europhysics
conference
abstracts

21st EPS Conference on Controlled Fusion and Plasma Physics

Montpellier, 27 June - 1 July 1994

Editors: E. Joffrin, P. Platz, P. E. Stott

Contributed Papers, Part II

ished by: The European Physical Society

es Editor: Prof. R. Pick, Paris

aging Editor: G. Thomas, Genève

Volume 18B
Part II

Max-Planck-Institut für Plasmaphysik
- 6. DEZ. 1994
Bibliothek

europhysics
conference
abstracts

21st EPS Conference on Controlled Fusion and Plasma Physics

Montpellier, 27 June - 1 July 1994

Editors: E. Joffrin, P. Platz, P. E. Stott

Contributed papers, Part II

Topics 4, 5, & 6

Published by : The European Physical Society
Series Editor : Prof. R. Pick, Paris
Managing Editor : G. Thomas, Genève

VOLUME
18B
Part II

94-0920

EUROPHYSICS CONFERENCE ABSTRACTS is published by the European Physical Society, © 1994.

Reproducing rights reserved.

This volume is published under copyright of the European Physical Society. We wish to inform the authors that the transfer of the copyright to the EPS should not prevent an author from publishing an article in a journal quoting the original first publication or to use the same abstract for another conference. This copyright is just to protect EPS against using the same material in similar publications.

The Proceedings may be purchased from "Association EURATOM-CEA sur la Fusion", Centre d'Etudes de Cadarache, 13108 Saint Paul lez Durance Cedex, FRANCE.

PREFACE

The 21st EPS Conference on Controlled Fusion and Plasma Physics was organized on behalf of the European Physical Society (EPS) by "Association EURATOM-CEA sur la Fusion". Following the guidelines of the EPS Plasma Physics Division, the 1994 Conference included topics from other areas of plasma physics in addition to fusion research (topics 9 to 14).

This year the Board of the EPS Plasma Physics Division agreed to an important change in the arrangements for contributed papers. The Proceedings were printed after the meeting allowing a later submission date for the abstracts and giving authors the opportunity to include latest results in the four-page papers. Because of this new arrangement, the authors of contributed papers were requested to hand in the four-page papers to the Conference Secretariat during the conference.

According to the EPS Plasma Physics Division regulations, the Conference Proceedings contain the four-page papers of all those contributions for which at least one author was registered at the Conference. There are 383 papers which satisfy this qualification. The three volumes of the Proceedings will be mailed to all registered participants of the Conference.

The papers of the 9 review lectures and 18 topical lectures will be published in a special issue of "Plasma Physics and Controlled Fusion", which will also be mailed to the participants.

Cadarache, July 1994 — The Editors

Acknowledgements:

The Conference Organizers acknowledge the financial support from:

- Commissariat à l'Energie Atomique.
- District de Montpellier.
- Commission of the European Communities.
- International Science Foundation.
- Ministère de la Défense.
- Ministère des Affaires Etrangères.
- Ministère de l'Enseignement Supérieur et de la Recherche.

PROGRAMME COMMITTEE:

P.E. Stott (JET, Abingdon, Chairman) ..... United Kingdom
F.C. Schüller (FOM Nieuwegein, Chairman Lisbon Conference) ..... Netherlands
F.W. Sluijter (Eindhoven, Chairman Plasma Physics Division EPS) Netherlands
P. Platz (Cadarache, Chairman of the Local Organizing Committee) ..... France
A. Bers (MIT Cambridge) ..... USA
J.A. Costa Cabral (IST, Lisbon) ..... Portugal
F. De Marco (ENEA Frascati) ..... Italy
V. Erckmann (MPI Garching) ..... Germany
V.E. Golant (Ioffe Institute, St Petersburg) ..... Russia
M. Haines (Imperial College, London) ..... United Kingdom
R. Koch (ERM - KMS, Brussels) ..... Belgium
A. Pochelon (CRPP, Lausanne) ..... Switzerland
S. Torven (RIT, Stockholm) ..... Sweden

LOCAL ORGANIZING COMMITTEE:

P. Platz (Chairman) ... Association EURATOM-CEA sur la Fusion, Cadarache
E. Joffrin (Scien Sec). Association EURATOM-CEA sur la Fusion, Cadarache
M. Capitain ..... Association EURATOM-CEA sur la Fusion, Cadarache
M. Giraud ..... Université Aix-Marseille I
B. Pégourié ..... Association EURATOM-CEA sur la Fusion, Cadarache
V. Poli ..... Association EURATOM-CEA sur la Fusion, Cadarache

CONTENTS

INDEX OF PAPERS VI

PART I
Topic 1: Tokamaks 1
Topic 2: Stellarators 359
Topic 3: Alternative Magnetic Confinement Schemes ..441

PART II
Topic 4: Magnetic Confinement Theory and Modelling ..507
Topic 5: Plasma Edge Physics 693
Topic 6: Plasma Heating 931

PART III
Topic 7: Current Drive and Profile Control 1041
Topic 8: Diagnostics 1167
Topic 9: Basic Collisionless Plasma Physics 1373
Topic 10: High Intensity Laser Produced Plasmas and Inertial Confinement 1443
Topic 11: Space and Astrophysical Plasmas 1469
Topic 12: Partially Ionized Plasmas 1499
Topic 13: Elementary Processes in Plasmas 1509
Topic 14: Plasma Applications 1519
Post Deadlines 1541

INDEX OF AUTHORS XVII

Part II

- A theory for the propagation of changes to confinement — Page: 508

  Christiansen, J.P.

- The impact of sawtooth effects on the prospects for ignition — Page: 512

  Turner, M.F.

- Prospects for improved confinement in hot plasmas — Page: 516

  Tendler, M.

- Global thermal transport and indications from the Alcator C-Mod experiment — Page: 520

  Coppi, B.

- Modelling of ITER operation — Page: 524

  Boucher, D.

- Transport changes due to the magnetic field shear, stochastic magnetic field and electric field shear — Page: 528

  Itoh, S.I.

- Nonlinear magnetic reconnection in low collisionality plasmas — Page: 532

  Porcelli, F.

- Self-consistent equilibrium in a cylindrical, dissipative reverse field pinch — Page: 536

  Guo, S.C.

- The evolution of a slightly non-ideal, neutral plasma — Page: 540

  Edenstrasser, J. W.

- Stabilization of pressure-driven external modes in tokamaks with a resistive wall and toroidal rotation — Page: 544

  Ward, D.J.

- Ideal MHD stability in tokamaks with external windings — Page: 548

  Moeckli, R.

- Tearing stability in ITER shaped plasma — Page: 552

  Pletzer, A.

Part II

- MHD limits and axisymmetric stability of doublets — Page: 556
  Medvedev, S.
- Electromagnetic effects on electron fluid drift turbulence — Page: 560
  Scott, B.
- High resolution simulations of 2-D dissipative drift-wave turbulence — Page: 564
  Camargo, S.J.
- Neoclassical transport scalings for stellarators in the long-mean-free-path regime — Page: 568
  Maassberg, H.
- Stochastic diffusion in reverse field pinch — Page: 572
  Paccagnella, R.
- Non-linear theory of magnetic line diffusion in a stochastic layer — Page: 576
  Misguich, J.
- Radially extended 2D toroidal mode structures and velocity shear effects — Page: 580
  Wilson, H.R.
- A wireframe model for toroidal magnetic field - plasma systems — Page: 584
  Montvai, A.
- Hamiltonian structure and stability of low-frequency nonlinear plasma dynamics — Page: 588
  Pegoraro, F.
- Drift-Alfvén vortices in a magnetized plasma — Page: 592
  Kuvshinov, B. N.
- Radiative-condensation instability in Be-seeded plasmas in tokamaks — Page: 596
  Abramov, V. A.
- Transport barrier formation due to turbulent spin-up of edge tokamak plasma during L-H transition — Page: 600
  Ossipenko, Marina V.

Part II

- Macroscopic modelling by lattice Boltzmann techniques — Page: 604

  Vahala, G.

- Effects of sheared poloidal rotations on neoclassical resistivity-gradient-driven turbulence transport — Page: 608

  Peng, X.

- Excitation of global Alfvén eigenmodes by RF heating in JET — Page: 612

  Kerner, W.

- Non-ideal effects on toroidal Alfvén Eigenmode stability — Page: 616

  Dendy, R.O.

- fast particle losses due to toroidal Alfvén modes in JET — Page: 620

  Hender, T. C.

- Nonlinear mode conversion of Toroidal Alfvén Eigenmodes — Page: 624

  Zonca, F.

- Linear stability analysis and nonlinear hybrid simulation of TAE mode — Page: 628

  Fu, G.Y.

- Test of theory of the L-H transition in ASDEX-Upgrade discharges — Page: 632

  De Blank, H. J.

- Neoclassical alpha-particle losses in tokamaks allowing for large orbit widths — Page: 636

  Cox, M.

- Possibility of using ion-Bernstein waves for alpha power extraction in tokamaks — Page: 640

  Fisch, N.J.

- Modelling of sawtooth induced redistribution of ICRF-heated minority ions — Page: 644

  Ödblom, A.

- Topology and slowing down of high energy ion orbits — Page: 648

  Porcelli, F.

Part II

- A mechanism for beam-driven excitation of ion cyclotron harmonic waves in TFTR — Page: 652
  Dendy, R.O.
- Current driven non-Maxwellian plasmas — Page: 656
  Haines, M. G.
- Direct emission in the ion cyclotron range of frequency — Page: 660
  Fraboulet, D.
- Radial current across the separatrix due to direct ion orbit loss of a fast ion population — Page: 664
  Kurki-Suonio, T.K.
- Parametric dependencies of JET electron temperature profiles — Page: 668
  Schunke, B.
- Boundary point collocation method to solve toroidal plasma flow of arbitrary aspect ratio and arbitrary cross section — Page: 672
  Cap, F. F.
- Influence of detailed neutral particle modelling on currents and cross-field drifts in a poloidally biassed divertor plasma — Page: 676
  Baelmans, M.
- Comparison of experimental MARFE observations in ASDEX-Upgrade with B2 calculations — Page: 680
  Junker, W.
- Simulations of reactivity transients in tokamak fusion reactors — Page: 684
  Mantsinen, M.J.
- Vertical instability dynamic analysis — Page: 688
  Brémond, S.
- A numerical study of plasma detachement conditions in JET divertor plasmas — Page: 694
  Simonini, R.
- Detached divertor plasmas in JET — Page: 698
  Horton, L.D.

Part II

- Divertor studies for optimized Helias configurations — Page: 702

  Strumberger, E.

- Divertor options for ITER and ASDEX-Upgrade : results of modeling — Page: 706

  Neuhauser, J.

- Bright spots on the divertor plates of ASDEX-Upgrade during stationay phases — Page: 710

  Büchl, K.

- Momentum removal from subsonic and supersonic plasma flows in the ITER divertor — Page: 714

  Igitkhanov, Yu. L.

- Erosion at the divertor tiles of ASDEX- Upgrade — Page: 718

  Garcia-Rosales, C.

- Spectroscopic investigation of molecular impurities in the ASDEX-Upgrade divertor — Page: 722

  Lieder, G.

- Bistable behaviour of the ASDEX-Upgrade divertor near the transition to the X-point Marfe — Page: 726

  Laux, M.

- Study of high-Z target plate materials in the divertor of ASDEX-Upgrade — Page: 730

  Radtke, R.

- Structure of the temperature and density fields in the boundary layer during ergodic divertor operation on Tore Supra — Page: 734

  De Michelis, C.

- Screening and radiating properties of Tore Supra ergodic divertor during impurity injection experiments — Page: 738

  Monier-Garbet, P.

- Numerical modeling of plasma flow target interaction for prediction of divertor behaviour under ITER typical disruption conditions — Page: 742

  Würz, H.

- The control of convection by fuelling and pumping in the JET pumped divertor — Page: 746

  Harbour, P.J.

Part II

- Experimental investigation of the power deposition on the the ergodic divertor target plates in Tore Supra — Page: 750
  Guilhem, D.
- Avtive density control with ergodic divertor on Tore Supra — Page: 754
  Loarer, T.
- New results obtained by finite element modelling of the plasma edge — Page: 758
  Pütz, Th.
- Probe measurements on drift patterns in RFP edge plasmas — Page: 762
  Bergsaker, H.
- The impact of kinetic effects on the ITER divertor plasma — Page: 766
  Igitkhanov, Yu. L.
- Revised formula for chemical sputtering of carbon — Page: 770
  Garcia-Rosales, C.
- The impact of chemical erosion on the global impurity balance in the ASDEX-Upgrade tokamak — Page: 774
  Kallenbach, A.
- Evolution of radiating vapour shield at divertor plates during disruption — Page: 778
  Lengyel, L. L.
- Time resolved measurements of hydrogen inventory in graphite under plasma exposure — Page: 782
  Langhoff, M.
- Radiation phenomena and particle fluxes in the X-event in JET — Page: 786
  Jäckel, H.-J.
- Radiative plasmas with ergodic divertor and additional power in Tore Supra — Page: 790
  Vallet, J.-C.
- Radiative thermal instability of the tokamak edge region — Page: 794
  Bachmann, P.

Part II

- Enhanced edge radiation induced by electrode biasing on TEXTOR — Page: 798
  Van Nieuwenhove, R.
- Radiation losses in FTU — Page: 802
  Apruzzese, G.
- Effective charge of the plasma resulting from the injection of neon into deuterium discharges on TEXTOR — Page: 806
  Telesca, G.
- Measurement of carbon sources on the limiter face in Tore Supra — Page: 810
  Monier-Garbet, P.
- Spectroscopic study of marfe-like ergodic edge plasmas on Tore Supra — Page: 814
  Hess, W.R.
- Siliconization of FTU — Page: 818
  Apicella, M.L.
- Self-consistent impurity modeling with edge/core plasma coupling — Page: 822
  Zanino, R.
- Impurity line emission due to thermal charge exchange in JET edge plasmas — Page: 826
  Maggi, C.F.
- Experimental study of vapor shield formation and divertor material erosion for ITER typical plasma disruptions — Page: 830
  Würz; H.
- Experimental measurements and modeling of impurity transport in the divertor and boundary plasma of DIII-D — Page: 834
  West, W. P.
- ICRF power modulation experiments on ASDEX-Upgrade — Page: 838
  Hoffmann, C.
- Changes in the edge plasma due to ELMs, a study using coupling measurements in the ICRF range — Page: 842
  Noterdaeme, J.-M.

Part II

- B2-EIRENE modelling of ELMs on ASDEX-Upgrade — Page: 846
  Coster, D.P.
- Investigation of the dynamics of the L-H transition in ASDEX-Upgrade — Page: 850
  Zohm, H.
- A study of edge fluctuations in L- and H-mode by phase contrast imaging on DIII-D — Page: 854
  Coda, S.
- The parametric dependence of the spatial structure of the radial electric field at the plasma edge in the DIII-D tokamak — Page: 858
  Gohil, P.
- Edge turbulence and transport studies with ergodic divertor on Tore Supra ohmic discharges — Page: 862
  Devynck, P.
- Edge plasma measurements on Extrap T1 reversed field pinch with Langmuir probe array — Page: 866
  Li, G.X.
- Influence of local neutral concentration on edge turbulence in the TJ-1 tokamak — Page: 870
  Pedrosa, M. A.
- Turbulent fluctuations in the scrape-off layer of the ASDEX tokamak and the W7-AS stellarator — Page: 874
  Niedermeyer, H.
- Stochastic ion trajectories in a potential landscape — Page: 878
  Krlin, L.
- The SOL width and the MHD interchange instability in tokamaks — Page: 882
  Pogutse, O.
- Comparison of T-10 edge turbulence with the drift resistive ballooning turbulence computer modelling — Page: 886
  Vershkov, V.A.
- Transport of high energy electrons in edge stochastic magnetic layer of tokamaks — Page: 890
  Takamura, S.

Part II

- Edge biasing and electron heating by Fermi acceleration in RF fields — Page: 894

  Myra, J. R.

- Experimental measurements of ICRF and edge plasma interactions on Tore Supra — Page: 898

  Harris, J.H.

- On the effect of a radial electric field on the edge of a takomak plasma — Page: 902

  Nocentini, A.

- Interpreting fluid models of tokamak edge plasmas — Page: 906

  Maddison, G.

- Validation of fluid modelling of edge plasmas on Compass-D — Page: 910

  Maddison, G.

- Shutdown of a burning plasma and examination of edge DT depletion — Page: 914

  Pacher, H. D.

- Plasma edge spectral profiles for discharges with high and low MHD activity in TBR-1 tokamak — Page: 918

  Caldas, I.L.

- Control of secondary electron emission from end plates of the Gamma 10 tandem mirror — Page: 922

  Saito, T.

- Space charge sheaths with electron emission — Page: 926

  Hantzsche, E.

- Fast access to neutral injection heating profiles applied for the stellarator W7-AS — Page: 932

  Penningsfeld, F.-P.

- Neutral beam heating in ASDEX-Upgrade — Page: 936

  Vollmer, O.

- Development of negative-ion-based NBI injector for large helical device — Page: 940

  Ando, A.

Part II

- The new JET phased ICRH array. First experiments and modelling — Page: 944

  Bures, M.

- Spatial distribution of gamma emissivity and fast ions during (3He)D ICRF heating experiments on JET — Page: 948

  Righi, E.

- An analysis of JET fast-wave heating and current drive experiments directly related to ITER — Page: 952

  Bhatnagar, V. P.

- Ion energy balance during fast wave heating in Tore Supra — Page: 956

  Hutter, T.

- Fast evaluation of the quasilinear ion distribution function during ion cyclotron heating — Page: 960

  Brambilla, M.

- Study of the third harmonic ICR heating of the beam heated deuterium plasma of TEXTOR — Page: 964

  Van Wassenhove, G.

- Ponderomotive effects on the coupling of ion Bernstein waves to tokamak plasma — Page: 968

  Cesario, R.

- Quasilinear analysis of the IBW electron absorption — Page: 972

  Cardinali, A.

- Observation of plasma expulsion from a powered screenless ICRF antenna — Page: 976

  Van Nieuwenhove, R.

- A study of antenna coupling during ICRF plasma build-up — Page: 980

  Moiseenko, V.E.

- ICRF antenna coupling and fast alpha heating models for fusion plasmas — Page: 984

  Scharer, J.E.

- Recent results from the TFTR ICRF DT program — Page: 988

  Rogers, J. H.

Part II

- ICRF experiments in the Alcator C-mod tokamak — Page: 992

  Golovato, S.N.

- Radial banana-transitional transport of alpha particles driven by ICRH in a tokamak fusion reactor — Page: 996

  Chang, C.S.

- ICRF heating in CHS — Page: 1000

  Kumazawa, R.

- Measurement of the optical depth at the third electron cyclotron harmonic in Tore Supra — Page: 1004

  Segui, J.-L.

- High density operation with 140 GHz ECRH : experiments at the W7-AS stellarator, prospects for the W7-X stellarator — Page: 1008

  Erckmann, V.

- Electron cyclotron heating & current drive in ITER — Page: 1012

  Lloyd, B.

- Experimental investigation of ECRH assisted low voltage ohmic start-up in HL-1 — Page: 1016

  Yao, L.H.

- Influence of different heating schemes on high-Z contamination from a tungsten test limiter in TEXTOR — Page: 1020

  Van Oost, G.

- Physics issues and design aspects of ITER ion and electron cyclotron systems — Page: 1024

  Nagashima T.

- Effective lower hybrid heating of electrons and ions in the FT-2 tokamak — Page: 1028

  Budnikov, V. N.

- Electron cyclotron heating & current drive in the presence of a lower hybrid wave;a finite element solution of the QRFPE — Page: 1032

  Tribeche, M.

- Parasitic absorption at the Alfvén resonance in scrape-off layers — Page: 1036

  Faulconer, D.W.

Topic 4

Magnetic Confinement

Theory and Modelling

A THEORY FOR THE PROPAGATION OF CHANGES TO CONFINEMENT

J.P. Christiansen
JET Joint Undertaking, Abingdon, Oxfordshire OX14 3EA, U.K

1. INTRODUCTION

A heat pulse triggered by a sawtooth near $q_\psi = 1$ surface propagates on a msec. timescale towards the edge in TFTR [1, 4] and JET [2, 3]. A cold pulse triggered by impurity injection propagates towards the $q_\psi = 1$ surface on a msec. timescale towards the $q_\psi = 1$ surface in TFTR [5]. The transitions from L to H and H to L-mode confinement propagate inwards on a msec. timescale in JET [6]. If a diffusive process is invoked to explain these phenomena then it requires a heat diffusivity χ which initially, in the ballistic phase [4], is one order of magnitude larger than the steady state value inferred from a power balance calculation. In the case of the rapid L to H transition [6] this implies that the relative change $\Delta\chi / \chi$ initially is of order + 10 and then has to relax towards $-\frac{1}{2}$.

The omnipresence of "some global mode" could be invoked to explain these rapid changes; such "a global mode" would switch on-off during the L to H transitions; however, heat pulses produced by sawteeth propagate at similar speeds in ohmic, L-mode and H-mode plasmas. At present no conventional theory can explain the rapid changes to confinement; conventional theory means in this context a theory which assumes that the rapid changes occur via diffusive processes. A recent study on TFTR [4] concludes that the inital phases of the heat pulse propagation is non-diffusive.

A physics model is being developed in an attempt to describe rapid changes to confinement. The work is divided into three parts: i) the derivation of a fluid model based on kinetic drifts; ii) a study of the linearized response from these drift-kinetic fluid equations to a perturbation; iii) the evaluation of the characteristic propagation speed of a finite amplitude perturbation through a toroidally confined plasma with varying shear and collisionality. This paper will summarise Part I and outline a simplified approach to Part III. The initial simplification made is to employ a spectral representation of a temperature perturbation $\tilde{T}$; i.e. $\tilde{T}$ varies as $e^{i\underline{k}\cdot\underline{r}}$, and then to apply standard approximations of weak turbulence theory. Work in progress replaces the spectral representation by a statistics based description.

2. FLUID EQUATIONS FOR TEMPERATURE ANISOTROPY BASED ON KINETIC DRIFTS

The Boltzmann equation is used to derive equations for velocity moments M of the distribution function f ($\underline{v}$) for plasma particles of mass m, velocity $\underline{v}$, and charge Ze in a magnetic field $\underline{B}$ and electric field $\underline{E}$. Four moment equations are derived with M = 1, $m\underline{v}$, $m\underline{vv}$, $m\underline{vvv}$ for respectively density n, momentum $m\underline{u}$, pressure tensor $\underline{P}$ and heat flow tensor $\underline{Q}$. The fifth moment enters the equation for $\underline{Q}$ and formal closure of the four equations is obtained by reducing the moment $m\underline{vvvv}$ into products $(m\underline{vv})$ $(\underline{vv})$ of dyadics. The four moment equations include on the RHS terms describing collisions between ions and electrons (ei) and between ions, electrons and an external source. The former leads via the collision operator C_{ei} to respectively for the four moments; 0, $\underline{R}^c$, $\underline{P}^c$, $\underline{Q}^c$. The external source leads to respectively: a source rate S, directional momentum $Sm\underline{U}$, power transfer $S\underline{\underline{\mathcal{E}}}$, collisional heat flow tensor $\underline{\underline{\Theta}}$. The external source can represent: i) low energy Frank-Condon neutral atoms undergoing charge-exchange in the edge, ii) neutrals being ionized, iii) neutral beam injection, iv) ICRF accelerated minority ions residing in the plasma. For any such source a separate calculation of S, $\underline{U}$, $\underline{\underline{\mathcal{E}}}$, $\underline{\underline{\Theta}}$ must be made. This is done in computer codes like TRANSP.

The derived equations for the anisotropic temperatures $T_\parallel$ and $T_\perp$ and density n are

$$\partial_t n + \underline{u}_F\cdot\nabla n + n\left(\frac{\underline{u}_\kappa}{T_\parallel}\cdot\nabla T_\parallel + \left(\frac{\underline{u}_B}{T_\perp} - \frac{\underline{u}_\kappa}{T_\parallel}\right)\cdot\nabla T_\perp\right) + n\left(1-\frac{T_\perp}{T_\parallel}\right)\Omega_\parallel + \Omega_E = C \quad (1)$$

$$\partial_t \frac{1}{2}T_\parallel + \left(\underline{u}_F + \underline{u}^{(\parallel)}\right)\cdot\nabla\frac{1}{2}T_\parallel + T_\parallel\underline{u}_\kappa\cdot\frac{\nabla n}{n} + (T_\parallel - T_\perp)\,\Omega_\parallel + T_\parallel\omega = \frac{1}{2}C_\parallel \quad (2)$$

$$\partial_t T_\perp + \left(\underline{u}_F + \underline{u}^{(\perp)}\right)\cdot\nabla T_\perp + T_\perp\left(\underline{u}_B - \frac{T_\perp}{T_\parallel}\underline{u}_\kappa\right)\cdot\frac{\nabla n}{n} + T_\perp(\Omega_\parallel + \Omega_E + \omega) = C_\perp. \quad (3)$$

The advective fluid velocities, $\underline{u}_F$, $\underline{u}^{(\parallel)}$, $\underline{u}^{(\perp)}$ contain $\underline{E}\times\underline{B}$ drift, curvature drift $\underline{u}_\kappa$, ∇B drift $\underline{u}_B$, but not diamagnetic and collisional drifts The inverse time scales $\Omega_\parallel$, Ω_E, ω in (1 - 3) do not contain ∇n, $\nabla T_\parallel$, $\nabla T_\perp$ and the RHS terms denote the collisional effects. Eqs. (1 - 3) are coupled non-linear hyperbolic equations and they show that diamagnetic drifts do not transport plasma or energy. In this drift kinetic formulation magnetic curvature $\underline{\kappa}$, $\nabla\times\hat{b}$ and ∇B can maintain anisotropy.

3. SIMPLIFIED TURBULENT TRANSPORT

In a toroidal configuration the stochastic nature of drift motion continuously generates fluctuations $\tilde{T}_\perp$, $\tilde{T}_\parallel$, $\tilde{n}$ on each magnetic surface. The advection of $\tilde{n}$ etc. and collisions will attempt to isothermalize $(\partial_t \tilde{n} \to o)$ each surface as described by Eqs. (1 - 3). The isothermalization rates $\partial_t \tilde{T}_\parallel$ etc. arise from drifts in three directions labelled β (along $\hat{b}$) μ (diamagnetic direction) and x (normal to a surface); the rate in the parallel directions is faster than in the other directions. $\partial_t \tilde{T}_\parallel$ therefore depends strongly on the mode rationality numbers ($q_\psi = m/n$) of a surface. In a tokamak these numbers have a rapid x variation. In the (x, μ) plane a disturbance $\tilde{T}_j$ induced on a field line j will propagate faster in the μ direction (via parallel flows and $\perp$ drifts) than in the x direction (via $\perp$ drifts). The displacement of a field line μ_2 after one toroidal turn is

$$\mu_2 \approx \frac{1}{m} \int_o^{2\pi} \frac{d\ell}{b\varphi} \tag{4}$$

while the maximum displacement of a particle from a magnetic surface $\Delta x \sim \varepsilon \rho_\theta$ (Larmor radius in poloidal field). Since μ_2 (x) differs strongly from μ_2 (x + Δx) the flow pattern associated with the disturbance $\tilde{T}_j$ at x becomes decorrelated from that at x + Δx after one toroidal transit time. The linear contributions to $\partial_t \tilde{T}$, $\underline{u}_F \cdot \nabla \tilde{T} + \tilde{\underline{u}}_F \cdot \nabla T$, will average out quickly and transport in the model presented will arise from the non-linear term $\tilde{\underline{u}}_F \cdot \nabla \tilde{T}$. An assessment of the random spatial displacements $\underline{\Delta}$ of energy (or $\tilde{T}$) are described by the evolution of the velocity correlation tensor

$$\underline{\underline{C}} = \left\langle \tilde{\underline{u}}_F(t)\ \tilde{\underline{u}}_F(t+\tau) \right\rangle = \underline{\alpha}\underline{\alpha} \left\langle \tilde{T}(t)\ \tilde{T}(t+\tau) \right\rangle \tag{5}$$

where $\underline{\alpha}$ contains the magnetic curvature $\underline{\kappa}$ and ∇B vectors. The non-linear solution for the temperature correlation function C_T is obtained from Eqs. (1 - 3) with the following simplifications: $\tilde{n} = o$, $\tilde{T}_\perp = \tilde{T}_\parallel = \tilde{T}$, $C = C_\parallel = C_\perp = \Omega_\parallel = \Omega_E = \omega = o$, and it involves calculating the evolution of harmonics in an assumed spectral representation

$$\tilde{T} = \sum_k \tilde{T}_k e^{i\underline{k}\cdot\underline{r}}, \quad \tilde{T}_k(t+\tau) = \tilde{T}_k(t)\, e^{P_k}, \quad P_k = i\underline{\alpha}\cdot\underline{k} \int_t^{t+\tau} \tilde{T}(t')dt' \tag{6}$$

The propagator P_k describes the probability that the entire history $\tilde{T}(t) \to \tilde{T}(t+\tau)$ takes place. From stochastic theory the expectation value of P_k is the following variance

$$E\{P_k\} = \left[(i\underline{\alpha}\cdot\underline{k})^2\ 2Q_T\right]^{1/2},\ Q_T = \frac{1}{2}\int_o^\tau \int_o^\tau C_T\ dt_1\ dt_2.$$

The resulting equation for Q_T has the first integral

$$\frac{1}{2}\left(\frac{dQ_T}{d\tau}\right)^2 = \iiint S_k \left(1 - e^{-(\underline{\alpha}\cdot\underline{k})^2 Q_T}\right) \frac{d\underline{k}}{\underline{\alpha}\cdot\underline{k}} \qquad (7)$$

where $S_k = \left\langle \tilde{T}_k{}^2(t_o) \right\rangle$ represents a stationary fluctuation spectrum. The immediate response to a disturbance (small τ) shows advective or wavelike transport with a propagation speed obtained from expanding (7) $2\left(\frac{d}{dt}\langle\Delta\Delta\rangle^{1/2}\right)^2 = \underline{\alpha}\underline{\alpha}\iiint S_k\ d\underline{k}$ or $\underline{v}_{prop} = \underline{\alpha}\langle S_k\rangle^{1/2} = \underline{u}_F\left\langle \tilde{T}_k^2 / T^2 \right\rangle^{1/2}$. This means that the disturbance in this simplified model propagates with the fluid drift velocity (appropriately scaled) independent of the nature or origin of the fluctuations. In a more complex model the propagation speed derived from Eqs. (1-3) will depend on $\left\langle \tilde{n}_k^2 / n^2 \right\rangle, \left\langle \tilde{T}_{\perp k}^2 / T_\perp^2 \right\rangle, \left\langle \tilde{T}_{\parallel k}^2 / T_\parallel^2 \right\rangle$. Experimental observations show fluctuation levels to be largest at the edge while the drift velocities themselves are largest at the centre.

4. SUMMARY

A drift kinetic fluid model has been developed. It shows that diamagnetic drifts do not contibute to transport of plasma and energy (no entropy generation). Application of the model to a simplified description of plasma turbulence shows that disturbances, such as heat-cold pulses, L to H transitions, all can propagate with the fluid advective drift velocity irrespective of the nature of these disturbances.

REFERENCES

[1] E.D. Frederickson, J.D. Callen, K. McGuire et al., Nucl. Fusion, 26, 849 (1986).
[2] B.J.D. Tubbing, et al. Nucl. Fusion, 27, 1843 (1987).
[3] A. Griguoli, A.C.C. Sips, Application of Dynamic Response to Analysis to JET Heat Pulse Data, JET Report, JET-R(93)04).
[4] E.D. Frederickson, A.C. Janos, K.M. McGuire, S.D. Scott, G. Taylor, Nucl. Fusion 33, 1759 (1993).
[5] M.W. Kissick, E.D. Frederickson, J.D. Callen, Nucl. Fusion 34, 349 (1994).
[6] S.V. Neudatchin, D.G. Muir, J.G. Cordey, The Time Behaviour of the L-H and H-L Transitions in JET, JET preprint JET-P(93)58, to appear in Nucl. Fusion.4

The Impact of Sawtooth Effects on the Prospects for Ignition

M F Turner and J W Connor
UKAEA Government Division, Fusion, Culham, Abingdon, Oxon, OX14 3DB, UK
(UKAEA/Euratom Fusion Association)

1 Introduction

In order to assess the limits on plasma current or the need for sawtooth avoidance or control activities in a fusion ignition device, it is important to understand the impact of sawteeth on the ignition margin. In the absence of a fully convincing theoretical model for predicting the energy confinement capability of proposed ignition devices such as ITER much reliance is placed on empirical scaling laws. These empirical scaling laws are derived from a database which is limited to safety factor values $q_\psi \geq 3.1$ so that sawteeth effects are not excessive. Operating at higher current could exploit the beneficial trends suggested by the scaling laws. It is important to assess whether the increased sawteeth effects that can be expected in association with the higher current, would degrade τ_E sufficiently to offset the promised gain. The work described here studies the effect which the presence of sawteeth may have on the location of the ignition boundary in $n-T$ space. Clearly the seriousness of the effect will be dependent upon the nature of the sawtooth characteristics; in particular the period of the sawtooth (τ_{saw}) will be important. In the absence of a full understanding of how the sawtooth period may be accurately predicted, a range of values has been studied. Other sawtooth properties which have been explored are different positions of the mixing radius (r_m) with respect to the $q = 1$ surface and the possibility that energetic α-particles may be ejected from the plasma centre during the sawtooth crash period. The investigations have been carried out using the TRINEX time-dependent transport code.

2 The Simulation Model

The $1\frac{1}{2}$D TRINEX code computes a self consistent evolution of toroidal and poloidal magnetic fields and plasma equilibrium. Shape is determined using an expansion in inverse aspect ratio, ellipticity and triangularity as a function of evolving pressure and q profiles. Neo-classical resistivity and bootstrap current are included. The electron density profile is fixed and determined from the initial main ion density profile, which is given by $[n_i = n_{ei}(0.1 + 0.9(1 - (r/a)^2)^{\gamma_n})]$, plus the effect of impurities. Ion density dilution due to Helium ash and other impurities is included. The α-particle heating model takes account of finite α-particle orbits and slowing down time. Since the objective is to provide a generic set of results, this assessment of sawtooth effects is carried out against a background of otherwise stationary plasma confinement properties: ie. a simple background energy transport model is used, ($n_e\chi_e = \kappa$ and $\chi_i = \chi_e = 0.4m^{-1}s^{-1}$); no radiation other than Bremsstrahlung is considered and the Helium ash fraction is fixed at a predetermined level (5%).

3 Sawtooth Model

The TRINEX code models the effect of the sawtooth instability by enhancing the thermal diffusivity χ, within a mixing radius r_m, to a large value χ_{saw} for a short interval τ_c to produce each sawtooth crash. r_m is linked in a fixed ratio to the computed position of the $q = 1$ surface. The sawtooth period τ_{saw} is fixed but the crash is only triggered if q_0 is less

than a prescribed critical value q_c (set at 0.8 for this study). Pre-determined values of τ_c, τ_{saw} and q_c are fixed for each simulation run. Also introduced during the interval τ_c is an anomalous resistivity η_a of sufficient magnitude to return q_0 to q_c. There is an option to allow the sawtooth crash to result in the prompt loss to the wall of 50% of α-particles. The enhanced sawtooth transport is given the radial profile:- $\chi_{saw} = \chi_1 \left(1 - \frac{r^2}{r_m^2}\right)$ where χ_1 is taken to be a large multiple of χ_0.

The temperature profile is assumed to be flattened within the mixing radius at the time of the sawtooth crash; this places a lower bound on χ_1. It must be sufficiently large to produce a thorough mixing of the plasma within the mixing radius (r_m) during the crash time (τ_c), ie. $\chi_1 > r_m^2/\tau_c$. In trials with the TRINEX code it has been found that $\chi_1 = r_m^2/\tau_c$ represents an approximate lower bound and the results are then largely independent of the choice of sawtooth crash time τ_c.

4 Chosen Parameters

The geometry of the proposed EDA version of ITER was chosen, ie: Plasma Current (I_P) = $25MA$; Major Radius (R_m)= 7.75m; Minor Radius (a) = 2.8m and Toroidal Field on axis ($B_{\phi 0}$) = 6T. Impurity levels were set at 1.0% Carbon and 0.05% Nickel, giving a $Z_{eff} \sim 1.7$, including the effect of 5% He. The investigations were carried out over a range of sawtooth periods (τ_{saw}), with and without ejection of energetic α-particles at the time of the sawtooth crash. The effect of varying the ratio $r_m/r_{q=1}$ was explored by the choice of two values: $r_m/r_{q=1}$ =1.0 and $r_m/r_{q=1}$ = 1.4.

5 Ignition Criterion

In each TRINEX simulation run, the plasma was initialised in some nominal low energy state and then provided with additional heating at an appropriate level until the rate of increase of plasma energy exceeded the total input power (ohmic + auxiliary); this was taken to be the ignition point. In order to ascertain the exact values of plasma parameters at the ignition point a stationary marginally ignited state needs to be generated. This was achieved by suitable adjustment of a small amount of supplementary heating. Plasma conditions at the second (high temperature) marginally ignited state were also investigated. This second point is stable and was simulated by removing the burn control and allowing the plasma to heat up until a steady state was reached. It was only possible to explore this state at low density due to the limitations on β for the TRINEX code. Plasma parameters recorded at the ignition points were: the volume averaged temperature, $< T >$ (which, except in the case of very severe sawtooth conditions at the high temperature ignited states, remained steady - not responding to the sawtooth oscillation); the time averaged α-particle heating, $\overline{P_\alpha}$; the global energy confinement time, τ_E.

6 Results

Fig.1(a-d) presents contour plots of the ignition boundaries in the $< T_i >$-$< n_e >$ plane for different values of τ_{E0}/τ_{saw} (where τ_{E0} = global energy confinement time without sawteeth. Each of the 4 plots depicts various combinations of the $r_m/r_{q=1}$ ratio and ejection or not of α-particles at the sawtooth crash. The low density parts of these contours are shown dotted to indicate that specific results were not obtained in that region. The high temperature results should also be treated with some caution, being obtained at the limits of operation of the TRINEX code. In the least severe case (r_m = $r_{q=1}$ with no α-particle ejection), which is depicted in Fig.1(a), the presence of sawteeth having $\tau_{saw} \approx \tau_E$ requires an increase in $< T_i >$ of between 5% and 25%, depending on

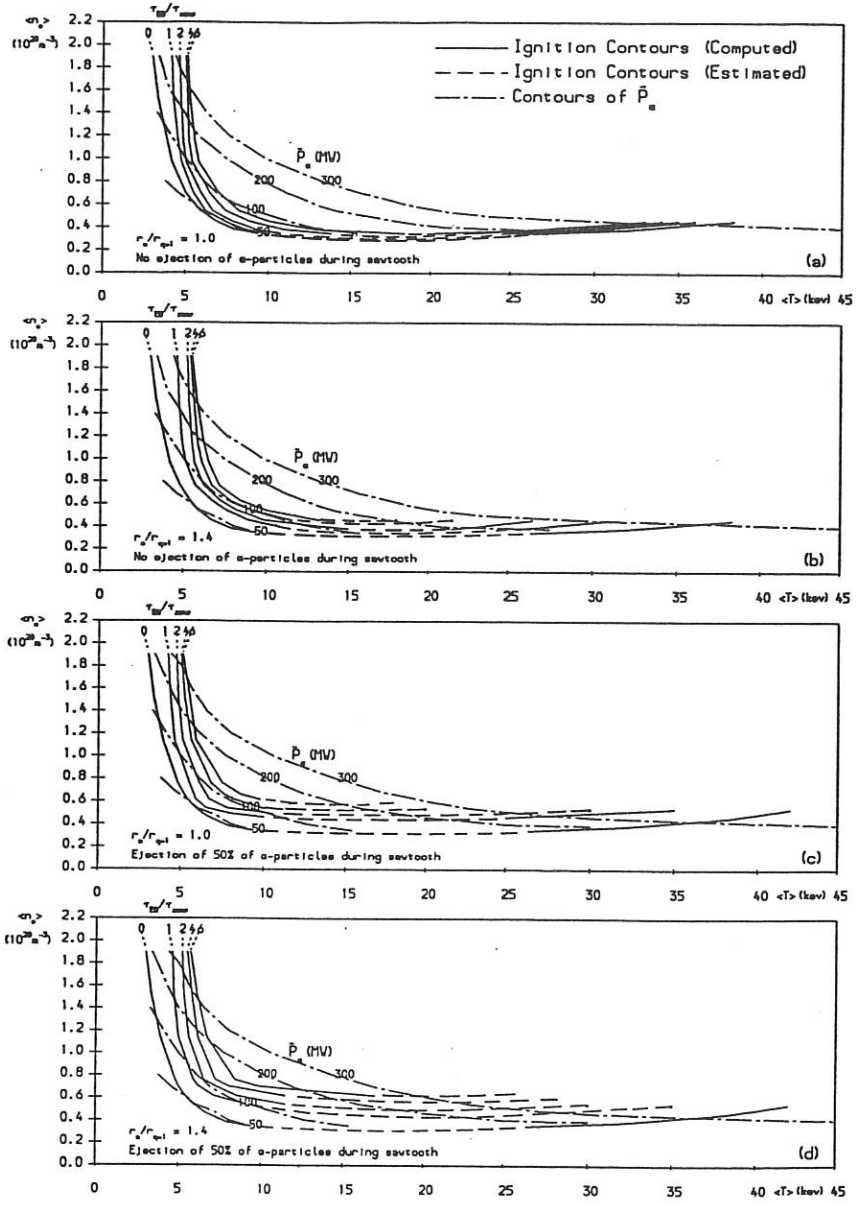


Fig 1. Sawtooth Effects on Ignition Boundaries

density. The minimum density required for ignition is $< n_e > \approx 0.32\ 10^{20} m^{-3}$ which is not significantly affected by the presence of sawteeth. In the most severe case ($r_m = 1.4 r_{q=1}$ with 50% α-particle ejection at the sawtooth crash) which is depicted in Fig.1(d), the presence of sawteeth having $\tau_{saw} \approx \tau_E$ causes the minimum density required for ignition to increase to $< n_e > \approx 0.46\ 10^{20} m^{-3}$. The ejection of α-particles is mostly responsible for this rise

which is due to the long slowing down time (τ_s) of the α-particles at the lower density ($\approx 1.5s$ at $< n_e >= 0.5\ 10^{20} m^{-3}$); in this case the α- power production has insufficient time to recover before the onset of the next sawtooth crash. At higher densities, the shorter slowing down time causes the ejection of α-particles to have little significant effect. The plots also show contours of mean α-power production ($\overline{P}_\alpha$). These contours indicate that the presence of sawteeth may require a significant increase in the P_α required to reach the marginally ignited state. Fig.2 shows plots of the confinement time degradation against τ_{E0}/τ_{saw}, for the two cases of most severe and least severe sawtoothing conditions, at various densities.

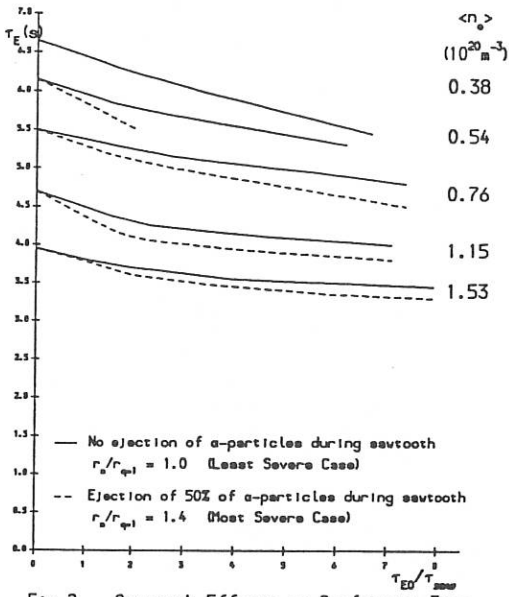


Fig 2. Sawtooth Effects on Confinment Time

7 Conclusions

The extent to which the presence of sawteeth may affect the location of the ignition boundary in $< n > - < T >$ space has been investigated. The result is seen to depend on sawtooth period, plasma density and the prescription for the position of the mixing radius with respect to the position of the $q = 1$ surface. A significant effect is observed under the conditions of $\tau_{saw} = \tau_E$ and $r_m = r_{q=1}$ which may be a plausible scenario. The ejection of high energy particles at the time of the sawtooth crash is seen to be of importance only if τ_{saw} approaches the slowing down time of the α-particles. A further consequence of the sawteeth is that higher P_α is required to achieve ignition. In practice this may lead to a further degradation of τ_E and the requirement for a higher current, or even a larger machine, to provide a compensating improvement in background transport. Higher densities need to be explored in order to completely map out both the unstable and stable branches of the ignition curve. Different currents and the extent to which the results are dependent upon background transport and the treatment of the Helium ash need to be investigated.

Acknowledgement:

This work is funded jointly by the UK department of Trade and Industry and Euratom.

Prospects for improved confinement in hot plasmas.

V.Rozhansky * & M.Tendler

Alfven Lab., Royal Institute of Technology, Stockholm, 10044, Sweden

A hot edge in the banana regime is addressed. It is demonstrated that a radial electric field differs from the neoclassical value in a hot plasma due to the strongly reduced neoclassical parallel viscosity. The focus is on the anomalous transport of the toroidal momentum. Equations for determining the poloidal flow and radial electric field profiles self - consistently in the banana regime are given. It is shown that for $\nu^* << 1$, the electric field profile varies significantly within the scale $L_n = (d\ln n/dr)^{-1}$ at the edge.Therefore, the resulting profile may obtain a large shear, which is beneficial for improved confinement, provided a steep density gradient emerges at the edge.

I. Introduction.

Recently, novel regimes with improved confinement (VH regime, High - β_p H - mode etc.) have been demonstrated on DIII - D, JET and JT - 60 . The transport barrier region, where confinement is significantly improved, broadens significantly as compared to the reference H - regime. Although a complete, quantitative theory of the regimes with improved confinement does not yet exist, combined theoretical and experimental work has merged into a paradigm that a highly sheared $\mathbf{E} \times \mathbf{B}$ flow in the plasma edge can lead to better confinement through decorrelation of the fluctuations, decreased radial correlation lengths, and reduced turbulent transport [1]. Yet, the fundamental question remains of how the crucial electric field shear can be created.

Here, the focus is on the anomalous radial transport of the toroidal momentum, which is borne out by numerous experiments. Since the edge is in the banana regime during a high performance, this transport is shown to differ dramatically in the banana and the plateau regimes [2, 3]. The profiles of the electric field and the poloidal and the toroidal rotations are obtained self - consistenly in the banana regime. This model extends the theory shown to yield both the profile of the electric field in the H -regime and the cross - field conductivity in experiments with biased electrode in the plateau regime [2,3].

In order to contrast the plateau and the banana regimes, we start from the case when $\nu^* >1$. Employing the flux surface average momentum balance reading

$$nm_i \frac{du_i}{dt} = \mathbf{j} \times \mathbf{B} - \nabla p - (\nabla \cdot \pi_i)^{(NEO)} - (\nabla \cdot \pi_i)^{(AN)} + \mathbf{F} \qquad (1)$$

In Eq.(1) the convective derivitive $(\mathbf{u}_i \cdot \nabla)$ takes into account the anomalous transport of momentum across field lines defined by $u_r^{(A)}$. It is assumed to be ambipolar $u_r^{(A)} = -D\frac{d\ln n}{dr}$, where D is the same for electrons and ions. The viscosity originates from two parts both the neoclassical parallel viscosity and the anomalous perpendicular viscosity. The external force F is caused by an unbalanced neutral beam injection.

For simplicity, the tokamak geometry with circular cross - sections and large aspect ratio

$$\mathbf{B} = B_0(\mathbf{e}_\phi + \Theta \mathbf{e}_\theta) / (1 + \varepsilon \cos\theta)$$

where $\varepsilon = r/R$ and $\Theta = B_\theta/B_\phi$ is the ratio of the poloidal to the toroidal magnetic fields. The radial dependence of the parallel ion velocity yields the anomalous viscosity

$$(\nabla\cdot\pi_i)^{(AN)} = \frac{1}{r}\frac{\partial}{\partial r}\left(r\,\eta\frac{\partial u_{i\parallel}}{\partial r}\right) \qquad (2)$$

Here, η is the coefficient of the anomalous perpendicular viscosity given by the estimate $\eta = -\gamma D m_i n$. Employing parallel and the toroidal components, one obtains

$$< B\cdot n m_i \frac{du_i}{dt} > = - < B\cdot\nabla\cdot\pi_i >^{(NEO)} - < B\cdot\nabla\cdot\pi_i >^{(AN)} + F \qquad (3)$$

$$B_0^2 < \frac{n m_i}{B^2} B_\phi \cdot \frac{du_i}{dt} > = B_0^2 < \frac{B_\phi}{B^2}\cdot\nabla\cdot\pi_i >^{(AN)} + F \qquad (4)$$

In Eq.(4) it has been taken into account that $< j_r > = 0$ and $< \frac{B_\phi}{B^2}\cdot\nabla\cdot\pi_i >^{(NEO)} = 0$.

Here, we assume that the toroidal rotation velocity is subsonic thereby neglecting poloidal variations of plasma density and potential within a magnetic surface.

Thus, the continuity equation is

$$\frac{\partial}{\partial\theta}[(1+\varepsilon\cos\theta)\,u_{i\theta}] = 0 \qquad (5)$$

yielding the velocity of poloidal rotation as

$$u_{i\theta} = \frac{\text{const.}}{1+\varepsilon\cos\theta} = \frac{u_\theta}{1+\varepsilon\cos\theta} \qquad (6)$$

where $u_\theta = < (1+\varepsilon\cos\theta)\,u_{i\theta} >$ is the flux surface average of the poloidal rotation.

Using the well - known expression obtained from the radial component of the momentum balance

$$u_{i\theta} = V_0 + u_{pi} + \Theta\,\overline{u_{i\phi}} \qquad (7)$$

where $V_0 = -\frac{E_r}{B}$ is the poloidal rotation velocity in the $\mathbf{E}\times\mathbf{B}$ fields, $u_{pi} = \frac{1}{eBn}\frac{dp_i}{dr}$ is the velocity of the diamagnetic drift. Combining Eqs.(6 &7) and accounting for the poloidal dependence of V_0 and u_{pi}, one obtains to the highest order of ε^2

$$u_{i\phi} = (-2q\cos\theta + 1.5\,\varepsilon^2\Theta^{-1} - \varepsilon^2\Theta^{-1}\cos^2\theta)\,(1+\varepsilon\cos\theta)^{-2}\,(V_0 + u_{pi})$$

$$+ \overline{u_\phi}\,(1+\varepsilon\cos\theta)^{-1} \qquad (8)$$

where $q = \varepsilon/\Theta$ is the safety factor and $\overline{u_\phi} = < (1 + \varepsilon\cos\theta)\, u_{i\phi} >$ is the flux surface average of toroidal rotation.

Substituting Eq.(8) into Eqs. (3 & 4) one obtains

$$nm_i B_0 \frac{d}{dt}[\overline{u_\phi} + \Theta(1 + 2q^2)(V_0 + u_{pi}) + \varepsilon^2 \overline{u_\phi}] -$$

$$-\frac{B_0}{r}\frac{d}{dr}\{ r\eta \frac{d}{dr}[\overline{u_\phi} + \Theta(1 + 2q^2)(V_0 + u_{pi}) + \varepsilon^2 \overline{u_\phi}]\} = - < \mathbf{B}\cdot\nabla\cdot\pi_i >^{(NEO)} + F \quad (9)$$

$$nm_i \frac{d\overline{u_\phi}}{dt} - \frac{1}{r}\frac{d}{dr}(r\eta \frac{d\overline{u_\phi}}{dr}) = F \quad (10)$$

Eqs.(9 & 10) yield the profiles of the flux surface average toroidal rotation $\overline{u_\phi}$, the electric field V_0 and the flux surface average poloidal rotation u_θ in the plateau regime.

II. Banana regime.

Now we will show that the anomalous inertia and viscosity are significantly amplified in the banana regime compared to the plateau. Considering the contributions of banana orbits on either side of r, the trapped ion flow emerges [4]. A steady state requires that momentum gained by the trapped ions in the process of collisional trapping is removed by collisional detrapping. Thus, by identifying the mean ion flow with the untrapped ion flow and employing a reference frame moving in the toroidal direction with velocity

cE_r/B_θ, one obtains an additional significant parallel flux $\sqrt{\varepsilon}n(V_0/\Theta + u_{pi}/\Theta)$ owing to the banana ions. Furthermore, it has been shown by us before [2&3] that this largest parallel flow results in the enhanced anomalous inertia and viscosity yielding the following equation instead of Eq.(9). Accounting for the average toroidal rotation $\overline{u_\phi}$, one obtains

$$\frac{nm_i\sqrt{\varepsilon}B_0}{\Theta}\frac{d}{dt}(V_0 + u_{pi} + \Theta\overline{u_\phi}) + nm_i B_0 \frac{d}{dt}[\overline{u_\phi} + \Theta(1 + 2q^2)(V_0 + u_{pi}) + \varepsilon^2 \overline{u_\phi}] -$$

$$-\frac{B_0}{r}\frac{d}{dr}\{ r\eta \frac{d}{dr}[\overline{u_\phi} + \Theta(1 + 2q^2)(V_0 + u_{pi}) + \varepsilon^2 \overline{u_\phi}] - \frac{B_0}{r}\frac{d}{dr}\{ r\eta \frac{d}{dr}[(\overline{u_\phi} + V_0 +$$

$$u_{pi})\sqrt{\varepsilon}\Theta^{-1}\overline{u_\phi}]\} = - < \mathbf{B}\cdot\nabla\cdot\pi_i >^{(NEO)} + F \quad (11)$$

In other words, the dominant radial flux of banana particles results from the combined effect of an anomalous transport in a spatially varying electric field (see Fig. 2 and Section VII in [3]). Analogously to the "Ware pinch", the similar effect emerges due to the force F. Hence, the $\overline{u_\phi}$ is included in Eq.(11). Given neoclassical parallel viscosity of ions as a function of the poloidal rotation velocity u_θ, reading for $|u_\theta| << \Theta C_S$

$$< \mathbf{B}\cdot\nabla\cdot\pi_i >^{(NEO)} = \frac{1.1\sqrt{\varepsilon}nm_i\nu_i B_0}{\Theta}(u_\theta - u_\theta^{(NEO)}) \quad (12)$$

where $u_\theta^{(NEO)} = \frac{k}{eB}\frac{dT_i}{dr}$

Eq.(11) yields the following equation exemplifying the impact of the trapped particles on the poloidal rotation , thereby affecting a profile of the radial electric field

$$\frac{nm_i\sqrt{\varepsilon}\,B_0}{\Theta}\frac{d}{dt}u_\theta + \frac{\sqrt{\varepsilon}}{\Theta}\frac{B_0}{r}\frac{d}{dr}\left(r\eta\frac{d}{dr}u_\theta\right) = -\frac{1.1\sqrt{\varepsilon}nm_i\nu_i B_0}{\Theta}\left(u_\theta - u_\theta^{(NEO)}\right) \quad (13)$$

Eq.(13) in combination with the well known flux surface averaged radial momentum balance

$$u_\theta = V_0 + u_{pi} + \Theta\overline{u_\phi}$$

yields the following conclusions. Two typical length scales emerge in the banana regime depending on the collisionality ν_i. The first is $L_{u_\theta} = \frac{u_r^{(A)}}{\nu_i} \approx \frac{D}{L_n\nu_i}$, where $L_n = \left(\frac{d\ln n}{dr}\right)^{-1}$ provided $\nu^* \approx 1$. In contrast, $L_{u_\theta} \approx L_n$ when $\nu^* \ll 1$ and $L_n^2 \ll \frac{D}{\nu_i}$ i.e. the poloidal rotation is reduced to zero within the scale L_n. Neglecting the neoclassical viscosity and employing $u_r^{(A)} = -D\frac{d\ln n}{dr}$ one obtains the equation for the poloidal rotation profile

$$\frac{dV_\theta}{dr} = \frac{const}{n^{1+\gamma}} \quad (14)$$

In summary, Eq.(14) yields the poloidal rotation profile decreasing to zero inwards from a separatrix within the length scale of the order L_n. It may be either positive or negative. For a given u_{pi} and $\overline{u_\phi}$, Eq.(14) also yields the radial electric field profile V_0 because $V_\theta \approx 0$ for $r < a - L_n$. A constant in Eq.(14) is determined by the density profile on the separatrix. Indeed, if the u_{pi} dominates, it governs the electric field there. In conclusion, variations of poloidal rotation and electric field profiles occur within L_n and not within the " squeezed" banana width due to radial electric field shear. The significance of the first two terms at the L.H Side of Eq.(13) as opposed to neoclassical viscosity appears to yield steep profiles of poloidal rotation velocity typical at the very edge for the H regime where $\overline{u_\phi} \sim 0$. Yet, the impact of terms at the R.H.Side due to a profile in toroidal rotation may be more dramatic deeper in a tokamak thereby bringing about the high - shear electric field in the plasma outer region.

* Permanent address : St.Petersburg Technical University, St.Petersburg, Russia

1. H.Biglari, P.Diamond & P.Terry Phys. Fluids B2, 1 (1990)

2.L.G.Askinazi, V.Golant, S.Lebedev, V.Rozhansky & M.Tendler Nuc.Fus.32, 271

3.V.Rozhansky & M.Tendler Phys.Fluids B4, 1877, 1992

4. A.Galeev & R.Sagdeev in Reviews of Plasma Physics v.7, p.237 1979

Global Thermal Transport and Indications from the Alcator C-Mod Experiment*

B. Coppi, L.E. Sugiyama, M. Greenwald, W. Daughton,
A. Hubbard, J. Irby, C. Fiore, T. Luke, J. Rice, E. Marmar, S. Wolfe, R. Granetz
Massachusetts Institute of Technology, Cambridge MA USA 02139-4307

I. Introduction

High field, compact experiments have a well demonstrated ability to produce a relatively large variety of regimes, that include plasmas with a high degree of purity as well as record values of the confinement parameter $n\tau_E$. The early operation of the Alcator C-Mod machine [1] has indicated that clean ohmic plasmas can reliably achieve, at low and moderate densities, confinement times that exceed those expected from the so–called 'neo-Alcator' scaling [2], where the energy confinement time improves with density, $\tau_E^{NA} \simeq 0.07\overline{n}_{e20}qR^2a$. The Alcator C-Mod experiment has a naturally large "dynamic range" in density at a given plasma current I_p because of the extreme purity of the produced plasmas. Taking advantage of this feature, it has been possible to identify a variation of the energy confinement time with plasma current throughout its present range of operation. Specifically, the neo-Alcator values of τ_E are exceeded at the lower densities. A regime, where τ_E increases with I_p and is greater than τ_E^{NA} by a factor of at least two at low density, has also been identified recently [3] in boronized ohmic plasmas in the Tuman-3 experiment. In order to understand the origin of this result and to address the problem of the intrinsic coupling of the plasma density and current, we have undertaken a detailed numerical simulation of the Alcator C-Mod ohmic data. We have identified a type of thermal diffusion coefficient that reproduces, with considerable accuracy, the observed electron temperature profile, the toroidal loop voltage, and the energy confinement time.

II. Electron Thermal Transport Coefficient

To clarify our argument, we refer to a large aspect ratio, toroidal configuration with a circular cross section and consider the electron thermal energy balance equation in which the electron thermal conductivity is the main form of power loss,

$$E_{||}J_{||} = -\frac{1}{r}\frac{d}{dr}\left(rnD_e^{th}\frac{dT_e}{dr}\right).$$

Therefore, the form of the diffusion coefficient D_e^{th} that would lead to a temperature profile $T_e \simeq T_{eo}\exp(-\alpha_T r^2/a^2)$, where α_T is a weak function of r^2/a^2, can be written as

$$D_e^{th} \simeq \left[\frac{eV_{||}}{2(2\pi)^2 T_e(r)}\right]\frac{I(r)}{en(r)}\frac{a^2}{\alpha_T r^2 R}, \tag{1}$$

where $V_{||}$ is the loop voltage that is independent of r, $I(r) = 2\pi\int_0^r J_{||}(r')r'\,dr'$. The Coppi-Mazzucato-Grüber D_{CMG} diffusion coefficient [4,5] complies with the form (1) and with the observation that in all ohmic heating experiments $V_{||}$ has a nearly constant canonical value. In the Alcator C-Mod discharges, $V_{||} \sim 1$ volt. Since under stationary conditions, $V_{||}$ is independent of r, a specific expression of D_e^{th} is obtained by prescribing a form of the dimensionless quantity $eV_{||}/[2(2\pi)^2 T_e(r)]$ that has nearly the same spatial dependence as $1/T_e(r)$ and that contains the physical factors which are considered to be involved in the observed form of transport. In the case of the CMG coefficient,

$$\frac{eV_{||}}{T_e(r)} \propto \left(\omega_{pi}d_e^2\frac{\nu_{ee}}{V_{the}^2}\right)^{2/5}\left\langle\frac{Z_*}{A_i}\right\rangle^{2/5}, \tag{2}$$

where $d_e \equiv c/\omega_{pe}$, A_i is the mass number of the main ion population, $Z_* = A_i\sum_j n_j Z_j^2/(n_e A_j)$ summed over the ions and $\langle\ \rangle$ is the volume average. On the other hand, it is reasonable to

* Supported in part by the U.S. Department of Energy

assume that the electron pressure gradient play a role in the transport process and guided by the criterion that there are regimes where D_e^{th} is independent of the magnitude of the density we may take instead of (2)

$$\frac{eV_{||}}{T_e(r)} \propto \left(\omega_{pi} d_e^2 \frac{\nu_{ee}}{V_{the}^2}\right)^{1/3} \left(\frac{8\pi p_{e*}}{B_{\theta*}^2}\right)^{5/6} \left\langle \frac{Z_*}{A_i} \right\rangle^{1/2}, \tag{3}$$

where $p_{e*} = -r dp_e/dr$ evaluated at the surface where it is maximum (typically around $a/3$) and $B_{\theta*} = r dB_\theta/dr$ evaluated at the same surface while $(\omega_{pi} d_e^2 \nu_{ee}/V_{the}^2)$ is evaluated as a function of r. Thus we argue that the Alcator C-Mod experiments can be described by the diffusion coefficient

$$\begin{aligned} D_{JA} &\simeq C \left(\omega_{pi} d_e^2 \frac{\nu_{ee}}{V_{the}^2}\right)^{1/3} \frac{I(r)}{en(r)} \frac{1}{R} \frac{a^2}{r^2} \left(\frac{8\pi p_{e*}}{B_{\theta*}^2}\right)^{5/6} \left\langle \frac{Z_*}{A_i} \right\rangle^{1/2} w(r), \\ &\propto \frac{a^{5/3}}{I_p^{2/3} R} \left\langle \frac{Z_*}{A_i} \right\rangle^{1/2}, \end{aligned} \tag{4}$$

where C is a numerical coefficient that is determined by fitting the electron temperature profile of a typical discharge under steady state conditions and $w(r)$ is a weak dimensionless function of r^2. Thus the scaling for the energy confinement time is

$$\tau_E \sim J_{||}^{2/3} a^{5/3} R \left\langle \frac{A_i}{Z_*} \right\rangle^{1/2}. \tag{5}$$

Equation (5) becomes a reminder of the so-called neo-Alcator scaling when the maximum particle density n_M is coupled to the current density and n_M replaces $J_{||}$. We also notice that the introduction of the pressure gradient through p_{e*} gives the expression (4) for D_{JA} the same driving factor as that considered [6] for the diffusion coefficient that we have used to reproduce experiments where ohmic heating is no longer prevalent, relative to injected heating, and that gives the scaling

$$\tau_E \sim I_p (n/P_H)^{1/2} aR, \tag{6}$$

where P_H is the total heating power. The form of D_{CMG} that we have used is, in general axisymmetric geometry [6] and mks units,

$$D_{CMG} \simeq 7.76 \times 10^8 \left(\frac{I_\phi}{n_e^{4/5} T_e}\right) \left(\frac{Z_* \ln\Lambda}{A_i}\right)^{2/5} \frac{\pi^{3/2} V_a^2}{A_a^{3/2}} \frac{1}{\langle\langle |\nabla V|^2 \rangle\rangle} \quad (\mathrm{m}^2/\mathrm{s}), \tag{7}$$

where I_ϕ is the toroidal current contained within a given flux surface, T_e is in keV, ln Λ is the Coulomb logarithm, V is the volume contained within a flux surface, V_a and A_a are the total volume and cross sectional area of the plasma, respectively, and the brackets $\langle\langle\ \rangle\rangle$ represent a flux surface average.

III. Results of the Transport Simulation

The Alcator C-Mod parameters covered a range of current, $I_p \simeq 0.38$–1.0 MA, and density, $\overline{n}_e \simeq 0.78$–$2.4 \times 10^{20}\mathrm{m}^{-3}$ (line average). For the transport simulation, representative discharges were selected that included a density scan at constant current, $\overline{n}_e \simeq 0.78$– $2.1 \times 10^{20}\mathrm{m}^{-3}$ at $I_p \simeq 0.61$–0.67 MA, and a sequence of discharges with varying current at $\overline{n}_e \simeq 1.1 \times 10^{20}\mathrm{m}^{-3}$. The major and minor radii and the toroidal magnetic field were held approximately constant for all discharges at $R \simeq 0.69$ m, horizontal $a \simeq 0.22$ m, and $B_T \simeq 5.2$ T, while the elongation κ had a small variation. The effective charge Z_{eff} varied from 1–3, but most of the steady state cases that we analyzed fell in the range 1–1.6. Cases were chosen to be as close as possible to steady state and to cover the range of parameter space over which the thermal diffusion coefficient varied. Parameters are given in Table 1.

The simulation was carried out with the 1 1/2D transport code BALDUR. For reasons of numerical convenience and timeliness, we have utilized the form of the CMG diffusion coefficient as given by Eq. (7) and taken, for simplicity,

$$D_e = C_e D_{CMG} \left(\frac{8\pi^2 p_* a^2}{\mu_o I_p^2/10} \right) w_o(\hat{\Phi}),$$

which is reasonably close to Eq. (4). Here C_e is a numerical coefficient, $\hat{\Phi}$ is the normalized toroidal magnetic flux, and p_* is approximated by $p_* = p_e(r_G)$, evaluated on the flux surface $r_G = r(\hat{\Phi}_G)$ corresponding to the maximum of the pressure gradient, which was typically $r_G \simeq (1/3)a$ for the cases considered. The weak function $w_o(\hat{\Phi})$ is taken to be $w_o = [(1.7\hat{\Phi} + 0.3)/(1+\hat{\Phi})]^{1/2}$, where $\hat{\Phi} \simeq r^2/a^2$. The ion thermal transport was assumed to be neoclassical, as was the electrical resistivity. The density profile was held fixed to match the experimentally determined one. This had little effect on the thermal energy balance, since the convective contribution is small in steady state.

One approximation that was made in the simulation was that the plasma shape possessed up–down symmetry, unlike the actual configurations, which had a bottom null point. This does not greatly affect the results, to the accuracy considered. The overall numerical coefficient C_e was found to have a constant value $C_e \simeq 2$, for all the deuterium discharges simulated. This value gave a good fit to the electron temperature profile, the plasma loop voltage, the electron stored energy, and the energy confinement time. The dependence of τ_E on A_i/Z_* has not yet been tested, as the steady state discharges available for analysis were all in deuterium.

The simulation results are compared to the experimental parameters in Table 1. Representative electron temperature profiles are shown in Fig. 1, compared to the measured ECE temperature profiles, and a representative density profile. The highest and lowest density cases in the current scan and a high current case are shown. The electron temperatures in the table are given at $r = (1/3)a$, since the simulation did not model the effects of the sawtooth oscillations, which could be large at the higher currents (e.g., Fig. 1). The profile of the ion temperature has a large uncertainty and is not reported. There is also a relatively large uncertainty in the central values T_{io} and the ion stored energies W_i.

IV. Interpretation of the Results

The results show that a thermal diffusion coefficient which corresponds to an energy confinement time that increases with the plasma current gives a good representation of the Alcator C-Mod ohmic plasmas, where R, a, and B_T are approximately fixed. Differences between the confinement scaling implied by the adopted transport coefficient and those obtained by statistical regression analyses suggest that there are interdependences among the plasma parameters considered, within the data set. We also mention that we have tried to simulate the Alcator C-Mod discharges indicated in this paper by the form for D_e^{th} [6], that we have proposed for injected heating regimes and gives the scaling (6), without succeeding to reproduce the relevant temperature profiles. It is evident that there remains a degree of uncertainty in the parameter dependence of the confinement that is due to the experimental uncertainties and to the small range of variation of some of the relevant parameters, that cannot be resolved on the basis of the available data. The present work has assumed one of the simplest possible forms for D_e^{th} that satisfy the physical constraints discussed in Section II. The considered set of discharges excludes those that have characteristics of the so called "H-mode" confinement regime.

Acknowledgements

The authors thank the entire Alcator C-Mod team for the use of the data and for their generous assistance in accessing and analyzing it.

References

[1] I.H. Hutchinson, R. Boivin, F. Bombarda, et al. *Phys. Plasmas* **1** 1511 (1994).
[2] W. Pfeiffer and R.E. Waltz, Nuclear Fusion **19** 51 (1979).
[3] V.E. Golant, private communication, 1994.
[4] B. Coppi and E. Mazzucato, Phys. Lett. A **71** 261 (1979).
[5] O. Grüber, Nuclear Fusion **22** 1349 (1982).
[6] B. Coppi, P. Detragiache, S. Migliuolo, L. Sugiyama, L. Zakharov, in Plasma Physics and Controlled Nuclear Fusion Research 1992, Würzburg (I.A.E.A., Vienna, 1993), Vol. 2, pp. 131–141.

Table 1. Comparison of plasma parameters for simulation and experiment.

shot	931021022		931008014		931021020		931006015		931013013		931021010	
I_p (MA)	0.565		0.608		0.624		0.672		0.80		0.85	
$\overline{n}_e$ (m^{-3})	1.06×10^{20}		0.939×10^{20}		2.14×10^{20}		0.781×10^{20}		1.75×10^{20}		1.15×10^{20}	
R_o (m)	0.691		0.690		0.691		0.689		0.692		0.693	
a (m)	0.221		0.218		0.217		0.217		0.222		0.224	
κ	1.50		1.54		1.48		1.55		1.51		1.53	
δ	0.25		0.30		0.30		0.30		0.30		0.29	
B_T (T)	5.24		5.24		5.24		5.23		5.27		5.27	
Z_{eff}	1.0		1.29		1.0		1.6		1.0		1.24	
	Exp.	Sim.	Exp.	Sim.	Exp.	Sim.	Exp.	Sim.	Exp.	Sim.	Exp.	Sim.
τ_E (msec)	42.0	42.8	40.0	41.0	33.0	34.6	38	45.4	40.0	42.9	44.0	46.1
V_s (volt)	0.996	1.01	0.988	1.06	1.75	1.59	1.01	0.976	1.29	1.21	1.19	1.05
W_e (MJ)	0.0117	0.0127	0.0142	0.0142	0.0149	0.0174	0.0152	0.0163	0.0225	0.0213	0.0198	0.0212
W_i (MJ)	0.0115	0.0118	0.0109	0.0123	0.0194	0.0170	0.0096	0.0128	0.0226	0.0202	0.0184	0.0199
$T_e(a/3)$ (keV)	0.96	1.02	1.40	1.18	0.685	0.664	1.83	1.75	1.12	1.32	1.46	1.65

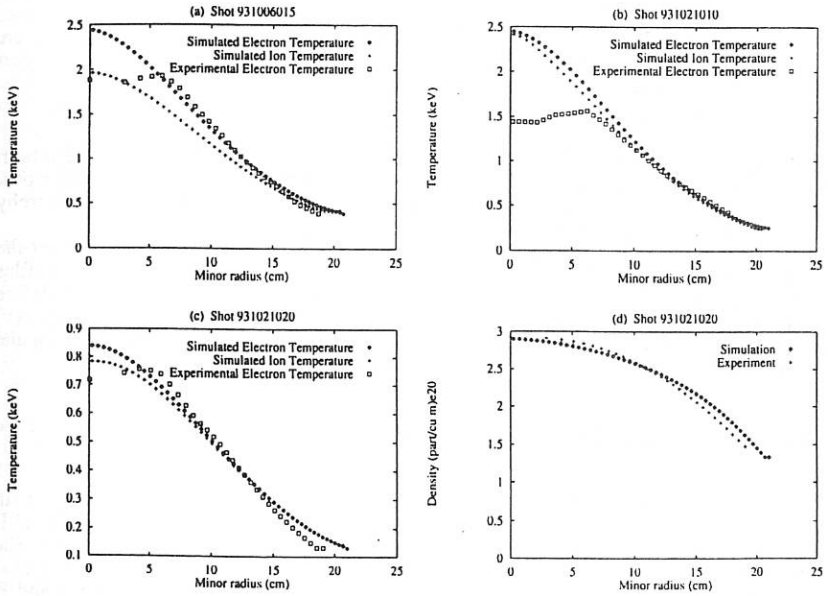


Figure 1. Representative temperature and density profiles. The radial coordinate is on the midplane from the magnetic axis outward. (a) Temperature profiles for shot 931006015 at I_p=0.672 MA and $\overline{n}_e$ =0.78 x10^{20} m^{-3} (b) Temperature profiles for shot 931021010 at I_p=0.85 MA and $\overline{n}_e$ =1.15 x10^{20} m^{-3} (c) Temperature profiles for shot 931021020 at I_p=0.624 MA and $\overline{n}_e$ =2.14 x10^{20} m^{-3} (d) Density profiles for shot 931021020 with units of 10^{20} m^{-3} on the vertical axis. Sawtooth flattening of the temperature profiles is evident in the experimental data. A sawtooth model was not included in the simulation.

Modelling of ITER operation

D. Boucher, J. Wesley

ITER San Diego co-center
11025, North Torrey Pines Road
La Jolla, CA 92037

Introduction

The principal parameters of the ITER Outline Design figuring in Protocol II of the ITER EDA Agreement are as follow:

Fusion Power (nominal)	1.5 GW
Burn Time (nominal)	1000 seconds
Plasma Current	24 MA
Geometric Major Radius	~ 8.1 m
Geometric Minor Radius	~ 3.0 m
Elongation	1.55
Vacuum Toroidal Field at geometric axis	5.7 T

The physics objectives include the demonstration of "controlled ignition and extended burn of deuterium-tritium plasmas, with steady state as an ultimate goal"[1]. In particular, a new regime will be reached where the fusion power becomes the main heating source thereby imposing a new relation between plasma density, plasma purity and heating power.
Local transport modelling is one of the main tool available to (i) define a strategy for the control of the fusion burn, (ii) predict the stability of the dynamic and equilibrium profiles with respect to MHD activity, (iii) define the optimal operation scenarios , (iv) define shutdown scenarios to stop the fusion power within a prescribed amount of time, and (v) specify the technical requirements for the design of the various systems required for the operation of the plasma.

ITER reference temperature and density profiles

A 1-1/2D transport code (PRETOR) implementing the RLW energy transport model with the particle transport model developed by D. Boucher [2] was used to generate typical L mode and H mode profiles that can be used as reference for further stability studies. The transport coefficients were varied to account for physics uncertainties and to include global scaling laws confinement predictions. Two options are studied: L mode operation and H mode regime. In H mode the main uncertainty for extrapolation comes from the prediction for the properties of the edge transport barrier: what fraction of the additional stored energy comes simply from an edge temperature pedestal and what fraction comes from a reduction of transport over the entire plasma volume ? How does it affect edge particle transport ? Figure 1 shows the L mode temperature and density profiles predicted by RLW model (solid lines) together with the H mode profiles (dotted lines) obtained by imposing a reduction of

transport at the plasma edge and increasing the core transport in order to keep the same (ignited) fusion power, the same energy confinement time. The pumping speed was adjusted to keep the same central helium density as for the L mode. This procedure allows to estimate extreme profiles from no edge pedestal to high edge pedestal thereby covering a wide range of possible profiles.

Fusion power control strategy

Three key observations can be used to define the main strategy for the control of the fusion power independently of any transport model:
(i)Whether the energy confinement time decreases with increasing input power or whether it saturates at high input power - as would be the case for an offset linear law - there always exist a thermally stable regime where the transport losses compensate the input power.
(ii)Since transport losses are weakly dependent on plasma composition - through isotopic and effective charge or mass dependence - whereas the fusion power is strongly dependent on the fuel - DT mix - density, it can be clearly asserted that the operating point where heat losses equal heat sources can be chosen by controlling the fuel dilution.
(iii) in steady state the fusion power is uniquely defined by the fuel injection rate (or net fuel particle flux crossing the plasma separatrix).
Local transport modelling is then used to precisely quantify the three previous observations and study their domain of validity. Figure 2 summarizes the fusion control strategy: the fusion power can be increased by increasing the fuel injection rate or by auxiliary heating, it can be decreased by decreasing the fuel injection rate or by injecting impurities. The time scale for any change in fusion power can be varied either through edge gas injection (slow) or by injecting pellet (fast). Figure 3 shows a PRETOR simulation where only the gas injection rate and the amount of auxiliary heating were varied according to a simple feedback command to force the fusion power to follow a required wave form.

Fusion Shutdown scenarios

Increasing the fuel dilution does not only move the plasma operating point towards a lower temperature but also increases the relative part of the Bremstrallung radiation in the overall transport losses. Since the temperature dependence of the Bremstrallung radiation is much weaker than that of the fusion power, one can rapidly reach the point where a thermal instability is triggered leading to a fast collapse of the fusion power. Figure 3 shows such a thermal instability triggered by simply stopping the fuel injection rate at t=5s, it also shows an even faster termination by impurity pellet injection at t=5s where the initial cooling of the plasma is obtained by the pellet ablation itself. These simulations show that the characteristic time to stop the fusion is between a fraction of a second with pellet to about 20s by stopping fueling.

Scenario for H mode operation

Recent scaling laws for the H mode power threshold [3] showed a requirement of the form: $P/S \propto n\,B$ where P is the power reaching the plasma edge in MW, S the plasma surface in m^2, n the edge density in $10^{19} m^{-3}$ and B the toroidal field in T. Following [4], the relation $P/S > 0.0044\ n\ B$ with a factor of 2 decrease for the reverse - H to L - transition was used

thereby imposing severe requirement on ITER operation. Figure 5 shows the trajectory of a typical discharge in the plane (P edge , n edge). The linear dependence of the threshold power on density was used to enter the H mode at low density at which point the edge power is roughly equal to the amount of auxiliary heating: 50 MW. The fusion power is then ramped up - and the auxiliary heating progressively reduced to zero - leading to the edge power increasing more than linearly with density which, together with a lower requirement for reverse transition, insured than the discharge stayed in H mode. However, helium would then accumulate leading to both a decrease of power reaching the edge - due to larger radiation losses - and higher edge density eventually leading to the end of the H mode. It is however conceivable that ELMs activity at a sufficiently high frequency would help reduce the helium accumulation thereby maintaining the H mode regime.

Plasma response to perturbations

Under normal operation, a typical ITER plasma will be submitted to various perturbations including sawtooth relaxation, ELMs activity, H mode transition or minor disruptions. Figure 6 shows the example of a worst case H mode transition. This transition occurs in an ignited plasma and is simulated by instantaneously reducing the transport over the entire plasma volume by a factor of two at t=10s. It is seen that the variation in fusion power can be less than about 10% by injecting impurity pellets (Be, 3mm, 1.5km/s) thereby rapidly offsetting the improved confinement by increasing the fuel dilution. Such simulations, once more closely validated against actual experiments, are planned to be used for the technical requirement specifications for the design of ITER poloidal field system and ITER divertor.

Conclusion

Local transport modelling and simulations are used to study the overall behavior of a fully ignited plasma and to identify those specific aspects of plasma transport for which present knowledge is not sufficient and that could be the subject of further ITER Physics R&D. However, many important conclusions concerning the controllability of such a plasma and the requirements for its operation are not dependent on any particular modelling assumption but can be derived from general principles.
H mode operation is clearly seen as the most difficult regime to extrapolate for ITER. In particular the power threshold requirements and the role of the edge transport barrier, likely to be responsible for both energy and particle improved confinement, are still uncertain and could have important consequences for ITER operation.

[1] *ITER Detailed Technical Objectives*, in Protocol II of the ITER EDA Agreement, Negotiators Shared Views Attachment 1.

[2] *Predictive Modelling and Simulation of Energy and Particle Transport in JET*, D. Boucher, in Advances in Simulation and Modeling of Thermonuclear Plasmas, (Proc. IAEA Technical Committee meeting, Montreal, Canada, 1992) IAEA, Vienna (1993) 142.

[3] *An examination of the ITER H mode Power Threshold DataBase*, H mode Database working group, 20th EPS Conf., Lisboa, July 1993, Part I, p.I-15.

[4] *Ohmic H mode and H mode Power Threshold in ASDEX Upgrade*, F. Ryter et al., 20th EPS Conf., Lisboa, July 1993, Part I, p.I-23

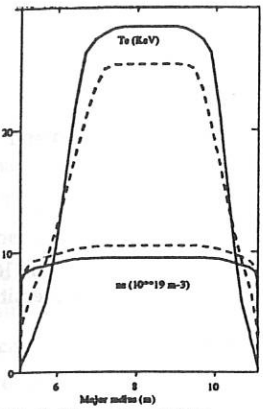


Fig.1: H mode profiles.

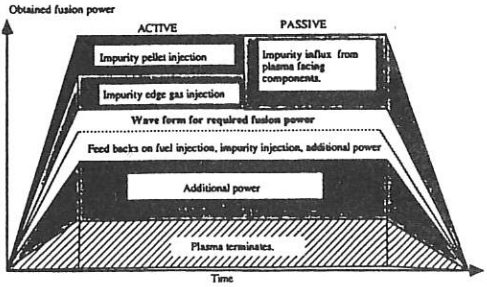


Fig.2: Fusion power control.

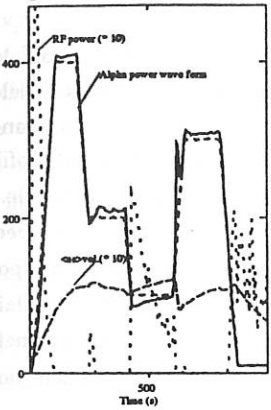


Fig.3: Fusion power wave form.

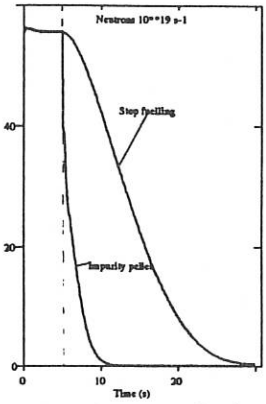


Fig.4: Fusion power shutdown.

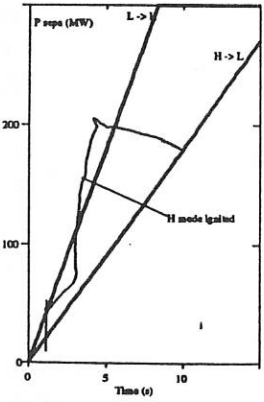


Fig.5:H mode trajectory.

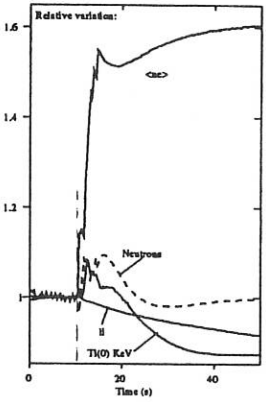


Fig.6: H mode transition.

Transport changes due to the magnetic field shear, stochastic magnetic field and electric field shear

Sanae-I. Itoh*, T. Kubota**, S. Toda**, H. Yamaguchi**,
A. Fukuyama+, Y. Fuji+ and K. Itoh++

* Research Institute for Applied Mechanics, Kyushu University 87, Kasuga 816
** Interdisciplinary Graduate School of Engineering Sciences, Kyushu Uiversity 39,Kasuga 816
\+ Faculty of Engineering, Okayama University, Okayama 700
++ National Institute for Fusion Science, Nagoya 464-01
Japan

Various improved modes other than H-mode have been discovered in tokamaks. The H-mode is characterized by the edge transport barrier due to radial electric field, $E_r(r)$. The electric field shear, dE_r/dr, plays an important role. On the other hand, high β_p mode is said to be characterized by the self-consistent plasma current profile J(r) where the bootstrap current(BSC) is included. The magnetic shear plays a role.

Theoretical model of transport coefficients for the L-mode plasma has been developed[1], which successfully explains the characteristics of anomalous transport in toroidal plasmas. The model has been extended to include dE_r/dr to explain H-mode transport[2]. We study effects of the magnetic shear, s=r(dq/dr), the magnetic axis shift as well as BSC and high β_p mode is also explained by another extension[3]. We explore roles of dE_r/dr and s on transport processes.

Transport coefficient and heat pulse propagation

Based on a self-sustained turbulence theory, anomalous heat conductivity, χ_H, is obtained as, [1),2)]

$$\chi_H=\frac{\chi_L}{1+G_1\omega_{E1}^2}, \qquad \chi_L=\frac{q^2}{f(s)}\left[R\frac{\partial\beta}{\partial r}\right]^{1/2}\delta^2\frac{V_A}{R} \tag{1}$$

$$G_1=\left[\frac{9}{8}\left(1+\frac{4}{3\alpha f}\right)^2+\frac{25(s-\alpha)^2}{4(1+2\alpha-2s)}\sqrt{\frac{2+C}{1+C}}\left(1+\frac{4}{3\alpha f}\right)\left(1+\frac{4}{5\alpha f}\right)\right]\frac{\alpha}{f^2}$$

where $\omega_{E1}\,(=\tau_{Ap}(dE_r/dr)(srB)^{-1})$ denotes the electric field shear effect and f(s) indicates the magnetic shear effect. When ω_{E1} is small (i.e., L-mode), χ_H has $|\nabla T|^{3/2}$ dependence.

We firstly examine various models of χ ,by use of heat pulse propagation analysis. Five cases are adopted, namely 1) χ=const, 2) $\chi=\alpha T$(Bohm type), 3) $\chi=\gamma T^{3/2}$(gyro-Bohm type), 4) $\chi=\beta\ |\nabla T|$ (R-L type) and 5) $\delta\ |\nabla T\ |^{3/2}$ (Itoh type). Coefficients $\alpha, \beta, \gamma, \delta$ and const. are chosen so that the internal energy W_p takes the same value (for given density) in a stationary state. In table 1, we compare the values of χ_{HP}/χ_{PB}, the ratio of χ (heat pulse) and χ (power balance) for various locations in the plasma (r/a=0.4, 0.5, 0.6). The case is for uniform heat deposition profile and the pulse perturbation is given at r/a=0.3. From the comparison study with experiments, we may say that R-L model and Itoh model survive. Magnetic shear effect is also examined for Itoh model, noting the relation that $J(r)\propto T(r)^{3/2}$. Usual L-mode transport is found less affected by s than by q value itself.

χ_{HP}/χ_{PB}

	$r/a=0.4$	$r/a=0.5$	$r/a=0.6$
$\chi=const$	1.00	1.00	1.00
$\chi=\alpha T$	1.04	1.02	1.01
$\chi=\gamma T^{3/2}$	1.07	1.03	1.02
$\chi=\beta\|\nabla T\|$	2.28	2.06	2.02
$\chi=\delta\|(\nabla T)^{3/2}\|$	3.12	2.57	2.52

High-β_p plasma and magnetic shear profile

The strong magnetic shear effect on the reduction of transport is expected, if the plasma is imbedded in a low shear or negative shear region. The transport simulations were made using Eq.(1) for given density profile. A JET class plasma is assumed with P_{in}=10MW, $n_0=5\times10^{19}m^{-3}$. The L-mode plasma (3MA) and high β_p plasma (1MA) are compared. In the high-β_p case, BS current is generated near the steep pressure gradient (r/a~0.6), which substantially flattens the current and q profiles and lowers s. Strong reduction of χ is predicted inside r/a~2/3.

Electric field formation in a stochastic magnetic field layer

In a sheared magnetic field appearance of stochastic magnetic field (magnetic chaos) layer has been predicted associated with the nonlinear interaction of global MHD modes [4]. When the mode amplitude becomes large enough , a global stochasticity sets in [5]. In this layer, the plasma transport becomes bipolar in radial direction, which gives rise to the formation of radial electric field E_r.

The case where the stochastic layer (2) is sandwiched in between two anomalous but regular transport regions (1,3) is modelled. We first formulate the

transport matrix for electrons and ions in the stochastic region. The shifted maxwellians are assumed for velocity distribution functions and the self- consistent electric field, $e\phi / \langle T \rangle$, is incorporated. The relation between fluxes and thermodynamic forces is given by.

$$\begin{pmatrix} \hat{\Gamma}_{xj} \\ \hat{P}_{xj} \\ \hat{Q}_{xj} \end{pmatrix} = -\frac{1}{\pi} D_M \exp\left[\frac{e\phi(x)}{\langle T \rangle}\right] \begin{pmatrix} 1 & X_{0j} & 1 \\ 2X_{0j} & 1 & 2X_{0j} \\ 1 & 3X_{0j} & 2 \end{pmatrix} \begin{pmatrix} X_{1j} \\ X_{2j} \\ X_{3j} \end{pmatrix}, \quad \begin{aligned} X_{1j} &= \frac{1}{n_j}\frac{dn_j}{dx} - \frac{1}{2}\frac{1}{T_j}\frac{dT_j}{dx} \pm \frac{e}{\langle T \rangle}\frac{d\phi}{dx} \\ X_{2j} &= \frac{2}{v_{Tj}}\frac{dU_{//}(x)}{dx} \\ X_{3j} &= \frac{1}{T_j}\frac{dT_j}{dx} \end{aligned} \qquad (2)$$

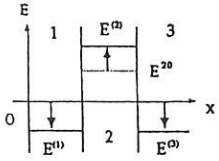
where $v_T = \sqrt{\frac{2T}{m}}$, $X_0 = \frac{U_{//}(x)}{v_T}$, $X_0 \ll 1$

For the stationary state, the formation of E_r is predicted, by matching the fluxes across three regions as

$$\begin{aligned} E^{(1,3)} &= \frac{\langle T \rangle}{e(\bar{D}_i + \bar{D}_e)}\left[-\kappa^{(1,3)}(\bar{D}_e - \bar{D}_i) - \frac{1}{2}(\bar{D}_e \kappa_{T_e}^{(1,3)} - \bar{D}_i \kappa_{T_i}^{(1,3)})\right] \\ E^{(2)} &= \frac{\langle T \rangle}{4e\alpha}\left[\bar{\chi}_e \kappa_{T_e}^{(1,3)} - \bar{\chi}_i \kappa_{T_i}^{(1,3)})\right], \quad \alpha = \frac{1}{\sqrt{\pi}} D_M \exp\left[\frac{e\phi(x)}{\langle T \rangle}\right] \end{aligned} \qquad (3)$$

where $\bar{D}$ and $\bar{\chi}$ denote the diffusion coefficient and thermal conductivity in (1,3) regions. κ and κ_T are the gradients. If $\bar{D}_e = \bar{D}_i$, and $\kappa_{Te} > \kappa_{Ti}$ in (1,3), the thermoelectric field, $E^{(1,3)}$ is generated. In the stochastic region, (2), positive E_r is generated because of the enhanced electron transport. The case for $e\phi / \langle T \rangle \ll 1$ is shown in Fig. 1.

Fig. 1



Dynamics due to edge electric field shear

The H-mode transition model, which contains the hysteresis curve $\Gamma(q)$- λ plane (Γ, q (particle, heat fluxes); λ (thermodynamic force i.e., gradients)), predicts a limit cycle as a dynamic solution[6]. This self-generated oscillation is found in a limited plasma parameter space near the L/H transition boundary. We attribute this to a small and frequent ELMs. The analysis was done for a transition model, where the electron anomalous loss due to microscopic instabilities and the ion orbit loss are

taken into account[6].The electric field shear effect was incorporated to the transition model[7]. Here, the dynamics is newly analyzed. We confirm the existence of limit cycle solutions in the presence of E_r and E_r'. The condition for the occurrence is obtained for the given λ as $0.4/(1+u_g/u_c)<d<1$ where $u_g=E_r'\rho_p/B_p v_{T_i}$, $u_c=2.76$, $d=\frac{D_e\sqrt{\epsilon}}{F\nu_i\rho_p^2}$, $\lambda=-\rho_p\frac{T_e}{T_i}\left(\frac{n_e'}{n_e}+\alpha\frac{T_e'}{T_e}\right)$. The parameter spaces for the occurrence of self-generated oscillation are shown in Fig. 2(a) (ELM region) for E_r model[6] and in Fig. 2(b) (hatched region) for the extended E_r-E_r' model. The wider region is predicted for negative E_r' ($u_g<0$).

Fig.2(a)

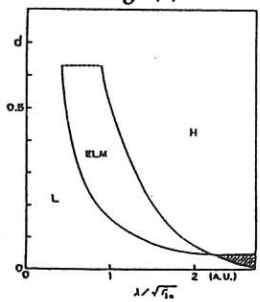
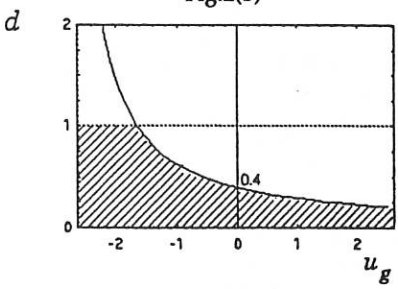


Fig.2(b)



In summary, we examined various transport changes due to magnetic field shear, stochastic magnetic field and electric field shear. They appear independently in different locations in the plasma column as different physics mechanisms. Some may interact with each other. The quantitative analyses are left for the future work.

1) K. Itoh, et al., Phys. Rev. Lett. 69 (1992) 1050; Plasma Phys. Control. Fusion 35 (1993) 543; Plasma Phys. Control.Fusion 36 (1994) 279.

2) S.-I. Itoh, et al., Phys. Rev. Lett. 72 (1994) 1200 .

3) A.Fukuyama, et al., submitted to Plasm. Phys. Control. Fusion (1994).

4) M. N. Rosenbluth, et al., Nucl. Fusion 6 (1966) 297.

5) A . J. Lichtenberg, et al., Nucl. Fusion 32 (1992) 495.

6) S.-I. Itoh, et al., Phys. Rev. Lett. 67 (1991) 2505; Nucl. Fusion 33 (1993) 1445.

7)S.-I. Itoh, et al., J. Phys. Soc. Japan 59 (1990) 3815.

NONLINEAR MAGNETIC RECONNECTION IN LOW COLLISIONALITY PLASMAS

Maurizio Ottaviani and Franco Porcelli*
JET Joint Undertaking, Abingdon, Oxfordshire OX14 3EA, U.K.
*Politecnico di Torino, C.so Duca degli Abruzzi 24, 10129 TORINO; porcelli@polito.it

INTRODUCTION. We discuss magnetic reconnection in collisionless regimes, where electron inertia is responsible for the decoupling of the plasma motion from that of the field lines. These regimes have become relevant in high temperature laboratory plasmas. For example, sawtooth relaxations at JET occur on a time scale shorter than the average collision time. The linear theory of m=1 modes has been recently extended to experimentally relevant regimes [1]. The conclusion from linear theory is that these modes can remain virulent at high temperature, with an initial growth rate, γ_L, which compares favourably with that observed in the experiments. Specifically, it was found that $\gamma_L \sim \omega_A d$ for $d > \rho$; $\gamma_L \sim \omega_A d^{1/3} \rho^{2/3}$ for $d < \rho$, where $d = d_e / r_s$, with $d_e = c/\omega_{pe}$ the inertial skin depth and r_s the q=1 radius; $\rho = \rho_i / r_s$, with ρ_i the ion (sound) Larmor radius; and $\omega_A = L_x / v_A$ is the Alfven frequency.

Since the linear theory breaks down for very small magnetic island widths, a nonlinear analysis is called for. Recent nonlinear studies [2,3], which assumed that collisionless magnetic reconnection evolves according to a Sweet-Parker process, gave contraddicting results.

In this paper, we analyze the behavior of a collisionless, 2-D fluid slab model in the limit $\rho/d \to 0$. Our main result is that, when the island size is larger than the linear layer but smaller than the equilibrium scale length, the reconnection rate exhibits a quasi-explosive time behaviour, during which a current density sub-layer narrower than the skin depth is formed [4].

THE MODEL. The equations we solve are

$$\partial_t U + [\varphi, U] = [J, \psi] \qquad \text{vorticity equation} \qquad (1)$$

$$\partial_t F + [\varphi, F] = 0 \qquad \text{inertial Ohm's law} \qquad (2)$$

where $[A,B] \equiv \mathbf{e}_z \cdot \nabla A \times \nabla B$, with $\boldsymbol{e}_z$ the unit vector along the ignorable z direction ($\partial_z = 0$), φ is the stream function, $\mathbf{v} = \mathbf{e}_z \times \nabla\varphi$ is the fluid velocity, ψ is the magnetic flux function, $U = \nabla^2\varphi$ is the *fluid vorticity;* $J = -\nabla^2\psi$ is the *current density;* $F \equiv \psi + d^2 J$ is the *z-canonical momentum.* Eq. (2) implies $dF/dt = 0$: F is conserved on moving fluid elements. The ***boundary conditions*** are *periodic.* The co-ordinates x and y vary in the intervals $x \in [-L_x, L_x]$ and $y \in [-L_y, L_y]$, with the slab aspect ratio $\varepsilon \equiv L_x/L_y < 1$. The magnetic field is $\mathbf{B} = B_o \mathbf{e}_z + \nabla\psi \times \mathbf{e}_z$, B_o =constant. All quantities are dimensionless, with $L_x = \pi$ and $\tau_A = (4\pi\rho_m)^{1/2} L_x / B_y$ determining the length and time scale normalisation. At ***equilibrium:*** $\varphi_o = U_o = 0$, $J_o = \psi_o = \cos x$, and $F_o = (1+d^2)\psi_o$. The ***initial conditions*** are the equilibrium plus a small tearing-parity perturbation of the form $(\varphi, \delta\psi) = \mathrm{Real}\left\{[\varphi_L(x), \delta\psi_L(x)] e^{\gamma t + iky}\right\}$, with $k = m\varepsilon$ and m an integer number. In the limit $d << L_x$, the solution of the linearized system can be obtained analytically using asymptotic matching techniques. For $0 < k^2 \le 1$, the logarithmic jump of $\delta\psi_L$ across the reconnecting layers is

$$\Delta' = 2\kappa \tan(\kappa\pi/2), \qquad \kappa \equiv \left(1 - k^2\right)^{1/2} \qquad (3)$$

We are interested in the *large-*Δ' regime, defined by

$$\Delta' d \ge 1 \quad \Rightarrow \quad \text{macroscopic convection cells, } L_{cell} \sim L_x. \qquad (4)$$

which can be obtained for low values of m and $\varepsilon^2 << 1$ such that $\Delta' \sim (8/\pi k^2)$. In this regime, *the structure of the stream function is macroscopic,* with $\varphi_L \approx \varphi_\infty \operatorname{sign} x$, $\varphi_\infty \equiv (\dot{\gamma}/k)\psi_\infty$, everywhere except in narrow layers near the reconnecting surfaces. The current channel in the linear stage has a width $\delta_L \sim d$. The linear growth rate is $\gamma_L \approx kd$.

NUMERICAL SOLUTION. The system of Eqs. (1,2) is solved numerically with a pseudospectral code truncated to 1024×64 (x,y) components. We concentrate on the ***early nonlinear phase,*** specified by the inequalities

$$d < w < 2L_x \qquad (5)$$

where w is the magnetic island width. An important consequence of the inertial Ohm law is that the value of F at $x = 0$ is frozen to its initial value, i.e. $F(x=0, y, t) = F_o(x=0) = 1 + d^2$. The solution shown in Figs. 1-4 has been obtained for $\varepsilon = 0.5$ and $d/(2L_x) = 0.04 \Rightarrow d\Delta' \approx 2.03$.

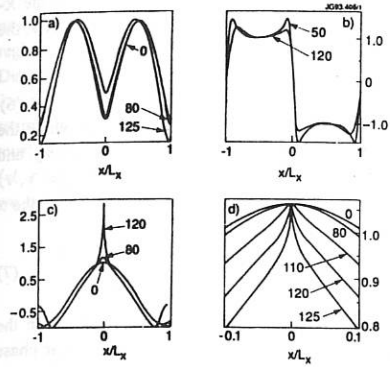


Fig. 1. *Cross sections of a) normalized* $\delta\psi$*; b) normalized* v_x*; c) J; d) F versus x at* $y = 0$ *and various times, indicated by arrows.*

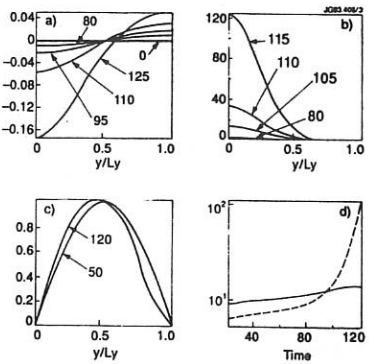


Fig. 2. *Cross sections of a)* $\delta\psi$*; b)* $\partial^2 F/\partial x^2$*; c) normalized* v_y *versus y at* $x = 0$*. Also, d) time dependence of the logarithm of the inverse scale lengths* δ_φ^{-1} *(solid line) and* δ_J^{-1} *(broken line).*

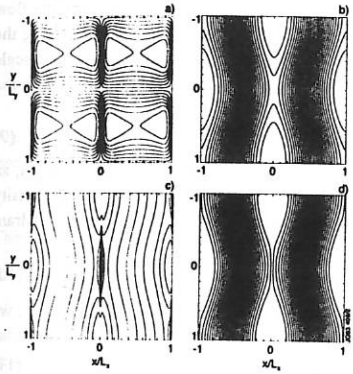


Fig. 3. *Contour plots at t=120: a)* φ*; b)* ψ*; c)* J*; d)* F*.*

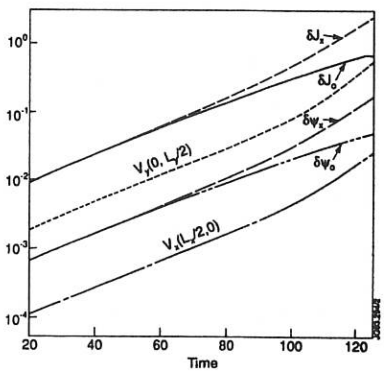


Fig. 4. *Time dependence of* $\delta\psi$ *and* δJ *at the X- and O-points, of* $v_x(-L_x/2,\ 0)$ *and of* $v_y(0,\ L_y/2)$.

RELEVANT PHENOMENOLOGY. The linear phase conventionally lasts until $t \sim 80$, when the magnetic island reaches a width of order d. For $t > 80$, the width of the profile of v_x, $\delta_\varphi \equiv (v_x)_{x=L_x/2} / (\partial_x v_x)_{x=0}$, as well as that of $\delta\psi$, remain of the order of the skin depth (Fig. 1a,b and Fig. 2d). Therefore, the convection cells retain approximately their linear shape well into the nonlinear phase (Fig. 3a). By contrast, the current density profile (Fig. 1c) develops a sub-layer whose width around the X-point, $\delta_J \equiv \left(\partial_x^2 \delta J / \delta J\right)^{-1/2} < d$, keeps shrinking with time (see also Fig. 2d). This sub-layer is also visible in the profile of F across the X-point (Fig. 1d). The contraction of this sub-layer is extremely rapid in time, as shown by the graph of $\partial^2 F/\partial x^2$ versus y for $x = 0$ and several times in Fig. 2b. Note the development of a current sheet around the reconnection line (Fig. 3c).

Also, note the preservation of the topology of the isolines of F (Fig. 3d). Finally (Fig. 4) the mode growth remains very rapid throughout the simulation. Indeed, the growth of φ, as well as that of $\delta\psi$ and δJ at the X-points, accelerate in the early nonlinear phase, which is symptomatic of an explosive behaviour (eventually, the mode growth slows down when w approaches L_x).

ANALYTIC TREATMENT. The numerical simulations suggest the following *ansatz:*

$$\varphi(x,\ y,\ t) = \mathrm{v}_o(t)g(x)h(y) + u(x,y,t) \tag{6}$$

where $h(y) \sim k^{-1}\sin(ky)$, $g(x) \sim \varphi_L(x)/\varphi_\infty$ contains the linear scale length d and $u(x,y,t)$ develops the rapid scale length $\delta(t) \sim \delta_J$ observed in the numerical simulation. The relevant ordering is $u << \mathrm{v}_o$ and $\partial_x u \sim \mathrm{v}_o \partial_x g$. Integration of the collisionless Ohm's law gives $F = F_o(x_o)$, where $x_o(x,\ y,\ t) = x - \xi(x,\ y,\ t)$ is the initial position of a fluid element situated at (x,y) at time t and ξ is the displacement along the x direction defined by the equation $d\xi/dt = \mathrm{v}_x$, $\xi(t=-\infty) = 0$. At $y = 0$,

$$-\int_{x_o}^{x} dx'/g(x') = \int_{-\infty}^{t} \mathrm{v}_o(t')dt' \equiv \lambda(t). \tag{7}$$

The function $\lambda(t) > 0$ represents the amplitude of ξ outside the reconnection layer, where $g(x) \approx 1$. In the linear phase, $-\psi_\infty \approx \lambda < d$. When $\lambda > d$, the magnetic island width $w \sim 2\lambda$, so that the early nonlinear phase can also be characterised by the inequality $d < \lambda < L_x$, or alternatively $t_0 < t < t_D$, with $\lambda(t_0) \sim d$ and t_D the characteristic turnover time of the macroscopic eddies in Fig. 3a. Inverting equation (4) in the limit $d < \lambda < L_x$, we obtain $x_o = x_o(x,\ t)$, which depends on the time-dependent scale length

$$\delta(t) \equiv d\exp\left[-\lambda(t)/d\right]. \tag{8}$$

Thus we see that near the X-point along the x direction, $F(x_o)$ (and hence J) varies over a distance $\delta(t)$ which becomes exponentially small in the ratio λ/d. Conversely, F flattens over a distance $|x| \sim \lambda$ around the O-point. The formation of a sub-layer is the combined result of the conservation of F on each fluid element and the flow pattern around the X-point, which acts to increase the local curvature of the F profile (Fig. 1d). Integrating the equation $\psi + d^2 J = F$, where $J \approx -\partial_x^2 \psi$, we find that ψ has an integral structure such that any fine scale variation of F is smoothed out over a distance $\sim d$. Asymptotic evaluation of ψ at the X- and O-points in the early nonlinear phase gives

$$\psi_X \equiv \psi(0,0,t) \sim 1 - \tfrac{1}{2}\lambda^2(t), \quad \psi_O \equiv \psi(0,\pm L_y,t) \sim 1 + \mathcal{O}\left(d^2\right) \tag{9}$$

Now set $F = F_o(x) + \delta F$. Then, $\delta\psi + d^2\delta J = \delta F$, and at $x = 0$, where $\delta F = 0$, we find $\delta J = -\delta\psi/d^2$. Thus, an asymmetry develops in the values of $\delta\psi$ and of J between the X- and O-points. The spike of the current density at the X-point has an amplitude $\delta J_X \sim 0.5(\lambda/d)^2$. Integrating the vorticity equation over the quadrant $S: \left[0 \le x \le L_x, 0 \le y \le L_y\right]$ gives

$$\partial_t \int_S U dx dy = \oint_C J d\psi. \tag{10}$$

where C is the boundary of S. With the ansatz (6), and neglecting corrections $\mathcal{O}\left(k^2 d^2\right)$ contributed by $\partial_y^2\varphi$, we find

$$\partial_t \int_S (\partial_x^2 \varphi) dx dy \approx -\left(4c/k^3 d\right) d^2\lambda/dt^2, \tag{11}$$

where $c > 0$ is a factor of order unity, which depends weakly on time (e.g. $1 \le c \le 1.4$ in Fig. 2d). The dominant contribution from the r.h.s. of Eq. (10) is

$$\oint_C J d\psi \approx \delta\psi_X - \delta\psi_O - \left(\delta\psi_X^2 - \delta\psi_O^2\right)/2d^2 \tag{12}$$

Finally, using an interpolation formula between the linear and early nonlinear limits of the r.h.s. of (12), we obtain an equation for the evolution of $\hat{\lambda}(t) \equiv \lambda(t)/d$:

$$d^2\hat{\lambda}/d\hat{t}^2 \approx \hat{\lambda} + c_2\hat{\lambda}^4 \tag{13}$$

where $\hat{t} \equiv \gamma_L t$ and $c_2 \approx 1/16 c > 0$ can be taken constant. The solution is $\hat{\lambda}(\hat{t}) = \left[\left(1-\alpha\right)/\left(1-\alpha\, e^{3t}\right)\right]^{\frac{1}{3}} e^t$, where $\alpha = \beta - \left(\beta^2 - 1\right)^{1/2}$, $\beta = 1 + 5/c_2$, and we have chosen the time origin so that $\hat{\lambda}(0) \equiv 1$. Thus, once the early nonlinear regime is entered, $\lambda(t)$ accelerates and reaches a macroscopic size over a fraction $\sim \ln\left(\alpha^{-1/3}\right)$ of the linear growth time. Eventually, we can expect this quasi-explosive growth to cease as λ approaches L_x.

DISCUSSION AND CONCLUSIONS. Collisionless reconnection in regimes where the instability parameter Δ' is large and global convection cells develop does not follow the standard Sweet-Parker scenario [5-7]. In

this context, we note a fundamental difference in the nonlinear flow pattern between the collisionless case (Fig. 3) and the resistive case (Fig. 5). The Sweet-Parker scenario applies to the regime $\eta^{1/2} >> d$, where η is the normalized resistivity (inverse Reynolds' number). It is of interest to study the limit $\eta^{1/2} << d << \eta^{1/3}$. In this regime, the linear phase is dominated by exponential evolution with the resistive growth rate $\gamma_L \sim \eta^{1/3}\omega_A$. During an initial nonlinear phase, where $\eta^{1/3} < \lambda < \eta/d^2$, the displacement λ grows algebraically in time, $\lambda \sim \eta t^2$, while the width of the current channel shrinks from $\delta_L \sim \eta^{1/3}$ to $\delta \sim (\eta/\lambda)^{1/2}$. This initial nonlinear regime is consistent with Sweet-Parker. When $\lambda \sim \eta/d^2$, also $\delta \sim d$. Therefore, the initial nonlinear behavior must change for $\lambda > \eta/d^2$, as for these values of λ the current in the layer is distributed mostly over a distance $\sim d$, independently of λ. Assuming that the formation of the current spike (cf Eq. 10) is impeded (see below), we can expect a resumption of exponential growth in this later nonlinear phase, with $\lambda \propto \exp(d \cdot t)$.

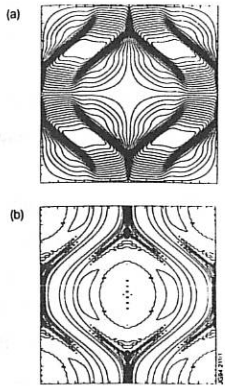


Fig. 5 *Contour plots of a) the stream function* φ *and b) the current density* J *in the resistive case.*

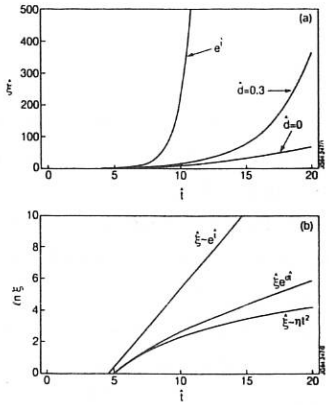


Fig. 6 *Time evolution of the normalized displacement* $\hat{\xi} = \lambda/\eta^{1/3}$ *in the regime* $\eta^{1/2} << d << \eta^{1/3}$*: a) linear plot; b) semi-log plot.*

This behavior can be summarized by the following phenomenological equation for $\xi \equiv \lambda/\eta^{1/3}$:

$$d\hat{\xi}/d\hat{t} = \left[(1+\hat{d}^2\hat{\xi})/(1+\hat{\xi})\right]^{1/2}\hat{\xi} \qquad (14)$$

where $\hat{t} = \eta^{1/3}t$ and $\hat{d} = d/\eta^{1/3}$. The numerical solution of Eq. (14) is shown in Fig. 6. The growth eventually saturates when the displacement reaches a macroscopic size ($\lambda \sim L_{cell}$). One expects that the current spike will be limited by effects not taken into account by the present analysis. Such effects may include collisions (most notably, electron viscosity), velocity-space instability associated with the current density gradient, 3-D effects, etc. Further work needs to be done to determine the relevant effects for interesting applications. While the current spike is being formed, the reconnection rate exhibits a quasi-explosive time behavior. Physically, the flow rotation accelerates following the intensification of the electromagnetic torque $\oint_C \mathbf{J}\times\mathbf{B}\cdot d\mathbf{l} = \oint_C J d\psi$ in the early nonlinear regime. This torque is mainly contributed by the average $J_z B_x$ force between the X- and O-points within a magnetic island.

In conclusion, we believe that the inclusion of the electron inertial term in Ohm's law opens the possibility to understand the rapidity of relaxation processes observed in low collisionality plasmas.

REFERENCES [1] F.Porcelli, Phys. Rev. Lett. **66**, 425 (1991). [2] J.Wesson, Nuclear Fusion **30**, 2545 (1990). [3] J.F.Drake and R.G.Kleva, Phys. Rev. Lett. **66**, 1458 (1991). [4] M. Ottaviani and F. Porcelli, Phys. Rev. Lett. **71**, 3802 (1993). [5] P.A.Sweet, in *Electromagnetic Phenomena in Cosmic Physics*, ed. by B.Lehnert (Cambridge University Press, 1958), p. 123. [6] E.N.Parker, J. Geophys. Research **62**, 509 (1957). [7] B.B.Kadomtsev, Fiz. Plasmy **1**, 710 (1975) [Sov. J. Plasma Phys. **1**, 389 (1975)].

Self-consistent Equilibrium in a Cylindrical, Dissipative Reverse Field Pinch

S.C. Guo[1], C. Lo Surdo[2], R. Paccagnella

Istituto Gas Ionizzati del CNR, EURATOM-ENEA-CNR Association
Padova, Italy
[1]Dipartimento di Ingegneria Elettrica, Universita' di Padova, Italy
[2]Associazione EURATOM-ENEA sulla Fusione, C.R.E.,
Frascati, Roma, Italy

Introduction

One of the authors (C.L.S) recently proposed a dissipative model to self-consistently solve the equilibrium problem in a free-boundary plasma column under cylindrical symmetry [1].

In the present paper, on one hand the problem is strongly specialized to circular symmetry and to Ohm's and Fourier's laws without off-diagonal contributions; on the other hand, it is generalized by adding a dynamo effective electric field $\mathbf{E}_d$ in Ohm's law, based on the standard turbulent model [2]. This seems appropriate enough to study RFP equilibria, since it is well known that a stationary and cylindrically symmetric RFP is incompatible with a classical Ohm's law. Reasonably, only numerical solutions are expected to be accessible in general; but the further simplified problem with scalar and constant electric resistivity η and constant dynamo coefficient α ($\mathbf{E}_d = \alpha\,\mathbf{B}$) can be solved analytically by elementary means.

The model

In the following we shall consider a stationary, cylindrically and circular symmetric plasma configuration bounded by a conductive shell of radius a. The full model is described as follows:

$$\begin{cases} \nabla\cdot(\rho\,\vec{v}) = 0 & 1_1 \\ \vec{j}\times\vec{B} = \nabla p & 1_2 \\ \vec{E}+\vec{v}\times\vec{B} = \vec{H}\cdot\vec{j} - \alpha\vec{B} & 1_3 \\ \vec{H} = \eta_{//}\,\hat{B}\,\hat{B} + \eta_{\perp}\left(1-\hat{B}\,\hat{B}\right) & 1_4 \\ \nabla\cdot\left(\frac{3}{2}p\,\vec{v}+\vec{q}\right) + p\,\nabla\cdot\vec{v} = (\vec{E}+\vec{v}\times\vec{B}+\alpha\vec{B})\cdot\vec{j} & 1_5 \\ \vec{q} = -\lambda_{\perp}\,\nabla T & 1_6 \end{cases}$$

where v is the velocity, ρ is the mass density, **j** is the current density, **B** is the magnetic field, p is the plasma pressure, T the temperature and $\eta_{\parallel}$, $\eta_{\perp}$, $\lambda_{\perp}$ are the parallel and perpendicular electric resistivity and the perpendicular thermal conductivity, respectively. Note that, because of the symmetry assumptions and the stationarity condition, the electric field can be written as:

$$\vec{E} = \nabla\Phi, \qquad \Phi = U z + \phi$$

with U = const. and ϕ independent of z, while the magnetic field is decomposed as:

$$\vec{B} = f\,\hat{z} + \hat{z} \times \nabla\Psi$$

with f, Ψ independent of z, Ψ being the poloidal flux. We assume also that the temperature is constant along the magnetic surface, so that $\mathbf{B}\cdot\nabla T = 0$.

The velocity field decouples (with $v_r = 0$) and after some lengthy but straightforward algebra [1], the following set of equations results:

$$\begin{cases} d_r \Psi = \chi & 2_1 \\ d_r \chi = \dfrac{-\chi}{r} - \dfrac{f}{\chi}\sigma - \dfrac{U}{\eta_{\perp}} & 2_2 \\ d_r f = \sigma & 2_3 \\ \sigma = \dfrac{Uf}{\chi\eta_{//}\eta_{\perp}}\left(\dfrac{\eta_{\perp}\chi^2 + \eta_{//} f^2}{\chi^2 + f^2} - \eta_{//}\right) - \dfrac{\alpha\chi}{\eta_{//}} & \\ d_r \delta = -\dfrac{\delta}{r}\left(1 + \dfrac{r}{\lambda_{\perp}} d_r \lambda_{\perp}\right) - \dfrac{(U - \alpha f)}{\lambda_{\perp}}\left(\dfrac{f\sigma}{\chi} + \dfrac{U}{\eta_{\perp}}\right) + \dfrac{\alpha\sigma\chi}{\lambda_{\perp}} & 2_4 \\ d_r T = \delta & 2_5 \\ d_r p = \dfrac{U\chi}{\eta_{\perp}} & 2_6 \end{cases}$$

where f is the axial component of the magnetic field and χ is the poloidal component. This 1st order ordinary differential system must be solved under the conditions:

$$\begin{cases} f(a) = f_w \\ \Psi(a) = 0 \\ \chi(0) = 0 \end{cases} \qquad \begin{cases} \delta(0) = 0 \\ T(a) = T_w \\ p(a) = 0 \end{cases}$$

This is a mixed two-point boundary value problem and some shooting technique has to be used to solve it numerically. Note that in Eq. 1_5 the effect of the dynamo term is

merely described by the term $\alpha\,\mathbf{j}\cdot\mathbf{B}$; this is certainly correct but very likely not exhaustive [3].

Analytical solution

Under the simplifying hypothesis, $\eta_{\|} = \eta_{\perp} = \eta$ = const. and α=const. the system of equation (2) can be solved analytically by elementary means, the energy equation being decoupled. The result is:

$$f(r) = -\mu\,\Psi(r) + f_w = B_0\,J_0(\mu r) + \frac{U}{\alpha} \quad , \quad \chi(r) = B_0\,J_1(\mu r)$$

$$\Psi(r) = \frac{B_0}{\mu}\left(J_0(\mu a) - J_0(\mu r)\right) \quad , \qquad p(r) = \frac{U}{\eta}\Psi(r)$$

where $B_0 = I/(2\pi a J_1(\mu a))$, $\mu = \alpha/\eta$ and I is the total zeta current.

We obtain a Bessel type solution for the magnetic field, similar to that derived by Taylor [4] on the basis of quite different arguments. Our solution, however, is not force-free because $U \neq 0$. The reversal of toroidal magnetic field is maintained by the dynamo effect.

Numerical results

The 1st order system of ordinary differential equation (2) has been solved numerically using a standard Runge-Kutta algorithm.

To determine the solution of the problem it is also clearly necessary to assign the relations which connect the plasma thermal and electrical conductivity to the unknowns, in particular to the temperature.

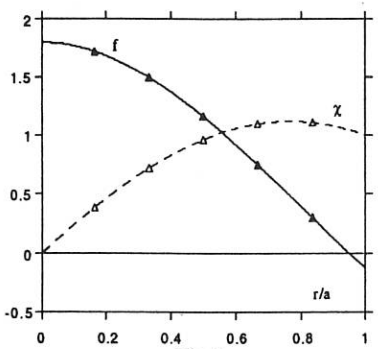


Fig.1

The analytical solution was used to test the numerical one (see Fig.1), the triangles represent the analytical solution. A more interesting case is obtained assuming the classical dependence of plasma resistivity on temperature, $\eta \approx \eta_0\,T^{-3/2}$ (and $2\,\eta_{\|} = \eta_{\perp}$), keeping constant α and $\lambda_{\perp}$. In this case energy and magnetic field equations are coupled, the numerical solution is shown in Fig.2.

The profiles reported in Fig.2 can be considered realistic as long as magnetic fields and pressure are concerned: the values of $F = f(1)/\langle f\rangle = -0.15$, $\Theta = \chi(1)/\langle f\rangle = 1.7$, $\langle\beta\rangle = \langle p/B^2\rangle = 0.04$, where $\langle\rangle$ is the cross section average, are in the range of the corresponding experimental measurements. The

feature which seems not realistic in Fig.2, is the high value for the edge temperature compared with the on axis value, i.e. the ratio $\tau = T(1)/T(0) = 0.27$ is too high.

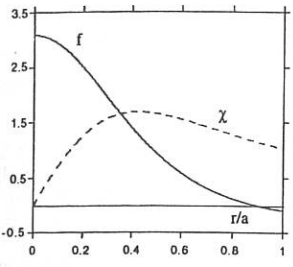
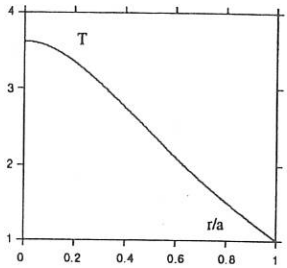


Fig.2



Experimentally this ratio, measured in the outside edge, is found to be quite low, $\tau < 0.1$. Therefore we attempted to find a combination of the parameters for which our model can simulate more satisfactorily the temperature profile.

It has been found that this can be obtained by lowering the value of the thermal conductivity, but in this way it is difficult to obtain values of $\tau < 0.2$. Moreover realistic values for F and Θ are obtained only at low $\langle\beta\rangle < 2\ \%$.

This difficulty is clearly connected to the strong non-linear coupling between temperature and magnetic field, but it is clear on the other hand, that a high degree of inaccuracy still affects our model, due to the too rough representation of $(\eta_{\parallel}, \eta_{\perp}, \alpha, \lambda_{\perp})$ as functions of the plasma state. We leave for the future the task of extending this research in the sense of above.

Moreover the symmetry assumptions and Eq. 1_1 pose severe constraint, in particular on the radial velocity component ($v_r = 0$). It is expected that relaxing these assumptions (in particular the circular symmetry) could produce more realistic profiles.

References

[1] C. Lo Surdo, "A consistent determination of the pressure/toroidal magnetic field profiles in Grad-Shafranov Equation", ENEA, RT/ERG/FUS/9408 (1994).

[2]H.K. Moffat, "Magnetic Field generation in electrically conducting fluids", Cambridge Un. Press, Cambridge (1978).

[3] K.F. Schoenberg, R.W. Moses, R.L. Hangenson, Phys. Fluids Vol.27, p.1671 (1984)

[4]J.B. Taylor, in Plasma Physics and Controlled Nuclear Fusion Research, Vol.1,p.161,IAEA Vienna (1975).

THE TIME EVOLUTION OF A SLIGHTLY NON–IDEAL, NEUTRAL PLASMA

J.W.Edenstrasser & M.M.Kassab*

Institute for Theoretical Physics, University of Innsbruck, Austria.

Abstract

The concept of a 'slightly non–ideal' plasma was first introduced by J.B.Taylor in the context of his famous theory of plasma relaxation in the following sense: a slightly non–ideal plasma relaxes towards a state of minimum magnetic energy under the constraint that the global magnetic helicity integral K and the total toroidal magnetic flux remain conserved. Based on a multiple time scale derivative expansion scheme, we have shown in a previous work, that Taylor's conjecture is indeed true on the MHD–collision (CMHD) timescale. In this paper, the invariance properties of the local mass integral M^Ψ are investigated on the ideal MHD (IMHD) and the CMHD timescales. It is shown that on the IMHD timescale both the local and the global mass integral are conserved. On the CMHD timescale it turns out that for an incompressible plasma the local and the global mass integral are still conserved, whereas for a compressible plasma only the global mass integral is conserved.

INTRODUCTION

It is well known that in the case of an ideal, perfectly conducting plasma, the motion of the plasma particle perpendicular to the magnetic field lines is not permitted since the field lines are frozen to the plasma. Consequently, the local mass integral, $M^\Psi=\int \rho \, d\tau^\Psi$ is thought to be constant for each flux tube, where ρ is the particle mass density and Ψ is the label of the magnetic surface. On the basis of Taylor's famous theory /1/, the constancy of M^Ψ represents an infinity of topological constraints. Clearly, because of these constraints a complete rearrangement of the plasma particles is not permitted in the ideal MHD limit. Let us now consider a slightly non–ideal plasma where the deviations from the ideal limit arise on account of resistivity effects. In the presence of a small but finite resistivity, however, the topological constraints associated with the magnetic field lines are no longer preserved, since the field lines may break and reconnect. In this case, it will be possible for the plasma particles to move across the field lines and to rearrange themselves within the whole volume such that the global mass integral M is constant. A similar argument has been used by K.Avinash /2/ to interpret the evolution of a slightly non–ideal, non–neutral plasma. On the other hand,

* *On leave from the Dept. of Eng. Physics, University of Cairo(Fayoum branch), Egypt.*

Y.Kondoh /3/ conjectured that, in the case of a slightly non–ideal, neutral plasma the local mass integral M^{Ψ} remains conserved.

In a previous contribution to this conference series /4/ we have, based on a multiple timescale derivative expansion scheme, shown that on the intermediate MHD–collision (CMHD) timescale, the plasma may be considered as slightly non–ideal. In this paper, the conjectures by K.Avinash and Y.Kondoh are analysed and the invariance properties of the local mass integral M^{Ψ} on the ideal MHD (IMHD) and the MHD–collision (CMHD) timescales are investigated.

BASIC EQUATIONS

Referring to the multiple timescale approach /5/, the dimensionless continuity equations on the IMHD and the CMHD timescale read

$$\textbf{IMHD}: \quad \frac{\partial n_0}{\partial t_1} + \nabla\cdot(n_0\vec{u}_0) = 0 \ , \tag{1a}$$

$$\textbf{CMHD}: \quad \frac{\partial n_0}{\partial t_2} + \frac{\partial n_1}{\partial t_1} + \nabla\cdot(n_0\vec{u}_1 + n_1\vec{u}_0) = 0 \ , \tag{1b}$$

where, n_k and $\vec{u}_k$ refer to the k^{th} order normalized particle density and normalized plasma velocity respectively, and t_1 and t_2 are related to the Alfven time (τ_A) and the collision time (τ_c), respectively. Furthermore the dimensionless equations for the time evolution of the volume element $d\tau^{\Psi}$, read

$$\textbf{IMHD}: \quad \frac{\partial \tau_0}{\partial t_1} = (\Omega_i \tau_A \delta)^{-1}(\vec{u}_0\cdot d\vec{s}_0) \ , \text{ and} \tag{2a}$$

$$\textbf{CMHD}: \quad \frac{\partial \tau_0}{\partial t_2} + \frac{\partial \tau_1}{\partial t_1} = -\left\{\vec{u}_0\cdot d\vec{s}_1 + \vec{u}_1\cdot d\vec{s}_0 - (\vec{G} + \vec{u}_0\times\nabla\mu)\cdot d\vec{s}_0\right\}(\Omega_i\tau_A\delta)^{-1} \ , \tag{2b}$$

where, $\vec{G}$ is a vector function defined by $\vec{\nabla}(\vec{G}\cdot\vec{\nabla}\Psi_0) = \vec{\nabla}\Psi_0\times\vec{\nabla}\left\{\frac{\partial\mu}{\partial t_1}\right\}$, and Ψ_0 is the zero order poloidal magnetic flux. In equation (2b) it is assumed that the system has already relaxed to its zero order equilibrium state [$\vec{J}_0 = a(\vec{x};t_1,t_2)\vec{B}_0$ and $\vec{u}_0 = \mu(\vec{x};t_1,t_2)\vec{B}_0$]. These equations are employed consistently with the boundary conditions /4/.

THE INVARIANCE PROPERTY OF THE LOCAL MASS INTEGRAL ON THE IMHD TIMESCALE

According to our expansion scheme /4/, we can write the local mass integral M^{Ψ} for each flux tube in the the following dimensionless form

$$M^{\Psi} = \int (n_0 + \delta n_1 + \delta^2 n_2)\,(d\tau_0 + \delta d\tau_1 + \delta^2 d\tau_2) \ . \tag{3}$$

where $d\tau^{\Psi} = (d\tau_0 + \delta d\tau_1 + \delta^2 d\tau_2)$, is a volume element enclosed between two neighbouring magnetic surfaces $\Psi = \Psi_0 + \delta\Psi_1 + \delta^2\Psi_2 = \text{const.}$, created by the magnetic

field ($\vec{B}_0 + \delta\vec{B}_1 + \delta^2\vec{B}_2$). The application of our multiple timescale expansion scheme, then yields to the order δ the following dimensionless equation for the time evolution of the local mass integral on the IMHD timescale;

$$\frac{\partial M^\Psi}{\partial t_1}\Big|_{IMHD} = \int \frac{\partial n_0}{\partial t_1}\, d\tau_0 + \int n_0 \frac{\partial \tau_0}{\partial t_1}. \tag{4}$$

By employing Eqs.(1a) and (2a), equation (4) takes on the following dimensional form;

$$\frac{\partial M^\Psi}{\partial t}\Big|_{IMHD} = \int \frac{\partial \rho_0}{\partial t}\, d\tau_0 + \int \rho_0 \frac{\partial \tau_0}{\partial t} = -\int \vec{\nabla}\cdot(\rho_0\vec{u}_0)\, d\tau_0 + \oint \rho_0\,(\vec{u}_0\cdot d\vec{s}_0) \equiv 0\,. \tag{5}$$

This means that on the IMHD timescale the local mass integral M^Ψ is conserved for each single flux tube. This result is consistent with Taylor's conjecture /1/ concerning the nature of the IMHD invariants of motion. If we assume that the plasma is surrounded by a rigid, perfectly conducting wall so that the plasma boundary is identical with the outermost magnetic surface, then naturally also the global mass integral M taken over the whole plasma volume is an invariant of motion.

THE INVARIANCE PROPERTY OF THE GLOBAL MASS INTEGRAL ON THE COLLISION TIMESCALE (CMHD)

First , we investigate the time evolution of the local M^Ψ for each single flux tube. Similarly, the next order in our expansion scheme yields for the time derivative on the collision timescale the following expression

$$\frac{\partial M^\Psi}{\partial t_2}\Big|_{CMHD} = \int\Big(\frac{\partial n_0}{\partial t_2} + \frac{\partial n_1}{\partial t_1}\Big)\, d\tau_0 + \int n_0\Big(\frac{\partial \tau_0}{\partial t_2} + \frac{\partial \tau_1}{\partial t_1}\Big) + \int \frac{\partial n_0}{\partial t_1}\, d\tau_1 + \delta\int n_1 \frac{\partial \tau_0}{\partial t_1}. \tag{6}$$

By employing equations (1a,b) and (2a,b), we then obtain $\frac{\partial M^\Psi}{\partial t_2}\Big|_{CMHD}$ in its dimensional form as follows:

$$\begin{aligned}\frac{\partial M^\Psi}{\partial t}\Big|_{CMHD} &= \int\Big(\frac{\partial \rho_0}{\partial t} + \delta\frac{\partial \rho_1}{\partial t}\Big)\, d\tau_0 + \int \rho_0\Big(\frac{\partial \tau_0}{\partial t} + \delta\frac{\partial \tau_1}{\partial t}\Big) + \delta\int \frac{\partial \rho_0}{\partial t}\, d\tau_1 + \delta\int \rho_1 \frac{\partial \tau_0}{\partial t} \\ &= -\delta\oint (\rho_0\vec{u}_1 + \rho_1\vec{u}_0)\cdot d\vec{s}_0 + \delta\oint \rho_0(\vec{u}_1\cdot d\vec{s}_0 - \mu\vec{B}_1\cdot d\vec{s}_0 - (\vec{G} + \vec{u}_0\times\vec{\nabla}\mu)\cdot d\vec{s}_0 + \\ &\quad \delta\oint \rho_0\vec{u}_0\cdot d\vec{s}_1 + \delta\oint \rho_1(\vec{u}_0\cdot d\vec{s}_0)\,.\end{aligned} \tag{7}$$

Assuming that the plasma has been relaxed to its zero order equilibrium state ($\vec{J}_0 = a(\vec{x};t)\vec{B}_0$ and $\vec{u}_0 = \mu(\vec{x};t)\vec{B}_0$), and employing the boundary condition /4/ , we obtain that

$$\frac{\partial M^\Psi}{\partial t}\Big|_{CMHD} = -\delta\oint \rho_0(\vec{G} + \vec{u}_0\times\vec{\nabla}\mu)\cdot d\vec{s}_0\,. \tag{8}$$

Thus, in the case of an ***incompressible*** plasma ($\vec{\nabla}\cdot\vec{u}_0 = 0$, $\mu = \mu(\Psi_0)$, $\vec{\nabla}\mu\uparrow\uparrow d\vec{s}_0$ and $[\partial\mu/\partial t_1] = 0$), it is obvious that, the right hand side of (8) will be identically zero. Thus one can conclude that, in the case of an ***incompressible*** plasma, the local mass integral M^Ψ is conserved on the MHD–collision (CMHD) timescale , whereas, it is no more an invariant of motion for a ***compressible*** plasma. On the other hand, by assuming that the plasma is surrounded by a perfectly conducting wall, it can be shown that the global mass integral M is an invariant of motion for both cases. Thus, it can be concluded that during the evolution of a ***compressible*** plasma on the CMHD timescale, plasma particle are allowed to move across the magnetic field lines and to rearrange themselves such that the global mass integral M remains constant. Earlier similar arguments have been used by Avinash /2/ to interpret the evolution of a slightly non–ideal, non–neutral plasma. Furthermore, it can be concluded that , the conjecture drawn by Y.Kondoh /3/ is only valid for an incompressible plasma.

SUMMARY

A multiple timescale approach has been applied to investigate the invariance property of the local and the global mass integrals. On the IMHD timescale, the local mass integral M^Ψ is conserved for each single flux tube. On the CMHD timescale, the invariance property of the local mass integral M^Ψ for each single flux tube is violated due to the compressibility of the plasma. Furthermore, it is concluded that, during the evolution of a compressible plasma on the CMHD timescale, a complete rearrangement of the plasma particles within the whole plasma volume is permitted such that the global mass integral M remains constant.

REFERENCES

/1/ J.B.Taylor, Phys. Lett. **33**, 1130 (1974).

/2/ K.Avinash, Phys. Fluids **B4** (8), 2658 (1992).

/3/ Y.Kondoh, J. Phys. Soc. Jpn. **54**, 1813 (1984).

/4/ J.W.Edenstrasser and M.M.Kassab, Proc. of the 20th EPS Conf. on Controlled Fusion and Plasma Physics, Lisboa 1993, Vol.IV, 1287.

/5/ J.W.Edenstrasser, Proc. Intern. Workshop on Plasma Physics, Pichl, 1992, Austria.

This work was supported in part by the Austrian Science Foundation (FWF) under contract P 8405 – PHY

Stabilization of Pressure-Driven External Modes in Tokamaks with a Resistive Wall and Toroidal Rotation

D. J. Ward[a] and A. Bondeson[a,b]
[a]Centre de Recherches en Physique des Plasmas,
Association Euratom–Confédération Suisse, EPFL, Lausanne
[b]Dept. of Technology, Euratom-NFR Association, Uppsala University, Uppsala, Sweden.

In recent work [1], we have shown that it is possible to completely stabilize low n, pressure-driven external modes in tokamaks by the combined effect of resistive walls and toroidal plasma rotation. We have used numerical computation to study the wall stabilization in toroidal geometry. The spectral codes MARS [2] and NOVA [3] have been modified to include a resistive shell in the vacuum region surrounding the plasma. Rigid toroidal rotation was modeled by making the resistive shell rotate with an externally imposed frequency $\omega_{\rm rot}$ while the equilibrium was static. The plasma was treated as ideally conducting and $\omega_{\rm rot}$ was some fraction of the sound frequency. Furthermore, the time-constant of the resistive wall, τ_w, was taken much larger than any ideal-MHD timescale.

Sonic rotation complicates the stability problem by coupling to sound waves, for which the MHD model predicts an unphysical resonant behavior. For realistic temperature ratios, the sound waves are strongly damped by ion Landau damping, and an accurate calculation requires a description that is kinetic along the field lines. However, reasonable approximations of the kinetic behavior can be obtained by adding dissipative terms to the fluid equations. We have applied three such modifications of the scalar-pressure ideal MHD equations. Two of these consist of adding a damping term for the Lagrangian pressure perturbations. The perturbed pressure is split into a convective and a Lagrangian part:

$$p_1 = -\vec{\xi}\cdot\nabla p_0 + p_{1L}, \qquad \text{where} \qquad \partial p_{1L}/\partial t = -\Gamma p_0 \nabla\cdot\vec{v} - \nu p_{1L} \tag{1}$$

The damping rate ν is taken either to be a fixed number or to represent a thermal diffusivity following the Hammet-Perkins [4] prescription, $\nu = \chi|k_\parallel v_{\rm thi}|$. As a third alternative, we use a term representing parallel viscosity in the equation of motion along the field lines so that $v_\parallel \equiv (\vec{B}_0/B_0)\cdot\vec{v}$ is computed from

$$\partial v_\parallel/\partial t = -(\vec{B}\cdot\nabla p)_1/B_0\rho_0 - \kappa|k_\parallel v_{\rm thi}|v_\parallel \tag{2}$$

When the pressure exceeds the stability limit with the wall at infinity, we find two classes of modes that can potentially be unstable: (a) one which has zero frequency in the frame of the plasma and hardly penetrates the resistive wall: the "plasma mode"; and (b) one which penetrates the wall and rotates slowly with respect to it (slip frequency = $O(\tau_w^{-1}) \ll \omega_{\rm rot}$): the "resistive wall mode." The resistive wall mode rotates with respect to the plasma at a frequency close to the imposed rotation frequency. A typical example of how the growth rates of the plasma and resistive wall modes depend on the wall radius d is shown in Fig. 1. The two modes are influenced in opposite ways by the wall distance—the plasma mode is *destabilized* as the wall is moved further from the plasma, while the resistive wall mode is *stabilized*.

The plasma mode rotates quickly (frequency $\approx \omega_{\rm rot} \gg \tau_w^{-1}$) with respect to the wall. It does not penetrate the wall and behaves as if the wall were ideal. The plasma mode is

unstable on the ideal MHD time scale when the wall radius exceeds the usual ideal MHD threshold for wall stabilization, $d_{\rm ideal}$. This marginal wall position approaches infinity at the conventional beta limit and decreases with increasing pressure.

The resistive wall mode becomes increasingly stable with increasing wall radius. This counter-intuitive behavior can be understood by a large-aspect-ratio calculation of Δ' at the resistive shell. We consider a magnetic perturbation in the vacuum, dominated by one poloidal harmonic m (assumed > 0). The perturbed magnetic flux function ψ satisfies $\nabla_1^2\psi = 0$ in the vacuum region, and the poloidal harmonic m is a linear combination of r^{-m} and r^m. The growth rate of the resistive wall mode is given by $\gamma = \tau_w^{-1} d\Delta'_w$, where $\Delta'_w = [\psi'(d_+) - \psi'(d_-)]/\psi(d)$. If we write the logarithmic derivative of ψ at the plasma edge $r = a$ as $(\psi'/\psi)_{r=a} = -(m/a)(1+z)$ (with $z = x + iy$, x and y real and $y \neq 0$ because of the rotation) a simple calculation gives Δ'_w:

$$d\Delta'_w/2m[1-(a/d)^{2m}] = z/(w-z) = [(wx - x^2 - y^2) + iwy]/[(w-x)^2 + y^2] \qquad (3)$$

where $w = 2/[(d/a)^{2m} - 1]$. In the case with no rotation ($y = 0$) and the plasma unstable in the absence of a wall ($x > 0$), Eq. (3) shows that the resistive wall mode is unstable ($\Delta'_w > 0$) for $a \leq d < d_{\rm ideal} \equiv a[1+2/x]^{1/2m}$. As the wall radius increases, $\Delta'_w \to \infty$ when $d \to d_{\rm ideal}$, and at this wall position, the resistive wall mode connects to the ideal MHD instability, which occurs for $d > d_{\rm ideal}$. In the region of ideal instability, plasma inertia is non-negligible and modifies $(\psi'/\psi)_{r=a}$ so as to keep $\Delta'_w \approx +\infty$. When the rotation frequency is finite, y is non-zero. This eliminates the zero in the denominator of Eq. (3). Consequently, Δ'_w remains finite and complex for all wall distances, and the resistive wall mode does not join the ideal instability. Rotation effectively separates the resistive wall mode from the plasma mode, and the growth rate of the resistive wall mode remains $O(\tau_w^{-1})$ for all d. The resistive wall mode is stabilized when $d_{\rm res} > a[1+2x/(x^2+y^2)]^{1/2m}$.

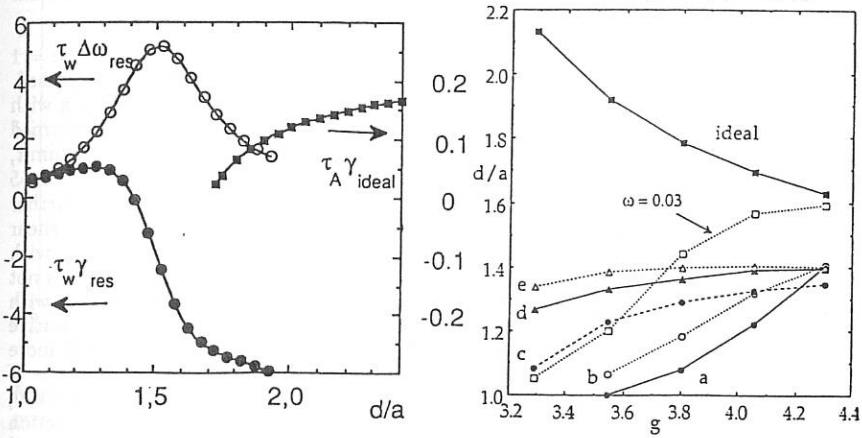


Figure 1: Growth rate $\gamma_{\rm res}$ and slip frequency $\Delta\omega_{\rm res}$ vs. wall radius for $\omega_{\rm rot}/\omega_A = 0.06$.
Figure 2: Marginal wall distance versus Troyon factor g for the plasma mode (marked "ideal") and the resistive wall mode using different assumptions. Curves (a)–(e) apply for $\omega_{\rm rot}/\omega_A = 0.06$. (a) and (b) give results for the pressure damping model, Eq. (1), with (a) $\nu/\omega_A = 0.025$ and (b) $\nu/\omega_A = 0.0025$. (c)–(e) give results for the parallel viscosity model Eq. (2) with (c) $\kappa = 0.1$, (d) $\kappa = 0.885$, and (e) $\kappa = 1.77$.

Thus, when a rotating plasma exceeds the pressure limit with the wall at infinity, there are two stability limits for the wall radius, $d_{\rm res}$ and $d_{\rm ideal}$. The plasma is stable when $d_{\rm res} < d < d_{\rm ideal}$, and this condition must apply for all n (except $n = 0$, which is usually stabilized by active feedback on the resistive shell time scale). We have computed stability limits, including rotation and resistive walls, for several MHD equilibria. Generally, the effect of wall stabilization is stronger when the pressure profile is broad so that the beta limit is set by external modes. An example is given in Fig. 2, which shows $d_{\rm ideal}$ and $d_{\rm res}$ versus normalized pressure g for $n = 1$ and rotation frequency $\omega_{\rm rot}/\omega_A = 0.06$. The computations were made for an equilibrium with JET shape (elongation = 1.7, triangularity = 0.3 and aspect ratio = 3) and a low pressure peaking factor, $p_0/\langle p\rangle \approx 1.7$. The current profile was adjusted to keep $q_0 = 1.2$ and $q_s = 2.55$. The resistive shell was conformal with the plasma boundary and we used different fluid approximations to show the dependence on model assumptions. Stability limits are shown for the $n = 1$ resistive wall mode using the model of Eq. (1) with $\nu/\omega_A = 0.0025$ and $\nu/\omega_A = 0.025$ and the parallel viscosity model Eq. (2) with $\Gamma = 1.5$ and $\kappa = 1.77$, 0.885 and 0.1. The Hammett-Perkins approximation with $\chi = 2/\pi$ gives a result almost identical to that for the pressure damping model with $\nu/\omega_A = 0.025$. Thus, the two pressure damping models of Eq. (1) give rather similar results, while the parallel viscosity model gives a stronger stabilizing effect. Furthermore, if the sound waves are eliminated by setting $\Gamma = 0$, the wall stabilization becomes much weaker. We conclude that the stabilization by resistive walls and rotation is sensitive to the dynamics of sound waves and an accurate theory must be kinetic along the field lines (e.g., drift kinetic).

Also shown in Fig. 2 is a comparison case with half the rotation frequency, $|\omega_{\rm rot}/\omega_A| = 0.03$ (and $\Gamma = 1.5$, $\kappa = 1.77$). The stabilization is much weaker for this lower rotation frequency and is almost lost when $\omega_{\rm rot}/\omega_A \leq 0.02$. Thus, there is a threshold behavior with respect to the rotation frequency. For this type of equilibrium, $\omega_{\rm rot}/\omega_A$ needs to be about 0.05 to give a significant stabilizing effect. This corresponds to a minimum rotation frequency of about 20% of the sound frequency at the $q = 2$ surface.

We find that when q_s is increased (holding the pressure profile fixed), $d_{\rm res}$ for $n = 1$ moves closer to the plasma boundary, and the maximum normalized beta is increased. Figure 3 shows the regions of stability with $q_s = 2.55$ and $q_s = 3.55$ for equilibria with identical pressure profiles and q_0 fixed at 1.20. The stability calculations are performed with the constant damping model and different damping coefficients. The stability limit, when expressed in terms of normalized beta, is higher at $q_s = 3.55$ than at $q_s = 2.55$ for both the resistive wall and the plasma mode. Increasing q_s to higher values further increases the stable g. We have also examined equilibria with negative central shear and high bootstrap fraction, similar to those discussed in [5]. For these equilibria, with peaked pressure profiles and only one integer-q surface ($q = 3$), wall stabilization is not very effective. However, even rather small modifications of the equilibrium profiles, with an increased pressure gradient close to the edge and a somewhat larger region of positive shear (to produce both a $q = 3$ and a $q = 4$ surface), make these equilibria much more susceptible to wall stabilization. Some results are shown in Fig. 4 for a sequence of equilibria with $q_0 = 2.5$ and $q_s = 4.1$. With a suitable wall position and $\omega_{\rm rot}/\omega_A = 0.10$, these equilibria remain stable to all ideal-MHD modes even at 100% bootstrap fraction and $\beta^* = 4.5\%$. Our study indicates that the $n = 1$ stability limit with rotation and resistive walls is rather sensitive to the detailed profiles near the wall.

CONCLUSION

In summary, we have shown that low n modes can be stabilized by resistive walls in combination with plasma rotation and that this wall stabilization leads to experimentally [illegible] beta limit. The effect is more pronounced for broad pressure pro-

files and high q_s. A numerical example with standard q-profile and broad pressure profile shows an increase in the beta limit by about 30% due to the wall stabilization. MHD stability analyses indicate that similar increases are observed experimentally in DIII-D [6]. Stabilization by resistive walls and rotation can give even more favorable results for advanced tokamak operation (non-monotonic q and $\approx$ 100% bootstrap fraction), but for such equilibria, global stability becomes sensitive to edge conditions.

ACKNOWLEDGMENT

This work was supported in part by the Swiss National Science Foundation.

REFERENCES

[1] A. Bondeson and D. J. Ward, Phys. Rev. Lett. **72** (1994) 2709.

[2] A. Bondeson, G. Vlad, and H. Lütjens, Phys. Fluids B 4 (1992) 1899.

[3] C. Z. Cheng and M. S. Chance, J. Comput. Phys. **71** (1987) 124; D. J. Ward, S. C. Jardin, and C. Z. Cheng, J. Comput. Phys. **104** (1993) 221.

[4] G. W. Hammett and F. W. Perkins, Phys. Rev. Lett. **64** (1990) 3019.

[5] C. Kessel, et al., Phys. Rev. Lett. **72**, (1994) 1212.

[6] A. D. Turnbull, et al., Int. Sherwood Theory Conf., Dallas, TX, 1994, paper 2B1.

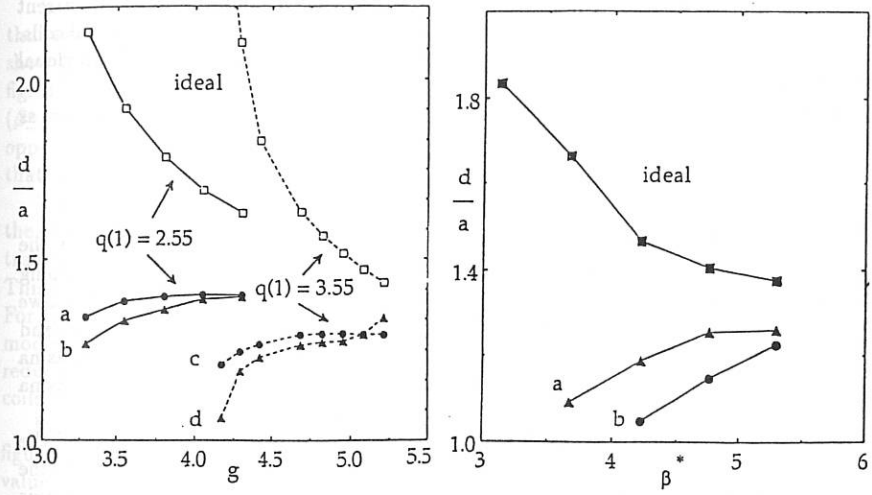


Figure 3: Marginal wall distance versus Troyon factor $\hat{g}$ for equilibria with the same pressure profile, with $q_s = 2.55$ and $q_s = 3.55$. (a)–(b) are the resistive wall modes for $q_s = 2.55$ with the pressure damping model, Eq. (1), with (a) $\nu/\omega_A = 0.025$ and (b) $\nu/\omega_A = 0.0025$. (c) and (d) are resistive wall modes for $q_s = 3.55$ equilibria with (c) $\nu/\omega_A = 0.025$ and (d) $\nu/\omega_A = 0.01$.

Figure 4: Stability boundaries for equilibria with negative central shear and high bootstrap fraction. Results are shown for (a) the pressure damping model, Eq. (1), with $\nu/\omega_A = 0.35$, and (b) the parallel viscosity model with $\kappa = 1.77$.

Ideal MHD Stability in Tokamaks with External Helical Windings

R. Moeckli, W. A. Cooper and F. Troyon
Centre de Recherches en Physique des Plasmas,
Association Euratom-Confédération Suisse,
Ecole Polytechnique Fédérale de Lausanne,
Lausanne, Switzerland

The ideal MHD stability properties of a tokamak with external L=3 windings are investigated with respect to local ballooning and Mercier modes and global external modes. The energy and particle confinement in standard tokamaks is known to improve with plasma current. Imposing external helical windings offers an additional knob to vary the toroidal plasma current independently of the value of the edge rotational transform. Therefore, we can reduce the plasma current and sustain a large fraction of the rotational transform with the helical windings or conversly increase the plasma current and correspondingly unwind the rotational transform with the current in the helical coils. The aim of this study is to try to investigate the effect of the winding on local and global ideal MHD stability.

We model the effect of $L = 3$ windings by prescribing the plasma-volume interface as

$$R = R_{00}(1) + R_{10}(1)\cos u + \delta\cos(2u - Nv) + \delta\cos(2u - 3Nv)$$
$$Z = R_{10}(1)\sin u + \delta\sin(2u - Nv) - \delta\sin(2u - 3Nv)$$

where $R_{00}(1)$ is the major axis, $R_{10}(1)$ is the minor axis, so that $A = R_{00}/R_{10}$ is the aspect ratio, u and v are the poloidal and toroidal angle-like respectively, δ is the shaping parameter of the helical coil currents and N is the periods number. The configurations we studied have the following parameters : $R_{00}(1) = 10$, $R_{10}(1) = 1$, $A = 10$, $\delta = 0.075$ and $N = 4$. The resulting magnetic field produces a triangular deformation of the plasma that only alters the external region of the plasma even when the bulk of the plasma (where the pressure concentrates) remains essentially a conventional tokamak.

In a previous study [1], we allowed the q-on-axis to approach 2 and investigated the inpact of external helical windings on access to the second region of MHD stability. In the work we present here, we have adjusted the plasma current profile to constrain q-on-axis to be approximately unity and consequently examine the first region of MHD stability. The equilibria were performed with the VMEC code [2].

We have applied the energy principle given by

$$\delta W_p - \omega^2 \delta W_k = 0$$

where

$$\delta W_p = \frac{1}{2}\int\int\int d^3x[C^2 + \gamma p|\nabla\cdot\xi|^2 - \mathrm{D}|\xi\cdot\nabla\mathrm{s}|^2]$$

to study the MHD stability of these configurations. The coefficients C^2 and D are described in Refs. [3] and [4]. Applying the ballooning mode transformation [5], we obtain

$$\frac{\partial}{\partial\theta}\left([C_p + C_s(\theta-\theta_k) + C_q(\theta-\theta_k)^2]\frac{\partial\chi}{\partial\theta}\right) + (1-\lambda)[d_p + d_s(\theta-\theta_k)]\chi = 0$$

The coefficients are given in Ref. [6]. The Mercier criterion can be derived from the asymptotic analysis of the ballooning mode equation [7]. A more detailed description for the global stability can be found in [6]. The TERPSICHORE code [8] has been used for all stability calculations. The pressure profiles are optimized to satisfy marginal stability to local modes uniformly across the plasma.

We have first examined a sequence of configurations in which we have kept the toroidal plasma current fixed. The pressure, iota and current profiles of the tokamak are shown in fig. 1. Adding helical windings modifies the iota profiles as in fig. 2. We obtain that the marginal β^* values (defined as $\beta^* = \frac{\sqrt{\iiint d^3x p^2}\sqrt{\iiint d^3x}}{\iiint d^3x B^2/2\mu_0}$) imposed by local ballooning/Mercier modes remain about the same. However, global external modes impose β^* limit in the configurations with external coils helical that are lower than that of the conventional axisymetric tokamak.

In the second sequence we have investigated, we have modified the current profiles so that each configuration has the same value of iota at the edge ($\iota(a) = 0.45$). Fig. 3 and 4 show the corresponding iota and current profiles. Using optimized pressure profiles (cf. fig. 5), we obtain that β^* increases slightly from $\beta^*_{tok} = 0.986\%$ (tokamak) to $\beta^*_- = 1.06\%$ (β^*_- means the marginal β^* value for the configuration with the current in the coils in the opposite sense than the toroidal plasma current). On the other hand, helical windings that add rotational transform make the marginal β^* value decrease to $\beta^*_+ = 0.804\%$.

The calculation of the β^* limit imposed by global modes were performed by rescaling the ballooning/Mercier optimized pressure profile for each case with fixed edge rotational transform. The $\beta^* = 0.905\%$ achieved in the axisymetric tokamak appears to be optimal. This limit decrease to $\beta^* = 0.65\%$ for the case in which the coils unwind the transform. For the case in which the transforms are additive, the β^* limit imposed by the global modes is $\beta^* = 0.75\%$. The plasma shaping that results from the external helical coils reduces the vacuum magnetic well regardless of the direction of the currents in these coils. This destabilizes the global external modes.

In conclusion, for local stability, the best marginal β^* value is obtained for a configuration that has higher total toroidal current than the tokamak. The marginal β^* value decreases for a lower total toroidal current. For global stability, the axisymetric configuration gives the best marginal beta value with $\beta^* = 0.905\%$. The problem of the transition and accessibility from the first stability regime with $q_0 \simeq 1$ to the second stability regime with $q_0 \geq 2$ still remains an open question that requires further investigation.

[1] **Cooper W. A. and Troyon F.**, *Proc. 20th EPS Conf. Lisbon*, 1993, Vol. 17C, Part IV, EPS (1993), IV-1283

[2] **Hirshman S. P. and Betancourt O.**, *J. Comput. Phys.* **96** (1991) 99.

[3] **Nührenberg J. and Zille R.**, in *Proc. of the Workshop on Theory of Fusion Plasmas*, EUR 11336 EN (1987), pp. 3-23. Editrice Compositori, Bologna.

[4] **Anderson D. V., Cooper W. A., Gruber R. and Schwenn U.**, *Scientific Comp-*

uting on Supercomputers II, (Editors: J. T. Devreese and P. E. Camp), Plenum Press, New York, 1990, p. 159.
[5] **Dewar R. L. and Glasser A. H.**, *Physics Fluids* **26** (1983) 3038.
[6] **Cooper W.A.**, *Plasma Physics and Controlled Fusion* **34** (1992) 1011.
[7] **Connor J. W., Hastie J. and Taylor J. B.**, *Proc. R. Soc. London,* **A365** (1979)
[8] **Anderson D. V., Cooper W. A., Gruber R., Merazzi S. and Schwenn U.**, *Int. J. Supercomp. Appl.* 4 (1990) 34.

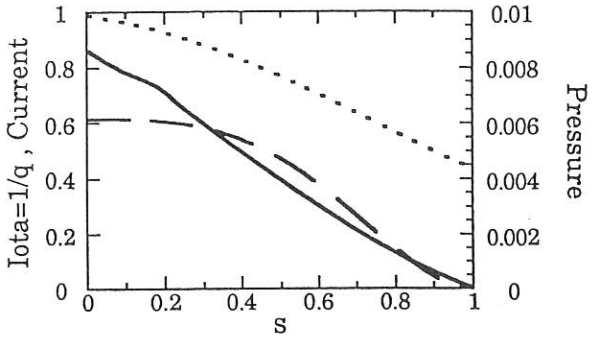


Fig. 1: Pressure (solid), iota (dotted) and current (dashed) profiles of the axisymetric tokamak configuration.

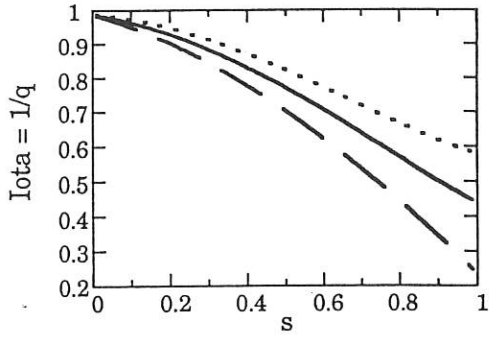


Fig. 2: Iota profiles for the sequence with constant toroidal plasma current. The solid line is the tokamak configuration. The dotted (dashed) curve corresponds to the configuration where the current in the helical coils is in the same (opposite) direction than the toroidal plasma current.

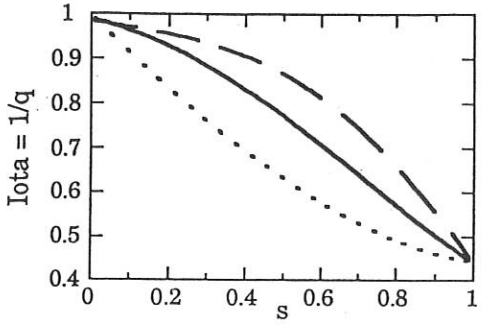


Fig. 3: The iota profiles for the sequence with constant iota value at the edge. The solid line is the tokamak configuration. The dotted (dashed) curve corresponds to the configuration where the current in the helical coils is in the same (opposite) direction than the toroidal plasma current.

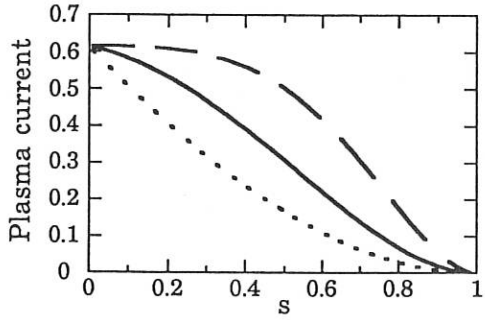


Fig. 4: The toroidal current profiles that correspond to the iota profiles of fig. 3. The solid line is the tokamak configuration. The dotted (dashed) curve corresponds to the configuration where the current in the helical coils is in the same (opposite) direction than the toroidal plasma current.

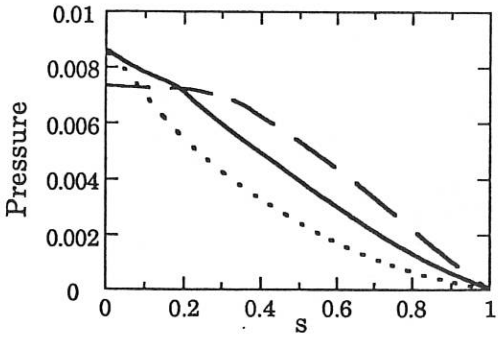


Fig. 5: The optimized pressure profiles for each configuration of the sequence with constant iota value at the edge. The solid line is the tokamak configuration. The dotted (dashed) curve corresponds to the configuration where the current in the helical coils is in the same (opposite) direction than the toroidal plasma current.

Tearing stability of an ITER shaped plasma

A. Pletzer, J. Manickam*, and D.A. Monticello*
Centre de Recherches en Physique des Plasmas
Association Euratom - Confédération Suisse
Ecole Polytechnique Fédérale de Lausanne
21 Av. des Bains, CH-1007 Lausanne, Switzerland
* *Plasma Physics Laboratory, Princeton University*
Princeton, New Jersey 08544, USA

1. Introduction

The focus of the present paper is to present calculations of the nonideal stability index Δ' using the toroidal axisymmetric code PEST-3 [1], which has recently been upgraded to treat plasmas with an up-down asymmetric cross-section. In the case of the ITER tokamak, this up-down asymmetry is due to the presence of a single magnetic divertor.

The code PEST-3 solves the ideal MHD marginal stability equation in the plasma bulk. The inner layers located at the $q = m/n$ rational surfaces appear as singularities. These are resolved as a separate problem involving nonideal physics. A variational principle is exploited to determine the coefficients of the recessive or "small" singular solutions normalized to the "large" singular solutions. Because we allow for the presence of $N > 1$ rational surfaces for a given toroidal mode number n, Δ' generalizes to a matrix Δ'_{ij} where $i, j = 1, 2 \cdots N$. For the sake of generality, we also compute the matching data A'_{ij}, B'_{ij} and Γ'_{ij} [2] which are associated with the coupling of tearing parity to interchange parity modes. These data are only important when Δ' is large or when $D_{I,i}$, the Mercier function at the rational surface $\psi = \psi_i$, differs significantly from the critical zero-β value of $-1/4$ for which the mode has a pure tearing parity (and for which the constant Ψ approximation is particularly adequate). These matching data are conveniently assembled to form the *outer region matching matrix*

$$\mathsf{D}' \equiv \tfrac{1}{2} \begin{pmatrix} \mathbf{A}' & \mathbf{B}' \\ \mathbf{\Gamma}' & \mathbf{\Delta}' \end{pmatrix}, \tag{1}$$

which condenses all the outer region information necessary to match the singular solutions to arbitrary inner layer solutions. It is apparent from the expression of D' in terms of small and large solutions, Eq.(46) in Ref. [3] or Eq.(99) in Ref. [1], that D' is symmetric for real singular solutions and that we must have $\mathsf{D}'^{\dagger} = \mathsf{D}'$ in the case of up-down asymmetry. This property is confirmed numerically.

To the outer region matching matrix D' corresponds, in the linear theory, an inner layer matching matrix $\mathsf{D}(\gamma)$. The matching condition then takes the form of a dispersion relation $\det[\mathsf{D}' - \mathsf{D}(\gamma)] = 0$, which is used to extract the growth rates γ's by scanning in the complex plane. In small β plasmas, we have $|\mathbf{A}'| >> |\mathbf{B}'| \sim |\mathbf{\Gamma}'| >> \mathbf{\Delta}'$, so that the dispersion relation can often be simplified to $\det[\mathbf{\Delta}' - \mathbf{\Delta}(\gamma)] = 0$. Furthermore it is well known that in the linear zero-β theory of tearing modes [4], $\Delta \sim \gamma^{5/4}$, so that the dispersion relation immediately gives the condition that $\mathbf{\Delta}'$ be negative definite for stability. This criterion remains valid in the collisionless limit [5,6], but becomes only

sufficient when pressure gradient and compressibility are accounted for [7] and when the resistive Mercier function $D_{R,i} < 0$. Rutherford [8] showed that in the nonlinear regime, the magnetic island width grows proportionally to Δ' and more recently, Waelbroeck [9] and Zakharov *et al.* [10] have shown that $\lambda_H \equiv \pi/\Delta'$ provides the basic matching condition to resolve the helical near equilibrium, magnetic configuration of the inner layer, which is thought to develop in the early nonlinear stage of sawtooth reconnection.

2. Δ' and linear resistive growth rates

We perform the matching of the tearing parity solutions arising in the ITER plasma shown in Fig. 1, to the resistive inner solutions of Glasser *et al.* [7]. In this case, we have the diagonal matrix

$$\Delta(\gamma) = \left(\frac{\Delta_i(\gamma)}{2\mu_i L_i^{2\mu_i}} \delta_{ij} \right), \tag{2}$$

and

$$\Delta_i(\gamma) = 2^{2\mu_i} \pi \frac{\Gamma(\frac{3}{4})}{\Gamma(\frac{1}{4})} \hat{Q}_i^{5/4} \left(1 - \frac{\pi D_{R,i}}{4\hat{Q}_i^{3/2}} \right) \tag{3}$$

as inner matching data defined in the inner layers $i = 1, 2 \cdots N$, where

$$\hat{Q}_i \equiv \gamma / Q_i \tag{4}$$

is the normalized growth rate, and $\mu_i \equiv \sqrt{-D_{I,i}}$ is assumed to be real by virtue of Mercier's criterion. Expressions for $D_{I,i}$, $D_{R,i}$, the characteristic growth rate Q_i and the layer width L_i are given by Eqs.(139)–(149) in Ref. [1]; they depend entirely on the equilibrium quantities evaluated at given flux coordinates. Recall that Q_i and the layer width L_i scale as the resistivity η to the power 1/3. A direct consequence of (2) and (3) plus the fact that D′ is Hermitian is that the growth rates always come as complex conjugate pairs.

The safety factor profile is monotonically increasing from $q_0 = 1.1$ to $q_a = 3.1$, yielding two rational surfaces, $m = 2/n = 1$ and $m = 3/n = 1$, which are located at 0.89% and 0.99% of the plasma boundary flux ψ_a, respectively. Figure 2 shows the convergence of the two eigenvalues $\lambda_{2/1}$ and $\lambda_{3/1}$ of the Δ' matrix. The boundary conditions applied on the displacement field are those of an infinitely conducting wall at the plasma surface ($b = a$), at distance $b = 1.2$ times the plasma boundary radius a and at infinity. The destabilizing effect of increasing b is particularly noticeable for the 3/1 tearing mode, which remains nevertheless stable (negative eigenvalue) even after complete removal of the wall. The 2/1 mode has a marginally positive eigenvalue $\lambda_{2/1} = 0.209$ for the fixed boundary case whereas $\lambda_{2/1} = 0.532$ for $b = 1.2a$ and $\lambda_{2/1} = 3.58$ for $b \to \infty$.

Due to finite pressure gradient effects ($D_{R,1} = -0.0027$), the instability only occurs when the eigenvalue exceeds a threshold Δ_c which increases as η decreases. This leads to complete stabilization for $\eta < \eta_c$, where η_c ranges from 10^{-6} to 10^{-9} depending on the boundary conditions. There is a second branch in the dispersion relation which gives a much smaller growth rate (not shown). As η decreases, this branch however merges to the dominant one to form two complex conjugate growth rates. The particular value of η where this takes place is made apparent by the abrupt rise of the imaginary part (only one complex root is shown).

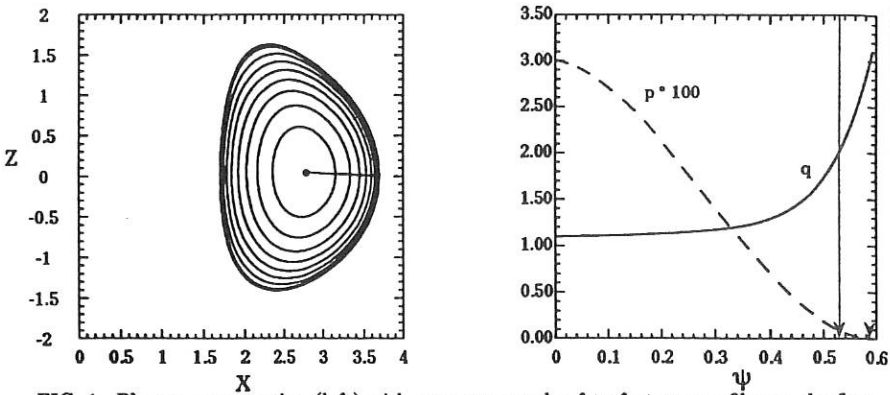


FIG. 1. Plasma cross-section (left) with pressure p and safety factor q profiles vs the flux coordinate ψ (right). The two vertical arrows indicate the positions of the $q = 2/1$ and $q = 3/1$ surfaces. The values for the inverse aspect ratio, the ellipticity, the triangularity and the average $\beta \equiv 2p/B^2$ are $\epsilon = 0.36$, $E = 1.43$, $T = 0.32$ and $< \beta >= 2.13\%$, respectively.

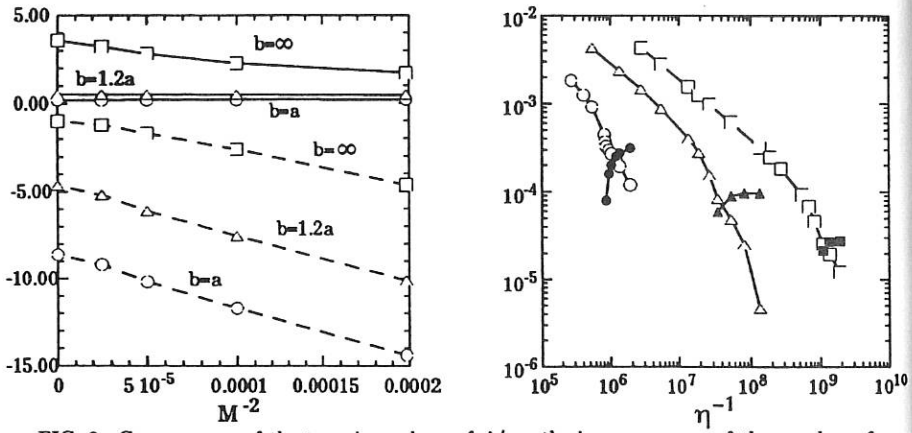


FIG. 2. Convergence of the two eigenvalues of Δ' vs the inverse square of the number of radial mesh nodes M (left) and dominant growth rates vs the inverse resistivity η (right). The growth rates are normalized to the Alfvén frequency. The boundary conditions are $b = a$ (circles), $b = 1.2a$ (triangles) and infinite vacuum (squares). Closed symbols refer to the imaginary part of the growth rates.

3. Summary

The latest PEST-3 version for plasmas with up-down asymmetric cross-section has been used to compute the outer region matching data of a two-rational surface ITER-shaped equilibrium. The code PEST-3 has previously been tested against a fully resistive code [1], but has not been applied to an up-down asymmetric plasma before. The convergence properties of the matching data suggest that the code is working properly.

Irrespectively of the boundary conditions applied at the plasma surface, the most interior rational surface $m = 2/n = 1$ is found to be unstable at moderate resistivity where $\gamma \sim \eta^{3/5}$ (the usual tearing mode scaling). As η approaches 10^{-6} to 10^{-9}, depending on the boundary conditions, finite pressure gradient effects become important and the growth rate becomes complex before being stabilized due to the threshold Δ_c in (3). Adopting typical ITER parameters: $R_0 = 9$ m, $a = 3$ m, $B_0 = 5$ T, $n = 2{\times}10^{20}$ m^{-3} and applying Spitzer's expression for the resistivity, one finds that the $\eta < 10^{-9}$ limit translates into requiring an electron temperature exceeding 1.6 keV in order to statisfy linear resistive stability. It should however be emphasized that this threshold is very sensitive to the local pressure profile at the rational surfaces: a flattening of the pressure induced by error fields, for instance, could remove this threshold so that the mode would remain, at least formally, unstable at any resistivity level. On the other hand, the growth rate would be so small at high temperature $\gg 1$ keV, that a one fluid, purely resistive description becomes inadequate.

REFERENCES

[1] A. Pletzer, A. Bondeson, and R. L. Dewar (1993). "Linear Stability of Resistive MHD Modes: Axisymmetric Toroidal Computation of the Outer Region Matching Data." LRP 487/93, CRPP-EPFL, 21 Av. des Bains CH-1007 Lausanne, Switzerland (submitted to J. Comp. Phys.).

[2] J. Manickam, R. C. Grimm, and R. L. Dewar, in *Energy Modeling and Simulation*, edited by A. K. et al. (North Holland, Amsterdam, 1983), pp. 355–359.

[3] A. Pletzer and R. L. Dewar, J. Plasma Phys. **45**, 427 (1991).

[4] H. P. Furth, J. Killeen, and M. N. Rosenbluth, Phys. Fluids **6**, 459 (1963).

[5] J. F. Drake and Y. C. Lee, Phys. Fluids **20**, 1341 (1977).

[6] F. Porcelli, Phys. Rev. Lett. **66**, 425 (1991).

[7] A. H. Glasser, J. M. Greene, and J. L. Johnson, Phys. Fluids **18**, 875 (1975).

[8] P. H. Rutherford, Phys. Fluids **16**, 1903 (1973).

[9] F. L. Waelbroeck, Phys. Fluids B **1**, 2372 (1989).

[10] L. E. Zakharov, B. Rogers, and S. Migliuolo, Phys. Fluids B **5**, 2498 (1993).

MHD LIMITS AND AXISYMMETRIC STABILITY OF DOUBLETS

L.Degtyarev, A.Martynov, S.Medvedev
Keldysh Institute of Applied Mathematics
Russian Academy of Sciences, Moscow

F.Troyon, L.Villard
Centre de Recherches en Physique des Plasmas
Association Euratom - Confédération Suisse
Ecole Polytechnique Fédérale de Lausanne

Abstract

MHD stability limits were studied for doublet plasma configurations using the equilibrium code CAXE and the stability code KINX [1]. Beta limits have been found against ballooning and n=1 external kink mode stability. For doublet plasmas in the TCV tokamak the beta limits are close to the values obtained for a plasma with a single magnetic axis and the same overall elongation. The current limit against kink modes is lower in doublets. But the maximal beta is obtained at almost the same value of the current.

Axisymmetric n=0 mode growth rates with resistive wall were obtained with the KINX-W code. A comparison shows that the axisymmetric stability of doublets is much better than that of a single axis plasma with the same overall elongation.

1 Equilibrium The equilibrium plasma boundary is chosen to obtain two magnetic axis equilibrium with prescribed profiles of the surface averaged toroidal current density I^* and $dp/d\psi$. The following parameterization is suitable to generate a boundary with indentations from both inner and outer sides:

$$r = R + a_i \cos(\theta + \delta_i \sin\theta)(1 - p_i \cos^2\theta), \quad z = Z + a\kappa_i \sin\theta, \\ i = 1 \quad 0 < \theta < \pi, \quad i = 2 \quad \pi < \theta < 2\pi. \tag{1}$$

The values of κ_1, δ_1 and κ_2, δ_2 can be varied independently thus controlling the elongation and the triangularity of the upper and lower parts of the plasma cross-section. The relation $a_1(1 - p_1) = a_2(1 - p_2)$ is needed to ensure the continuity of the shape.

For the profiles of I^* the following expression was chosen:

$$I^* = (1 - \psi^{j_1})^{j_2} + I_m, \tag{2}$$

where ψ is the normalized poloidal flux in each plasma subdomain with nested flux surfaces and I_m is chosen to ensure the continuity of I^* across subdomains boundaries.

To obtain a sequence of equilibria for β-limit computations we fix the profile of I^* and perform pressure gradient optimization to get the equilibrium marginally stable against ballooning modes. The β-limit for kink modes is obtained by rescaling the optimized $dp/d\psi$ profile until marginal stability is reached.

2 External kink limits The following plasma boundary parameters were chosen for up-down symmetric doublet configurations: $a/R = 0.65, \kappa = 1.25, \delta = 0.1, p = 0.8$, which gives the boundary aspect ratio $A = 3.47$ and total elongation $E = 2.89$. This shape fits into the TCV vacuum vessel (Fig.2a). The mantle outside separatrix was chosen pressureless and currentless ($I_m = 0$). The parameter j_2 was fixed and the plasma current varied by changing j_1 in equation (2). The value of q at the upper magnetic axis was set to 1.05 for all cases. In Fig.1a β-limits vs normalized current for $j_2 = 1$ are shown. Note that the definitions here are $\beta = 2\int p\,dV/B_{vac}^2$, $I_N = I_p(MA)/a(m)B_{vac}(T)$

and the integrals are over plasma volume without mantle. B_{vac} is the vacuum field in the plasma centre. The same is shown in Fig.1b for the case $j_2 = 2$ which corresponds to larger values of l_i. Maximum beta and current are somewhat higher in this case but the kink β-limit degradation is more pronounced when approaching the current limit.

The influence of the current in the mantle on the stability was studied by introducing $I^* = I_m(1-\psi)$ with $I_m = 0.1, 0.2$ and $j_2 = 1$ in plasma. The β–limits do not change much . But the current limit degrades with increasing I_m. In the table below limits in total current (I_{tot}) and current inside separatrix (I_{int}) are given.

I_m	0.0	0.1	0.2
I_{tot}	2.18	2.08	1.75
I_{int}	2.18	2.03	1.66

Comparing doublet plasmas (dt) with corresponding single–null plasmas inside separatrix taken alone (sn), it was found that the n=1 external kink β-limit in doublets is about 5% lower than in single–null plasmas. The difference in current limit is even smaller. In the table below the beta limits are given for three types of current profiles. I_{Ndt} is the normalized current at the beta limit for doublets.

j_1	j_2	I_m	β_{dt}	β_{sn}	I_{Ndt}
1	1	0.0	2.1%	2.2%	1.00
1	1	0.1	2.6%	2.75%	1.16
2	2	0.0	2.7%	2.8%	1.06

3 Up–down asymmetric doublets Two examples of up–down asymmetric doublet equilibria were considered. The first one was obtained using the parameterization (1) with $a_1/R = 0.65, a_2/R = 0.65, \kappa = 1.7, \delta = 0.1, p_1 = 0.85$ (Fig.2b). The current density profiles were $I^* = 1-\psi$ for the upper domain and $I^* = 0.3(1-\psi)$ for the lower domain. The flux outside separatrix is very small in this case (about 100 times smaller than inside the upper domain) and the separatrix closely follows the external boundary shape which has a low triangularity.

The second equilibrium boundary was obtained from the asymmetric "TCV-D" parameterization:

$$
\begin{aligned}
&r = R + a\cos(\theta + \delta\sin\theta - \lambda\sin 2\theta), \quad z = a\kappa\sin\theta,\\
&\kappa = 0.5(\kappa_1 + \kappa_2 + (\kappa_1 - \kappa_2)\sin\theta),\\
&\delta = 0.5(\delta_1 + \delta_2 + (\delta_1 - \delta_2)\sin\theta),\\
&\lambda = 0.5(\lambda_1 + \lambda_2 + (\lambda_1 - \lambda_2)\sin\theta),\\
&0 < \theta < 2\pi.
\end{aligned}
\tag{3}
$$

This shape with $a/R = 0.3, \kappa_1 = 3.7, \kappa_2 = 1.7, \delta = 0.5, \lambda = 0.2$ was indented from both inner and outer sides by $0.3a$ and a respectively (Fig.2c). The current density was $I^* = 1-\psi$ for both upper and lower domains.

The ballooning β–limit is higher for the second case of Fig.2c because of its more triangular boundary ($g = \beta/I_N = 2.75\%/0.76 = 3.6\%$ for Fig.2b vs $g = \beta/I_N = 3.5\%/0.81 = 4.3\%$ for Fig.2c; the values are computed over upper domains only, lower domains were kept force–free). The same holds for the kink limit ($g = 3.0\%$ vs $g = 4.2\%$). Again no substantial differences were revealed between the kink limits for doublets and single–null plasmas.

4 Axisymmetric stability A wall shape close to that of TCV vacuum chamber was chosen for n=0 stability studies (using the parameterization (3) with $a/R =$

$a_w/R_w = 0.34, \kappa = 2.7, \delta = 0.2, \lambda = 0.8$). Two versions of the KINX–W code were used to compute the growth rates of doublet and single axis equilibria surrounded by the resistive wall.

Four equilibria with $\beta = 0$ were compared : a symmetric doublet (Fig.2a) with $I^* = 1 - \psi, I_N = 1.15$, two asymmetric doublets Fig.2b and 2c with $I_N = 0.90$ and $I_N = 1.24$ and a single axis highly elongated equilibrium of "TCV–D" shape (Fig.2d) with $R/a = 3.67, \kappa = 3, \delta = 0.5, \lambda = 0.2, I^* = 1 - \psi, I_N = 2.07$.

The table below shows the instability growth rates in s^{-1} obtained assuming the plasma major radius R=0.88m and a resistivity/wall thickness ratio of 10^{-5}Ohm (the growth rates scale linearly with increasing the resistivity up to $5 \cdot 10^{-5}$ which is closer to the experimental value). The resistive growth rates for doublets (first two rows in

	sym. doublet (a)	asym. doublet (b)	asym. doublet (c)
doublet (1)	44	62	360
doublet (2)	28	ideally unstable	27
single top	43	62	800

the table) and for the corresponding single–null plasmas from the upper domains inside separatrix (single top) are close to each other in the two first cases where the separatrix is near the external boundary at the top. For the asymmetric doublet (c) the growth rates are higher due to a more triangular boundary which is not following the wall shape like in the two other cases. The stabilizing influence of the plasma outside the separatrix is considerable in this case and the growth rate for the single–null plasma is much higher than for the doublet.

A characteristic feature of n=0 stability of up–down symmetric doublets is the presence of two unstable modes [1]. The same is valid for the resistive wall modes: for the most unstable mode the displacements in the two domains inside the separatrix are mirror symmetric, the plasma is displaced mainly as a whole for the more stable mode. The growth rates of the two modes are close to each other for the symmetric doublet. For asymmetric doublets the two modes are mainly independent displacements of each domain inside the separatrix. For the asymmetric doublet (b) the plasma in the lower smaller domain is ideally unstable due to its relatively high elongation and large distance from the wall. For the asymmetric doublet (c) the mode in the lower domain is ideally stable and has a much lower resistive growth rate because its shape follows the wall more closely.

For the TCV wall position with $a_w/R_w = 0.34$ the highly elongated equilibrium is ideally unstable. Even for a wall with $a_w/R_w = 0.31$ the growth rate is much higher than for the doublets: $1300s^{-1}$.

5 Conclusions Comparisons of the β and current limits against external n=1 kink stability for doublets and for corresponding single–null plasmas inside the separatrix show that the limits are very close to each other. No substantial influence of the mantle on the stability was revealed.

The maximal β obtained for doublet configurations is almost the same as for plasmas having a single axis and the same overall elongation. The current limit for the doublet imposed by n=1 external kink mode appears to be lower by 30%. But the optimum β [2] is obtained at approximately the same current.

The $n = 0$ mode stability properties of doublet equilibria can be influenced by the plasma outside the separatrix. The displacements for the two unstable modes in asymmetric doublets are localized in either one or the other domain inside the separatrix. However the interaction between the plasma domains can be considerable. A comparison shows that the n=0 mode growth rate with resistive wall stabilization are much lower for doublets than for a single axis plasma with the same overall elongation.

Acknowledgement This work was partly supported by the Fonds National Suisse de la Recherche Scientifique.

References

[1] Medvedev S., Villard L., Degtyarev L.M., Martynov A., Gruber R., Troyon F. MHD equilibrium and stability of doublet configurations. 20th EPS Conf. on Controlled Fusion and Plasma Phys., Lisbon, Proc. Contrib. Papers vol.IV (1993) 1279

[2] Jardin S.C. *et al.*, MHD constraints for advanced tokamak operation Proc. 14th Conf. Plasma Phys. Controlled Nucl. Fusion Research, Würzburg, vol.2 (1992) 285

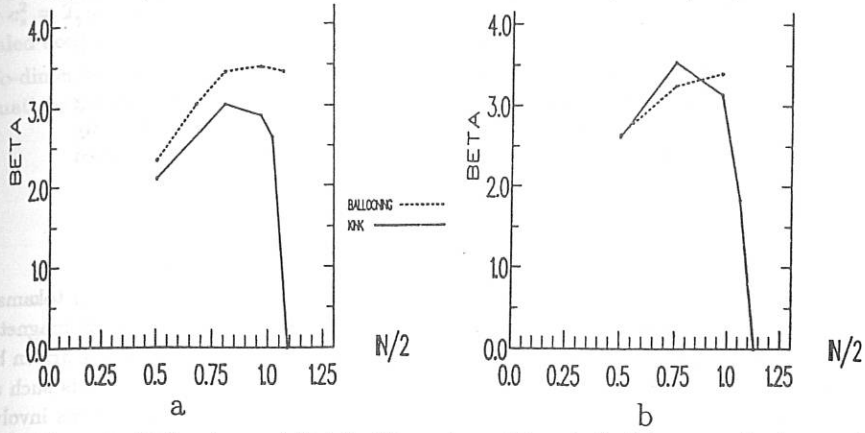


Figure 1: *Ballooning and kink limiting values of β vs half of the normalized current inside separatrix: (a) current density parameter $j_2 = 1$ (b) $j_2 = 2$.*

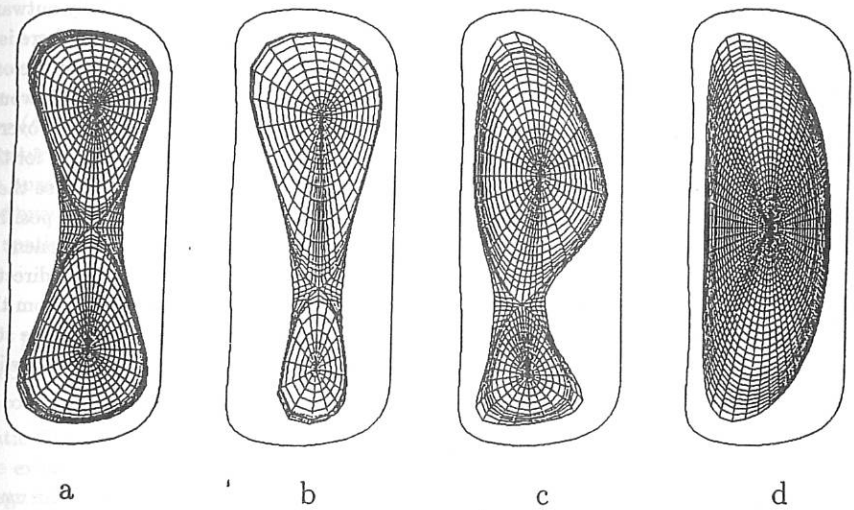


Figure 2: *Equilibrium grid adapted to magnetic surfaces inside the wall: (a) symmetric doublet (b) asymmetric doublet (c) asymmetric doublet (d) highly elongated single axis equilibrium.*

Electromagnetic Effects on Electron Fluid Drift Turbulence

B. Scott, Max-Planck-Institut für Plasmaphysik, Garching, Germany

Previous work on the physics of collisional drift-wave turbulence studied via high-resolution simulation is extended by re-incorporating all the effects of the attendant magnetic fluctuations. For typical edge parameters for Ohmic or L-mode tokamak discharges the effects of magnetic fluctuations on both the linear waves and the turbulence are minimal. Although there is a slight tendency to more strongly excite current fluctuations at very small scales, the effect of this is limited to constraining the numerics. Transport due to the magnetic fluctuations is directly computed, with the result that it is negligible compared to that caused by the ExB turbulence.

I. Introduction

One of the outstanding problems in the theory of anomalous transport in tokamak plasmas is the degree to which the transport is effected by electrostatic or electromagnetic mechanisms. In the most likely scenarios the transport results from turbulence driven by gradients in the background density and temperature, mediated by other effects such as finite resistivity or an inhomogeneous magnetic field. The turbulent fluctuations involve the electric and magnetic fields as well as the density and temperature, giving rise to a net flux in particles and energy which can be carried either through advection by ExB flow eddies or nonlinear divergences of parallel current and heat flux. For radially outward transport by ExB flow eddies the electrostatic component is sufficient, provided there is a positive average phase shift between fluctuations in the transported quantities on the one hand and fluctuations in the electrostatic potential on the other. The phase shift would be measured in the electron drift direction, parallel to $\nabla p \times \mathbf{B}$, and the average is over a flux surface. For a finite net transport by fluctuating magnetic fields it is necessary for the flux surfaces to be broken by turbulent magnetic field fluctuations, since otherwise there can be no angle-averaged parallel divergences. For this to occur there must be a positive average correlation between the parallel current fluctuation and the radial component of the fluctuating magnetic field. It is only recently that ExB transport has been directly measured in an experiment with the temperature fluctuation properly separated from the others [1], and measurements of similar quality for the electromagnetic transport are still lacking. It is of considerable interest, therefore, to study this question in detail with computations.

II. Electromagnetic Drift-Fluid Equations

The model equations follow from the Braginskii two-fluid equations [2] and the usual microturbulence ordering. Fluctuation activity is assumed to occur over a range of scales

about some average, Δ, for which $L \gg \Delta \gtrsim \rho_s$, where L represents profile scales and ρ_s is the drift-dispersion scale given by $\rho_s^2 = c^2 M_i T_e / e^2 B^2$. With the further simplification of cold ions, $T_i \ll T_e \equiv T$, the perpendicular velocities are given by the ExB and diamagnetic drift for electrons and the ExB and polarisation drifts for the ions. Fluctuations are scaled according to: $\delta_0 \tilde{\phi} \leftarrow e\tilde{\phi}/T$, $\delta_0 \tilde{n} \leftarrow \tilde{n}/n$, $\delta_0 \tilde{T} \leftarrow \tilde{T}/T$, $\delta_0 \tilde{u}_\parallel \leftarrow \tilde{u}_\parallel / c_s$, $\delta_0 \tilde{\psi} \leftarrow \tilde{\psi}/\epsilon_s B \rho_s$, $\delta_0 \tilde{q}_\parallel \leftarrow \epsilon_s \tilde{q}_\parallel / n T c_s$, and $\delta_0 \tilde{J}_\parallel \leftarrow \epsilon_s \tilde{J}_\parallel / n e c_s$, where $\delta_0 = \rho_s / L_n$, $\epsilon_s = L_n / L_s$, c_s is given by $c_s^2 = T_e / M_i$, and L_s and L_n are the shear and density scale lengths. Derivatives are scaled according to $\nabla_\perp \leftarrow \rho_s \nabla_\perp$, $\nabla_\parallel \leftarrow L_s \nabla_\parallel$, and $(\partial/\partial t) \leftarrow (L_n/c_s)(\partial/\partial t)$. In a simple two-dimensional sheared-slab geometry, $\mathbf{b}^{(0)} = \hat{\mathbf{z}} - (x/L_s)\hat{\mathbf{y}}$, so that $\nabla_\parallel^{(0)} = -x(\partial/\partial y)$, the equations are:

$$\frac{\partial}{\partial t}\nabla_\perp^2 \tilde{\phi} = -\mathbf{v}_E \cdot \nabla \nabla_\perp^2 \tilde{\phi} + \nabla_\parallel \tilde{J}_\parallel, \tag{1}$$

$$\frac{\partial \tilde{n}}{\partial t} = -\frac{\partial \tilde{\phi}}{\partial y} - \mathbf{v}_E \cdot \nabla \tilde{n} + \nabla_\parallel \tilde{J}_\parallel - \epsilon_s \nabla_\parallel \tilde{u}_\parallel, \tag{2}$$

$$\frac{3}{2}\frac{\partial}{\partial t}\tilde{T} = -\frac{3}{2}\eta_e \frac{\partial \tilde{\phi}}{\partial y} - \frac{3}{2}\mathbf{v}_E \cdot \nabla \tilde{T} + \nabla_\parallel \tilde{J}_\parallel - \nabla_\parallel \tilde{q}_\parallel - \epsilon_s \nabla_\parallel \tilde{u}_\parallel, \tag{3}$$

$$\frac{\partial}{\partial t}\tilde{u}_\parallel = -\mathbf{v}_E \cdot \nabla \tilde{u}_\parallel - \epsilon_s \nabla_\parallel \left(\tilde{n} + \tilde{T}\right) + \mu_\parallel \left[\nabla_\parallel^{(0)}\right]^2 \tilde{u}_\parallel, \tag{4}$$

$$\frac{\partial}{\partial t}\tilde{\psi} = -D^{-1}\tilde{J}_\parallel + \nabla_\parallel \left(1.71\tilde{T} + \tilde{n} - \tilde{\phi}\right), \tag{5}$$

$$c_\nu \frac{\partial}{\partial t}\tilde{q}_\parallel = -1.6 D \nabla_\parallel \tilde{T} - \tilde{q}_\parallel - 0.71 \tilde{J}_\parallel, \tag{6}$$

where $\tilde{J}_\parallel = -\hat{\beta}^{-1}\nabla_\perp^2 \tilde{\psi}$, $\mathbf{v}_E \cdot \nabla = \hat{\mathbf{z}} \cdot \nabla_\perp \tilde{\phi} \times \nabla_\perp$, $\nabla_\parallel = -x(\partial/\partial y) - \hat{\mathbf{z}} \cdot \nabla_\perp \tilde{\psi} \times \nabla_\perp$, and the parameters are given by $D = (c_s / 0.51 \nu_e L_n)(M_i/m_e)(L_n^2/L_s^2)$ for parallel dissipation, $\hat{\beta} = (4\pi n T / B^2)(L_s^2/L_n^2)$ for electromagnetic induction, $\eta_e = L_n/L_T$ for the relative temperature gradient, and $\epsilon_s = L_n/L_s$ for ion sound coupling. (The numerical constants hold for pure hydrogen, the small constant c_ν is employed to create a separate equation for $\tilde{q}_\parallel$ and avoid the need to compute a nonlinear $\nabla_\parallel^2$, and the parallel viscosity $\mu_\parallel$ is added solely to spatially contain the turbulence.)

III. Electromagnetic Drift-Wave Turbulence

In the above equations, it is clear that $\hat{\beta}$ controls the emergence of electromagnetic effects. When $\hat{\beta} \ll 1$ the usual currents produced by the drift-wave turbulence correspond to comparatively weak magnetic fields ($\tilde{\psi}$), so that the corrections to $\nabla_\parallel^{(0)}$ and the electrostatic Ohm's law (Eq. [4] with $\tilde{\psi} \to 0$) are negligible. For larger $\hat{\beta}$ two things occur. First, the existence of parallel force imbalance on the electrons ("nonadiabaticity") produces a magnetic field somewhat out of phase with the producers of the parallel forces: $\tilde{\phi}$, $\tilde{n}$, and $\tilde{T}$. This would tend to weaken the current produced by a given level of nonadiabaticity,

and hence weaken the overall dissipation thereby excited. The system would become more nonadiabatic on average for a given D, which has the same effect as would an increase of D: weaker linear modes but stronger turbulence. The second new effect is the nonlinear transfer tendency of the nonlinearities in $\nabla_\parallel$ introduced by a finite $\tilde{\psi}$: these tend toward small scales, which would tend to weaken the inverse cascade dynamics in $\tilde{\phi}$ which support the collisional drift-wave mode structure [3].

These changes actually emerge for $\hat{\beta}$ somewhat greater than unity, since $\tilde{\psi}$ is driven according to the nonadiabatic fraction of the electron dynamics, not the whole. Scaling the right side of Eq. (5), one finds that $\tilde{\psi}/\tilde{\phi} \sim \hat{\beta} D k_\parallel{}^2 \Delta^2 \alpha$, with Δ the perpendicular scale, $k_\parallel$ the average parallel wavenumber, and α the nonadiabatic fraction. For linear waves with $\hat{\beta} \sim 1$, the other factors combine for a $\tilde{\psi}/\tilde{\phi}$ ratio of about 0.2. As a result of this, the growth rate for a linear wave externally driven by multiplying the linear gradient term in Eq. (2) by $(1 + i\gamma)$, with $\gamma = 0.3$, starts to decrease only for $\hat{\beta} > 3.0$, about an order of magnitude larger than it ever is in a tokamak edge plasma (the other parameters were set to $D = 2.0$, $\eta_e = 0.6$, $\epsilon_s = 0.1$, and $k_y \rho_s = 0.2$).

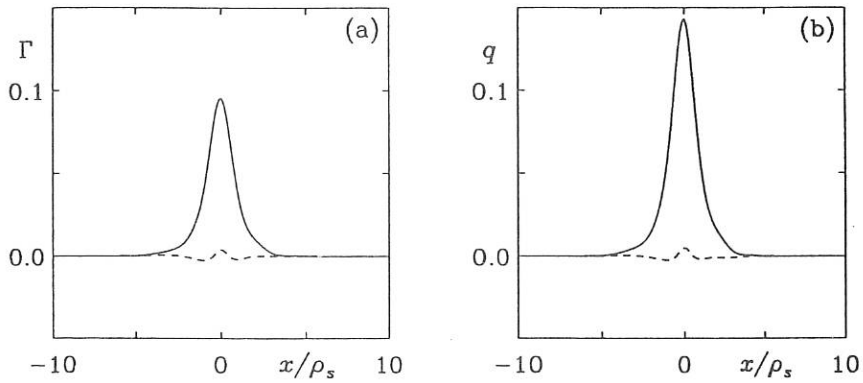


Fig. 1. Particle flux (a) and conductive part of heat flux (b), electrostatic (solid) and electromagnetic (dashed) parts. The transport is dominantly electrostatic, through the turbulent ExB eddies.

The results for the turbulence are no different, even with the extremely powerful kinetic Alfvén physics constraining the timestep to absurdly low values as $\hat{\beta}$ approaches unity ($\tau = 5 \times 10^{-3}$ led to run crashes for $\hat{\beta} = 1.0$, while $\tau = 0.1$ is normal for the electrostatic case). The kinetic Alfvén physics consists of $\nabla_\parallel \tilde{J}_\parallel$ in Eqs. (2,3) and the $\nabla_\parallel$ terms in Eq. (5), with the terms involving $\tilde{q}_\parallel$ also entering. Although the mode structure for turbulence is rather different from that of linear waves [3], the same situation regarding the size of $\tilde{\psi}$ continues to hold. Additionally, $\tilde{\psi}$ emerges in phase with its excitors, $\tilde{h} = \tilde{n} - \tilde{\phi}$

and $\widetilde{T}$, as does $\widetilde{J}_\parallel$, at the energy-producing scales. The measured average $\langle {k_\parallel}^2 \rangle$ has only a very small nonlinear component, except at very small scales where the dissipative forcing through the parallel dynamics is of the least relative importance compared to the turbulence. The main effect of the finite $\widetilde{\psi}$ is to exacerbate $\widetilde{J}_\parallel$ and $\widetilde{q}_\parallel$ at very small scales ($k_\perp \rho_s > 3$), which is of no consequence to the physics but important for the numerics. Fortunately for future numerical tokamak efforts, the scales involved in microturbulence can usually be kept electrostatic. This is made clear by measuring the fluxes, shown in Figure 1, for the case of $D = 2.0$, $\hat{\beta} = 0.3$, $\eta_e = 0.6$, $\epsilon_s = 0.1$. The fluxes were measured by profile, averaged over $800 < t < 1800$ in saturation (the profile gives the transport at the given x, averaged over y). Both particle and conductive heat fluxes are shown; these are $\mathbf{v}_E \cdot \nabla \widetilde{n}$ and $\nabla_\parallel \widetilde{J}_\parallel$, and $\mathbf{v}_E \cdot \nabla \widetilde{T}$ and $\nabla_\parallel \widetilde{q}_\parallel$, respectively. The solid lines give the electrostatic component ($\mathbf{v}_E \cdot \nabla$ terms), and the dashed lines give the electromagnetic component (nonlinear $\nabla_\parallel$ terms). Note that since the results are flux-surface averaged (here, an average over y), only the part involving $\widetilde{\psi}$ contributes to the electromagnetic component. The electromagnetic component is negligible for these parameters, not only to transport, but also to mode structure, as the package of diagnostics used in Ref. [3] verified. (Note that $\hat{\beta} = 0.3$ is typical for an L-H transition phase with $T_e \sim 200\,\mathrm{eV}$ and $n \sim 2 \times 10^{13}\,\mathrm{cm}^{-3}$.)

IV. Conclusion

In a simulation whose model equations are capable of representing both electrostatic transport by ExB turbulence and electromagnetic transport by fluctuations in magnetic field, and parallel current and heat flux, it has been found that the transport is overwhelmingly electrostatic at the highest levels of plasma beta expected in tokamak edge plasmas. Although the model is restricted to parallel electron dynamics, this part of the physical system is self-consistently treated, with separate equations for the three fluctuations important to drift-wave turbulence: $\widetilde{\phi}$, $\widetilde{n}$, and $\widetilde{T}$. Further, it is this part of the overall dynamics present in a magnetised plasma through which turbulent fluctuations interact with the parallel current and magnetic field, at low plasma beta. It is therefore to be expected that the results of this study are quite relevant to the long-standing question whether tokamak edge transport is primarily electostatic or electromagnetic, and the results indicate that it is electrostatic. It should be added, however, that possible contributions from exotic, fast-particle effects are not ruled out.

References

[1] Ch. P. Ritz, R. V. Bravanec, P. M. Schoch *et al* (1989) *Phys. Rev. Lett.* 62, 1844.

[2] S. I. Braginskii (1965) in *Reviews of Plasma Physics*, M. A. Leontovich, ed. (Consultants Bureau, New York), Vol. 1, p. 205. See also J. F. Drake and T. M. Antonsen Jr. (1984) *Phys. Fluids* 27, 898.

[3] B. D. Scott (1990) *Phys. Rev. Lett.* 65, 3289; (1992) *Phys. Fluids B* 4, 2468.

High resolution simulations of 2-D dissipative drift-wave turbulence

Suzana J. Camargo, Dieter Biskamp, and Bruce D. Scott
Max-Planck-Institut für Plasmaphysik, 85748 Garching, Germany

Drift-wave turbulence is considered as a possible cause of anomalous transport, in particular in the plasma edge region of tokamaks and stellarators. Hasegawa and Wakatani [1] proposed a simple model to study two-dimensional drift-wave turbulence in a collision dominated plasma with a constant magnetic field in the z direction and a constant mean density gradient in the negative x direction. In this paper, the Hasegawa-Wakatani model is studied by high-resolution numerical simulations for high-Reynolds numbers.

The Hasegawa-Wakatani model consists of two coupled nonlinear equations for the normalized potential $\tilde{\phi}(x,y)$ and density $\tilde{n}(x,y)$ fluctuations [1]:

$$\frac{\partial}{\partial t}\nabla_\perp^2\tilde{\phi} + \left(\hat{z}\times\nabla_\perp\tilde{\phi}\right)\cdot\nabla_\perp\nabla_\perp^2\tilde{\phi} = C\left(\tilde{\phi}-\tilde{n}\right) + \mathcal{D}^\phi, \tag{1}$$

$$\frac{\partial}{\partial t}\tilde{n} + \left(\hat{z}\times\nabla_\perp\tilde{\phi}\right)\cdot\nabla_\perp\tilde{n} + \frac{\partial\tilde{\phi}}{\partial y} = C\left(\tilde{\phi}-\tilde{n}\right) + \mathcal{D}^n, \tag{2}$$

where the usual dimensionless variables are used [2]. $\mathcal{D}^\phi$ and $\mathcal{D}^n$ are ad-hoc dissipation terms $\mathcal{D}^\phi = \nu\nabla_\perp^6\nabla_\perp^2\tilde{\phi}$ and $\mathcal{D}^n = \nu\nabla_\perp^6\tilde{n}$, which are chosen in order to confine dissipation to the smallest scales resolved in the numerical system [3]. In the limit of small ν, where viscous energy dissipation vanishes, which we call the non-viscous limit, the only relevant parameter is the adiabaticity parameter $C \propto k_\parallel^2/\eta_\parallel$. For $C \gg 1$, the electron response is nearly adiabatic and Eqs. (1) and (2) reduce to the Hasegawa-Mima equation, while for $C \ll 1$, Eq. (1) reduces to the 2-D Navier-Stokes equation, while $\tilde{n}$ is passively advected.

The invariants of the purely nonlinear subset of the Hasegawa-Wakatani system are the total energy $E = E^N + E^V = 1/2\int d^2x\left(\tilde{n}^2 + |\nabla_\perp\tilde{\phi}|^2\right)$ and the generalized enstrophy $U = 1/2\int d^2x\left(\tilde{n}-\tilde{\Omega}\right)^2$, where $\tilde{\Omega} = \nabla_\perp^2\tilde{\phi}$ is the E×B vorticity. These quantities evolve with time as $\partial E/\partial t = \Gamma_n - \Gamma_c - \mathcal{D}^E$ and $\partial U/\partial t = \Gamma_n - \mathcal{D}^U$. Only Γ_n can act as a source, the other quantities are sinks. $\Gamma_n = -\int d^2x\tilde{n}\left(\partial\tilde{\phi}/\partial y\right)$ is the rate at which the system extracts free energy from the density gradient. $\Gamma_c = C\int d^2x\left(\tilde{n}-\tilde{\phi}\right)^2$ is the resistive energy dissipation rate. These two quantities represent the collisional drift-wave energetics in the non-viscous limit. It is important to note that they are only active if the dynamics is nonadiabatic. $\mathcal{D}^E$ and $\mathcal{D}^U$ are viscous sinks and in the non-viscous limit $\mathcal{D}^E$ is negligible compared to Γ_n and Γ_c while $\mathcal{D}^U$ is finite.

Eqs. (1) and (2) are solved on a square box of size $L^2 = (2\pi/K_0)^2$ with periodic boundary conditions using a de-aliased pseudo-spectral algorithm similar to the one used in [4]. Two different boxes sizes are chosen concentrating primarily on either high-k ($K_0 = 0.15$) or low-k ($K_0 = 0.0375$) properties. The grid-size is varied from 128^2 to 1024^2 nodes. The dissipation parameter ν was kept just large enough to prevent piling up of mode energy at large k, varying

from $\nu = 10^{-4}$ to $\nu = 5 \times 10^{-10}$ depending on the size of the box and number of nodes. Three values of C are used in the computations, representing the hydrodynamic ($C = 0.1$), adiabatic ($C = 5$) and transition ($C = 1$) regimes.

The numerical simulations are initialized by a random-phase, broad-band field for the density and potential fluctuations. The evolution of the system follows a standard pattern, a linear growth phase followed by a quasi-stationary turbulent phase. The saturation time uniformly decreases with C, which cannot be explained by the linear growth rate, which peaks for $C = 0.3$ and decreases for smaller and greater values of C, but is due to the increasing decoupling of $\tilde{n}$ and $\tilde{\phi}$ in the hydrodynamice regime. The energy saturation level is minimum for $C = 1$, which is a further indication that the evolution is determined more by the nonlinear properties than by the linear growth rate. It is important to note that the variation of E with C is almost entirely due to E^N. The saturated enstrophy level, on the other hand, decreases uniformly towards the adiabaticity limit, due to the presence of the vorticity cascade to small scales in all regimes, coupled with a lower Γ_n in the adiabatic regime. All this serves to demonstrate that the nonlinear drive and damping rates, together with the strength of inter-scale transfer, not the linear growth rates determine the character of the saturated state.

The angle-integrated energy spectrum E_k exhibits a maximum at a certain wave-number k_0. On the high-k side there is an inertial range in which E_k follows a power law ($E_k \simeq k^{-\alpha}$) up to the viscous cut-off, with $\alpha = 1.6 - 3.5$. Let us analyse separately the kinetic energy and the density spectra E_k^V and E_k^N. Since the effect of the collisional term is small in the inertial range, Eq. (1) essentially reduces to the 2-D Navier Stokes equation, where the spectrum $E_k^V \simeq k^{-3}(\ln kL)^{-1/3}$ is predicted. This explains the spectral index for E_k^V, which is not very sensitive to C, $\alpha_V = 3.1 - 3.5$. On the other hand, E_k^N depends strongly on C. In the hydrodynamic limit the density behaves essentially as a passive scalar, which suggests the form $E_k^N \simeq k^2 E_k^V$, which is in fact observed ($\alpha_N = 1.6$), hence E_k^N dominates the energy spectrum at high-k in this regime. In the adiabatic limit the kinetic energy is dominant at high-k since $\tilde{n}$ is forced by the strong cross-coupling to have the same spectrum as $\tilde{\phi}$ ($\alpha_N = 4.2$). It is then clear that the sensivity of E_k to C is essentially due to that of E_k^N. The angle-integrated enstrophy spectrum U_k also has a maximum at k_0 and follows a power law for $k > k_0$. The variation of the spectral index of U_k with C is much smaller than that of E_k. U_k is dominated by the vorticity component, hence the spectral index of $U_k \simeq k^{-\beta}$ is approximately given by that of the vorticity $\beta = 1.3 - 1.6$.

The energy spectra $E(k_x)$ and $E(k_y)$ show that for k_x, $k_y > k_0$, the spectral distribution is isotropic, while for k_x, $k_y \lesssim k_0$ it is strongly anisotropic. Contour plots of E_k for $k \lesssim k_0$ are similar to those of the linear growth rate γ, indicating that the behavior for $k < k_0$ is essentially determined by the linear forcing, since γ is proportional to k_y with a maximum at $\mathrm{k}_m = (0, k_m)$. For $C \ll 1$ we find that $k_0 \simeq k_m$, while for $C > 1$, where k_m becomes independent of C, the actual spectrum is shifted to lower k as C increases. This is another manifestation of the inverse energy cascade in the adiabatic regime.

The angle integrated turbulent flux $\Gamma_{nk} = i \int d^2k\, k_y \tilde{n}_{\mathbf{k}} \tilde{\phi}^*_{\mathbf{k}}$ is compared with its quasilinear prediction Γ_k^{ql}, in which $\tilde{n}_{\mathbf{k}}$ is substituted by $(1 + f_k)\tilde{\phi}_{\mathbf{k}}$, where f_k is the linear response function [3]. In the adiabatic limit ($C \gg 1$), $\Gamma_n \simeq \Gamma^{ql}$, while for $C \lesssim 1$, $\Gamma_n < \Gamma^{ql}$ Their ratio, Γ_n/Γ^{ql}, decreases with decreasing C approximately as $\Gamma_n/\Gamma^{ql} \sim C^{1/3}$ for $C \lesssim 1$. Comparison of the spectral behavior of the two quantities shows that for $k \lesssim k_0$, $\Gamma_{nk} \simeq \Gamma_k^{ql}$ for all values of C. This good agreement between Γ_n and Γ^{ql} at low-k shows that although $\tilde{\phi}$ is nonlinear, the response of $\tilde{n}$ to it is linear, in the sense that the nonlinearity in Eq. (2) is weak compared to the forcing terms. For $C = 5$, $\Gamma_{nk} = \Gamma_k^{ql}$ over the entire spectrum, which can be explained by the strong

cross-coupling.

In most transport models, it is assumed that the nonadiabatic response is small, entering purely as a small phase-shift between $\tilde{n}_{\mathbf{k}}$ and $\tilde{\phi}_{\mathbf{k}}$: $\tilde{n}_{\mathbf{k}} = (1 - \delta_{\mathbf{k}})\tilde{\phi}_{\mathbf{k}}$, with a given $\delta_{\mathbf{k}} \ll 1$ for each Fourier component. In general, $\tilde{n}_{\mathbf{k}}$ and $\tilde{\phi}_{\mathbf{k}}$ are two complex numbers whose ratio can be given in terms of an amplitude and a phase-shift given by $\delta_{\mathbf{k}} = Im \log \tilde{n}^*_{\mathbf{k}} \tilde{\phi}_{\mathbf{k}}$. For linear waves, the phase-shift $\delta^L_{\mathbf{k}}$ is obtained as a function of the linear response function $f_{\mathbf{k}}$ [3]. The tendency of the parallel dissipation C to enforce adiabaticity is opposed for the linear waves by the mean density gradient and by ion inertia. As these effects are weak for low k, $\delta^L_{\mathbf{k}}$ is small in this range. As C increases, the inertia with its higher k dependence gives the dominant contribution to the linear phase-shift $\delta^L_{\mathbf{k}}$. In the turbulent case, the E × B advection also opposes parallel dissipation, because it tends to randomise the relation between $\tilde{n}$ and $\tilde{\phi}$. When the E × B advection is dominant, as at high-k and low C, the two quantities become statistically independent. So the average phase-shift is less than a linear estimate would suggest, especially at the smaller scales where the turbulent advection overwhelms linear forcing. The small-scale phase-shift is larger when the electrons are adiabatic, which is quite counter-intuitive from the standpoint of linear theory.

The statistical properties are conveniently described by the normalized structure functions of the density, potential and vorticity increments [2]. For instance, the normalized density structure functions are defined as $F^{(2j)} = \left\langle (\delta\tilde{n}_r)^{2j} \right\rangle / \left\langle (\delta\tilde{n}_r)^2 \right\rangle^j$, where $\delta\tilde{n}_r$ is the density increment $\delta\tilde{n}_r = \tilde{n}(\mathbf{x} + \mathbf{r}) - \tilde{n}(\mathbf{x})$. While for $r > k_0^{-1}$ the large scale statistics are found to be Gaussian, the statistics become increasingly non-Gaussian for $r < k_0^{-1}$, indicating the existence of small-scale intermittency. While the structure functions of the density are strongly dependent on C, the potential and the vorticity are practically independent of C. The structure functions of the potential being approximately Gaussian even for the smallest scales. The Gaussian statistics at large scales is consistent with the absence of large scale coherent structures in the non-viscous limit. Similar diagnostics performed on cases reproducing the calculations of [5], which considered much more strongly viscous conditions, long-living coherent structures were observed and the statistics were far from Gaussian.

A useful diagnostic is the measurement of the spectral transfer function for the energy. We compute the spectral transfer of kinetic T^V, density T^N and vorticity T^W from mode k′ to mode k. Since in a homogeneus system one is interested in scale transfer, the interesting quantities are those between "shells" of modes (corresponding to angle integrations). In the three regimes considered averages over sufficiently long periods of quasi-stationary turbulence are taken to provide good statistics. Most activity is concentrated at $k \simeq k'$, which shows that the transfer occurs between scales of motion which are within a factor of two of each other, therefore the transfer can be described as a local cascade. T^V shows an inverse cascade (towards large scales), while T^W has a direct cascade towards small scales. Hence the E × B nonlinearity exhibits the familiar dual cascade of 2D fluid. T^N shows a direct cascade, since $\tilde{n}$ is passively advected by the E × B eddies. Although the character of the system differs substantially between the adiabatic and hydrodynamic limits, the function and actual behaviour of each nonlinearity remains the same throughout. Only the magnitude of T^N is sensitive to C; this merely reflects that for high C the system does not tolerate strong departures from electron adiabaticity. Therefore, only the relative magnitudes of the different cascade tendencies are affected by the strength of the cross-coupling.

In summary, the Hasegawa-Wakatani model has been solved using high-resolution numerical simulations in the non-viscous limit, such that the controlling parameter is the dissipative

cross-coupling C between the two fluctuating variables $\tilde{n}$ and $\tilde{\phi}$. Though the characteristics of the turbulence are quite different in the hydrodynamic and adiabatic regimes, the essential ingredients of the system (gradient driving, dissipative cross-coupling and turbulent $\mathbf{E} \times \mathbf{B}$ advection) have the same qualitative effect in all regimes, the different properties being only due to the different relative strenght of these ingredients for different values of C. High resolution computations play an essential role in understanding the turbulence properties. The most obvious manifestation of this is the disappearance of coherent structures when the viscous damping is reduced. The inertial range spectral power laws agree surpringly well with simple scaling predictions. The statistical properties are found to be perfectly Gaussian for $k \lesssim k_0$, but exhibit the non-Gaussian behavior, typical for small-scale intermittency in the inertial range. When the quasilinear flux estimate fails it overestimates the value of the flux, as the density tends to get randomised with respect to the potential in the strongly nonlinear, nonadiabatic regime. The transfer of energy and vorticity confirms the persistence of local cascade dynamics in all regimes: a dual cascade for the $\mathbf{E} \times \mathbf{B}$ flow eddies and a direct cascade for the density.

[1] A. Hasegawa and M. Wakatani, *Phys. Rev. Lett.* **50**, 682 (1985).

[2] D. Biskamp, S.J. Camargo and B.D. Scott, *Phys. Lett.* A **186** 239 (1994).

[3] S.J. Camargo, D. Biskamp and B.D. Scott submitted to *Phys. Plasmas.*

[4] B.D. Scott, *J. Comp. Phys.* **78**, 114 (1988).

[5] A.E. Koniges, J.A. Crotinger and P.H. Diamond, *Phys. Fluids* **B4**, 2785 (1992).

Neoclassical Transport Scalings For Stellarators in the Long-Mean-Free-Path Regime

C.D. Beidler, W. Lotz, H. Maaßberg
Max-Planck-Institut für Plasmaphysik, IPP-EURATOM Association
D-85748 Garching bei München, Germany

Introduction. One of the most fundamental differences distinguishing the toroidal confinement concepts of tokamak and stellarator is that the latter's magnetic field is produced entirely through the use of external coils. Although this has obvious advantages (steady-state, disruption-free operation), the necessarily three-dimensional nature of such a magnetic field implies a significant fraction of localized particles and an accompanying neoclassical transport rate in the long-mean-free-path (*lmfp*) regime which dwarfs that of a tokamak. The importance of neoclassical losses has already been documented in the current generation of modest-sized stellarator experiments [1] and is expected to increase further in the large devices of the next generation.

Theoretical efforts to understand and describe neoclassical transport in stellarators have been numerous, but a general consensus on all aspects of the problem has yet to emerge. One uncertainty concerns the correct scalings of the transport coefficients with collision frequency, ν, and radial electric field, E_r ($E_r = -d\Phi/dr$, where $\Phi(r)$ is the potential necessary to insure that the losses are ambipolar). A further question is the validity of predictions based on simple magnetic-field models, given the often complex B spectra of actual stellarator devices. These two topics are considered in the following.

Traditional Analytic Theory. In the simplest approximation, a classical stellarator represents the superposition of a toroidal and a helical magnetic field, with magnitude $B/B_0 = 1 - \epsilon\cos\theta + \epsilon_h\cos(\ell\theta - p\phi)$, where θ [ϕ] is the poloidal [toroidal] angle, ϵ [ϵ_h] is the average toroidal [helical] curvature of B (ϵ need not be equal to $\epsilon_t = r/R_0$, the inverse aspect ratio) and ℓ [p] is the helical field multipolarity [period number]. In the *lmfp* regime particles localized in the helical ripple may experience significant radial drift and are generally expected to provide the dominant contribution to the overall neoclassical transport. The form this contribution takes is determined by the relative magnitudes of the effective collision frequency, $\nu_{eff} = \nu/2\epsilon_h$, and the $\mathbf{E}\times\mathbf{B}$ precessional frequency, $\Omega_E = E_r/rB_0$. The results may be summarized by the "mono-energetic" diffusion coefficients [2]

$$D_{1/\nu} = \frac{4}{9\pi}\left(v_d\frac{\epsilon}{\epsilon_t}\right)^2\frac{(2\epsilon_h)^{3/2}}{\nu}, \qquad D_{\sqrt{\nu}} = \frac{4\sqrt{2}}{9\pi}\left(v_d\frac{\epsilon}{\epsilon_t}\right)^2\frac{\nu^{1/2}}{|\Omega_E|^{3/2}}, \qquad D_{\nu} = \left(\frac{v_d}{\Omega_E}\frac{\epsilon}{\epsilon_t}\right)^2\frac{\nu}{2\mathcal{F}_{bl}},$$

which are predicted analytically for $\nu_{eff} \gg \Omega_E$, $\nu_{eff} \lesssim \Omega_E$ and $\nu_{eff} \ll \Omega_E$, respectively. (In these expressions, $v_d = \kappa/qB_0R_0$ where $\kappa = mv^2/2$ is the kinetic energy of the monoenergetic particles and q is their charge, and $\mathcal{F}_{bl} = \sqrt{\epsilon + 2\epsilon_h} - \sqrt{2\epsilon_h}$.) A difference of opinion exists as to whether the $\sqrt{\nu}$ scaling is actually observed in numerical simulations

of neoclassical transport [2-4] or whether $D_{1/\nu}$ and D_ν alone are sufficient to explain the results [5,6]. This question is of more than academic interest as the inclusion of the $\sqrt{\nu}$ scaling will generally lead to more pessimistic expectations for the neoclassical confinement.

DKES Code Results. The DKES code [7] solves the mono-energetic drift kinetic equation for a complex magnetic field geometry which is defined by the Fourier spectrum of B on a flux surface, $\Psi \propto r^2$,

$$B(r,\theta,\phi) = B_0 \sum_{m,n} \beta_{mn}(r) \cdot \cos(m\theta - np\phi)$$

with θ and ϕ being the poloidal and toroidal angles in magnetic (Boozer) co-ordinates ($\epsilon \equiv -\beta_{10}$ and $\epsilon_h \equiv \beta_{\ell 1}$, see above). The mono-energetic transport matrix, Γ_{ij} obtained from DKES depends on ν/v and E_r/v, where $\nu(v)$ is the collision frequency, E_r the radial electric field, and v the particle velocity. For different magnetic field configurations, the three transport coefficients, Γ_{11}, Γ_{13} and Γ_{33} (where the indices 1 and 3 define the radial and the parallel directions, respectively) are stored in a database with respect to "effective" radius, r, "collisionality", ν/v, and E_r/v. For each particle species, the full "thermal" transport matrix, D_{ij}, is obtained by an energy convolution algorithm based on this mono-energetic database. For comparing the transport properties of different magnetic configurations in the *lmfp* regime, however, the mono-energetic Γ_{11}^* are well suited, where the star indicates normalization to the plateau value, $\Gamma_{11}^p = \pi/(8R_0\iota B_0^2)$ (in DKES notation [7]), of the equivalent axisymmetric configuration with circular cross section ($\beta_{10} = -\epsilon_t$).

The magnetic configuration of classical stellarators is characterized by one dominating Fourier harmonic β_{m1}: e.g., $\beta_{11} \simeq 0.8\%$ ($\beta_{21} \simeq 0.3\%$) for W7-A at $\epsilon_t = 0.025$ and $\iota = 0.51$, and $\beta_{21} \simeq 4.3\%$ for L-2 at $\epsilon_t = 0.06$ (clean spectrum); see [8] for more details. Consequently, these configurations are most suited for a quantitative comparison with the analytic predictions. In Figure 1, the DKES results, $\Gamma_{11}^*(\nu/v, E_r/v)$, are shown together with the equivalent normalized D^* where the different regimes are smoothly connected using $D^{-1} = D_{1/\nu}^{-1} + D_{\sqrt{\nu}}^{-1} + D_\nu^{-1}$. Please note in this context that the rather poor convergence of DKES as indicated by the error bars in the very-*lmfp* regime (e.g., up to 500 Fourier modes and 180 Legendre polynomials were used) may mask the $\sqrt{\nu}$- and ν-dependencies of Γ_{11}^* for fixed E_r/v. However, for both W7-A and L-2 the analytic approach is in reasonable agreement with the DKES results confirming the $\sqrt{\nu}$ dependence. As expected due to the $\mathcal{F}_{bl}$-term in the analytic results, the $\sqrt{\nu}$ regime is more extended for the L-2 configuration ($\epsilon \simeq \epsilon_t \simeq \epsilon_h$) than for W7-A ($\epsilon \simeq \epsilon_t \simeq 3 \cdot \epsilon_h$). A significant difference is obtained at the boundary of the $1/\nu$ and the plateau regimes. The axisymmetric contribution also indicated in Fig. 1 is obtained from least-squares fitting of DKES results for an extended database of axisymmetric configurations (elongation is taken into account by $\epsilon \leq \epsilon_t$). This stellarator specific deviation is attributed to the interaction of localized (e.g., "helically" trapped) and non-localized (e.g., "tokamak-like"

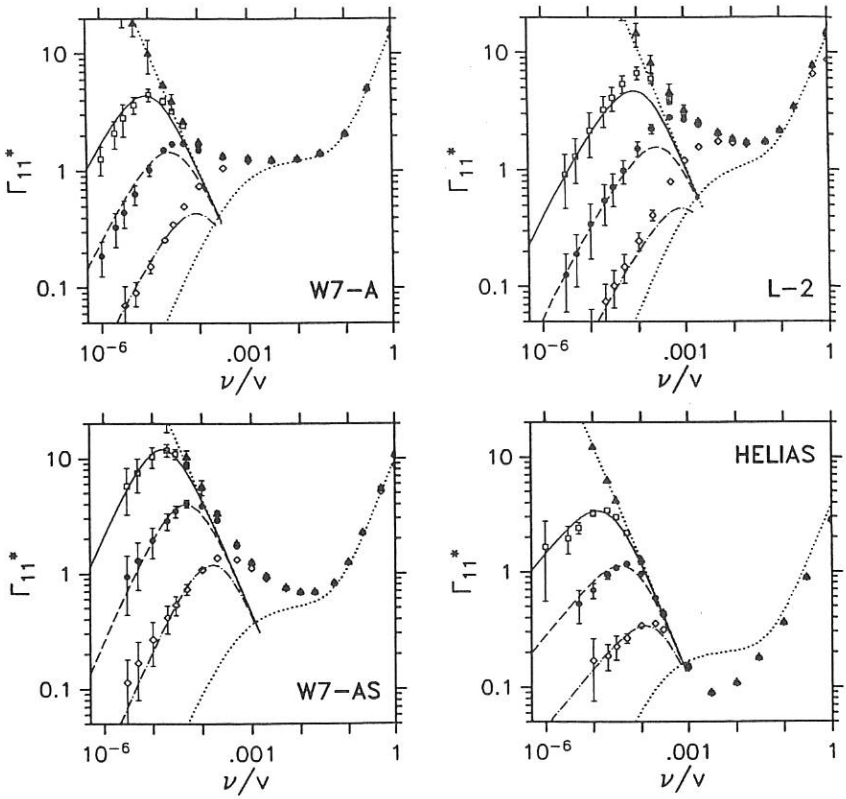


Fig. 1: *Normalized mono-energetic transport coefficients, Γ_{11}^*, at about half the plasma radius versus ν/v for* **W7-A** *($\epsilon_t = 0.025$, upper left plot), for* **L-2** *($\epsilon_t = 0.06$, upper right), for* **W7-AS** *($\epsilon_t = 0.05$, $\iota \simeq 0.31$, lower left) and for a* **Helias** *configuration ($\epsilon_t = 0.05$, lower right plot) at different E_r/v: 0 ($\blacktriangle$, dotted line), 10^{-4} ($\square$, solid line), $3 \cdot 10^{-4}$ ($\bullet$, dashed line), and 10^{-3} ($\diamond$, dot-dashed line), respectively. The axisymmetric contribution is indicated (additional dotted line).*

banana orbits) particles, and can also decrease the plateau value when reduced average curvature is taken into account (see the Helias-case in Fig. 1).

For a broader spectrum of Fourier harmonics, the analytic approach fails. However, the $1/\nu$ regime as well as something like the $\sqrt{\nu}$ or ν regime are clearly indicated. By a standard least-squares fit technique to the DKES database, the numerical coefficients for the different regimes are obtained; e.g., the "effective helical ripple", $\langle \epsilon_h \rangle$, as used in the next section is estimated. By using these numerical coefficients with the dependence on ν/v and E_r/v being fixed, fairly good fits of the DKES-Γ_{11}^* in the *lmfp* regime are

obtained. For the W7-AS [8] (with $\beta_{10} \simeq -0.7 \cdot \epsilon_t$) and the optimized Helias [9] (with $\beta_{10} \simeq -0.43 \cdot \epsilon_t$) configurations also shown in Fig. 1, quite different results are obtained: whereas for this W7-AS configuration (the "standard case") the $\sqrt{\nu}$ contribution is small and quickly gives way to a ν scaling, no ν-regime is found for the Helias configuration at all (although the ν scaling may be "masked" by convergence problems of DKES in the very-*lmfp*, an extended $\sqrt{\nu}$-regime was also obtained by Monte-Carlo technique; see [4]). In the Helias configuration the "geometrical ripple" is larger than in the W7-AS case, however, the "effective ripple" is smaller. This result demonstrates that an additional degree of freedom exists in the optimization of the Fourier B spectrum in addition to the reduction of the avaraged toroidal curvature. In this sense, partly optimized configurations for W7-AS (by adjusting the toroidal mirror term, β_{01}, at nearly idential β_{10}), with Γ_{11}^* being reduced in the *lmfp* regime by more than a factor of 2, are also found, and the $\sqrt{\nu}$ regime becomes much more pronounced.

Effective Helical Ripple. Corresponding to the analytic approach, the "effective helical ripple", $\langle \epsilon_h \rangle$, is defined within the $1/\nu$ regime from the $D_{1/\nu}$ transport coefficients for configurations with a complex B Fourier spectrum where a flux-surface-averaged "geometrical helical ripple" cannot be used. For optimized magnetic configurations, as for the Helias case shown in Fig. 2, $\langle \epsilon_h \rangle$ is significantly smaller than the leading β_{mn} coefficients. In addition to the reduction of the β_{10}-term, (which is included in the definition of $\langle \epsilon_h \rangle$), the reduction of the fraction of particles trapped in the region of strong toroidal curvature is most essential for the optimization in the *lmfp* regime. As shown in [9], the addition of toroidal mirror contributions β_{0n} in these regions significantly reduces Γ_{11}^*.

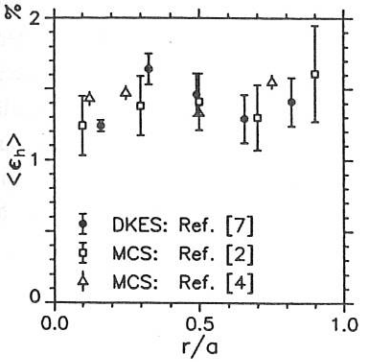


Fig. 2: *The "effective helical ripple", $\langle \epsilon_h \rangle$, versus the normalized effective radius for a Helias configuration (an intermediate step within the evolution of the W7-X concept) obtained by DKES and by different Monte-Carlo techniques (MCS). Within the $1/\nu$ regime, $\langle \epsilon_h \rangle$ is defined by*

$$D_{1/\nu} = \frac{8\sqrt{2}}{9\pi} \cdot v_d^2 \cdot \frac{1}{\nu} \cdot \langle \epsilon_h \rangle^{3/2}.$$

[1] Maaßberg et al., Plasma Phys. Control. Fusion **35** (1993) B319.
[2] Beidler, Proc. 9th Int. Stellarator Workshop (1993) 138.
[3] Mynick and Hitchon, Nucl. Fusion **26** (1986) 425.
[4] Lotz and Nührenberg, Phys. Fluids **31** (1988) 2984.
[5] Crume et al., Phys. Fluids **31** (1988) 11.
[6] Ogawa et al., Nucl. Fusion **32** (1992) 119.
[7] van Rij and Hirshman, Phys. Fluids B 1 (1989) 563.
[8] Maaßberg et al., Phys. Fluids B **5** (1993) 3627.
[9] Maaßberg et al., Phys. Fluids B **5** (1993) 3728.

" Stochastic diffusion in Reverse Field Pinch"

[1]F. D'Angelo, R. Paccagnella

Istituto Gas Ionizzati del CNR, EURATOM-ENEA-CNR Association
Padova (Italy)
[1]Dipartimento di Fisica, "G. Galilei", Padova (Italy)

Introduction:

The island overlapping criterion can quite well describe the transition to chaotic dynamic in many physical systems [1]. This idea has been also usefully applied to study the confinement properties of plasmas in magnetic fusion devices [2]. Defining the stochasticity parameter as in Ref. [2], the stochasticity threshold is determined by the s=1 condition. Clearly the transition to chaotic dynamics is easier if many resonant modes are present in the plasma and the spacing between the modes is such to fulfil the $s \geq 1$ condition. Unfortunately this seems to be the typical condition in the Reverse Field Pinch (RFP). Nevertheless many aspects of the stochastic diffusion process remain to be clarified. First of all, there is the basic problem that the physical domain in a fusion device is finite, therefore the problem of diffusion cannot be approached like Brownian motion in an unconstrained domain [3]. Moreover, although quite well established for tokamaks, it is not clear, in our opinion, for RFPs whether or not the quasi-linear approximation [2] can describe the diffusion rate of magnetic field lines. Other questions are: the role of m=0 modes, still quite controversial, and the gaussian-like behaviour of the diffusion process. Moreover in this paper we try to establish a relationship between stochastic diffusion rate and positive Lyapunov exponents.

Field line Hamiltonian

The field line equations can be cast [4] in hamiltonian form, which in particular in the action-angle representation reads as:

$$\begin{cases} \dfrac{dI}{d\theta} = -\varepsilon\, f(I) \sum_{m,n} b_{m,n} \sin(m\theta - n\varphi + \mu_{mn}) \\ \dfrac{d\varphi}{d\theta} = \omega(I) + \varepsilon\, f'(I) \sum_{m,n} \dfrac{b_{m,n}}{n} \cos(m\theta - n\varphi + \mu_{mn}) \end{cases} \qquad (1)$$

where f(I) is a given function of I, f'=df/dI, $\omega = q(I)$, is the safety factor, μ_{mn} is a random phase and ε determines the amplitude of the perturbation (assuming $b_{m,n} \approx 1$). From (1) it is easily seen that the zero-order hamiltonian is the unperturbed toroidal flux, while it is clear that the action I is proportional to the poloidal flux. In the following we use a simplified model [5] which make it possible to identify $I=r^2$, where r is the radial co-ordinate.

The stochastic diffusion

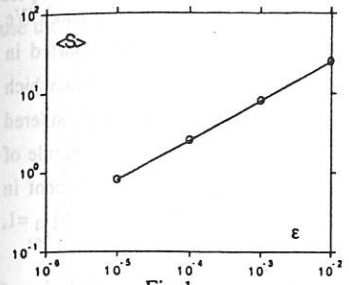


Fig.1

To show how critical is the s=1 condition for RFP in Fig.1 the average stochasticity parameter is plotted versus ε in the case of m=1 modes with n=10÷30 ($b_{1,n} = 1$). Only if the perturbation is equal or less 10^{-5} the non-overlapping condition is satisfied.

To characterize chaotic motion it is often used the concept of the diffusion coefficient defined as:

$$D_{st} = \lim_{t\to\infty} \frac{< (r - r_0)^2 >}{2t}$$

where r_0 is the initial position of the some physical quantity (i.e. magnetic field lines) and t is a time "like" variable.

From the definition, it follows that for bounded domain $D_{st}=0$. The point is quite clearly discussed in Ref. [3]. A direct and intuitive physical approach is given in Ref.[6], in which it has been shown that the field line spreading for a bounded domain is saturating in time, so that it is clear that the diffusion rate in such situation has some meaning only at an initial stage (when the spreading of field lines increases in time). More, precisely following Ref. [6], it is possible to define:

$$D_{st} = \int_0^{L_c} < b_r\, b'_r > dL \qquad (2)$$

where $<b_r\, b'_r>$ is the ensemble average of the correlation of the radial field and L_c is the so called auto-correlation length, defined as the length for which the integrand of (2) vanishes.

With this definition in mind it is clear that, only if $L_c < L_{sat}$, where L_{sat} is the length at which $<(r-r_0)^2>$ saturates, a meaningful diffusion coefficient can be defined for the problem. In other words only if there is a rapid decay of correlation [2], it is possible to characterize the spreading

of field lines (in a bounded domain) as a diffusion process. For the RFP, we have found that the correlation length is of the order of the plasma minor radius, $L_c \approx a$, while $L_{sat} = 4 \div 5\ a$.

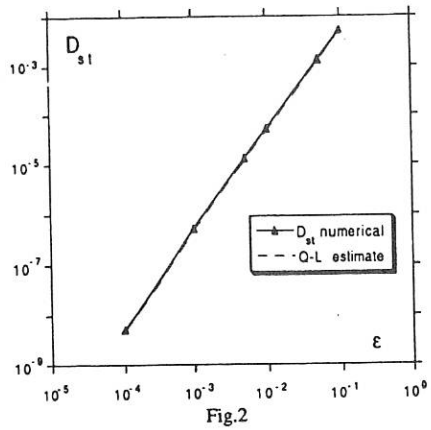


Fig.2

We now analyze the behaviour of the diffusion coefficient in a RFP. Fig.2 shows the comparison between the numerical calculated D_{st} (normalized to plasma minor radius) and the quasi-linear estimate [2], $D_{st} \approx L_c\,(b/B)^2$. The agreement is very good. We note that the result reported in Fig.2 refers to a case in which only m=1 modes are considered (n=10÷30) and the amplitude of the (1,n) Fourier component in the spectrum is constant: $b_{1,n} = 1$, so that the amplitude of the perturbation is actually given by ε (see Eq.(1)).

The role of m=0 modes is another open question in the problem of stochastic diffusion of magnetic field lines. Clarifying this role is particularly important for the RFP in which many m=0 modes, resonant at the reversal surfaces, can rise. A preliminary observation is that the system (1) becomes autonomous when only m=0 modes are considered. Since it is well known that a 1 degree of freedom hamiltonian system cannot be stochastic [7], it is clear that m=0 modes alone cannot give rise to stochastic diffusion.

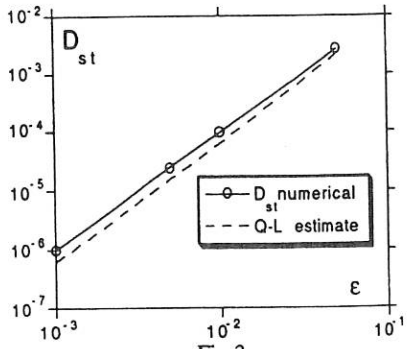


Fig.3

But, although not stochastic, an enhanced diffusion is certainly expected, due to m=0 modes. In fact they produce "islands" which make it possible for a magnetic field line to move at least for a radial extension comparable with the island width. If the correlation length is of the same order of the length necessary to move radially over the island size, this process can appear like stochastic diffusion. Numerically we have verified that the simultaneous

presence of m=0,1 modes enhances the diffusion rate (Fig.3) slightly above the quasi-linear estimate.

Another interesting point is to understand if the diffusion process can be described by a gaussian process. To this purpose we follow the evolution in time of an ensemble of initially Dirac-distributed field lines. It has been found that in the diffusive region ($L < L_c$) the process can be well approximated by a gaussian probability distribution of the field lines, whereas when $L \simeq L_{sat}$ the probability distribution function becomes flat over the diffusion region.

As last topic we address the question of calculating the maximum Lyapunov exponent for the problem and of analyzing its relationship with D_{st}. To calculate Lyapunov exponents we use the method proposed in Ref. [8].

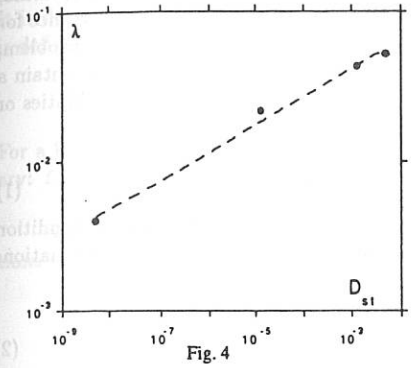


Fig. 4

In Fig.4 the maximum positive Lyapunov exponent is plotted vs. D_{st}.(the spectrum is the same as in Fig.1) A good correlation is found with a power law of the type: $\lambda \propto D_{st}^{0.186}$. In Ref. [9] a quasi-linear evaluation gives $L_k \propto 1/\lambda \propto D_{st}^{-1/3} L_s^{2/3}$, showing a dependence of the Kolmogorov-length on magnetic diffusivity and shear length. Our scaling with D_{st} is different (probably due to a slightly different definition), instead we have found a good agreement for the dependence of λ on L_s. Finally we note that the presence of m=0 modes gives rise to ordered structures and has generally the effect of lowering the Lyapunov exponent of the system.

References

[1] G.M. Zavlavskii, B.V. Chirikov, Sov. Phys. Uzspekhi, Vol.14, (1972) 549.

[2] A. B. Rechester, M.N. Rosenbluth, Phys. Rev. Lett., Vol.40 (1978) 38.

[3] S. Benkadda et. al., Phys. Rev. Lett., Vol.72 (1994) 2859.

[4] J. Cary, R.G. Littlejohn, Ann. of Phys., Vol.151 (1983) 1.

[5] A. Bazzani et. al., Nuovo Cimento B, Vol.103 (1989).

[6] A. Gurevich et al., Sov. Phys. JETP, Vol.6 (1991) 976.

[7] A. J. Lichtenberg, M.A. Liebermann, "Regular and stochastic motion", Springer Verlag (1983).

[8] G. Benettin et al. , Meccanica, Vol.15 (1980) 21.

[9] J. A. Krommes, C. Oberman, R.G. Kleva, J. Plasma Phys., Vol.30 (1983) 11.

NON-LINEAR THEORY OF MAGNETIC LINE DIFFUSION IN A STOCHASTIC LAYER

R. Balescu°, J. Misguich*, F. Spineanu*•, E. Vanden Eijden°, M. Vlad*•, H. Wang°.

* Association Euratom-C.E.A. sur la Fusion, DRFC, Centre d'Etudes de Cadarache, F-13108 St.-Paul-lez-Durance Cedex, France.

° Association Euratom-Etat Belge sur la Fusion, Physique Statistique et Plasmas, CP 231, Université Libre de Bruxelles, Campus Plaine, Bvd. du Triomphe, B-1050 Bruxelles, Belgium.

• On leave of absence from the Institute of Atomic Physics, P.O. Box MG-7, Magurele, Bucharest, Romania.

The problem of particle and energy transport in a magnetically confined plasma, in a region where the magnetic field is completely stochastic, is of major importance for controlled fusion. Here we concentrate on the purely magnetic aspect of the problem, i.e. the spatial diffusion of magnetic lines. The magnetic field is supposed to contain a fluctuating component, perpendicular to the main field, due to internal instabilities or to irregularities in the external coils ("braided field"):

$$\underline{B}(\underline{x}) = B_0 \left(\underline{e}_z + b_x(\underline{x})\underline{e}_x + b_y(\underline{x})\underline{e}_y\right) \tag{1}$$

where $B_0 = const.$ and $b_x, b_y \ll 1$. In order to ensure the divergence-free condition $\underline{\nabla}_\perp \cdot \underline{b}(\underline{x}) = 0$, $\underline{b}$ is represented by the vector potential $\underline{a}(\underline{x}) = \Psi(\underline{x})\underline{e}_z$. The equations for the magnetic line are Hamiltonian ($1^{1/2}$ degrees of freedom):

$$\frac{d\underline{x}_\perp}{dz} = \underline{b}(\underline{x}_\perp, z) = \underline{\nabla} \times (\psi(\underline{x})\,\underline{e}_z) \tag{2}$$

This is a 2-D Langevin type equation (where z plays the role of time). It contains the **Lagrangian nonlinearity** which comes from the $\underline{x}_\perp$ dependence of the magnetic field.

The total magnetic field in such a "stochastic layer" must be described statistically. The statistical assumptions are introduced at the level of the potential $\psi(\underline{x})$ which is taken as a Gaussian random field, spatially homogeneous and isotropic in the (x, y) plane. Its Eulerian (fixed points) autocorrelation function is supposed to be Gaussian:

$$\mathcal{A}(\underline{r}) \equiv \langle \psi(\underline{x} + \underline{r})\psi(\underline{x})\rangle = \langle \psi(\underline{r})\psi(0)\rangle = \beta^2 \lambda_\perp^2 exp\left(-\frac{r_z^2}{2\lambda_{/\!/}^2} - \frac{r_\perp^2}{2\lambda_\perp^2}\right) \tag{3}$$

(the average $\langle ... \rangle$ is taken over an ensemble of realizations of the $\underline{b}$-field).

The Eulerian autocorrelation functions for the magnetic field components are derived. They form a **nondiagonal matrix**. This is a consequence of the divergence-free condition.

$$\mathcal{B}_{mn}(\underline{r}) = \beta^2 \left\{\left(1 - \frac{r_\perp^2}{\lambda_\perp^2}\right)\delta_{mn} + \frac{r_m r_n}{\lambda_\perp^2}\right\}\mathcal{E}(\underline{r}) \tag{4}$$

where: $\mathcal{E}(\underline{r}) \equiv \mathcal{E}(r_z, r_\perp) = exp\left(-\frac{r_z^2}{2\lambda_{/\!/}^2} - \frac{r_\perp^2}{2\lambda_\perp^2}\right)$. Similar expressions are obtained for the Eulerian correlations of the gradients of the magnetic field $b_{m,\alpha}(\underline{x}) \equiv \nabla_\alpha b_m(\underline{x})$, $m, \alpha = x, y$: $\mathcal{B}_{mn}^{\alpha\beta}(\underline{r}) = \langle b_{m,\alpha}(\underline{x}+\underline{r})\, b_{n,\beta}(\underline{x})\rangle = \langle b_{m,\alpha}(\underline{r})\, b_{n,\beta}(0)\rangle$.

The solution of Eq.(2) is obtained by integrating $\underline{b}$ along the magnetic field line:

$$\delta\underline{x}_\perp(\zeta) = \int_0^\zeta d\zeta_1\, \underline{b}[\underline{x}_\perp(\zeta_1), \zeta_1] \tag{5}$$

where $\delta\underline{x}_\perp(\zeta) = \underline{x}_\perp(\zeta) - \langle\underline{x}_\perp(\zeta)\rangle = \underline{x}_\perp(\zeta) - \underline{x}_\perp(0)$. The Mean Square Deviation in the x-direction at "time" ζ is:

$$\Gamma(\zeta) \equiv \langle\delta x^2(\zeta)\rangle = \int_0^\zeta d\zeta_1 \int_0^\zeta d\zeta_2\, \mathcal{L}_{xx}(\zeta_1, \zeta_2) \tag{6}$$

It is determined by the Lagrangian correlation of the magnetic field fluctuations which is defined as:

$$\mathcal{L}_{mn}(\zeta_1+\zeta, \zeta_1) \equiv \langle b_m[\underline{x}_\perp(\zeta_1+\zeta), \zeta_1+\zeta]\, b_n[\underline{x}_\perp(\zeta_1), \zeta_1]\rangle \tag{7}$$

For a homogeneous and stationary turbulence, the Lagrangian correlations are stationary: $\mathcal{L}_{mn}(\zeta_1+\zeta, \zeta_1) = \mathcal{L}_{mn}(\zeta)$

We have adopted **Corrsin approximation** which relates the Lagrangian correlations to the corresponding Eulerian ones:

$$\mathcal{L}_{mn}(\zeta) \cong \int d\underline{r}_\perp\, \mathcal{B}_{mn}(\underline{r}_\perp, \zeta)\, \gamma(\underline{r}_\perp, \zeta) \tag{8}$$

where $\gamma(\underline{r}_\perp, \zeta) = \langle\delta[\underline{r}_\perp - \underline{x}_\perp(\zeta)]\rangle$ is the probability of finding the current point on a field line at the perpendicular position $\underline{r}_\perp$ at "time" ζ, starting from $\underline{x}_\perp(0)$ at "time" 0.

We have shown that, in a homogeneous, stationary and gyrotropic state:

1) the Lagrangian correlation matrix of the field components is **diagonal**:

$$\mathcal{L}_{mn}(\zeta) = \delta_{mn}\, \mathcal{L}(\zeta) \tag{9}$$

and $\mathcal{L}(\zeta)$ is the solution of the following nonlinear integral equation:

$$\mathcal{L}(\zeta) = \beta^2 exp\left(-\frac{\zeta^2}{2\lambda_{/\!/}^2}\right) \frac{\lambda_\perp^4}{\left[\lambda_\perp^2 + 2\int_0^\zeta d\zeta_r\, (\zeta - \zeta_r)\, \mathcal{L}(\zeta_r)\right]^2} \tag{10}$$

2) the Lagrangian correlations of the field gradients are expressed in terms of a single scalar function $\mathcal{K}(\zeta)$ as:

$$\mathcal{L}_{xx}^{xx}(\zeta) = \mathcal{L}_{yy}^{yy}(\zeta) = -\mathcal{L}_{xy}^{xy}(\zeta) = -\mathcal{L}_{xy}^{yx}(\zeta) = \mathcal{K}(\zeta) \tag{11}$$

$$\mathcal{L}_{xx}^{yy}(\zeta) = \mathcal{L}_{yy}^{xx}(\zeta) = 3\mathcal{K}(\zeta) \tag{12}$$

$$\mathcal{L}_{xx}^{xy}(\zeta) = \mathcal{L}_{xy}^{yy}(\zeta) = \mathcal{L}_{yy}^{xy}(\zeta) = \mathcal{L}_{yx}^{xx}(\zeta) = 0 \tag{13}$$

where $\mathcal{K}(\zeta)$ is given by:

$$\mathcal{K}(\zeta) = \beta^2 exp\left(-\frac{\zeta^2}{2\lambda_{//}^2}\right) \frac{\lambda_\perp^4}{\left[\lambda_\perp^2 + 2\int_0^\zeta d\zeta_r\,(\zeta - \zeta_r)\,\mathcal{L}(\zeta_r)\right]^3} \tag{14}$$

The integral equation (10) can be transformed into a differential equation for $\Gamma(\zeta)$ given by Eq.(6):

$$\frac{d^2\Gamma(\zeta)}{d\zeta^2} = 2\beta^2 exp\left(-\frac{\zeta^2}{2\lambda_{//}^2}\right) \frac{\lambda_\perp^4}{[\lambda_\perp^2 + \Gamma(\zeta)]^2} \tag{15}$$

with the initial condition $\Gamma(0) = 0$ and $\Gamma'(0) = 0$. The diffusion coefficient is defined as $D_m = \lim_{\zeta \longrightarrow \infty} D_m(\zeta)$, with:

$$D_m(\zeta) = \frac{1}{2}\frac{d\Gamma(\zeta)}{d\zeta} = \int_0^\zeta d\zeta_1 \mathcal{L}(\zeta_1) \tag{16}$$

Analytical solution for Eq.(15) can be obtained for two limits:

1) $\lambda_\perp \rightarrow \infty$ *(quasilinear, small* α *limit)*: $D_m = D_{QL} \equiv \sqrt{\frac{\pi}{2}}\beta^2\lambda_{//}$

2) $\lambda_{//} \rightarrow \infty$ *(percolation, large* α *limit)*: $D_m = \beta\lambda_\perp$

The numerical solution of Eq.(15) shows the transition from the quadratic to the linear regime as $\alpha = \beta\frac{\lambda_{//}}{\lambda_\perp}$ increases. The resulting diffusion coefficient of the magnetic lines is plotted in Fig.1 as a function of α.

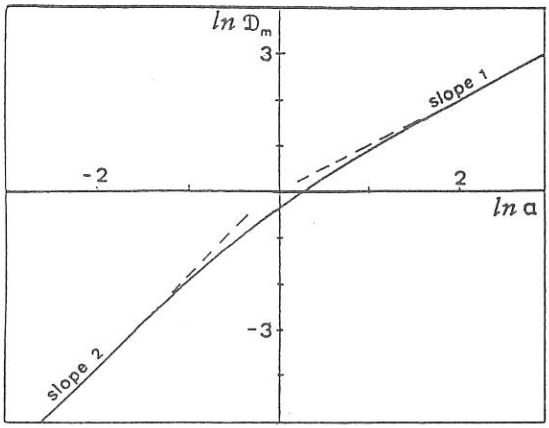


Fig.1: Dimensionless magnetic diffusion coefficient ($\mathcal{D}_m = \lambda_{//} D_m/\lambda_\perp^2$) as function of α.

The relative diffusion of the magnetic lines was also studied. The equation for the distance between two magnetic lines ($\Delta \underline{x}_\perp(\zeta) = \underline{x}_{\perp 2}(\zeta) - \underline{x}_{\perp 1}(\zeta)$), linearised around $\underline{x}_{\perp 1}(\zeta)$ is:

$$\frac{d\Delta x(\zeta)}{d\zeta} = b_{x,x}(\zeta)\,\Delta x(\zeta) + b_{x,y}(\zeta)\,\Delta y(\zeta) \tag{17}$$

Using the Lagrangian correlations for the field gradients and the quasi-linear and markovian approximations, the following equations are obtained for the first stage of the evolution of the relative distance:

$$\begin{aligned}
\frac{d}{d\zeta}\left\langle \Delta x^2(\zeta)\right\rangle &= 2\mathcal{K}\left\langle \Delta x^2(\zeta)\right\rangle + 6\mathcal{K}\left\langle \Delta y^2(\zeta)\right\rangle \\
\frac{d}{d\zeta}\left\langle \Delta y^2(\zeta)\right\rangle &= 6\mathcal{K}\left\langle \Delta x^2(\zeta)\right\rangle + 2\mathcal{K}\left\langle \Delta y^2(\zeta)\right\rangle \\
\frac{d}{d\zeta}\langle \Delta x(\zeta)\Delta y(\zeta)\rangle &= -4\mathcal{K}\langle \Delta x(\zeta)\Delta y(\zeta)\rangle
\end{aligned} \tag{18}$$

with the solution:

$$\begin{aligned}
\left\langle \Delta r^2(\zeta)\right\rangle &\equiv \left\langle \Delta x^2(\zeta)\right\rangle + \left\langle \Delta y^2(\zeta)\right\rangle = \Delta r^2(0) exp\left(2\frac{\zeta}{L_k}\right) \\
\left\langle \Delta x^2(\zeta)\right\rangle &- \left\langle \Delta y^2(\zeta)\right\rangle = [\Delta x^2(0) - \Delta y^2(0)] exp\left(-\frac{\zeta}{L_k}\right)
\end{aligned} \tag{19}$$

which shows that in the average picture the distance between magnetic lines grows gyrotropically (the initial differences are washed out). Here, $\mathcal{K} \equiv \frac{1}{4L_k} = \int_0^\infty d\zeta\, \mathcal{K}(\zeta)$ ($L_K = \frac{\lambda_\perp^2}{4D_{QL}}$ = Kolmogorov length).

This study shows that the effects of the Lagragian nonlinearity (finite $\lambda_\perp$) result in:

- a transition of the adimensional diffusion coefficient $\mathcal{D}_m \equiv D_m \frac{\lambda_{/\!/}}{\lambda_\perp^2}$ from α^2 to α or equivalently the decrease of the dimensional D_m when $\lambda_\perp$ decreases (at fixed $\beta, \lambda_{/\!/}$).
- the onset of the chaoticity of the magnetic lines (finite Kolmogorov length) as soon as $\alpha \neq 0$.

The condition $\underline{\nabla} \cdot \underline{b} = 0$ is responsible for the gyrotropization (19) of the mean square distance between magnetic lines and for an increase of the nonlinear effects (squaring the nonlinearity in Eqs.(10) and (15)).

The study of the diffusion problem through the solution of a differential equation is a rather new methodology. It leads in particular to an analytic expression of the diffusion coefficient, both in the quasilinear limit and in the oposite, percolation limit. In between, the numerical solution of the equation exhibits a transition from a regime $D_m \sim \beta^2$ to a regime $D_m \sim \beta$: this is very reminiscent of the transition from the quasilinear to the "Bohm-like" regime in the electrostatic drift wave turbulence. The same method is also applied to particle diffusion.

Radially Extended 2D Toroidal Mode Structures and Velocity Shear Effects

J W Connor, J B Taylor and H R Wilson
UKAEA Government Division, Fusion, Culham, Abingdon, Oxfordshire, OX14 3DB, UK
(UKAEA/Euratom Fusion Association)

For drift waves with high toroidal mode number, when the separation of rational surfaces is small compared to equilibrium radial profile scalelengths, the ballooning representation can be exploited to simplify the 2-D problem. The theory of such toroidal drift waves [1,2] was originally formulated using techniques which were first employed for MHD ballooning theory [3]. The resulting modes are confined by two WKB turning points to be highly localised around the position where the diamagnetic frequency, ω_*, is a maximum, with a width $\sim r/n^{1/2}$ (where r is the minor radius and n is the toroidal mode number). Away from such a position, or in a region of sheared plasma flow, these modes cannot exist. Therefore, although the localised modes are interesting in that they are less stable than their cylindrical analogues, they are probably not important for plasma transport. Recently, a new type of drift wave structure has been identified using a wave number representation, which is not constrained to be localised in a region where ω_* is stationary, but can exist anywhere in the plasma [4]. Furthermore, the distance between WKB turning points of this new mode is found to be much larger than that of the original mode ($\sim \epsilon r$, where ϵ is the toroidicity) and we therefore refer to these two types as 'extended' and 'localised' respectively. Note, however, that in the presence of dissipation the actual mode width may not extend as far as the turning point separation suggests; this is the subject of future work.

Both ballooning [5] and wavenumber [4] representations reduce the original 2-D partial differential equation to a more tractable system of 1-D ordinary differential equations. In both cases the same leading order equation is obtained with an eigenvalue $\omega(k)$ that is a periodic function of the radial wavenumber, k, which appears as a parameter in this equation. The radially localised modes correspond to a localised range of k about a value k_0 which maximises the growth rate as $\gamma(k_0)$ while the extended modes span a whole period in k and their growth rate is the average $\oint \gamma(k)dk$. Thus the extended modes tend to be more stable than the localised modes and have a growth rate which is close to the slab value, but may be more relevant for transport because of their greater radial extent and their ability to exist at any radial location.

In the H-mode, edge pressure gradients can be steep and flows with strong radial shear have been observed. Clearly the 'ballooning' theory results break down in this region and it is necessary to solve the full 2-D equation. This is the subject of the work presented here. In particular, we are interested in possible explanations of the improved confinement observed in the H-mode and we therefore concentrate on results for the extended mode, although we shall discuss the localised mode briefly as it allows a convenient validation test of our 2-D calculation.

We begin with a brief discussion of our model instability which is based on a simplified electron drift wave [6]. The instability drive is not addressed in this work; instead we calculate the shear damping and assume that a sufficiently strong drive exists to destabilise the mode. In this way we are able to employ a relatively simple drift wave model, which includes toroidal coupling and shear damping, to outline the essential features of two dimensional extended toroidal modes and make comparisons with the predictions of the 'ballooning' theory. Analysis of a more realistic model is the subject of future research.

We define a radial variable $x = nqs(r - r_0)/r$ and a poloidal angle θ. Here q is the safety factor, s is the magnetic shear and r_0 is the minor radius of the reference flux surface (assumed circular). In these coordinates the model equation becomes [6]:

$$\left\{\frac{\partial^2}{\partial x^2} - \sigma^2\left(\frac{\partial}{\partial\theta} + ix\right)^2 - \epsilon\left[\cos\theta + is\sin\theta\frac{\partial}{\partial x}\right] - K_1 x - K_2 x^2 - \lambda\right\}\phi = 0 \qquad (1)$$

All variables have the same definition as given in [6] except that, in the case of a toroidal rotation, we have $\omega \to \omega - n\Omega$ where ω is the mode frequency and Ω is the toroidal angular rotation frequency. This modifies the λ, K_1 and K_2 parameters:

$$\lambda = \left[\frac{1}{bs^2(1+\tau)}\right]\left[\frac{\omega - n\Omega}{\omega_*} - 1 + b(1+\tau)\right] \tag{2}$$

$$K_1 = -\frac{r}{nqbs^3(1+\tau)}\left\{\frac{1}{L_*^{(1)}} + n\hat{\Omega}\left[\frac{1}{L_\Omega^{(1)}} - \frac{1}{L_*^{(1)}}\right]\right\} \tag{3}$$

$$K_2 = -\frac{r^2}{2n^2q^2bs^4(1+\tau)}\left\{\frac{1}{L_*^{(2)}} - \frac{2}{(L_*^{(1)})^2} + n\hat{\Omega}\left[\frac{1}{L_\Omega^{(2)}} - \frac{2}{L_\Omega^{(1)}L_*^{(1)}} - \frac{1}{L_*^{(2)}} + \frac{2}{(L_*^{(1)})^2}\right]\right\} \tag{4}$$

where $\hat{\Omega} = \Omega/\omega_*$, $(L_*^{(n)})^{-1} = (1/\omega_*)(d^n\omega_*/dr^n)$ and $(L_\Omega^{(n)})^{-1} = (1/\Omega)(d^n\Omega/dr^n)$. Note that the model retains the essential physics required to describe the mode; i.e. shear damping through σ, toroidal coupling through ϵ and radial variation of the equilibrium through K_1 and K_2.

For sheared toroidal rotation, with $\Omega \sim \omega_*$ the approximation K_1, $K_2 \ll 1$ becomes invalid and it is not possible to use the ballooning formalism; it is then necessary to solve the full 2–D equation. In order to do this we employ a series expansion in terms of Hermite polynomials in the radial direction and Fourier harmonics in the poloidal direction, where the expansion coefficients and the argument of the Hermite polynomials are treated as variational parameters determined by requiring stationarity of the functional

$$J = \int_{-\infty}^{\infty} dx \int_{-\pi}^{\pi} d\theta \quad \left\{\frac{\partial\phi^\dagger}{\partial x}\frac{\partial\phi}{\partial x} - \sigma^2\left(\frac{\partial}{\partial\theta} - ix\right)\phi^\dagger\left(\frac{\partial}{\partial\theta} + ix\right)\phi + (K_1x + K_2x^2)\phi^\dagger\phi \right.$$
$$\left. + \epsilon\left[\cos\theta\,\phi^\dagger\phi + \frac{is}{2}\sin\theta\left(\phi^\dagger\frac{\partial\phi}{\partial x} - \phi\frac{\partial\phi^\dagger}{\partial x}\right)\right]\right\} \tag{5}$$

subject to the normalisation condition

$$\int_{-\infty}^{\infty} dx \int_{-\pi}^{\pi} d\theta\, \phi^\dagger\phi = 1 \tag{6}$$

Thus we choose for the trial functions

$$\phi = \sum_{m=-\infty}^{\infty}\sum_{n=0}^{\infty} c_m^n e^{-im\theta}\exp\left\{-\frac{\alpha^2}{2}(x-\beta_m^+)^2\right\} H_n[\alpha(x-\beta_m^+)] \tag{7}$$

$$\phi^\dagger = \sum_{m=-\infty}^{\infty}\sum_{n=0}^{\infty} c_m^{n\dagger} e^{-im\theta}\exp\left\{-\frac{\alpha^2}{2}(x+\beta_m^-)^2\right\} H_n[-\alpha(x+\beta_m^-)] \tag{8}$$

where $\beta^\pm = (2m\sigma^2 \pm K_1)/(2(\sigma^2 - K_2))$. Here we have constructed ϕ to be a linear combination of a set of basis functions that are similar to the slab eigenfunctions, but we have allowed for toroidal modifications to the radial mode structure through the variational parameter, α. The conjugate function, $\phi^\dagger$, is constructed using the condition that $\phi^\dagger(x,\theta;K_1) = \phi(-x,\theta;-K_1)$ which can be seen by varying the functional J with respect to ϕ. Finding stationary points of J with respect to $c_m^{n\dagger}$ and α then yields a system of equations which can be solved using matrix techniques to evaluate the 'eigenvectors' c_m^n, the eigenvalue λ and the variational parameter α.

It is interesting to use the 2-D calculation to first investigate the small K_1 and K_2 limits and compare with the results of the 'ballooning' theory discussed above. First let us consider the localised mode, which exists in the limit $K_1 \ll K_2 \ll 1$; thus we take $K_1 = 0$, $K_2 = 0.01$, $\sigma = \epsilon = s = 1$. Retaining 31 Fourier modes and 3 Hermite polynomials, the matrix system is solved for

the eigenvector c_m^n and the eigenvalue λ. As illustrated in figure 1a, this is sufficient to describe the mode (more harmonics must be retained for lower K_2 and in the limit $K_2 = 0$ an infinite number of harmonics are coupled) and the eigenvalue of $\lambda_{2d} = 1.05 - 0.771i$ compares well with the 'ballooning' result of $\lambda_{lb} = 1.13 - 0.77i$. The 2-D eigenfunction can be re-constructed and, as illustrated in figure 1b, this 'balloons' around $\theta = \pi$ (this is consistent with the 'ballooning' theory which requires $k = \pi$). The radial envelope for the 2-D calculation is compared with the result for the ballooning formalism in figure 1c and again good agreement is obtained.

The extended mode structure can be investigated by setting $K_2 = 0$, $K_1 = 0.1$ and retaining 41 Fourier harmonics and 5 Hermite polynomials. The series is terminated by the finite value of K_1 as illustrated in figure 2a and the eigenvalue of $\lambda_{2d} = -0.015 - 0.973i$ agrees well with the result obtained from the wave number representation of $\lambda_{eb} = -0.011 - 0.975i$ (note that this is close to the slab eigenvalue of $\lambda_{\text{slab}} = -i$). The eigenfunction, shown in figure 2b, has no unique poloidal angle about which it balloons, and the radial structure, shown in figure 2c, is very different to that of the localised mode.

We now consider the effects of a finite velocity shear, modelled by an $O(1)$ value of K_1. The localised modes cannot exist in such a region and we are interested in the effect of velocity shear on the extended drift waves. Three effects are apparent as K_1 is increased from 0.1 through 1 and finally to 5. The results for $K_1 = 0.1$ are illustrated in figure 2 where it will be seen that $\sim$ 30 Fourier harmonics couple to give the mode structure. Increasing K_1 to 1 reduces this number to just 6 Fourier harmonics and the radial extent of the mode is also reduced (see figure 3). The eigenvalue, $\lambda = -0.26 - 0.98i$ exhibits almost the same level of shear damping. Increasing K_1 to 5 further reduces the radial mode width and then the mode is dominated by a single Fourier harmonic, with the eigenvalue $\lambda_{2d} = -0.12 - 0.99i$ very close to the slab result.

To summarise, we have calculated the 2-D eigenmode structure for a simple toroidal electron drift wave model and have identified two distinct mode structures which agree well with earlier calculations using 'ballooning' theory or a wave number representation in the limit of small K_1, K_2. However, the 2-D calculation presented here is not restricted to small values of K_1 and K_2 and can be used to investigate the effect of finite velocity shear on the extended mode structures. While the shear damping is only weakly affected by the velocity shear, the number of coupled Fourier harmonics and radial mode width are reduced and this may be related to the improvement in confinement observed in the H-mode where strong velocity shears are observed.

Acknowledgement Discussions with S Sen are acknowledged. This work was funded jointly by the UK Department of Trade and Industry and by Euratom.

[1] Hastie R.J., Hesketh K.W. and Taylor J.B. Nucl.Fus. **19** (1979) 1223

[2] Chen L. and Cheng C.Z. Phys.Fluids **23** (1980) 2242

[3] Connor J.W., Hastie R.J. and Taylor J.B. Proc.Roy.Soc. **365** (1979) 1

[4] Connor J.W., Taylor J.B. and Wilson H.R. Phys.Rev.Lett. **70** (1993) 1803

[5] Taylor J.B., Connor J.W. and Wilson H.R. Plas.Phys.Cont.Fus.**35** (1993) 1063

[6] Connor J.W. and Taylor J.B. Phys.Fluids **30** (1987) 3180

Figure Captions

Figure 1: Eigenvectors (a), 2-D mode structure (b) and radial envelope (c) (full curve is the 2-D result) for localised mode ($K_1 = 0$, $K_2 = 0.01$, $\sigma = \epsilon = s = 1$). Note, negative eigenvector coefficients are hidden.

Figure 2: As figure 1, but for extended mode ($K_1 = 0.1$, $K_2 = 0$).

Figure 3: Eigenvector for extended mode with increased velocity shear ($K_1 = 1$).

Fig 1a

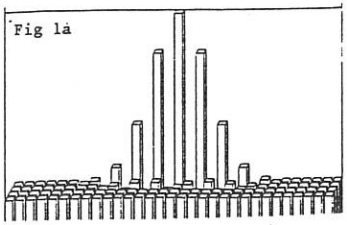


Fig 2a

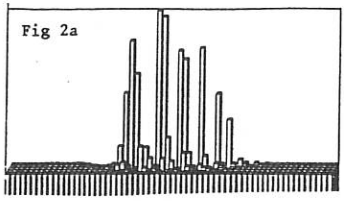


Fig 1b

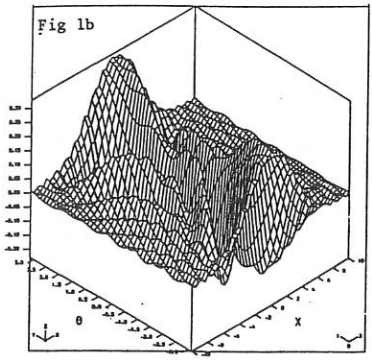


Fig 2b

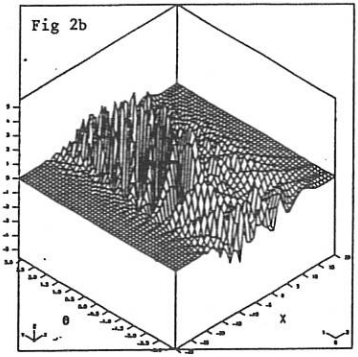


Fig 1c

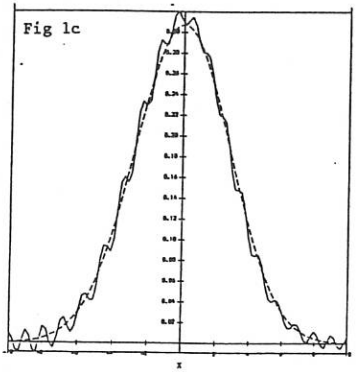


Fig 2c

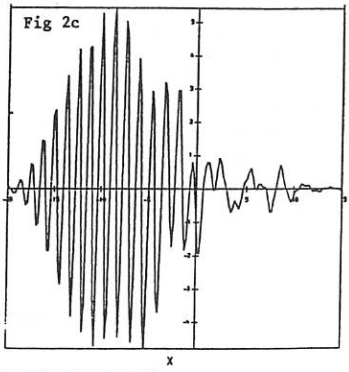
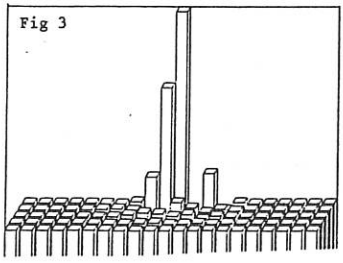


Fig 3



A wireframe model for toroidal magnetic field - plasma systems

A. Montvai, N.J Lopes Cardozo, M. de Rover
FOM-Instituut voor Plasmafysica 'Rijnhuizen'
P.O.Box 1207 3430 BE Nieuwegein, The Netherlands

Abstract

A numerical procedure to compute the magnetic equilibrium in a toroidal plasma is described. The existence of flux surfaces is ***not*** presumed, the procedure does ***not*** solve the Grad-Shafranov equation. Instead the plasma current is represented by a large number of current elements. Local pressure balance is achieved by iteration. First results show a numerically stable equilibrium with a set of good and 'fuzzy' surfaces.

1 Introduction

Recent measurements in the RTP tokamak [1] show longlived spatial fluctuations and asymmetries of the electron temperature distribution. These measurements are hard to interpret in terms of a configuration consisting of nested, toroidal magnetic surfaces.

In the MHD approximation the equation of motion is simplified to a form containing a scalar pressure. It can be shown that this implies - mathematically - the presence of perfect magnetic surfaces. In order to avoid these mathematical rather than physical constraints a system of programs has been constructed to model toroidal discharges.

2 Numerical procedure

Essential features of the algorithm implemented are the following:

- the system of programs delivers a Grad-Shafranov - like equilibrium with magnetic surfaces in the limit of axial symmetry and exact validity of the force balance equation;
- local violation of the equilibrium equation is an easily controllable parameter,
- CPU time needed to compute a (numerically) stable field configuration was kept within practical limits by the use of the so-called mapping technique [2]. One of its main features is that the field variables are stored on a 3-D grid in an always accessible and easily computable way, which drastically reduces the total CPU time needed.

The 3-D grid consists of a sufficiently dense set of poloidal sections of the plasma torus along the toroidal angle. On this sequence of planes the $\mathcal{M}$ map generated by the field lines is computed on a 2-D grid. (Fig.1.) These maps are defined by the:

$$\mathcal{M}^k = P_k(R_i, Z_l) \rightarrow P_{k+1}(\tilde{R}_i, \tilde{Z}_l)$$
$$P_{k+1}(\tilde{R}_i, \tilde{Z}_l) = P_k(R_i, Z_l) + \int_{\phi_k}^{\phi_{k+1}} \frac{\partial \vec{B}^j}{\partial l} dl \qquad (1)$$
$$1 \leq i \leq N_i, \quad 1 \leq l \leq N_l, \quad 1 \leq k \leq N_k,$$

relations. Here R, Z ϕ defines a cylindrical coordinate system. The N_i, N_l and N_k integers give the gridsize in the R, Z and ϕ directions respectively. The j index of $\vec{B}$ reflects that the procedure itself is an iteration constructed as follows.

First the vector field defining the magnetic configuration is used to compute the corresponding current density distribution.

The current field contains $N_K \times N_i \times N_l$ straight current segments ('wires') started over the grid at each of the poloidal sections and ending on the next one. Consequently one has to specify a current value and a direction for this current carrying 'wires'.

To do this the total current value and the type of the current density distribution are predetermined. As a rule they are consistent with an equilibrium configuration of a typical shot on the RTP tokamak. ($q_a = 4.4$t; $B_0 = 2T$)

A pressure distribution is chosen of the form [3]:

$$p(r) = P_0\{1 + \frac{r^2}{a^2}(const)\}^2 \qquad (2)$$

With these assumptions a current density distribution and a current vector field can be devised. It exactly fulfills the force-balance equation on the three-dimensional grid.

Naturally the discretisation (and the linear elements used) result in violation of the force balance between adjacent gridpoints. This level of violation can be controlled by using current tubes of finite radius with uniform internal current distribution. A typical value of $\rho \sim a/40 = 5mm$ corresponding to $\tilde{B}/B \leq 10^{-3}$ is used.

Using the Biot-Savart law in a form taking into account the finite length of a current element it is possible to compute a $\vec{B}^{j+1}$ vector field.

This is used as input for the subsequent loop of iteration.

3 Results

- The final configuration is sensitively dependent on the correctness of the pressure gradient distribution.
- The stable configuration is in wide limits independent of the input magnetic field.
- The evolution goes through a Grad-Shafranov like equilibrium to a so-called 'fuzzy' configuration which contains conserved and destructed magnetic surfaces.
- The destruction of surfaces does not lead to a complete randomistaion of the field lines. Very strong, slowly decaying correlations remain in the system. The dominant local structure of field lines is still close to a set of nested toroidal regions.

- The spreading out of the field lines is a strong function of the distance from the magnetic axis along the small radius.
- There is a poloidal dependence in the 'fuzzyness' of the configuration 'more fuzzyness on the low field side'.

4 Discussion

This was the first step towards a new way of computing 3-D equlibria in Tokamaks. The necessary extensions: better modeling of the current field, more realistic constraints on pressure distribution, etc. are underway. Nevertheless the first results: a new class of possible field structures and correlations with recent measurements are encourageing signs. A potentially useful feature is, that the procedure can deliver the vector potential of the magnetic field as well.

5 References

[1] N.J. Lopes Cardorzo et al.: Phys. Rev. Lett. accepted for publication.
[2] A. Montvai et al.: JET Report: JET-R(92)05 1992.
[3] F.C. Schüller et al.: Proc of 18th Eur. Conf. on Contr. Fus and Pl. Phys. Berlin,1991, IV-185

6 Acknowledgement

Constructive discussions with F.C Schüller, T.J. Schep and J.P Goedbloed are gratefully acknowledged.

This work was performed under the Euratom-FOM association agreement with financial support from NWO and Euratom.

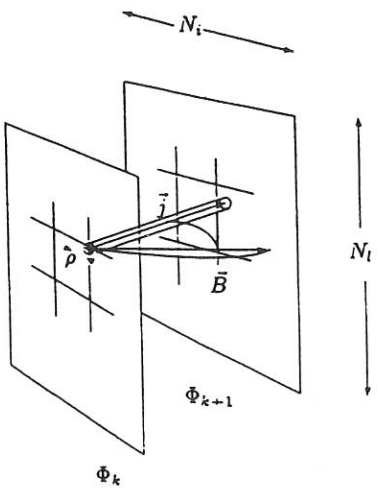


Fig. 1. The WIREFRAME model.
It consists of a discretised current field defined over $\sim$ 50 poloidal sections on which a regular grid of size $\sim 50 \times 50$ is defined. The current segments start at the gridpoints of a poloidal section and end at the next one. The cruicial point of the numerical procedure is to iterate the scheme up to a state when these segments ('wires') form a consistent pair with the magnetic field and observe the predetermined pressure distribution.

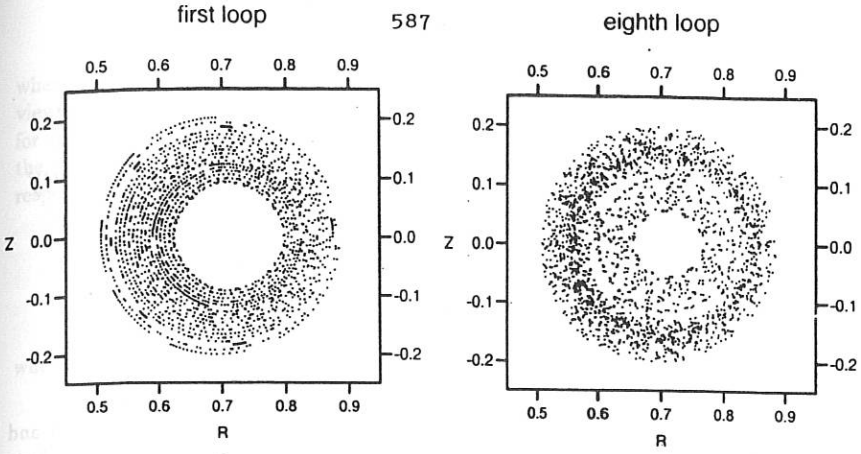


Fig. 2. Poincaré plot of 18 trajectories started at Z=0 and 6 $cm \leq r_i \leq$ 18 cm. Each field line has 80 revolutions around the main axis.
a.) State of the configuration after one loop of iteration completed.
b.) State of the configuration after eight loops.

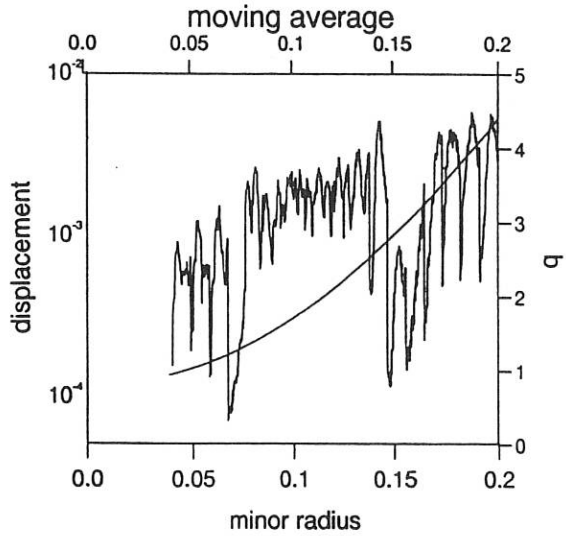


Fig. 3. Moving average of the mean squared displacement of 20 consecutive crossings of the Poincaré section along a sample consisting of $\sim$ 2000 points. The points are computed using 30 trajectories started at Z=0 and 4 $cm \leq r_i \leq 20cm$. In each trajectories the first 20 crossings are discarded.

Hamiltonian structure and stability of low-frequency nonlinear plasma dynamics

F. Pegoraro, B. N. Kuvshinov* and T. J. Schep*

Dipartimento di Fisica Teorica, Università di Torino, 10125 Torino, Italy

Abstract In this paper we generalize the "reduced" MHD (RMHD) model and include electron and ion diamagnetism, finite ion gyroradii and finite electron mass effects which dominate the plasma dynamics at small scales. In a high-temperature plasma, the electron inertial skin depth is smaller than the gyro-radius of a thermal ion. These equations can be cast in (noncanonical) Hamiltonian form. It is shown that infinite sets of conserved quantities (Casimirs) exist. Sufficient conditions for stability are discussed on the basis of the second variation, at constant Casimirs, of the Hamiltonian functional.

We consider a geometry with magnetic field $\vec{B}$ and electric field $\vec{E}$

$$\vec{B} = B_0(\vec{e}_z + \vec{e}_z \times \nabla\Psi), \qquad \vec{E} = -\nabla\phi + \frac{B_0}{c}\frac{\partial\Psi}{\partial t}\vec{e}_z, \tag{1}$$

where Ψ is the flux function, ϕ is the electrostatic potential. Assuming that the parallel ion velocity is much smaller than the electron velocity v_z, Ampere's law reads $v_z \approx -J_z/en_0 = -(cB_0/4\pi en_0)\nabla^2\Psi$, where n_0 is a reference value. The parallel momentum balance and the continuity equation of the electrons are

$$\frac{1}{a}\frac{\partial\Psi_e}{\partial t} + [\Phi\ ,\ \Psi_e] + [\Psi\ ,\ \ln\frac{n}{n_0}] = \frac{\partial\Phi}{\partial z} - \frac{\partial}{\partial z}\ln\frac{n}{n_0}, \tag{2}$$

and

$$\frac{1}{a}\frac{\partial}{\partial t}\ln\frac{n}{n_0} + [\Phi\ ,\ \ln\frac{n}{n_0}] - \frac{1}{\beta_e}[\Psi\ ,\ J] = \frac{1}{\beta_e}\frac{\partial J}{\partial z}, \tag{3}$$

respectively. Here, $\Psi_e = \Psi - {d_e}^2\nabla_\perp^2\Psi$ is the generalized flux function, $d_e = c/\omega_{pe}$ is the electron inertial skin depth, the brackets are defined by $[f,g] = \vec{e}_z\cdot\nabla f\times\nabla g$, $\Phi = e\phi/T$, $J = \nabla_\perp^2\Psi$, $a = cT/(eB_0)$, and $\beta_e = 4\pi n_0 T/{B_0}^2$. Finite electron mass effects are taken into account. Temperatures are taken to be constant throughout the fluid.
The electron density n is related to the ion density through the quasi-neutrality condition. The ion response is given by:

$$\frac{1}{a}\frac{\partial}{\partial t}(\ln\frac{n}{n_0} - {\rho_i}^2\nabla_\perp^2 h) + [\Phi,\ \ln\frac{n}{n_0}] - {\rho_i}^2\nabla_\perp\cdot[\Phi,\ \nabla_\perp h] = 0, \tag{4}$$

*FOM-Instituut voor Plasmafysica, "Rijnhuizen", Nieuwegein, the Netherlands

where $\rho_i^2 = T_i m_i c^2/(eB_0)^2$, $\tau_i = T/T_i$, and $h = \tau_i\Phi + \ln n/n_0$. Since Eq.(4) can be viewed as a nonlinear generalization of the Padé approximation to the linear ion response for arbitrary values of the ion gyroradius[1] we assume it to be valid for all values of the gyroradius. Its leading order solution in the large gyroradius limit is the adiabatic response $\ln n/n_0(\vec{x}) + \tau_i\Phi = 0$.

The nonlinear equations [2, 3, 4] can be written in Hamiltonian form[2]

$$\frac{\partial \xi_i}{\partial t} = \Big\{\xi_i\ ,\ H\Big\}, \qquad i = 1,2,3, \tag{5}$$

where the noncanonical variables ξ_i are

$$\xi_1 = \Psi_e, \quad \xi_2 = d_e\beta_e^{1/2}\ln\frac{n}{n_0}, \quad \xi_3 = d_e\beta_e^{1/2}\Big(\rho_i{}^2\nabla^2 h - \ln\frac{n}{n_0}\Big). \tag{6}$$

The Hamiltonian is the energy functional

$$H = \frac{1}{2}\int d^3x\Big(-\xi_1\frac{\nabla_\perp^2}{1-d_e^2\nabla_\perp^2}\xi_1 + (1+\frac{1}{\tau_i})\frac{\xi_2^2}{d_e^2} - \frac{1}{d_e^2}(\xi_2+\xi_3)\frac{1}{\tau_i\rho_i^2\nabla_\perp^2}(\xi_2+\xi_3)\Big). \tag{7}$$

The noncanonical Poisson brackets are a generalization of the brackets given in[3,4]

$$\Big\{F\ ,\ G\Big\} = \frac{ad_e}{\beta_e^{1/2}}\int d^3x\ W_{ij}\Big[\frac{\delta F}{\delta\xi_i}\ ,\ \frac{\delta G}{\delta\xi_j}\Big] - \frac{ad_e}{\beta_e^{1/2}}\int d^3x\ W_{ij}^{(z)}\frac{\delta F}{\delta\xi_i}\frac{\partial}{\partial z}\frac{\delta G}{\delta\xi_j}$$
$$-\frac{ad_e}{\beta_e^{1/2}}\rho_i{}^2\int d^3x\ \xi_2\Big[\frac{\partial}{\partial x_k}\frac{\delta F}{\delta\xi_3}\ ,\ \frac{\partial}{\partial x_k}\frac{\delta G}{\delta\xi_3}\Big], \tag{8}$$

where $x_k = (x,y)$ and the symmetric matrices W_{ij} and $W_{ij}{}^{(z)}$ are defined by

$$W_{ij} = \begin{pmatrix}\xi_2 & \xi_1 & 0\\ \xi_1 & \xi_2 & 0\\ 0 & 0 & \xi_3\end{pmatrix}, \quad W_{ij}^{(z)} = \begin{pmatrix}0 & 1 & 0\\ 1 & 0 & 0\\ 0 & 0 & 0\end{pmatrix}, \tag{9}$$

We consider localized phenomena and disregard boundary effects. The brackets (8) are antisymmetric and satisfy the Jacobi identity $\{F,\{G,H\}\}+\{G,\{H,F\}\}+\{H,\{F,G\}\} = 0$. Apart from the ξ_2 contribution to the integrand in the second term in Eq.(8), we see from the form of the matrices (9) that the Poisson brackets do not contain any coupling between $\xi_{1,2}$ and ξ_3. Coupling arises when ion currents are no longer negligible and/or when charge neutrality is violated. It can easily be seen that the choice of new variables $\xi_\pm = 1/2(\xi_1 \pm \xi_2)$ diagonalizes the Poisson brackets. but not the Hamiltonian.

The system of Eqs.(5) has two types of invariants: those related with the symmetries of the Hamiltonian and those related with the algebraic structure of the Poisson brackets. When the Hamiltonian has a continuous translational symmetry in x, y and/or rotational symmetry, the functionals P_x and/or P_y, that generate translations, and the angular momentum functional L_z, that generates rotations in (x,y),

$$P_{(x,y)} = \int d^3x\ (y,-x)(\xi_2+\xi_3), \quad L_z = -\int d^3x\ r^2(\xi_2+\xi_3)/2 \tag{10}$$

are conserved, as is the case for the Hamiltonian (7). The operators $P_{x,y}$ and L_z satisfy the appropriate commutation relations $\{L_z, P_x\} = P_y$, $\{L_z, P_y\} = -P_x$ and $\{P_x, P_y\} = \int d^3x(\xi_2 + \xi_3)$.

The invariants of the second set are called Casimirs and are functionals that commute with all functionals F, i.e. $\{C, F\} = 0$. We treat 2D cases and take all quantities to depend on t, x, and y. In these cases the brackets (8) admit two infinite sets of Casimirs,

$$C_\pm = \int d^2x\ f_\pm(\xi_1 \pm \xi_2) = \int d^2x\ f_\pm(\Psi_e \pm \beta_e^{1/2} d_e \ln n/n_0), \tag{11}$$

with $f_\pm$ arbitrary functions. These functionals depend only on the dynamics of the electrons and do not depend on the ion response.

In the limits $m_e \to 0$, $\ln n/n_0 \to \rho_s^2 \nabla^2 \Phi$, the Casimir (11) become those of RMHD[4] In the cold ion limit, $T_i \to 0$, the last term in (8) vanishes. Then the system contains an infinite number of Casimirs involving ξ_3

$$C_3 = \int d^3x\ G(\xi_3), \tag{12}$$

with G an arbitrary function. Note that in this limit $\xi_3 = d_e \beta_e^{1/2}(\rho_s^2 \nabla^2 \Phi - \ln(n/n_0))$ with $\rho_s^2 = \tau_i \rho_i^2$. In the model of reduced magnetohydrodynamics (RMHD) ξ_3 vanishes. Then the Casimirs (12) become trivial. Eq.(11) implies that magnetic reconnection in Ψ_e and/or Ψ can occur in the presence of an infinite set of conservation laws. This is related with the fact that inertia is particularly important in regions where the reconnection process can occur. The existence of these infinite sets of Casimirs is equivalent to the special properties of the equations of motion (2, 3) and (4) under time transformations.

In terms of the variables $(\xi_+,\ \xi_-,\ \xi_3)$, where $\xi_\pm = \frac{1}{2}(\xi_1 \pm \xi_2)$ so that $\delta H/\delta \xi_\pm = \delta H/\delta \xi_1 \pm \delta H/\delta \xi_2$, the equations of motion (5) read in the limit $T_i \to 0$,

$$\frac{\partial \xi_\pm}{\partial t} = \mp \frac{a d_e}{\beta_e^{1/2}} [\xi_\pm,\ \frac{\delta H}{\delta \xi_\pm}]. \quad \frac{\partial \xi_3}{\partial t} = -\frac{a d_e}{\beta_e^{1/2}} [\xi_3,\ \frac{\delta H}{\delta \xi_3}], \tag{13}$$

We remark that Eqs.(13) and the corresponding Poisson brackets (8) are invariant under coordinate transformations in the plane that leave the Jacobian equal to unity. The Hamiltonian, however, is only invariant under translations and rotations. Equations (13) also take the same form after the transformations $g_i(\xi_i) d\tau \to d\tau_i$ and $\delta H/\delta \xi_i \to g_i^{-1} \delta H/\delta \xi_i$. This is equivalent to redefining the time in Eq.(5) and changing the diagonal matrix W_{ij} according to $\xi_i \to g_i^{-1} \xi_i$. Since the $g_i(\xi_i)$'s are arbitrary, this invariance is equivalent to the existence of three infinite sets of Casimirs. In terms of the new Poisson brackets the translation and rotation operators (10) become

$$P^g_{(x,y)},\ \ L^g_z\ = \int d^2x\ (y,\ -x,\ -r^2/2)\ [g_+(\xi_+)\xi_+ - g_-(\xi_-)\xi_- + g_3(\xi_3)\xi_3], \tag{14}$$

The existence of the Casimir invariants restricts the possible plasma motions to hypersurfaces in the infinite dimensional phase space. This restriction can be used to describe the stationary solutions and the stability of the Hamilton equations (5) with the help of a variational principle. Variations of the field variables that conserve automatically all Casimir invariants, have been introduced by Arnold[5] for the Euler equation. A generic variation Δ which conserves all the Casimir invariants is $\Delta \xi_i = \delta \xi_i + \frac{1}{2!} \delta^2 \xi_i + \ldots$, with

$$\delta \xi_\pm = [\mu_\pm,\ \xi_\pm], \qquad \delta \xi_3 = [\sigma\ , \xi_3], \tag{15}$$

$\mu_\pm(x,y)$ and $\sigma(x,y)$ being arbitrary functions. The first variation of H gives the stationary solutions of Eqs. (13),

$$\frac{\delta H}{\delta \xi_\pm} = F_\pm(\xi_\pm), \quad \frac{\delta H}{\delta \xi_3} = U'(\xi_3). \tag{16}$$

These equations can be written as $F_\pm(\xi_\pm) = -J \pm \beta_e^{1/2} d_e^{-1}(\ln n/n_0 - \Phi)$, and $U(\xi_3) = -\beta_e^{1/2} d_e^{-1}\Phi$. When the Hamiltonian is minimized under the constraint of a constant operator (14), propagating solutions are obtained where each ξ_i propagates with a velocity that is constant on the corresponding $\xi_i = const$ surfaces. When all $g_i = 1$, all velocities are equal and a stationary equilibrium is obtained.
The second variation of the Hamiltonian functional is

$$\delta^2 H = \int d^2x \left(-\delta\xi_1 \delta J + A_1 (F'_+ \delta\xi_+ + F'_- \delta\xi_-)^2 + A_2 (\delta\xi_+ - \delta\xi_-)^2/d_e^2 \right.$$
$$\left. - \beta_e \delta\Phi \rho_s^2 \nabla^2 \delta\Phi - U'(\xi_3)(\delta\xi_3)^2 \right), \tag{17}$$

where $\delta J = (1 - d_e^2\nabla^2)^{-1}\nabla^2 \delta\xi_1$, $\delta\Phi = (d_e \beta_e^{1/2} \rho_s^2 \nabla^2)^{-1}(\delta\xi_2 + \delta\xi_3)$, and $A_1 = -(F'_+ + F'_-)^{-1}$, $A_2 = 1 - d_e^2(F'_+ F'_-)/(F'_+ + F'_-)$. The first and fourth terms in (17) are positive definite. Sufficient conditions for stability are $A_{1,2} \geq 0$

$$F'_+ + F'_- \leq 0, \qquad -(F'_+ + F'_-) \geq -d_e^2 F'_+ F'_-, \qquad U' \leq 0. \tag{18}$$

In the RMHD limit, ξ_3 is not an independent variable and the last contribution to (17) has to be omitted and the last condition of (18) does not apply. Also in the large-ρ_i limit, ξ_3 is not an independent variable. The equilibrium is given by the first two eqs in (16) and by the relationship $\ln n/n_0(\vec{x}) + \tau_i \Phi = 0$. Instead of (17), we obtain

$$\delta^2 H = \int d^2x \left(-\delta\xi_1 \delta J + A_1 (F'_+ \delta\xi_+ + F'_- \delta\xi_-)^2 + \frac{\hat{A}_2}{d_e^2}(\delta\xi_+ - \delta\xi_-)^2 \right), \tag{19}$$

where $\hat{A}_2 = \tau_i^{-1} + A_2$. In this case the sufficient conditions for stability read $A_1, \hat{A}_2 \geq 0$ In the limit of zero electron mass $d_e \to 0$. these two conditions reduce to a single one on the profile of the equilibrium current density[6] $\partial J/\partial\xi_1 = \partial J/\partial\Psi \geq 0$.

Acknowledgements This work was performed as part of the research programme of the association Euratom-FOM and of the Italian CNR.

References

[1] F. Pegoraro and T. J. Schep. *Plasma Phys. Contr. Fusion*, **28**, 647 (1986).

[2] T. J. Schep, F. Pegoraro and B. N. Kuvshinov. to be published.

[3] R. D. Hazeltine, C. T. Hsu, P. J. Morrison. *Phys.Fluids*, **30**,3204 (1987).

[4] P. J. Morrison and R. D. Hazeltine. *Phys. Fluids*. **27**, 886 (1984).

[5] V. I. Arnold. *J. Appl.Math. Mech.*. **29**. 1002 (1965)

[6] R. D. Hazeltine, D. D Holm, J. E. Marsden and P. J. Morrison, *Proc.ICCP* Lausanne 1984, Vol.I, 203 (1984).

Drift-Alfvén vortices in magnetized plasmas

B. N. Kuvshinov, F. Pegoraro*, J. Rem, and T. J. Schep

FOM-Instituut voor Plasmafysica, "Rijnhuizen", Nieuwegein, the Netherlands

Abstract

We consider a set of nonlinear equations that governs the dynamics of low-frequency perturbations in nonuniform magnetized plasmas and takes into account diamagnetic drift, finite ion-sound gyroradius, and finite electron mass effects. The solutions of this set in the form of spatially localized propagating dipole vortices are investigated.

In this paper we consider vortex motions in a plasma slab embedded in a strong uniform magnetic field $B_0\vec{e}_z$. The linear density gradient is in the transverse x-direction. We adopt a collisionless two-fluid model. The electrons are described by the parallel (to $B_0\vec{e}_z$) momentum balance (Ohm) including inertia and by the continuity equation. The ions are taken to be cold and their parallel motion is neglected. Temperature gradients are omitted. This system of equations is treated in Ref. 1, where it is shown that it can be put in noncanonical Hamiltonian form.

The solutions we are interested in correspond to vortices that propagate uniformly in the $(x-y)$ plane perpendicular to the density gradient.

In the cold ion limit the equations of Ref. 1 have the form

$$(\partial\Psi_e/\partial\tau)+[\Phi,\Psi_e]+[\Psi,\ln n/n_0]=0,\ (\partial/\partial\tau)\ln n/n_0+[\Phi,\ln n/n_0]-(1/\beta_e)[\Psi,\nabla^2\Psi]=0,$$

$$(\partial/\partial\tau)(\ln n/n_0-{\rho_s}^2\nabla^2\Phi)+[\Phi,\ln n/n_0-{\rho_s}^2\nabla^2\Phi]=0, \qquad (1)$$

where $\rho_s=(T_e m_i)^{1/2}c/(eB_0)$, is the ion-gyroradius at the electron temperature, $\Psi_e=\Psi-d_e^2\nabla^2\Psi$, $d_e=c/\omega_{pe}$ is the inertial skin-depth, $\beta_e=4\pi n_0 T_e/B_0^2$, and the square brackets denote Jacobians, $[a,b]=\mathrm{e}_z\cdot\nabla a\times\nabla b$. All variables are supposed to be functions of x, $\eta=y+\alpha z-ut$, and $\tau=(cT_e/eB_0)t$, where u is the propagation velocity along y and $\alpha\equiv u/v$ with v the parallel velocity. The poloidal magnetic flux Ψ and the electric potential $\Phi=e\phi/T_e$ are related with their values $\tilde{\Psi}$, $\tilde{\Phi}$ calculated in the laboratory frame by $\Psi=\tilde{\Psi}+\alpha x$, $\Phi=\tilde{\Phi}-\hat{u}x/l_n$, where l_n is the scale-length of the density gradient, $\hat{u}=u/u_*$, and $u_*=cT_e/eB_0l_n$ is the diamagnetic drift velocity of the electrons.

Stationary equilibria are described by (see Eq. (15) of Ref. 1)

$$-\nabla^2\Psi\pm\beta_e^{1/2}d_e^{-1}(\ln n/n_0-\Phi)=F_\pm(\xi_\pm),\qquad -\beta_e^{1/2}d_e^{-1}\Phi=U(\xi_3), \qquad (2)$$

where $F_\pm$ and U are arbitrary functions of

$$\xi_\pm\equiv(\Psi-d_e^2\nabla^2\Psi\pm\beta_e^{1/2}d_e\ln n/n_0)/2,\quad \xi_3\equiv\beta_e^{1/2}d_e(\rho_s^2\nabla^2\Phi-\ln n/n_0). \qquad (3)$$

*Dipartimento di Fisica Teorica, Università di Torino, 10125 Torino, Italy

Equations (2), (3) describe generic stationary propagating nonlinear structures and, as a particular case, drift-Alfvén vortices.

We are interested in solutions for which $\bar{\Psi}$ and $\bar{\Phi}$ are localized. This implies that, at infinity, $\Psi \to \alpha x$, $\ln n/n_0 \to -x/l_n$ and $\Phi \to -\hat{u}x/l_n$. These boundary conditions can be satisfied by taking $F_\pm$ and U to be linear in their arguments. As is usual in vortex theory, these relationships are taken to be linear everywhere. As is well known, for regular solutions the proportionality factors $F'_\pm$ and U' cannot be the same over all space and must be allowed to change at specific surfaces.

Adding and subtracting Eqs. (2) and eliminating $\ln n/n_0$, one obtains the equations

$$\rho_s^2\nabla^2\Psi = h_1\Psi + \beta_e^{1/2}\rho_s h_2\Phi, \quad \rho_s^2\nabla^2\Phi = -(h_2/\beta_e^{1/2}\rho_s)\Psi + [1 - 1/p - (d_e^2/\rho_s^2)h_1]\Phi, \quad (4)$$

where $h_1 = -\rho_s^2(F'_+ + F'_- - d_e^2F'_+F'_-)/D$, $h_2 = -\rho_s d_e(F'_+ - F'_-)/D$, $p = d_e^2U'$ and $D = (2 - d_e^2F'_+)(2 - d_e^2F'_-)$. The eigenvalues of the matrix in Eq. (4) are

$$\kappa_1^2 + \kappa_2^2 = (1 - 1/p) + (1 - d_e^2/\rho_s^2)\, h_1, \quad \kappa_1^2\kappa_2^2 = h_1(1 - 1/p) + h_2^2 - (d_e^2/\rho_s^2)h_1^2. \quad (5)$$

It follows from Eqs. (2), (3) and from the boundary conditions that the values of $F'_\pm$ and of p in the external region are $F'_{\pm e} = 2(\beta_e^{1/2}/d_e)(\hat{u} - 1)(-\beta_e^{1/2}d_e \pm \alpha l_n)^{-1}$, and $p_e = \hat{u}$. These expressions yield

$$h_{1e} = -u_A^2(1 - 1/\hat{u})[1 - (d_e^2/\rho_s^2)u_A^2]^{-1}, \quad h_{2e} = h_{1e}/u_A, \quad p_e = \hat{u}, \quad (6)$$

where $u_A = u/(\alpha c_A)$ and c_A is the Alfvén velocity. In the outer region one of the eigenvalues $\kappa_{1,2}^2$ vanishes and the other is equal to

$$\kappa_e^2 = (1 - 1/\hat{u})\,(1 - u_A^2)\,[1 - (d_e^2/\rho_s^2)u_A^2]^{-1}. \quad (7)$$

Localized modes can exist if $\kappa_e^2 > 0$. It follows from (7) that electron inertia effects are dominant if

$$(d_e^2/\rho_s^2)u_A^2 = [m_e/(m_i\beta_e)]\,[u^2/(\alpha^2c_A^2)] \;>\; 1, \quad (8)$$

which is valid if the electrons are taken to be cold and/or in the limit of purely perpendicular propagation ($\alpha \to 0$). In these cases the limit $d_e \to 0$ cannot be taken[2]. In the opposite limit, all coefficients in (4) are regular for $d_e \to 0$. Note that in these two limits localized vortices exist in complementary velocity intervals. Vortices that satisfy (8), and are thus localized on the electron inertia skin depth, will be considered in a future paper. Regular solutions require that either F'_+, F'_- or p exhibit jumps at separatrix surfaces. Imposing that both sides of Eqs. (2) be continuous, we find that a jump in F'_+ or F'_- may occur at surfaces where the arguments of the functions $F_\pm$ vanish, which corresponds to

$$\Psi \pm \beta_e^{1/2}d_e\Phi = 0, \quad (9)$$

and jumps in p at surfaces where $\Phi = 0$. In principle, only a jump in a single quantity is required. Also the three surfaces will not coincide in general.

In the remainder of this paper we will limit ourselves to the case of vanishing electron inertia. In this limit the surfaces where $F'_\pm$ jump coalesce. Jumps in the quantity $F'_+ + F'_-$ with continuous $F'_+ - F'_-$ can occur at surfaces $\Psi = 0$, and jumps in $F'_+ - F'_-$ with $F'_+ + F'_-$ continuous can occur at $\Phi = \ln n/n_0 = \Psi = \nabla^2\Psi = 0$. We will ignore this latter, rather special case, and will only consider discontinuities in h_1 with h_2 continuous.

The eigenvalues (5) in the inner region are

$$\kappa_{1,2}^2 = \frac{\hat{u}-1}{2\hat{u}}\left[1-u_A^2+\varepsilon_h-\varepsilon_p \pm \sqrt{\left[(1+u_A)^2-\varepsilon_h-\varepsilon_p\right]\left[(1-u_A)^2-\varepsilon_h-\varepsilon_p\right]}\right]. \quad (10)$$

Here $\varepsilon_h \equiv (1-1/\hat{u})^{-1}\Delta h_1$ and $\varepsilon_p \equiv (1-1/\hat{u})^{-1}\Delta(1/p)$ characterize the jumps of the functions h_1 and p at the surfaces $\Psi = 0$ and $\Phi = 0$ respectively. We will limit the discussion to cases in which $\kappa_{1,2}^2$ are real and a single jump occurs. We will label the corresponding vortex solutions as Ψ and Φ vortices. All these solutions represent drift-Alfvén vortices.

We look for solutions of Eqs. (4) in the form of dipole vortices, $\Psi = \Psi_0(r)\cos\theta$, $\Phi = \Phi_0(r)\cos\theta$, where r and θ are the polar coordinates, $r^2 = x^2+\eta^2$, $\tan\theta = \eta/x$.

It is convenient to represent the solutions in terms of functions χ_1, χ_2. Here χ_1 is proportional to the potential ($\Psi_0(r)$ or $\Phi_0(r)$) which goes to zero at the separatrix, and χ_2 is proportional to the parallel electric field. Explicitly,

$$\chi_1(r) = \begin{cases} \hat{\phi} \\ \hat{\psi} \end{cases}, \quad \chi_2(r) = \frac{\hat{\phi}-\hat{\psi}}{1-u_A^2}\begin{cases} 1 & \text{(for } \Phi\text{-vortices)} \\ u_A^2 & \text{(for } \Psi\text{-vortices)} \end{cases}, \quad (11)$$

where $\hat{\phi} = -l_n\Phi_0/\hat{u}r_0$, $\hat{\psi} = \Psi_0/\alpha r_0$. Solutions of Eqs. (4) which satisfy the condition $\chi_1(r_0) = 0$, and which are bounded at $r \to \infty$ and at $r = 0$ have the form

$$\chi_1(r) = \varrho - \frac{1}{\varrho} + C^e\left(\frac{K_1(\hat{\kappa}_e\varrho)}{K_1(\hat{\kappa}_e)} - \frac{1}{\varrho}\right), \quad \chi_2(r) = C^e\,\frac{K_1(\hat{\kappa}_e\varrho)}{K_1(\hat{\kappa}_e)}, \quad r > r_0, \quad (12)$$

$$\chi_1(r) = C^i\left[\mathcal{B}_1(\hat{\kappa}_1\varrho)/\mathcal{B}_1(\hat{\kappa}_1) - \mathcal{B}_1(\hat{\kappa}_2\varrho)/\mathcal{B}_1(\hat{\kappa}_2)\right],$$

$$\chi_2(r) = \frac{C^i}{\hat{\kappa}_e^2}\left[(\hat{\kappa}_e^2-\hat{\kappa}_2^2)\frac{\mathcal{B}_1(\hat{\kappa}_1\varrho)}{\mathcal{B}_1(\hat{\kappa}_1)} - (\hat{\kappa}_e^2-\hat{\kappa}_1^2)\frac{\mathcal{B}_1(\hat{\kappa}_2\varrho)}{\mathcal{B}_1(\hat{\kappa}_2)}\right], \quad r < r_0. \quad (13)$$

Here $\varrho = r/r_0$, $\hat{\kappa}_{e,1,2} = (r_0/\rho_s)\kappa_{e,1,2}$, $\mathcal{B}_1$ is a Bessel function of first order, $\mathcal{B}_1(\hat{\kappa}\varrho) = I_1(|\hat{\kappa}|\varrho)$ if $\hat{\kappa}^2 > 0$ and $\mathcal{B}_1(\hat{\kappa}\varrho) = J_1(|\hat{\kappa}|\varrho)$ if $\hat{\kappa}^2 < 0$.
Matching $\chi_2(r)$ and $\chi_2'(r)$ at the separatrix $r = r_0$ one obtains

$$\hat{\kappa}_e^2 C^e = C^i(\hat{\kappa}_1^2-\hat{\kappa}_2^2), \quad (\hat{\kappa}_1^2-\hat{\kappa}_2^2)\hat{K}(\hat{\kappa}_e) + (\hat{\kappa}_e^2-\hat{\kappa}_2^2)\hat{\mathcal{B}}(\hat{\kappa}_1) - (\hat{\kappa}_e^2-\hat{\kappa}_1^2)\hat{\mathcal{B}}(\hat{\kappa}_2) = 0, \quad (14)$$

where $\hat{K} = \hat{\kappa}_e K_2(\hat{\kappa}_e)/K_1(\hat{\kappa}_e)$, $\hat{\mathcal{B}} = \mathrm{sgn}(\hat{\kappa}^2)|\hat{\kappa}|\mathcal{B}_2(\hat{\kappa})/\mathcal{B}_1(\hat{\kappa})$, and $\mathcal{B}_2$ is a Bessel function of second order which is determined similar to $\mathcal{B}_1$. Matching $\chi_1'(r)$, one obtains

$$C^e\left[\hat{\kappa}_1^2\hat{\mathcal{B}}(\hat{\kappa}_2) - \hat{\kappa}_2^2\hat{\mathcal{B}}(\hat{\kappa}_1)\right] = 2(\rho_s/r_0)(\hat{\kappa}_1^2-\hat{\kappa}_2^2)(1+C^e). \quad (15)$$

In the above equations $\kappa_{1,2}^2$ are given by Eq. (10).

The second of Eqs. (14) can be considered as the dispersion relation. Then Eq. (15) defines the vortex amplitude. Equations (14) and (15) provide three relations between the unknown amplitudes $C^{e,i}$, the normalized vortex radius r_0/ρ_s, the velocities u and α (through $\hat{u}$ and u_A) and either of the jumps ε_h and ε_p. Hence, given the background plasma, the structure of vortices is determined by specifying three parameters.

Equations (12) and (13) describe so-called two-potential vortices[3-5] which are characterized by a slow decay ($\sim 1/r$) in the external region, and by two nonvanishing wave numbers $\hat{\kappa}_{1,2}^2$ in the internal region. In either of the limits $u_A^2 \to 0$ and $u_A^2 \to \infty$ one of the

two eigenvalues in the internal region vanishes and the vortices reduce to one-potential vortices. The first limit corresponds to Φ-vortices[6], the second to Ψ- vortices[7]. In both limits $C^e = -1$ and the slow spatial decay does not occur so that the one-potential vortices decay exponentially. Both cases are characterized by a dispersion relation of the Larichev-Reznik[8] type $\hat{\kappa}_i^2 \hat{K}(\hat{\kappa}_e) + \hat{\kappa}_e^2 \hat{B}(\hat{\kappa}_i) = 0$, where $\hat{\kappa}_i^2$ is the eigenvalue in the inner region.

We have analyzed the dispersion relation (14) numerically and found that it has no roots in the region where both $\hat{\kappa}_1^2 \geq 0$ and $\hat{\kappa}_2^2 \geq 0$. Then from Eq. (10) it follows, that either $\varepsilon_{p,h} < 0$ or $\varepsilon_{p,h} > (1 + |u_A|)^2$. The product $\hat{\kappa}_1^2 \hat{\kappa}_2^2$ has the same sign as $\varepsilon_{p,h}$. A dipole vortex solution can always be found if $\hat{\kappa}_e^2 > 0$. Ψ-vortices with $u_A^2 < 1$ and Φ-vortices with $u_A^2 > 1$ must satisfy the condition $\hat{\kappa}_1^2 \hat{\kappa}_2^2 < 0$. Ψ-vortices with $u_A^2 > 1$ and Φ-vortices with $u_A^2 < 1$ can have both $\hat{\kappa}_1^2 < 0$, $\hat{\kappa}_2^2 < 0$ and $\hat{\kappa}_1^2 \hat{\kappa}_2^2 < 0$. While the former always exist, the latter only exist in the range $1 < u_A^2 < 1 - \hat{\kappa}_e^2/\hat{\kappa}_{cr}^2$ for Ψ-vortices, and $(1 - \hat{\kappa}_e^2/\hat{\kappa}_{cr}^2)^{-1} < u_A^2 < 1$ for Φ-vortices. Here $\hat{\kappa}_{cr}^2 < 0$ is a function of $\hat{\kappa}_e$ which is determined by the equation $|\hat{\kappa}_{cr}| J_2(|\hat{\kappa}_{cr}|)/J_1(|\hat{\kappa}_{cr}|) = \hat{\kappa}_e K_2(\hat{\kappa}_e)/K_1(\hat{\kappa}_e)$.

The general Hamiltonian formalism presented in Ref. 1 can be used for a first investigation of the vortex stability. Sufficient conditions for stability are (see Eq. (17) of Ref. 1)

$$F'_+ + F'_- < 0, \qquad -(F'_+ + F'_-) > -d_e^2 F'_+ F'_-, \qquad p < 0. \tag{16}$$

We refer to the limit $d_e \to 0$. The second condition is stronger than the first one and gives $h_1 > 0$. Inserting the expressions for $F'_\pm$ in the external region, it follows that the contributions from this region to localized vortices never lead to sufficient conditions for stability. However, global stability of Ψ-vortices, propagating in the range $0 < \hat{u} < 1$, $u_A^2 > 1$, can be proven with respect to a special class of perturbations, $\delta\xi_3 = 0$, when the third condition in (16) does not apply. These vortices are stable if $\varepsilon_h < 0$.

Acknowledgements This work was performed as part of the research programme of the association agreement of Euratom and the "Stichting voor Fundamenteel Onderzoek der Materie" (FOM) with financial support from the "Nederlandse Organisatie voor Wetenschappelijk Onderzoek" (NWO) and Euratom. Financial support from the Italian Research Council (CNR) and from the "Associazione per lo Sviluppo Scientifico e Tecnologico del Piemonte" of Turin is also acknowledged.

References

[1] F. Pegoraro et al., *This Conference*, paper C 65.

[2] D. Jovanovich and W. Horton, to appear in *Physics of Plasmas* (1994).

[3] T. D. Kaladze et al., *Sov. Phys. JETP*, **64**, 62 (1986).

[4] J. Liu and W. Horton, *J. Plasma Phys.*, **36**, 1 (1986).

[5] A. B. Mikhailovskii et al., *Plasma Phys. Contr. Fusion*, **29**, 1 (1987).

[6] J. D. Meiss and W. Horton, *Phys. Fluids*, **26**, 990 (1983).

[7] V. P. Lakhin et al., *Sov. J. Plasma Phys.* **12**, 326 (1986).

[8] V. D. Larichev and G. M. Reznik, *Doklad. Akad. Nauk. SSSR*, **231**, 1077 (1976).

RADIATIVE-CONDENSATION INSTABILITY IN Be-SEEDED PLASMAS IN TOKAMAKS

V.A.ABRAMOV,D.KH.MOROZOV
INSTITUTE OF NUCLEAR FUSION,RRC "KURCHATOV INSTITUTE"
123182,MOSCOW,THE RUSSIAN FEDERATION

1.INTRODUCTION

The experiments at JET with Be-limiter show that MARFE's typically form at ~40% radiated power whereas in the regimes with C-limiter MARFE's generally occur at ~ 100% radiated power,just a disruption[1].The reasons for such plasma behaviour have been discussed in [2,3].The detailed dependence of the radiative cooling rate Q on the electron temperature T_e has not been used in these papers.For carbon-seeded plasmas the function $Q(T_e)$ with taking into account the charge exchange effects and the corresponding criterion for the MARFE formation has been calculated in [4]. The destabilizing effect of the hydrogen atom density fluctuations due to dependence of the ionization rate on T_e has been revealed for Carbon-seeded plasmas [5]. In this paper we present the investigation of the radiative-condensation instability for Be-seeded plasma.Both the charge exchange effects leading to the departure from the corona model and the destabilizing influence of the hydrogen atom density fluctuations are taken into account.It is shown that the overlapping of the region where the strong dependence of the ionization rate on T_e exists and the region of the strong dependence of Q-function on the hydrogen atom density is more essential for Be-seeded plasmas than one for Carbon-seded plasmas.The last effect gives the main contribution to the instability onset.The numerical calculations have showed that for Be-seeded plasmas the critical value of the fraction of the re-radiated power (P_{rad}/P_{tot}) is about 15% without taking into account some stabilizing effects`.It must be noted that for Carbon-seeded plasmas the destabilizing role of the hydrogen atom density fluctuations leads to the non-essential lowering of the critical value of the re-radiated power fraction P_{rad}/P_{tot} and this value is about 100% [5].

2.The radiative cooling rate for Be-seeded plasmas

The numerical calculations of the non-coronal radiative cooling rate Q have been performed in the frame of the next model.The system of the balance equations for the different ionization stages of Be ions have been solved with taking into account the charge exchange between Be-ions and neutral hydrogen atoms.The atomic data base includes the recommended data on the electron impact ionization [6],the recommended data on the electron impact excitation [7].The direct radiative recombination rates have been calculated in the Kramers approximation.The dielectronic recombination rates have been

taken from [8].The cross-sections for the charge-exchange processes of Be(+2),Be(+3),Be(+4) with hydrogen atoms are taken from [9,10,11],correspondingly.The charge exchange process of Be(+1) with H(1s) is negligible.The function Q has been calculated for the different values of the parameter N/n_e (N is a hydrogen atom density, n_e is an electron density).Fig.1 illustrates the results of the calculations.

3.The mathematical model and the stability criterion

Fig.1 shows that the function $Q(T_e, N/n_e)$ is a relatively weak function at $T_e > 10$ eV. It is a reason to use the Drake model [12]. We assume(for sake of simplicity) that in the boundary plasma the heat transport is provided mainly due to the heat conductivity. Then in the region with the closed magnetic surfaces the heat balance equation is

$$\kappa_\perp \frac{d^2T}{dx^2} = Q \qquad (1)$$

The solution of this equation is

$$x = \frac{2\kappa_\perp}{q_0} \frac{T_L - T_W}{q_1^2} \left[\left(1 - q_1^2 \frac{T_L - T}{T_L - T_W} \right)^{1/2} - \left(1 - q_1^2 \right)^{1/2} \right] \qquad (2)$$

Here T_W is a wall temperature, q_0 is a heat flux density entering into the radiating layer from the plasma core, $q_1^2 = 2\kappa_\perp Q_0 (T_L - T_W)/ q_0^2$, Q_0 and T_L are the parameters of the Drake model for the radiative cooling rate Q. It is easily to see that the next relation is

$$P_{rad}/ P_{tot} = 1 - \left(1 - q_1^2 \right)^{1/2} .$$

For the perturbed temperature the equation with taking into account the hydrogen atom fluctuations is [5]

$$(\kappa_\perp + n D_\perp) \frac{d^2\tilde{T}}{dx^2} - g \tilde{T} = \left(\frac{\partial Q}{\partial N} + T n K_i \right) \tilde{N} \qquad (3)$$

where $g = 2.5\gamma + \kappa_\parallel k_\parallel^2 - n N \left(K_i/T - \frac{\partial K_i}{\partial T} \right) \tilde{T} - \frac{2Q}{T} + \frac{\partial Q}{\partial T}$,

K_i is an ionization rate, γ is a growth rate.

For $\kappa_\parallel$ we use the simple model: $\kappa_\parallel = 0$ at $T < T_c$, $\kappa_\parallel = \infty$ at $T > T_c$ ($T_c < T_L$).

For our aims we may use for $\tilde{N}$ the expression offered [5]

from the kinetic consideration:

$$\tilde{N} = - N_w \int_0^x dy \frac{n\tilde{T}}{v_T} \left(\frac{\partial}{\partial T} - \frac{3}{2T}\right)(K_i + K_{CX}) \qquad (4)$$

where K_{CX} is a charge exchange rate, V_T is a neutral atom thermal velocity.

Substitution of expression (4) into Eq.(3) gives

$$\frac{d^3\tilde{T}}{d\xi^3} + K^2 \frac{d\tilde{T}}{d\xi} + \lambda_0^3 K^2 \tilde{T} = 0. \qquad (5)$$

Here $\xi = x/x_L$, $K^2 = 4 \frac{T_L - T_W}{T q_1^2} \left(1 - \left(1 - q_1^2\right)^{1/2}\right)$,

$$\lambda_0 = \frac{nK_i}{2v_T} \frac{\partial \ln K_i}{\partial \ln T} \frac{\partial \ln Q}{\partial \ln N}.$$

The total radiating zone may be separated on two zones. At zone where $T < T_i$ =15-20 eV the parameter $\frac{\partial \ln K_i}{\partial \ln T}$ is large. In this temperature region the parameter $\frac{\partial \ln Q}{\partial \ln N}$ is about 1,5 ,according to the results of Section 2.

In the zone where $T > T_i$ the parameter $\frac{\partial \ln K_i}{\partial \ln T}$ is small. Hence, the parameter λ_0 is practically zero in this region. Matching of the heat balance equation solutions in these zones gives the critical value of q_1 corresponding to the instability margin:

$$\lambda_0^2 K^{4/3} \xi_c = 2, \qquad (6)$$

where $\xi_c = \xi(T_c)$.

The dependence of the criterion on ξ_c is a rather weak. It is a reason to put $\xi_c = 1/3$ but don't calculate accurately. For typical edge plasma conditions it is easily to obtain the estimation $\lambda_0^3 = 4$. Hence, we have $q_1^2 = 0.25$ and $P_{rad}/P_{tot} = 0.13$.

4. Conclusions

The performed calculations have showed the strong dependence of the radiative cooling rate on the hydrogen atom density at $T_e > 5$ eV. The combined effect of the dependence of Q on T_e and N/n_e and the ionization rate dependence on T_e leads to the conclusion that for Be-seeded plasmas the critical fraction of radiated power for the MARFE formation is about (10-15)% .The calculation shows the mode is stable at N/n_e less than 0.1 if the fluctuations of

the hydrogen atom densities are neglected. Authors believe that the better agreement between the experimental values and the calculated ones for P_{rad}/P_{tot} may be achieved if some stabilizing effects will be taken into account.

One of the authors (V.A.A) is grateful to the JSPS for a research fellowship and to the NIFS where the essential part of this study has been performed for its warm hospitality in the course of this work.

References

1. S. Clement, D. Campbell, S.K. Erents et al. Proc. 17-th Europ. Conf. on Contr. Fusion and Plasma Heating, Amsterdam, 1990, v. 14B, part III, pp. 1373-1376
2. T.C. Hender, J.A. Wesson, Proc. 18-th Europ. Conf. on Contr. Fusion and Plasma Physics, Berlin, 1991, v. 15c, part IV, pp. 81-83
3. A.V. Gruzinov, D.Kh. Morozov, JETP Letters 54(1991), 316-319
4. V.A. Abramov et al., JETP Letters 56(1992), pp. 445-448
5. P. Bachman, D.Kh. Morozov, D. Sunder, Contribution to Plasma Phys. 32(1992), 395.
6. K.L. Bell, H..B. Gilbody, J.F. Hughes et al. J. Phys. Chem. Ref. Data 12, 891 (1983)
7. K.A. Berrington, R.E.H. Clark, Atomic and Plasma Material Interactoin Data For Fusion 3, 87 (1992)
8. M.S. Pindzola, N.R. Badnell , ibid. 3, 101 (1992)
9. A.E. Wetmore, H.R. Cole, R.E. Olson J. Phys. B19, 1515(1986)
10. N. Shimakura, J. Phys. B21, 2485 (1988)
11. M.I. Chibisov JETP Letters, 24, 46 (1976)
12. J.F. Drake, Phys. Fluids 30, 2429 (1987)

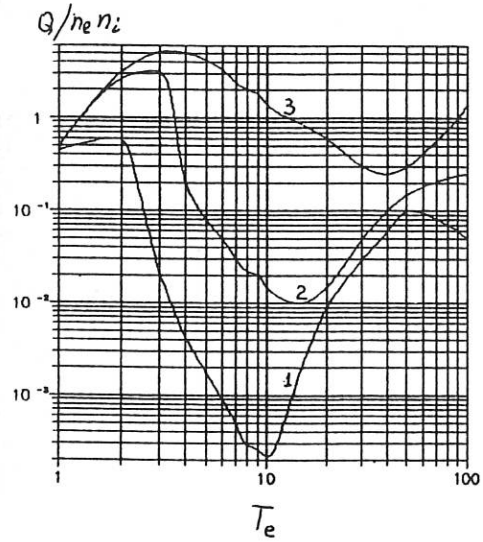


Fig.1. $Q/n_i n_e$ vs. T_e, (n_i is total density of impurity ions, T_e in eV, Q in $10^{-26} W \cdot cm^3$)

1 $N/n_e = 10^{-5}$
2 $N/n_e = 10^{-3}$
3 $N/n_e = 10^{-1}$

TRANSPORT BARRIER FORMATION DUE TO TURBULENT SPIN-UP OF EDGE TOKAMAK PLASMA DURING L-H TRANSITION

M.V. Osipenko, A. R. Polevoy, S.V. Bazdenkov

RRC "Kurchatov Institute", 123182 Moscow, Russia

INTRODUCTION

The commonly accepted brick stone in modern L-H transition theories is the experimentally verified assertion that edge turbulence and corresponding transport are dramatically suppressed by sheared poloidal rotation at the transition. But the following questions are still open: what triggers the transition from L- to H-mode operation, what is the mechanism of sheared poloidal flow generation and what is the nature of turbulent transport at the edge? The proposed model permits the self-consistent analysis of these questions using a convective cell turbulence as a representative paradigm to describe turbulent transport at the edge. We follow the concept of "transport barrier" assuming that there are no changes in core plasma confinement through the transition and all dynamics of temperature and density profiles are controlled by the thin edge layer with steep gradients just inside separatrix. Thus, to simulate evolution of temperature, density and current profiles in the core plasma ASTRA transport code [1] is used. The boundary conditions for this code (turbulent fluxes) are taken from the nonlinear self-regulated model of coupled convective cell turbulence and sheared flow evolution at the plasma edge [2,3]. And vice versa the boundary values of temperature and density obtained from ASTRA are used as input parameters for turbulent layer dynamics calculations.

NONLINEAR MODEL OF TRANSPORT IN THE VICINITY OF SEPARATRIX

Although all attempts to identify the type of instabilities responsible for observed edge turbulent transport led to a very little progress, the universal character of edge turbulence for different devices allows to say that on the nonlinear stage different instabilities exhibit more or less similar dynamics, which seems to be mainly determined by convective nonlinearities. To model these nonlinear transfer processes convective cell turbulence (similar to nonstationary Rayleigh thermoconvection) appears to be very appropriate object, because it's complicated chaotic behavior can be qualitatively described by Lorenz system of three ordinary differential equations. Thus we generalize Lorenz model to include effects of mean shear flow generation and to get the self-regulated system of convective cell turbulence and sheared flow. Two mechanisms of spontaneous spin-up are considered simultaneously: 1) peeling convective cell instability due to nonlinear energy exchange between turbulence and flow; 2) Stringer instability driven by the poloidally asymmetric turbulent particle flux, where instead of neoclassical flux anomalous flux is substituted.

Drift resistive ballooning instability equations

including ion parallel dynamics are used as a basic model. Curvature driven instability is chosen because there are experimental indications [4] that the dynamics of turbulence at the inboard midplane shows no changes during L-H transition while at the outboard midplane noticeable reduction of turbulence takes place and then ELM activity begins. The normalized equations appear as

$$\frac{\partial \Delta\varphi}{\partial t} + [\vec{e}_z \times \nabla\varphi]\nabla\Delta\varphi + g_B \frac{\partial \tilde{n}}{\partial y} \cos\lambda y - \sigma(\varphi - \tilde{n}) = \mu\Delta^2\varphi,$$

$$\frac{\partial \tilde{n}}{\partial t} + [\vec{e}_z \times \nabla\varphi]\nabla\tilde{n} + g_N \frac{\partial \varphi}{\partial y} + \frac{\varepsilon}{q}\frac{\partial V_\parallel}{\partial y} - \sigma(\varphi - \tilde{n}) = D\nabla^2\tilde{n}\ , \qquad (1)$$

$$\frac{\partial V_\parallel}{\partial t} + [\vec{e}_z \times \nabla\varphi]\nabla V_\parallel + \frac{\varepsilon}{q}\frac{\partial n}{\partial y} = \mu_\parallel \Delta V_\parallel$$

where dimensionless variables and parameters are introduced: potential $\varphi \to e\varphi/T$, density $n \to n/n_0 = \langle n\rangle + n$, $\langle n\rangle = 1 - x/L_N$, $g_N = \rho/L_N$, $g_B = \rho/R$, $\rho^2 = \omega_c^2 T/M$, $T = T_e$, $\omega_c = eB_0/mc$, $V_\parallel \to V_\parallel/\rho\omega_c$, $t \to \omega_c t$, $x,y \to x,y/\rho$, $\mu, \mu_\parallel, \chi \to \mu, \chi/\rho^2\omega$, $\sigma \to \sigma k_\parallel^2 B/(nce)$, $k_\parallel = 1/qR$, x corresponds to radial direction, y - to poloidal direction, $\lambda = \rho/r$, $\varepsilon = r/R$.

To minimize the phase space dimensionality of nonlinear model of edge plasma dynamics two methods of plasma turbulence description are combined: Galerkin method, which provides evolution equations for most unstable harmonics and evolution equations for energy exchange between different parts of the system. To describe Stringer spin-up, terms with slow poloidal variation are added to modes used in [2]:

$$\tilde{n} = \hat{N} \sin k_x x \sin\lambda y + (Y \sin k_x x \cos k_y y + N \sin 2k_x x \sin k_y y) *$$

$$*(1+\varepsilon\cos\lambda y) + Z \sin 2k_x x + \varepsilon Z_1 \sin 2k_x x \cos\lambda y,$$

$$\varphi = V \sin k_x x + (X \sin k_x x \sin k_y y + \hat{W} \sin 2k_x x \cos k_y y)(1+\varepsilon\cos\lambda y)$$

$$V_\parallel = u_1 \sin k_x x \cos k_y y + u_2 \sin 2k_x x \sin\lambda y.$$

Modes X,Y,Z,V,N,$\hat{W}$ are used to estimate nonlinear terms and flux in the following space averaged equations, where periodicity conditions are expected in y direction and zero φ, $\partial\varphi/\partial y$ and n for $x = 0, L_N$

$$\frac{\partial U}{\partial t} + \frac{1}{U}\int_0^\delta W'\varphi_0' \frac{dx}{\delta} = \frac{1}{U} g_B \lambda \langle n * \sin\lambda y\rangle - \frac{1}{U}\mu \langle \varphi_0''^2\rangle$$

$$\frac{\partial I}{\partial t} - \int_0^\delta W'\varphi_0' \frac{dx}{\delta} = g_B \Gamma - \sigma\langle\varphi^2\rangle - \mu \langle\Delta\varphi^2\rangle$$

$$\frac{\partial N}{\partial t} + \frac{1}{N}\int_0^{\delta} \Gamma' N' \frac{dx}{\delta} = -\frac{1}{N} D \langle N'^2 \rangle \qquad (2)$$

$$\frac{\partial J}{\partial t} - \int_0^{\delta} \Gamma' N' \frac{dx}{\delta} = g_N \Gamma - D \langle \nabla N^2 \rangle$$

Here $\varphi=\varphi_0(x,t)+\tilde{\varphi}(x,y,t)$, $n=N_0(x,t)+\tilde{N}(x,y,t)$, $\Gamma(x)=-n\partial\varphi/\partial y$ - particle flux, $W(x)=-\partial\varphi/\partial x * \partial\varphi/\partial y$ -Reynolds stress, $U=\langle\varphi_0'^2\rangle^{1/2}$ is proportional to mean velocity, $I=\langle|\nabla\varphi|^2/2\rangle$ - turbulent kinetic energy , $N=\langle N_0^2\rangle^{1/2}$ - mean density profile variation, $J=\langle\tilde{N}^2/2\rangle$ - internal energy of the fluctuations. Terms proportional to particle flux provide energy transfer from density gradient to turbulence by means of instability. The case of strong nonlinearity which transfers energy from the unstable to damping modes is considered. In the lowest order in ε Eqs. (2) are coupled with parallel flow due to poloidal asymmetry of particle transport only through the generation of the mean flow U by $\hat{N}$ mode. According to the ideas presented in [5] one can obtain the following relations

$$\dot{u}_1=-\lambda k_x V u_2-(\varepsilon/q)\lambda\hat{N}-\mu_{\parallel}k^2 u_1, \quad \dot{Z}_1=k_y XY-(\lambda/q)u_2-(\lambda/2\varepsilon)k_x V\hat{N}-Dk^2 Z_1.$$

Assuming u_1, Z_1 to be stable modes we get

$$\hat{N}=(q^2/\lambda\varepsilon)\Gamma k_x V/(1+(q^2/2\varepsilon^2)k_x^2 V^2).$$

As a result we obtain generalized Lorenz like model:

$$\begin{aligned}
\frac{dV}{dt} &= C_{vx}X^2 V + S\,XYV/(1+sV^2) - A_{vv}V,\\
\frac{dX}{dt} &= -C_{vx}XV^2 + A_{xy}Y - A_{xx}X,\\
\frac{dY}{dt} &= -C_{yz}XZ + A_{yx}X - A_{yy}Y,\\
\frac{dZ}{dt} &= C_{yz}XY - A_{zz}Z + \frac{1}{n_0(b,0)}\frac{dn_0(r=b,t)}{dt},
\end{aligned} \qquad (3)$$

$C_{vx}=0.15\,k_y^2\,\tau$, $S=g_B\varepsilon s$, $s=q^2/2\varepsilon^2$, $A_{vv}=\mu_{nc}\,k_x^2$,
$A_{xy}=0.5\,k_y g_B/k$, $A_{xx}=0.5\,(\sigma/k^2+\mu\,k^2)$, $C_{yz}=0.5\,k_y/k$,
$A_{yx}=0.5\,k_y g_N/k$, $A_{yy}=0.5\,D\,k^2$, $A_{zz}=4\,D\,k^2$, $\tau=0.4/(\mu k^2)$.

Here V and X are characteristic mean and turbulent velocities normalized to sound speed, Y and Z turbulent and mean variation of density profile normalized to mean density. τ is the time scale, which is determined by nonlinear energy transfer between stable and unstable modes. Although S coefficient in Stringer drive is small compare to C_{vx} Reynolds stress it could change an equilibrium.

NUMERICAL SIMULATIONS

To make more explicit an effect of transport barrier formation the simplest model of particle balance, which includes the source of particles due to neutral injection and Bohm-like diffusive transport, has been used for core plasma. At the boundary core flux $-D_B \nabla n|_{r=b}$ is equal to $\{n_0(r=b,t)+2\pi n_0(r=b,t=0)|Z|\}/L_N$, where Z is calculated from (3) with $n_0(r=b,t)$ taken from the core calculations.

Two different modes of operation are seen. L-mode confinement takes place for V=0, when the viscosity for poloidal μ_{nc} flow is high. Due to increase of temperature μ_{nc} goes down [6] permitting flow generation. When small seed V is present it is effectively amplified by turbulence so that the system comes to the equilibrium with improved confinement. Increase of electron temperature leads to stabilization of the turbulence due to conductivity and system returns to L-mode. Qualitative explanation of this transition is based on the analysis of equilibrium of eqs. 1. When the level of fluctuations exceeds $X^2_{cr}=A_{vv}/C_{vx}$, bifurcation happens. Two states are possible: one corresponds to L-mode with V=0 and high flux proportional to $Z_L=(A_{xy}A_{yx}-A_{xx}A_{yy})/(C_{yz}A_{xy})$, and another state corresponding to H-mode with high V and suppressed flux proportional to $Z_H=C_{yz}A_{yx}/(C^2_{yz}+A_{zz}C_{vx}A_{yy}/A_{vv})$. It is interesting to note that in frame of assumptions of our model the relation of confinement in L and H-mode depends only on Prandtl number $Pr=\mu/D$: $Z_L/Z_H=1+0.12/Pr^2$. In our calculations Pr=0.4.

Transitions between these two equilibriums can be used to model ELMing H-mode.

CONCLUSIONS

Three regimes of confinement are possible in frame of the model: under the threshold of spin up instability high level turbulent convection takes place (L-mode); when the critical gradient is achieved or ion temperature becomes high enough to reduce neoclassical viscosity second-order phase transition is seen which is controlled by amplitude of the sheared flow V as an order parameter. Equilibrium with nonzero flow and reduced transport can be achieved (ELM-free H-mode). The transition back to L-mode is possible due to electron temperature increase. Because the high gradients and low conductivity are necessary for instability in question, the self-supporting transport barrier arises at the plasma edge just inside separatrix.

REFERENCES

1. G.V. Pereverzev, et al., Preprint IPP 5/42, Garching, 1991.
2. O.P. Pogutse, et al., Preprint JET-P(93)106, 1994.
3. N.N. Kukharkin, et al., in Plasma Phys. and Contr. Nucl. Fus. Research 1992 (Proc. of 14th Int. Conf. Wurzburg, 1992), Vol.2, IAEA, Vienna, (1993), 293.
4. E.J. Doyle, et al., Ibid. Vol.1, 235.
5. A.B. Hassam, et al., Phys. Fluids B 5, 1993, 2519.
6. H. Sugama, W. Horton, Phys. Plasmas, 1 (1994) 345.

MACROSCOPIC MODELING BY LATTICE BOLTZMANN TECHNIQUES

George Vahala, Department of Physics, William & Mary, Williamsburg, VA, USA

Pavol Pavlo, Institute of Plasma Physics, Czech Academy of Sciences, Praha 8, Czech Republic

Linda Vahala, Department of Electrical & Computer Engineering, Old Dominion University, Norfolk, VA, USA

Abstract

The Lattice Boltzmann (LBE) approach to solving nonlinear moment equations is investigated for the case of the evolution of a very thin 2D shear layer in a compressible fluid. The importance of LBE, and its extensions, lies in the fact that these methods are microscopically linear, can handle difficult geometries easily, and they are ideally suited for parallel computations. These techniques should find application in divertor design for fusion tokamaks.

I. Introduction

Nonlinear macroscopic systems in nontrivial geometries abound in plasma physics and in turbulence. For example, one very useful model[1] to study the divertor region of a tokamak consists of a coupled set of continuity, momentum and energy equations for a plasma interacting with a neutral fluid in a backward facing step geometry. The region before the backstep corresponds to the SOL before the separatrix, while the region in the expanded channel corresponds to SOL after the separatrix. Because of the extreme difficulty in directly solving these inherently nonlinear models with the appropriate boundary/initial conditions in nontrivial geometries, it seems appropriate to consider new solution techniques.

One such technique is the lattice Boltzmann method (LBE)[2,3] with its linearized Krook collision operator. LBE, in some respects, improves on the lattice gas automata (LGA)[4,5] approach by eliminating statistical noise, non-Galilean invariance as well as a pressure that is velocity dependent. This is accomplished at the expense of working with floating point rather than Boolean variables and the need to specify an appropriate equilibrium distribution function to which the collisions drive the microscopic system.

In LBE, the set of nonlinear macroscopic equations is replaced by a linear microscopic model which is solved on a spatial grid with discretized phase space velocities. If the LBE model can be so constructed that only local interactions are needed, then this kinetic model is ideally suited for multiprocessor machines. The underlying principle in the LBE is that there is an infinite number of microscopic models that will yield the desired moment equations and one needs only work with that which is most efficient computationally. The spatial grid is so chosen so that after the appropriate moments are taken, the final macroscopic system does not exhibit any of the discrete lattice symmetries[4,5]. For two-dimensional (2D) problems, a suitable spatial lattice is the hexagonal lattice[4,5]. Moreover, nontrivial geometries and macroscopic boundary conditions are much easier to handle in LBE just by incorporating appropriate microscopic collision rules on those particles interacting with the boundaries.

2. Thermo-LBE Model[6]

In 2D LBE, one introduces a velocity distribution function $f_{\sigma i}(\mathbf{x},t)$ at the lattice node site $\mathbf{x}$ at time t for particles moving in direction "i" with speed $|\mathbf{e}_{\sigma i}|$. On the hexagonal grid, each lattice node is connected to 6 other spatial sites (i=1, ..., 6). Let N be the number of speeds (σ = 0, 1, ... N), with lattice vectors $\mathbf{e}_{\sigma i}$ of length $|\mathbf{e}_{\sigma i}| = \sigma$. The σ = 0 particles are rest particles, and are introduced so that one can recover the correct macroscopic behavior[2]. Since we will be using this LBE approach for divertor problems, we explore the properties of the an extended LBE model introduced by Alexander et. al.[6] that goes beyond the standard Navier-Stokes equation and incorporates effects of heat conductivity.

In LBE, one solves the linearized evolution equation for $f_{\sigma i}(\mathbf{x},t)$

$$f_{\sigma i}(\mathbf{x}+\mathbf{e}_{\sigma i}, t+1) - f_{\sigma i}(\mathbf{x}, t) = \Omega_{\sigma i} \equiv -\frac{1}{\tau}\left[f_{\sigma i}(\mathbf{x}, t) - f^{eq}_{\sigma i}(\mathbf{x}, t) \right] \tag{1}$$

where τ is the rate at which the distribution function relaxes to the local equilibrium distribution f^{eq} in the collision operator $\Omega_{\sigma i}$. The macroscopic density, velocity and temperature are obtain from the appropriate moments of $f_{\sigma i}(\mathbf{x},t)$:

$$\text{density } n(\mathbf{x}, t) = \sum_{\sigma,i} f_{\sigma i}(\mathbf{x}, t) \ , \quad \text{mean velocity } n(\mathbf{x},t)\,\mathbf{u}(\mathbf{x},t) = \sum_{\sigma,i} \mathbf{e}_{\sigma i}\, f_{\sigma i}(\mathbf{x}, t)$$

$$\text{temperature : } \quad n(\mathbf{x},t)\,T(\mathbf{x},t) = \frac{1}{3}\sum_{\sigma,i} \left[\mathbf{e}_{\sigma i} - \mathbf{u}(\mathbf{x}, t) \right]^2 f_{\sigma i}(\mathbf{x}, t) \tag{2}$$

Critical to the success of the LBE approach is the choice of the equilibrium distribution f^{eq}. Certain constraints must be satistifed, since the collision operator $\Omega_{\sigma i}$ conserves local density, momentum and kinetic energy. Typically, f^{eq} is chosen as a power series in the local mean velocity $\mathbf{u}$:

$$f^{eq}_{\sigma i}(\mathbf{x}, t) \equiv A_\sigma(n,T) + B_\sigma(n,T)\, \mathbf{e}_{\sigma i} \cdot \mathbf{u} + C_\sigma(n,T)\, [\mathbf{e}_{\sigma i} \cdot \mathbf{u}]^2 + D_\sigma(n,T)\, u^2 + \\ + E_\sigma(n,T)\, [\mathbf{e}_{\sigma i} \cdot \mathbf{u}]^2 + F_\sigma(n,T)\, [\mathbf{e}_{\sigma i} \cdot \mathbf{u}]\, u^2 + O(u^4) \tag{3}$$

where the coefficients $A_\sigma \ldots F_\sigma$ are functions of the local density n and temperature T and are determined from a Chapman-Enskog expansion of (1) in the long-wavelength, low-frequency limit so as to recover the macroscopic equations[6]

$$\frac{\partial n}{\partial t} + \nabla \cdot (n\,\mathbf{u}) = 0 \tag{4}$$

$$n\left[\frac{\partial}{\partial t} + \mathbf{u} \cdot \nabla \right] u_\alpha = -\frac{\partial p}{\partial x_\alpha} + \frac{\partial}{\partial x_\alpha}\left[\lambda \nabla \cdot \mathbf{u} \right] + \frac{\partial}{\partial x_\beta}\left[\mu\left(\frac{\partial u_\alpha}{\partial x_\beta} + \frac{\partial u_\beta}{\partial x_\alpha} \right) \right], \tag{5}$$

$$n\left[\frac{\partial}{\partial t} + \mathbf{u} \cdot \nabla \right] \frac{3\,T}{2} = -p\,\nabla \cdot \mathbf{u} + \frac{\partial}{\partial \beta}\left[\kappa \frac{\partial T}{\partial x_\beta} \right] + \lambda\,(\nabla \cdot \mathbf{u})^2 + \\ + \mu \frac{\partial u_\beta}{\partial x_\alpha}\left[\frac{\partial u_\alpha}{\partial x_\beta} + \frac{\partial u_\beta}{\partial x_\alpha} \right] , \tag{6}$$

with the transport coefficients :

shear viscosity $\mu = n\dfrac{3\,T\,(2\,\tau - 1)}{4}$, thermal conductivity $\kappa = n\dfrac{3\,T\,(2\,\tau - 1)}{2}$, (7)

with the viscosity $\lambda = -\,\mu$, so that the bulk viscosity is zero. This thermo-LBE model[6] satisfies the ideal (monatomic) equation of state $p = 3nT/2$. To obtain (4)-(6), one must use a 13-speed model, with $N = 2$ (i.e., $\sigma = 0, 1, 2$).

III. Evolution of a Very Thin Shear Layer in Thermo-LBE

We consider the evolution of a 2D very thin (tanh) shear layer in $u_x(y)$. The thermo-LBE system (1) and (3) is solved in a 512 x 512 periodic box, with an initial small perturbation of wavelength ≈ 1/6 of the box length. The Reynolds number of the flow is directly related to the collision relaxation time τ, and on this 512^2 grid the

$$\text{Reynolds Number} \quad R_e = \frac{26.1}{(2\,\tau - 1)} \ , \tag{8}$$

with the characteristic eddy turnover time ≈ 2000 LBE time-steps. In Fig. 1, we show the time evolution of vorticity contour plots of this shear layer for

column (a) : $R_e = 261$ (laminar flow)

column (b) : $R_e = 2610$ (turbulent flow)

For $R_e = 261$, the vorticity contour plots [Fig. 1(a)] are shown at eddy turnover times $t_{eddy} = 0.5$, 1.5, 4.5 and 8.0 respectively. Within one teddy, the shear layer develops into 6 well developed vortices. Because of the inverse cascade of energy in 2D, these vortice structures coalesce - even in laminar flow.

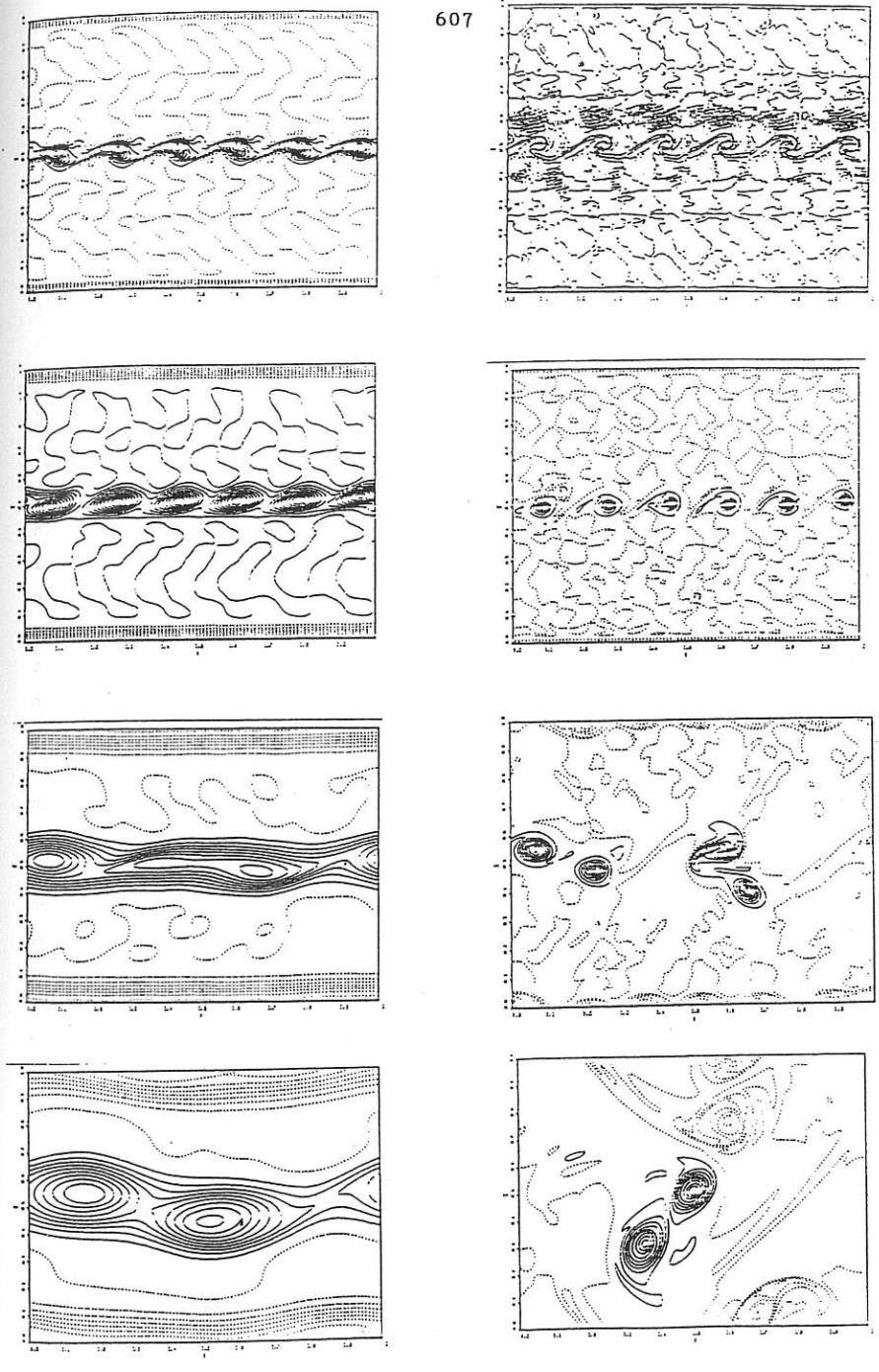
When the Reynolds number is increased to $R_e = 2610$, the vorticity contour plots [Fig. 1(b)] are shown at $t_{eddy} = 0.5$, 2.0, 4.0 and 8.0. One again sees the coalescence of the vortex patterns in this turbulent situation. At this higher Reynolds number, the vortices are stronger and distort the flow field considerably.

Acknowledgments

The authors are grateful for discussions with Hudong Chen, and to Shiyi Chen for sending us preprints of his work. This work was supported by U.S-Czech Science and Technology Joint Fund Grant 930-66

References

1 S. Krasheninnikov, private communcation (1993)
2 H. Chen, S. Chen & W. H. Matthaeus, Phys. Rev. **A45**, 5339 (1992)
3 Y. Qian, D. d'Humieres & P. Lallemand, Europhys. Lett. **17**, 479 (1992)
4 U. Frisch et. al., Complex Systems **1**, 649 (1987)
5 S. Wolfram, J. Stat. Phys. **45**, 471 (1986)
6 F. J. Alexander, S. Chen & J. D. Sterling, Phys. Rev. **E47**. R2249 (1993)



(a) (b)

Effects of Sheared Poloidal Rotations on Neoclassical Resistivity-Gradient-Driven Turbulence Transport

Xiaodong PENG Qingdi GAO Caigen LIU

(Southwestern Institute of Physics, P.O.Box 432, Chengdu 610041,P.R.China)

INTRODUCTION

H-mode found in 1982 is an enhanced confinement mode in tokamak plasmas[1]. It is important to understand the L-H mode transition and the properties of H-mode. It is shown by experiments [2] that L-H mode transition is accompanied by the onset of a rapid poloidal plasma flow at the plasma boundary. The effects of sheared rotations on turbulence were addressed in Ref.3. pointing out that the poloidal shearing can couple with radial scattering so that the turbulent decorrelation is enhanced while the turbulence is suppressed. Y.B.Kim *et al.*[4] investigated the effects of poloidal rotations on the resistivity-gradient-driven turbulence(RGDT). It was shown that the turbulent diffusion coefficient D_k varies with $|k_\theta V_\theta'|^{-1/2}$ in the limit case of strong shear, i.e., the turbulent diffusion decreases slowly as poloidal shearing increasing. However, this model is valid only in the Pfirsch-Schlüter collisionality regime [5] with characteristic frequency ω less than the collision frequency $\omega \ll \nu$. In order to extend the validity regime of RGDT into the experimentally relevant banana-plateau regime, the neoclassical resistivity-gradient-driven turbulence(NRGDT) was proposed by O.J.Kwon *et al.*[6]. It was shown that the turbulence depends on the profile of electron temperature as well as that of density. As tokamak experiments have demonstrated that the L-H transition is accompanied with strong enhancement of poloidal flow, it is interested to investigate the effects of poloidal rotations in the NRGDT theory.

NONLINEAR THEORY

NRGDT is described by the Ohmic law, the vorticity equation, and the electron temperature and density evolution equation. But $(V_\theta/r)\frac{\partial}{\partial\theta}$ is included in the differentiation operator d/dt in this paper. First, we eliminate the vorticity by employing ''decoupling approximation'', i.e., letting $\tilde{J}_\parallel \simeq 0$. Then, a transformation is taken as $t' = t$, $x = r - r_s$, $\theta' = \theta - V_\theta(r_s)t/r_s$, $\zeta' = \zeta$, and for any fluctuation field $\tilde{\phi} = \sum \phi_k(x,t')\exp[i(m\theta' - n\zeta')]$, where k represents the poloidal and toroidal mode number (m,n), V_θ is the velocity of poloidal rotation. Finally, by employing a standard direct iterative approximation(DIA) the renormalized equations are obtained

$$\frac{\partial}{\partial t}T_{ek}+\chi_{\parallel}k_{\parallel}^{2}T_{ek}+ik_{\theta}V_{\theta}'xT_{ek}-D_k^{T}\frac{\partial^2}{\partial x^2}T_{ek}=\frac{E_0}{B_z}\frac{k_{\theta}T_e}{k_{\parallel}L_n}\left(C_t\frac{T_{ek}}{T_e}+C_n\frac{n_k}{n_0}\right), \quad (1)$$

$$\frac{\partial}{\partial t}n_k+\chi_n k_{\parallel}^{2}n_k+ik_{\theta}V_{\theta}'xn_k-D_k^{n}\frac{\partial^2}{\partial x^2}n_k=\frac{E_0k_{\theta}n_0}{B_zk_{\parallel}L_n}\left(C_t\frac{T_{ek}}{T_e}+C_n\frac{n_k}{n_0}\right), \quad (2)$$

where $V_{\theta}'=dV_{\theta}(r_s)/dr-V_{\theta}(r_s)/r_s$ is the shear of poloidal rotations, L_n, L_t, k_{θ}, $k_{\parallel}$, $\chi_{\parallel}$, χ_n, C_n and C_t are the same as Ref.6. The turbulent diffusion coefficient $D_k^{T}\simeq\langle V_r^2\rangle/\Delta\omega_k^{(T)}$ and $D_k^{n}\simeq\langle V_r^2\rangle/\Delta\omega_k^{(n)}$ with $\langle V_r^2\rangle=\sum_{k_{\theta}}k_{\theta}^2|\phi_k|^2$. Estimating decorrelation rate $\Delta\omega_k^{(T)}\simeq(D_k^{T})^*/(\Delta_k^{T})^2$, $\Delta\omega_k^{(n)}\simeq(D_k^{n})^*/(\Delta_k^{n})^2$, we obtain $\langle V_r^2\rangle\simeq|D_k^{T}|^2/(\Delta_k^{T})^2\simeq|D_k^{n}|^2/(\Delta_k^{n})^2$, here Δ_k^{α} is the characteristic length of turbulence. On the other hand, the natural radial scales for turbulent fluctuations at saturation are determined by the asymptotic balance of both parallel dissipation and poloidal shearing with the turbulent diffusion. From Eqs.(1) and (2), we obtain $D_k^{T}=(\chi_{\parallel}k_{\theta}^2/L_s^2)(\Delta_k^{T})^4+ik_{\theta}V_{\theta}'(\Delta_k^{T})^3$, $D_k^{n}=(\chi_n k_{\theta}^2/L_s^2)(\Delta_k^{n})^4+ik_{\theta}V_{\theta}'(\Delta_k^{n})^3$. Hence

$$\langle V_r^2\rangle=\left(\chi_{\parallel}k_{\theta}^2/L_s^2\right)^2(\Delta_k^{T})^6+(k_{\theta}V_{\theta}')^2(\Delta_k^{T})^4=\left(\chi_n k_{\theta}^2/L_s^2\right)^2(\Delta_k^{n})^6+(k_{\theta}V_{\theta}')^2(\Delta_k^{n})^4. \quad (3)$$

To determine fluctuation levels at saturation, Eqs.(1) and (2) is multiplied by $\tilde{n}^*$ and integrated over x so as to yield a close set of coupled algebraic equations for the quantities $\int dx\,\tilde{n}^*\tilde{T}_e$ and $\int dx\,|\tilde{n}|^2$. In order to obtain a nontrivial solution, it is necessary that

$$\begin{vmatrix} \langle\tilde{n}|\mathcal{L}^{T}|\tilde{T}_e\rangle & -C_n\frac{E_0L_s}{B_zL_t}\frac{T_e}{n_0}\langle\tilde{n}|1/x|\tilde{n}\rangle \\ -C_t\frac{E_0L_sn_0}{B_zL_nT_e}\langle\tilde{n}|1/x|\tilde{T}_e\rangle & \langle\tilde{n}|\mathcal{L}^{n}|\tilde{n}\rangle \end{vmatrix}=0, \quad (4)$$

where $\mathcal{L}^{T}$ and $\mathcal{L}^{n}$ are the same as Ref.7. Hence, we obtain $\langle V_r^2\rangle^{1/2}=\left(E_0L_s/B_zL_n\right)(C_n+C_t\eta_e)$, where $\eta_e=L_n/L_t$. The characteristic length of turbulence can be determined by Eq.(3), $(\Delta_k^{T})^2=(a_t/3)F(S_T)$, where a_t is the same as Ref.7,

$$F(S_T)=\begin{cases} -1+2\cos\left[\frac{1}{3}\cos^{-1}(-1+\frac{1}{2S_T})\right], & (S_T\geq 1/4) \\ -1+\left[-1+\frac{1}{2S_T}+\sqrt{\frac{1}{S_T}\left(\frac{1}{4S_T}-1\right)}\right]^{1/3}+\left[-1+\frac{1}{2S_T}-\sqrt{\frac{1}{S_T}\left(\frac{1}{4S_T}-1\right)}\right]^{1/3}, & (0<S_T\leq 1/4) \end{cases}$$

where $S_T=(k_{\theta}V_{\theta}')^6/27\langle V_r^2\rangle(\chi_{\parallel}k_{\theta}^2/L_s^2)^4$. so that the turbulent diffusion

coefficient of temperature is $\mathrm{Re}(D_k^T)=S_T^{2/3}F^2(S_T)D_{k0}^T$, where D_{k0}^T is the temperature diffusion coefficient without poloidal shearing(see Ref.6). Similarly, we can obtain $(\Delta_k^n)^2=(a_n/3)F(S_n)$, where S_n, a_n are the same as Ref.7. And the turbulent diffusion coefficient of density is $\mathrm{Re}(D_k^n)=S_n^{2/3}F^2(S_n)D_{k0}^n$, where D_{k0}^n is the density diffusion coefficient without poloidal shearing[6].

In the weak shear limit($S_\alpha \to 0$), $D_k^\alpha = D_{k0}^\alpha$ ($\alpha = T, n$), which is the results of Ref.6. The turbulent diffusion coefficients are determined by $\chi_\parallel^{-1/3}$ and $\chi_n^{-1/3}$.

In the strong shear limit($S_\alpha \gg 1/4$), $D_k^T = [(E_0L_s/B_zL_n)(C_n + C_t\eta_e)]^2(\chi_\parallel k_\theta^2/L_s^2)(k_\theta V_\theta')^{-2}$ and $D_k^n = [(E_0L_s/B_zL_n)(C_n + C_t\eta_e)]^2(\chi_n k_\theta^2/L_s^2)(k_\theta V_\theta')^{-2}$. Clearly, D_k^α should decrease as $|k_\theta V_\theta'|$ increasing, but the turbulent diffusion coefficients obtained here vary with $(k_\theta V_\theta')^{-2}$ rather than $|k_\theta V_\theta'|^{-1/2}$ as in Ref.4.

In fact, the criterion of $S_T > 1/4$, i.e., $|k_\theta V_\theta'| > 1.375\langle V_r^2\rangle^{1/6}\cdot(\chi_\parallel k_\theta^2/L_s^2)^{2/3}$ is similar to that of the strong shear limit of Ref.4. It is noted that the transition from the weak to the strong shear regime will occur for low m modes first.

FLUCTUATION LEVEL AND TRANSPORT

The characteristic length of turbulence can be written as $\Delta_k^\alpha = S_\alpha^{1/6}F^{1/2}(S_\alpha)\Delta_{k0}^\alpha$, ($\alpha$=$T$, n), where Δ_{k0}^T and Δ_{k0}^n are the characteristic length of turbulence without poloidal shearing[6]. Hence, the electron temperature and density fluctuation levels at saturation are estimated as $(\tilde{T}_e/T_e)_{rms} \simeq S_T^{1/6}F^{1/2}(S_T)(\tilde{T}_e/T_e)_{rms}^{(0)}$, $(\tilde{n}/n_0)_{rms} \simeq S_n^{1/6}F^{1/2}(S_n)(\tilde{n}/n_0)_{rms}^{(0)}$, where $(\tilde{T}_e/T_e)_{rms}^{(0)}$ and $(\tilde{n}/n_0)_{rms}^{(0)}$ are the fluctuation levels without velocity shear[6].

In the weak shear limit, $(\tilde{T}_e/T_e)_{rms} \simeq (\tilde{T}_e/T_e)_{rms}^{(0)}$ and $(\tilde{n}/n_0)_{rms} \simeq (\tilde{n}/n_0)_{rms}^{(0)}$.

In the strong shear limit, $(\tilde{T}_e/T_e)_{rms} = L_t^{-1}[(E_0L_s/B_zL_n)(C_n + C_t\eta_e)]^{1/2}\cdot|k_\theta V_\theta'|^{-1/2}$ and $(\tilde{n}_0/n)_{rms} = L_n^{-1}[(E_0L_s/B_zL_n)(C_n + C_t\eta_e)]^{1/2}|k_\theta V_\theta'|^{-1/2}$.

From Ref.6, the temperature fluctuation level is lower than that of density in the case of weak shear. In the strong shear limit, the ratio of temperature and density fluctuation is η_e. It is shown by experiments[8] that $\eta_e < 1$ at the edge of tokamak plasma , implying that the temperature fluctuation is lower than that of density as well.

The particle flux is given by $\Gamma_k^n \simeq S_n^{2/3}F^2(S_n)\Gamma_{k0}^n$, and the thermal flux is given by $Q_k = S_n^{2/3}F^2(S_n)T_e\Gamma_{k0}^n + S_T^{2/3}F^2(S_T)n_0\Gamma_{k0}^T$, where Γ_{k0}^n and Γ_{k0}^T are the particle flux and thermal flux without poloidal shearing[6].

Clearly, the fluctuation levels vary with $|k_\theta V_\theta'|^{-1/2}$ in the strong shear limit. However, the transport fluxes are dependent on $(k_\theta V_\theta')^{-2}$.

SUMMARIES AND CONCLUSIONS

The effects of sheared poloidal rotation on the structure of NRGDT in tokamak plasmas are investigated. The turbulent diffusivity, and the fluctuation level and transport fluxes at saturation, which are highly dependent on poloidal shearing, are evaluated analytically. The principal results are summarized as follows.

a). NRGDT with effects of poloidal rotations is investigated. We have obtained the diffusivity, the fluctuation level and the transport fluxes any shear parameter S_α.

b). The turbulent diffusion coefficients at saturation decrease with shearing parameter S_α increasing. In the strong shear limit, D_k^α varies with $(k_\theta V_\theta')^{-2}$ rather than $|k_\theta V_\theta'|^{-1/2}$, which is different from Ref.4.

c). The poloidal shearing can reduce the fluctuation level and plasma transport at saturation. In the strong shear limit, the fluctuation levels vary with $|k_\theta V_\theta'|^{-1/2}$ while the transport fluxes vary with $(k_\theta V_\theta')^{-2}$.

d). The fluctuation level of temperature is lower than that of density even in the presence of shearing poloidal rotations.

e). Clearly, the sign of poloidal rotation shearing does not affect the turbulent diffusion, and the fluctuation and transport etc..

ACKNOWLEDGMENTS

This work is supported by the Nuclear Science Foundation under Grant No.192010.

[1]F.Wangner, G.Becker, K.Behringer, et al., Phys.Rev.Lett.49, 1408 (1982)

[2]K.H.Burrel, Bull.Am.Phys.Soc.34, 2073 (1989)

[3]H.Biglari, P.H.Diamond, and P.W.Terry, Phys.Fluids B2, 1 (1990)

[4]Y.B.Kim, P.H.Diamond, H.Biglari, *et al*, Phys.Fluids B2, 2143 (1990)

[5]R.D.Hazeltine, and F.L.Hinton, Phys.Fluids 16, 1883 (1973)

[6]O.J.Kwon, P.H.Diamond, and T.S.Hahm, Phys.Fluids B1, 2172 (1989)

[7]X.D.Peng, Q.D.Gao, *CNIC*-00848 *SIP*-0071, 1994

[8]P.W.Terry. and P.H.Diamond, Phys.Fluids 28, 1419 (1985)

EXCITATION OF GLOBAL ALFVÉN EIGENMODES BY RF HEATING IN JET

W. Kerner, D. Borba, A. Fasoli*, C. Gormezano, G. Huysmans, F. Porcelli, S. Sharapov and D. Start.**
Jet Joint Undertaking, Abingdon, Oxfordshire OX14 3EA, U.K.
*CRPP, Lausanne, Switzerland
**RRC Kurchatov Institute, Moscow,Russia

INTRODUCTION

The alpha-particle confinement of future D-T experiments at JET can be severly degraded by Global Alfvén Eigenmodes (AE). Scenarios for the excitation of Alfvén eigenmodes in usual (e.g. D-D) plasmas are proposed, which provide a MHD diagnostic and allow the study of the transport of super-Alfvénic ions.

Active studies with separate control of TAE amplitude and energetic particle destabilisation, measuring the plasma response, give more information than passive studies, in particular concerning the damping mechanisms. The linear regime of the Alfvén physics can be exploited for a MHD diagnostic, where no significant perturbation of the plasma is required.

The TAE excitation can be achieved by means of the saddle coils, modelled in Ref. [1,2], and the ICRH antenna. In this paper the experimental method is introduced together with a theoretical model for RF excitation.'

EXPERIMENTAL METHOD

Whereas the saddle coils constitute a direct drive of global Alfvén waves via oscillatory currents with a frequency range of 20 - 500kHz (covering BAE, TAE and EAE), the ICRH antenna operates at much higher frequencies. Direct excitation has, consequently, to be achieved by frequency/amplitude modulation or by the nonlinear interaction of two fast waves whose frequency differ by the AE frequency. The beat wave excitation, satisfying energy $\left(\omega_1 - \omega_2 = \omega_{TAE}\right)$ and momentum $\left(\bar{k}_1 - \bar{k}_2 = \bar{k}_{TAE}\right)$ balance, relies on the generation of a volume current, $\bar{j}_{h\ell}$, inside the plasma with a power transfer $\left\langle \bar{j}_{h\ell} \cdot \bar{E}^{*}_{TAE} \right\rangle$ into the TAE. The corresponding radial magnetic field amplitude can be large at marginal stability $\left(\gamma_{TAE} \to 0\right)$, $\delta B_r / B_0 \approx \omega_{TAE} / \gamma_{TAE} \cdot v^2_{osc} / v^2_A$. A second method is given by the generation of high-energy ions, which subsequently provide the drive for AE destabilisation. Due to the high power of the JET ICRH antennae, these methods could generate finite-amplitude AE, allowing a systematic study of the AE enhanced energetic particle transport.

In the active studies the frequency in the driver is swept, correspondingly the modulation amplitude/frequency or the difference between the two driving RF wave frequencies. When a global Alfvén eigenmode is encountered, a resonance appears in the plasma response. The corresponding width gives a measure for the damping.

Synchronous detectors, whose reference signal is taken directly from the saddle coil exciter or, in the beat wave case, from the frequency difference of the two fast waves, are used to diagnose the plasma response. In phase ('real') and quadrature ('imaginary') components are provided. Different signals (up to 48) are considered, namely the active saddle coils for the antenna impedance, the passive saddle coils for the perturbed $\vec{B}_r$ (n-mode analysis), the magnetic probes for the perturbed $\vec{B}_\theta$ (n- and m-mode analysis) and other space-resolved, non-magnetic diagnostics, such as ECE and reflectometry, to resolve the spatial mode structure

The Data analysis fits the antenna-plasma-detectors transfer function with a rational fraction, with the discrete AE resonances being represented as poles in the complex plane, where the real part corresponds to the frequency and the imaginary part to the damping or drive. When Alfvénic fast particles ($v \sim v_{Alfvén}$) are produced in the plasma, e.g. by ICRH or NBI, an AE instability driving effect is produced and the imaginary part of these poles is modified.

WAVE-PARTICLE INTERACTION

Theoretical estimates for the RF drive of the TAE mode are based on a perturbative approach valid for a small drive. In the hybrid kinetic-MHD model a quadratic form is constructed, where the non-adiabatic, kinetic contribution $\delta W_{hot} = -\frac{1}{2}\int d^3x d^3v\, L^{(1)*} f^{(1)}$ is defined by the perturbed Lagrangian of the particle motion in the drift approximation and the perturbed distribution function $f^{(1)}$ Ref. [3]. The growth rate is proportional to its imaginary part, i.e. $\gamma \propto \mathrm{Im}\{\delta W_{hot}\}$. Here $L^{(1)} = -(mv_\parallel^2 - \mu B)\,\vec{\xi}\cdot\vec{\kappa} + \mu B\,\nabla\cdot\vec{\xi} \approx -(mv_\parallel^2 + \mu B)\,\vec{\xi}\cdot\vec{\kappa}$, where $\vec{\kappa}$ denotes the curvature of the magnetic field and $\vec{\xi}$ the MHD perturbation. It holds that $\tilde{L}^{(1)} = \hat{L}^{(1)} \exp\left(-\,in^\circ\varphi^{(\sim)}\right)$ is periodic in τ. Therefore, a Fourier expansion is possible $\tilde{L}^{(1)}(\tau) = \sum_{-\infty}^{\infty}{}_p\, Y_p\left(E,\ \mu,\ P_\varphi;\ \sigma\right) \exp\left(-\,ip\omega_b\tau\right)$, where $\omega_b \equiv 2\pi/\tau_b$. The Fourier coefficients are defined as $Y_p\left(E,\ \mu,\ P_\varphi;\ \sigma\right) = \oint \frac{d\tau}{\tau_b}\,\tilde{L}^{(1)} \exp\left(ip\omega_b\tau\right)$. Integration over the gyro angle and poloidal angle leads to

$$\delta W_{hot} = -\frac{2\pi^2 c}{Zem^2}\int\sum_{\sigma} dP_\varphi dE d\mu \tau_b \left(\omega - n^\circ \omega_*\right)\frac{\partial F}{\partial E}\sum_{p}^{\infty}\frac{\left|Y_p\right|^2}{\omega + n^\circ\langle\dot{\varphi}\rangle + p\omega_b}. \qquad (1)$$

Resonaces appear for $\omega + n^0\langle\dot{\varphi}\rangle + p\omega_b = 0$. The equilibrium distribution function $F = f^{(o)}$ is a function of the adiabatic invariants, i.e. $F = F\left(E,\ \mu,\ P_\varphi\right)$.

In order to enable a fast analysis of JET discharges several approximations are introduced in form of a analytic, small-orbit approximation and a local treatment on a flux surface. The evaluation of δW_{hot} requires still the calculation of the bounce-average Fourier components, Y_p and the sum of the resonant contributions integrated over $\Lambda = \mu B_o/E$.

In the case of passing particles good agreement with the results of Betti and Freidberg, [4], is found as shown in Fig. 1. For RF heated JET discharges the fast particle distribution is modelled by a slowing down distribution, Fig. 2, and by the Stix approximation $f_h^{(0)} = \exp\left(-\frac{E}{T_{eff}}\left(1 + H\left(\frac{E}{E_j}\right)\right)\right)$ [5], Fig. 3. The results for deeply trapped particles, i.e. $\Lambda = 1$, and for on-axis heated particles, i.e. $\Lambda = 1\text{-}\varepsilon$, are displayed in the figures.

CONCLUSIONS

RF Heating provides interesting schemes to: i) excite TAE directly by nonlinear wave-wave drive and ii) generate sufficiently many energetic ions to destabilise the TAE, i.e wave-particle drive.

The stability analysis shows that it is possible to destabilise TAE modes in JET discharges via particle resonances for relatively low $\beta_{hot} \sim 10^{-4}$ in low density plasmas, $n_e \sim 10^{19}$ m^{-3}, if ions with very high energy ($\geq$ 1 MeV) are generated by RF heating. These results are in qualitative agreement with the reported observation of TAE activity in JET [6]. It is emphasised that improved high-frequency diagnostics will enable more detailed comparison between theory and experiments.

Utilising the high-accuracy detection installed for the saddle coils excitation, i.e. frequency sweeping, synchronous detection and measurement of the plasma response, allows for accurate, independent determination of the damping effects and the destabilisation.

REFERENCES

[1] L. Villard, J. Vaclavik, S. Brunner, H. Lütgens and A. Bondeson, Proc. 20th Eur. Conf. on Controlled Fusion and Plasma Physics, ed. by J.A. Costa Cabral, M.E. Manso, F.M. Serra, F.C. Schuller, EPS Lisbon, (1993) IV, 1347.

[2] G.T.A. Huysmans, H. Holties, W. Kerner, J.P. Goedbloed, D. Borba and F. Porcelli, ibidem I, 187.

[3] F. Porcelli, R Stankiewicz, W. Kerner, H.L. Berk Phys. Plasmas 1, 470, 1994.

[4] R. Betti and J.P. Freidberg Phys Fluids B4, 1465, 1992.

[5] T.H. Stix, Nuclear Fusion 15, 737, 1975.

[6] S. Ali-Arshad, D.J. Campbell, JET-P(94)12

STABILITY DIAGRAMS

Local stability analysis of TAE modes with n=3, m=3,4 localised at q=7/6, as a function of β_{hot} for the following plasma parameters: Te=Ti=10 Kev, E_{hot}= 1->3 Mev, BT=2.8 T, $n_e=n_i=10^{19}m^{-3}$ at $V_\alpha/V_A=1$. Different values of V_α/V_A are scanned by changing the density n_e and keeping the magnetic field constant.

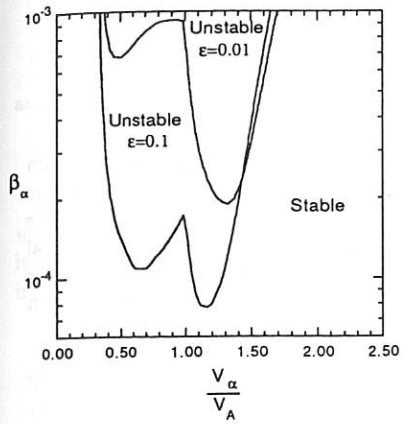


Figure 1 Isotropic slowing down distribution for particles with the birth energy of 3.5 MeV

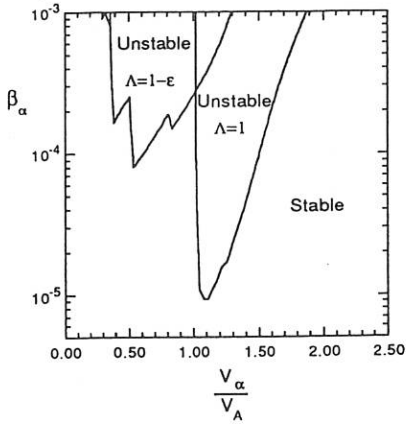


Figure 2 Anisotropic slowing down distributions for different pitch angles

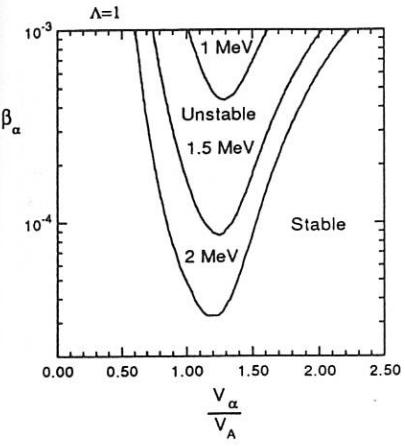


Figure 3a Stix distribution function for deeply trapped particles

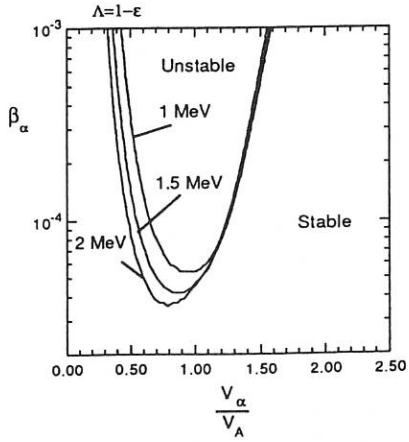


Figure 3b Stix distribution function for on-axis heated trapped particles

Non-ideal Effects on Toroidal Alfvén Eigenmode Stability

J W Connor, R O Dendy and R J Hastie
D Borba*, G Huysmans*, W Kerner* and S Sharapov*

UKAEA Government Division, Fusion, Culham, Abingdon,
Oxon OX14 3DB, UK
(UKAEA/Euratom Fusion Association)
*JET Joint Undertaking, Culham, Abingdon, Oxon, OX14 3EA, UK

1 Introduction Toroidal Alfvén Eigenmodes (TAE) and the associated Kinetic Alfvén Eigenmodes (KTAE) can be excited by fusion alpha-particles and can lead to anomalous alpha-particle transport. To calculate the threshold alpha-particle pressure needed to excite such modes, one must evaluate all the damping mechanisms. Within the framework of ideal MHD there is only continuum damping[1,2]. Here we derive improved analytic expressions for radiative damping and for ion resonant damping, and present results from an mhd code with complex resistivity, which generates a realistic spectrum of KTAE modes.

2 Radiative damping We first develop a ballooning formalism for non-ideal TAE modes and consider the effects of FLR and $\delta E_{\|} \neq 0$ within the layer surrounding the TAE resonant surface. Writing the scalar potential $\Phi(\theta) = \Psi_c(\theta)\cos(\theta/2) + \Psi_s(\theta)\sin(\theta/2)$, the first order FLR and toroidal coupling effects lead to a Schrödinger-type ballooning equation for the function $\Psi_c(\theta)$:

$$\frac{d^2\Psi_c}{dk^2} + \left[(\lambda^2 k^2 - g)^2 - 1\right]\Psi_c = 0, \tag{1}$$

$$k \equiv \epsilon\theta/4 \; ; \quad \lambda^2 \equiv 16\left(\frac{m\rho_i}{r}\right)^2 \frac{s^2}{\epsilon^3}\left(\frac{3}{4} + \frac{T_e}{T_i}(1 - i\delta(\nu_e))\right)$$

$$\delta(\nu_e) \simeq 0.44\sqrt{\frac{\nu_e}{\omega}}\left(\ln 16\sqrt{\frac{\epsilon\omega}{2\nu_e}}\right)^{-\frac{3}{2}} \; ; \; g \equiv \frac{1}{\epsilon}\left(\frac{2qR\omega}{v_A}\right) \; ; \quad s = rq'(r)/q(r) \; ; \quad \epsilon \approx \frac{5}{2}\frac{r}{R} \; ;$$

and ν_e is the electron collision frequency. If the shear is small ($s \ll 1$), the TAE eigenfrequency lies near the lower boundary of the frequency gap ($g \approx -1$) and the FLR effects produce a hill in the Schrödinger potential, providing some tunnelling of TAE energy into the high-k_r dissipative region (ie radiative damping). Asymptotic matching gives a TAE radiative damping rate

$$\left(\frac{\gamma}{\omega}\right) = -\frac{\pi^2}{8}\epsilon s^2 \exp\left(-\frac{\pi^3 s^2}{2^{7/2}\lambda}\right) \; , \text{ for } \; s \ll 1 \; , \tag{2}$$

and this damping becomes large when $\lambda \sim s^2$ (ie when $k_\theta\rho_i \gtrsim 0.2\epsilon^{3/2}$).

Near the upper boundary of the gap ($g \approx +1$) FLR effects provide a local well, leading to a quasi-stationary discrete spectrum of KTAE modes above the gap. The dispersion relation for KTAE modes is obtained using asymptotic analysis:

$$\frac{\pi s(g-1)}{2^{13/4}\lambda^{1/2}} = \mathrm{tg}\pi\left(\frac{1}{4} + \frac{a}{2}\right)\frac{\Gamma(3/4 - a/2)}{\Gamma(1/4 - a/2)}\,\frac{1 - i\Delta\mathrm{ctg}\pi(1/4 + a/2)}{l + i\Delta\mathrm{tg}\pi(1/4 + a/2)} \tag{3}$$

$$\Delta \equiv \frac{\sqrt{2\pi}(-a)^{-a}}{\Gamma(1/2-a)} \exp\left(-\frac{2^{5/2}}{3\lambda}\right) \; ; \quad a \equiv \frac{1-g^2}{2^{3/2}\lambda} \; ; \quad s \ll 1$$

Eq (3) gives the local dispersion relation for the KTAE discrete spectrum,

$$g = 1 + \frac{\lambda}{\sqrt{2}}(4p+1)\left(1 + \frac{s\sqrt{\lambda}}{2^{7/2}} \frac{\Gamma(p+1/2)}{\Gamma(p+1)}\right) \text{ , for } s \ll 1 \text{ ,} \tag{4}$$

as well as KTAE radiative damping

$$\left(\frac{\gamma}{\omega}\right)_{KTAE} = -\frac{\epsilon s \lambda^{3/2}}{2^{5/4}} \exp\left(-\frac{2^{5/2}}{3\lambda}\right) \text{ ,} \tag{5}$$

which becomes large at $\lambda \sim 1$ ($k_\theta \rho_i \gtrsim 0.2\epsilon^{3/2}s^{-1}$). An analogous study of radiative damping for the $s \gtrsim 1$ case shows that both TAE and KTAE radiative damping effects become important when $k_\theta \rho_i \gtrsim 0.2\epsilon^{3/2}s^{-1}$ and can be estimated as:

$$\left(\frac{\gamma}{\omega}\right)_{\text{TAE}} \simeq -\frac{\pi^{3/2}}{48}\frac{\epsilon\lambda^a}{s^4} \exp\left(-\frac{2^{5/2}}{3\lambda}\right) \text{ , } a \simeq \frac{\pi^2\sqrt{2}}{144 s^4 \lambda} \text{ ,}$$
$$\left(\frac{\gamma}{\omega}\right)_{KTAE} \simeq -\frac{24}{\pi^2 2^{1/4}} \epsilon s^2 \lambda^{3/2} \exp\left(-\frac{2^{5/2}}{3\lambda}\right) \cdot \tag{6}$$

3 Ion resonant damping In Refs 3 and 4 the damping rate of TAEs due to ion resonance was estimated as

$$\gamma_i/\omega_o \simeq -(\pi^{1/2}/4)\beta_i q^2 \lambda_3 \left\{1 + (1 + 2\lambda_3^2)^2\right\} \exp(-\lambda_3^2) \tag{7}$$

where $\lambda_n^2 = 1/n^2\beta_i$ and $\omega_o = v_A/2Rq$ with q evaluated at the gap centre where $nq \simeq (m + \frac{1}{2})$ with n the toroidal mode number and m and $m+1$ the poloidal mode numbers of the dominant TAE harmonics. The ion damping is determined by the perturbed ion distribution function, $\delta f_i \propto \boldsymbol{V}_d \cdot \delta \mathbf{E}_\perp \propto \omega_\kappa \Phi$ where $\omega_\kappa = (\boldsymbol{B} \times \boldsymbol{\kappa} \cdot \boldsymbol{k}_\perp) T_i/m_i\omega_c$ and $\boldsymbol{\kappa} = (\boldsymbol{b} \cdot \nabla)\boldsymbol{b}$ is the field line curvature. Because of the $(\cos\theta, \sin\theta)$ dependence of ω_κ, the perturbed ion distribution δf_i contains the poloidal harmonics $m-1, m+2$, corresponding to $k_\parallel \simeq 3/2Rq$ at the mode centre, and high energy ions with $mv_\parallel^2/2T_i = 1/9\beta_i \equiv \lambda_3^2$ give ion transit time damping. However, the estimate Eq (7) neglects $\delta E_\parallel$ and the effect of side-band harmonics in $\Phi(\theta)$ and $\omega_\kappa(\theta)$.

When $\delta E_\parallel$ is retained and evaluated using the quasi-neutrality condition, one finds[3] $\Psi = 2\tau\Phi\omega_\kappa/\omega$, where $\delta E_\parallel = -\nabla_\parallel \Psi$ and $\tau = T_e/T_i$. The resulting damping, obtained using the quadratic form in Ref 4, is $\gamma_i/\omega_o = -\sqrt{\pi}/4\beta_i q^2 F(\lambda_3, \tau)$ where $F(x,\tau) = x\{1 + (1 + 2\tau + 2x^2)^2\} \exp(-x^2)$. The increase in damping due to $\delta E_\parallel$ becomes significant only at larger values of $\beta_i (> 1\%)$. Thus, for $\tau = 1, \gamma_i$ is increased by 35% at $\beta_i = 2\%$ and by 52% at $\beta_i = 3\%$.

As a result of toroidal and shaped cross section effects, $\omega_\kappa(\theta)$ and $\Phi(\theta)$ contain small amounts of other poloidal harmonics. These drive components in δf_i with $k_\parallel = 5/2Rq$ and $7/2Rq$ at the mode centre, for which lower energy ions are resonant with $mv_\parallel^2/2T_i = \lambda_5^2$ and λ_7^2. We have calculated the first order corrections to $G(\theta) \equiv \omega_\kappa(\theta)\Phi(\theta)$ using the ballooning

formalism for a large aspect ratio, elliptic tokamak equilibrium. The resulting expression has been used in the quadratic form of Ref 2 to calculate ion resonant damping of TAE for $s \ll 1$:

$$\frac{\gamma_i}{\omega_o} = -\frac{\sqrt{\pi}}{4}\beta_i q^2 \left\{ F(\lambda_3^2,\tau) + \left[\frac{3}{4}\Delta' + \frac{3}{4}\frac{E}{r} - \frac{5}{4}E'\right]^2 F(\lambda_5^2,\tau) + \left[\frac{7}{12}E' - \frac{3}{4}\frac{E}{r}\right]^2 F(\lambda_7^2,\tau)\right\} \quad (8)$$

where $\Delta(r)$ is the equilibrium Shafranov shift and $E/r = (\kappa-1)/(\kappa+1)$ is the ellipticity parameter. At small values of $\beta_i(< 1\%)$ the new sideband corrections dominate ion damping which is, however, negligible compared to trapped electron damping given by

$$\frac{\gamma_e}{\omega} = -\left(\frac{\nu_e}{\omega}\right)^{\frac{1}{2}} \left[\ln 16 \left(\frac{\epsilon\omega}{2\nu_e}\right)^{\frac{1}{2}}\right]^{-\frac{3}{2}} \left[3.9\beta_e q^2 + 0.44(\rho_s/\Delta_{TAE})^2\right] \quad (9)$$

where for $s \ll 1, \Delta_{TAE} \simeq \epsilon r/m$. For higher values of $\beta_i(\gtrsim 2\%)$ $\delta E_\parallel$ causes significant enhancement of ion damping. In the interesting intermediate range $1\% < \beta_i < 2\%$, ion damping is important and Eq (8) provides a more accurate estimate than was previously available.

4 Complex resistivity approximation for KTAE in CASTOR[5] code First order FLR of core ions and $\delta E_\parallel \neq 0$ give the following corrections to the vorticity equation:

$$\underbrace{(\boldsymbol{b}\cdot\nabla)\left(\nabla^2(\boldsymbol{b}\cdot\nabla)\phi\right) + \nabla\left(\frac{\omega^2}{v_A^2}\nabla_\perp\phi\right)}_{\text{Ideal MHD Part}} + \underbrace{\frac{3}{4}\frac{\omega^2}{v_A^2}\rho_i^2\nabla_\perp^4\phi}_{\text{FLR}} + \underbrace{(1 - i\delta(\nu_e))\frac{\omega^2}{v_A^2}\rho_s^2\nabla_\perp^4\phi}_{\delta E_\parallel \neq 0 \text{ Term}} = 0 \quad (10)$$

The structure of this equation is analogous to that of the resistive MHD equations in the limit of $|\eta k_r^2/\omega| \ll 1$ with "complex resistivity" defined by:

$$\eta = 4\pi\omega\rho_s^2\left(\frac{2\omega}{\omega_A}\right)^2 \delta(\nu_e) + i4\pi\omega\left(\frac{3}{4} + \frac{T_e}{T_i}\right)\rho_s^2\left(\frac{2\omega}{\omega_A}\right)^2, \quad (11)$$

with $\omega_A = v_A/Rq$. The spectrum of Alfvén waves can be solved in compressible MHD in

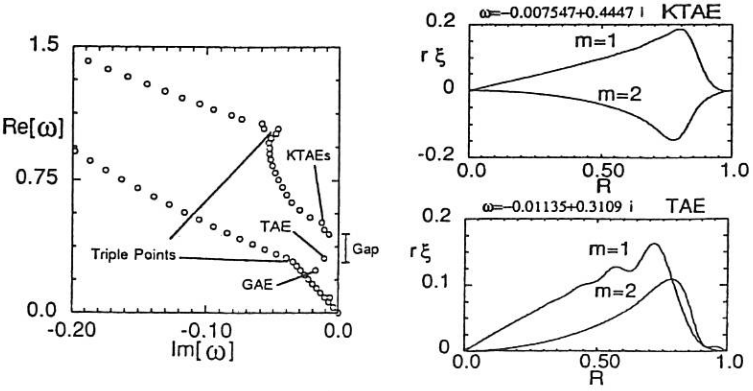


Fig 1 Alfvén spectrum for $\eta = 2.5 \times 10^{-5} + 10^{-4}i$, showing TAE and KTAE eigenfunctions.

cylindrical geometry, using a finite element numerical method. Solving in an equilibrium with a parabolic current profile having q=1 on axis and q=2 at the edge, with an artificial term coupling the two poloidal Fourier harmonics, we find: two Global Alfvén Eigenmodes (GAE); a TAE within the continuum gap; and a spectrum of KTAE, shown in Fig 1.

5 Conclusions Quantitative results are shown in Fig 2, which displays TAE damping rates for the mechanisms considered under JET and ITER conditions.

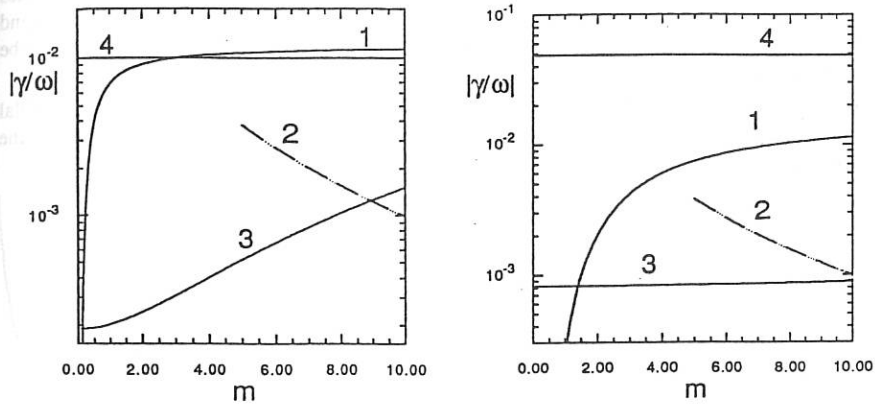


Fig 2 TAE damping rates for (left) JET (a = 1m, R = 3m, $B = 2T, T_e = T_i$ = 7 keV, n_o = 3 x $10^{19}m^{-3}, r_{TAE}$ = 0.3m, s = 0.2, ϵ = 0.25) and (right) ITER (a = 2.8m, R = 7.8m, B = $6T, T_e = T_i$ =19 keV, n_o = 1.4 x $10^{20}m^{-3}, r_{TAE}$ =0.7m, s = 0.2, ϵ = 0.29) for (1) radiative damping, (2) continuum damping for high m, (3) trapped electron collisional damping and (4) ion Landau damping.

Acknowledgement: This work was funded jointly by the UK Department of Trade and Industry and Euratom.

References

1 M N Rosenbluth, H L Berk, J W Van Dam and D M Lindberg, Phys Rev Lett 68, 596 (1992).
2 F Zonca and L Chen, Phys Rev Lett 68, 592 (1992).
3 R Betti and J P Freidberg, Phys Fluids B4, 1465 (1992).
4 G Y Fu and C Z Cheng, Phys Fluids B4, 3722 (1992).
5 W Kerner et al, Proc 18^{th} Eur Conf Contr Fusion & Plasma Phys, Berlin, 1991, IV, 89.

FAST PARTICLE LOSSES DUE TO TOROIDAL ALFVEN MODES IN JET

L C Appel*, T C Hender*, G T A Huysmans, W Kerner, S D Pinches+ and S Sharapov

JET Joint Undertaking, Abingdon, Oxon, OX14 3EA, UK
*UKAEA Government Division, Fusion, Culham, Abingdon, Oxon, OX14 3DB, UK
(UKAEA/EURATOM Fusion Association)
+University of Nottingham, University Park, Nottingham, NG7 2RD, UK

Introduction Toroidal Alfven Eigenmodes (TAE's) [1] can be destabilised in thermo-nuclear tokamak plasmas by a resonant interaction with a super-Alfvenic α-population. This interaction leads to an exchange of energy and canonical momentum between the particle and wave, which in-turn can lead to 'anomalous' losses or diffusion of α-particles by several mechanisms. In this paper we consider these α-particle loss and diffusion mechanisms for JET. In a previous study [2] the stability of a high performance deuterium JET discharge (26087) to TAE modes was analysed, but with $n_D=n_T$. It was found for this case that a modest decrease in density (and increase in temperature) would destabilise the Alfven modes, and thus permit their effects to be studied. The most likely candidates for TAE instability were found to be the n=3 modes.

Computational Methods The TAE mode eigenfunctions are calculated using the toroidal linear stability code CASTOR [2]. Figure 1 shows a typical n=3 eigenfunction along with the associated q-profile

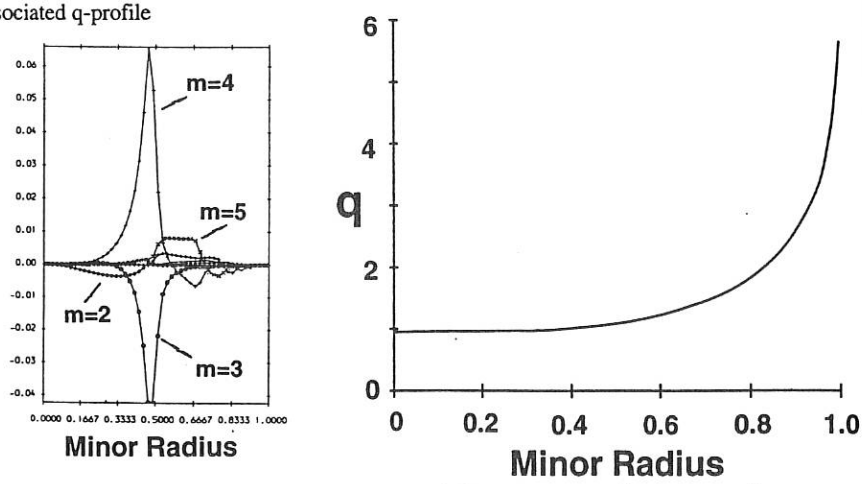


Fig 1 (a) n=3 TAE radial velocity eigenfunction and (b) q versus normalised minor radius

These eigenfunctions together with the associated equilibrium provide the magnetic field input for a new guiding centre particle following code. This code is based on a Hamiltonian formalism [3] to enhance numerical accuracy; without the Alfven mode perturbations for the worst case (Pinch orbit) the invariants of energy (E) and canonical toroidal angular momentum (P_ϕ) are conserved to better than the integrator tolerance (typically 10^{-10}) over a poloidal transit, while with a non-axisymmetric perturbation, the invariant $E-\omega P_\phi/n$ is conserved to $O(10^{-6})$ per transit. The widths of the particle islands, induced by resonant interactions with the TAE modes, have also been favourably compared with analytic estimations [4].

α-Loss and Diffusion Mechanisms As in Ref [5] two main mechanisms for α-losses and diffusion have been identified for the JET cases studied:-

- Firstly the TAE modes may cause relatively prompt losses of α-particles near loss boundaries.
- Secondly stochastic radial diffusion of the α-particles may occur. This class includes the possibility of α–particle loss by diffusion into loss cones.

The locations in the phase space λ-Pϕ (where $\lambda=\mu B_0/E$) of trapped and passing particle loss boundaries for the JET case studied are shown in Fig 2(a) and an orbit where an n=3 TAE perturbation converts a counter-passing particle into an unconfined trapped particle is shown in Fig 2(b).

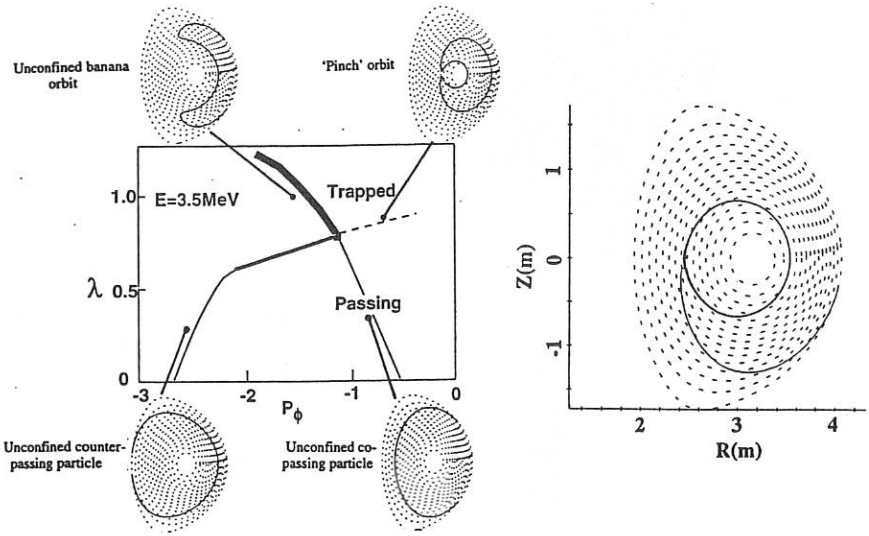


Fig 2(a) Locations in the λ-Pϕ plane of trapped-passing boundaries for 3.5MeV α–particle here; Pϕ is normalised to eΨ_{edge} . To the left of each solid line a particular class of particles is lost. In decreasing thickness the lines are trapped confined to unconfined, counter-passing confined to trapped unconfined, counter-passing confined to unconfined and co-passing confined to unconfined. The broken line is the (pinch-orbit) boundary between passing and trapped particles. (b) n=3 TAE mode causing a barely passing α to be converted into an unconfined trapped orbit.

To study collisionless particle losses due to TAE modes, Monte-Carlo simulations of 50,000 α-particles have been made. The α-particles have a slowing down distribution with energies in the range 3.5MeV to 1.5MeV, a radial distribution varying as $(1-\Psi)^3$ and a random distribution in pitch angle, poloidal angle and toroidal angle. For these studies three n=3 TAE modes with

normalised frequencies ω/ω_A=0.41, 0.51 and 0.58 have been used (the poloidal Fourier components for the ω/ω_A=0.58 case are shown in Fig 1(a)). Since these eigenmodes have been obtained from a linear simulation their amplitudes are arbitrary; here they are normalised so each eigenfunction has the same maximum radial field amplitude. These Monte-Carlo simulations show two distinct classes of lost particles due to the n=3 TAE modes (see Fig 3(a) and (b)). Firstly there is a prompt loss of α-particles born near a loss boundary; co and counter-passing particle prompt losses peak at ~3μs and trapped losses at ~6μs. Secondly above a stochastic threshold there is a steady long term loss of α-particles by stochastic diffusion into a loss boundary. Below the stochastic threshold losses scale linearly with the applied TAE perturbation.

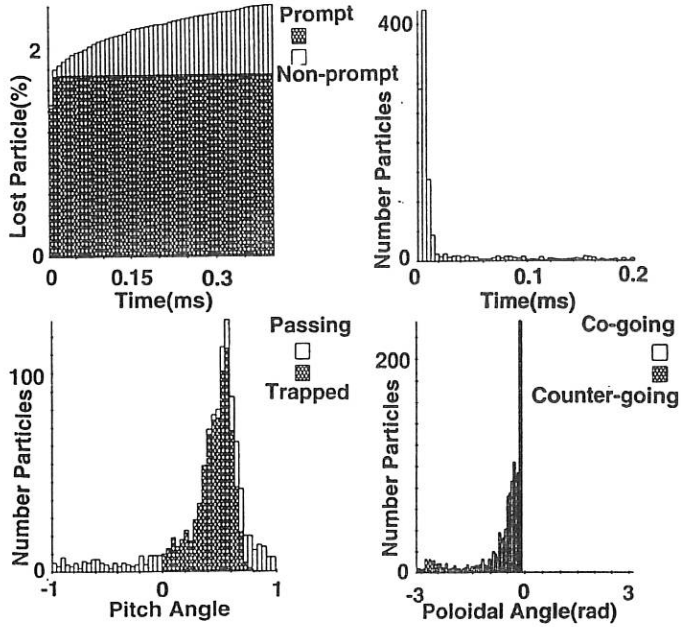


Fig 3(a) Fraction of lost particles as function of time (b) Number of lost particles in 4μs bins with the birth type of the particles distinguished (c) and (d) total number of lost particles versus pitch angle and poloidal angle, respectively.

It can be seen from Fig 3 (d) that the majority of particles are lost just below the outboard mid-plane for the particular ∇B-drift direction used; this is due mainly to co-directed trapped particle orbits (see Fig 3(c)) intercepting the 'wall' (at $\theta \leq 0$).

The second class of particle loss and diffusion is due to stochastic motion. For passing particles the stochastic diffusion occurs in the presence of the TAE perturbations because the particle orbits and flux surfaces are relatively displaced causing side-band resonances. Stochasticity occurs when the particle excursions due to the primary and side-band resonances overlap. For a single TAE mode the stochasticity threshold can be determined by examining the particle orbit in

a frame of reference which moves at the TAE frequency (ie ϕ–$\omega t/n$). In this frame of reference the particle islands and the transition to stochasticity as the islands overlap can be seen. With multiple TAE perturbations (of different frequency) it is not possible to define an equivalent frame of reference in which to view the particle orbits. Instead stochasticity must be determined by the particle diffusion (or loss) which the TAE perturbations cause. As in Ref [5] diffusion is measured by evaluating for an initially mono-energetic and mono-P_ϕ particle distribution, the spread of $\langle \Delta P_\phi^2 \rangle = \langle P_\phi^2 \rangle - \langle P_\phi \rangle^2$ in time (where $\langle\rangle$ denotes an ensemble average). Figure 4 (a) shows for the same n=3 TAE perturbations as used for Fig 3 the variation of $\langle \Delta P_\phi^2 \rangle$ with time for $\delta B_r/B=3\times10^{-3}$ and 5×10^{-4}; for these cases 500 particles are launched with an initial E=2.5MeV, $P_\phi=3.6\times10^{-19}$kgm^{2}s^{-1} and the particles are randomly distributed in pitch, poloidal and toroidal angles. For this case the stochasticity threshold is fairly high since the n=3 eigenmodes peak in a low shear region (see Fig 1) which increases the field amplitude required for island overlap [4]. Figure 4(b) shows for the $\delta B_r/B=3\times10^{-3}$ case the number of particles experiencing a given variation in P_ϕ. The smaller class experiencing a large variation are passing particles while the trapped particles have a small variation in P_ϕ.

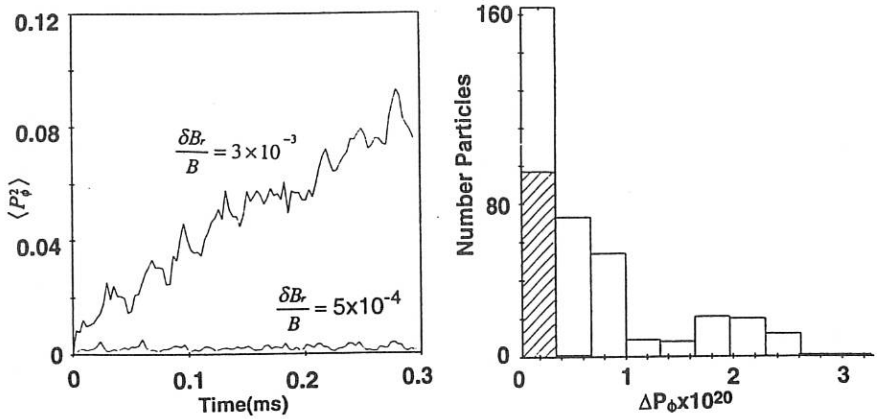


Fig 4(a) Variation of $\langle \Delta P_\phi^2 \rangle \times 10^{40}$ with time for $\delta B_r/B=3\times10^{-3}$ and 5×10^{-4} (b) Number of particles with a given variation ΔP_ϕ for $\delta B_r/B=3\times10^{-3}$, the shaded bars are trapped particles.

Summary For the high performance JET discharge studied the most likely candidates for TAE instability are the n=3 modes. Studies of particle orbits under the influence of these TAE modes have shown two dominant processes; firstly there is a relatively prompt loss of barely confined α-particles and secondly over a longer time stochastic diffusion of the α-particles can occur; this latter class includes the possibility of stochastic diffusion into a loss cone.

Acknowledgement The UKAEA authors were funded by the UK Department of Trade and Industry and EURATOM.

References

[1] G.Y.Fu and J.W.Van Dam, Phys Fluids B 1 (1989) 2404.
[2] W Kerner et al, Proc 1993 EPS Lisbon, 1 paper I-46.
[3] R.B.White et al, Phys Fluids 25 (1982) 2455.
[4] H.L.Berk et al, Phys Fluids B 5 (1993) 1506.
[5] C.T.Hsu and D.J.Sigmar, Phys Fluids B 4 (1992) 1506.

Nonlinear mode conversion of Toroidal Alfvén Eigenmodes

F. Zonca
Associazione Euratom-ENEA sulla Fusione,
C.P. 65 - 00044 - Frascati, Rome, Italy.

The fluid nonlinear saturation mechanism for Toroidal Alfvén Eigenmodes proposed previously[1,2] is considered in further detail. It is shown that the physical mechanism, leading to saturation above a critical mode amplitude, may be viewed as a nonlinear mode conversion of TAE's into short wavelength waves, which are strongly damped in the presence of a small dissipation.

1. Introduction

It has been recently shown that Toroidal Alfvén Eigenmodes (TAE) may nonlinearly saturate due to fluid nonlinearities only.[1] In analogy to linear toroidal coupling, nonlinear effects are important only in a thin region around the radial positions in the plasma discharge, where frequency gaps are opened in the shear Alfvén continuous spectrum. The nonlinear mode dynamics, then, turns out to be determined within these *boundary layers*, while the remainder of the plasma provides the inertia and the magnetic field line tension for the propagation of shear Alfvén waves associated to TAE modes.

The nonlinear equations for the boundary layers, derived previously,[1] are further analyzed in the present work. Essentially, it will be shown that nonlinearities change the linear eigenfunctions till, above a certain threshold in the mode amplitude, infinitely short scales are ideally excited. At this point, resistivity, e.g., becomes crucial for the dynamic mode evolution and it dissipates all the energy pumped into the wave, yielding nonlinear saturation.

This mechanism is analogous to what happens to linear TAE's, when resistivity (or finite Larmor radius effects) is made so large that TAE modes merge into kinetic TAE's.[3] The basic difference is that now, resistive dissipation is made larger by nonlinearities. In fact, it will be shown that the nonlinear boundary layer equations may be viewed as those describing a *nonlinear mode conversion* of a TAE into the continuum, above a certain threshold.

2. The Model

We consider a pressureless, large aspect ratio ($R_o/a \equiv 1/\epsilon >> 1$, R_o and a being major and minor radii), axisymmetric toroidal equilibrium with shifted circular magnetic surfaces. For the sake of simplicity, we also consider a single frequency gap in the shear Alfvén continuous spectrum, due to the toroidal coupling of the $(1,1)$ and $(2,1)$ Fourier harmonics.[1] Each fluctuation is assumed to be written in the form $F(\vec{x},t) = \sum_{m,n} e^{i(n\phi - m\theta)} F_{m,n}(r,t)$, (r,ϕ,θ) being toroidal coordinates, cho-

sen such that the inverse Jacobian $(\vec{\nabla}r \times \vec{\nabla}\phi)\cdot\vec{\nabla}\theta = R_o/rR^2$ and the safety factor $q = q(r)$. With this assumption, the nonlinear dynamic evolution of the system is determined within a single *boundary layer* at $q(r_o) = 3/2$, the remainder of the plasma providing only inertia and magnetic potential energy. When many *boundary layers*, or *frequency gaps*, are considered,[2] the boundary layer solutions must be matched to the external solutions at each gap radial location. The formalism is, thus, more complicated, but the physical picture remains essentially unaltered.[2] The purpose of the following analysis is to give a simple example of nonlinear dynamic evolution of TAE modes. The $(1,1)$ and $(2,1)$ Fourier harmonics will be considered as *test shear Alfvén waves*, generating nonlinear beat waves which couple back to $(1,1)$ and $(2,1)$ modes.

Outside the boundary layer at $q_o = q(r_o) = 3/2$, the time evolution of the two (uncoupled) test waves is determined by inertia, balancing magnetic field line bending. Thus, on the Alfvén time scale ($\omega_o^{-1} = 2q_oR_o/v_A$, v_A being the Alfvén speed), the dynamics of the $(1,1)$ and $(2,1)$ components of the vorticity U, related to the component of the fluid velocity perpendicular to $\vec{\nabla}\phi$ as $\vec{v}_\perp = (R^2/R_o)\,\vec{\nabla}U \times \vec{\nabla}\phi$, is described by the linear cylindrical vorticity equation[4]

$$\begin{aligned} \partial_r\left(\hat{U}_{m,n}(r,T)/r\right) &= \hat{C}_{m,n}(r,T)/[r^2 D_{m,n}(r)]\ , \\ \partial_r\left(r\,\hat{C}_{m,n}(r,T)\right) &= \left(m^2-1\right) D_{m,n}(r)\,\hat{U}_{m,n}(r,T)\ , \end{aligned} \qquad (1)$$

with $U_{m,1} = e^{-i\omega_o t_o}\hat{U}_{m,1}(r,T)$, $(m = 1,2)$, and $D_{m,n}(r) = [1/9 - (n - m/q(r))^2]$. It is worth to note that the nonlinear time scale $T = O(1/\epsilon\omega_o)$ enters only as a parameter in Eqs. (1), confirming that the nonlinear dynamic evolution of the system is determined within the boundary layer.

Substituting the solutions of the beat fluctuations equations into the nonlinear coupling terms of the vorticity equation,[1] nonlinear equations are derived, which determine the time evolution of $\hat{U}_{1,1}$ and $\hat{U}_{2,1}$ on the nonlinear scale within the boundary layer:

$$\begin{aligned} \left(i\partial_T - i\Gamma_\alpha - 4i\nu\partial_x^2 - 2sx\right)\partial_x u + \partial_x v - C_u(T) - 4\partial_x u\,\partial_x^2|v|^2 &= 0 \\ \left(i\partial_T - i\Gamma_\alpha - 4i\nu\partial_x^2 + 4sx\right)\partial_x v + \partial_x u - C_v(T) - 4\partial_x v\,\partial_x^2|u|^2 &= 0\ . \end{aligned} \qquad (2)$$

Here, $T \equiv \epsilon_o\omega_o t/2$, $\epsilon_o = 2\Delta' + r_o/R_o$, Δ' being the derivative of the Shafranov shift, $\nu = \eta/(\omega_o r_o^2\epsilon_o^3)$, $s = r_o q_o'/q_o$ is the magnetic shear and $x \equiv 2(r - r_o)/(r_o\epsilon_o)$. A term $-i\Gamma_\alpha$, has been also inserted *ad hoc* to model a linear drive associated to the energetic particles. Furthermore, $u(x,T)$ and $v(x,T)$ are the Fourier components of the vorticity normalized to $U_o^{-1} \equiv (2/\epsilon_o)^{3/2}(1/\omega_o r_o^2)$; $u(x,T) \equiv \hat{U}_{1,1}/U_o$, $v(x,T) \equiv \hat{U}_{2,1}/U_o$, and the quantities $C_u(T) \equiv 2q_o^2\hat{C}_{1,1}(r_o,T)/U_o$ and $C_v(T) \equiv 2q_o^2\hat{C}_{2,1}(r_o,T)/U_o$ are obtained from the dissipationless linear cylindrical equations outside the gap region.

From the second of Eqs. (1), it follows $C_u = 0$, and $\hat{U}_{1,1} = U_o A(T)(r/a)$ for $r < r_o$ and $\hat{U}_{1,1} = 0$ for $r > r_o$, with $A(T)$ given by the jump condition $A(T)(r_o/a) = -\int_{-\infty}^{+\infty} dx\partial_x u$. As to the $(2,1)$ component, the jump condition yields[4] $[\hat{U}_{2,1}(r_{o+}) - \hat{U}_{2,1}(r_{o-})]/U_o = -K C_v = \int_{-\infty}^{+\infty} dx\partial_x v \equiv \delta v(C_v)$, with K being a constant which depends only on the q-profile. Such a condition determines the time behaviour

of C_v, thus defining, together with Eqs. (2), a well posed problem for studying the nonlinear dynamics of TAE modes.

3. Nonlinear mode conversion of TAE modes

In the linear limit, Eq. (2) has solutions of the form $C_v(T) = \bar{C}_v e^{-i\lambda T + \Gamma_\alpha T}$, with $\bar{C}_v$ being independent of T. In this case, $\delta v(C_v)$ is linearly proportional to C_v and the $(2,1)$ jump condition determines the eigenvalue λ. Following the analysis of Ref. [3], it can be shown that $Im(\lambda)$ is related to the effect of dissipation, yielding $Im(\lambda) \approx \nu s^2$ in the case $\nu s^2 << 1$.

Also at saturation, i.e., when the mode amplitude does not grow in time, solutions of the form $C_v(T) = \bar{C}_v e^{-i\lambda T + \Gamma_\alpha T}$ satisfy Eq.(2) with the nonlinear terms included, provided the condition $Im(\lambda) = -\Gamma_\alpha$ is satisfied. Taking, for simplicity, the small magnetic shear limit, $s << 1$, the nonlinear system, Eqs. (2), yields two coupled nonlinear ordinary differential equations for the functions $f \equiv e^{i\lambda T - \Gamma_\alpha T}\partial_x u$ and $g \equiv e^{i\lambda T - \Gamma_\alpha T}\partial_x v$:

$$\begin{aligned} \left(\lambda - 4i\nu s^2\partial_z^2 - 2z\right) f + g - 8|g|^2 f &= 0 \ , \\ \left(\lambda - 4i\nu s^2\partial_z^2 + 4z\right) g + f - 8|f|^2 g &= \bar{C}_v \ , \end{aligned} \tag{3}$$

with $z \equiv sx$. In terms of g, the $(2,1)$ jump condition, together with the saturation condition $Im(\lambda) = -\Gamma_\alpha$, yields

$$\int_{-\infty}^{+\infty} g_R dz = -sK\,\bar{C}_v \ , \qquad \Gamma_\alpha = \frac{4\nu s^2 \int_{-\infty}^{+\infty} \left(|\partial_z f|^2 + |\partial_z g|^2\right) dz}{\int_{-\infty}^{+\infty} \left(|f|^2 + |g|^2\right) dz} \ , \tag{4}$$

with $g_R \equiv Re(g)$ and $g_I \equiv Im(g)$. Equations (4) determine the two unknowns of the problem, namely $Re(\lambda)$ and $\bar{C}_v$ at saturation.[1]

From the second of Eqs. (4), it is clear that the saturation condition can be satisfied only if very small scales are excited nonlinearly. This can happen only if the Jacobian of Eq. (3) in the dissipationless limit, $J(z,\bar{C}_v) \equiv (\lambda - 2z - 8g^2(z))(\lambda + 4z - 8f^2(z)) - (1 - 16g(z)f(z))^2$, tends to vanish.[1,2] It is interesting to note that the condition $J = 0$ defines, in the linear limit, the shear Alfvén continuum. The condition $J = 0$ will occur first at the local maximum ($z = z_o$) of J, since for $|z| \to \infty$ the Jacobian is always negative ($J \approx -8z^2$). Furthermore, the first of Eqs. (4) determines λ as a function of $\bar{C}_v$ and sK. Thus, the maximum of the Jacobian, $J_o \equiv J(z_o, \bar{C}_v, \lambda)$, turns out to be a function of $\bar{C}_v$ and sK, with $J_o < 0$ for $\bar{C}_v \to 0$. The condition that $J_o = 0$ determines then the critical mode amplitude $\bar{C}_{vo}$, above which nonlinear saturation may occur.

For small dissipation, $\nu s^2 << 1$, it has been shown that the true saturation level is close to $\bar{C}_{vo}$, i.e. $|\bar{C}_v - \bar{C}_{vo}| = |\Delta C_v| << |\bar{C}_{vo}|$.[1,2] The mode amplitude at saturation is then well estimated as $\delta B_{m,1;r}/B \approx -i(U_{m,1}/mU_o)(1 - m/q_o)(r_o/R_o)(\epsilon_o/2)^{3/2} \approx \bar{C}_{vo}\epsilon_o^{5/2}$. Since the amount by which this level is exceeded at saturation is small, we may let $\Delta f \equiv f(z) - f_o(z)$, $\Delta g \equiv g(z) - g_o(z)$, and solve for Δf_R, Δf_I, Δg_I, in terms

of Δg_R. An equation for Δg_R near $z = z_o$ can be obtained,[1,2] yielding

$$\partial_y^4 G + G^2 + 2G\sqrt{\frac{J_o^2}{J_\nu^2} + y^2} = \Lambda \ , \tag{5}$$

with $y \equiv \Delta z/z_L$, $G \approx \Delta g_R/z_L$, $\Lambda \approx -\Delta C_v/z_L^2 ln(z_L)$, $z_L \approx (4\nu s^2)^{2/5}$, and $J_\nu^2 \approx (4\nu s^2)^{4/5}$. Equation (5) and the second of Eqs. (4), i.e. the saturation condition, yield[1,2]

$$\Gamma_\alpha \approx (4\nu s^2)^{7/5} \int_0^\infty dy |\partial_y G(y,\Lambda)|^2 \ . \tag{6}$$

Once Γ_α and ν are given, Eq. (6) determines ΔC_v and hence the saturated TAE amplitude $\bar{C}_v = \bar{C}_{vo} + \Delta C_v$. Saturation can occur only for $\Lambda < -J_o^2/J_\nu^2$. In such a case, $I(\Lambda) = \int_0^\infty dy |\partial_y G(y,\Lambda)|^2$, as determined by numerical integration of Eq. (5) for $J_o^2 = J_\nu^2$, is well represented by the following interpolating expression: $I(\Lambda) = 0.0138\exp(-0.6563\Lambda)$. This yields $\Delta C_v \approx -(4\nu s^2)^{4/5}\ln(4\nu s^2)\ln[(4\nu s^2)^{7/5}/\Gamma_\alpha]$, explicitly showing the relevance of $\bar{C}_{vo}$ in estimating the mode saturation level.

An interesting point, concerning the physical mechanism behind the nonlinear mode saturation, emerges from the analysis of Eq. (5). It is readily verified that $G \simeq -\sqrt{y^2 + J_o^2/J_\nu^2} + \sqrt{y^2 + J_o^2/J_\nu^2 + \Lambda}$ is a good solution as long as $J_o^2/J_\nu^2 + \Lambda > 0$. In this case the fourth derivative, representing dissipation, can be neglected. Dissipation, on the contrary, plays a major role for $y^2 < y_T^2 \equiv -\Lambda - J_o^2/J_\nu^2$. At $\pm y_T$, ***nonlinear mode conversion*** into a strongly damped "kinetic"[3] Alfvén wave takes place: mode saturation then occurs, since the linear power input is dissipated on short scales in the interval $-y_T < y < y_T$. The nonlinear character of this ***mode conversion*** above a critical threshold is evident, since we clearly need $\Lambda < 0$ [1] and to be close enough to the critical threshold $J_o = 0$ [2], i.e. $J_o^2/J_\nu^2 \lesssim 1$, in order not to need too large and negative values of Λ. The dependence of Λ, or ΔC_v, on the linear drive Γ_α, as it emerges from Eq. (6), may be understood since the bigger the linear power input for the mode is, the bigger the region $-y_T < y < y_T$ must be, where the mode converted "kinetic" Alfvén wave can be dissipated. Furthermore, above the $\bar{C}_{vo}$ threshold, the Jacobian of Eq. (3) is $J \simeq J_\nu\sqrt{y^2 + J_o^2/J_\nu^2 + \Lambda}$. Thus, an attractive way to interpret the positions $\pm y_T$ is as the points where the mode interacts with the ***nonlinearly modified continuum***, although care must be used in extending the concept of a continuous spectrum to the nonlinear case.[1,2]

References

[1] G. Vlad, S. Briguglio, C. Kar, F. Zonca and F. Romanelli, in Theory of Fusion Plasmas, pp. 361-382, Ed. E. Sindoni and J. Vaclavik, (Editrice Compositori, Bologna, 1992). F. Zonca, F. Romanelli, G. Vlad and C. Kar, submitted to Phys. Rev. Lett.

[2] G. Vlad, C. Kar, F. Zonca and F. Romanelli, submitted to Physics of Plasmas.

[3] R.R. Mett and S.M. Mahajan, Phys. Fluids B 4, 2885, (1992); F. Zonca, Plasma Phys. 35, B307, (1993).

[4] H.L. Berk, J.W. Van Dam, Z. Guo, and D.M. Lindberg, Phys. Fluids B 4, 1806, (1992).

[1] I.e., $\Delta C_v < 0$. Note that also $\bar{C}_{vo} < 0$, for monotonically increasing $q(r)$.
[2] Recall that $J_o = 0$ is the condition defining the critical threshold $\bar{C}_{vo}$.

Linear Stability Analysis and Nonlinear Hybrid Simulation of TAE Mode

G. Y. Fu, C. Z. Cheng and W. Park
Princeton Plasma Physics Laboratory, Princeton University
Princeton, New Jersey 08543, U.S.A.

I. Introduction

The toroidicity-induced Alfvén eigenmode (TAE) has received a great deal of attention recently. Experiments have shown that TAE mode can be strongly destabilized by energetic ions introduced by NBI heating or ICRF heating in tokamak plasmas. The unstable TAE mode can in turn lead to large losses of energetic particles. This will have important implications for tokamak reactor design since the lost alpha particles can seriously damage the first wall. At prsent, D-T experiments in TFTR are being carried out to study the influence of fusion alpha particles on the TAE modes. Thus, it is of interest to assess the linear stability and the nonlinear saturation of the TAE modes. In this work, we briefly describe the main results of a linear stability calculation of the TAE modes in TFTR D-T plasmas using the kinetic MHD stability code NOVA-K [1-2], and the results of nonlinear hybrid simulation using the gyrokinetic MHD code MH3D-K [3].

II. Linear Stability Analysis

The stability of TAE modes in TFTR D-T supershot plasmas has been analyzed using the NOVA-K code. The code includes physics of alpha particle destabilizing contribution with the finite orbit width effects taken into account. The code also includes several damping mechanisms such as the Landau damping of thermal ions and electrons, the Landau damping of fast beam ions, and the collisional damping of the trapped electrons. For TAE mode to be unstable, the alpha drive must overcome the sum of the all dampings.

Figure 1 shows the critical central alpha beta for TAE instability versus toroidal mode number for TFTR shot #73268 in which 6.2 MW of fusion power was generated [4]. We observe that the alpha beta is about 1/3 of the critical value for the n=5 mode and all the TAE modes considered here are stable in this case. We have also analyzed other D-T shots and found that the TAE modes are stable for the most cases, with alpha beta value about a factor of two smaller than the critical value. The calculations done here use the experimental paramenters and profiles as simulated by the TRANSP code [5]. The safety factor q profile is quite flat near the center of plasma such that the $q = 1.5$ surface is at about 2/3 minor radius. The plasma pressure profile is peaked near the center. The TAE modes corresponding to the first continuum gap near the plasma center (at $q \approx 1.0$) usually do not exist due to the large pressure gradient. The TAE modes that do exist localize

radially around the second or the third gap at about 2/3 minor radius. It is found that the Landau damping of the deuterium beam ions is the most important damping mechanism for these TAE modes. The tritium beam Landau damping is smaller than the deuterium beam damping due to slower velocity. The electron Landau damping is also smaller. The Landau damping of thermal ions and the collisional damping of the trapped electrons are usually negligible.

In the future TFTR D-T experiments, the TAE modes may be destabilized by reducing the deuterium beam damping, or by enhancing the alpha drive. The deuterium beam Landau damping can be reduced with lower injection energy (i.e., slower beam particle speed to avoid the wave particle resonance). For one particular case, we find that the beam damping can be reduced by a factor of four if the the beam energy is reduced by 30%. The alpha particle drive can be significantly enhanced by allowing TAE mode to exist near the center of plasma where alpha pressure is highly peaked and the destabilizing contribution is largest. Numerically, we find that such core localized TAE mode can exist if the plasma pressure profile is slightly broader than the typical TFTR super shot profiles.

III. Nonlinear Hybrid Simulation

Nonlinear gyrokinetic MHD hybrid simulation have been carried out to study the TAE instability driven by energetic particles in tokamak plasma. The aim of this study is to determine the nonlinear saturation mechanism and associated fast particle transport. To this end, a hybrid model is used to describe the MHD feature of the mode and the kinetic effects of fast particle destabilization through wave particle interaction. The plasma is divided into two parts: the bulk part of the plasma which contains thermal electrons and ions, and the energetic part of hot ions. The bulk part is described by the ideal MHD equations, whereas the hot ions are described by the gyrokinetic equations. The effects of hot ions is coupled to bulk part motion through the pressure stress tensor term in the momentum equation as follows:

$$\rho_b \frac{d\mathbf{v}_b}{dt} = -\nabla P_b - \nabla \cdot \mathbf{P}_h + \mathbf{J} \times \mathbf{B} \tag{1}$$

where the subscript b denotes the bulk part, the subscript h denotes the hot ion component, P_b is the isotropic pressure of the bulk plasma, and the P_h is the pressure stress tensor of the hot ions. Equation 1 is closed by the ideal MHD Ohm's law and the Faraday's law. The stress tensor is calculated from a set of particles that are followed using the gyrokinetic equations with the self-consistent electromagnetic field. This system of equations is solved as an initial value problem. It can be shown analytically that our model conserves the total energy. Our numerical results indicate that the total energy is indeed well conserved.

In the simulations, we use the following parameters and profiles for most cases: the aspect ratio $R/a = 6$, the q profile $q = 1.2 + 0.9(r/a)^2$, the plasma density profile $\rho = \rho_0(1 - 0.8(r/a)^2)$, the bulk plasma beta $\beta_b(0) = 0.2\%$, the central hot particle beta $\beta_h(0)$

is on the order of percent, the hot particle velocity distribution is a Maxwellian in parallel direction with the mean value equals to the Alfvén speed at the center of plasma, and the perpendicular velocity is negligible. The number of particles used ranges from twenty thousands to two hundred thousands.

In the linear regime, the results show a robustly growing n=1 TAE mode. Figure 2 plots the evolution of the fluid kinetic energy of the bulk part. The slope of the straight line gives the linear growth rate of a converged mode. The corresponding TAE eigenmode structure is shown in Fig. 3. The calculated mode frequency agrees well with the NOVA-K result. The growth rate is also similar. In the nonlinear regime, the mode saturates in about one hundred Alfvén time, as shown in Fig. 4. Let's discuss briefly possible saturation mechanisms. First, large loss of resonant hot particles can be induced by the TAE mode with finite amplitude. As a result, the hot particle drive is diminished and the mode saturates. Second, the nonlinear mode coupling can modify the the continuum gap structure [6] such that the continuum damping is induced and the mode saturates when the continuum damping balances the hot particle drive. Third, the resonant particles can be trapped in the TAE wave at finite amplitude. As a result, the hot particle density profile is flattened locally and the drive diminishes to zero. In this case, the mode saturates at $\omega_b \sim \gamma_h$, where $\omega_b \propto \sqrt{\delta B_r}$ is the nonlinear bounce frequency of the resonant particles trapped in the wave. Our numerical results support this wave particle trapping mechanism. Figure 5 shows the saturation level δB_r as a function of the linear growth rate, where δB_r is the perturbed radial magnetic field. We see that our numerical results (solid dots) agree with the expected scaling of $\delta B_r \propto \gamma_h^2$ which is indicated by the solid line. Furthermore, a local flattening in the hot particle density profile is observed when a special distribution is used for which all particles have velocities close to the Alfvén speed. In addition to these results, we also find that the mode coupling is not important for the saturation. Figure 6 shows the the nonlinear saturation of the $n = 1$ TAE mode. We see that the saturation level obtained with a single $n = 1$ perturbation is almost the same as that with multiple toroidal mode number case (the solid line). Lastly, our results show that the particle loss is negligible and is not responsible for the mode saturation. In conclusion, we have demonstrated that the wave particle trapping is the dominating mechanism for the TAE saturation. Future work will assess the importance of other mechanisms in more realistic cases, including the situation of multiple unstable modes and associated hot particle transport.

[1]C. Z. Cheng, Phys. Reports 211, 1 (1992).
[2]G. Y. Fu, C. Z. Cheng and K. L. Wong, Phys. Fluids B5, 4040 (1993).
[3] W. Park et al., Phys. Fluids B4, 2033 (1992).
[4] R. J. Hawryluk et al., Phys. Rev. Lett. 72, 3530 (1994).
[5] R. V. Budny et al., Nucl. Fusion 32, 429 (1992).
[6] G. Vlad et al., Proceeding of 20th EPS Conference on Controlled Fusion and Plasma Physics, Volume 17C, IV-1351 (1993).

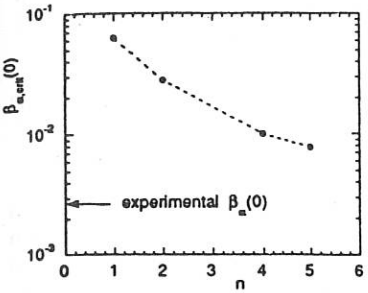


Fig. 1

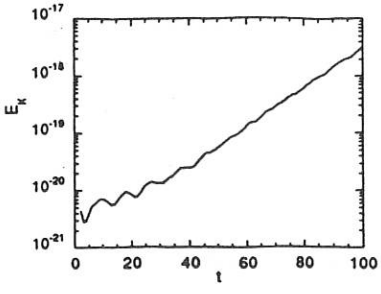


Fig. 2

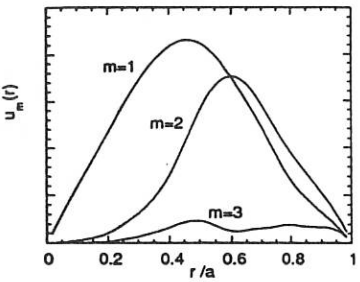


Fig. 3

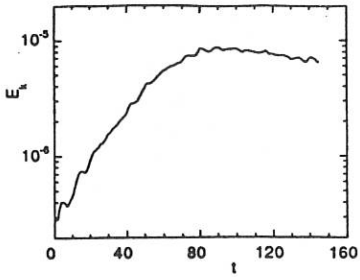


Fig. 4

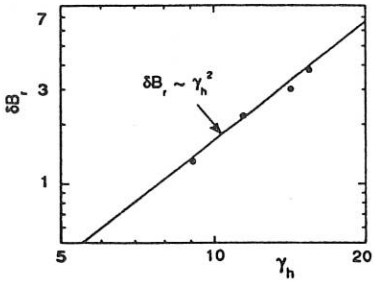


Fig. 5

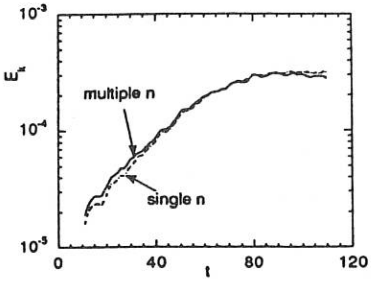


Fig. 6

TEST OF THEORY OF THE L-H TRANSITION IN ASDEX UPGRADE DISCHARGES

H.J. DE BLANK, H. ZOHM, ASDEX UPGRADE TEAM

Max-Planck Institut für Plasmaphysik, EURATOM-Association, 85740 Garching, FRG

Preliminaries

Significant progress in our understanding of the H-mode has come from bifurcation models of the L-H transition. The aim of this paper is to clarify the relation between such bifurcation models and the experiments on the ASDEX-Upgrade tokamak in which prolonged dithering at the L-H transition is observed when the ICR heating power ramp-up through the H-mode threshold is sufficiently slow.[1] These observations provide a novel test for models of the transition, since oscillatory L-H transitions do not only require the existence of a bifurcation, but also the capability of the particle and energy fluxes, modified by the electric field, to prevent a hard transition.

This paper addresses models in which a bifurcation in the radial electric field is deduced from the radial current balance. To this current various non-ambipolar particle loss mechanisms may contribute, such as ion orbit loss, anomalous electron loss, anomalous ion viscosity, electron ripple loss, and charge exchange. The non-linear dependence on E_r of some of these fluxes causes the bifurcation. We shall limit ourselves to the case of circular flux surfaces and equal electron and ion temperatures.

As pointed out by Shaing *et al.*[2,3] and Stringer[4,5], the resulting current is balanced by the neo-classical ion flux for which they give, for bulk viscosity in the collisional and plateau regimes, expressions that depend strongly and non-linearly on E_r. The ion flux in terms of the normalized electric field $Z = U_t/v_{ti} - E_r/B_p v_{ti}$ is

$$\Gamma^{NC} = 2\frac{nD_i}{\rho_{pi}}(\lambda - Z)I_p(Z), \qquad D_i = \tfrac{1}{2}\pi^{1/2}\frac{\epsilon^2\rho_{pi}T}{reB}, \qquad \lambda = -\tfrac{1}{2}\rho_{pi}\left(\frac{n'}{n} + \gamma\frac{T'}{T}\right). \quad (1)$$

Here $\rho_{pi} = mv_{ti}/eB_p$ is the poloidal ion gyroradius, and I_p is defined in Refs. [2,3]. It is of order unity for $|Z| \ll 1$ and $\sim \epsilon^{-Z^2}$ in the plateau regime, $\sim Z^{-2}$ in the collisional regime, for $|Z| \gg 1$. It depends on ϵ and on the collisionality $\nu_* = r\nu_{ii}B/v_{ti}B_p(\epsilon S)^{3/2}$. The orbit squeezing factor $S = |1 - \rho_{pi}Z'|$ may be important ($S > 1$) in the transition region. A prime denotes d/dr. The factor γ depends weakly on ϵ, ν_*, and Z as well.

Important for the present discussion is that the density and temperature gradients, enter the model as a combination $\lambda - Z$. This is also the case for the model of Itoh *et al.*[6,7] who assume that the anomalous electron transport is non-ambipolar and proportional to $-\lambda - Z$ times an anomalous diffusivity. This leads to a qualitatively similar bifurcation, not by a transformation $\lambda \to -\lambda$ but, since the bifurcation turns out to occur at $Z < 0$, by a transformation $Z \to -Z$.

We follow Refs. [2,6] in choosing ion orbit loss as the additional non-ambipolar process. It gives rise to an ion flux

$$\Gamma_i^{\text{orbit}} = n_i\nu_{ii}\rho_{pi}S^{-1}F(Z).$$

Itoh and Itoh [8] find $F \sim \exp(-\sigma Z^2)$, where σ is of order unity and depends on the shape of the separatrix. If it is too large, a bifurcation is not possible. Shaing [9] finds

a weak dependence of F on ν_* and describes the exponential decay $\sim \exp(x/\Delta x)^2$ away from the separatrix. Here $x = r - r_{\rm sep}$ and the loss layer width is $\Delta x = \rho_{pi}(2\epsilon/S)^{1/2}$. In the following sections we cannot retain this radial dependence. Instead we assume that the L-H transition occurs within the loss zone. Somewhat conflicting with this is our need to take S constant, neglecting its explicit dependence on $Z'(x,t)$

Bifurcation

The stationary state is given by the radial current balance, $j_r = e\Gamma_i^{NC} + e\Gamma_i^{\rm orbit} = 0$. The electrostatic stability can be seen from Poisson's equation, $\epsilon_\perp \partial E_r/\partial t = -j_r$. We rewrite this in a normalized form,

$$\hat{\epsilon}_\perp \frac{\partial Z}{\partial t} = I_p(Z)(\lambda + N(Z)), \qquad N(Z) = \frac{\rho_{pi}}{2nD_i}\frac{\Gamma_i^{\rm orbit}}{I_p} - Z. \tag{2}$$

The stationary state corresponds to $\lambda + N = 0$. A bifurcation occurs if $\lambda + N(Z)$ has multiple zeroes. Solutions with $dN/dZ > 0$ are unstable when λ is kept fixed. From here on we shall assume that $I_p(Z)$ and $F(Z)$ are such that $dN/dZ > 0$ in a single interval $Z_{\rm min} < Z < Z_{\rm max}$.

In the dynamical system of the next section we shall be able to find a relation between the changes in λ and Z. Then stability against space charge perturbations (much faster than the changes described by that system) then yields the requirement $(d/dZ)(\lambda(Z) + N(Z)) < 0$. We shall interpret this criterion as a necessary condition for a limit cycle.

This condition, effectively applied to a simple model with constant temperature in Ref. [7], will be applied here to the extended dynamic system of Ref. [1]. Subsequently, the function N(Z,g) will be constructed from the expressions for ion orbit losses[9] and the non-ambipolar neoclassical ion flux[2,3,5].

Dynamic system

In Ref. [7] oscillatory behaviour was found in a simple model in which Z, subject to a bifurcation as described above, modifies the anomalous particle diffusivity, while the particle flux in turn modifies λ and non-linearly influences Z.

This system was extended in Ref. [1] to include the effects of heat conductivity and will be used here. The particle and heat fluxes Γ and q are given in terms of the anomalous particle diffusivity D and heat conductivity χ. Particle and energy conservation in the absence of local sources and sinks is assumed,

$$\begin{aligned} \frac{\partial n}{\partial t} &= -\Gamma', \qquad \Gamma = -Dn', \\ \frac{\partial}{\partial t}(\tfrac{3}{2}nT) &= -q', \qquad q = -n\chi T' + \tfrac{3}{2}\Gamma T, \end{aligned} \tag{3}$$

Suppression of turbulent transport by the radial electric field is modelled by functions $D(Z)$ and $\chi(Z)$, such that for sufficiently large $Z > Z_{\rm max}$ the coefficients have (high) L-mode values D_L, χ_L, while for small $Z < Z_{\rm min}$ they have (low) H-mode values D_H, χ_H. In Ref. [7] this was implemented as

$$D(Z) = \tfrac{1}{2}(D_L + D_H) + \tfrac{1}{2}(D_L - D_H)\tanh(Z - Z_0), \tag{4}$$

where Z_0 is in the bifurcation interval. A similar expression is used for $\chi(Z)$.

The equation for Z is given by current balance. The parameter $\epsilon_\perp$ in Eq. (2) is small and causes a faster response of Z than the timescale on which n and T change. We put $\epsilon_\perp = 0$ so that Z adjusts to satisfy current balance instantaneously. In order to resolve the jump of Z in the L-H transition region we introduce in the curent balance the perpendicular shear viscosity $\mu_\perp$, as in Refs. [1,7], $\Gamma^{\rm shear} = (\mu_\perp Z')'$. We obtain the equation

$$(\mu_\perp Z')' = 2\frac{nD_i}{\rho_{pi}}(\lambda - Z)I_p(Z) + \frac{n\rho_{pi}\nu_{ii}}{S}F(Z). \tag{5}$$

In Ref. [7] the bifurcation in this equation was modelled by a cubic function. Using an equation of the form

$$\mu Z'' = \alpha Z - \beta Z^3 + d(n,T)(\lambda - \lambda_1),$$

dithering behaviour resembling experimental observations was obtained. Here we will keep the more general expression (5). The boundary conditions are: given fluxes Γ, q from the plasma centre, and fixed gradient lengths at the separatrix $\lambda_n = -n/n'\big|_{x=0}$ and $\lambda_T = -T/T'\big|_{x=0}$.

The Static L-H transition layer

We shall discuss here the case of sufficiently small $\mu_\perp$, so that spatially the transition between the L-state ($Z < Z_0, D \approx D_{\rm max}$) and the H-state ($Z > Z_0, D \approx D_{\rm min}$) occurs in a narrow region of width $\Delta \sim \left((Z_{\rm max} - Z_{\rm min})/2\mu_\perp\right)^{-1/2}$. Outside this layer D and χ are constant. Inside the layer we treat the fluxes as spatially constant, while n', T', Z, D, and χ may vary considerably. If the transition zone is close to the separatrix, we obtain from Eq. (3)

$$n'(Z) = -\frac{\Gamma}{D}, \qquad T'(Z) = \frac{\frac{3}{2}\Gamma T - q}{n\chi}. \tag{6}$$

Now that the radial dependence of n and T is given by Z alone, it is possible to integrate Eq. (6). The result is

$$x(\tilde{Z}) = 2^{1/2}\mu_\perp \int_{Z_2} d\tilde{Z} \left[\int_{Z_1}^{Z} dZ\, I_p(Z)\big(g(Z) + N(Z)\big)\right]^{-1/2}, \tag{7}$$

where

$$g(Z) = \frac{2nD_i\mu_\perp}{\rho_{pi}}\lambda, \qquad \text{and} \qquad N(Z) = \frac{n\rho_{pi}\nu_{ii}\mu_\perp}{S}\frac{F}{I_p} - \frac{2nD_i\mu_\perp}{\rho_{pi}}Z.$$

Again, the function $N(Z)$ increases in approximately the interval $[Z_{\rm min}, Z_{\rm max}]$ and decreases everywhere outside it. Furthermore, it is negative in the entire bifurcation interval. The function $g(Z)$ is positive and increases in this interval from its L-mode value for ($Z < Z_{\rm min}$) to its H-mode value ($Z > Z_{\rm max}$) because $\lambda(x) \sim D^{-1}, \chi^{-1}$. Hence $g+N$ has at least one zero. The integration boundary $Z = Z_1$ has to be at such a zero in order to ensure that the solution (7) extends to $x \to -\infty$. To the right of this root one either finds an unstable root or no root at all. Therefore, the solution cannot extend to $x \to +\infty$, which shows that the stationary transition layer solution is necessarily bounded to the right by the plasma edge. The L-mode solution exists for $g(Z_{\rm max}) + N(Z_{\rm max}) \lesssim 0$ and the condition for the H-mode solution is $g(Z_{\rm min}) + N(Z_{\rm min}) \gtrsim 0$. These two criteria overlap.

Existence of a limit cycle

In a dynamical situation the function $g(Z)$ may be shifted with respect to $N(Z)$ and destroy the stable solutions found before. However, as long as the more stringent condition $g(Z_{\min})+N(Z_{\max}) > 0$, the H-mode solution survives. Similarly, the stable L-mode solution exists as long as $g(Z_{\max}) + N(Z_{\min}) < 0$.

These conditions can be given in terms of the fluxes Γ and q. We use $D_i \sim T^{3/2}$, $\nu_{ii} \sim nT^{-3/2}$, $\rho_{pi} \sim T^{1/2}$, expressions (6), and normalize λ to $T^{1/2}\hat{\lambda}$. Using Eq. (6) and the boundary conditions we find $n = \lambda_n \Gamma/D$ and $T \sim q/\Gamma$. The dZ integrand in Eq. (7) is found to be proportional to

$$(\tfrac{q}{\Gamma})^{3/2}\hat{\lambda}(Z) - (\tfrac{q}{\Gamma})Z + \Gamma(\tfrac{q}{\Gamma})^{-1}\frac{\hat{F}(Z)}{I_p(Z)}.$$

Hence, the criterion for a stable H-mode becomes

$$(\tfrac{q}{\Gamma})^{5/2}\hat{\lambda}(Z_{\min}) - (\tfrac{q}{\Gamma})^{2} Z_{\max} + \Gamma\frac{\hat{F}(Z_{\max})}{I_p(Z_{\max})} > 0, \tag{8}$$

The criterion for L-mode is similar. The criteria for the heat flux have the form

$$\text{L-mode:} \quad q < q^{L}_{\text{crit}}(\Gamma), \qquad \text{H-mode:} \quad q > q^{H}_{\text{crit}}(\Gamma).$$

If $q^{H}_{\text{crit}} < q^{L}_{\text{crit}}$ there exists a window in q for which L and H mode are both stable. This is the bifurcated state. There, $g+N$ has three zeroes, of which the middle is unstable. If however $q^{H}_{\text{crit}} > q^{L}_{\text{crit}}$, for values of q within this interval both the L-state and the H-state can be unstable. It is in this regime that oscillatory behaviour is possible and has been found numerically in Ref. [1]. The precise relation q_{crit} and Γ depends in detail on the functions I_p and F, but for reasonable values, inspection of expression (8) shows that

$$q_{\text{crit}} \propto \Gamma^{c}, \qquad 1 \lesssim c \lesssim \tfrac{3}{2},$$

i.e., the thresholds in the heating power are expected to depend linearly or slightly stronger on the density.

Summarizing, we have obtained, in addition to the conditions under which the L-H bifurcation exists, a more stringent necessary condition for dithering behaviour at the L-H transition. For the transport mechanisms considered, the correct scaling between density and power threshold is found.[1,10]

References

[1] H. Zohm , ASDEX-Upgrade Team, NI and ICRH Group, Phys. Rev. Lett. **72** (1994) 222.
[2] K.C. Shaing, and E.C. Crume, Phys. Rev. Lett. **63** (1989) 2369.
[3] K.C. Shaing, E.C. Crume, and W.A. Houlberg, Phys. Fluids B **2** (1990) 1496.
[4] T.E. Stringer, Nucl. Fusion **32** (1992) 1421.
[5] T.E. Stringer, Nucl. Fusion **33** (1993) 1249.
[6] S.-I. Itoh, and K. Itoh, Phys. Rev. Lett. **60** (1988) 2276.
[7] S.-I. Itoh, K. Itoh, A. Fukuyama, and Y. Miura, Phys. Rev. Lett. **67** (1991) 2485.
[8] S.-I. Itoh, and K. Itoh, Nucl. Fusion. **29** (1989) 1031.
[9] K.C. Shaing, Phys. Fluids B **4** (1992) 3310.
[10] H. Zohm, et al., *This Conference.*

NEOCLASSICAL ALPHA-PARTICLE LOSSES IN TOKAMAKS ALLOWING FOR LARGE ORBIT WIDTHS

M Cox, M R O'Brien and F S Zaitsev[†]
UKAEA Government Division, Fusion, Culham, Abingdon, Oxon, OX14 3DB, UK.
(UKAEA/EURATOM Fusion Association)
[†]Moscow State University, Moscow, Russia.

INTRODUCTION

Alpha-particle physics is of particular importance now that research into controlled fusion has reached thermonuclear parameters and D-T fuel has been used in JET and TFTR. Here we address the important topic of α-particle transport: if transport is too low helium ash accumulates quenching the burn; if it is too high heating of the plasma by fast α-particles is insufficient to maintain the burn. We give results from simulations of α-particle distributions (f_α) which self-consistently treat α-particle birth, collisional slowing down and neoclassical radial transport. The (steady-state) f_α is calculated by the FPP code [1] as a function of speed (v), pitch-angle (θ) and flux surface radius (r). This code is based on a 3D Fokker-Planck theory of "banana regime" neoclassical effects in tokamaks [2] which can treat large deviations of fast ion orbits from flux surfaces and non-Maxwellian distributions. The code reproduces standard neoclassical results for Maxwellian distributions in the large aspect ratio (ϵ) and small orbit width (Δ) limits (e.g. radial fluxes, conductivities and bootstrap currents), but can also be used for small ϵ and large Δ which are difficult to treat analytically. The code is particularly useful for α-particle studies as (a) the experimental evidence is that fast ion transport is usually consistent with neoclassical theory, unlike electron or thermal ion transport, and (b) trapped fast ion orbits can deviate greatly from flux surfaces. An alternative to this Fokker-Planck treatment is Monte Carlo modelling. However, representation of the detailed structure of $f_\alpha(\theta, v, r)$ would require very large numbers of particles, and hence be very slow.

Calculations have been made for parameters typical of TFTR, JET, SSTR (an "advanced tokamak" reactor [3]) and STR (a tight aspect ratio or "spherical" tokamak reactor [4]), though only the JET results are discussed in detail. The aim is to investigate the general topic of neoclassical α transport, and not the specific details of D-T shots in TFTR or JET, though this is the subject of separate work. (In this latter work the time evolution of f_α is studied and direct orbit losses are included but these are neglected here for simplicity.) Only thermal-thermal fusion reactions were included in the α-particle source term for the results presented here, though a treatment including beam-thermal fusion is important for quantitative comparison with α-particle detectors in the TFTR D-T experiments for example.

RESULTS

For JET an up-down symmetric D-shaped plasma without X-points was used, with R_o=3m, $R_{magaxis}$=3.25m, a=1.2m, κ=1.5, B_o=3T. The plasma current (I_p) was varied between 1 and 5 MA to vary both the deviations of orbits from flux surfaces and the strength of neoclassical transport. Equal deuterium and tritium densities and temperatures were assumed ($n_D(0)$=$n_T(0)$=2×10^{19}m^{-3}, $n_e(0)$=6×10^{19}m^{-3}, $T_D(0)$=$T_T(0)$=20keV and $T_e(0)$=10keV). Parabolic density profiles ($n(r{=}a){=}0.1n(0)$), (parabolic)^2 temperature profiles ($T(r{=}a){=}0.05T(0)$) and a (parabolic)^2 current profile ($q_0 \sim 1$ for I_p = 3MA) were used.

JET calculations were performed for three currents, I_p = 1, 3 and 5 MA. For each I_p there were two calculations: one in which the full orbits were used and one in which the orbits were assumed to stay close to flux surfaces (as in standard neoclassical theory). Figure 1 shows the

predicted profiles for I_p=1MA: Fig 1(a) shows the density profile $n_\alpha(r)$ and Fig 1(b) shows the α-particle source and the predicted plasma heating profile. Similarly Figs 2 and 3 shows profiles for I_p=3 and 5 MA. Note that the source profile is the same for all the calculations as it is determined only by the deuterium and tritium profiles ($\sim n^2T^2$). In Fig 2(b) the heating profiles for electrons, deuterium and tritium are given separately: as the electron heating clearly dominates only the total heating profile is given in Figs 1(b) and 3(b). The algorithm for calculating the heating profiles is accurate for the surface-averaged calculations but only approximate for the orbit-averaged ones. This is because the algorithm spreads the power transferred through collisions by an individual α-particle evenly along the orbit whereas in fact it is uneven (varying approximately as $n_e T_e^{-3/2}/|v_\parallel|$). This means that the predicted power deposition profiles for the orbit-averaged calculations may be narrower than they should be, since $n_e T_e^{-3/2}$ increases with r. This algorithm will be improved for future work.

The results are qualitatively broadly as anticipated. The α-particle density decreases with increasing I_p as expected neoclassically. The α-particle "temperature" increases with decreasing I_p as the stronger the transport the less time the α-particles have to slow down. (The densities and temperatures quoted are integrals over the whole distribution and include the thermalised particles.) Also, the difference between surface-averaging and orbit-averaging is most marked at low I_p for which the orbit deviations from flux surfaces are largest. In all cases the α-particles have thermalised by the time they are lost through the collisional radial flux at the edge (there is no other loss mechanism), and so almost all the α-particle energy is deposited in the plasma. The power deposition profile most closely matches the source profile for I_p=5MA, as anticipated, though the difference between I_p=3MA and I_p=5MA is not as large as perhaps one might have expected. In all cases the central α-particle density is lower if orbit deviations are included. The interpretation of this is that the fast α-particles have a lower confinement time since their initial orbits pass through regions away from the magnetic axis, which means that they have less far to be transported before reaching the edge.

Contour plots of f_α in (speed, pitch-angle, flux surface radius) space reveal a structure which will be valuable for comparison with α-particle diagnostics on JET (such a comparison is already underway for TFTR). In particular on a given flux surface the distribution varies greatly around a flux surface and at any point on the flux surface is not isotropic in pitch-angle. At the inside of the flux surface f_α peaks for counter-travelling particles, whereas at the outside it peaks for co-travelling particles. This behaviour arises since the α-particle source is centrally peaked and counter-particles on the inside (outside) come from smaller (larger) flux surface radii, whereas co-particles come from larger (smaller) radii. Figures 4(a) and 4(b) illustrate this point showing contours of f_α as a function of speed and pitch-angle at the inside and outside of the flux surface with $r \simeq 0.5a$ for the I_p=5MA orbit-averaged calculation. It is clear that slowing-down approximations to the local distribution function (isotropic with $f_\alpha \sim 1/(v^3 + v_c^3)$) are unlikely to compare well with detailed diagnostic measurements, though they do give the strong peaking at low v

The distribution functions peak strongly at low energy ("helium ash"), though since the transport of slow α-particles is likely to be anomalous, these energies are not treated accurately in the present calculations.

CONCLUSIONS AND FUTURE PLANS

The results show that excursions of α-particle orbits from flux surfaces can give a significant broadening of the profile of power deposition on the background plasma (in practice, almost

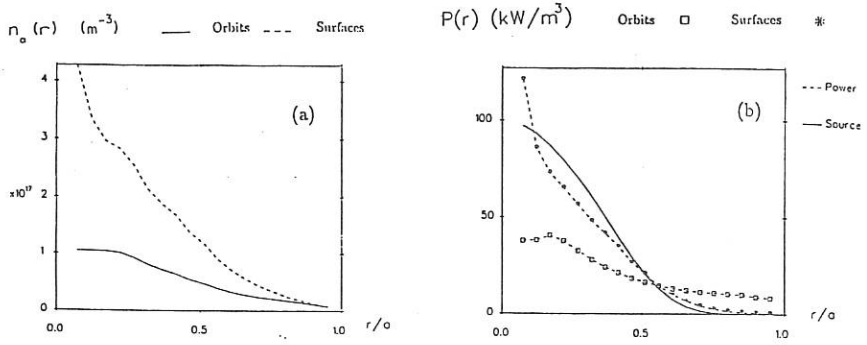


Figure 1 Comparison between surface- and orbit-averaged calcluations for JET $I_p = 1$MA: (a) Alpha-particle density profile, (b) Alpha-particle source and deposition profile.

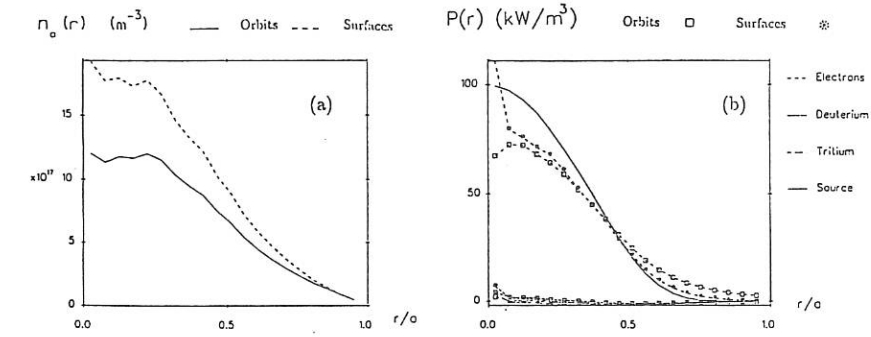


Figure 2 As Figure 1 but for $I_p = 3$MA. The power deposited on each species is shown.

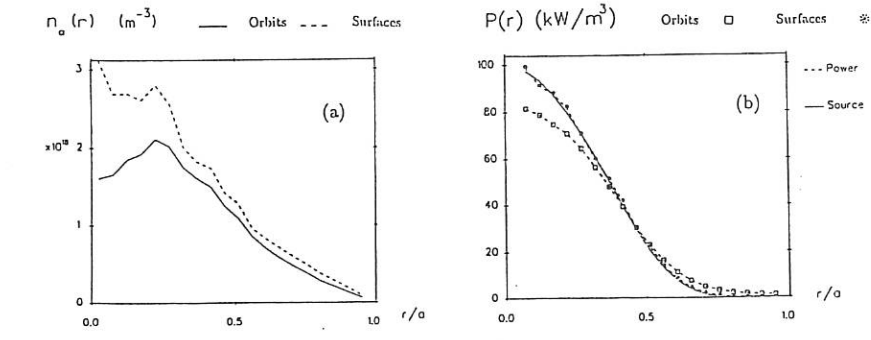


Figure 3 As Figure 1 but for $I_p = 5$MA.

entirely on the electrons) particularly at low I_p. This broadening should be included in transport simulations of D-T shots. Inclusion of these excursions gives lower α-particle content as it results in a lower α-particle confinement time. These effects are mainly due to trapped α-particles which have the largest excursions, particularly if born in the low poloidal field centre of the tokamak. The calculations for TFTR showed more pronounced effects with its smaller current and size (we took $I_p = 1.5$MA, $R = 2.5$m, $a = 0.8$m). Also, in TFTR direct loss terms can influence f_α away from the edge unlike in JET or the other devices studied (though ripple losses may be important in these machines). The calculations for SSTR ($I_p = 12$MA, $R = 7$m, $a = 1.7$m) showed a smaller effect than for JET due both to its larger current and its large aspect ratio (i.e. low trapped particle fraction). However a calculation for STR which has an even higher current ($I_p = 30$MA, $R = 2$m, $a = 1.5$m) shows a sizeable effect because of the large trapped particle content (aspect ratio = 1.33).

In this paper only neoclassical transport has been considered. This is unlikely to be sufficient for slow α-particles since thermal ion transport generally exceeds neoclassical levels so ad hoc transport operators will be included for studies of helium ash build-up. There may be other processes that affect the confinement of fast particles (e.g. TAE modes, ripple losses) and these will also be included in the code. Another enhancement planned is an ICRF heating operator to study fast ion tail distributions.

Acknowledgements

This work was funded by the UK Department of Trade and Industry and by Euratom. Part of the work undertaken as part of a Task Agreement between UKAEA and the JET Joint Undertaking.

References

[1] M R O'Brien et al., IAEA Technical Committee Meeting on Advances in Simulation and Modelling Thermonuclear Plasmas, Montreal 1992, p527.
[2] F S Zaitsev, M R O'Brien and M Cox, Physics of Fluids B **5** (1993) p509.
[3] M Kikuchi, Plasma Physics and Controlled Fusion **35** (1993) B39.
[4] T C Hender et al., Proc. 14th Int Conf on Plasma Physics and Controlled Nuclear Fusion Research, Würzburg 1992, Vol 3 p399.

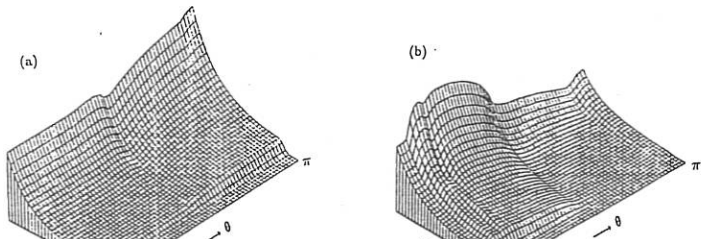


Figure 4 Contour plots of $f_\alpha(\theta, v)$ for JET, $I_p = 5$MA on inside (a) and (b) outside of flux surface $r \simeq 0.5a$. The minimum and maximum energies are 0.56MeV and 4.5MeV. The distribution falls rapidly above 3.5MeV.

Possibility of Using Ion-Bernstein Waves for Alpha Power Extraction in Tokamaks

N. J. Fisch, E. J. Valeo, C. F. F. Karney, and R. Majeski
Princeton Plasma Physics Laboratory, Princeton, NJ 08543, USA

1. Introduction

If the fusion α-particle power is directly channeled to do useful things rather than simply undergo collisional absorption, there is an opportunity for significantly improved tokamak reactor performance. In the absence of the channeling, the α-particle power results predominantly in electron heating, which is a poor use of this power.

One possibility is to direct this power into waves that damp on electrons traveling in one direction to sustain the plasma current [1]. Since the power required to drive the toroidal current is about 10% of the fusion power output, whereas the α-particle power is 20% of the fusion power output, using even a fraction of the α-particle power to amplify the waves used for current drive can result in very significant savings in the required power for the current drive.

A second possibility is to direct this power into waves that damp on fuel ions to increase the plasma reactivity [2]. Such a channeling of the α-particle power could make possible the operation of fusion reactors in regimes in which the fuel ion temperature can be much greater than the electron temperature.[3] It may also be possible to sustain a hot, nonmaxwellian component of the fuel ions, further enhancing the reactivity. By these means, if 75% of the α-particle power is diverted, the plasma reactivity, at constant pressure, can be increased by about a factor of two. [4] It may even be possible to achieve at once the increased reactivity and the current drive, if, for example the α-particle power is channeled into waves that damp on fast ions traveling in one toroidal direction.

2. Basics of the Energy Extraction

Although there is free energy in the energetic α-particles, how to tap a large fraction of this power is challenging. For example, wave interactions that drive particles primarily in velocity space tend not to extract most of the recoverable energy [e.g. 5-7]. A more promising way of tapping this power appears to be through a resonant quasilinear interaction with a poloidally and toroidally propagating short wavelength electrostatic wave [1]. Such a wave diffuses the α-particles both in space and energy, rather than just in energy.

For simplicity, consider a cylindrical geometry. Suppose an electrostatic wave such that $k_\perp \rho_\alpha \gg 1$, where $\rho_\alpha \equiv v_\alpha/\Omega_\alpha$ is the α-particle gyroradius, and where, for radial diffusion, $k_\perp \simeq k_\theta$. Upon experiencing a velocity impulse due to the wave-particle interaction, the change in the radial guiding center displacement is $\Delta r_{gc} = \Delta v_\theta/\Omega_\alpha$, and the energy change is $\Delta E = m_\alpha(v_\theta \Delta v_\theta + v_\parallel \Delta v_\parallel)$. Note also that, since $k_\perp \rho_\alpha \gg 1$, the velocity impulse occurs when the α-particle is Landau resonant, i.e., when $v_\theta = (\omega - k_\parallel v_\parallel)/k_\theta$. Also, successive impulses from the wave add if $v_\parallel = (\omega - n\Omega_\alpha)/k_\parallel$. It is also the case, by energy conservation in the wave frame, that the direction of the impulse must be along the path $v_\perp \Delta v_\perp + (v_\parallel - \omega/k_\parallel)\Delta v_\parallel = 0$. It then follows that the diffusion takes place along the path in r_{gc}–E space such that

$$\Delta r_{gc} = \Delta E k_\theta / m_\alpha \Omega_\alpha \omega. \tag{1}$$

Note that in extracting its energy, an α-particle can be made to move many gyroradii.

The diffusion path indicated by Eq.(1) is modified in toroidal geometry, particularly for trapped particles. Similar to the gyrocenter motion induced by perpendicular impulses, a velocity space impulse in the parallel direction results in banana center motion for toroidally trapped particles. A suitable formalism for studying these toroidal effects is found, e.g., in Ref. 8.

3. Optimal Wave Characteristics

Note that Δr_{gc} is related linearly to ΔE, so that, depending upon the sign of ω/k_θ, as E decreases r either increases or decreases. The sign of ω/k_θ can and ought to be chosen to assure the former event, for then α-particles are extracted cold at the plasma periphery, giving up energy to the wave. This is the situation depicted in Fig. 1, which shows a diffusion path such that α-particles are diffused from high energy at the plasma center ($r = 0$), to low energy at the plasma periphery ($r = a$). Depicted here for didactic purposes is an α-particle distibution function f_α that is monotonocally decreasing in energy on any magnetic surface, yet energy extraction takes place so long as there is a population inversion along the diffusion path.

Note that a population inversion along the diffusion path can normally be achieved with $\omega/k_\theta \to 0$. However, that would result in α-particles being ejected at $r = a$ with little change in energy, which, in fact, is highly undesirable. In the opposite limit, $\omega/k_\theta \to \infty$, the diffusion occurs in velocity space only, so that there is no population inversion (i.e., the wave is damped. The optimum choice of ω/k_θ results in $\Delta r_{gc}/\Delta E \simeq 3.5\,\mathrm{MeV}/a$, where clearly a population inversion occurs as α-particles may be extracted cold at the periphery. Fig. 1 depicts a nearly optimum diffusion path.

4. The Ion Bernstein Wave

To achieve the necessary $\Delta r_{gc}/\Delta E$, it is necessary to launch large-k_θ waves. In this regard, one possibility is the lower hybrid wave, but it is difficult to define a large k_θ with slow wave structures at the plasma periphery. An attractive possibility, depicted in Fig. 2, is to launch a fast wave that mode-converts at the ion-ion resonance surface into an ion Bernstein wave (IBW). The idea here is that the resonance surface is vertical, so the IBW emerges with a high horizontal wavenumber, which, if the mode conversion takes place sufficiently off the horizontal midplane, as depicted in the figure, is essentially with a high poloidal wavenumber. By poloidally phasing the ICRF antenna, the required sign of ω/k_θ can be accomplished. Note that a significant simplification of the antenna geometry would be produced with an off-midplane, high field side antenna site in a large reactor.

In Fig. 3, we depict the interaction of α-particles with the IBW, which occurs in a narrow vertical slab. On any magnetic surface, essentially all the α-particles sample the wave region. Those α-particles satifying the resonance condition as they pass through the vertical slab are kicked to a larger minor radius if they lose energy to the wave, and are kicked to a smaller minor radius if they gain energy from the wave. Particles are extracted as they near the periphery, so that a diffusion gradient is maintained along the path stretching from the center at high energy to the edge at low energy.

For the IBW, the upshift in poloidal wavenumber that occurs at the mode conversion surface can be dramatic. In Fig. 4, we calculate the upshift for the case of a 50:50 D-T mix, with ion temperatures of 20 KeV and electron temperatures of 10 KeV. Incidentally, note that, because of the upshift, care must be taken not to approximate the wave using the conventional finite $k_\perp\rho$ approximations (dotted line). Most of the

IBW experimentation and analysis has been carried out with a view towards power deposition at or near the horizontal midplane. For example, current drive on axis is a very interesting possibility [9]. However, to achieve the channeling effect, mode-conversion off the midplane is required, where the poloidal magnetic field must be taken into account. An account of the wave propagation and damping, presented elsewhere [10], shows that the required waves can be excited off axis, if a suitable choice is made of certain parameters, such as the toroidal phasing and the fuel mix.

5. Suggested Experiments

A test of the channeling effect is, in principle, possible on TFTR, where the effect of the ion Bernstein waves on the α-particles might be observed. A preliminary calculation shows that, if at least 1 MW of ICRF power is converted to an IBW, a significant number of α-particles might be diffused about 30 cm in less than a slowing down time.

The best experiment would be to conduct experiments with both poloidal and toroidal phasing. Then, by reversing the poloidal phasing, one should be able to observe that α-particles are diffused out while losing energy in one case, and diffused out by gaining energy in the other case. TFTR is suited well for this experiment, not only because of the existence of α-particles, but also because the ICRF antennas, being center-grounded and end-fed, can be modified easily to achieve the poloidal phasing.

Acknowledgements: Much of this work is an outgrowth of the joint work of one of the authors (NJF) and Dr. Jean-Marcel Rax. This work was supported by the United States Department of Energy under contract number DE–AC02–76–CHO3073.

---

1. N. J. Fisch and J. M. Rax, Phys. Rev. Lett. **69**, 612 (1992).

2. N. J. Fisch and J. M. Rax, in Plasma Physics and Controlled Nuclear Fusion Research (Proc. 14th Int. Conf. on Plasma Phys. and Controlled Thermonuclear Fusion, Würzburg, 1992) IAEA, Vienna, Vol. 1, 769 (1993).

3. J. F. Clarke, Nucl. Fusion **20**, 563 (1980).

4. N. J. Fisch and M. C. Herrmann, Princeton Plasma Physics Laboratory Report 2989 (1994).

5. D. J. Sigmar, in Proc. Physics of Plasmas Close to Thermonuclear Conditions, Varenna, Italy (Int. School of Plasma Physics, 1979) p. 271.

6. W. R. Sutton III, D. J. Sigmar, and G. H. Miley, Fusion Tech. **7**, 374 (1985).

7. K. R. Chen, Phys. Rev. Lett. **72**, 3534 (1994).

8. Z. Gášek, L. Krlín, and Z. Tlučhoř, Phys Lett. A **135**, 284 (1989).

9. R. Majeski et al., in Proc. 10th Top. Conf. on rf Heating, ed. M. Porkolab and J. Hosea (AIP, NY) AIP Conf. Proc. Vol. 289, 401 (1994).

10. E. J. Valeo and N. J. Fisch, Princeton Plasma Physics Laboratory Report 3000 (1994).

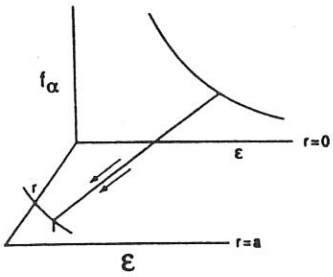


Fig. 1. f_α vs. energy ϵ and radius r. Population inversion exists along diffusion path.

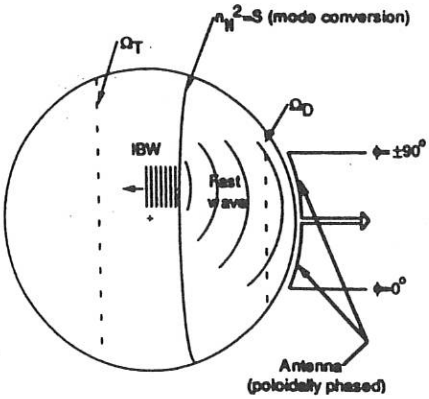


Fig. 2. Mode conversion of fast wave viewed in poloidal cross-section. Note IBW has short poloidal wavelength.

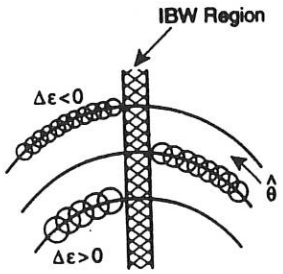


Fig. 3. Gyrating α-particle viewed in poloidal cross-section as it enters resonant region from right. Subsequent motion is either along lower (more energetic) orbit or upper (less energetic) orbit.

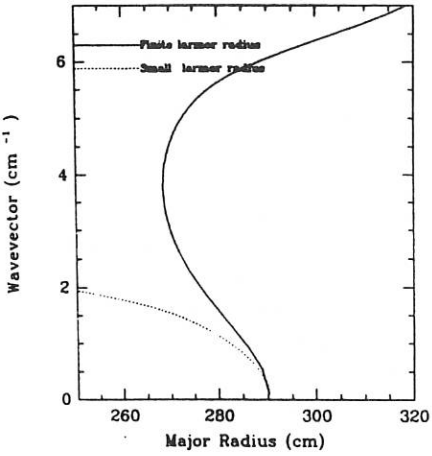


Fig. 4. Ray-tracing of IBW following mode conversion (solid line) showing upshift in $k_\perp$. Note that the group velocity reverses direction. Dotted line shows small Larmor radius approximation.

Modelling of sawtooth induced redistribution of ICRF-heated minority ions

D. Anderson, L.-G. Eriksson* and A. Ödblom

Institute for Electromagnetic Field Theory
Chalmers Univ. of Technology
S-412 96 Göteborg, Sweden

* JET Joint Undertaking, Abingdon, England

1. Introduction

Experimental evidence indicate that sawtooth crashes tend to redistribute ICRF-heated particles [1, 2]. In particular, the redistribution may be inferred from the rapid reduction in the total fast ion energy following a sawtooth crash [1] and the reheating rate of the central electron temperature [2].

In the present work a qualitative model is given to describe the redistribution of ICRF-heated minority ions at sawtooth crashes in Tokamak plasmas. A crucial feature of the model is that it takes into account the finite width of the ICRF-heated particle orbits. Predictions of the model are compared, and found to be in agreement with, numerical simulations as well as experimental results from JET.

2. Simple model for finite orbit width effects on fast-ion energy density profile

Strong ICRF-heating creates an almost perpendicular velocity tail of high energy trapped particles with turning points in the resonant layer. The fast ions slow down on, and transfer energy to, the background species by collisions. Due to the finite orbit widths of the RF-heated particles, the profile of the collisionally deposited electron heating is broadened. The analysis is based on a simplified model, which prescribes the broadening effect by a suitably chosen weighted velocity and space average of the orbit width. For on-axis heating the RF-heated ions trace out potato-shaped rather than banana-shaped orbits. The resulting width, δ_{eff}, characterizing the broadening of the power deposition on the electrons is

$$\delta_{eff} \cong 0.7\ A^{1/3}\ (q_o\, \rho_L(o))^{2/3} \qquad (1)$$

where A is the aspect ratio, q_o is the central safety factor. $\rho_L(o)$ denotes the Larmor radius corresponding to the axial, tail temperature $T_\perp(o)$, which may be determined from the centrally absorbed RF-power density.

The collisionally deposited electron heating, p, may be modelled by a gaussian profile $p(x) \sim \exp[-(x/b)^2]$, where $x=r/a$ is the normalized minor radius which equals unity at the plasma edge. To account for the finite orbit width effects we increase the e-folding width with δ_{eff}, but conserve the total power. The fast-ion energy density, w, is given by

$$w(x) = \frac{1}{2} t_s(x)\ p(x) \qquad (2)$$

where the slowing down time is modelled by a generalized parabola, $t_s \sim (1-x^2)^{\mu}$. The importance of finite orbit-widths for fast-ion profile properties is exemplified in Fig. 1, which also shows the good agreement with the results from more complete numerical simulations of JET discharges.

3. Effect of finite orbit width on total fast-ion energy

It has been observed on JET that the increase of the total energy of the RF-heated minority ions tends to saturate at high absorbed RF powers. A simple model to account for the saturation can be given based on the model of the previous paragraph.

The peaked, gaussian, power deposition profile may with good agreement be approximated by a generalized parabola. Integrating eq. (2) over the plasma volume, which is approximated with a straight, circular cylinder, the finite orbit-width degradation of the total fast-ion energy W is, cf Fig. 2,

$$\frac{W}{W_o} = \frac{1+\mu b^2}{1+\mu b^2 \left(1+\left(\frac{T_\perp(0)}{T_*}\right)^{1/3}\right)^2} \qquad (3)$$

where W_o is the total fast energy neglecting finite orbit-width effects and

$$T_* \equiv 1.4 \cdot 10^{-4} \frac{b^3}{MA} \left(\frac{Za(cm)\ B(kG)}{q_o}\right)^2 \qquad (MeV)$$

M and Z denote the mass number and the charge number respectively of the heated ion and B is the magnetic field. Application to JET discharges yield good agreement, cf Table 1.

4. Sawtooth induced redistribution of ICRF-heated ions

Experimental evidence indicate that sawtooth crashes tend to redistribute ICRF-heated particles [1, 2]. Since the spatial resolution is limited by the typical orbit width the present work is based on a recently presented "smoothed" model for fast ion redistribution [3]. The model redistributes the fast energy density profile shaped as a generalized parabola, by prediction of the change in amplitude and peaking exponent, conserving the total fast energy on the crash time scale. The two most important parameters determining the redistribution is the peaking factor of the fast energy profile and the location of the q=1 surface (x_s). A measure of the redistributing efficiency is the ratio, K, of the fast-ion energy within the q=1 surface after the crash compared to the corresponding energy before the crash, cf. Fig. 3. Note, when finite orbit-widths are included the peaking factor of the fast energy profile is diminished, reducing the redistributing efficiency. Application to JET discharges, show that the present model including finite orbit-widths is able to reproduce the measured rate of reheating of the central electrons after the crash, cf Table 1. The model has also been applied to estimate the sawtooth-induced change of total fast-ion energy following a sawtooth crash as observed in JET experiments.

5. Conclusions

A qualitative model is given to describe the redistribution of ICRF-heated minority ions at sawtooth crashes in Tokamak plasmas.

The finite orbit widths of the ICRF-heated ions are important for:

- the fast-ion energy and power transfer profiles
- the total fast energy content
- the redistributing efficiency of the fast ions

Comparison with numerical simulations and experimental results shows an improved agreement when the finite orbit-widths are included.

References:

[1] L.-G. Eriksson, T Hellsten, and U Willén, Nucl. Fus. 33 (1993), 1037.

[2] L.-G. Eriksson et al, Nucl. Fus. 29 (1989), 87.

[3] D Anderson, P Batistoni, M Lisak, and F Wising, Plasma Phys. Control Fusion 35 (1993), 733.

Table 1: Comparison between the results from the present model and from the JET experiments for the total fast-ion energy and for the sawtooth induced redistribution of the ICRF-heated ions including the finite orbit-widths. The post-crash fast-ion energy density $w_{+\,exp}(0)$ is obtained from the central electrons' reheating rate, cf [2].

pulse	δ_{eff}	W_o [MJ]	W [MJ]	W_{exp} [MJ]	x_s	K	$w_+(0)$ [kJ/m^3]	$w_{+\,exp}(0)$ [kJ/m^3]
12298	0.19	1.5	1.1	1.0	-	-	-	-
19650	0.12	1.3	1.0	1.1	0.32	0.59	61	60
15374	0.15	1.0	0.8	0.7	0.32	0.40	47	50
15380	0.11	0.9	0.8	0.9	0.34	0.41	41	43
15433	0.10	0.7	0.6	0.6	0.40	0.44	23	21

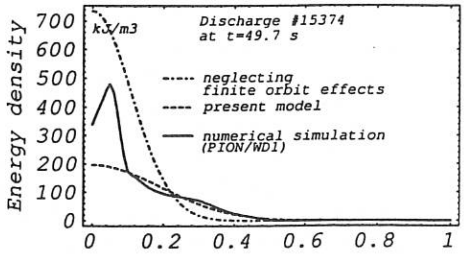


Fig. 1: Comparison between numerical simulations, including the finite orbit width effects on the energy density profile of the rf-heated ions, and the simplified present model .

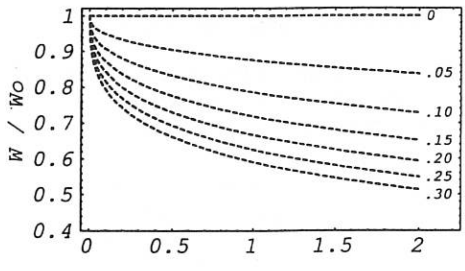


Fig. 2: Degradation of total fast-ion energy with increasing orbit width as characterized by the normalized on-axis tail temperature $T_\perp(0)/T^*$ for different values of the parameter μb^2.

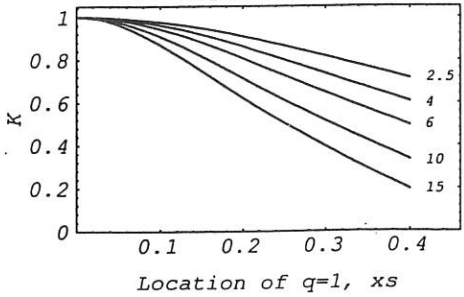


Fig. 3: The ratio, K, of the fast energy content inside the q=1 surface after the crash to the corresponding energy before the crash, for different peaking factors, γ, of the pre-crash energy density profile.

TOPOLOGY AND SLOWING DOWN OF HIGH ENERGY ION ORBITS

F. Porcelli*, L.-G. Eriksson and H.L. Berk**
JET Joint Undertaking, Abingdon, Oxon, OX14 2BN, UK.
*Politecnico di Torino, C.so Duca degli Abruzzi, 24, 10129 TORINO; porcelli@polito.it
**Institute for Fusion Studies, University of Texas, Austin, TX 78712

INTRODUCTION. A correct description of high energy ion orbits is important to assess their effects on the energy balance and on MHD modes active in the central region of a Tokamak plasma (internal kinks, fishbones, TAE). We consider the regime $\delta_b \geq r$, where $\delta_b \sim \varepsilon^{-1/2} q\rho$ is the standard banana orbit width, $\varepsilon \equiv r/R$, $q_0 \equiv q(0)$ and ρ is the Larmor radius. In this regime, the banana-shaped orbit is distorted into a *potato*-shaped orbit with a characteristic width of the order of $\delta_p = \Delta^{2/3} R$, $\Delta \equiv 2q_0\rho / R$. For a 1 MeV Hydrogen ion and typical parameters of the JET Tokamak, $\delta_p \sim 0.3$ m is about one third of the plasma minor radius.

ORBIT EQUATION. The orbit equation for the particle guiding centres can be obtained from the invariance of the energy, $\mathcal{E} \equiv mv^2/2$, magnetic moment, $\mu \equiv mv_\perp^2/2B$, and toroidal canonical momentum in axisymmetric plasmas, $P_\varphi = (Ze/c)\psi - mRv_\parallel B_\varphi / B$, where $\psi \geq 0$ is the poloidal flux function. We consider a standard low-β Tokamak equilibrium where the departure from concentric flux surfaces is of order ε. Neglecting higher order corrections, let us set $v_\parallel = \pm v_{\perp 0}(\lambda + \varepsilon\cos\vartheta)^{1/2}$, where $v_{\perp 0} \equiv (2\mu B_0/m)^{1/2}$ and $\lambda \equiv (\mathcal{E}/\mu B_0) - 1$ are constants of the motion. We define $\psi_\varphi \equiv cP_\varphi/Ze$. The orbit equation can be written as

$$v_\parallel / v_{\perp 0} = \pm(\lambda + \varepsilon\cos\vartheta)^{1/2} = (Ze/mcR_0 v_{\perp 0})(\psi - \psi_\varphi). \tag{1}$$

Let us introduce the dimensionless variables $\hat{r} \equiv r/\delta_p$, $\hat{\lambda} \equiv (R/\delta_p)\lambda$, $\hat{\psi} \equiv (2q_0/B\delta_p^2)\psi$, $\hat{\psi}_\varphi \equiv (2q_0/B\delta_p^2)\psi_\varphi$, where the characteristic potato width

$$\delta_p \equiv (2q_0 v_{\perp 0}/\Omega_0 R_0)^{1/3} R_0 \tag{2}$$

is defined here as a constant of the motion. For the sake of analytic progress, we shall assume that the fast ions are confined near the magnetic axis in a region of low magnetic shear, i.e. $(d\ln q / d\ln r) << 1$ for $r \leq \delta_p$. In this case, we can approximate $\hat{\psi} \approx \hat{r}^2$. Then, the orbit equation can be cast in the more compact form:

$$\pm(\hat{\lambda} + \hat{r}\cos\vartheta)^{1/2} = \hat{r}^2 - \hat{\psi}_\varphi. \tag{3}$$

The potato range is defined by the inequalities

$$\hat{\psi}_\varphi \leq 1, \qquad \hat{\lambda} \leq 1. \tag{4}$$

ORBIT CLASSIFICATION. A classification of the orbit types can be obtained by studying the intersections of the orbits with the poloidal midplane. Squaring Eq. (3), we are led to consider the real non-negative roots of the quartic polynomial

$$F(\hat{r}) = \hat{\lambda} \pm \hat{r} - (\hat{r}^2 - \hat{\psi}_\varphi)^2, \tag{5}$$

where the plus sign corresponds to intersections on the low field side ($\vartheta = 0$) and the minus sign corresponds to intersections on the high field side ($\vartheta = \pi$). The total number of intersections can be either 0, 2 or 4, corresponding to 0, 1 or 2 orbits. Limiting orbits correspond to the tangency of the straight lines $g_\pm(\hat{r}) = \hat{\lambda} \pm \hat{r}$ with the quartic $f(\hat{r}) = (\hat{r}^2 - \hat{\psi}_\varphi)^2$. Thus, the loci of these orbits in the $(\hat{\lambda}, \hat{\psi}_\varphi)$ plane are obtained from the solution of the system

$$\begin{cases} F = 0 \\ \partial F/\partial \hat{r} = 0 \end{cases} \Rightarrow \begin{cases} \hat{\lambda} = \mp\hat{r} + 1/16\hat{r}^2 \\ \hat{\psi}_\varphi = \hat{r}^2 \mp 1/4\hat{r} \end{cases} \tag{6}$$

Eliminating $\hat{r}$, we obtain two curves in the $(\hat{\lambda}, \hat{\psi}_\varphi)$ plane (Fig. 1). The curve obtained choosing the minus sign, $\lambda_-(\hat{\psi}_\varphi)$, corresponds to the locus of the counter-passing stagnation orbits. No orbits exist below this curve. The curve obtained choosing the plus sign has a cusp at $\hat{r} = 1/2 \Rightarrow \hat{\lambda} = \hat{\psi}_\varphi = 3/4$. Thus we can identify two branches: the lower branch, $\lambda_{-,l}(\hat{\psi}_\varphi)$ which corresponds to the locus of the pinch orbits, and the upper branch, $\lambda_{-,u}(\hat{\psi}_\varphi)$, which corresponds to the locus of the co-passing stagnation orbits. The cusp itself corresponds to a triple zero of F, i.e. to a pinch orbit where the inner loop degenerates to a point. The two branches together form the boundary between the one-orbit and the two-orbit regions of Fig. 1. Transitional orbits correspond to values of $\hat{\lambda}$ and $\hat{\psi}_\varphi$ such that the

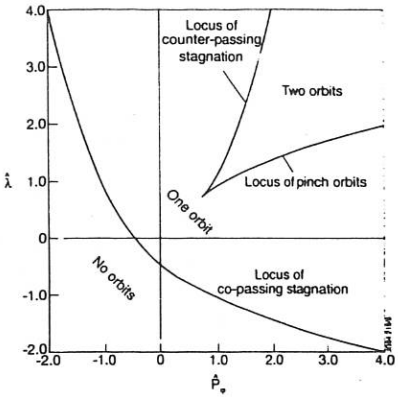


Figure 1

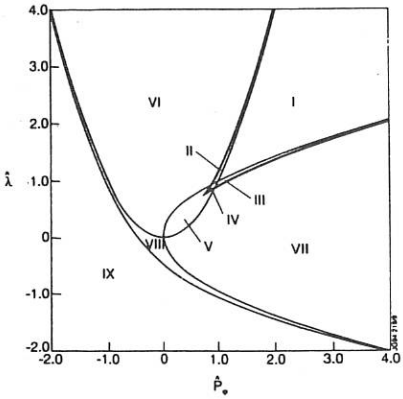


Figure 2

intersections between the curves $g_+(\hat{r})$ and $f(\hat{r})$ occur either at $\hat{r}=0$ (orbits tangent to the axis) or at $\hat{r}=\hat{r}_\varphi$ (marginally trapped orbits). Thus we are led to consider the two additional parabolic curves $\hat{\lambda}=\hat{\psi}_\varphi^2$ (locus of the orbits that are tangent to the magnetic axis) and $\hat{\lambda}=\left(\hat{\psi}_\varphi\right)^{1/2}$ for $\hat{\psi}_\varphi \geq 0$ (locus of the marginally trapped orbits). These two parabolas, in addition to the two curves of Fig. 1, give rise to eight regions in the $(\hat{\lambda},\hat{\psi}_\varphi)$ plane, corresponding to as many distinct topological orbit types, plus a ninth region where no orbits exist, as shown in Fig. 2. Limiting and transitional orbits can be found on the boundaries and corners among these regions. A complete orbit classification and representative examples are given in Table 1 and Figure 3.

TABLE 1: ORBITS IN REGIONS I-IX.

REGION	ORBITS	ORBIT TYPE(S)
I: $\hat{r}_\varphi < \hat{\lambda} < \hat{r}_\varphi^4$	two	-co-passing, encircling the axis -counter-passing, encircling the axis
II: $\max\{\hat{r}_\varphi,\hat{r}_\varphi^4\} < \hat{\lambda} < \hat{\lambda}_{+\infty}$	two	-co-passing, encircling the axis -counter-passing, high field side
III: $\hat{\lambda}_{+\nu} < \hat{\lambda} < \min\{\hat{r}_\varphi,\hat{r}_\varphi^4\}$	two	-mirror-trapped, encircling the axis -counter-passing, encircling the axis
IV: $\max\{\hat{\lambda}_{+\nu},\hat{r}_\varphi^4\} < \hat{\lambda} < \min\{\hat{r}_\varphi,\hat{\lambda}_{-\infty}\}$	two	-mirror-trapped, encircling the axis -counter-passing, high field side
V: $\hat{r}_\varphi^4 < \hat{\lambda} < \hat{r}_\varphi$ – IV	one	-mirror-trapped, encircling the axis
VI: $\hat{\lambda} > \max\{\hat{\lambda}_{+\infty},\hat{r}_\varphi,\hat{\psi}_\varphi^2\}$	one	-co-passing, encircling the axis
VII: $-\hat{r}_\varphi < \hat{\lambda} < \min\{\hat{r}_\varphi^4,\hat{\lambda}_{+\nu}\}$	one	-mirror-trapped, not encircling the axis
VIII: $\hat{\lambda}_- < \hat{\lambda} < \min\{\hat{\psi}_\varphi^2,\hat{r}_\varphi\}$	one	-co-passing, low field side
IX: $\hat{\lambda} < \hat{\lambda}_-$	no orbits	

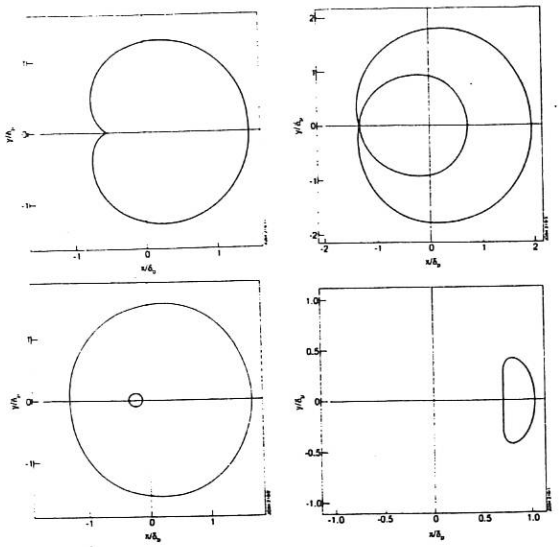


Fig. 3. Representative orbits: a) cusp orbit; b) pinch orbit; c) Pair of orbits in region II of Fig. 2, the inner orbit is close to the limiting counter-passing stagnation orbit; d) transitional orbit at the boundary between regions VII and VIII of Fig 2 (marginally trapped, not encircling the axis).

SLOWING-DOWN CHARACTERISTICS. In the high energy limit, only the collisional drag by the thermal electrons is important. The bounce-averaged Fokker-Plank equation for the fast ion distribution function, f_0, has the form

$$\frac{\partial f_0}{\partial t} = \left\langle \frac{1}{\tau_s} \right\rangle \frac{1}{v^2} \frac{\partial}{\partial v}\left(v^3 f_0\right) + \left\langle \frac{P_\varphi - Ze\psi/c}{\tau_s} \right\rangle \frac{\partial f_0}{\partial P_\varphi} + \langle S \rangle, \tag{7}$$

where angle brackets denote bounce averaging, τ_s is the slowing-down time and S is the fast ion source term. Using the variables $\hat{\psi}_\varphi, \hat{\lambda}$, assuming $\tau_s \approx$ const, and introducing the normalized time $\hat{t} \equiv t/\tau_s$, we obtain

$$\frac{dF}{d\hat{t}} = \frac{\partial F}{\partial \hat{t}} + \frac{2}{3}\hat{\lambda}\frac{\partial F}{\partial \hat{\lambda}} + \left[g(\hat{\psi}_\varphi, \hat{\lambda}; \sigma) + \frac{4}{3}\hat{\psi}_\varphi \right] \frac{\partial F}{\partial \hat{\psi}_\varphi} = \tau_s \langle S \rangle, \tag{8}$$

where $F \equiv v^3 f_0$ and the function $g(\hat{\psi}_\varphi, \hat{\lambda}; \sigma) \equiv \langle \hat{\psi} - \hat{\psi}_\varphi \rangle$, which is proportional to the fast ion toroidal

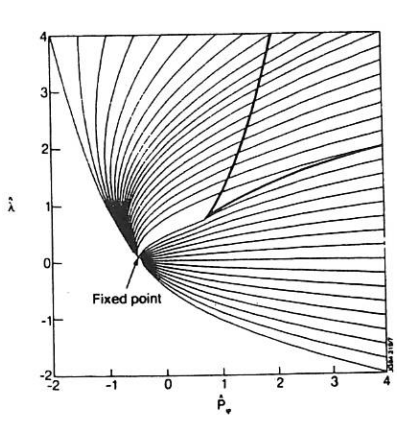


Figure 4

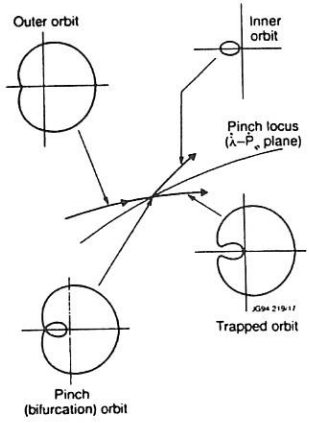


Figure 5

precession frequency, can be expressed in terms of elliptic integrals. The characteristic equations are

$$\frac{d\hat{\psi}_*}{d\hat{t}} = g\left(\hat{\psi}_*, \hat{\lambda}; \sigma\right) + \frac{4\hat{\psi}_*}{3}, \qquad \frac{d\hat{\lambda}}{d\hat{t}} = \frac{2\hat{\lambda}}{3} \tag{9}$$

Analysis of this system reveals the existence of an unstable fixed point at

$$\hat{\lambda}_f = 0, \qquad \hat{\psi}_{*f} = -3(16)^{-1/3} \approx -0.47 \tag{10}$$

The characteristic curves in the $(\hat{\lambda}, \hat{\psi}_*)$ plane can be thought of as originating from this fixed point at $\hat{t} \to -\infty$, as shown in Fig. 4. Some of these curves intersect the pinch locus. At this time, a bifurcation occurs, as represented by the diagram of Fig. 5. Part of the orbits will become trapped (region VII of Fig. 2), while the remaining orbits will become counter-passing (regions I-III). The characteristic curves of the latter orbits are shown in Fig. 6. In order to assign a probability of transition to either of the two branches of the bifurcation diagram, the basins of attraction need to be studied.

The loci of co- and counter-passing stagnation orbits are mapped onto themselves during the slowing-down evolution. A significant inward radial transport has been found for those high energy ions that initially do not encircle the axis. An example is shown in Fig. 7a. Note that, as the particle loses energy, its orbit must eventually become a standard one. Therefore, particles that initially do not encircle the axis, either move onto the axis and then become a passing orbit, as in the case of Fig. 7a, or move a finite distance toward the axis and then become a standard banana orbit, as in the example of Fig. 7b.

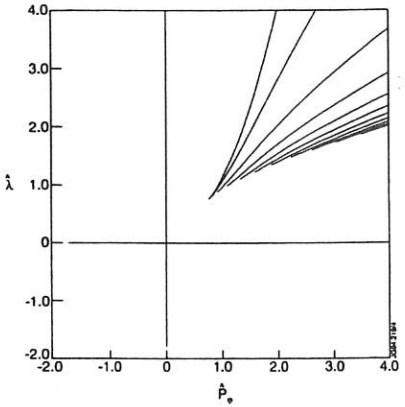


Figure 6

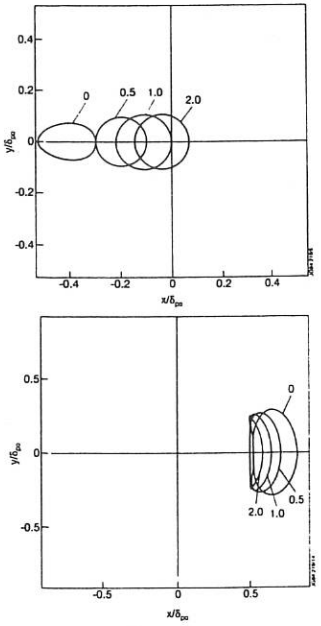


Figure 7

CONCLUSIONS. We have presented an analysis of nonstandard guiding centre orbits, which is relevant to MeV ions in a Tokamak. The orbit equation has been simplified from the start, so to enable us to present an analytic classification of the possible orbits. We have described the topological transitions of the orbits during collisional slowing down. In particular, the characteristic equations reveal the existence of a single fixed point in the relevant phase plane, and the presence of a bifurcation curve corresponding to the locus of the pinch orbits. A significant particle inward pinch has been discovered.

A MECHANISM FOR BEAM–DRIVEN EXCITATION OF ION CYCLOTRON HARMONIC WAVES IN TFTR

K. G. McClements, R. O. Dendy and C. N. Lashmore–Davies

UKAEA Government Division, Fusion, Culham, Abingdon, Oxfordshire, OX14 3DB, UK (Euratom/UKAEA Fusion Association)

R. Majeski and S. Cauffman

Princeton Plasma Physics Laboratory, Princeton University, Princeton NJ 08543, U.S.A.

1 Introduction

Observations from deuterium and tritium neutral beam–heated discharges in TFTR [1,2] indicate that ion cyclotron emission (ICE) can be driven by injected beam ions as well as by fusion products. Spectra obtained with edge–mounted probes located approximately in the vertical plane of the magnetic axis sometimes display peaks whose frequencies correspond to multiple cyclotron harmonics $\ell\Omega_b$ of the injected beam species at the outer mid–plane edge: examples are shown in Figs.1 and 2. Once the emission mechanism for ICE has been identified, observed spectral properties can be used to infer values for the parameters describing the energetic ion velocity distribution, as was done for the case of fusion–product–driven ICE from JET [3–6]. We outline here a candidate mechanism for the injected beam–driven component of ICE in TFTR.

2 Stability of Beam Ion Distributions

We adopt the following model for the normalized beam ion distribution:

$$f_b = \frac{1}{2\pi^{3/2} u v_r} \exp\left(-\frac{(v_\parallel - v_d)^2}{v_r^2}\right) \delta(v_\perp - u), \tag{1}$$

where $v_\parallel$, $v_\perp$ are parallel and perpendicular velocity components, and u, v_d, v_r define respectively the perpendicular speed, average beam speed, and parallel velocity spread of the beam: u is much smaller than the Alfvén speed, and so wave–particle interactions involving the electromagnetic fast Alfvén wave [6] are not relevant. We therefore concentrate on the excitation of electrostatic modes, whose dispersion relation is

$$\sum_s \frac{\omega_{ps}^2}{k^2} \sum_{\ell=-\infty}^{\infty} \int d^3v \frac{J_\ell^2(k_\perp v_\perp/\Omega_s)}{k_\parallel v_\parallel + \ell\Omega_s - \omega} \left[\frac{\ell\Omega_s}{v_\perp}\frac{\partial f_s}{\partial v_\perp} + k_\parallel \frac{\partial f_s}{\partial v_\parallel}\right] = 1, \tag{2}$$

where particle species are labelled by s, plasma and cyclotron frequencies are denoted by ω_p and Ω respectively, ω is the wave frequency, $\mathbf{k} = (k_\perp, 0, k_\parallel)$ is the wavevector, and J_ℓ denotes the Bessel function of order ℓ. Evaluating the integrals in Eq.(2) gives

$$-\frac{\omega_{pe}^2}{\Omega_e^2}\frac{k_\perp^2}{k^2} - 2\frac{\omega_{pe}^2}{k^2 v_e^2}\left[1+\nu_0 Z(\nu_0)\right] - \frac{\omega_{pi}^2}{\Omega_i^2}\frac{k_\perp^2}{k^2}\sum_{n=-\infty}^{\infty}\frac{e^{-z_i^2} I_n}{z_i^2}\left[1+\zeta_0 Z(\zeta_n)\right]$$

$$-\frac{\omega_{pb}^2}{\Omega_b^2}\sum_{\ell=-\infty}^{\infty}\left[\frac{\ell\Omega_b}{k_\parallel v_r}\frac{k_\perp^2}{k^2}Z(\eta_\ell)\frac{1}{z_b}\frac{dJ_\ell^2}{dz_b} + \frac{2\Omega_b^2}{k^2 v_r^2}\left[1+\eta_\ell Z(\eta_\ell)\right]J_\ell^2\right] = 1. \qquad (3)$$

Electrons and bulk ions are denoted by e and i. I_n is the modified Bessel function of order n, with argument $z_i^2 = k_\perp^2 v_i^2/2\Omega_i^2$, v_i being the bulk ion thermal speed. The argument of J_ℓ is $z_b = k_\perp u/\Omega_b$. The plasma dispersion function Z has arguments $\nu_0 = \omega/k_\parallel v_e$ (v_e the electron thermal speed), $\zeta_n = (\omega - n\Omega_i)/k_\parallel v_i$ and $\eta_\ell = (\omega - k_\parallel v_d - \ell\Omega_b)/k_\parallel v_r$. Solutions of Eq. (3) for ω/Ω_α as a function of z_b and $\theta \equiv \cos^{-1} k_\parallel/k$ depend on seven dimensionless parameters: the ratio of ion beam number density to total ion number density, ξ; the ratio of the Alfvén speed to the speed of light, c_A/c; the bulk ion plasma beta, $\beta_i \equiv (1-\xi)v_i^2/c_A^2$; u/c_A; v_d/u; v_r/u; and the electron–ion temperature ratio, T_e/T_i. Appropriate values for c/c_A, β_i and T_e/T_i are 15, 10^{-3} and 0.5.

We consider a high power beam of deuterium atoms, injected with energies of 120 keV at 45° to the magnetic field in the edge plasma, so that $v_d/u = 1$ and $u/c_A \simeq 0.12$, and set $\xi = 0.01$ and $v_r/u = 0.01$. Eq.(3) yields instability for values of θ lying close to (but not equal to) 90°: waves with $\theta < 86°$ are strongly damped. Fig.2 shows the growth rate γ as a function of real frequency ω for cyclotron harmonics up to $\ell = 10$: only positive values of γ are shown. For each harmonic, there is a narrow band of frequencies, lying slightly above $\ell\Omega_b$, at which instability occurs. A similar instability occurs when 120 keV tritons are injected into the TFTR edge plasma (Fig.4). The trend apparent in Fig.3, of γ increasing uniformly with harmonic number, is not as clear-cut in Fig.4: the growth rates at $\omega \simeq 3\Omega_b$ and $\omega \simeq 6\Omega_b$, in particular, are comparatively low.

In the rest frame of the beam ion guiding centres, the real frequencies of the unstable modes lie very close to Ω_b and its harmonics. Putting $v_e = v_r = 0$ in Eq. (3) reveals a beam–driven instability with $\omega \simeq k_\parallel v_d + \ell\Omega_b$ and maximum growth rate [2]

$$\gamma = \Omega_b \frac{\omega_{pb}}{\omega_{pi}}\cot\theta\, J_{\ell,m}\left[\frac{\Omega_b^2}{\Omega_i^2}\sum_{n=-\infty}^{\infty}\frac{n e^{-z_i^2} I_n}{z_i^2}\frac{\Omega_i}{\ell\Omega_b + k_\parallel v_d - n\Omega_i} + \frac{\omega_{pe}^2}{\omega_{pi}^2}\frac{\Omega_b^2\cot^2\theta}{(\ell\Omega_b + k_\parallel v_d)^2}\right]^{-1/2}, \qquad (4)$$

where $J_{\ell,m}$ is the first maximum of $J_\ell(z_b)$. These waves are distinct from the Bernstein modes associated with the bulk ions: they cease to exist when the beam terms in Eq.(3) are zero. For deuteron beam ions (Fig.3), the unstable frequencies are slightly greater than $n\Omega_i$, and so the bulk ion cyclotron resonance term in Eq.(4) reduces γ. In the tritium beam case (Fig.4), this reduction only occurs at every third harmonic, since $3\Omega_b = 2\Omega_i$. Degeneracy of deuteron and triton cyclotron harmonics may account for the fact that, in some ICE spectra obtained during tritium beam–heated discharges, the third and sixth harmonics are observed to be less intense than other low harmonics (Fig.2).

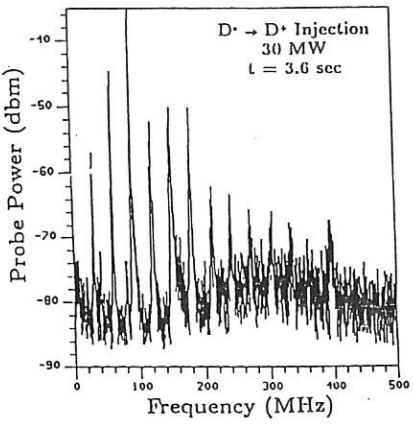


Fig. 1. ICE spectrum obtained during 30 MW deuterium neutral beam injection in TFTR [1].

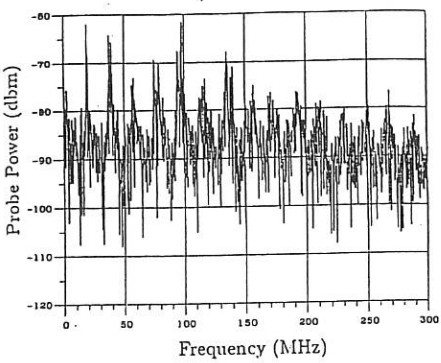


Fig. 2. ICE spectrum obtained during tritium neutral beam injection in TFTR (shot number 73273).

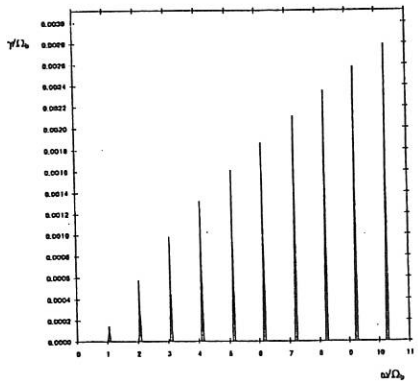


Fig. 3. Growth rate of cyclotron harmonic waves as a function of ω_r for the case of deuterium beam and bulk ions. The plasma parameters are: $c/c_A = 15$, $T_e/T_i = 0.5$, $\beta_i = 10^{-3}$, $\xi = 0.01$, $u/c_A = 0.12$, $v_r/u = 10^{-2}$, and $v_d/u = 1$. The wave propagation angle is 88.5°.

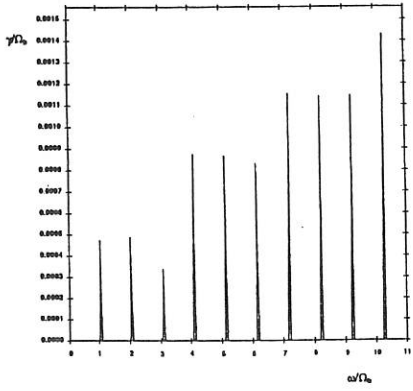


Fig. 4. As Fig. 2 except that the beam ions are tritons and $u/c_A = 0.1$.

3 Discussion and Conclusions

An important question is how narrow in velocity space the beam distribution must be for instability. In our model the lower harmonics are the first to be stabilized when v_r/u is increased or ξ is reduced. Instability is observed at $\omega \simeq \Omega_b$ in deuterium beam–heated discharges. To account for this, our model requires either high ξ or small v_r/u. As the beam penetrates the plasma, both ξ and v_r/u will increase, but eventually the beam thermal spread will suppress instability. The sensitivity of γ to v_r/u may account for the observation that beam–driven ICE in TFTR originates from the outer mid–plane edge.

Because the Doppler–shifted frequency lies close to $\ell\Omega_b$ over a broad range of values of $k_\perp$, the group velocity $v_{g\perp} \equiv \partial\omega/\partial k_\perp$ is very small: typically three orders of magnitude smaller than c_A. The model requires that waves remain in cyclotron resonance with beam ions for long enough to be amplified to the observed levels, which can be as high as 50 dbm above the noise (cf. Fig.1). In the present case, $v_{g\perp}$ is so small that 50 dbm amplification can be achieved over a distance of about 10 cm. Since, in the midplane, the total magnetic field B is approximately constant in the poloidal direction, a poloidally–propagating wave packet can remain in resonance over the required distances. On the other hand, the inverse linear dependence of B on major radius implies that radially–propagating waves will not remain in cyclotron resonance for long enough to undergo 50 dbm amplification.

We conclude that the excitation of ICE at beam ion cyclotron harmonics in deuterium neutral–beam–heated TFTR discharges may be due to an instability which requires a narrow velocity–space distribution for the beam ions. The presence of such distributions close to the injection point may account for the localization of the observed signal to the outer mid–plane. In the case of tritium beam injection, cyclotron resonance with the bulk ions may account for the fact that the third and sixth cyclotron harmonics are observed to be less intense than other low harmonics. The low group velocity of the waves perpendicular to the magnetic field implies that amplification to the observed levels can easily occur within the outer midplane.

Acknowledgements

This work was funded jointly by the UK Department of Trade and Industry and Euratom. We are grateful to T. J. Martin for providing us with a zero finding code, and to W. G. F. Core, G. A. Cottrell, M. Cox, D. Darrow, M. O'Brien, C. M. Roach, M. Von Hellermann and S. Zweben for helpful discussions.

References

[1] G. J. Greene and the TFTR Team, EPS 1990, ECA 14B 4, 1540 (1990).
[2] R. O. Dendy, K. G. McClements, C. N. Lashmore–Davies, R. Majeski, and S. Cauffman, Phys. Plasmas, submitted (1994).
[3] G. A. Cottrell and R. O. Dendy, Phys. Rev. Lett. 60, 33 (1988).
[4] R. O. Dendy, C. N. Lashmore–Davies and K. F. Kam, Phys. Fluids B 4, 3996 (1992).
[5] G. A. Cottrell et al., Nucl. Fusion 33, 1365 (1993).
[6] R. O. Dendy, C. N. Lashmore–Davies, K. G. McClements, and G. A. Cottrell, Phys. Plasmas 1, 1918 (1994).

Max-Planck-Institut für Plasmaphysik
- Bibliothek -

Current driven non-Maxwellian plasmas

M. G. Haines
Blackett Laboratory, Imperial College London SW7 2BZ, UK

Abstract

Linear transport theory assumes infinitesimally small electric fields, current densities, heat fluxes and spatial gradients. Any finite transport leads to a corresponding departure of the lowest order isotropic distribution function from a Maxwellian. The Fokker-Planck equation is considered in its tensor expansion form, $f = f_0 + \underline{f}_1 . \underline{v}/|\underline{v}| + \ldots$ and applied to the case of a current driven by an electric field. The various conditions when $|f_1| \geq f_m$; or when the heating exceeds the down-scattering; or when the Dreicer runaway occurs are derived. A simplified case is solved analytically showing that the departure from a Maxwellian occurs first in a v^5 term in a Taylor expansion of f_0. Application to the DIII-D tokamak shows that "non-linear neoclassical transport" might well explain the inward electron heat flux when electron cyclotron heating (ECH) is applied off-axis; essentially the trapped component of the heated electrons convect inwards by the Ware pinch. In absence of a toroidal electric field their suprathermal energy would be lost by down-scattering to cold electrons and to ions, but in the presence of the parallel electric field the suprathermal electrons can retain or even increase their energy. The trapped component of the isotropic energetic group carries the inward heat flux. A more complete Fokker-Planck model with equipartition and bremsstrahlung is discussed.

Introduction

This work is inspired by the intriguing experimental results on the DIII-D tokamak in which ECH is absorbed half-way between the minor axis and the wall, yet electron temperature profiles are strongly peaked on the minor axis [1,2]. Indeed the electron temperature on axis is 1.7keV and only 0.6keV at the position of ECH deposition. It therefore appears that heat actually flows *up* the temperature gradient, a phenomenon inconsistent with a simple diffusive model of heat flow. Any explanation of this must of course be consistent with the Second Law of Thermodynamics; indeed the *local* generation of entropy must be positive. We will see that if $\underline{q}.\nabla T/T^2$ is positive there must be a larger positive contribution from the $\underline{J}.\underline{E}/T$ contribution and also from the equilibriation (arising from electron-electron and electron-ion collisions) and this thermodynamic reasoning gives us the correct insight into the physics at work here.

In an analogous recent study [3,4] the combined effects of the Ettinghausen and Nernst effects in a Z-pinch showed in a one dimensional simulation that the inward heat flow in the direction of $\underline{J} \times \underline{B}$ in combination with the inward convection of magnetic flux by the heat flux [5,6,7](or by the temperature gradient) drastically reduces the high surface temperature

and current density and leads to a slight peaking of electron temperature on axis. However this is based on linear transport, though in an example applied to laser fusion this off-diagonal transport is also very effective in non-linear transport [8,9].

To complete the background to this study let us examine what *linear* neoclassical transport[10] would give. The total inward electron energy flux is $\left(Q_e + \frac{5}{2}\Gamma T_e\right)$ where Q_e is the electron heat flux and Γ is the particle flux. In a quasi-steady state in which there is no net inward particle flux we find that Q_e has contributions that are outwards both for a negative value of $\partial T_e/\partial\Gamma$ and for the E_ϕ contribution. (The sign of the latter term is perhaps surprising and was noted by Balescu [11], but it can be explained because in the inward Ware pinch of trapped particles [12] their energy is not increased by a simple gas compression law; indeed their magnetic moment is conserved in absence of collisions and so a heat flux must be subtracted from their inward enthalpy flux to reflect this condition.) The only large inward contribution to heat flux arises in the $\partial n/\partial r$ term and, for $\Gamma = 0$, the condition that Q_e is negative is that

$$-\frac{1}{n}\frac{\partial n}{\partial r} > 1.13\left(-\frac{1}{T_e}\frac{\partial T_e}{\partial r}\right) \qquad (1)$$

for $T_e = T_i$, the numerical factor increasing to 2.05 if $T_i << T_e$. Such a peaking of electron density is not observed. Another effect must be considered.

If we assume that in the region of ECH heating there is a substantial population of suprathermal electrons created, the trapped component of these will drift inwards with a convection time τ_c given by

$$\tau_c = r_1\frac{B_\theta}{E_\phi} \qquad (2)$$

where B_θ is the poloidal magnetic field and r_1 is the distance to the minor axis. The effective time τ_e for a hot electron to lose energy by electron-electron collisions is

$$\tau_e = 0.51\frac{m_e}{n_e e^2}\frac{J_\phi}{E_\phi}\left(\frac{v}{v_T}\right)^3 \qquad (3)$$

where $v_T^2 = T_e/m_e$ and trapped particle and other effects in Ohm's law are neglected. Using $B_\theta = \frac{1}{2}\mu_0 r_1 J_\phi$ we obtain the ratio

$$\frac{\tau_c}{\tau_e} = \frac{\omega_{pe}^2}{c^2}r_1^2\left(\frac{v_T}{v}\right)^3 \qquad (4)$$

For DIII-D parameters, $n = 2.2 \times 10^{19}m^{-3}$, $r_1 = 0.34m$, $T_e = 0.5$ keV, we find that τ_c is equal to τ_e only for 1 MeV electrons. Fokker-Planck simulations [13] show that there is a negligible number of electrons with energy above 50 keV. Therefore there is no enhanced inward heat flux by suprathermal electrons unless their energy is maintained or increased. This effect is considered next.

Fokker-Planck expansion and estimates

Taking the tensor expansion of the Fokker-Planck equation [14,15] and limiting our attention to f_0 and $\underline{f}_1$ we write, where $\underline{f}_1$ is replaced by the ϕ component only, f_ϕ

$$\frac{\partial f_\varphi}{\partial t} = \frac{e}{m} E_\varphi \frac{\partial f_0}{\partial v} - \nu_0 f_\phi \frac{v_T^3}{v^3} + C_{ee\phi} \tag{5}$$

For a Maxwellian lowest order isotropic component, ie.

$$f_0 = f_m = a_0 \exp\left(-v^2/v_T^2\right) \tag{6}$$

the condition that $|f_\phi| > f_m$ is

$$\frac{v}{v_T} > \left(\frac{v_T}{v_d}\right)^{1/4} \tag{7}$$

where the effective drift velocity v_d taking into account trapped electrons is given by

$$E_\varphi = \frac{m_e \nu_0}{e} v_d \Big/ \left[1 - 1.95(r/R)^{1/2}\right] \tag{8}$$

The well known Dreicer condition [16] for the runaway electrons is given by the condition

$$\frac{v}{v_T} > \left(\frac{v_T}{v_d}\right)^{1/2} \tag{9}$$

for the unlimited acceleration of electrons.

The effect of f_ϕ on f_0 is given by (10)

$$\frac{\partial f_0}{\partial t} - \frac{1}{3v^2}\frac{\partial}{\partial v}\left(v^2 \frac{e}{m} E_\varphi f_\varphi\right) = \frac{\nu_{ee}}{n_e} v \frac{\partial}{\partial v}\left[f_0 4\pi \int_0^v f_0 v^2 dv + \frac{v}{3}\left\{\frac{4\pi}{v^2}\int_0^v f_0 v^4 dv + 4\pi v \int_v^\infty f_0 v dv\right\}\frac{\partial f_0}{\partial v}\right]$$

where the RHS represents electron-electron collisions with $\nu_{ee} = \nu_{eeT} v_T^3/v^3$. If we take this term to be of order $\nu_{eeT}\frac{v_T^3}{v^2}\frac{\partial f_0}{\partial v}$ we arrive at the condition which Dreicer also found for the isotropic velocity of electrons above which Joule heating exceeds the down-scatter by electron-electron collisions,

$$\frac{v}{v_T} > \left(\frac{v_T}{v_d}\right)^{1/3} \tag{11}$$

We note that this is intermediate to conditions (7) and (9).

For a tokamak we find that

$$\frac{v_T}{v_d} = \frac{\mu_0 R q n e \nu_T}{B\phi}\left[1 - 1.95(r/R)^{1/2}\right] \tag{12}$$

and typically for DIII-D has a value of 8. Therefore for electron velocities of $1.68v_T$ there is a strong departure of f_0 from Maxwellian and if above $2v_T$ there will be enhancement of the random energy. This is just the velocity group most effective in heat flow as is well known in finding the non-linear classical heat flux in laser fusion [17].

If this is translated into an estimate of the inward heat flux we find that for DIII-D E_ϕ/B_θ, taking into account trapped particle effects, is 4.6m/s and an inward heat flow of $10^3 Wm^{-3}$ (which is the experimentally estimated value) would require an additional non-linear increase in the advected trapped particle energy density of 7%. The fraction of electrons with a suprathermal component is of order $\exp(-1.68^2)$ which is 6%. These estimates appear to give a plausible explanation of the inward heat flux.

Fokker-Planck solution

We consider the non-linear Fokker-Planck equation in the steady state in which the effect of E_ϕ on f_ϕ leads to a non-Maxwellian f_0. Specifically, neglecting the electron-electron collisions on f_ϕ, $C_{ee\phi}$, eq.(5) is substituted into eq.(10). On integrating with respect to v, in dimensionless form we have

$$-\frac{A}{3}V^5\frac{\partial F_0}{\partial V} = F_0\int_0^V F_0V^2dV + \frac{V}{3}\left\{\frac{1}{V^2}\int_0^V F_0V^4dV + V\int_V^\infty F_0VdV\right\}\frac{\partial F_0}{\partial V} \qquad (13)$$

where

$$A = \left(\frac{eE_\varphi}{m}\right)^2\frac{1}{\nu_{eio}\nu_{eeo}v_T^2} \qquad (14)$$

$$F_0 = \frac{4\pi v_T^3}{n_e}f_0 \quad \text{and} \quad V = \frac{v}{v_T} \qquad (15)$$

The parameter $A\left(=v_d^2/v_T^2\right)$ is the driving term for causing F_0 to be non-Maxwellian.

A series solution $F_0 = \sum_{n=0}^{\infty} a_nV^n$ is employed and reproduces a Maxwellian exp(-V^2) up to V^5 when a new term, specifically $a_5 = 0.8A$ appears. (There appears to be no connection to the Langdon effect.) Expansion up to V^{12} has been carried out and is relatively simple. However we estimate that about 40 terms will be required. More important an energy sink is required for this Joule heating, and recently terms in equipartition to the ions and bremsstrahlung have been introduced. The former indicate the strong coupling of cold electrons to the ions, but the suprathermal group is relatively unaffected. The energy flow channel is therefore into the suprathermals from E_ϕ, through to colder electrons by electron-electron collisions and then to ions. It is expected that within a few months this analytic technique of solving the non-linear Fokker-Planck equation will confirm the estimates of the previous section.

References

[1] C. C. Petty et al.
Eur. Conf. on Controlled Fusion & Plasma Physics, Vol 1, 241 (1990)
[2] T. C. Luce, C. C. Petty & J. C. M. de Haas, *Phys. Rev. Lett.* 68, 52 (1991)
[3] M. G. Haines & J. P. Chittenden
1992 Int. Conf. on Plasma Physics, Innsbruck, Vol 1, 655 (1992)
[4] J. P. Chittenden & M. G. Haines, *J. Phys. D: Appl. Phys*, 26, 1048 (1993)
[5] A. Nishigushi et al., *Phys. Rev. Lett.* 53, 262 (1984)
[6] A. Nishigushi, T. Yabe & M. G. Haines, *Phys. Fluids* 28, 3683 (1985)
[7] M. G. Haines, *Plasma Phys. & Controlled Fusion* 28, 1705 (1986)
[8] T. H. Kho & M. G. Haines, *Phys. Rev. Lett.* 55, 825 (1985)
[9] T. H. Kho & M. G. Haines, *Phys. Fluids* 29, 2665 (1986)
[10] M. N. Rosenbluth, R. D. Hazeltine & F. L. Hilton, *Phys. Fluids* 15, 116 (1972)
[11] R. Balescu, *Transport Processes in Plasmas*, (Elsevier, Amsterdam, 1988) Vol 2
[12] A. A. Ware, *Phys. Rev. Lett.* 25, 916 (1970)
[13] M. O'Brien, private communication
[14] T. W. Johnston, *Phys. Rev.* 120, 1103 (1960)
[15] I. P. Shkarovsky, *Can. J. Phys.* 41, 1753 (1963)
[16] H. Dreicer, *Phys. Rev.* 117, 329 (1960)
[17] A. R. Bell, R. G. Evans & D. J. Nicholas, *Phys. Rev. Lett.* 46, 243 (1981)

DIRECT EMISSION IN THE ION CYCLOTRON RANGE OF FREQUENCY

D. Fraboulet, A. Bécoulet, B. Saoutic.
Association EURATOM-CEA sur la Fusion Contrôlée
C.E. Cadarache, 13108 St Paul-lez-Durance cedex, FRANCE

G. Pelletier
Laboratoire d'Astrophysique de l'Observatoire,
Domaine Universitaire de St Martin d'Hères,
BP53X, 38041 Grenoble cedex, FRANCE

C. Thomas
Oak Ridge National Laboratory, P.O.Box 2009, Oak Ridge, USA

A diagnostic of the fast alpha particle content is of major importance in a tokamak reactor to monitor the fusion reactivity. Among the various methods, the measurement of the direct cyclotron emission, if possible, appears to be one of the simplest. The paper first presents a theoretical approach of the direct emission of the fast magnetosonic wave in the ion cyclotron range of frequency (~10-500 MHz). The radiated spectra are then computed in several situations, and the role of the various parameters is discussed.

I. The energy transport model

The model solves the continuity equation which governs the behaviour of $N^\sigma(\omega, \mathbf{x}, t)$, the *occupation number* of the mode σ, at the location $\mathbf{x}$, at the time t, and for the frequency ω. The label σ characterises a given solution of the WKB dispersion equation $\Lambda(\mathbf{k}, \omega, \mathbf{x}, t) = 0$, so that a single-valued relationship exists between the wave vector $\mathbf{k}^\sigma$ and the position $\mathbf{x}$, for a given frequency ω. The continuity equation reads:

$$\frac{\partial N^\sigma}{\partial t} + \nabla(\mathbf{v}_g{}^\sigma N^\sigma) = \mathcal{E}^\sigma + \mathcal{A}^\sigma + \sum_{\sigma'} \mathcal{C}^{\sigma\sigma'} \qquad (1)$$

where $\mathbf{v}_g{}^\sigma(\omega, \mathbf{x}, t)$ is the group velocity of the mode, $\mathcal{E}^\sigma$ accounts for the emission on σ, $\mathcal{A}^\sigma$ for the absorption and $\mathcal{C}^{\sigma\sigma'}$ for the possible mode conversion between σ and σ'. Note that the energy locally (in $\mathbf{k}$ and/or in $\mathbf{x}$) contained in σ is $N^\sigma \hbar\omega$.

The expression of $\mathcal{A}^\sigma$ could in principle be derived from the dielectric tensor $\mathbb{K}$. However, due to necessary approximations (Larmor radius expansion, aspect ratio expansion, Maxwellian distribution functions...) the self-consistency existing between the elementary absorption-emission processes is extremely difficult to insure. One can alleviate this difficulty with proper quantum mechanics considerations. In fact, eq.1 derives from a master equation[1] accounting for spontaneous emission, absorption and stimulated emission. Each process appears through a probability of transition between an initial ($\mathbf{p}$) and a final ($\mathbf{p}'=\mathbf{p}\pm\Delta\mathbf{p}$) quantum state of a test particle interacting with the mode σ. Resulting from the existence of the Einstein relations, the three probabilities of transition are equal. This is closely linked to the possible existence of an equilibrium state, the so-called "black body". Performing a statistical treatment for each plasma species (labelled s), in the presence of a magnetic field and for the classical limit $\hbar \to 0$, $\mathcal{E}^\sigma$ and $\mathcal{A}^\sigma$ read:

$$\mathcal{E}^{\sigma}(\omega,\mathbf{x},t) = \sum_{s}\int d\mathbf{p}\; w_{\mathcal{G}}\, f_s \qquad (2)$$

$$\mathcal{A}^{\sigma}(\omega,\mathbf{x},t)=N^{\sigma}\sum_{s}\int d\mathbf{p}\; w_{\mathcal{G}}\left(\hbar\frac{(\omega-k_{//}v_{//})}{v_{\perp}}\frac{\partial f_s}{\partial p_{\perp}}+\hbar k_{//}\frac{\partial f_s}{\partial p_{//}}\right)=N^{\sigma}\,\mathcal{B}^{\sigma} \qquad (3)$$

where $f_s(\mathbf{p},\mathbf{x},t)$ is the distribution function of the species s which depends on the particle phase space variables $(\mathbf{p},\mathbf{x})$ and on time. $w_{\mathcal{G}}(\mathbf{p},\mathbf{k}^{\sigma}(\mathbf{x}),t)$ is the transition probability per unit time and $\mathbf{k}$ of, say, the spontaneous emission process. The projections // and $\perp$ refer to the confinement magnetic field. Note that $\mathcal{A}^{\sigma}$ accounts for both absorption and stimulated emission (the so-called "net absorption") and is thus proportional to N^{σ}. The conversion term $\mathcal{C}^{\sigma\sigma'}$ couples the evolution equations of different modes. In the present paper, we deal with a given mode (here the fast wave) and carefully avoid any conversion process (on Alfvén resonances, ion-ion hybrid layers, Bernstein waves, ...).

The spontaneous emission probability density per unit time $w_{\mathcal{G}}$ is directly the emitted power density P^{σ} divided by the elementary energy $\hbar\omega$. P^{σ} is evaluated with the particle current $\mathbf{j}_{part}$ and the field amplitude $\mathbf{E}$ through:

$$P^{\sigma}(\mathbf{p},\mathbf{k}^{\sigma}(\mathbf{x}),t) = -\,\mathbf{j}_{part}(\mathbf{p},\mathbf{x},t)\;.\;\mathbf{E}^{*}(\mathbf{k}^{\sigma}(\mathbf{x}),t) \qquad (4)$$

The field amplitude in (4) is linked to $\mathbf{j}_{part}$ through the propagation equation:

$$\mathbf{L}\mathbf{E} = \frac{c^2}{\omega^2}\mathbf{k}\times(\mathbf{k}\times\mathbf{E}) + \mathbf{K}^{h}\mathbf{E} = -\,i\,/(\varepsilon_0\,\omega)\,\mathbf{j}_{part} - \mathbf{K}^{a}\mathbf{E} \qquad (5)$$

where the dielectric tensor is splitted in hermitic $\mathbf{K}^{h}$ and antihermitic $\mathbf{K}^{a}$ contributions and where $\mathbf{K}^{\hat{a}}$, which represents the absorption, is neglected. One then obtains([1]):

$$w_{\mathcal{G}}(\mathbf{p},\mathbf{k}^{\sigma},\mathbf{x},t) = \frac{2\pi q_s^2}{\hbar\omega\varepsilon_0}\frac{tr\lambda}{\omega(\partial\Lambda/\partial\omega)}\sum_{n=-\infty}^{\infty}|\mathbf{e}_{\sigma}^{*}.\mathbf{V}(n)|^2\,\delta(\omega-k_{//}v_{//}+n\omega_{cs}) \qquad (6)$$

where q_s is the charge of the species s, ω_{cs} its gyrofrequency, $tr\lambda$ the trace of transposed matrix of the cofactors of $\mathbf{L}$, $\mathbf{e}_{\sigma}$ the polarisation vector of the mode σ. Moreover,

$$\mathbf{V}(n)=\left[\; v_{\perp}\frac{n}{u}J_n\;,\; -iv_{\perp}J_n'\;,\; v_{//}J_n\;\right] \qquad (7)$$

where $u=k_{\perp}v_{\perp}/\omega_{cs}$, and J_n represents the Bessel function of order n and argument u. Finally, note that the group velocity is computed from the dispersion equation $\Lambda(\mathbf{k},\omega,\mathbf{x},t) = \det(\mathbf{L}) = 0$, which is itself derived from the hermitic part of (5), also neglecting $\mathbf{j}_{part}$.

II. Direct emission of the fast magnetosonic wave

The equation (1) is now solved for the fast magnetosonic wave, emitted and absorbed by tokamak plasma particles, in the 10-500 MHz range. The present description allows a clear disconnection between the wave propagation and the source terms. In fact, the propagation equation is solved using the cold plasma dielectric tensor, in order to derive the local values of the group velocity, the polarisation vector, the wave vector $\mathbf{k}^{\sigma}$, $tr\lambda$ and $\partial\Lambda/\partial\omega$, i.e. of all the propagation characteristics. Note that a hot tensor description would simply yield corrections on the former values, and allow new mode conversions. On the opposite, the particle kinetics $\mathbf{V}(n)$ is computed exactly for the required set of the cyclotron harmonics n.

An axisymmetrical one-dimensional tokamak plasma ($-a\le x\le a$), with proper magnetic field, density and temperature profiles is studied. The

large aspect ratio limit is assumed, so that the parallel and toroidal directions merge. For each frequency ω, the wave propagation is computed, $\mathcal{E}^\sigma$ and $\mathcal{A}^\sigma$ are estimated including all particle and harmonics contributions (thermal ions, thermal electrons, suprathermal particles), leading to $N^\sigma(\omega, x, t)$. The boundary problem exists. In the present model, the fast wave propagates with a constant toroidal mode number $N_{//}$ ($k_{//}=N_{//}/R$) and experiments a reflection on a limit density layer at the plasma edge. This limit density increases with $k_{//}$. The 1-D model thus deals with a forward(σ+) and a backward(σ-) mode for a given $N_{//}$, having locally the same group velocity and k modules. An analytical solution can be found for (1):

$$N^{\sigma\pm}(x) = \frac{e^{-\Psi(x)}}{v_g^{\pm}(x)}\left(c^{\sigma\pm} + \int_{-a}^{x} dx\ \mathcal{E}^\sigma(x')e^{\Psi(x')}\right);\ \Psi(x) = -\int_{-a}^{x} dx' \frac{\mathcal{B}^\sigma(x')}{v_g^{\pm}(x')} \qquad (8)$$

where $c^{\sigma\pm}$ are constants ($\mathcal{E}^\sigma$ and $\mathcal{B}^\sigma$ are identical for both modes). Moreover, a realistic model must take into account parasitic edge absorptions or conversions, representing a certain amount of losses. The boundary condition is thus represented by a certain energy reflection coefficient R, chosen as a free parameter, which influence can be studied. Out of the emitting area(s), the N^σ profile satisfies roughly $\nabla(v_g{}^\sigma N^\sigma)=0$, i.e. N^σ is inversely proportional to $v_g{}^\sigma$. In the limit ($R=1$, $T_{//}=T_\perp=T_i$), the order of magnitude of N^σ is given by the Rayleigh-Jeans law:

$$N^\sigma \approx -\frac{\mathcal{E}^\sigma}{\mathcal{B}^\sigma} \approx \frac{k_B T_i}{\hbar\omega} \qquad (9)$$

where $k_B T_i$ is the thermal energy of the ion species i, assumed to be dominant in the process. For R->0, $\mathcal{E}^\sigma$ is much larger than $\mathcal{A}^\sigma$ so that $\nabla(v_g{}^\sigma N^\sigma) \approx \mathcal{E}^\sigma$ leading for u<<1 to N^σ proportional to $T_i{}^n$. This reveals that the interaction process is not strong enough to insure a local "black body" solution, but needs edge reflections or strong plasma temperatures(2).

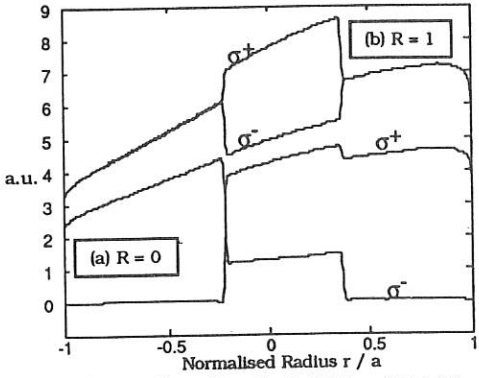


fig1: $N^{\sigma+}$ and $N^{\sigma-}$ profiles, for R=0 (a) and R=1 (b)

As an example, a stationary ITER-like plasma is studied (B0=6T, R0=7.75m, a=3m, $T_D=T_T=T_e=25$ keV parabolic profiles, T_{alpha}=1MeV peaked, $n_e=1.5\ 10^{20}m^{-3}$, flat profile). For $\omega/2\pi$=200 MHz and $k_{//}=1$, fig.1 shows the $N^{\sigma+}$ and $N^{\sigma-}$ profiles, in the cases R=0 (a) and R=1 (b). Fig.2 displays the radiated power spectrum (proportional to $N^\sigma(x=a)$) for $k_{//}=1m^{-1}$, R=1. The frequency range avoids the mode conversion on the ion-ion hybrid layers. The spectrum exhibits the various alpha cyclotron harmonics n=2,3,4..., centred on $\omega=n\omega_{c\alpha}(x=0)$ and which width is consistent with the alpha particle pressure profile, also taking into account the (small) Döppler effect. The visible downshift of the peaks in frequency is due to a profile effect combined with the presence of several harmonic layers at high frequency in the plasma. The typical power level raises up to -70dBm per cm^2 and per toroidal mode number. This is to be compared to -100dBm, predicted and measured on typical Tore Supra plasmas. This gives

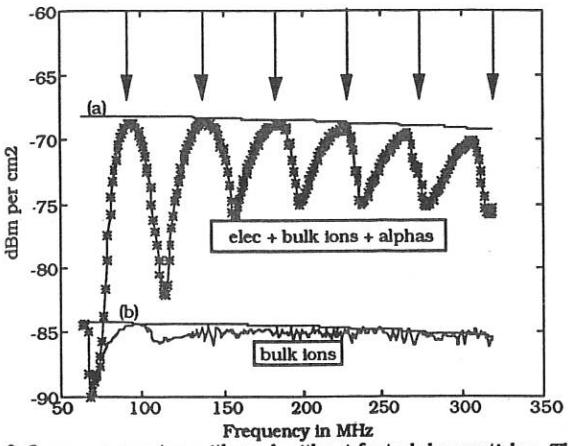


fig2: power spectra with and without fast alpha particles. The arrows display the alpha particle cyclotron harmonics at the plasma centre. The Rayleigh-Jeans predictions (with central temperatures values) are plotted in (a) (with alphas) and (b) (without).

confidence for possible direct measurements on ITER of the alpha particle temperature by a simple RF probe. One can also notice that the electronic contribution affects the low-frequency part of the spectrum, especially at high $k_{//}$-values, symmetrically to the ELD/TTMP damping of a launched fast wave on electrons[3]. This could possibly lead to a diagnostic of the electron parallel temperature, during LHCD for instance. Finally, the introduction of an ad-hoc population inversion (fast alpha particles at the plasma edge for instance) reveals the occurence of possible instability effect, leading to radiation levels well above the Rayleigh-Jeans predictions[4].

CONCLUSION

A fluid description of the fast wave emission-absorption-propagation is presented, in order to address the ion cyclotron direct emission in a tokamak plasma. This method can easily be extended to possible mode conversion effects (coupled equations), kinetic effects (arbitrary distribution functions), as well as be used for more classical heating considerations (propagation, single-pass absorption...). On a tokamak reactor, the "black body" level seems to be obtained, almost independently of the exact edge reflection coefficient. The question of measuring this radiation through an RF probe system requires further studies (edge propagation, other propagation branches,...), but seems possible.

Unfortunately, the alpha particle density effect is small, or even inexistent. A way to obtain the alpha particle density profile could be a measurement of the phase of the radiation, through probe correlations, coupled to a complete field reconstruction[5]. This requires further developments.

ACKNOWLEDGEMENTS

The authors are very grateful to F. Restagno for his active collaboration.

REFERENCES

[1]D.B. MELROSE, *Plasma Astrophysics*, Gordon & Breach, London, 1980.
[2]M.V. DMITRIEVA, private communication.
[3]Equipe Tore Supra, presented by B. SAOUTIC, this conference.
[4]R.O. DENDY, this conference.
[5]D. GAMBIER, A. SAMAIN, Proc. of the 1st Conf. on Plasma Physics, Lausanne, 1984.

RADIAL CURRENT ACROSS THE SEPARATRIX DUE TO DIRECT ION ORBIT LOSS OF A FAST ION POPULATION

T.K. Kurki-Suonio, M.J. Alava, and S.K. Sipilä

Department of Technical Physics
Helsinki University of Technology
FIN-02150 Espoo, FINLAND

Understanding and controlling the plasma confinement is crucial for the development of a fusion reactor. In a so-called L–H transition the plasma confinement suddenly increases when the auxiliary heating exceeds a critical value. Experimentally, an L–H transition seems to be always accompanied with the generation of a strong, sheared radial electric field near the edge [1]. Moreover, such a transition can be triggered even in the absence of any auxiliary heating by externally imposing an edge radial electric field [2]. It is the shear in the poloidal rotation corresponding to this radial electric field that is believed to suppress the microturbulence, thus reducing anomalous transport [1]. Therefore, it is very important to understand how the radial electric field is generated.

According to the most successful theory so far, the radial current due to high energy ions leaving the plasma produces the radial electric field and the poloidal rotation necessary for the suppression of microturbulence [3]. The critical quantity in the original theory was the collisionality of the edge plasma – as the edge plasma gets collisionless, the high energy ions with wide banana orbits are able to leave the plasma through direct ion orbit loss. Therefore this model ran into difficulties when the L–H transition was achieved on the JFT-2M -tokamak under very collisional circumstances [4]. According to a revision of the original theory, this problem is removed when the radial current is caused by a non-thermal hot ion component in the edge plasma [5]. A Monte Carlo simulation, in which a group of fast ions scatters off a stationary background plasma, should be an appropriate tool for evaluating the ion orbit loss current of the revised theory.

In this paper we study the radial current across the tokamak separatrix that is generated by the direct ion orbit loss of fast ions. Such a fast ion component could be caused by, e.g., neutral beams. We use a guiding center following code ASCOT [6] to trace the ion orbits in a fully toroidal geometry. The effect of Coulomb collisions is simulated by using binomially distributed Monte Carlo scattering operators derived from the Fokker-Planck equation [7]. Only the thermal distribution (i.e. background plasma) is included in evaluating the scattering operators because the contribution of a super-thermal component is insignificant. Also the assumption of a stationary background plasma is reasonable if we have a steady-state situation, in which the neutral beams replenish the fast ion population at the same rate they are lost from the plasma.

We evaluate the radial current for L– and H–mode cases to find out, if there are any significant differences between the two modes. We also investigate how a non-uniform radial electric field might affect the radial current. The magnetic geometry is similar to the DIII-D tokamak: $R = 1.75$ m, $a = 0.6$ m, $B_0 = 2.1$ T, and $I_p = 1$ MA.

The plasma is assumed to have only two components: deuterons and electrons. In the code the plasma profiles are given in a simple form, $A = A_0(1-(r/a)^2)^\alpha$, and thus it is not in general possible to match an experimental profile exactly. The L– and H–mode profiles used in the code have been tailored to match the experimentally measured ones [8–10] in the edge region as closely as possible. The density and temperature profiles thus obtained are shown in Fig. 1(a) and (b), respectively. The magnetic geometry in each case is calculated from the given magnetic field strength, plasma current, and plasma profiles [11], and is shown in Fig. 2.

First we evaluate the current in the absence of a radial electric field. Later, we repeat the simulations with linearly varying radial electric fields. It should be emphasized that these are not the self-consistent fields generated by the direct ion orbit loss of the simulation because, as we already mentioned, our test particle approach does not allow for such self-consistent effects.

The test particles are the same species as the plasma, i.e., deuterons. In the absence of experimental data on the fast ion population in the edge region, we choose 4 keV for the energy of the test particles. Even in the H–mode case this value is above the local temperature in the region that we are interested in. On the other hand, it is low enough, so that the banana widths remain sufficiently small as compared to the minor radius and we can limit our considerations to the edge region. The dissimilarity of the magnetic geometries in L– and H–mode poses a problem in choosing the proper initial distribution for the ions: the same radial distance in real space corresponds to quite different ranges in the flux surface coordinate ρ (and, thus, in banana widths) in L– and H–mode. Therefore the initial distribution should be chosen carefully to allow for a meaningful comparison between the different modes. The test ions are distributed uniformly in the flux surface label on eleven surfaces. In the L–mode case the innermost starting flux surface is at $\rho = 0.469$ m and the outermost at $\rho = 0.531$ m. This region corresponds to a distance of 5 cm in the major radius along the outer midplane. In the H-mode case the corresponding ρ-values are 0.45 m and 0.538 m, and the distance in the major radius is 4 cm. We do not extend the launching surfaces all the way to the separatrix because, with this high launching energy, the ions starting close to the separatrix would be lost right away before any of the dynamics we are interested in would have had any impact. Thus such ions would not only be wasted, but would also contribute an initial spike in the radial current hampering the evaluation of a steady-state current. To obtain the best possible statistics from our ensemble we chose the outermost flux surface to be at the distance of one banana width (from the separatrix) of a test ion with the pitch $\xi = -0.5$. The innermost surface was chosen not to be smaller than $\rho = 0.45$ m, inside which the profiles do not necessarily resemble the experimental ones. Since in the H-mode case these criteria led to the distance of only 4 cm in real space, the innermost flux surface for the L-mode was chosen so that it did not differ dramatically from the H-mode case either in the flux surface coordinate or in real space. On each flux surface the ions are launched at 30 different poloidal locations, and at each location there are 30 ions, uniformly distributed in pitch.

The duration of the simulation is long enough to cover many banana orbits but

shorter than the time required for the ions to leave the plasma diffusively. During a simulation run we keep a record of the ions leaving the plasma. The ions can leave the plasma in two ways: (1) they hit the vessel wall, which in the L-mode case is 8 mm but in the H-mode case only 3.5 mm from the separatrix, or (2) they enter a simplified upper divertor cone within the scrape-off layer. The upper divertor cone is specified as the region between the poloidal angles of 90 and 120 degrees. The radial current is evaluated as the time derivative of the accumulated charge outside the plasma. The radial current for the L- mode case without and with a radial electric field is shown in Fig. 3(a) and (b), respectively. The electric field extends from $\rho/a = 0.65$ ($E_r = +50$ kV/m) all the way to the vessel wall (E_r = -20 kV/m) [12]. Thus the radial electric field is positive deeper in the plasma, becomes zero at $\rho/a = 0.9$, and is negative near the separatrix. Figure 4 shows the current for the H-mode case without a radial electric field. Unfortunately, the combination of the large Grad-Shafranov shift and the strongly non-uniform radial electric field did not allow for reliable statistics in reasonable computing time for the case of an H-mode discharge with $E_r(r)$. For this case, a more robust algorithm needs to be installed.

The effect of the non-uniform radial electric field on the radial current is clear from the Fig. 3: the radial field reduces the current by about a factor of two. However, no significant difference is seen between the L- and H-mode. Before drawing any conclusions on this comparison, however, one should recall the significant differences in the magnetic geometries and the fact that the initial spatial distributions could not be made identical. Therefore, to reliably study the differences between L- and H-mode discharges, the code has to be modified so that, instead of calculating the magnetic surfaces, the magnetic geometry can be given as input. This way we can use different plasma profiles on the same magnetic geometry and, thus, see the effect of just the profiles on the radial current.

References:

[1] Burrell *et al.*, Phys. Plasmas **1** (1994) 1536 and references therein.
[2] Taylor *et al.*, Phys. Rev. Lett. **63** (1989) 2365.
[3] Shaing *et al.*, Phys. Fluids B **2** (1990) 1492.
[4] Ida *et al.*, Phys. Rev. Lett. **65** (1990) 1364.
[5] Shaing *et al.*, Phys. Fluids B **5** (1993) 666.
[6] Heikkinen *et al.*, Comput. Phys. Comm. **76** (1993) 215.
[7] Boozer *et al.*, Phys. Fluids **24** (1981) 851.
[8] Burrell, *'Physics of the L-mode to H-mode Transition in Tokamaks'*, at The Internatinal Conference on Plasma Physics, Innsbruck Austria, 1992.
[9] Matsumoto *et al.*, Plasma Physics and Contr. Fusion, **34** (1992) 615.
[10] Groebner *et al.*, Proc. 13th International Conference on Plasma Physics and Contr. Fusion,Washington, D.C., 1990, Vol. I, p. 453.
[11] Private communication between Stringer and Heikkinen.
[12] Burrell, *'Role of Radial Electric Field in the Transition from L-mode to H-mode to VH-mode in the DIII-D Tokamak'*, at The 35th Annual Meeting of the Division of Plasma Physics, St. Louis, Missouri, USA.

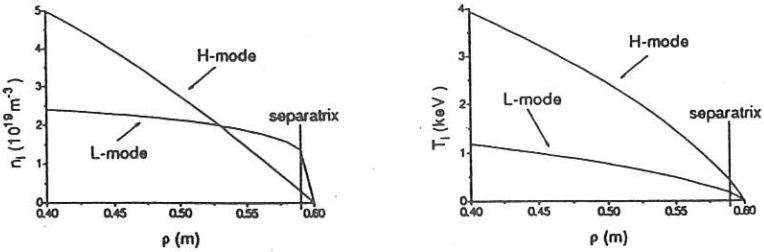


Fig. 1. Plasma density and temperature profiles near the edge.

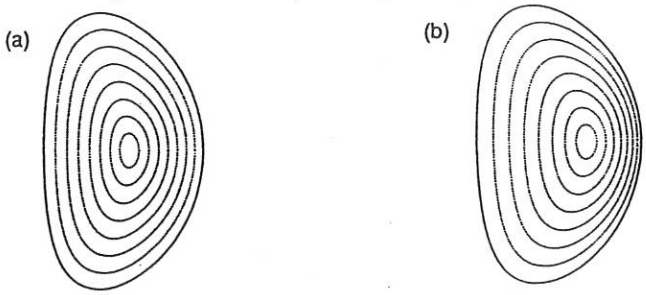


Fig. 2. The flux surfaces for L-mode (a) and H-mode (b) plasma.

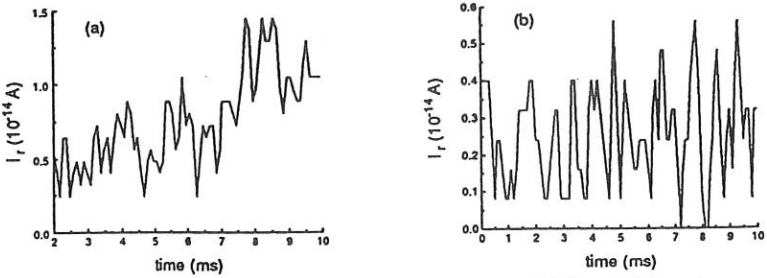


Fig. 3. The radial current for an L-mode plasma with $E_r = 0$ (a), and with a linearly varying electric field, E_r = +40kV/m ... -20kV/m (b).

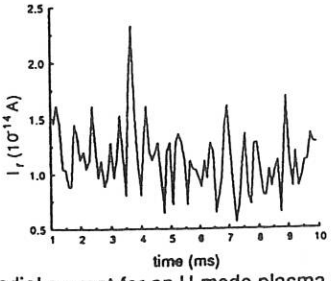


Fig. 4. The radial current for an H-mode plasma without a radial electric field.

Parametric Dependencies of JET Electron Temperature Profiles

Beatrix Schunke, Kaya Imre*, Kurt S. Riedel*

JET Joint Undertaking, Abingdon, Oxon, OX14 3EA, UK

*** New York University, 251 Mercier St., New York NY 10012-1185**

The JET Ohmic, L-Mode and H-Mode electron temperature profiles obtained from the LIDAR Thomson Scattering Diagnostic [1] are parameterised in terms of the normalised flux parameter ψ and a set of the engineering parameters like plasma current I_p, toroidal field B_T, line averaged electron density $\bar{n}$,... We intend to use the same model to predict the profile shape for D-T discharges in JET and in ITER.

1. The log-additive temperature profile model

Assuming that the electron temperature profile in a tokamak depends only on the global parameters, we adopt a generalised log-additive model to describe the electron temperature profile [2] $\ln\left[\theta\left(\psi,\bar{u}\right)\right] = f_0(\psi) + \sum_{l=1}^{L} f_l(\psi) h_l\left(\bar{u}\right)$ with $h_l\left(\bar{u}\right) = (\ln[I_P], \ln[B_t], \ln[\bar{n}], \ln[\kappa], .)$,

where all variables are normalised to their mean values in the data set.

To estimate the unknown $f_l(\psi)$ we expand in B-splines: $f_l(\psi) = \sum_{k=1}^{K} \alpha_{lk} \beta_k(\psi)$ using cubic spline functions $\beta_k(\psi)$. All spline coefficients are estimated simultaneously with a penalised least square regression by minimising $\sum_{i,j} \left(\frac{\ln[T_i(\psi_j^i)] - \theta(\psi_j^i, \overline{u_i})}{\sigma_{i,j}}\right)^2 + \sum_l \lambda_l \int_0^1 | \bar{f}_l(\psi) |^2 d\psi$.

$T_i\left(\psi_j^i\right)$ is the jth radial measurement of the ith measured temperature profile and $\sigma_{i,j}$ is the associated error. The second term is the smoothness penalty function, which damps down artificial oscillations in the estimated $f_l(\psi)$. We use the Rice criterion C_R to estimate the total predicted error, which consists of variance plus smoothing bias plus the model bias (the error arising from the use of an incorrect model):

$$C_R = \frac{\sum_{i,j} (yij - \theta ij)/\sigma_i)^2}{(N - 2 \times degrees\ of\ freedom)} \quad \text{where } y_{i,j} = \ln[T_i(\psi)].$$

The Rice criterion differs from a least square fit by the denominator and enables us to compare models and optimise a given model with respect to the smoothing parameters, choosing λ_l, adding one parameter at a time during a sequential selection procedure and minimising C_R.

2. Advantages of the log-additive model:

- Discharge specific phenomena are eliminated by fitting all profiles simultaneously.
- Physics insight into which global variables influence temperature profile.
- Compact representation for a class of discharges.
- The fitted profiles may easily be input into analysis codes.

- Extrapolation to new values of engineering parameters possible.
- Self consistent errors, including discharge variability, are estimated using repeated measurements.

3. JET electron temperature profile parameterisation

We have compiled and, using the fitting method described above, statistically analysed a 43-profile Ohmic data set, a 55-profile L-Mode data set and a 51-profile H-Mode data set. The data were taken from experimental campaigns from 89 to 92 (see Figure 1 for examples of the fit obtained). Our parameter range is: I_p = 1.-5. MA, B_T= 1.1-3.4 T, q_{95}=2.8-17. Each profile is measured at 50 locations along the mid-plane of the JET vessel. The raw profile data show much radial structure and vary slowly in parameter. We remove the outermost points near the inner wall, where the dumping of the laser light causes a spurious spike on the profile.

Ohmic temperature analysis: Table 1 visualises the selection procedure of the dominant covariants for the Ohmic data set. Fitting all candidates in a one variable fit, one finds that I_P minimises C_R. This parameter is then selected and paired with all other variables in a two variable fit. The variable that minimises C_R in combination with I_P is then selected as second parameter, and we continue to add another variable to minimise CR.

Table 1: Rice Table for Ohmic data set

Vars	1 Var	2 Var	3 Var	4 Var	5 Var
$\ln[\bar{n}]$	8.58	3.07	**1.90**	seed	seed
$\ln[q_{95}]$	5.70	3.23	2.42	**1.50**	seed
$\ln[I_p]$	**3.49**	seed	seed	seed	seed
$\ln[B_T]$	7.20	**2.81**	seed	seed	seed
$\ln[\kappa]$	7.92	3.49	2.76	1.86	1.49
a	8.48	3.44	2.79	1.88	1.46
V_{loop}	8.51	3.45	2.71	1.85	1.46
Z_{eff}	8.01	3.24	2.78	1.87	1.43
ℓ_i	7.79	2.91	2.61	1.77	1.47

The sequential selection procedure shows that I_P is the most important variable in determining the plasma temperature, followed by the toroidal field B_T, the line average density $\bar{n}$ and q_{95}. Adding a fifth variable does not appreciably decrease C_R, so we choose the four variable model. The Rice table shows that the plasma inductance is not particularly influencing the temperature.

The resulting model for the JET Ohmic temperature profile is:

$$T(\psi) = \mu_o(\psi)\, I_P^{f_I(\psi)}\, B_t^{f_B(\psi)}\, \bar{n}^{f_n(\psi)}\, q_{95}^{f_q(\psi)} \qquad \text{with } \mu_o(\psi) = \exp(f_0(\psi)) \tag{1}$$

Because Eq(1) already contains B_T and I_P, q_{95} seems to account for changes in R, a and κ. Thus we can reparameterise (1) using $q_{95}I_P/B_T$ as the fourth variable. As seen in Figure 2 the electron temperature profile broadens and becomes slightly hollow with increasing current when the other parameters are held constant. The same effect is also seen with decreasing toroidal magnetic field for constant current. Since $f_I(\psi) \neq c - f_B(\psi)$ the profile shape depends primarily but not exclusively on the ratio I_P/B_T. Our best fit has an average error of 183 eV, which is 12.6 % of the typical line average temperature. The error bar for predicting new measurements is larger than the typical residual fit error. With $C_R \approx 1.5$ the error bar for

predictions is 22% larger than the typical measurement error.
A similar fit to the Ohmic density profiles shows that $n(\psi)$ depends only on $\bar{n}$ and B_T and that a good approximation is $f_B(\psi) = c - f_n(\psi)$.

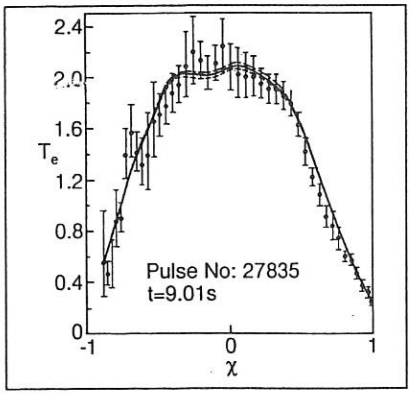


Figure 1: Example of predicted temperature profile from model with raw data

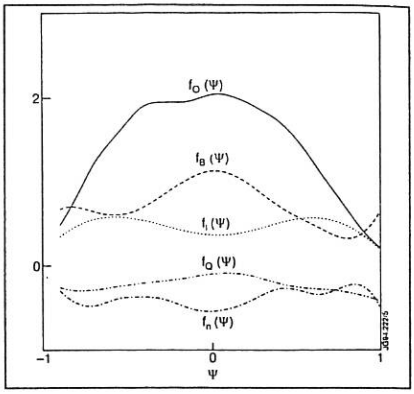


Figure 2: Spline functions for Ohmic electron temperature profile fits

L- Mode temperature fit: Repeating the analysis on the L-Mode data, we find the dependency on B_T to be stronger than in Ohmic discharges. T_e decreases and broadens with $\bar{n}$. The dependency on the current is weaker ($\sim I_P^{0.4}$) then in the Ohmic case. ICRH heated discharges are more peaked than NB heated discharges, therefore we introduce the parameter $\gamma = P_{RF}/P_{tot}$ into the set of covariants.

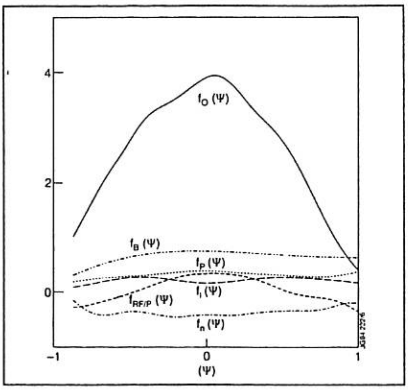


Figure 3: Spline functions for L-Mode temperature profile fits

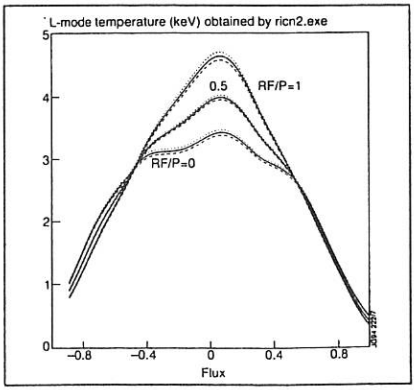
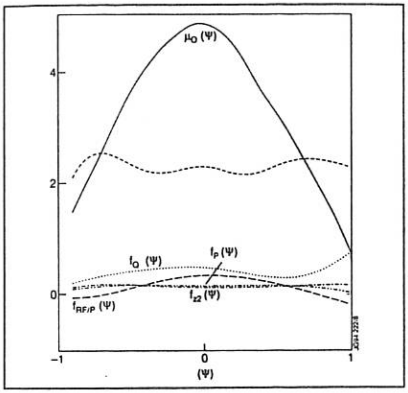


Figure 4: L-Mode temperature profiles varying γ

Best fit model: $T(\psi) = \mu_o(\psi)\, P_{tot}^{f_{P_{tot}}(\psi)} \exp\{\gamma^{f_\gamma(\psi)}\}\, n^{f_n(\psi)}\, B_t^{f_{B_t}(\psi)}\, I_p^{f_{I_p}(\psi)}$ (Figure 3)

Figure 4 shows how the L-Mode temperature profiles change according to our model when varying γ. Regardless of the value of γ the profile shape stays the same outside 0.5 χ, inside 0.5 χ the application of radio frequency heating alone produces a more peaked temperature profile than the application of neutral beam heating.



H-Mode temperature fit: Our best fit parameterisation shows a strong dependency on the current (~ Ip^2). We found that q_{95} has an influence on the electron temperature profile in the H-Mode case, but there is no significant dependency on the density as in the L-Mode data set. Again we find ICRH heated discharges to be more peaked than NB heated discharges, and the parameter $\gamma = P_{RF}/P_{tot}$ appears also in the parametric description of the H-Mode profile as a covariant. We also found that Z_{eff} strongly influences the H-Mode temperature.

Figure 5: Spline functions for H-Mode temperature profile fits

Best fit model: $T(\psi) = \mu_o(\psi)\, z_{eff}^{f_{z_{eff}}(\psi)}\, P_{tot}^{f_{P_{tot}}(\psi)}\, I_p^{f_{I_p}(\psi)}\, q_{95}^{f_{q_{95}}(\psi)} \exp\{\gamma^{f_\gamma(\psi)}\}$ (Figure 5)

Conclusions

The statistical analysis of JET Ohmic, L- and H-Mode data sets shows that the electron temperature profiles fit a log-additive model well. The further analysis of JET L- and H-Mode discharges, e.g. the inclusion of parameters describing the sawtooth phase or the power deposition profile - if feasible, will clarify the parametric dependencies. The parameterisation and characterisation of the corresponding density profiles is nearly completed and will be reported later. A Multimachine database for extrapolation to ITER performance seems possible.

[1] H.Salzmann, J.Bundgaard, A.Gadd, et.al., Rev.Sci.Instrum.**59**, 1451(1988)

[2] McCarthy, P.J., Riedęl, K.S., Kardaun, O.J.W.F., Murmann, H., Lackner, K., Nuclear Fusion, **31**, 1595 (1991)

Boundary point collocation method to solve toroidal plasma flow of arbitrary aspect ratio and arbitrary cross section.

Ferdinand F. CAP, University of Innsbruck

According to TAYLOR's theory a plasma relaxes to a force-free state described by curl $\vec{B} = \lambda \vec{B}$, where λ is constant for a homogeneous initial condition due to div $\vec{B} = \nabla\lambda \cdot \vec{B} = 0$. Since the equation of motion for an incompressible force-free plasma reads [curl $\vec{v} \times \vec{v}$] + $\nabla(\vec{v}/2) + \nabla p/\rho = 0$, scalar multiplication with $\vec{v}$ delivers the BERNOULLI-equation and curl $\vec{v} = \gamma\vec{v}$ with $\gamma = const.$ We thus have a BELTRAMI-flow and compatibility with $\vec{v} = const\vec{B}$ (aligned flow) [1] as well as with the MHD-CROCCO-theorem [2] and the PEYRET-transform [3]. If curl $\vec{v} = \gamma\vec{v}$ is written down in cylindrical coordinates r, z, φ it can be shown for tokamak-symmetry ($\partial/\partial\varphi = 0$) that the solution is given by

$$v_r = -\frac{1}{\gamma}\frac{\partial v_\varphi}{\partial z}, \quad v_z = \frac{1}{\gamma}\frac{1}{r}\frac{\partial}{\partial r} r v_\varphi, \tag{1}$$

where v_r, v_φ, v_z depend on r and z. v_φ is given by

$$v_\varphi(r,z) = \sum_{l=1}^{N} \left[A_l \mathrm{J}_1\left(\sqrt{\gamma^2 - k_l^2}\, r\right) + B_l N_1\left(\sqrt{\gamma^2 - k_l^2}\, r\right)\right] \cos k_l z. \tag{2}$$

In order to satisfy the boundary condition on a rigid wall of a vanishing normal velocity component $v_n = 0$ we consider a cross section curve $z^* = z(r)$ of the toroidal containment of major radius R. In cylindrical coordinates r, z the boundary condition reads [4]

$$v_n = -v_r \sin\alpha + v_z \cos\alpha = 0, \tag{3}$$

where $\tan\alpha = \mathrm{d}z^*/\mathrm{d}r$. If $N \to \infty$, the solutions (1), (2) can satisfy the boundary condition (3) exactly by an appropriate set of the $3N + 1$ unknown parameters A_l, B_l, k_l and γ. For a boundary point collocation method [5] to be used on a computer, N must be finite. If P boundary points $r_i, z_i = z^*(r_i), i = 1 \ldots P$ are chosen on the toroidal boundary curve $z^* = z(r)$ then the P boundary conditions of type (3) read

$$-v_r(r_i, z_i)\left(\frac{\mathrm{d}z^*}{\mathrm{d}r}\right)_{r_i} + v_z(r_i, z_i) = 0, \quad i = 1 \ldots P. \tag{4}$$

These P equations determine the $3N + 1 = P$ unknown parameters in (1) and (2). Several methods have been worked out to solve this problem [5]. It is thus possible to calculate the eigenvalue γ (and also λ [6]) and its dependence from the aspect ratio and the form of the cross section, be it circular, elliptic, D-shaped or a CASSINI-curve etc. $v_r(r,z), v_z(r,z)$ being given it is possible to produce graphic flow pictures.

Another possibility to satisfy (4) is the transformation into

$$\frac{\mathrm{d}z^*}{v_z} = \frac{\mathrm{d}r}{v_r}, \tag{5}$$

which describes the streamlines of $\vec{v}$. Insertion of (1) yields

$$\frac{\partial r v_\varphi}{\partial z} \mathrm{d}z^* + \frac{\partial r v_\varphi}{\partial r} \mathrm{d}r = 0 \tag{6}$$

or

$$r v_\varphi = const \qquad \text{or} \qquad r_i v_\varphi(r_i, z^*(r_i)) = const \tag{7}$$

as an alternative form for (4), which has also been used.

The numerical solution of P transcendental equations (4) or (7) for the $3N+1$ unknowns A_l, B_l, k_l, γ of (2) can be quite tricky with a Macintosh II. Since the number P of the collocation points apparently determines the accuracy of the solution, one may fix P and transform the transcendental equations (4) or (7) into a system of homogeneous linear equations for the $2N$ variables A_l, B_l, $l = 1 \ldots P$ with $P = 2N$ by choosing arbitrarily the N parameters k_l in the interval $0 \leq k_l \leq \gamma$. The eigenvalue γ is then determined by the vanishing of the determinant of the coefficients of the homogeneous linear system. Since now $P = 2N$, the same accuracy measured by P can be obtained by increasing the number N of the modes in (2). FORTRAN- and MATHEMATICA-codes have been written for the calculations presented for various cross-sections and aspect ratios.

From the calculations made with a Macintosh IIfx following conclusions may be drawn:

1. The codes BESSJO, BESSYO, BESSJ1, BESSY1 of the collection Numerical Receipes, W. Press et al, Cambridge University Press, Cambridge, 1986 deliver *wrong* results for arguments $2 \leq r \leq 7$ as compared with results from MATHEMATICA or from numerical tables, e.g. for $J_1(2.8) = 0.56711$ instead of 0.379378.
2. The code LUDCMP to calculate determinants, published by the same source is not able to give exact results. Values calculated differ from values calculated by MATHEMATICA.
3. The influence on the eigenvalue γ of the arbitrary choice of the constants k_l is small (about 4 %), if $N \gtrsim 8$.
4. The difference between calculating with an accuracy REAL*8 or REAL*12 is negligible.
5. The number N of modes used gives small differences in the eigenvalue. For $n = 4$ one obtains $\gamma = 5.15407$, for $N = 6$ $\gamma = 5.28647$, for $N = 8$ one has $\gamma = 5.34299$, but for $N = 10$ (and higher values) one obtains $\gamma = 5.36388$.
6. The influence of small aspect ratio is considerable.
7. The theorems by COURANT on the coherence of domains in boundary problems [7] and the theorem by FABER on the lowest eigenvalue of twodimensional bounded domains [8] are satisfied. For higher eigenvalues the flow picture is more complicated.
8. The method to use (7) instead of using (3) gives similar results, for example $\gamma = 5.340219$ instead of 5.34299.

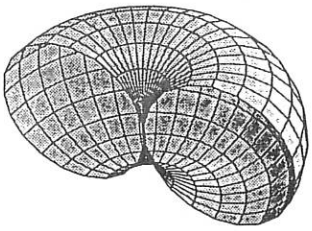
References

[1] N. van KAMPEN, B. FELDERHOF, Theoretical Methods in Plasma Physics, North Holland, Amsterdam, 1967, p 40

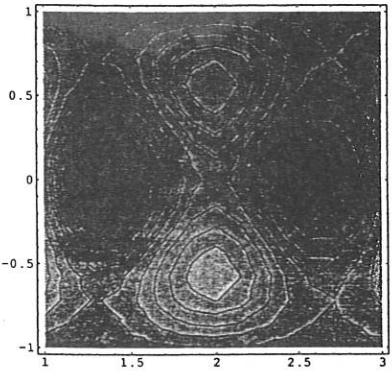
[2] see e.g. F. CAP, Lehrbuch der Plasmaphysik und Magnetohydrodynamik, Springer, Wien, 1994

[3] H. PEYRET, Compt Rendus 250, (1960), 1971–1973
[4] F. CAP, Phys. Fluids 26(6), (1985), p 1766
[5] F. CAP, Wie löst man Randwertprobleme in Physik und Technik, de Gruyter, Berlin, 1993
[6] F. CAP, S. KHALIL, Eigenvalues of relaxed axisymmetric toroidal plasmas of arbitrary aspect ratio and arbitrary cross section, Nuclear Fusion 29, Nr 7 (1989), 1166-1170
[7] R. Courant, Nachr. Ges. Göttingen (math.-phys. Kl.) 1923, Sitzung vom 13. Juli, according to [9]
[8] G. Faber, Sitz. Ber. Bayr. Akad. Wiss. (math.-phys. Kl.) 1923, pp 169-172, according to [9]
[9] R. Courant, D. Hilbert, Methods of Mathematical Physics, Interscience, New York, 1953

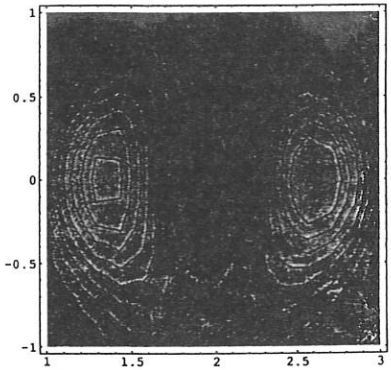
```
(*Give values *)
n=8; np=2*n; R=2.0; RR=1.; elb=2.0 ;r[1]=1.0048; z[1]= 0.1960;
r[2]=1.0431; z[2]=0.5806; etc g[1]=0.5000; g[2]=1.0000; etc
(*Calculation of Eigenvalue*)
a=Table[BesselJ[0,r[i]*Sqrt[u^2-g[j]^2]]*Sqrt[u^2-g[j]^2]*
Cos[g[j]*z[i]]+elb^2*(r[i]-R)/(z[i]*RR^2)*g[j]*Sin[g[j]*z[i]]*
BesselJ[1,r[i]*Sqrt[u^2-g[j]^2]],{i,1,np},{j,1,n}]/u;
bneu=Table[BesselY[0,r[i]*Sqrt[u^2-g[j]^2]]*Sqrt[u^2-g[j]^2]*
Cos[g[j]*z[i]]+elb^2*(r[i]-R)/(z[i]*RR^2)*g[j]*Sin[g[j]*z[i]]*
BesselY[1,r[i]*Sqrt[u^2-g[j]^2]],{i,1,np},{j,1,n}]/u;
at=Transpose[a];bt=Transpose[bneu];dt=Join[at,bt];
et=Transpose[dt];Table[Det[et],{u,5.01,5.02,0.001}]
ka=Table[BesselJ[0,r[i]*Sqrt[u^2-g[j]^2]]*Sqrt[u^2-g[j]^2]*
Cos[g[j]*z[i]]+elb^2*(r[i]-R)/(z[i]*RR^2)*g[j]*Sin[g[j]*z[i]]*
BesselJ[1,r[i]*Sqrt[u^2-g[j]^2]],{i,1,np-1},{j,1,n}]/u;
kb=Table[BesselY[0,r[i]*Sqrt[u^2-g[j]^2]]*Sqrt[u^2-g[j]^2]*
Cos[g[j]*z[i]]+elb^2*(r[i]-R)/(z[i]*RR^2)*g[j]*Sin[g[j]*z[i]]*
BesselY[1,r[i]*Sqrt[u^2-g[j]^2]],{i,1,np-1},{j,1,n-1}]/u;
tka=Transpose[ka];tkb=Transpose[kb];jtk=Join[tka,tkb];
ttj=Transpose[jtk]; j=n;bbb=-Table[BesselY[0,r[i]*
Sqrt[u^2-g[j]^2]]*Sqrt[u^2-g[j]^2]*Cos[g[j]*z[i]]+
elb^2*(r[i]-R)/(z[i]*RR^2)*g[j]*Sin[g[j]*z[i]]*BesselY[1,r[i]*
Sqrt[u^2-g[j]^2]],{i,1,np-1}]/u ;xx=LinearSolve[ttj,bbb];
aa[1]=xx[[1]]; aa[2]=xx[[2]];...b[1]=xx[[9]]; b[8]=1.000
vr[r_,z_]:=Sum[g[j]*(aa[j]*BesselJ[1,r*Sqrt[u^2-g[j]^2]]+
b[j]*BesselY[1,r*Sqrt[u^2-g[j]^2]])*Sin[g[j]*z],{j,1,n}]/u;
vz[r_,z_]:=Sum[Sqrt[u^2-g[j]^2]*(aa[j]*BesselJ[0,r*Sqrt[u^2-
g[j]^2]]+b[j]*BesselY[0,r*Sqrt[u^2-g[j]^2]])*Cos[g[j]*z],
{j,1,n}]/u; gesv[r_,z_]:=vr[r,z]*elb^2*(r-R)/(z*RR^2)+vz[r,z]
Table[N[gesv[r[i],z[i]]],{i,1,np}] //Timing
ListPlot[{{r[1],z[1]},{r[2],z[2]},{r[3],z[3]},.z[16]}},
AspectRatio->1,PlotJoined->True];
ContourPlot[gesv[r,z],{r,R-RR,R+RR},{z,-elb,elb}] //Timing
Needs["Graphics`PlotField`"];PlotVectorField[{vr[r,z],vz[r,z]}
,{r,R-RR,R+RR},{z,-RR,RR}] //Timing
```



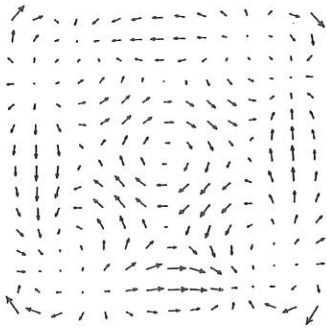
1. Torus of aspect ratio 1.



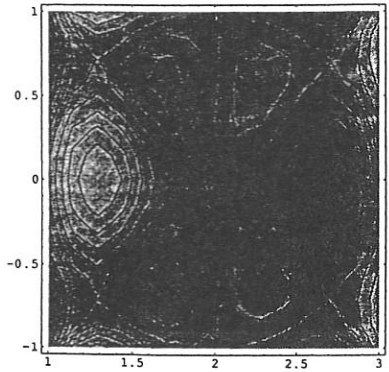
2. Circle, $N = 4, \gamma = 5.1541, A = 2, k_1 = 5.0990,$ $k_2 = 3.8240, k_3 = 2.5490, k_4 = 1.2740,$.



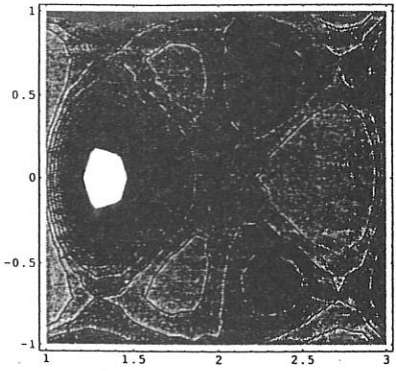
3. Circle,$N = 8, \gamma = 5.4892, A = 1,$.



4. Circle, see left contour.



5. Circle $N = 10, \gamma = 5.3639, A = 2,$ $k_i = 0.5, 1., 1.5, 2., 3., 3.5, 4., 4.5.$



6. Circle, $N = 8, \gamma = 5.8719, A = 2,$ $k_i = 1., 2., 2.5, 3., 3.5, 4., 4.4, 4.5.$

Influence of detailed neutral particle modelling on currents and cross-field drifts in a poloidally biassed divertor plasma

M. Baelmans[a], D. Reiter[b], P. Börner[b]

[a] Department of Mechanical Engineering, Katholieke Universiteit Leuven, Celestijnenlaan 300A, B3001 Heverlee, Belgium
[b] Institut für Plasmaphysik, Forschungszentrum Jülich Gmbh, Association EURATOM-KFA, D-52425 Jülich, Germany

Abstract
The application of external electrostatic fields to divertor and limiter configurations provides some control of plasma behaviour in general and of scrape-off layer profiles in particular [1]. Therefore, it might play an important role in next generation tokamaks. The analysis of such control mechanism on larger devices requires plasma edge codes which are capable to compute electric currents and electric fields. Therefore, the B2-edge plasma code [2] is modified to include the effects of classical fluid drifts across the magnetic field lines and electric plasma currents. In this paper this extended code (EB2) is used to examine effects of electrically biassing between divertor plates. In addition the EB2 code is coupled with the Monte Carlo code EIRENE [3] to describe more accurately the neutral particle behaviour. Differences between a simplified analytic and a Monte Carlo neutral model are investigated.

1 Introduction

In recent experiments particle and heat flows in the scrape-off layer could actively be modified by poloidally biassing of divertor plates [4]. The potential of edge plasma control by electric fields has triggered development of improved edge plasma codes permitting a more complete description.
To study biassing experiments, the B2 code [2] is extended to compute the electric potential Φ, the electric current density $\mathbf{j}$ and diamagnetic as well as $\mathbf{E} \times \mathbf{B}$ particle drifts. These extensions are based on neoclassical collisional dominated momentum equations [5]. In particular, it contains a neoclassical expression for the radial current density, which allows to determine the radial electric field inside the last closed flux surface.

2 Model description

2.1 Basic equations

We add to the B2 code the equations for Φ, $\mathbf{j}$ and particle drifts.
The electron momentum equation in the parallel direction is used to define the parallel electric current density :

$$j_\parallel = \frac{\sigma_\parallel}{en}\frac{B_\theta}{B}\frac{1}{h_\theta}\left(\frac{\partial p_e}{\partial u^\theta} - en\frac{\partial \Phi}{\partial u^\theta} + 0.71n\frac{\partial T_e}{\partial u^\theta}\right) \tag{1}$$

and, in combination with the current continuity equation gives rise to a second-order partial differential equation in θ for Φ :

$$\frac{\partial}{\partial u^\theta}\frac{\sqrt{g}}{h_\theta^2}\sigma_\parallel\frac{B_\theta^2}{B^2}\frac{\partial \Phi}{\partial u^\theta} = \frac{\partial}{\partial u^\theta}\frac{\sqrt{g}}{h_\theta}\left[\frac{\sigma_\parallel}{en}\frac{B_\theta^2}{B^2}\frac{1}{h_\theta}\left(\frac{\partial p_e}{\partial u^\theta} + 0.71n\frac{\partial}{\partial u^\theta}T_e\right) + \frac{B_\phi}{B}j_\perp\right] + \frac{\partial}{\partial u^r}\left(\frac{\sqrt{g}}{h_r}j_r\right) \tag{2}$$

The radial ion momentum equation is used to obtain the diamagnetic component of the ion velocity $V_\perp$, neglecting inertial, viscous and perpendicular conductivity effects in comparison with the radial pressure and electric potential gradients :

$$V_\perp = -\frac{1}{B}\left(\frac{1}{enh_r}\frac{\partial p_i}{\partial u^r} + \frac{1}{h_r}\frac{\partial \Phi}{\partial u^r} - \frac{1}{en}S_{mv,r}\right) \tag{3}$$

The radial component of the total momentum equation is similarly reduced to the equilibrium equation :

$$j_\perp = -\frac{1}{B}\left(\frac{1}{h_r}\frac{\partial p}{\partial u^r} - S_{mv,r}\right) \tag{4}$$

The radial current density j_r is obtained by evaluating the total momentum equation in the diamagnetic direction. In this equation inertia terms are omitted :

$$j_r = \frac{1}{B}\left\{\frac{B_\phi}{B}\frac{\partial p}{h_\theta \partial u^\theta} + \frac{1}{\sqrt{g}}\frac{\partial}{\partial u^\theta}\left[\frac{\sqrt{g}}{h_\theta^2}\eta_0\left(\frac{2}{3}\frac{B_\theta B_\phi}{B^2}\frac{\partial}{\partial u^\theta}V_\parallel - \frac{1}{3}\frac{B_\phi^2}{B^2}\frac{\partial}{\partial u^\theta}V_\perp\right)\right] - S_{mv,\perp}\right\} \quad . \tag{5}$$

For the radial component of the ion velocity V_r the anomalous expression is supplemented with neoclassical terms :

$$V_r = -\frac{D}{h_r}\frac{\partial}{\partial r}\ln(n) + \frac{1}{B}\left[\frac{B_\phi}{B}\left(\frac{1}{enh_\theta}\frac{\partial p_i}{\partial u^\theta} + \frac{1}{h_\theta}\frac{\partial \Phi}{\partial u^\theta}\right) - \frac{1}{en}S_{mv,\perp}\right] \quad . \tag{6}$$

Contributions from these additional plasma parameters ($V_\perp$, V_r, j and Φ) to the plasma density, the parallel ion velocity and to the ion and electron temperature are likewise incorporated.

2.2 Geometry, transport coefficients and boundary conditions

The model was applied to typical ohmic ASDEX-Upgrade conditions (see figure 1) where the MHD equilibrium is provided by a grid generator code SONNET [6]. Three regions can be distinguished : the scrape-off layer (SOL), the private flux region (PF) and an outer section of the core. A modification of the standard B2 allows to handle adequately the divertor magnetic configuration near the X-point. The direction of the toroidal magnetic field B_Φ is taken antiparallel to the plasma current I_p for those computations where drift flows are incorporated.
For the parallel transport coefficients the Braginskii expressions are used without any flux limiting factor. The radial anomalous diffusion coefficient D equals 2 m^2/s. The radial transport coefficients for parallel momentum, electron and ion energy are respectively $\eta = mnD_\eta$ with $D_\eta = 0.2 m^2/s$, $\kappa^e = nD_{\kappa,e}$ with $D_{\kappa,e} = 4 m^2/s$ and $\kappa^i = nD_{\kappa,i}$ with $D_{\kappa,i} = 1 m^2/s$.
On the magnetic flux surface at the core plasma interface $n = 2 \times 10^{19}$ m^{-3}, $Q_r^e = 1.17 \times 10^4 W/m^2$ and $Q_r^i = 5.83 \times 10^3 W/m^2$ are prescribed. This leads to a total radial heat flow from the core into the scrape-off layer of 700 kW.
At the targets, plasma sheath edge conditions are imposed on both sides with a transmission coefficient $\delta_i = 3.5$ for the ions and $\delta_e = (0.9 + e\Delta\Phi/Te)$ for the electrons.
We allow some particle flux to the wall ($V_r = 100 m/s$). The wall temperatures are set to 2 eV.

2.3 Neutral modelling

In order to save computing time the standard "minimal" model is often used, with neutral particles restricted to the divertor legs (i.e. they cannot penetrate further than the topological cuts) [5], [7]. The code is then consistently linked to the Monte Carlo code EIRENE to examine effects of detailed neutral particle description on the additional flows in EB2 [8].
For the analytic model, the global recycling coefficient at the plates is set equal to 0.7. In the Monte Carlo runs a pumping duct is modelled by an effective albedo resulting in 20000 l/s at the outer divertor leg.

3 Results

3.1 Poloidal biassing of divertor plates

The code extensions have been implemented stepwise : In a first step, in order to investigate biassing experiments, $j_\parallel$ and E_θ are introduced, solving Eqs. (1) and (2) and posing j_r and $j_\perp$ equal to zero. This will further be referred to as EB2[1].
Three sets of calculations are performed with the EB2[1] code with varying applied voltage at the outer divertor plate. Figure 2 shows the induced electric current towards the outer target and the saturation currents towards both targets I_{sat} as a function of the applied voltage. When the analytic neutral model is used (solid line in figure 2, left), the I-V characteristic is dominated by the sheaths. When the density at the plasma core boundary is increased (see figure 2, right) from $2 \times 10^{19} m^{-3}$ to $4 \times 10^{19} m^{-3}$ the peak temperatures at the target decrease and the density increases (see table 1). This results in a plasma resistance dominated regime with higher saturation currents to the targets. Conform to experimental data on DIII-D [4], the I-V characteristic is not double-probe like and the SOL currents can influence the ion saturation currents. However, it should be noted that the computed electric resistance of the SOL is much lower than the one measured in DIII-D. When the Monte Carlo code is used, the electron and ion peak temperatures are reduced. Despite its influence on the target parameters, causing lower saturation currents, the I-V characteristic is not much altered and a typical double-probe like characteristic is obtained. For higher densities the plasma parameters at the target will more influence the global solution and the use of EIRENE seems necessary. Until now no stationary solution was obtained, but the time-dependent EIRENE recently linked to B2 [9] gave promising results.
For all cases it turned out that the heat load at the targets was shifted from the cathode to the anode during biassing in a limited range from -10 V to 10 V. With higher voltages the supplied bias energy overrules this effect and heat power increases at both targets.

Case	n_{core} in m^{-3}	Neutral Model	$T_{e,in}$ in eV	$T_{e,out}$ in eV	$T_{i,in}$ in eV	$T_{i,out}$ in eV	n_{in} in m^{-3}	n_{out} in m^{-3}
A	2×10^{19}	Anal.	10.64	12.73	7.55	8.36	1.7×10^{19}	1.6×10^{19}
B	4×10^{19}	Anal.	3.38	4.26	3.84	4.14	8.3×10^{19}	7.0×10^{19}
C	2×10^{19}	M.C.	5.54	10.31	4.43	4.87	1.0×10^{19}	9.9×10^{18}

Table 1: Target parameter for three cases without biassing

3.2 Calculations including drift terms

For the evaluation of the diamagnetic and E × B drifts the knowledge of the radial electric field is required. Outside the separatrix this can easily be obtained by solving equation (2). Inside the separatrix the boundary condition for the poloidal direction is a periodic condition and thus determines the electric potential only up to an unknown constant value. For the radial electric potential profile we need a relation between j_r and E_r. Using the neoclassical equations, this relation is indirectly given via the diamagnetic component of the ion velocity (Eqs. (5) and (3)). This extension of B2 code will be further referred to as EB2[2].
With the analytic neutral model it turned out that SOL currents and plasma peak temperatures are not much influenced by applying drift terms (see table 2). In figure 3 it can be seen that the cross field

Case	I in A	$I_{sat,in}$ in A	$I_{sat,out}$ in A	$T_{e,in}$ in eV	$T_{e,out}$ in eV
A EB2[1]	-819.3	4161	4964	10.64	12.72
A EB2[2]	-944.1	4159	4947	10.88	12.54
B EB2[1]	-133.9	-10522	11832	3.38	4.26
B EB2[2]	-83.3	-10257	11844	3.63	4.14

Table 2: Effects on SOL currents and plasma temperature by introducing cross-field drifts

currents are equally spread over the SOL. The circuit is closed in the PF region near the X-point.
From data obtained with the Monte Carlo code using EB2 as postprocessor, we see that the radial current profile in the divertor region is determined by two competitive forces induced by the pressure gradient and parallel viscosity. Forces from neutral particle interactions are 2 orders of magnitude smaller. However some impact might exist in the SOL above the X-point.

4 Conclusions

Simulations with the EB2 code for differential biassing show two regimes for the I-V characteristic: a sheath dominated regime for low density plasmas and a resistance dominated regime for high density plasmas. Although Monte Carlo computations for neutral particle modelling have a relevant impact on target parameters they hardly effect the SOL currents in the low density regime. For high density plasmas, a larger influence of detailed neutral particle modelling is expected. For both regimes it turned out that due to the low plasma resistivity, the range in which the heat load can be shifted from cathode to anode is limited.
Implementation of drift terms with the analytic neutral model has only a small influence on the plasma parameters. Monte Carlo calculations show that pressure gradients and parallel viscous terms dominate the current density profile in the divertor region.

References

[1] R.R. Weynants and G. Van Oost, Plasma Phys. and Contr. Fus., 35B (1993) 177.

[2] B.J. Braams, Proc. 11th Eur. Conf. on Contr. Fus. and Plasma Phys., Aachen, Germany (1983).

[3] D. Reiter, KFA-Report, JÜL-2599 (1992).

[4] M.G. Schaffer, M. ali Mahdavi, C.C. Klepper et al., Nucl. Fus., 32 (1992), 855.

[5] M. Baelmans, KFA-Report, JÜL-2891 and LPP-ERM/KMS-Rep N° 100 (1994)

[6] R. Schneider, B.J. Braams, D. Reiter et al., Contrib. to Plasma Phys., 32 (1992), 450.

[7] M. Baelmans et. al, PSI conference, J. Nucl. Mat., to be published.

[8] D. Reiter, J. Nucl. Mat., 196-198 (1992), 241.

[9] D. Reiter, PSI conference, J. Nucl. Mat., to be published.

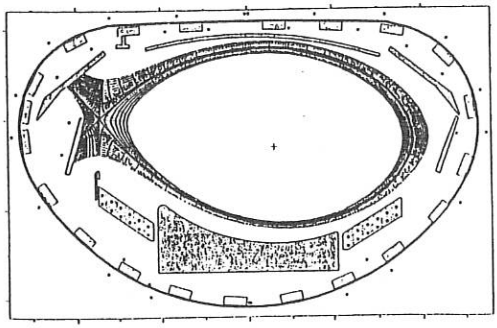


Figure 1: Magnetic configuration of ASDEX-Upgrade

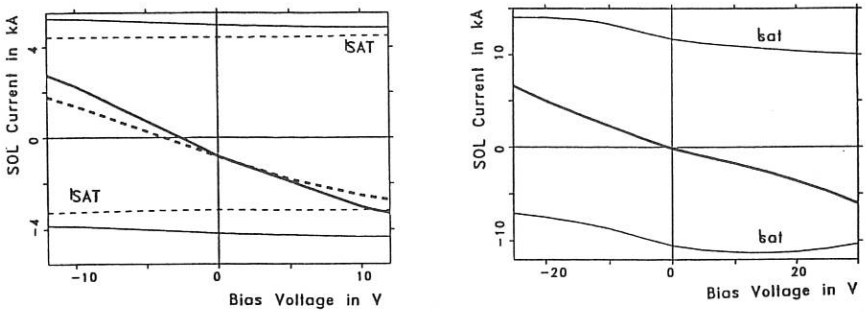


Figure 2: SOL current for biassing simulations (left: case A (solid line), case C (dashed line) and right: case B)

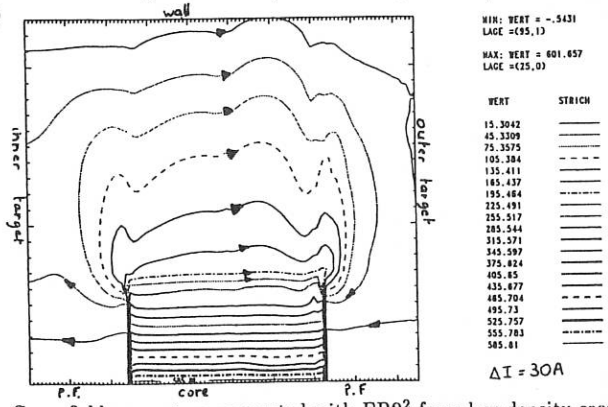


Figure 3: Cross-field currents as computed with EB2[2] for a low density case.

Comparison of Experimental MARFE Observations in ASDEX Upgrade with B2 Calculations

W. Junker, H.-S. Bosch, K. Büchl, O. Gruber, G. Haas, H. Kastelewicz*, M. Kaufmann, W. Köppendörfer, K. Lackner, M. Laux*, V. Mertens, J. Neuhauser, C.S. Pitcher#, H.Röhr, R. Schneider, K.-H. Steuer, ASDEX Upgrade & NI Teams
*Max-Planck-Institut für Plasmaphysik, EURATOM Association, D-85748 Garching, *D-10117 Berlin, Germany*
#PPPL Princeton, USA and CFFTP, Toronto, Canada

Introduction

Future large tokamak reactors will operate at high plasma density, low edge temperature and strong impurity radiation at the edge in order to reduce peak power loads on the divertor plates and physical sputtering. Such discharges are likely to develop toroidally symmetric poloidally localized dense edge regions. These regions will be referred to as MARFEs, only if they are highly radiating and if they appear in the main plasma chamber or close to the X-point. In this paper, high density regions in front of the target plates are called high recycling zones. MARFEs may beneficially influence the discharge characteristics, as they can radiate away a substantial amount of the power flowing into the plasma edge; thus controlled creation of a MARFE can be an efficient means to reduce the power load onto the divertor plates. High recycling zones in the divertor in front of the target plates may broaden the energy flux distribution in the divertor by charge exchange collisions. The high energy fluxes associated with ELMs may be prevented from penetrating to the target plates by establishing such high recycling zones. In this paper, the characteristics of cold divertor scenarios in ASDEX Upgrade neutral beam injection heated and Ohmically heated discharges are described. The divertor dynamics due to ELMs is discussed.

Diagnostics

In order to identify cold and dense plasma regions two different methods of measurement were applied: 1.) The emission coefficient of plasma bremsstrahlung in the near infrared wavelength region is proportional to $n_e^2/\sqrt{T_e}$, so that measurement of bremsstrahlung is a particular sensitive means of identifying dense cold plasma regions as MARFEs. On ASDEX Upgrade the wavelength region around $1035nm \pm 10nm$ was found to be suitable for bremsstrahlung measurements, i.e. free of disturbing spectral lines, by spectroscopic investigations [1]. In addition to bremsstrahlung in this wavelength range recombination radiation may make up a non - neglegible contribution to continuum radiation. Calculations with the B2 code show that in realistic situations the contribution of recombination radiation can be neglected for temperatures above $10eV$ and reaches the order of 30% in cases of lower temperatures ($\approx 1eV$).

2.) An estimate for the plasma temperature can be derived from the power radiated by the transition $3p\ ^3P \rightarrow 3s\ ^3P$ ($\lambda = 464.9\ nm$) of Carbon^{2+} (CIII) ions. The excitation rate coefficient of this line exhibits a weak temperature dependence above 10 eV and sharply drops towards lower temperatures [2].

The plasma was observed by three arrays of lines of sight across the ASDEX Upgrade vessel (fig. 1). Detectors were silicon diodes and silicon avalanche diodes, 16 of which were simultaneously used for Nd - YAG Thomson scattering. While the arrays with essentially horizontal direction were dedicated to bremsstrahlung measurement in all

cases, the array with vertical view was alternately equipped with a bremsstrahlung or CIII filter.

Experiments

Experiments were done on Ohmically and neutral beam heated discharges with plasma current $I_p = 0.8\ MA$, heating power $P = 1...7\ MW$, line integrated density $\bar{n}_e = 3...9 \times 10^{19} m^{-3}$ and safety factors ranging from $q_{95} = 2.8$ to 5.0.

In order to exclude the additional complications imposed by the dynamics of ELMs the characteristics of Ohmically heated plasmas are described first. In Ohmically heated discharges with low $\bar{n}_e$ high recycling zones with high plasma density ($\approx 10^{20} m^{-3}$) in front of each target plate form. The formation of these high density zones can essentially be explained by the pressure constancy along field lines in combination with a temperature drop from the midplane scrape off layer (SOL) towards the divertor due to radiation power losses. While the bremsstrahlung channels observing the outer target plate show hardly any increase in intensity during the density rise, channels observing the inner side sharply increase. Interferometric measurements of the edge density and edge temperatures obtained from Nd-YAG laser Thomson scattering indicate within their spatial resolution ($\approx 5cm$) that the density rise might occur at constant pressure in the main chamber SOL. When the density is raised increased recycling and increased neutral pressure induce growing charge exchange friction and consequently a pressure drop in the divertor along field lines, so that the plasma density in front of the outer plate saturates. The lines of sight of the channels observing the inner target plate cross the plasma region inside the separatrix just above the X-point. When the edge temperature becomes low enough the formation of MARFEs inside the separatrix in all cases (i.e. for all values of the safety factor q and for both directions of the ion-∇B drift) starts here [4, 3, 10]. Thus the increase of the signals that view the inner divertor in fig 2 is caused by the X-point MARFE formation. Densities in the MARFE and in the high recycling zones are derived from near infrared bremsstrahlung measurements in combination with B2 calculations (s. figs. 2,3,4). In the calculations an advanced version of the B2 multi-fluid code is used [5]. Simple recycling models yield a good agreement between measurement and calculation for plasmas with low and medium line averaged densities. High plasma densities seem to require coupling B2 to the EIRENE neutral gas Monte-Carlo Code [6]. In ASDEX Upgrade Carbon and Oxygen are the main impurities with respect to radiation power [8]. Thus in the calculations 15 fluids ($D^+, C^{1+}, ..., C^{6+}, O^{1+}, ..., O^{8+}$) are taken into account. Typical parameters are separatrix densities of $n_{sep} = 2...3 \times 10^{19} m^{-3}$, power input at the inner grid boundary $P = 1MW$, $Z_{eff} = 1.3$ due to carbon and oxygen impurities and an empirical diffusion coefficient $D = 1m^2/s$.

CIII profiles measured by the vertical system in fig. 1 show peaks in channels observing the inner and outer divertor legs in low and medium density Ohmically heated discharges. As in this type of discharge the divertor temperature stays so low [7] that physical target plate sputtering does not significantly contribute to the carbon concentration in the plasma these peaks indicate regions of temperature hotter than about 10 eV, but low enough to allow more CIII ions to exist than in any other part of the divertor. When the density is raised the divertor becomes so cold that both excitation of the observed spectral line and target plate sputtering become unlikely here and the maximum moves towards the channels passing through the X-point region.

In neutral beam injection heated plasmas, which are usually H-mode, the highest intensities in CIII radiation are observed in front of the target plates during ELMs (s. fig. 5). This is very likely an effect indicating the onset of physical sputtering. In between ELMs

CIII radiation profiles become similar to those of Ohmically heated plasmas indicating temperatures low enough to exclude physical sputtering.
Experiments with Neon-, Argon- and Deuterium puffing showed that in spite of the high values of $P_{rad}/P_{input} \approx 0.8$ (P_{rad} is integrated over ELMs and inter-ELM-periods) that could be reached by noble gas radiation, the most efficient cooling of the divertor was achieved when the neutral gas pressure in the divertor was high (s. fig. 6). In these cases CIII radiation profiles in between ELMs were identical to profiles of Ohmic discharges with an X-point MARFE. As shown in fig. 6, in discharges with high neutral gas pressure ELMs hardly burn through on the inner divertor. Apparently the plasma density in front of the inner target plate and the neutral gas pressure are high enough on this side to efficiently broaden and absorb the energy flux of an ELM.
In the outer divertor a higher energy flux in between ELMs and a shorter distance between X-point and target plate may yield increased heat conduction along field lines to the plate and a smaller zone where interaction between neutral gas and plasma occurs. Thus there is a lower efficiency with respect to damping the impact of ELMs.

Conclusions

In ASDEX Upgrade experimental investigations by near infrared and CIII diagnostics show that regions of high density and low temperature in front of the target plates can be established. In Ohmically heated plasmas these high density zones can exist when the density is high enough, yet significantly ($\approx 30\%$) below the density limit. For these cases a quantitative agreement between measurements and B2 calculations is obtained. Operation with cold divertor in NBI heated plasmas was shown to be possible when the neutral gas pressure in the divertor was high ($\approx 8 \times 10^{-3} mbar$). In phases between ELMs both inner and outer divertor are cold. The high plasma density in front of the target plate and neutral gas recycling prevent ELMs from burning through on the inner side. The outer divertor so far could not be kept cold during ELMs; this may be possible when the divertor neutral gas pressure is further increased.
B2 calculations for ELMy H-mode plasmas will require a model for ELMs, which is currently being developed [9] and a full Monte-Carlo description of the neutrals like the coupled code package B2-EIRENE [6].

References

[1] S. dePeña-Hempel, Diploma Thesis, Technische Universität München 1993
[2] K. Behringer, H.P. Summers, B. Denne, M. Forrest, M. Stamp, Plasma Physics and Controlled Fusion, Vol.31, No.14, 2059, 1989
[3] V. Mertens, W. Junker, M. Laux, M. Schittenhelm, K. Büchl, F. Mast et al., accepted for publication in Plasma Physics and Controlled Fusion 1994
[4] K.-H. Steuer, W. Junker, H. Röhr, K. Büchl, W. Engelhardt et al.: Proc. 19th EPS Conference Innsbruck 1992, Vol.II, p.743
[5] R. Schneider, D. Reiter, H.P. Zehrfeld, B. Braams et al., Journal of Nuclear Materials 196-198 (1992) 810-815
[6] H.-S. Bosch et al., PSI Conference 1994
[7] C.S. Pitcher et al., PSI Conference 1994
[8] R. Neu et al., this conference
[9] D. Coster et al., this conference
[10] M. Laux et al., this conference

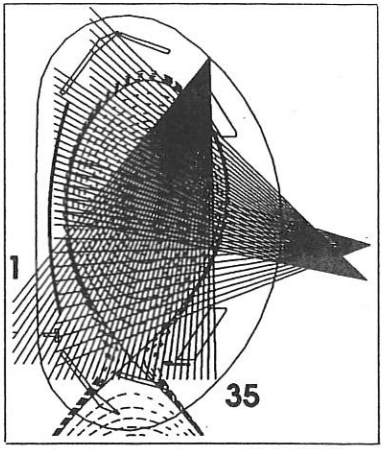


Figure 1: *Cross section of ASDEX Upgrade and lines of sight of the bremsstrahlung and CIII diagnostics*

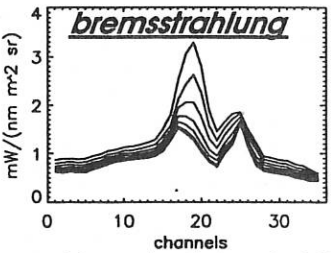


Figure 2: *Measured evolution of a MARFE during the density rise* ($\bar{n}_e = 3.7...4.2 \cdot 10^{19} m^{-3}$) *in an Ohmically heated discharge* (#4489)

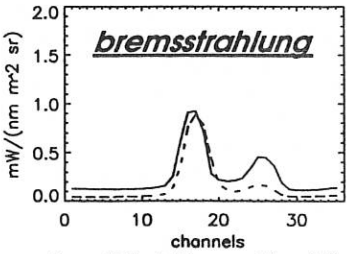


Figure 3: *Calculations with different* P/n_{sep}; *dashed line:* $960kW/(2 \cdot 10^{19} m^{-3})$, *solid line:* $1.6MW/(2.5 \cdot 10^{19} m^{-3})$; *pure B2 output, poloidally symmetric contribution due to bremsstrahlung from the core plasma* ($\approx 1mW/(nm\ m^2\ sr)$) *not added*

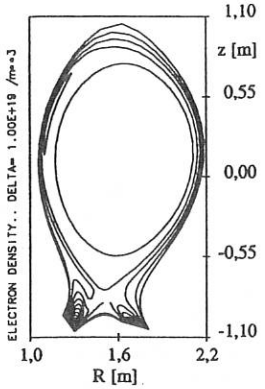


Figure 4: *Contours of* n_e *calculated with the B2 multi-fluid code, maxima in front of the target plates:* $10^{20} m^3$

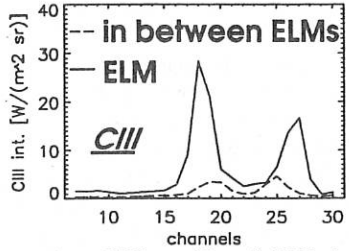


Figure 5: *CIII profile of NBI heated discharge* (#4286, $P_{NI} = 6.8MW$, $\bar{n}_e = 8.6 \times 10^{19} m^{-3}$, $t = 2.1s$); *neutral gas pressure below X-point low:* $p_n = 3 \times 10^{-3} mbar$; $T_{divertor} > 10eV$ *in between ELMs*

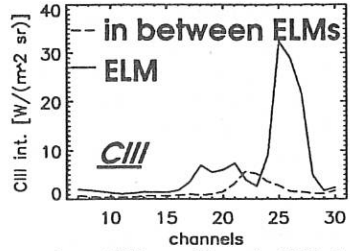


Figure 6: *CIII profile of NBI heated discharge* (#4286, $t = 3.9s$); *neutral gas pressure below X-point high:* $p_n = 8 \times 10^{-3} mbar$; $T_{divertor} < 10eV$ *in between ELMs; inner divertor stays cold even during ELM*

SIMULATIONS OF REACTIVITY TRANSIENTS IN TOKAMAK FUSION REACTORS

M.J. Mantsinen and R.R.E. Salomaa
Helsinki University of Technology, Department of Technical Physics
Rakentajanaukio 2C, FIN-02150 Espoo, Finland

1. Introduction: In this paper we present a study of transients in near-term experimental DT tokamak fusion reactors and in advanced D^3He-tokamaks. Cases considered include reactor start-up and shut-down, fuelling interruptions, helium ash accumulation, and sudden changes in plasma confinement.

Understanding the start-up behaviour of fusion reactors is important for the design of external heating and current drive systems. In the case of D^3He-reactors, we have considered the use of tritium injection to alleviate the extremely demanding heating power requirements. After ignition, helium ash accumulation determines the plasma evolution. During plasma burn, severe power and temperature excursions may occur when fuel injection or plasma confinement properties suddenly change. A gentle shut-down of a burning plasma must be accomplished by a proper ramp-down of the plasma current, a decrease in the fuelling rates and, when necessary, by plasma stabilization and impurity injection.

2. Model: We have developed a zero-dimensional (volume-averaged) time-dependent particle and power balance code for our transient studies. The balance equations, similar to those used in ASPECT [1] and DYNASTY [2], describe global dynamics of a tokamak. Steady state operating points are consistent with those given by POPCON [3]. Preliminary comparisons with transport calculations [4,5,6] show good agreement. The advantage of our code as compared to transport codes is the possibility to scan quickly the dependencies of different reactor parameters.

In our model we assume prescribed profiles for the plasma parameters; usually in the form $x(r) = x(0)(1 - r^2/a^2)^{\alpha_x}$. The code includes external and ohmic heating; fuelling; DD, DT, and D^3He fusion reactions; temperature relaxation between ions and electrons; diffusion and radiation losses; bootstrap current (optional); and stability limits to beta, density, and safety factor. The division of the alpha-particle heating between ions and electrons is as given in [7], and the beta of fast fusion products according to [1]. The code assumes plasma neutrality and follows the evolution of ash concentration self-consistently. The time-dependence of impurity concentrations, profile exponents, and the H-mode factor f_H multiplying the empirical confinement time τ_E are specified as an input. In the present paper diffusion losses are estimated using ITER89-P scaling law [8], other options are available.

We have applied our model to ITER, compact tokamaks, and advanced D^3He-tokamaks. The reference designs are ITER-CDA [9]; Burning Plasma Experiment (BPX) Physics Design [10]; and APOLLO [11] and ARIES-III [12] studies. In DT-tokamaks, where diffusion losses dominate the power balance, the choice of confinement scaling is crucial; in D^3He-tokamaks radiation losses are a key issue and have to be described properly. We have checked the validity of Trubnikov's formula for cyclotron radiation [13] with the 1D transport code CYTRAN [14].

3. ITER-studies: We have investigated the effect of τ_{ash}/τ_E on the start-up and fusion burn (Fig. 1). During the start-up, plasma density, temperature and current are ramped up. The ramp-up of the plasma current and the evolution of the plasma configuration are according to the reference ignition scenario of ref. [15]. The plasma density is increased linearly with 50:50 DT-injection until the average electron density reaches its design value of $1.2\times10^{20}\mathrm{m}^{-3}$ at $t = 95$ s. Thereafter the electron density is maintained at a constant level. Simultaneously with the current and density ramp-up, the plasma is heated to the ignition temperature of about 7.5 keV with ca. 27 MW of external heating power (the peak value). The ignition happens at $t \simeq 100$ s.

During the start-up, τ_{ash}/τ_E has only a minor effect on fusion power and ash concentration as seen in Fig. 1. After the ignition the fusion gain is high (the plasma is still rather pure, the ash concentration being about 2% and Z_{eff} about 1.5), and a power excursion lasting about 20 s occurs. However, the final steady state fusion power depends on τ_{ash}/τ_E. According to our calculations, ITER will sustain stable fusion burn if $\tau_{ash}/\tau_E \leq 9$; the critical value of τ_{ash}/τ_E decreases slightly with the plasma density. Our results are in good agreement with ITER-CDA where it is estimated that $\tau_{ash}/\tau_E < 5 - 10$ is required to keep the helium concentration at or below its design value of 10%.

Interesting burn-time transients can take place due to sudden changes in plasma fuelling. Such events are displayed in Fig. 2. Initially, the plasma is in the steady state given by Fig. 1 with $\tau_{ash} = \tau_{part} = 8\tau_E$. A change in fuelling (small enough not to quench the burn (< 20%) or to trigger a disruption because of density or beta limits) gives rise to oscillations in plasma parameters. The oscillations are a clear manifestation of the highly nonlinear nature of burn dynamics and can be explained as follows: A drop in the fuelling rate leads to a decrease in the fuel density and to a momentary increase in the plasma temperature as alpha particles heat up a smaller number of particles. The decrease in fuel density results in a decrease of the alpha particle heating and the plasma starts to cool down. During the cool-down, the fuel burn-up fraction diminishes and the plasma particles are better confined (the confinement time becomes longer due to its power dependence), leading to an increase in the fuel density and, consequently, to an increase in alpha particle heating power and plasma temperature. After a few oscillations, the plasma reaches a new steady state. The sequence of events following an increase in the fuelling rate is similar; in this case the disturbance leads to a build-up of fuel density. When τ_{part}/τ_E decreases, oscillations gradually disappear. These results are consistent with ref. [16] where different equilibrium points of burning DT-plasmas are discussed. Here, however, the dynamical system has a higher dimension as the evolution of ash concentration as well as the temperature relaxation between ions and electrons are taken into account. Because of these effects the centre of oscillation in the (n,T)-plane does not remain fixed during the plasma evolution in Fig. 2.

As a second category of burn-time events we have considered transients caused by sudden changes in the plasma confinement (Fig. 3). Again, the initial state is that of Fig. 1 with $\tau_{ash} = 8\tau_E$. At $t = 400$ s, f_H and the profile exponents are assumed to change within 100 ms. The fuelling rate is kept at a constant level. The basic mechanism of the oscillations in Fig. 3 is the same as in Fig. 2: changes in the fuel density lead to changes in the plasma temperature. From Fig. 3, also the effects due to changes in the plasma profiles are clearly evident. A slight deterioration ($|\delta f_H| < 0.1$) of the confinement, if accompanied by a narrowing of the density profile ($\alpha_n : 0.5 \rightarrow 1$), is not detrimental

to the fusion burn. When, on the other hand, no narrowing of the density profile takes place, an abrupt termination of the fusion burn follows if $|\delta f_H| \geq 0.02$. Because of the density limit, a disruption may appear (due to its power dependence, the confinement time becomes longer as the plasma cools down). An improvement in the confinement leads to an increase in the fuel density and fusion power. In the case of a hard beta limit, a risk of a disruption in a few seconds after the change appears. When a flattening of the temperature profile ($\alpha_T : 1 \rightarrow 0.5$) is included, $\delta f_H > 0.075$ is necessary to sustain the burn.

4. Advanced and compact tokamaks: We have considered the start-up of a D^3He-tokamak [17], both with D^3He-mixture, with DT-ignition (after ignition switching to a D^3He-plasma), and with DT-assistance. In the DT-ignited scheme there is a long (about 5 min) power overshoot with a peak power of approximately 1.6 times the steady state value. By reducing the tritium injection, the duration and peak of the overshoot can be considerably reduced. When compared to the pure D^3He-ignition, the external heating power requirements are reduced in the DT-assisted case from about 175 MW to about 55 MW when the tritium concentration is about 5% during the ramp-up phase.

Qualitatively, burn-time transients in advanced and compact tokamaks are similar to those of ITER described above. The shut-down of D^3He reactors, however, is more demanding. This is because of the higher operating densities and temperatures as compared to DT reactors. In our studies [17] acceptable shut-down scenarios with a simultaneous ramp-down of the plasma current and fuelling rate have been found.

References

[1] D. P. Stotler, et al., Computer Physics Communications, in press

[2] S. K. Ho, et al., Fusion Tech., Vol. **19**, 1322–1326 (1991)

[3] W. A. Houlberg, et al., Nucl. Fusion, Vol. **22**, 935–945 (1982)

[4] G. Kamelander, et al., Fusion Tech., Vol. **25**, 241–248 (1994)

[5] M. H. Redi, and S. A. Cohen, Fusion Tech., Vol. **20**, 48–57 (1991)

[6] W. A. Houlberg, and N. A. Uckan, Fusion Tech., Vol. **21**, 1421–1426 (1992)

[7] T. H. Stix, Plasma Physics, Vol. **14**, No. 4, 367–384 (1972)

[8] P. N. Yushmanov, et al., Nucl. Fusion, Vol. **30**, 1999–2006 (1990)

[9] Anon., *ITER Conceptual Design Report*, ITER Doc. Series No. 18, IAEA, 1991

[10] R. J. Goldston, et al., Fusion Tech., Vol. **21** (1992)

[11] G. L. Kulcinski, et al., Fusion Tech., Vol. **21**, 2292–2296 (1992)

[12] R. L. Miller, R. A. Krakowski, and the ARIES Team, Fusion Tech., Vol. **19**, 802–806 (1991)

[13] B. A. Trubnikov, Rev. of Plasma Physics, Vol. **7**, 345–379 (1979)

[14] S. Tamor, UC–20 Report No. LAPS–72 SAI–023–81–189–LJ (1981)

[15] D. E. Post, et al., *ITER Physics*, ITER Doc. Series No. 21, IAEA, 1991

[16] K. Schoepf, et al., Emerging Nuclear Energy Systems, ICENES'93, 261–265, World Scientific, 1994

[17] M. J. Mantsinen and R. R. E. Salomaa, Emerging Nuclear Energy Systems, ICENES'93, 41–46, World Scientific, 1994

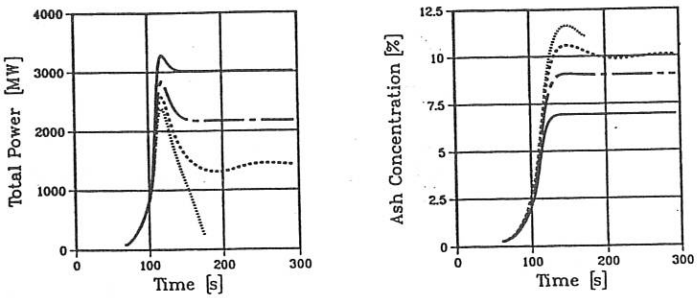


Figure 1. *Fusion power and ash concentration during the start-up and fusion burn when τ_{ash}/τ_E is 4 (solid curve), 6 (chain-dashed), 8 (dashed) and 10 (dotted).*

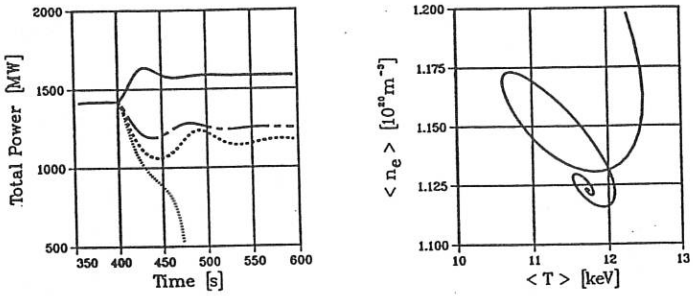


Figure 2. *Evolution of fusion power after fuelling rate is increased by 10% (solid curve) and decreased by 10% (chain-dashed), 15% (dashed), and 20% (dotted) at $t = 400$ s. The trajectory in (density,temperature)-plane after a 15% drop in fuelling.*

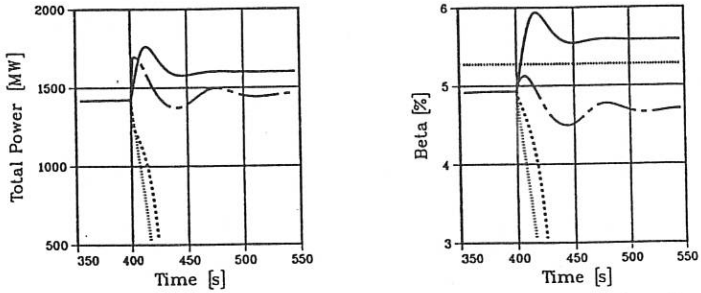


Figure 3. *Evolution of fusion power and total beta after a transition where $f_H : 2 \rightarrow 2.1$, no changes in the profiles (solid curve); $f_H : 2 \rightarrow 1.85$ and $\alpha_n : 0.5 \rightarrow 1$ (chain-dashed); $f_H : 2 \rightarrow 2.1$ and $\alpha_T : 1 \rightarrow 0.5$ (dashed); and $f_H : 2 \rightarrow 1.85$ with constant profiles (dotted). The dotted horizontal line is the Troyon beta limit.*

Vertical instability dynamics analysis

S. Brémond, J.M. Ané, G. Urquijo

Association EURATOM-CEA
Département de Recherches sur la Fusion Contrôlée
Centre d'Etudes de Cadarache, F-13108 Saint-Paul-Lez-Durance, France.

Introduction The problem of the vertical instability of elongated plasmas and/or iron core tokamak plasmas remains a crucial issue for the feedback synthesis of present machines [1] and the design of future ones [2]. The aim of the paper is to characterise the open-loop behaviour of the complete plasma-vessel-coils coupled system, and to analyse the consequences on the feedback design. Analytical expressions are derived from a lumped parameters description. Applications to TORE SUPRA and ITER are presented.

Model The vertical instability, due to the negative curvature of the equilibrium field (fig 1.), is characterised by the well-known decay index $n < 0$, such as :

$$\delta F_{z\,destab} = -\,n\gamma_0^2\delta z \quad NKg^{-1}$$

where $\gamma_0 = \sqrt{\dfrac{|2\pi I_{p0} B_{zext0}|}{m_p}} \approx 10^6\, s^{-1}$

corresponds to the Alfven growth rate.

We consider the axisymmetric rigid-displacement model of a plasma coupled with:

- a passive structure (vacuum vessel, shield...) represented by the leading mode of an expansion of the structure current in harmonic or orthogonal modes [3].
- an active structure (poloidal field control coils) represented by a pair of PF coils (fig 1.)

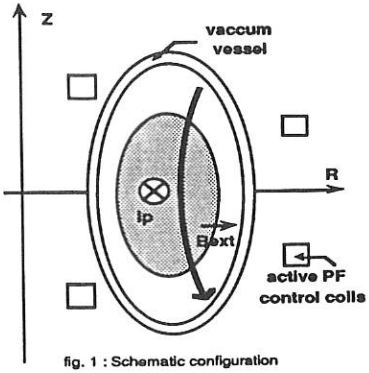


fig. 1 : Schematic configuration

Basic equations The basic equations are the vertical equation of motion and the circuits equations of both structures:

$$\ddot{\delta z} = -\,n\gamma_0^2\delta z + \frac{n_v}{w_v}\gamma_0^2\delta I_v + \frac{n_a}{w_a}\gamma_0^2\delta I_a$$

$$\dot{\delta I_v} = -\gamma_v\delta I_v - w_v\dot{\delta z} - \frac{m_{va}}{l_v}\dot{\delta I_a} \quad \text{and} \quad \dot{\delta I_a} = -\gamma_a\delta I_a - w_a\dot{\delta z} - \frac{m_{av}}{l_a}\dot{\delta I_v} + \frac{1}{l_a}\delta U_a$$

where : γ_v, γ_a are the r/l decay rate of induced current in the passive and active structure respectively. l_v, l_a, m_{va} are the self and mutual inductance of the structures. w_v, w_a are the current induced in an ideal conducting structure by an unit displacement.

n_v, n_a are their critical indexes: $n_{v,a} = \dfrac{I_{p0}}{-\pi B_{ext0} l_{v,a}}\left(\dfrac{\partial M_{pv,a}}{\partial z}\right)^2$. It represents the value of $|n|$ up to which an ideal conducting structure alone can marginally stabilize the plasma displacement. Weighting up the stabilizing efficiency of a structure, it essentially depends on the distance between the structure and the plasma (we suppose $n_v > n_a$).

$\delta I_{v,a}$ and $\delta U_{v,a}$ refers to the antisymmetric part of the structures' currents and voltages.

By Laplace transformations of these equations, the overall transfer function G of the system can be obtained: $G(s) = \frac{\delta z(s)}{\delta U_a(s)} = \frac{num(s)}{den(s)}$

Poles analysis The denominator of G is the characteristic equation of the problem :

$$(1-\lambda^2)x^4 + (\gamma_v+\gamma_a)x^3 + [\gamma_v\gamma_a + \gamma_0^2((1-\lambda^2)n + n_v + n_a - 2\lambda\sqrt{n_v n_a}]x^2$$
$$+\gamma_0^2[\gamma_v(n+n_a)+\gamma_a(n+n_v)]x + n\gamma_0^2\gamma_v\gamma_a = 0$$

where λ is the coefficient of inductive coupling between the active and passive structures : $\lambda = \sqrt{\frac{m_{va}\, m_{av}}{l_v\, l_a}}$

Given the ordering on the growth rates: $\gamma_0 >> \gamma_v >> \gamma_a$ ($\gamma_0 \approx 10^6 s^{-1}$; $\gamma_v \approx 10^2 s^{-1}$ and $\gamma_a \approx 1 s^{-1}$ for TORE SUPRA; $\gamma_v \approx 5 s^{-1}$ and $\gamma_a \approx 0 s^{-1}$ for ITER), we can define two small parameters :

$\varepsilon = \gamma_v / \gamma_0 << 1$ and $\alpha = \gamma_a / \gamma_v << 1$.

Dividing the above equation by γ_0^4, we get a polynomial equation :

$P(n, n_v, n_a, \lambda, \varepsilon, \alpha, x_n) = 0$

where x_n denotes x normalized to the Alfven growth rate. The implicit functions theorem guarantees the existence of an expansion of the solutions in powers of ε and α. By identification, we find (using Landau notation):

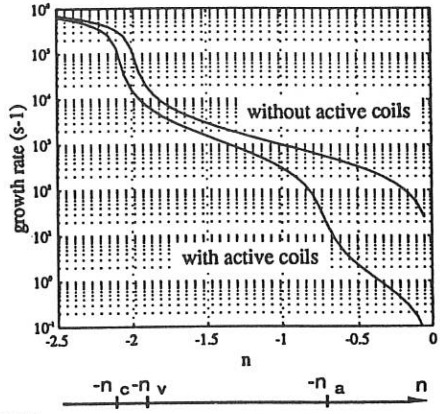


fig. 2 : Growth rate of the open-loop instability as a function of n for typical parameters

$$x_{1,2} = \pm\sqrt{-(n+n_c)\gamma_0} + \frac{n_a - n_c}{2(1-\lambda^2)(n+n_c)}\gamma_v(1+O(\varepsilon+\alpha)), \quad x_3 = -\frac{n+n_a}{(1-\lambda^2)(n+n_c)}\gamma_v(1+O(\varepsilon+\alpha))$$

and $x_4 = -\frac{n}{n+n_a}\gamma_a(1+O(\varepsilon+\alpha))$ where $n_c = \frac{1-2\lambda\mu+\mu^2}{1-\lambda^2}n_v$ and $\mu = \sqrt{\frac{n_a}{n_v}}$

The growth rate of the instability, i.e the maximum real part (noted real) of the roots, is: real(x_1) when $n < -n_c$, real(x_3) when $-n_c < n < -n_a$, and real(x_4) when $-n_a < n < 0$. It is plotted in fig. 2 . The result obtained on the plasma-vessel system alone is given to be compared with.

Two points should be noticed:

- the critical decay index n_c , beyond which the damping effect of eddy currents is unefficient -instability growth rate being then of the order of Alfven growth rate, is found to be higher than the index n_v usually considered (fig.3). This gain on the stability boundary is due to the "passive effect" of the active structure. It occurs even if the only active structure can't passively stabilize the displacement.

It depends on the two parameters λ and μ and is all the more important as these parameters are differents. This result can be explained as follows : the effect of the active structure, which interacts both with the

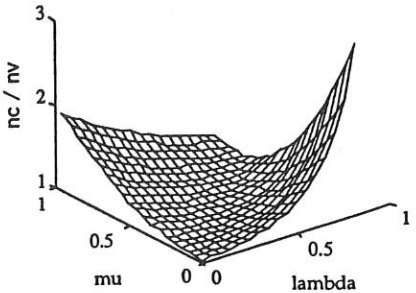


fig. 3 : Dependance of the critical index on the coefficient of inductive coupling and on the stabilizing efficiency ratio of the active and passive structures

passive structure (λ) and the plasma (μ) is all the more favourable as the two interactions do not compete with each other. Close results were noticed in [4].

• when n is higher than n_a , the instability growth rate can be reduced to the decay rate of the active structure.

Zeros analysis The numerator of G is : $K_0\ [(1-\frac{\lambda}{\mu})s+\gamma_v]$ where K_0 is a simple gain.

If $\lambda > \mu$, we find a positive zero: $z = (\frac{\lambda}{\mu}-1)^{-1}\gamma_v$. It means that a counter-effect appears in the response of the system (fig. 5). In this case, when a voltage is applied to the poloidal control coils, the plasma tends initially -typically during a period of the order of the passive structure time constant- to react in the opposite way of his steady state response. As a matter of fact, during this period, the eddy currents in the passive structure, which play the main part in the displacement of the plasma, oppose the control coils voltage.

This effect, which characterises what is called in control theory a "non minimum phase system", may have serious implications as we shall see in the following.

Applications

TORE SUPRA: The condition $n > -n_a$ is most of the time fulfilled in Tore Supra (fig 4). It could explain that no violent vertical instability has been observed despite the destabilizing effect of the transformer iron core. The counter effect, if present, doesn't cause any trouble in pratice, as his time scale is by several orders lower than the dominant dynamics of the system [6].

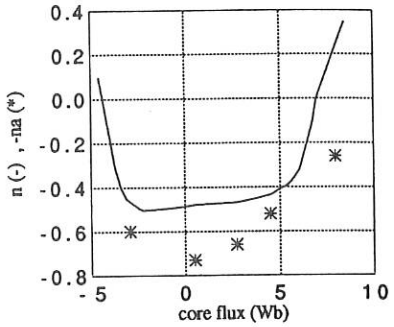


fig. 4 : Decay index and active critical index versus the iron core flux in TORE SUPRA

ITER: We have typically [5] : $n \approx -0{,}5$; $n_v \approx 2$ (from the ideal stability margin with the only passive structure $m_s \approx 3$); $n_a \leq 0.2$ so $\mu \leq 0.35$ and $\lambda \approx 0.6$

Hence we find $\gamma \approx 0.28\gamma_v$, which is approximatively 20% lower than the value we get if we only consider the passive structure. This order of the gain is confirmed by the codes simulations (PF coils open or shorted [5]).

Yet, a counter-effect (fig. 5) will certainly occur as the critical active index is low. It is of great importance for ITER, as the counter-effect duration is of the order of the growth time of the open-loop instability, which indicates the time scale on which the feedback must efficiently react. It imposes intrinsic constraints on the feedback design, notably with regard to robustness.

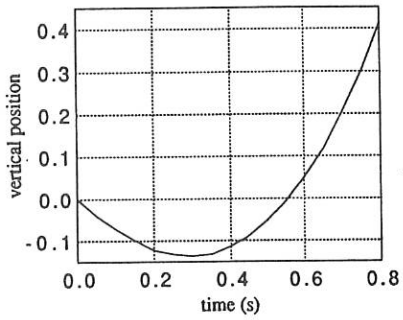


fig. 5 : Response to a step in the control coils voltage

More precisely, these limitations on performances can be expressed in terms of the sensitivity function of the problem. Let's consider the standard feedback configuration (fig 6) where G represents the transfer function of the tokamak and K the feedback compensator. d represents input disturbance and/or error modelling and m measurements errors.

From fig.6., we can write:

$$z = T\ z_{ref} + S\ d - T\ m$$

where T is the closed-loop transfer function and S is called the sensitivity function:

$$S = \frac{1}{1+GK}$$

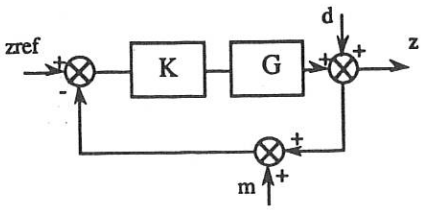


fig. 6 : Standard feedback configuration

$S(j\omega)$ characterises the rejection of input disturbance and/or error modelling as a function of the frequency ω. Moreover, $1/\|S\|_\infty$ ($\|S\|_\infty = \max_\omega |S(j\omega)|$) measures the distance from the critical point of the Nyquist stability diagram, and so denotes a closed-loop stability margin.

The open-loop unstable pole imposes a lower bound on GK bandwith [6] and consequently imposes to keep S small up to frequencies about γ_v. Intuitively, it means that we must "keep in the loop" the signals whose frequencies are on the range of the open-loop instability growth rate, in order to significally counter-react against them, and so assure stability.

On the contrary, the positive zero roughly imposes an upper bound on GK bandwith [6] and therefore prevent S to be very small up to γ_v. Intuitively, the presence of a systematic counter-effect limits the capability of tracking signals on a faster time scale than the counter-effect period. If one tries to push the sensitivity lower on a larger frequency range, we get a peak value of S at some higher frequency and consequently a worse stability margin. This phenomenon, known as the waterbed effect [7] is all the more serious as the unstable pole and the positive zeros are close together [8].

In brief, we are likely to have very difficult tradeoffs to make, and that, whatever the feedback design method, as these limitations are independant of the compensator.

Conclusion The analytical expressions obtained through a simple description of the plasma-vessel-active coil system sets:

- the passive role of the PF control coils, which can lower the open-loop instability growth rate (e.g about 20 % in ITER), and even reduce it to a low active decay rate (e.g. in Tore Supra).
- the major importance of the relative value of the inductive coupling coefficient of the structures, and the ratio of their damping efficiency, on the dynamics of the system.

More precise conclusions would require full MHD equilibrium calculations. Yet, the counter effect seems to raise a crucial issue for ITER plasma controllability and robustness. This is all the more important as it puts limitations on close-loop performances which are independant of any particular feedback design.

Acknowledgements: S. Bremond wants to thank Dr. D. Viault for fruitful discussions and Dr. F. Colledani for precious advices concerning feedback notions.

References:

[1] : T. Bonicelli, M. Garribba, P.L. Mondino, P. Noll, in JET Contributions to the 15th SOFE, Hyannis, Mass, USA, JET-P88 (1993).
[2] : S. Nishio, M. Sugihara, Y. Shimomura, in Fusion Engineering and Design 23, 17 (1993).
[3] : E.A. Lazarus, J.B. Lister, G.H. Neilson, Nuclear Fusion 30, 111 (1990).
[4] : E.A. Lazarus et al., Phys. Fluids B3(8), 2220 (1991).
[5] : ITER TAC 4-05, Poloidal field system (1994).
[6] : J.M. Maciejowski, Multivariable feedback design, Addison-Wesley, 24-36 (1989).
[7] : J.S. Freubenberg, D.P. Looze, IEEE Transactions on automatic control, AC-30, 555 (1985).
[8] : J.C Doyle, B. A. Francis, A.R. Tannebaum, Feedback Control Theory, Mac Millan, 90-104 (1992).

Topic 5

Plasma Edge Physics

A Numerical Study of Plasma Detachment Conditions in JET Divertor Plasmas

R Simonini, G Corrigan, G Radford, J Spence, A Taroni, S Weber
JET Joint Undertaking, Abingdon, Oxon., OX14 3EA, UK

Introduction

The problem of determining the conditions for plasma detachment and extinction in JET divertor plasmas, in order to reduce particle and energy loading onto the dump plates, has been studied by means of the EDGE2D/U chain of codes [1].

Detachment is characterised by a drop in particle, pressure and energy fluxes to the target. This phenomenon has been observed in several Tokamaks, including JET. A possible explanation for the pressure drop [2,3] is that if a region of low temperature (a few eV) and not too high density can be established in front of the targets, then in this region charge exchange dominates over ionisation and becomes an efficient means to remove "parallel" momentum from the plasma to the vessel. However, efficient power dissipation cannot be obtained at relevant values of SOL input power in a pure plasma, as found in predictions for the JET Mk I divertor [4], where the need was shown for a means of dissipating enough power to achieve extinction. Experiments show evidence [5] for the role of carbon in detachment in JET. The results reported here refer to two ('gas box') divertor configurations being considered for possible future upgrade of the JET divertor for extrapolations to ITER.

The modelling assumptions can be found in Refs. [6] and [7]. For boundary conditions, we have assumed that no energy is conducted to the vessel wall ($\nabla_\perp T=0$), but density has a prescribed radial decay length of λ_n = 0.5 and 0.2 cm at the outer mid plane and in the private region, respectively.

Dependence of Detachment on Density, Power, Geometry and Radiation

Table 1 summarises the results obtained for an equilibrium configuration (I_p=4.5 MA) in the gas box divertor with either flat (F) dump plates (cf. Fig. 2), or with the plasma hitting the side walls (V). By changing the particle inventory $2\pi N$ in the boundary region we have performed scans of the density at the separatrix mid-plane, n_s, for several values of the power input to the SOL. In the case of a pure plasma (impurity radiation P_{RI}=0) and input power P_e=P_i=5 MW, as n_s increases from about 2.3×10^{19} m^{-3} to 5.5×10^{19} m^{-3}, the fraction $P_t/(P_e+P_i)$ of input power onto the targets drops from 47% to 14% in the F configuration.

The ratio f_p of the pressure at the mid-plane to the pressure at the targets, which depends on the efficiency of dissipating parallel momentum either by interaction with the neutrals or by radial transport to the vessel wall, rises from 2 to 12, and from 4 to 60, along the separatrix and along a field line approximately 1 cm outboard, respectively. An average of the pressure at the targets is taken, the in-out asymmetry being small, less than 20%.

Similar calculations performed for the JET Mk I divertor [4], where no power is allowed to flow to the wall ($\nabla_\perp n=0$) have shown that, although the volume power loss terms in a pure plasma are more efficient at higher densities, they do not seem sufficient to cause detachment at this power level. In the present case, however, an additional power dissipation mechanism is at work, namely wall loading P_W, which rises from 23% to 48% of the input power as n_s increases. The power loss P_{RH} (charge exchange + hydrogen radiation), instead, does not vary much.

Since a high flow of hot particles to the walls may not be desirable, and in order to achieve better detachment with a larger drop of the particle flow to targets, radiation induced by impurities (either sputtered from the walls or puffed in) could be exploited to reduce the energy content of the SOL. However, the additional power loss would be offset to a certain amount by a reduction in the power removed by hydrogenic atomic physics processes, owing to a reduction in recycled neutrals.

For this purpose, we carried out a series of simulations using a simple formula for the radiation efficiency proposed in [8] to simulate the radiation due to a mixture of carbon and oxygen in an otherwise pure plasma, rescaled in order to obtain a prescribed value of the total radiated power, P_{RI}. The main results obtained with this approach have also been reproduced by simulations with a consistent treatment of impurities, as discussed later.

It is found that if sufficient power is radiated such that T<5 eV at the targets, namely when the ionisation rate starts to drop rapidly with respect to charge exchange, detachment can be obtained at large enough values of P_{RI} for a given input power P, and it improves as P-P_{RI} decreases, as shown by f_p and the particle flux onto the targets, Γ_t.

The V configuration enters the regime of detachment more easily than the F configuration, since in the V configuration, the neutrals are recycled preferentially toward the separatrix, thus reducing the temperature there.

It is apparent that similar levels of detachment are obtained for similar values of P-P_{RI}, while P itself, the input power flowing into the SOL, is less important.

Effect of a Recycling Impurity and Gas Puffing.

A proper assessment of all the consequences of impurity radiation requires the simulation of the spatial impurity distribution by taking impurity transport into account. Several runs have been performed with the full multi-species EDGE2D/U code.

Since carbon or beryllium alone are unlikely [4] to produce the required amount of radiation by physical sputtering alone, we have considered the injection of neon, a recyclable impurity, into the SOL from all round the vessel. In the calculations reported here for the F configuration, the neon injected amounts to 0.3% of the hydrogen inventory, the input power is $P_i=P_e=$ 5 MW. Since the injected impurity could contaminate the bulk plasma, we have also assessed whether an induced flow of plasma is able to keep the impurity in the divertor region.

To this end, gas is extracted from the bottom of the divertor chamber. The pumping efficiency has been estimated by Monte Carlo calculations [9]. The neutral albedoes are A_1=92% and A_2=45%, at the bottom of the divertor box. The deuterium extracted is then fed back into the SOL, at the top in order to maximise the extension of the induced flow which by friction tends to carry the impurities toward the dump plates.

Fig. 1 shows the average impurity density in the plasma boundary, from the outer target to the inner target, for $N=10x10^{19}$, without and with puffing. The enhanced entrenchment of neon due to the deuterium flow is clear. Better retention here implies that with deuterium puffing the neon radiation decreases from 3.5 MW to 2.5 MW. The pressure drop fits well with that computed from the simple formula for the same level of radiation.

We present in Fig. 2 contour plots for the impurity radiation, with neutral deuterium pumping. The induced flow makes the radiation pattern more in-out symmetric, and whereas without puffing the maximum radiation is near the X point, the enhanced impurity retention due to the puffing moves the maximum near the outer dump plate.

Conclusions

Results obtained so far confirm that for a given particle inventory in the SOL (including the divertor), the main parameter determining whether or not particle, momentum and energy detachment occurs is the residual power $P-P_{lost}$, where P is the total power entering the SOL and P_{lost} is the power lost by transport to walls and by volume losses in the SOL outside the region where detachment takes place.

For particle contents leading to reasonable values of the separatrix mid-plane density ($n_s<4x10^{19}$ m^{-3} in JET), detachment is found if the residual power is low enough. Typically the residual power must be $\leq$3 MW for good detachment, with the exact value depending on the geometry of the divertor, the transport assumptions and the neutral recirculation scheme.

The results show that divertor plasma conditions relevant for the study of power exhaust and impurity control problems are possible in JET.

Acknowledgements: K Borras, E Deksnis, P Harbour, L Horton, A Loarte, G Matthews and G Vlases are acknowledged for useful discussions.

References

[1] R Simonini, G Corrigan, G Radford, J Spence, A Taroni, Contrib. to Plasma Phys. 34(1994)368

[2] K Borras, P Stangeby, 20th EPS Conf., Lisbon 1993

[3] P Stangeby, Nucl. Fus. 33(1993)1695

[4] A Taroni, G Corrigan, R Simonini, J Spence, S Weber, 11th PSI Conf. Mito, Japan (1994)

[5] L D Horton, "Detached Plasmas in JET", this Conference.

[6] A Loarte et al, 11th PSI Conference, Mito, Japan(1994)

[7] A Taroni, G Corrigan, R Simonini, J Spence, G Vlases, Contrib. to Plasma Phys. 34(1994)448

[8] R Schneider, B Braams, D Reiter et al., Contrib. to Plasma Phys. 33(1992)450

[9] E Deksnis, private communication

Cf	N 10^{19}	$P_{e,i}$ MW	P_{RI} MW	n_s 10^{19} m^{-3}	P_t MW	P_w MW	f_p sep	f_p 1cm	P_{RH} MW	Γ_t 10^{23} s^{-1}
F	5	5	0	2.3	4.7	2.3	2	4	3.1	5.8
"	"	"	2	2.3	3.2	2.0	2	8	2.7	3.8
"	"	"	4	2.2	1.9	1.7	3	10	2.3	3.4
"	"	"	6	2.0	0.7	1.4	20	40	1.8	1.6
"	10	5	0	3.9	2.7	3.7	4	10	3.4	5.0
"	"	"	2	3.8	1.7	3.3	7	30	3.0	3.4
"	"	"	4	3.4	0.7	2.7	26	67	2.5	1.8
"	"	"	6	3.1	0.3	1.7	300	300	2.0	0.4
"	"	10	0	4.0	8.9	5.2	2	8	5.8	11.8
"	"	"	5	3.8	6.0	4.1	2	11	4.8	9.1
"	"	"	10	3.5	2.6	3.3	5	40	3.6	5.1
"	"	"	15	2.6	0.5	1.9	160	300	1.6	0.7
"	15	5	0	5.5	1.4	4.8	12	60	3.5	3.1
V	5	"	0	3.0	3.9	2.4	10	5	3.6	6.2
"	"	"	3	2.8	2.0	2.0	34	11	3.0	3.8
"	"	"	6	2.3	0.6	1.5	150	55	2.0	1.4
"	10	"	0	5.0	2.2	4.0	40	17	3.8	5.0

Table 1

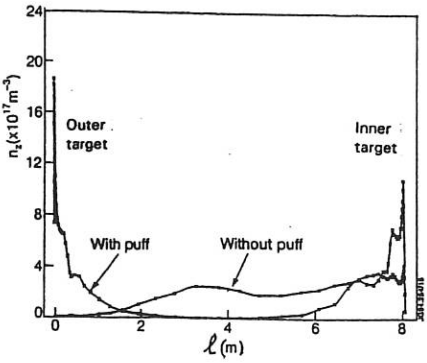


Fig.1 Average impurity density in SOL, F configuration, N=10x10^{19}

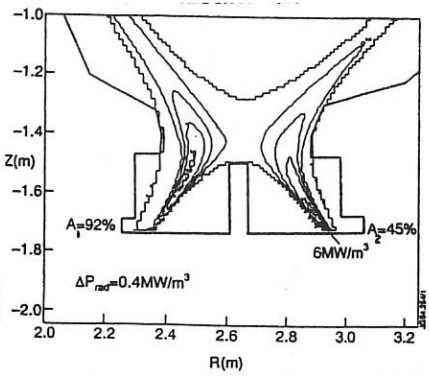


Fig 2 Contour plot of radiation with deuterium puffing. P_{RI}=2.5 MW

Detached Divertor Plasmas in JET

L.D. Horton, K. Borrass, G. Corrigan, N. Gottardi, J. Lingertat, A. Loarte, R. Simonini, M.F. Stamp, P.C. Stangeby[1], and A. Taroni
JET Joint Undertaking, Abingdon, Oxon, United Kingdom, OX14 3EA
[1]Institute for Aerospace Studies, University of Toronto, North York, Ontario, Canada

During 1991/92 a series of experiments was performed in which the divertor density was raised to the point where a sudden reduction of the particle flux to the target plates occurred [1]. The radiation from these detached plasmas can be as high as 90% of the input power, thus making it possible to run discharges with input energies far above what would otherwise be the limit of the target tiles. The primary diagnostics for assessing the radiation from these plasmas are, of course, the bolometer arrays. During 1991/92 there were three such arrays, two spanning the entire plasma as viewed from a main horizontal port (R = 5.8 m, Z = +/-0.5 m), and one vertical camera which viewed virtually the entire plasma except the divertor. In addition, there is data available from a CCD camera and from several discrete visible spectroscopy views. The geometry of the plasma and of these visible lines-of-sight are shown in Fig. 1. The divertor target tiles shown as boxes in Fig. 1 were made of beryllium while the rest of the divertor region was covered with graphite. This significantly complicates the analysis, since both surfaces quickly become a mixture of the two elements.

PLASMA MODELS

In order to estimate the power radiated from detached plasmas, some model of the background plasma is required. Ideally, one would construct a completely self-consistent model including the radiation losses from the various plasma species. In reality this is still not possible and compromises are necessary. Here two models of the background plasma are constructed and the resulting radiation patterns compared with experiment.

An analytic model for detached plasmas has been proposed whereby the plasma momentum along open field lines is reduced by neutral-ion charge exchange collisions [2,3]. In this model the SOL is divided into two regions, one dominated by ion-neutral collisions and the other by ionisation and electron heat conduction:

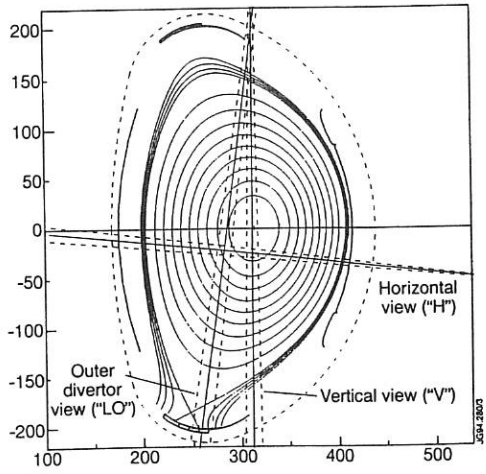
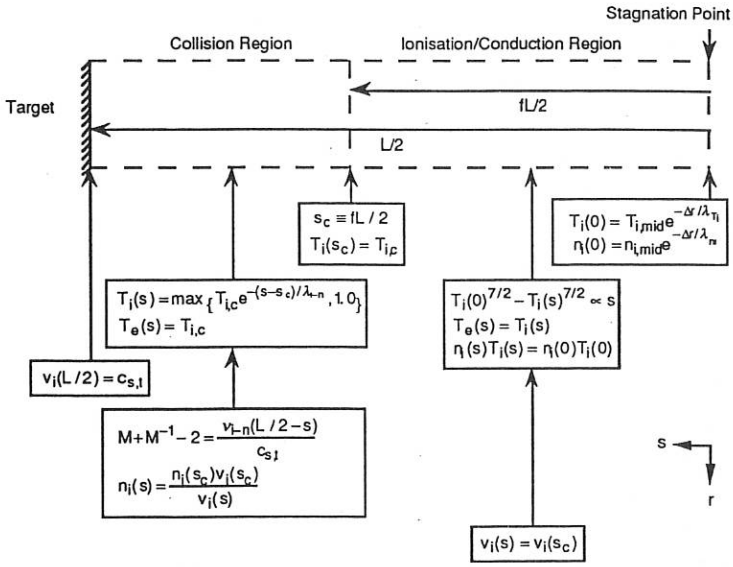


Figure 1: Viewing lines of the visible spectroscopy overlaid on the plasma magnetic geometry for JET pulse 26848.



There are seven inputs to this model: f, the position of the entrance of the collision region as a fraction of the SOL length (0.55 in the simulations shown below); $T_{i,mid}$, the ion temperature on the separatrix at the stagnation point (75 eV); $n_{i,mid}$, the ion density on the separatrix at the stagnation point (4.3×10^{19} m^{-3}); λ_{T_i}, the ion temperature scrape-off length at the outer midplane (2 cm); λ_{n_i}, the ion density scrape-off length at the outer midplane (2 cm); $T_{i,c}$, the ion temperature at the entrance to the collision region (2 eV); and λ_{i-n},the ion-neutral elastic collision mean-free-path (50 cm). The advantage of this model is its flexibility in describing different lengths and therefore volumes of the collision region. This must be set against the fact that the plasma so derived is not self-consistent.

Recently, the two dimensional fluid code EDGE2D/U has been applied to the simulations of detached plasmas [4]. In some of these simulations, a first attempt at assessing the effects of impurity radiation was made using a radiation loss term first used to model carbon radiation from ASDEX plasmas [5]:

$$Q_{rad} = \alpha_{imp} n_e^2 \left(\frac{2 \cdot 10^{-18} \, \text{erg} - \text{cm}^3/\text{s}}{(T_e/15\text{eV})^{1.5} + (T_e/15\text{eV})^{-3}} \right)$$

In these simulations, the value of α_{imp} is spatially constant and is adjusted at each time step so as to give a prescribed total radiated power. When this total power is raised to a certain level the divertor plasma detaches, with a significant drop in the ion current to the target plates, as observed in experiment. For the background plasma used below it was assumed that 10 MW of the 15 MW input power enter the annular calculational grid, with the other

5 MW supposed lost due to radiation from the core. In addition, 6 MW of impurity radiation was assumed, roughly matching the measured total radiated power.

COMPARISON WITH EXPERIMENTAL RESULTS

In order to assess the radiation from different hydrogen and impurity species, the two background plasmas were used as input to the DIVIMP impurity transport code [6], which has been coupled to NIMBUS, the same neutral transport code used with EDGE2D/U. In each case, two DIVIMP runs were performed, one assuming the targets to be pure beryllium (run A/Be for the analytic plasma background and run E/Be for the EDGE2D/U background plasma) and the other pure carbon (runs A/C and E/C). Comparison of the code results with experiment is given in Table 1.

The most obvious discrepancy between model and experiment is in the radiated power. In addition, neither carbon simulation can reproduce the observed carbon emission even assuming that the beryllium tiles behave as though they were pure carbon. In contrast, there is generally good agreement between simulation and experiment for the beryllium signals. Thus, it is concluded that beryllium cannot be the main radiating species.

In contrast to the beryllium profiles, the deuterium radiation is not well modelled by the EDGE2D/U simulation. The ratio of measured to simulated D_α is 3 at the target, suggesting the source there is approximately correct, while the same ratio is 70 along the vertical chord. By varying the length of the collision region in the analytic model, it is possible to study the variation in deuterium leakage from the divertor and the accompanying affect on radiated power. The analytic background plasma shown in Table 1 was the most successful attempt at reproducing the deuterium signals. Such a match requires a cold plasma which extends far beyond the X-point into the SOL. Even in such an extreme example, the total deuterium radiation is less than 1 MW and does not account for the measured radiated power.

There are three possible reasons for the discrepancy between the predicted and measured carbon content of the plasma. Firstly, the plasma is not in steady state. These plasmas were ELMy throughout. Due to the limitations of the probes, the plasma we model is that which is seen between ELMs. Secondly, chemical sputtering from the targets and from the walls may play an important role in carbon release at the these low temperatures. Thirdly, non-thermal distribution functions may be important. In cases where the bulk of the plasma is below the physical sputtering threshold, a small fraction of fast particles would dominate the impurity yield. With this in mind, it is tempting to scale the carbon content of the plasma to the influx measured at the outer target. This would result in a radiated power of 16 MW. It also, however, results in an order of magnitude overprediction of the carbon signals along the vertical and horizontal channels. The carbon radiation will, however, be dominated by such a large source at the target.

	Exp.	E/C	E/Be	A/Be	A/C
Total Radiated Power (MW)	11.5	0.41	0.54	0.96	0.86
Impurity Radiation (MW)	-	0.026	0.16	0.10	0.003
Hydrogen Radiation (MW)	-	0.38	0.38	0.86	0.86
Isat inner (A/cm^2)	1-2*	14	14	7.3	7.3
Isat outer (A/cm^2)	3-4	10	10	2.3	2.3
D_α (LO)	5^{20}	1.6^{20}	1.6^{20}	4.5^{20}	4.5^{20}
D_α (V)	9^{19}	1.3^{18}	1.3^{18}	5.6^{19}	5.6^{19}
D_α (H)	1^{19}	3.2^{17}	3.2^{17}	1.2^{18}	1.2^{18}
Be II 4361 (LO)	5^{17}	-	2.5^{17}	9.9^{16}	-
Be II 5270 (V)	1^{16}	-	7.5^{15}	2.8^{15}	-
Be II 5270 (H)	2^{15}	-	3.0^{15}	1.9^{15}	-
C II 6578 (LO)	1.5^{18}	2.5^{15}	-	-	2.0^{14}
C III 4647 (V)	1.5^{18}	3.1^{16}	-	-	1.0^{15}
C III 4647 (H)	7.5^{17}	2.0^{16}	-	-	4.5^{15}

*Table 1: Comparison of experimental measurements with signals synthesized from the four different simulations described in the text. *The measured ion saturation current from the inner probe is known to be low due to shadowing by the target tile .*

CONCLUSIONS

In simulations with high radiated power fractions, it is possible to produce the drop in ion current to the divertor targets typical of detached plasmas. Despite the fact that these experiments were performed on beryllium target tiles, radiation from deuterium and beryllium cannot account for the measured power losses. The neutral deuterium levels in the SOL in these plasmas are higher than the model predicts. This may be due to leakage from the divertor or to additional wall sources related to the non-steady nature of these plasmas. In contrast, a surprisingly high level of carbon is present in these discharges; higher even than would be predicted were the divertor target tiles pure carbon. This level may well be large enough to produce the measured radiation, but more detailed information on the source profile is required.

[1] S. Clement, S.K. Erents, N. Gottardi, *et al.*, 19th EPS Conf. on Contr. Fusion and Plasma Phys., Innsbruck (1992) II-723.
[2] K. Borrass and P.C. Stangeby, 20th EPS Conf. on Contr. Fusion and Plasma Phys., Lisboa (1993) II-763.
[3] P.C. Stangeby, Nucl. Fusion **33** (1993) 1695.
[4] A. Taroni, G. Corrigan, R. Simonini, J. Spence, and S. Weber, to be published in the proceedings of the 11th PSI Conference, Mito (1994).
[5] R. Schneider, B. Brahms, D. Reiter, *et al.*, Contributions to Plasma Phys. **33** (1992) 450.
[6] P.C. Stangeby and J.D. Elder, J. Nucl. Mater. **196-198** (1992) 258.

DIVERTOR STUDIES FOR OPTIMIZED HELIAS CONFIGURATIONS

E. Strumberger

Max-Planck-Institut für Plasmaphysik
IPP-EURATOM Association, D-85748 Garching bei München

Divertor design plays an important role for present and future fusion devices in order to overcome the problems of power and particle exhaust, and of impurity control. The diversion properties of optimized Helias configurations [1] had therefore been investigated in order to assess these difficulties. Although divertor operation was not an original objective of the optimization procedure, these investigations led to a divertor concept [2]: positioning of five divertor plates called helical troughs at a distance of $\frac{1}{5}$ of the plasma radius outside the last closed magnetic surface (lcms) along the so-called helical edges [3]. Given this situation and structural differences as compared to the axisymmetric tokamak, namely significantly larger aspect ratio and an ergodized edge, it appears worthwhile to pursue a divertor concept based upon small angles of incidence and large wetted areas to obtain a moderate and as uniformly as possible distributed power load on the divertor plates. A suitable way has been found to design such divertor plates. Here, the divertor design is briefly described and the most important results are summed up, while a more detailed account of this work will be given in the near future [4].

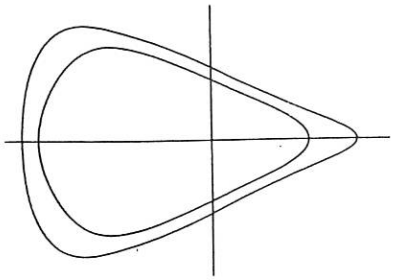


FIG. 1. Last closed magnetic surface (inner line) and 'fictitious' flux surface (outer line) in the edge region for the triangular cross-section.

Using a typical vacuum magnetic field configuration for W7-X [5], the NEMEC code [6] is an effective tool in order to find surfaces with small angles of incidence and a relatively homogeneous distribution of intersecting field lines, because it is shown to construct surfaces nearly tangential to the field lines in the region beyond the lcms. Figure 1 shows such a surface in the edge region. The average intersection angle of the field lines at this surface is $\approx 0.2°$ and the maximum angle is below $2.5°$ which confirms that this surface is nearly tangential to the field lines in the edge region.

Previous calculations showed that field lines coming close to the lcms - these field lines carry most of the particle and power load to the divertor plates - intersect a surface outside the last closed magnetic surface only on narrow stripes along the helical edges. Therefore, again so-called 'helical troughs' are defined as divertor plates which are parts of the 'fictitious' flux surface obtained by the NEMEC code. Figure 2 shows two examples for three characteristic cross-sections. In case 1 the 'fictitious' flux surface, shown in Fig. 1, is used. Because of the structure of the magnetic field configuration and, therefore, of the surface approximating this structure, the outer parts of the helical troughs (close to their poloidal and toroidal boundaries) come close to the lcms at certain positions, e.g. ≈ 3 cm distance between lcms and edges of the troughs at the bean-shaped cross-section ($v = 0$) (the coordinates (s, u, v) are explained in [2]). At these positions the leading

edge problem occurs. In order to overcome this problem and to preserve the positive properties, namely small angles and large wetted areas, in case 2 the outer parts of the plasma-facing surfaces of the troughs are bent away from the lcms while the inner parts are kept fixed. Here the minimum distance between lcms and plasma-facing surfaces of the troughs is ≈ 5 cm at $v = 0$. As the figure of the triangular cross-section ($v = 0.5$) shows, the plasma-facing surfaces of the troughs intersect the first wall used here (dotted line) at certain positions. This means, that using the present coil configuration there may not be enough space for this kind of divertor plates. One possibility to solve this problem is to create more space at these positions by varying the form of the coils. This variation or even the incorporation of the divertor operation into the coil optimization procedure is an aim for future investigations [7].

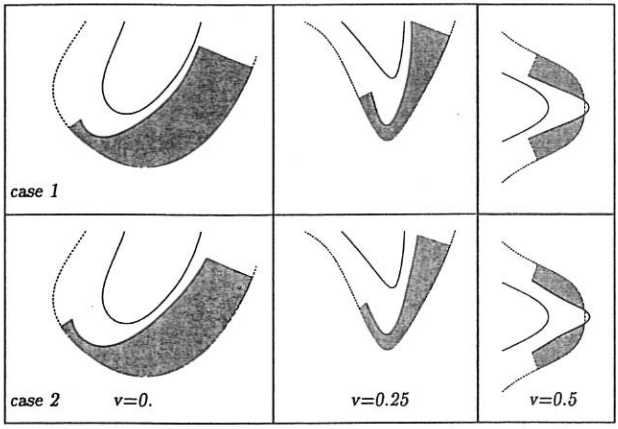


FIG. 2. Parts of three characteristic cross-sections (columns 1-3) for two different troughs (rows 1-2). The innermost lines show the lcms, and the dashed lines mark the first wall. The lines in front of the helical edge show the plasma-facing surfaces of the troughs, while the grey areas represent the space available for the divertor equipment between the plasma-facing surfaces and the first wall.

To study the divertor properties of the helical troughs defined above, magnetic field lines are started at the plasma-facing surfaces of the troughs and traced until they and at the troughs. When these field lines are ordered according to their lengths, ordered layers are found. The longest field lines ($2L > 200$ m) form the innermost layer close to the lcms, while the field line length decreases with increasing distance from the lcms. The magnetic field lines forming the different layers map ordered areas on the helical troughs onto each other. Field lines forming the innermost layer intersect the central parts of the plasma-facing surfaces of the helical troughs in more or less narrow stripes. These parts of the intersection pattern are surrounded by areas formed by field lines of the next layers, while the field lines of the outermost layer intersect the outer regions of the divertor plates. That is, ordered areas on the troughs correspond to ordered layers in the edge region [4, 8, 9].

Calculation of the mean angle of incidence, $\langle\Psi\rangle$, and the intersection area, A, of the magnetic field lines belonging to one layer (layer 1: $2L > 200$ m, layer 2: $100 < 2L \leq 200$ m, layer 3: $45 < 2L \leq 100$ m, layer 4: $15 < 2L \leq 45$ m, layer 5: $2L \leq 15$ m) yields the results presented in Table I. There clear improvements are shown with respect of large wetted areas and small angles of incidence for the divertor configurations case 1 and 2 in comparison with a previously used plate configuration named case 3 [8, 9]. For the cases 1 and 2 an increase of at least a factor 5 has been obtained for the areas formed by the

very long field lines (layer 1 and 2), while for the third layer the increase is even larger. Furthermore, in connection with the increase of the wetted areas the mean intersection angles decrease by approximately the same factor for the inner layers.

TABLE 1

layer	case 1		case 2		case 3	
	$\langle\Psi\rangle$ (°)	A (m^2)	$\langle\Psi\rangle$ (°)	A (m^2)	$\langle\Psi\rangle$ (°)	A (m^2)
1	0.7	1.2	0.8	1.1	2.3	0.2
2	0.6	1.4	0.7	1.3	2.6	0.3
3	0.4	10.5	0.9	8.0	2.0	0.2
4	0.4	23.7	1.2	15.4	2.1	4.9
5	0.2	18.8	1.6	33.5	2.7	32.7

Perpendicular electron transport in the edge region of tokamaks as well as stellarators is found to be anomalous as a consequence of turbulence and/or destruction of magnetic surfaces [10]. Therefore, Monte Carlo methods which make use of standard assumptions of scrape-off layer (SOL) modeling [11], and which are described in detail in [2,3], are used to simulate the energy transport across the field lines by 'diffusion' of field lines. With diffusion taken into account, the foot points of the long field lines are spread over a larger area on the troughs as shown in Table II. The wetted area formed by field lines which are longer than 100 m is more than twice as large as in the case without diffusion, and the mean field line length of the long field lines $2L > 100$ m is also reduced.

TABLE II

layer	without diffusion		with diffusion	
	A (m^2)	$\langle 2L\rangle$ (m)	A (m^2)	$\langle 2L\rangle$ (m)
1	1.1	545	2.0	298
2	1.3	151	3.8	143
3	8.0	70	5.9	63
4	15.4	28	16.3	28
5	33.5	7	31.2	7

The wetted area for field lines which are longer than 100 m and which form the inner part of the SOL amounts to ≈ 6 m^2. Assuming that a substantial part of the power flows along these field lines to the divertor plates, one obtains a quite small average power load of $P_e/A < 2$ MW/m^2 for a power flow of $P_e \approx 10$ MW, which is a typical value expected for W7-X.

In order to obtain a more detailed estimate of the power load which makes use of the detailed field line structure of the SOL, the Monte Carlo calculations have been combined with a simple 1D transport model which is described in detail in [9]. Whithin this model simple 1D transport equations are solved along 3D field lines for which diffusion has been taken into account. In order to solve these 1D transport equations, a scrape-off layer has been defined, i.e. a region in which the volume heat source - representing the flow of heat from the main plasma - loads the field lines. Its thickness is a parameter that has to be determined by energy conservation within the model used here. Together with typical SOL parameters for W7-X, the information on the field line positions relative to

the SOL plasma region and boundary conditions corresponding to small temperatures at the plates, one-dimensional fluid solutions along the field lines have been obtained.

Averaging over the power flux which flows along the 'diffusive' field lines to the divertor plates yields the power load on the plasma-facing surfaces of the helical troughs. The maximum power load is less than 9 MW/m^2, and only a small part of the total power of 10 MW, namely $\approx$ 0.6 MW, flows to the divertor plates with a power load greater than 5 MW as Fig. 3 shows. Figure 4 shows the spatial distribution of the power load as a function of the poloidal length measured from the upper boundary of the helical trough for a certain toroidal region, namely for $0.453 < v < 0.458$, which contains an area with a relatively high power load. The maximum power load in this area is $\approx$ 6 MW and its poloidal width is $\approx$ 0.025 m. The total width of the helical trough at this toroidal position is given by $\approx$ 0.9 m. The peak value of the power load occurs at the triangular cross-section and amounts to 8.5 MW/m^2, while the poloidal width of this peak is $\approx$ 0.01 m.

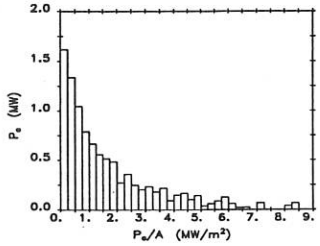


FIG. 3: Histogram of the total power flow reaching the five troughs as a function of the power load.

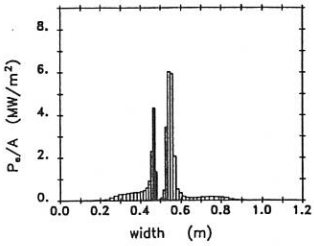


FIG. 4: Histogram of the power load as function of the poloidal width of the plasma-facing surface of a trough at the toroidal cross-sections $0.453 < v < 0.458$.

Up to now, in this simple model many physics ingredients (e.g. the interaction with neutrals in front of the plates, the simulation of the cross-field transport with local SOL parameters) have not been considered so that it is likely that these few isolated peaks of the power load existing on areas of a few cm^2 disappear or at least become smoothed out in a more detailed model.

REFERENCES

[1] Nührenberg, J., Zille, R., Phys. Lett. A **114** (1986) 129, Phys. Lett. A **129** (1988) 113.
[2] Strumberger, E., Nuclear Fusion **32** (1992) 737.
[3] Nührenberg. J., Strumberger, E., Contrib. Plasma Phys. **32** (1992) 204.
[4] Strumberger, E., et. al., to be submitted for publication.
[5] Merkel, P., Kisslinger, J., Proc. 19th Europ. Conf. on Contr. Fusion and Plasma Physics, Innsbruck 1992, ECA, **16C**, Part I, 585.
[6] Hirshman, S.P., Van Rij, W.I., Merkel, P., Comput. Phys. Comm. **43** (1986) 143.
[7] Merkel, P., private communication.
[8] Strumberger, E., Proc. 20th EPS Conf. on Contr. Fusion and Plasma Physics, Lisboa 1993, ECA, **17C**, Part II, 791.
[9] Strumberger E., Contrib. Plasma Phys. **34** (1994) 120.
[10] Neuhauser, J., Plasma Physics and Controlled Fusion **34** (1992) 2015.
[11] Keilhacker, M., et. al., Physica Scripta Vol. **T2/2** (1982) 443.

Divertor Options for ITER and ASDEX-Upgrade: Results of Modeling

J. Neuhauser, H.-S. Bosch, B. Braams*, D. Coster, O. Gruber, M. Kaufmann, K. Lackner, D. Reiter**, R. Schneider, B. Streibl, H.-P. Zehrfeld and the ASDEX-Upgrade Team
Max-Planck-Institut für Plasmaphysik, EURATOM Association, D-75748 Garching, Germany
* Courant Institute, New York University,
** Forschungszentrum Jülich, EURATOM Association

Introduction

One of the most challenging issues in the design of ITER is a divertor concept which simultaneously provides tolerable power loads on the target plates and sufficient particle exhaust. No validated divertor concept exists so far, which could cope with the extreme power flow levels envisaged for ITER and to be expected in a subsequent DEMO. An assessment of the relative merits of different divertor schemes requires elaborate numerical models and codes, which are able to treat all the atomic physics processes as well as the complicated geometries involved, and which must be sufficiently validated against running experiments like ASDEX-Upgrade over a relevant range of parameters. In this paper, we describe results obtained with the B2-EIRENE code package for two specific ITER divertor configurations (V-shape and gas bag) and give an outline of the design, properties and physics basis of an improved ASDEX-Upgrade divertor (Divertor II), to be operational in about two years.

Status of B2-EIRENE and model validation

The B2-EIRENE package was developed and is still being improved in a joint effort between Garching, Jülich and New York University [1, 2]. The most recent version applied here involves an advanced version of the 2d multifluid tokamak edge code B2, coupled with a fully time dependent version of the EIRENE Monte Carlo neutral particle code [2] called by B2 at each iteration step. Mostly stationary solutions are presented here, but the package can handle time dependent scenarios as well, e.g. ELMs [3]. Both are running on realistic geometries taken directly from experiment or detailed technical designs of future machines, respectively.
In parallel to the simulation of future experiments, model validation on ASDEX-Upgrade is going on, yielding e.g. $D = 0.1..\ 0.3$; $\chi \approx 1...1.5$ for the radial transport in ohmic discharges [4, 5]. While for ASDEX-Upgrade Divertor II the transport coefficients of the present configuration seem to be an adequate choice, the extrapolation to ITER requires some assumption on size scaling. B2-EIRENE modeling results of ASDEX-Upgrade [4] and the old ASDEX [9] together with EDGE2D simulations of JET [6] seem to indicate that there is no significant size dependence of the anomalous radial transport coefficients. However, in ASDEX-Upgrade H-mode discharges, rather narrow power deposition profiles at the target plates are frequently obtained, which - for standard model assumptions - would result in

extremely small χ values. Since the physics behind this is still unresolved (fast particles, ∇TxB terms, ...), it is clear that much more work has to be done in this field. For the moment, we take typical ASDEX-Upgrade transport coefficients as a starting point.

ITER simulation results

Based on qualitative physical considerations supported by numerical scoping studies for various possible ASDEX-Upgrade, JET and ITER divertor variants, we have finally chosen two distinct ITER configurations for a more detailed study [7]: a V-shaped target geometry and a gas bag case more similar to the present ITER JCT proposal [8] (fig. 1). An extensive density scan with pure hydrogen plasma assuming 100 MW power into the edge (i.e. two thirds of the nominal α-power are assumed to be radiated) shows that the V offers several advantages: because of the relatively localised recycling inside the V-targets, the recycling and, above a critical density, the momentum and energy detachment from the target is obviously in a sense self-controlling, which results in a more stable and symmetric behaviour of both plasma fans. This is obvious from the bottom part of fig. 2, which represents the pressure drop factor from midplan to divertor (essentially the inverse of fp as defined in ref. [8]). The V also seems to buffer grassy ELMs more efficiently, probably because of the fast neutral recycling response inside the V-target, as shown by a few ELM runs in the detachment regime [3]. A study has been made also with impurities (sputtered Be together with externally controlled Ne puffing; now 200 MW into the edge, i.e. assuming that one third of the α-power radiated in the bulk). For both geometries a strong radiation especially close to the x-point is obtained, but again the V-configuration is rather symmetric, while in the gas bag divertor the inner divertor leg cools much stronger than the outer one.

ASDEX-Upgrade divertor plans

As seen above, the detailed target and baffle configuration inside the divertor chamber can significantly change the divertor performance. These structures control the neutral recycling pattern, which in turn has a strong influence on the symmetry and stability of the divertor plasma fans and finally on the whole edge region. Therefore, in addition to numerical predictions, these different divertor structures must be intensively tested in experiments like ASDEX-Upgrade. The Divertor II proposed for this purpose is being designed as flexible as possible. There is some cooled base structure on the high and low field side of the divertor plasma region, which can be equipped with target plates of different shape. The Lyra and gas bag divertors are the basic configurations in discussion. These can be complemented by various uncooled structures in the private flux region (fig.3). By exchanging these baffle structures one should be able to vary the neutral recycling pattern and to test its influence on the divertor performance.

Various preliminary simulations relevant for Divertor II have been done in the past in parallel to the ITER simulations. At present, detailed scans are being done for the new geometries in comparison with the present Divertor I. An interesting indication is that Divertor I shows qualitatively features similar to those of a deep gas bag. This means that the present divertor (to be operational till about 1996) - in connection with modeling and model validation - can substantially contribute to ITER.

References

[1] R. Schneider et al.; Contib. Plasma Physics **32** (1992) 450-455
R. Schneider et al.; J. Nucl. Mater. **196-198** (1992) 810-815

[2] D. Reiter et al.; Time dependent neutral gas transport in tokamak edge plasmas;
Proc. 11th PSI Conference, Mito (Japan) May 1994; to be publ. in J. Nucl. Mater.
D. Reiter et al.; J. Nucl. Mater. **196-198** (1992) 80-89

[3] D. Coster et al.; B2-EIRENE modeling of ELMs in ASDEX-Upgrade; this conference

[4] H.-S. Bosch et al.; 2d modeling of the ASDEX-Upgrade sol and divertor plasma;
Proc. 11th PSI Conference, Mito (Japan) May 1994; to be publ. in J. Nucl. Mater.

[5] W. Junker et al.; Comparison of experimental Marfe observations in ASDEX-Upgrade with B2 calculations; this conference

[6] A. Loarte et al.; Comparison between measurements and 2d model calculations for JET x-point discharges;
Proc. 11th PSI Conference, Mito (Japan) May 1994; to be publ. in J. Nucl. Mater.

[7] R. Schneider et al.; Analysis of cold divertor concepts for ITER;
Proc. 11th PSI Conference, Mito (Japan) May 1994; to be publ. in J. Nucl. Mater.

[8] G. Janeschitz et al.; The ITER divertor concept;
Proc. 11th PSI Conference, Mito (Japan) May 1994; to be publ. in J. Nucl. Mater.

[9] K. McCormick et al.; J. Nucl. Mater. **196-198** (1992) 264-270

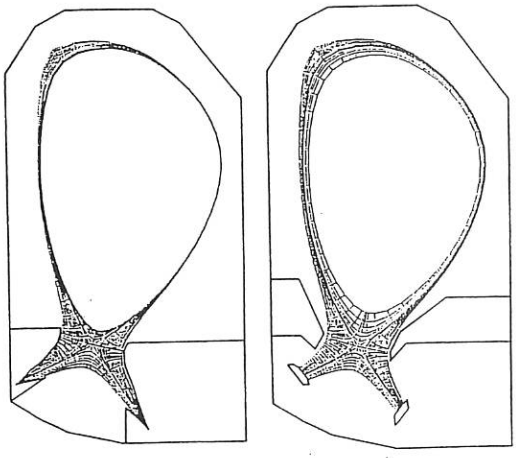


Fig. 1. Numerical grid and wall contours for the ITER divertor configurations modeled: V-shape target (left) and gas bag (right).

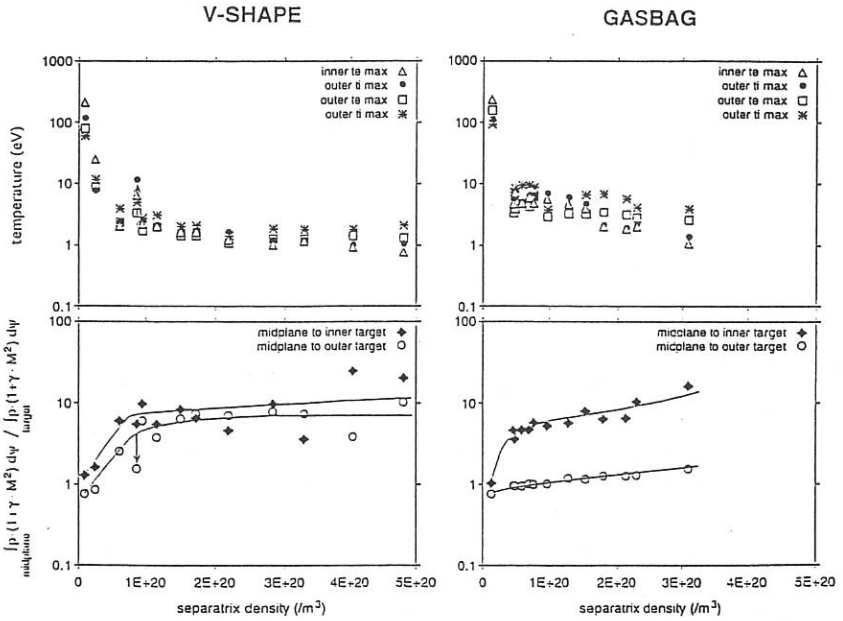


Fig. 2. Divertor temperature and radially averaged pressure drop factor (midplan to divertor) for both ITER configurations as function of midplane density.

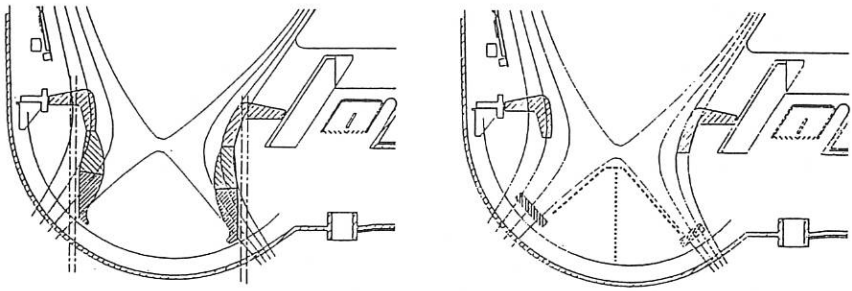


Fig. 3. The two basic ASDEX-Upgrade Divertor II configurations in discussion are shown: the Lyra (left) and the gasbag (right; the target shape may still be changed). Additional, uncooled baffle structures in the private flux region, a dome-like baffle and a vertical septum, are indicated in the gas bag case, but could be used in this or a modified form also with the Lyra.

Bright Spots on the Divertor Plates of ASDEX-Upgrade during Stationary Phases

K. Büchl, A. Carlson, A. Herrmann, J. Neuhauser, U. Seidel, M. Ulrich, M. Weinlich
and the ASDEX-Upgrade Team
Max-Planck-Institut für Plasmaphysik, EURATOM Association, D-85748 Garching

The appearance of bright spots at several parts in the tokamak vessel during disruptions is a well known phenomenon (ref.1 and 2). In ASDEX-Upgrade an enormous number of bright spots is observed at the lower target plate and at the diaphragm ring of the divertor as shown in figure 1 from a density limit disruption.The investigation of carbon tiles after an operation period of the tokamak shows,that arcs are the reason for the bright spots (ref.3).
In ASDEX-Upgrade, however, bright spots at the divertor plates are observed also during the stationary phases of the tokamak operation. These spots seem to arise from uneven power deposition on the target plates. The energy of the bulk plasma enters the scrape-off layer crossing the seperatrix so far it is not radiated from the bulk and the boundary of the plasma. Along the SOL the energy is transfered to the divertor plates. During the stationary state ASDEX-Upgrade is heated with a power up to 10 MW. Power loads of about 10 MW/m^2 at the target plates are measured by thermography supposing uniform deposition. However due the tile geometry (fig.2) and other irregularities on the surface of the tiles a local power overload will occur unavoidably. Then the sublimation temperature on the carbon tiles may be exceeded. The increased impurity production can produce carbon blooms and following plasma disruptions. Also damage of divertor tiles is possible.

Diagnostics

The target plates are monitored by several CCD cameras with time resolution of 20 msec. We are using remote-head cameras, which operate perfectly also in magnetic fields of 3 Tesla. The movies are recorded on tape using commercial video tape recorders.
An overview of the discharge is given by a wide-angle colour CCD. Due the poor spatial resolution of 5 - 10 mm just the bright edges of the carbon tiles are visible, but only extrem bright spots with smaller diameters are observable (fig.3).
A better resolution of about 1 mm on the target plates can be reached with two CCD´s looking from top of the vessel. They will be used with different focal length objectives (4.8 - 24 mm). These cameras are able to observe single bright spots.
Additional information will be delivered from another two CCD´s. One of them looks in radial direction across the outer divertor plate and can be used with different focal lengths. The line of sight of the second one is in toroidal direction close to the x-line of the plasma configuration and sees also a part of the outer divertor plates.
For all CCD cameras supplied with objectives of long focal length interference filters can be applied for spectral lines of H, CI, CII, and CIII. An infrared filter near 1 µm wavelength in

a line free region of the plasma spectrum is applied to one of the CCD´s on top of the vessel. It is calibrated with a W - lamp and a pyrometer in the temperature range from 1500 K to 2500 K. With this camera the temperature of the bright edges of the carbon tiles and of large bright spots is measured during the discharge.

Currents from insulated carbon tiles of the target plates to the wall of the vacuum vessel are measured, too.The measurement is integrated over the surface of the tile of about 70 cm^2 . The sampling rate is 5 kHz. This measurement can contribute to answer the question, if the observed bright spots during the stationary phases of operation are connected with arcs.

Results

* Bright spots are observed in ASDEX-Upgrade as well in instationary phases, e.g. disruptions (fig.1) as in stationary phases during ohmic and additional heating (fig.4).
* During the stationary phase bright spots occur predominantly on the outer divertor plate in contradiction to disruptions, when bright spots are detected on both target plates.
* Bright spots are concentrated in the zone on the target plate, where the SOL hits the surface, with increasing number of spots towards the strike line (fig.4). No bright spots are observed in the private region.
* Bright spots do not move around the surface of the tiles. During motion of the strike line on the divertor plate bright spots appear and disappear relativ to the strike line position.
* Bright spots appear in subsequent discharges at the same geometrical location.
* Arc traces seem not to start at hot spots but this has to be clarified.
* Material is erupted in some cases from bright spots. It moves along the magnetic field lines.
* The number of bright spots in the ohmic phase is relativly small, but during ELM´y H-mode the number can be very large.
* Bright spots are observed at low density. They disappear, when a critical mean electron density is exceeded or equivalent T_e in the divertor is fallen below a certain value. (fig.5).
* In the ohmic phase the current through the outer divertor tiles is proportional to the number of bright spots. From the measurement of the current through the whole tile (fig.6) a current less then 1 A / spot can be estimated.
* At heating powers above 2 MW the edges of the tiles start to get bright , in addition to the bright spots on the surface of the tiles.
* The edges of the tiles heat up to more then 2500 K during NI (fig.6). Bright spots are measured to reach up to 2000 K.
* Although Ha and CIII emission in the outer divertor is constant during NI (4 MW) the current through the tiles increases in the same way as the edge temperature of the tiles (fig.6).

Conclusion

The observed bright spots during the stationary phases of ASDEX - Upgrade operation are not identical with arcs detected by the traces on the tiles. However at the hot spots non-

selfsustained arcs seem to exist with a current less then 1 A / arc .
The bright spots develop on the carbon tiles in the divertor at positions, where a higher power density exists due non-grazing incidence of the magnetic field lines. This occurs as well at the edge of the tiles as at imperfections of the tiles .

References

(1) K.Ertl and the Asdex-Team,B.Jüttner Nucl.Fus. 25 (1985),1413
(2) K.H.Finken et al. Nucl.Fus. 32 (1992), 915
(3) C.Garcia-Rosales ,this conference

Figures

Fig.1 Bright spots at the outer divertor plate during a density limit disruption
Fig.2 Geometry of the inner and outer divertor plates
Fig.3 Bright edges at the outer carbon tiles during a 800 kA / 6 MW NI discharge
Fig.4 Bright spots at the outer target plates (800 kA / 6 MW NI)
Fig.5 Critical density vs. plasma curent for ohmic discharges
Fig.6 NI power, electron density, tile edge temperature, current through outer tiles, CIII and Ha emission above the outer divertor vs. time

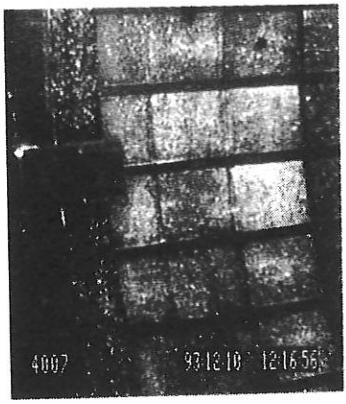


Fig. 1

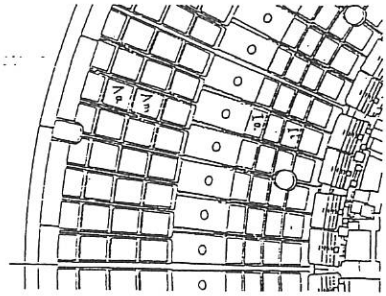


Fig. 2

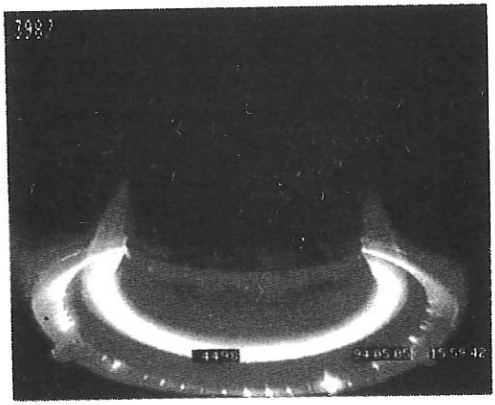


Fig. 3

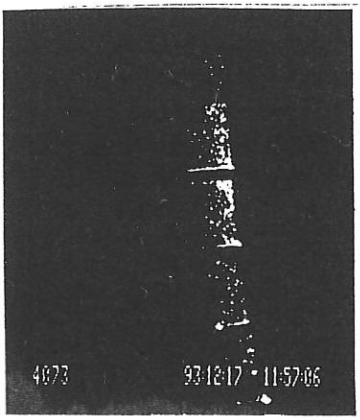


Fig. 4

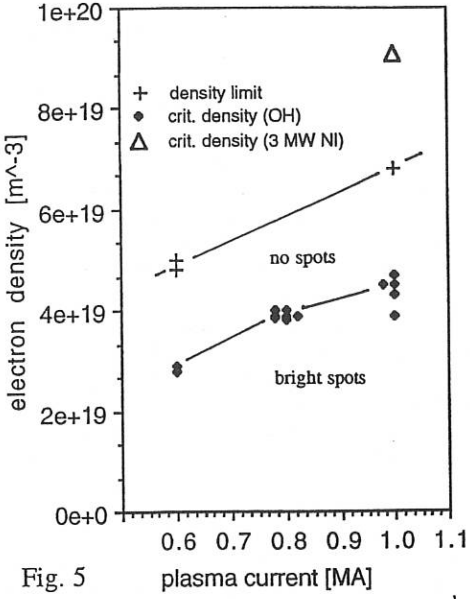
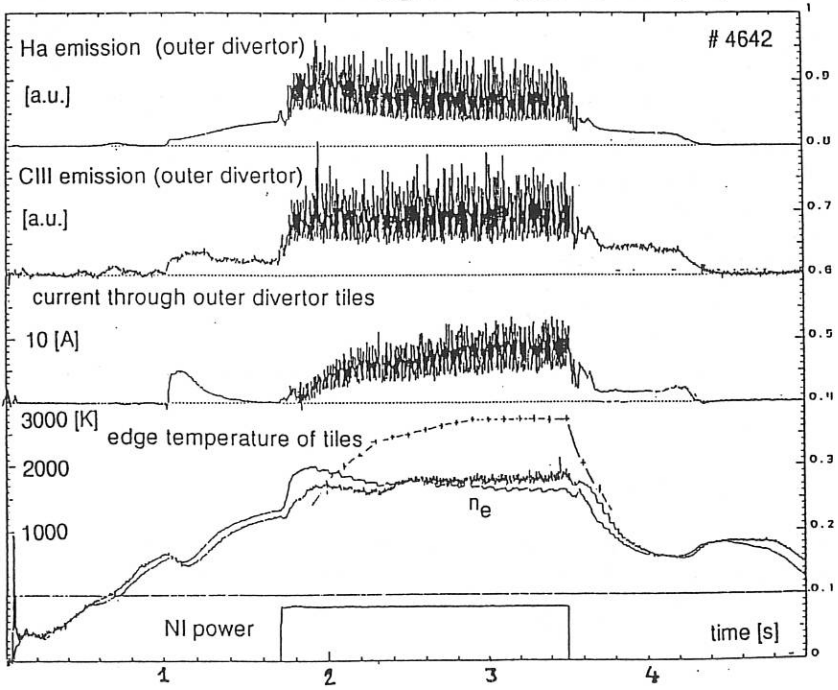


Fig. 5

Fig. 6



Momentum removal from subsonic and supersonic plasma flows in the ITER divertor

Yu.Igitkhanov, G. Janeschitz*, A.S.Kukushkin*, M.Sugihara*
Max-Planck-Institut für Plasmaphysik, Garching,
*ITER-JCT, JWS- Garching, Germany.

1. Introduction.

The concept of the ITER divertor is based on the Dynamic Gas Target, where a low density cushion develops upstream of the plate. In order to sustain such a regime most of the power has to be radiated upstream of the cushion which in turn requires a significant pressure drop >80% along field lines. This pressure drop occurs in the low density cushion due to cx neutrals which remove momentum from the plasma to the wall [1].

The momentum transfer by cx neutrals is very efficient provided they can leave the plasma collisionless and deposit momentum and energy directly onto the side walls. If, however, the mean free path for neutral-neutral collisions is shorter than, or comparable to, the distance between the divertor plasma and the wall, the hot cx neutrals collide with cold neutrals surrounding the plasma column. This makes the momentum transfer to the wall viscous rather than prompt and thus less efficient.

2. Efficiency of Momentum Removal from a Plasma surrounded by Gas.

In the Dynamic Gas Target Concept three zones can be distinguished in radial direction: a central (hot) plasma SOL region, where cx neutrals enhance the cross field transport of momentum and energy (inside the cushion where ionisation is negligible => Te<5eV). This region extends beyond the neutral penetration length $(\lambda_i \lambda_{cx})^{1/2}$ and provides the momentum source to the second region at the plasma edge which has a width of order λ_{cx}. In this second region direct exchange of momentum (energy) through mutual collisions of ions with cold neutrals takes place. The third region is the gas cloud between the plasma and the wall where neutral-neutral collisions are important at higher density.

The momentum balance equation describing the volumetric losses in the second region is used in order to estimate the momentum loss inflicted on the plasma (pressure drop along the field) by cx neutrals.

$$\nabla_{//}\left(m_i n_i v_{i,//}^2 + p\right) + \nabla_{\perp}\left(m_i n_i v_{i,x} v_{i,//}\right) = -m n_0 n_i \left(v_{i,//} - v_{0,//}\right)\langle\sigma v\rangle_{cx} \qquad (1)$$

where $v_{i,//}$ and $v_{0,//}$ are the parallel velocities of the ions and neutrals, respectively, v_x is the crossfield velocity and $<\sigma v>_{cx}$ is the rate coefficient for cx. Assuming that the volumetric losses in this region prevail over the cross-field ones, one can estimated:

$$\lambda_{i-n}\frac{\partial \Pi_{//}}{\partial x} \approx -\Pi_{//}\left(1-\frac{v_0}{v_i}\right)\frac{\sqrt{2\gamma}}{\left(1+\gamma M^2\right)} \qquad (2)$$

where $\Pi_{//} = m n v_i^2 + p$, and $\gamma = 5/3$. Equation (2) can be integrated from some upstream region (say X-point) to the target. A direct measure of momentum removal efficiency is lateral momentum loss fraction $\Pi_{Wall}/\left(\Pi_{Wall}+\Pi_{Target}\right)$, i. e. the

momentum transferred to the side walls normalised to the momentum to side walls + target. This can be written as

$$f_w = 1 - \exp(-L/\lambda_*), \qquad \lambda_* = \lambda_{i\text{-}n}/(1 - v_0/v_i)\sqrt{2\gamma}\, M/(1+\gamma M^2), \tag{3}$$

where λ_* is an effective length for the momentum loss, L is the length along which neutral -plasma interaction takes place, M is the Mach number for plasma ions taken at the plasma surface and $\lambda_{i\text{-}n}$ is the cx collision length. The velocity differenc in (3) can be estimated from the total momentum loss of the plasma per unit poloidal length. This amount of momentum is transported by neutrals through the third region to the wall and it can be expressed as:

$$f(Kn)\eta_0 \left.\frac{\partial v_0}{\partial x}\right|_{edge} = m \int_0^{\Delta_m} n_0 n_i (v_i - v_0)\langle\sigma v\rangle_{cx} dx \tag{4}$$

on the left h.s. of Eq.(4) there is a generalized expression for the shear stress, valid for an arbitrary level of collisionality. f(Kn) is a function which is defined by kinetic treatment (see below) and η_0 is the neutral viscosity coefficient. Note that the left h.s. of Eq.4 is assumed to be constant across the gas layer due to the uniformity of neutral gas along the field while neutrals are assumed to decay as $\exp(-x/(\lambda_i \lambda_{cx})^{1/2})$ inside the plasma. The velocity difference can then be assessed from (4) as:

$$1 - v_0/v_i = 1/(1 + 0.6\sqrt{\pi}/f(Kn)Kn)\ . \tag{5}$$

f(Kn) varies between one and zero therefore v_0 approaches 0 at high Kn number and, v_0 tends to v_i in the opposite case. This implies that the effective length for momentum losses λ_* depends on the competition of two processes, momentum transfer via charge exchange from ions to neutrals (increasing with neutral density) and momentum transfer via the neutral gas to the wall (decreasing with n_0 because v_0 approaches v_i).

3. Shear stress for arbitrary collisionality.

To evaluate f(Kn) which is a normalised general shear stress value for arbitrary neutral density, a kinetic approach, similar to that for rarefied gases [2], is employed . Cold and hot neutrals, moving in opposite directions are assumed to be distributed as a local Maxwellian function of six unspecified low moments: n, T and radial velocity v_x, which are different for cold and hot atoms. In the limiting case of low density these distributions are reduced to two-streaming Maxwellian functions $F^{\pm}$. and start to depend appreciably on the conditions at the wall and at the plasma edge, respectively. In the opposite limiting case they combine to one Maxwellian distribution. All required moments can be found from the momentum equations, which can be derived from

$$\frac{\partial}{\partial x}\left(\int v_x F^{\pm} v_x^i v_z^k dv\right) = \int St\, v_x^i v_z^k dv \tag{6}$$

where x denotes the radial direction and the collisional term St is chosen for the elastic interaction of neutrals, obeying the inverse fifth-power law of repulsion. Six different collisional invariants $v_x^i v_z^k$ are taken, two for n, T, two for the two components of velocity v_x , v_y , and two for radial heat and viscous fluxes. For example, the momentum equation can then be written from (6) as

$$\frac{\partial}{\partial x}\pi_{xz}=0,\quad \pi_{xz}=-\frac{\eta}{p}\frac{\partial}{\partial x}\int mF^{\pm}v_z v_x^2\,dv=Const. \tag{7}$$

assuming uniformity of the neutral distribution along the field. The integration constants are evaluated from the boundary conditions. In order to formulate the boundary condition we assume that neutrals acquire the ion velocity at the plasma edge, and that they are reflected from the wall with complete energy and momentum accommodation. The result is determined by three independent parameters: the Kn number, which characterize the density level and distance d between plasma and the wall, the Mach number, the dissipation parameter due to the generation of heat as a result of viscosity, and the temperature ratio $\theta = T_{plasma} / T_{wall}$. The result of this evaluation is presented in Fig.1 showing that the shear stress varies smoothly with the Kn number. In the limiting case of low Kn, f(Kn) approaches 1, which agrees with the well-known classical value for π_{xz}:

$$\pi_{xz}=\eta_0\frac{v_i}{d}\frac{1}{2}\left(1+\left(1+\frac{2}{27}M^2\right)\theta\right) \tag{8}$$

At high density (low Kn) $\pi_{x,z}$ becomes independent of density, while when Kn is high, π_{xz} asymptotically approaches the free-streaming value:

$$\pi_{xz}=(mv_i)j^{+}=(mv_i)\frac{1}{4}n\sqrt{\frac{8T_*}{m\pi}},\quad T_*=T_{plasma}\left(1+\frac{1+\kappa}{1-\kappa}\sqrt{\theta}\right) \tag{9}$$

and is linearly dependent on density. In (9) κ is the ratio of ionization rate tothe sum of cx and ionization. Fig.1 shows that f(Kn) decreases weakly with increasing Mach number, because the collisional viscosity depends only weakly on M.

4. Results and Conclusions.

As described above the efficiency of momentum transfer to the wall is influenced by a number of parameters: the neutral density, the plasma-wall distance in the divertor, the Mach number, and the divertor (connection) length. For typical ITER dimensions the neutral collisionality is the most likely the intermediate (Kn~1). The transition from one limiting case to another occurs over an interval of the order of the Kn number (Fig. 1), which corresponds to the expected neutral

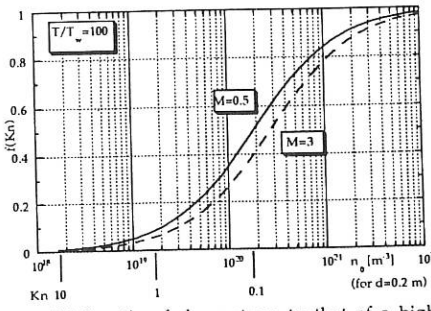


Fig.1 f(Kn), ratio of shear stress to that of a highly collisional gas, versus neutral density at the plasma edge (for d=0.2 m) calculated for M=0.5 and M=3

density range in ITER. The efficiency of the lateral momentum loss evaluated from (4) is plotted as a function of neutral density in Fig.2 for two Mach numbers and two lengths L (connection length) assuming that θ is typically ~ 100. The Momentum transfer to the wall improves with both Mach number and length. Fig.3 shows the lateral momentum loss for two different plasma-wall distances "d" and two different lengths at M=0.5. The efficiency of momentum removal from the plasma increases with density and with M, whereas the efficiency of momentum transport to the wall decreases almost at the same degree (independent of Mach number or θ). As a result the total momentum losses to the wall saturate at some neutral density level, which depends on θ), Mach number and the distance to the wall.

A dependence on "d" is seen at high neutral densities when the classical viscosity dominates (see equ. 8). However, it is only pronounced for a relatively low L values. For such a short length (L=5m and n > $10^{20}m^{-3}$), a factor 1.5 can be gained by moving the wall closer to the plasma (from 0.8 m to 0.2 m), while for L=20 m, this gain is negligible. In ITER ,"L" can vary from 5m to 35m depending on the length of the neutral cushion. From the work presented in this paper it is clear that a long cushion (L~20m) will allow to remove all the momentum with a relatively low neutral density (5.1019m-3) in the divertor and at the same time relaxes the requirement for a wall close to the plasma.

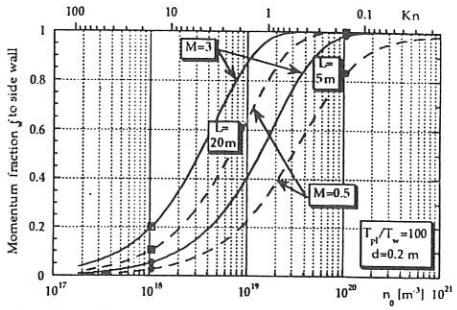


Fig. 2 Lateral momentum loss fraction (momentum lost to side wall normalised to momentum lost to side walls and target) vs. neutral density at plasma edge. Neutral density evenly distributed along divertor length. Calculations for along-field length 5 m and 20 m, Mach number at plasma edge 0,5 and 3, and plasma-wall distance 0.2 m.

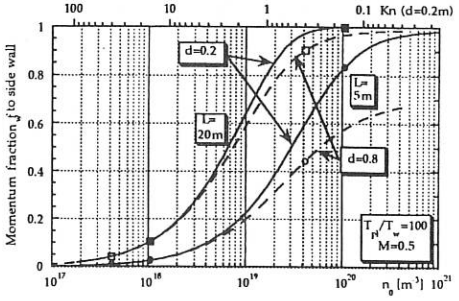


Fig.3 Same as Fig.2 but for M= 0.5 and plasma-wall distance 0.2 m and 0.8 m.

References.

1. Janeschitz G., et al., PSI 94
2. Lifshiz,E.M., and Pitaevskii ,L.P.,1981,Physical Kinetics.

Erosion at the divertor tiles of ASDEX-Upgrade

C. García-Rosales, R. Behrisch, D. Hildebrandt*, B. Jüttner*, W. Schneider*, H. Wolf*

and the ASDEX-Upgrade Team

Max-Planck-Institut für Plasmaphysik, EURATOM Association, D-85748 Garching, Germany
* Bereich Berlin, D-10117 Berlin, Germany

1. Introduction

For a magnetically confined hot plasma major erosion is expected at the vessel walls around areas where the separatrix, i.e. the least closed magnetic surface intersects. In a divertor tokamak these are the divertor tiles receiving the highest power and particle fluxes. Recent investigations have shown that besides sputtering arcing at inner tokamak surfaces can be a frequent event leading to a remarkable surface erosion [1].

The present paper reports about detailed analysis of divertor tiles from the ASDEX-Upgrade tokamak exploring the contributions to surface erosion of sputtering and of arcing phenomena during a defined number of discharges.

2. Experimental Conditions and Methods

Several tiles of the lower divertor plates (inner and outer) of ASDEX-Upgrade have been inspected by Scanning Electron microscopy (SEM), Auger Electron Spectroscopy (AES) and Profilometry, the latter having a vertical resolution ≤ 100 nm. These tiles have been exposed to different discharge periods: a relatively long period with plasma currents of 600 - 800 kA and electron densities mostly $\overline{n}_e = (2-4)\times10^{19}\,\mathrm{m}^{-3}$ (period I), and two short periods (II, III) with 800 kA plasma current, $\overline{n}_e = (4-6)\times10^{19}\,\mathrm{m}^{-3}$ and neutral beam injection (NI) with a power up to 7 MW. Electron density and temperature in front of the divertor plates were of the order of $n_e = (1-3)\times10^{19}\,\mathrm{m}^{-3}$ and $T_e = 10-50$ eV, respectively [2,3]. The toroidal magnetic field was mostly -2 T. The tiles differed by material and surface treatment (prior to exposure): graphite (fine grain, EK98) as received, graphite polished and weakly degassed at 300°C, graphite polished and thoroughly degassed at 1100°C in a vacuum of about 10^{-5} Pa, and tungsten intarsia plates (3 samples, soldered on graphite tiles located side by side in poloidal direction at the lower outer divertor).

Run	Tile material	Surface treatment	Tile name	Position divertor	No. of discharges		No. of disruptions	Direction of disrupt.
					total	with NI		
I	graphite	none	C	inner	850 - 900	20	250	↑↓
II	graphite	polished, 300°C	CP	outer	112	57	26	↓
II	graphite	polished, 1100°C	CPD	outer	112	57	26	↓
III	tungsten	polished	WP	outer	214	85	49	↓

Table 1: Analysed divertor tiles, experimental conditions and discharge numbers.

3. Results

All tiles (C,CP,CPD,WP, s. table 1) showed surface changes of geometry and chemical state on a µm-scale that can be attributed to arcing events. In addition a depression on a larger scale was detected at tile C (inner divertor) as shown in fig. 1. From the surface profile in fig. 1 a total carbon mass loss of about 1 (± 0.3) g can be deduced for tile C after exposure to discharge period I which corresponds to 210 (± 65) mg/m² per discharge.

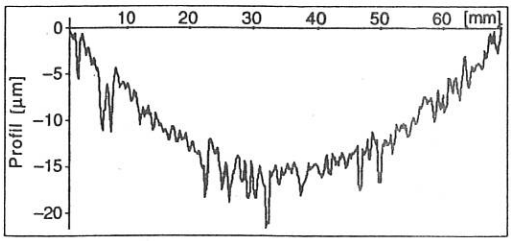


Fig. 1: Surface profile of tile C (inner divertor) in the direction perpendicular to the magnetic field after exposure to 850-900 ohmically heated discharges.

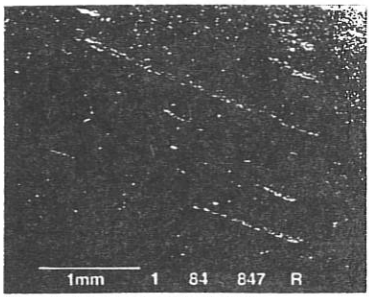


Fig. 2: Arc traces at a CP tile

Arc traces are oriented perpendicular to the magnetic field, i.e. in fig. 1 nearly parallel to the surface scan so that the probability of crossing a trace is small. Fig. 1 shows also some spikes due to arc traces with a depth of about 6 µm. A SEM picture of arc traces at the surface of tile CP (graphite, polished) is shown in fig. 2 while fig. 3 shows a surface scan of this tile perpendicular to the traces (parallel to the magnetic field). The trace profiles can clearly be distinguished from the surface roughness and have a mean depth of about 7 µm and a mean width of 20 - 50 µm. The mean trace length is 2 to 5 mm.

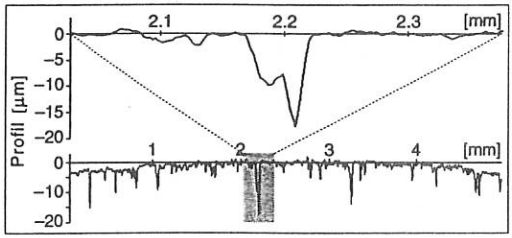


Fig. 3: Surface profile of CP tile (lower outer divertor) in the direction parallel to the magnetic fieldafter exposure to period II.

Still deeper arc traces of up to 30 µm have been found for the degassed tile CPD, as shown in fig. 4. Their width reaches 100 µm, and they are more frequent than for the CP tile (figs. 2,3), leading to a complete roughening of the surface. From length, width and depth of the traces a carbon mass loss of 10 mg (± 4 mg) and 34 mg (± 14 mg) can be deduced for the CP and CPD tiles, respectively, after exposure to discharge period II.

Arc traces on tungsten (WP) are smaller and longer than for graphite, thus indicating a higher arc velocity. The depth was < 0.5 µm, and the arcs mostly run from the starting point to the end of the tile. Fig. 5 shows a picture of a W-surface with a nearly perfect circle which

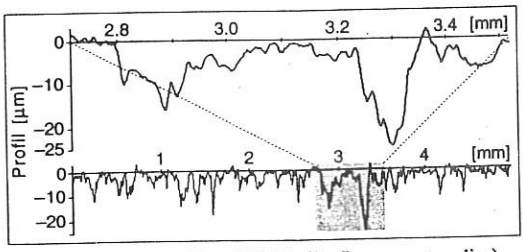


Fig. 4: Surface profile of CPD tile (lower outer div.) in the direction parallel to the magnetic field.

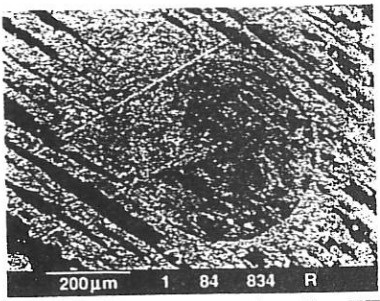


Fig. 5: Surface topography of a WP tile with a starting point of arc traces.

served as starting point of a multitude of arcs. Elemental analysis revealed that the circle area is enriched in contaminants such as Na, K, Cl, Ca, and Mg. The area of the tiles corresponding to the private flux region is covered with a 170 nm thick amorphous B:H layer -as measured by AES depth profiling- originating from boronization. At the intersection area with the separatrix the boron layer is eroded by physical sputtering and a clean tungsten surface appears. Outside the decay length of the separatrix a boron layer containing about 30% C, probably due to redeposition, can be detected. The boron and carbon containing areas of the tungsten tiles show a remarkable higher arc trace density than the clean tungsten surface, where only a few arc traces mostly starting at contamination spots can be observed.

4. Discussion

4.1 Large scale changes (Tile C)

The depression shown in fig. 1 cannot be explained by sputtering alone. On the one hand this depression was also observed on other tiles of the inner divertor at different poloidal positions. At the outer divertor such a depression was not observed. On the other hand, from measured D^+ fluxes and electron temperature profiles at the lower divertor during discharge period I [3] and from known sputtering yield values [4] the sputtered carbon mass can be estimated to about 43 (± 22) mg/m² per tile and ohmically heated discharge without taking into account redeposition effects. This is a factor of about 5 smaller than the value of about 210 (± 65) mg/m² per discharge deduced from the depression. This discrepancy is an indication that also additional effects may contribute to surface erosion.

4.2 Arcing

Arcing events can be deduced in situ from video-pictures [5] and thermography [6,7]. However, due to the limited resolution of the cameras, these methods register only immobile bright spots, rather than the rapidly moving arc spots with a velocity of the order of 100 m/s [1,8]. Fig. 5 is likely an example of such a bright spot where arcs start. Under the premises that most of the observed bright spots are associated with arcs, the optical investigations [1,5-7] indicate that arcing is frequent under the following conditions:

(i) NI (intensive) and transitions from double null to single null at the beginning of a discharge (moderate), preferentially at the outer tiles.

(ii) Disruptions, preferentially at the inner tiles.

While it is difficult to separate the mass loss for case (ii) from erosion by sputtering, the conditions of the present experiment allows a more quantitative estimate for case (i). This carbon mass loss due to arcing per NI-discharge and m^2 amounts to 120 (± 45) mg/m^2 and 34 (±14) mg/m^2 for the degassed (CPD) and undegassed (CP) tiles, respectively. From the known arc erosion rate of 17 µg/C for clean carbon [9] a total transported charge of 2000 C per degassed tile CPD and period II can be deduced. For a total number of NI pulses of 57 with a mean duration of 1.5 s we obtain an arcing current of about 20 A per degassed tile and NI pulse.

The difference between the weakly degassed sample CP and the highly degassed sample CPD indicates that the desorbed gas provides the atoms to form the arc plasma, thus leading to a lower surface erosion, while for well degassed tiles the arc plasma is fed from material of the cathode spot, i.e. carbon, resulting in a stronger surface erosion.

On tile W, the observation of contaminant spots as starting points of arcs is an indication that surface contamination may considerably reduce workfunction and thus electron emission from the cathode occur at much lower electric fields for contaminated surfaces than for clean ones. The presence of boron and carbon containing layers may enhance ignition probability of arcs because of its insulating nature or a possible reduction of workfunction.

5. Conclusions

- Under the given discharge conditions the maximum net erosion of graphite divertor tiles due to sputtering as calculated from flux, electron temperature and sputtering yields amounts to about 43 (± 22) mg/m^2 per ohmic discharge. Additional effects which also contribute to surface erosion make a quantitative evaluation on plasma exposed tiles difficult.
- The minimum erosion in NI-discharges due to arcs at the lower outer divertor plates amounts to about 34 (± 14) mg/m^2 per discharge for polished and undegassed tiles, thus being a non-negligible fraction of the total erosion. The arcing current per degassed tile and NI pulse is about 20 A.
- Arc erosion is larger at degassed tiles. It seems that gas desorption during arcing provides the atoms to form the arc plasma, thus leading to a lower surface erosion at undegassed tiles than at degassed ones, where the arc plasma is fed from carbon atoms from the surface.
- Arcs on a polished tungsten surface ignite easily at surface contaminants and have a higher velocity than on carbon. Boron and carbon containing layers have a lower ignition voltage than tungsten.

References

[1] B. Jüttner, K. Büchl, M. Weinlich et al., Contrib. Plasma Phys. 34 (1994) 2/3, 472.
[2] A. Field et al., Proc. 11st Conf. Plasma Surface Interaction, Mito (Japan), 1994.
[3] A. Kallenbach and A. Field, Max-Planck-Institut f. Plasmaphysik, private communication
[4] W. Eckstein, C. García-Rosales, J. Roth and W. Ottenberger, Sputtering Data, IPP-Report, IPP-9/82 (1993).
[5] K. Büchl et al., this conference.
[6] G. Pautasso et al., this conference.
[7] A. Herrmann, Proc. 20th EPS Conf. Control Fusion and Plasma Phys., Lisbon 1993.
[8] R. Behrisch, in: „Physics of Plasma Wall Interaction in Controlled Fusion", Eds. E.D. Post, R. Behrisch, NATO-ASI Series B, Phys. Vol. 131 (Plenum Publ. Corp. 1986), p. 495.
[9] Kimblin, J. Appl. Phys., Vol 44 (1973) 3074.

SPECTROSCOPIC INVESTIGATION OF MOLECULAR IMPURITIES IN THE ASDEX UPGRADE DIVERTOR

G. Lieder, K. Behringer, A.R. Field*, C. Garcia-Rosales*, S. Hirsch*
A. Kallenbach*, B. Napiontek*, D. Naujoks* C.S. Pitcher+, W. Poschenrieder*
R. Radtke*, J. Roth*, M. Weinlich* and the ASDEX-Upgrade Team
Institut für Plasmaforschung der Universität Stuttgart, Pfaffenwaldring 31, 70569 Stuttgart
**Max-Planck-Institut für Plasmaphysik, EURATOM Association, D-85748 Garching, FRG*
+*PPPL, Princeton, USA and CFFTP, Toronto, Canada*

Introduction

Design studies for reactor-like devices, like ITER, have emphasized the importance of erosion and transport of material from the divertor target plates. In the ASDEX Upgrade divertor tokamak graphite is used as material for the target plates and heat shields. However, carbon reacts strongly with oxygen and atomic deuterium leading to enhanced erosion by chemical sputtering[1]. Recent results of spectroscopic investigations of the global impurity balance in ASDEX Upgrade have shown the strong influence of chemical erosion[2].

Here, we study the behavior of molecules close to the target plates by means of emission spectroscopy. Spectra and emission profiles measured with the multi-chord "divertor spectrometer" are discussed in comparison with other spectrometers[2,3] and mass spectroscopy[4].

Experiment

The divertor spectrometer views along 16 lines of sight parallel to the target plates at distances of 1.5–225 mm with a maximum spatial resolution of about 2 mm close to the tiles. Two detection systems are simultaneously available: A 1m Czerny-Turner spectrometer fitted with a 2D CCD-camera and a spectral resolution of $\Delta\lambda \gtrsim 0.01$nm and two 16 channel photomultiplier arrays equipped with different interference filters ($\Delta\lambda \gtrsim 1$nm)[5]. Measurements were performed mainly in front of tungsten intarsia plates soldered on graphite tiles[3,6,7].

The experiments were ohmically-heated deuterium discharges with $I_p = 800$ kA, $B_t = 2$T (grad-B drift towards the X-point) and an elongation of 1.7. Profiles of n_e and T_e along the divertor plate were obtained from two independent Langmuir probes. At moderate plasma densities of $\bar{n}_e = 4 * 10^{19}$ m^{-3} values of n_e and T_e at the target are $1 * 10^{19}$ m^{-3} and 15 eV.

Results and discussion

Strong emission bands of CD/CH, C_2 and BD/BH are observed especially at high densities. These indicate that hydrocarbons play a role as a carbon impurity source. Apart from the CD_4 production C_2D_x molecules are probably also of importance. The absence of carbon oxides (CO) or hydroxides (OD) is a result of the strong oxygen reduction by boronization, which is consistent with observations by mass spectrometry[4].

The observed CD transition is well-known and consists of the $A^2\Delta \Rightarrow X^2\Pi$ electronic transition at 431 nm (see Fig.1). These molecules are formed during the CD_4 break-up process. Interpretation requires model calculations. The dissociation model predicts a high CD^+ density, which should give rise to strong CD_4 bands in the same wavelength range, but these bands are of very low intensity. Thus, it must be concluded that molecular ions are very effectively redeposited at the target and do not enter the plasma. Fig.2 shows spatial emission profiles of the CD bands above the plate for two plasma densities $\bar{n}_e$. From these profiles penetration depths of about 0.8 cm were derived, which are important for studying the break-up processes. The profile of a C^o line is also shown for comparison.

The observed C_2 molecular band belongs to the Swan-System, i.e. the $A^3\Pi_g \Rightarrow X'\Pi_u$ transition at 516.5 nm (see Fig.3). C_2 molecules may be formed either by break-up processes of higher hydrocarbons, like ethane and ethylene, or as a result of sublimation However, the temperature rise of the plates during Ohmic discharges is only about $\Delta T \simeq 40\,K$ and thus sublimation can be ruled out[8]. From spatial emission profiles of the C_2 band penetration depths of about 0.6 cm are derived.

The boronized vessel state is characterized by the appearance of strong bands of boron hydrides which originate from the $^1\Pi \Rightarrow {}^1\Sigma$ transitions with bandheads at 433.2 nm (BH) and 432.8 nm (BD). After fresh boronization the intensity of the BD bands may exceed the intensity of the neighboring D_γ line. Little is known about the formation of BD molecules. Release of BH_2 from a:B-H layers upon exposure to thermal H has been reported[9]. From the thermodynamical point of view the formation of boranes is unlikely to occur, because these reactions are strongly endotherm. As shown in Fig.4 the emission profiles of the BD bands peak at the plate in contrast to the hydrocarbons. The penetration depth is about 1.8 cm. A further point of interest is the emission profile of a B^o line, which is also shown in Fig.4. In contrast to C^o (see Fig.2), its maximum is about 5 mm from the plate[5]. This may be explained by dissociation of the BD molecules providing the dominant source of B^o.

As a first step towards interpretation of the observed molecular bands, their appearance was modelled by computer programs[10]. For an interpretation of the CD band intensities in terms of methane fluxes, the number of CD_4 dissociation processes associated with each CD photon has been calculated on the basis of the respective excitation rate coefficients and calculations for the molecular CD_4 break-up. This quantity is usually called S/XB. Transport is included by defining particle confinement times for charged and neutral molecules τ_i and τ_n, respectively. All these methods were tested on microwave produced CD_4 discharges.

The conversion of intensities to influxes under the geometrical conditions of our observation is given by $\Gamma = \frac{4\pi}{h\nu} \frac{S}{XB} \frac{1}{d} \int I\,dl$ assuming that the line emission I is localized within a region of width d along the lines of sight. Table 1 shows particle influxes determined from the above relation with the usual values for S/XB[10–12]. The total flux is determined by taking into account fractional population of metastable levels[10]. For *d* a value of 6 cm is used as obtained from other diagnostics. The results for the influx are in good agreement with measurements of the "boundary layer spectrometer"[3]. Surprisingly, influxes measured in front of the tungsten plate are equal to the fluxes from the original graphite plate. This behavior can be explained by B and C deposition on the tungsten inlays. From the molecular influxes the chemical sputtering yield $Y_m = \Gamma_m / \Gamma_{D^o}$ for methane and higher hydrocarbons could be estimated to be about 0.03 and 0.06, respectively. The result for CD_4 is in agreement with mass spectroscopy measurements and similar to those reported from JET[10]. The higher value for C_2D_x may reflect the increasing production rate of heavier hydrocarbons at low energy bombardment[1]. Table 1 shows that the influx of O is only 10 % of the C flux. Therefore, only 10 % of the C flux is attributed to CO recycling.

For a precise determination of influxes the knowledge of the local plasma parameters is indispensable, because S/XB depends strongly on T_e, especially at temperatures below 20 eV[10,11]. If $\bar{n}_e$ increases towards the density limit, the intensity of the molecular bands also increases and remains high, although the plasma eventually 'detaches' from the target plate and T_e drops to ≤ 5 eV. (see Fig.5). This can be partly explained by the fact that the emitting layer width may double due to the broadening of the power deposition profile[3]. However, the

Species	Line (λ [nm])	S/XB	λ_e [cm]	Γ [$10^{20}m^{-2}s^{-1}$]
D	D^o (656.1)	15	14.0	70
C	C^+ (657.8)	10	2.0	2.2
CD	CD^o (431.0)	20	0.8	0.43
CD_4	CD^o (431.0)	100	0.8	2.1
C_2	$C_2{}^o$ (516.5)	2	0.7	0.02
C_2D_x	$C_2{}^o$ (516.5)	500[12]	0.7	4.2
B	B^o (249.7)	4.0	1.0	0.06
B	B^+ (345.1)	1.5	1.4	0.25
BD	BD^o (432.9)	1.2	1.8	0.02
O	O^+ (441.4)	6	2.2	0.2

Tab.1: Integrated particle fluxes Γ of atoms, molecules and ions released from the divertor plate. Also given are the line wavelengths λ, the number of ionizations/dissociations per photon S/XB at T_e = 15 eV and n_e, = $1 * 10^{19}\ m^{-3}$ and the decay length λ_e.

determination of molecular influxes as a function of $\bar{n}_e$ shows, that they depend on $\bar{n}_e$ in a similar way as the local plasma density. The density dependence of the strong C^+ line at 426.7 nm and the molecular bands in Fig.1 is quite different. Increasing $\bar{n}_e$ from 3 to 4 $* 10^{19}\ m^{-3}$ leads to higher intensities of both species, but at $5 * 10^{19}\ m^{-3}$ the intensity of the C^+ line starts to drop. This can be explained by the strong temperature dependence of physical sputtering, which is reduced at low values of T_e. The decrease of the C^+ influx is much more pronounced than the reduction of the observed intensities, since the drop of S/XB must also be taken into account.

An interpretation model which simulates the many reaction paths of the molecules allows simulation of the measured emission profiles (see Fig.6). The necessary mean confinement times are obtained from calculations of the transport of the molecules by the ERO code[13].

Summary

We have presented first measurements of molecular spectra and emission profiles near the divertor target plates of ASDEX Upgrade. From the measured intensities particle influxes and sputtering yields for chemical erosion have been derived. The important findings are : chemical erosion is present even at low incident ion energies. The respective yields for CD_4 and C_2D_x of 3 % and 6 %, respectively, reflect the expected higher rate of the heavier hydrocarbons. Molecular ions e.g. $CD_4{}^+$ are very effective redeposited. The influx scales with the local plasma density.

References

[1] Roth J., Vietzke E., Haasz A.,Supplement to Nuclear Fusion 1 (1991) 63
[2] Kallenbach, A. et.al , this conf.
[3] Field, A.R., et al., Proc. 11st Conf. Plasma Surface Interaction, Mito 1994
[4] Poschenrieder W., et al., Proc. 11st Conf. Plasma Surface Interaction, Mito 1994
[5] Lieder G., et al, 20th EPS Conference, Lisbon 1993, Europhysics conf. abstracts 17C Part II (1993) 579
[6] Hirsch, S., et.al, this conf.
[7] Garcia-Rosales, C. , et.al, this conf.
[8] Herrmann, private communication
[9] Vietzke, E., et al. Proc. 10th Int. Symp. Plasma Chemie, Bochum 1991
[10] Behringer K., J. Nucl. Mat. 176&177 (1990) 606 and private communications
[11] Behringer K., et al., J. Nucl. Mat. 145–147 (1987) 145
[12] Pospieszczyk A., et al., UCLA report PPG-1251 (1989)
[13] Naujoks, D., et al., J. Nucl. Mat. 210 (1994) 43

Figures

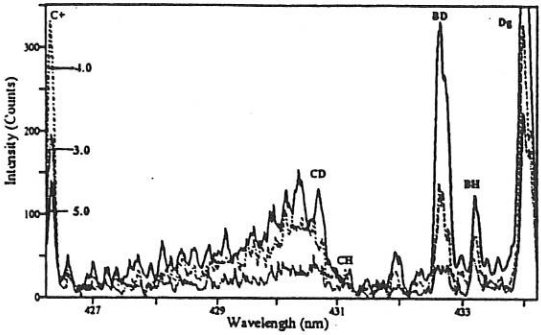


Fig. 1 Survey spectra around 430 nm at different plasma densities $\bar{n}$

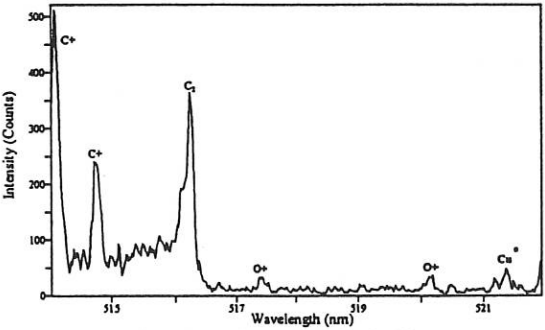


Fig. 3 Spectra shows molecular bands of C_2

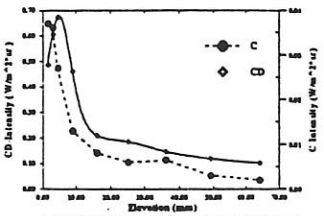


Fig. 2 Emission profiles of CD bands and a C line

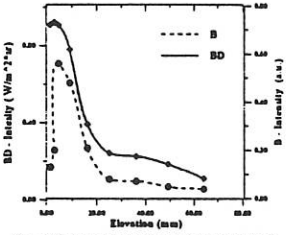


Fig. 4 Emission profil of BD bands and a B line

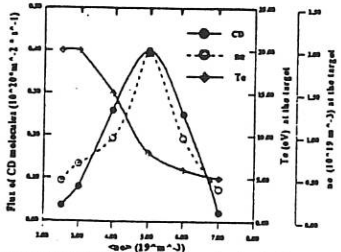


Fig.5 Local plasma density, temperature and molecular fluxes versus <n>

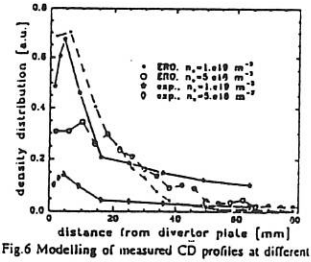


Fig.6 Modelling of measured CD profiles at different densities

Bistable Behaviour of the ASDEX-Upgrade Divertor Near the Transition to the X-Point MARFE

M. Laux, W. Junker, A. Herrmann, K. Büchl, A. Field, G. Haas, F. Mast, V. Mertens, B. Napiontek, J. Neuhauser, M. Weinlich, U. Wenzel, *ASDEX Upgrade Team*

Max-Planck-Institut für Plasmaphysik - EURATOM Assoziation

Introduction :

For plasma densities above n_{crit} a toroidally symmetric radiating structure (MARFE) is established at the x-point of ASDEX-Upgrade [1]. The transition is rather complex, starting with a cooling of the divertor plasma below 5 eV, a subsequent partial detachment from the plate [8] influencing strongly the particle and power deposition profiles on the plates, and, finally, a quick movement of the fully developed MARFE to the x-point where it stabilizes [2]. If the density is held sufficiently close to n_{crit} a bistable behaviour of the divertor plasma occurs and will be discussed in this paper to gain further inside into the mechanism of the transition. Dedicated experiments have been performed with the density varying around n_{crit} at different safety factors q to shed more light on the causes and consequences of different phases during the transition from a well attached divertor plasma to the x-point MARFE.

Experiments :

All experiments were carried out as ohmically heated single null discharges in deuterium with plasma currents around I_p=800 kA and at toroidal fields between -1.5 and -2.5 T (ion ΔB-drift towards the divertor) and +2 T (the reversed field orientation). The power flowing into the scrape-off layer (SOL) is about 600 kW. The density was ramped slowly allowing a clear distinction of different phases or events.

Diagnostics :

Arrays of Dα diodes and of bremsstrahlung detectors were used to monitor the cold and dense MARFE plasma. The power radiated by the bulk and the divertor plasma is measured by a bolometer system. Arrays of Langmuir triple-probes have been flush-mounted into the divertor plates to measure the plasma parameters. Two multichannel optical spectrometers (one looking horizontally, one vertically) observe the intensity of spectral lines emitted by the plasma in front of the outer target plate. The neutral gas pressure in the divertor region is measured by gauges installed below the x-point and behind the lower passive stabilizing coil.

Experimental Results and Discussion :

As reported elsewhere [2], a toroidally symmetric radiating structure is created in the divertor of ASDEX-Upgrade during density ramp experiments. It starts when the electron temperature at the plate drops below about 5 eV. In its early stage (pre-MARFE) the radiating structure has a rather diffuse shape but it flattens the flux profiles along the divertor plate. The bolometer and the spectrometers indicate a movement of the global radiation and the impurity radiation away from the plate towards the x-point. This stage (pre-MARFE in the divertor) is often interpreted as a detachment from the plate, but only a 20 ... 30 % reduction of the fluxes of particles and energy to the plate is observed. Clear indications of the strike point are still detectable at the plate. The rather slow development of the pre-MARFE (characteristic time 100 ms) is terminated by a fast movement (10 ... 20 ms) directly to the x-point now forming a well developed MARFE. This structure is essentially stable even if the density ramp is continued until the density limit is approached.

The principal difference is that the x-point MARFE obviously influences regions with closed magnetic surfaces slightly inside the separatrix most remarkably expressed as a rise of the central density indicating an improvement of the particle confinement (fig. 1) [9]. This must be a consequence of the additional heat sink due to the MARFE, probably changing profiles just inside separatrix. In experiments with the line averaged density feedback controlled at a value slightly exceeding n_{crit} the MARFE fell back to its pre-stage and became re-established again. This bistable behaviour is, however, rather a consequence of time shifts between gas puff and central density and the improvement of particle confinement by the MARFE than a self-sustained oscillation as reported in [3]. The MARFE switches into its pre-stage at the maximum of the central density indicating a kind of hysteresis or the fact that edge parameters (edge density, edge temperature, or gradients at the edge) are essential for the switching rather than the central density itself. X-point MARFEs and hysteresis effects for their existence have been found in numerical modelling of ASDEX-Upgrade [4] but there the switch-back density is lower than the density needed for the creation. An interferometer channel looking through outer plasma regions indicates a drop of edge density already during the existence of the x-point MARFE as would be expected from the observed confinement behaviour (fig. 1) . All observations indicate that the radiating structure never completely vanishes, so the divertor never returns to its well attached state. The repeated switching of the MARFE between the divertor and x-point stage reveals the following typical features: By jumping to the x-point the MARFE opens the part of the divertor farer away from the separatrix to particle fluxes now bypassing the MARFE. $D\alpha$ and the neutral pressure rise imediately in those regions (fig. 2). To the contrary, the particle fluxes close to the outer strike point fall indicating an intersection of transport channel known to be crucial in divertor tokamaks [5]. The neutral pressure below the x-point and the $H\alpha$-signal from the inner strike zone demonstrate the same prompt disconnection (fig. 3). If the MARFE falls back into the divertor pre-stage the particle fluxes to the strike points as well as $D\alpha$ light and neutral pressure are re-established, but now the fluxes to the outer parts are reduced : the bypass is closed. Now, the slow shaping of the MARFE repeats and the fluxes to the outer parts of the divertor rise gradually until the x-point stage is switched-on again. The intensity of observed impurity lines is reduced by establishing the x-point MARFE (see fig. 4 for O and [1] for C) indicating that fluxes close to the strike zone are essential for impurity production. The observed CII radiation indicates the switching but the location of maximum intensity is clearly not at the x-point but in the SOL. In a series of dedicated experiments the dependence of n_{crit} on the q value was investigated by applying a density ramp well exceeding n_{crit} and than returning to subcritical values. Again the edge density seems to govern the transitions rather than the central density. The critical density deminishes for rising q (fig. 5) pointing to the fact that a longer connection to the upstream sources is favourable for MARFE creation as can be expected from MARFE models balancing the locally radiated energy and the heat conduction along the field lines [6].

Conclusions :

With rising density the divertor plasma of ASDEX-Upgrade cools down and a diffuse pre-MARFE appears that redirects particle and energy fluxes away from the separatrix flattening the deposition profiles. This structure develops by shaping and slow movement into a well localised ring moving quickly to the x-point localized at least partly inside the

separatrix. The fully developed x-point MARFE improves the particle confinement. It interrupts particle and energy fluxes close to the separatrix, but can be bypassed in the outer part of the SOL. Changes in edge conditions may cause it to fall back into its pre-stage in the divertor, indicating, that this stage is at least marginally stable, too. The q dependence of the threshold density reveals the expected influence of the connection length. Impurity production at the plates is influenced by the MARFE development but the fact that the maximum CII radiation is not centered around the MARFEs location is not well understood yet. Until the transition of the fully developed MARFE to the x-point all features are essentially the same for the reversed field case, whereas afterwards the scenario is different. Some details of the MARFE and its development observed experimentally can be confirmed by model calculations [7].

References

[1] M. Laux, K. Büchl, A. Carlson, A. Field, Ch. Fuchs, et al. : Detachment of the Divertor Plasma in ASDEX Upgrade, 20th EPS, Lisboa 1993

[2] V. Mertens, W. Junker, M. Laux, M. Schittenhelm, K. Büchl et al.:Experimental Investigation of Marfes and the Density Limit in ASDEX Upgrade, to be published in Plasma Physics and Controlled Fusion

[3]S.I. Krasheninnikov, A.S. Kukushkin, V.I. Pistunovich, V.A. Posharov: Nuclear Fusion Vol. 27 No.11(1987)

[4] H. Kastelewicz, R. Schneider, J. Neuhauser, D. Reiter B. Braams et al.: Numerical Marfe Studies at ASDEX Upgrade, IPP 8/3, April 1994

[5] A. Herrmann, M. Laux, D. Coster, J. Neuhauser, D. Reiter et al.: Energy Transport to the Divertor Plates of ASDEX Upgrade during ELMy H-Mode Phases, 11th PSI, Mito 1994

[6] J. Neuhauser, W. Schneider, R. Wunderlich Nuclear Fusion, Vol.26, No. 12 (1986)

[7] W. Junker, H.-S. Bosch, O. Gruber, G. Haas, H. Kastelewicz et al.: Comparison of Experimental MARFE Observations in ASDEX Upgrade with B2 Calculations, this conference

[8] S. Pitcher, H.-S. Bosch, K. Büchl, A. Field et al. : The effect of density on divertor conditions in ASDEX Upgrade, 11th PSI, Mito 1994

[9] P.C. Stangeby , Nuclear Fusion, Vol.33 (1993) p. 1695

Figure Captions

fig. 1 :Temporal evolution of central and edge chord densities and the gas flow (residence periods of the MARFE at the x-point are indicated)

fig. 2 : Neutral gas pressure behind PSL, Dα-intensity in front of the outer part of the plate and particle flux to a probe at the strike point

fig. 3 : Neutral gas pressure below the x-point, Dα-intensity at the inner strike zone, and particle flux to a probe in the private flux region

fig. 4 : Temporal evolution of a spectral line of neutral O close to the outer plate

fig. 5 : Dependence of the critical density for MARFE creation on the q(95) value

Corresponding Address : Max-Planck-Institut für Plasmaphysik
Bereich Berlin
Mohrenstraße 40/41
10117 Berlin

fig. 1

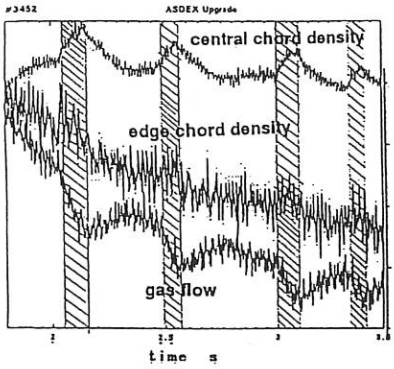


fig. 2

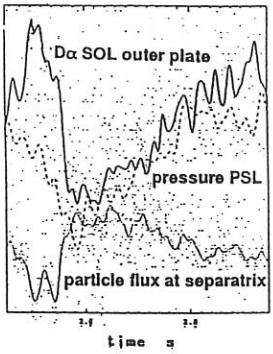


fig. 4

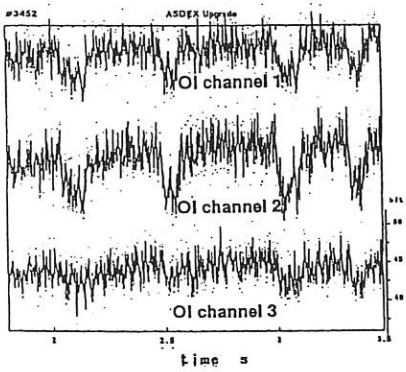


fig. 3

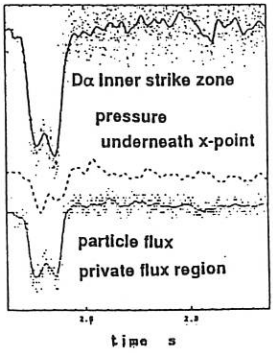
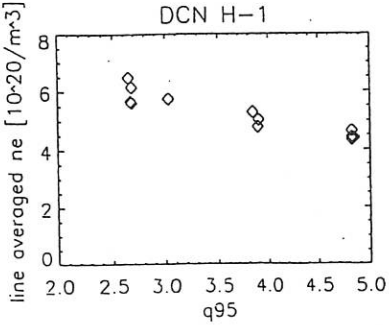


fig. 5



Study of High-Z Target Plate Materials in the Divertor of ASDEX-Upgrade

S. Hirsch, K. Asmussen, W. Engelhardt, A.R. Field, G. Fussmann, G. Lieder, D. Naujoks, R. Neu, R. Radtke, U. Wenzel and the ASDEX-Upgrade Team

Max-Planck-Institut für Plasmaphysik Garching, Association EURATOM Division Berlin, 10117 Berlin, Mohrenstraße 40-41, Germany

1. Introduction:

The reduction of divertor tile erosion is a challenging problem in present and future tokamaks. Until now, graphite has almost exclusively been used for divertor plates, and it is estimated that unacceptable amounts of material would be eroded under reactor relevant conditions where power fluxes to the target plates as high as 20 MW/m^2 are expected [1].

In a high-recycling divertor with relatively low temperature ($5eV<T_e<30eV$) and high density ($n_e \approx 10^{19}m^{-3}$) high-Z materials, e.g. tungsten, offer a possible solution to the target erosion problem. The reason is that the sputtering rates for these materials are extremely low under low temperature conditions. In addition, at high density the ionization lengths can be smaller than the gyro-radius leading to a high probability for prompt redeposition of the eroded ions. [2].

To provide a test of the suitability of high-Z materials for the divertor plates, in-situ studies of the erosion of various divertor target materials have been performed by means of passive spectroscopy. From our spectroscopic observations we infer that under high density divertor conditions the advantages of high-Z materials become fully efficient.

2. Experimental:

ASDEX-Upgrade is a divertor tokamak where graphite is used as material for the target plates. In order to study the erosion of high-Z materials narrow stripes of Cr, Ni, Mo and W have been inlaid across the outer target plate. These were observed by the boundary layer spectrometer [3] viewing perpendicularly to the target. A similar plate of W has been embedded into the target under the tangentially viewing multi-chord divertor spectrometer [4]. With a spatial resolution of about 2 mm, the divertor spectrometer allows direct measurements of the ionization length of the sputtered atoms. A schematic diagram of both spectrometer systems is shown in Fig. 1.

Although highly charged impurity ions are not produced under low temperature divertor conditions, we cannot exclude that such ions are created in the hot plasma regions and flow towards the target plates. In this case, self-sputtering can be a problem due to the energy that highly charged ions gain over the sheath potential. In order to study the role of self-sputtering in the erosion of high-Z materials, a laser-blow-off system has been used to inject W ($1\text{-}4\cdot10^{17}$ atoms per pulse) into the hot plasma remote from the divertor region. Following injection, the W emission (x-ray to visible region) was observed by several spectrometers and bolometer arrays viewing in the central and SOL plasma.

The experiments were conducted in ohmically heated deuterium discharges (I_p=800kA, B_t=-2T, $\bar{n}_e = 2\text{-}5\cdot10^{19}m^{-3}$) as well as in discharges with additional heating ($P \leq$ 8MW) where the line averaged density $\bar{n}_e$ was as high as $8\cdot10^{19}m^{-3}$.

3. Results and Discussion:

During divertor operation several lines of atoms sputtered from the target plate inlays were observed. Generally, the line intensities became weaker with increasing Z due to the increasingly complex atomic structure. Concentrating on a discussion of our data for W (W is the most promising alternative to graphite), with the divertor spectrometer several WI lines were observed (WI 400.8, 407.4, 429.5, 430.2 nm) , the strongest being the WI 400.8 nm ($a^7 S_3 - z^7 P_4$) transition. No lines of W II (and Mo II) ions could be detected with the divertor or boundary layer spectrometers.

The WI 400.8 nm line was used to plot intensity profiles above the target plate. Fig. 2 shows the variation of the profile as function of the line averaged density during an Ohmic discharge before boronisation. The corresponding values for n_e and T_e at the target were derived from in-vessel probe measurements. At $\bar{n}_e = 3.2\cdot10^{19}m^{-3}$, $T_e \leq 10$ eV and $n_e \approx 5\cdot10^{18}m^{-3}$ at the target. The decay lengths of the emission λ_0 estimated from these profiles of about 2-3 mm are consistent with ionization lengths λ_i calculated using appropriate ionization rates for neutral W^0 [5]. The ionization length is given by $\lambda_i = v_0/n_e S(T_e)$ where $S(T_e)$ is the ionization rate coefficient and v_0 is the initial velocity of the eroded W^0 atoms. If we assume an incident ion energy of 110 eV for the light impurities O and C ($E_0 = 2T_i+3Z_iT_e = 110$ eV with $T_e = T_i = 10$ eV and $Z_i = 3$), an average energy of 4 eV is estimated for the sputtered tungsten atoms. Assuming $T_e = 10$ eV and $n_e = 5\cdot10^{18}cm^{-3}$ for target facing plasma gives $\lambda_i = 1.3$ mm which is in reasonably good agreement with the measured decay length.

The fact that the ionization length λ_i is so short ensures that prompt redeposition of sputtered W^+ ions should be highly efficient. After leaving the surface sputtered neutrals are ionized and, once charged, are constrained to gyrate around the B-field.

With B tangential to the target, some of these ions are promptly redeposited at the surface within their first gyro-orbit. The redeposition probability is independent of the energy of the sputtered atoms and increases with decreasing $p = \lambda_i/\rho$ where $\rho = v_i m/eB \approx 2$ mm is the gyro-radius of the W^+ ion. Analytic calculations, including the ionization distribution, suggest that the redeposition probability can be almost unity provided n_e at the target is sufficiently high [6]. At $n_e = 5 \cdot 10^{18} m^{-3}$, $T_e = 10$ eV and B = 2T for W we find $p \approx 0.6$ corresponding to a redeposition probability of 0.75.

The WI line intensity decreases markedly as soon as the bulk plasma density is increased confirming that the sputtering yield for W is strongly temperature dependent. Under higher density Ohmic conditions ($\bar{n}_e \geq 5.10^{19} cm^{-3}$) the WI lines are no longer detectable because the divertor temperature is to low to sputter W^0 atoms. Measurements with additional heating (8 MW NI power) at higher $\bar{n}_e$ ($\approx 6.10^{19} cm^{-3}$) show that the W^0 influx increases as expected, but the intensity of the observed line peaks sharply at the target plate. This indicates that the decay length is less than our spatial resolution (2 mm).

Although the WI 400.8 nm line intensity is proportional to the W-influx, the gross flux cannot be derived accurately from our spectroscopic measurements. The reason is that a large fraction of atoms can be in the many unobserved metastable states. With a simple model, using the same excitation rates for all levels, we have estimated that as much as 95% of the W atoms can be in such states. A reliable spectroscopic flux measurement for W requires, therefore, further quantitative studies.

Turning to the observations following W injection by the laser-blow-off system, the total radiation profiles from the bolometer arrays show a general enhancement of the emissivity in the central and SOL plasma. However, there is no pronounced peaking of the radiation indicating little tendency for the injected W to accumulate. The decay time of the W emission to the pre-injection level is typically 100 ms resulting in a mean W-flux of about $2 \cdot 10^{18}$ s^{-1} to the target plates. No enhancement of the WI 400.8 nm line could be detected by the divertor spectrometer following W injection. This indicates that substantial self-sputtering does not occur, probably due to a cooling of the divertor plasma.

References

[1] J.N. Brooks, Fusion Technology, 18 (1990) 239

[2] J. Roth, et al., Nucl. Materials (1994), to be published

[3] A.R. Field, et al., IPP Report, 1-278 (1994)

[4] G. Lieder, et al., Proc. 20th Europ. Conf. Contr. Fus. and Plasma Phys., 17C, Lisbon (1993) 579

[5] M.S. Pindzola, D.C. Griffin, Phys.Rev.A, 16 (1992) 2486

[6] G. Fussmann, Field et al., Nucl. Materials (1994), to be published

Figure captions

Fig. 1 Schematic diagram of the boundary layer (BLS) and divertor (DS) spectrometers on ASDEX-Upgrade.

Fig. 2.a) Intensity distribution around 404 nm showing WI lines at 400.8 and 407.4 nm
b) Measured intensity profiles of the WI 400.8 nm line above the target:
Δ-$\bar{n}_e = 2.1 \cdot 10^{19}$ m^{-3}, $\lambda_o = 3.3$ mm; $*$ - $\bar{n}_e = 3.2 \cdot 10^{19}$cm^{-3}, $\lambda_o = 1.8$ mm.

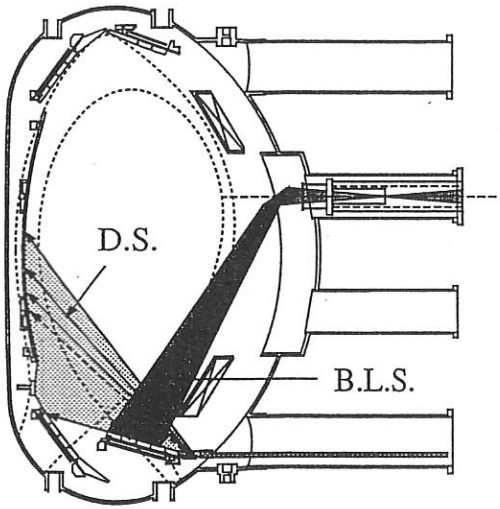


Fig. 1

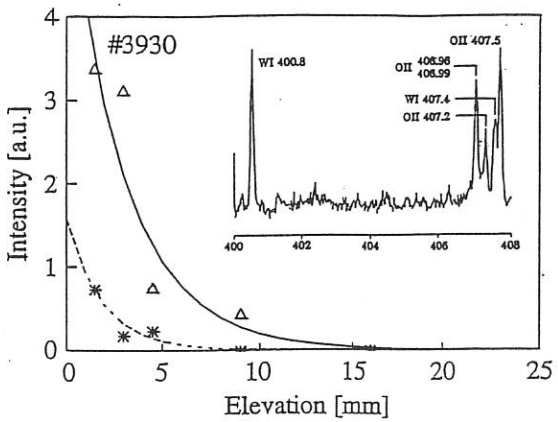


Fig. 2

STRUCTURE OF THE TEMPERATURE AND DENSITY FIELDS IN THE BOUNDARY LAYER DURING ERGODIC DIVERTOR OPERATION IN TORE SUPRA

DeMichelis C., Ghendrih Ph., Guirlet R., Hess W., Monier-Garbet P., Capes H., Grosman A., Guilhem D., Nguyen F., Vallet J.C., Valter J.

Association EURATOM-CEA, DRFC/SPPF,
C.E. Cadarache, 13108 Saint Paul-lez-Durance, France

Active control of the edge plasma (in view of minimizing the impurity influx) is one of the crucial issues to be solved for tokamaks. Much work has been recently devoted to axisymmetric poloidal divertor configurations /1/. An alternative possible solution, the ergodic divertor (ED), is being studied in the Tore Supra tokamak. Here, the idea is to destroy the magnetic surfaces in the edge plasma with a weak resonant perturbation /2/, thus leading to an edge layer where the field lines are stochastic. The expected result is an enhancement of both the particle and heat transport coefficients /3/. We have already demonstrated the ED capability to screen the main plasma from impurities /4/, and to stabilize the (2,1) MHD mode /5/.

Tore Supra is the first tokamak in which the ED concept has been integrated in the machine design. The ED configuration consists of six, toroidally equally spaced, octopolar coils installed inside the vacuum vessel. Their toroidal and poloidal extensions are 13° and 120°, respectively. The ED toroidal and poloidal mode numbers are $n = 6$ and $m = 18 \pm 3$ in the correct magnetic coordinates (i.e., the system is resonant for a safety factor value $q = 3$), thus providing an ergodic layer that is well located in the plasma edge (with a thickness 10-20 % of the plasma radius), with a rapid spatial decay towards the plasma core /6/.

A theoretical analysis of transport in presence of the ED, including the effect of the wall, shows that one can expect two domains in the edge layer: a laminar region, where the field line connection lengths are short (and therefore there is little stochasticity), and the proper ergodic region, where the connection lengths to the wall are large. As a result of the transport properties imposed by the presence of different flux tube lengths and by the existence of localized sources and sinks, one expects some modulation of the electron temperature and density /7/.

Figure 1 shows a few experimental data for an ED deuterium discharge with $R = 2.39$ m, $a = 0.75$ m (set by a carbon limiter, 4 cm ahead of the ED modules), $I_p = 1.4$ MA, and $B_t = 3.4$ T, with the ED coils activated at their maximum current from the beginning. This series of discharges was characterized by an almost completely saturated carbon wall, since in the reference (no ED, same n_e) ohmic discharge the electron density was built up without gas injection (apart from a small pre-fill for breakdown). The central electron density and temperature values were $n_e(0) = 5.5 \times 10^{-19}$ m^{-3} and $T_e(0) = 1.7$ keV, with $T_i(0) \equiv T_e(0)$. As expected, due to the ED effect, both the dominant impurity (carbon) and the injected deuterium gas were screened out ($Z_{eff} = 1.05$), and a large quantity of D_2 had to be injected to reach the requested n_e value. The radiative behaviour of these discharges is shown in figure 2, giving the total ohmic and radiated (calculated from bolometry) powers, as well as two bolometric radial profiles. ED ohmic discharges of not too high n_e are characterized by a low field side (exterior) radiating layer, possibly not completely toroidally uniform (because of the recycling pattern on the discrete ED coils). However, as the electron density is pushed up by the strong gas injection, recycling on the inner wall becomes important, the radiating layer moves to the high field side (interior), and a Marfe-like structure develops. Note that the Marfe is stable, and that a large fraction (≥ 75 %) of the ohmic power is radiated away.

Tangential views of the plasma with a visible (unfiltered) CCD camera show, when the internal Marfe appears, an "island"-like structure of the magnetic flux tubes on the high field side /8/. The visible light (essentially deuterium emission) structure is interpreted as due to the temperature and/or density modulations associated with the modulation of the field line connections. Such T_e and n_e edge modulations have actually been detected with a reciprocating Langmuir probe /6/; in the following we shall show that they also affect the emission of light impurity peripheral ions.

Spatially resolved profiles of several peripheral light impurity ions have been obtained with the experimental set-up schematically shown in figure 3. A grazing incidence vuv spectrometer (spectral range 50 - 2000 Å, spectral resolution 1.3 Å), equipped with two movable, metallic anodes, microchannel plate detectors /9/, views the plasma through a gold-coated, grazing incidence, vibrating mirror (vibration frequency 2 Hz, i.e., four profiles per second, acquisition time 2 ms, time for an entire scan of the plasma lower half 90 ms, spatial resolution 4 cm). Figure 4 shows the profiles of three carbon ion lines as a function of the mirror angle α defined in figure 3. The three lines are: CIV 312 Å $1s^2 2s - 1s^2 3p$ (a $\Delta n = 1$ transition, n being the principal quantum number), CIII 538 Å $1s^2 2s2p - 1s^2 2s3s$ ($\Delta n = 1$), and CIII 977 Å $1s^2 2s^2 - 1s^2 2s2p$ ($\Delta n = 0$). For each line we have shown one profile before the Marfe (i.e., when the radiating layer is on the low field side), and one during the Marfe (radiating layer on the high field side), at approximately the same times as the two bolometric profiles of figure 2. The most striking feature is the strong modulation observed on all the $\Delta n = 1$ transitions of low ionization potential E_i impurity ions (but not on $\Delta n = 0$ transitions), when the Marfe appears. Other, higher E_i, impurity ion lines (such as CVI 182 Å 2s - 3p, OV 630 Å $1s^2 2s^2 - 1s^2 2s2p$, or OVI 1032 Å $1s^2 2s - 1s^2 2p$) do not show any modulation, probably because they are emitted further inside the plasma, where the ergodic perturbation has become negligible. The observed modulation structure is stable during the current plateau, as well as from shot to shot in a series of approximately reproducible plasmas (but its observation requires always the presence, at the same time, of the ergodic divertor and the interior Marfe). There are six peaks in the lower half plasma profile, corresponding to a poloidal angle of 120°, i.e. a poloidal number ≤ 18 (the dominant mode of the ergodic perturbation).

The observed radiance of a given spectral line being given by

$$B_Z^n = \int n_e\, n_Z\, Q_Z^n(T_e)\, \Gamma_n \, dr \,/\, 4\pi$$

(photons $cm^{-2}\, s^{-1}\, sr^{-1}$; n_e and n_Z are the electron and ion impurity density, respectively, $Q_Z^n(T_e)$ the effective exitation rate coefficient, and Γ_n the branching ratio of the line transition), the high field side structure modulation cannot be due to a modulation of n_e and/or n_Z, since in this case it would result in a modulation of both $\Delta n = 1$ and $\Delta n = 0$ transitions. It is therefore due to a T_e modulation, as a consequence of the different T_e dependence of $Q_Z^n(T_e)$ for the two types of transitions; indeed, the intensity ratio of the two CIII lines indicates that T_e varies between 7 and 10 eV, a T_e range where $Q_Z^n(T_e)$ for the $\Delta n = 1$ transition is a strong increasing T_e function (also for the CIV line), whereas it is approximately constant for the $\Delta n = 0$ transition /10/.

Going back to figure 4, some structure is also seen on the profiles before the Marfe, when bolometry shows an external radiating layer. However, in contrast to what is seen during the Marfe, these broader modulations are seen on all the ion lines emitted in the ergodic region (independently of their $\Delta n = 0$ or 1 nature). Also, there are only between two and three modulations, mainly because of the smaller poloidal angle spanned on the low field side (60°), thus corresponding to a poloidal mode number between 12 and 18. The fact that the structure is now seen on all the lines emitted by ions in the ergodic layer indicates that it is not due to T_e, but rather to n_e or n_Z modulations. This implies that the peripheral T_e value is higher in the low field side (since T_e must be large enough to have approximately constant

$Q_z^n(T_e)$ values); indeed, a Langmuir probe in one of the ED modules shows T_e = 20 eV, probably due to the lower n_e value. As far as the n_e and/or n_z modulations are concerned, it is not possible to discriminate between them from the spectroscopic results. Electron density modulations have been seen by Langmuir probe measurements, but impurity source modulations are also possible, since for these low ionization potential carbon ions there is no time to achieve complete poloidal and toroidal uniformity.

The spectroscopic results discussed above give clear evidence of poloidal density modulations when the radiating layer is on the low field side (the usual ED situation when the electron density is not too high), and temperature modulations when the radiating layer is on the high field side (at high electron density, where, in the ED presence, a stable Marfe-like structure develops). Density and temperature modulations are predicted by the ED theory. They originate outboards (where the ED modules are located), from the connections of the flux tubes either towards the plasma core (yielding a large heat source) or towards the wall (yielding a small heat source), depending on the direction of the local radial magnetic perturbation due to the ED. From there, they propagate along field lines. On the low field side the peripheral T_e value is large enough not to have any effect on the impurity line brightness (because in this temperature range the relevant excitation rate coefficients are approximately constant), which is therefore affected only by the density (electron and/or impurity) modulations (of course, only the emission from ions existing in the ED peripheral layer is affected). However, as the modulations propagate from the exterior along flux lines, the density modulations are smoothed out, because the ED induced particle transport is of the same order as the usual radial transport, and they do not propagate very far. On the other hand, the ED induced parallel heat transport is much larger than the usual perpendicular transport, and therefore the T_e modulation is not easily destroyed. Moreover, when the interior Marfe develops, the peripheral T_e value is lower, because of the larger electron density, and is such that $\Delta n = 1$ transitions are modulated (because in this temperature range, below or of the order of 10 eV, the Q_z^n rate coefficients are an increasing T_e function), but not $\Delta n = 0$ transitions (because their Q_z^n rate coefficients are roughly T_e independent). Lines from more ionized ions (having $E_i \geq 100$ eV) do not show any modulation, since they are emitted further inside the plasma, where the ED perturbation has become negligible.

A field line tracing code (MASTOC) /11/ has been used to study the intersection of the laminar layer and the wall. The derived connection lengths to various parts of the wall are used to analyse heat and particle flux deposition. Since the geometrical features of the laminar region are closely related to the structure of the field lines, most of the observed effects can be modeled by using the properties of the field lines. This simple model, based on the connection properties, allows the expected modulation to be calculated for different dominant poloidal numbers. A comparison with the impurity profiles shows that the observed modulations are characterized by a poloidal wave number m = 16, thus allowing to locate radially the emission region at r = 0.71 m. Note, however, that there is no atomic , nor plasma-wall interaction, physics in these calculations.

REFERENCES

/1/ VLASES G.C., Plasma Phys. Control. Fusion 35 (1993) B67
/2/ ENGELHARDT W. and FENEBERG W., J. Nucl. Mater. 76-77 (1978) 520
/3/ SAMAIN A. et al, Contr. Plasma Phys. 30 (1990) 157
/4/ BRETON C. et al, Nucl. Fusion 31 (1991) 1774
/5/ VALLET J.C. et al, Phys. Rev. Letters 67 (1991) 2262
/6/ GHENDRIH Ph. et al, Plasma Phys; Control. Fusion 34 (1992) 2007
/7/ NGUYEN F. et al, J. Nucl. Mater. 176-177 (1990) 499
/8/ GROSMAN A. et al, J. Nucl. Mater. 196-198 (1992) 59
/9/ DEMICHELIS C. et al, Meas. Sci. Technol. 4 (1993) 109
/10/ MAGGI C.F., JET-IR(93)05 (1993)
/11/ NGUYEN F. et al, 19th EPS, Innsbruck, Europhys. Abstracts 16c (1992) 851

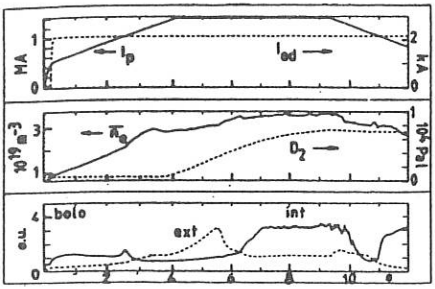


Figure 1

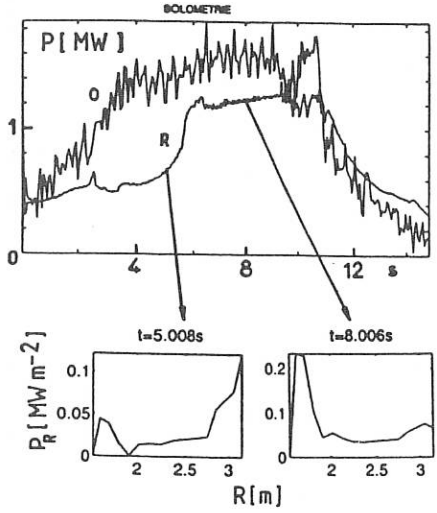


Figure 2

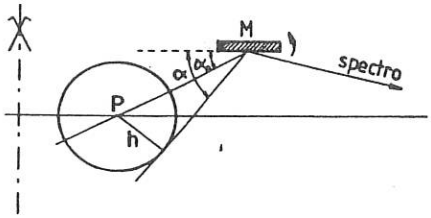


Figure 3

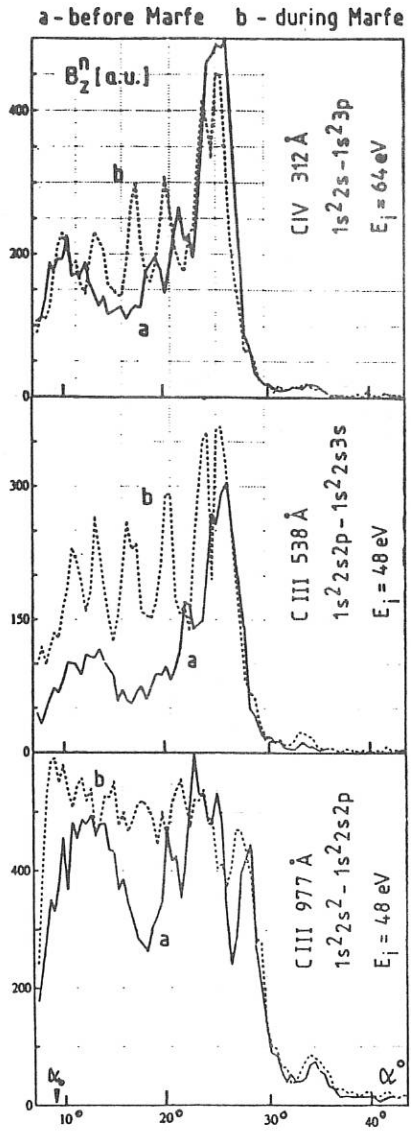


Figure 4

Screening and radiating properties of Tore-Supra ergodic divertor during impurity injection experiments.

P. Monier-Garbet, C. Chamouard, C. DeMichelis, E. Gauthier, Ph. Ghendrih, C. Grisolia, A. Grosman, R. Guirlet, W. Hess, J.C. Vallet

Association EURATOM-CEA sur la Fusion Contrôlée
Centre d'Etudes de Cadarache, 13108 St-Paul-lez-Durance, France

I.Introduction

Edge radiative layers are a possible solution for energy exhaust in the next step tokamak. For this scenario, the high radiative loss is triggered either by deuterium or gaseous impurity injection. Therefore the main difficulty lies in minimizing the plasma core contamination by the injected species. In Tore-Supra, the impurity seeding technique is used and the ergodic divertor (ED) is activated to shield the plasma core from the impurity influx. Indeed, the ED configuration in Tore-Supra has given evidence of good screening properties for most species. A purification of the plasma core has been observed in ohmic plasmas, both for intrinsic carbon and for injected nitrogen and argon (1). The scope of this paper is to assess the efficiency of the ED configuration to produce a controlled radiating edge in auxiliary heated plasmas, by an impurity injection technique, and with low plasma core contamination. A series of experiments with up to 5 MW of ion cyclotron resonant waves heating (ICRH) and neon injection is analysed. A few experiments with argon and methane injection are also shortly discussed. Similar experiments with neon injections, in a limiter configuration, are reported from Textor in reference (2).

II.Edge radiative layer experiment

The main plasma characteristics are : deuterium gas, a=0.74m, R=2.41m, B_t=3.6T, I_p=1.56MA satisfying the resonant ED conditions ($q_\psi(a) \approx 3$). The outboard carbon limiter is inserted 0.03m radially ahead of the ED modules. A total input power of up to 6.5 MW is achieved by means of up to 5 MW of ICRH and 1.5 MW of Joule heating. In a first series of experiments the ED is activated all along the plasma discharge. In a second series the ED is not active (limiter configuration, comparable to Textor experiments). The volume averaged electron density is 3.2 10^{19} m^{-3} in the ED configuration, and 4.5 10^{19} m^{-3} in the limiter configuration. The impurity is puffed into the plasma 0.5s after the ICRH pulse is started. The impurity injection is monitored by a set of visible and VUV spectrometers. The global power balance of the discharge is deduced from both bolometric measurements for the radiative fraction, and infra-red thermography of the main plasma-facing components for the conductive-convective fraction. The bolometer array gives a measurement of the radiative power profile in a complete poloidal section, but only at one toroidal location. The infra-red thermography measurement is a useful cross-check for the calculation of the total radiative losses in case of toroidal inhomogeneities. It is also directly relevant to the goal of the experiment which is to reduce the heat flux to the wall. The duration of the impurity puff is increased from shot to shot to maximize the radiated power.

Argon, methane and neon have been used. However an extensive set of experiments has been performed only for neon for reasons related to the sake of simplicity in the discharge analysis. For argon, the wall retention plays a prominent role. Indeed the quantity of argon injected during a shot is not completely recovered at the end of the plasma discharge. Consequently the argon wall inventory increases from shot to shot during the day, reaching saturation after less than 3. 10^{19} argon atoms in the wall. Their subsequent desorption from the wall results in a shot to shot modification of the gas quantity which it is necessary to inject. Nevertheless,

the few experiments performed with argon before the wall is saturated indicate that only a low quantity of this impurity, typically 40 Pal = 1. 10^{19} atoms, is enough to radiate close to 100% of the total input power ($P_{tot} \cong 3.5$MW in this particular experiment) when the ED is activated. The resulting argon concentration in the plasma core n_{Ar}/n_e is lower than 0.3%. For methane, a high quantity has to be injected, close to 1500 Pal. This is of the same order as the quantity of deuterium which is necessary to inject to radiate the same power. Only less than 1% of the injected carbon atoms penetrate into the confined plasma, yielding an increase of the carbon concentration in the plasma core lower than 0.5%. Results on the low fuelling efficiency of methane and carbon monoxide in Textor and Asdex are reported in (2) and (3). The experiments with neon are easier to analyse than with argon, because they have no shot-to-shot retention and release problem. The rest of this paper is devoted to neon injection experiments.

III.Neon injection : comparison of ED and limiter configurations

III.1.Radiative fraction

Figure 1 shows the ratio of the radiated power measured by bolometry to the total input power as a function of the number of injected neon atoms in the limiter and ED configurations. In the limiter case the radiated fraction reaches 80%, when 12. 10^{19} neon atoms are injected.The radiation profile is roughly poloidally symmetrical up to 9.0 10^{19} injected neon. The electron temperature measured by Thomson scattering at r=0.70±0.03m is practically unaffected by neon injection, at approximately 200 eV. For 9.0 $10^{19} < N_{inj} <$ 12. 10^{19} a high-field MARFE appears, and a higher injection level leads to a disruption. In the ED case, the radiative fraction is P_{rad}/P_{tot} = 50% before neon is injected. However the effective charge is low, close to 1.3. The edge electron temperature at r=0.70±0.03m is 90 eV. Radiation is located on the plasma low-field-side (lfs), close to the ED modules. In this configuration, less than 2.0 10^{19} injected neon are enough to bring the radiative fraction in the 80% range for 3MW < P_{ICRH} < 5MW. The radiation profile remains poloidally located on the plasma lfs. The edge electron temperature drops to about 60 eV (at r=0.70±0.03m). Hence, when comparing the two configurations, the first point to notice is that the limiter configuration requires much more injection than the ED one (about 7 times more) for a similar radiative loss increase of about 1MW.

III.2.Neon penetration probability

The number of neon atoms in the confined plasma is measured by the NeX Lyman α (1.2nm) line brightness, correlated with soft X-rays and visible bremstrahlung absolute brightness values. The neon experimental penetration probability (P) is calculated by dividing the number of neon atoms in the confined plasma by the number of injected neon atoms. The penetration probability is shown on figure 2 for the limiter and ED configurations. The penetration probability is found to be 4.5 times higher in the ED configuration than in the limiter one. In other words, although the ED configuration requires 7 times less injection through the valve, the resulting neon density in the plasma core is only lower by a factor 7/4.5 = 1.6 compared to the limiter case. Indeed, the neon density in the plasma core corresponding to a peripheral radiation loss increase of 1 MW is close to 2.5 $10^{17} m^{-3}$ in the ED case and 4.0 10^{17} m^{-3} in the limiter case. Note that, due to the different values of the plasma electron density in the two cases, the corresponding neon concentrations n_{Ne}/n_e are roughly equal : 0.8% in the ED case, and 0.9% in the limiter one.
In order to understand this lower apparent screening of the injected species in the ED case, the wall retention has been investigated (no pumping system was activated). The residual gas analyser data show that the exponential decrease of the neon partial pressure in the torus is slower in the limiter configuration than in the ED one. In both cases the time constants (45s

and 15s) are larger than the pumping time constant (7s) if the origin of neon was only recombination at the end of the shot. Thus, a transient retention is clearly shown and it is much higher for the limiter configuration than for the ED one. It is important to note that the retention time is much longer than the neon residence time in the plasma, but much smaller than the delay between shots. As a consequence, a major part of the injected neon could stay in the wall during the shot but would have disappeared before the next one.
These observations show that an impurity which is not pumped (either by the wall or any other pumping system) eventually contaminates the plasma core despite the ergodic region. Its penetration probability is of the order of 1. In the case of neon, the lower apparent screening in the ED configuration is due to the measured lower retention in the wall and not, as could be first proposed, to deleterious transport effects in the edge region. In this frame, when using a recycling impurity to produce edge radiative layers, the problem to be solved is to distribute a given number of impurity ions (≡ the number of injected impurity atoms) as adequately as possible in the edge so as to maximize the radiated power.

III.3.Neon radiation capability

The radiation capability of neon can be defined by the volume integrated radiation function :

$$\frac{P_{rad}(neon)}{\langle n_e \rangle \langle n_{neon} \rangle} = \int L(T_e) dV$$

where $P_{rad}(neon)$ is the power radiated by neon, $L(T_e)$ is the cooling rate and the integral is over the volume of the radiating zone. The radiation capability of neon has been measured for the ED and limiter configurations in our experiments, the power radiated by neon in the edge being estimated from the peripheral NeVII (55.8nm) line brightness. The result is shown on figure 3 where the radiation capability of neon is indicated by the slope of the two lines. It is 3 times higher in the ED case than in the limiter one, i.e. for a given neon density in the plasma core, the neon radiation is 3 times higher in the ED configuration than in the limiter one. These observations indicate that the distribution of neon ions achieved by the ED is better compared to the distribution achieved by the limiter configuration. This optimized distribution can be due either to a modification of the electron temperature profile, or to a modification of the impurity transport in the edge.

IV.Conclusion

Controlled radiating edge layers have been obtained in Tore Supra both in limiter and ED configurations, the latter having shown some advantages. The plasmas were heated with up to 5 MW of ICRH, added to 1.5 MW of Joule heating. A highly radiating edge was obtained by neon injection. Conditions where more than 80% of the total power is radiated were achieved in both limiter and ED cases, but with an order of magnitude more neon injected in the former case. Nevertheless the neon concentration in the plasma core remains low in both configurations : 0.8% in the ED one, 0.9% in the limiter one. This result is explained by the retention of neon in the wall, which has been shown to be much higher in the limiter case. Yet the radiation capability of neon has been proved to be larger in the ED case, the neon density in the plasma core corresponding to a typical edge neon radiation being 3 times lower in the ED configuration than in the limiter one.

References :

(1) Monier-Garbet, P., et al., IAEA-CN-56/A-5-4, 14th IAEA Conference, Würzburg, 30 Sept-7Oct 1992.
(2) McCracken, G.M., et al., Nucl. Fusion **33** (1993) 1409.
(3) Krieger, K., et al., Nucl. Fusion **33** (1993) 1591.

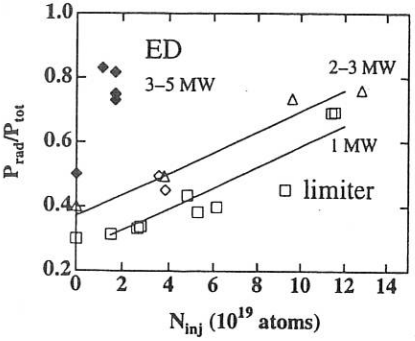


Figure 1

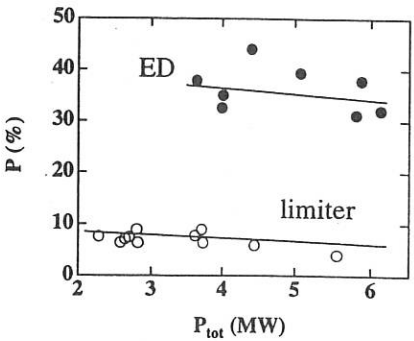


Figure 2

Figure 1 : Ratio of the radiated power to the total input power, as a function of the number of injected neon atoms through the valve : (□) limiter configuration, P_{ICRH}=1MW; (△) limiter configuration, P_{ICRH}=2-3MW; (◆) ED configuration, P_{ICRH}=3-5MW.
Figure 2 : Neon experimental penetration probability as a function of the total input power, in the limiter (○), and ED (●) configurations.

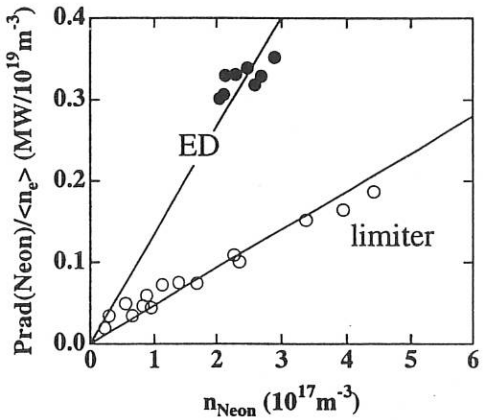


Figure 3 : Radiation capability of neon in the limiter (○), and ED (●) configurations

Numerical modeling of plasma flow target interaction for prediction of divertor behavior under ITER typical disruption conditions

B. Basylev[1], I. Landman[2], H. Würz[3]

1 Lykov Institute of Heat and Mass Transfer, 220086 Minsk Belarus
2 Troitsk Institute für Innovation and Fusion Research, 142092 Troitsk Russia
3 Kernforschungszentrum Karlsruhe, INR, Posfach 36 40, D-76021 Karlsruhe

Introduction

During the thermal quench phase of a plasma disruption and during ELM's the divertor plates are hit by an intense plasma flow consisting of electrons and ions. In ITER this flow has the following parameters: particle energy around 10 keV pulse duration larger than 100 μs, energy density up to 150 MJ/m^2 for disruptions and up to 10 MJ/m^2 for ELMs. Presently existing tokamaks are achieving energy densities up to 1.5 MJ/m^2 in the disrupting plasma flow and thus even are unable to reach the power density of an ITER ELM. Therefore for prediction of material behavior under typical ITER conditions simulated disruption testing is required. Pulsed plasma streams from plasma guns [1] and pulsed electron beams from vacuum diodes [2 - 3] are used and numerical modeling of the plasma flow target interaction is performed [4 - 6].

An important problem in the disruption simulation work is the investigation of the shielding effect of the target plasma formed in front of the divertor plates under the influence of the impinging plasma flow and the inclined magnetic field lines. Once a protective target plasma layer is formed, radiative energy transfer becomes the most important energy transfer path from the impinging plasma flow to the target. In all modeling work up to now rather low target plasma temperatures are reported [4 - 6]. New experimental results from disruption simulation however have shown that for low Z target materials a hot low dense plasma edge with temperatures up to 80 eV is formed which emits intense soft x-ray (SXR) line radiation. For carbon mainly two CV lines with photon energies of 308 eV and 356 eV were observed [7]. The role and the importance of this radiation for the radiative energy transfer to the target and for the effectiveness of the vapor shield is discussed in this paper.

Modeling of plasma flow target interaction

To identify the most important parameters influencing the target plasma temperature and the effectiveness of the vapor shield and to demonstrate the need for detailed optical data and for line radiation transport a simple plasma multilayer model as shown in Fig. 1 was used without hydrodynamics, without magnetic field diffusion and without vaporization and melt front propagation. Radiation transport is treated in forward reverse transport approximation, by using the multigroup Planck opacity concept. Power deposition by ions and Maxwellian distributed electrons is modeled.

A collisional radiative model is used for calculation of the optical properties [8] being described by the absorption and emission coefficients κ and η. These include contributions form free-free (ff, bremsstrahlung), bound-free (bf, ionization), and bound-bound (bb, excitation) transitions. For photon energies below 2 eV κ and η are dominated by ff transitions and above 40 eV mainly by bf transitions. In the photon energy region from 5 to 40 eV bb transitions are important. As this region is the most important one for plasma temperatures of a few eV the contribution of lines to the radiation transport becomes important. In carbon and beryllium plasmas with temperatures above 10 eV bb transitions in helium and hydrogen like ions for carbon and hydrogen like ions for beryllium produce SXR line radiation in the photon energy region above 100 eV. To describe the frequency dependence of κ and η by Planck group averaging adequately several hundred frequency groups were used.

The plasma emissivities are calculated assuming an optically thin plasma. This is appropriate for the continuum radiation. For the most prominent lines however the plasma is not optically thin. The plasma emissivities in the frequency range of these lines are additionally calculated assuming LTE and applying the Kirchhoff law. Both variants represent the extreme cases. The realistic line emissivity values should lie in between. Their calculation presently is performed applying an escape probability method.

Modeling results

The evolution of plasma temperature, radiation flux and ion beam energy depositon is shown in Fig. 2 for a carbon plasma layer of thickness of 10 cm having an exponentially rising plasma density with densities ranging from 5×10^{16} cm^{-3} up to 5×10^{18} cm^{-3}. The plasma flow enters the plasma layer at the low density side. The density profile approximately describes the real situation corresponding to an erosion of 1 µm and a target plasma expansion across a 5 T magnetic field. The energy of the impacting protons is 10 keV. Increasing the power density of the beam to 100 MW/cm^2 increases the plasma temperature to 77 eV and results in deeper penetration of the heat front into the plasma layer due to an increased contribution of electron heat conduction. The plasma emissivities used are valid for an optically thin plasma. A comparison of Fig. 2a and b shows that the radiative heat flux is locally correlated with the plasma temperature. The radiative heat load at the wall therefore is only weakly influenced by the temperature of the plasma edge (plasma corona).

Assuming validity of LTE for the emissivities of the SXR lines the temperature of the plasma corona reduces to 23 eV because of higher reradiation. Assuming LTE for the emissivities of the continuum radiation finally brings down the temperature to values below 10 eV for a power density of 10 MW/cm^2. A comparison of photon energy dependent boundary radiation fluxes is shown in Fig. 3. For SXR line emissivities under LTE the hot photons contribute with 50 % to the backradiated flux in rough agreement with the experimental results [7]. No hot photons are arriving at the wall. The opacity concept is only able to describe the transport of photons being in equilibrium with the local plasma temperature and

thus fails to predict the transport of hot photons through cold plasma layers with a steep temperature gradient.

Results for beryllium are shown in Fig. 4 for emissivities derived for an optically thin plasma. The temperature in the plasma corona reaches about 13 eV at plasma densities up to 4 x 10^{17} cm^{-3} due to a larger beam penetration. Fig. 5 shows boundary radiation fluxes. The backradiated flux is mainly due to hot photons from hydrogen like ions with energies of 123 eV. The radiative flux to the wall is due to photons from the energy region 1 to 10 eV.

Conclusions

For low Z materials the existence of a hot plasma corona confirmed in disruption simulation experiments was reproduced. The Be corona despite it's moderate temperature of around 13 eV mainly emits SXR photons with energy of 123 eV. A considerable fraction of the carbon corona emission consists of photons of energy of 308 and 356 eV. Calculation of the transmission probability of such hot photons through cold plasma layers with steep temperature gradients requires a self consistent method which takes into account the influence of the SXR radiation on the local level population of ions. Then finally the question can be answered whether the hot plasma corona contributes to the radiative heat load at the target.

Acknowledgement

The support of Dr. Vladimir Tolkach from Lykov Institute Minsk who provided updated and improved data on optical properties is greatly acknowledged. Dr. Friedbert Kappler from Kernforschungszentrum Karlsruhe assisted in comparing optical data of different origin and in it's visualization.

References

[1] N.I. Arkhipov et al., Fusion Technology 1992, North Holland Amsterdam 1993, Vol. 1, p. 171.

[2] V. Engelko et al., 11th International Conf. on Plasma Surface Interactions in controlled Fusion Devices, Mito, May 23 - 27, 1994.

[3] A. Burdakov et al., 20th EPS Conf. on Controlled Fusion and Plasma Physics, Lisboa, 26 - 30 July 1993, Vol. 17c Part II p. 747.

[4] H. Würz et al., 6th Int. Conf. on Fusion Reactor Materials, Stresa, Sept. 27 - Oct. 1, 1993.

[5] A. Hassanein et al., 11th Int. Conf. on Plasma Surface Interactions in Controlled Fusion Devices, Mito, May 23 - 27, 1994.

[6] P. Spathis, L. Lengyel, 20th EPS Conf. on Controlled Fusion and Plasma Physics, Lisboa, July 26 - 30, 1993, Vol. 17c, Part II, p. 1443.

[7] H. Würz et al., 11th Int. Conf. on Plasma Surface Interactions in controlled Fusion Devices, Mito, May 23 - 27, 1994.

[8] B.N. Basylev, L.V. Golub, G.S. Romanov, V.I. Tolkach, Physical Engineering Journal, Vol 58 No. 6 (1990), p. 1012 (in russian).

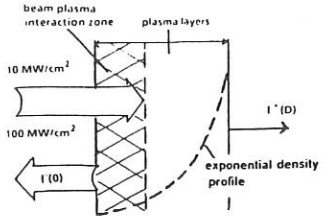


Fig. 1

Plasma multilayer model schematically.
$I^-(0)$ backradiated flux
$I^+(D)$ radiative flux to wall

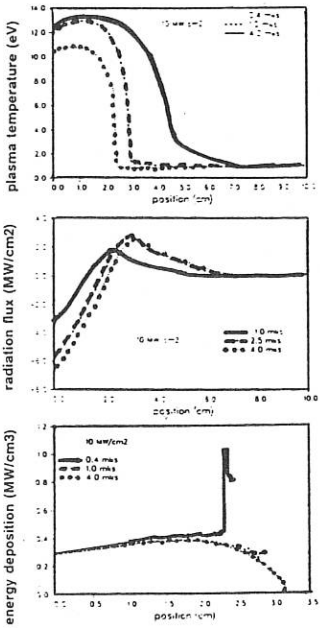


Fig. 4 Time evolution of plasma temperature radiation flux and beam energy deposition in a beryllium plasma. Proton impact energy is 10 keV, beam power density is 10 MW/cm^2.

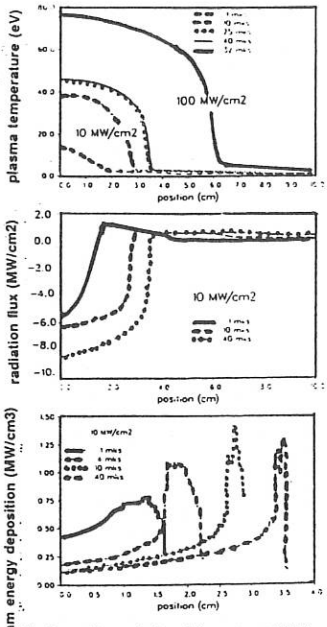


Fig. 2 Time evolution of plasma temperature radiation flux and ion beam energy deposition in a carbon plasma with exponentially rising plasma density. Proton impact energy is 10 keV.

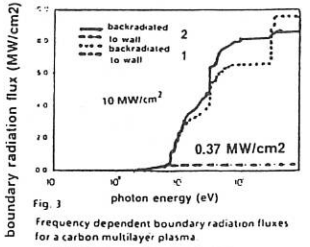


Fig. 3

Frequency dependent boundary radiation fluxes for a carbon multilayer plasma

1. SXR line emissivity for LTE
2. SXR line emissivity for optically thin plasma

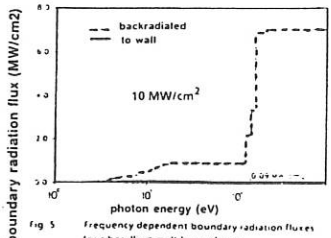


Fig. 5 Frequency dependent boundary radiation fluxes for a beryllium multilayer plasma

The Control of Convection by Fuelling and Pumping in the JET Pumped Divertor

P J Harbour, P Andrew, D Campbell, S Clement, S Davies, J Ehrenberg, S K Erents, A Gondhalekar, M Gadeberg, N Gottardi, M von Hellermann, L Horton, A Loarte, C Lowry, C Maggi, K McCormick, D O'Brien, R Reichle, G Saibene, R Simonini, J Spence, M Stamp, D Stork, A Taroni, G Vlases
JET Joint Undertaking, Abingdon, Oxon, OX14 3EA, UK

1 INTRODUCTION

Convection from the scrape-off layer (SOL) to the divertor will control core impurities, if it retains them in a cold, dense, divertor plasma. This implies a high impurity concentration in the divertor, low at its entrance. Particle flux into the divertor entrance, Γ_d, can be varied systematically in JET, using the new fuelling and pumping systems. We estimate the **convection ratio**, Γ_d/Γ_t, where Γ_t is the particle flux to the divertor target, for various conditions of operation. Particle convection into the divertor should increase thermal convection, decreasing thermal conduction, and temperature and density gradients along the magnetic field, hence increasing the frictional force and decreasing the thermal force on impurities.

The **convection ratio**, Γ_d/Γ_t,is estimated as follows ($n_S \approx 2\times10^{19}$ m^{-3}), based on EDGE2D [1].

Open configuration (horizontal target)	0.15	0.35
Closed configuration (vertical target)	0.03	0.19
Typical conditions	Low pumping/wall pumping and/or fuelling in divertor	High pumping/wall pumping & fuelling in torus

The limited range is due to ionisation in the divertor. The configuration is more "open" at low density and with hydrogen, giving higher Mach number at the divertor entrance.

The control of convection is important, so is studied in JET, using the new fuelling system. We discuss a limited study, using the Mk I Divertor, with horizontal target, and no pumping. It is expected that the control of impurities may be sensitive to small changes in Mach number, $-0.1 \le M \le 0.1$, say. The study of fuelling is supported by modelling with EDGE2D, as described in Sections 5,6.

2 THE EXPERIMENT IN JET AND THE MODEL PLASMA FOR EDGE2D

Fuelling ("puff" in Figures) is now provided at three poloidal locations in JET (Fig 1a), top (thick SOL), outer midplane, OMP (thin SOL, hence deeper penetration), and in the divertor, just below the X-point. The divertor system has 24 toroidally distributed inlet pipes, controllable in quadrants (six pipes each), via four independent fast gas valves. Pumping will be via a cryopump, stronger in the outer divertor, but not yet available, so we use wall-pumping in this study. Wall-pumping is assumed to occur mainly in the divertor and is found to decrease in strength throughout the day, from ~ 4×10^{21}s^{-1} to ~ 2×10^{21}s^{-1} in high density Ohmic discharges. The plasma configuration studied is shown in Fig 1a and the model geometry in Fig 1b. Fuelling in EDGE2D is simulated by introducing D atoms (T≈0.1eV) at the walls where indicated, while pumping is simulated by absorbing 10% of the flux of neutrals onto the divertor walls. Steady state is achieved by matching the fuelling rate to the wall pumping rate found in experiment and model respectively.

3 EXPERIMENTAL PROCEDURE

An Ohmic density scan was made in a series of discharges (2.8T, 2MA), with deuterium fuelling in the divertor (1,2 or 4 quadrants). Several discharges had top or OMP fuelling for comparison. The total electron content, N, increased until fairly constant. The pumping rate, ϕ_{pump}, is given by

$$\phi_{pump} = \phi_{fuel} - dN/dt \qquad (1),$$

and in every discharge $|dN/dt| \ll \phi_{pump}, \phi_{fuel}$ during the ≈ constant density phase. On the first day, with purely Ohmic discharges (#29756-66), data were taken at $t_{data} = 14-16s$. On the second day (#29810-23), $t_{data} = 13.5s$, avoiding the NBI commissioning time ($t_{NBI} \ge 16s$; $P_{NBI} \le 12\,MW$).

4 EXPERIMENTAL RESULTS

Figure 2 shows the density scan. The specific pumping rate, ϕ_{pump}/N(Fig 2a), lies mostly between 1 s^{-1} and 3.3 s^{-1}. Considering the pumping observations sequentially, there was first a density limit pulse

(29756) with top fuelling, then a low density pulse (fuelling off), where ϕ_{pump}/N was much lower. Divertor fuelling was used in **61**, which showed 20% less pumping than **56**, and the specific pumping rate continued to fall throughout the sequence **62-65**, with divertor fuelling, and **66**, with top fuelling. There seems little to distinguish the pumping in these Ohmic discharges, with top or divertor fuelling. On the second day, ϕ_{pump}/N was almost twice as large (only partly due to the timing of the observation, 1.5 s earlier). Again the specific pumping rate fell, the sequence 29**810-15** showing this clearly. The trend was resumed during **17,18 & 19**, the latter with top fuelling, and if we allow for the density variation there is nothing to suggest that **19** (top fuelling) or **20** (OMP fuelling) lie outside the sequence. In contrast, **23** (OMP fuelling) has at least 50% more pumping than expected. The specific pumping rate falls by 3% to 10% per discharge, increasing with plasma density as expected under high recycling conditions. A regression fit to the data in Fig.2a shows that ϕ_{pump} varies approximately as $N^{1.3}$ and that it increased by a factor greater than two on the second day. All measured values of ϕ_{pump} lay within about 10% of the regression line (apart from #29823) and, for those observations with fuelling in the main SOL, the deviations from the regression fit were random in sign as well as being of similar magnitude to those with divertor fuelling. This confirms the analysis of data given above.

The global $Z_{effective}$ varies with density as usual, but is higher for four of the five plasmas with SOL fuelling (Fig2b). This implies greater carbon content, due either to sputtering at the fuelling location or increased sputtering and escape of carbon from the divertor. In contrast, the bulk radiation is not affected fuelling location (Fig2d): either it is dominated by high Z species (e.g. Cl), little affected by changes at the edge, or we have an inconsistency. However the trends do appear to be significant.

Radiation in the divertor shows consistent trends in line with expectations. With divertor fuelling, the D_α intensity at both targets increases rapidly with N, D_α/N increasing linearly with N up to $N=10^{21}$, with about 10% greater intensity in the inner divertor. Above $N=10^{21}$ the increase, still linear in the outer diveretor, is faster than linear in the inner, indicating a cold plasma. The D_α intensity is up to 25% lower with fuelling in the SOL (Fig.2e,f). There is a similar trend in the total divertor radiation obtained bolometrically (Fig 2c).

Overall, there is clear evidence (D_α /bolometry) that particle fluxes in the divertor increase with density ($D_\alpha \sim N^2$ or more) as well as with divertor fuelling. Also the specific pumping rate increases with density ($\phi_{pump} \sim N^{1.3}$), but at a lower rate than the increase in particle fluxes in the divertor. It is surprising that the specific pumping rate is not increased by fuelling in the divertor, when fluxes are higher. Can it be that pumping occurs near the fuel inlet, possibly due to charge exchange?

SOL profiles, measured with a movable Langmuir probe in discharges 29**810-20**, showed a fairly constant narrow layer. In 29**819** (top fuelling) the scrape-off thickness increased substantially compared to 29**818** with divertor fuelling, (λ_n, 13.7→21mm; λ_Γ, 8.8→14mm; λ_T, 23→27mm). We expect broadening with fuelling in the SOL, especially at the top of the vessel, which would exaggerate differences between torus and divertor fuelling. No significant difference is apparent in Fig.2 for discharge 29**819**. Plasma profiles at the target were unavailable in these discharges.

5 MODELING WITH EDGE2D: PROCEDURE

Nine steady state runs with EDGE2D and NIMBUS were performed ($P_i^{SOL}=P_e^{SOL}=12.5MW$; $D_\perp=0.2\ m^2s^{-1}$, $\chi_\perp=1.5\ m^2s^{-1}$; L-mode values), with three densities and three fuelling assumptions: top or outer midplane (OMP) fuelling and no fuelling (≈divertor fuelling). The plasma geometry is similar to that used experimentally (Fig 1). The interaction between plasma and walls in the torus was minimised, so that changes due to changing fuelling point would be detectable. To this end, a diffusive flux boundary condition with shallow gradient (λ_n=3cm) was set at the outer surface of the plasma region used in EDGE2D (Fig.1b). Plasma crossing this outer surface was recycled at the divertor target. About half of the recycling was of this type, the other half flowing to the target via the model plasma

region (Fig.1b). This outer boundary condition produced relatively flat radial density profiles in the SOL, so, although the average density simulates experimental results, details of density profiles do not. The temperature profiles are consistent with typical observations, however.

6 MODELLING WITH EDGE2D: RESULTS AND DISCUSSION

Total plasma flow to the targets, Γ_t, is tabulated below, with other flows of interest. The prescribed wall pumping removes up to 8% of the target flow, which is then re-injected as fuel. Pumping and fuelling has a predictably small effect on parameters in the SOL and divertor channel. At all three

	No fuelling			Top fuelling			OMP fuelling		
Albedo in divertor	100%			90%			90%		
Edge density/$10^{19}m^{-3}$	2.45	1.84	1.31	2.50	1.91	1.32	2.67	2.04	1.41
Flow to target, $\Gamma_t/10^{21}s^{-1}$	202	202	197	210	210	201	208	210	200
Fuel/pump flow/$10^{21}s^{-1}$	0	0	0	16.2	13.2	10.1	16.3	12.7	9.6
Flow into divertor/$10^{21}s^{-1}$	54.9	47.3	36.8	58.8	48.4	38.8	60.2	50.7	38.2

Edge plasma densities and global flows obtained in simulations of fuelling and pumping with EDGE2D/NIMBUS.

densities, T_i is reduced (more so at the fuelling point) by ~5eV at the separatrix, and T_e fell by 1 to 2eV (Fig.3a). Although impurities were not studied, the dip in T_i implies the thermal force on impurity ions is directed from the fuelling point towards the divertor. Frictional forces increase due to reduced T_i and to flow induced by fuelling. Mach number profiles (Fig.3b) show SOL fuelling moves the stagnation point in the SOL towards the fuelling point from its location with no fuel, and increases the gradient of M.

SOL fuelling had little influence on ***separatrix*** Mach number at the divertor entrance, radial profiles (Fig.4) showing strong flow (M≈0.3) into each divertor. The outer part of the profile shows a tendency to flow reversal, reduced by SOL fuelling. Detailed study shows flow reversal at/or near each divertor entrance, only in the outer part of the profile. SOL fuelling diminishes the flow reversal zone and increases plasma density away from the separatrix. Fuelled neutrals are attenuated within a few mm. Those surviving, having charge-exchanged, penetrate easily, especially at the outer mid-plane.

7. SUMMARY AND CONCLUSIONS

Changes in convection in the SOL, caused by gaseous fuelling, have been studied, both experimentally in the JET Mk I divertor, and with EDGE2D/NIMBUS. In Ohmic plasmas (2MA, 2.8T), divertor fuelling gave low $Z_{effective}$ with increased radiation intensity (D_α/bolometry) in the divertor. Fuelling in the main SOL gave higher $Z_{effective}$ but not bulk radiation, and decreased radiation in the divertor. The wall-pumping speed varied day by day by at least a factor of two. On a given day, $\phi_{pump} \sim N^{1.3}$. and $D_\alpha \sim N^2$ (or more). Despite extra fluxes with divertor fuelling, there was no increase in wall-pumping speed, suggesting that pumping may occur at the fuelling point. Preliminary measurements with a movable Langmuir probe show a thicker SOL with top fuelling, in qualitative agreement with EDGE2D. One aim of the experiment was to investigate the need for toroidally uniform fuelling. Preliminary results, though unclear, help to define a future investigation. The experiment described was part of a larger study, to include controlled pumping with a cryo-pump. When commissioned, it will be possible to test whether wall-pumping occurs at the fuelling point. With EDGE2D, a 90% albedo on the divertor side-plates pumped ≤8% of the target plasma flow. Fuelling in the main SOL reduced T_i, with a minimum near the fuelling point. This suggests fuelling in the SOL might control impurities, via frictional and thermal forces. In contrast, increased impurity content was found in JET, using the Bremsstrahlung measurements, but not the bolometry. Impurities generated at the fuelling point might be implicated here, further work being needed. EDGE2D showed that fuelling alters profiles at the divertor throat, flow reversal regions being diminished if not removed. Although details may be model dependent, the sensitivity to fuelling procedure implies that a versatile fuelling system such as now installed in JET, is needed to optimise performance.

[1] R Simonini, G Corrigan, J Spence, A Taroni and G Vlases, 20th EPS, Lisbon, 26-30 July 1993.

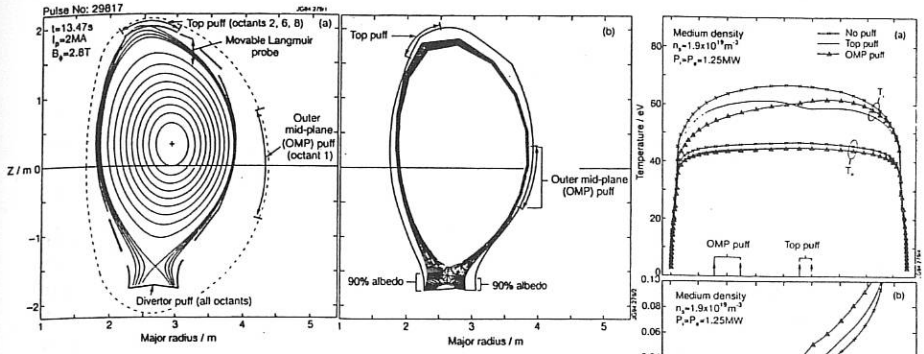


Figure 1: The geometric configuration, with fuelling locations of a) the experiment in JET, and b) the model plasma used in EDGE2D.

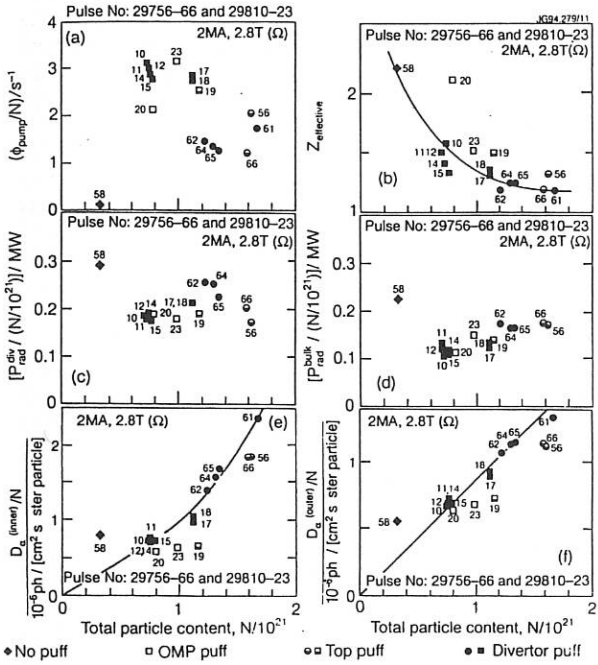


Figure 2: The density (total electron content, N) scaling of a) the specific wall-pumping rate, ϕ_{pump} / N (see Equ. 1), b) the global $Z_{effective}$, c,d) radiation power in divertor and bulk plasma (power/particle is plotted), and e,f) D_α intensity in inner and outer divertors (radiation intensity per particle is plotted). Solid symbols represent fuelling in the divertor; open/half-solid symbols represent SOL fuelling. With SOL fuelling we see higher $Z_{effective}$ and lower divertor radiation (total and D_α) but no change in bulk plasma radiation or in wall pumping.

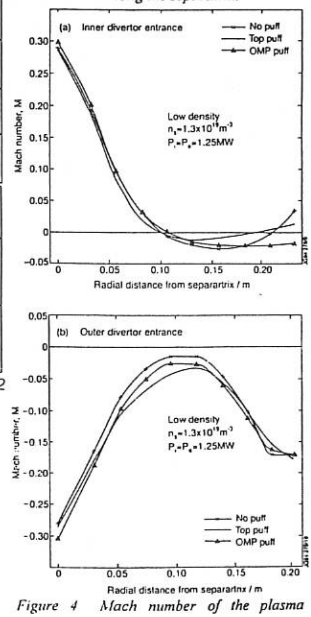


Figure 3: Poloidal profiles on the separatrix, fuelling as shown: a) T_i,T_e, b) Mach number along the separatrix.

Figure 4 Mach number of the plasma outside the divertor entrance, against radial distance from the separatrix, a) inner divertor entrance, b) outer entrance.

Experimental investigation of power deposition on the ergodic divertor target plates in TORE-SUPRA.

D.Guilhem, P.Ghendrih, A.Grosman, F.Nguyen, J.J.Cordier, P.Deschamps, H.Renner*, E.Gauthier, M.Lipa

Association EURATOM-CEA sur la Fusion
Centre d'études de Cadarache. 13108 Saint-Paul-lez-Durance (France)
* W7X Group, IPP Garching, D-85748 (Germany)

It is widely accepted that achieving the relevant central plasma performances in steady state requires control of the plasma wall interaction. Indeed, in order to keep under control the central plasma impurity concentration it is necessary to ease the power deposition on walls (power density < 5 MW/m²) in order to minimise the main impurity sources. However, if some impurities are generated at the plasma edge, it is also necessary to reduce their penetration depth into the main plasma. For these purposes axisymmetric divertor configurations are used worldwide /1/. On Tore-Supra the ergodic divertor (E.D.) is used as an alternative scheme /2/. The plasma edge physics is quite the same in spite of the different approach. The goal of the E.D. is to destroy the magnetic surfaces at the plasma edge (last 20% of the plasma volume) with a weak ($<\delta B_r> / B\varphi \sim 10^{-3}$) resonant magnetic perturbation. Two main regions can be identified within this controlled plasma volume /3/. The laminar zone where one can find open field lines as in axisymmetric divertors (defining the heat load pattern) and a stochastic zone (close to the main plasma) where field lines experience long connexion length ($>10^3$m) before impinging on the wall /4/. From the properties of such an E.D. system, one can expect an enhancement of the transport of heat and fast particles in the periphery /5/. This paper presents new results on power deposition on plasma facing components and especially on a dedicated target plate designed for this study. 5 such plates equip each E.D. module. Six identical modules are equally spaced toroidally in the main vacuum vessel of Tore-Supra /6/. The extension of each module is 120° poloidally and 13° toroidally. The set of 6 coils has a poloidal mode number m=18±3 and a toroidal number n=6 being therefore resonant for q~3 when the Shafranov shift is small (q~3 for $\beta p+l_i/2=0.7$ and q~4 for $\beta p+l_i/2=1.5$). Since the radial perturbation of the magnetic field line is rapidly decreasing away from the E.D. bars, only resonant field lines will experience a large radial excursion into the main plasma (δr~2 to 3cm per poloidal turn). Each time a field line encounters the radial magnetic field very close to the bars, it will receive a small radial kick. Only field lines having coherent deflections will be able to escape from the confined plasma. As a result, we can find a number of flux tubes connected very deep into the main plasma (down to r/a = 0.7). We shall show that the heat load pattern on the main plasma facing components, namely the E.D. target plates or the main limiter, presents such localized hot spots due to flux tubes connected with the hot plasma, visualised and predicted at the very edge. They correspond to strong modulations of the density and/or temperature at the plasma edge /7/. For the sake of simplicity only shots 13360, 13361 (to compare the relative power depositions with/without E.D.) and 12797 (to compare code prediction and temperature surface measurements), will be analysed. Shots 13360 and 13361 correspond to Ip=1.51MA, V-loop=1.1V, $<n_e.l>=6.10^{13}m^{-2}$, $T_e0=$ 1.8keV, R=2.41m, r=0.76m, B_t=3.3T so that q-psi~3 at the very edge. The plasma is limited by the E.D. coils. The current in the divertor coils for shot 13360 is I_{div}=27kA, constant during the entire plasma. For shot 13361 I_{div}=0 but all other macroscopic parameters are identical to shot 13360.

The radial position of each coil has been measured (figure 1). One can see that there is a radial excursion of ±5mm with respect to the average value. Since we have measured that the e-folding length for power deposition is 12mm when Ip=1.51MA and I_{div}=0 /8/, we can expect a non uniform toroidal power deposition when the plasma is leaning on the E.D. module even if no current is flowing in the E.D. modules. This can be seen figure 2 which shows the power density on different actively cooled plasma facing components. However, there is almost no E.D. induced modification of the average surface power deposition on the target plates, which varies from 1.5 to 3.0MW/m². This is due to a reorganisation of the power density distribution on the plates with a constant extracted power. When I_{div}=0, only the part of the target plate emerging from the coil casing (δr=20mm) limits the plasma (more or less uniformely illuminated). On the other hand, when I_{div}=27kA deeper regions of the target plates between bars (δr=40mm) collect power by direct deflection of heat along field lines. The "apparent" e-folding length for power deposition is increased, on average, by a factor of 2 when I_{div}=27kA. More power is then spread out on remote plasma facing components (such as the inner wall located on the high field side) than on the E.D coils located on the low field side. The casing of the E.D. coils then takes less power (from 0.15MW/m² to 0.10MW/m²), but the overall power is conserved. All these relative observations can be seen on figure 3, where the variation is ±20% on the target plates (0.061m²), -20 to -70% on the E.D. casing (3.6m²) and +40 to +100% on the remote inner wall (12m²) located 0.1m away from the last closed flux surface when I_{div}=0. It is interesting to note by comparing figure 1 and figure 3 that the power loading reduction corresponds to the closest target plates with respect to the plasma. This shows clearly the robustness of such a system with respect of gross misalignments of more than ±5mm.

The presence of a limiter in front of the E.D. coils has several consequences. Firstly, field lines directly connected to two of the E.D target plates are intercepted by this object. The consequence is that the power deposition on the limiter is strongly affected by the E.D. These modifications have already been described /9/. The symmetry of power deposition on electron/ion, top/bottom sides of the limiter is no longer preserved. A strong modulation is observed with some hot and cold zones, qualitatively reproduced by the MASTOC field line code /4/. These strong modulations can be correlated to the modulations seen on the target plates as described below. When the limiter is in front of the E.D. coils, if the difference in radial position is < 0.03m only 2 target plates are affected, (one on each module on the sides of the limiter) but with no consequence on the physics within the plasma volume affected by the E.D. If the radial distance is increased then the number of E.D. modules concerned is increased, but only one target plate on each module is concerned. However, the limiter is always located in the laminar zone; consequently a well defined pattern is observed.

Each E.D. coil consists of 8 actively cooled current bars. The current in the bars ensures a self protection by channelling the field lines in between bars where the target plates are located. In fact the channelling is more or less efficient depending on the local pitch angle since the bars have been designed to accomodate pitch angles corresponding to q=3 (for $\beta p+l_i/2=0.7$). For different q values, some shadowing of the target plates by the casing of the coils is observed. Figure 4 shows surface temperatures of one of the target plates, obtained with an infrared camera during shot#12797. One can clearly see a non uniform power deposition corresponding to different flux tubes which penetrate to different minor radii.

The dedicated target plate is made of an actively cooled copper structure covered with a 60μm B_4C layer. The thermal conductivity of such layer has been measured to be ~1.0 W / m. °K. The time constant of such a structure has been calculated with a 2D mesh code (CASTEM) with the real geometry. Two very different time constants can be identified: a 4ms time constant for the B_4C layer (an analytic formula gives ~11ms) and a 5 seconds time constant (25 seconds to reach true steady state) for the copper structure. The large difference

between these time constants indicates that if measurements are made with a good temporal resolution (as with infrared cameras, integration time = 20ms) on a short sequence, any rapid surface temperature change can be attributed to the gradient temperature change of the B_4C layer. Moreover, the change in surface temperature reflects directly the change of the power flux density at the surface of the target plate, since $Q(W/m^2) = (T_S-T_{CU}) * \lambda / e$, where T_S is the B_4C surface temperature, T_{CU} is the copper surface temperature, e=60μm is the thickness of the B_4C layer and λ is its thermal conductivity.

In our experiment the direct change of surface temperature gives information on the power flux associated to the different flux tubes. It can be seen (figure 5), that during the plasma current ramp up, the safety factor varies at the very edge as well as the radial excursion experienced by the flux tubes impinging on the target plate. The power deposition can strongly vary on a very short spatial scale, here from 0.5MW/m² to 3.2MW/m² within 0.03m. It can change from less than 1MW/m² up to 10MW/m² depending on the experimental scenario. All these observations can be computed as will be described below.

Numerical computations are used to predict both, the magnetic perturbation in the vicinity of the E.D. coils when current is flowing, and the field line excursion /4/. Field line penetrations are derived along a typical toroidal length. This figure of merit is supposed to give an estimate of the power conducted along the field lines since the perpendicular transport is not dominant. Figure 6 shows the image ($q \sim 3.2$) of a target plate in a (r,θ) plane as a function of the radial penetration of field lines in the plasma (different colors). This code result is very similar to the experimental surface temperature map (which can be directly interpreted in terms of power density) presented in figure 4. The magnetic surfaces are modified, leading to a significant enhancement of the transport along well defined flux tubes. This corresponds to the pattern observed on the target plate (or on the main limiter /9/). Small scale structures can be identified corresponding to a succession of "hot" and "cold" flux tubes suggesting that the turbulence is small in the perturbed zone /11/. Theoretical predictions and observations of such phenomena have been made in stellarators and especially at the boundary of W7AS /10/.

Conclusion. Ergodic divertor experiments in Tore-Supra have shown valuable effects. The reorganisation of the plasma wall interaction was discussed in this paper. The dominant effects are: 1) an increase of the "average" e-folding length for heat and particle deposition at the expense of large asymmetries, leading to a marked heat load pattern on the main plasma facing components; 2) the power deposition on target plates is not strongly affected by gross misalignments of the E.D. modules; 3) the absolute temperature map, and hence the power density map on a dedicated target plate, has been obtained; 4) the heat load channeling at the very edge presents a small spatial scale pattern (<< average heat load e-folding length) and is therefore not affected by any plasma edge turbulence (which is however decreased by the E.D., as measured by infrared scattering turbulence measurements [11]).

/1/ Vlases G.C. and al — Plasma Phys. Control. Fusion 35 (1993) B67
/2/ Samain A. and al — JNM 128-129 (1984) 395
/3/ Ghendrih P. and al — IAEA-CN-53/A-VII-7
/4/ Nguyen F. and al — JNM 176-177 (1990)
/5/ Grosman A. and al — JNM 196-198 (1992) 59-70
/6/ Lipa M. and al — Fusion Technologie Vol.19 July 1991
/7/ DeMichelis C. and al — This conference
/8/ Guilhem D. and al — JNM 196-198 (1992) 759-764
JNM 176-177 (1990) 240-244

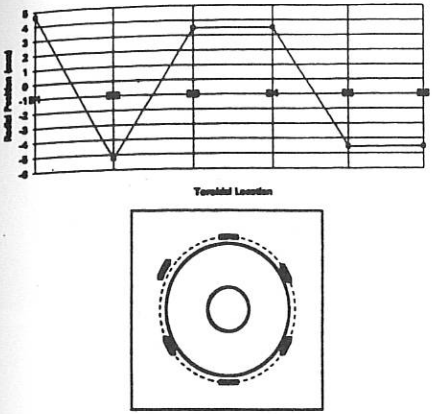


Figure 1: Variation of the Radial position of the E.D. coils (1 to 6 for the six coils).

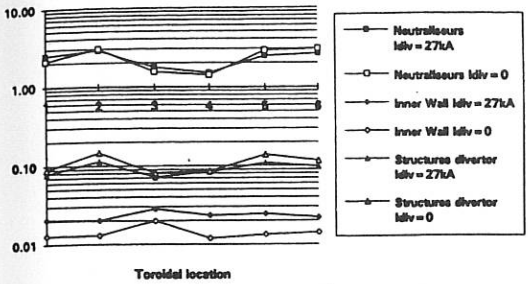


Figure 2: Power density on the main plasma facing components as a function of the toroidal location when I_{div}= 0 and I_{div}=27kA.

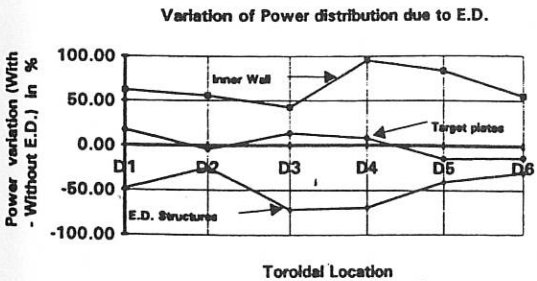


Figure 3: Relative variation (With - Without E.D.) of the power distribution as a function of the toroidal location

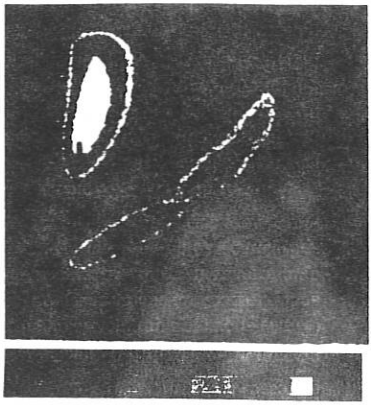


Figure 4: Infrared image of the surface temperature of the dedicated target plate (note the heat load pattern) .

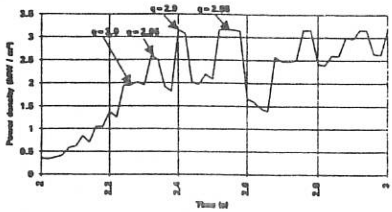


Figure 5: Power density modulation due to the modification of q-edge when plasma current is ramped up (at the cross location figure 4).

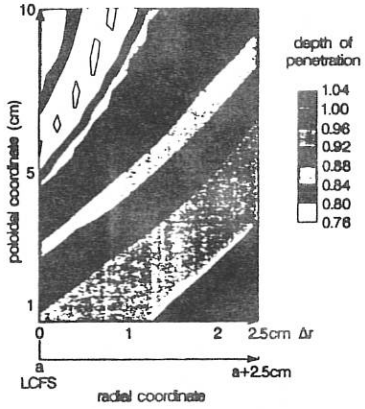


Figure 6: MASTOC code prediction to b compared to figure 4.

Active density control with ergodic divertor on Tore Supra

T. Loarer, M. Chatelier, Ph. Ghendrih, A. Grosman, C. Chamouard, and P. Sonato*

Association EURATOM-CEA sur la fusion contrôlée
CEN Cadarache, 13108 Saint-Paul-Lez-Durance Cédex, FRANCE.

* Association EURATOM-ENEA-CNR, Instituto Gas Ionizzati,
35020 Padova, ITALY.

Introduction

The next step device will have to demonstrate the compatibility between the heat removal with very high radiation level, in order to reduce the convective heat flux in the scrape off layer (SOL), and the particle exhaust in order to maintain the ash density sufficiently low in the core plasma. The superconducting tokamak Tore Supra has been equipped with ergodic divertor (ED) modules and six vertical pump limiters (VPL) designed to simultaneously control the plasma density and to extract the heat flux. The ED is described in [1] and previous experiments have shown that it reduces the convected heat flux on the plasma facing components (PFC) by increasing the rate of radiated power at the edge and by preventing the plasma contamination via impurity edge screening [2, 3].

In this paper, it will be shown that with an ergodized boundary, the active pumping by the ED modules is a means to control the plasma density and the wall particle content, while the radiation level and the screening properties at the edge are preserved. In the first part of this paper, the experimental sequence and the pumping efficiency are discussed. The second part is devoted to the global particle balance (including the wall retention).

Plasma density control

In order to determine the efficiency of plasma density control by the ED, a series of (10-15) consecutive shots with deuterium plasmas "leaning" on the ED modules have been realized. The plasma heating is restricted to ohmic with a plasma current of I_p=1.6MA, a toroidal field B_T=3.2 T (in order to obtain a safety factor : $q_{edge} \approx 3$). The volume averaged plasma density is varied between 2 and 4.5 $10^{19}m^{-3}$. During this series of shots the density is feedback-controlled by gas puffing up to 2s before the end of the current plateau when injection is stopped. Assuming N to be the total number of particles in the discharge, the global particle balance can be described by the simple equilibrium $dN/dt=\Gamma-N/\tau_p^*$, where Γ is the injected flux, τ_p^* the apparent confinement time $\tau_p^* = \tau_p /(1-R)$ where τ_p is the particle confinement time and R the global recycling coefficient. The titanium getters, which ensure the pumping, are generally activated for only half of the experiments in order to compare the data to similar unpumped shots. The exhaust efficiency ε is deduced from the pumping : $\varepsilon = \tau_p (1/\tau_{p(w)}^* - 1/\tau_{p(w/o)}^*)$.

Figure 1 displays the time evolution of the average plasma density and the gas injection for similar shots, without (#10517) and with active pumping (#10518). In these experiments, the plasma is leaning on the ED which is energized at its maximum value (I_{div}=45kA). For the non-pumped case (#10517), the wall particle content is nearly large enough to maintain the density at a steady state indicating a wall status close to the saturation. For the pumped shot (#10518), when the titanium getters of the ED modules are activated, the gas injection required to maintain the plasma density is 5 to 6 times larger than in the non-pumped case. This injection tends to a steady state gas puff as high as 1.5 Pam^3s^{-1} and when the gas injection is stopped at t=6s, the density strongly decreases (τ_p^*≈3s). In these experiments the exhaust efficiency is ε≈5% (τ_p≈200ms) which is close to those previously recorded with the outboard pump limiter (OPL) [4]. The exhaust efficiency also increases with the average plasma density and it does not depend on the wall saturation status [5]. It has also to be noted that for similar plasma conditions, the activation of the pumping with the ED energized does not modify either the radiation fraction (up to 70% of the total power for the described experiments) or the screening properties of the ED at the edge.

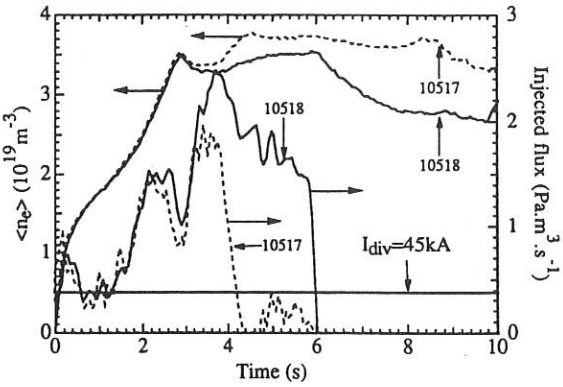


Figure 1 : Evolution of the average plasma density and of the injected gas versus time for a non-pumped shot (10517) and a pumped shot (10518) respectively

Particle balance

As previously demonstrated for the OPL experiments [5, 8], the particle balance shows that the ED configuration allows one to control the plasma density while partially depleting the wall particle content. The particle balance can be divided into three sequences:

The current ramp-up [0-4s], the steady state phase for the plasma density [4-7.5s] and finally the density decay before the end of the plateau current [7.5-8.7s] when the gas puff is turned off.

The time evolution of the plasma density and of the plasma current for a pumped shot lea-ning on the ED modules when the ED is energized (I_{div}=27kA i.e 60% of the maximum perturbation) are displayed on figure 2a. For the same shot, the injected particle flux (gas puff) and the exhaust particle flux by the ED pumps are decribed in figure 2b. The plasma

particle content variation (V $d\langle n_e \rangle/dt$ where V is the plasma volume) and the wall particle content variation are displayed on figure 2c. The plasma and wall particle content equilibrium is expressed in the form :

$$\frac{dN_{wall}}{dt} = \text{Injection} - V\frac{d\langle n_e \rangle}{dt} - \text{Exhaust}$$

where N_{wall} is the total number of particles in the wall.

In these experiments, the injection is the gas puff and the exhaust term is given by : Exhaust=P. S_{ti} where P is the D_2 pressure (simultaneously measured by both a baratron and an ionisation gauge [10]) in the pumping chamber and S_{ti} is the pumping speed of the titanium getters.

For the overall shot duration the following analysis is suggested:
During the current ramp-up phase, typically 3 times the plasma particle content has to be injected to obtain the prescribed density. This behaviour is always observed whether the pumping is activated or not and independently of the wall saturation state. When the edge safety factor approaches the resonant value ($q_{edge} \approx 3.5$ at $t \approx 3.5s$) a strong injection is needed to increase the density, indica-ting an enhanced wall pumping. This phenomenon is noticeable to in the current ramp down a $t \approx 10.5s$ when moving out of the resonance and is also similar to the "pump out" effect observed on JET at the "X point formation".
During the steady state phase of the discharge, equilibrium between gas injection and extraction by the pumps is reached. However, for typically the three first pumped shots of the series, the number of particles extracted by the pumps is larger by 20% than the number of particles injected. For

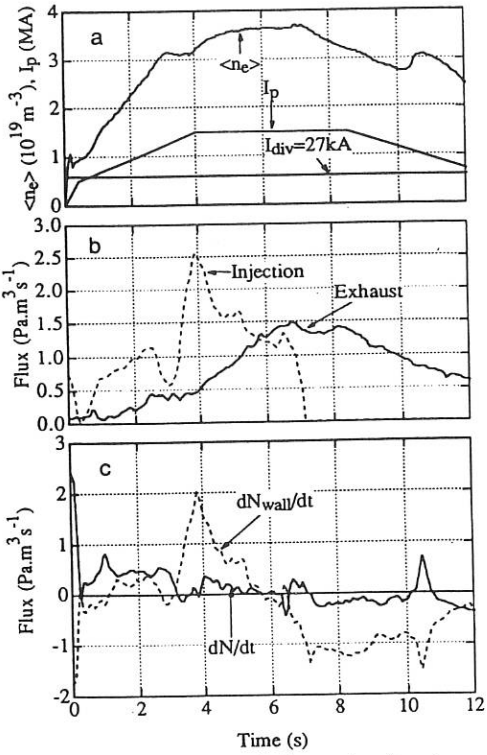


Figure 2 : a : Volume averaged plasma density, plasma current and total current in the ergodic coils for a pumped shot
b : Time evolution of the gas injection, the exhaust by active pumping and the plasma density variation
c : Variation of the plasma and wall particle content as a function of time

the non pumped shots of this series, the gas puff does not drop completely to zero during this phase and the wall does not appear totally saturated when the ED is energized and when the plasma is leaning on the ED.
The final part of the discharge, between 7.5 and 8.7s, shows that the exhaust by the pumps of the ED exceeds typically 3 to 4 times the density decay. During this phase, the particle balance shows that the wall is depleted (figure 2c). The depletion of the wall by the active pumping is also confirmed by the partial D_2 pressure measurement at the end of the shot with a quadrupole mass spectrometer in the pumping system of the torus. The D_2 partial pressure is 2 times lower at the end of the series (15 shots) of experiments than at the beginning. Also, just after a an over-night helium glow conditioning, the overall quantity of gas required to maintain the density is quite high in the absence of active pumping. From shot to shot, in spite of a higher density, the total quantity of gas required to obtain this density remains roughly constant. In contrast, for the pumped shots which are all realized after the non pumped shots, the gas injection necessary to obtain the density depends strongly on the plasma density. The recent results of DIII-D, in which the axisymmetric divertor extracts neutrals from both the plasma and the wall [9], supports the idea that this is a ge-neral phenomenon not particularly linked to the precise edge configuration [8].

Summary

The reported experiments show that the plasma density and the wall particles content can be actively controlled with an ergodic layer when the plasma is leaning on the ED modules when the ED is energized without modifying plasma parameters. That means that the ergodic divertor can simultaneously provide a screening of the impurities, and a plasma density control with a fraction of radiated power as high as 70% with intrinsic impurities.

Acknowledgments

The authors gratefully acknowledge the efficient and permanent technical assistance of J.Y. Pascal and S.J. Vartanian.

References

[1] Grosman A. et al. J. Nucl. Mater. 176-177 (1990) 493.
[2] Ghendrih Ph. et al. Proc. 19th EPS Conf. , Insbrück, (1992).
[3] Monier-Garbet P. et al. 14th IAEA Conf. on Plasma Fusion, 317-322, Würzburg (1992).
[4] Chatelier M. et al. 14th IAEA Conf. on Plasma Fusion, 341-349, Würzburg (1992).
[5] Loarer T. et al. Proc. 20th EPS Conf., Lisboa, (1993), Vol 17C, 4-14.
[6] Klepper C.C. et al. J. Nucl. Mater. 176-177 (1990) pp 798-802.
[7] Loarer T. et al. 11th PSI Conf. Japan (1994) to be published.
[8] Mioduszewski P.K. et al. 11th PSI Conf. Japan (1994) to be published.
[9] Madhavi A. et al. Proc. 20th EPS Conf., Lisboa, (1993), Vol 17C, 4-24.
[10] Haas G. et al., J. Nucl. Mater. 121 (1984) 151.

New results obtained by finite element modelling of the plasma edge

Th. Pütz, A. Kaleck, D. Reiter, P. Börner
Institut für Plasmaphysik, Forschungszentrum Jülich GmbH
Association EURATOM-KFA Jülich, P.O. Box 1913, D-52425 Jülich, Germany

Abstract

First results of the SAFE-code (Solution Adaptive Finite Element) had emphasized the importance of a geometrically realistic treatment of complex wall structures in the scrape off layer (SOL) of tokamaks [1]. In a single fluid approximation and with fixed electron temperature profile the plasma flow has been calculated for the limiter configuration of TEXTOR. The source terms, generated by the recycling neutrals, are computed using the Monte Carlo code EIRENE.
Now the SAFE-code is extended to take into account the electron temperature selfconsistently. To save computer time, for the first approximation of the particle and energy sources and sinks due to reionisation and charge exchange a fast analytical neutral particle model was developed. This modified SAFE-EIRENE code system is applied again to the SOL of TEXTOR. Since the SOL is not completely collision-dominated the classical dissipative fluxes of electrons and ions along the magnetic field should be limited by collision-free fluxes. The influence of these flux limitations are studied.

1 Introduction

Finite element codes with triangular meshes are more appropriate in modelling complex geometrical structures than finite difference codes. For the SOL of TEXTOR including the toroidal pumplimiter ALT II we observed qualitatively new effects. On top of this limiter a flow reversal in poloidal and radial direction appears. Underneath the blades the recycling is strongly localized and thereby an effective cooling of the plasma is achieved [1]. But until now all these results were evaluated in a single fluid approach, calculating only the density, momentum and the energy of the ions. For the electrons a fixed temperature distribution was assumed. The strong impact of neutral particles on the electron temperature profile had been taken into account only by using a fixed temperature gradient length in poloidal direction. Now we have extended the code to include selfconsistently also the electron energy equation. The interactions of the plasma with the neutral particles are described either by the Monte-Carlo code EIRENE or by a faster analytical model, developed for the FEM-code. In the next sections the improvements of the SAFE-code with respect to [1] are described, including the implementation of flux limits. Then the influence of the selfconsistent electron temperature and of the flux limitation is demonstrated.

2 Model description

2.1 Transport Equations

The transport equations are primarily based on a **modified version of Braginskij's plasma equations** [2]. A major change is the "ad-hoc" introduced **Diffusion Ansatz for the radial transport**, due to the experimentally observed "anomalous" high particle and energy flux perpendicular to the magnetic field. The plasma is considered to be quasineutral; electric currents and diamagnetic fluxes are neglected. **Assuming toroidal symmetry**, one gets a set of simplified fluid equations used in many other numerical 2D-transport-codes as well (e.g. [3]). This set consists of one continuity equation (quasineutrality), a momentum equation for the parallel ion flow velocity, a Diffusion equation for the radial plasma flow and the energy equations for ions and electrons.
The radial anomalous diffusion coefficient D is set to $0.6\mathrm{m}^2/\mathrm{s}$ and the radial transport coefficients for parallel momentum, ion and electron energy are respectively $\eta_r = mnD, \kappa_r^i = nD$ and $\kappa_r^e = 2nD$.

2.2 Calculation of source terms

We have two options to calculate the interaction processes of the plasma with recycled neutral particles: The Monte-Carlo code EIRENE [4] and a simpler but faster analytical model, simulating a neutral fluid in an FEM-mesh. (CPU-time: EIRENE $\approx 1-100$ sec; analytical model ≈ 50 msec).
First we use the analytical model to get an initial solution In this model we consider two groups of neutrals, one with a Franck-Condon energy of 3 eV and the other with thermal energy. From each boundary element both species flow with their characteristic velocity into the SOL (perpendicular to the wall). Because of reionization, a fraction of the neutral flux is lost per element. According to the flow direction relative to the element sides the remaining flux is divided up into the adjacent elements. This process is repeated until all neutrals are reionized ore lost at the boundaries. One finds the total particle and energy sources by summing up the contributions from all outflow-cells to each element. Per Ionization of a neutral particle the ions receive an averaged energy of 3 eV and the electrons are loosing 25 eV.
To couple the plasma code to EIRENE, an interface has been installed, which transfers the geometry and the plasma quantities. Based on fixed plasma conditions, the particle-, momentum- and energy-sources for each element are computed and transferred back to the plasma code. This procedure is repeated until the particle, momentum and energy balances are fulfilled.

2.3 Limitation of the dissipative fluxes

Since the plasma in the SOL is not everywhere collision-dominated, in regions of steep gradients the Braginskij form of e.g. the heat flux vector will lead to values larger than the the collision-free heat flux. This is avoided by limiting the transport coefficients in the following way (see also [3]):

$$\kappa_{\parallel}^{e} = \frac{\kappa_{\parallel,class}^{e}}{1+\left|\frac{\kappa \frac{\partial T}{\partial x}}{F^{e} \cdot v_{th}^{e} p^{e}}\right|} \tag{1}$$

(The factor F^e has to be adjusted, to fit results of kinetic calculations and is chosen to be 0.4).

2.4 Numerical Implementation of the electron energy equation

To solve the equations we use an explicit time dependent method. As indicated in a previous work [1] the timestep must be limited such that the fastest transport process can transfer information only to the neighbouring nodes. For the continuity and the momentum equation this timestep is given by the quotient of the element length $\|\vec{B}$ and the maximal flow velocity, i.e. the sound velocity. For the energy equations it is determined by the heat conduction process, which is about 60 times faster for the electrons than for the ions. So we use the following time marching procedure (see Fig.1): Density, flow velocity and pressure are calculated for a half timestep in advance. Using these results the electron temperature is calculated dividing the ion-timestep into sufficiently small steps. Then the new electron temperature is used to correct the ion energy equation and also the continuity and the momentum equation for $V_{\parallel}$.

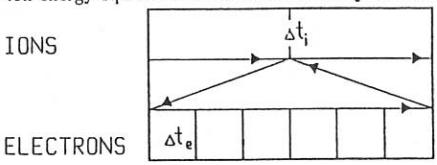


Figure 1: Time marching procedure to solve transport equations

3 Application to the SOL of TEXTOR

3.1 Specification of geometry, boundary conditions

The model was applied to the TEXTOR-SOL including the pumplimiter ALT II. The magnetic flux surfaces are calculated using the equilibrium code CATI [5]. Our finite element mesh is then generated aligned to

these flux surfaces and during the calculation automatically refined in regions where steep gradients occur, in particular near the limiter.

On the magnetic flux surface at the **core plasma interface** we use as boundary conditions: $V_\vartheta = 0$ m/s; $n = 7 \times 10^{18}$ m^{-3}. Temperatures are set to 70 eV.

At the **limiter tips and at the target plates**, plasma sheath edge conditions are imposed on both sides : $V_\vartheta = \frac{B_\vartheta}{B} c_s$; $Q^i_\vartheta = V_\vartheta(2.5T_i n + \frac{1}{2}mnV_\parallel^2)$; $Q^e_\vartheta = 4.8T_e n V_\vartheta$; At the limiter tips all particles are recycled, whereas in the scoops 25% will be pumped. The parts of the **limiter** $\parallel \vec{B}$ behave like ideal walls, i.e. no forces and no fluxes are directed onto the surfaces.
The boundary conditions at the **outermost flux surface** are : $V_r = 0$ m/s; $\frac{\partial V_\parallel}{\partial r} = 0$; $Q^i_\vartheta = 0$;$Q^e_\vartheta = 0$.

3.2 Results

3.3 Heat flux limit for the electrons

Applying the solution procedure described before with no limitation of the dissipative fluxes, no stationary solution is achieved. This can be explained by looking at the various parts of the energy fluxes: Even in regions of high convective flow the electron heat flux is larger by more than a factor of ten than all other fluxes, so that the electrons and ions are almost decoupled. This in front of the limiter leads to a nearly homogeneous and high electron temperature, whereas the ions are cooled more and more by neutral particles and by the strong convective flux, imposed as boundary condition.
We get a stable solution, when we limit the classical electron heat flux as described above. Starting now from the solution with fixec electron temperature [1], we achieve a stationary solution after 12000 timesteps and 3 additional runs of EIRENE. After that, the plasma flow onto the targets is changing by not more than 2% within 3000 timesteps ($\approx 5 \cdot 10^{-4}$ sec). The selfconsistent calculation of the electron temperature has only marginal influence on the density profile and the flow pattern. We therefore show only the temperature profiles for ions and electrons.

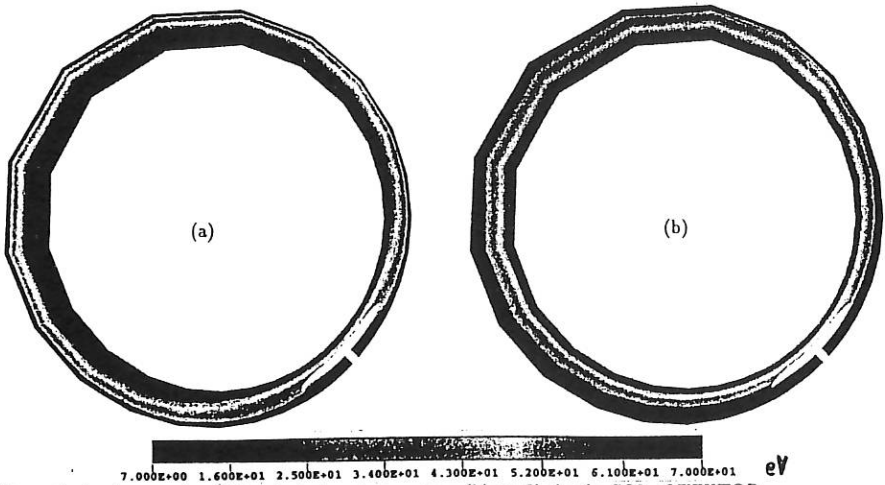


Figure 2: Ion temperature (a) and electron temperature (b) profile in the SOL of TEXTOR

3.4 Heat flux limit for the ions

Consistent with the treatment of the electrons and following proposals discussed in earlier works [1,6] a flux limit also for the ions is introduced in the same form as written above for the electrons. Instead of $F^e \cdot v^e_{th} p^e$ for the electrons here we have to use $F^i \cdot c_s p^{tot}$.
Figure 3 shows for different F^e and F^i the value of the ion -timestep and the number of iterations needed for the electrons per needed per "ion"-timestep. ion-timestep. The magnitude of the Δt_i should be quite

universal for TOKAMAKS, since it is mainly determined by the sound velocity, which only depends on T_e and T_i. The ratio of the electron to ion-timestep is essentially determined by the factors F^i and F^e.

F for IONS	∞	∞	10	0.4
F for ELECTRONS	∞	0.4	0.4	0.4
Δt_i / s	1.E-7	1.E-7	6.E-6	1.E-5
Δt_e / s	2.E-9	5.E-7	5.E-7	5.E-7
Number of Iterations	40	1	12	20

Figure 3: Characteristic timesteps for electrons and ions using different flux limiting factors

Using the strong flux limit for the electrons ($F^e = 0.4$) and the fast neutral particle model we have solved the transport equations for different ion heat flux limits. As a result the ion temperature on the flux surface with radius $r = 0.48\,m$ is shown (Figure 4). As Figure 4 suggested, there is only a slightly change in the values over a wide range of flux limiting factors.

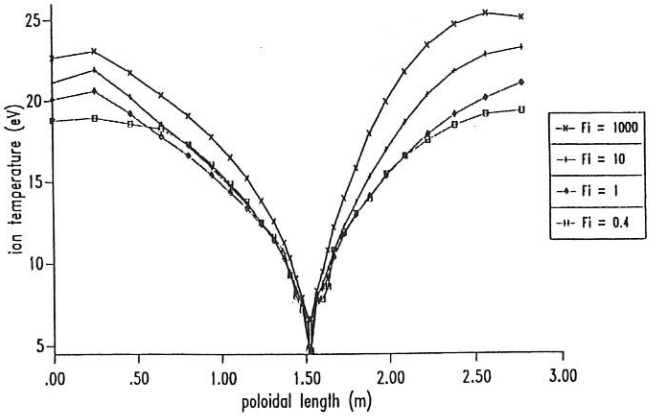


Figure 4: Poloidal variation of the ion temperature for different ion flux limits on a magnetic surface ($r = 0.48m$)

4 Conclusions and Outlook

The results show that the SAFE-EIRENE code system permits a realistic treatment of the plasma and the neutral particles in geometrically complex boundary structures. Because of the small changes in the plasma temperature we suggest to use for ions and electrons the physically more reasonable flux limits. Further studies of the overall stability of the code system and applications to simplified geometries will be carried out, to get comparable results to e.g. B2-EIRENE [7].

References

[1] Th. Pütz, M.W. Wuttke, D. Reiter: *Contribution to plasma physics* **34; 2/3** (1994), 404
[2] S.I. Braginskij: *Review of Plasma Physics* **1** (1965), 205
[3] B.J. Braams: *NET-REPORT EUR-FU IXII-80-87-68* (1987)
[4] P. Börner, A. Kaleck: *12. EPS-Conference* **9F/I** (1985), 187
[5] D. Reiter: *The EIRENE Code*Jül-2599 1992
[6] G.P. Maddison, P.C. Stangeby, G.J. Radford, J. Hugill: *Contr. to plasma physics* **34; 2/3** (1994), 226
[7] D. Reiter: *Journal of Nuclear Materials* **196-198** (1992), 80

PROBE MEASUREMENTS ON DRIFT PATTERNS IN RFP EDGE PLASMAS.

H. Bergsåker[1], V. Antoni, D. Desideri, I. Gudowska[1], E. Martines, A. Möller[1], V. Rigato[2], G. Serianni, L. Tramontin and S. Zandolin[2]

Gruppo Padova per Ricerche sulla Fusione Euratom-ENEA-CNR-Università di Padova, Association, Italy.

1) Royal Institute of Technology, Stockholm, Sweden, Ass. NFR-Euratom.

2) INFN Laboratori Nazionali di Legnaro, Italy.

Introduction. Edge plasma rotation in tokamaks, due to e.g. $E \times B$ or grad B drift has attracted interest in recent years due to its relevance for understanding enhanced confinement modes. Probe measurements have been applied in studying both parallel and perpendicular drift motion [1]. A rapid perpendicular drift has been observed with probe measurements in reversed field pinch experiments [2,3] and was used to estimate the edge ion temperature, assuming that it can be identified with diamagnetic drift [2]. The drift complicates the interpretation of probe measurements, and a comparative study has been made in two RFP experiments of vastly different dimensions, with the aim to identify the causes of drift motion.

Experimental. In RFX, with $R = 2$ m and $a = 0.456$ m, a rotatable Langmuir probe array with four single probes facing different directions with respect to the magnetic field has been used [4], as well as passive collector probes mounted on an identical manipulator. In T1, with $R = 0.5$ m and $a = 0.057$ m, rotatable double probe and passive probes have been used [2,5].

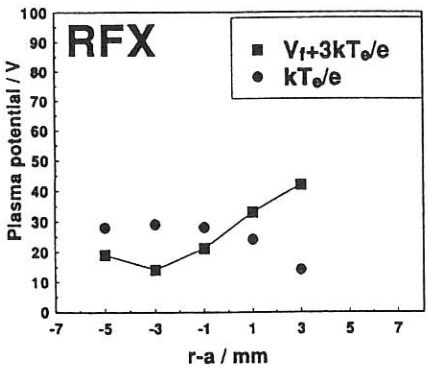


Figure 1.

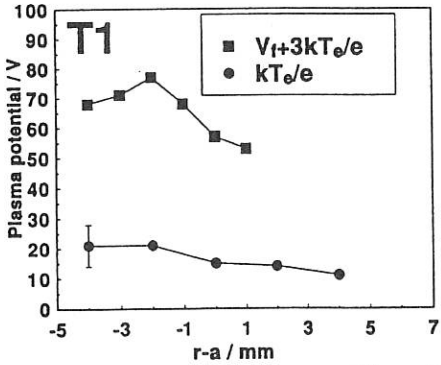


Figure 2.

Results and discussion. Figures 1 and 2 show the radial profiles in RFX and T1 of T_e and the plasma potential V_p, assuming that the latter can be calculated from the probe floating potential V_f as $V_p \approx V_f + 3kTe/e$. The data from RFX are taken from the drift measurement series of discharges to be presented below, whereas the T1 data are from typical 80-90 kA discharges. In both cases the density decay length is of order $\lambda_n \approx 3mm$. Figures 3-5 show examples of the asymmetric particle flux on probes, which will be interpreted in terms of plasma drift. In figure 3 the steady state ion saturation currents on differently oriented probes in RFX are presented; in every discharge the Langmuir probes collect particles in four different directions, the probe array is turned between discharges and the shot to shot density scatter has been

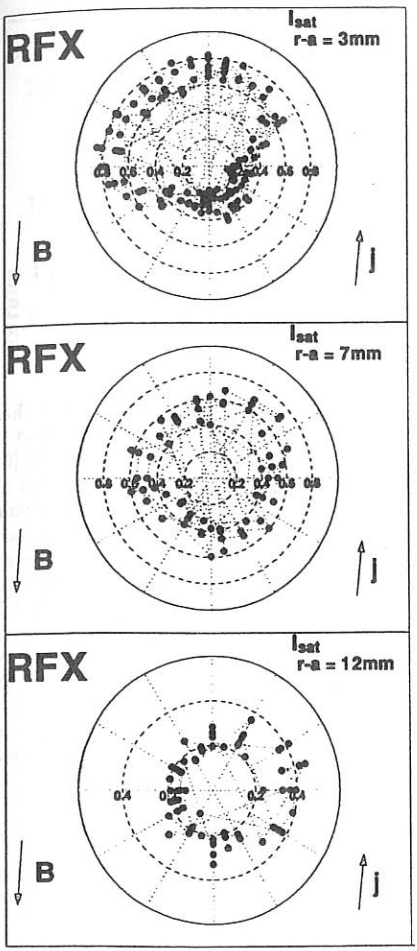


Figure 3.

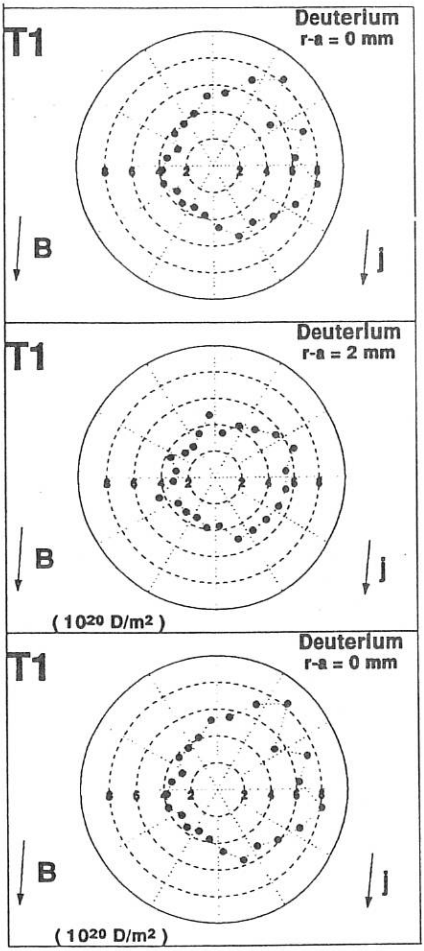


Figure 4.

eliminated by normalising to the sum of the four I_{sat} in different directions. The angle of maximum I_{sat} changes gradually with the minor radius. Figure 4 shows analogous angular distributions of deuterium trapping on a cylindrical graphite probe which was exposed to 220 RFP discharges; this time the maximum trapping rate remains fixed on the right hand side, as seen from the plasma. A qualitatively similar behaviour is observed for the deposition rate of impurities, as the examples of carbon collection on silicon probes in figure 5 show, this time from RFX.

Different models have been suggested for translating the flux asymmetry to probes into drift velocities, or Mach numbers. Four examples are given in figure 6. The solid line marked with a in figure 6 corresponds to a particle model according to which the ions move with a drifting Maxwellian distribution [2]. Such a model would seem ap-

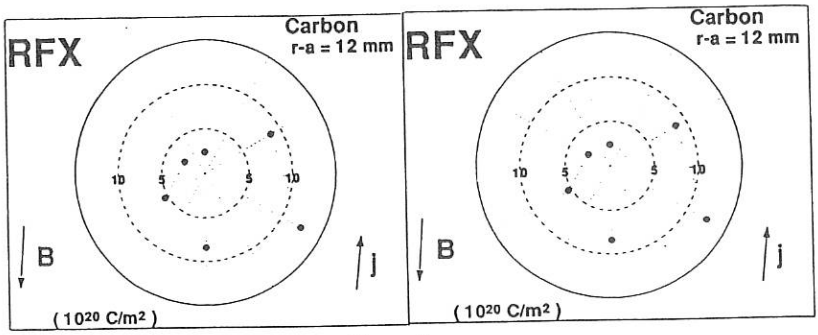


Figure 5.

propriate for instance if $T_i \gg T_e$ and in particular if the ion gyro radii are larger than the probe dimensions. The dashed curve b is is the simple model which was used in [3], the dashdotted curve c results from Hutchinsons one dimensional fluid model [6] and the dotted curve d shows Stangebys analytical fluid model [7]. MacLatchy et al. incorporated the Hutchinson model in a more elaborate treatment [1]. That scheme may not necessarily be the most natural choice in cases where the drift is predominately perpendicular. To make a simple estimate of the main trends in the measured asymmetries we have chosen to proceed as follows: the overall drift direction is determined directly from the angle of maximum particle flux in the diagrams such as figures 3-5. An effective Mach number is calculated from the upstream to downstream flux ratio using curve c in figure 6. The parallel and perpendicular drifts are finally calculated by taking the projection of the overall drift in the parallel and perpendicular directions. The results are shown in figures 7 and 8. Far away from the plasma the electric field is directed outwards and the $E \times B$ drift is in the same direction as the diamagnetic drift. Further into the plasma the directions are opposite. In RFX the perpendicular drift changes sign at smaller minor radius, whereas in T1 it remains high and in the diamagnetic direction. Qualitatively this is explained by higher edge ion temperature in T1, since the density gradient and radial electric field are similar in the two machines.

Conclusions. The edge plasma drifts in RFX and T1 have been studied with Langmuir and passive probes. The perpendicular drift seems to be largely of diamagnetic, nature particularly in T1 where the diamagnetic drift prevails over the $E \times B$ drift in the region where they are opposite in direction.

References.

[1] C.S. MacLatchy, C. Boucher, D.A. Poirier et al. Rev. Sci. Instr. 63(1992)3923.

[2] H. Bergsåker, I. Gudowska, B. Emmoth and E. Tennfors, Proc. 19th Eur.Conf. Contr.Fus. Plasm.Phys. Innsbruck 1992, part I p. 607.

[3] V. Antoni, M. Bagatin, H. Bergsåker et al. Proc. 20th Eur.Conf. Contr.Fus. Plasm.Phys. Lisabon 1993, part II p. 695.

[4] V. Antoni, M. Bagatin, D. Desideri et al. Rev. Sci. Instr. 63(1992)4711.

[5] A. Möller, H. Bergsåker, G. Hellblom et al. Proc. 20th Eur.Conf. Contr.Fus. Plasm.Phys. Lisabon 1993, part II p. 471.

[6] I.H. Hutchinson, Phys. Fluids 30(1987)3777.

[7] P.C. Stangeby, Phys. Fluids 27(1984)2699.

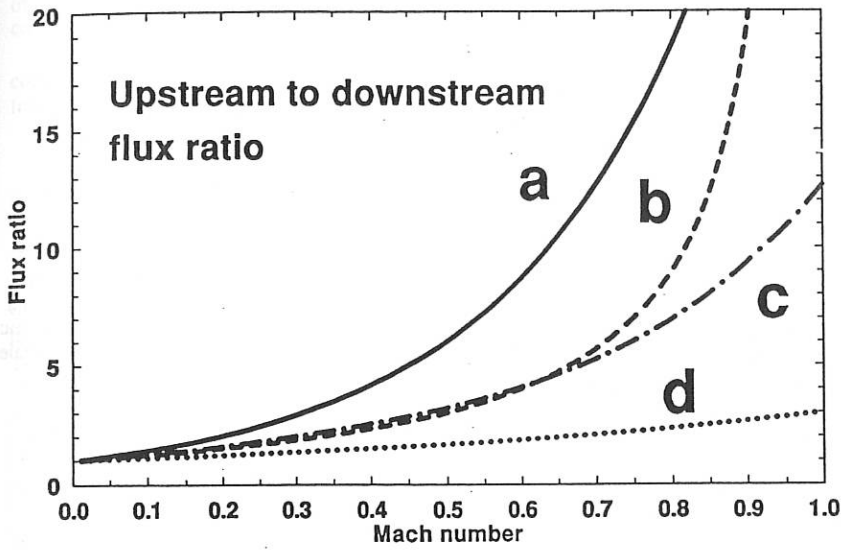


Figure 6.

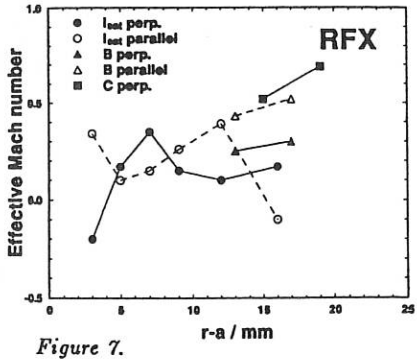


Figure 7.

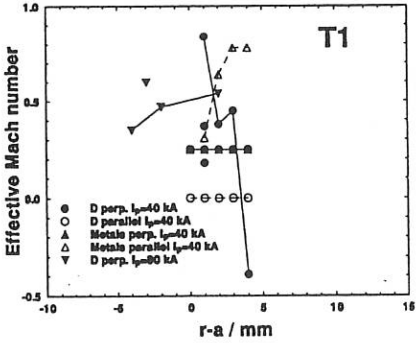


Figure 8.

The impact of kinetic effects on the ITER divertor plasma.

Yu. L. Igitkhanov†, A. S. Kukushkin, A. M. Runov‡

ITER EDA Co-centre, Boltzmannstr. 2, 85748, Garching, Germany
†Max-Planck Institut für Plasmaphysik, Boltzmannstr. 2, 85748, Garching, Germany
‡Kurchatov Institute, Kurchatov str. 46, 123182, Moscow, Russia

1. Introduction

The equations of fluid dynamics, which are in wide use now in computational models of transport of particles and energy within the scrape-off layer (SOL) and divertor region of a tokamak, are well known to be inaccurate for a significant part of the parameter range specific for the edge plasma. The principal reason for this lies in the long - as compared with the scale length of the SOL - mean-free-path, $\lambda_{st} \approx L$, of the suprathermal particles which are largely responsible for the energy transport. The behaviour of these particles is non-local, i.e. they carry energy from distant points of the SOL. Thus the corresponding transport phenomena cannot be described accurately with usual fluid approach dealing only with local values and derivatives, even when the mean-free-path of the bulk particles, λ_b, satisfies the usual condition for validity of the fluid approach, $\lambda_b << L$. Corrections of parallel heat flows with so-called "flux-limit factors" (FLF), when the fluxes are assumed to be limited to some fraction of free-streaming flow, is also not so helpful – there is no reason to assume this fraction to be constant

A rather simple and computationally efficient hybrid approach, where the two-dimensional fluid equations are solved in order to find the plasma parameters, and the parallel heat flows appearing in these equations are found from simplified kinetic equations allowing one to take into account the effects related to the long-range particles, has recently been proposed [1]. The aim of the present paper is the application of this approach to modelling the ITER divertor and the assessment of the possible effect of the non-local heat flows on the conditions of the plasma detachment from the divertor targets.

2. Kinetic model

Simplified kinetic equations [2] which are used in our code can be written as

$$v_z \frac{\partial \Phi_\alpha}{dz} + \frac{e_\alpha E}{m_\alpha} \frac{\partial \Phi_\alpha}{dv_z} = \frac{n\varphi_\alpha - \Phi_\alpha}{\tau_m} + S_\perp + S_{\alpha N} + S_{\alpha C} \qquad (1)$$

The first term on the right-hand side describes the relaxation of distribution functions of electrons and ions $\Phi_\alpha(v,z), \alpha = i,e$, to the local Maxwellian functions φ_α (φ_i is biased by the fluid velocity in Z direction); $S_\perp$ is the cross-field exchange term; $S_{\alpha N}$ describes the interaction with neutrals; and $S_{\alpha C}$ stands for the electron-ion coupling. Only terms with characteristic times shorter than τ_m should be retained on the right-hand side of Eq.(1) - all the rest is already taken into account in the fluid equations - thus S_{eN} and $S_{\alpha C}$ terms can always be neglected. The term with electric field on the left-hand side of Eq.(1) can be simplified by the assumption that it is relatively weak for hot particles - and just these particles are believed to play a major role in the heat (and momentum) transfer. In this case one can replace $\partial\Phi_\alpha/\partial v_z$ with $\partial\varphi_\alpha/\partial v_z$[3], and find the field from the requirements that $n_i = n_e$ and $j_i = j_e$.

Boundary conditions at the sheath are: absorption of all impinging ions, and reflection of electrons having energy above the sheath potential, which is in turn determined from the condition of zero net current to the target.

The principal improvement which allows us to avoid the well-known problem of incorrect asymptotic behaviour of the BGK operator when $\tau_m \to 0$ [4] is to introduce two differently weighted distribution functions, f and F :

$$f_\alpha(x,v_z) = \iint \Phi_\alpha dv_y dv_x \ , \quad F_\alpha(x,v_z) = \iint \Phi_\alpha v^2 dv_y dv_x \qquad (2)$$

and to write for them separate equations like Eq.(1). The boundary conditions can also be expressed in terms of f and F, and one has to solve a series of 1D linear ODE in co-ordinate space for each value of velocity v_z . The point here is that we do not need to use the same value of τ_m for f and F - that is, we approximate each particle distribution with two different functions and find the lower moments, n, V, and Π, from f, and the higher moments, T and q, from F and f. This allows us to take into account - though in a rather crude way - the dependence of τ_m on v and to abstain from specifying the distributions in cross-field velocities.

The kinetics package is coupled to the fluid code DDC83 [5] like a Monte-Carlo package for the neutral particle transport is: it is invoked after the fluid equations are advanced by a number of time steps, and then its output is used for calculation of the kinetic corrections to the transport coefficients and boundary conditions for the fluid equations. The only difference is that the Monte-Carlo code provides one immediately with the source terms which are needed for the equations, whereas the transport coefficients have yet to be derived from the kinetics output. In order to separate the conductive heat flow, we subtract from the total flow, obtained from integration of the distribution functions, the convective flow calculated with the kinetic values of n, V, and T. It is worth noting that the boundary conditions for the fluid equations are obtained automatically with such an approach from the distribution functions calculated at the sheath, and they are essentially non-local in terms of Ref.[6].

3. First results for the ITER divertor

Full implementation of the BGK kinetics package into the fluid code is still in progress. Here we present the results of 2D calculations, where only the BGK relaxation term in the right-hand side of Eq.(1) was included for electrons and ions, and only the heat flows were corrected. The slab model with enhanced distance from x-point to the target, absorbing target and side wall, and a "gas bag" outside the plasma in the divertor [7] was used, the total power input to the SOL being 50 MW. The density of the neutral gas in the divertor was an adjustable parameter, and variation of this density allowed one to obtain a scan over a range of the upstream plasma density at the separatrix, n_s which is commonly used for comparisons.

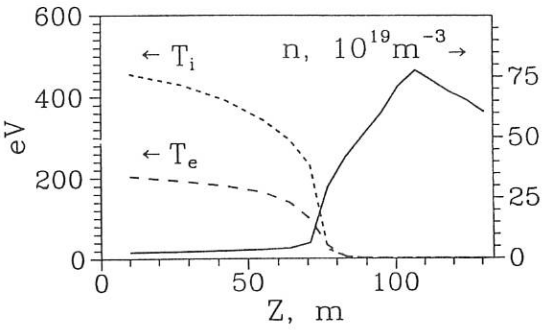


Fig. 1. Profiles of plasma density and temperature along magnetic field near the separatrix for 50 MW power entering the full SOL with the plasma. Slab model, Z = 0 corresponds to the symmetry plane, the x-point is located at Z = 74 m

Fig. 1 shows the typical profiles of the plasma temperature and density along the magnetic field. One can easily see a sharp temperature front and a

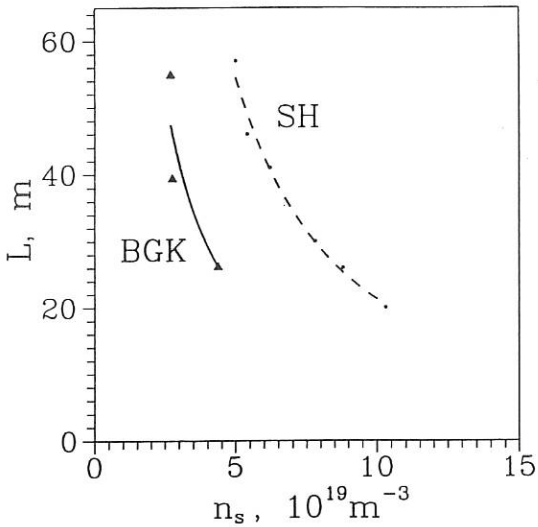


Fig. 2. The flame extinction length, L, as a function of the upstream plasma density, n_s, calculated with the hybrid model (solid line) and with fluid model [7] (dashed line)

density peak displaced from the target, the features indicative of the detachment. The major kinetic effect here is the drastic reduction of the parallel heat conductance. This increases the temperature drop between the mid-plane and the target, and the same plasma pressure in the divertor can be sustained at much lower values of n_s consistent with pressure balance between the mid-plane and the divertor. This effect is shown in Fig. 2 where, following Ref.[7], the flame extinction length L (the distance along the field from the x-point to the point where the parallel heat flow carried by plasma goes below 10 MW/m^2) is plotted against n_s. The major effect of the kinetic corrections to the power flows is thus the reduction – by a factor of approximately 2 – of the upstream plasma density necessary to achieve the detachment. Given the importance of the n_s value matching the plasma density profile in the discharge, this effect can be quite substantial: it allows one to have two times higher power flux into the ITER divertor, as compared with the previous calculations [7].

While this effect could be qualitatively reproduced by introducing a small enough value of the FLF, the physical correctness of the latter seems to be doubtful. The profiles of the effective FLF values, restored from the comparison of the kinetic heat flows with those obtained from the classical Spitzer-Harm expressions, are shown in Fig. 3 for the electrons and ions. An order of magnitude variation of the effective FLF values is clearly seen there. Moreover, the effective FLF values become even negative downstream the temperature front, reflecting an increase of the heat conductivity due to the presence of the fast, long-range particles, which come from the upstream part of the SOL. Such an effect of the plasma pre-heating before the temperature front has been observed in calculations [1] for the old ASDEX parameters. It is however strongly damped by the prevailing convective transport of energy in the downstream part of the detached divertor, therefore the total effect of this pre-heating is insignificant – at least, under the considered conditions. Fig. 4 shows the ratios of the kinetic heat flows to the

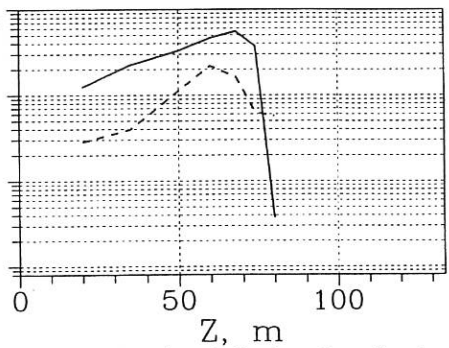


Fig. 3. Profiles of the effective – i. e. calculated *post factum* from the result – FLF values for the ion (solid line) and electron (dashed line) heat conductivity, taken along the field line near the separatrix. This value becomes even negative (not shown here) downstream

flows calculated from the classical heat conductivity for the same plasma profiles, and the enhancement of the heat flow due to the kinetic effects below the temperature front is seen to be within 3% at most.

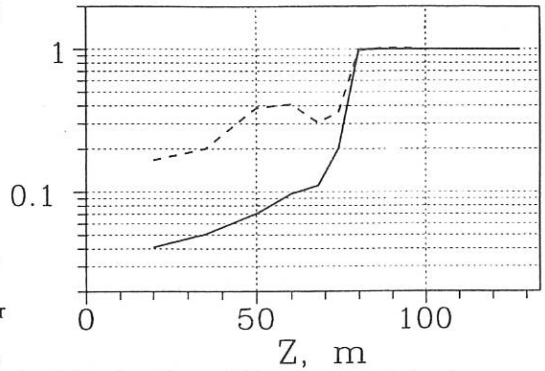


Fig. 4. The ratios of the parallel heat flows – conductive plus convective – for ions (solid line) and electron (dashed line) to those calculated with use of the classical heat conductivity on the same plasma profiles. The plato downstream corresponds to the convection-dominated region below the flame

4. Conclusions

A simple kinetics package has been implemented into the 2D fluid model in order to extend its applicability to regimes with lower collisionality, which are common for divertor plasmas. The package is rather efficient computationally, and it allows one to consider the effect of long-range hot particles in the energy transport by electrons and ions simultaneously. The main effect of the kinetic corrections to the heat flows is to increase the temperature gradients along the magnetic field and thus shift pressure balance between the mid-plane and the divertor plasmas towards lower upstream plasma densities. Since ions make a significant contribution to the upstream plasma pressure, it is important to use kinetic corrections to ion heat conductivity also. In contrast to the usual flow correction with "flux-limit factor", the proposed approach provides a physically motivated model of the non-local energy transport due to the presence of energetic particles.

The first results for the ITER parameter range indicate that the upstream plasma density may be considerably over-estimated in the previous calculations with the fluid transport model [7]. This could imply that the achievement of the divertor operation regime envisaged in ITER [8] would require somewhat less radiated power, reducing thus demands for the momentum removal. On the other hand, the non-local heat transport just below the thermal front, which could spoil the picture of the plasma flame, seems to be not so important.

Considerable effort still has to be made to introduce the kinetic corrections also to the momentum flow, although they might be less significant because the bulk of momentum transfer is normally attributed to a group of particles with energy somewhat lower than that of the particles responsible for energy transfer. Finally, validation of this transport model against experimental data remains crucial.

References

1. A. S. Kukushkin, A. M. Runov, *Contr. Plasma Phys., Berlin*, **34** (1994) 204
2. D. L. Bhatnagar, E. P. Gross, M. Krook, *Phys. Rev.* **94** (1954) 511
3. I. P. Stakhanov, *Sov. J. Appl. Mathem. and Theor. Phys.*, 1969, No. 3, p. 47
4. C. Cercignani. Mathematical Methods in Kinetic Theory. Plenum Press, New York, 1969
5. Yu. L. Igitkhanov, A. S. Kukushkin, A. Yu. Pigarov, et al., *Plasma Phys. Controlled Nucl. Fusion Res.* Proc. 9th Int. Conf., London, 1984. IAEA, Vienna, **2** (1985) 113
6. Yu. L. Igitkhanov, A. M. Runov, *Contributions to Plasma Physics*, **32** (1992) 308
7. A. S. Kukushkin, *Contr. Plasma Phys., Berlin*, **34** (1994) 282
8. G. Janeschitz, et al., The ITER divertor concept. Presented at the 11th Int. Conf. on Plasma Surface Interactions, Mito, Japan, 1994; to be published in *J. Nucl. Mater.*

Revised Formula for Chemical Sputtering of Carbon

C. García-Rosales and J. Roth

Max-Planck-Institut für Plasmaphysik, EURATOM Association, D-85748 Garching, Germany

Introduction

One critical problem in today's fusion devices using graphite as first wall material concerns the erosion of surface material by chemical sputtering via hydrocarbon formation due to hydrogen bombardment from the plasma. This effect may lead to a considerable impurity flux into the plasma, as shown in recent measurements at the ASDEX-Upgrade tokamak [1,2]. In order to calculate the contribution of chemical sputtering to carbon erosion and impurity flux into the plasma it is convenient to have at disposal an analytic expression based on laboratory experiments. Up to now an empirical formula was proposed [3] which only crudely describes the broadening of the temperature dependence of the chemical sputtering at incident energies ≤ 200 eV [4]. This low energy effect leads to a considerable erosion already at room temperature and to the absence of a threshold energy for carbon erosion. In fusion experiments this low energy erosion regime is of particular importance especially in regions with high hydrogen recycling, such as the divertor chamber, where strong impurity fluxes were found [1,2].

Boronized graphites as well as thin boron films deposited on the first wall were used in several fusion experiments to getter the oxygen and to reduce the contribution of chemical sputtering, because in laboratory experiments a strong reduction of chemical sputtering was observed for boronized graphites at 1 keV hydrogen bombardment and temperatures around 800 K, where a maximum for chemical sputtering on pure graphite occurs [4]. However, in fusion experiments chemical erosion was observed spectroscopically also after boronisation [1]. Indeed, it was measured later in laboratory experiments that also for boron doped graphites no reduction of chemical sputtering is observed at low ion energies (≤ 200 eV) and low temperatures (≤ 700 K) compared to pure graphite [4]. It is presumed that this low energy effect being similar for both pure graphite and boron doped graphite is due to a different mechanism than the one leading to the maximum at 800 K, which is nearly suppressed for boronized graphite. Due to the relevance of this low energy regime for fusion application, the mentioned formula is revised by introducing a new term for the low energy mechanism.

Results

The original formula described the contribution of chemical sputtering to total erosion (for deuterium bombardment) with an only mechanism which reproduces the observed maximum at 800 K [3] and which in the following will be denoted $Y_{ch,th}$ ($th \equiv$ thermal activated). The broadening of the temperature dependence at low energies was taken into account rather crudely by an additional condition which did not describe satisfactory the available experimental data as a function of target temperature.

In order to properly describe the temperature dependence at low energies, a new term can be added to the original equation which corresponds to a different chemical mechanism of hydrocarbon formation than the one leading to the peak at 800 K and which in the following will be denoted $Y_{ch,ath}$ ($ath \equiv$ athermal). Thus, the total sputtering yield for deuterium

bombardment of carbon for an incident deuterium energy E_0, a target temperature T in K, and a deuterium flux Γ_{D^+} in $cm^{-2}s^{-1}$ is

$$Y_{tot}(E_0,T) = Y_{phys}(E_0) + Y_{chem}(E_0,T,\Gamma_{D^+}) \quad . \tag{1}$$

$Y_{phys}(E_0)$ is the physical sputtering yield, which for normal incidence can be calculated with the revised Bohdansky formula [5]

$$Y_{phys}(E_0) = Q \cdot S_n(E_0) \left(1-\left(\frac{E_{th}}{E_0}\right)^{2/3}\right)\left(1-\frac{E_{th}}{E_0}\right)^2 \quad , \tag{2}$$

where Q and the threshold energy E_{th} are fitting parameters. For D → C these parameters are $Q = 0.1$ and $E_{th} = 28$ eV [5]. $S_n(E_0)$ is the stopping power which can be approximated by [5]

$$S_n(E_0) = \frac{0.5\ \ln\left(1+1.2288\left(E_0/E_{TF}\right)\right)}{E_0/E_{TF} + 0.1728\sqrt{E_0/E_{TF}} + 0.008\left(E_0/E_{TF}\right)^{0.1504}} \quad . \tag{3}$$

E_{TF} is the Thomas-Fermi energy which for D → C amounts to 447 eV.

The chemical sputtering yield is given by

$$Y_{chem}(E_0,T,\Gamma_{D^+}) = Y_{ch,th}(E_0,T,\Gamma_{D^+}) + Y_{ch,ath}(E_0,T) \quad \text{with} \tag{4}$$

$$Y_{ch,th}(E_0,T,\Gamma_{D^+}) = \frac{6\times10^{19}\exp(-1\text{ eV}/kT)}{1\times10^{15}+3\times10^{27}\exp(-2\text{ eV}/kT)}\left(2+200Y(E_0)\right)\left(\frac{\Gamma_{D^+}}{10^{16}}\right)^{-0.1} \quad , \tag{5}$$

which is the original term, and the new term

$$Y_{ch,ath}(E_0,T) = \frac{0.05\ \exp\left(E_0\times10^{-3}(20-1/kT)\right)}{\left[1+\exp\left((E_0-150)/25\right)\right]\left[1+\exp\left((T-740)/25\right)\right]} \quad . \tag{6}$$

The thermal activated mechanism $Y_{ch,th}$(eq. (5)) is composed of three terms: the first term is based on a model which explains the occurrence of a peak in the erosion yield as a function of temperature as the result of the competition between CD_4 formation and D_2 recombination, with activation energies of 1 and 2 eV, respectively. These activation energies were obtained from fits to the temperature dependence for 1 keV D^+ ions and are lower than inferred from thermal desorption spectroscopy [6]. However, during simultaneous ion bombardment ion induced processes lead to smaller activation energies [7]. The second term takes into account the energy deposited into nuclear damage in the surface layer, which has a maximum between 300 eV and 2 keV, enhancing the chemical erosion. Finally, the last term is an attempt to include the dependence of chemical erosion on ion flux, which is based on a scarce number of experimental data. The new athermal mechanism $Y_{ch,ath}$ (eq. (6)) is an empirical fit to the experimental data. The two terms in denominator restrict this process to energies and temperatures below 150 eV and 740 K, respectively. Within this range the process is only weakly energy and temperature dependent.

As shown in figs. 1 and 2 the new formula leads to a good agreement with all available experimental data both for the temperature and the energy dependence of the chemical sputtering yield. The contributions of $Y_{ch,th}$, eq. (5), and $Y_{ch,ath}$, eq. (6), are plotted separately. In fig. 2 the physical sputtering yield Y_{phys} is also shown. The experimental data in fig. 2 correspond to the total sputtering yield $Y_{tot} = Y_{phys} + Y_{ch,th} + Y_{ch,ath}$, while the ones in fig. 1 correspond to

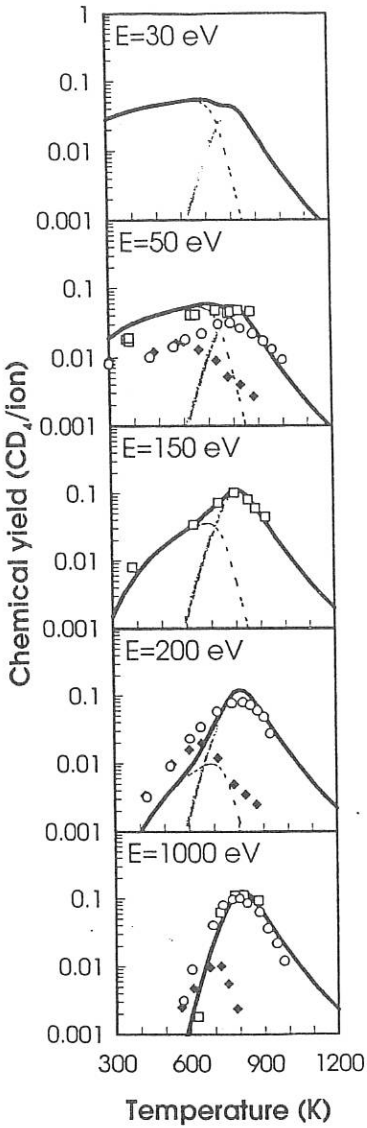


Fig.1: Temperature dependence of the chemical sputtering yield at different ion energies. □,○: exp. data for C; ♦: exp. data for C+15%B. ▒▒ $Y_{ch,th}$; ---- $Y_{ch,ath}$; ▬▬ $Y_{ch,th}$+ $Y_{ch,ath}$.

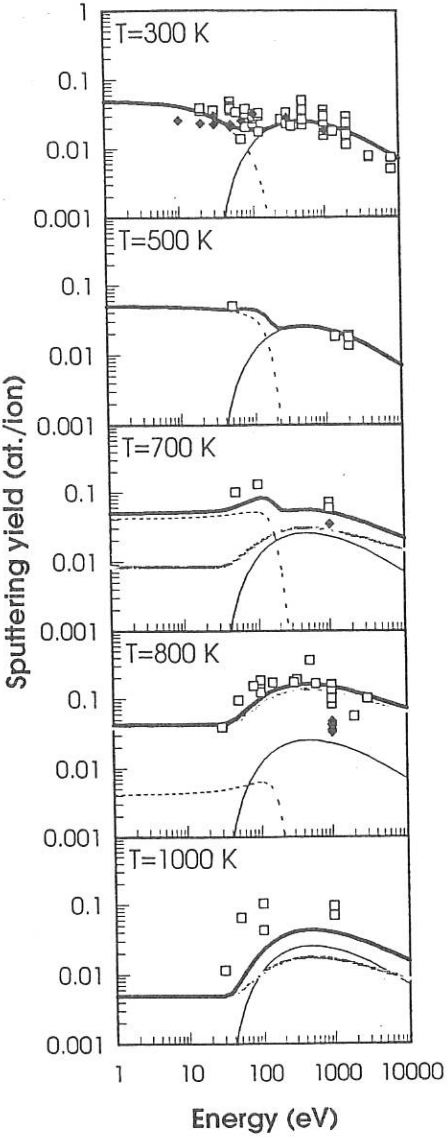


Fig.2: Energy dependence of the total sputtering yield at different target temperatures. □,○: exp. data for C; ♦: exp. data for C+15%B. — Y_{phys}; ▒▒ $Y_{ch,th}$; ---- $Y_{ch,ath}$; ▬▬ Y_{phys} + $Y_{ch,th}$+ $Y_{ch,ath}$.

the chemical sputtering yield $Y_{ch,th} + Y_{ch,ath}$, however neglecting higher hydrocarbons.

Discussion

Figs. 1 and 2 clearly show that in some energy and temperature regions only a scarce number of experimental data is available. For the temperature dependence at 50 eV (fig. 1) one set of experimental data is about a factor 3 lower than the values predicted by eq. (4) for the second mechanism ($Y_{ch,ath}$). The difficulties in absolutely calibrating mass spectrometer signals and the emission of higher hydrocarbons [2,3] may be the origin of such discrepancies. For the energy dependence (fig. 2) the experimental values are in general slightly higher than predicted by eq. (4). This is often attributed to surface roughness of graphite samples, while at temperatures above 1000 K the contribution of radiation enhanced sublimation begins to be notable [3] leading to higher values of the total sputtering yield.

Küppers et al. [8] investigated in recent studies the surface chemistry of thin C:H films by impact of thermal hydrogen. Besides thermal activated erosion via methyl and methane by C-CH_3 bondbreaking, which corresponds to our first process $Y_{ch,th}$ in eq. (4), they identified a second erosion process where a methyl or heavier group is released by deexcitation of sp^3 radicals to sp^2 by forming a double bond with a neighbour C atom. This process is most effective at temperatures around 600 K, in agreement with our second process $Y_{ch,ath}$ in eq. (4), see fig. 1. Contrary to the finding by Küppers, we do not find a decrease of the athermal process towards low ion energy and low temperature. While well annealed carbon surfaces show very little chemical erosion at temperatures < 700 K, chemical erosion increases drastically when the surface is prebombarded with energetic hydrogen [9]. This last situation corresponds to the conditions expected in a fusion machine, where the vessel walls receive large charge exchange hydrogen fluxes with an energy distribution strongly peaking at Franck-Condon energies and with a high energy tail responsible for surface damage. Under such conditions, chemical erosion at energies below 30 eV will remain about constant. This effect was taken into account in eq. (4), where for $E_0 \rightarrow 0$ the second term $Y_{ch,ath}$ tends to a yield of 0.05.

Figs. 1 and 2 also show experimental data from boron doped graphites which suggest that the thermal activated process $Y_{ch,th}$ is strongly reduced while the second process $Y_{ch,ath}$ remains unchanged. Thermal desorption spectroscopy (TDS) measurements after 1 keV D implantation have shown that boron addition to graphite shifts the balance of deuterium release towards the formation of D_2 rather than CD_4 due to a decrease of the desorption maximum of D_2 [4,6]. Therefore, in order to describe chemical erosion of boron doped graphites eq. (5) can be modified merely by reducing the activation energy of D_2 recombination from 2 eV to 1.7 eV. Already this small change in activation energy results in a strong reduction of the thermal activated erosion, $Y_{ch,th}$.

References

[1] A. Kallenbach et al., this conference.
[2] W. Poschenrieder et al., Proc. 11st Conf. Plasma Surface Interaction, Mito (Japan), 1994.
[3] J. Roth, E. Vietzke and A.A. Haasz, Supplement to Nucl. Fusion 1 (1991) 63.
[4] C. García-Rosales and J. Roth, J. Nucl. Mater. 196-198 (1992) 573.
[5] W. Eckstein, C. García-Rosales, J. Roth and W. Ottenberger, Sputtering Data, IPP Report, IPP-9/82 (1993); and C. García-Rosales, W. Eckstein and J. Roth, submitted to J. Nucl. Mater.
[6] C. García-Rosales, J. Roth and R. Behrisch, J. Nucl. Mater. (1994), in print.
[7] B.L. Doyle, W.R. Wampler and D.K. Brice, J. Nucl. Mater. 103 & 104 (1981) 513.
[8] J. Küppers, J. Biener, A. Schenk, B. Winter and C. Lutterloh, this conference.
[9] E. Vietzke and V. Philipps, Fusion Technol. 15 (1989) 108.

THE IMPACT OF CHEMICAL EROSION ON THE GLOBAL IMPURITY BALANCE IN THE ASDEX UPGRADE TOKAMAK

A. Kallenbach, A. Field, C. García-Rosales, M. Kaufmann, G. Lieder*, R. Neu, S. de Peña Hempel, W. Poschenrieder, K.-H. Steuer, ASDEX Upgrade Team

MPI für Plasmaphysik, EURATOM Association, D-85748 Garching, Germany
* IPF Universität Stuttgart, Germany

1 Introduction

Besides physical sputtering of surface material by energetic particles, fusion experiments using graphite as first wall material experience chemical erosion of carbon by hydrogen via the formation of hydrocarbon molecules followed by desorption. The absence of a (lower) threshold energy for chemical erosion gives rise to large impurity fluxes due to chemical erosion at low plasma temperatures. In particular regions with high hydrogen recycling, such as the divertor chamber, may make a considerable contribution to the carbon content of the main plasma. Erosion yields due to methane formation are of the order of a few per cent [1], even comparable to the maximum values for physical sputtering of carbon due to D bombardment. However, the main plasma fuelling efficiency for carbon atoms released by hydrocarbon formation is expected to be lower than for physically sputtered carbon atoms: the molecules leave the surface with wall temperature, and can therefore be effectively redeposited. The impact of chemical erosion processes on the impurity content in ASDEX Upgrade is investigated using spectroscopic measurements and statistical analysis.

2 Experimental results

Particle influx measurements are performed by means of visible spectroscopy using a freely programmable, gateable CCD camera and a 1-m Czerny-Turner spectrometer /2/. The geometry of the corresponding lines-of-sight, looking nearly horizontally through the main plasma, is shown in Fig. 1. Photon fluxes integrated along these viewing lines originate predominantly from the high-field side of the plasma, with the maximum of the local emission situated around or outside the separatrix /3/. The spectrometer is routinely tuned to impurity lines. The corresponding D_α-flux is in each case obtained from a diode equipped with an interference filter situated in a different toroidal position (120 degrees), which has been cross-calibrated against the absolutely calibrated camera-spectrometer arrangement.

The observed photon fluxes are converted to the corresponding particle fluxes by the well-known relation $\Gamma_{part} = S/XB \cdot \Gamma_{phot}$. The total C^{2+} flux is derived from the triplet

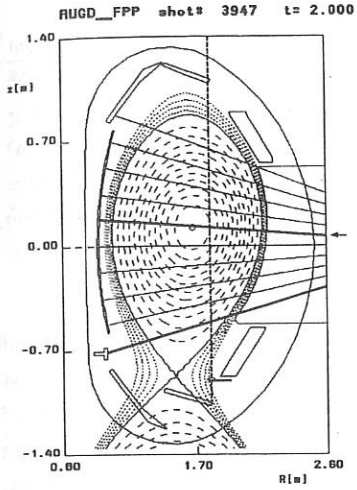


Figure 1: *Poloidal cross section of ASDEX Upgrade, typical flux surface structure and viewing lines used for particle influx measurements (solid lines) and C and O density measurements (dashed, vertical line).*

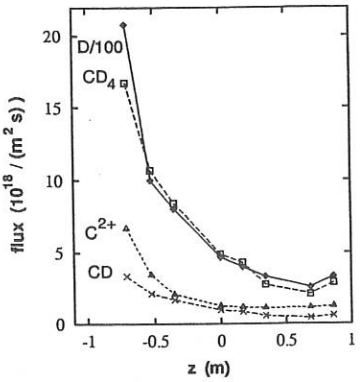


Figure 2: *Measured fluxes of D^0, C^{2+}, CD and recalculated CD_4 fluxes for comparable discharges along the sightlines shown in Fig. 1. z is the vertical position of the crossing of the sightlines with the inner plasma boundary and the viewing lines used for particle influx measurements.* *(I_p=0.6 MA, $\overline{n}_e = 3 \cdot 10^{19}\ m^{-3}$).*

line at 464.7 nm using an effective S/XB obtained with a simple 1-d transport code for the line-of-sight averaging of the local photon emission /3/. The hydrogen flux is evaluated from D_α measurements using S/XB=const=25, where the original Johnson-Hinnov value for typical edge conditions has been increased to account for direct D^+ release from breakup of D_2^+ molecular ions. The D^0 flux evaluated in this way is believed to be equal to the total hydrogenic flux to the wall, since the recycling coefficient for hydrogen is usually close to 1. CD molecular fluxes are determined from band emission around 431 nm. We use D/XB (CD)=const=20, the value for the CD_4 flux recalculated from CD emission following various molecular breakup chains is D/XB (CD_4)=100 /4/. About one fifth of the methane flux is expected to show up as CD. However, this factor is a rough estimate and may change considerably, if redeposition of molecular ions to the wall is accounted for more quantitatively.

Figure 2 shows spatial influx profiles of D^0, C^{2+}, CD and CD_4 molecules recalculated from CD flux. The fluxes increase towards the bottom, which is explained by the outflow of particles from the inner divertor chamber. The divertor is quite open against the inner heat shield, as can be seen in Fig. 1. The spatial variation of the various fluxes are very similar. Disregarding the large experimental uncertainties connected to the evaluation of

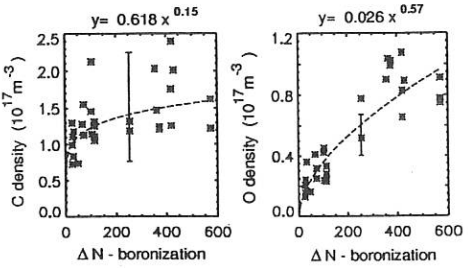


Figure 3: *Carbon and oxygen densities for the discharges of the database. ΔN denotes the number of discharges after the last boronization. The impurity densities were simply obtained by multiplication of the corresponding concentrations with $\overline{n}_e$.*

spectroscopic flux measurements, Fig. 2 is interpreted in the following: CD_4 is produced with a yield of 1 % by the impinging hydrogen flux. Owing to the high losses of carbon atoms during the molecular breakup chain, the resulting CD flux amounts to 0.2 % of the hydrogen flux and is responsible for part of the C^{2+} flux observed. The remaining part of the C^{2+} flux can be attributed to CO recycling, as will be shown in the following.

Carbon and oxygen densities are derived from the Lyman-α radiation of the corresponding hydrogen-like ions. The line intensities are measured with two Bragg spectrometers operating routinely with fixed wavelength setting. They are converted into impurity densities by transport calculations using measured electron temperature and density profiles. The carbon and oxygen densities of the database are displayed in Fig. 3 versus the number of shots made after the preceding boronization. The result of the regression analysis is given on top of each figure, and is plotted as a dashed line.

The wall condition is the dominant parameter for the oxygen density, showing a partial recovering of the oxygen content during a few hundred discharges after boronization. The carbon density is much less affected by the boronization, the slight long-term increase after the boronization is similar to the absolute increase of the oxygen density. This behaviour can be attributed to a similar fuelling efficiency for C and O stemming from recycling carbon oxide. It should be noted, that the first 15 discharges after a boronization have been omitted from the analysis. These discharges show also a significant reduction of carbon fluxes as well as concentrations, which may be attributed to an impermeable coverage of the graphite surface by boron layers.

The measurement of relative carbon and oxygen concentrations in the main plasma allows one to subtract that fraction of the C^{2+} influx which is attributed to CO recycling. The quantity $f_s^C = \frac{\%C-\%O}{\%C}$ is attributed to that fraction of the carbon ions *not* originating from CO recycling (assuming equal fuelling probabilities for C and O). For vanishing oxygen concentration, the C^{2+} flux amounts to about 0.45 % of the hydrogen flux (see Fig. 4). If the carbon influx is reduced by f_s^C, finally a good correlation between this CO-resolved C^{2+} flux and the D^0 flux is obtained. As can be seen in Fig. 5, the CO-resolved C^{2+} flux is nearly proportional to the hydrogen flux, with the effective yield

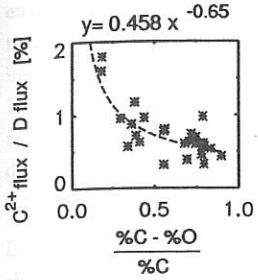


Figure 4: *Ratio of C^{2+} and D^0 fluxes versus the fraction of the measured carbon concentration not attributed to CO recycling.*

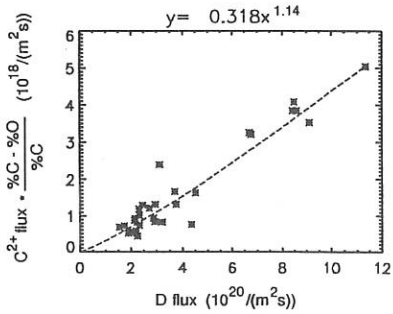


Figure 5: *Measured carbon flux, reduced by the fraction owing to CO recycling, versus D_0 flux.*

$\Gamma_{C^{2+}}/\Gamma_D \approx 0.45$ %.

Influx measurements for O^+ and CD were performed for a smaller number of discharges. Generally, the oxygen fluxes also increase with the electron density. This behaviour is probably due to the decrease of the particle confinement time ($\tau_p \propto 1/\overline{n}_e$), which leads to an increase of the recycling speed of the oxygen inventory. The CD_4 flux derived from CD band emission preserves the level of 1-2 % of the hydrogen flux, even during neutral-beam heating and H-mode (averaged over ELMs).

3 Conclusions

Chemical erosion via hydrocarbon and carbon oxide formation and desorption are responsible for major parts of the carbon and oxygen concentrations observed in the main plasma of ASDEX Upgrade. The measured fluxes and concentrations reveal a consistent picture: Hydrocarbons are produced at graphite walls with a yield of a few per cent. The hydrocarbon fluxes cause a lower C^{2+} ion flux $\Gamma_{C^{2+}}/\Gamma_D \approx 0.45$ %. CO recycling is an additional source for carbon and oxygen, which becomes dominant for impure wall conditions. The penetration probability for C and O released by CO is comparable, and the impurity concentrations in the main plasma reflect the ratio of their fluxes in comparison to the hydrogen flux for these ohmic conditions.

References

/1/ C. Garcia-Rosales et al., this conference.

/2/ A. Kallenbach et al., Rev. Sci. Instr. **64** (1993) 1257.

/3/ A. Kallenbach et al., Plasma Phys. Contr. Fusion (1994), in press.

/4/ K. Behringer, J. Nucl. Mater. **176+177** (1990) 606.

Evolution of radiating vapour shield at divertor plates during disruption

L. L. Lengyel and P. N. Spathis
Max-Planck Institut für Plasmaphysik - EURATOM Association
D-85748 Garching bei München, Germany

During off-normal operational regimes in large-scale tokamaks, as in the case of hard disruptions or giant ELM-s, an intense flux of high-energy plasma particles impacts the plasma facing machine components. In the case of ITER, it is estimated that the energy flux affecting the divertor plates during the thermal quench phase of a disruption is of the order of 10^{10} to 10^{11} W/m^2 (12 MJ/m^2 are damped within 0.1 to 3.0 ms). The plasma energy transported by particles presumably distributed over the SOL. The energy flux incident at the divertor plates raises the temperature of the solid until phase transition takes place: a vapour layer forms at the surface which, depending upon the physical properties of the substance used for coating the plates, may stop the incident particles and, at the same time, dissipate their energy by radiation to the environment. As a result of this, the erosion rate of the surface may rapidly reduce to tolerable values [1]. An accurate description of this process requires considering a number of physical phenomena that occur simultaneously:
(a) collisional energy transfer to the solide surface and the vapor layer evolving over it (stopping-length calculations with simultaneous determination of the self-consistent electrostatic shielding field induced; the energy distribution of the plasma particles being approximated by a discrete number of energy groups);
(b) phase transition at the surface that determines the erosion rate;
(c) gasdynamic expansion of the vapor and the resulting hydrodynamic and state parameter distributions;
(d) atomic processes such as radiation emission and finite rate ionization and recombination;
(e) MHD interaction of the high-beta ionized vapor fraction with the magnetic field (slowing-down and stopping of the cross-field motion) and the distortion of the magnetic field topology;
(g) energy transport in the cloud interior by thermal conduction and radiation;
(f) energy losses to the environment by conduction (into the solid) and radiation.

The effectiveness of surface shielding by an evolving vapour layer is demonstrated by means of a scenario calculation: a graphite-coated divertor plate is exposed to the action of thermal electrons originating from a thermonuclear plasma. The Maxwellian energy distribution of the energy carriers is approximated by a discrete number of

energy groups. The geometry considered corresponds to a SOL in a high-aspect-ratio-tokamak ($R/a \rightarrow \infty$) and is represented by a straight strip of given width extending to infinity (see Fig. 1). Parameter variation across the SOL is neglected in the present $1\frac{1}{2}$-D approximation, only the effects of the lateral expansion of the vaporized material and the lateral radiative losses are taken into account (the lateral direction is the direction across the SOL, see the x-axis in Fig. 1). Results corresponding to an infinitely wide SOL (infinite plate approximation) are described in [2].

In this work, quantitative data are presented on the effectiveness of radiative vapor shields, i.e. on the relative magnitudes of $\dot{Q}_{rad}$ and $\dot{Q}_{input}$, where $\dot{Q}_{input}$ and $\dot{Q}_{rad}$ represent the energy flux incident on the wall and that dissipated through radiation by the vaporized wall particles, respectively. Results of a scenario calculation are presented below.

Representative results

The disruption scenario considered corresponds to a thermal background plasma with temperature $T_0 = 5\ keV$ and density $n_0 = 10^{19}\ m^{-3}$ dumped on the divertor plates within a SOL of width l = 3 cm. The corresponding thermal flux carried by the electrons is $\approx 1.9 \times 10^{11}\ W/m^2$. This value is about 1.6 times higher than the upper limit given by ITER specifications (12 MJ/m^2 dumped within 100 μs). The applied magnetic field strength was assumed to be B = 4 tesla. Figures 2 to 5 represent parameter distributions at $t = 92\mu s$ vapor shield evolution time.

Figure 1 shows the geometry considered: the applied magnetic field B_0 of an angle of incidence α is aligned with the y, z plane. The SOL width is measured in the x-direction.

Figure 2 shows the electron density distribution across the vapor layer at a time instant $92\mu s$ after exposing the graphite surface to the incident plasma particles.

Figure 3 shows the distributions of the first two ionization levels across the vapor layer at $t = 92\mu s$ after the start of the disruption; these distributions could readily be compared with results of spectroscopic (line emission) measurements.

Figure 4 represents the energy flux depletion chart for the energy carriers in the five-group approximation used: the particles in the group with the highest initial energy (≈25 keV) have the largest penetration depth. In the case shown here, the high-energy particles do reach the plate also after 92 μs.

Figure 5 shows the distribution of the radiant energy flux across the vapor layer. Negative values correspond to radiant energy transport towards the plate.

Figure 6 represents the total radiant energy lost through the lateral surfaces of the scrape-off layer (in the ±x direction).

Figure 7 represents the time variation of the surface erosion rate. The process may turn out be self-regulating: the quasi-stedy value of the erosion rate being defined by the mutual feed-back between the incident energy flux and the dissipative processes

present.
Figure 8 shows the time evolution of the energy balance per unit SOL length (l = 1 cm) for a SOL 3 cm wide. As can be seen, the radiated energy approaches the value of the input energy. The energy expended on ionization, internal energy, and kinetic energy is about 10 per cent of the input energy. The lowest curve, $E_{incident}$, represents the energy transferred directly to the wall by incident plasma electrons. In the scenario here considered, the energetic particles do reach the plate even after $92\mu s$ physical time.

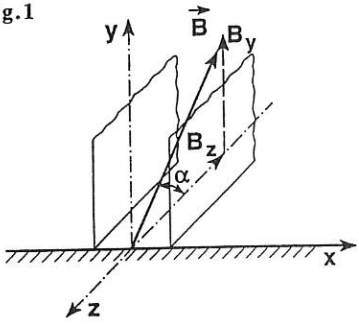
The calculations show that the magnetic field distribution becomes notably disturbed by the expanding high-beta ionized vapor. The magnitude of the field dilution strongly depends upon the incident energy flux and the magnetic field strength applied. For example, assuming classical resistive magnetic diffusivity, an increase of the background plasma temperature from 3 keV to 7 keV causes a reduction of the normalized average magnetic field strength in the vapor layer, B/B_0, ($B_0 = 4\ tesla$), by approximately 60 per cent. Keeping the plasma temperature constant ($T_{e0} = 4\ keV$) and changing the value of B_0 from 6 $tesla$ down to 2 $tesla$ causes an increase of the diamagnetic dilution factor (i.e. a reduction of the average magnetic field strength in the cloud) by $\approx$ 64 per cent. In these computations, the effect of the magnetic field dilution on the incident energy flux was not yet taken into account.
The quantitative effect of the magnetic field distortion on the global shielding characteristics is subject to further studies.

REFERENCES

[1] L.L. LENGYEL (compiled by), "Studies on Wall Erosion during Off-Normal (Disruptive) Tokamak Operation", IPP Progress Report 1993 in "Report on European ITER Task ETA-EC-DPI-1-3: Development of Divertor Materials, Modelling of Off-Normal Plasma-Material Interaction." Report No. NET PM 94-003, March 1994.

[2]P.SPATHIS and L.L. LENGYEL, Proc. 20th EPS Conf. on Contr. Fusion and Pl. Physics, Lisboa 1993, 17C, Part IV, p. 1443.

Fig.1



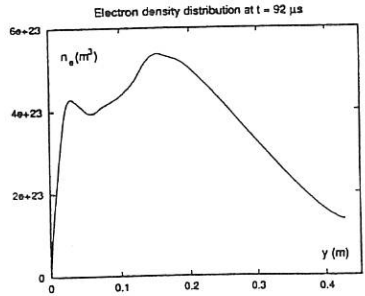


Fig.2

Fig. 3

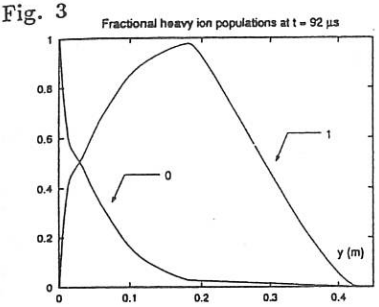


Fig. 4

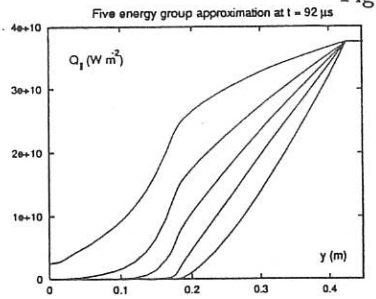


Fig. 5

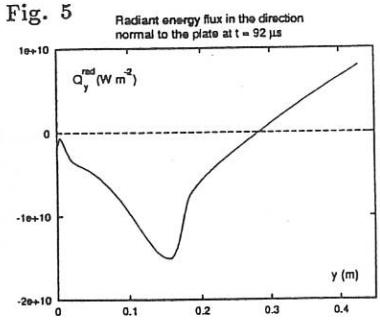


Fig. 6

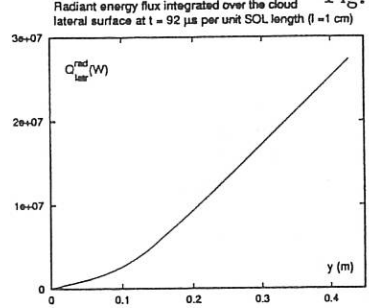


Fig. 7

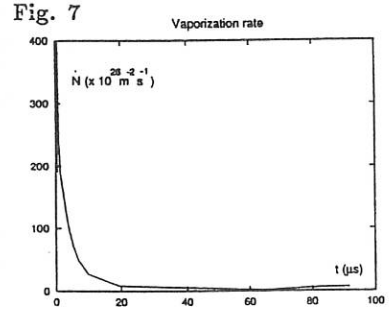
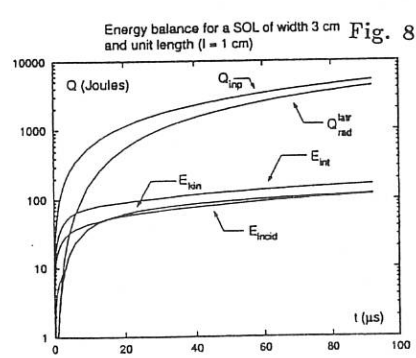


Fig. 8



Time resolved measurements of hydrogen inventory in graphite under plasma exposure

M.Langhoff, B.M.U.Scherzer
Max-Planck-Institut für Plasmaphysik
EURATOM Association
85748 Garching

Introduction

The hydrogen inventory in graphite used as a first wall material of magnetically confined fusion plasma experiments has been subject to many investigations. In fusion devices at temperatures below 300K a transient hydrogen inventory during plasma discharges is observed [1,2], which is contradictory to results of ion beam implantation experiments [3,4,5]. Latter show that for hydrogen implantation in graphite at room temperature 100% trapping occurs below a saturation concentration of H/C = 0.42. Further implanted hydrogen is reemitted instantaneously. Differences in hydrogen impact parameters between plasma exposure and ion beam implantation (i.e. lower ion energies, higher flux, additional neutral flux, impurity contaminated walls) could be responsible for the different behaviour in fusion experiments.

Experimental

Therefore an RF plasma experiment was used to clarify the existance of such a "dynamic" inventory. The experimental setup has already been described by Jandl et al. [6,7]. The RF reactor consists basically of a parallel plate reactor (Volume 1l) powered by an RF transmitter (50W) operated at 13.56 MHz. The electrodes are of stainless steel, the powered electrode is covered by an a-C:H layer. The carbon target (Ringsdorff EK98) was placed in the grounded electrode. The experiments were performed with a deuterium discharge at 10 Pa, resulting in a DC-bias of 150V. A 2.6 MeV $^4He^+$-beam provided in-situ ion beam analysis of the target by means of Rutherford backscattering spectrometry (RBS) for detection of heavy elements ($Z \geq 6$) and elastic recoil detection for hydrogen and deuterium analysis. The target was heatable to 1000K by a resistance heater mounted at the back of the target.
The experimental procedure was as follows: The plasma was switched on (for 300s) and off (for 900s) periodically. During this time the total amount of deuterium was determined every 30s. To reduce statistical effects the data shown below (fig.1) are averaged over 10 plasma cycles. During these 10 cycles a hydrogen depth profile and an RBS spectrum was taken.

Results and Discussion

As expected from ion beam implantation the graphite target starts to reach saturation during the first five cycles. Unexpected is the decrease of the inventory after plasma shut down (fig.1). Interrupting the ion beam analysis after plasma exposure for 300s showed, that the high energy beam is responsible for the release rather than a spontaneous process. Ion induced desorption by high energy ions has already been observed by Roth et.al. [8]. They have determined a cross section of $9.4 \cdot 10\text{-}19$ cm^{-2} for 2.5 MeV ^{3}He on pyrolytic graphite. For EK98 we have determined a value of $5 \cdot 10\text{-}18$ cm^{-2}with ion beam implantation. In the plasma experiment, assuming an exponential behaviour, a cross section as high as 10^{-16} cm^{-2} is obtained. Only a fraction of 20% to 30% of the total inventory exhibits this enhanced ion induced desorption (furtheron called desorbed inventory). As the analysis beam has energies in the MeV range, the interaction with the hydrogen in the implantated layer is dominated by inelastic collisions [8,9].

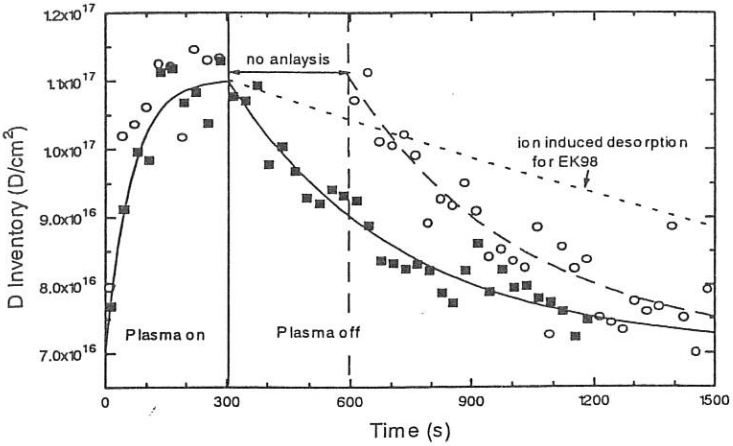


Fig.1: The deuterium inventory during and after plasma exposure (squares). To study the influence of the beam the analyses were interrupted for 300s after plasma shut down (open circles). The lines are exponential fits to the data. The ion induced desorption of ion beam implanted EK98 is also shown (dotted line).

The deuterium inventory was observed over a long time of plasma exposure. Fig. 2 shows the increase of the inventory and the desorbed part with plasma irradiation time. Also shown is the increase of impurities (i.e. iron and oxygen) on the target. As the powered electrode is covered by an a-C:H layer, they arise from sputtering of the surrounding grounded electrode and deposition onto the target. Experiments were also performed with a tungsten covered electrode, which shows basically no differences. The coverage of metal impurities is on the same order as of limiter tiles in JET [10]. As Sawicki et.al. showed, iron droplets on the ASDEX limiter consist of a mixture of cementite and austenite [11]. It has been confirmed by XPS measurements that this is also the case for the impurities on our plasma exposed surfaces. So with respect to wall contamination the graphite target in our plasma experiment is comparable with limiter tiles from fusion machines.

In addition to the impurities on the target a build up of a surface structure is observed. Probably due to preferential sputtering the surface is covered with needles a few microns long and a few tenth of a micron in diameter. A SEM picture of the surface after 13 hours of plasma irradiation is shown in fig.3. Towards the tip of these needles the concentration of the metal impurities increases. The formation of this structure is not completly understood as the metal has to be deposited, whereas the complete surface is eroded several 10 microns. This structure, however, exhibits an enhanced surface area for ion implantation, so the deuterium inventory should increase with plasma exposure. The decrease of the static inventory at the beginning of the plasma exposure supports this assumption as the formation of needles could be observed only after at least 3 hours of plasma impact.

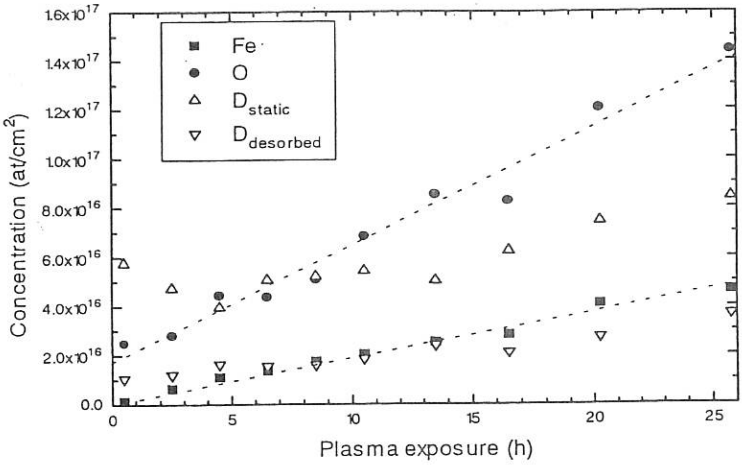


Fig.2: The deuterium inventory (desorbed: down triangle;static: up traingle), and the impurities (Fe: squares, O:circles) increase with plasma exposure time.

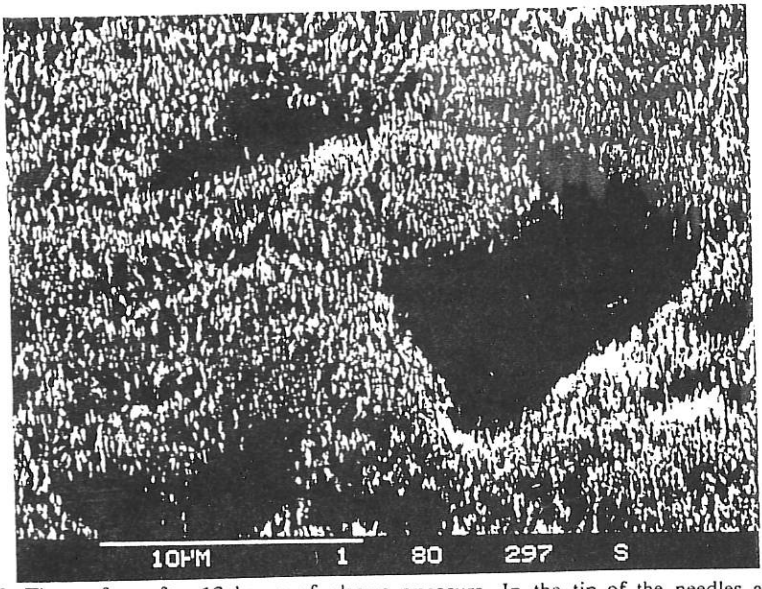


Fig.3: The surface after 13 hours of plasma exposure. In the tip of the needles a higher concentration of Fe is found.

Unfortunately the surface modification is coupled to the metallic impurities. Using carbon as electrode material for the RF reactor leads to a build up of an a-C:H layer, which exhibits an extremely low ion induced desorption. So no definite claim can be made, wether the metal impurities or the properties of plasma impact is responsible for the fast ion induced desorption. This experiment was also done at a target temperature of 600K, which has been the wall temperature of the fusion experiments described by Ehrenberg et.al. [1]. Even at these elevated temperatures no dynamic inventory could be found.

Conclusion

The recent experiment showed, that there is no transient uptake of hydrogen in graphite by plasma impact. We have taken into account the influence of low energy ions, additional neutral flux and we have investigated impurity covered graphite similar to limiter tiles. The model of Grisolia [2] and Ehrenberg [1] assuming a hydrogen diffusion below 300K could not be confirmed.

The nonsaturating pumping capability of fusion walls could be explained by an enlarged surface area due to erosion.

In addition to that a large amount of hydrogen can be released from the walls easily induced by fast charge exchange neutrals, which has not yet been taken into account.

References

[1] J.Ehrenberg, P.J.Harbour, Nucl.Fusion **31**(2) (1991) 287.

[2] C.Grisolia, Ph.Ghendrih, B.Pegourie, A.Grosman, J.Nucl.Mater. **196-198** (1992) 281.

[3] G.Staudenmaier, J.Roth, R.Behrisch, J.Bohdansky, W.Eckstein, P.Staib, S.Matteson, S.K.Erents, J.Nucl.Mater. **84** (1979) 149.

[4] B.M.U.Scherzer, P.Borgesen, W.Möller, IPP-JET-Report No.32 (1986)

[5] W.Möller, J.Nucl.Mater. **162-164** (1989) 138.

[6] C.Jandl, W.Möller, B.M.U.Scherzer, in 'Proceedings of the 18th European Conference on Controlled Fusion and Plama Physics', Berlin 1991.

[7] C.Jandl, Dissertation TU Munich 1993.

[8] J.Roth, B.M.U.Scherzer, R.S.Blewer, D.K.Brice, S.T.Picraux, W.R.Wampler, J.Nucl.Mater. **93&94** (1980) 601.

[9] H.Bergsaker, S.Nagata, M.Rubel, B.Emmoth, in 'Amorphous Hydrogenated Carbon Films', edited by P.Koidl, P.Oelhafen (Les Editions de Physique, Paris, 1987).

[10] R.Behrisch, J.Ehrenberg, H.Bergsaker, J.P.Coad, L.de Kock, B.Emmoth, H.Kukral, A.P.Martinelli, G.M.McCracken, J.W.Partridge, J.Nucl.Mater. **145-147** (1987) 731.

[11] B.D.Sawicka, J.A.Sawicki, R.Behrisch, J.Appl.Phys. **62**(12) (1987) 4844.

Radiation Phenomena and Particle Fluxes in the X-event in Jet

H.J. Jäckel, D.V. Bartlett, H. Falter, J. Lingertat, R. Reichle
JET Joint Undertaking, Abingdon, Oxon OX14 3EA, U.K.

Introduction

The highest fusion yield of $\Gamma_n \approx 4 \times 10^{16}$n/s has been observed in JET in hot ion H-mode discharges at a heating power of $P_{heat} \approx 15$ MW with average electron densities of $\bar{n}_e \leq 4 \times 10^{19}$ m^{-3}[1,2,3]. The energy confinement during the H-mode was typically 3 times better than in the L-mode. The final termination of the high confinement regime can take place within milli-seconds. The sudden loss of stored energy then causes an intense heat-flash on the divertor dump plates, accompanied by a dramatic increase of divertor particle fluxes (X-event).

Several typical patterns of the H-mode termination have been observed, showing different dynamic and radial range of the confinement deterioration, as reflected in the response of stored energy, W_p, the total neutron rate, Γ_n, and the electron and ion temperature profiles:

The diffusive decay: Γ_n and W_p degrade gradually on a time scale of up to several hundred milli-seconds. The plasma temperature starts to decrease from the edge. A 'cold wave' appears to travel towards the plasma centre.

The fast edge, diffusive core decay: The core ($r \leq a/2$) confinement degradation takes place on a diffusive time scale, while the outer half is deteriorating fast.

The sudden decay: Core and edge confinement decay simultaneously on a sub milli-second time scale.

A final power flash, dumped on the divertor target plates, resulting from the final fall-back into L-mode, can reach more than 100 MW and is observed in all three types.

Experimental:

The radiation build-up and the particle fluxes in the phase, immediately preceding the X-event, has been studied with bolometry and spectroscopy. Only the D_α data have a time resolution (≈ 2 ms), which comes close to the dynamic of the X-event itself. Bolometry, spectroscopy and the infrared diagnostic have resolution in the 20 to 100 ms range.

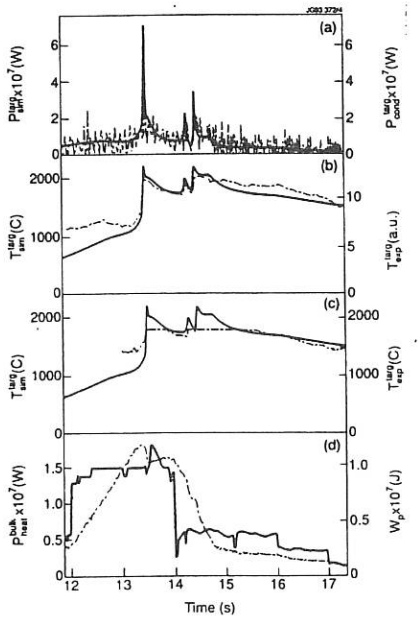


Fig. 1: a: Total heating power (solid) and stored energy; b+c: Fitted temperature (solid) and measured one; d: Fitted (solid) and measured target power.

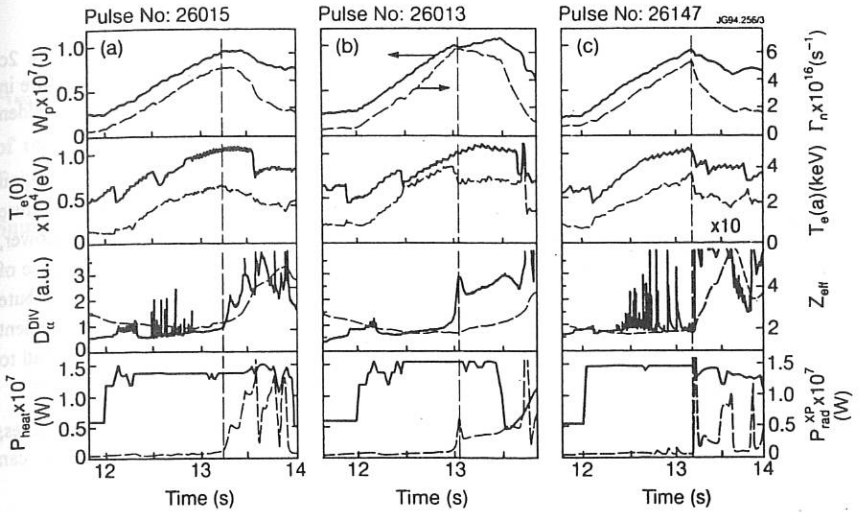


Fig. 2: Three HMI discharges with differing X-event pre-phase. The curves depict (bottom to top, solid refers to left scale): Total heating power and total divertor radiation, divertor D_α-emission and Z_{eff}, central and edge electron temperature, stored energy and total neutron rate, respectively.

The measurement of the target temperature, T_{targ}, was fraught with difficulties. The measuring range of the CCD and infrared cameras did not cover the fast rise of T_{targ} and the temperature pattern was complicated by mechanical alignment errors of the target tiles. For the graphite divertor an attempt had been made [4] to fit the target temparature, calculated from the conductive power into the divertor to experimental data. Figure 1 shows, for a HIM discharge with X-event, the development of the measured and calculated target temperature.

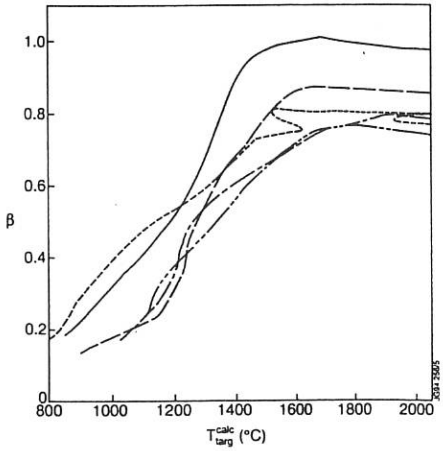


Fig. 3: development of β as a function of the calculated target temperature during the course of the high performance regime of 5 HIM discharges.

Results and Discussion:

Figure 2 depicts relevant plasma parameters during the H-mode of representative hot-ion mode (HIM) discharges for the above classification. The discharges of figure 2a (pulse 26015) and 2b (pulse 26013) show a gradual degradation of the confinement before the actual X-event, which is marked by the sharp drop of the central electron

temperature. The edge electron temperature decays well before the central one. Figure 2c (pulse 26147) demonstrates the simultaneous and sudden decay of the electron temperature in the centre and the edge and, not shown, of the ion temperature and, accordingly, the sudden drop of stored energy and total neutron rate.

Although MHD-activities are often coinciding with the termination, there is no clear correlation to a critical β. Figure 3 shows the relation between β and the calculated target temperature during the course of the H-mode for 5 HIM-discharges with similar heating power, $P_{heat} \approx 15$ MW, and electron density, $\bar{n}_e \leq 4 \cdot 10^{19}$ m^{-3}. The run-away target temperature of about 1400 °C is reached at different β-values. The temperature is too low, to contribute through sublimation to the divertor carbon flux. However, any further confinement deterioration increases the power load on the target and can, at this temperature level, lead to run-away conditions:

MHD-activities: A fast loss of stored energy leads to high target surface temperatures, even if ΔW_p is small. If a sawtooth is coupling to an ELM, as in discharge 26147, $\dot{W}_p$ can easily reach 50 to 100 MW.

Recycling losses: High target bulk temperature can cause a significant release of deuterium, trapped in the graphite and, due to the enhanced recycling, can lead to an effective edge cooling.

Thermally decoupled carbon: Recent NBI test-bed experiments on graphite tiles [5] have demonstrated the existance of a partial coverage of particles without or with reduced thermal contact to the bulk. This carbon can be vapourised and/or ejected into the plasma on a ms time scale, even with relatively small heat pulses, similar to a laser blow-off. The particle coverage can not be removed completely, even at intensive pulsing. Redeposited carbon might also contribute in the same way.

The development of the calculated target temperature T_{targ} and the time-integrated target ower

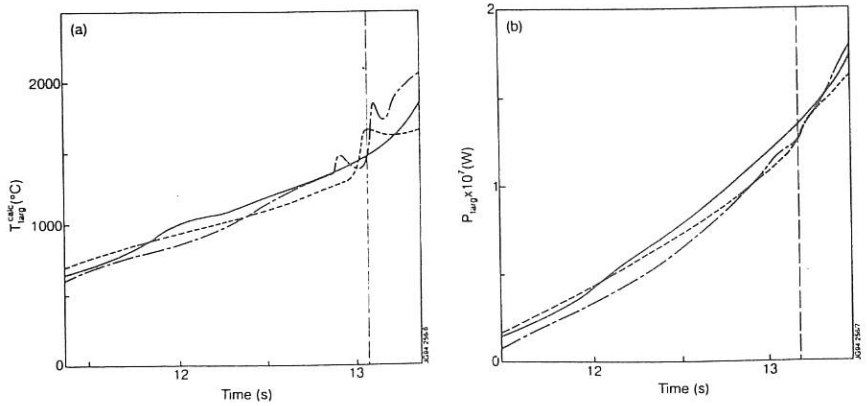


Fig. 4: The development of target temperature (left) and integrated target load (right) during the high performance regime for the 3 discharges of picture 2. The vertical dotted line marks the onset of the X-event, the start of the decline of the total neutron rate.

$E_{targ} = \int_{t_{xp-s}}^{t_0} P_{targ} dt$ are depicted in figure 4 (t_{xp-s}=start of the X-point configuration). At the time of the X-event, marked by the vertical dotted line, typical values are $T_{targ} \approx 1400\,°C$ and $E_{targ} \approx 13\,MJ$.

Summary:

- The H-mode phase in high performance discharges tends to collapse irreversibly. The (calculated) target temperature just before the X-event amounts to about 1400 °C. Any deterioration of confinement at this temperature leads to run-away conditions of the target temperature and a final fall-back into L-mode. However, there is no clear of a correlation between a critical β and the H-mode termination.
- Possible causes of the confinement deterioration are:
  1. MHD activitives can cause a fast plasma loss and, hence, a power flash, dumped on the divertor target, leading to a temperature jump of up to 1000 °C. At a bulk temperature $T \geq 1400\,°C$ this leads to run-away conditions of confinement and target surface temperature.
  2. Enhanced recycling, due to thermal release of trapped deuterium from the graphite target plates causes an efective plasma edge cooling.
  3. Loose graphite on the target tiles with virtually no thermal coupling to the target bulk can be sublimated and ejected into the main plasma with even small power levels.
- Apart from major instabilities, the bulk temperature of the divertor dump plates appears to play an important role. Increasing temperature reduces the equilibrium pressure of trapped deuterium in the graphite and leads to higher recycling fluxes and hence, stronger edge cooling, making the discharge vulnerable to any further confinement deterioration. An active cooling, keeping the bulk target at ambient temperature could make the discharge more resilient against even medium MHD instabilities, as e.g. giant ELMs.

References:

[1] E. Thompson, D.Stork, H.P.L. de Esch and the JET Team, Phys. Fluids B 5 (1993) 2468

[2] The JET Team, Nucl. Fus. 32 (1992) 187

[3] J.G. Cordey, R. Reichle, D. Stork and the JET Team, "The enhanced Confinement Regime in JET", submitted for publication in Plasma Phys. and Contr. Fus.

[4] H.J. Jäckel et al., Proc. 20th EPS Conf. Contr. Fus. & Plasma Phys., Vol. I (1993) 287

[5] D. Ciric et al., to be published in Proc. 18th Symp. on Fus. Techn.

RADIATIVE PLASMAS WITH ERGODIC DIVERTOR AND ADDITIONAL POWER IN TORE SUPRA

J.-C.Vallet, A.Grosman, B.Beaumont, C.DeMichelis, E.Gauthier,M.Goniche, D.Guilhem, R.Guirlet,W.Hess, P.Monier-Garbet, B.Saoutic
Association EURATOM-CEA sur la fusion contrôlée
Centre d'Etudes de Cadarache, F-13108 St-Paul-Lez-Durance, France

INTRODUCTION Over the past years, the TORE SUPRA ergodic divertor has demonstrated some capabilities to stabilize both edge radiating layers -as Marfes or detached plasmas- and edge MHD activity -as the m=2,n=1 tearing mode- usually encountered simultaneously close to the ohmic density limit[1]. Moreover, it has been shown that in TORE SUPRA the ergodic layer induces an effective screening of most of the chemical species -except helium- which may be present at the plasma edge.

During the last campaign, taking advantage of the ergodic divertor properties, part of the experimental program has been dedicated to the production of stationary edge radiating layers in plasmas heated by waves. Two problems had to be solved: 1) waves coupling in the presence of the ergodic divertor magnetic perturbation and 2) the control of the radiated power at a level close to the total input power.

1)So far it has been possible to couple up to 3MW of lower hybrid power and up to 5.5 MW of ICRH in two different plasma geometries depending on the specific interaction of the launchers with the stochastic magnetic field at the edge. This resulted in target plasmas with about 4.5MW and 7MW of total heating power respectively. Note that in all these experiments launchers were in the shadow of the outboard inertial limiter.

With lower hybrid waves an excessive heating of neutralizer plates connected to launchers by magnetic field line performing less than one third of toroidal turn has been observed. This power loss by conduction is coming from the high N// part of the wave spectrum (N//≥6) which can be absorbed at the very plasma edge [2] Thus for these first experiments a conservative geometry has been used: The limiter and launchers have been further off from the divertor coils (R_{coils}=3.18m, R_{lim}=3.11m, $R_{launchers}$=3.13m) leading to a somewhat lower stochasticity of the plasma edge. The "safety factor" at the limiter radius is $q_{Rlim}\approx 3.2$ corresponding to $q_{coils}\approx 3.8$ while the resonant value is $q_{coils}\approx 3.4$. In these experiments the plasma column was centered at $R_0\approx 2.35$ It has to be noticed that it exists conservative geometries which may provide also a better agreement with the resonant condition -They will be used in future experiments.

With ICRH due to the resonant absorption far away from the ED coils it has been possible to use the standard geometry which fullfils the ED resonant condition ($R_{lim}\approx 3.15$m $R_0\approx 2.4$m $q_{Rlim}\approx 3.2$).

2) To maximize the radiated power two different scenarios, based either on intrinsic impurities (C, O, Cl) and charge exhange at high plasma density (volume averaged density>4 $10^{19}m^{-3}$)-in that case the radiation pattern takes the form of a stationary high field side extended Marfe [3]- or on gaseous extrinsic impurity injections (CD_4-N_2-Ne-Ar) at low or moderate plasma density, have been used to produce stationary radiating rates in the range of 70% to 100% of the total input power. -Neon experiments are reported in this paper.

NEON EXPERIMENTS Compared to other gaseous impurities Neon exhibits three interesting properties: i) it is a fully recycling impurity thus even without pumping and without feedback loop stationnarity can be easily obtained, ii) between two shots the injected Neon is fully pumped which provides a good reproductibility of the experiments, and iii) the effective power exhaust per injected atom is quite high - of the order of 300 to 700keV/s

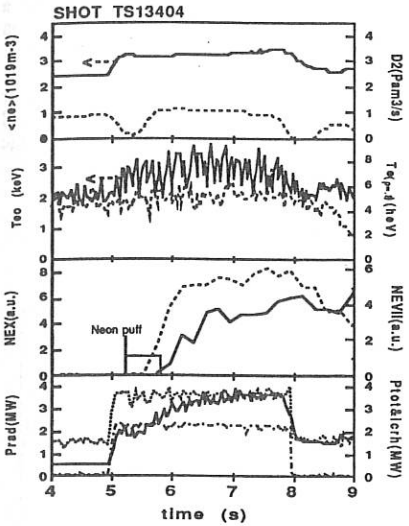


Fig1.a ED exp. with Neon puff &ICRH

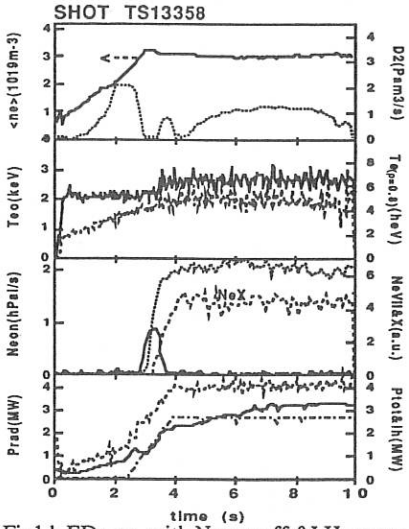


Fig1.b ED exp. with Neon puff &LH power

depending on plasma parameters (density and temperature). Fig.1.a&b show two typical ED experiments with ICRH and LH power respectively. In both cases a Neon puff of about 50Pal (1Pal≈2.610^{17}Ne) leads to an increase of the total radiated power. The behaviour of the NeVII&NeX lines brightness points out the high value of the Neon recycling coefficient. Thermographic analysis of the limiter and neutralizer plates indicates that in the ICRH case the radiated power deduced from bolometers is overestimated by at least 1MW. In this case the radiating layer being localized in front of divertor coils is probably sensitive to the toroidal modulation of the ED magnetic perturbation. This also indicates that probably the radiated ratio is not larger than 70%.-these discharges are analysed in details in [4].

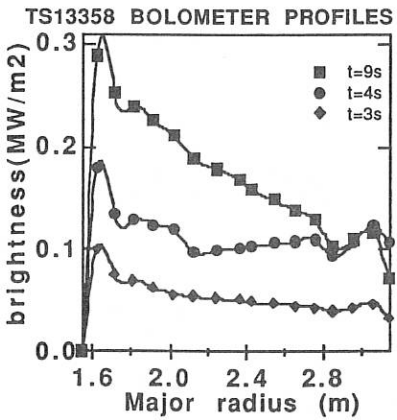


Fig.2 SHOT TS13358 Bolometer profles

In the case of LH experiments the low temperature of the various pfc's is in agreement with the high radiated ratio deduced from bolometry. This is due to a more favorable geometry of the radiating layer which evolves from a poloidally symmetric ring -due to the radiation of Neon [5]- to a stable high field side Marfe both being less

sensitive to toroidal asymmetries induced by the ED. Fig.2 shows the behaviour of the bolometer brightnesses for the shot 13358 (Fig.1.b). At t=4s the radiation is at 50% due to Neon and is poloidally symmetric then from t=5s to t=10s the bolometer profile evolves toward a very extended marfe. This is interpreted as a synergetic effect between the neon radiation and the edge thermal equilibrium: the neon radiation decreases the convective power to such a level that at this working density the condensation instability takes place and that a marfe develops. As already observed [3,5,6] the marfe in the presence of ED perturbation reaches a saturation level and finally corresponds to a stationary radiating layer with a maximum of emissivity located on the high field side of the torus and with a poloidal extension larger than 180° as inferred from both tangential CCD camera and bolometer measurements. This synergetic effect may lead to an appearent power exhaust per injected atom of Neon larger than 1MeV/s. In these experiments a rough estimation of the average Zeff gives a value variing between 2 and 2.5. At lower density this synergetic effect is expected for a lower residual convective power thus to reach high radiation rate it is necessary to increase the Neon injection.

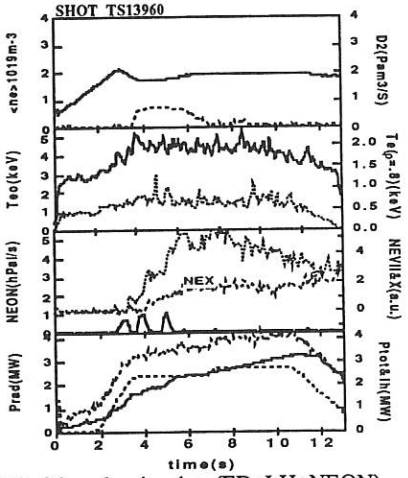


Fig.3 low density shot (ED+LH+NEON)

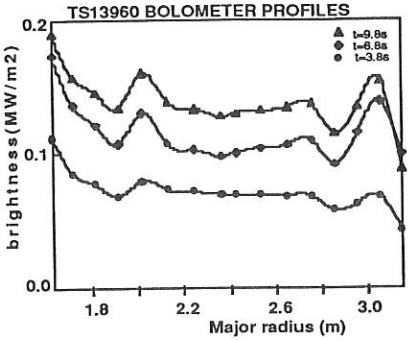


Fig.4 Bolometer profiles (brightness)

An experiment at lower density is shown on Fig.3. In this case the low natural emissivity of this less collisional plasma has to be compensate by a Neon injection of about 100Pal which leads to an increase of about 1.6MW of the radiated power. In contrast with the NeVII line brightness shown on fig.1b (λ=56.16nm) the NeVII line brightness shown on Fig.3 (λ= 10.62nm) is sensitive to the local temperature -The stationarity of the recycling Neon being infered from the stationarity of the NeX line brightness. The behaviour of this NeVII line for t >8.s compared to the evolution of the radiated power may indicate an evolution of the thermal equilibrium favorable to the increase of the neon emissivity - but part of the increase of the radiated power can also be attributed to an increase of high Z impurities produced by the LH launchers. Nevertheless the bolometer profile behaviour for this shot (Fig.4) shows that the radiated power remains dominated by the neon radiation -i.e. the bolometer profile remains rather poloidally symmetric- showing that at this density the residual convective power of about 800kW is higher than the threshold at which the Marfe develops. A rough comparison with the shot 13358 indicates that the condensation instability starts at Pcond/ne<300kW/10^{19}m^{-3}. The Abel inversion of bolometer profiles shown on Fig.4 indicates a local emissivity peaked at the edge with a maximum value of about .2MW/m^{-3} which is a rather low value and it confirmes that at t>8s part of the increase of the radiated power is coming from the center. In such shot the Zeff is higher typically in the range of 3-3.5 than those obtained in higher density discharges.

DATABASE ANALYSIS: Series of shot with and without ED made at different plasmadensity, LH power and Neon puff has been made. In each shot -as on Fig.3- series of small neon puff allows to follow the evolution of both the Neon emissivity (fast response) and of the thermal equilibrium (time scale typically 2-4s). Results are summarized on Fig5&6. They are plotted versus a parameter $A= nl.Te^{-|\alpha|}$ - nl being the line average density and Te the electron temperature measured at the edge of the confined plasma -. The temperature dependance is introduce phenomelogically to somewhat takes into account temperature effects on screening and radiating properties of Neon . α is arbitrarily set to 3/2. Note that the right experimental determination of the temperature dependance requires further experiments. Fig.5 shows the power exhaust per injected atom of neon. It shows that the neon emission increases with A and is higher with the ED -by a factor variing between 1.5 and 2- Fig.6 shows the brightness ratio NeX(λ=1.2nm) on NeVII(λ=10.62nm) vs A. The NeX emitted in the confined plasma is linked with the increase of Zeff while the NeVII emitted at the edge - in the ergodic domain - is linked with the exhausted power. Fig.6 shows that the ED decreases very much this ratio, improving the neon efficiency and the plasma screening. With the ED the high A branch is dominated by the increase of the NeVII brightness (thus by the improvement of the exhausted power) while the low A branch is dominated by the decrease of the NeX brightness -thus by the increase of the screening effect.

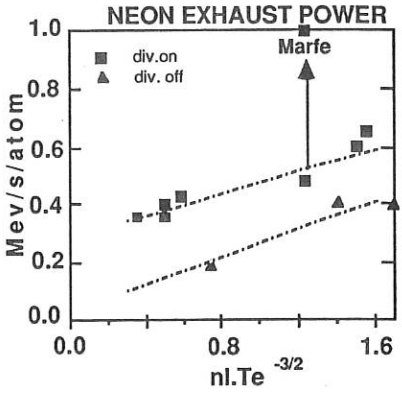


Fig.5 Neon exhaust power vs $nlTe^{-3/2}$

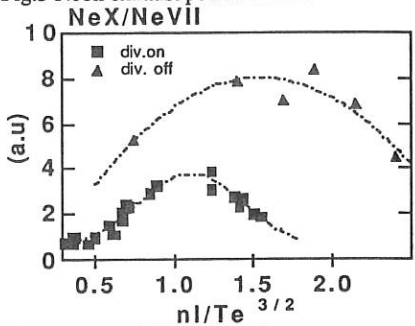


Fig.6 brightness ratio NeX/NeVII vs $nlTe^{-3/2}$

CONCLUSIONS: these preliminary experiments have demonstrated that it is possible to produce stationary edge radiating layers with a fully recycling impurity - even without feedback loop and without active pumping.

They demonstrate the capability of the ED to maximize the neon radiation and to minimize the plasma contamination.

The appearent neon emissivity can be increased - up to 1MeV/s/atom- by a synergetic effect with a Marfe for Pcond/ne<300kW/$10^{19}m^{-3}$.

Nevertheless in LH experiments the screening efficiency has still to be improved -possibly with the use of a more adequate geometry- to keep the Zeff typically below 2 as it is in ICRH experiments[4].

REFERENCES:

[1]VALLET;J.-C.&al. PRL 1991 (Vol67)
[2]GONICHE;M &al. EPS 1994
[3]VALLET;J.-C.&al. EPS 1993
[4]MONIER-GARBET;P &al. EPS 1994
[5]SAMM;U &al. Plas. Phys&Cont. Fus 1993 (Vol35(12)B)
[6]HESS;W &al. EPS 1994
[7] DeMICHELIS;C &al. EPS 1994

RADIATIVE THERMAL INSTABILITY OF THE TOKAMAK EDGE REGION

P. Bachmann, D. Sünder
Max-Planck-Institut für Plasmaphysik Garching, Association
EURATOM, Division Berlin, 10117 Berlin, Mohrenstr. 40-41, Germany

A radial hydrodynamic model, which describes the dynamics of the plasma and neutral particles self-consistently, is used to investigate the radiative thermal instability in the scrape-off layer by applying a linear stability analysis of existing equilibrium states. Phase space trajectories are analyzed to derive conditions of their existence and bifurcation. Neutrals are shown to force bifurcation. Unstable perturbations, localized in the SOL, may lead to a strongly radiating cold plasma belt which is shifted to the wall with increasing energy input and connection length.

1 Fundamentals

The stability of a tokamak plasma depends significantly on the processes that take place in the scrape-off layer. The formation of a Marfe and the onset of density disruptions, which limit the maximum plasma density, result from thermal instabilities, triggered by impurity radiation in the edge plasma. If the plasma density reaches a first threshold, the radiative condensation thermal instability is excited and a Marfe appears. Above a second density threshold, an unstable detached plasma state is formed owing to the radiative thermal instability (RTI), which can lead to a terminating disruption.

This paper deals with the effect of neutral particles, of heating and loss processes on the RTI. The dynamics of the plasma and neutral particles is described by a self-consistent set of 1D hydrodynamic equations, averaged along the magnetic field lines [1], which can be written in vector notation as

$$\left(\hat{A}\partial_t + \hat{E}\partial_x\right)\cdot\vec{y} = \vec{f},\quad \vec{y} := (n,\Gamma_n,T,\Gamma_T,N,\Gamma_N)^T, \tag{1}$$

with n (N) - plasma (neutral particle) density, Γ_n (Γ_N) - plasma (neutral particle) flux perpendicular to the magnetic field, T - plasma temperature, Γ_T - perpendicular heat flux ; $\hat{A}(\vec{y})$ is a 6×6 matrix function with the only non-vanishing elements $A_{11} = A_{25} = 1, A_{31} = 3y_3, A_{33} = 3y_1$, and $\hat{E}$ is the identity matrix. The rhs vector function $\vec{f}$ contains the gain and loss functions due to ionization, charge exchange, ohmic and external local heating, particle and energy loss due to the limiter ($\sim 1/L$ with L being the connection length) and radiation caused by carbon impurities (with the loss function Q_R of [1] which takes especially charge exchange between carbon impurities and atomic hydrogen into consideration). $\partial_{t,x}$ denote the partial derivates with respect to the time $t, x := r - r_s$(r_s - separatrix radius).

2 Equilibrium and Bifurcation

We investigate steady-state solutions $\vec{y}(x)$ to (1) ($\partial_t = 0 \Rightarrow \partial_x \vec{y}_0 = \vec{f}$) on the domain $X = [x_c, x_w]$ (x_c - position in the central plasma, x_w - distance from the separatrix, located at $x = 0$, to the wall). We consider initial and boundary value problems (BVP), and start with an *existence theorem* [2]: An equilibrium state exists if the following inequalities are fulfilled:

$$\Gamma_B^2 \geq 0, \quad B \geq 0 \ \forall\, x \in X, \quad B = n, N, T. \tag{2}$$

These conditions restrict physically relevant solution manifolds to be within limited existence domains in the phase space $S := \{\vec{y}\}$. A point $\vec{y}_0 \in S$ is said to be *quasi-singular* if it is an element of the hypersurface $S_i := \{\vec{y} \,|\, f_i = 0\} \subseteq S$, where f_i is the ith component of $\vec{f}$. The case of equality in (2) are related to conditions $f_i = 0$. Thus quasi-singular points limit existence domains in S. We define $S^{(6-m)} := \bigcap_i^{(m)} S_i$ where m is the total number of the hypersurfaces S_i. If $m = 6$, $S^{(0)}$ is identical with the *singular point* where $\vec{f} = 0$ holds. To prove existence, it is necessary to analyze phase space portraits in the vicinity of a quasi-singular point $\vec{y}_0$. If this point is the singular point, $\vec{y}_0 = \vec{y}^0 \equiv S^{(0)}$, this analysis is simple. The linearized equation

$$\partial_x \vec{\xi} = \hat{J}_f(\vec{y}^0) \cdot \vec{\xi}, \quad \vec{\xi} := \vec{y} - \vec{y}^0, \tag{3}$$

($\hat{J}_f := \partial \vec{f} / \partial \vec{y}$ is the Jacobian matrix) can be solved with the ansatz $\vec{\xi} \sim exp(\lambda x)$. The eigenvalues λ_i are the roots of the characteristic equation $det\,(\hat{J}_f - \lambda \hat{E}) = 0$. The two essential eigenvalues $\lambda_{1,2} = \pm\sqrt{\alpha}$, $\alpha := (c\sqrt{T}/L - k_i(T)N)^0/D$ (D - diffusion coefficient, k_i - ionization rate coefficient, c is a constant) are either real or imaginary with different sign. For the first case the phase portrait for $(n, \partial_x n)^0$ is a saddle point, for the latter it is a vortex. The phase portrait is changed from a saddle point to a vortex at $\alpha = 0$, i.e. *bifurcation* occurs [3]. Only for the first case BVP can be solvable. This analysis of phase portraits is valid only for phase trajectories in the vicinity of the singular point. Otherwise phase space analysis becomes much more complicated. How the neutrals determine α, reveals their general influence to force bifurcation.

Numerically computed equilibrium states for different BVP (fluxes give at x_c, densities and temperature given at x_w) and connection length are shown in Fig. 2.

3 Stability Analysis

The stability property of these equilibrium states $\vec{y}_0$ are investigated by means of a linear analysis. The expansion of the steady-state equation at $\vec{y}_0$ leads to

$$\left[\hat{A}(\vec{y}_0)\partial_t + \hat{E}\partial_x\right] \cdot \delta\vec{y} = \hat{J}_f(\vec{y}_0) \cdot \delta\vec{y}, \quad \delta\vec{y} := \vec{y} - \vec{y}_0. \tag{4}$$

We look for *absolute instabilities*, and try to solve this equation with the ansatz $\delta\vec{y} \sim exp(\gamma t)$, which leads to

$$\partial_x \delta\vec{y} = \left[\hat{J}_f(\vec{y}_0) - \gamma \hat{A}(\vec{y}_0)\right] \cdot \delta\vec{y}. \tag{5}$$

To solve the eigenvalue problem (5), a BVP was formulated with boundary conditions which describe fluctuations that may appear in the SOL: Positive eigenvalues $\gamma = const > 0$ with

vanishing perturbed fluxes in the plasma center and a sufficiently small perturbation of the remaining quantities at the wall are assumed. The reason for the excitation of the RTI is the existence of a part of the radiation profile which decreases with increasing temperature ($\partial Q_R/\partial T < 0$). The radiation is localized in the SOL (Fig. 2) with a maximum which is shifted to the wall with increasing Γ_{Tc} and connection length L (this means increasing power input and decreasing limiter losses). These properties are reflected in the location of the fluctuations in the SOL which is pointed out for the temperature fluctuation for the three calculated equilibrium states in Fig. 1. The fluctuations lead to the temporal development of the profiles which is shown in Fig. 2. The lowering of the temperature and the enhancement of the densities in the plasma edge result in a strong increase of the radiation. This shows that the RTI can lead to the formation of a strongly radiating, cold plasma belt.

However, only the onset of these unstable solutions can be described within the frame of the linear approach. But a small change of the phase space trajectory in the vicinity of quasi-singular points may lead to non-existence with regard to (2), which can be understood as bifurcation. Bifurcation is revealed as the essential mechanism that disrupt the equilibrium state.

[1] Abramov, V.A., Bachmann, P., et al, D., Contrib. Plasma Phys. 34(1994)271
[2] Abramov, V.A., Bachmann, P., et al., 20th EPS, Lisboa 1993. Contributed Papers II-823
[3] Neimark, Yu.I., et al, P.S., Stochastic and Chaotic Oscillations, Kl. Acad. Pub. 1992

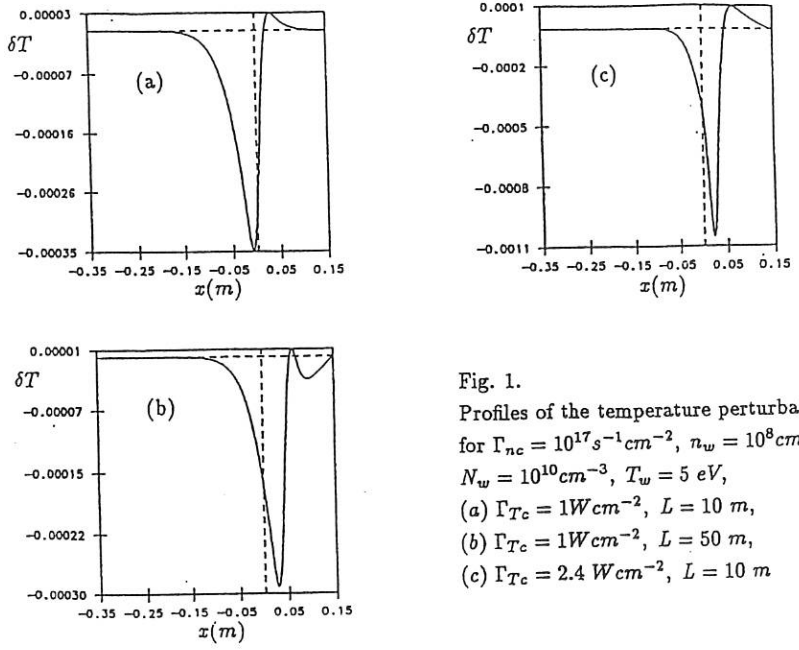


Fig. 1.
Profiles of the temperature perturbation for $\Gamma_{nc} = 10^{17} s^{-1} cm^{-2}$, $n_w = 10^8 cm^{-3}$, $N_w = 10^{10} cm^{-3}$, $T_w = 5\ eV$,
(a) $\Gamma_{Tc} = 1 W cm^{-2}$, $L = 10\ m$,
(b) $\Gamma_{Tc} = 1 W cm^{-2}$, $L = 50\ m$,
(c) $\Gamma_{Tc} = 2.4\ W cm^{-2}$, $L = 10\ m$

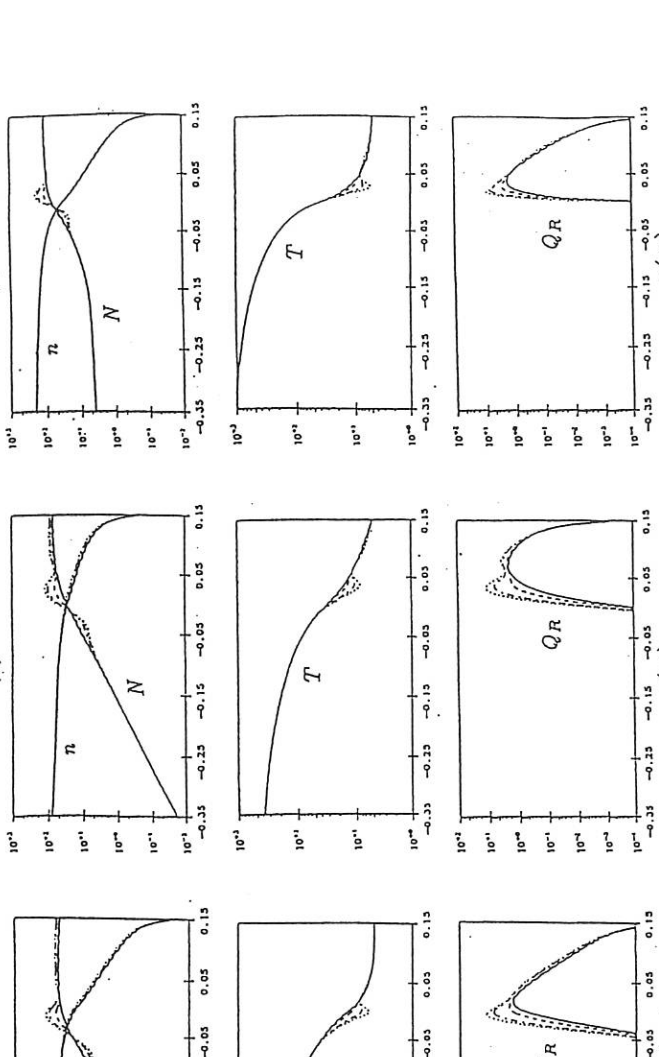


Fig. 2. Profile evolution of the plasma density $n(10^{12}cm^{-3})$, neutral particle density $N(10^{8}cm^{-3})$, temperature $T(eV)$ and radiation density $Q_R(Wcm^{-3})$ for $\gamma t = 0$ (—), 4 (– –), 5 (–·–), 5.3 (·····), $\gamma = 25s^{-1}$ for the cases (a), (b) and (c) of Fig. 1.

ENHANCED EDGE RADIATION INDUCED BY ELECTRODE BIASING ON TEXTOR

R. Van Nieuwenhove *, G. Van Oost, R. Weynants, A. Pospieszczyk [1], U. Samm [1], B. Schweer [1], B. Unterberg [1]

Laboratoire de Physique des Plasmas - Laboratorium voor Plasmafysica
Association "Euratom-Belgian State" Ecole Royale Militaire - Koninklijke Militaire School
1040 Brussels - Belgium
* Researcher at NFSR Belgium
[1] Institut für Plasmaphysik, Forschungszentrum Jülich, GmbH, D-52425 Jülich

Abstract
It is shown that enhanced edge radiation can be achieved by a biased electrode inserted into the plasma. Even under standard TEXTOR plasma conditions ($I_p = 350\ kA$, $B_T = 2.25\ T$, $\bar{n}_{e0} = 2 - 3\ 10^{13}\ cm^{-3}$) with 650 kW of neutral beam power it is found that it is possible to radiate about 95 % of the total input power by positive electrode biasing (below transition to H-mode).

1) Introduction

In polarization experiments on TEXTOR, radial electric fields in the plasma edge are set up by means of a biased electrode (relative to the ALT limiter, which is electrically connected to the liner) which is inserted inside the last closed flux surface. Above a critical value of the electrode voltage, the electrode current suddenly drops and the plasma switches to the so-called polarization induced H-mode [1]. Confinement and profile changes induced by the presence of positive and negative radial electric fields have been investigated [2]. In this paper however, we will concentrate on the effect of polarization on the radiated power and the edge temperature in the Ohmic as well as in the neutral beam heated (NBI) case. The radiated power can be described by means of the radiation potential E_{Rad} [3] , which represents the total energy which is radiated per particle during its dwell time in the plasma. The total radiated power P_{Rad} is then given by $P_{Rad} = E_{Rad} \times \Gamma_i$, where Γ_i is the surface integrated impurity flux (from wall and limiters). The term E_{Rad} depends on the impurity species, the transport and also strongly on the edge electron temperature (T_e). Below temperatures of about 20 eV, E_{Rad} of carbon (C) and oxygen (O) shows an almost exponential increase with decreasing T_e [4]. Enhanced radiation can thus be due to an enhancement of E_{Rad} and/or an increase of Γ_i.

2) Experiments.

2.a) Ohmic case :

In previous polarization experiments on TEXTOR [5], it was already observed that the polarization induced H-mode is accompanied by a strong increase of the radiated power and a concommitant decrease of the edge temperature. When the radiation level attains 100 % of the input power (case of bad wall conditions), a new type of H-mode can occur, the so-called detached H-mode [5]. Even for subtransition voltages, an increase of the radiated power (bolometry) (Fig.1) as well as a small reduction of the edge temperature can already be observed. An example of a transition into a detached H-mode is shown in Fig.2. The CI and CII lines were monitored on the electrode head as well as on one of the ALT-II limiter blades. At both locations an increase of their brilliances could be observed. It was verified however that this increase can be completely attributed to the increasing sensitivity of these lines with decreasing T_e (as measured by a He-beam diagnostic [6]). Thus the car-

bon fluxes are not increasing. This is consistent with the fact that for these Ohmic conditions and relatively low electrode current the heat load to the electrode is too small to increase the temperature of the electrode head (made out 2D CFC carbon) to the level needed for strong thermal evaporation. Enhanced physical sputtering (with bias voltage) is also not likely since the electrode is biased positively with respect to the plasma. The initial decrease of T_e (as well as the strong drop at the transition) could be attributed to an increase of the bulk plasma density (since the same input power is distributed over more particles), which in turn results from an enhanced particle confinement induced by the radial electric field and the concommittant poloidal rotation in the plasma edge. The decrease of T_e leads to an enhancement of the radiation potential of carbon (as well as of oxygen for which E_{Rad} is even higher) and explains the increase of P_{Rad}. From the radiation profile (bolometry), it is found that all the radiation comes from the plasma edge. After the transition, the heat flux (thermographic camera observation) to the electrode becomes negligible. Therefore, no active cooling for the electrode is required, even for long pulse (several seconds) plasma operation.

2.b) Neutral beam heated case

Two neutral beam heated shots ($P_{NBI} = 500\ kW$) are compared : one in which the electrode is floating (case a ; Fig3a) and one in which +200 V is applied (case b ; Fig.3b). In case a, 26 % of the input power is radiated, while 95 % is radiated (from the plasma edge) in case b. Despite the larger fraction of radiated power in case b, and the larger contamination of the plasma edge by carbon (see below), the energy confinement time is 25 % higher as compared to case a. For a subtransition voltage of only +200 V, this is most surprising. For negative polarization (-300 V), the above mentioned effects did not occur. A very strong increase of the C lines at the electrode and the ALT limiter was observed. Even after correcting the brilliances of the C lines for their dependence on T_e an increase of the C fluxes has to be concluded since in this case the application of NBI leads to an increase of the edge temperature (outer ECE channel). The strong increase of radiation in case b could therefore be attributed to a strongly enhanced impurity (carbon and oxygen) flux, whereas E_{Rad} is probably no changed substantially. For negative polarization (-300 V), no enhancement of the radiated power was observed.

From the known dependence of the thermally evaporated carbon flux on the surface temperature , an estimated value of E_{Rad} (1.5 keV) and the radiated power one can deduce the surface temperature T_s of the electrode. For case b (corresponding to a radiated power of 800 kW, i.e. 95 % of the total input power) this results in $T_s = 3000\ K$, corresponding to a tremendous carbon flux of $2.5\ 10^{21}\ s^{-1}$ (which is comparable to the total deuterium flux from wall and limiters). This high value of the electrode temperature is supported by spectroscopic observations of the electrode head, revealing a release of Cr (which from experience always occurs on this particular head when the surface temperature attains at least 2150 K (melting point of chromium)). From probe theory [7], it is known that the heat flux to a probe increases exponentially with applied voltage, above the floating potential. In our case, the heat flux (due to electrons) can be estimated by multiplying the number of electrons arriving at the electrode surface with their typical energy. The resulting heat flux is then $Q = I_E \times T_e [eV]$ (in case the electron current is much larger than the ion current). For case b, this results in a heat flux of about 50 kW, which is sufficient to heat the surface (not the bulk) of the electrode head by by 2000 K or more during a single discharge. Inspection of the electrode head did not reveal any noticeable erosion or damage.

3) Conclusions.

In the Ohmic case, the enhanced radiated power with polarization can be understood as being due to the following chain of events : 1) increase of particle confinement induced by the radial electric field 2) increased plasma density leading to a decrease of the electron temperature 3) increase of E_{Rad} (of C and O) and consequently of P_{Rad} whereas Γ_i is not increased. In high power discharges (with NBI), positive biasing leads to a very strong enhancement of the heat flux to the electrode. This is interpreted as being due to the fact that biasing allows a current to the electrode which is substantially above the ion saturation current. Due to this effect the electrode becomes sufficiently hot to evaporate enough carbon to radiate (from the edge) up to 95 % of the input power. At the same time, the energy confinement time is increased (with respect to the floating case).

References

1. Weynants, R.R. and Taylor, R.J., Nuclear Fusion 30 (1990) 945.
2. Weynants, R.R., Van Oost, G., et al., Nuclear Fusion 32 (1992) 837
3. Samm, U., et al., Proc. of the 18 th European Conf. on Plasma Physics and Controlled Fusion Berlin (1991), Vol.3, 157
4. Tokar, M., 18 th EPS Conf. on Contr. Fus. and Plasma Heat., Berlin 1991, Europh. Conf. Abstr., 15C, Vol.3, p.1
5. Van Nieuwenhove, R., Van Oost, G., Weynants, R.R., et al., IAEA Technical Committee Meeting on Tokamak Plasma Biasing, Varennes, September 1992.
6. Schweer, B., Pospieszczyk, A., Mank, G., et al., J. Nucl. Mater., 196-198 (1992) 174-178
7. Stangeby, P.C., Journal of Nuclear Materials 111&112 (1982), 84

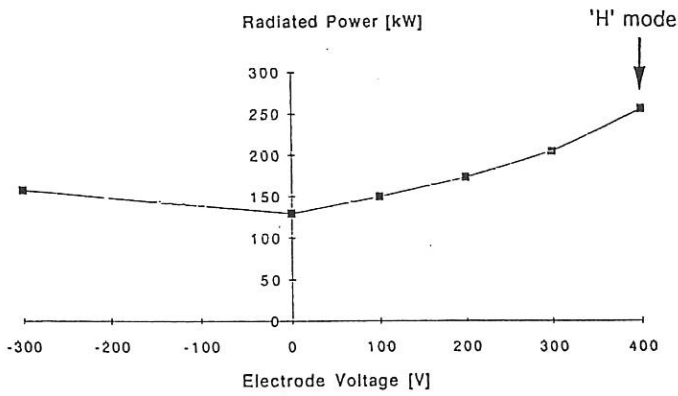


Fig.1 : Dependence of radiated power on electrode voltage. The plasma parameters are : I_p = 250 kA, BT = 2.35 T, n_e = 1. 10^{13} cm^{-3}, siliconized walls, electrode positioned at r_E = 42 cm (#53241-53252)

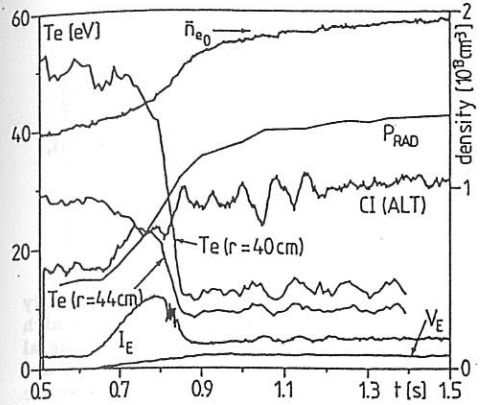


Fig.2 : Transition into a detached H-mode. The plasma parameters are : I_p = 250 kA, BT = 2.25 T, $n_e = 1.2\ 10^{13}$ cm^{-3}, r_E = 42 cm, boronised walls, applied electrode voltage V_E = 700 V (#49180)

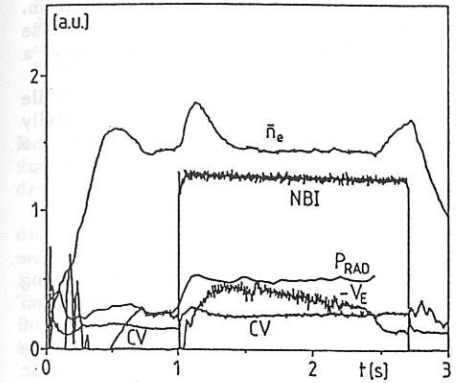


Fig.3.a : Polarization (floating electrode ; V_E = - 150 V at t = 1.5 s) combined with NBI (P_{NBI} = 500 kW, co - beam injection). The plasma parameters are : I_p = 350 kA, BT = 2.25 T, n_e = $2.2\ 10^{13}$ cm^{-3}, r_E = 42 cm, boronised walls. The electrode is positioned at 42 cm (the limiters are at r = 46 cm) (#54963)

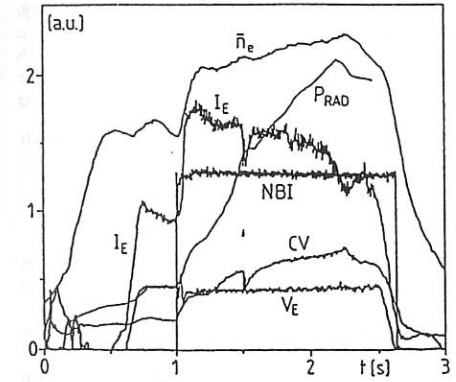


Fig.3.b. : Polarized discharge (V_E = + 200 V, electrode current I_E = 325 A (at t = 1.5 s) combined with NBI (conditions similar to those of fig.3.a) in which 90 % of the input power is radiated from the plasma edge. The electrode is positioned at 42 cm (#54964)

RADIATION LOSSES IN FTU

G. Apruzzese, L. Gabellieri, H. Kroegler, G. Mazzitelli, L. Pieroni

Associazione EURATOM- ENEA sulla Fusione, Centro Ricerche Energia Frascati,
C.P. 65 - 00044 Frascati, Rome (Italy)

1 - INTRODUCTION

Radiation losses from the FTU plasma are measured (temporally and spatially resolved) with a 16 channel bolometer array, arranged in a pin-hole-camera, which observes the lower half plasma cross-section. The bolometer consists in a metal resistor bridge [1]. The total radiated power and the radial profiles of emissivity are calculated by the standard Abel inversion technique, assuming poloidally symmetric emission. The radiation emission is calculated utilizing a 1-D impurity transport code with an expression for the anomalous flux with a diffusive term plus a pinch term. The absolute values of the central impurity densities are obtained by x-ray Pulse Height Analyzer (PHA) measurements, and are used as input to the code to have a comparison with the experimental results.

For FTU plasmas the capability of reconstructing the radiative heat loss profile is limited by the presence of Marfes [2], since they are characterized by a poloidally asymmetric radiation emission. A method has been developed to calculate the radiation emission from the Marfe, in order to derive the contribution to the total radiated power and to characterize the Marfe itself.

2 - RADIATION LOSSES

Pulse Height Analysis soft x-ray diagnostic is routinely used on FTU to give quantitative estimates of heavy (K_α emission lines) and light (bremsstrahlung enhancement) impurity density in the plasma. In Fig.1 the density of nickel, cromium and oxygen (assumed to be the dominant light impurity), measured at the centre of the plasma column, is shown versus the electronic density for I_p=600 kA. In the discharges performed with inconel poloidal limiter nickel is the dominant metallic impurity mainly at low density. Z_{eff} of the discharge measured by PHA shows a good agreement with visible bremsstrahlung (540 nm) measurement [3].

The data collected by PHA have been utilized as input for a 1-D impurity transport code which solves the following equation for each ion of charge Z:

$$\frac{\partial n}{\partial t} + \frac{1}{r}\frac{\partial (r\Gamma_Z)}{\partial r} = S_Z n_e n_Z - S_{Z-1} n_e n_{Z-1} - \alpha_{Z+1} n_e n_{Z+1} + \alpha_Z n_e n_Z$$

where S_Z is the ionization rate and α_Z the radiative plus dielectronic recombination rate. For the flux we assume the usual expression:

$$\Gamma_Z = - D \frac{\partial n_z}{\partial r} + n_Z v_0 \frac{r}{a} \quad .$$

where D is the diffusion coefficient and v_0 is an inward velocity, these parameters are assumed constant along the minor radius. The total radiated power is one of the outputs of the code and the result is compared with the measurement.

In the code only one impurity species is considered and, since more species are generally present in the discharge, results of several code runs are summed up. For comparison, radiation losses are also calculated under pure coronal equilibrium [illegible] the radial impurity profile is assumed quite flat as used in

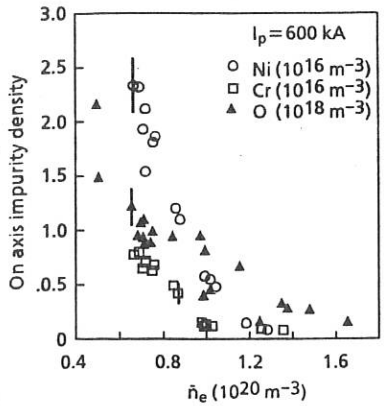


Fig.1 - PHA soft x-ray measured impurity density versus line averaged electron density. Heavy ions density are calculated from K_α emission lines

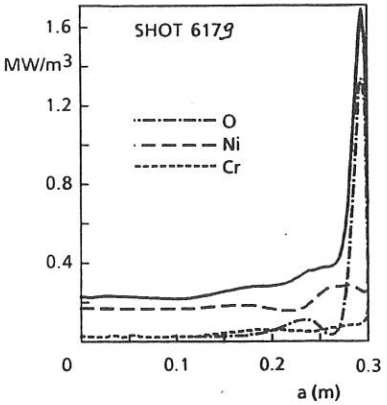


Fig 2 - Calculated emission density profiles. The continous line is the total radiated power density

Ref. [4]. The experimental electron temperature and density profiles are used and a matching is performed to adjust the values at the last closed magnetic surface to the data given by Langmuir probes measurements.

Simulations have been executed for a wide range of electron density for discharges in steady state condition and in absence of Marfe, to avoid localized radiation source. Experimental radiative losses are reproduced assuming a value of D=0.3 m^{-2} s^{-1} for the diffusion coefficient and v_0=-1.5 m s^{-1} for the inward velocity. These values are consistent with those previously quoted on FTU [5]. As an example, in Fig.2 the total computed emission profiles together with the contribution of single impurity species are shown.

In Table 1 the total experimental radiative losses are compared with the results of the diffusion code and with the corona equilibrium calculations.

Generally good agreement is found for the intermediate and high electron density discharges both for the diffusion as well as for corona calculations. At low density great discrepancy is found with corona calculation while the result from the diffusion code is more acceptable. From the data it seems that a dependence of anomalous flux with density must be envisaged and it will be the object of further investigations.

The difference at low electron density between corona and diffusion calculations is due to the contribution of the oxygen emission: the oxygen emits at the boundary of the plasma and it is strongly dependent from the electron temperature profile at the edge. The effect of transport is to displace the emission

Table 1

Shot	Electron Density	P_{rad} Experim.	P_{rad} Corona	P_{rad} Diffusion
7193	0.6×10^{20} (m^{-3})	800 (kW)	370 (kW)	580 (kW)
6179	1.4×10^{20} (m^{-3})	700 (kW)	640 (kW)	740 (kW)
6242	2.0×10^{20} (m^{-3})	480 (kW)	440 (kW)	540 (kW)

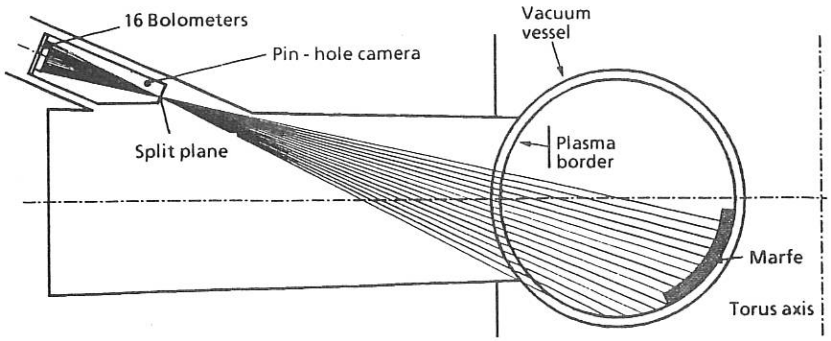


Fig.3: Viewing chords of the bolometer array in FTU and a typical position of a Marfe

peak toward the centre with an obvious increase of the radiation losses. This is less important for medium Z impurity which emits more inside the LCMS.

3 - RADIATION ASYMMETRY

The total radiated power and the radial profiles of plasma emissivity are derived by an Abel inversion of the line integrated bolometer signals performed by using the Zernicke technique coupled with the equilibrium reconstruction code (ODIN) [6]: the magnetic flux surfaces are taken as surfaces of constant emissivity. The assumption of poloidal symmetry for the plasma emissivity is no more valid in presence of a poloidal asymmetric radiative structure as a Marfe. When the Marfe is localized inside the view of the bolometric measurement, see Fig.3, the corresponding increase of signals is seen as an increase of plasma emission over the plasma cross-section, determining in this way an overestimation of the total radiated power. On the other hand if the Marfe is localized outside the view, the total radiated power is understimated.

On the FTU tokamak, the Marfe radiative emission is observed also in the H_α and visible bremsstrahlung wavelengths, both with horizontal and vertical sight lines. Sometimes the Marfe is seen by the inner vertical chord of IR interferometer which lies at 18 cm from inward to the plasma center, when it intercepts the Marfe region. The Marfe is a toroidally symmetric and poloidally asymmetric band of impurity radiating plasma, resulted by a radiative thermal instability [7] and characterized by high electron density and low electron temperature. The formation of the Marfe occurs at the inner plasma edge in tokamaks with toroidal or poloidal limiter as FTU. The variable Marfe surfaces can be evalutated by the signals of the H_α or visible bremsstrahlung arrays. In Fig.4. it is shown how we estimate the Marfe poloidal length. The width of the Marfe in the radial direction is taken approximately between 2-4 cm. Since the Marfe is an edge plasma phenomenon, we assume that the bulk plasma properties do not change during the presence of the Marfe. This means that the increase of radiative emission signals are due only to the formation of the Marfe. Taking an average value of the increase only on the integrated line signals which see the central part of the Marfe, as described before, the Marfe average emission is derived. The Marfe total radiated power is then estimated considering its volume.

For this analysis, only discharges with Marfes whose central part is seen by the bolometric detectors are analyzed. These discharges have plasma current I_p = 300-1100 kA and toroidal magnetic field B_t = 6-7 T. Over the electron density range of $0.9\text{-}1.9\times10^{20}$ m^{-3}, the radiation emissivity in the Marfe ranges between 2-12 MW/m^3 without showing any dependence on the electron density. A clear correlation instead appears with the conduction power, P_{ohm}-P_{rad}, calculated at the time before the Marfe onset, as shown in Fig.5.

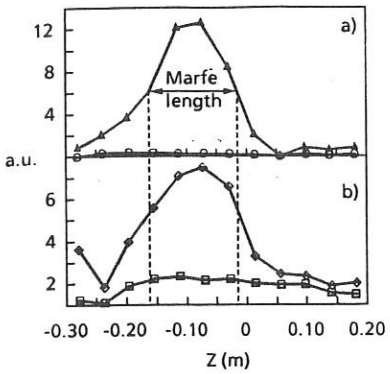


Fig.4 - Line integrated emissivity of horizontal H_α (a) and visible bremsstrahlung (b) radiation vs the impact parameter, before and after the Marfe onset

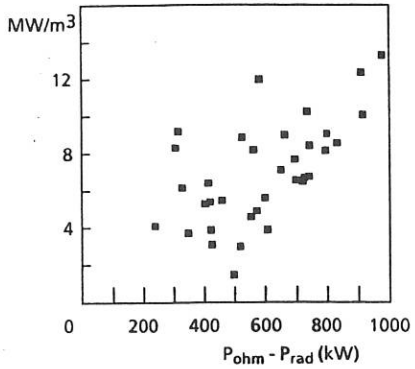


Fig.5 - Radiation emissivity in the Marfe versus the conduction power, P_{ohm}-P_{rad}

4 - CONCLUSION

Calculation of total radiated emission in FTU plasma assuming impurity density as obtained from PHA soft x-ray measurements generally agrees with the experimental results, provided that a diffusion coefficient of 0.3 m^{-2} s^{-1} and a value of -1.5 m s^{-1} for the inward velocity are assumed in the transport model. The results seem to suggest that a dependence of the transport coefficients with the density has to be investigated.

The Marfe formation is connected with the presence of light impurities in the discharge. During the FTU operation with the poloidal limiter in inconel or in molybdenum, the oxygen is responsible of the Marfe onset. We have also observed Marfes in discharges dominated by neon (from injection) and silicon (soon after the silanization of the vacuum vessel). The contribution of the Marfe radiation to the total plasma radiation is 5-30 % over an electron density range of $0.9\text{-}1.9\times10^{20}$ m^{-3}. There is evidence of a correlation between the Marfe emissivity and the conduction power. An evaluation of the Marfe electron density n_e can be obtained considering that the emissivity is given by the relation $\varepsilon=n_e\, n_i\, R(T)$ where n_i is the impurity density and R(T) is the cooling rate of the impurity. Taking the maximum value of R(T) and considering an approximated value for the impurity fraction $n_i/n_e$the Marfe density is derived. For a plasma with a fraction of 1% of oxygen, as the dominant impurity, the corresponding values of Marfe density are between 20-50 % of the line average plasma electron density.

REFERENCES

[1] K. F. Mast, J.C. Vallet, C. Andelfinger, P. Betzler, H. Kraus, and G. Schramm, Rew. Sci.Ins. 62 ,(1991) 744
[2] J.L. Terry, E.S. Marmar, and S.M. Wolfe, Bull. Am. Phys. Soc. 26, (1981) 886
[3] G. Bracco, S.E. Segre, V. Zanza et al., accepted for publication in Nucl. Fusion
[4] V. Pericoli Ridolfini, R. Zagorski, F. Crisanti et al., paper OB7 11th PSI Conf. on Plasma Surface Interactions in Controlled Fusion Device May 94 Japan
[5] I.Condrea, R. De Angelis, L. Gabellieri, Proceeding of 20th EPS Conference on Controlled Fusion and Plasma Physics July 93 Portugal
[6] F. Alladio and P. Micozzi, submitted to Nucl. Fusion
[7] J. Neuhauser, W.Schneider, and R. Wunderlich, Nucl. Fusion 26, (1986) 1679.

EFFECTIVE CHARGE OF THE PLASMA RESULTING FROM THE INJECTION OF NEON INTO DEUTERIUM DISCHARGES IN TEXTOR.

G. Telesca, R. Koch*, A.E. Messiaen*, U. Samm, B. Unterberg

Institut für Plasmaphysik, Forschungszentrum Jülich,
Association EURATOM-KFA, Germany

*Laboratoire de Physique des Plasmas - Laboratorium voor Plasmafysica -
Association "Euratom-Belgian State", Ecole Royale Militaire - Koninklijke Militaire School,
B-1040 Brussels - Belgium

I. Introduction

The concept of the cold radiation boundary could be a possible solution for the problem of power exhaust in a fusion reactor. By injecting impurities into hydrogenic plasmas the heat flow tends, indeed, to be uniformly distributed around the plasma periphery. Experiments with neon injection into auxiliary heated hydrogenic discharges on TEXTOR have shown the following properties [1-3]:

i) Strong enhancement of the radiated power (P_{rad}) up to a value of the ratio γ of the radiated power to the input power of the order of 0.9
ii) The emitting volume is localized in the plasma periphery
iii) The edge temperature is reduced while the central one stays constant or slightly increases for a given electron density
iiii) The confinement properties are at least maintained; in some cases the confinement increases
iiiii) The incremental plasma contamination due to the presence of neon is estimated to be low in most cases (from conductivity, SXR continuum, charge-exchange and neutron yield)

This paper deals on the one hand with an analysis of the mechanisms responsible for the plasma contamination during the injection of neon and on the other hand with the comparison, for different experimental situations, of the relation between the increase of P_{rad} and the increase of the contamination. These two quantities are, indeed, different functions of the amount of the injected neon and of plasma parameters like the electron density, temperature and of level of input power. Their ratio $\Delta P_{rad}/\Delta Z_{eff}$, which is the figure of merit to determine the quality of the edge cooling, changes depending on the specific experimental situation.

The ionic effective charge (Z_{eff}) is measured by detection of continuum radiation in the visible range [4] along a horizontal chord which crosses the plasma center. This method, [5], is suitable for large tokamaks but could be marginal for TEXTOR (R = 175 cm, a = 46 cm). An additional chord which detects only the continuum radiation emitted at the plasma periphery allows the related error to be estimated. Due to the dependence of bremsstrahlung on the square of the electron density, the reported Z_{eff} has to be considered as a core plasma parameter. The absolute value of the bremsstrahlung Z_{eff} tends to be higher, at low density, than other estimates of the plasma contamination (like conductivity). We limit the discussion to the increments of Z_{eff}, ΔZ_{eff}.

II. Fluxes and densities of the intrinsic impurities.

By reducing the edge temperature of a hydrogenic plasma the release of the physically sputtered light impurities decreases, as the plasma contamination does. The new equilibrium situation is in reality the result of different interdependent mechanisms ; e.g. less impurities means less radiated power, decrease of the edge temperature means also that the radiation potential increases (radiation potential = radiated energy per atom entering the plasma) [1]. These mechanisms depend on and affect the edge temperature thus a nonlinear dependence is established. However, in a first approximation, the reduction of the intrinsic impurity concentration can simply be related to the reduction of the sputtering yields.
By injecting neon the edge temperature decreases and we expect a reduction of the fluxes of intrinsic impurities. In Fig. 1 the edge electron temperature and the fluxes of the intrinsic impurities for a siliconized machine [6] are shown as a function of γ. γ is increased by increasing the neon puffing rate. The data refer to a series of NB heated discharges, for a total input power (P_{in}) of 1.5 MW, at constant averaged density $\bar{n}_{e0}$ = 4.7 10^{13} cm^{-3} . The ratio of Si:C:O fluxes is about 4:2:1 and the resulting oxygen level is very low considering the high purity of plasmas under siliconized conditions. Together with the fluxes, the densities of the intrinsic impurities also decrease by injecting neon. In agreement with the relation between fluxes and densities a direct independent measurement of the brilliance of a CV line , which in a first approximation is proportional to the carbon density [7], confirms the validity of our statement (Fig.1).
At lower electron densities ($\bar{n}_{e0} < 3\ 10^{13}$ cm^{-3}), however, the increase of γ does no longer lead to a reduction of the fluxes. Also the brilliance of the CV line does not decrease, as compared to pure (without neon) deuterium discharges at identical power. This behaviour can be explained i) at high density by a low concentration of neon (< 1 %) and ii) at low density by considering that the deuteron impact energies are (for these discharges) of the order of 250 - 300 eV. In this range the sputtering yields are not very sensitive to a change of $T_e(a)$. At higher density the impact energies are in the range 100-150 eV where the sputtering yields decrease significantly with $T_e(a)$.
In case of boronized machine a similar behaviour is observed.
Unlike carbonization, for boronized and even more for siliconized walls the chemical processes play a very marginal role also at high electron densities. Primarily owing to the low oxygen level, the plasma contamination is dominated by physical sputtering.

III. Relation between ΔP_{rad} and ΔZ_{eff}

Since the presence of neon can modify the concentration of the intrinsic impurities, one can write:

$$\frac{dZ_{eff}}{dn_{Ne}} = \frac{\partial Z_{eff}}{\partial n_{Ne}} + \sum_i \frac{\partial Z_{eff}}{\partial n_i} \frac{\partial n_i}{\partial n_{Ne}}$$

where the sum extends to all the intrinsic impurities. Excluding discharges at low electron density, the second term on the right hand side is negative, so that the incremental Z_{eff} resulting from the injection of neon is lower than the one calculated on the basis of the density of neon. The incremental Z_{eff} is a function of the neon density, of the electron temperature (input power), of the electron density and of the sputtering yields. On the other hand also ΔP_{rad} is not simply related to the density of neon. It depends on the same parameters as Z_{eff} does, but in a different way. Therefore the ratio between these two quantities, which determines the quality of the edge radiation cooling, changes depending on the discharge parameters. We will comment on some significative examples.

a) Different impurities and different γ

With boronized walls for an input power of 1.6 MW and $\bar{n}_{e0} = 4.3\ 10^{13}\ cm^{-3}$ the radiated power without neon is 400 KW ($\gamma = 0.25$) with neon is 1,050 KW ($\gamma = 0.66$). The corresponding Z_{eff} are 1.7 and 2. From spectroscopic data a reduction of 25% of the carbon density can be estimated during neon injection for these discharges. Assuming constant $T_e(a)$ about the 80 % of the measured incremental radiated power (~600 KW) can be explained. 25% due to the substitution of carbon with neon (neon radiates more than carbon at constant Z_{eff}), and 55 % to an increase of density of neon which corresponds to the change of Z_{eff}. The existence of a missing part shows that the reduction of $T_e(a)$ plays a role in the increase of P_{rad}.
By increasing γ this effect is amplified. For similar input power and density (siliconized walls) but for $P_{rad} = 500$ KW without neon ($\gamma = 0.33$) and 1,280 KW with neon ($\gamma =$ 0.85) only 40 % of the total incremental radiated power (~800 KW) can be explained under the same assumption. In this case, indeed, the substitution of Si and C with Ne does not result in an increase of P_{rad} at constant Z_{eff} .(In the considered range of temperatures Si radiates more than Ne and C less than Ne at constant Z_{eff}). Only 40% of the increase P_{rad} is due to the increase of neon density.

b) Density scan.

In Fig.2 Z_{eff} is plotted versus density for two series of discharges, one with Ne the other without. Input power 1.5 MW , siliconized machine. At the lower electron densities ΔZ_{eff} resulting from the injection of neon is of the order of 1, while at the higher densities is of the order of 0.3 (in both cases for $\gamma =$ 0.8 - 0.85). This strong dependence on the electron density can be explained by considering that P_{rad} is proportional to $n_e n_{Ne}$ and to the radiation potential which is a decreasing function of the edge temperature. At low density and high temperature one needs much more neon to radiate an important fraction of the input power than at higher density and lower temperature. Considering that the input power is approximately constant, we can conclude that at higher density the cooling efficiency is about a factor of three higher than at low density.

c) Power scan

Table I shows Z_{eff} versus input power (NBI + ICRH) at nearly constant $\bar{n}_e$ for a boronized and siliconized machine. In spite of the slow increase of the electron density (first 4 shots) Z_{eff} increases with power. This can be clarified as follows: by increasing the input power the power flow increases too and one needs more neon to keep γ constant. Simultaneously the temperature increases, so that the cooling efficiency is reduced, making it necessary to further increase the level of neon. Therefore the rise in Z_{eff} is due both to the usual enhanced release of the intrinsic impurities with input power and to the stronger neon puffing. However, even at higher power, Z_{eff} can be reduced to acceptable values by working at much higher densities (siliconized machine) as shown on the last line of Table I.
In conclusion we have shown that i) at high densities the contamination due to the intrinsic impurities is reduced by injecting neon ii) the quality of the neon cooling (ΔP_{rad} to ΔZ_{eff}) depends on the electron temperature and density and iii) a large ratio ΔP_{rad} to ΔZ_{eff} can be achieved also at high heat fluxes (up to 0.1 MW / m^2) if the electron density is sufficiently high.

REFERENCES

[1] U.Samm, "Radiation Control in a Limiter Tokamak", KFA-Jülich Report 2378 (1990)
[2] U.Samm et al., Plasma Physics and Controlled Fusion, Vol. 35, 12 B, B167 (1993)
[3] A.E.Messiaen et al., "Improved Confinement with Edge Radiation Cooling at High Densities and High Power in TEXTOR", to be published in Nuclear Fusion (1994)
[4] J.Ongena et al., Proc. of the 17th EPS- Conf., Amsterdam, Vol. IV, p. 1532 (1990)
[5] Foord et al., Rev. Sci. Instrum. 53 (9), 1407 (1982)
[6] Winter et al., Phys. Rev. Lettr., Vol. 71 (10), 1549 (1993)
[7] Telesca et al., "Study of Plasma Contamination during ICRF- Heating under boronized Wall Conditions in TEXTOR", to be published in Nuclear Fusion (1994)

Acknowledgments

We wish to thank J. Ongena, A. Pospieszczyk, N. Schoon, B. Schweer, M. Tokar and G.Van Oost for experimental help and discussions.

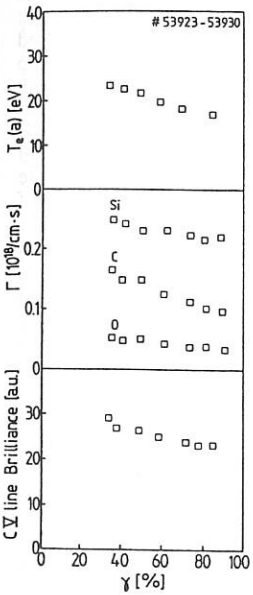


Fig. 1: T_e at LCFS, impurity fluxes, and C density as a function of γ

TABLE I Z_{eff} as a funtion of the input power at constant γ

	I_p [kA]	Power [MW]	n_{e0} [10^{13} cm^{-3}]	γ	Z_{eff}	τ_E [ms]
		Boronized	NBI + ICRH			
# 55787	400	2.6	3.9	0.60	2.8	45
# 55790	"	2.8	4.4	0.65	2.9	45
# 55791	"	3.0	4.4	0.70	3.15	41
# 55792	"	3.2	4.8	0.68	3.5	40
		Silconized	NBI + ICRH			
# 55045	480	4.0	6.9	0.65	2.2	47

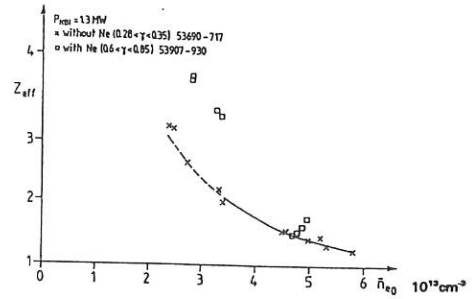


Fig. 2: Z_{eff} as a function of density for input power of 1.5 MW with (boxes) and without neon injection (crosses)

Measurement of the Carbon Source on the Limiter Face in Tore Supra

S.J. Tobin§*, P. Monier-Garbet, J.T. Hogan*, C.C. Klepper*
C. DeMichelis, P. Ghendrih, D. Guilhem, R. Guirlet, W.R Hess, R.C. Isler*, A.I. Ledyankin

Assoc. EURATOM- CEA, DRFC/SPPF, Centre d'Etudes de Cadarache
F-13108 Saint Paul-lez-Durance, France

*Fusion Energy Division, Oak Ridge National Laboratory
Oak Ridge, TN 37831-8072

1. Introduction. In a steady-state tokamak, the impurity production and transport from plasma facing components will have to be controlled. An understanding of these processes in the edge plasma is necessary for the design and operation of plasma facing components. In this frame, an experiment has been carried out to study impurity generation and transport processes on an inertial limiter on Tore Supra as a baseline for upcoming experiments on an actively cooled limiter. A system has been implemented to permit quantitative measurement of impurity sources from the outboard limiter in Tore Supra.

2. Experimental setup and plasma conditions. The principal diagnostic is a visible endoscope that combines a spectroscopic view of the limiter with a CCD camera view. Light emitted near the limiter surface is guided to the endoscope imaging system by a mirror located on the top of the torus and then to a beam splitter for simultaneous measurements by the two systems. The light is guided from the beam splitter by fiber optics to a visible spectrometer with an Optical Multichannel Analyzer (OMA) detector. The other path from the beam splitter leads to a CCD camera equipped with interchangeable interference filters for the D_α (6561Å), CII (5150Å) and CIII (4647Å) lines. The two systems thus provide both a detailed spatial resolution (CCD, 2.5 mm/pixel), and an absolute calibration (spectrometer+OMA). The absolute brightness of the entire CCD images is determined from the known brightness of several spots on the limiter. A limitation of the experimental system is the progressive deterioration of the endoscope transmission due to particle deposition on the optical surfaces in the torus. To minimize the impact of this difficulty on the absolute calibration, the optical system was absolutely calibrated whenever access into the torus was possible. A second experimental limitation in the interpretation of the CCD images is that, because of the viewing angle, the electron side leading edge of the limiter is partially shadowed by the limiter tip (see figure 1a).

A reciprocating Langmuir probe located 60° toroidally and 90° poloidally away from the limiter gives the electron temperature T_e and density n_e in the scrape-off layer (SOL) for the region 0.01m to 0.05m outwards in the radial direction from the last closed flux surface (LCFS). The temperature just inside the LCFS is measured by Thomson scattering. The surface temperature of the limiter is deduced from an infrared camera which has the same optical view of the limiter as the visible endoscope.

The deuterium plasma parameters are the following: toroidal magnetic field $B_t = 3.75$ T, minor radius $a = 0.70$ m, major radius $R = 2.44$ m, toroidal plasma current $I_p = 1.24$ MA, and volume averaged electron density $\langle n_e \rangle = 3.0\ 10^{19}$ m^{-3}. The limiter dimensions are 0.5 m in the toroidal direction and 0.6 m in the poloidal direction. A particularly small minor radius has been chosen in order to isolate, as much as possible, the limiter as the primary impurity source.

3. Experimental results. Fig. 1a shows that the temperature distribution across the center of the limiter face is symmetric, thus indicating a uniform incident heat flux. However, an asymmetry is seen between the ion-side and electron-side, leading edges (LE); it is not clear if

§ Supported by a fellowship from the Oak Ridge Institute of Science and Education.

this asymmetry can be attributed totally to the geometric shadowing effect. The temperature at the central tip of the limiter is close to 600°C and the highest overall temperature of 740°C is reached on the ion-side, leading edge (ISLE). Fig. 1b and 1c show the CII, CIII and D_α brightness distributions across the limiter equatorial plane. In contrast to the symmetrical central temperature distribution, the three central peaks are shifted to the ion-side of the limiter. The CIII distribution, unlike the CII distribution, does not have LE peaks, but only one peak centered 0.12 m toroidally away from the tip, towards the ion side.

The ion fluxes φ have been determined from the experimental brightness distributions using theoretical values for the number of ionizations per photon [1]. Fig. 2a shows as an example the flux distribution for C^+. Fig. 2b shows that the φ(CII) to $\varphi(D_\alpha)$ ratio peaks at the tip. The value of this ratio is an empirical estimate of the total sputtering yield, which decreases gradually to each side of the tip, until the decrease becomes very abrupt at the LE. Fig. 2c illustrates that the φ(CIII) to φ(CII) ratio has a relatively constant value over the central part of the limiter, while decreasing significantly on the LE.

Integration of the C^+ flux over the entire limiter gives a carbon production rate of a few 10^{22} atoms per second. On the other hand, the core plasma carbon density (estimated from ultra-violet spectroscopy and impurity transport calculations) is of the order of 10^{17} m^{-3}. Consequently, if we assume an average particle confinement time of 0.1 seconds, the ratio of the carbon content in the core plasma to the carbon produced on the limiter face is approximately 0.1%.

4. Discussion. The experimental plasma conditions and limiter temperature show that both chemical and physical sputtering can be important impurity production mechanisms on the limiter. To assess the relative importance of these two production mechanisms from the brightness distributions it is necessary to evaluate the impurity ionization lengths (which depend on their production mechanism). On the LE, where $\langle n_e \rangle = 1.5\ 10^{18}$ m^{-3} and $T_e = 20$ eV, the ionization lengths are 0.02 m, 0.14 m and 1.1 m for chemically sputtered neutrals (0.1 eV), physically sputtered neutrals (5 eV), and C^+ ions (7 eV), respectively. On the tip of the limiter, where $\langle n_e \rangle = 6\ 10^{18}$ m^{-3} and $T_e = 70$ eV, the ionization lengths drop to 2.3 10^{-3} m (0.1 eV), 16 10^{-3} m (5 eV) and 0.15 m (23 eV), respectively.

The CII brightness distribution is assumed to represent the neutral carbon source, since the C ionization rate is very large for the measured plasma parameters, and the CII radiation is emitted rapidly after C ionizes. Therefore, fig. 1b shows that the C neutrals are localized on the LE, indicating that chemical sputtering, because of its resulting shorter ionization length, is more important on the LE than physical sputtering. Indeed, physically sputtered carbon, with an ionization length of 0.14 m, would result in a much less localized peak.. Note that fig. 1a shows that the ISLE has a temperature compatible with high chemical sputtering (a process which has a maximum around 600°C).

The central tip region of the limiter is also at a temperature which would produce high chemical sputtering. However, both chemically and physically sputtered carbon neutrals have here very short ionization lengths, and it is therefore not possible to infer the dominant source from the brightness localization. However, fig. 2b can be interpreted to show that physical sputtering is of primary importance in the central region of the limiter. Indeed, since (for the carbon energies considered here) the surface temperature is the principal variable in chemical sputtering and since both the LE and tip are at the maximum chemical sputtering temperature range, one would expect the empirically estimated, total sputtering ratio of φ(CII) to $\varphi(D_\alpha)$ to be about constant if chemical sputtering had the same importance in the two regions. Instead, a 10 fold difference is observed. Thus, a production mechanism other than chemical sputtering is important on the tip.

Physical sputtering increases with incident ion energy. The incident ion energy is greater near the tip than on the LE. This indicates that physical sputtering is more important on the tip than on the LE. It is therefore probable that physical sputtering is the production mechanism responsible for the 10 fold difference in the ratio of φ(CII) to $\varphi(D_\alpha)$ between the LE and the tip. A few experimental physical sputtering data [2] have been included in Fig. 2b to indicate that this empirical estimate of the total sputtering yield is of a reasonable order of magnitude. Note, however, that these data are for normal incidence with the ion impact energy taken to be

$3kT_e$, whereas on the face we have near grazing incidence and there can possibly be a significant D flux amplification value. Finally, the low value of the $\varphi(CII)$ to $\varphi(D_\alpha)$ ratio at the LE, where chemical sputtering is important, is probably a consequence of the increased D production that accompanies the liberation of CD_4 via chemical sputtering.

The ratio of $\varphi(CIII)$ to $\varphi(CII)$ shown in Fig. 2c is consistent with the much larger value of the C^+ ionization length on the tip. The ratio of $\varphi(CIII)$ to $\varphi(CII)$ is constant for the central region of the limiter since C^+ does not travel far before becoming C^{2+}. On the LE, however, there is not a strong source for C^{2+} since C^+ travels, on average, two times the dimension of the limiter before ionizing to become C^{2+}.

Physical sputtering also depends on the angle of incidence. The angular dependence has an effect on the CII, CIII and D_α brightness distributions (Fig. 1b and 1c) and on the C^+ flux distribution (Fig. 2a) near the central tip of the limiter. Indeed, in each distribution the peak is shifted away from the tip by 3 to 5 cm; these shifts are interpreted as being due to the reduction in the angle between the magnetic field lines and the tangent to the limiter surface.

5. Impurity transport calculations. To further differentiate the possible impurity production mechanisms, the data have been modeled with the impurity code BBQ. This code incorporates a 3D Monte-Carlo description of both neutral and charged impurity transport in Tore Supra geometry. Impurity generation processes related to physical and chemical sputtering are included. Given the limiter temperature distribution and the incident D+ flux parameters, BBQ calculates the evolution of both physical (C) and chemical (CD_4) sputter products. The code calculates spatial distributions of CII and CIII brightnesses. The physical sputter products are emitted with a Thomson energy distribution, with energies as high as 5-10 eV; the chemical products are emitted at the wall temperature (0.1 eV) as CD_4, which then experiences a break-up chain.

The BBQ code with physical sputtering alone produces a CII brightness distribution which is too diffuse [3]; the emission is not localized on the LE. With chemical sputtering added to the code, the toroidal spatial structure of the experimental brightness data is qualitatively reproduced. Fig. 3 shows the absolute BBQ CII brightness distribution obtained when a representative poloidal average temperature distribution was taken from the IR camera. The experimental data is given for comparison. The sputtering dependence on the angle of incidence of the flux is also illustrated by BBQ since there are two peaks 5 cm on each side of the tip.

6. Conclusion. In an effort to better understand the processes of impurity production and transport from the Tore Supra outboard limiter, we have used an absolutely calibrated, visible endoscope. The experimental data have been interpreted as evidence that chemical sputtering is the most important impurity production mechanism on the leading edges, while physical sputtering is probably the most important one in the central region of the limiter. With the BBQ code, it was necessary to include chemical sputtering in order to qualitatively match the experimental spatial distributions.

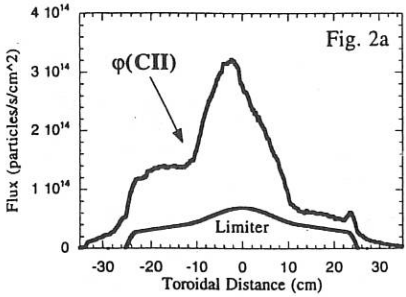
7. References.

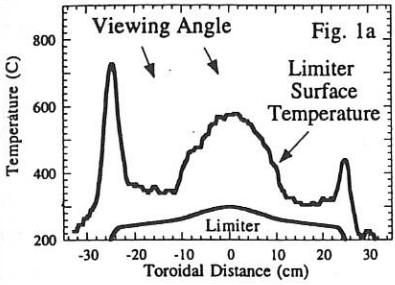
[1] K. Behringer,et al., *Plasma Phys. Contr. Fusion* **31**, 2059 (1989)
[2] Roth et al., *Max-Planck-Institut für Plasmaphysik: Data on Low Energy Light Ion Sputtering*, IPP 9/26 (1079)
[3] Klepper et al., *Measurements and Modeling of Impurity Source Distributions from the Tore Supra Outboard Pump Limiter* , PSI (1994)

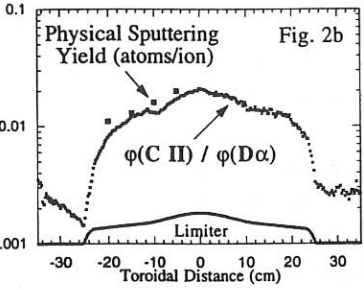
8. Acknowledgment. We would like to thank Prof. T. Kammash (University of Michigan, US), M. Chatelier, H. Garcin, J.H. Harris, K. Mony and P. Mioduszewski for their valued assistance.

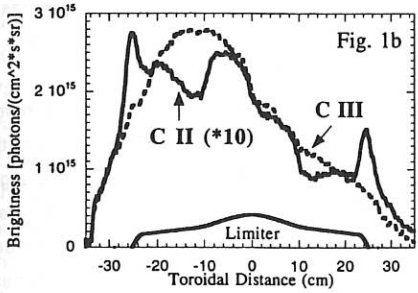
9. Figures

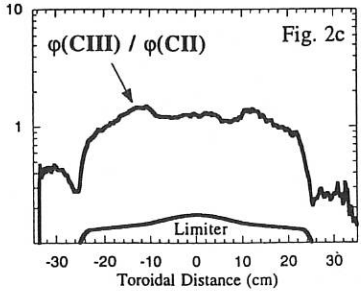
Fig. 1a Limiter surface temperature vs toroidal distance in the equatorial plane.
Fig. 1b CII and CIII brightness vs toroidal distance.
Fig. 1c Dα brightness vs toroidal distance.
Fig. 2a CII flux vs toroidal distance in the equatorial plane.
Fig. 2b Flux ratio of CII to Dα vs toroidal distance.
Fig. 2c Flux ratio of CIII to CII vs toroidal distance.
Fig.3 Absolute BBQ and experimental CII brightness vs toroidal distance in the equatorial plane.

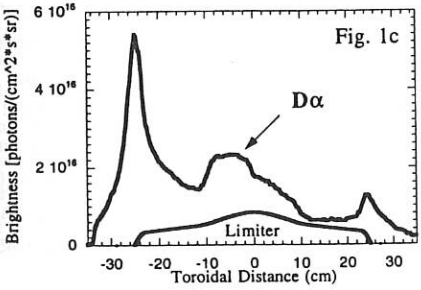


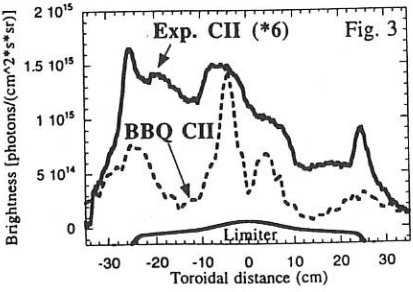












Spectroscopic study of Marfe-like ergodic edge plasmas on TORE SUPRA

W.R.Hess, C.DeMichelis, M.Mattioli, M.Druetta*, R. Guirlet, A.I.Ledyankin, P.Monier-Garbet, J.C.Vallet
Association EURATOM-CEA sur la Fusion Contrôlée
CEN-Cadarache, 13108 Saint-Paul-Lez-Durance Cedex, FRANCE
*Univ. de St. Etienne, F-42023 St. Etienne Cedex 2

Introduction: Asymmetric radiation features at the plasma edge (Marfe) are always observed on high density plasmas before the plasma detaches or disrupts. They have been studied in 'limiter' plasmas and also with toroidally symmetric 'X'-point divertors. This 'classical' Marfe and a new type of ergodic divertor Marfe (ED-Marfe) are observed on TORE SUPRA. In contrast to the 'classical' Marfe, the ED-Marfe has a large poloidal extension and is stable without radiation collapse. It appears when the electron density is pushed up by strong gas injection (necessary because of the ED screening property). The radiating layer 'swings' from the divertor plates (LFS) to the inner wall (HFS). In fact, within its cold and high density layer the intrinsic structure of the magnetic perturbation is revealed. Careful analysis of the bolometric, visible and XUV spectral radiation combined with density and temperature profiles at all available viewing lines show the asymmetries characteristic of the ergodised plasma edge. The ergodic divertor (ED) configuration of TS has an intrinsic topological relation to the 'X'-point divertor. Instead of using one gross perturbation (n=0, low m) of the poloidal field, a multiplicity of weaker perturbations (n=6, m≈18) creates a series of small kicks (δB_r) on the field lines which (when the resonance condition is fulfilled) connects the field lines to the target plates and walls or to the hot core.

Experiment: This section briefly reviews the experimental conditions. The ohmic discharges (I_p=1.4 MA, B=3.4 T, a=0.75m, R=2.4m, q(a)=3.2) were initiated on the outboard limiter (3 cm ahead of the Divertor plates, R=3.18m). This series of discharges was characterized by an almost completely saturated carbon wall. Apart from a small prefill no gas was injected in the reference shot without divertor. The latter has the same bulk density and temperature profile as the following shot with the ED activated (at max. current) from the very beginning. This discharge can be divided into three phases: 1) the plasma current ramps up and resonance with the ED (for q(a)~3) is attained at 3s. Then the ergodic zone acts as an efficient screen for impurities (i.e. the intensity of CVI (Lα) drops) 2) between 3 and 6s (as n_e is pushed up by strong gas injection) the radiating layer in front of the divertor plates 'swings' to the inner wall and 3) at 6s an ED-Marfe develops which stays stable until the current ramps down. Fig. 1a compares the total and radiated powers (as measured by the bolometer) of the reference and the diverter shot. The onset of the ED-Marfe is clearly linked to the radiation 'swing' (fig. 1b). The radiated power increases from 45%

(LFS at 5s) to about 80% at 8s during the ED-Marfe. A Langmuir probe (close to a neutralizer plate of the divertor) shows that the plasma pressure decreases by a factor of 2.4 after the transition of the radiating zone to the inner wall. This means that the plasma slightly 'detaches' from the divertor plates. At the same time the heat flux on the (outboard) limiter and the divertor plates diminishes. The impurity content is very low (Zeff=1.1). A cross check between XUV line emission, bremsstrahlung, tomography and code simulation indicates: $n_C/n_e=1.5.10^{-3}$ and $n_O/n_e=3.10^{-4}$.in the plasma core Thus an important quantity of the radiated power must be due to deuterium radiation within the high density and low temperature ED-Marfe.

Structure of the Divertor Marfe: The structure of the ergodized plasma edge is in some way 'revealed' within the cold and dense ED-Marfe. This means that density, temperature and radiation measurements at different poloidal positions show specific asymmetries due to the (rigid) magnetic divertor structure. A first example is shown in fig.2 where the electron densities, measured in a vertical (Thomson-scattering) and an equatorial direction (reflectometry at LFS), are compared. The edge density is measured by a vertically reciprocating Langmuir probe. At 5s, before the radiation swing from the divertor plates to the inner wall, a density bulge is seen by the equatorial reflectometry. The latter disappears after the radiation swing. A simple argument based upon pressure constancy is used to explain this: as the temperature decreases due to (ED increased) radiation losses at the LFS (in front of the divertor plates) the density increases. It is expected that this density bulge is displaced on the HFS as the ED-Marfe radiates an even higher part of the total power (0.15MW for the divertor and 0.7MW for the ED-Marfe). In fact, fig.3 shows that the entire plasma edge is affected by the ED-Marfe radiation. At the upper plasma edge (Thomson scattering at r/a=0.94) T_e decreases from 80 to 40 eV and at the LFS (divertor Langmuir probe at r/a=1.04) T_e decreases from 22 to 12 eV.

Extension of the ED-Marfe:1) A tangential view with an (unfiltered) CCD-camera shows the lower half of the inner carbon wall. A luminous zone with a width of 15 cm and a homogeneous extension over the entire covered poloidal angle is seen. This is interpreted as the extension of the cloud of neutral deuterium particles. Thus, an important neutral density is expected 5 cm within the LCFS (of the unergodized plasma) with a poloidal extension of ≥120°. **2)** A poloidal intensity modulation of CIII and CIV lines (see below) is observed with a rotating mirror VUV spectrometer (the lower half of the HFS plasma edge is scanned) /1/. **3)** Dα emission is recorded from the upper half of the inner wall by a fan of 9 chords. They confirm the extension of the ED-Marfe showing also Dα-fluctuations which are clearly linked to the exhaust of energetic ions due to the sawtooth activity of the plasma interior.

In conclusion: The ED-Marfe is not a sharply limited region (as the classical Marfe) but extends over the wholé inner wall (i.e. over the 120° of the carbon tiled inner wall). As

already reported /2/ the boundary of the 'classical' Marfe (in its stable phase) is the LCFS and its poloidal extension does not exceed 40°. The volume of the ED-Marfe (~1.6m^3) is much bigger (about 4x) than the (classical) Marfe volume. Thus, the smaller radiated power per volume (≤0.4 MW/m^3) and the (higher) ergodic heat flow into the ED-Marfe are important differences in comparing it to the unstable Marfe. Combining all informations about the mean temperature within the radiating layers it appears that **a)** the classical Marfe is the coldest -close to the recombination limit of hydrogen (~5 eV) /3/, **b)** the ED-Marfe is somewhat hotter (≥5 eV) but still the deuterium radiation is important, **c)** the temperature of the radiating layer in front of the divertor pannels is ≥15 eV (at 5s). This is consistent with the fact that impurities (e.g.Neon injection) are necessary if a substantial part of the heating power is to be radiated with a edge temperature between 20 and 100 eV /4/.

ED-Marfe temperature: The above mentioned intensity modulations of CIII and CIV indicate an electron temperature of the order of or below 10 eV. Surprisingly low ion temperatures of 10 eV have been observed (CX-line of CVI (8-7)) with Marfes /2/ whereas a temperature of 20 eV is measured in similar conditions with the ED-Marfe.

Temperature profiles: As for the density profile, only the plasma edge ($r/a \geq 0.7$) is affected. Fig.:4 shows the evolution of the electron temperature profile within this region where the heat flow is strongly modified by the ergodic divertor: **1)** An almost flat Te profile is observed between r/a=0.96 and 1.02. This region is not ergodic since the connection lengths from wall to wall are short ($L<\pi qR$) as in the 'classical' SOL /5/. **2)** Further inside ($0.8 \leq r/a \leq 0.94$ within the ergodic zone), the temperature gradient is steepened with the application of the divertor.

Plasma edge ion temperature: Ti (measured at the LFS in the vicinity of the neutralizer plates of the div.) is significantly higher (2x) than the electron temperature (Te=12 eV). A careful analysis of the Doppler broadened Zeeman structure of CIII (4647 Å) /6/,/7/ gives an ion temperature of 25±5 eV during the ED-Marfe (w/o divertor this edge temperature is typically 2x higher).

Neutral density: Direct measurements of n_o in the plasma edge are unfortunately lacking. Thus indirect information via CX sensible intensity ratios of impurity ions are used. **1)** A hint about n_o within the ergodic layer is obtained by the simulation of the observed carbon line ratio ρ=[CVI(Lα)/CV(resonance line=R)] and of the 'G-ratio'. The latter is the intensity ratio between the intercombination (I) and the resonance line of CV: G=I/R. Typical values when reaching the ED resonance are: $\rho=2 \rightarrow 1$ and $G=0.4 \rightarrow 0.6$. The ED values can be simulated (simultaneously) only by a) enhancing the diffusion coefficient and/or reducing the parallel confinement time for $r/a \geq 0.85$ and b) introducing n_o values in the 10^{16} m^{-3} range in the CV emitting layer (r/a~0.85). (CX recombination favours the triplet state population which enhances the I-line). **2)** A similar approach has been used for the estimation of n_o within the

classical Marfe. Simulations of the CVI(8-7) line intensity show that CX with excited deuterium can account for the measured signal. In this case a neutral density (at r/a=1) between 10^{17} and 10^{18} is necessary /2/.

References

/1/ De Michelis et al. this conf.

/2/ Hess W. et al. EPS 1993

/3/ Sergienko G. et al. EPS 1993

/4/ Monier-Garbet P. et al this conf

/5/ Nguyen F. et al. EPS 1992

/6/ Klepper C. et al this conf.

/7/ Hey J. et al. EPS 1993

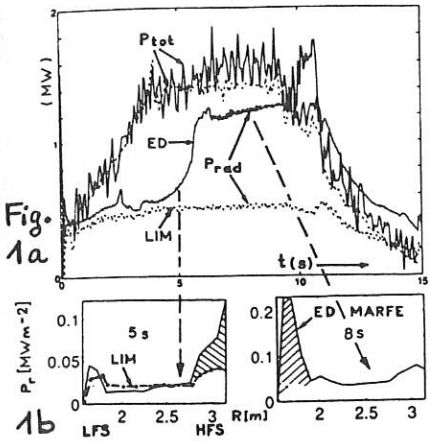
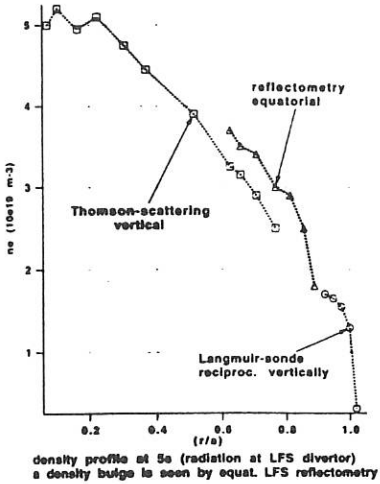


Fig.1a total and radiated power of limiter and diverter shot

Fig.1b radiation swing from (LFS) divertor plates to inner wall



density profile at 5s (radiation at LFS divertor) a density bulge is seen by equat. LFS reflectometry

Fig. 2

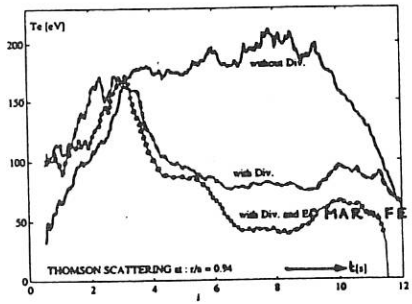
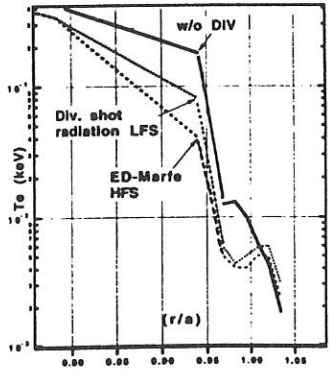


Fig.3 comparison of plasma edge T_e w/o & with divertor



Te from Thomson scat. and recipr. Langmuir probe limiter shot: solid line, divertor shot: dotted line

Fig. 4

SILICONIZATION ON FTU

M.L.Apicella, R.Bartiromo, G.Mazzitelli, L.Pieroni, D.Frigione

Associazione EURATOM- ENEA sulla Fusione, Centro Ricerche Energia Frascati, C.P. 65 - 00044 Frascati, Rome (Italy)

INTRODUCTION

FTU is a compact tokamak operating usually with an inconel poloidal limiter and stainless steel walls maintained at 77 K(liquid nitrogen temperature).

For well conditioned discharges, the density limit at I_p=0.5MA extends beyond the Greenwald limit by 1.7 times, in a regime where all the impurities are practically absent in the plasma ($Z_{eff} \simeq 1$) [1]. At higher current, the experimentally obtained density limit does not increase with respect to the previous value. In this condition oxygen and low traces of metallic impurities are still present.

In order to better assess the role of low-Z impurities with regard to the operational regime of FTU, a silicon coating of the wall has been attempted "in situ" for the first time by using a dc glow discharge and a mixture of helium with a minority of silane as feeding gas. Indeed silicon is known for its chemical property to form tight bonds with oxygen.

Furthermore, a plasma with silicon as the dominant impurity is obtained during the first phase when the limiter is still Si-coated and this has allowed the comparison of plasma characteristics with low-Z (silicon), and medium-Z (nickel) first wall materials.

In this paper, after a brief description of the experimental apparatus and the deposition procedure, the main properties of the plasma before and after siliconization are described and conclusions are then drawn.

EXPERIMENTAL APPARATUS AND DEPOSITION PROCEDURE

A test apparatus especially arranged for the safe handling of a hazardous gas such as silane, was installed on the machine in September 1993. Four vertical ports located 90° toroidally from each other are employed to introduce the gas (90% He+ 10%SiH_4) by a piezoelectric inlet valve, which is automatically regulated to maintain the pressure in the chamber at 7×10^{-3} mbar. The gas is pumped using two evacuation lines of the main vacuum system placed at the opposite side of the torus and connected to two standard 2000 l/s turbomolecular pumps and two 60 m^3/h rotary pumps, which have been modified to assure very good vacuum tightness and to allow the dilution of silane at the exhaust with a flux of gaseous nitrogen before contact with the air. With this geometrical configuration a good uniformity of the film deposition along the torus can be obtained by a suitable adjusting of the feeding gas.

The discharge develops between two electrodes inserted up to the centre of the vacuum chamber and toroidally displaced by 180° and the walls. Its conditions are: voltage drop of about 400÷450 V, total current of 1 A corresponding to 8 $\mu A/cm^2$. Unlike other tokamak devices, siliconization in FTU is performed on cold walls (273÷298 K) to avoid waste of time for heating at higher temperature, since the machine usually operates at 77 K. Typically, with these discharge parameters, a deposition time of 3h is required to produce a 1000Å thick film. Extensive preliminary tests have been previously carried out [2] on physical and chemical properties of silicon films deposited on cold surfaces (77,273 and 298 K). They show that bad adherence and traces of peeling are observed only at 77 K.

PLASMA RESULTS

To evaluate the effect of siliconization on plasma performances we compare the results obtained during three different experimental phases of FTU characterized by different materials facing the plasma: phase I (inconel limiter and SS walls), phase II (silicon limiter and walls), phase III (inconel limiter and siliconized walls). In the second phase, which is limited to a short period immediately after siliconization, silicon is the dominant impurity of the discharges.

The first indication of the oxygen reduction in the plasma due to siliconization, came from the fact that at the restart of the machine the standard good plasma was produced immediately, like when the machine is well conditioned by careful baking and discharge cleaning [3].

The plasma results in the phase II show very good properties of the silicon as getter for oxygen and as a protection against sputtering of metals from the limiter. In fact, up to a plasma current of 0.7 MA and at low electron density (0.8×10^{20} m^{-3}), a drastic reduction of oxygen and metallic lines radiation have been observed by UV spectroscopy. The intensity of the most prominent line of OV decreased by about a factor 10, while silicon lines of SiXII, SiXI, SiX appeared in the spectra, in the energy range before dominated by nickel lines (fig 1a,1b). In addition, the ratio of the radiated power to the ohmic power decreased from about 68% to 40%, (fig.2) while no change of Z_{eff} and confinement time was evident.

The reduction of the radiated power was consistent with the increase of the energy on the limiter, as measured by thermocouples poloidally distributed.

The impurity production mechanism is essentially the release from the limiter via physical sputtering, as suggested by the density dependence of the ratio of $SiII/H_\beta$ line intensities which decreases with density. This behaviour is typical of processes which present a pronounced energy dependence.

Despite of the reduction of oxygen, the operational density limit obtained with silicon as limiter material at 0.7 MA has been lower by a factor 1.5 than the value obtained with inconel limiter, connected with the onset of Marfes at lower density.

A different behaviour has been observed further after siliconization (phase III). During this phase, due to the consumption of the silicon coating on the limiter, nickel lines reappear and dominate the UV spectra, while oxygen is practically absent (fig.1c). The intensity of the metal emission lines is higher than before siliconization (fig.1a) due to an increase of metal released from the limiter. This can be explained

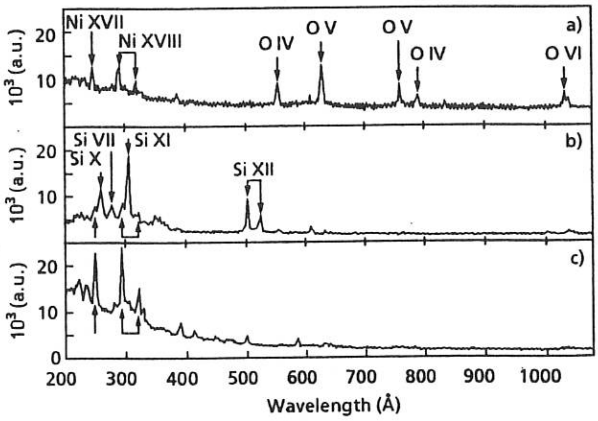


Fig. 1 - UV spectra for $I_p=0.5$ MA, $B_T=6$T and $\bar{n}_e=0.8\times10^{20}$ m^{-3} plasma discharges with a) inconel limiter and SS walls, b) silicon limiter and walls, c) inconel limiter and siliconized walls

by a value of the radiated power (60%) lower than before siliconization (68%) and by the consequent increase of the power flux onto the limiter.

With inconel limiter and siliconized walls, the density limit observed at 0.7MA does not change with respect to the case of SS walls (n_e=2.5×10^{20} m^{-3}).

All these experimental findings suggest that the silicon radiation losses and its production mechanism are crucial for plasma performances. To clarify this behaviour plasma discharges whose dominant impurities are Ni and Si have been compared with a plasma discharge with oxygen as dominant impurity.

Figure 3 shows the temporal evolution of the electron temperature at r=0.24m (r/a= 0.8) during the density ramp up at I_p=0.7 MA, B_T=6T.

At low density, around 0.8×10^{20} m^{-3}, T_e is different in the three cases with the highest value for siliconized discharge (T_e=300 eV) which rapidly decreases after 400 ms when the onset of Marfe occurs. Nevertheless no detached plasma was observed: as evidenced by the value of the electron temperature at r=0.28 m, equal to $T_e \geq 10$ eV. It is important to note that Marfe appears at different densities: for silicon discharge is n_e=1.0×10^{20} m^{-3}, for oxygen discharge is n_e=1.5×10^{20} m^{-3} and, finally, for nickel discharge is n_e=2.0×10^{20} m^{-3}.

The radiative cooling rate of these impurities computed in coronal equilibrium as a function of electron temperature [4] shows that both silicon and oxygen curves

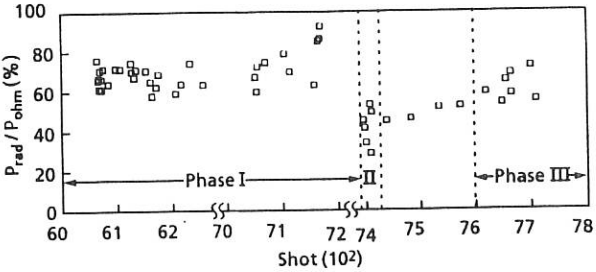


Fig. 2 - Fraction of radiated power P_{rad} (in %) to the ohmic power P_{ohm} as a function of the number of shot for I_p=0.5 MA, B_T=6T plasma discharges obtained before (phase I), immediately after (phase II) and further after (phase III) siliconization

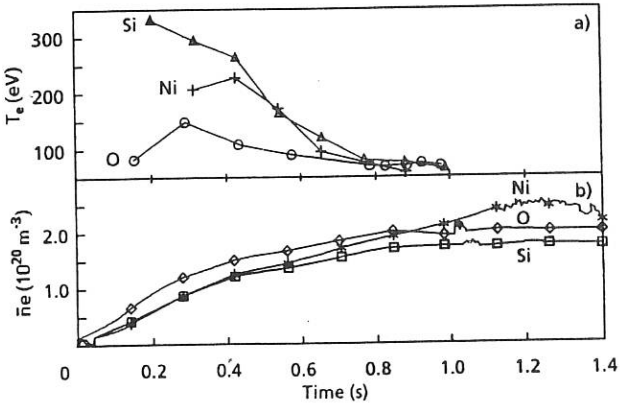


Fig. 3 - Temporal evolution of: a) electron temperature at 0.24 m, b) average electron density for I_p=0.7 MA, B_T=6T with Si, Ni and O dominated plasma discharges

are confined within a narrow range, up to about 100 eV for silicon and to 20 eV for oxygen, while the curve for nickel extends at higher electron temperatures.

The phenomenology described above can therefore been understood with the following arguments. In the Si-dominated discharge steep temperature gradients develop in the edge plasma at low density, as it can be seen from fig.3 and from the fact that temperature at the last closed magnetic surface(LCMS) has been measured to range always between 20 and 40 eV [5] in FTU. This reduces the radial extension of the Si radiating layer and therefore the amount of the total radiated power.

At higher density the T_e gradient decreases and the layer, where the Si cooling rate curve has a negative slope, broadens. In this layer the plasma has a high emissivity and shows a large thermal instability so that the Marfe develops and finally a disruption occurs.

For the oxygen dominated case temperature at the edge are always lower since oxygen radiates mainly at the far edge (>0.28m). This in turn causes flatter Te profile than for Si-case, therefore larger radiating volumes are involved and more power is lost by radiation. However, the low temperature required for having a high radiation together with a high thermal instability, causes the onset of Marfe to occur at higher density, as indeed experimentally observed.

In the discharge dominated by nickel the maximum emissivity at low density is displaced at the bulk of the plasma and the total radiation power is lower than for oxygen dominated discharge (50% against 60%). On the basis of the cooling rate much higher for Ni than for O for T_e>20eV, we expect therefore a much lower concentration of Ni($\simeq 2\times10^{-4}$ of the average electron density) in the discharge as confirmed by Z_{eff} measurements which are very similar in both cases ($\simeq$ 1.5).

At high density the nickel production decreases faster than for silicon due to the higher threshold for physical sputtering and the condition of high emissivity does not occur. The fact that the onset of Marfe happens at higher density in Ni dominated plasma can be attributed to the very small concentration of oxygen still present in the discharge.

Experimentally, the total radiated power for silicon discharges is lower than for nickel discharges (a factor 0.6) while Z_{eff} is very similar. This last observation implies a Si ion concentration 4 times higher than Ni, due to the different atomic numbers, 14 and 28 respectively.

The larger power input in the SOL is consistent with the factor 2 increase observed for the particles flux in the SOL by Langmuir probes.

The higher impurity density can be qualitatively accounted for this fact and by the different sputtering yields (higher for Si).

An exact evaluation of the last term is not possible because the temperature is found to vary poloidally in the range (T_e=20÷40 eV) where steep variation of the sputtering yield occurs [6].

A model coupling the plasma edge and the SOL plasma [7], is able to reproduce satisfactorily the experimental results, assuming the physical sputtering as the only mechanism for impurity generation in the case of Si and Ni.

REFERENCES

[1] D. Frigione, L. Pieroni and FTU Team, Proc. 20th EPS Eur. Conf. on Control. Fusion and Plasma Physics, Abs. Vol. 20 (Lisboa 1993).

[2] M.L.Apicella et al., 6th ICFRM Int. Conf. on Fusion Reactor Materials, Stresa, Italy, 27 September-1 October,1993, to be published on J. Nucl. Materials

[3] M.L. Apicella et al., Proc. 20th EPS Eur. Conf. on Control. Fusion and Plasma Physics Vol.17C, partII, p.619 (Lisboa 1993).

[4] D.E.Post and R.V.Jensen,Atomic Data and Nuclear Data Tables 20,397 (1977).

[5] V.Pericoli Ridolfini et al., 11th PSI Int. Conf. on Plasma Surface Interactions, Mito, Japan, 23-27May, 1994, to be published on J. Nucl. Materials.

[6] W.Eckstein et al., Sputtering Data, Max-Planck-Institut für Plasmaphysik, IPP Report 9/82(1993).

[7] F.Alladio et al., Invited Paper, this Conference.

Self-Consistent Impurity Modeling with Edge/Core Plasma Coupling

R.Zanino and C.Ferro (†)

Dipartimento di Energetica, Politecnico, I-10129 Torino
(†) Associazione Euratom-ENEA sulla Fusione, I-00044 Frascati

ABSTRACT

A simplified model for impurity screening in a limiter SOL has been coupled to an impurity transport code for the main plasma. The structure of the resulting SCOUT code (Self-COnsistent impUriTies) is summarized, and results are presented for the case of the Frascati Tokamak Upgrade (FTU).

1. Introduction

Impurities presently constitute one of the major problem areas in plasma-surface interactions and for fusion as a whole. In the recent past we have developed a simple self-consistent iterative model for the study of impurity screening and contamination in limiter tokamak plasmas [1]. The model was used to analyze the possible edge conditions of a high density ignited tokamak design [2], and was compared to some experimental results of FTU [3]. The model was subsequently improved [4] allowing for the distinction between the impurities recycling near the limiter and those diffusing out of the main plasma; good agreement was found when comparing with FTU in several relevant quantities, e.g., edge plasma densities and temperatures, and main plasma contamination parameter Z_{eff}. However, the main plasma description was admittedly very rough, as for instance the related estimate of the radiated power fraction.
In the present work we try to partially overcome these limitations by coupling the edge part of our model to a 1-D impurity code of the main plasma, which is a relative of the STRAHL code [5] available at Frascati. Our model provides the neutral impurity influx from the SOL into the main plasma (and edge electron density and temperature) as a source to the impurity code; alternately, the impurity code provides the radial profiles of the charged impurity ionization stages and the radiated power fraction in the main plasma.
In Section 2 the main plasma and SOL models contained in the SCOUT code are briefly reviewed, and the structure of their coupling is described. In Section 3 an application to the case of limiter produced impurities in FTU is presented. Some conclusions are drawn in Section 4.

2. Coupling of main/SOL plasma models

Main plasma model

In the main plasma 1-D radial transport equations are solved (see [5,6] and references therein) for the N ionization stages of a single given impurity species

$$\frac{\partial n_j}{\partial t} = -\frac{1}{r}\frac{\partial}{\partial r}(r\Gamma_{rj}) + Q_j \qquad j = 1,...,N \tag{1}$$

where the (anomalous) fluxes are specified by

$$\Gamma_{rj} = -D(r)\frac{\partial n_j}{\partial r} - n_j V_{in} \qquad j = 1,...,N \tag{2}$$

with common diffusion coefficient and inward pinch velocity, and the sources are

$$Q_j = [I_{j-1}n_{j-1} - (I_j + C_j)n_j + C_{j+1}n_{j+1}]n_e \qquad j = 1,...,N \tag{3}$$

with the strong temperature dependence of ionization and recombination rates I and C respectively, given as referenced in [5].
From our point of view it is essential to observe that: 1) boundary conditions are imposed at the separatrix r=a (continuity of fluxes from the main into the SOL plasma)

$$\Gamma_{rj}(a) = n_j(a)V_{eff} = \frac{D(a)}{\lambda_n} n_j(a) \qquad j = 1,...,N \tag{4}$$

where λ_n is the density SOL thickness; 2) specification of the sources in (3) requires the neutral impurity density n_0 to be known: the latter is obtained from the neutral impurity influx from the SOL to the main $\Gamma_0^{SOL\to main}$, assuming that the neutrals reach an instantaneous ionization equilibrium streaming freely with velocity V_0 into the main plasma; neglecting recombination of singly ionized ions one gets

$$n_0(r) = \frac{\Gamma_0^{SOL\to main}}{V_0} \frac{a}{r} \exp[-\int_r^a \frac{n_e I_0}{V_0} dr'] \tag{5}$$

Main plasma density and temperature profiles are needed. Here we parametrize them in the form

$$n_e(r) = a1[1 - \alpha(\frac{r}{a})^{a2}]^{a3} + a4 \tag{6a}$$

$$T_e(r) = b1[1 - \alpha(\frac{r}{a})^{b2}]^{b3} + b4 \tag{6b}$$

where the unknown a1,...,a4,b1,...,b4 are determined such as to fit the respective measured volume averaged and peak values, and the computed edge value and SOL thickness (typically α=0.99).

SOL plasma model

Details of the SOL plasma model are to be found in [1-4], and here we will only review those features which are most relevant to the coupling. The SOL model is partly 0-D and partly 1-D in the radial and/or in the parallel direction. It computes edge density and temperature of the plasma, together with their values in front of the solid target, neutral impurity influx Γ_0 produced by physical sputtering, the fraction η of Γ_0 which makes it to the main plasma without being ionized, and the radiated power fraction in the SOL.
We assume that (for the surface integrated fluxes) $\Gamma_0^{SOL\to main} = \eta\Gamma_0$, i.e., all those impurities which are ionized in the SOL recycle at the target without entering the main plasma, with screening efficiency $1-\eta$. Direct contamination of the main plasma by neutral impurities produced by sputtering of charged particles is obviously mostly relevant to the limiter case, whereas it will not typically apply to a divertor configuration. Essential input parameters which must be provided, e.g., by the main plasma transport code, are the fraction of the input power $P_{conv} = P_{in} - P_{rad}^{main}$ conducted/convected by charged particles into the SOL, and the impurity influx into the SOL from the main plasma $\Gamma_Z^{main\to SOL} = \sum_{j=1}^{N} \Gamma_{rj}(a)$. We do not attempt to follow the single ionization stages in the SOL, but instead assume an average charge $Z_{SOL} = \sum_{j=1}^{N}[j\ n_j(a)]/\sum_{j=1}^{N} n_j(a)$. A different charge (typically 1 or 2) is assumed for the non-thermalized impurities recycling in the limiter proximity.

Coupling

The evolution of the impurity concentration in a given discharge is followed for a given time or up to steady state. The plasma background (with the exception of the $n_e(a)$, $T_e(a)$ pedestals computed by SCOUT) and the input power P_{in} are given and fixed in time.
We march forward in time alternating a time step of the main plasma with a steady state (fast time scale equilibrium) computation of the SOL; the following procedure (explained below) is used

$$n_j(r)^{(k)} \to Z_{eff}, P_{rad}^{main}, \Gamma_Z^{main\to SOL} \to T_w, T(a), \Gamma_0 \to \eta \to \Gamma_0^{SOL\to main} \to n_j(r)^{(k+1)}. \tag{7}$$

Assume that at a given time $t = k\,\Delta t$ we have just computed P_{rad}^{main} and $\Gamma_Z^{main\to SOL}$. The former (actually P_{conv}) gives roughly speaking the edge plasma temperature at $t + \Delta t$, whereas the latter contributes with

plasma ions and recycling impurities (the latter computed iteratively) to the sputtering of the limiter (Γ_0). Depending on the limiter geometry, material, and on the plasma density and temperature in its proximity the screening efficiency of the SOL is computed, counting the fraction η of impurities reaching the main as neutrals. These are used as the source in the main plasma transport step to compute impurity and energy fluxes into the SOL at $t + \Delta t$, closing the cycle. The same procedure is then repeated in the subsequent steps.

3. Results

The SCOUT code is being applied to the study of impurities in FTU. In this Section we will describe some preliminary results for the case of Ni produced at an Inconel poloidal limiter; we follow a transient which starts without impurities in the main plasma and lasts about 1s.
As to the main plasma computation the following parameters (shot # 4347, high density) were used: main plasma densities $n_e(0) = 2.09 \times 10^{20}$, $< n_e >= 1.14 \times 10^{20}$, temperatures $T(0) = 1.12$ keV, $< T >= 0.35$ keV, input power 0.92 MW. Furthermore D(r) varies monotonically from 0.1 m^2/s in the center [7] to about 3 times the Bohm value at the edge [8], and $V_{in} = 2$ m/s.
The typical time step was 2.5 ms, a much larger Δt giving rise to oscillations in time. A large number of discretization points, typically 1001, was distributed between r=0 and r=a, quadratically or cubically denser near r=a [6]. This is necessary to adequately resolve the source, which at t=1s decreases from r=a inward by 3 orders of magnitude in 1mm, but also to resolve the lower ionization stages and in particular their gradients at the separatrix, which then determine $\Gamma_Z^{main \rightarrow SOL}$.
[Standalone runs of the main plasma code at fixed neutral impurity influx seem to indicate that using a much smaller number of points in r, say 51 as is sometimes done, can easily lead, depending on density and temperature profiles, to underestimating the correct P_{rad}^{main} by a factor of 1.5 to 3. Spatial convergence often starts only when one uses several hundreds of points.]
In Fig.1 we show the time evolution of: edge (far from the wall) and wall temperature, volume averaged Z_{eff}, convected power fraction P_{conv}/P_{in}, and penetration probability η (in all cases the initial transient is due to the fact that the input power is turned progressively on and reaches its final value in the code after 10 time steps). One sees that only about 15 % of the neutral impurities emitted from the limiter make it to the main, this high screening efficiency being due to the high edge density ($\sim 4 \times 10^{19}$). Thanks to this $< Z_{eff} >$ stays low, although the low plasma temperature and high density lead to a relatively high power radiated in the main. All of these results compare reasonably with measured values; edge n: 3.5×10^{19} (exp), 3.1/3.9 (model); edge T: 23 eV (exp), 15/25 (model); $< Z_{eff} >$: 0.91/1.45 (exp), 1.06 (model); P_{rad}^{main}/P_{in}: 54 % (exp), 62 % (model). As to the impurity influx (not shown), at t=1s $\Gamma_0^{SOL \rightarrow main} \sim 3 \times 10^{17}/m^2 s$ computed dividing the number of neutral impurities reaching the main in unit time by the plasma surface area. Finally, the radial profile of Z_{eff} after 1s is shown in Fig.2.
Detailed results obtained with SCOUT and comparing cases with different plasma densities and/or different choice of main plasma transport coefficients will be published elsewhere. A preliminary study indicates however that the trends of lower $< Z_{eff} >$ and lower P_{rad}^{main}/P_{in} with increasing density seem to be reproduced by the model.

4. Conclusion and perspective

A first albeit simple self-consistent treatment of impurity production and transport in both the central and boundary regions of a limiter tokamak plasma has been discussed as implemented in the SCOUT code. Future developments of this work could include: treatment of a toroidal limiter geometry, addition of another impurity species, simultaneous evolution of the background plasma.

Acknowledgments

We wish to thank G.Mazzitelli for making the main plasma impurity code available to us. This work was partially supported by a research contract between ENEA and Politecnico di Torino. R.Z. also thanks ASP for support.

References

[1] R.Zanino, Politecnico di Torino Report DE IN 247 (1990).
[2] C.Ferro and R.Zanino, *J. Nucl. Mater.* 176-177 (1990) 543.
[3] C.Ferro and R.Zanino, *J. Nucl. Mater.* 196-198 (1992) 321.
[4] R.Zanino and C.Ferro, *Contrib. Plasma. Phys.* 34 (1994)337.
[5] K.Behringer, JET Report R(87)08.
[6] K.Lackner, et al., *Z. Naturforsch.* 37a (1982) 931.
[7] F.Bombarda, et al., EPS Lisboa (1993); R.Giannella, et al., EPS Lisboa (1993).
[8] G.Granucci and V.Pericoli Ridolfini, EPS Lisboa (1993).

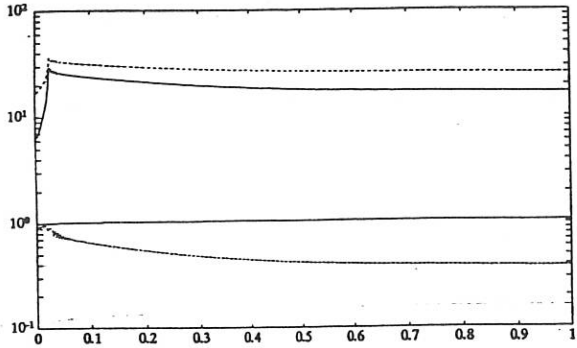


Fig.1: (top to bottom) $T(a)$ [eV], T_w [eV], $< Z_{eff} >$, P_{rad}^{main}/P_{in}, η, vs. t [s].

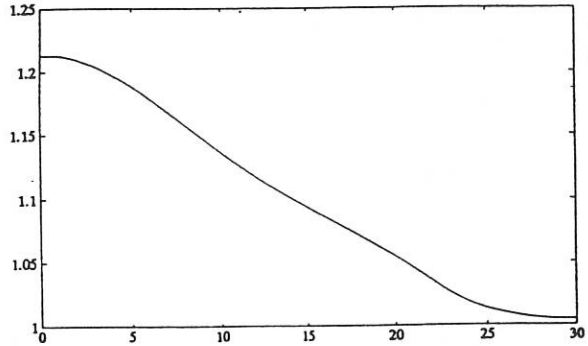


Fig.2: Z_{eff} vs. r [cm] at t=1s.

Impurity Line Emission due to Thermal Charge Exchange in JET Edge Plasmas

*C.F. Maggi, L.D. Horton, R. König, M. Stamp, H.P. Summers**
JET Joint Undertaking, Abingdon, OXON, OX14 3EA, UK
**Dept. of Physics and Applied Physics, University of Strathclyde, Glasgow, UK*

Introduction

High n-shell emission from hydrogen-like carbon (C VI, n=8-7) has been routinely observed from the plasma edge of JET. The C VI observation is along an absolutely calibrated visible chord traversing the plasma cross section vertically from top to bottom of the vessel, just outside the outer strike point during upper X-point configurations (fig.1). Supplementary observations of D I, C II and C III spectral line signals have been made along an identical chord and at nearby chords directed at the divertor strike zones. By comparing the measured spectral line intensities with the signals predicted by advanced atomic physics modelling of carbon and hydrogen radiation, integrated with modelling of the divertor and edge plasma, it is concluded that charge transfer from excited state hydrogen donors into fully stripped carbon ions can account for the observed spectral emission, but that the hydrogen distribution and to a lesser extent the carbon distribution away from the strike zone predicted by the transport model are too low. The data presented here are those of three upper X-point discharges - performed during the 1991/92 JET experimental campaign - where the target material was carbon.

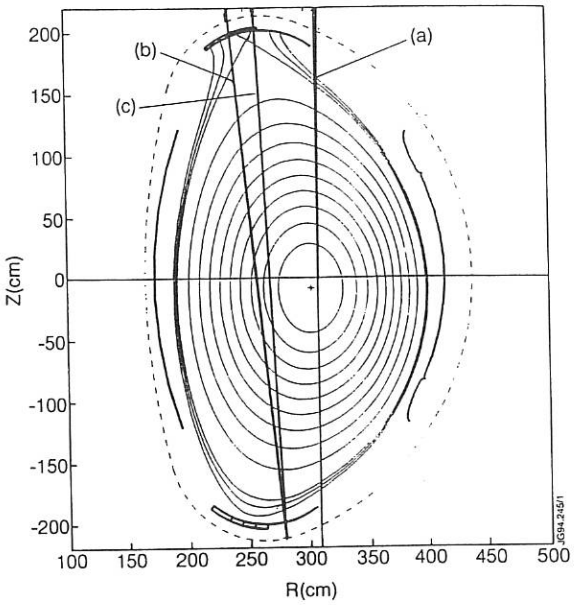


Figure 1. Plasma equilibrium for JET pulse #24174 with superimposed geometries for the visible chord at 3.1 m (a) and two supplementary visible viewing lines at the inner (b) and outer (c) strike point.

Thermal Charge Exchange and Excited Neutral Hydrogen

The calculated C VI (n=8-7) emission due to electron impact excitation is estimated to be a factor 2 to 15 lower than that due to charge exchange. This estimate depends strongly on

the mixing of the l-states in the C VI (n=8) level. More detailed calculations are in progress. In this paper the charge exchange origin of the line is assumed. In the edge region, rich with recycling neutral hydrogen, thermal charge exchange processes with fully stripped carbon impurity ions represent a suitable candidate. Due to the highly excited emitting state of the receiver species, however, charge transfer from ground state hydrogen is a negligible populating mechanism. On the contrary, charge exchange from excited states of hydrogen populates levels of the carbon ions high enough to contribute to the observed emission. Of hydrogen excited states, n=2 has the largest population density and its partial charge transfer cross section peaks at C VI (n=8). Therefore direct charge transfer from D I (n=2) into C VI (n=8), followed by radiative decay into C VI (n=7), is the mechanism considered.

Modelling

The characteristic spectral emission is well localised in the region of overlap of the spatial profiles of the neutral hydrogen donor and the fully stripped carbon ions. Thus the modelling of these spectral line intensities strongly depends upon an accurate transport picture of the reacting species at the edge. A steady state background plasma has been analytically constructed, defining the electron temperature and density profiles at the divertor target plates and, using classical transport, mapped around the scrape-off layer (SOL) [1]. This procedure draws upon experimental measurements from an array of Langmuir probes imbedded in the target tiles. The 2-D Monte Carlo code DIVIMP [2] is then used to model the production and transport of the carbon impurities. It is linked to the 2-D Monte Carlo code NIMBUS [3], which models the neutral hydrogen transport and recycling at the edge. A full collisional-radiative atomic model [4] relates the hydrogen excited state population densities to that of the ground state, whose spatial distribution is given by the transport codes. The atomic model also provides the modifications to the carbon ionization balance, resulting from charge exchange with neutral hydrogen [5] and the effective emission rate coefficients, necessary for the interpretation of the line intensity spectroscopic measurements.

Discussion

Three discharges have been selected for comparison with the model. The main plasma parameters are listed in Table 1. Comparison of the model to the observed spectral emission is extended by including additional spectroscopic signals directly related to the presence of carbon and hydrogen in the emission region. An additional absolutely calibrated visible observation, along an identical viewing line as the one measuring the C VI emission (see fig.1), measures the line intensity of the C III multiplet (λ = 4647 Å) and the H_α radiation. A visible viewing line to the outer strike point (for #24174 and #24175) or to the inner strike point (#26291) on the divertor target tiles (see fig.1) monitors the H_α, H_γ and the C II (λ = 6579.7Å) line intensities. Table 2 shows the observed and predicted line-of-sight integrated emission from H and C for #24174, #24175 and #26291 at the time of the probe

measurements. Table 3 shows the comparison between the observed C VI (n=8-7) spectral line intensities, integrated along the vertical line of sight through the plasma, and the model predictions.

Table 1. Main plasma parameters of the selected discharges.

Discharge	time(s)	$B_T(T)$	$I_p(MA)$	$P_{in}(MW)$	$T_e(0)(keV)$	$n_e(0)(m^{-3})$
#24174	12.18	2.1	3.1	13.0	4.0	1.8×10^{19}
#24175	13.59	2.1	3.1	5.6	3.5	1.6×10^{19}
#26291	13.90	2.8	3.1	3.1	3.0	2.1×10^{19}

Table 2. Comparison between observed and predicted line-of-sight integrated spectral emission from H and C (photons/cm2/s/sr), using the viewing lines at 3.1 m and at the outer strike point, for JET pulse #24174 and #24175, and at the inner strike point for #26291.

	#24174		#24175		#26291	
	Exp.	Model	Exp.	Model	Exp.	Model
$I(H_\alpha)$ @ 3.1 m $\times 10^{14}$	1.50 ± 0.35	0.48	1.40 ± 0.35	0.40	0.75 ± 0.19	0.43
I(CIII,4647Å) @ 3.1 m $\times 10^{13}$	2.50 ± 0.62	1.99	2.60 ± 0.65	1.67	1.35 ± 0.34	0.93
$I(H_\alpha)$ @ strike point $\times 10^{15}$	1.30 ± 0.32	1.55	1.09 ± 0.27	1.34	3.20 ± 0.80	3.70
$I(H_\gamma)$ @ strike point $\times 10^{13}$	1.75 ± 0.87	3.97	1.50 ± 0.75	3.48	6.00 ± 3.00	7.20
I(CII,6580 Å) @ strike point $\times 10^{13}$	0.91 ± 0.23	2.30	0.91 ± 0.23	1.77	12.0 ± 3.0	31.0

Table 3. C VI (n=8-7) LOS integrated (see fig.1) spectral line intensities (photons/cm2/s/sr). Comparison between observations and model predictions. The time of the measurements coincides with that of the Langmuir probe data.

JET Discharge	I(experiment)	I(model)	I(model, normalized)
#24174	$(2.0 \pm 0.4) \times 10^{11}$	2.2×10^{10}	8.6×10^{10}
#24175	$(1.6 \pm 0.4) \times 10^{11}$	2.3×10^{10}	1.2×10^{11}
#26291	$(1.2 \pm 0.6) \times 10^{11}$	6.2×10^{10}	1.6×10^{11}

The relatively large error bars on the experimental values are due to the weakness of the C VI edge charge exchange signal in these discharges. The simulated values are lower than the experimental measurements, particularly for #24174 and #24175. These discrepancies originate from the fact that for these discharges the model fails to give an adequate description of the neutral and impurity transport in the SOL. For both #24174 and #24175, in fact, the H_α signal at the outer strike point matches quite well with the observed one. At 3.1 m, on the other hand, the H_α signal is underestimated by a factor 3 to 4 (see Table 2) with respect to the observed emission. Since the intensity of the H_α signal marks the neutral hydrogen abundance in the emission region, this leads to a corresponding underestimation of the predicted neutral hydrogen density at 3.1 m. Similarly, the C III density in the same region is underestimated by the model, in spite of the C II line intensity being about a factor two higher than the observed one at the outer strike point. Such trends suggest that the hydrogen and the carbon impurities do not spread as far away from the strike point as appears experimentally. By scaling the modelled C VI emission using the ratio of measured to modelled H_α emission and the ratio of measured to modelled C III emission, one obtains much better agreement with experiment (see Table 3).

Conclusions

Thermal charge exchange from excited state hydrogen (n=2) to C^{+6} ions can account for the measured spectral line emission from hydrogen-like carbon (C VI, n=8-7) in JET edge plasmas. The emission due to electron impact excitation is estimated to be a factor 4 to 50 lower than the normalized charge exchange emission, this variation strongly depending on the mixing of the l-states in the C VI (n=8) level. The analysis is complicated by the failure of the simulations to describe correctly the leakage of hydrogenic and impurity particles from the divertor. However, if the experimental values of H_α and C III signals are used to normalise the model results, the predicted C VI line emission agrees within a factor 2 of the measurements. The observation and modelling of impurity line emission due to thermal charge exchange constitutes a promising diagnostic for the derivation of neutral hydrogen density spatial profiles in the edge region of JET. In fact, these studies have demonstrated a deficiency in the transport model for neutral deuterium and/or impurities, which is being investigated. These studies will also be extended to the very low temperature, high density divertor regimes planned for the 1994 experimental campaign.

References

[1] G.F. Matthews et al., J. Nucl. Mater. **196-198** (1992) 374.

[2] P.C. Stangeby, J.D. Elder, J. Nucl. Mater. **196-198** (1992) 258.

[3] E. Cupini, A. De Matteis, R. Simonini, NET Report EUR XII (1984) 324.

[4] H.P. Summers, ADAS, JET Report, in progress.

[5] C.F. Maggi, Laurea Thesis, (1992).

Experimental study of vapor shield formation and divertor material erosion for ITER typical plasma disruptions

N.I. Arkhipov[1], V.P. Bakhtin[1], V.M. Safronov[1], D.A. Toporkov[1], A.M. Zhitlukhin[1], H. Würz[2]

[1] Troitsk Institute for Innovation and Fusion Research, 142092 Troitsk, Russia

[2] Kernforschungszentrum Karlsruhe, INR, Postfach 36 40, D-76021 Karlsruhe

Introduction

Vapor shield formation can drastically decrease the heat load to divertors during the impact of disrupting plasma streams and during ELMS and thus can reduce the material erosion [1]. In this paper vapor shield formation under the impact of a pulsed, high intense, hot plasma stream is investigated experimentally. Experiments were carried out at the 2MK-200 facility at Troitsk [2]. The vapor shield is formed under high temperature plasma exposure with a beam power density of up to 10 MW/cm^2. Properties and dynamics of the vapor shield are studied by means of laser interferometry, laser Thomson scattering, and optical and soft x-ray spectroscopy. Time dependent erosion is measured by applying optical interferometry.

Facility and Diagnostics

The 2MK-200 facility is a magnetic trap with a central solenoid (1.2 m length) and two CUSPs at either end of the solenoid. Two pulsed plasma guns inject deuterium plasma streams into the central solenoid (see Fig. 1) at opposite directions through the magnetic field of the CUSPs. Collision of the counter streaming plasmas causes thermalization of the plasma stream kinetic energy and produces a high temperature plasma with $T_e + T_i \approx 0.7$ keV. The total plasma energy stored in the trap can be up to 50 kJ. The high temperature plasma diffuses across the magnetic field lines in the solenoid and then escapes along magnetic field lines (B = 2 T) through the CUSP slits.

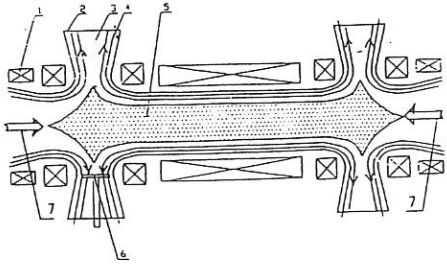


Fig. 1 Experimental facility 2MK-200

1 - magnetic coils, 2 - vacuum chamber, 3 - plasma flow leaving the trap, 4 - magnetic field lines, 5 - plasma column with $\beta \approx 1$, 6 - target position in the CUSP ring slit, 7 - plasma streams from two plasma guns

Samples can be placed in the CUSP ring slit where the magnetic field lines are parallel and the magnetized plasma flow is non - diverging. The plasma stream parameters at this region are as follows: density $n \approx 10^{16}$ cm^{-3}, deuteron ion temperature $T_i \approx 500$ eV, electron temperature $T_e \approx 120$ eV, plasma beta 0.25, plasma flow width 1 cm, power density 10 MW/cm^2, and time duration of the pulse 20 μs. The main positive features of the 2MK-200 facility for disruption simulation are the magnetized hot plasma stream with $\beta < 1$, the plasma stream power density of 10 MW/cm^2 and the rather pure deuterium plasma stream with only very low impurity densities from carbon and plasma gun structural materials.

Thus allowing experiments under favorable and well defined conditions, being similar to a tokamak situation. Disadvantages of the 2MK-200 facility are the short duration, the rather low temperature of the plasma stream and the rather short distance between the target and the central trap plasma what results in a continuous removal of vapor from the expanding vapor shield layer.
However the 2MK-200 facility is very well suited to simulate under quite realistic tokamak conditions the initial stages of the disruptive plasma stream target interaction, and to study formation, behavior and properties of the target plasma cloud for different target materials under the influence of a magnetic field. Experiments at the 2MK-200 facility allow to study the principal physical processes during such an event and thus allow a validation of the numerical modeling. Because of the limited energy density of the plasma stream the target surface in the interaction experiments up to now was oriented perpendicular to the guiding magnetic field lines. Plasma expansion across magnetic field lines was not investigated up to now. Target materials such as graphite, boron nitrite, quartz, aluminum, copper and tungsten were used.
The facility is equipped with a set of diagnostics including magnetic probes for measurement of the gas kinetic plasma pressure, pressure sensors at the target surface, calorimeters for measurement of the energy of the plasma flow and energy absorbed by the sample, a laser interferometer, optical and soft x-ray spectroscopy and laser Thomson scattering for analysis of the target plasma properties and for energy balance measurements and a laser interferometer for erosion rate measurements.

Experimental results

Optical interferometry was used for determination of plasma electron densities in the target plasma [3]. The interferometer has a two dimensional spatial resolution of 1 mm perpendicular to the probing beam and a temporal resolution of 30 ns. Interferometry results are shown in Fig. 2 for a graphite target. Two zones of

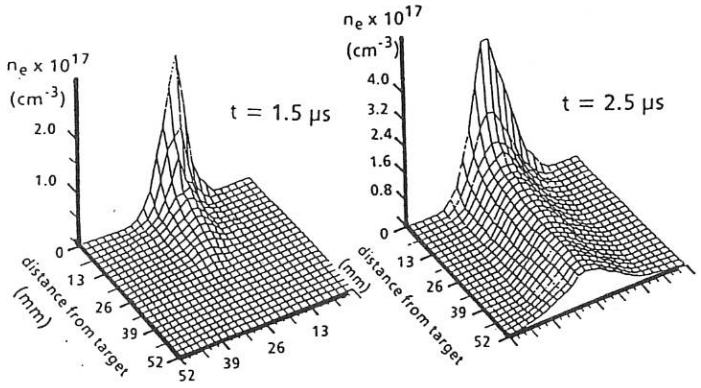


Fig. 2 Plasma electron density distribution for graphite

different plasma densities are observed. The low dense plasma cloud "corona" (electron density around 5 x 10^{16} cm^{-3}) expands along the magnetic field lines with velocities of around (3 - 4) 10^6 cm/s. The dense plasma cloud close to the target is formed within 1 μs (density up to 5 x 10^{17} cm^{-3}) and expands with a velocity of around 2 x 10^5 cm/s. For tungsten a plasma corona extending over a wide region is not seen. The electron density near the surface is around 3 x 10^{17} cm^{-3}. The thickness of the dense cloud remains at around 1 cm.

Results of Thomson laser scattering measurements are shown in Fig. 3 for a graphite target. The probing laser beam is focused to a 1 mm spot at the measurement position. At times below 1 μs the plasma parameters in experiments with and without target are approximately the same. The drastic difference afterwards shows the appearance of the carbon plasma corona.

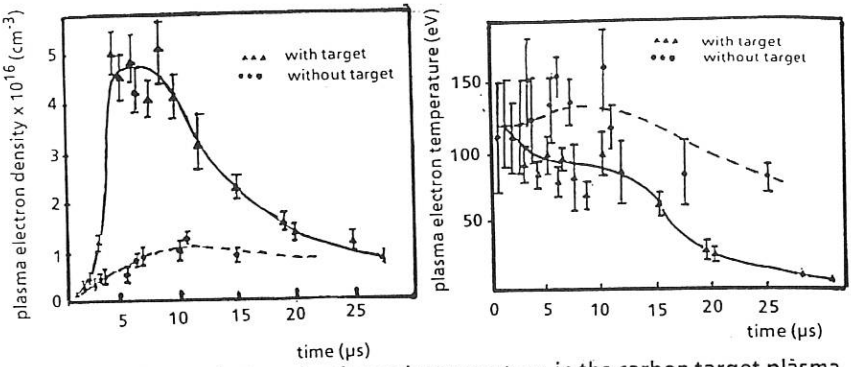


Fig. 3 Plasma electron density and temperature in the carbon target plasma corona at a distance of 3 cm from the graphite target.

The electron temperature is less than without target but up to 15 μs remains at the rather high value of 80 eV and drops afterwards due to radiative cooling. For tungsten the plasma electron density at distances above 3 cm from the target is around (2 - 3) 10^{16} cm^{-3}. Contamination with ablated tungsten is negligible or at least not sufficient to radiatively cool the plasma stream.
Space resolved, time integrated and time resolved (resolution 0.1 μs) soft x-ray spectroscopy (SXR) was applied for analysis of the plasma corona. A column length of 7 cm, with space resolution of 2.5 mm was observed. For carbon according to Fig. 4 radiation mainly from CV lines is observed, thus roughly indicating plasma temperatures between 40 - 50 eV. From time and space resolved SXR measurements it is concluded that the radiation after 1 μs is distributed quite homogeneously over the observable volume of the corona. This quasistationary situation is 2MK-200 typical, and is due to the short distance of the target from the solenoid being less than the range of the plasma stream in the corona. So the fastly expanding plasma corona continuously is damped into the solenoid and continuously is reproduced at the cold end by the still impinging plasma stream. Quite

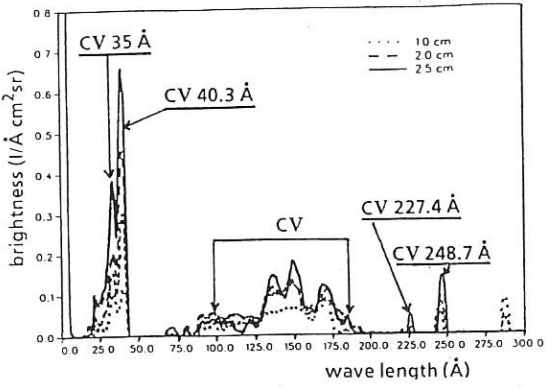


Fig. 4 Time integrated soft x-ray spectrogram for carbon plasma corona at different distances from the target.

similar results were obtained for boron nitrite (BN), for quartz targets and for aluminum. Again a hot plasma corona is produced. Radiation in these cases is observed from BV and NVI lines at 48.6 Å and 29 Å, from SiVII lines at 55 Å and from AlVI lines at 59 Å. In all these spectrograms only very weak radiation from CV lines were detected, their intensity being below 10 % of the line intensity for a carbon target plasma. Therefore contamination of the plasma stream with carbon is negligible small. For tungsten the radiation intensity grows sharply towards the target surface and at a distance of 1 cm it is 10 times larger than at 3 cm. A corona is not observed.
Optical spectroscopy was performed for regions close to the target surface. For carbon mainly radiation from CIV at a wavelength of 4658.3 Å is observed. A rough estimation of the plasma temperature yields values below 5 eV. For tungsten the plasma layer close to the target shows only continuum radiation. It remains for the whole interaction period within a distance of 10 mm from the target. The temperature is estimated to be around 3 eV.
Time dependent erosion measurements were performed applying optical interferometry. A high speed streak camera with time resolution of 0.4 µs is used for registration. As the sample has to be transparent for the probing light source a quartz sample was used. The radiation passing through the target was determined with a calorimeter and amounted up to 1 % of the incident plasma energy. Erosion starts at an energy density of 40 J/cm^2 and approximately is proportional to the energy density of the plasma stream. The quartz erosion rate for an incident energy density of 150 J/cm^2 is constant and with 0.024 µm/µs rather small. The overall erosion remains as for carbon and tungsten below 1 µm.

Conclusion

In the 2MK-200 plasma stream target experiments for materials such as carbon, boron and aluminum a rather hot but low dense target plasma corona is produced. For carbon the plasma edge expands with velocities of about (3 - 4) 10^6 cm/s along the magnetic field lines. The temperature in the corona amounts up to 80 eV.The impinging plasma stream penetrates up to 10 cm into the corona. It's energy is volumetrically converted into soft x-ray line radiation. The corona is optically thin and the radiation escapes through the surfaces of the corona. Thus it acts as an effective energy dissipation system.Close to the carbon target there is a rather dense cold plasma layer which expands with velocities of around 2 x 10^5 cm/s. The fraction of radiative energy finally reaching the region close to the target is less than 5 % of the energy density of the plasma stream.
For high Z materials such as tungsten no hot target plasma corona is observed in the 2MK-200 experiments. The plasma stream penetrates only a few mm into the rather dense target plasma cloud. The energy of the plasma stream is mainly converted into radiation in the rather thin interaction zone. Most of the energy is backradiated and only a fraction in the order of a few % is transported across the plasma layer to the target.

Acknowledgement

The authors thank Paul Rockett and John Hunter from Sandia National Laboratory for providing a transmission grate spectrometer and for assistance in the first SXR measurements.

References

[1] A. Sestero, Nucl. Fusion, 17 (1977), 115.
[2] N.I. Arkhipov et al., Proc. 12th, Int. Conf. Plasma Phys. and Controlled Nucl. Fus. Research, Nice France (1988) Vol. 2, p. 683.
[3] N.I. Arkhipov et al., Fusion Technology 1992 (North Holland, Amsterdam 1993), Vol. 1, p. 171.

EXPERIMENTAL MEASUREMENTS AND MODELING OF IMPURITY TRANSPORT IN THE DIVERTOR AND BOUNDARY PLASMA OF DIII–D*

W.P. West, S.L. Allen,† N.H. Brooks, R.D. Campbell,Δ D.N. Hill,† K. Krieger,◊ A.W. Leonard, T.W. Petrie, G.T. Sager, M.J. Schaffer, G.M. Staebler, D. Whyte,# and R.D. Wood†

General Atomics, P.O. Box 85608, San Diego, CA 92138-9784

Analysis of trace impurity injection experiments on DIII–D during a beam power scan is presented. Spectroscopic measurements indicate that as beam power is increased, and concomitantly ELM frequency and scrape-off-layer thickness increase while energy confinement decreases, the core impurity content decreases only slightly. Modeling of the edge plasma using the UEDGE 2D and NEWT1D plasma fluid codes indicate that as beam power is increased, the parallel forces on an impurity ion increase in the direction from the divertor and toward the core plasma. Experiments using the divertor cryopump to induce higher parallel particle flow toward the divertor demonstrate significant reduction in core impurity content. These results indicate that parallel forces on impurity ions in the scrape off layer are playing a significant role in core impurity content.

Introduction

Containment of impurities within the divertor of a tokamak has long been an important issue, since the large heat and particle flux to the divertor plates naturally generates large impurity influxes which would be deleterious to the core plasma. With the recent effort to demonstrate the ability to actively reduce and control the heat flux to the divertor plates, in order to demonstrate realistic operating scenarios for the next generation long pulse tokamaks, there is renewed interest in impurity containment. This interest is focused on containment of impurities which are intentionally injected in order to enhance radiated power in the divertor and thus reduce the heat flux carried along field lines to the divertor plate. Since the real need for heat flux reduction is in long pulse and/or steady state operation, injection of recycling impurities, such as rare gases, is needed. The purpose of this paper is to briefly examine some experiments on DIII–D in which trace levels of rare gas impurities were puffed into the plasma, and through modeling to examine the various transport mechanisms that were contributing to the observed impurity core content.

The ability to maintain a high concentration of a recycling impurity in the divertor while maintaining low core plasma impurity levels is related to a number of transport mechanisms. The primary mechanism in the scrape off layer (SOL) that keeps the impurity ions from migrating back to the core plasma is the flow of the background plasma toward the divertor plate. Working against the flow is the thermal gradient force.[1] For recycling impurities, the flight of neutrals in the tenuous plasma region between the SOL and the vacuum wall is also important. When the neutral impacts the SOL plasma, the mean free path for ionization is important. Once an ion has reached the core plasma, it will remain there until is diffuses back to the SOL or is expelled by an ELM.[2] The distribution of the impurity within the divertor and core plasma will thus be determined by these various transport mechanisms.

Experiment

To begin exploring this important physics area on DIII–D, an experimental run was carried out in which a trace amount of argon or neon was injected into steady ELMing H–mode discharges. Parametric scans of beam power, plasma current, and toroidal field strength were conducted on a shot to shot basis. Spectroscopic measurements of line emission from the core plasma using the SPRED VUV instrument in the wavelength range of 100 to 1100 Å provided information on the core content of argon and neon. In the case of neon, charge exchange emission from a neutral heating beam which crosses the SPRED viewing cord near the central axis was observed. By modulating the neutral beam, and modeling its attenuation,[3] accurate core neon densities could be obtained. With argon, such charge exchange emission was not observed and core densities are obtained

*Work supported by the U.S. Department of Energy under Contract Nos. DE-AC03-89ER51114, W-7405-ENG-48, and DE-AC03-76DP00789.

†Lawrence Livermore National Laboratory.

ΔSandia National Laboratory, Albuquerque.

◊Max Planck, Garching.

#Centre Canadien de Fusion Magnetique .

with the aid of modeling using the MIST transport code.[4] Electron density and temperature profiles of the core plasma, needed for the MIST modeling, are obtained using the multipulse Thomson scattering system. A six chord visible spectrometer (MDS),[5] with a spectral window of about 140 Å, setable from 3900 Å to 7100 Å views the divertor from above. The view chords are fixed in position, viewing 2 cm diameter spots placed at about 15 cm intervals across the floor of DIII–D from near the inner wall to beyond the typical outer strike point. This spectrometer was set to view emission from either ArII or NeII ions.

Here we will focus on the beam power scans with neon and argon injection. The effect on the core content for both species as a function of beam power is shown in Table 1. For both species, the core content is not observed to change dramatically with beam power. The neon content, which is derived from charge exchange emission, is more accurate than the argon content, which is obtained using emissivities derived from MIST. The neon data indicate some drop in core content as the beam power is increased. ArII line intensities as a function of beam power measured with MDS for two chords, one viewing through the vicinity of the X-point into the private flux region and one viewing near the outer strike point, are also given in Table 1. As beam power is increased, the ArII emission near the strike point does not change appreciably, indicating that the recycling of Ar at the plate is not affected by increasing beam power. However the emission from near the X-point drops dramatically as beam power increases, which reflects the fact that the electron temperature predicted by UEDGE[6] at the 1 cm flux surface begins to exceed the ionization potential of ArII near the X-point..

TABLE 1

Impurity	Beam Power (MW)	τ_E (ms)	Integral n_e Across SOL (a.u.)	ELM Frequency (Hz)	Core Impurity Density (a.u.)	MDS X-point (a.u.)	MDS OSP
Argon	4.6	165	4.2	30	0.83	230	315
	9.1	130	8.4	85	1.00	120	340
	13.2	100	12.4	220	1.01	50	340
Neon	7.0	190	8.4	45	1.15	190	88
	9.0	160	10.9	60	1.00	100	58
	13.5	110	13.3	215	0.88	30	73

Modeling

The UEDGE two dimensional fluid model and the NEWT1D[7] one dimensional fluid model have been used to investigate the effects of plasma flow and thermal gradient terms in the beam power scan. Both codes are based on the Braginski equations.[8] The UEDGE code input includes the power flux across the separatrix and the recycling coefficient at the plate. The electron and ion particle and thermal diffusivities are also inputs, and are adjusted until reasonable agreement is obtained with available midplane plasma data, such as Thomson scattering electron densities and temperatures and charge exchange spectroscopy ion temperatures just inside the separatrix and in the SOL. In previous work, the UEDGE results have been benchmarked against DIII–D discharges by comparing the resulting plasma density, temperature, and heat flux profiles against measured values. Best agreement is usually obtained when the ambipolar field is included in the model, and when an ad-hoc model for impurity radiation (constant carbon fraction of a few percent) is included. At the present time, UEDGE does not routinely include impurity transport, so the NEWT1D code was used to investigate impurity phenomena.

The predicted forces from the plasma flow and the thermal gradients along a flux tube lying about 6 mm outside the separatrix at the midplane for the 9.1 and 13.2 MW beam power discharges are shown in Fig. 1. These forces are calculated from the UEDGE predicted plasma following Neuhauser et al.[7] In this case, although the fluid flow is every where toward the plate, the ion thermal gradient force away from the plate becomes dominant just a few centimeters poloidally away from the plate. Impurity ions in this region will be forced toward the midplane, and thus toward the core plasma. As expected, this thermal gradient term is seen to increase as the beam heating power is increased. This effect can be dramatically illustrated using the NEWT1D code. In Fig 2, the predicted neon ion poloidal distribution is shown for two cases of trace impurity injection. In both cases the neon injection is very small, and the resulting background plasmas are essentially identical.

In case 1 the neon is injected into the divertor along a 1 cm long region just above the plate. The injection is assumed to be steady state and to achieve a steady state solution an impurity recycling coefficient at the plate of 0.985 is assumed. In the injection region the viscous force strongly dominates and essentially no neon is able

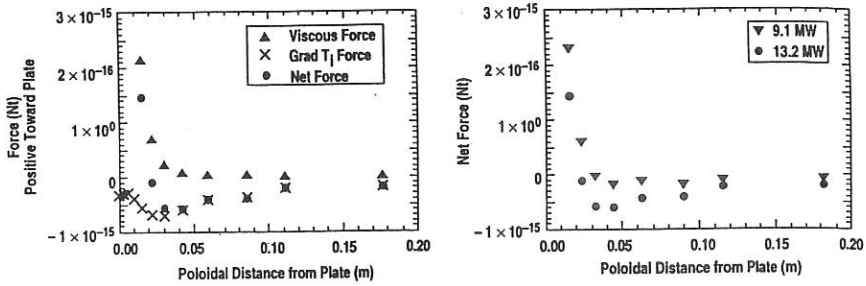


Fig. 1. The forces on a test ion (Ar+6) with zero velocity in the lab frame due to the plasma flow and thermal gradient terms are shown as a function of poloidal distance from the outer strike plate. On the left are the three most important terms using plasma parameters are obtained from the UEDGE code, for an injected beam power of 13.2 MW. On the right the net forces are shown for discharges with 13.2 and 9.1 MW of injected beam power.

of 0.985 is assumed. In the injection region the viscous force strongly dominates and essentially no neon is able to reach the SOL above the X-point. In case 2 the same neon throughput is injected along a 5 cm length poloidally above the plate. The injection reaches into the region where the thermal gradient force dominates, and a significant neon density is seen to build up above the X-point. In the open divertor configuration of DIII–D, normal recycling of neutral neon on the divertor plate should result in a significant flux of neutral neon reaching the divertor plasma a few centimeters above the plate, this net force away from the divertor and toward the core could be quite deleterious.

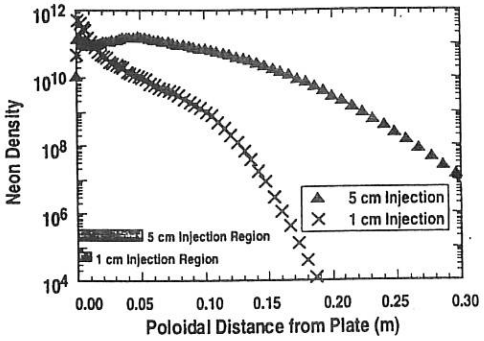


Fig. 2. Neon distribution along flux tube modeled using NEWT1D for plasma forces similar to those shown in Fig. 1(a). The circles are for injection of neon along a 1 cm distance just above the divertor plate, the crosses are for injection along a 5 cm distance above the plate.

Induced Flow Experiment

Direct experimental evidence has been produced on DIII–D that indicates a strong flow can be induced in the SOL and can keep the core plasma clean in the presence of a strong, steady argon puff.[9] A lower single-null configuration is used with a plasma current of 1.5 MA and neutral beam injection of 8.5 MW. In this case, the plasma is positioned such that a strong pumping condition is achieved with the cryopump which lies within a pumping plenum near the divertor floor at the outer wall. Deuterium can be steadily puffed in at the midplane and pumped at the outer strike point at a rate of 200 torr liters/s and a steady plasma density maintained. Simultaneously, argon can be puffed at the midplane, yet very little argon is observed in the core plasma with SPRED and little effect on radiated power is seen. Table 2 gives the observed core Ar content of four pumped discharges on DIII–D, with and without deuterium puffing and at two levels of Ar puffing. Also given is an effective Ar confinement time, given by the core plasma Ar content divided by the Ar puffing rate.

TABLE 2

	Case 1	Case 2	Case 3	Case 4
D_2 puff (torr-l/s)	200	0	200	0
$n_e(0)$ (10^{20} m^{-3})	1.0	0.7	1.0	0.7
Ar puff (torr-l/s)	0.5	0.5	1	1
Puff location	Divertor	Divertor	Midplane	Midplane
Central (r=0) Ar (10^{15} m^{-3})	2.9	56	20	190
τ_{Ar} (ms)	1	20	4	40

Using the plasma electron temperatures and densities from the UEDGE model as shown in Fig. 1, a rough estimate of the flow required to overcome the thermal gradient forces can be obtained by artificially increasing the plasma flow velocities until the viscous force toward the plate equals the temperature gradient forces away from the plate at a location just below the X-point. This adjusted flow can then be used to estimate the additional particle throughput required to provide a net force toward the plate. For this case an increased throughput of about 400 torr·l/s is required, in reasonable agreement with the experiment where 200 torr·l/s was observed to profoundly influence the core Ar content.

Discussion

The measurement of neon core plasma content during trace neon injection using charge exchange recombination radiation indicates that as beam power is increased (resulting in decreased core energy confinement time, increased ELM rate and a thicker SOL) the neon concentration in the core drops only slightly. Edge plasma modeling using both the UEGDE and NEWT1D codes indicates that the parallel ion temperature gradient from the divertor plate to the midplane is sufficiently strong to overcome the viscous drag and results in a net force on an impurity ion driving it toward the midplane (except very near the plate). As beam power is increased, the ion temperature gradient also increases, and may be limiting the beneficial effects discussed above. Using the cryopump on DIII–D, direct experimental evidence has been obtained that increased particle flow can reduce significantly the core argon content during argon injection experiments.

These results indicate that baffling of the divertor region to block the passage of recycling impurity neutrals around the plasma boundary may not be sufficient to provide good radiative divertor operation. Increased particle flow to overcome parallel thermal gradients may also be required. Along with new baffling structures, the radiative divertor configuration currently planned for installation on DIII–D willl include new cryopumps, two each in the lower and upper divertors. The combination of baffling and increased pumping speed should provide enhanced particle throughput and improved impurity containment.

[1]J. Neuhauser et al., Nucl. Fusion **24**, 39 (1984).
[2]M. Perry et al., Nucl. Fusion **4**, 701 (1990).
[3]D.F. Finkenthal et al, Proceedings 19th EPS Conference on Controlled Fusion and Plasma Physics, Innsbruck (1992).
[4]R.A. Hulse, Nuclear Technology/Fusion **3**, 259 (1983).
[5]N.H. Brooks et al., Rev. Sci. Instrum. **63**, 4941 (1992).
[6]T.D. Rognlien et al., J. Nucl. Materials **196-198**, 347 (1992).
[7]R.B.Campbell et al., J. Nucl. Materials **196-198**, 426 (1992).
[8]S.I. Braginski, Rev. of Plasma Phys. **1**, Consultants Bureau, New York, p. 205 (1965).
[9]M.J. Schaffer et al., to be submitted to Nucl. Fusion..

ICRF POWER MODULATION EXPERIMENTS ON ASDEX-UPGRADE

C. Hoffmann, F. Braun, W. Suttrop, J.-M. Noterdaeme, H.-U. Fahrbach, W. Hermann
ASDEX-Upgrade Team and ICRH Team

Max-Planck-Institut für Plasmaphysik, EURATOM Association,
D-85748 Garching, Fed. Rep. of Germany

1 Introduction First power modulation experiments with ICRF heating were conducted on ASDEX-Upgrade. For these experiments we chose rather low modulation frequencies (18 Hz and 38 Hz) and strong modulation (squarewave: max. > 1 MW, min. < 0.1 MW, duty cycle 50%). For various diagnostic signals, phase and amplitude spectra and profiles were obtained. The experiment was simulated by a transport calculation that takes transport of the fast particles into account.

2 Set-up of the experiments Five similar discharges of $\approx 15\%$ H in D at $B = 2$ T and $I_p = 800$ kA were performed where modulated ICRH was the only additional heating. All discharges remained in L-Mode. Three ICRF generators were simultaneously modulated, all of them working on the H-fundamental frequency, two of them at 30 MHz and one at 31.6 MHz. The difference in frequency amounts to a 9 cm shift in the resonance location. In two shots the modulation frequency was 18 Hz and for three shots 38 Hz. The 50% duty cycle implies that only the odd harmonics are present in the power spectrum. The largest modulation depth was between 120 kW and 1340 kW (# 4599). Even switching to zero was technically feasible (#4596: 0 - 800 kW). The line averaged density through the center was $6 \cdot 10^{19} \mathrm{m}^{-3}$. The peak electron temperature was 1500 eV, with heavy sawtooth activity of $\Delta T|_{r=0} = 300 - 500$ eV.

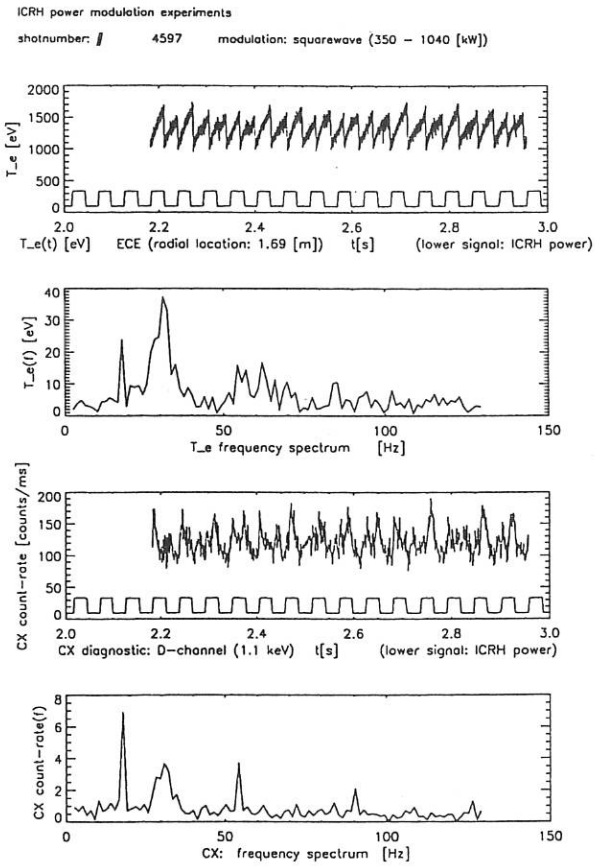
3 Diagnostics The key diagnostics investigated encompass two independent measurements of the electron temperature and the ion energy distribution. They are (τ_s = sample time):

- Electron cyclotron emission measured by a Radiometer ($\tau_s = 5 \cdot 10^{-5}$ s).
- Thomson scattering by a YAG-Laser ($\tau_s = 2.425 \cdot 10^{-2}$ s).
- Charge exchange analyzer for neutralized fast H and D particles ($\tau_s = 1 \cdot 10^{-3}$ s).
- Neutron rate with two different counters (U235, He231) ($\tau_s = 10 \cdot 10^{-2}$ s).

The measurements relating to the ion energy distribution allow of course only integral properties of the ion distribution. For the lower modulation frequency the sample frequency of the Thomson scattering diagnostic is marginal. The modulation frequency was chosen such that the ratio is not an integer but $\tau_{Thomson}/\tau_{Modulation} \approx 2.3$. Therefore after fourier-analyzing a larger time interval (≈ 800 ms), phases and amplitudes could well be extracted. At 38 Hz modulation frequency the Thomson scattering could not be used for phase measurements. - The plasma edge density and temperature were measured with a DCN-interferometer ($\tau_s = 1.2 \cdot 10^{-3}$ s) and H_α photo diode arrays ($\tau_s = 4 \cdot 10^{-4}$ s).

4 Fourier spectra Fig. 1 shows the time traces of the ECE-signal at a major radius of 1.69 m and the charge exchange signal of D^0 in the lowest energy channel (1.1 keV) and their respective spectra. The average sawtooth frequency of this discharge was ≈ 31 Hz. Due to the irregularity of the sawtooth period its spectral broadening shrinks the amplitude so much that it is of the same order as the modulation fundamental

Figure 1



at 18 Hz. The ECE and the CX-spectrum show obvious similarities. The frequency components of the sawteeth also appear in the CX-spectrum. The ratio of modulation to sawtooth amplitude is inverse for the two spectra. We conclude that the fast H ions preferentially heat the D majority ions. Calculations show that for the rather high H minority concentration of $\approx$ 15% this is indeed the case. For the same reason the CX-signal for D shows the higher odd harmonics very clearly which can hardly be identified in the ECE spectrum.

Fig. 2 shows the phase lag of the H and D signal with respect to the modulation frequency plotted over the particle energy. The H measurement extends up to 30 keV and the D measurement up to 15 keV. The count rate for D in the lower energy channels is 100 - 200 counts/ms. For the H channels it is 5 - 10 counts/ms. Since D stays close to a maxwellian at 1.5 keV, the count rate in channels above 7 keV becomes too small to be useful for phase measurements. On the other hand due to the RF-drive the count rate of the H-minority is sufficient up to the highest energies. Theory predicts that direct RF

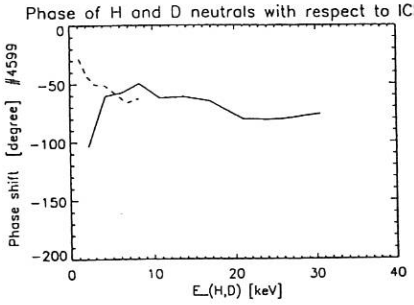


Figure 2

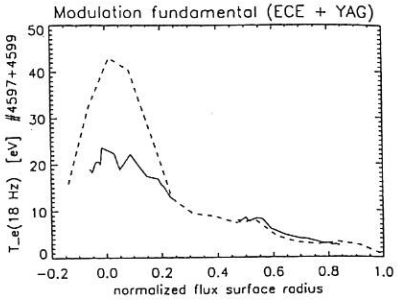


Figure 3

absorption through D at its second harmonic frequency is negligible. The Deuterium is thus only heated through collisions with the minority. The D-signal should therefore lag behind the H-signal. This is not the case for energies below 5 keV. We think that at low energies particles coming from the edge conceal the phase relationship in the center.

5 Amplitude and phase profiles Fig. 3 shows the amplitude profile of the modulation fundamental for the ECE (solid line) and the Thomson scattering diagnostic (dashed line) over the normalized flux coordinate. Presently the radiometer covers only about 1/3 of the minor radius due to the limited number of amplifiers on the intermediate frequency. To get a more complete profile in one discharge (#4597) the central part of the profile was measured and in another (#4599) the outer part. For the same magnetic field strength the gap inbetween is presently not accessible at all. Since the modulation depth and maximal power was different for these shots (#4597: ΔP = 690 kW and #4599: ΔP = 1220 kW) the amplitude of #4599 was accordingly scaled both for the ECE as for the YAG profile to make the profiles comparable. The difference is small outside the central deposition region but substantial in the center. We have to postpone definite conclusions until the ECE measurements cover the whole radius. A kink appears in the temperature profile at $\approx$ 0.58 of the minor radius. Reasons for this could either be a power deposition at this point or otherwise drastic local changes in the transport. Concerning the latter we ascertained that the location of the kink coincides rather well with the q=2 surface. But how this may affect the profile in this way is unclear. Since two independent diagnostics show this behaviour as weli as there are 6 ECE channels that map this region this might be significant, but we did not determine the error bars yet.

6 Determination of deposition and χ_e profile The direct method to determine the deposition profile is to increase the modulation frequency so that broadening of the $\tilde{T}$-profile through transport decreases. For ECR heating modulation frequencies up to the kHz region were already used. For ICRH the limiting factor of frequency increase is the dynamics of the fast particles and their collisional coupling to the electrons. We have not yet tried where this limit is. Without a good estimate of the deposition profile it is futile to derive a χ_e-profile. Fitting the phase profile under the assumption of δ-peaked deposition in the center we found χ_e to vary from 3 - 16 m^2/s from inside to outside. But if power is locally coupled to the electrons away from the ion resonance zone these values for χ_e are meaningless.

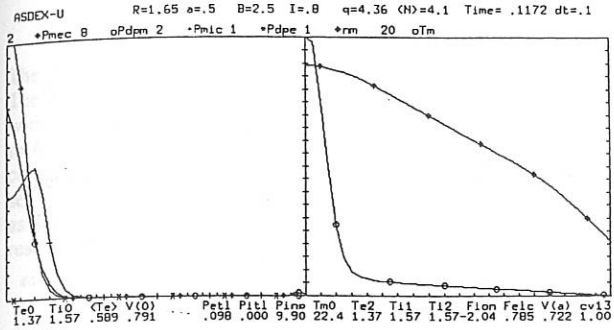


Figure 4: The collisional power coupled to the background drops very fast outside the deposition region. The majority absorbs less in the center where T_m is high and electrons are favored but more outside where T_m is low.

Pmec: Collisional power from minority to electrons; Pmic: - to ions; Pdpm: Power deposited in the minority; nm,Tm: minority density- and temperature profile

7 Transport simulation Minority heating with ICRH was calculated with the two-fluid transport code ASTRA which was extended by a third equation for the minority temperature. In principle a RF-heated minority has to be described kinetically since the distribution function deviates strongly from a maxwellian. There are two arguments that make it possible to use but one temperature equation to describe the minority: a) for low concentration/strong heating the distribution is mainly characterized by the tail temperature, b) the collisional interaction with the background is an integral property of the distribution: a mean minority temperature can be defined that has the same collisional interaction with the background (ratio of power fluxes) as the *true* distribution. The validity of the approximation was checked against Fokker-Planck calculations. The transport matrix was extended by coefficients that relate the heat flux of the minority to the thermodynamic forces:

$$q_m/(n_m T_m) \;=\; -HM \cdot \frac{1}{T_e}\nabla T_e - XM \cdot \frac{1}{T_i}\nabla T_i - DM \cdot \frac{1}{n_e}\nabla n_e - EM \cdot \frac{1}{T_m}\nabla T_m$$

The coefficient XM that links the ion temperature gradient to the minority heat flux was assumed to be the most important one. Fig. 4 shows the profiles of the minority temperature and the collisional powers that are coupled to electrons and ions as a result of a transport calculation with parameters as in the experiments. The legend on top of the pictures explains which marker belongs to what profile. The moment in time for which the profiles are shown is at the end of one modulation half cycle at maximum power.

8 Conclusions and Outlook The first ICRF-modulation experiments on ASDEX-Upgrade have shown that the phase information can be filtered from all relevant electron- and in particular the ion diagnostics. The ratio of the collisional power flux to electrons and majority ions can be derived from the available data. The discharges were in a regime that favours the majority ions over the electrons. To address the deposition profile and plasma transport further experiments will be conducted with higher modulation frequencies, multiple frequencies, lower minority concentration and heating without ion resonance.

Changes in the edge plasma due to ELMs, a study using coupling measurements in the ICRF range

J.-M. Noterdaeme, M. Brambilla, D. Coster, J. Gernhardt, C. Hoffmann, F. Hofmeister, J. Neuhauser, D. Reiter*, R. Schneider, H. Zohm,
ASDEX Upgrade Team, ICRH Team, NI Team
Max-Planck-Institut für Plasmaphysik
Euratom Association - D-85748 Garching bei München, Germany
* Forschungscentrum Jülich, KFA, Jülich, Germany

ABSTRACT - During an ELM the density at the separatrix increases and the density profile in the scrape-off layer flattens. From fast measurements (20 μs) of the resulting variation of the ICRF antenna resistance, conclusions can be drawn on the time evolution of those changes. This allows a refinement of the ELM models in fluid codes and indicates that, for ASDEX Upgrade and a power through the separatrix (excluding radiation power) of 1.6 MW, the time interval during which the ELM increases the transport at the separatrix is of the order 1 ms.

INTRODUCTION

The sudden expulsion of energy and particles during an ELM[1] provides an increased transient load in the divertor which complicates the power handling capability of future devices. The transients, measured in or near the divertor with high time resolution as changes in H_α, in the radiation of impurities[2] or as increased power loading using fast thermography, are used to calibrate codes which model[3] the ELM behaviour *and* the transport in the scrape-off to the divertor. A more direct validation of the ELM model itself is provided by comparing the predicted variation in time and space of temperature and density at the plasma edge, with measurements. The coupling of the ICRF to the plasma is sensitive to edge density and edge profile. Fast measurements (time resolution of 20 μs) of the antenna resistance thus allow conclusions to be drawn on the evolution of these parameters.

EXPERIMENTAL DATA

ELMs are obtained over a wide range of parameters in the H-mode. The measurements were performed on ASDEX Upgrade, a tokamak with R=1.65m, a=0.5m, b=0.8m, in single null configuration. The plasma current was 800 kA and the magnetic field 2 T, with the ion gradient-B drift towards the X-point.

Data were obtained for discharges heated with ICRH (up to 2.8 MW) alone or in combination with NI, in the H-minority heating regime (D-majority, H/D=15 %).

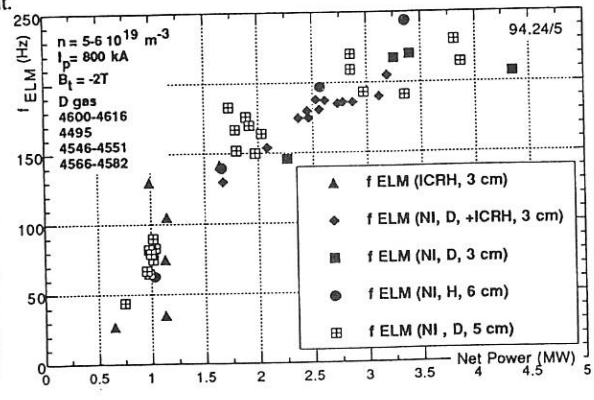


Fig. 1. Variation of the ELM frequency as a function of the power through the separatrix (P_{OH} + 0.75 P_{ICRH} + 0.85 P_{NI} - P_{rad}, where P_{ICRH} is the RF generator net output power, P_{NI} the net power injected in the torus and P_{rad} the power radiated inside the separatrix, calculated from bolometric measurements).

The distance from the separatrix to the antenna was feedback controlled to a constant 3 cm. The ELM frequency in these discharges behaves similarly to the ELM frequency in discharges with purely NI heated plasmas (H_0 in D or D_0 in D), and with antenna-separatrix distances up to 6 cm (Fig 1.) so that within this range of distance and for these heating methods or combination thereof, the ICRF heated discharges can be considered representative of the whole set. For a discharge with 2.8 MW ICRH power (net power through the separatrix of 1.6 MW, as defined in fig. 1), the time traces and the evolution of the antenna resistance with high time resolution are shown in fig 2.

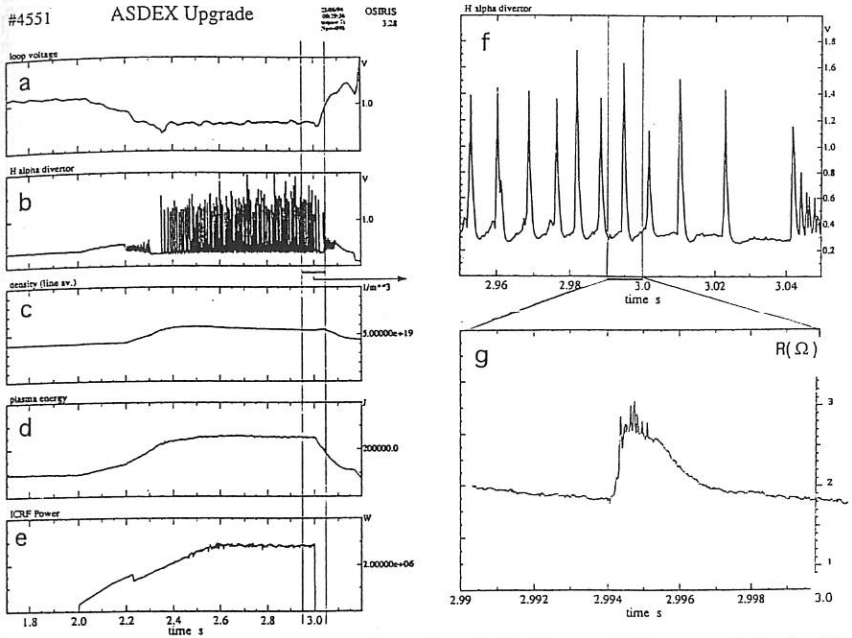


Fig 2. Experimental traces for (a) the loop voltage, (b) Hα in the divertor, (c) line averaged density, (d) plasma energy, and (e) ICRF power. Expanded (f) the traces for Hα in the divertor and with even higher time resolution (g) the variation of the antenna resistance during an ELM .

B2-EIRENE ELM MODELLING

The ELMs are simulated in the code by an ad hoc change of the transport parameters[3] during a imposed time interval : the particle diffusivity is switched from 0.5 m^2s^{-1} between ELMs to 5 m^2s^{-1} during the ELM, and the electron and ion thermal diffusivities from 0.1 to 5 m^2s^{-1}. Experimental inputs are the value of the separatrix density between ELMs, the power through the separatrix and the time between ELMs.

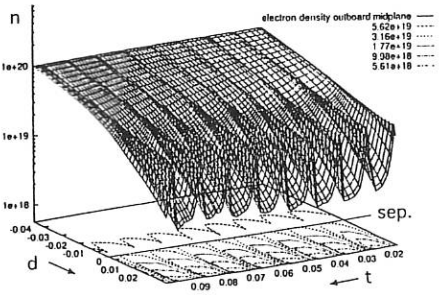


Fig. 3. 3-D plot of the time evolution of edge density based on the B2-EIRENE code

B2-EIRENE provides the time evolution of the separatrix density and of the density gradient length at the separatrix. They were used as input for the coupling code which calculates the antenna resistance. The time interval during which the transport parameters in B2-EIRENE have to be increased was varied to match the calculated time evolution of the antenna resistance to the experimentally measured one. Fig. 3 shows the predicted effect of the ELM on the density profile at the edge : the density at the separatrix increases and the profile flattens. The coupled variation of separatrix density and density gradient length in the course of consecutive ELMs is shown in fig. 4 for two values of the time interval (100 μs, 1 ms) the increased transport is switched on. Also shown is the variation of the separatrix density, as a function of time.

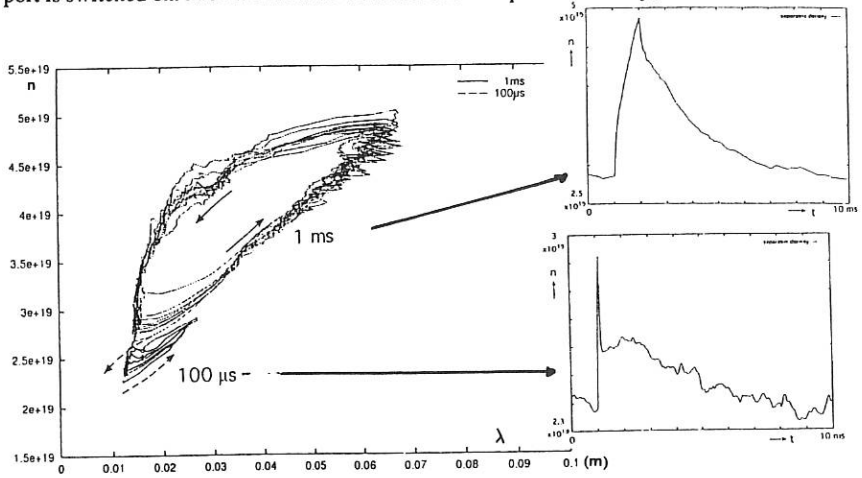


Fig. 4. Variation of the edge density and edge gradient length during ELMs as modelled by the B2-EIRENE code for two values of the time interval (100μs and 1ms) during which transport is increased , with the corresponding temporal evolution of the separatrix density for both values of this time interval.

CALCULATION OF THE ANTENNA RESISTANCE

The loading resistance was calculated with the FELICE[4] coupling code for the different combinations of density at the separatrix and density gradient length outside the separatrix predicted by the B2-EIRENE code (fig. 4) during an ELM. Inside the separatrix the density was connected to a parabolic density profile, using an exponential such that the gradient at the separatrix was continuous. Outward radiation conditions were imposed to avoid the appearance of standing waves, otherwise overestimated in the model because of the slab geometry. Fig 5. shows some examples of the profiles used.

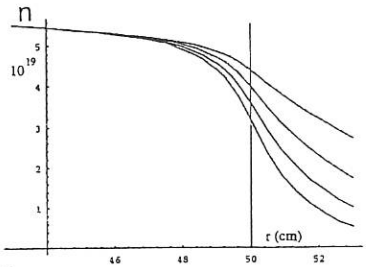


Fig. 5. Model for the variation of the edge density and gradient length for the FELICE code.

COMPARISON OF MODEL AND EXPERIMENT

Using the time evolution of the separatrix density and the density gradient length at the separatrix predicted by B2-EIRENE, the calculated antenna resistance can be plotted as a function of time. This can be done for different values of the time interval during which the

transport in the ELM model is increased. Comparison of the calculated loading resistance with the measured antenna resistance indicates that, to match the time evolution of the experimental data, the time interval of increased transport in the ELM model of the B2-EIRENE code should be of the order of 1 ms. Interestingly, the combination of the change of density at the separatrix and of the density gradient length has the effect that after a fast rise, the antenna resistance saturates and starts to decrease even during the phase of the ELM where the separatrix density still increases. During this time the experimental curve is rather spiky while, when the ELM relaxes, it is much smoother. This tends to confirm that the increased transport phase and the ELM relaxation phase are not separated by the maximum in the antenna resistance but rather by the different smoothness of the curve. Other fast measurements (e.g. a loop voltage, Fig. 7) similarly indicate that during a time of the order of 1 ms, very fast transients (on the order of 10μs) occur. This work identifies the 1 ms time scale as the time interval during which the transport due to the ELM is increased. Future direct measurements of the edge density by reflectometry will allow a check of this hypothesis.

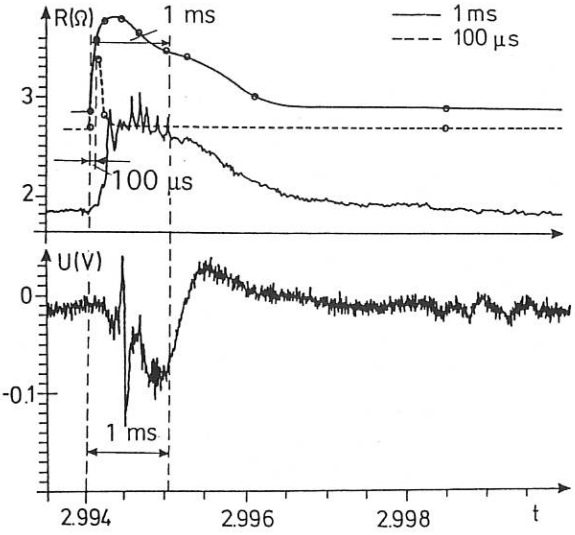


Fig. 7. Comparison of the measured antenna resistance for the discharge shown in fig. 2, and the loading resistance, calculated by FELICE based on the prediction of the plasma density and gradient length at the separatrix and its evolution during the ELM by the B2-EIRENE code from fig.4. Time of increased transport in the ELM model is 100 μs and 1 ms. Shown is further a fast measurement of a loop voltage indicating similarly a variation on the time scale of 1 ms.

CONCLUSION

The fast measurement of the antenna resistance provides information on the changes of edge density and edge gradients and allows a better validation of the ELM model for the scrape-off layer codes. To match the calculated loading resistance and the measured antenna resistance, the time interval during which the transport has to be changed to model the ELM in ASDEX Upgrade and for the power considered, is of the order of 1 ms, on the higher side of the expected range. From the comparison, it is further clear that prudence is recommended when evaluating ELM time scales from the measurements of their effects. Some signals can react to the fast energy pulse due to the ELMs; others can, for different reasons, mimic a faster rise time than the time during which the transport is increased.

REFERENCES

1. H. Zohm et al. Characterisation of ELMs on ASDEX Upgrade, 20th EPS, 1993, Vol. 1, 19.
2. A. Field et al. Spectroscopic Investigation of ELM Phenomena in the ASDEX Upgrade Divertor with high time Resolution, 20th EPS, 1993, Vol. 2, 575.
3. D. Coster et al. B2-EIRENE Modelling of ELMs on ASDEX Upgrade, this Conference.
4. M. Brambilla Plasma Physics Contr. Fus. 31 (1989) 723.

B2-EIRENE Modelling of ELMs on ASDEX-Upgrade.

Coster, D.P., Braams, B.[a], Neuhauser, J., Reiter, D.[b],
Schneider, R., Zohm, H.
and the ASDEX-Upgrade and NBI Teams.
Max-Planck-Institut für Plasmaphysik, Garching, FRG

[a]Courant Institute, New York, USA
[b]Forschungszentrum Jülich (KFA), IPP, Jülich, FRG

In order to accurately calculate edge conditions in a tokamak plasma, a number of fluid and neutral codes have been used in the community. The fluid codes share the characteristic of being two-dimensional multi-fluid codes. The packages that best capture the effects of recycling neutrals, are based on Monte-Carlo techniques. In this work the plasma fluid code B2 [BRAAMS, 1986] and the neutrals Monte-Carlo code EIRENE [REITER, 1992] are used together. Up until the beginning of this year, most coupled calculations had been done using the Monte-Carlo code to calculate the equilibrium neutral distribution and consequent particle and energy sources. Recently a time dependent version of EIRENE has become available [REITER and MAY, 1994], allowing time dependent calculations of the edge plasma. This work expands on the work of Neuhauser *et al* [ZOHM *et al.*, 1994] where ELM simulations were done using the B2 code with a fairly simple semi-analytic model describing the neutrals. Some aspects of this work have been described briefly elsewhere ([SCHNEIDER *et al.*, 1994, HERRMAN *et al.*, 1994, REITER and MAY, 1994]).

ELMs are periodic perturbations occurring during H-mode discharges which dump additional particles and energy to the divertor plates and wall. A type I ELM can change the energy content of the plasma by as much as 15%, while a type III ELM can cause a 5% change in energy content [ZOHM *et al.*, 1992]. As a start in modelling ELMs, we impose periodic changes on the transport coefficients used in simulating the edge. While a fully consistent picture with a triggering mechanism based on the density and temperature profiles would be nice, this *ad hoc* scheme provides a useful starting point. Key parameters used are given in table 1. Results for two different densities, two different powers, three different elm periods and for the time-dependent/time-independent have been calculated.

n_e	P	τ_D	τ_I	D	χ_e	χ_i	D'	χ'_e	χ'_i
5.0e19	3 MW	1 ms	10ms	0.5	0.1	0.1	5	5	5
1.0e20	3 MW	1 ms	10ms	0.5	0.1	0.1	5	5	5
1.0e20	1.5 MW	1 ms	7.1ms	0.5	0.1	0.1	5	5	5
1.0e20	3 MW	100 μs	10ms	0.5	0.1	0.1	5	5	5
1.0e20	3 MW	500 μs	10ms	0.5	0.1	0.1	5	5	5
1.0e20	1.5 MW	100 μs	10ms	0.5	0.1	0.1	5	5	5

Table 1: Parameters used to simulate ELMs. Note that higher equilibrium χ's were used in the core to simulate an H-mode profile. n_e is the density used on the inner, core, computational boundary (m^{-3}), P the power passing through that boundary, τ_D is the ELM duration, τ_I the time separating ELM starts, D the particle diffusivity ($m^2.s^{-1}$), χ_e and χ_i the electron and ion thermal diffusivities ($m^2.s^{-1}$). Primed quantities are the values during the ELM, unprimed quantities the values between ELMs.

In the runs done, the changes in the input parameters changed the observed ELMs in expected

ways:

- lowering the density changed the plasma conditions so that higher divertor temperatures were observed (time steps were too large to allow changes in arrival times to have been seen);
- for the longer ELM durations, there was an increased particle and energy flux to the wall, and the energy flux to the divertor plates after the ELM was considerably smaller than just before the ELM, whereas for the shorter ELMs the energy flux to the divertor plates during the ELM appeared as a spike against a more constant baseline;
- halving the input power roughly halved the temperatures.

See figure 1 for the power and particle fluxes.

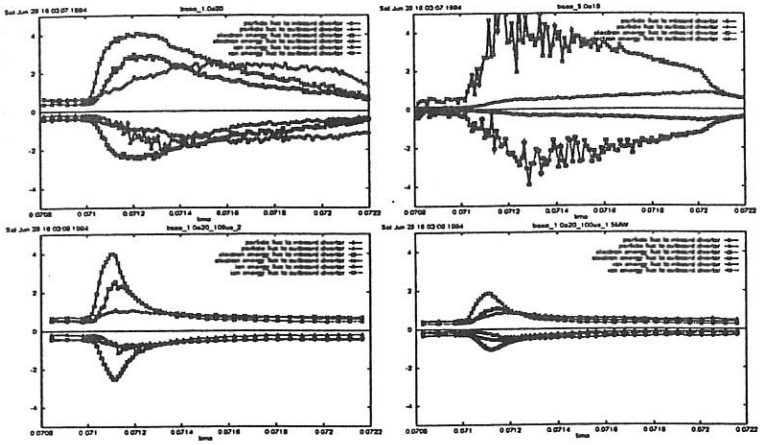


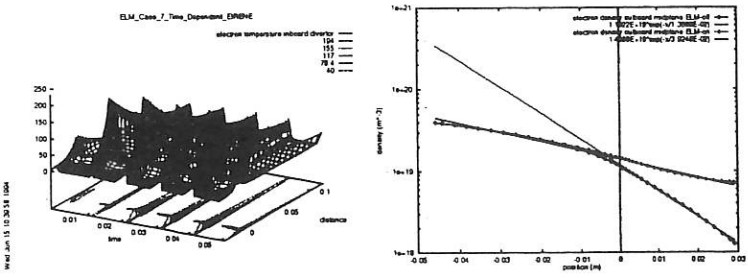
Figure 1: Fluxes to the divertor plates for the 1e20-1ms-3MW, 5e19-1ms-3MW, 1e20-100μs-3MW and 1e20-100μs-1.5MW cases. Energy fluxes have been normalized by 1e6W and particle fluxes by 1e23m^{-3}.

In figure 2a we see how a series of ELMs affects the electron temperature on the inboard divertor.

In figure 2b we show the outboard midplane density profiles for two time points, one during the ELM and one between the ELMs. An exponential is fitted to the density outside the separatrix, and figure 3 shows the variation of separatrix density and scale-length with time. These data have been used by Noterdaeme [NOTERDAEME *et al.*, 1994] to calculate the change induced by ELMs on the ICF antenna voltage. The equivalent scale lengths for the inside midplane seem to be in reasonable agreement with data obtained from reflectometry.

Figure 4 shows the H-α signal from the experiment, and from the code.

The possibility of modelling time-dependent phenomena including the proper time-dependent behaviour of the neutrals opens up new horizons in the realms of model validation. It is to be hoped that transitory occurrences in the plasma will give a better indication of edge transport coefficients than can be obtained by analysis of equilibrium scenarios alone.



a b

Figure 2: (a) Electron temperature at the inboard divertor plate as a function of position and time. (b) Electron density at the outboard midplane as a function of position for two times, together with the exponentials fitted to the data outside the separatrix (note the logarithmic scale for the density plot).

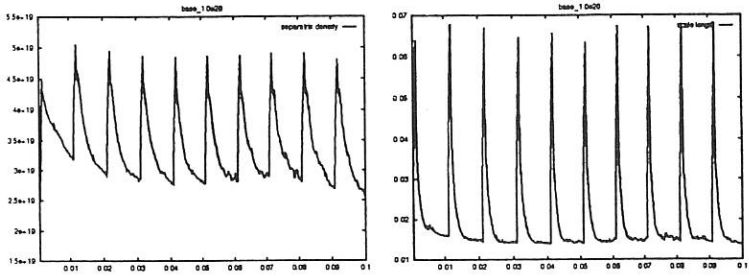


Figure 3: Separatrix density and scale length as a function of time.

The occurrence of ELMs in H-mode plasmas could provide for challenges in designing divertors for future machines (ITER, TPX). This phenomenological simulation of ELMs can be used to examine the impact of different sorts of ELMs on future divertor designs. To do this, a better theoretical understanding of the causes of ELMs would be useful, but in its absence, scalings of ELM parameters with plasma parameters might suffice. A start to this has been made with some preliminary work on ITER being reported at the recent PSI meeting ([SCHNEIDER *et al.*, 1994]).

A reasonable match between experiment and the phenomenological model has been obtained. A closer match should be possible once a fully diagnosed set of discharges are available — at the moment the data consists of thermography data for one set of discharges, ICH coupling data from a different set of discharges, reflectometry from a third set, and Langmuir Probe measurements from a fourth set. The plasma equilibrium differs between these shots, as does the input power. The resultant ELMs have different intervals, as well as different durations. Rather than trying to match the experimental data in detail, a (somewhat) limited parameter scan of the model has been done to see if we can match the range of observed phenomena.

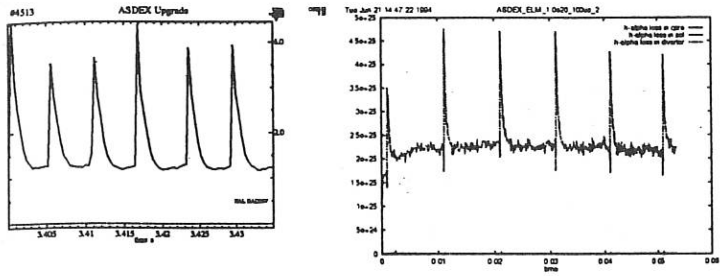


Figure 4: H-α signal as observed on the experiment, and the simulated signal from the code.

References

[Braams, 1986] Braams, B. J. (1986). *Computational Studies in Tokamak Equilibrium and Transport.* PhD thesis, Rijksuniversiteit, Utrecht, Nederland.

[Herrman *et al.*, 1994] Herrman, A., Laux, M., Coster, D., Neuhauser, J., Schneider, R., Weinlich, M., and ASDEX-Upgrade team (1994). Energy transport to the divertor plates of ASDEX-Upgrade during ELMy H-mode phases. In *International Conference on Plasma Surface Interactions in Controlled Fusion Devices.*

[Noterdaeme *et al.*, 1994] Noterdaeme, J.-M., Brambilla, M., Coster, D., Hoffmann, C., Hofmeister, F., Neuhauser, J., Reiter, D., Schneider, R., Zohm, H., ASDEX Upgrade Team, and ICRH Team (1994). Changes in the edge plasma due to ELMs, a study using coupling measurements in the ICRF range. In *this conference.*

[Reiter, 1992] Reiter, D. (1992). The EIRENE Code, Version: Jan. 92 Users Manual. Technical Report Jül-2599, KFA Jülich, Germany.

[Reiter and May, 1994] Reiter, D. and May, C. (1994). Time dependent neutral gas transport in tokamak edge plasmas. In *International Conference on Plasma Surface Interactions in Controlled Fusion Devices.*, Mito, Japan.

[Schneider *et al.*, 1994] Schneider, R. *et al.* (1994). Cold divertor concepts for ITER. In *International Conference on Plasma Surface Interactions in Controlled Fusion Devices.*, Mito, Japan.

[Zohm *et al.*, 1992] Zohm, H., Osborne, T., Burrell, K., Chu, M., Doyle, E., Gohil, P., Hill, D., Lao, L., Taylor, T., and Turnbull, A. (1992). ELM studies on DIII-D and a comparison to ASDEX results. In *European Physical Society Conference on Plasma Physics*, Innsbruck.

[Zohm *et al.*, 1994] Zohm, H., Ryter, F., Fuchs, J., Herrmann, A., Kaufmann, M., Neuhauser, J., Salmon, N., ASDEX Upgrade Team, and ICRH- and NBI-Group (1994). Dynamic behaviour of the H-mode in ASDEX Upgrade. To be published in *Plasma Physics and Controlled Fusion.*

Investigation of the Dynamics of the L-H Transition in ASDEX Upgrade

H. Zohm, K. Büchl, H.J. de Blank, A. Kallenbach, M. Kaufmann,
F. Ryter, W. Suttrop, ASDEX Upgrade Team, ICRH-, NBI-Group
MPI für Plasmaphysik, EURATOM Association, D-85748 Garching, Germany

1. Introduction

Since the discovery of the H-mode [1], progress in experimental und theoretical understanding of the phenomenon has been made [2]. One aspect of the phenomenon is its bifurcation character. In operating space, this manifests in the hysteresis in the power threshold P_{thr} for the L-H transition with $P_{thr}^{L-H} > P_{thr}^{H-L}$ for given plasma parameters (see e.g. [3]). At the transition, the bifurcating system may oscillate between L- and H-mode. These so-called dithering cycles can be interpreted as a limit cycle oscillation of the system [4]. The study of the dynamics of the L-H transition may therefore yield insight into the physics of the process. It is the aim of this work to experimentally characterize the occurrence of dithering cycles in the ASDEX Upgrade tokamak [5]. We interpret the findings in terms of the bifurcation model discussed in [4].

2. Occurrence of Dithering Cycles

In previous work [4], we found that the number of dithering cycles occuring at the transition decreases with the ramp rate γ_P of power in excess of the L-H transition threshold power P_{thr}. In NBI heated cases, the power is switched on rapidly; as a measure for γ_P at the separatrix, we take the excess power divided by the confinement time τ_E:

$$\gamma_P \approx \frac{1}{\tau_E P_{thr}}(P_{NBI} - P_{thr}) \tag{1}$$

We now examine the occurrence of dithering cycles at different values of P_{thr}. In ASDEX Upgrade, we have used three methods of varying P_{thr} by a wide extent:

a) Change of the parameter $\bar{n}_e B_t$: In various tokamaks, it was found that $P_{thr} \propto B_t \bar{n}_e$ [6]. Therefore, variation of density and toroidal field allows to adjust P_{thr}. In ASDEX Upgrade, we have varied B_t by a factor of 2 (1.35 T $\rightarrow$ 2.7T) and found no qualitative changes in the occurrence of the cycles.

b) Reversal of B_t: As in other tokamaks, the sign of the ion ∇B drift has a strong influence on P_{thr}: With the drift towards the active X-point ('favorable direction') P_{thr} is lower than for the other ('unfavorable') direction by a factor of ≈ 1.8. As shown below, this introduces a new feature: With the unfavorable direction, dithering cycles do not occur.

c) Change of the working gas: With H-NBI into an H target plasma, the threshold is nearly twice that of a D plasma. Values for He are somewhere inbetween these two. Inspite of this variation, there is no qualitative difference to a) and b): Cycles occur in cases with the favorable drift direction, but not with the unfavorable one.

The effect of a) and b) is documented in Fig. 1 for cases with ± 1.85 T and ± 2 T. The other plasma parameters ($I_p = 0.8$MA, $\bar{n}_e = 0.5 \times 10^{20}\mathrm{m}^{-3}$) and NBI timing and power are the same for all 4 shots. A negative sign of B_t corresponds to the favorable direction, a positive sign to the unfavorable. For the pair with positive B_t, one can see the effect of γ_P, i.e. at the higher B_t, P_{thr} is higher and γ_P smaller, resulting in more dithers to occur. For the unfavorable direction, no dithers are seen. The enhanced fluctuation level in the preceding L-mode can be distinguished from dithers by the fluctuation pattern [7] or the effect on plasma parameters.

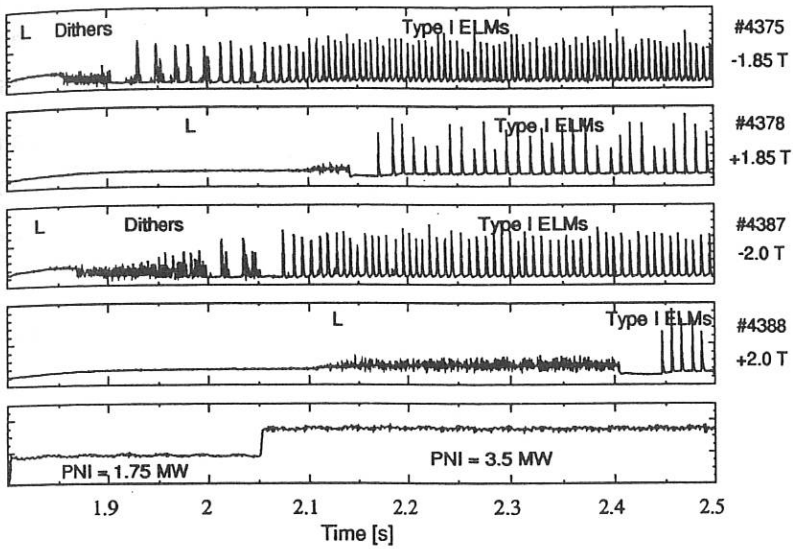


Figure 1: *Example for the variation in the occurrence of dithering cycles with varying P_{thr} as seen in the D_α emission in the divertor.*

We now examine the occurrence of dithering cycles at the H-L transition. Due to the hysteresis, P_{thr} is lower in this case. In addition, the plasma drops out of an H-mode state, i.e. τ_E in Eq. 1 is higher by a factor of ≈ 1.8 and therefore γ_P is lower. Fig. 2 shows the H-L transition for the cases shown in Fig. 1. It can be seen that the dithering phase in shots with the favorable direction is longer at the H-L transition due to the decrease in γ_P. Nevertheless, even with the lower γ_P, no cycles are observed with unfavorable drift direction.

Therefore, the absence of dithering cycles with the unfavorable drift direction cannot be explained by an effect of γ_P. This is further confirmed by the observation that even at $B_t = -2.7$ T, when P_{thr} is close to the + 1.85 T case, long dithering phases are observed.

3. Comparison with theory

We now try to relate these findings to the model presented in [4]. There, the L-H transition occurs at a given value of the gradient parameter

$$g(n,T) = g_0 \frac{T}{n}\left(\frac{n'}{n} + \gamma \frac{T'}{T}\right) \tag{2}$$

With fixed gradient lengths, this corresponds to a certain value of T/n. As the bifurcation occurs in this parameter, dithering cycles can be found when the increase in n at the L-H transition is strong enough to effectively decrease g even though T increases at the transition. With this model, we can draw a schematic picture of the cycles in terms of the operation diagram P_{heat} versus $\bar{n}_e B_t$ as shown in [3]. For that purpose, we make the assumption that the L-H transition is governed by the local values at the plasma edge and therefore translate $\bar{n}_e$ into $n(a)$. In this diagram, an unambiguous translation of P_{heat} into $T(a)$ is not possible.

Fig. 3 a) shows a path for a dithering discharge: We have indicated the stationary L-mode

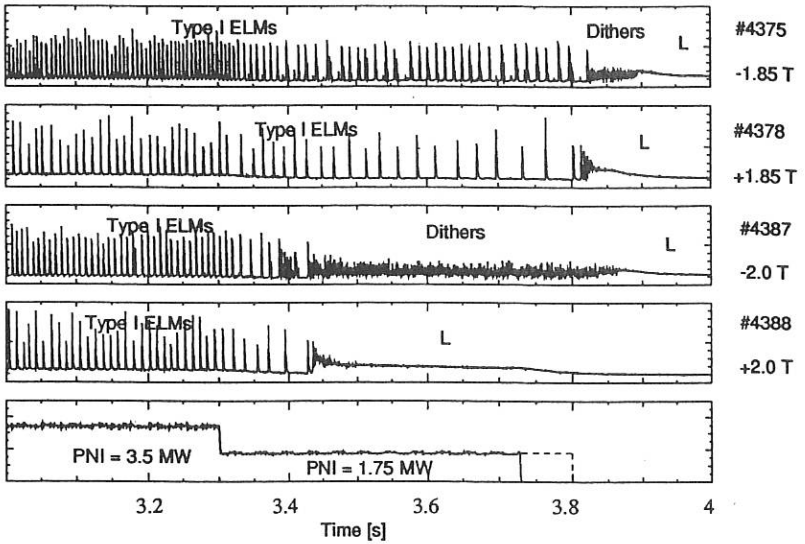


Figure 2: *Occurrence of dithering cyles at the H-L transition in the divertor D_α emission. NI power shown is for #4388, the dashed line indicates the timing of the other shots.*

edge density n_L and the stationary H-mode edge density n_H by vertical lines in the diagram. The boundaries for the L-H and the H-L transition are shown as obtained from ASDEX Upgrade data for the favorable drift direction, i.e. $P_{sep}^{L-H} \approx 1.8 P_{sep}^{H-L}$. We approach the threshold at n_L $(1 \rightarrow 2)$. At the threshold, $n(a)$ rises. At low γ_P, the path reaches the H-L threshold $(2 \rightarrow 3)$ and the back transition occurs. Due to the increase in power flux, the return point at the L-H boundary (4) is shifted in P. This goes on until the path reaches the n_H line before it reaches the H-L boundary (7). Then, the path follows the n_H line to its final point (8).

In this diagram, we can modify the path in several ways to avoid dithers. One is to increase γ_P and therefore increase the slope of $2 \rightarrow 3$. In [8], a necessary condition on γ_P is given for the model used here. Another way is to change the width of the hysteresis. This is shown in Fig. 3 b), where we have kept the H-L boundary from a) and have increased the L-H boundary by a factor of 1.8 in order to match the higher P_{thr} with the unfavorable drift direction. Now, on the path into $(1 \rightarrow 4)$ and out of the H-mode $(4 \rightarrow 6)$, no dithers occur. An increase in the H-L boundary by the same factor would have given a picture similar to a). Thus, we find that in order to explain our findings, we have to increase the width of the bifurcation zone in the diagram for the unfavorable direction. An experimental indication for this can be seen in Fig. 2: the back transition to L-mode resp. dithering cycles occurs for approximately the same power for pairs with opposite sign of B_t.

Within this interpretation, the change of P_{thr} with the working gas may be a profile effect: As stated above, P_{thr} varies by a factor of ≤ 2 with a change from D to H, but still dithers occur only with the favorable drift direction. Therefore, the relative width of the bifurcation only changes with the sign of the ∇B drift. The change in the absolute value of P_{thr} may be explained by the T/n dependence of g in eq. 2: in ASDEX, at constant $\bar{n}_e$, the value of $n(a)$ in Hydrogen was higher by a factor of ≈ 1.3 than in Deuterium [9]. At constant power flux into the edge, $T_e(a)$ is reduced by the same factor. Therefore, to obtain a constant $T(a)/n(a)$,

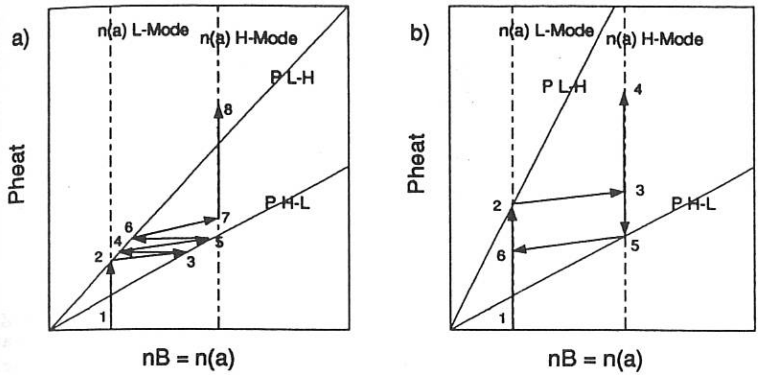


Figure 3: *Schematic operation diagram: Path a) corresponds to a dithering transition, path b) to one without dithers. In b), P_{thr}^{L-H} has been increased by a factor of 1.8 with respect to a), whereas P_{thr}^{H-L} was not varied.*

the value of $T(a)$ has to be higher in Hydrogen discharges by a factor of $1.3^2 = 1.7$, requiring an increase in P by at least this factor.

4. Conclusions

The occurrence of dithering cycles in ASDEX Upgrade is studied. One factor to influence the number of cycles occurring at the transition is γ_P, the ramp rate of power in excess of the L-H threshold. A variation of P_{thr} reveals that varying the threshold by the magnitude of $n_e B_t$ or by changing the working gas does not essentially change the picture. Changing the direction of the ∇B drift introduces a qualitatively new feature: With the ion ∇B drift away from the active X-point, no dithers occur. We demonstrate that this is not the effect of a change in γ_P. An interpretation in terms of a schematic operational diagram is given; the observation that the bifurcation zone is wider with the unfavorable drift direction can be used to qualitatively explain why no dithers occur.

References

[1] The ASDEX Team, Nucl. Fusion **29** (1989) 1959.
[2] GROEBNER, R. J., Phys. Fluids B **5** (1993) 2343.
[3] RYTER, F. et al., 4th H-Mode workshop, Naka, Japan, to appear in Plasma Physics and Controlled Fusion (1993).
[4] ZOHM, H., Phys. Rev. Lett. **72** (1994) 222.
[5] KÖPPENDÖRFER, W. et al., 14th International Conference on Plasma Physics and Controlled Nuclear Fusion Research, Würzburg, IAEA-CN-56 / A-2-3 (1992).
[6] H-Mode Database Working Group, 14th International Conference on Plasma Physics and Controlled Nuclear Fusion Research, Würzburg, IAEA-CN-36 / IF-1-3 (1992).
[7] ZOHM, H. et al., Nucl. Fusion **32** (1992) 489.
[8] DE BLANK, H. et al., this conference (1994).
[9] BESSENRODT-WEBERPALS, M. et al., Nucl. Fusion **33** (1993) 1205.

A STUDY OF EDGE FLUCTUATIONS IN L– AND H–MODE BY PHASE CONTRAST IMAGING ON DIII–D*

S. CODA† AND M. PORKOLAB

Department of Physics and Plasma Fusion Center,
Massachusetts Institute of Technology, Cambridge, Mass. 02139, U.S.A.

1. INTRODUCTION

A density fluctuation imaging diagnostic based on the Zernike phase contrast imaging (PCI) technique [1] has been employed to investigate long wavelength turbulence at the outer edge of the DIII–D tokamak [2]. When applied to a transmitted CO_2 laser beam [3,4], the PCI method has several attractive properties, including high sensitivity ($\tilde{n}_e \gtrsim 10^9$ cm^{-3}) and broad wave number range (1 cm$^{-1} \leq k_R \leq 16$ cm^{-1}). The radial resolution of the DIII–D PCI system is also excellent (~ 0.5 cm); however, the measurement is not well localized in the poloidal direction. The impact of this limitation on data interpretation can be greatly reduced with the aid of analytical and numerical modeling based on the geometrical constraints of the measurement [5], as discussed in section 2. The results of a study of the L– to H–mode transition are presented in section 3. It is shown that the radial spectrum of turbulence in the L–mode phase is characterized by net inward propagation. The transition to H–mode is accompanied by decorrelation of the fluctuations and loss of directionality.

2. THE PHASE CONTRAST IMAGING TECHNIQUE

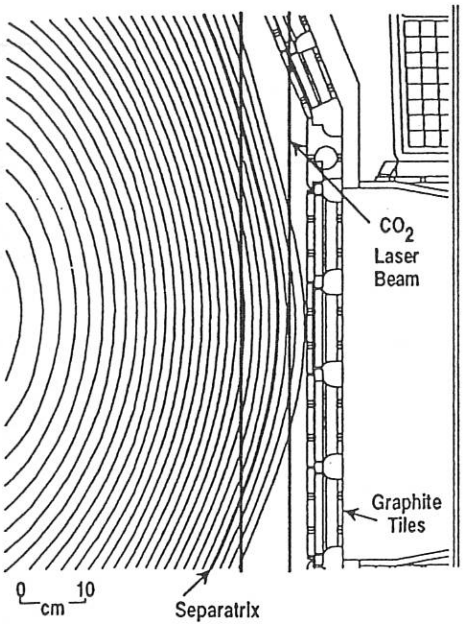
The PCI technique [2-4] and the specific DIII–D apparatus [2,4,5] have been described elsewhere. The system employs a 20 W CO_2 laser beam expanded to a width of 7.6 cm. The beam propagates vertically through the outer edge of the plasma (Fig. 1a) and is then spatially filtered and imaged onto a linear detector array. The final result is a radially-resolved, 16-point image of line-integrated density fluctuations. The data acquisition bandwidth is 1 MHz.

A common difficulty shared by fluctuation diagnostics based on the interaction of electromagnetic waves with plasma is the finiteness volume, which limits the localization of the measurement. The pointwise correlation function (a function of four spatial coordinates, if toroidal invariance is assumed) can be derived in principle from the measured correlation function between line integrals (a function of two coordinates) only if two variables are eliminated from the problem with the aid of symmetry considerations. Homogeneity [6], and local isotropy combined with flux surface invariance [7], are examples of symmetry assumptions that lead to unique analytical inversion procedures.

Such assumptions are not well supported by experimental observations [8,9]. We have investigated the properties of our system by considering a more general case of separate radial and poloidal local wave number spectra superimposed on an arbitrary spatial distribution [5]. Although an unambiguous inversion is not possible in this case, the peculiar geometry of our measurement aids greatly in selecting the correct interpretation. An intuitive approach to the problem is provided by the following mathematical observation: the spatial Fourier spectrum of a line integrated measurement can only

* This work was supported by the U.S. Department of Energy under Grant No. DE-FG02-91ER54109 at MIT and Contract No. DE-AC03-89ER51114 at General Atomics.

† Present address: General Atomics, San Diego, CA 92186-9784, U.S.A.



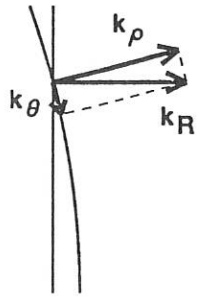


Fig. 1. a) Phase contrast imaging geometry on DIII–D. b) Decomposition of a horizontal wave vector into its radial and poloidal components.

contain wave vectors that are perpendicular to the direction of integration, which is vertical in our case. Any vertically varying component clearly will be averaged out. Since the poloidal angle subtended by the laser beam path in the plasma is generally $< 30°$, owing to its edge location (Fig. 1a), the poloidal fraction of a horizontal wave vector can be at most 25%, as shown in Fig. 1b. Thus the DIII–D PCI diagnostic is mostly sensitive to *radial* wave vectors.

This statement can be reformulated in a rigorously quantitative form [5], which is beyond the scope of this paper. Here we merely wish to provide an illustration of its significance. Our analysis uses the additional assumption that the poloidal and radial spectra are gaussian, centered respectively at $k_{\theta 0}$ and $k_{\rho 0}$, with half-widths $\bar{\kappa}_\theta$ and $\bar{\kappa}_\rho$. The correlation function between line integrals is then calculated numerically, using experimentally determined flux surface geometries. We call the spatial Fourier transform of this correlation function the *apparent PCI spectrum*. We find that for realistic spectral parameters [8,9] the apparent PCI spectrum approximates closely the radial fluctuation spectrum (Fig. 2).

3. EDGE TURBULENCE IN L– AND H–MODE

Our study is based on a set of 10 discharges, which differed for the position of the last closed flux surface but otherwise had identical plasma parameters (single null divertor configuration, $B_T = 2.1$ T, $I_p = 1.37$ MA, $\bar{n}_e = 4 \times 10^{13}$ cm^{-3}). This was effectively equivalent to a radial scan of the position of the PCI beam in the plasma. Such a scan cannot be performed directly because the position of the beam is fixed by machine constraints.

Max-Planck-Institut für Plasmaphysik
- Bibliothek -

The rms fluctuation signals are reduced at the transition from L– to H–mode. The suppressed component of the frequency spectrum is centered around 50 kHz, with a width of 60-80 kHz (Fig. 3). The signal level generally peaks at a major radius 3 to 4 cm inside the separatrix: this behavior is readily explained as the result of the competition between the fluctuation level, which increases with radius, and the integration length, which decreases with radius. The cross-correlation function between PCI signals in L–mode displays consistently an inward propagating pattern. The average phase velocity is approximately $(1.7 - 2.0) \times 10^5$ cm/s. This feature is unexplained at present. A study of both the correlation coefficient in the time domain, and of the coherence function in the frequency domain, shows that during H–mode the signals are thoroughly uncorrelated at distances ≥ 0.5 cm, and no net propagation is observed. The decorrelation of the fluctuations can be expected to cause a decrease in the rms signal level, which can be expressed as $\left(\int \tilde{n}_e^2 L_{cz} dz\right)^{1/2}$, where z is the integration variable and L_{cz} is an effective correlation length. It is unclear at this point whether this effect alone accounts for the observed suppression or whether the absolute $\tilde{n}_e^2$ level is also reduced.

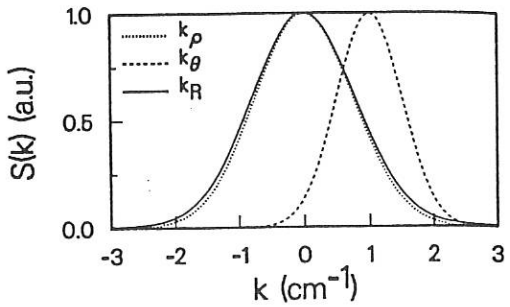


Fig. 2. Sample radial (k_ρ) and poloidal (k_θ) wave number spectra with parameters $k_{\rho 0} = 0$, $\bar{\kappa}_\rho = 1.5$ cm^{-1}, $k_{\theta 0} = 1$ cm^{-1}, and $\bar{\kappa}_\theta = 1$ cm^{-1}. The resulting apparent PCI spectrum (k_R) is computed numerically.

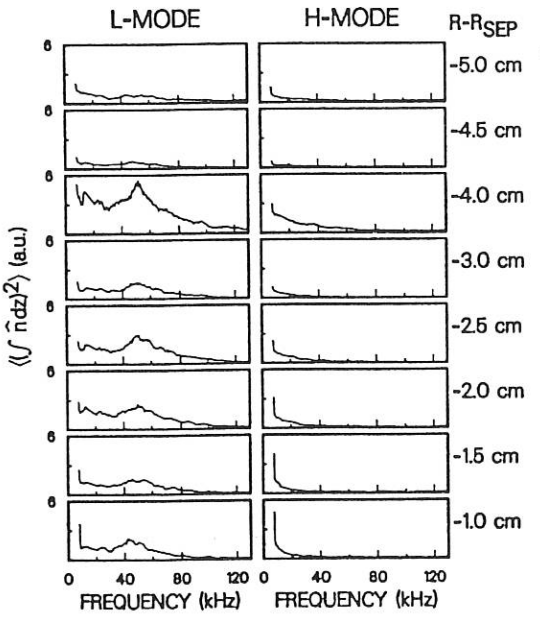


Fig. 3. Calibrated PCI power spectral density functions in L– and H–mode at varying distances from the separatrix (the innermost chord is at the top).

A global picture of the properties of the turbulence is obtained by calculating the conditional apparent PCI spectrum $S(k_R|\omega)$, which is the spatial Fourier transform of the normalized complex cross-spectral function. The spectra for L– and H–mode are plotted in Fig. 4. The plot is limited to the range 30–80 kHz to highlight the difference between L– and

H–mode. In Fig. 4a the spectrum peaks at negative values of k_R, a reflection of the inward propagation discussed above. The suppression and broadening of the spectrum in H–mode is evident from Fig. 4b.

These observations, especially the novel features of the L–mode spectrum, will be put on a more quantitative footing by a substantial expansion of our L– and H–mode database which is planned for the near future. Comparative studies with the other fluctuation diagnostics that exist on DIII–D will also be carried out.

ACKNOWLEDGEMENTS

We wish to thank the DIII–D team, particularly Drs. K.H. Burrell, T.N. Carlstrom, P. Gohil, and J.G. Watkins, for their assistance during the experiments described in this paper.

REFERENCES

[1] F. Zernike, Physica **9**, 686, 974 (1942).
[2] S. Coda, M. Porkolab, K.H. Burrell, and T.N. Carlstrom, Proc. 20th EPS Conference, Lisboa, Vol. 17C, Part III (1993), p. 1179.
[3] H. Weisen, Rev. Sci. Instrum. **59**, 1544 (1988).
[4] S. Coda, M. Porkolab, and T.N. Carlstrom, Rev. Sci. Instrum. **63**, 4974 (1992).
[5] S. Coda and M. Porkolab, submitted to Rev. Sci. Instrum.
[6] H. Weisen, Ch. Hollenstein, and R. Behn, Plasma Phys. and Contr. Fusion **30**, 293 (1988).
[7] A. Lazarian, Plasma Phys. and Contr. Fusion **36**, 1013 (1994).
[8] D.L. Brower, W.A. Peebles, and N.C. Luhmann, Jr., Nucl. Fusion **27**, 2055 (1987).
[9] R.J. Fonck, G. Cosby, R.D. Durst, *et al.*, Phys. Rev. Lett. **70**, 3736 (1993).

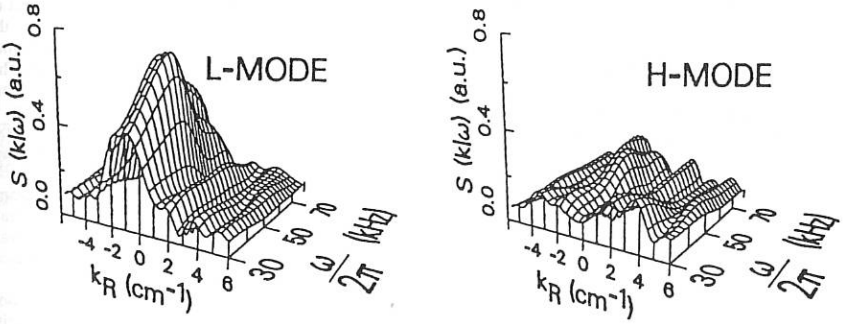


Fig. 4. Conditional apparent PCI spectrum: a) L–mode, b) H–mode.

THE PARAMETRIC DEPENDENCE OF THE SPATIAL STRUCTURE OF THE RADIAL ELECTRIC FIELD AT THE PLASMA EDGE IN THE DIII–D TOKAMAK.

P. Gohil, K.H. Burrell, R.J. Groebner, J. Kim, and R.P. Seraydarian
General Atomics, P.O. Box 84508, San Diego, California 92186-9784

Much recent theoretical and experimental work has focused on the mechanisms controlling the transition from L–mode to H–mode and the subsequent improvement in transport and confinement.[1–13] Measurements of the radial electric field, E_r, with high spatial and time resolution at the L–H transition have led to an understanding of the improved confinement of the plasma edge in H–mode plasmas based on the stabilization of plasma turbulence by sheared *E×B* flow.[1–6] The radial electric field just inside the last closed flux surface (LCFS) changes dramatically at the L–H transition and a well-like structure in E_r forms simultaneously at the transition. At present, there is no accepted theory which gives the spatial structure of E_r near the plasma edge and which can predict its time evolution.

Present theories propose mechanisms for the generation of a negative E_r at the L–H transition, the bifurcation conditions for the transition and the stabilization of turbulence by sheared *E×B* flow.[7–13] Although the various theories invoke different mechanisms to derive the negative E_r (e.g., ion orbit losses,[8,13] Stringer spin-up,[10] nonlinear transport theory,[9] self-regulating turbulence[11,12]), they have as yet to come into full agreement with the observed experimental results and, in particular, the observed behavior of the poloidal rotation and pressure gradient of the *main* ions at the transition.[14,15] Furthermore, these theories need to be extended to explain the formation of the spatial structure of E_r at the transition and its temporal development into the H–mode. In order to help development of theories on the E_r profile, we have examined the dependence of the radial profile of E_r on different plasma parameters.

Experimental Conditions

The experimental investigations of the parametric dependence of the edge radial electric field were coordinated with investigations of the power threshold required for the H–mode transition. For each set of plasma parameters studied, a power scan with time was performed during each discharge. For cases where the H–mode power threshold was less than the injected power from an integral number of DIII–D neutral beams, one neutral beam was modulated at duty cycles of 25%, 50% and 75% of the full cycle period of 20 ms. This allowed for a more sensitive determination of the H–mode power threshold, but subsequently reduced the times at which data was available from the Charge Exchange Recombination (CER) spectroscopy diagnostic system.[16] Typically, time points were available every 20 ms during the discharge. The full beam power was about 2.6 MW. The plasma conditions investigated covered the following range of plasma parameters in a lower single-null diverted configuration: plasma current, I_p = 1.0–2.0 MA; toroidal magnetic field, B_T = 1.5– 2.1 T; ohmic target density, $\bar{n}_e$ = 2.0–4.0 x 10^{19} m^{-3}; X-point height above the floor, ΔZ_x = 0–24 cm; the plasma elongation, κ = 1.8–2.0; the gap between the LCFS at the z-location of the magnetic axis and the outside wall, gap_{out} = 0–15 cm; the gap between the inner LCFS at the z-location of the magnetic axis and the inner wall, gap_{in} = 0–8 cm. The following plasma parameters were investigated in a double-null diverted configuration: toroidal magnetic field, B_T = 1.3–2.1 T; plasma triangularity, δ = 0.7, 0.85; inside gap, gap_{in} = 1–8 cm.

Measurements of the edge values of the ion temperature, T_i, the poloidal rotation, v_θ, and toroidal rotation, v_ϕ, in the DIII–D tokamak were made using a high resolution spectroscopy diagnostic system utilizing the active charge exchange recombination between the neutral atoms in the heating beams and impurity ions in the plasma. The C VI 5290.5 Å spectroscopic line was used for the measurements presented in this paper, whereby the ion temperature is determined from the widths of the Doppler broadened lineshape, the plasma rotation velocities, v_θ and v_ϕ, are determined from the Doppler shifted line centers and the relative impurity density is determined from the signal intensity of the line. The radial electric field, E_r, is calculated from the lowest order radial force balance equation for a single species, $E_r = (Z_I e n_I)^{-1} dP_I/d_r - v_{\theta I} B_\phi + v_{\phi I} B_\theta$, where Z_I is the charge of the ion, n_I is the ion density, e is the electronic charge, P_I is the ion pressure, and B_ϕ and B_θ are the toroidal and poloidal magnetic fields, respectively. The CER system has the highest spatial resolution over a spatial extent of 4.6 cm at the outside plasma edge such that the spatial resolution of the flow velocities and E_r measurements is 0.6 cm and the spatial resolution of the T_i measurements is 0.3 cm. The minimum possible integration time for the measurements is 0.52 ms.

Parametric Dependence Of E_r

For all the plasma parameters investigated, both in single-null diverted and double-null diverted configurations, the general shape of the spatial profiles of the radial electric field was the same. This shape consisted of a negative well-like structure with the minimum of the E_r well located at or just inside the LCFS. The E_r values just inside the LCFS were negative for all the plasma parameters and conditions investigated, *with no exceptions*. The available data are too numerous to be represented adequately within the limited space of this paper and only E_r profiles for a high plasma current (2.0 MA) and a low plasma current (1.0 MA) case are shown (Figs. 1 and 2 respectively). Figures 1 and 2 show the edge E_r profiles for two plasma discharges which are nearly identical in their plasma parameters and shape apart from the plasma current. Profiles of E_r are shown for L–mode conditions, early in the H–mode phase and later in time into the H–mode. The localization of the sheared region in E_r is well-defined with respect to the location of the separatrix, which is well resolved from the variation in the signal amplitudes of the CER chords spanning the separatrix. There is a decrease in the signal intensity of chords outside the separatrix and an increase in signal intensity inside the separatrix at the L–H transition.[17] This allows us to determine the separatrix location in our data set independent of fits to magnetic probe data, although the separatrix location from both measurements typically agrees within the ±0.5 cm error bars. Exact knowledge of the separatrix location is crucial because the E_r well is quite narrow. The depth of the E_r well in H–mode with respect to the L–mode value was the largest at the higher plasma currents and toroidal fields. This can be seen in Figs. 1 and 2 and in Table 1. The widths (FWHM) of the E_r wells are similar at about 1 cm, and a more critical determination of the E_r widths is limited to about ±0.3 cm by the spatial resolution of the E_r measurement. No discernible structure in the E_r profile was observed during the L–mode phase of the discharge for any of the different plasma conditions.

The sharpest L–H transitions were observed in cases where the E_r profiles exhibited large minima. For example, in the plasma discharge corresponding to Fig. 1, the L–H transition (as observed on the divertor photodiode signal) occurred within 1 ms, whereas the photodiode signal for the plasma discharge corresponding to Fig. 2 indicated a gradual and dithering transition over a timescale of about 20 ms before the H–mode was firmly established. This seems to indicate that large values of E'_r are correlated with faster L–H transitions and that once a critical value of E'_r has been achieved the transition proceeds unhindered (or vice versa). This behavior does not prove causality. It only associates high E'_r with faster L–H transitions. Nevertheless, the L–H transition for different plasma conditions occurs for an observed range of E_r values at the separatrix (Table 1) and the requirements for the change in E_r at the L–H transition may vary with different plasma conditions. The total input power (ohmic plus auxiliary heating) into the plasma discharge was maintained close to the threshold

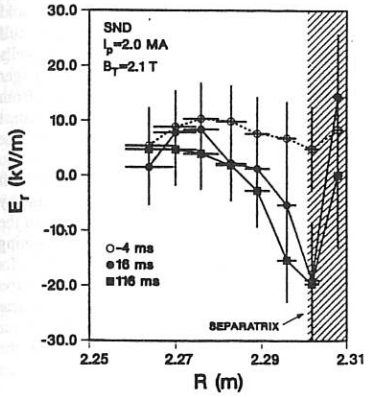


Fig.1. The E_r profile for a plasma current of 2.0 MA. The shaded region is the uncertainty in the determination of the separatrix from fits to magnetic probe data. The times shown are with respect to the time of the L-H transition. The integration time of the measurement is 2.5 ms.

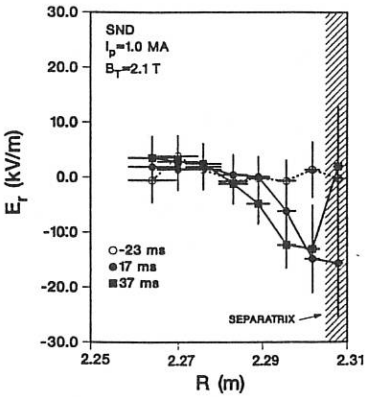


Fig. 2. The E_r profile for a plasma current of 1.0 MA. There is a movement of the separatrix of about 0.5 cm towards a lower major radius for the later H-mode time and does not represent a broadening of the E_r well. The integration time of the measurement was 2.5 ms.

TABLE 1
DESCRIPTIONS OF THE PLASMA CONDITIONS AND THE ASSOCIATED WIDTHS AND DEPTHS OF THE E_r WELL AND THE VALUE OF $|\nabla E_r/B_T|$

All tabulated values are at the first available time after the L–H transition (i.e., within 20 ms after the transition). The value of $|\nabla E_r/B_T|$ is the largest determined value along the negative slope of the E_r well. The plasma conditions represent the departure of one parameter from the reference set of parameters. The reference set of parameters is: I_p = 1.35 MA; B_T = 2.1 T; $\bar{n}_e$ (ohmic) = 4 x 10^{19} m^{-3}; ΔZ_x = 14 cm (for SND); outside gap = 6 cm; inside gap = 4 cm; triangularity = 0.85 (for DND).

Plasma Condition	E_r Width (FWHM) (cm)	E_{min}–E_{L-mode} (kV m^{-1})	$\lvert\nabla E_r/B_T\rvert$ $\times 10^5$ Hz
SND reference condition SND; I_p = 1.35 MA; B_T = 2.1 T	1.1	– 30	15.7
High plasma current SND; I_p = 2.0 MA; B_T = 2.1 T	1.2	– 25	15.8
Low plasma current SND; I_p = 1.0 MA; B_T = 2.1 T	1.3	– 16	6.2
Low toroidal field SND; I_p = 1.35 MA; B_T = 1.5 T	1.2	– 14	6.7
Low plasma current and toroidal field SND; I_p = 1.0 MA, B_T = 1.5 T	1.2	– 12	6.6
Low ohmic electron density SND; I_p = 1.35 MA; B_T = 2.1 T; n_e (ohmic) = 2×10^{19} m^{-3}	1.1	– 13	5.7
Low divertor X-point location SND; I_p = 1.35 MA; B_T = 2.1 T; ΔZ_x = 0 cm	1.0	– 12	8.1
High divertor X-point location SND; I_p = 1.35 MA; B_T = 2.1 T; ΔZ_x = 24 cm	1.2	– 18	7.1
High plasma elongation SND; I_p = 1.35 MA; B_T = 2.1 T; κ = 2.0	1.2	– 12	9.5
DND reference condition DND; I_p = 1.35 MA; B_T = 2.1 T	1.1	– 25	9.5
Low toroidal field DND; I_p = 1.35 MA; B_T = 1.3 T	0.9	– 15	15.4
Large inside gap DND; I_p = 1.35 MA; B_T = 2.1 T; G_I = 8 cm	0.8	– 12	8.1

power required for the H–mode transition for times before, during and after the L–H transition so that any influence of excess heating power is reduced.[18] The depth of the E_r well after the L–H transition appears to be lower at lower plasma current, lower toroidal field and lower ohmic electron density. Also, the power threshold for the H–mode for these cases is lower than for higher values of these plasma parameters in a single-null diverted discharge.[19] Therefore, it seems as if the low power thresholds correspondingly have less deep E_r wells for these parameters However, it is difficult to resolve as yet whether the depth of the E_r well is a stronger function of the input power or of the plasma parameters. The contributions to the total radial electric field from the diamagnetic and rotational terms of the force balance equation were examined. For *all* cases, the greatest contribution to E_r at the L–H transitions resulted from the change in the impurity ion poloidal rotation. The influence of the impurity ion pressure gradient term becomes appreciable 10's of milliseconds later in time into the H–mode. However, it has been shown[14,15] that the main ion poloidal rotation 3.5 ms after the L–H transition is in the ion diamagnetic direction and opposite to the impurity ion poloidal rotation, as pointed out by neoclassical theory.[20] By this time, the main ion pressure gradient term is the dominant, negative term in the determination of E_r and remains so thereafter through the H-mode. No conclusions can be made discriminating between the $\partial P_I/\partial_r$ and V×B terms for the impurity ions and main ions in this study, apart from the fact that for all the plasma parameters studied, the poloidal rotation *for the impurity ions* is consistently in the electron diamagnetic direction and is the important term at the time of the L–H transition. Even though there is no clear disagreement with the observed E_r widths and Shaing's modified theory[21] which includes the influence of the shear in E_r on the banana orbit widths, the dominance of the main ion pressure gradient milliseconds after the L–H transition[14,15] would imply that the observed E_r structures reflect the behavior of the main ion pressure gradient profiles[9] for the various plasma parameters.

The E_r shear suppression theory of Biglari, et al.[7] predicts that shear in E_r can nonlinearly stabilize a range of flute-like turbulent modes with the criterion for effective suppression being $|\nabla E_r/B_T| \geq (\Delta\omega_t/k_\theta \Delta r_t)$ where B_T is the toroidal field, $\Delta\omega_t$ is the turbulent decorrelation frequency, Δr_t is the radial correlation length, and k_θ is the mean poloidal wave number of the turbulence. The values of $\Delta\omega_t$ and Δr_t are in the absence of the electric field shear. Using typical values of $2\pi \times 40$ kHz for $\Delta\omega_t$ (from reflectometry measurements), 0.7 cm for the radial correlation length Δr_t and 1 cm^{-1} for k_θ, the RHS of the above criterion is equivalent to 3.6×10^5 Hz. The E_r profiles at the L–H transition for the various plasma parameters studied were analyzed for the value of the $|\nabla E_r/B_T|$. These values are shown in Table 1 and represent the largest shear in E_r inside the separatrix. Note that the values of $|\nabla E_r/B_T|$ are underestimates since the spatial resolution of the E_r measurements leads to averaged

determinations of E_r over a finite spatial region. Nevertheless, Table 1 clearly shows that the criterionof Biglari et al., for E_r shear stabilization of turbulence is satisfied by between a factor of 2–5 for $k\theta \geq 1$ cm^{-1} for all the plasma conditions investigated.

The greatest changes in the E_r profile after the L–H transition were observed for the case of the low ohmic target electron density discharge. The E_r profiles for this discharge are shown in Fig. 3. There is an increase in the depth of the E_r well and a broadening of the well with time into the H–mode at constant input power. The main reason for the broadening is the increasing spatial extent of the region with the high pressure gradient, which is much more important later in the H–mode for the low density discharge than in the other cases. This is qualitatively in agreement with the theory of Hinton and Staebler, which links the mean free paths of incoming neutrals with the width of the region of high pressure gradient. The deeper penetration of neutrals at lower electron densities would then favor a broadening of the E_r profile.

In summary, there is no clear variation in the shape or width of the E_r well at the L–H transition with any of the different plasma parameters investigated. The value of E_r is negative just inside the LCFS for all cases. There is a variation in the depth of the E_r well for different conditions and the largest broadening of the E_r width later into the H–mode is observed in the case with a low ohmic electron density. The criterion of Biglari et al., for the suppression of turbulence by sheared *E×B* flow is satisfied for all the cases.

[1] K. H. Burrell, et al., Phys. Fluids B **2**, 1405 (1990).

[2] R. J. Groebner, et al., *Plasma Physics and Controlled Nuclear Fusion Research*, 1990 (International Atomic Energy Agency, Vienna, 1991), Vol. 1, p.453.

[3] E. J. Doyle, et al., Phys. Fluids B **3**, 2300 (1991).

[4] P. Gohil, et al., in *Proceedings of the 18th European Conference on Controlled Fusion and Plasma Physics*, Berlin, 1991 (European Physical Society, Petit-Lancy, Switzerland, 1991), Vol. 15C, p. 289.

[5] K. Ida, et al., Phys. Fluids B **4**, 2552 (1992).

[6] K. H. Burrell, et al., Plasma Phys. Controlled Fusion **34**, 1859 (1992).

[7] H. Biglari, et al, Phys. Fluids B **2**, 1 (1990).

[8] K. C. Shaing, et al, Phys. Fluids B **2**, 1492 (1990).

[9] F. L. Hinton et al, Phys. Fluids. B **5**, 1281 (1993).

[10] A. B. Hassam, et al, Phys. Rev. Lett. **66**, 309 (1991).

[11] P.H. Diamond, et al, Phys. Rev. Lett. **72**, 2565 (1994).

[12] B. A. Carreras, et al, Phys. Fluids B **5**, 1491 (1993).

[13] K. C. Shaing, Phys. Plasmas **1**, 219 (1994)

[14] J. Kim, et al, Phys. Rev. Lett. **72**, 2199 (1994).

[15] K. H. Burrell , et al., Phys. Plasmas **1**, 1536 (1994).

[16] P. Gohil, et al., in *Proceedings of the 14th IEEE/NPSS Symposium on Fusion Technology* (Institute of Electrical and Electronics Engineers, Princeton, NJ, 1992), Vol. II p. 1199

[17] P. Gohil, et al., GA-A 21265 to be published Nuc. Fus.

[18] R. J. Groebner, et al., in *Proceedings of the 19th EPS Conf. Contr. Fusion & Plasma Phys.* (Innsbruch, 1992)

[19] T.N. Carlstrom, et al., GA-A21541, to be published in Plas. Physics and Contr. Fusion.

[20] Y. B. Kim, et al., Phys. Fluids B **3**, 2050 (1991).

[21] C. Shaing, Phys. Fluids B **4**, 171 (1992).

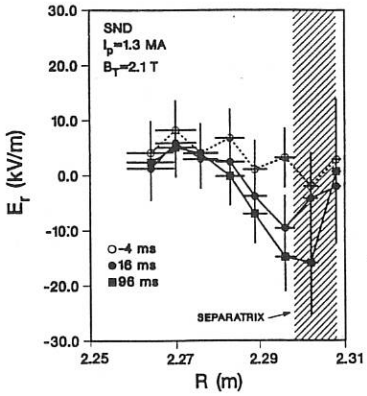


Fig. 3. Profiles of E_r at various times for a plasma discharge with low ohmic electron density, $\bar{n}_e$, of 2×10^{19} cm^{-3}. The times shown are with respect to the time of the L–H transition. The integration time for each profile is 2.5 ms.

Edge turbulence and transport studies with Ergodic Divertor, on TORE SUPRA ohmic discharges

J. Payan, X. Garbet, F. Clairet, P. Devynck, C. Laviron,
J.H. Chatenet, P.N. Ghendrih, A. Grosman
Association Euratom-CEA, CE Cadarache, 13108 Saint Paul lez Durance, France

F. Gervais*, P. Hennequin*, A. Quémeneur*, A. Truc*
*PMI, Ecole Polytechnique, 91128 Palaiseau, France

1) Introduction

The ergodic divertor (ED) on TORE SUPRA is a set of six coils equally spaced in the toroidal direction, producing magnetic perturbations and overlapping magnetic islands for $r/a>\rho_s=0.83\pm0.05$. Within this layer, the electrons tend to diffuse faster than ions and the ambipolarity is ensured by a positive radial electric field which confines electrons. Since the field is negative in the bulk, there is an inversion point of the radial electric field, whose position is expected to be close to ρ_s [1]. Edge turbulence and transport studies have been performed when the ergodic divertor is applied on TORE SUPRA ohmic discharges. A modification of radial electric field profiles is expected. Such a change could influence edge transport and turbulence. A CO_2 laser scattering diagnostic, ALTAIR [2], has been used to study the turbulence changes at the plasma edge. Reflectometry (used at fixed frequency) gives also access to localized turbulence measurements. Preliminary results from reflectometry are presented and compared to ALTAIR results.

2) Profile analysis and transport studies

For this studies, experiments have been performed in a set of stationary helium ohmic discharges with Ip=1.4MA, B=3.2T, R=2.37m, $a_{limitor}$=0.78m, q_ψ=3 and the average electron density is scanned from $\langle n_e\rangle$=1 to 4 $10^{19}m^{-3}$. The electron temperature is given by Thomson scattering in the plasma bulk and by Langmuir probe at the edge. The electron density profile is measured by interferometry, Thomson scattering and reflectometry. No change appears on the normalized radial shape of density with ED, but temperature profiles are strongly modified (see Fig.1).

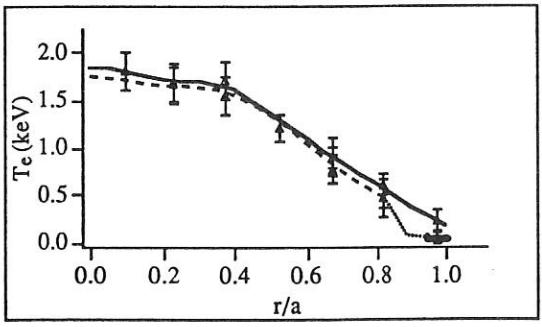


Fig.1 Radial temperature profile. Thomson scattering measurements are indicated by black and open triangles, respectively with and without ED. Circles at the edge represent Langmuir probe measurements whith ED. Dashed line represents an extrapolation of the profile in the intermediate zone.

Three regions may be identified on temperature profiles: **the plasma bulk ($r/a<\rho_S$) where no change appears, the ergodic zone at the edge for $r/a>y_T$, where the temperature is flattened (the value of y_T being smaller than 0.93) and an intermediate zone, where a steep temperature gradient exists.**

A heat transport analysis has been achieved. In the plasma bulk, the profiles described above have been analysed with the LOCO code [3], without including convective term and radiative losses, which are negligible for $r/a<y_T$. In this set of helium discharges, no ion temperature exists. So an effective diffusivity $\chi_{eff} = \chi_e + n_i T_i / n_e T_e \chi_i$ is estimated and no change appears within the error bars. At the edge, for $r/a>y_T$, the heat conductivity is very high with ED, in agreement with a flat temperature profile. In the intermediate zone, where the temperature gradient is steep, the heat flux is not changed. No significative change is observed on average density, $<n_e>$ is only slighly lowered at large density when the ED is switched on. Thus, the heat conductivity is locally divised by 2, in the intermediate zone.

3) Inversion point of the radial electric field

Density fluctuations are measured in TORE SUPRA with the ALTAIR diagnostic. Heterodyne detection allows discrimination between waves propagating in the electron or in the ion diamagnetic direction. The measured frequency spectra exhibit two humps, one drifting in the electron diamagnetic direction, and the other one in the ion diamagnetic direction. This two humps structure is attributed to a sharp change of sign of the radial electric field in the plasma edge. The dispersion relation of any turbulence driven by electrons is given by:

$$\omega = \frac{k_\theta T_e}{eB_\phi}\left[\frac{dn_e}{n_e dr} + \alpha_o \frac{dT_e}{T_e dr}\right] - \frac{k_\theta E_r}{B_\phi} \qquad (1)$$

where α_o depends on the kind of waves ($\alpha_o=0$ for electrostatic drift waves). k_θ is the poloidal wave number observed by Thomson scattering and B_ϕ the toroidal magnetic field. In the ergodic layer, the positive electric field value is:

$$\frac{e E_r}{T_e} = \left[\frac{dn_e}{n_e dr} + \alpha_E \frac{dT_e}{T_e dr}\right] \qquad (2)$$

where α_E increases with collisionality from 0.5 to 1.7. Taking into account relations (1) and (2), we obtain ω_+ value, corresponding to the mean frequency of the ionic frequency part of density fluctuation spectrum:

$$\omega_+ = \frac{k_\theta}{eB}\left(\alpha_o - \alpha_E\right)\frac{dT_e}{dr} \qquad (3)$$

At the edge, for $r/a>y_S$, the temperature gradient is close to zero so that $\omega_+ \approx 0$. A peak centered on $\omega=0$ should appear on frequency spectra. Such a peak is not observed, so that a modification of the radial fluctuation profile is needed.

4) Radial density fluctuation profiles

During activation of ED, density fluctuation spectra are strongly modified. The ionic hump becomes more important than the electronic one. This leads to an inversion radius y_S of the radial electric field E_r moving toward the center at the position $y_S=0.83\pm0.05$. Furthermore, the total level of relative fluctuation level $<\delta n^2>/<n_e>^2$ decreases with ED, and we can distinguish fluctuations coming from the inside ($r/a<y_S$) from that coming from the outside($r/a>y_S$). ALTAIR diagnostic does not have a good spatial localization, so that a modelization is involved in order to estimate ED effects on density fluctuations profile. We shall consider a simple model in the shape of triangle. For $r/a<y_S\approx0.83$, transport is

unchanged and we assume no change on density fluctuations. Taking into consideration the ratios between fluctuations coming from $r/a<y_S$ and those coming from $r/a>y_S$, with and without ED, it is possible to estimate fluctuations profile (see Fig.2).

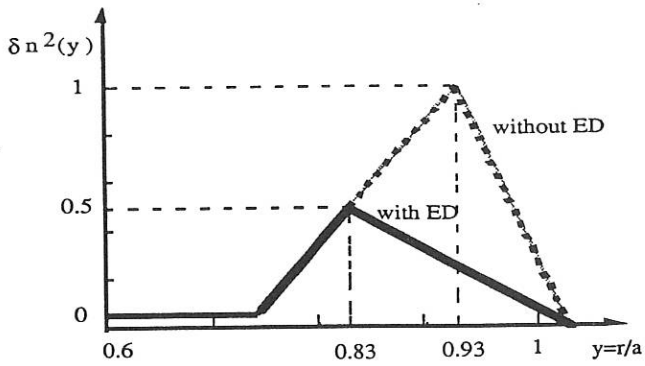


Fig.2: Radial density fluctuations profile with ED(straight line) and without ED(dotted line) .

It is important to notice that even if the density fluctuations level does not fully vanish for $r/a>y_T$, this level is very low. The frequency peak at $\omega=0$ is low enough so that it cannot be seen on frequency spectra.

5) Reflectometry measurements

Preliminary results are obtained by reflectometry measurements at different fixed frequencies i.e for a given density. The reflectometry signal is proportional to density fluctuations. This diagnostic gives very localized measurements but integrated over wave numbers. The probed region differs from coherent Thomson scattering, toroidally and even poloidally. The microwaves probe a region in the plane $\theta=0$ [4], from the low field side of the tokamak. We therefore compare the results coming from our modelization with these results. The ratio between fluctuations with and without ergodic divertor perturbation is plotted on Fig.3.

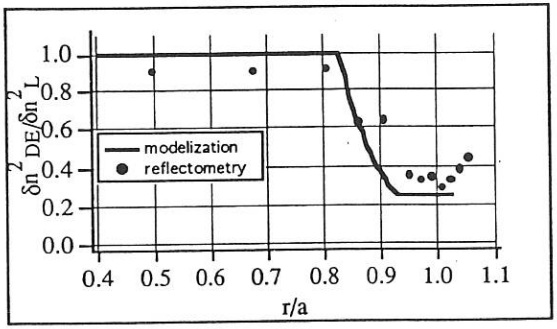


Fig.3 Ratio between fluctuations level with (δn^2_{ED}) and without ED(δn^2_L). Results coming from our modelization with data from coherent Thomson scattering are indicated with straight line. Reflectometry results are represented with circles for another discharge.

The reduction profile given by the reflectometry agrees with the one given in the previous model. However, reflectometry measurements come from one particular shot, where Thomson scattering whas exceptionally scanning the plasma on an internal line of sight shifted from 17cm on the high field side. In this particular configuration, the relative level of

fluctuations measured by coherent scattering is weakly modified when the E.D is switched on. Two explanations can be drawn. A change of the wavenumber spectrum, with ED, remains possible. Poloidal asymmetries may exist. Such asymmetries have been recently observed on the CCT tokamak [5].

6) Discussion

Transport and turbulence levels decrease from a factor larger than 2 in an intermediate zone between r/a≈0.83 and r/a≈0.93, when ergodic divertor perturbations exist on the edge of TORE SUPRA tokamak. No change is observed in the bulk (r/a<0.83) and at the edge (for r/a>0.93) transport increases and density fluctuations level decreases. A modification of radial electric field profiles may explain this. Although we cannot measure such profiles, we are able to estimate a change of the radial electric field jump at the $r/a=y_S$ transition by using Eq(1). The intermediate zone is not completely ergodic while transport is improved, but the radial electric field remains positive, so that the turbulence is mainly electrostatic with $\alpha_o=0$ [6]. Even if the gradient is very steep with ED, according to equation (1), the radial electric field jump can be written:

$$\Delta E_r = k_\theta \, \Delta\omega / B_\phi$$

The radial electric field jump is plotted (Fig.4) versus the average electron density, with and without ED. No significative change is observed.

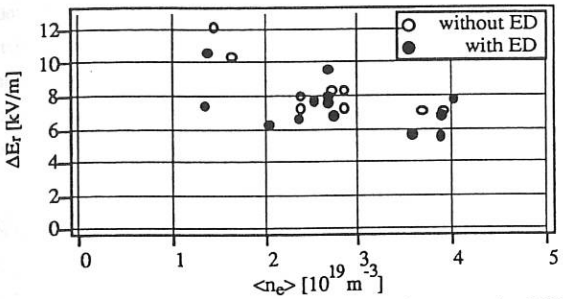


Fig.4 Radial electric field jump with ED (open circle) and without ED

Transport and turbulence improvements between r/a=0.83 and r/a=0.93 are not correlated with a modification of the radial electric field jump, but a modification of the radial electric field shear cannot be excluded as well as a modification of the radial electric field bend. On TORE SUPRA, preliminary density fluctuations measurements are obtained with reflectometry. The general trend seems to be in agreement with coherent Thomson scattering measurements although wavenumber spectra or/and poloidal asymetries may exist.

References:

[1] : X.Z. Yang, B.Z. Zhang, A.J. Wootton, et al., Phys. Fluids B3 (1991) 3448.

[2] : P.Devynck, X. Garbet, C. Laviron, et al., Plasma. Phys. Cont. Fusion. 35 (1993) 65.

[3] : G.R. Harris, H. Capes, X. Garbet, Nuclear Fusion 32, n°11 (1992), 1967.

[4] : M. Paume, F. Clairet, X.L. Zou, IAEA Techn. Commit. Meeting on microwave reflectometry for fusion plasma diagnostics, JET, England (1992).

[5] : T.L. Rhodes, R.J. Thaylor, E.J. Doyle, et al., Nuclear Fusion 33, n°12 (1993), 1787.

[6] : C.X. Yu, D.L. Brower, S.J. Zhao, et al., Phys. Fluids B4 (1992) 381.

Edge Plasma Measurements on Extrap T1 Reversed Field Pinch with Langmuir Probe Array

G.X. Li, G. Hellblom, H. Bergsåker*, A. Möller, J.H. Brzozowski and J. R. Drake

Dept. of Fusion Plasma Physics, Alfvén Laboratory, Royal Institute of Technology, S-100 44 Stockholm, Sweden

**Dept. of Physics Frescati, Royal Institute of Technology, S-104 05 Stockholm, Sweden*

1. Introduction Langmuir probe array measurements have been performed on the high aspect ratio (R/a = 8.8) and high plasma current density Extrap T1 reversed field pinch[1]. The study is focused on two goals. First, to measure the characteristics of the edge plasma including the steady state parameters and the fluctuations, which play an important role in the determination of the global plasma confinement in tokamak, stellarator as well as reversed field pinch(RFP)[2]. Second, we hope to provide an edge data base for the global RFP confinement study[3].

The probe array consists of four 0.5-mm-diameter molybdenum pins 1-mm long arranged in a square array 2 mm on edge. It is mounted on a manipulator which is located at 20° below the horizontal mid plane at the large major radius side and its radial position can be changed shot by shot. A rotating vacuum seal allowed the probe to be rotated to verify different alignment, with a precision of 1.5°. The triple probe technique was used to measure electron temperature, electron density, plasma potential including their fluctuated components. The frequency bandwidth of the electronics is 1 MHz. The fluctuation induced radial particle and heat fluxes can be calculated based on above fluctuated parameters, although we do not present such results in this contribution.

2. Edge Plasma Characteristics Due to the high parallel heat flux (of the order of 100 MW/cm^2 [4]) at the edge of Extrap T1 RFP the edge parameters have been measured only in the region $r/a_l > 0.93$ (a_l is the limiter minor radius, illustrated in Fig.1b, and r is the plasma minor radius) to avoid the arcing and the thermal electron emitting of the probe. During the ramp up phase (~ 200 μs) of the plasma current large spikes appear on the ion saturation current signal because of high initial plasma density(3~6 x $10^{14}cm^{-3}$, central chord averaged) and negative spikes appear on the floating potential signals, possibly caused by high energy electrons. During the sustained phase (~ 300 μs) of the plasma current the chord averaged density drops to around 1.0 x $10^{14}cm^{-3}$ and the spikes disappear from the probe signals, and all the data presented in this contribution were taken in this phase.

Fig.1 shows the radial profiles of the edge electron temperature, density and plasma potential and their relative fluctuation levels in the lower plasma current I_p (= 45 kA) discharges with pinch parameter $\Theta = B_\theta(a)/\langle B_t \rangle = 2.0$, reversal parameter $F = B_t(a)/\langle B_t \rangle = -0.5$ and central chord averaged density $\langle n_e \rangle = 0.8 \times 10^{14}cm^{-3}$. The data at each radial position is the average of 5 shots and the error bars reflect the data scattering and the system error. The edge electron density is nearly one order less than the chord averaged density and the edge electron temperature is also roughly one order

smaller than the central chord averaged electron temperature (~120 eV, from existed data base [1]). The scale lengths of the electron density and temperature are nearly the same: L_n = 0.82 cm and L_{Te} = 0.78 cm. An inward radial electric field E_r =13 V/cm was measured (Fig. 1b, with about 100% error bars of the plasma potential φ_{pl}) and a nearly toroidal E x B drift of velocity $u_{Er} = 8.0 \times 10^5$ cm/s, comparable to the electron diamagnetic drift velocity $u_{de} = T_e/(eBL_n) = 4.7 \times 10^5$ cm/s, was in the electron diamagnetic drift direction. The relative rms fluctuation levels of the plasma potential, the electron density and temperature (Fig.1c) have relations, as in tokamak[5], as $\tilde{\varphi}_{pl} / T_e > \tilde{n}_e / n_e > \tilde{T}_e / T_e$ which also means the Boltzmann relationship ($\tilde{\varphi}_{pl} / T_e = \tilde{n}_e / n_e$) is not satisfied (here $e\tilde{\varphi}_{pl} / k_B T_e$ is simplified as $\tilde{\varphi}_{pl} / T_e$, and k_B is Boltzmann constant). It is interesting to note that the relative fluctuation levels in the high current density Extrap T1 are nearly the same as in the other RFP's (ZT-40M[6], MST[7] and TPE-1RM20 [8]), and are slightly larger (about 50%) than that in tokamak [5].

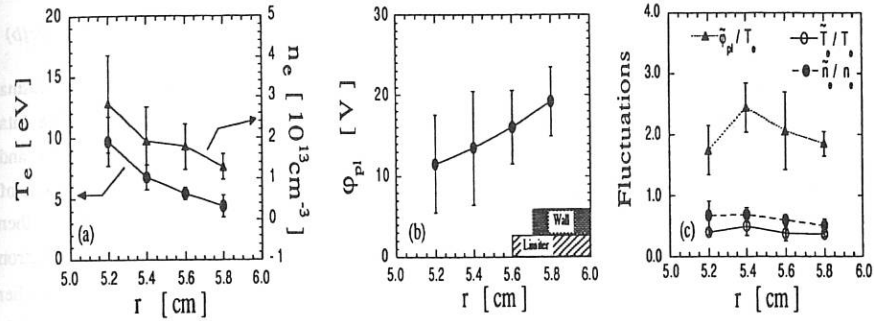


Fig. 1 Radial profiles of the electron temperature and density(a), the plasma potential(b) and their relative fluctuation levels(c).

Fig. 2 shows the fluctuation spectra at r =5.7 cm (the minor radius of the wall) of discharges of I_p = 60 kA, Θ = 1.65, F = – 0.25 and $\langle n_e \rangle = 0.8 \times 10^{14} cm^{-3}$. The frequency spectra of electron temperature, electron density and plasma potential (Fig.2a) are broader than that in larger RFPs [6,7,8], and are much broader than the magnetic fluctuation spectrum, of which the power density at 200 kHz is about two order less than the peak power density at lower frequency, measured at the edge of Extrap T1 RFP by internal coils[9]. Fig.2a shows that up to 500 kHz the power densities of all the three spectra just drop to values about 5 times smaller than their maximum values at frequencies below 200 kHz. The fast decrease at 500 kHz is due to the use of 500 kHz low pass filters. Coherent peaks can be seen on the three spectra at less than 300 kHz frequencies. The mode number spectra were estimated from the two-point method from the two floating potential signals. Fig.2b and Fig.2c show that the coherent modes of m=0, 1 and n=(0 to 16) ± 3, which have been identified as the internal resistive tearing modes associated with the dynamo process[1], superpose on the gauss-like distributed incoherent (turbulent) components. It is clear that the edge fluctuations of the plasma potential, the electron density and electron temperature, which determine the edge particle transport observed on the

other RFPs[6,7,8], are not dominated only by the dynamo related magnetic fluctuations, although magnetic fluctuations may contribute to the electron density/temperature fluctuations as indicated by the spectra difference between the plasma potential and the electron density/temperature (Fig.2a).

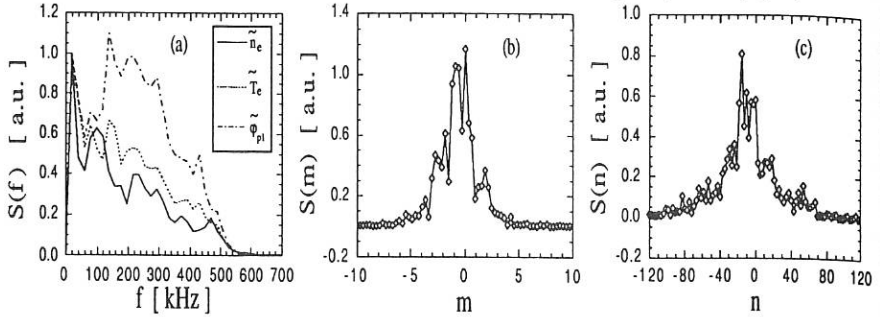


Fig. 2 Spectra of fluctuations near the wall in the domains of frequency (a), poloidal mode number(b) and toroidal mode number(c).

3. Edge Data base for Confinement Study Edge electron density, electron temperature and plasma potential and their fluctuation levels have been collected in a plasma confinement study. The data shown in Fig.3 are the results of a plasma current scan with constant Θ (= 1.65 ± 0.05, Fig.3a) and constant $\langle n_e \rangle$ = (0.75 ± 0.25) x $10^{14} cm^{-3}$ at r = 5.7 cm . Fig.3a also shows that the absolute value of field reversal parameter |F| decreases when the plasma current I_p increases from 60 kA to 100 kA then slightly increases around I_p = 110 kA. When I_p increases from 60 kA to 110 kA the edge electron density almost linearly increases although the chord averaged density does not increase, on the other hand the edge electron temperature linearly decreases from I_p = 60 kA till I_p = 100 kA then roughly maintains unchanged to I_p = 110 kA (Fig. 3b). Such variations can not be due to the displacement of plasma column since the electron density and temperature change in opposite directions. Simultaneous measurements showed that the central electron temperature and ion temperature were higher in the higher I_p discharges[3]. Therefore when I_p was increased, the consequences were that the temperature gradient was increased and the resistivity profile was changed, and presumably the resistive tearing mode activities and other instabilities, like resistive g-modes, should be different, which may affect the dynamo process and the plasma confinement[10]. We did observe that the edge relative fluctuation levels of electron temperature and density (Fig.3c) and plasma potential (Fig.3d) were larger in the higher plasma current discharges.

4. Summary The electron density, electron temperature and plasma potential and their fluctuations in the edge plasma of Extrap T1 RFP have been investigated. Near the limiter the electron density and temperature are about one order smaller then the central chord averaged electron density and electron temperature respectively. In lower plasma current discharges, the electron density and temperature almost have the same scale length. An inward radial electric field E_r = 1300 V/M was measured, which caused a toroidal ExB drift in the same direction and of the same order velocity as that of the

electron diamagnetic drift. The relative fluctuation levels of the plasma potential, the electron temperature and density are nearly the same as in other lower aspect ratio and lower current density RFPs, and are about 50% larger than that in tokamak. In the Extrap T1 RFP the frequency spectra of the edge fluctuations of the plasma potential, the electron density and temperature are broader than that in other RFPs, and the edge fluctuations are not solely dominated by the dynamo associated magnetic fluctuations. In a plasma current scan experiment of constant Θ and constant central chord averaged density the edge electron temperature was observed to be decreasing with the increasing of plasma current, while the edge density and the edge relative fluctuation levels of the plasma potential, the electron density and temperature were increasing.

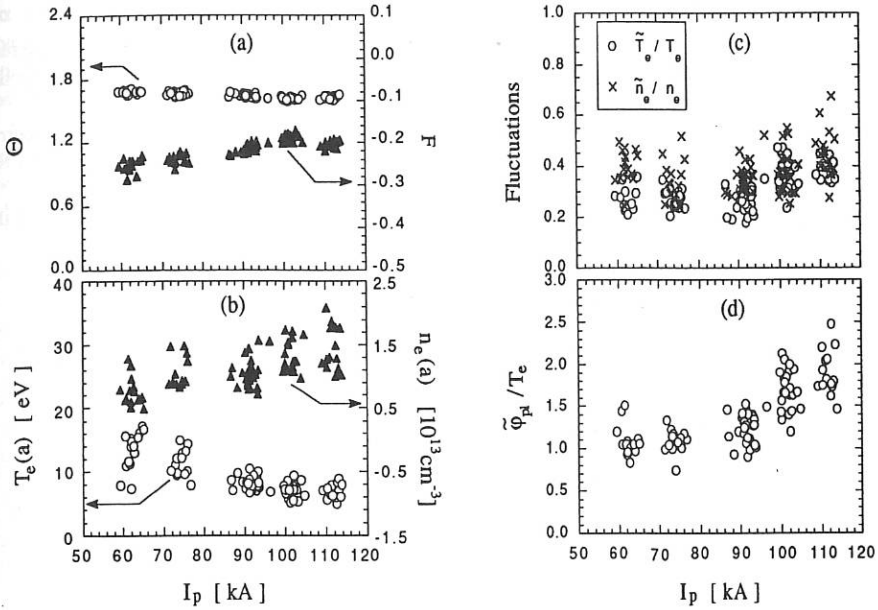


Fig. 3 A plasma current scan with constant pinch parameter and constant central chord averaged density. (a) Pinch and reversal parameters. (b) Edge electron temperature and density. (c) Relative edge temperature and density fluctuation levels. (d) Relative edge plasma potential fluctuation levels.

Acknowledgements and References We would like to thank S. Mazur, P. Nordlund and Dr. P. Brunsell for discussions on our measurement results. This research is sponsored by the European communities under an association contract between Euratom and Sweden.

[1] S. Mazur, P. Nordlund, K.-D. Zastrow, J.H. Brzozowski & J.R. Drake, Nucl. Fusion 34(1994) 427.
[2] A. J. Wootton, et. al., research report of FRC, University of Texas, FRCR#423, 1992.
[3] J.H. Brzozowski, et. al., in this proceeding.
[4] A. Möller, et.,al., in proc. 20th EPS conf. Contr. Fusion & Plas. Phys.,Vol.17C, Part II, 471(1993).
[5] Ch. P. Ritz, et. al., Phys. Rev. Lett. 62, (1989) 1844..
[6] H. Y. W. Tsui, et. al., Nuclear Fusion 31, (1991) 2371.
[7] T. D. Rempel, et. al., Phys. Rev. Lett. 67, (1991) 1438.
[8] P. R. Brunsell, et. al., to be published in Phys. Plasmas, July 1994.
[9] S. Mazur and P. Nordlund, private communication(1994).
[10] P. Nordlund, et. al., in preparation.

INFLUENCE OF LOCAL NEUTRAL CONCENTRATION ON EDGE TURBULENCE IN THE TJ-I TOKAMAK

M. A. Pedrosa, B. Brañas, I. García-Cortés, R. Balbín, C. Hidalgo, T. Estrada, E. de la Luna, F. Medina, M. A. Ochando, J. Qin, J. Sánchez, F. Tabarés, D. Tafalla, V. Zhuravlev and TJ-I Team
Asociación EURATOM/CIEMAT. 28040 Madrid. Spain

1.- Introduction

The role of neutrals on plasma confinement has been experimentally studied in different devices [1,2]. Ionization and charge exchange mechanisms can be directly affected by the presence of neutral particles [3].

Although there exist experimental indications of edge turbulence and edge electric fields modified by the presence of neutrals, the processes through which neutrals affect the plasma confinement are not understood yet.

The goal of this research is to investigate the role of neutrals as a driving force of the turbulence, by modifying the toroidal symmetry in the local neutral density.

2.- Experimental set-up

To study the effects of neutrals in the structure of the edge turbulence in the ohmically heated TJ-I tokamak (R=0.3m, a=0.1m, B=1 T, $\bar{n}_e \approx 1.0\text{-}4.0 \times 10^{19}$ m^{-3} and $I_p \approx 35$ kA), a specific experimental set-up has been designed: The working gas (hydrogen) was puffed during the plasma discharge by any of the two piezoelectric valves located in two different sectors 60° toroidally apart. Two Hα detectors were placed at the injection ports and looking at the plasma volume where two Langmuir probes arrays (2 mm x 2 mm four tips, 2 mm long and 0.4 mm in diameter) were inserted. One of the tips of each probe array was used to measure ion saturation current ($I_s \propto A n_e T_e^{1/2}$, A=Area of the probe) and its fluctuations ($\tilde{I}_s/I_s$). Two tips of each system were used to measure the poloidal phase velocity of the fluctuations (v_{ph}) deduced from the floating potential (V_f) and the fourth tip, working as a fast swept probe, was used to measure the edge electron temperature (T_e). The experimental method has been described previously [4,5,6]. The level of the ion saturation current fluctuations has been used as a monitor for the turbulence, however, this magnitude does not give a direct measurement of density fluctuations since electron temperature fluctuations are not negligible [4].

A dual heterodyne-AM reflectometer (33.7 GHz, X mode), placed in one of the above mentioned toroidal sectors, was used to measure turbulence at the radial location where the electron density was $n_e \approx 4\text{-}5 \times 10^{18}$ m^{-3}. The frequency and phase of the reflected beam, as well as the time delay were measured. The frequency signal has a large bandwidth (3 MHz) and is very sensitive to high frequencies. The time delay is an useful magnitude to monitor the position of the reflecting point and to check the reproducibility of discharges [7].

3.- Results

Measurements were carried out in series of repetitive shots with different line averaged densities ($1.5\text{-}4\times10^{19}$ m^{-3}) obtained by puffing different hydrogen levels. The gas was puffed from each of the valves in the different series.

Under the experimental conditions used, the intensity of the Hα emission is proportional, in first approximation, to the local electron density, to the edge local neutral density and to the excitation rate coefficient for the Hα transition, that depends on the electron temperature but only changes abruptly when $T_e<13$eV [8].

The values of the edge electron density and temperature measured simultaneously by the probes in the two toroidal positions were very similar, therefore, the ratio between the two Hα signals ($H\alpha^{(puff)}/H\alpha^{(no\ puff)}$) can be used as a measure of the degree of toroidal asymmetry in the local neutral density. Fig. 1 shows the ratio between the normalized ion saturation current fluctuations, measured in the flat top of the discharges, at the two toroidal positions versus the degree of asymmetry. Mean average electron density has been modified in a wide range ($1\text{-}4\times10^{19}$ m^{-3}), as well as edge electron temperature (10-40 eV) and independently of the values of these magnitudes, toroidal asymmetries in the turbulence have not been observed, within the range of change of the degree of asymmetry that has been induced in the experiment (up to a factor 3.5).

A detailed study of the turbulent spectral behavior has also been done. Fig. 2a shows the spectra of $\tilde{I}_s/I_s$ measured in the proximity and far from the neutral source; no modes induced by the neutral asymmetric density have been observed. In agreement with probe results, measurements obtained by the reflectometer in series of shots with the gas puffed by one of the two valves indistinctly, show no relevant differences in turbulence levels for frequencies in the range of the drift plasma frequencies (below 200 kHz), as is shown in Fig. 2b.

Turbulence was also measured in plasmas with the same average density achieved with different amounts of gas puffing and therefore with different recycling/impurity levels. Fig.3a shows the turbulence level in the reflectometer frequency signal as a function of Hα signal at the puffing location. Each symbol denotes a different average electron density $\bar{n}_e$. It can be observed that, for a given $\bar{n}_e$, turbulence level is sensitive to the puffing level and increases for a larger amount of puffing. The same behavior is observed in the phase signal above 300 kHz (Fig. 3b). The asymmetry in the Hα signal varies up to a factor of four.

Turbulence spectra were compared in the plateau of two discharges with different puffing level but the same $\bar{n}_e$. The time delay of the amplitude modulated microwave beam reflected at the plasma indicates that the reflecting position has not varied considerably, comparing the two shots, and consequently the electron density at this location has not changed either. Fig. 4 shows the spectra of the phase signals. The increase in the turbulence level with higher puffing level (i.e. with lower recycling/impurity levels) is systematic only for the higher frequency part of the spectrum (f>300 kHz). This suggests that either the increase of fluctuation level due to neutral concentration is significantly slighter or non existent for the lower frequencies or that it is masked by other effects. It should be noticed that any change in the density profile would modify the fluctuation level in the whole frequency range.

Fig. 5 shows the influence of a plasma density scan on the edge plasma parameters, for a probe placed at a fixed radial position ($r/a\approx0.99$). At the higher densities, obtained

increasing the level of gas puffing (i.e. increasing neutral influx), magnitudes measured in the edge by Langmuir probes change from values typical of the edge plasma to values typical of the scrape-off layer. Above a mean density value ($\bar{n}_e \approx 3.x10^{19}m^{-3}$), the poloidal phase velocity of fluctuations changes sign, $\tilde{I}_s/I_s$ increases up to a factor of 2 and mean values of I_s and T_e measured by the probes decrease. These results suggest that plasma profiles at high density are peaked in the center and flattened at the edge. The sharp change observed in v_{ph} indicates a variation of the velocity shear location to a position radially inwards. Measurements for an inner radial position of the probe ($r/a \approx 0.92$), are also shown in Fig.5: typical values of the probe parameters at the bulk side are obtained again for this probe position, corroborating the interpretation of changes in density profile and shear layer position. The change in the velocity shear position can be directly related with a change in the radial electric field.

Electron temperatures of the order or lower than the corresponding to the ionization potential for hydrogen, have not been obtained in the bulk region of the velocity shear layer of the TJ-I. This may be due to the fact that below this temperature neutral density increases strongly not only because of the neutral influx but also due to neutralization of the ions. It is in this case when all the reported changes of density and temperature profiles and radial electric field take place. Charge exchange and/or ionization can be considered as a possible explanation of the electric field modification [9].

4.-Summary and Conclusions

By changing the degree of toroidal asymmetry in the local neutral density up to a factor of 3.5, no asymmetric effects have been found in the edge turbulence of TJ-I. This result call into question the importance of ionization effects on edge turbulence [3]. Therefore, if the increase in the local neutral density induces changes in turbulence, these changes should occur via a global plasma parameter (e.g. the electron temperature).

Turbulence levels measured with reflectometry increase in the high frequency range when the local neutral source is larger. In the range of studied plasma conditions, the observed increment of phase fluctuations is only a factor 1.3. If the density profile at the reflection layer does not change it would represent a 30% increment in $\tilde{n}/n$ (for f>300 kHz), and even a change in the density gradient could not account for the change observed in the turbulence spectra, that is not the same in all frequencies.

Changes in plasma profiles have been observed when the electron density increases up to a critical value.

Low electron temperatures, below 13 eV, have not been obtained in the plasma bulk side of the velocity shear layer location of the TJ-I.

[1] M. Ali Mahdavi, N. Brooks et al., J. Nucl. Mater. **176 &177** (1990) 32.
[2] K. Mc. Cormick, G. Kyriakakis et al., J. Nucl. Mater. **196 &198** (1992) 264.
[3] J.N. Lebouef, D.K. Lee, et al. Phys. Fluids B **3** (8), 2291 (1991).
[4] C. Hidalgo, R. Balbín, M.A. Pedrosa, I. García-Cortés, M.A. Ochando, Phys. Rev Lett. **69** (1992) 1205
[5] R. Balbín, C. Hidalgo, M.A. Pedrosa, I. García-Cortés, J. Vega. Rev. Sci. Instrum. **63** (1992) 4605
[6] R. Balbín, A. Carlson, et al. Proc. 19th European Conference on Controlled Fusion and Plasma Physics, Innsbruck. **16C-II** (1992) 783
[7] V. Zhuravlev, B. Brañas et al. This Conference.
[8] K.H. Behringer, J. Nucl. Mater. **145 &147** (1987) 145.
[9] K.C. Shaing, W.A. Houlberg and E.C. Crume, Comments Plasma Phys. Controlled Fusion **12** (1989) 69.

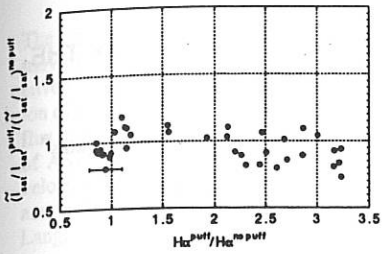


Fig. 1.- Ratio of $\tilde{I}s/Is$ measured at the gas puffing position over the one measured at the other toroidal position, versus the degree of asymmetry.

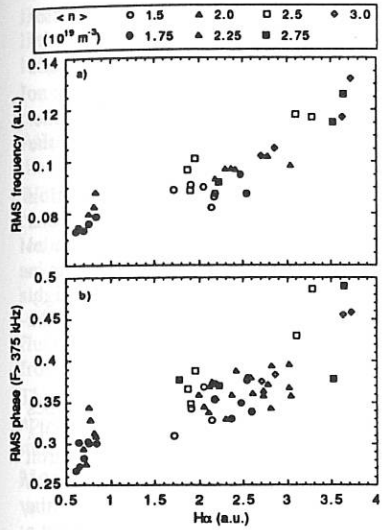


Fig. 3.- Turbulence level in the reflectometer frequency (a) and phase (b) signals as a function of Hα signal at the puffing location.

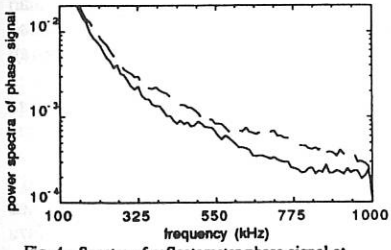


Fig. 4.- Spectra of reflectometer phase signal at the density plateau of two discharges with different puffing level but the same n_e. Dotted line corresponds to higher puffing level than solid one.

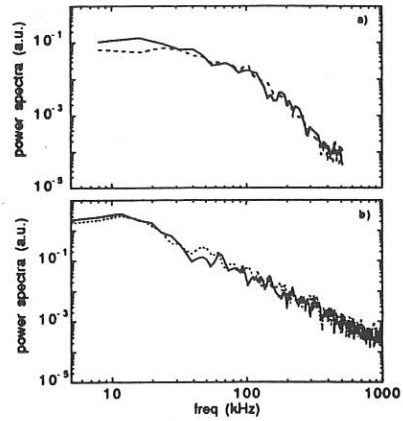


Fig. 2.- a) Spectra of $\tilde{I}s/Is$ measured for both tips in the same shot and b) reflectometer phase spectrum with puffing in two different valves, solid line correspond to the valve in the same port as the reflectometer.

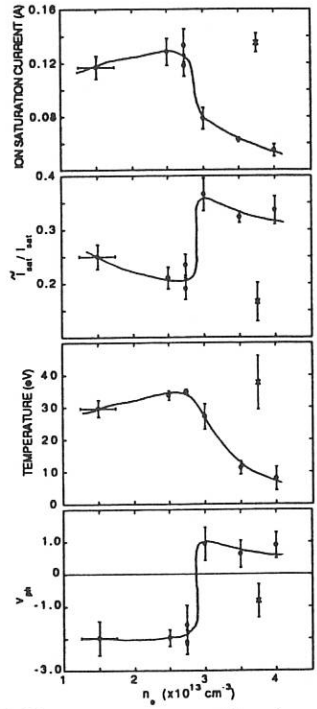


Fig. 5.- Plasma parameters measured for probe array at one fixed radial position (o r/a=0.99) versus mean density and at a radial position further inside (x r/a=0.92).

TURBULENT FLUCTUATIONS IN THE SCRAPE-OFF LAYER OF THE ASDEX TOKAMAK AND THE W7-AS STELLARATOR

M. Endler, L. Giannone, K. McCormick, H. Niedermeyer, A. Rudyj, G. Theimer, N. Tsois*, S. Zoletnik+, ASDEX Team and W7-AS Team

Max-Planck-Institut für Plasmaphysik, EURATOM Association, Garching, Germany

* NCSR Demokritos, Athens, Greece

\+ KFKI-Research Institute for Particle and Nuclear Physics, Budapest, Hungary

Introduction

The power density at the limiter or divertor target plates in tokamaks and stellarators is a function of the SOL width which is strongly determined by turbulent processes. In a reactor technical constraints require limiting the power density, and broadening the SOL by controlling the turbulent transport would be a desirable solution. Understanding the basic effects involved in the SOL turbulence is necessary for developing control schemes.

Turbulence in the SOL might also influence the anomalous transport in the confinement zone. Fluctuations will spread out from the zone where they are driven. The turbulent plasma in the SOL could even be involved in the formation of the H-mode thermal barrier.

In the edge plasmas of the ASDEX tokamak and the W7-AS stellarator fluctuation measurements were carried out. Based on the results a linear theoretical model has been developed predicting unstable modes which can explain the turbulence. From this model mixing length estimates for the radial transport and resulting density and pressure gradients in the SOL are derived and compared to measurements on ASDEX. In order to get more insight into the nonlinear development of structures in the turbulence we decompose data from probe arrays into space-time functions called "events" and analyse these events statistically.

Experimental Investigation of Turbulence

Floating potential or ion saturation current were measured with arrays of Langmuir probes (typically 16 pins) oriented in poloidal direction and inserted into the outboard SOL. Neglecting temperature fluctuations the probes measure the plasma potential Φ or the electron density n_e, respectively. H_α (or D_α) light emitted from the plasma edge in the vicinity of a gas puffing valve mainly reflects fluctuations of electron density integrated radially over the layer with significant neutral density. Signals from both diagnostics were usually sampled at a rate of 1 MHz and 16–19 Langmuir probe tips separated poloidally by 2–2.5 mm were used. For the 16 H_α channels a poloidal resolution of 6 mm was achieved [1,2].

A beam of neutral Li atoms with an energy of 20 - 66 keV is injected radially into the plasma. Measuring the Li I line emission at 670.8 nm along the beam path permits computing radial electron density profiles at W7-AS with a spatial resolution of 5 mm and a temporal resolution of typically 200 µs.

In ASDEX the measurements were performed under a wide variety of discharge conditions. The similarity of the SOL fluctuations on ASDEX and W7-AS is so striking that results from both machines can be discussed together.

The spatially resolved raw data reveal structures with high amplitudes (typically 30 % for n_e) moving poloidally in most discharges (see fig. 1 top and centre). Frequency spectra are broad with decreasing power density towards high frequencies up to typically a few 10 to 100 kHz. We prefer to describe the fluctuations in terms of their spatial-temporal correlation function. By a fitting procedure correlation time, poloidal correlation length, wavelength and velocity were determined from the correlation function in a wide range of plasma parameters [2,3,4].

The typical values obtained this way for the SOL are a correlation time of several 10 μs in the moving frame of reference, a poloidal wavelength of 4–8 cm and a poloidal half width (of the envelope to the periodic function) of 1–4 cm. In the SOL the fluctuation events move in the ion diamagnetic drift direction with a velocity of up to several 100 m/s, inside the last closed flux surface the direction changes sign. At high n_e (and correspondingly low T_e) in the SOL of ASDEX velocities of nearly 0 were observed. At low n_e and low magnetic field the velocity may reach 4000 m/s (W7-AS in discharges at 1.25 T). These fluctuation parameters are in good agreement for all three observed fluctuating quantities ($\tilde{I}_{sat}$ and $\tilde{\Phi}_{fl}$ from Langmuir probes and H_α intensity) for identical discharge conditions.

In some earlier experiments the radial correlation length of the fluctuations in the SOL of ASDEX was measured [5] and found to be in the order of 1 cm which is the same order of magnitude as both poloidal correlation length (see above) and radial width (scale length of the SOL). Measurements with the Li beam at low time resolution (200 μs) show rather high fluctuation amplitudes of the density and a high radial correlation over the whole SOL with little delay indicating that a large fraction of the fluctuation amplitude must be attributed to long-lived structures extending over the whole width of the SOL.

Ion saturation current fluctuations were found to be highly correlated (>82 %) and in phase over a distance of 10 m parallel to the magnetic field between mid-plane and divertor of ASDEX [1,6]. The fluctuations are flute-like and a 2d description in a plane perpendicular to the magnetic field seems to be justified.

With different tips of the poloidal probe array $\tilde{I}_{sat}$ and $\tilde{\Phi}_{fl}$ could be measured simultaneously. Neglecting temperature fluctuations one can derive the fluctuation-induced time-dependent local radial particle flux $\Gamma_r = \tilde{E}_{pol} \cdot \tilde{n}/B$. Its amplitude distribution function is strongly asymmetric: the transport is almost completely directed radially outwards and displays signatures of intermittency (see fig 1 bottom) [2]. The fluctuations of I_{sat} are phase-shifted by $-\pi/2$ poloidally as compared to $\tilde{\Phi}_{fl}$, resulting in a maximum outwards transport for a given fluctuation amplitude. This turbulent particle flux explains the total particle flux estimated from recycling measurements within the uncertainty [1].

The fluctuations are driven on the outboard side of the torus. In ASDEX the fluctuations appear at the inboard (high field) side of the torus only in single null configurations when the inboard and outboard parts of the SOL are connected [1].

Model for a SOL-specific instability

We developed a simplified linear 2d SOL fluctuation model based on the same effects as used in [7,8] but included temperature fluctuations simultaneously with density and potential fluctuations [2]. In this electrostatic single fluid model we retained only those effects which in our opinion are basic for the instability mechanism in the SOL, guided by the experimental results. The curvature (inboard-outboard asymmetry!) and the sheath at the target plates (long correlation $\parallel$ B!) are essential for this model.

Classical dissipative effects are neglected. Polarization drifts are neglected because the experimentally observed frequencies are well below the ion cyclotron frequency. We assume cylindrical geometry with helical magnetic field lines connecting an upper and a lower annular target plate. By choosing the direction of the radial n and T gradients this geometry can approximate either the outboard or the inboard side of the SOL.

The resulting system of three equations in n, T and electric potential Φ is linearized around equilibrium parameters to be taken from the experiment. At the outboard side waves are unstable below a certain wavelength limit. In the limit $\lambda \to 0$ this mode is similar to a resistive interchange mode with the plasma resistance replaced by the sheath resistance. In [4] it was shown that experimental correlation data and grow times or wavelengths from the model, respectively, agree well.

By mixing length arguments an "anomalous diffusion coefficient" $D_\perp$ can be estimated. We add as a crude correction for colder plasmas ($T < 10$ eV) the plasma resistance to the sheath resistance and obtain

$$D_\perp \approx \frac{2T_0 L|\partial p_0/\partial r|}{B^2 R p_0}\left(\frac{T_0}{c_s V} + 1.3\cdot 10^{-5}\frac{e n_0 L \ln\Lambda}{T_0^{3/2}}\right)$$

T_0 is in eV, all other quantities in SI units; L is the magnetic connection length and V is the mean ratio of electron to ion current onto the target plates; ln Λ is the Coulomb logarithm.

This expression together with the equilibrium balance equations for the SOL yield a "self-consistent" expressions for $D_\perp$ and for the scale lengths of pressure and density [2,3,4]. For several different parameter scans in ASDEX these were compared to values measured with Langmuir probes in the divertor or with a neutral Li beam at the midplane. All absolute values agree better than within a factor of three, some much better. Parameter dependencies have always the same tendency. The agreement is best for parameters where the assumption of negligible gradients of temperature and density along the field lines is best justified.

Analysis of single events

Short correlation lengths and short correlation times of the fluctuation patterns as observed in ASDEX and W7-AS suggests to investigate the evolution of fluctuations within short time intervals and small volumes ("events"). A localized potential hill with a limited lifetime is the prototype of an event. Around its centre the plasma flows along circular streamlines. Volume elements of different densities are exchanged resulting in particle transport. The correlation functions computed from experimental data are well reproduced by a random superposition of events with proper probability distribution functions of the parameters [9].

We identify events by a fitting method in multi-channel raw data (see also [10]). Position in time and space, amplitude, size, growth time, decay time and velocity are fitting parameters. A fit minimizing the sum of absolute deviations was chosen because it is less sensitive to superimposed smaller structures than a least-squares fit. Identified events were subtracted from the data set, and the procedure was iterated until only 10 % of the original energy remained. The data base of parameters obtained is used for further analysis.

The probability distribution of the size is $\propto \exp(-D/D_0)$, $D_0 = 2$ mm. There is no fixed relation between size and lifetime, smaller events are, however, in the average shorter lived than larger ones. The amplitude distribution (integrated over all sizes) is Gaussian. Larger events have in the average slightly higher amplitudes.

Data around about 40 selected events with large values of the ratio amplitude / size were averaged. At one side of the events with positive potential there is a cluster of negative events (fig. 2) and vice versa. The "companions" are spread out in time. Pairs are oriented in such a way that the plasma flows radially outward between the poles.

Discussion and conclusion

Based on magnetic curvature, E×B drifts and the potential perturbations caused by parallel electric currents onto the target plates an electrostatic instability mechanism similar to the resistive interchange has been described which qualitatively and quantitatively explains many features of the fluctuations observed in the SOLs of ASDEX and W7-AS. Transport properties estimated with this model agree with experimental values within the uncertainties.

Effects like the following should be tested in the framework of the model and, if necessary, included: viscosity, polarization drift, atomic processes, gradients parallel to the magnetic field, realistic geometry. The understanding of the basic effects reached so far seems to be sufficient to develop control schemes for the SOL width. It is useful to get more insight into localized nonlinear processes from the experiment or from a computer simulation to be performed. The "event" analysis is able to clear up such phenomena, for example the formation of oriented dipoles as shown.

References

[1] A. Rudyj, PhD thesis, Technische Universität München, 1990, report IPP III/160.

[2] M. Endler, PhD thesis, Technische Universität München, 1994, report IPP III/197.

[3] M. Endler et al., PSI conference 1994, to appear in J. Nucl. Mater.

[4] M. Endler et al., Proc. 20th EPS Conf. on Controlled Fusion and Plasma Physics, Lisboa 1993, volume 17C, part II, pp. 583-586.

[5] M. Krämer and A. Carlson, Proc. 16th EPS Conf. on Controlled Fusion and Plasma Physics, Venice 1989, volume 13B, part III, pp. 923-926.

[6] A. Rudyj et al., Proc. 16th EPS Conf. on Controlled Fusion and Plasma Physics, Venice 1989, volume 13B, part I (European Physical Society, 1989) pp. 27-30.

[7] A. V. Nedospasov, Soviet Journal of Plasma Physics 15 (1989) 659.

[8] X. Garbet, L. Laurent, J.-P. Roubin and A. Samain, Nucl. Fusion 31(1991) 967.

[9] M. Endler et al., Proc. 1992 Int. Conf. on Plasma Physics, Innsbruck 1992, volume 16C, part II (European Physical Society, 1992) pp. 787-790.

[10] O. Kofoed-Hansen, H. L. Pécseli and J. Trulsen, Physica Scripta 40 (1989) 280-294

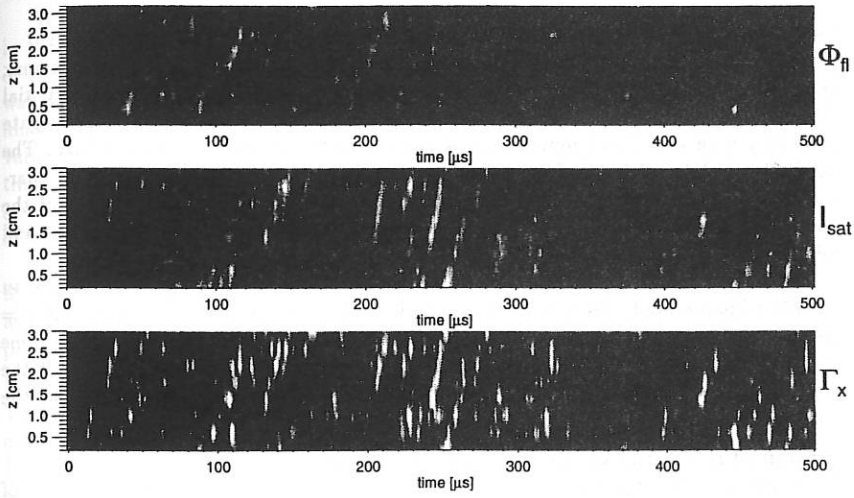


Fig. 1 Floating potential (top) and saturation current fluctuations (centre) measured simultaneously with a 17-pin Langmuir probe array. The radial particle flux $\tilde{n}\cdot\tilde{v}$, caused by the E×B drift is shown at the bottom. Amplitudes are encoded in grey shades: white means maximum (positive) value, black means minimum value.

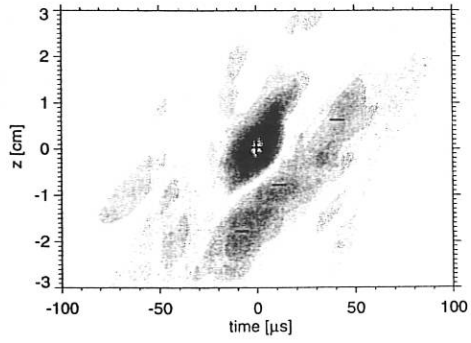


Fig. 2 Averaged surroundings of events with positive potential in the centre.

Stochastic ion trajectories in a potential landscape

L. Krlín, J. Stöckel, V. Svoboda, J. Holakovský
Institute of Plasma Physics, Czech Academy of Sciences
Za Slovankou 3, P.O.B.17, 182 11 Praha 8, Czech Republic

Abstract
Recently, Bellan [1] proposed a mechanism of test ion transport in magnetized plasmas with *time-varying* perturbations of the plasma potential ("blobs"). Transport appears as a result of jumps of test ions from a dying to a newly forming blob.

Here, we analyze the transport of test ions in *stationary* perturbations of the plasma potential. We use a model potential which is spatially periodical in the poloidal plane, similar in dimensions and amplitudes to the real situation in the poloidal plane of tokamaks . Then we calculate trajectories of test ions in such a potential landscape so as to estimate the diffusion coefficient and to compare it with the typical experimental value.

Potential fluctuations on the CASTOR tokamak($R_0 = 0.4\ m,\ a = 0.085\ m$)
The correlation analysis, performed in the edge plasma on the CASTOR tokamak by multiple tip probes, has identified localized perturbations of the plasma potential ("blobs"). These blobs, elongated in the poloidal direction $\lambda_p/\lambda_r = 2 - 4$, propagate poloidally with $v = 1 - 3\ mm/\mu s$ in the ion diamagnetic drift direction in SOL. The poloidal correlation length of the potential blobs is $\lambda_p = 10 - 20\ \ mm$, and their characteristic lifetime is greater then $t_{life} \sim 10 - 15\ \mu s$. The typical RMS values of the potential fluctuations are $\tilde{\phi} \sim 10 \div 20\ V$, and so the difference between the maxima and minima of potential is $U^{max} - U^{min} < 2\sqrt{2}\tilde{\phi} \doteq 60\ V$.

Let us assume an individual blob in the poloidal plane ($B = 1\ T$), which has an idealized "paraboloid" form with $U = 30\ V$ and with the base of diameter $2r_0 = 15\ mm$. The test ion circumnavigates around the blob [1] with a characteristic time $\tau_{circ} = \pi r_0^2 B/U \sim 5\ \mu s$, which is noticeably shorter than the typical lifetime of the blob. Therefore, we assume it is worthwhile to analyze the ion trajectories assuming the potential is *stationary*.

Motion of a test ion in the potential landscape
We model the ion trajectories in the poloidal plane, assuming an orthogonal system of coordinates x,y. The idealized model of 2D- potential, chosen as

$$U(x,y) = U_0[sin^2(k.x) + sin^2(k.y)] \tag{1}$$

is plotted (in 3D and 2D) in Fig.1a,b. The landscape is a periodical mesh of maxima (hill) and minima (valley) of potential. The distance between adjacent hills (or valleys) is $\lambda = \pi/k$. The equipotential lines with $U = U_0/2$, which are the *separatrixes*, divide the potential landscape into the rectangular cells, each containing either an individual hill or valley. The cross-points between the separatrixes are the *saddle points*.

The trajectory of a test ion in such potential landscape is described by the equation of motion with $\vec{E} = (E_x, E_y, 0)$, $\vec{B} = (0, 0, B)$

$$\ddot{x} = +\omega_{ci}[\dot{y} - v_d.sin(2kx)] \qquad \ddot{y} = -\omega_{ci}[\dot{x} + v_d.sin(2ky)] \quad , \tag{2}$$

where $v_d = U_0 k/B$ is the characteristic velocity of the $\vec{E} \times \vec{B}$ drift.

Frozen and stochastic trajectories

Fig. 1b. shows the trajectories of two test protons starting their motion at a hill and at a valley The initial velocity corresponds to a thermal velocity at $T_i = 16\ eV$. The maximum potential is chosen as $U_0 = 20\ V$, the distance between maxima is $\lambda = \pi/k = 6.28\ mm$, $(k = 0.5\ mm^{-1})$ and $B = 1\ T$.

The trajectories are vortex-like and represent a superposition of the cyclotron motion and the circumnavigation around the selected potential maximum (minimum). Trajectories are frozen to a local potential hill (valley) under these conditions.The Larmor radius is $\rho_i \doteq 0.5\ mm << \lambda$. Note the different form of the trajectories of ions bounded either to a hill or to a valley.

The picture changes dramatically for higher amplitudes of potential perturbations. Some test ions are no longer trapped and they wander in the potential landscape, as shown in Fig.2 for $U_0 = 80\ V$. The Larmor radius of the wandering ions is comparable with the blob diameter and their trajectories cross the saddle points.

We have found that the test ion behaviour depends strongly on the starting position in the potential landscape. Therefore we performed a systematic investigation. A part of the landscape was divided into $M \times M$ pixels ($M \sim 10$) and N test ions ($N \sim 10$) was launched randomly from every of them. The time interval t_f during which the test ion remains "confined" to the corresponding hill/valley was determined. The average value of t_f over a pixel is $\bar{t}_f$. The grayscale plot of the pixels with a finite confinement time (emphasized by dark colors) is shown in Fig.3 for $U_0 = 80\ V$. We see that the starting points most favourable for future wandering are located close to the hill—side of the separatrix.

This procedure allow us to characterize the diffusion in such a potential landscape by defining the "statistical" diffusion coefficient $D =< \lambda^2/\bar{t}_f >$ where $< ... >$ means an averaging over all $M \times M$ pixels. Variation of D with the amplitude of potential perturbations is shown in Fig.4.

Hamiltonian approach and possible mechanisms of the diffusion

The motion of a particle in a constant magnetic field B_z and in a spatially periodically variable electrostatic potential $U = U_0[\sin^2 kx + \sin^2 ky]$ (valley- type) and $U = U_0[\cos^2 kx + \cos^2 ky]$ (hill-type) can be described in the poloidal plane (here referred as coordinates x, y) by means of the Hamiltonian H

$$
\begin{aligned}
H \;=\; & \omega_c J_1 + eU_0[1 + \frac{1}{2}k^2\frac{2J_1}{m\omega_c} \pm (\frac{1}{2} - \frac{1}{4}k^2\frac{2J_1}{m\omega_c}) \times \\
& \times[\cos(2k\sqrt{\frac{2J_2}{m\omega_c}}\cos w_2) + \cos(2k\sqrt{\frac{2J_2}{m\omega_c}}\sin w_2)\,] - \\
& \mp k\sqrt{\frac{2J_1}{m\omega_c}}\,[\sin w_1 \times \sin(2k\sqrt{\frac{2J_2}{m\omega_c}}\cos w_2) + \cos w_1 \times \sin(2k\sqrt{\frac{2J_2}{m\omega_c}}\sin w_2)\,] + \\
& \pm\frac{1}{4}k^2\frac{2J_1}{m\omega_c}\cos 2w_1[\cos 2k\sqrt{\frac{2J_2}{m\omega_c}}\cos w_2 - \cos 2k\sqrt{\frac{2J_2}{m\omega_c}}\sin w_2]\,]. \qquad (3)
\end{aligned}
$$

Here, $\omega_c J_1$ represents the perpendicular energy (ω_c is the cyclotron frequency, $\omega_c J_1 = \frac{1}{2}mv_\perp^2$ is the energy of the cyclotron motion). The meaning of the new coordinates J_i,

w_i is quite simple. The generalized momentum J_1 is allied to the cyclotron radius r_c as $r_c = \sqrt{\frac{2J_1}{m\omega_c}}$, and the canonically conjugated coordinate w_1 is simply the angle of the cyclotron rotation $w_1 = \omega_c t + w_{10}$. The generalized momentum J_2 is analogously connected with the radius of the guiding centre r_D, $r_D = \sqrt{\frac{2J_2}{m\omega_c}}$, and the conjugated coordinate w_2 is the angle of the guiding centre in the plane x, y. The upper sign corresponds to the hill-type of the potential, the lower to the valley-type. For this canonical formalism, see e.g. [3].

This form of the Hamiltonian suitable describes the particle motion for the case when the drift velocity is substantially smaller than the velocity of the cyclotron motion. In this approximation, and using perturbation analysis, it is possible to find a lot of nonlinear resonances between the cyclotron and drift motion of the type $\omega_c - n\omega_D = 0$ where ω_D is the angular frequency of the drift motion. Changing its radial position, the particle can enter into the whole set of these resonances.

Due to the nonlinear character of the dynamics, the resonant change of J_2, and consequently, of r, is limited to some value δJ_2 and δr.

Let us label $\triangle r_{n,n+1}$ as the mean radial distance between neighbouring resonances. The approximative expression for the stochasticity threshold is given by the requirement $\delta r > \triangle r_{n,n+1}$. Using the perturbation analysis, we have estimated this stochasticity threshold for $U_0 = 50\ V$ and for the energy of protons $16eV$ and have found that in the region of the separatrix the interaction just exceeds this stochasticity threshold and particles move in a form of a random walk. For $U_0 = 100\ V$, the system starts to be globally stochastic. This seems to be in an agreement with the numerical results, discussed previously.

The conditions for the stochastic threshold depends strongly on three parameters U_0, k, and ω_c. The stochasticity regime requires larger values of U_0, and lower values of ω_c. Consequently, the stochasticity - and the corresponding diffusion in the potential landscape - can be reached for large-scale turbulent regime, and for ions with lower cyclotron frequency (e.g. for D-, T-, alpha-particles and for heavy ions impurities). For particles with Larmor radii comparable with the dimensions of the hill (and, therefore, not describable by our perturbation analysis), the stochasticity also strongly increases.

Summary

The present contribution has been inspired by the paper of Bellan [1]. We try to show here that the diffusion of ions in a spatially periodical potential (which simulates the edge turbulence) can appear even if the potential structures are quasi-stationary.

Using both the numerical and analytical approaches, we found that such diffusion, caused by non-linear effects, appears for plasma parameters close to the experimental ones. This phenomenon can be regarded as an additive mechanism of particles transport, being obviously relevant to the well-developed turbulence and for heavier ions.

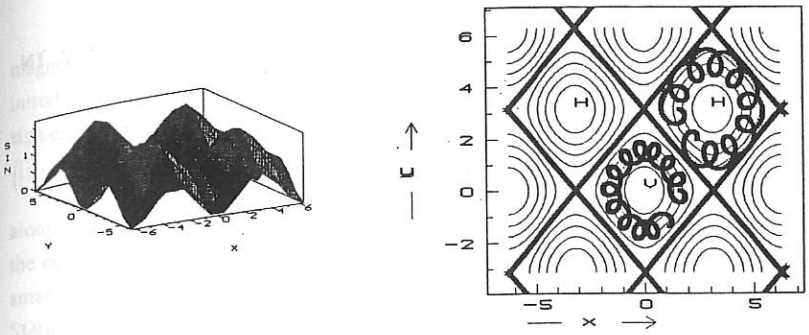


Fig. 1. a) 3D plot of the potential landscape
b) 2D plot with proton trajectories around hill (H) and valley (V) ; $U_0 = 25\ V$.

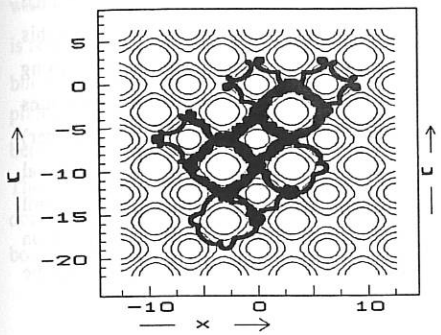


Fig. 2. "Chaotic" trajectory; $U_0 = 80\ V$

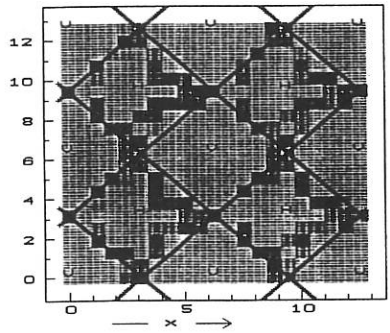


Fig. 3. Grayscale plot of the "confinement time" t_f, $(v_y(0) = 0)$.

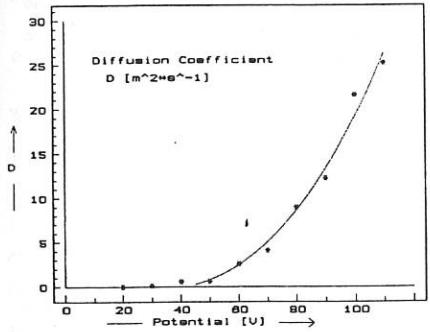


Fig. 4. "Statistical" diffusion coefficient versus potential U_0

Acknowledgement: Work was performed under GACR - grant No. 202/0711 and supported by IAEA contract No. 6702/RB.

References

/1/ Bellan P.M.: Plasma Phys. and Contr. Fus., 35, 1993, 169-178
/2/ Stöckel J., et al: 20th EPS-conf., Lisabon 1994, Vol.2, 691
/3/ Krlín L. et al: Plasma Phys. and Contr. Fus.,29,1987,1653

THE SOL WIDTH AND THE MHD INTERCHANGE INSTABILITY IN TOKAMAKS

O. Pogutse* and W. Kerner
JET Joint Undertaking, Abingdon, Oxfordshire OX14 3EA, U.K
*RRC Kurchatov Institute, Moscow, Russia.

1. INTRODUCTION

The hot core plasma in tokamaks is surrounded by the scrape-off-layer (SOL), a region of relatively cold plasma with open field lines intersecting the limiter or the divertor target plates. Previous theoretical work has revealed that instabilities in the SOL plasma can strongly influence the SOL plasma behaviour and, in particular, the SOL width, x_0 [1-4]. The SOL stability analysis (resembling that of open traps) shows that there exists a critical ratio of the thermal energy and the magnetic energy, β_{cr}. If the SOL beta is greater than this critical value, β_{cr}, the magnetic field cannot prevent the plasma displacement and a strong MHD instability in the SOL occurs. In the opposite case only slower resistive instabilities can develop. The resistive instabilities depend strongly on both the volume (Spitzer) conductivity and the sheath conductivity near the end plates. In this paper a theoretical investigation of the SOL plasma stability is presented for JET single-null and double-null divertor configurations. The dependence of the stability threshold on the SOL beta and on the sheath resistance is established. Applying a simple mixing length argument gives the scaling of the SOL width.

2. DISPERSION RELATION

The plasma is described by the macroscopic single-fluid MHD model. For the case of a strong magnetic field a simplified system of reduced equations can be applied [3]. The behaviour of linearised perturbations around an equilibrium state are studied by means of the Fourier Ansatz $e^{i\underline{k}\cdot\underline{r}}$ leading to the following dispersion relation for the growth rate γ.

$$\left[\gamma + k_\perp^2 \mu_\perp\right] - \frac{G(\ell)}{\left[\gamma + k_\parallel^2 \cdot \chi_\parallel + k_\perp^2 \cdot \chi_\perp\right]} + \frac{k_\parallel^2 \cdot C_A^2}{\left[\gamma + k_\perp^2 \cdot D_M\right]} = 0, \qquad (1)$$

where $$G(\ell) = \omega_g^2 \cdot \left(k_y^2 / k_\perp^2\right), \quad \omega_g^2 = \frac{1}{R(\ell)M} \cdot \frac{dP_0}{n_0 dx} \equiv \frac{C_s^2}{x_0 R(\ell)},$$

$$\frac{1}{x_0} = -\frac{dP_0}{P_0 dx}, \quad C_A^2 = \frac{B_0^2}{4\pi M n_0}, \quad D_M = \frac{c^2}{4\pi\sigma_s}, \quad C_s = \left(P_0 / (M \cdot n_0)\right)^{1/2},$$

$\mu_\perp$ denotes the transverse viscosity, $\chi_\parallel$ ($\chi_\perp$) the parallel (perpendicular) thermal conductivity and σ_s the Spitzer conductivity. A new coordinate system with ℓ the coordinate along the

magnetic field line and the local orthogonal coordinates (x, y) in the transverse (R, Z) plane is introduced. In this system all quantities have only weak dependence on ℓ and do not change sign except the quantity $R(\ell)$ which is defined by $\left(\left[\vec{k}\times\nabla(1/B)\right]\cdot\left[\vec{k}\times\nabla P_0\right]\right)\cdot B_0/n_0 \equiv \frac{1}{R(\ell)}\cdot\frac{dP_0}{n_0 dx}\cdot k_y^2$, and does change its sign along ℓ as indicated in Fig. 1. Since $R(\ell)$ is the most important term, the weak dependence of the other quantities on ℓ can be neglected. This ordering is suitable for taking into account small-scale transverse perturbations, where the transverse wave length is smaller than the SOL width. From Eq. (1) we can restore the differential equation. In particular, the component along the magnetic field line, i.e. along ℓ, is given by

$$\frac{\partial}{\partial\ell}\frac{C_A^2}{\left[\gamma+k_\perp^2\cdot D_M\right]}\frac{\partial}{\partial\ell}\Phi' - \left[\gamma+k_y^2\cdot\mu\right]\cdot\Phi' + \frac{G(\ell)}{\left[\gamma+1/\tau_\parallel+k_\perp^2\cdot\chi_\perp\right]}\Phi' = 0, \quad (2)$$

where Φ' is the perturbed electrostatic potential, $\left(\vec{b}\nabla\right)\equiv\nabla_\parallel\equiv\partial/\partial\ell$, and the operator $k_\parallel^2\cdot\chi_\parallel$ is replaced by the constant $1/\tau_\parallel$. This allows to reduce the order of the differential equation but still accounts for longitudinal losses. In the case of free-streaming losses onto the target plates at ion sound velocity, C_s, $\tau_\parallel$ is estimated as $\tau_\parallel = L_\parallel/C_s$, where $2L_\parallel$ is the distance between the target plates along $\vec{B}$. The hydrodynamic region is characterised by $\tau_\parallel = L_\parallel^2/\chi_\parallel$. The differential equation needs to be completed by an appropriate boundary condition as done in Ref. [5]. Neglecting small dissipative terms, i.e. $\mu_\perp$, $\chi_\perp$ and $1/\tau_\parallel$, equation (2) and the boundary condition are rewritten in more convenient, dimensionless variables

$$\frac{\partial}{\partial s}\frac{1}{\beta^*\cdot\left[\bar{\gamma}+\delta\right]}\frac{\partial}{\partial s}\phi - \bar{\gamma}\cdot\phi + \frac{\bar{G}(\ell)}{\bar{\gamma}}\cdot\phi = 0, \quad \frac{\partial}{\partial s}\phi\Big|_{s=\pm1} = (\mp1)\cdot\alpha\cdot\phi. \quad (3)$$

Here $\phi = e\cdot\Phi'/T$, $s = \ell/L_\parallel$, $\bar{G}(\ell) = G(\ell)/G$, where G is a characteristic value such that $-1 < \bar{G}(\ell) < +1$, $\beta^* = L_\parallel^2\cdot G/C_A^2 = L_\parallel^2/(x_0\cdot R)\cdot\beta$, where $\beta = 4\pi P/B_0^2$ is the usual beta for SOL parameters, $\bar{\gamma} = \gamma/(G)^{1/2}$, $\delta = k_\perp^2\cdot D_M/(G)^{1/2}$, $\alpha = \alpha_1\cdot\left(\bar{\gamma}+\delta\right)$ with $\alpha_1 = \left(\frac{L_\parallel^2}{x_o\cdot R}\right)^{1/2}\left(\frac{\omega_{pi}}{k_\perp\cdot c}\right)^2$. It is emphasised that in this dimensionless form β^* appears, which is of order unity, instead of the small $\beta\ \left(\approx 10^{-4}\right)$.

The pumped divertor, which was recently installed at JET, is a single-null divertor. For this magnetic field line geometry the curvature term $G(\ell)$ in Eq. (2), plotted in Fig. 1, changes sign while the average part is approximately zero. Numerical evaluation shows that the closer the field is to the separatrix the more $G(\ell)$ assumes a step-function dependence. For analytical treatment we assume that $G(\ell) = \theta\left(\ell-\ell_\parallel\right)$ is a step function. However, the simplest situation with constant $G(\ell)\equiv 1$ can be regarded as a suitable model for a double-null divertor. For the **single-null divertor** the step-function model for the curvature term

$G(\ell)$ is adopted.

The eigenfunction in the unstable region I (see Fig. 2) is given by the ansatz

$$\phi_1(s) = C_1 \cdot \left[k \cdot \cos\left(k \cdot (1-s)\right) + \alpha \cdot \sin\left(k \cdot (1-s)\right)\right], \quad k^2 = \beta^* \cdot \left(\bar{\gamma} + \delta\right) \cdot \left(1/\bar{\gamma} - \bar{\gamma}\right). \tag{4}$$

For the stable region II the eigenfunction has the following dependence

$$\phi_2(s) = C_2 \cdot \left[\kappa \cdot ch\left(\kappa \cdot (1-s)\right) + \alpha \cdot sh\left(\kappa \cdot (1-s)\right)\right], \quad \kappa^2 = \beta^* \cdot \left(\bar{\gamma} + \delta\right) \cdot \left(1/\bar{\gamma} + \bar{\gamma}\right). \tag{5}$$

It is easily verified that these eigenfunctions satisfy the boundary conditions at both target plates. Using the matching conditions between the two regions

$\phi_1(0) = \phi_2(0)$, $\partial\phi_1(0)/\partial s = \partial\phi_2(0)/\partial s$ yields the dispersion relation

$$\frac{k + \alpha \cdot \tan(k)}{k \cdot \left(k \cdot \tan(k) - \alpha\right)} = \frac{k + \alpha \cdot \tanh(\kappa)}{\kappa \cdot \left(\kappa \cdot \tanh(\kappa) + \alpha\right)}, \tag{6}$$

The stability threshold is given by $\beta^*_{cr} = (2.365)^2 \approx 5.6$. The growth rate for arbitrary β^* is displayed in Fig. 2.

The corresponding diffusion coefficient obtained from the mixing length argument is in physical variables

$$\chi_\perp = D_\perp = c^2/\omega_{pi}^2 \cdot \left(\beta^*/\beta^*_{cr}\right)^2 \cdot C_s/L_\parallel. \tag{7}$$

In comparison with the linear dependence on β^* for the double-null case a quadratic dependence occurs. Making use of the diffusion equation the SOL width for the single-null divertor is estimated as

$$x_0 = \left(\beta^*/\beta^*_{cr}\right) \cdot c/\omega_{pi} \quad \text{with the scaling } x_0 \sim L_\parallel \cdot R^{-1/2} \cdot n^{1/4} \cdot T^{1/2} \cdot B^{-1}. \tag{8}$$

The final result states that x_0 cannot exceed the value c/ω_{pi}.

DISCUSSION

The stability analysis concerning interchange modes in SOL plasmas has been carried out for single-null and double-null divertor geometry. Applying a mixing length argument scalings for the transport coefficients and the SOL width were derived in different regimes. The longitudinal loss mechanisms take into account the hydrodynamical regime $(\lambda_i < L_\parallel)$ with $\tau_\parallel = L_\parallel^2/\chi_\parallel$ and the kinetic regime $(\lambda_i > L_\parallel)$ with $\tau_\parallel = L_\parallel/C_s$. The ideal MHD interchange instabilities define a stability limit for the SOL plasma beta, β^*_{cr}. At lower beta values $\left(\beta^* < \beta^*_{cr}\right)$ resistive interchange instabilities occur and the resulting turbulence determines the SOL width. It is shown that for the volume (Spitzer) resistive being the dominant dissipation process the perpendicular transport $\chi_\perp \sim \chi^S_\perp \sim D_M\ \beta^*/\beta^*_{cr}$ is the same for single-null and double-null divertor configurations. For the sheath resistance the transport coefficient scales as $\chi^{sh}_\perp \sim \frac{c^2}{\omega_{pi}^2}\left(\frac{\beta^*}{\beta^*_{cr}}\right)^2 \frac{C_s}{L_\parallel}$ for the single-null divertor and $\chi^{sh}_\perp \sim \frac{c^2}{\omega_{pi}^2}\left(\frac{\beta^*}{\beta^*_{cr}}\right) \frac{C_s}{L_\parallel}$ for the

double-null divertor. The dependence on beta is stronger for the single-null geometry due to the partial compensation of regimes with favourable and unfavourable curvature. The basic result is that with increasing SOL beta the difference between single-null and double-null disappears. Near the ideal MHD stability threshold the transport coefficient is $\chi_\perp \sim \frac{c^2}{\omega_{pi}^2} \frac{c_s}{L_\parallel}$. Consequently, the MHD instabilities regulate the SOL width and allow values up to $x_0 \sim \frac{c}{\omega_{pi}}$.

REFERENCES

1. M. Endler, L. Giannone, N. Niedermeyer, A. Rudyj, G. Theimer and the ASDEX Team in proceedings of 20th EPS Conference, 4-8, Lisboa, 1993.
2. A.V. Nedospasov in Sov. J. of Plasma Physics 15 (1989) 10, 659-661.
3. O. Pogutse, W. Kerner, V. Gribkov, S. Bazdenkov, M. Osipenko, JET-P(93) 106.
4. H.L. Berk, D.D. Ryutov, Yu. A. Tsidulko, Physics of Fluids B3 (6) (1993), 1346-1354.
5. W. Kerner and O. Pogutse to be published.

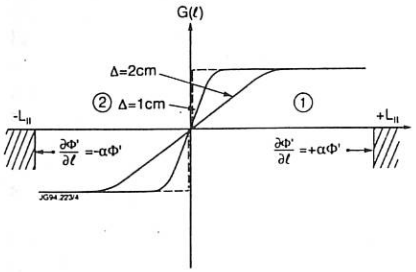


Fig. 1) The dependence of the driving curvature term along the field line for single-null divertor.

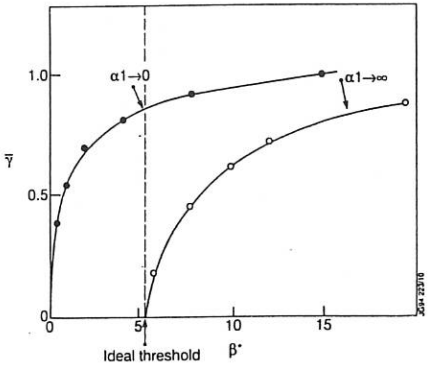


Fig. 2) The growth rate for single-null divertor

COMPARISON OF T-10 EDGE TURBULENCE WITH THE DRIFT RESISTIVE BALLOONING TURBULENCE COMPUTER MODELLING

Vershkov V.A, Bazdenkov S.V, Grashin S.A, Dreval V.V, Osipenko M.V,
Piterskii V.V., Sushkov A.V., Soldatov S.V., Jakovets A.N.
RRC "Kurchatov Institute",123182, Moscow, Russia.

The main goal of present investigations was to identify the possible different types of edge turbulence and compare them with theoretical models There are several different approaches to the driving forces of the edge turbulence, which consider either resistive ballooning mechanism [1,2] or interactions with the limiters [3] or hydrogen neutrals influx [4] and impurity radiation [5]. We compare the experimental results of the edge turbulence with the predictions of the nonlinear drift resistive ballooning instability in this paper.

THE EXPERIMENTAL SET UP AND RESULTS

The scheme of T-10 limiters and probes positions is presented on Fig. 1. In order to have wide range of edge parameters and to avoid the effects connected with the walls and circular limiter it was chosen the discharge with the rail limiter deeply introduced into the plasma at minor radius of 22 cm, while the circular carbon limiter was at 33 cm and the wall at 38 cm. The magnetic field line from the probe in both positions can hit the rail limiter at least after two turns around the major axis of tokamak.

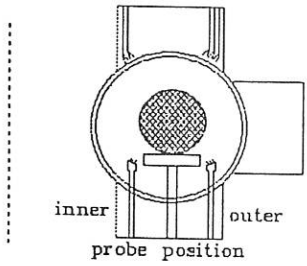


Fig. 1

The major plasma radius - 1.5m. Plasma current was 200 kA, magnetic field 2.65 T, average density 2.5-2.7x10^{13} cm^{-3}.

Turbulent density fluctuations were investigated in T-10 SOL with the moving from one discharge to another multipin and a set of flush with limiters Langmuir probes. Multipine probe has 7 pines with the distance of 3 mm in poloidal direction, thus enabling us to determine the length and velocity of the turbulent waves. Two probe positions (the "outer" and "inner") were used in experiment, as it is shown on Fig. 1. The rail limiter was equipped with four probes mounted near the limiter tip on "ion" and "e" sides plus-minus 6 cm from it's center.

Two channels were registered each discharge with 1 MHz sampling rate for 0.5 sec. The plasma position under toroidal field reversal was monitored with two 46 channels obscure chambers and with 8 channels 1 mm interferometer. The density profile was obtained with the interferometer in 16 channels mode. Two technique were used for the calculation of the density and temperature from the probes data. The triple probe technique was used for the Multipin probes and usual current-voltage characteristics for the rail limiter probes.

The density, the temperature and the floating potential of the SOL are presented on Fig. 2 a,b,c. The different characters corresponds to the inner and outer probe position with two opposite directions of the toroidal field. It is seen, that all parameters is very similar for all four cases. It is seen also, that the density, measured with probes agree very well at radius bigger 26 cm., but became less at the smaller radius. The possible reason is the secondary electron emission at higher temperatures. The floating potential is positive and reverses the sign practically only at the rail limiter tip.

The typical fluctuations of the ion saturation current are presented on Fig.3 a,b together with the results of computer modelling for two probe radial positions. The first trace on Fig 3a is for the radius 30 cm. It is clearly seen, that the fluctuations near the wall are of the relaxation type, like "events" measured on ASDEX [6]. The amplitude of the bursts is higher, than the average current. It is seen, that the type of the fluctuations is radically changes at the radius 24 cm in hotter plasma near the rail limiter (the first trace of Fig 3 b). They became more stochastic. The difference in the fluctuations types is well correlated with the difference in their poloidal rotation. Figure 4 presents the experimental poloidal velocity of the ion saturation current fluctuations and calculated poloidal velocity of the

plasma. The velocity of the fluctuations was found from the phase shift between the data of two probes, separated poloidally by 0.6 cm. The typical spectra, phases and coherency at the three radial probe positions are presented on Fig. 5.for the three typical radii. Fig. 5a and c for the probe positions near the wall and rail limiter correspondingly. Fig. 5b for the intermediate radius. It is seen, that near the wall fluctuations rotates in the ion diamagnetic drift direction, while near the limiter in electron diamagnetic drift direction. At intermediate radius low frequency rotates in ion and higher frequencies rotates in electron diamagnetic drift direction. This observation well correlate with the two mode regime at the periphery, found on TFTR [7].The plasma poloidal rotation was calculated from the radial momentum balance equation: $n_i Q_i [V_\theta B_\phi + V_\phi B_\theta - E_r] + \nabla P_i = 0$where n_i, Q_i, P_i, are the ion density charge, and pressure. θ and ϕ refer to poloidal and toroidal direction. The pressure and electric field were calculated using the experimental measured values of density, temperature and floating potential. The plasma potential was taken as $\phi = \gamma T + \phi_{fl}$, with γ equal to 2, which can account for the secondary electron emission [8]. It is seen, that while at the periphery the fluctuations rotates together with the plasma in ion diamagnetic drift direction, they propagate near the limiter in the electron diamagnetic drift direction with respect to plasma with the velocity about two times higher then calculated electron diamagnetic velocity.

The measurements at inner probe position showed the reduction of the ion saturation current fluctuations amplitude in two-four times, which supports their ballooning nature. For all probe positions the measurements of the cross-correlation between the ion saturation current and electric field showed the relative phase, which always corresponds to the maximal outward turbulent flux.

THEORETICAL MODEL

To interpret experimental observations two-dimensional version of drift-resistive ballooning instability which is essentially the only curvature-driven instability for edge tokamak plasma is considered, where dimensionless variables and parameters are introduced:

potential $\varphi \to e\varphi / T$, density $n \to n / n_0 = < n > + \tilde{n}$, $< n > = 1 - X / L_N$,

$g_N = \rho / L_N$, $g_B = \rho / R$, $\rho^2 = \omega_c^2 T / M$, $T = T_e$, $\omega_c = eB_0 / mc$

$t \to t\omega_c$, $x,y \to x,y / \rho$, $\mu,\chi \to \mu,\chi / \rho^2\omega$, $\sigma \to \sigma k_{II}^2 B / (nce)$, $k_{II} = 1 / qR$.

Temperature and magnetic fluctuations were not taken into account.

Linear dispersion relation for eq. (1) shows that increment has a maximum in space of wave numbers so that only modes with small and moderate k are unstable. For these modes m and D terms can be neglected, so that dispersion relation has the form

$$k_\perp^2 \omega^2 + i\omega\sigma(1 + k_\perp^2) - ik_y\sigma(g_N - g_B) + g_B g_N k_y^2 = 0 \qquad (2)$$

$\omega = \omega_0 + i\gamma$

Two different turbulent regimes are possible:

I. In the adiabatic regime $\sigma(\varphi - \tilde{n})$ terms are dominant in eq. (1) leading to appearance of drift waves with $\varphi \propto n$ and $\omega_0 = k_y\sigma(g_N - g_B) / [\sigma(1 + k_\perp^2) + 2\gamma k_\perp^2]$, $\gamma^2 = g_B g_N k_y^2 / k_\perp^2$

In dimensional variables phase velocity of this waves corresponds to electron diamagnetic drift velocity, but an increment can exceed usual dissipative drift instability increment because of the curvature drive.

In case g =0 weak turbulence regime takes place $\omega_0 >> \gamma$

II. In the hydrodynamic regime $\sigma << \gamma k_\perp^2$

$$\omega_o = k_y \sigma (g_N - g_B) / [\sigma(1 + k_\perp^2) + 2\gamma k_\perp^2], \quad \gamma = g_N g_B k_\perp^2 / k_\perp^2$$

Here $\omega_o << \gamma$, so that strong nonlinear coupling between the modes is possible. Note that in this limit eq.(1) coincident with the well known Boussinesq eq. for thermal convection with all their rich nonlinear dynamics. Phase velocity of these type of fluctuations is by $\sigma / 2\gamma k_\perp^2$ times less than electron diamagnetic drift velocity so they can be standing and rotate with the plasma in ion diamagnetic drift direction.

For typical T-10 parameters: B=2.65T, q=2.3, Z_{ef} =2, M_{ef}=2, a=0.24m, R=1.5m, n=10^{13} cm^{-3}, T =40eV, L_N =4.5cm modelling shows the transition between this different turbulent states around r=0.26-0.27m because the decrease of the conductivity with temperature. The characteristic dimensions of fluctuations are about 0.4cm for r<0.26m and about 2cm. for r>0.26m. Frequency spectrum is very close to the experimental one for more peripheral region (see Fig.2b), but for smaller radius the high frequency component is absent in simulation. May be it is connected with the numerical limitations, because high frequencies correspond to small scale modes which are smoothed by viscosity to provide stability of calculation procedure.

To compare the phase velocities of fluctuations with the experiment plasma rotation must be taken into account. The case is that spontaneous shear flow generation by turbulence is present in the model [2]. The difference of plasma velocities between r=0.25m and r=0.28m is about 1.5 of electron drift velocity V_{de} calculated for r=0.24m. An estimation of phase velocity of fluctuations with respect to plasma is $0.25V_{de}$ in ion drift direction at r=0.28m and 1.25 V_{de} in electron drift direction at the r=0.25m, which is in qualitative agreement with the experiment.

CONCLUSIONS

The experimental results show strong ballooning turbulence at the plasma edge. The amplitude of the fluctuations at the inner torus circumference is 2 - 4 times less, than at the outer one. The fluctuations character is radically changes with the radius. The burst type oscillations near the wall converts to the chaotic type at smaller radii. Near the wall fluctuation rotates together with plasma, while at smaller radii they travels in respect to plasma in electron diamagnetic drift direction with the velocity two times higher, than electron diamagnetic drift. Those observations are in good qualitative correlation with the results of computer drift resistive ballooning modelling. It reasonably well describes the change of the type of fluctuations and their propagation velocities at different radii. The frequency of oscillations is well described near the wall, but it is significantly less at smaller radii.

The work was carried out under support of Russian Foundation for Fundamental Researches. The Grant Number # 94-02-06521-a and RRC "Kurchatov Institute" support for young researches

REFERENCES

1. Drake J.F. et al., in Plasma Physics and Contr. Nucl. Fusion Research, Proc. of the 14th Int. Conference, Wurzburg, 1992 (IAEA, Vienna, 1993), Vol.2, p.115.
2. Pogutse O.P. et al., in Plasma Physics and Contr. Nucl. Fusion Research, Proc. of the 14th Int. Conference, Wurzburg, 1992 (IAEA, Vienna, 1993)
3. Nedospasov A.V. Journal of Nuclear Materials, 196-198 (1992)90-100.
4. Ware A.S. et al. Phys. Fluids B 4, 877, 1992.
5. Ware A.S. et al. Phys. Fluids B 4, 102, 1992.
6. Endler M.,Giannone L., 20th Eur. Conf. Lisbon 1993, v17C, part 2, p583-586.
7. Fonk R.J. et al, 1993 APS-DPP Meeting, St.Louis, MO, 1-5 Nov. 1993.
8. Matthews G.F. et al., Journ. of Nucl. Materials, 145-147(1987) 225-230.

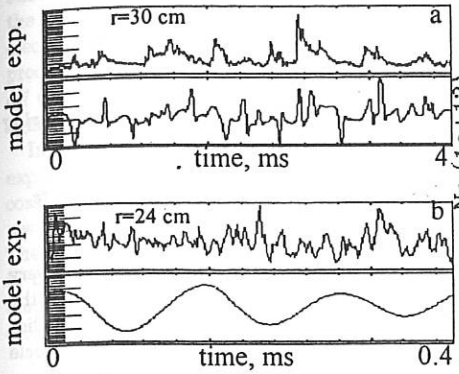


Fig. 3

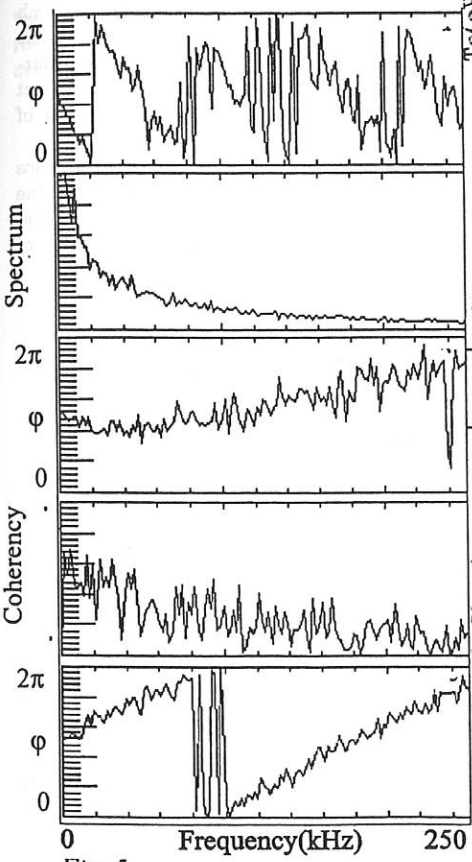


Fig. 5

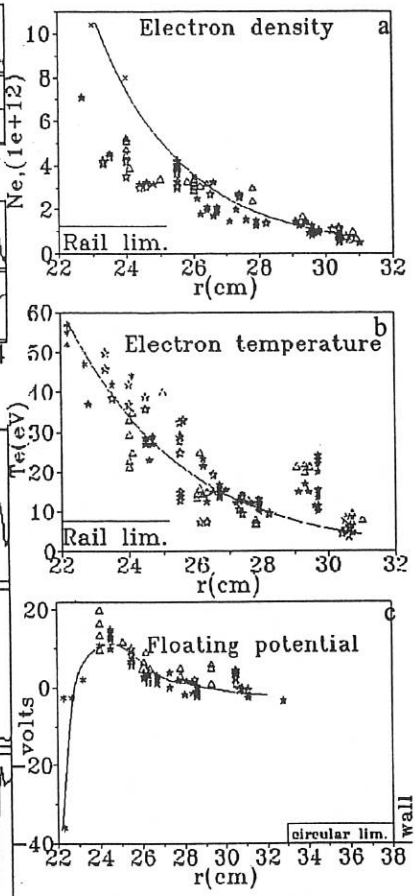


Fig. 2

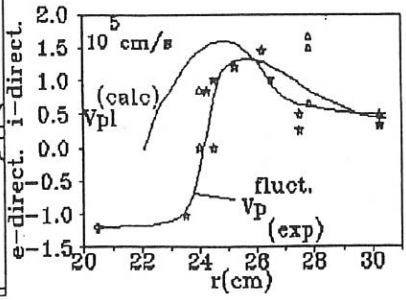


Fig. 4

TRANSPORT OF HIGH ENERGY ELECTRONS IN EDGE STOCHASTIC MAGNETIC LAYER OF TOKAMAKS

S. Takamura and S. Sakurai*
*Department of Energy Engineering and Science, *Department of Electrical Engineering*
School of Engineering, Nagoya University, Nagoya 464-01, Japan
H. Kawashima
Department of Fusion Plasma Research, Japan Atomic Energy Research Institute,
Naka-gun, Naka-machi, Ibaraki 311-01, Japan

1. Introduction Transport of energetic electrons in stochastic magnetic field is very important in behaviors of runaway electrons in magnetic island overlapping at the moment of disruption, confinement of current-carrying high energy electrons in radio-frequency current drive combined with ergodic magnetic divertor, physics on particle and energy confinement, etc.

Experimental and numerical studies on transport of high energy electrons in edge stochastic magnetic layer have been carried out in JFT-2M [1] and the small research tokamak CSTN-3 [2]. The hard X-ray analysis in JFT-2M gives the diffusion coefficient of runaway electrons which is much smaller than the value estimated by Rechester-Rosenbluth collisionless model based on the diffusion of magnetic field lines. The direct observation of electron orbits in CSTN-3 shows an energy dependent modification of drift orbit of energetic electrons.

The electron drift motions are followed numerically by orbit tracing computer codes both in JFT-2M with a simplified EML magnetic configuration but considering the relativistic effect, and in CSTN-3 with the rigorous EML structure for nonrelativistic electrons. These give the diffusion coefficient of electrons as well as a suppression of orbit stochasticity.

2. Transport of Runaway Electrons in EML of JFT-2M Figure 1 shows a typical time evolution of hard x-ray emission accompanied with runaway electrons in Ohmic discharge of JFT-2M tokamak (R_0 = 1.31 m, a×b = 0.33×0.43 m, Ip ~ 230 kA, Bt~1.3 T, $\overline{n_e}$~2×10^{19} m^{-3}) with an external helical magnetic field (m/n~5/2) of $b_r/Bt\sim2\times10^{-3}$ at r/a≥0.8, without which the x-ray emission decreases slowly by a factor of two at the end of Ih. It indicates that no new strong source of runaway electrons grow up. The initial spike of phase 1 shows that the runaway electrons at the extreme edge are pumped out promptly. The

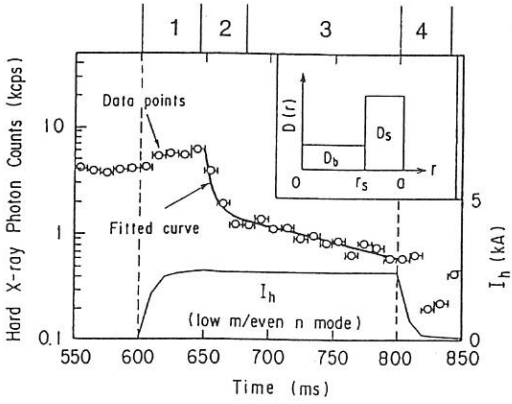


Fig.1 Details of the hard x-ray emission (open circles) with the helical field. The best fit curve from the numerical analysis is shown by solid line. Insertion shows the two area diffusion model for runaway electrons. Ds is the diffusion coefficient in the stochastic magnetic layer outside of the stochastic boundary r_s, while Db is the coefficient inside of r_s.

subsequent sharp decrease in phase 2 shows the out flux of the runaway electrons from the magnetic stochastic layer. A moderate decrease in phase 3 shows that the runaway electrons inside the stochastic boundary r_s are diffusing slowly out to the edge. The process is regulated by the transport in the core region. After the helical field is turned off (phase 4), the stochastic field disappears and the runaway electrons are confined again in the edge, which causes a sudden drop of x-ray emission.

In phase 2 and 3, the solution of diffusion equation for runaway electrons fitted with experimental decays give two different diffusion coefficients, Ds and Db for the edge and core regions, respectively. $Ds=1.0m^2/s$ and $Db=0.1m^2/s$ are obtained by appropriate assumption concerning the spatial profile of runaway electrons, slowing-down time, etc. The magnetic field line diffusion coefficient, $Dm=<(\Delta r)^2>/2L$ [3] amounts to 3×10^{-5}m in the edge stochastic layer.The collisionless Rechester model gives $Ds^{cl}=D_m v_{\parallel}$ which amounts to $10^4 m^2/s$ for runaway electrons with the energy of Mev. This value is four order of magnitude larger than the value of Ds obtained in the experiment.

Figure 2(a) shows the puncture plot of the magnetic field line on the poloidal cross section. Peripheral scattered points show that the magnetic surfaces are destroyed by the overlapping of the neighboring magnetic islands. Figure 2(b) through (d) also show the plots of drift orbits of electrons with the energies of 1keV, 1MeV and 10MeV, respectively. The stochastic behavior in the case of 1 keV is very similar to that for the magnetic field line. Instead, the stochasticity is greatly suppressed when increasing the

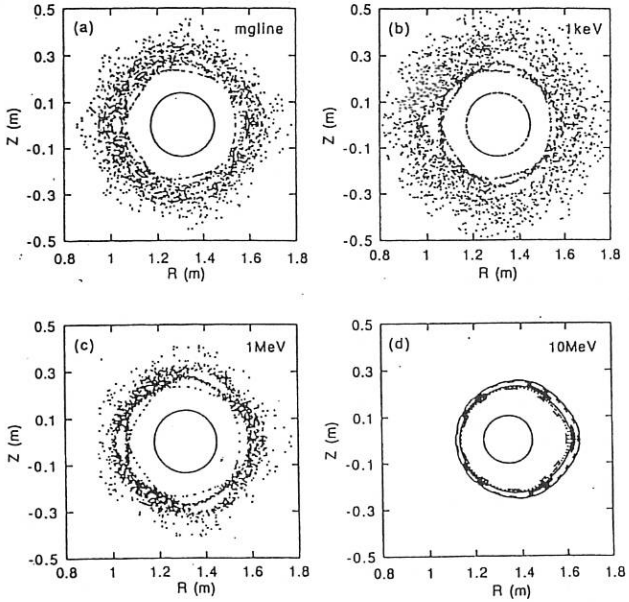


Fig.2 (a)Puncture plot of the magnetic field line on the poloidal cross section. The analytical formula for b_r is employed with the safety factor $q(r) = 1 + 3(r/a)^2$, a = 0.35 m. The starting points are R = 1.45, 1.60, 1.61, 1.62, 1.63, 1.64, 1.65 and 1.66 m on the mid plane. The total number of toroidal turns is 500. (b) - (d) Puncture plots of drift orbits for electrons with the energies of 1 keV, 1 MeV and 10 MeV under the same condition as in (a).

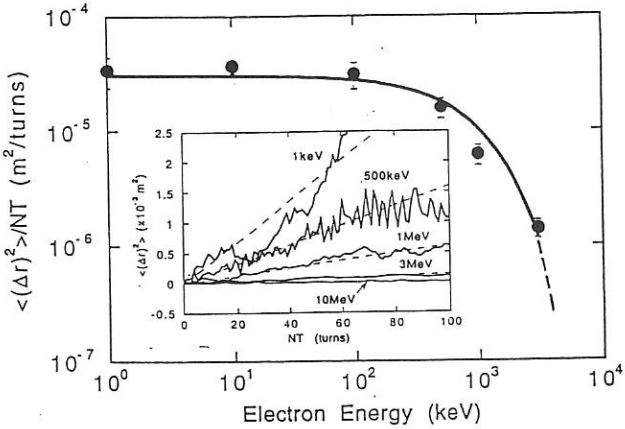


Fig.3 Electron energy dependence of $<(\Delta r)^2>/NT$. Insertion shows mean squared radial displacement $<(\Delta r)^2>$ of drift orbits for electrons with several energies vs. toroidal turn NT.

energy above 1 MeV. The insertion in Fig.3 shows $<(\Delta r)^2>$ vs. toroidal turn NT for the drift orbits of electrons. Then, $<(\Delta r)^2>/NT$ are plotted as a function of electron energy, suggesting that the diffusivity for MeV energy electrons becomes much smaller than the value given by Ds^{c1}.

Rechester transport model due to magnetic stochasticity assumes that an electron runs along a perturbed magnetic field line. The large shift of drift surface of high energy electrons from the intrinsic magnetic surface may explain this significant reduction of diffusivity in the stochastic magnetic layer.

3. Orbit of High Energy Electrons in Fine Helical Magnetic Layer The orbit of high energy electrons having a substantial shift of drift surface from their intrinsic magnetic surface has been detected in the small tokamak (R_0=0.4m, a=0.1m, Ip≤1kA, Bt≤0.1T, n_e~1×10^{18} m^{-3}, Te~10 eV, τ_{dis}~2ms) by using the sophisticated technique combining the electron beam probing with boxcar imaging [4]. The helical coil (m/n=6/1) are installed in the eight toroidal sections and those (m/n=18/2) are in four sections. The movement of the electron orbits associated with perturbed helical fields is summarized as the puncture points on the poloidal plane as shown in Fig.4, from the view point of electron energy dependence. Peak positions of

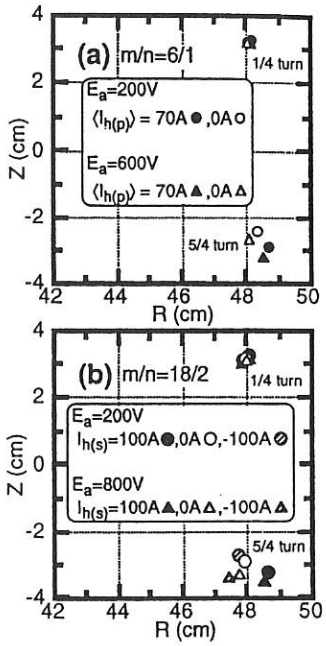


Fig.4 Effect of electron beam energy Ea on the electron drift orbit. (a) with m/n = 6/1 and (b) with m/n = 18/2 helical coil.

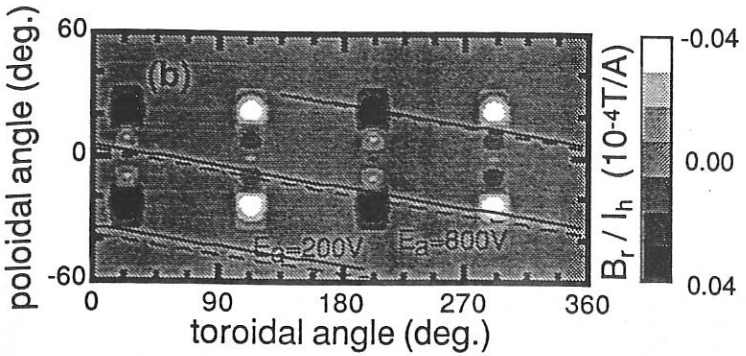


Fig.5 Schematic intensity map of radial helical field on a toroidal-poloidal two-dimensional space at r = 8 cm. Solid and dashed lines show the electron orbits for the energy of Ea = 200 eV and 800 eV, respectively.

fluorescent intensity were plotted by circles and triangles. When the beam energy increases from 200 to 600 eV, puncture points shifted a few mm in the poloidal direction after 5/4 toroidal turns in the case of low poloidal mode number as shown in Fig.4(a). The helical field makes them to move in the radial direction for both energies.

On the other hand, the beam energy has some influence on the direction of movement of puncture points as shown in Fig.4(b). The perturbed field of high poloidal mode number (m/n =18/2) makes slightly different directions when the electron beam energy Ea is different. The point moves radially in the low energy (Ea = 200 eV), while that moves horizontally in the high energy (Ea = 800 eV). Such an energy dependence of the movement was in a good agreement with the numerical analysis using the electron orbit tracing code taking account of the helical magnetic field.

These response can be explained by tracing the experience of local external magnetic field influencing the electron beam orbit. Figure 5 shows the intensity profile of helical field numerically obtained on a toroidal-poloidal two-dimensional space at r = 8 cm as well as the projection of intrinsic electron orbit without perturbed field. In the case of the high m number, the electrons having different energy such as Ea = 200 and 800 eV move along the different path on which b_r is different because the high m number makes a rapid change of b_r poloidally, so that the small deviation of drift orbits makes an extremely different orbit modification. This effect is thought one of the important mechanisms to explain the reduction of diffusion coefficient for runaway electrons discussed in the previous section.

4. Conclusion Experimental and numerical analysis show that the transport of high energy electrons is greatly influenced especially with increasing the energy by the phase averaging effect in such a small-scale magnetic perturbation, coming from the difference in rotational transform between drift orbits and magnetic field lines due to the shift of drift surfaces from their intrinsic magnetic surfaces.

References

[1]H. Kawashima et al., to be published in J. Plasma Fusion Res.
[2]S. Sakurai, N. Ohno and S. Takamura, J. Plasma Fusion Res. **70**(1994)173.
[3]A.B. Rechester and M.N. Rosenbluth, Phys. Rev. Lett. **40**(1978)38.
[4]S. Sakurai, N. Ohno and S. Takamura, Jpn. J. Appl. Phys. **33**(1994)1161.

Edge Biasing and Electron Heating by Fermi Acceleration in RF Fields

J.R. Myra and D.A. D'Ippolito
Lodestar Research Corporation, Boulder CO, USA

R. Majeski
Princeton Plasma Physics Laboratory, Princeton NJ, USA

A theory of electron interaction with rf fields in the vicinity of conducting surfaces is developed and applied to ICRF heating experiments. The crucial parameter is $\alpha = \omega\Delta/v_e\sin\theta$, which determines whether the electron response is Maxwell-Boltzmann (MB) or hydrodynamic across the rf sheaths of width Δ. (Here θ is the grazing angle of the B field with respect to the surface.) In the MB regime, $\alpha < 1$, we recover the usual process of rf rectification. In the opposite limit where ponderomotive effects would be expected to enter, the rectification effect, and all of its consequences, are reduced. The Fermi acceleration kick $\delta v_\parallel$ that the electrons receive from each interaction with the sheaths is computed by a Monte-Carlo technique and shown to maximize at $\delta v_\parallel \sim v_e$ for $\alpha \sim 1$, implying strong electron heating. The theory is applied to edge interactions in TFTR and shown to provide a candidate explanation of observed glows.

Introduction

The electron response to rf fields is fundamental to the formation of rf sheaths[1-3] on antennas, walls and limiters. The rf fields are rectified because the potential must adjust itself during nearly all phases of the rf cycle to be a deeply confining well for the mobile electrons, in order to maintain equality of the net electron and ion loss rates. Sheath rectification gives rise to rf-driven impurity sputtering, power dissipation and convective cells.[4] The Maxwell-Boltzmann (MB) regime for which $\alpha = \omega\Delta/v_e\sin\theta < 1$, where v_e is the electron thermal velocity, θ is the grazing angle of **B** with respect to the surface, ω is the rf frequency, and Δ is the rf sheath width, has been the basis of much rf sheath work.

In the opposite regime, $\alpha > 1$ where the electrons have a jitter response to the applied fields, the ponderomotive force can be significant especially near an rf launcher. The ponderomotive force has been proposed as a means of edge plasma control by creating a virtual ponderomotive limiter.[5] The ponderomotive force arising from the evanescent slow wave fields of an IBW (ion Bernstein wave) antenna has also been proposed for feedback stabilization of MHD modes.[6]

Here, we investigate the transition between these regimes. For $\alpha \sim 1$, strong Fermi acceleration[7] of electrons is expected. It will be shown that Fermi interactions are relevant to the observation of rf induced glows on the antennas in ICRF heating experiments. The interest in understanding rf sheaths and electron interaction in the regime for general α, is underscored by the need to understand the relationship of ponderomotive and sheath effects in IBW experiments.[8]

Geometry

Figure 1 shows the model geometry. Field lines strike a conducting surface, the Faraday screen or the leading edge of the antenna side protection tiles, at a near glancing angle, $\theta << 1$. The electron response is governed by the parameter

$$\alpha = \omega\Delta/v_e\sin\theta = 6.4 \times 10^3\ [V(\text{volts})/T_e(\text{eV})]^{3/4}\ f(\text{MHz})\ [n_e(\text{cm}^{-3})]^{-1/2}[\theta(\text{deg})]^{-1}. \quad (1)$$

For typical SOL conditions ($n_e \sim 10^{12}\text{cm}^{-3}$, $T_e \sim 20$ - 50 eV) and for typical rf sheaths (V ~ 500 - 1000 V, f ~ 50 MHz), Eq. (1) yields $\alpha \sim 1$ for experimentally relevant angles $\theta \sim 2$ - 4 deg. Thus, electrons can be in both the hydrodynamic and MB regimes, and also in the transition regime where strong heating is expected.

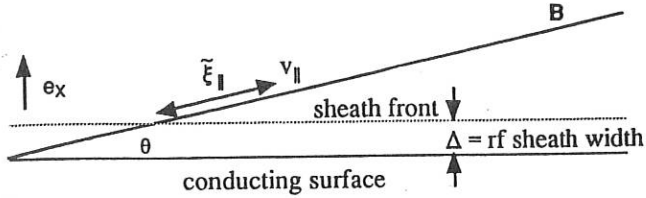


Fig. 1 Model geometry of field lines striking a surface at glancing angle θ. The electrons bounce off of the moving rf sheath front. In the hydrodynamic regime, the jitter excursion distance along the field line due to the rf is $\xi_{\|}$.

The Maxwell Boltzmann Regime

In the MB regime, $\alpha < 1$, rf sheaths and the concomitant edge biasing have been previously studied.[1-4] Qualitatively, the electric field and potential may be modeled as

$$E_x = - (V/\Delta) \exp(-x/\Delta) = - \partial\Phi/\partial x, \qquad (2)$$

where $x = 0$ is the conducting surface, $\Delta \sim \lambda_{de} (eV/T_e)^{3/4}$ is the rf sheath width, and λ_{de} is the Debye length. In the MB regime, V is approximately related to the peak-peak applied rf voltage V_0, by $V = V_e + (V_0/2)(1+\cos\omega t)$ where $V_e \sim 3T_e$ is the thermal Debye sheath, and the dc term $V_0/2$ represents the sheath rectification effect.[1] Two features should be noted: i) at all times Φ given by Eq. (2) provides a potential well for electrons so that only a few electrons can escape to $x = 0$, and ii) the electric field is localized in sheaths within a few Debye lengths of the wall.

In order to understand the electron heating that results from the field structure given by Eq. (2), we have carried out Monte-Carlo simulations. The electrons are launched at $x >> \Delta$, heading into the sheath with an initial parallel velocity $v_{\|0}$. Upon reflection from the sheath they acquire a velocity kick due to the Fermi acceleration mechanism. Figure 2a shows the resulting rms kick $\delta v_{\|}$ vs. α. The rms average is over the phase of the rf with respect to the launch time, and 16 phase points were employed. The kick is strongest when the electron velocity is comparable to the velocity of the moving sheath front. In order of magnitude, the Fermi-induced velocity kick takes the form

$$\begin{aligned} \delta v_{\|} &\sim \omega\Delta/v_e, & v_{\|} \sin\theta > \omega\Delta, \\ &\sim 0, & v_{\|} \sin\theta << \omega\Delta. \end{aligned} \qquad (3)$$

The fields employed in this part of the study are those of Eq. (2), and are invalid when α is sufficiently large, as discussed subsequently.

The Hydrodynamic Regime

In the hydrodynamic regime, $\alpha >> 1$, the electric fields may be determined by invoking a separation of time scales. On the slow (dc) time scale, the electrons are still MB and have a spatial distribution along the magnetic field given by

$$n_e = n_{e0} \exp(e\langle\Phi\rangle/T_e) \qquad (4)$$

where $\langle\Phi\rangle$ is the potential averaged over an rf cycle. On the fast time scale, the electrons jitter with amplitude $\xi_{\|} = eE_{\|}/m\omega^2$, where the rf field $E_{\|}$ must be determined self-consistently. Qualitatively, we expect that if $\xi_x \equiv \sin\theta\, \xi_{\|} << \Delta$, then linearization of the motion should be valid and rf modifications to the usual $3T_e$ Debye sheath should be negligible. In the opposite case $\xi_x >> \Delta$, sheath induced nonlinearities should be strong. The possibility of direct electron losses by jittering into the conductor now exists, and a dc potential $\langle\Phi\rangle$ must build up to confine the electrons away from it, much like in the MB regime.

As an ansatz, we take the dc potential to have the form of the usual Debye sheath with wall to plasma potential $3T_e + \Phi_r$, where the rectified voltage $\Phi_r > 0$ is to be determined. The spatial structure of the rf field is determined from integrating Poisson's equation to obtain

$$\varepsilon_{\|} E_{\|} = \text{const.} \qquad (5)$$

where the spatial dependence of the equilibrium density n_e in $\varepsilon_\parallel$ is determined from Eq. (4). Note that Eq. (5) results in the largest $E_\parallel$ in the sheaths, and that some electrons will bounce before seeing this $E_\parallel$.

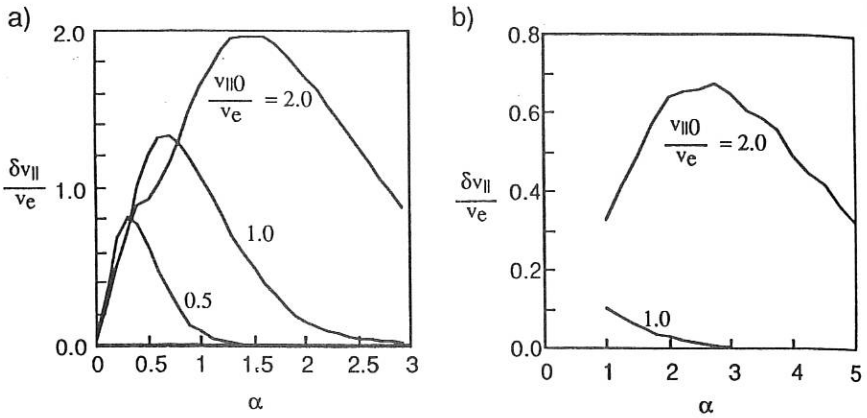


Fig. 2 Monte-Carlo results for the rms kick received by an electron on one bounce off of the rf sheath for a) the MB sheath model, and b) the hydrodynamic sheath model. The transition between regimes occurs at $\alpha \sim 3$.

The quantity Φ_r must be determined to give equality of the time-averaged electron and ion loss rates. The Monte-Carlo runs show that electrons tend to escape from the system when their jitter energy, $K \equiv m\langle\omega^2\xi_\parallel^2\rangle/2$, is comparable to Φ_r. Consequently, we define an effective confining potential for the electrons $U \equiv -e\langle\Phi\rangle - K$ and pick Φ_r by demanding that the barrier height $\Delta U \equiv U_{max} - U_\infty \sim (2 - 3)\, T_e$, just as it would be in the absence of rf. Here, U_{max} is the maximum U over all x on $(0,\infty)$, which occurs near the sheath entrance. Finally, we note in passing that K is the ponderomotive potential.

Figure 2b shows the resulting rms Fermi kicks, which match qualitatively onto the MB regime. At large α the kicks are small, and as α is reduced, the kick rises, and maximizes near $\omega\Delta = v_\parallel \sin\theta$. The transition between the MB and hydrodynamic regimes apparently occurs when a barely confined electron ($mv_e^2 = 3T_e$) transits the sheath (a total length of 2Δ) in half a wave period (a time of π/ω) which yields $\alpha \sim 3$.

In the process of computing the Fermi kicks, we have also obtained the rectified dc potential, Φ_r vs. α (not shown). In the limit of $\alpha \to \infty$, Φ_r vanishes, and as one approaches the MB regime, Φ_r becomes an order unity fraction of the applied rf voltage V_0, consistent with sheath theory from the MB regime. For the Monte-Carlo runs shown in Fig. 2, eV_0/T_e was taken to be 30.

Application

We now apply these results to estimate the rise in T_e along a flux tube connecting to the Bay-M ICRF antenna in TFTR. Two situations are of interest. In the old Bay-M geometry discussed in Ref. 9, field line connections between the Faraday screen and an rf limiter 1.7 m away were possible. In the present Bay-M antenna, more extended antenna bumper limiters intercept such field lines, but strong sheaths are still possible near the corners of the antenna.[10] Parameters for the two cases are similar, so they will be treated together.

The velocity space diffusion coefficient for the electrons is related to the Fermi acceleration kick by $D_v \sim \delta v_\parallel^2/\tau_{\parallel e}$ where $\tau_{\parallel e} = L_\parallel/v_e \sim 7.6 \times 10^{-7}$ s, where $L_\parallel$ is the total length of the field line between contact points. We estimate $\delta v_\parallel \sim \eta\, v_e$ where η is to be determined

from the Monte-Carlo simulations. This yields $m_e D_v \sim 3.3 \times 10^7\ \eta^2$ eV/s, where m_e is the electron mass. The resulting rise in the edge T_e along the affected flux tubes may be estimated from the diffusion that can occur during an energy confinement time of the electrons in the scrape off layer, viz. $\Delta T_e \sim m_e D_v \tau_E$. For sheath end losses $\tau_E = \tau_{\|E} = L_\| / 2\gamma_e c_s \sim 2.8 \times 10^{-6}$ s, where $\gamma_e \sim 5$ is the sheath energy transmission factor. Thus, when end loss is the dominant energy sink, we obtain

$$\Delta T_e \sim \eta^2\ 90\ \text{eV} \qquad (6)$$

where $0 < \eta < 1$ is obtained from the Monte-Carlo simulations for $0 < \theta < 3°$. This ΔT_e will be mitigated and spread by rf driven convective cells[4] which can reduce the confinement time from $\tau_{\|E}$ to $\tau_{cc} = L_T / v_{ExB}$ (with L_T the gradient length of T_e) when the latter is smaller. Equation (6) predicts a temperature rise on the order of a few tens of eV, which is adequate to change any atomic cross-sections that could be responsible for the observed antenna glow.

Summary and Conclusions

Simple models of the electric fields for rf sheaths in both the MB and hydrodynamic regimes have been obtained and employed in Monte-Carlo simulations of the electron motion. It has been shown that these models permit the two regimes to be qualitatively patched together, with an approximate transition occurring at $\alpha \sim 3$. The models show that for large α, which occurs for very small grazing angles θ, both the Fermi acceleration and the rectification effects, that characterize the usual MB sheaths, are reduced. Thus, by matching the plasma facing components of the antenna to the flux surfaces to within an angular tolerance of better than $\omega\Delta / v_e$ (typically of order 1 degree), the rectification that gives rise to rf-enhanced impurity sputtering, anomalous power dissipation in the sheaths, and convective cells are mitigated.

Normally, such fine tolerances are not achieved in experiments, and there is a group of field lines for which $\alpha \sim 1$ pertains. For TFTR parameters, we have shown that Fermi acceleration is a viable mechanism for explaining the observed glow in ICRF experiments.

The present work suggests that a unification of sheath and ponderomotive physics phenomena may be possible, and that when a variety of field lines with different grazing angles exist in a experimental situation, sheath and ponderomotive effects can be expected to coexist with strong electron heating occurring at the juncture of the two regimes.

Acknowledgments

This work was supported by USDOE contracts DE-FG03-93ER54212, DE-FG02-88ER53263 and DE-AC02-76CH03073.

References

1. J.R. Myra, D. A. D'Ippolito and M. J. Gerver, Nucl. Fusion **30**, 845 (1990).
2. F.W. Perkins, Nucl. Fusion **29**, 583 (1989).
3. R. Chodura, Fusion Eng. Des. **12**, 111 (1990).
4. D.A. D'Ippolito, J.R. Myra, M. Bures, and J. Jacquinot, Plasma Phys. Cont. Fusion, **33**, 607 (1991); and refs. therein; D.A. D'Ippolito, J.R. Myra, J. Jacquinot and M. Bures, Phys. Fluids B **5**, 3603 (1993).
5. T. Shoji. A. Grossman, R. Conn et al., J. Nucl. Mater. **176-177**, 830 (1990).
6. D.A. D'Ippolito and J.R. Myra, presented at the 1994 International Sherwood Theory Conference, Dallas, Texas, USA, paper 2C6.
7. M.D. Carter, D.B. Batchelor, and E.F. Jaeger, Phys. Fluids **4**, 1081 (1992); and refs. therein.
8. M. Ono, Phys. Fluids B **5**, 241 (1993); R.I Pinsker et al., GA Report No. GA-A20820 (1993).
9. R. Majeski, et al., presented at the *20th European Physical Society Conference*, Lisbon, Portugal, July 26-30, 1993.
10. J.R. Myra, D.A. D'Ippolito, R. Majeski, J.R. Wilson, J.H. Rogers, J. Stevens, G.R. Hanson, J.B. Wilgen, A.E. England and Y.L. Ho, presented at the *7th Boulder International RF AT Workshop*, Boulder CO, USA, April 6 - 8, 1994.

Experimental Measurements of ICRF and Edge Plasma Interactions on Tore Supra

J. H. Harris, C. E. Thomas, Jr., J. T. Hogan, G. R. Haste, S. Tobin, C. C. Klepper
Oak Ridge National Laboratory, Oak Ridge, Tennessee, USA

B. Saoutic, B. Beaumont, A. Becoulet, H. Kuus, D. Fraboulet, A. Grosman, D. Guilhem, J. Walter, Équipe Tore Supra
Centre d'Études de Cadarache, Association EURATOM-CEA sur la Fusion St. Paul lez Durance, France

Experiments to explore the interaction of Ion Cyclotron Range of Frequencies (ICRF) heating with the edge plasmas on the Tore Supra tokamak have been undertaken. The actively cooled, lateral protection (bumper limiters) on the three ICRF antennas in Tore Supra can experience overheating for power levels > 2 MW per antenna and pulse lengths > 2 seconds (depending on the power level) even when the antennas are operated in dipole mode. It appears that the local power fluxes on the lateral protection may exceed the nominally expected fluxes of 5 MW/m^2. Concentrated heat fluxes can result in hot spots with temperatures > 1000° C and can result in damage to the carbon tiles that make up the armor on the lateral protection.

Initial experiments with plasmas having I_p = 0.8–1.6 MA, $q(a)$ = 3–6, and P_{RF} = 1–2 MW have been carried out to characterize the phenomena that could contribute to the overheating and develop the diagnostic tools to be used in more comprehensive studies. Reciprocating magnetic and Langmuir probes have been used to measure the RF magnetic field amplitudes in the edge plasma and to measure the potential, electron density, and temperature on field lines connected to an antenna. Current steps are used to vary $q(a)$ during a discharge and move the Langmuir probe field line along the antenna in the poloidal direction. Figure 1 shows plots of the plasma potential and density profiles determined from one series of probe movements with and without rf power and at three different values of $q(a)$. When the probe field line touches the lower corner of the ICRH antenna, a 50 V peak in the floating potential profile and a steep density gradient appear near the last closed flux surface when 1 MW of ICRF power is applied to the antenna; these features fade when the probe field line is moved off of the antenna corner. These potential structures might be evidence of an rf potential sheath [1, 2].

A CCD camera system has been used to observe visible carbon III (4647 Å) and infrared (IR) emission from the antennas. Relatively faint carbon III emission is seen from an unpowered antenna, even when ICRF power is applied to another antenna. This emission increases markedly when the antenna is powered, and is distributed across the face of the Faraday screen. Figure 2 shows the time behavior of the image-integrated CIII emission measured using a CCD camera aimed at the Tore Supra Q1 antenna, together with the IR temperatures of three hot spots on the Q5 antenna that were monitored using the IR camera. In this shot, the rf power was applied in two pulses, one to the Q1 antenna and one to the Q5 antenna . The CIII emission from the Q1 antenna rises rapidly (on a time scale ≤ 100 ms; this value is limited by diagnostic resolution time) when rf power is applied to Q1 and then decreases strongly part way through the heating pulse; the reduction in rf power during this pulse was caused by power regulating circuitry in the transmitter system and is not due to a breakdown or

abrupt change in antenna coupling. The CIII emission from Q1 also increases rapidly when rf power is applied to the Q5 antenna (which is not in the field of view of the visible CCD camera) in the second rf pulse, but this increase is significantly smaller than for the first pulse. Note that the caution is in order in interpreting this data: the

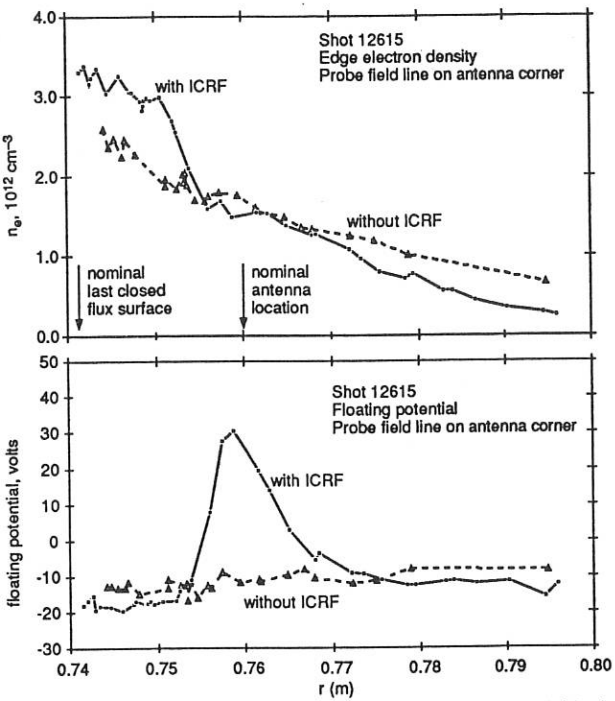


Fig. 1. Langmuir probe measurements of density and floating potential in the plasma edge.

finite spectral bandwidth, stray light, and integration over emitting zones all add considerable uncertainty. However, the relative variations and time scales of the signals do provide preliminary information on the antenna-plasma interactions.

The IR temperature traces in Fig. 2 show that the temperatures of the three hot spots on the Q5 antenna change very little when power is applied to the Q1 antenna, but rise significantly (with a time constant ~ seconds) when rf power is applied to the Q5 antenna.

The surface temperature distribution (derived from the IR images) on the lateral protection can be varied significantly by using the Tore Supra ergodic divertor to modify the magnetic configuration of the edge plasma. The locations of the maximum temperatures shift along the lateral protection in response to changes in the field line connection geometry, suggesting that the hot zones are not simply "frozen" to the locations of damaged tiles or locally reduced cooling efficiency—the contact geometry of the magnetic field lines also plays a role.

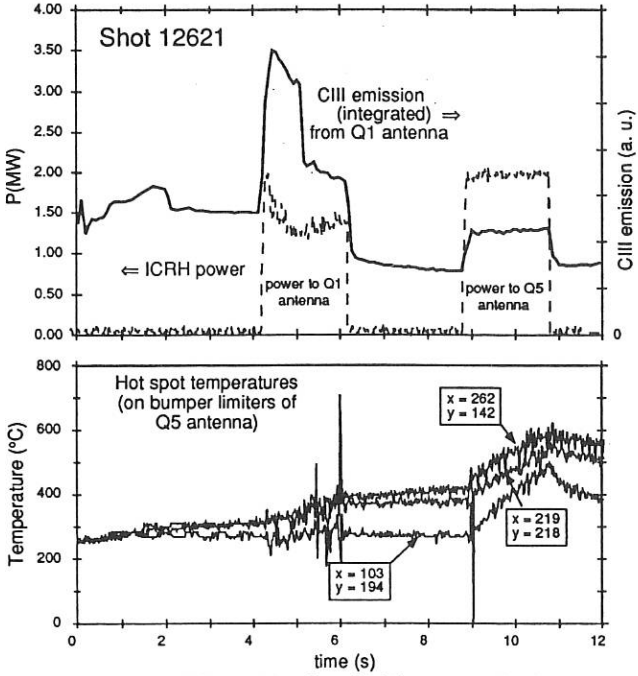


Fig. 2. Time history of CIII emission from the Q1 antenna and IR hot spot temperatures on the Q5 antenna. Note that the threshold level of the IR system was set for about 260° C. The coordinates of the hot spots refer to their pixel locations in the infrared images.

These observations suggest that the interaction of the antenna and the plasma edge involve rf-plasma phenomena (both global and local to the antenna region), the magnetic connections of the antenna to other plasma facing components (e.g., inner wall, outboard limiters), and thermal effects in the lateral protection. Future experiments will combine measurements of edge plasma parameters with spectroscopic studies and antenna imaging in CII, CIII, and infrared light.

We have also begun work on developing modelling techniques that will help evaluate the relative importance of the many possible physical effects that could be important in the antenna-plasma interaction. We have added the exact Tore Supra ICRF antenna geometries to the BBQ three-dimensional impurity transport code previously used to study limiter surface interactions, and have begun model calculations. The code uses the measured SOL background plasma parameters to compute the D^+ particle flux and ambient sheath potential (typically ~ 50 V) at the lateral protection surface. From this flux, and the detailed geometry of the protection (angle of incidence), the predicted CI emission due to physical sputtering and CD_4 emission due to chemical sputtering is computed. Emission of CI due to self-sputtering by (assumed) CIV emitted from distant surfaces is also estimated. The CI which arises directly from physical sputtering has an assumed Thomson distribution (which

can produce a high energy tail) while the chemically produced CD_4 is assumed to be emitted with the wall 'temperature (0.1 eV). Thus, carbon impurities produced by physical sputtering have a broader region of localization then the C from the CD_4 breakup process, which may acquire a Franck-Condon energy of ~1 eV from the dissociation. The spatial distribution of other possible chemical evolutes (e.g., C_2D_2) is expected to be similar, but has not yet been considered in detail. The characteristic spatial emission is shown in Fig. 3 (calculated CIII brightness distributions for t=9, 10.8, 11.2 and 12 secs, using the hot spot temperature data in Fig. 2). Note that the peak temperatures in Fig. 2 lie at the maximum of predicted chemical sputter yield curves.

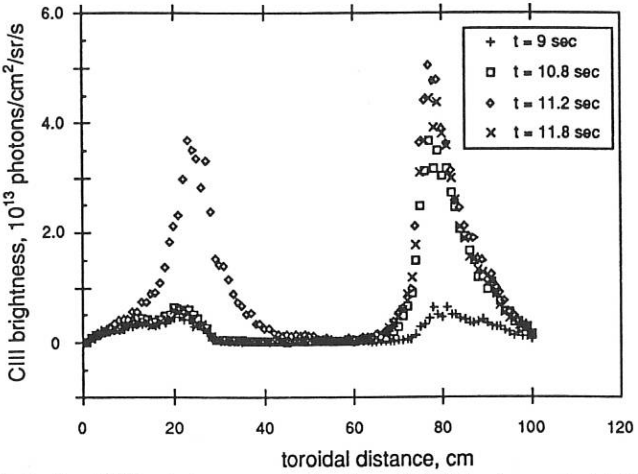


Fig. 3. Profile of CIII emission across the Tore Supra Q5 ICRF antenna calculated by the BBQ SOL impurity transport code at four times during a sample discharge, using the temperature evolution data shown in Fig. 2. The locations of three hot spots due to cooling defects are assumed, and the CIII emission is due to combined physical and chemical sputtering.

The observed temperatures on hot spots on the antenna lateral protection are near the expected maximum of chemical sputtering yields. However, the time scale of the decay of the CIII emission predicted from model calculations of chemical sputtering (CD4 emission) based on the observed temperatures of hot spots on the antenna bumper limiters can be much longer than that seen in the experiment (~ 1 sec vs 0.2s). Our preliminary conclusion is thus that further consideration of plasma (e.g., hot particle interactions) and rf specific effects (e.g., rf sheaths, such as those discussed in Refs. 1 and 2) is required in order to fully explain the experimental observations.

This research was sponsored in part by the Office of Fusion Energy, U.S. Department of Energy, under contract DE-AC05-84OR21400 with Martin Marietta Energy Systems, Inc.

References

1. J. M. Noterdaeme and G. Van Oost, Plas. Phys., 11, No. 35 (1993), p. 1481.
2. C. E. Thomas, Jr, et al, 11th Plasma Surface Interactions Conf, to be published in J. Nucl. Mater.

ON THE EFFECT OF A RADIAL ELECTRIC FIELD ON THE EDGE OF A TOKAMAK PLASMA

Aldo Nocentini
Dipartimento di Scienze Matematiche, Università di Trieste, Italy

and

Yang-Zhong Zhang
International Centre for Theoretical Physics, Trieste, Italy

Introduction

Radial electric fields on the edge of a tokamak plasma play an important rôle in determining its transport properties. Experiments aiming to understand this effect have been done, in which the radial electric field was induced in the plasma edge and controlled by using electrodes /1/.

Here, we consider the problem of particle transport in the tokamak edge for a plasma in the collision-dominated regime and in the presence of a radial (i.e. orthogonal to the magnetic surfaces) electric field.

The physics of the problem is the following. The radial electric field drives an $\underline{E} \times \underline{B}$ plasma flow on the magnetic surface (perpendicularly to the magnetic lines: in the following, we will denote this direction with $\perp$ and call it perpendicular). The $\underline{E} \times \underline{B}$ speed is smaller on the inner part (nearer to the symmetry axis) of the magnetic surface, where there is less space. Hence, poloidal asymmetries appear, which drive parallel fluxes, as regions at different poloidal locations are connected to each other along magnetic field lines. A stationary solution is possible when the resulting total (along plus across the magnetic field lines) flux on the magnetic surface is divergenceless. Of course, the final solution strongly depends on the capability of the system to efficiently redistribute the plasma on the magnetic surface along magnetic field lines. The capability is high when the $\underline{E} \times \underline{B}$ speed is much smaller than $v_{th} B_p / B$ (where v_{th} denotes the ion thermal speed and B_p the poloidal magnetic field). In this case the time required by the typical ion to reach a different poloidal location by moving along a magnetic field line is much shorter than by $\underline{E} \times \underline{B}$ drift; hence, only very small poloidal asymmetries are sufficient to drive relatively strong parallel flows whose divergence compensates for the divergence of the perpendicular ones. This is the usual situation (in the presence of an $\underline{E} \times \underline{B}$ speed of the same order or smaller than the diamagnetic speed). If, on the other hand, the $\underline{E} \times \underline{B}$ speed is much larger than $v_{th} B_p / B$, the capability mentioned above is very small, so that only very small parallel flow can appear; hence, poloidal dependencies of the density build up, which make the plasma flow on the magnetic surface divergenceless, in spite of the geometry and the poloidal dependence of the $\underline{E} \times \underline{B}$ speed. This implies that the plasma density is larger on the inner than on the outer side of the

torus.

Being the perpendicular speed the important driving parameter, the basic effect of the radial electric field does not depend on its sign, provided no other sources of perpendicular rotation are present. In practice, the ion diamagnetic drift, although small, is always present, so that the effect is symmetric with respect to that value of the electric field at which the $\underline{E} \times \underline{B}$ rotation exactly compensates the ion diamagnetic drift. This implies that, generally, positive (pointing outward) electric fields have a stronger effect. For the same reason, a neutral beam injection driving a poloidal rotation can enhance or decrease the effect of the electric field depending on its sign. Of course other effects not taken into account here, like the radial plasma current driven by the radial electric field in the presence of ion-neutral collisions, break this symmetry.

The model

We consider an electrically neutral, two-species (electrons plus singly ionized ions) plasma in the collision dominated (Pfirsch-Schlüter) regime, embedded in a tokamak magnetic field with magnetic surfaces having circular, concentric cross sections. The radial coordinate is denoted by ρ. Viscosity is neglected. The effect of ion-neutral collisions is included as the dissipation mechanism necessary to determine the ion parallel velocity. Ion inertia is included. The temperature is assumed uniform (the heat transport problem is not considered). Two-fluid equations are used.

The equations considered are the equation of motion of the ions,

$$m\,N\,\underline{V}\cdot\underline{\nabla V} = -\underline{\nabla} P_i + e\,N\left[\underline{E} + \frac{1}{c}\,\underline{V}\times\underline{B}\right] - \underline{R}_{e,i} - m\,N\,\nu_{i,n}\underline{V} \tag{1}$$

(where e, m, V and $P_i = NT$ denote respectively charge, mass, velocity and pressure of the ions, c denotes the speed of light, $\underline{R}_{e,i}$ is the density of the momentum acquired by electrons due to e-i collisions and $\nu_{i,n}$ is the frequency for momentum transfer of collisions of ions with neutral particles), the equilibrium equation,

$$m\,N\,\underline{V}\cdot\underline{\nabla V} = -\underline{\nabla} P + \frac{1}{c}\,\underline{j}\times\underline{B} - m\,N\,\nu_{i,n}\underline{V} \tag{2}$$

(where $P = 2NT$ is the total plasma pressure) and the continuity equations for the ion species, $\underline{\nabla}\cdot\left[N\,\underline{V}\right] = 0$.

From the radial component of eq.(1), by neglecting inertia and drag on electrons and neutral particles, we obtain the expression of the perpendicular component of the ion velocity on the magnetic surface,

$$V_\perp = -\frac{c}{B}\,E_\rho + \frac{c}{e\,N\,B}\,\frac{\partial P}{\partial \rho}, \tag{3}$$

where E_ρ is the radial electric field.

The continuity equation determines the parallel component of the ion flux but for a divergenceless term, $B\,C(\rho)$, where $C(\rho)$ is an arbitrary surface function. Then, the

poloidal and toroidal components of the ion velocity, V_p and V_T, read

$$V_p = \frac{B_p}{N}\, C(\rho), \qquad V_T = \frac{B_T}{B_p} V_p - \frac{B}{B_p} V_\perp. \tag{4}$$

We are interested in situations where the $\underline{E} \times \underline{B}$ rotation is much larger than the diamagnetic rotation, hence neglect the second term on the r.h.s. of eq.(3). Then, the parallel component of the equilibrium equation reads

$$\frac{m\,N}{\rho}\,\frac{B}{2B_p}\,\frac{\partial}{\partial\vartheta}\left(V_p^2 - V_\perp^2\right) = -\frac{B_p}{\rho B}\,\frac{\partial P}{\partial\vartheta} - m\,N\,\nu_{i,n} V_\parallel. \tag{5}$$

Its solubility condition determines $C(\rho)$ as

$$C(\rho) = \frac{B_T B}{B_p}\,\frac{\overline{N}}{\overline{B^2}}\, V_\perp, \qquad \text{where} \qquad \overline{Q} = \frac{\oint d\vartheta\, R\, \nu_{i,n} Q}{\oint d\vartheta\, R\, \nu_{i,n}},$$

and its solution determines the dependence on the poloidal angle ϑ of the density and, hence, of the poloidal and toroidal components of the ion velocity. The radius $R = R_0(1 + \varepsilon\, cos\vartheta)$ denotes the distance from the symmetry axis, ε is the inverse aspect ratio.

In the figures numerical results are reported for the parameters of the TEXTOR experiment /1/. The first three figures report the poloidal dependence of the poloidal and parallel velocity, normalized to the ion thermal speed, and of the density, normalized to its average value. The number labelling the lines is the ratio of the $\underline{E} \times \underline{B}$ speed evaluated at $R = R_0$ to the critical speed (see below). In the fourth figure the diffusion coefficient for particles is reported, normalized to the value it has in the absence of the radial electric field (its Pfirsch-Schlüter value), as a function of the electric field intensity.

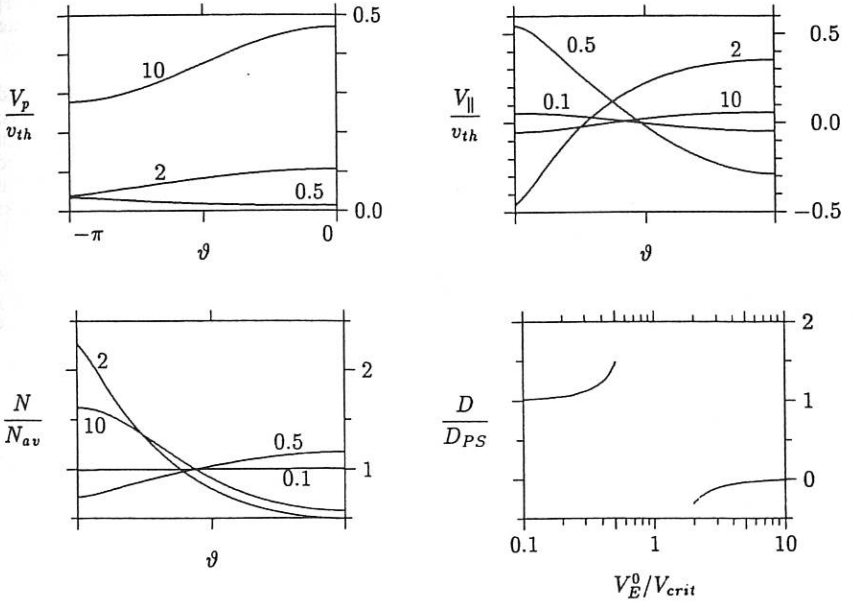
The results

As expected, a "critical" speed in the problem is found to be the ion thermal speed multiplied by the ratio of the poloidal to the total magnetic field, $V_{crit} = v_{th} B_p / B$. No solution can be found when the $\underline{E} \times \underline{B}$ perpendicular speed is of the order of V_{crit}. For TEXTOR parameters, the range where the equilibrium does not exist extends from half to twice the critical speed, corresponding to a jump by a factor four between the maximum of the lower values and the minimum of the higher values of the electric field allowed in the plasma. This is in agreement with the experiment /1/, where low voltages (up to roughly 500 V applied between electrode and limiter) tend to create an almost uniform radial electric field in the 5 cm plasma layer between the electrode and the limiter, of the order of up to roughly 100 V/cm, while higher voltages (above 500 V, up to 1000 V) tend to accumulate in front of the limiter, where electric fields of the order of 500 V/cm and higher appear, while the remaining part of the layer is interested by a much smaller radial electric field. For comparison with the experiment, it should be

noted that the value at which the electric field compensates the diamagnetic rotation is there of the order of -20 V/cm so that the magnitude of the negative voltages necessary to jump from the uniform to the non-uniform radial distribution of the electric fields is higher than that of the positive ones by roughly 200 V. The case where the $\underline{E} \times \underline{B}$ is of the order of V_{crit} was investigated in /2/.

At low values of the electric field, i.e. of the perpendicular speed, $V_\perp \ll V_{crit}$, the usual Pfirsch-Schlüter regime is obtained. By increasing the electric field, a density accumulation on the low-magnetic-field side appears. It is very weak because the building up of poloidal inhomogeneities is effectively impeded by relatively strong parallel flows. The cross-magnetic-field diffusion coefficient of particles, D, increases above its Pfirsch-Schlüter value, D_{PS} (see fig.1).

In the opposite limit of very strong values of the per[endicular rotation, $V_\perp \gg V_{crit}$, the parallel velocity is extremely small, as if there were no connection via the parallel direction between the diferent poloidal locations. The density depends on the poloidal angle as $1/R^2$. The cross-magnetic-field diffusion of particles vanishes. By decreasing the electric field, i.e. by reducing the rotation, the density unbalance between the low- and the high-magnetic-field sides increases, and the diffusion coefficient of particles become negative, i.e. the particle diffusion becomes inward (see the last figure).



/1/ R. R. Weynants et al., Nucl. Fusion 32, 837 (1992).

/2/ K. C. Shaing, R. D. Hazeltine and H. Sanuki, Phys. Fluids B4, 404 (1992).

INTERPRETING FLUID MODELS OF TOKAMAK EDGE PLASMAS

P. C. Stangeby* and G. P. Maddison**

*University of Toronto Institute for Aerospace Studies
Toronto, Ontario, Canada, M3H 5T6
and
JET Joint Undertaking, Abingdon, Oxon, OX14 3EA, U.K.

**UKAEA Government Division, Fusion, Culham Abingdon, Oxon, OX14 3DB, U.K.
(Euratom/UKAEA Fusion Association)

The concept of interpreting experimental data is a familiar one, but fluid model codes — particularly of the plasma edge — have now grown to be so complex and non-transparent, that the need has arisen for the interpretation of edge code results in terms of simpler, more basic, analytic models. Otherwise one is at risk of accepting code results which may be in error, or at least misleading. Code results are also most useful, clearly when one understands their basic features.

Consider two examples of surprising behaviour of edge code results:

(a) While simple fluid models lead one to anticipate that the plasma pressure will drop along the SOL by a factor of 2 as the flow accelerates to the Bohm speed (or to drop more if friction is present), code results often show dramatic pressure *increases*, approaching the sheath. The simple model expectations seem so undeniable that one is obliged to investigate. The problem turned out to be that the Braginski parallel viscosity is in error near the sheath [1] and when this is allowed for [2], pressure profiles in accord with analytic expectations are found.

(b) Many edge fluid codes show a very strong sensitivity of nt, plasma density at the target, and T_t, plasma temperature at the target, when the pumping is changed even by small amounts; see, for example, Fig. 26 of [3]. This is apparently inconsistent with analytic Two Point Models, 2PM. This finding not only raises the question of whether we really understand edge behaviour, but has the most practical of consequences: if such extremely important quantities as n_t and T_t can be manipulated so easily, then the engineering design of tokamaks ought to fully exploit this.

The present paper addresses this second problem. In the next section a (modified) 2PM is outlined and the reasoning is given as to why n_t and T_t should not be strongly influenced by pumping. In the subsequent section, B2 fluid edge code results are given which illustrate the strong sensitivity of n_t and T_t to pumping. In the last section the discrepancy is resolved.

A Modified Two-Point Model

2PM's are simply expressions of conservation of momentum and power. One therefore must insist that code results be in accord with them, approximately. Momentum or pressure balance gives:

$$n_t(kT_{et} + kT_{it}) = f_p n_m(kT_{em} + kT_{im}) \qquad (1)$$

where m refers to the mid-plane, or upstream, point and f_p allows for pressure drop due to acceleration and friction. For no friction and flow Mach number $M_t = 1$ at the sheath, $f_p = 1/2$. Conservation of power gives:

$$(1 - f_E)\, q_{\parallel} = \gamma_{sh}\, n_t\, c_{st}\, kT_{et} \qquad (2)$$

where $q_{\parallel} = Q_{tot}/A_{SOL}$, the power flux density along $\vec{B}$; Q_{tot} = total power into the SOL and A_{SOL} = cross-sectional area of SOL for power flow; γ_{sh} = sheath heat transmission coefficient; c_{st} = sound speed and $M_t = 1$ is assumed here; f_E is the fractional power loss in the divertor due to volume energy losses such as radiation and charge-exchange, and by transport into the private plasma. For illustration, taking $T_e = T_i$ one can combine (1) and (2) to give the simple relation for target temperature:

$$kT_t = \frac{m}{2}\left[\frac{(1-f_E)\, q_{\parallel}}{\gamma f_p\, n_m\, kT_m}\right]^2 \qquad (3)$$

and n_t is given by a similarly simple expression. As is evident from Eq. (3) there is no indication that T_t or n_t should have any particular sensitivity to pumping: none of the quantities on the RHS has any obvious, significant dependence on pumping.

The high recycling divertor mode of operation is generally sought where $T_t << T_m$ and most of the parallel heat transport is thus, necessarily, carried by conduction rather than convection. This operating mode is indeed termed "high recycling" since most of the neutral hydrogen recycling from the targets is ionized in the divertor plasma near the target, with only a small fraction either leaking naturally to the core plasma, or being pumped at/near the target — and then re-supplied by, say, pellet or NBI refueling the core. Thus convection is only significant near the target and large T_m/T_t ratios are then possible due to the basic nature of conductive heat transport. The parallel heat conductivity $\kappa_{\parallel} = \kappa_0 T^{5/2}$ leads, in the case of $T_m >> T_t$ to:

$$T_m = \left[\frac{7}{2}\frac{f_{cond}\, q_{\parallel}\, L}{\kappa_0}\right]^{2/7} \qquad (4)$$

where f_{cond} = fraction of the power flow carried by conduction (along most of the length of the SOL). As is evident from Eq. (4), T_m is very insensitive to any of the control variables. Admittedly one does now note a mechanism by which pumping would influence n_t and T_t: as pumping is increased, f_{cond} decreases, lowering T_m, raising T_t. This effect, however, is clearly small unless the pumping is extremely strong: even if one could pump half the target flux, practically not achievable (and inconsistent with the high recycling mode), resulting in $f_{cond} \simeq 1/2$, one would only raise T_t by ~50%. Code results, by contrast, are far more dramatic; from [3], for example, a pumping fraction of just 1.7% caused the peak value of T_t to rise ~4X, compared with zero pumping. This effect, therefore, would not appear to be the basic explanation of the code results, although it should be noted that the target conditions are rather "volatile", in that T_t and n_t are dependent on f_p, for example, as the second or third power, and therefore positive feedback or runaway effects may arise.

B2 Fluid Code Results

As in the earlier studies [2], the B2 edge fluid code was run with an ITER CDA grid and using either the EIRENE Monte Carlo neutral code, or the Hotston analytic model. For details, see [2]. Assumed here: $3D_{\perp} = 3\kappa_{\perp}^{i} = \kappa_{\perp}^{e} = 2$ m^2/s. The results shown used the Hotston model, but results are similar using EIRENE. The constrained parallel viscosity [1] was used here, but the conclusions were the same using unconstrained (Braginskii) viscosity (although the actual n_t and T_t values were much affected). Four values of pumping speed were

employed, specified by the number F_{OL} = 20, 50, 100, 670; the fraction of the target particle flux pumped = $1/F_{OL}$.

Figure 1 shows the radial profiles of n_e at the mid-plane and immediately reveals the first cause of the strong sensitivity of n_t and T_t to pumping in the code: as in virtually all code work, what is kept fixed as pumping (or other control parameters) are varied is the value of $n_{e,ref}$ at a reference grid ring located some distance inside the separatrix, here about 6 cm at the outside mid-plane. That, however, causes $n_{e,sep}$ to vary rather strongly with F_{OL} (depending on the value of $D_\perp$ also) since the pumped particle flux is assumed here to be resupplied by cross-field diffusion from the reference ring (the "core"), causing $n_{e,sep}/n_{e,ref}$ to decrease as F_{OL} decreases. One notes from Eq. (3) that T_t is a very strong function of n_m, $T_t \propto n_m^{-2}$. This, then, is a principal — and essentially artificial, or at least misleading — cause of the strong dependence of n_t and T_t on pumping. In Fig. 2 are shown the radial profiles at the target (but mapped back to the outside mid-plane) of n_{et}, $(T_{et} + T_{it})/2$ showing how very spectacular the sensitivity of these quantities can apparently be to pumping.

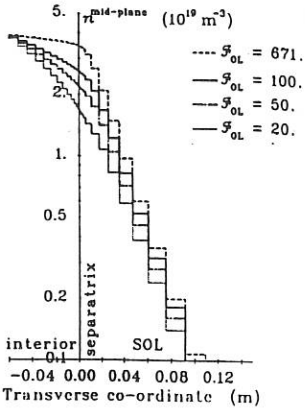


Fig. 1. Radial profiles of electron density at the mid-plane, $n_{e,mid}$, for various pumping speeds, as specified by F_{OL}.

Demonstrating the Consistency of the Two-Point Model with the B2 Edge Fluid Code Results

For each flux tube, and for each value of F_{OL}, the following quantities were extracted from the B2 code output: (a) f_p, (b) $q_\parallel$, calculated nearest the X-point, i.e., the "divertor entrance", (c) f_E, from the power loss between the divertor entrance and the target, (d) T_{em}, T_{im}, (e) n_{em}. These quantities were then used in Eq. (3) to generate the 2PM values of T_t which are compared in Fig. 3 with the code results. Figure 4 does the same for n_t. It is clear that the B2 code results are, flux-tube-by-flux-tube, in good agreement with the 2PM, generally. It is thus evident that there are not any basic "surprises" in the code results for n_t and T_t. Everything is approximately in accord with simple models.

It must be noted, of course, that the values of f_p and f_E *themselves* have to be explained, and the contributions to *them* identified — in order to complete one's understanding of what is going on. Nevertheless, if one looks upon the present exercise in code interpretation as an "onion skin peeling" exercise, where one builds up one's understanding one step at a time, then the first step or first "onion skin" of understanding — is achieved when, as here, one has established the consistency of the code results and the 2PM, on an individual flux tube basis. This second part of the exercise will be reported on elsewhere.

Support (PCS) by the Canadian Fusion Fuels Technology Project is acknowledged. This work (GPM) is partially funded by the U.K. Department of Trade and Industry.

References

1. G. J. Radford, *Contrib. Plas. Phys.* 32 (1992) 297.
2. G. P. Maddison, P. C. Stangeby, G. J. Radford and J. Hugill, *Contrib. to Plasma Phys.* 34 (1994) 226.
3. H. D. Pacher, W. D. D'Haeseleer, G. W. Pacher, *Nucl. Fusion* 32 (1992) 1373.

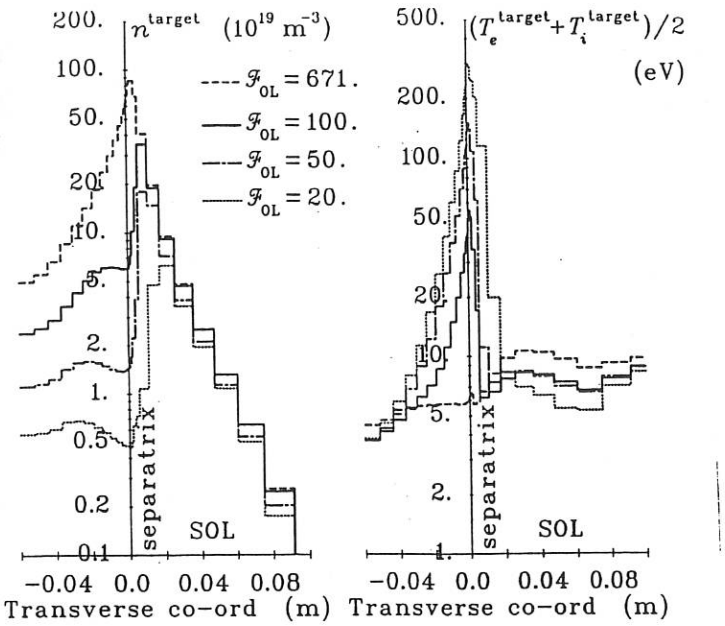


Fig. 2. Radial profiles of plasma temperature and density at the target for various values of F_{OL}.

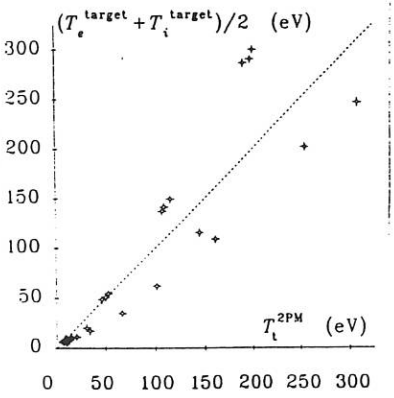


Fig. 3. For individual flux tubes and different values of pumping speed F_{OL}, the value of plasma temperature at the target (vertical scale) plotted against the value predicted by the Two Point Model, Eq. (3).

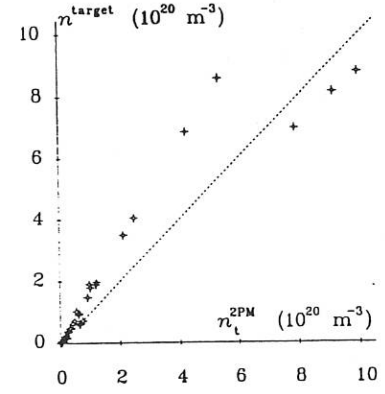


Fig. 4. As Fig. 3 but for plasma density at the target.

Validation of fluid modelling of edge plasmas on COMPASS-D

G P Maddison, K B Axon, M Booth, J Ferreira, S J Fielding & J Hugill
UKAEA Government Division, Fusion, Culham, Abingdon, Oxon. OX14 3DB, UK.
(UKAEA/EURATOM Fusion Association)

1. Introduction

Detailed numerical models for axisymmetric, steady states of tokamak edges include the BRAAMS "B2" fluid model of edge plasma transport[1], and the EIRENE Monte Carlo simulator of recycled neutral gas transport[2], which also incorporates various representations of surface interactions. A consistent, automatic linkage of these two codes now allows their integrated application (see ref.3 and references therein).

Such comprehensive treatments merit testing against experimental data. Indeed, this "validation" is essential, before the models can be used with confidence to predict behaviour in future devices, like ITER. We present a preliminary report on a programme of validation studies for "B2"-EIRENE being conducted on the COMPASS-D tokamak at Culham.

2. COMPASS experiment and computational model

The COMPASS device is a medium-sized, D-shaped cross-section tokamak, capable of forming single X-point plasmas impinging on an axisymmetric, instrumented set of carbon tiles (denoted the IXPL) for flat-top durations of order 100 ms. Basic parameters of pulses used in the present exercise are listed in Table 1. Shown in Fig.1 is its discrete rendition generated[4] for "B2"-EIRENE. A magnetic reconstruction code DFIT involving magnetic coil and flux loop signals indicates this geometry is accurately realized.

Restriction of the current version of "B2" to orthogonal co-ordinates leads to approximation of target sections by magnetic-surface-orthogonal contours exactly through their strike-point positions. Furthermore, standard "B2" omits[1] electric currents and plasma drifts across field lines within magnetic surfaces. To compensate for the latter, pulses are executed in COMPASS in *field-reversed* pairs. By duplicating discharges with normal field directions (designated (++)), then simultaneous reversal of *both* toroidal field *and* plasma current (designated (−−)), the helicity of field lines is preserved while reversing drifts. Hence joint *average* properties might be more closely approached by "B2".

All "B2" cases presented include a constrained form of parallel ion stress, shown previously to be important in preventing unphysical pressure profiles[4]. For consistency, parallel electron conductivity is also flux-limited[1]. Strictly steady results are ensured by securing always asymptotic convergence of "B2"-EIRENE as defined in ref.3.

3. Validation approach

Uncertain quantities such as cross-field transport coefficients $D_\perp$; $\chi_\perp^e$; $\chi_\perp^i$ enter into models effectively as undetermined parameters. In order to check a model, it is necessary first to fix the latter, or "calibrate" it, by matching to certain observed data, before next "testing" it, through comparisons of other features with their independent measurements. The initial matching procedure itself cannot alone verify a model.

In the following, we discuss three "B2"-EIRENE cases, distinguished by the choice of transverse diffusivities (see Table 1): Bohm-related values (A); smaller, constant values (C); and intermediate, constant values with a more extreme thermal to particle ratio (B). Remarkably, despite differing particle through-puts, the recycling regime solved for with EIRENE is nearly identical for each one, $\approx 26\%$ of neutral particles escaping through the interior boundary into the core.

"CALIBRATION"

A top-mounted, reciprocating probe (RCP) in COMPASS is able to detect edge plasma profiles within an individual discharge, and advantageously is remote from target diagnostics to be exploited subsequently in testing. Comparisons are shown in Fig.2 of measured and calculated profiles of ion saturation current density j_{sat} and electron temperature T_e during a reversed pair of pulses. Each probe data point is averaged over a 2.5 ms interval, and all are shifted inwards by ≈ 5 mm, within experimental uncertainty, for best alignment with the calculated curves. Note there is evidence of a narrower SOL width with normal (++) fields (ion ∇B-drift towards the X-point). This could correspond with spectroscopic and magnetic suggestions of a marginal H-mode in this instance. A shift in the L to H threshold with reversed fields would be consistent with identification in JET and other machines of its dependence on the direction of plasma drifts.

Examination of j_{sat} curves allows full use to be made of the distinct T_e; T_i profiles determined by "B2"-EIRENE, giving a more complete comparison. Bohm diffusivity (A) derived is of order $2 \rightarrow 3$ m$^2\cdot$s^{-1}, and appears most closely to recover at least the broader, reversed (−−) profiles. The smaller, constant diffusivities (B; C), while giving steeper j_{sat} curves, cannot then fit the very flat T_e data at the given total power efflux and parallel transport ($q_{\|} \sim nT^{3/2}$). An even more extreme ratio of $\{\chi_\perp/D_\perp\}$ on its own therefore could not lower calculated T_e to the probe points.

To identify $D_\perp$ it is not sufficient just to fit a j_{sat} (density) profile; its accompanying diffusive flux must be matched too. Future RCP measurements in COMPASS will estimate local flux from plasma fluctuations, but a global upper bound may be deduced roughly from conventions $\Gamma = (N/\tau_P) \lesssim (N/\tau_E)$. For COMPASS conditions specified, $\tau_E \approx 10$ ms, implying $\Gamma \lesssim 1.8 \times 10^{21}$ s^{-1}. Figures in Table 1 show each calculation to be within this limit, although these include ion effluxes at the "B2" outermost surface permitted by pedestal boundary conditions. Furthermore, a Balmer-α photomultiplier detects photons at its top viewing position equivalent to an axisymmetric emission of $\approx 5 \times 10^{20}$ s^{-1}. Future EIRENE applications will in turn evaluate Balmer-α distributions directly, but

Table 1. Main details of plasmas & calculations

COMPASS-D R_0 ; I_p ; B_0	species ; $\overline{n_e}$	$Q^{SOL} = P^{inp} - P^{rad}$
0.56 m ; 0.15 MA ; 1 T	^{2}H ; 3.5×10^{19} m^{-3}	≈ 0.13 MW

"B2"-EIRENE : interior $Q_e/Q_i = 2$; Bohm target-sheaths ; exterior pedestals				
Case	Diffusivities	interior n (10^{19} m^{-3})	*computed* Γ^{sep} (10^{21} s^{-1})	*computed* $\Gamma^{targets}$ (10^{21} s^{-1})
(A)	$\chi^e_\perp = \chi^i_\perp = 4D_\perp = 4D_{Bohm}$	1.0	1.4	2.5
(B)	$\chi^e_\perp = 2\chi^i_\perp = 10D_\perp = 2$ m$^2\cdot$s^{-1}	0.8	0.45	1.3
(C)	$\chi^e_\perp = \chi^i_\perp = 4D_\perp = 0.8$ m$^2\cdot$s^{-1}	0.8	0.45	1.3

corresponding total ionization source strength of $\approx 5.5 \times 10^{21}$ s^{-1} here is again within a factor of 2 of the Bohm case (A).

"TESTING"

The IXPL tiles are imaged by a matrix infra-red camera (IRC), which maps their surface temperature in 20 ms frames. A simple surface heating relation would predict their temperature rise $\Delta T \propto q\, t^{1/2}$ in a time t, where q is incident power density. Hence for a steady plasma, one would expect that normalized temperature distributions at each instant would tend to a constant shape, proportional to q. Normalized values along a major radius are plotted in Fig.3 at 20 ms intervals during the flat-tops of a (++); (−−) pair of pulses. Very steady shapes are indeed seen to occur. Curves shown dotted from 60 ms earlier in each discharge indicate their genuine approach to stationarity. Note there is only a small outward shift of the outboard strike-point between opposite field directions. Relative heights of inboard to outboard peaks now reveal the in/out asymmetry in target power density. This is clearly changed between reversed orientations, pointing to an average imbalance of ($\approx 0.93 : 1$).

Calculated profiles of target power density for each "B2"-EIRENE case are also shown in Fig.3. Surface recombination is included, but this contributes only a few percent. Angle factors between the numerical and actual target surfaces are almost identical at either strike-point, and so cancel in normalized peaks, positions and heights of which are superimposed on the IRC signals. There is good agreement on positions, while Bohm case (A) finds approximate in/out balance, again closest to the (−−) observations. Constants cases (B); (C) are clearly discriminated by predicting *inverted* in/out asymmetries (> 1).

Finally, shown in Fig.4 are "B2"-EIRENE profiles of target-facing electron temperature, together with flat-top data from a probe embedded within an IXPL tile. This measures higher inboard temperatures for (−−) fields, consistent with increased power density recorded by the IRC. Bohm case (A) here agrees very well with a (++),(−−) average.

4. Discussion

Preliminary validation tests on COMPASS suggest that features of its X-point SOL behaviour can be described by the "B2"-EIRENE fluid model, using large, Bohm-related transverse diffusivities. Field-reversed pairs of COMPASS pulses indicate the impact of plasma drifts omitted from standard "B2". However, while such pairs may be accurately anti-symmetric with respect to these drifts, they are unlikely to be so regarding currents flowing in the SOL, and also neglected in "B2". Moreover, examination of gradient scale-lengths[4] in preceding "B2"-EIRENE solutions shows that they do *not* in fact conform to a fluid plasma regime[4]. Further work will next extend testing over ranges in power and density, in particular to higher densities where fluid criteria should best be fulfilled.

This work is jointly funded by the UK Department of Trade & Industry and by Euratom.

References

1 – B J Braams, PhD thesis, University of Utrecht, 1986
2 – D Reiter, KFA Jülich report JÜL-1947, 1984
3 – G P Maddison & D Reiter, KFA Jülich report JÜL-2872, 1994
4 – G P Maddison, P C Stangeby *et al*, Contrib. Plasma Phys. 34 (1994) 226

Fig.1 COMPASS-D single null configuration

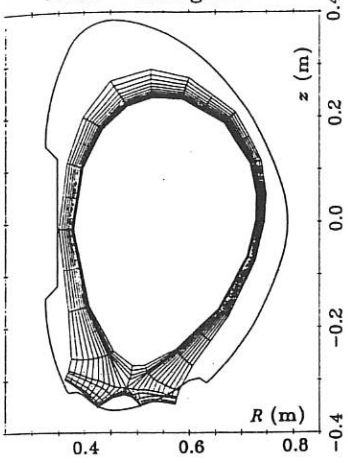


Fig.2 Calibration against top-mounted probe data

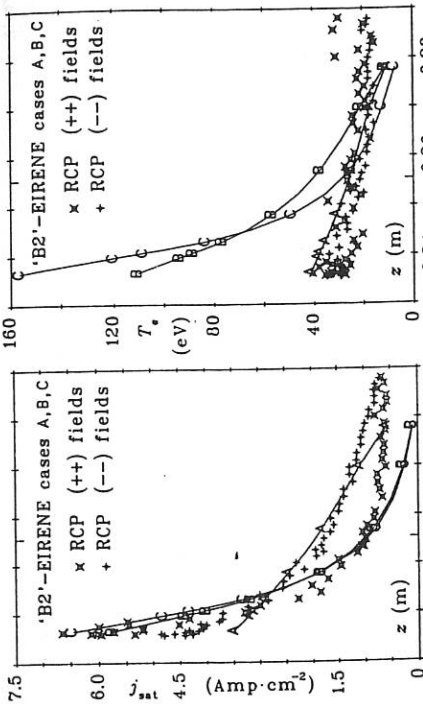
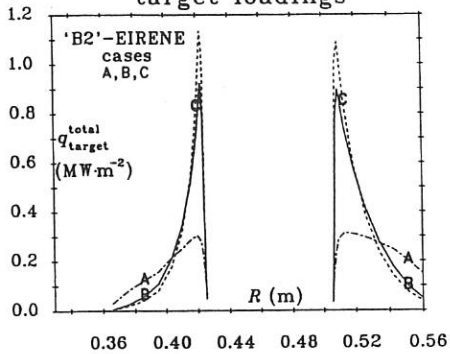


Fig.3 Comparison of target loadings



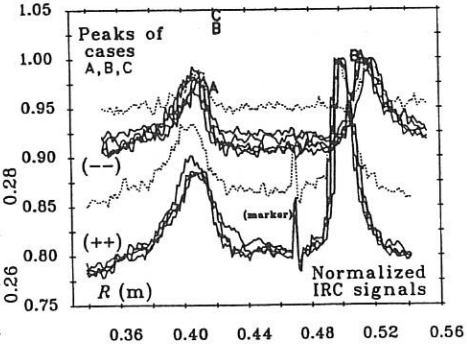
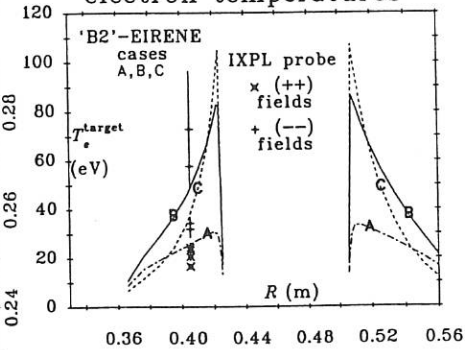


Fig.4 Comparison of target electron temperatures



Shutdown of a Burning Plasma and Examination of Edge DT Depletion

G.W. Pacher and H.D. Pacher

The NET Team,
c/o Max-Planck-Institut für Plasmaphysik, D-85748 Garching,Germany

Introduction

During start-up of the tokamak plasma, the gas stored in the plasma-facing components during the previous discharge can be desorbed and lead to overfuelling of the ohmic phase of the next discharge. In order to reduce the inventory available for desorption, it has been suggested [1] that the final stage of the discharge be performed in helium to degas the walls. Simulations to investigate this mode of operation are carried out with the 1.5 D ASTRA transport code, starting from an ITER plasma near end of burn. Calculations were performed for the Outline Design geometry with the full RLW transport model in order to determine a self-consistent evolution of plasma parameters. The operating point is determined by edge fuelling compatible with the Borrass edge density limit [2]. During the shutdown phase, the loop voltage is put to zero, so that no primary volt-seconds are consumed and the plasma current decays. Additional heating is applied to keep the density limit acceptably high. Normal shutdown in DT with up to 50 MW of additional heating results in fusion power shutdown in ~50 s with edge density maintained near the Borrass density limit. In the subsequent evolution, helium fuelling is applied to minimise the edge D+T concentration whenever possible according to density limit criteria.

Description of the Model

The transport calculations were carried out with the 1.5 D ASTRA transport code [3] developed at the Kurchatov Institute. The (fixed-boundary) equilibrium is determined from a moment expansion at each time step, and the profiles of the main plasma parameters (j, T_e, T_i, n_e, and, in addition, n_{He}) are evolved in time. The transport coefficients used correspond to the RLW transport coefficients given in [4]. For particle transport, the expressions of [5] were used:

$$\Gamma_e = \Gamma_{e,neo} - n_e D_e \nabla n_e - n_e D_e \frac{eE_r}{T_e} + n_e v_0 \qquad \Gamma_i = \Gamma_{i,neo} - D_i \nabla n_i + D_i n_i \frac{Z_i e E_r}{T_i}$$

$$\text{where} \qquad v_0 = -0.5 \frac{n_e + \sum n_i}{n_e} \frac{\nabla q}{q} \qquad D_e = D_i = 0.5 \chi_i$$

Particle diffusion coefficients for electrons, ions, and helium were taken to be equal. The pinch velocity for these species was calculated by eliminating E_r in the above equation using quasineutrality. The electron and helium pinch velocities are then:

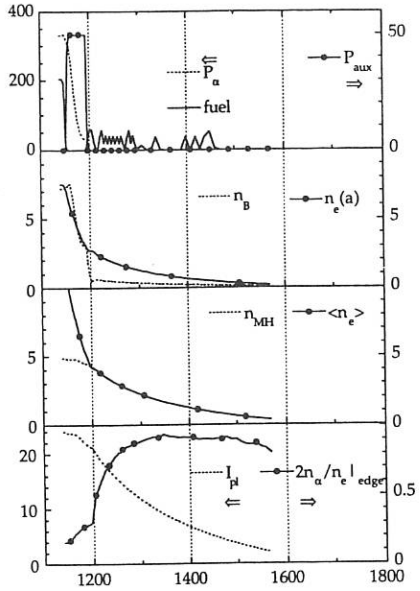
$$v_e = v_0 \frac{(1-Zc)T_e/T_i + 2c_\alpha T_e/T_i}{(1-Zc)(1+T_e/T_i) + 2c_\alpha T_e/T_i} \qquad v_{He} = 2v_0 \frac{1-Zc}{(1-Zc)(1+T_e/T_i) + 2c_\alpha T_e/T_i}$$

where Z and c are the charge and concentration of an impurity other than He. A time-averaged sawtooth model is incorporated, which artificially decreases the electrical conductivity, flattening j inside the q=1 surface and thereby constrain q_0 to be close to unity. The heat and particle transport coefficients are not explicitly modified, but are affected only by the shear dependence inherent in the RLW

coefficients. While a local beta-limiting algorithm is implemented, it is not called upon here, since the local pressure gradient is below the limit even before shutdown.

Beryllium is the only impurity considered, at a density of 0.8% of electron density, independent of radius. Impurity radiation is taken to be given by corona equilibrium.

The simulations include no neutral model. Electron and ion temperatures at the boundary of the calculation are held fixed at a value of 100 eV. The edge electron and helium densities $n_e(a)$ and $n_{He}(a)$ are boundary conditions for the transport problem, determined via an algorithm which approximates fuelling/pumping, as follows. 0D particle continuity is applied to the SOL region outside the transport calculation. The inflow into this region from the plasma plus a gas valve is balanced against a pumped flux, which is determined from an effective pumping speed applied to the species density at the plasma boundary (rather than to a density at the pump duct). This pumping speed for He is such that, in steady-state, the ratio $\tau_\alpha / \tau_E \sim 10.5$. The central helium concentration obtained is then ~15%, similar to the values obtained in 1-D modelling by the ITER Joint Central Team with PRETOR [5]. For hydrogenic species, this pumping speed is taken 1.5 times larger than for He. This implies fuelling at approximately 1×10^{22} atoms per second (about one-fifth of the maximum fuelling rate foreseen for ITER).



Case a): Shutdown, P_{aux} only until $<n_e>=n_{M\text{-}H}$, He fuelling at $<n_e>=n_{M\text{-}H}$

The heating power profile is taken to be $(1-r^2/a^2)^4$. Maximum heating power applied is 50 MW.

Description of Shutdown Simulation

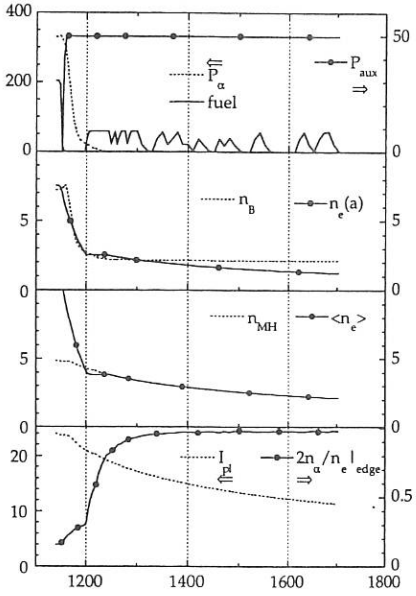
The initial condition for all cases investigated corresponds to a burning plasma in steady-state with a fusion power of 1650 MW (i.e. P_α=330 MW) and no additional heating. Specifically, $n_e(r)$ and j(r) have become stationary. At t=1150 s on the time scale of the figures, the DT fuelling is turned off and the loop voltage at the plasma edge is set to zero. Thus, no further primary volt-seconds are consumed during the shutdown. From this time onward, the additional heating power is applied such as to maintain the alpha power at a level of 320 MW as long as this is possible, and continues at full power (50 MW) thereafter for a time depending on the scenario. In all cases, additional heating remains on at least until the average density has fallen below the Murakami-Hugill value (taken to be the maximum density compatible with ohmic operation). Fuelling performed after t=1150 s is helium fuelling. During the burn phase, the edge electron density is approximately equal to n_B, the Borrass

value. Should $n_e(a)$ briefly exceed n_B, (it is about equal at 1175 s), either more pumping speed or higher additional power would be required.

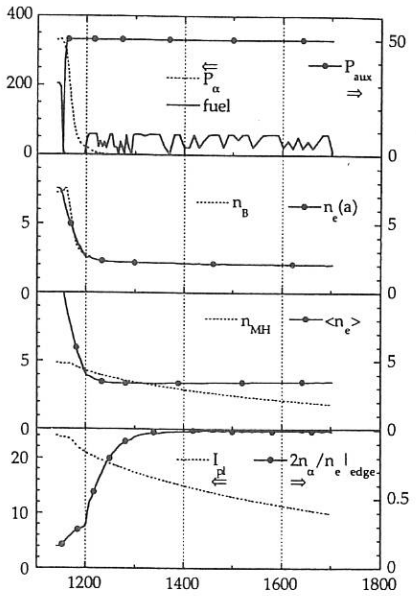
Shutdown Scenarios

Three main variants of the shutdown scenario were investigated:

a) Additional power is turned on as the fusion power drops. It is turned off as soon as the Murakami-Hugill limit is reached (after ~50 s). Helium fuelling maintains the average density at the Murakami-Hugill limit. The total plasma current drops by two thirds to 8 MA at t=1350 s, 200 s after shutdown begins . The edge He concentration is ~46% at 1400 s and then drops slowly. The edge helium density at the time of the maximum concentration is ~0.5×10^{19} m^{-3}.



Case b): Shutdown, P_{aux}=50 MW, He fuelling at $\langle n_e \rangle = n_{M\text{-}H}$



Case c): Shutdown, P_{aux}=50 MW, He fuelling at $n_{e,edge} = n_{Borrass}$

b) Additional power is turned on as the fusion power drops. It is maintained at 50 MW. Helium fuelling maintains the average density at the Murakami-Hugill limit The additional power conserves a hotter plasma, so that the current drops much more slowly than for case (a) and is still > 15 MA at t=1350 s, 200 s after start of shutdown . As a result, the Murakami-Hugill limit is higher, more fuelling is allowed, and more time is available. The edge He concentration is > 48% at 1400 s and $n_{He}(a)$ is ~ 10^{19} m^{-3} at that time and decreases thereafter as the Murakami-Hugill limit decreases with decreasing current.

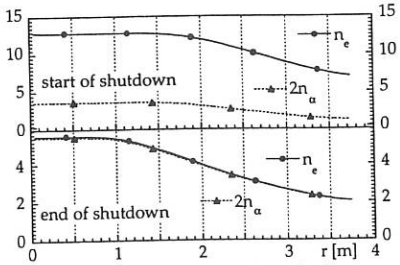
c) Additional power is turned on as the fusion power drops. It is maintained at 50 MW. Helium fuelling maintains the edge electron density at the Borrass limit. As for case (b), the current decreases slowly but faster than in case b). The edge

He concentration is > 48% at 1400 s and $n_{He}(a)$ remains constant at ~ 10^{19} m^{-3} thereafter. This mode of operation at constant edge helium density could be continued for > 1000 s with the inductive flux stored in the plasma. At any convenient time, the density can be ramped down to the Murakami-Hugill density and the additional power can then be shut off. The density profiles at the start and end of shutdown are also shown below.

Conclusion

At the start of shutdown from burn, of the order of 50 MW additional heating power is required in order to prevent the edge density limit (Borrass limit $\propto P^{0.66}$) from decreasing faster than the edge density. All three shutdown scenarios presented here have edge helium concentrations > 46% . If the additional power is shut off as soon as the average plasma density becomes compatible with ohmic operation (equals the Murakami-Hugill density), the edge D+T concentration is nevertheless of the order of almost 10% and the edge helium density is low. Operation at high helium concentration is limited to ~ 200 s. Both density and duration are too low to expect appreciable degassing of hydrogenic species by helium impact to take place. More efficient degassing can be obtained if the additional heating is maintained. For this case, fuelling such that $\langle n_e \rangle = n_{Murakami-Hugill}$ results in edge helium densities of ~10^{19} m^{-3}, decreasing in time, whereas fuelling such that $n_e(a) = n_{Borrass}$ maintains this density.

The last option, maintaining P_{aux} at 50 MW and fuelling such that $n_e(a) = n_{Borrass}$, would therefore be the most attractive variant to remove the hydrogenic species for the next discharge. Questions to be resolved include the capacity of the plasma-facing components to handle heating power of 50 MW at an edge density of 2x10^{19} m^{-3}, as well as the scaling of the plasma-wall processes, i.e. degassing efficiency.



Profile case c) at start and end of shutdown

Acknowledgements

We thank G. V. Pereverzev for providing the ASTRA code package and many discussions on its use.

References

1. J. Ehrenberg, JET, private communication, 1989
2. K.Borrass et al, Nucl. Fusion 33, no.1, (1993), p.63
3. G. Pereverzev et al, "ASTRA - An Automatic System for Tranport Analysis in a Tokamak", IPP report 5/42, Aug. 1991
4. P.-H. Rebut et al, "A Program toward a Fusion Reactor", Phys. Fluids B3 (8), Aug. 1991, p.2209
5. D. Boucher, Thesis, Sept 1992

PLASMA EDGE SPECTRAL PROFILES FOR DISCHARGES WITH HIGH AND LOW MHD ACTIVITY IN TBR-1 TOKAMAK

M.V.A.P. Heller, Z.A. Brasilio, R.M. Castro, I.L. Caldas, R.P. da Silva, TBR-1 Team.
Institute of Physics, University of São Paulo
C.P.20516, 01452-990 São Paulo-SP, Brazil

1. Introduction

Plasma edge turbulence was investigated in the TBR-1 small tokamak for two different discharge regimes, one with high ($\tilde{B}_\theta/B_\theta(a) \simeq 9\times10^{-4}$) and the other with low ($\tilde{B}_\theta/B_\theta(a) \simeq 3\times10^{-4}$) MHD activity. The last regime was achieved by using resonant helical fields (**rhf**), created by a set of external helical coils /1/. The experimental data were obtained from a set of specially designed system of Langmuir and magnetic probes /2,3/.

The digital spectral analysis technique, used to obtain the degree of correlation and phase difference between the probe signals, showed an unusual superposition between the electrostatic and magnetic spectra in MHD frequency region. The bispectrum /4/ was estimated to characterise the non linear nature of the broadband edge fluctuations. We also calculated, for the plasma parameter fluctuations, typical quantities as skewness and kurtosis to detect eventual deviations from normal distributions. The characteristic differences between the two regimes (with high or low MHD activity) were analysed to investigate the possibility of coupling between density and magnetic poloidal field fluctuations.

2. Experimental

The work was carried in the TBR-1, a small Ohmically heated tokamak filled with hydrogen as working gas. Details of the experiment can be found in references /2,3/.

The diagnostic measures simultaneously electrostatic and magnetic fluctuations besides the average values of the density, the potential and the temperature. The plasma density as measured by Lagmuir probes in the scrape-of-layer (SOL) are in the range $n \approx (0.5-5.0)\times 10^{17}\ m^{-3}$ and $T_e \approx (5-40)\ eV$ respectively, the density scale length is $L_n \simeq 1.1\times10^{-2}\ m$ and the temperature scale length $L_{Te} \simeq 1.0\times10^{-2}\ m$, the safety factor is $q(a) = 5$. Data were recorded at 1 MHz sampling rate.

The external magnetic perturbation was created by electric currents ($I_h = 180A$) circulating in a set of helical windings located externally around the torus. The current was switched on after the plasma current has reached steady values, during time intervals greater than two miliseconds. These coils produce a perturbation field with dominant helicity $m/n = 4/1$.

3. Discussion and Conclusions

The measured equilibrium radial profiles do not show any significant modification with the application of **rhf**. The direction of the phase velocity is unaffected by the resonant fields, but its value decreases inside the plasma. On the other hand, the turbulent induced particle flux, computed at different radial positions, increases with **rhf** inside the plasma /2/.

Fig 1 shows the autopower spectrum levels with and without **rhf**, for density fluctuations ($\tilde{n}$) as a function of radial coordinate. With **rhf** we note a reduction of the region of maximal amplitude, a shift of this region to outer plasma region and a broadening of the spectrum in frequency. However, in the case of potential fluctuations these spectra show the same frequency broadening but no radial amplitude alteration.

Fig 2 shows the autopower spectra of magnetic poloidal field fluctuations $\tilde{B}_\theta$; with **rhf**

a shift to lower frequencies for high fluctuation power and the same broadening of spectrum in frequency are observed.

The density and magnetic fluctuation power is located basically below 200 kHz. Unlike most present tokamaks /5/, in the TBR-1 the main electrostatic frequencies are smaller than the Mirnov frequencies. Furthermore, there is an unusual partial superposition of the frequency power spectra of these two kinds of oscillations. These characteristics create favourable conditions to the investigation of coupling between these two spectra, even for the observed low linear coherence ($0.3 < \gamma < 0.5$). In this situation, the **rhf** introduces a decorrelation in the coherence between the magnetic and density fluctuations (Fig 3- a,b).

Fig 4- a,b show the integrated bicoherence $b^2(f) = \sum_{f=f_1+f_2} b^2(f_1, f_2)$ for density fluctuations and magnetic poloidal field fluctuations. The observed alteration induced by **rhf** are similar and reveal an enhancement on the quadratically nonlinear coupling, with peaks in the broadband turbulence. The **rhf** causes a small reduction of the magnetic fluctuations in the low frequency region. The reduction of integrated bicoherence is specially significant for the cross bicoherence computed from the $\tilde{n}$ and $\tilde{B}_\theta$ fluctuations. Fig 5 shows the total squared cross-bicoherence between $\tilde{n}$ and $\tilde{B}_\theta$, without **rhf** a high total cross-bicoherence in the MHD region and also in the broadband between 100 and 150 kHz was detected. Thus, the **rhf** destroys the quadratically coupling previously present in the signals. These changes indicate that the control of the Mirnov oscillations may modify the eletrostatic transport at the plasma edge and consequently influence the plasma-wall interaction. However, the biphases calculated for density, potential and magnetic field fluctuations, with and without **rhf**, are rather constant in the range of the significant bicoherence; this means that the waveforms of these signals are quadratically symmetric.

Skewness and kurtosis calculated for potential and density fluctuations did not indicate deviations from normal distributions for the two discharge regimes. Only in the case of broadband magnetic poloidal fluctuations the parameters skewness ($S = 1$) and kurtosis ($K = 17$) indicate a possible departure from Gaussian distribution.

The results described in this work show that, $m = 4/n = 1$ resonant helical fields, used in this work, change the electrostatic frequency spectra, and constitute another new example of the use of ergodic divertor in tokamaks /6/.

References

/1/ F. Karger, O. Kluber, Nucl. Fus. 25, 1059 (1985).

/2/ M.V.A.P. Heller, R.M. Castro, I.L. Caldas, R.P. da Silva, Z.A. Brasilio, Proc. of the 19^{th} EPS Conference, Innsbruck, 1992, Vol II, 803,(1992); Proc of the 20^{th} EPS Conference, Lisboa, 1993, Vol II, 683 (1993).

/3/ R.M. Castro, M.V.A.P. Heller, I.L. Caldas, R.P. da Silva, Z.A. Brasilio, Il Nuovo Cimento 15D, 983 (1993).

/4/ Ch. P. Ritz, E. J. Powers and R.D. Bengtson, Phys. Fluids B1, 153 (1989).

/5/ D.C. Robinson, Plasma Phys. Control. Fusion 35 B1 (1993).

/6/ J.C. Vallet et. al., Phys. Rev. Letters 67,2662 (1991).

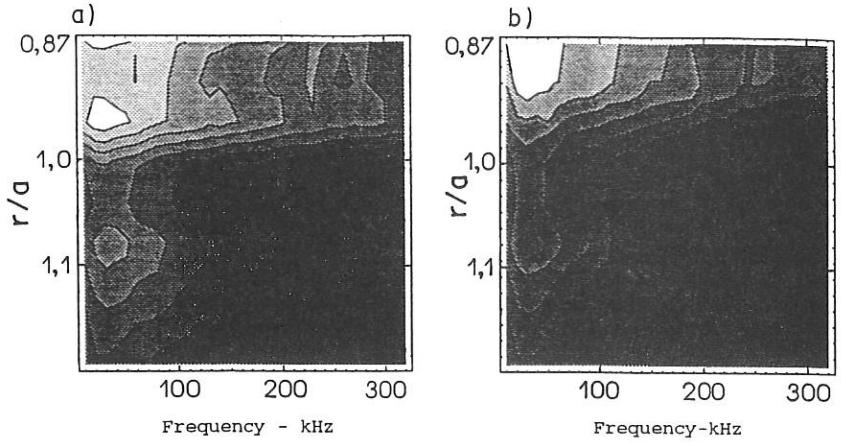


Fig 1- a) Autopower spectrum level of density fluctuations with rhf as a function of radial coordinate, in log-scale (the brightest area corresponds to the highest fluctuation power and the darkest area to the lower). b) The same without rhf.

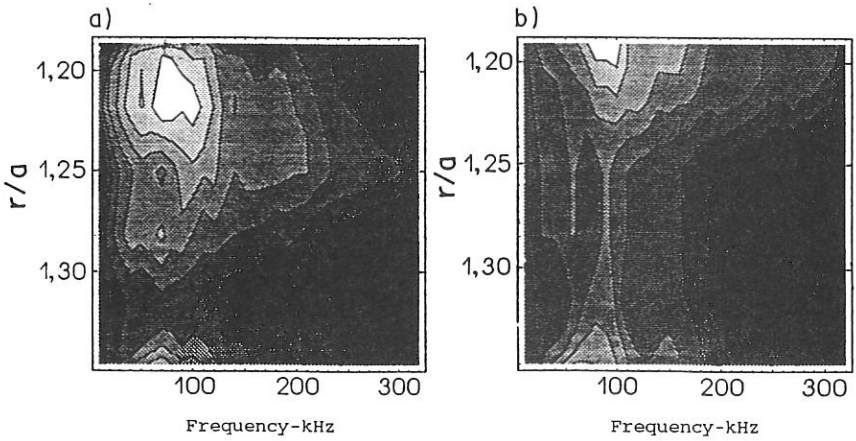


Fig 2- a) Autopower spectrum level of magnetic poloidal field fluctuations with rhf as a function of radial coordinate, in log-scale. b) The same without rhf.

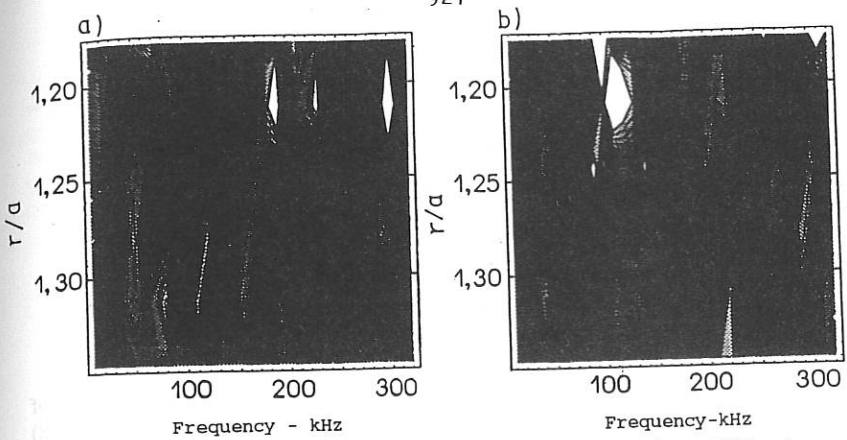


Fig 3- a) Radial coherence between density fluctuations at $r/a = 0.87$ and magnetic poloidal field fluctuations at $r/a = 1.16$ with **rhf** as a fuction of radial coordinate in log-scale. b) The same without **rhf**.

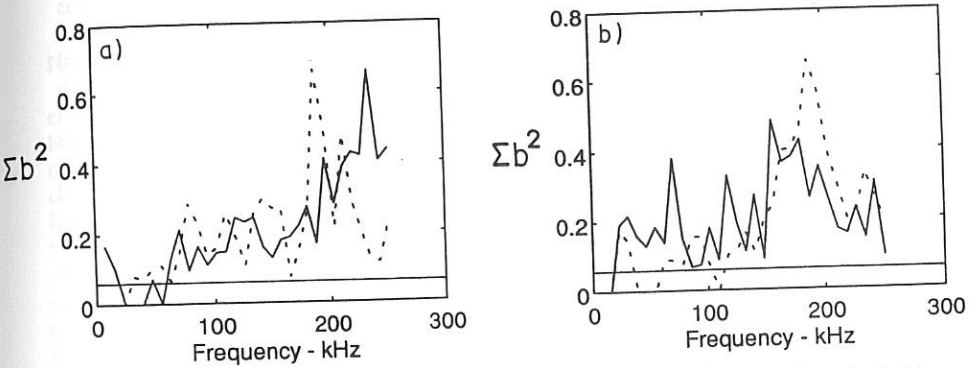


Fig 4- a) The sum of $\tilde{n}$ bicoherence at $r/a = 0.87$ with **rhf** (- - -) and without (—). b) The same for $\tilde{B}_\theta$ at $r/a = 1.16$ (Straight line denotes the statistical uncertainty).

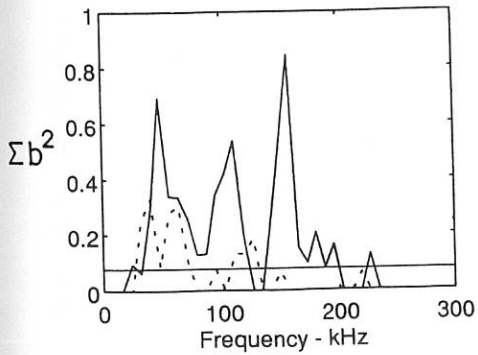


Fig- 5) The sum of the cross-bicoherence between $\tilde{n}$ and $\tilde{B}_\theta$ (at $r/a = 0.87$ and $r/a = 1.16$, respectively with **rhf** (- - -) and without (—) (Straight line denotes the statistical uncertainty).

Control of Secondary Electron Emission from End Plates of the GAMMA 10 Tandem Mirror

T. Saito, Y. Kiwamoto, Y. Tatematsu, Y. Yoshimura, T. Takahashi, M. Kurata, T. Cho, M. Ichimura, M. Inutake, K. Ishii, T. Tamano

Plasma Research Center, University of Tsukuba
Tsukuba City, Ibaraki 305 Japan

INTRODUCTION

Secondary electrons are emitted from plasma facing materials, e.g., divertor plates of a tokamak and end plates of a tandem mirror [1-3]. Secondary electron emission (SEE) strongly affects the potential distribution as well as the energy flow in the edge region. Moreover, SEE is an important factor of confinement of a tandem mirror plasma because cold secondary electrons emitted from end plates flow back to the confinement region along field lines and take the place of heated electrons. Thus control of SEE from the end wall material is one of important tasks of the mirror fusion study.

In the GAMMA 10 tandem mirror, an intense end-loss warm electron flux generated by ECRH induces SEE from end plates [4] and two experiments of controlling the SEE are in progress. In one experiment, negatively biased meshes placed on end plates are used to reflect secondary electrons. Since the mean energy of secondary electrons is very small, a low bias voltage should be effective. The second plan is a thermal dike [5]. Cold electrons emitted from the end plates located in a low field region are ECR heated perpendicularly to the field lines by 2.45 GHz microwave power and mirror-reflected on way to the higher field region. Back flow of secondary electrons to the confinement region is consequently reduced.

This paper describes experimental results of the mesh-bias experiment and the feasibility study of the thermal dike planed in GAMMA 10.

EXPERIMENTAL SETUP

Figure 1 illustrates the configuration of the end mirror cell and the end region of GAMMA 10. The outer mirror throat is the boundary between the confinement region and the end region. The magnetic field strength B_{th} at the mirror throat is 3.0 T and decreases down to B_{ep} = 0.01 T at the endplate. This large mirror ratio is utilized in the thermal dike. The endplates are composed of five annular rings made of stainless steel numbered outward from #1 to #5. Each piece of the plates is connected to the machine earth through a high resistance and hence virtually floating. For suppression of SEE, #1 to #3 plates of both ends are covered by stainless steel meshes highly permeable to end-loss particles. Bias voltage negative to the endplates is applied to these meshes. The three plates are mapped back along field lines to the cross section at the central cell midplane of about 12 cm in diameter, which is about two third of the plasma radius.

The position of the thermal dike is also shown in Fig. 1. The microwave power up to 5 kW is delivered from a magnetron of 2.45 GHz and transmitted to a hoghorn antenna. The magnetron can be pulse-modulated. The antenna radiates the microwave in X-mode onto the resonance layer of 0.0875 T from the high field side. The beam diameter of the microwave is 30 ~ 40 cm and it corresponds to the whole cross section of the plasma at the central cell. At the moment the thermal dike is installed only in one end region.

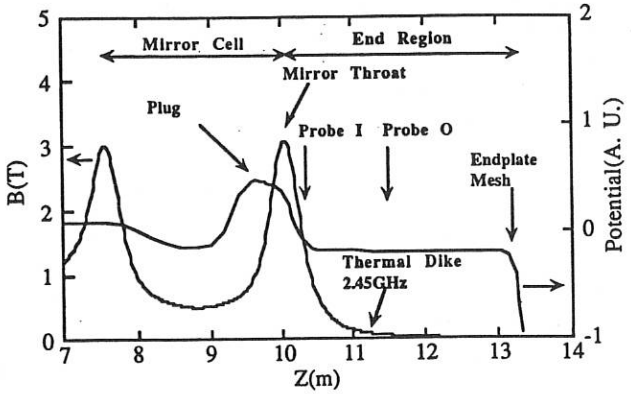


Fig. 1 Configuration of the end mirror cell and the end region.

PREDICTIONS FROM MODEL CALCULATION

Secondary electrons emitted from the endplates compensates the end-loss warm electron flow. Therefore, suppression of SEE should lead to reflection of warm electrons before the endplates. This is realized by deepening of the endplate potential. A recently developed potential model calculates the endplate potential as a function of the secondary electron emission coefficient γ [6,7]. This model has been experimentally confirmed [8]. Figure 2 plots the calculated endplate potential ψ_{EP}. In the model it is measured from the mirror throat and normalized by the temperature T_{ew} of the end-loss warm electrons ($\psi = (\Phi - \Phi_{th})/T_{ew}$).The typical value of T_{ew} is 500 ~ 600 eV. The calculated potential ψ_{EP} decreases with decreasing γ. The model predicts sheath formation in front of the endplate and it also calculates the potential before the sheath as represented by ψ_S in Fig. 2. The value of ψ_S little varies with γ. Thus only the sheath potential drop, which acts as decelerating potential of the end-loss electrons out of the mirror throat, increases under suppression of SEE and consequently the end-loss electron flux decreases. The normalized end-loss electron flux I depends on ψ_{EP}.

$$I(\psi_{EP}) = \exp(\psi_{EP}) - \frac{B_{th} - B_{ep}}{B_{th}} \exp\left(\frac{B_{th}}{B_{th} - B_{ep}} \psi_{EP}\right)$$

When the secondary electrons are completely suppressed, ψ_{EP} decreases to about −4.5 and the end-loss electron flux is expected to decrease to about 30 % of the value at ψ_{EP} of −3.0 with no suppression of SEE. Then we can expect a drastic decrease of the heat flow to the endplates carried by the warm electrons.

The function of the thermal dike is indirect compared to mesh-biasing. Secondary electrons are mirror-reflected as a consequence of perpendicular heating at the ECR zone. The response of the secondary electrons to the thermal dike ECRH is reduced to a response function [9]. Electrons with the energy ε and the magnetic moment μ are reflected before the mirror throat when the condition $\varepsilon < \mu B_m - e\Phi_m$ holds. The fraction $R(E)$ of the secondary electrons which are reflected before the mirror throat can be estimated by using the response function. Here, E stands for the electric field of the heating wave, B_m is equal to B_{th} and Φ_m

is the accelerating potential after the resonance region. Figure 3 plots the reduction of the effective secondary electron emission coefficient $\gamma/\gamma_0 = (1 - R(E))/(1 - R(0))$. In the figure the sheath potential $\Phi_{Sheath} = \Phi_S - \Phi_{EP}$ is 800 V according to the GAMMA 10 experiment. The estimated wave field of 6 kV/m in our experiment yields γ of 0.4 for Φ_m of 700 V by equating γ_0 to 0.7. Then, the thermal dike will reduce the power flow carried by warm electrons to the endplates by 50 %.

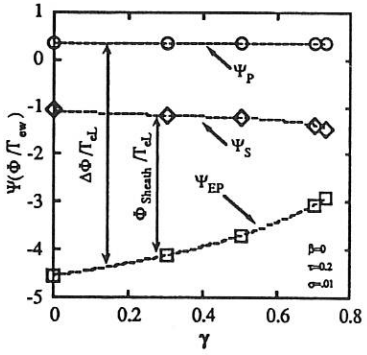


Fig. 2 Calculated potentials as fuctions of secondary electron emission coefficient γ.

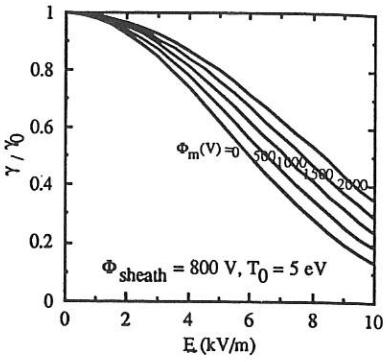


Fig. 3 Reduction of secondary electron emission coefficient due to thermal dike

RESULTS OF MESH BIASING EXPERIMENT

In this experiment the potentials at the central cell Φ_C and at the barrier midplane Φ_B are measured by heavy neutral beam probes. The plug potential Φ_P is evaluated from the energy spectrum of the end-loss ions. Two Langmuir probes shown in Fig. 1 are used to obtain the space potentials Φ_I and Φ_O in the end region. The voltage drop through the resistance reads Φ_{EP}. The energy spectrum of the end-loss electrons is obtained with a multi-grid energy analyzer called as LED.

The response of the measured potentials to the mesh bias V_M is shown in Fig. 4. Here, V_M is the voltage between the mesh and the endplate. On-axis values are plotted for Φ_C, Φ_B and Φ_P. All the plotted potentials denoted by capital Φ are measured from the machine earth. The floating potential Φ_{EP} promptly descends with V_M and then saturates at V_M larger than 10 V. This behavior of Φ_{EP} is understood if secondary electrons with a mean energy of around 10 eV are reflected to the endplate by the mesh. The floating potential descends to reflect end-loss electrons on way to the endplate. Consequently, the net current flowing to the end plate is kept to be zero with reduced SEE.

On the contrary to the behavior of the endplate potential Φ_{EP}, other potentials do not vary with V_M. Figure 4 also plots the potentials before the sheath region measured by the Langmuir probes. The difference between Φ_O and Φ_{EP} stands for the sheath potential drop Φ_{Sheath} in front of the endplate. The plug potential does not vary with V_M. The experimental result indicates that most of the increment of $\Delta\Phi \equiv \Phi_P - \Phi_{EP}$ stems from the increase of Φ_{Sheath}. This is consistent with the model prediction as represented in Fig. 2.

Next we compare the observed increment of $\Delta\Phi$ with that of the calculation. Figure 5 plots $\Delta\Phi/T_{ew}$ as a function of V_M. The energy spectrum of the end-loss electrons is measured

by LED and T_{ew} is determined from the spectrum for each V_M. The value of T_{ew} does not change

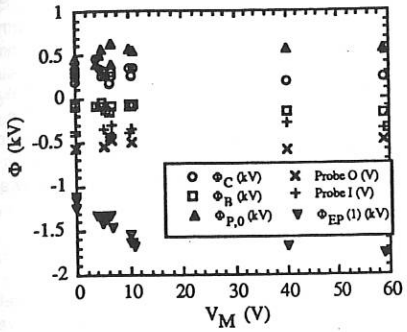


Fig. 4 Response of the plasma potentials to the mesh bias V_M.

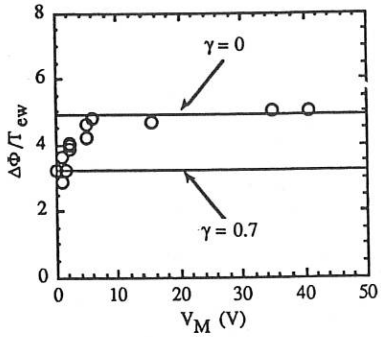


Fig. 5 Potential difference from the plug to the endplate normalized by the warm electron temperature T_{ew}.

very much with V_M. The normalized potential difference quickly increases with V_M from around 3 and then saturates at about 5. The quantity $\Delta\Phi/T_{ew}$ compares with $\psi_P - \psi_{EP}$ shown in Fig. 4, which varies from 3.3 to 4.8 with decreasing γ. Thus the experiment is consistent with the calculation if all the secondary electrons are reflected at V_M larger than 10 ~ 20 V and γ is regarded as zero.

In summary, a negatively biased mesh effectively suppresses secondary electrons emitted from the endplate and produces an increase of the sheath potential drop in front of the endplate. The maximum increment is about two times the temperature of the end-loss electrons which is sufficient to reflect almost all the end-loss electrons. The feasibility of the thermal dike experiment in GAMMA 10 is studied by using a heating response function. Detailed measurement of heat flow to the endplates under mesh biasing and the thermal dike is the next task.

The authors express their gratitude to the members of the GAMMA 10 group for valuable discussion and collaboration during the present study.

REFERENCES

[1] P. C. Stangeby, in *Physics of Plasma-Wall Interactions in Controlled Fusion* edited by D.E. Post and R. Behrisch (NATO ASI series B-131, Plenum Press, New York, 1984) p. 41.
[2] L. S. Hall, Nucl. Fusion **17**, 681 (1977).
[3] G. D. Porter, Nucl. Fusion **22**, 1279 (1982).
[4] K. Kurihara et al, J. Phys. Soc. Jpn. **58**, 3453 (1989)
[5] T. Ohkawa, Kakuyugo-Kenkyuu (J. Plasma Fusion Res.) **64**, 305 (1990).
[6] K. Kurihara et al, J. Phys. Soc. Jpn. **61**, 3153 (1992)
[7] Y. Tatematsu et al, J. Phys. Soc. Jpn. **63**, 558 (1994)
[8[T. Saito et al, Phys Fluids **B5**, 866 (1993).
[9] Y. Kiwamoto et al, Phys. Plasmas 1, 834 (1994)

Space charge sheaths with electron emission

E. Hantzsche

Humboldt-Universität Berlin, Institut für Physik / Max-Planck-Institut für Plasmaphysik Garching, Bereich Berlin, Germany

Abstract: The probability of ignition of plasma-induced arcs in fusion devices depends on the parameters of the space charge sheath between plasma and wall, especially on the potential drop and the power input. Both are calculated by simple balance equations in case of electron-emitting surfaces. The results show: The more electrons are emitted, the lower is the potential drop, the higher is the power density. With increasing net currents the sheath potential is enhanced, while the power is reduced at first and then strongly enhanced.

1. Introduction

The Langmuir sheath between plasma and wall may become unstable in case of high-temperature plasmas (with electron temperatures $kT_e \geq 10$ eV and with sufficient density). Locally it may develop into a plasma-induced arc. Especially in fusion devices such conditions often are fulfilled. Since these arcs are of importance because they generate considerable amounts of plasma impurities and change the plasma parameters within the adjacent magnetic flux tubes, the development of the sheath parameters in case of such an instability is of great interest. The existence of arc spots is identifyable by their tracks engraved in the surface of walls and other solid structures [1], and they are often hidden below visible bright speckles, which are caused by plasma hot spots near the walls. The generation of such hot spots and their properties have been discussed e.g. in [2,3].

The further transition of a plasma hot spot at the wall into a plasma-induced arc is expected to happen in case of an emission instability at the surface. Such instabilities may develop in different ways; the most probable seems to be a runaway-heating of localized surface inhomogeneities resulting in an increasing thermionic electron emission, further enhanced by the electric surface field strength. The emission current itself increases the temperature still more by Joule heating. This feedback may rapidly develop into an explosion with a sudden production of a cloud of dense metal plasma and great amounts of free electrons. Other sources of electrons are secondary electron emission by ion and electron impact, or photoelectric emission by plasma radiation. Therefore, electron emission is a normal component of sheaths in high temperature plasmas.

Primarily, both surface heating and surface field strength are caused by the contact between plasma and wall, that is: they are determined by the conditions within the Langmuir sheath, which depend decisively on the plasma parameters, especially the electron density n_e and the electron temperature T_e in front of the wall. In case of fusion devices these are mainly the plasma parameters near to divertor plates or to limiters; they are considered here to be largely fixed by the parameters of the main discharge and by the geometric boundaries.

However, the emission processes themselves, especially the electrons emitted from the walls, necessarily change the parameters of the plasma layer into which they penetrate. As a consequence, the space charge sheath and the power input into the wall also must change, and this again will influence the emission yield. The question is, whether an initiated emission causes a positive or negative feedback for the further development of an instability. Similar situations are investigated e.g. in [4,5] as to the time dependence and stability conditions, respectively. We will confine ourselves to the consequences of stationary balances.

2. Model assumptions and balance equations

Thus, we consider a very simple special case: The stationary equilibrium conditions of a sheath with electron emission, and without magnetic field effects. This example is approximately applicable if 1) the

change of plasma parameters and of the emission is sufficiently slow to remain near equilibrium, if 2) the plasma composition is not changed significantly by sputtering or evaporation, and if 3) the external magnetic field vectors enter the surface at a sufficiently steep angle, i.e. no grazing incidence (see [6]).

The main difference compared with a plasma sheath at an inactive surface is the existence of two electron ensembles near the sheath edge: the primary electrons from the plasma, and the secondary electrons from the wall. The plasma electrons are partly pushed away by the emitted electrons. Normally, both have different densities and temperatures. Because of interactions between these components the temperatures will gradually balance and equalize, more or less, depending on the available time and the distance from the wall. We consider two simple and extreme model situations only:
Short-time case 1): The temperatures of both ensembles are different, resembling their original state (i.e. there is no exchange or balancing at all).
Long-time case 2): Both temperatures are equal (complete balancing), that is: the electrons from both sources merge to one electron ensemble only.
We may expect that the real situation is somewhere in between.

Further model assumptions are: 1. the emitted electrons are randomized and thermalized at first mainly by collisions with plasma ions and neutral atoms, and by mutual collisions, 2. density and temperature of the ions are constant, 3. the energy distributions of the electrons are (almost) Boltzmann distributions, 4. the mean energy of the ions at the sheath edge is given by a generalized Bohm condition.

With these presuppositions the net current density j between plasma and wall is composed of

$$j = j_i + j_{ep} + j_{ee} \qquad (1)$$

with the plasma ion current density j_i (> 0), the plasma electron current density j_{ep} (< 0), and the electron emission current j_{ee} (> 0). j_{ep} must be divided into the current density of the primary plasma electrons (j_{ep1}) and of secondary electrons from the wall (j_{ep2}) after randomization. j_{ee} may be caused by ion or electron impact or by other sources, such as thermionic emission, field emission, or photoelectric emission. The plasma is assumed to be quasi-neutral (density n_0), with different temperatures of its constituents T_i, T_e (with T_{e1} and T_{e2}). Between plasma and wall exists a potential difference U (> 0) across the space-charge sheath. The components of (1) are applied in the form

$$j_i = eZ_i n_i \left[\left(\frac{k}{m_i}\right) \left(c_1 \frac{T_i}{Z_i} + T_{e1}\frac{n_{e1}}{n_0} + T_{e2}\frac{n_{e2}}{n_0}\right) \right]^{1/2} \qquad (2)$$

(ion charge eZ_i, ion density $n_i = n_0/Z_i$, and $n_{e1,2}$ density of the two electron components, c_1 = const), and

$$j_{epx} = -\xi_x n_{ex} e \left[\frac{kT_{ex}}{2\pi m_e}\right]^{1/2} \exp\left[-\frac{eU}{kT_{ex}}\right] \qquad (3)$$

with x = (1,2); $\xi_x < 1$ considers deviations from the Boltzmann distribution due to the loss of high energy electrons to the wall; $n_{e1} + n_{e2} + n_{ee}$ (density of emitted electrons at the plasma edge) = n_0; and from energy conservation we get $kT_{e2} = (2/3)(eU + 2kT_0)$; T_0 is the surface temperature. Moreover, we assume that only the part α_2 (< 1) of the emitted electrons is converted into the secondary electron gas returning j_{ep2} to the surface. After introducing the dimensionless quantities $i = j/j_i$, $\gamma = j_{ee}/j_i$, $i_{ex} = -j_{epx}/j_i$, $u = eU/kT_{e1}$, $\tau_i = T_i/T_{e1}$, $\tau_0 = T_0/T_{e1}$, $\nu_{ex} = n_{ex}/n_0$, $\mu = m_e/m_i$ we get from (1) the equation

$$i + i_{e1} + i_{e2} - \gamma - 1 = 0 \qquad (4)$$

which determines u. Both i_{e1} and i_{e2} are functions of γ.

Equ. (4) is valid in the limiting case 1, that is: the emitted electrons are randomized, but there is not sufficient time for an effective interaction between primary and secondary electrons. In the other limiting case 2, if both electron groups have time to merge completely and to reach together LTE conditions, we get in (4) only one reduced plasma electron current density i_e with an effective (mean) temperature T_e which is composed of T_{e1} and T_{e2} according to the contributions of the two electron groups to the electron density at the plasma edge.

Additionally, the power flux density P at the surface caused by the plasma is calculated. In dimensionless quantities with $\omega = eP/(j_i kT_{e1})$ we have (in case 1)

$$\omega = u + f(\tau_i, \tau_0, \nu_1) + \epsilon_{i1} - \phi_1 + i_{e1}(2 + \phi_1) + \\ + i_{e2}\left[\frac{4}{3}(u + \tau_0) + \phi_1\right] - \gamma(2\tau_0 + \phi_1) \qquad (5)$$

where $\varepsilon_{i1} = E_i/kT_{e1}$ is the dimensionless ionization energy, $\phi_1 = e\varphi/kT_{e1}$ the dimensionless work function, while f is a term determined mainly by the temperatures of both electrons and ions according to the Bohm condition. The power flux in case 2 can be written in an analogous way.

3. Results and Discussion

The reduced sheath potential drop u and the reduced power flux ω are functions of the main independent parameters γ and i; moreover, the results depend on further input parameters which are fixed here. As an example, we choose the following constants: $\xi_1 = \xi_2 = 0.9$; $\alpha_2 = 0.5$; $\tau_i = 0.5$; $\tau_0 = 0.02$; $Z_i = 1$; $\varepsilon_{i1} = 0.75$; $\phi_1 = 0.25$; $c_1 = 1$; $\mu = 0.000\ 27244$ (Deuterium).

In the simplest case $i = 0$, $\gamma = 0$ we get $u = u_0 = 2.8770$ and $\omega = \omega_0 = 7.6805$ in this example. The dependence of u and ω on γ and i is shown in fig.s 1 - 4. All results are averages of the two limiting cases; generally, the differences between them are small (mostly a few percent, at large negative i even < 1 %, and increasing to more than 10 % in case of $\gamma \gg 1$ only).

The results can be summarized as follows:

1. With increasing electron emission (γ) the sheath potential u decreases (with fixed i), approaching a minimum (almost zero) if $\gamma = \gamma_{max} \approx 7 \ldots 9$ (case 1), or $\gamma_{max} \approx 11 \ldots 13$ (case 2), almost independent of the net current density i (e.g., if $-2 \le i \le +2$; space charge limited emission). Approximately, with $\gamma \ll 1$, we have $u \approx u_0 - \gamma\zeta/(1 - i)$; with $\zeta = \text{const}$, $(1\text{-}0.22\xi_2) < \zeta < 1$.
2. The higher i, the higher becomes u (at fixed γ); the increase is slow at first, but becomes very rapid up to a maximum near the positive limit $i = i_{max}$ ($\approx 1 + \gamma$). There is no solution if either $i > i_{max}$ (almost complete suppression of j_{ep}) or if $i < i_{min} \approx i_{max} - \xi/\sqrt{(2\pi\mu)} < 0$ (since u becomes zero, and j_{ep} reaches its saturation value at $u = 0$).
3. Generally, the power input increases with γ, exceeding about the twofold of $\omega(\gamma{=}0)$ if $\gamma \ge 5$. However, in case of $i \ge 1$ and low secondary emission γ, i.e. with dominating ion current heating, ω increases again with decreasing γ. Thus, there is a minimum of the power density, and we have everywhere $\omega > \omega_{min} \approx 7$.
4. Due to dominating plasma electron heating, the power input increases considerably with decreasing net current density i (as far as $i < \gamma + 0.5$, especially with $-i \gg 1$, assuming a fixed γ).

With these results we come to the statements: 1) The yield of sputtering (dependent on the ion energy and therefore on u) is enhanced with increasing net current i and decreasing emission yield γ; 2) in contrast to this, the yield of evaporation (dependent on the surface temperature and therefore on ω) is enhanced with decreasing i and with increasing γ, with the exception of the case of high $i > 0$ ($\approx i_{max}$) where the dependence is reversed. This is the situation in which a positive feedback is indicated and which is best suited to develop into an instability with the formation of a plasma-induced arc spot. However, for the determination of realistic limits of sheath stability a more developed model should be applied.

References:

[1] B.Jüttner, K.Büchl, M.Weinlich, ASDEX-U-Team: "Arcing in ASDEX-Upgrade", 4th Int. Workshop on Plasma Edge Theory in Fusion Dev., Varenna 1993; Contrib. Plasma Phys. **34** (1994) 472

[2] M.Z.Tokar, A.V.Nedospasov, A.V.Yarochkin: "The possible nature of hot spots on Tokamak walls", Nucl. Fusion **32** (1992) 15

[3] V.Philipps, U.Samm, M.Z.Tokar, B.Unterberg, A.Pospieszczyk, B.Schweer: "Evidence of hot spot formation due to thermal electron emission", Nucl. Fusion **33** (1993) 953

[4] N.Anderson: "The formation of a plasma sheath with secondary electron emission"; Int. J. Electronics **32** (1972) 425

[5] R.N.Franklin, W.E.Han: "The stability of the plasma-sheath with secondary emission", Plasma Phys. Contr. Fusion **30** (1988) 771

[6] R.Chodura: "Numerical analysis of plasma-wall interaction for an oblique magnetic field", J. Nucl. Mat. **111/112** (1982) 420

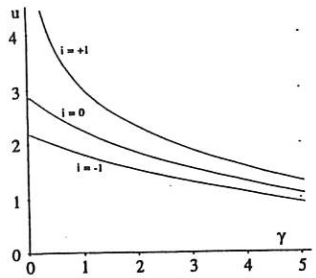


Fig. 1: Reduced sheath potential drop $u = eU/kT_{e1}$ as a function of the electron emission yield γ (= j_{ee}/j_i) in case of three values of the net current density $i = j/j_i$ (= 1, 0, -1, respectively)

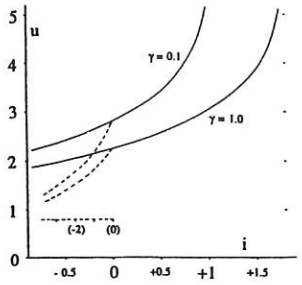


Fig. 2: Potential drop u as in fig. 1 as a function of the reduced net current density i in case of two values of γ (= 0.1 and 1, respectively)

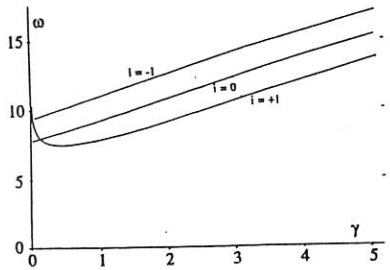


Fig. 3: Reduced power density at the wall $\omega = eP/j_i kT_{e1}$ as a function of the electron emission coefficient γ, and with three values of the current density i (= 1, 0, -1, respectively)

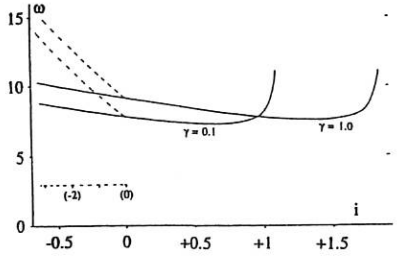


Fig. 4: Power density ω as in fig. 3 as a function of the current density i, and with two values of the emission coefficient γ (= 0.1 and 1, respectively)

Topic 6

Plasma Heating

Fast Access to Neutral Injection Heating Profiles Applied to the Stellarator W7-AS

F.-P. Penningsfeld
Max-Planck-Institut für Plasmaphysik, D-85748 Garching, Germany

1) Abstract

Global heating powers and their profiles of neutral injection systems are usually computed with Monte Carlo codes for diagnosed plasma targets.These computations are very time-consuming, therefore a fast code has been developed to calculate these quantities for given plasma profiles and heating scenarios using existing data sets. This code, named NIPOR (Neutral Injection Power using ORACLE data base), was applied to the stellarator W7-AS. It uses data sets of the local power deposition and the total heating power of the neutral beams obtained by previous runs of FAFNER1, a 3D Monte Carlo code for simulating the NI heating [1]. For global analysis of the total NI heating power $P_{heat}(t)$ the electron line density $\int ndl(t)$ and the mean electron temperature $\langle T_e(t) \rangle$ are used. For the calculation of the heating power profiles $p_{heat}(r,t_o)$ the measured profiles of electron density $n_e(r)$ and temperature $T_e(r)$ at time t_o are necessary. The influence of $n_0(a)$, the neutral gas density at the plasma edge, on the global heating efficiency via charge exchange losses is also included.

2) Method

The calculation of the neutral beam heating profiles is split into two steps: firstly, the global heating power $P_{heat,j}(t)$ is calculated using fit formulas for each source j as function of line density and secondly, the radial profile $p_{heat}(r,t)$ at $t = t_o$ is estimated using normalized profiles $p_{norm,j}$ corresponding to the measured density and temperature profiles of the target plasma [2]:

$$(1) \quad p_{heat}(r,t) = \sum_j \left(p_{norm,j}(r,t)\ P_{heat,j}(t) \right)$$

2a) Global NI-heating

The global heating efficiency η_j^0 of each NI-source was calculated over a wide range of plasma density using the FAFNER1 code for two standard magnetic configurations (B_0= 2.50 and 1.25 T, with $\iota = 0.38$, tangential injection into W7-AS). Typical measured density profiles were used for these scans and the central density was varied only. The results could be fitted [3] in the range $0.35 < T_e(0) < 0.55$ [keV] by equ.(2) with parameters $A_{i,j}(i=1,4)$ for each source j. The sum Σ_k adds the three species k of each beam with different cross-sections σ_k of the neutral beam species mix given by s_k. An example of these fits of the FAFNER1 results is shown in fig.1 for two inner sources of W7-AS. The differences in the efficiencies are mainly caused by the effect of CO and COUNTER-injection and the implication on the orbits of the injected particles.

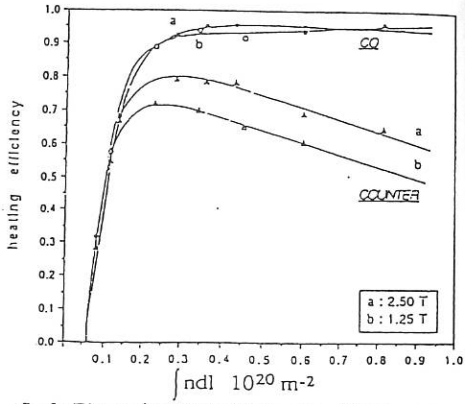


fig.1: Fits on heating efficiencies of the inner NI/W7-AS sources calculated by FAFNER1

$$(2) \quad \eta_j^0 = A_{3,j} \sum_{k=1}^{3} s_k \left(1 - e^{-\sigma_k A_{1,j} (n_e - A_{4,j})} \right) e^{-\sigma_k n_e A_{2,j}}; \quad \text{with } n_e = \frac{1}{2a} \int n\, dl$$

The difference of η_j^0 between full and half field target is only significant for COUNTER beams. The global heating power is then obtained by the sum over all active sources j, where $P_{NI,j}$

means the neutral beam input power, measured in the torus:

(3) $P_{heat}(t) = f_{T_e n_e} f_{cx} \sum P_{heat,j}(t) = f_{T_e n_e} f_{cx} \sum P_{NI,j} \eta_j^0(t)$

The factors $f_{Te,ne}$ and f_{cx} describe the influences of T_e and $n_0(a)$ on the heating efficiencies related to the standard data sets $\eta_j^0(t)$ (see equ.7 and equ.8).

2b) Reconstruction of the NI heating profile

To reach a higher flexibility of the data sets, the normalized profiles are not stored directly, but as a function of the variable $\xi(r)$, which is defined as the line-integrated density between the plasma edge at r=a and the radius r, divided by the volume of the corresponding plasma shell.

(4) $\xi(r) = \left(\int_a^r n\,dl : \int_a^r dV \right) : \left(\int_a^0 n\,dl : \int_a^0 dV \right)$ normalized to $0 < \xi(r) < 1$.

$\xi(r)$ combines both: the line-integrated density from edge to center, which is responsible for the beam absorption, and the different volume of the toroidal shells, which is needed to calculate the local heating power density (see fig.2). An example for two different target plasmas with similar $\int ndl$ is given in fig.3. The normalized heating power $P_j(\xi)$ is interpolated in between the stored data sets to $\langle P_j(\xi) \rangle$, in accordance with the actual line density of the plasma target. The power deposition per source is then obtained by the projection of $\langle P_j(\xi) \rangle$ to $P_{norm,j}(r)$ (see fig.3c,d) and renormalized to $\int P_{norm,j}(r)\,dr = 1$. To obtain the power density profile $p_{norm,j}(r)$ used in eq.(1) the radial heating power is divided by the volume V(r) of the corresponding plasma shell :

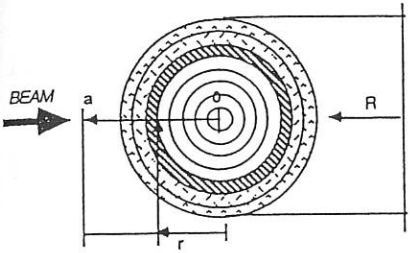


fig.2: geometry for the definition of $\xi(r)$

(5) $p_{norm,j}(r) = P_{norm,j} / V(r)$ [W cm^{-3}] , with

$V(r) = 2R_0\pi^2 (r_a^2 - r_b^2)$ where $r_{a,b} = r \pm 1$ [cm]

2c) Estimation of the ion/electron heating

The partition of the total NI heating to electrons and ions is recalculated from the total heating power density profile $p_{heat}(r)$ by means of the fit formula:

(6) $p_{ion}(r) = \frac{E_{crit}(r)}{\bar{E}(r)} p_{heat}(r)$ with $E_{crit}(r) = 14.8\, T_e(r)\, A_b\, A_p^{-2/3}$ and $\bar{E}(r) = 6.5$ keV $+ 9.7\, T_e(r)$

The fit for E(r) for W7-AS was obtained from FAFNER1 results for pure NI heating and combined heating with ECRH in the range $0.150 < T_e(0) < 2.500$ keV. The beam mass A_b=1 and the mass of plasma particles A_p=2, corresponding to H^0-injection into a D^+-plasma was used. The electron heating profile is then given by $p_{elec}(r) = p_{heat}(r) - p_{ion}(r)$.

3) Application to NI-W7AS

The application of NIPOR was tested for a large number of NI heated discharges by additional FAFNER1 runs.The influence of electron temperature in the range $0.150 < T_e(0) < 2.500$ [keV] obtained in NI+ ECRH heated discharges can be roughly fitted by :

(7) $f_{T_e n_e} = (b - c \sqrt{T_e(0)})$ for $\int ndl \le 0.40\ 10^{20}$ m^{-2} and $f_{T_e n_e} = 1$ for higher densities with

$b = 2.038 - 1.700 \sqrt{\int ndl}$ and $c = 1.664 - 2.693 \sqrt{\int ndl}$.

The influence of CX-losses by the neutral gas on the edge, a dominant effect at low target densities $n_e(0)$, can be fitted by equ.(8) with factors given in table 1 for $0.7 \le n_0(a) \le 2.5$ [10^{10}cm-3]

table 1	B = 1.25 T		B = 2.50 T	
c1	-0,05		0,32	
c2	0,53		0,34	
sources:	inner	outer	inner	outer
c3	0,03	0,02	00,06	00,04
c4	2,70	0,80	15,60	10,80
c5	7,54	4,70	10,00	9,60

(8) $f_{cx} = (c_1 + c_2\, n_0(a)) \cdot (c_3 + c_4\, e^{-c_5\, n_e(0)})$

An example for the time evolution of the global heating is shown in fig.4. The shot starts with ECRH. At t=0.1 s two inner NI-sources carry the plasma as shown by the input power $P_{NI,j}$. Only about 10% of the input power are coupled to the thin plasma target at the beginning with $n_e(0) \approx 0.2 \times 10^{20}$ m^{-3}. The coupling increases then nearly linearly with plasma density. At t = 0.250 s the COUNTER source was switched off to avoid further density increase. The CO-source heats then alone at $n_e(0) \approx 0.6\ 10^{20}$ m^{-3} with a power $P_{heat}(t) \approx 0.85 \times P_{NI,1} \approx 320$kW.

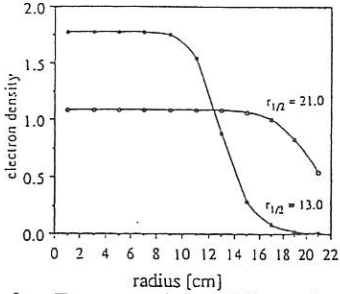


fig.3a: Two examples of different density profiles with ∫ndl ≈ const.

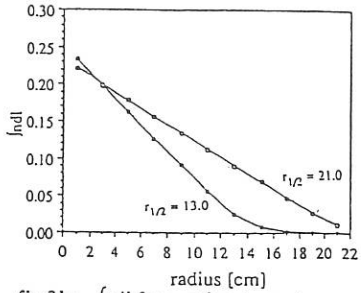


fig.3b: ∫ndl from edge to centre as used to calculate ξ(r) shown in fig.3d.

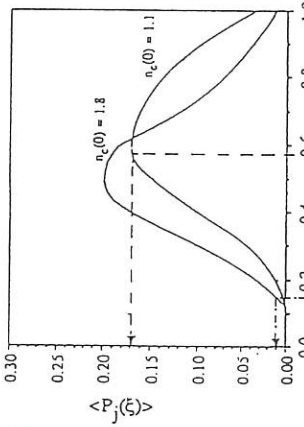


fig. 3c: Normalized heating power of source inner CO for the two target densities. The arrows indicate the heating power $< P_j(\xi) >$ used .

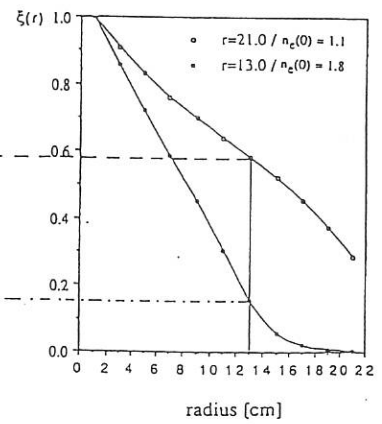


fig. 3d: Normalized variable ξ(r) for the two profiles of fig.3a. The arrows indicate the projection of the radius r to ξ(r).

An estimation of the NI heating profile by NIPOR is shown in fig.5. Measured $n_e(r)$ and $T_e(r)$ profiles were available at t=0.350 s and used as input.The calculated heating profile is compared with an elaborate calculation of FAFNER1 for this situation, indicated by crosses for

p_{heat} and triangles for p_{ion}. Very good consistency is obtained. Nevertheless, a difference of up to 20% in the inner part (r < 0.05 m) may occur,this being caused by the very small volume of the corresponding shell and the larger statistical error of the FAFNER1 results in the center. An absolute error bar for the estimations is in the range of 0.1W cm^{-3} over the whole radius.The effect of radial electric fields onto the NI heating in W7-AS was studied earlier and found to be low [4]. This parameter is therefore not included in this set of parameters.

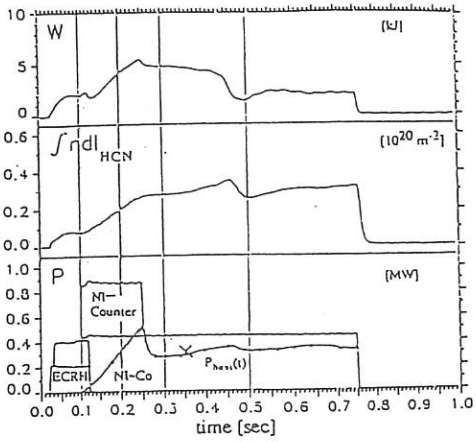
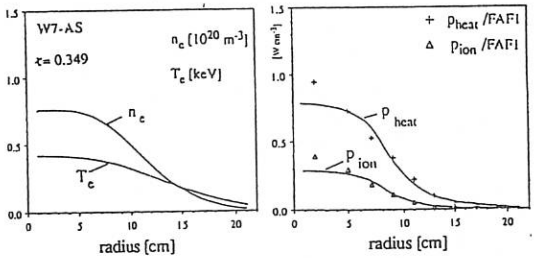


fig 4: Time development of shot 25133. $P_{heat}(t)$ of NI is calculated using ∫ndl(t) and $T_{e,softX}(t)$

fig. 5: Comparison of the NI heating profiles calculated by NIPOR with the FAFNER1 results for shot 25133 at t = 0.350 s. The global results of both methods are listed in the table. P_{NI} is indicated by a cross in fig.4 .

Global results for shot 25133		
B = 1,26 T	NIPOR	FAFNER1
Pion (kW)	98	97
Pelec (kW)	211	210
Pni (kW)	309	307



Summary and Conclusion

A method for the fast estimation of neutral heating profiles as functions of space and time was developed. It is realized by using data sets generated by sophisticated and time-consuming Monte-Carlo-simulations for the target plasma scenarios of the actual device (e.g. FAFNER1 for W7-AS). A high flexibility was obtained by transforming the actual target density profile into a new variable ξ, defined as normalized line density from plasma edge to the center. In this way the beam absorption in different radial shells with strongly varying volumes can be quickly calculated for the actual target using standard data sets. The application of this method to other devices is possible by checking the set of parameters and creating the corresponding data sets.

Acknowledgements

I would like to thank W.Ott and E. Speth (NI-team), H. Maaßberg and U.Stroth (W7-AS-team) for fruitful discussions and A. Kus for the implementation of the code in the data base of W7-AS.

References

[1] *G.G.Lister*,FAFNER: A fully 3-D neutral beam injection code using Monte Carlo methods, *IPP/Report 4/222, Garching (1985)*

[2] *F.-P. Penningsfeld* :Fast access to NI-heating profiles in W7AS, *IPP report 4/265, Nov 93*

[3] *W. Ott* Analytic fit to the calculated heating efficiencies *(private communication)*

[4] *A. Teubel, F.-P. Penningsfeld* Influence of the electric field on the heating efficiency in the W7-AS stellarator, *Proc.19th EPS. Conf.Plas.Phys., vol.16c, part 1, pp537, (1992)*

Neutral Beam Heating in ASDEX Upgrade

O. Vollmer , P.J. McCarthy*, A. Stäbler, F. Ryter, M. Fahy*, J.H. Feist, O. Gruber, A. Hermann, A. Kallenbach, O.Kardaun, V. Mertens, E. Speth, H. Zohm, and the ASDEX Upgrade Team

Max-Planck-Institut für Plasmaphysik, EURATOM Association, D-85748 Garching, Germany

* University College Cork, Ireland

1. Introduction

Neutral beam injection on the divertor tokamak ASDEX Upgrade (R_o =1.65 m, a = 0.5 m, elongation κ = 1.7) is in operation since June 1993, and experiments in ASDEX Upgrade have been using neutral beam heating extensively since then. Meanwhile up to 7 MW beam power using hydrogen and 10 MW using deuterium have been injected for pulse lengths of several seconds. This paper describes the injection system and its performance, a method for the fast recovery of beam power deposition profiles and neutral beam heated steady state ELMing H-mode discharges.

2. The ASDEX Upgrade (AUG) Neutral Beam Injection (NBI) System

At present the neutral beam system of AUG consists of one injector with a nominal injected beam power of 10 MW for deuterium operation (2). This was commissioned in spring 1993. The installation of a second injector is planned for 1996. The nominal performance of the first injector can be summarized by 6 MW injected neutral beam power with 55 kV with hydrogen beams, and 9 MW with 65 kV deuterium beams.

The first injector is equipped with modified JET-type Pinis (55kV/85A for hydrogen beams). Standard bucket sources are used as plasma generators. The beamline design (Fig.2) has to cope with a radial port of 0.9 m length, 0.8 m height and 0.4 m width. The length of the beamline is minimized by a compact rectangular arrangement of the 4 ion sources and a 180^0 reflecting magnet. An injection angle of 26.5^o off-normal as measured at R_o was chosen as a compromise between transmission losses and fast ion losses in the plasma. A pumping speed of 2.8 x 10^6 l/s is provided by four titanium evaporation pump modules.

No serious problems arose during the commissioning of the NBI system: The first injection experiments started in June1993 and provided useful data from the outset. The screening of the tokamak stray fields turned out to be sufficient, at least up to a plasma current of 1.2 MA. During the first year the system could be operated with nearly 100 % availability and about 90 % reliability.

The beams can be switched with frequencies of up to100 Hz by the tetrodes for the HV regulation. In this way the injected power can be adjusted by the duty cycles of the beams without changing the accelaration voltage and thus the beam deposition profile. The exploration of the H-mode window at low B_T (1.2 T), using beam power levels well below the maximum power of one ion source, is shown in Fig. 4. With confinement times around 100 ms, the plasma acts as an integrator and limits the oscillation in the plasma energy content. Calorimetric measurements show that the average beam power closely follows the duty cycle. Thus the injected power can be calculated from the actual duty cycle. Feedback control of the NBI power by the AUG fast control system are envisaged.

3. Fast Recovery of Neutral Beam Deposition Profiles

The moderate beam energy results in a high system efficiency (ca. 54 % for 60 kV deuterium operation), but at the cost of reduced central plasma heating. Typical deposition profiles calculated for a circular plasma shape with a Monte Carlo code (FREYA) are plotted in Fig.3. Noticeably peaked deposition profiles are obtained for moderate densities only. At high densities

deuterium operation produces hollow deposition profiles. Up to now no deleterious effects have been observed at the highest densities used. To allow shot-by-shot evaluation, a fast recovery procedure has been developed to calculate the beam deposition:

The conventional method for calculating the spatial dependence of the neutral beam heating power absorbed by various plasma species involves time-consuming Monte Carlo codes. Using the technique of Function Parameterization (1), a statistically well-designed database of electron and ion power deposition profiles generated with the FREYA Monte Carlo code (so far for circular ASDEX plasmas) has been analyzed with the goal of direct recovery of power deposition profiles from available diagnostic information. This consists of the fixed ASDEX neutral beam (D^0->D^+) co-injection geometry, the electron density $n_e(\rho)$, electron temperature $T_e(\rho)$, impurity n_{imp} (ρ) and background neutral density n_o (ρ) flux surface profiles. The toroidal field, plasma current, beam energy and injected power were fixed at 2.15 T, 350 kA, 52 keV and 4 MW, respectively. All injected neutrals carry the full beam energy. Since the velocities of the various species obey $v_{electrons} \gg v_{beam\ ions} \gg v_{plasma\ ions}$, the slowing-down physics is independent of the ion temperature, and hence T_i (ρ) was not varied independently of $T_e(\rho)$. A total of seven independent parameters were varied to generate the 42 cases in the database.

A standard FP regression of the power deposition profiles using a full quadratic model built from principal components of the profile data was successful; however, the number of second order terms in the model was large relative to the size of the dataset making interpretation of the results difficult. Instead, a two-step recovery involving a mixture of analytical and statistical procedures was developed. Firstly, the recovery of the normalized fast ion birth profile $H(\rho)$ was easily accomplished by exponential attenuation ($\lambda = 1/n_e\ \sigma_{coll.}$) of the injected neutrals along the beam path. A principal components analysis yielded 3 significant moments for the log $(H\ (\rho))$ profile, consistent with the 3-parameter family of density profiles used to generate the database. The regression model for the logarithmic power profiles combined these 3 moments with 5 linear, 2 quadratic and 3 interaction terms involving a total of seven principal components of the $\log(n_e)$, $\log(T_e)$ n_o and $\log(n_{imp})$ profiles.

The profiles of power deposited to the ions $p_i(\rho)$, to the electrons $p_e(\rho)$ and the total power $p_t(\rho) = p_i(\rho) + p_e(\rho)$ recovered with this model had error bars close to the Monte Carlo scatter of FREYA power profiles (8000 fast particles were followed per profile). The typical fractional errors in the recovered $p_i(\rho)$ profiles ranges from 3% at the centre of the plasma to 7% at the edge. The corresponding errors for the $p_e(\rho)$ profile were 20% and 4%. Fig 1 shows an example of $p_i(\rho)$ and $p_e(\rho)$ recovery for (a) a profile arising from typical background plasma profiles and (b) a high density case ($n_e = 8.8 \times 10^{19}$ m^{-3}). The online evaluation time for this recovery method is of the order of seconds in contrast to 2 hours Cray time per profile needed to generate the database. Work is in progress to adapt this procedure for on-line analysis of non-circular ASDEX Upgrade plasmas where the addition of equilibrium magnetic measurements to the set of diagnostic data required for profile recovery will be essential.

4. ASDEX Upgrade H-Mode Discharges

In the single null configuration with the ion grad-B drift towards the X-point the H-mode power threshold of AUG is low ($Pt_{hres} \sim 1.7\ n_e\ B_T$ in MW, 10^{20} m^{-3}) (3). With increasing total heating power different H-mode forms develop: Dithering phase, ELMing with type III ELMs, ELM free and ELMing with type I ELMs. (Type I ELMs can be identified by the increase in their frequency with increasing power across the separatrix.) A steady AUG discharge with type I ELMs is plotted in Fig.5. After a short L-phase the discharge develops into a H-phase with type I ELMs. The inserts in Fig.5 show the very stable behavior and the narrow frequency distribution of the type I ELMs. Electron density, radiation (lower than 50% of P_{tot}) and confinement time remain constant for a time exceeding $30\tau_E$. On AUG steady ELMing discharges occur over a wide window of operation provided the heating power P_{tot} sufficiently exceeds the power threshold for the L-H transition (3). This is in contrast to the quasi steady H-mode in ASDEX (4) where type III ELMs were observed (5) and stable discharges were possible only after careful adjustment of the plasma wall separation (7).

The global confinement time of type I ELM discharges is about 1.8 times the ITER 89-P L-mode scaling. Global confinement agrees with the extended DIII-D/JET scaling for ELM free discharges (6) as shown in Fig.6. The observed positive isotope effect is at least qualitatively in agreement with the observations on ASDEX. The stable behavior of ELMing discharges with type I ELMs is clearly favorable for reactor operation. Type I ELMs however increase the load on the divertor temporarily by a factor of 5 with peak power densities up to 20 MW m^{-2}. (Divertor heat loads by type III ELMs are considerably lower.)
In order to reduce the divertor problemsrecentl Ne puff experiments into the main chamber have been performed (Fig.7).The Ne puff increases the radiated power to about 65% of the total heating power. The plasma remains in the H-mode with a nearly constant energy content indicating that the Ne radiation is predominantly edge localized. In addition the ELM losses are reduced by the decreased ELM frequency during the phase with increased radiation. Therefore the cooling mantle concept seems to be compatible with the type I ELM H-Mode.

(1) P.J. Mc Carthy, et al. and ASDEX-Upgrade Team, MHD Equilibrium Identification on ASDEX-Upgrade. (19th Europ. Conf. on Contr. Fusion and Plasma Physics, Innsbruck, 1992) Europ. Conf. Abstracts **16C-I** (1992), 459-462.

(2) A. Stäbler et al., Design of the neutral beam injection system for Asdex-Upgrade, 15th SOFT, Utrecht, Vol 1, 620-624, Sep. 88

(3) F. Ryter et al., 4th H-Mode Workshop, to be published in Plasma Phys. and Contr. Fusion, Naka (Japan) Nov. 1993.

(4) F. Wagner et al., Recent results of H-mode studies on ASDEX, in Plasma Physics and Controlled Fusion Research, Vol. 1, IAEA, Vienna (1991) 277-290.

(5) H. Zohm et al., Studies of Edge Localized Modes on ASDEX. Nuclear Fusion, Vol. 32, No. 3 (1992) 489

(6) F. Ryter, et. al., Condition of the L-H and H-L transitions and operating regimes in ASDEX-Upgrade. 21st EPS, Montpellier (1994).

(7) O. Vollmer et al. in Contr. Fusion and Plasma Heating (Proc. 17th Eur. Conf. Amsterdam 1990), Vol. 14B, Part I, EPS (1990) 295.

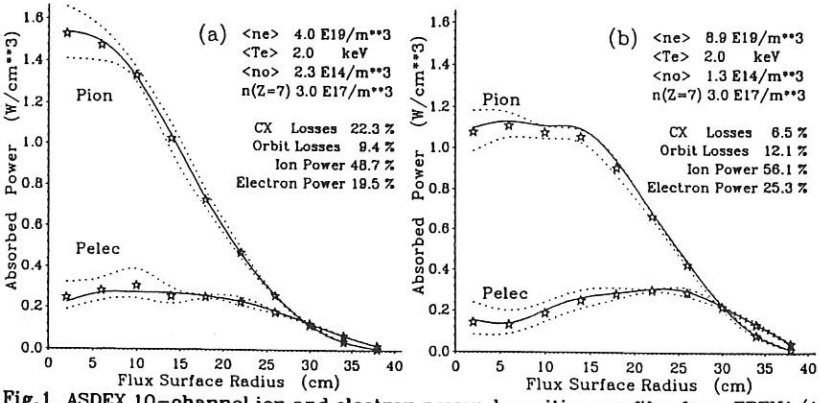


Fig.1 ASDEX 10-channel ion and electron power deposition profiles from FREYA (☆). Dotted curves show Monte Carlo scatter (95% bands). Full curves show recovered profiles.

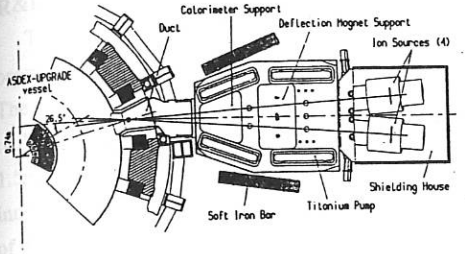


Fig.2 ASDEX-Upgrade Neutral Beam Injector

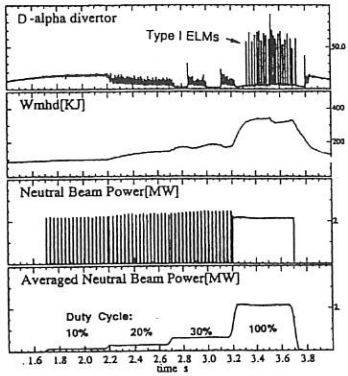


Fig.4 Modulation of the Beam Power

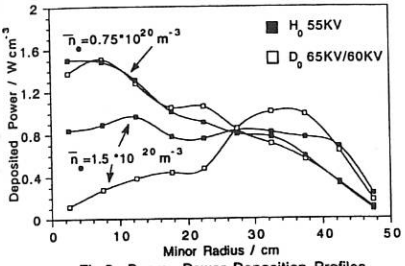


Fig.3 Beam Power Deposition Profiles

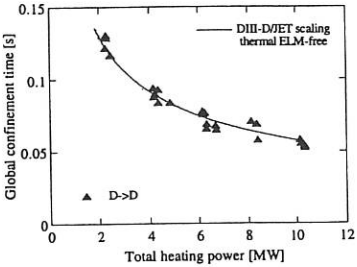


Fig.6 Global Confinement of Type I ELM H-Mode

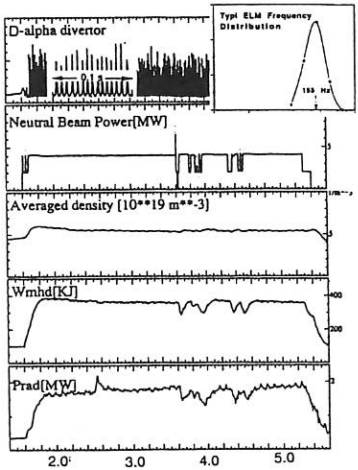


Fig.5 H-Mode Discharge with Type I ELMs

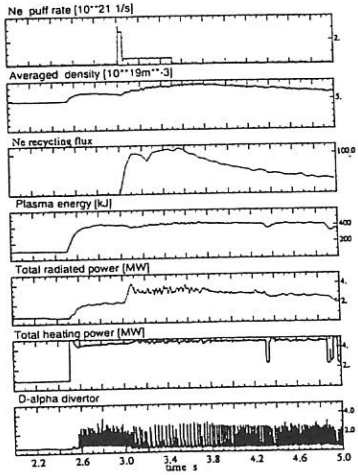


Fig.7 Ne Puffing for Radiating Edge

Development of Negative-ion-based NBI injector for Large Helical Device

A.Ando, K.Tsumori, Y.Takeiri, O.Kaneko, Y.Oka, M.Okamoto, T.Amano, N.Nakajima, S.Murakami, E.Asano, T.Kawamoto, R.Akiyama, and T.Kuroda

National Institute for Fusion Science
Nagoya, 464-01, Japan

Introduction

Large Helical Device (LHD) is a large super conducting Heliotron/Torsatron device with a major radius of 3.9m and an average minor radius of 0.6m.[1] The high power neutral beam injection (total port through power 20MW, pulse length 10seconds) is required as a main heating method of the LHD.[2] In the LHD-NBI, the required energy is so high that the negative-ion-based injector is to be installed. We have been developing a large current negative ion source since 1989, and recently achieved our target current density. This paper presents the basic parameters of the LHD-NBI system and R&D results of the negative-ion-based injector of the NBI system.

Determination of basic system parameters

Since the LHD is a machine with a moderate shear, it has a loss-cone in the velocity space, and the passing particle heating is necessary to heat the core plasma. In the perpendicular injection, the high energy ions are deeply trapped in helical ripples and easily lose away. Therefore, the tangential beam injection is essential for the efficient LHD plasma heating. The beam energy is selected at 125keV for hydrogen and 250keV for deuterium, because more than 50% of beam power is absorbed within the half minor radius and the shine through ratio is kept below 30% even in the low target plasma density. Considering the small tangential port size, the beam divergence angle should be below 0.5deg. If the beam divergence angle is 1.0 deg, the aperture loss is 20% of the beam power. Since the neutralization efficiency of negative ions is much higher than that of positive ions and negative ions has a potential to realize the small beam divergence angle, we have adopted the negative-ion-based NBI system. A large amount of negative ion current of 360A is needed to inject the power of 20MW with the acceleration voltage of 125keV, where the neutralization efficiency is 59%. We have designed the injection system which consist of 4 beam lines with 2 ion sources, each of which can deliver 45A negative ion current. The size of extraction area is 150cm x 25cm and the required current density is 30mA/cm^2 considering the transparency efficiency of 40%.

R&D of the negative ion source

The R&D of the negative ion source has been carried out at the high power negative ion beam teststand [3] with a 1/3-scale ion source which has a beam extraction area of 25 × 44 cm^2. The schematic diagram of the 1/3-scale ion source is shown in Fig.1. The size of the multicusp source chamber is 37cm(W) × 62.5cm(H) × 18.5cm(D). 24 tungsten filaments of 1.5mm in diameter are used in the experiment. The line cusp field strength is 0.8 kG on the inner wall. Water-cooled rod type magnetic filters and the EggBox Cell [4] are installed in front of the plasma grid. They suppress the electron current extracted with negative ions. The beam acceleration electrode system consists of four grids, each of which has 560 holes of 9mm in diameter in the area of 356cm^2 with the transparency of 32%. The plasma grid facing the arc plasma is made of molybdenum without water-cooling. Permanent magnets are buried in the extraction grid to eliminate electrons extracted together with negative ions. The power supply system is listed in Table 1. In these experiments we seed a small amount of cesium(Cs) vapor into the source chamber. By Cs-seeding the H^- current is enhanced several times larger than that in the pure hydrogen discharge and the decrease of electron current and the reduction of the operating pressure are observed, though there observed no harmful Cs effect such as the breakdown between the electrodes. The total H^- ion current is measured with a two-dimensional (2D) calorimeter array placed at 2.3m downstream from the plasma grid.

Figure 2 shows the dependence of H^- ion current on an input arc power P_{arc}.[3] The H^- current obtained in a pure hydrogen discharge is indicated as a dotted line in the figure, and it tends to saturate at higher P_{arc}. By Cs-seeding H^- current becomes several times larger than that in the pure hydrogen discharge and increases linearly with P_{arc}.

It is considered that the enhancement of H^- current is caused by the increase of surface production of H^- ions on the cesiated plasma grid. The maximum H^- current of 16A is

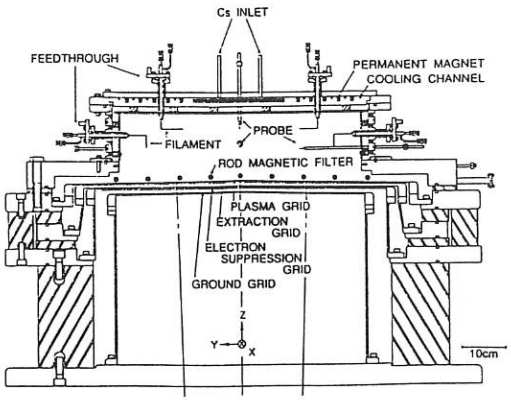


Fig.1 Schematic diagram of the 1/3-scale negative hydrogen ion source

obtained at P_{arc} = 265kW, V_{ext} = 7.5kV, V_{acc} = 33kV, and an operating gas pressure p = 0.9Pa (7mTorr). The corresponding current density is 45 mA/cm^2. As shown in the figure, V_{ext} is changed from 4kV to 7.5kV to avoid current saturation at high P_{arc} region. The current saturation value changes according to the Child-Langmuir $V_{ext}^{3/2}$ law.

The ratio of the extraction current I_{ext} to H^- current, I_{ext} / H^-, is reduced from 24 to 3 at P_{arc}=100kW in the Cs-seeded discharge, which indicates that the extracted electron current is reduced by the Cs-seeding. Here, I_{ext} is the sum of the H^- current and the electron current.

A low operating gas pressure is very important for high energy negative ion beam acceleration. H^- ions are easily stripped by collisions with neutral molecules. Figure 3 shows the dependence of the H^- current on p. In the pure hydrogen discharge the H^- current increases as p increases as shown by a dotted line in the figure. The optimum pressure, p_{opt}, to obtain the maximum H^- current increases as P_{arc} increases. In the Cs-seeded discharge p_{opt} is reduced to 0.8Pa and almost constant irrespective of Parc. The p_{opt} is more reduced when the plasma confinement in the source chamber is improved.

The 1/3-scale negative ion source with stronger cusp field (B_{cusp} = 1.8kG) is also constructed and tested. It has an external-type magnetic filter in front of the plasma grid. The electrodes has 522 extraction holes of 11.3mm in diameter in an area of 25 × 50 cm^2, where the total extraction area is 522 cm^2 and the transparency is 42 %.

Figure 4 shows the dependence of the H^- current on P_{arc} . The maximum H^- current of 16.2A is obtained at P_{arc} = 170kW, V_{ext} = 9.3kV, V_{acc} = 38 kV, and p = 0.5 Pa (3.8mTorr). The corresponding current density is 31 mA/cm^2. In the external filter source the arc efficiency (the ratio of H^- current to P_{arc}) is larger and p_{opt} is lower than those of the rod filter one, which is considered to be caused by the better source plasma confinement due to the strong cusp field in the external source.

Summary

In order to heat the core plasma in the LHD device, it is required to inject the neutral beams tangentially with the beam energy of 125keV for hydrogen and of 250keV for deuterium. The negative hydrogen/deuterium source is required for its high neutralization efficiency and potential to realize the small divergence angle. The R&D experiments have been done to realize the ion source which can deliver 45A of H^- current with the current density more than 30mA/cm^2. A negative hydrogen ion beam of 16A is extracted from the 1/3-scale ion source with the current density of 45 mA/cm^2. The value are obtained by seeding a small amount of Cs vapor into a conventional multicusp ion source with the magnetic filter in front of the plasma grid. The Cs-seeding into the source chamber results in not only an enhancement of the H^- current but also the reduction of the electron current and the operating gas pressure. The

operation gas pressure can be more reduced by improvement of the source plasma. It is reduced to 0.5Pa in the source with strong cusp field and external filter configuration.

Acknowledgment

Dr. T.Okuyama, Mr. Y.Suzuki and Mr. M.Tanaka are greatly acknowledged for their help in the experiments.

References

1) A.Iiyoshi, Proc. of the 13th Symp. on Fusion Engineering, (Knoxville, 1989), p.1007.
2) T.Mutoh, et.al., Proc. of the 15th Symp. on Fusion Technology (Utrecht, 1988), p.552.
3) O.Kaneko, et.al., Proc. of the 17th Symp. on Fusion Technology (Rome, 1992), p.544.
4) A.Ando., et.al., Proc. of the 5th Int. Symp. on Production and Neutralization of Negative Ions and Beams, (Brookhaven, 1992), AIP Conf. Proc. No.287, p.339.
5) A.Ando, et.al., to be published in Phys. of Plasmas.

Filament	12V / 10kA /30sec
Arc	120V / 8kA /15sec
Extraction	-10kV /150A / 1sec or -5kV /200A /10sec
Electron Suppression	3kV / 5 A / 1sec
Acceleration	
1st	-90 kV / 50A /10sec
2nd	-120 kV / 90 A / 1sec

Table 1 Specification of power supplies

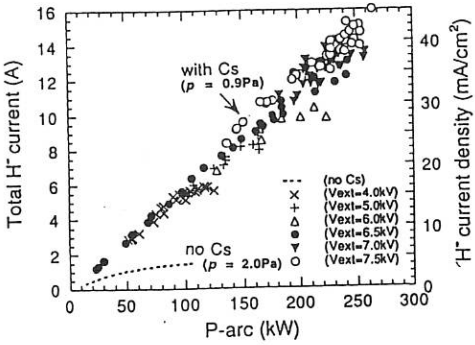


Fig.2 Dependence of H^- current on P_{arc} in the rod filter source

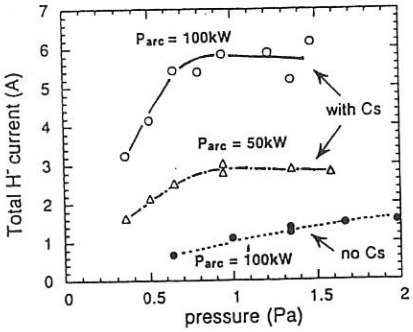


Fig.3 Dependence of H^- current on p

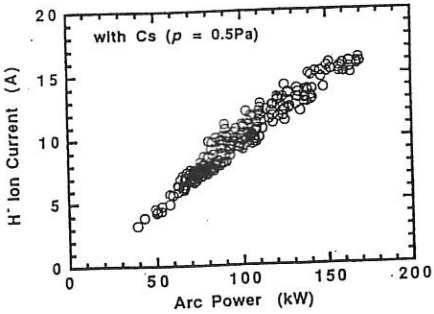


Fig.4 Dependence of H^- current on P_{arc} in the external filter source

The New JET Phased ICRH Array. First Experiments and Modelling.

M.Bureš, V.Bhatnagar, T.Brown, B.Fechner, C.Gormezano, R.Goulding*, A.Kaye, P.Lamalle+, M.Lennholm, F.Nguyen#, E.Righi, F.Rimini, A.Sibley, D.Start ,T.Wade.

JET Joint Undertaking, Abingdon,OXON OX14 3EA, UK
*Oak Ridge National Laboratory, Oak Ridge, Tennessee, USA
+Plasma Phys. Lab.,ERM, Av. de la Renaissance, Brussels, Belgium
#CEA, Centre d' Etudes de Cadarache, France

Introduction. New ICRH antennas on JET were designed to couple to the new JET divertor plasma configurations and to improve the Fast Wave Current Drive (FWCD) capabilities. The A2 antenna consists of 4 straps whose currents can be phased at arbitrary angles. In total 4 antennas are installed with a 2MW amplifier per strap. The real time automatic tuning acts on frequency, line length (line phase shifters) and stub length. As in the past provision is made for the coupling resistance/plasma position feedback to accommodate the fast changes in antenna loading. In this paper we report on the first coupling, tuning and heating results in $0\pi0\pi$, 0000 and $00\pi\pi$ phasing. Also we describe a new antenna model which was developed to simulate the measured antenna loading in terms of plasma parameters and to provide a starting point for the real time automatic tuning.

Antenna conditioning. The high power ICRH requires conditioning of all antennas. This is due to: a) novel design where a ceramic cone separating the vessel vacuum from the antenna vacuum transmission line (VTL) was removed thus allowing the pressure rises, in the VTL, associated with vessel conditioning and gas pulses, b) getter pumps previously active on the VTL were moved to pump only the double feedthrough interspace separating the VTL and main transmission lines (MTL). Conditioning sequence was 1) low voltage, short pulse multipactor vacuum conditioning, 2) high voltage, short pulse vacuum conditioning and 3) high power, long pulse plasma conditioning. Approximately 10 plasma pulses were required. To protect the VTL and the feedthroughs the RF generators are tripped, in addition to reflected power trips, when the VTL pressure reaches 10^{-4} mbar.

ICRH plasma heating. During the initial JET operations, until the new set of diagnostic coils are fully commissioned, the magnetic equilibrium reconstruction depending on the old set of coils is not accurate. The present data have large error bars but some estimates and conclusions about the initial performance of ICRH system and heating efficiency can be made. 1) P_{rf}=6 MW was coupled into a 1.5MA/2.8T plasma in $0\pi0\pi$ phasing and D(H), 42 MHz for 4s and max.power reached ≈9MW. 2) $P_{rf} \leq$ 4 MW was coupled for 8s. 3)$T_e(0)^{max}$ = 7-8 keV was achieved and sawteeth were stabilised for 1.4 s. 4) Heating in $0\pi0\pi$ is consistent with the L-mode scaling and $T_e(0)/n_e$ scales with RF power as observed previously. 5) Heating in 0000 phasing at low power ≤ 2 MW has very low efficiency. The final conclusion about these results requires a future comparison at high power. Possible reasons for the lack of heating are: i) all power in 0000 spectrum is contained in $k_{//} < 2.5 m^{-1}$. The low $k_{//}$ waves tend to reflect from the resonance zone and do not suffer sufficient damping. At high power the increasing temperature broadens the minority cyclotron layer, the cyclotron damping is enhanced and the minority tail can form. Also the direct electron damping becomes more efficient. ii) H concentration is too high. At high

concentrations the distance of cut-off layer to the minority cyclotron layer increases and the waves are readily reflected. Support for this hypothesis follows from the lack of 5.5MeV gamma radiation resulting from the reactions between the high energy protons and deuterons. iii) Parasitic dissipation in RF sheaths. Previous experiments (ref.1) with the 2 strap A1 antennas on JET in 00 phasing and large angle between the edge magnetic field and Faraday screen (FS) elements have shown that a large fraction of RF power can be dissipated in the RF sheaths at the front surface of antenna. RF sheaths are driven by the radial oscillating magnetic flux passing through electrical circuits formed by magnetic field lines connecting material surfaces on FS and/or protection tiles/limiters. Large convective cells (ref.2) are formed in front of FS which cause a strong interaction with the SOL/plasma edge. Indeed strong interaction plasma edge/poloidal limiter was observed with A2 antennas (0000) resulting in enhanced radiation. The possible circuits driving the convective cells result from magnetic field lines connecting FS and the poloidal limiter and the lines connecting poloidal limiters on both sides of antenna.

Results on antenna/plasma RF coupling. The initial operational constraints on JET control parameters implied plasma configurations which were not optimised for RF coupling. In particular the misalignment of the plasma boundary/antenna FS in the poloidal plane affects the coupling of large fractions of antenna straps which lowers the effective antenna loading. The uncertainty about the magnetic configuration means that most of JET plasmas were significantly detached. The initial operational experience nevertheless shows that the RF coupling resistance, measured on the transmission lines $R_c=2P_{rf}(Z_o/V_{max})^2$, depends on:

- antenna/plasma distance as shown in fig.1. $d_{a\text{-}p}$ is the distance of the Last closed flux surface (LCFS) from a surface $\approx$ 3 cm in front of FS measured at the mid plane. The solid lines are calculated from the model discussed below.
- phasing. Coupling in 0000 is significantly higher than in $0\pi0\pi$. Also $R_c{}^{00\pi\pi} \geq R_c{}^{0\pi0\pi}$
- SOL density e-folding length λ_n which is substantiated by the high coupling observed at low plasma current 1 MA.
- density. Present data set shows a weak density dependence which we attribute to lack of accurate data. Regression analysis shows the strongest dependence of R_c on $d_{a\text{-}p}$.
- frequency, $R_c{}^{32MHz} \approx 0.5R_c{}^{42MHz}$. This can be explained by two effects. First the 32MHz operation was done at low magnetic field 2.1T which implies short λ_n , second the A2 antenna is resonating at rather high frequency 42 MHz.
- the observed dependencies are in satisfactory agreement with model predictions.

In addition the divertor sweeping modulates R_c by up to 20%. During Elmy H-modes the ELMs modulate the reflected generator power by a significant fraction.

Automatic matching. Tuning of the antenna/transmission line system requires a generator load equal to the characteristic impedance of line Z_o. It is based on control of relative phase between the forward voltage on the MTL and the reflected voltage on the generator output line(OTL) e.g. $Re\{V_r{}^{OTL}/V_f{}^{MTL}\}=0$ as well as the amplitude of the OTL reflected voltage, $Im\{V_r{}^{OTL}/V_f{}^{MTL}\}=0$. The first condition is satisfied by feedback loop on frequency and MTL phase shifters and the second by feedback on stubs. Example of the automatic tuning is shown in fig.2. Voltages $V_r{}^{OTL}$ on all four lines are very low. The frequency and stub error signals are zero when the match is achieved. Time response of tuning is determined by the speed of stubs. Fast changes of loading have to be accommodated by the feedback R_c/radial plasma position as in the past.

Antenna/plasma RF coupling model . The model antenna consists of 4 toroidal straps, each strap has 4 poloidal sections of which 2 are shorted. The loading impedance matrix $\mathbf{Z_s}$ is calculated using the 5-region model shown in fig.3. TE waves are excited in vacuum regions I and II, FW are excited in the exponential plasma density region III, linear $k_\perp^2$ region IV and constant plasma density region V. The antenna capacitance matrix $\mathbf{C_s}$ is calculated from TM waves as described in ref.4. Antenna currents and their phases are defined at the antenna strap shorts as current vector $\mathbf{I_{vec}}$. The vacuum solutions assume $\omega/c << k_{//}$ and the FW dispersion in region III is derived (ref.2) for $k_o^2 S >> k_{//}^2$. S is the cold dielectric tensor element in Stix's (ref.3) notation. The FW wave field solution can be found for the poloidal electric field $E_y(x)^{III}$ in form:

$$E_y^{III}(x) = A^{III} J_\nu(\xi) + B^{III} J_{-\nu}(\xi) \quad \text{where}$$

$$\xi = 2\lambda_n \alpha \exp(x/2\lambda_n) \; ; \; \alpha^2 = \mu_o m_H (A\omega^2/B^2) n(0) \; ; \; \nu^2 = 4\lambda_n^2 k_{//}^2 (1 + \omega/\omega_{ci})$$

and $J_{\pm\nu}(\xi)$ are Bessel functions of fractional order ν.

In region IV the oscillating and evanescent FW fields are derived (ref.3) from the singular turning--point equations in terms of Bessel functions $J_{\pm 1/3}$ and $I_{\pm 1/3}$. In the constant plasma parameters region V we consider only the single pass fields. Poloidal variation of the fields is neglected, $k_y = 0$. The solutions of 5 regions are matched across their boundaries in standard fashion. Knowing $\mathbf{Z_s}$ and $\mathbf{Y_s} = i\omega \mathbf{C_s}$ we analyze wave propagation along the antenna in terms of TEM modes (ref.4):

- Calculate the matrices **K,L,D,G** and $\mathbf{Z_c}$, the columns of **K** and **L** are voltage and current eigenvectors

  $\mathbf{D = K^{-1} Z_s Y_s K = L^{-1} Y_s Z_s L}$ $\qquad$ $\mathbf{G = \sqrt{D}} = \text{diagonal}(\gamma_i)$, i=1-4

  $\mathbf{Z_c = G^{-1} K^{-1} Z_s L}$ $\qquad$ $\mathbf{Y_c = Z_c^{-1}}$

- Define matrix **T** and equivalent impedance $\mathbf{Z_{eq}}$ for the shorted strap sections of length l_1 and matrices **C** and **S** for the main strap sections of length l_2

  $\mathbf{T} = \text{diagonal}[\text{th}(\gamma_i l_1)]$ $\quad$ $\mathbf{Z_{eq} = KTZ_c L^{-1}}$ $\quad$ $\mathbf{C} = \cosh(\gamma_i l_2)$ $\quad$ $\mathbf{S} = \sinh(\gamma_i l_2)$

- Define transfer matrices (ref.5) to calculate the input voltages and currents into strap sections l_2 from the current vector $\mathbf{I_{vec}}$ defined at the input of sections l_1

  $\mathbf{X_V = K[CK^{-1} Z_{eq} + Z_c S L^{-1}]}$ $\qquad$ $\mathbf{X_I = L[Y_c S K Z_{eq} + C L^{-1}]}$

- Define antenna impedance matrix $\mathbf{Z_A}$ and total input voltages and currents

  $\mathbf{Z_A = X_V (2X_I)}$ $\qquad$ $\mathbf{I_{in} = 2X_I I_{vec}}$ $\qquad$ $\mathbf{V_{in} = Z_A I_{in}}$

- $\mathbf{R_c}$ is calculated on transmission lines from antenna input impedance $\mathbf{V_{in}/I_{in}}$, where the division is performed on the corresponding components of the $\mathbf{V_{in}}$ and $\mathbf{I_{in}}$ vectors.

References.
[1] M.Bureš et al, Nucl.Fus. 32, 7(1992)1139.
[2] D.A.D'Ippolito et al.,Phys.Fluids B5(10),1993 p.3603
[3]T.H.Stix, Theory of Plasma Waves, McGraw-Hill, 1962.
[4]P.V.Lamalle et al., IEEE Transactions on Plasma Science,Vol.PS-15, 1(1987)60
[5]R.H.Goulding et al, Bull.Am.Phys.Soc., APS1993.

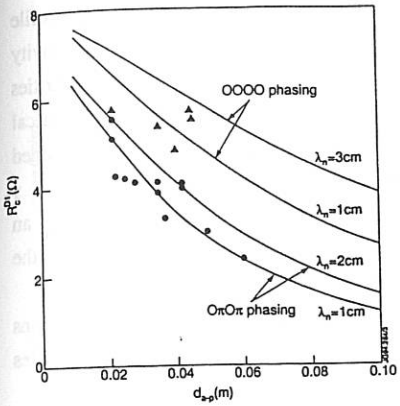


Fig.1 Coupling resistance R_C as a function of distance LCFS/FS+3cm

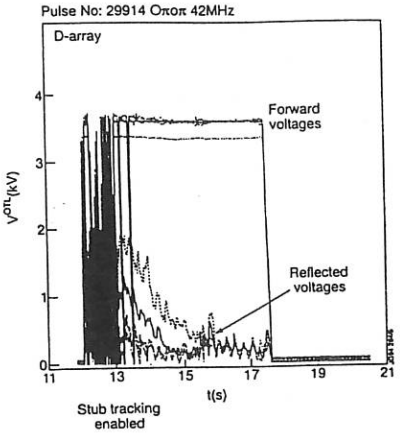


Fig.2 Forward and reflected voltages on OTL with automatic tuning enabled

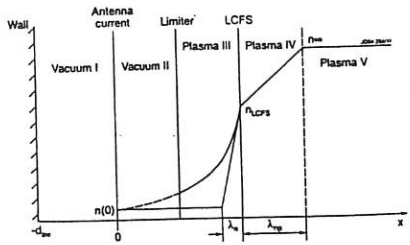


Fig.3 Schematic drawing of the 5-regions in the antenna/plasma RF coupling model

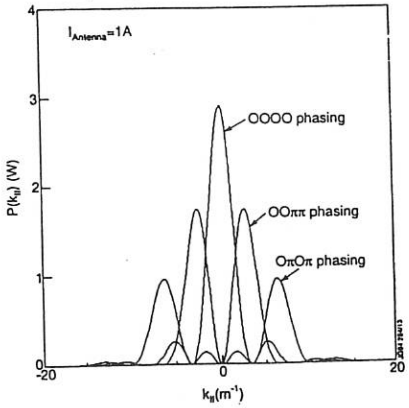


Fig.4 Antenna radiation power spectra for the phasings indicated in figure

Spatial distribution of γ emissivity and fast ions during (^{3}He)D ICRF heating experiments on JET

E. Righi*, D.F.H. Start, C. Warrick+
JET Joint Undertaking, Abingdon, OXON OX14 3EA, UK
*Imperial College of Science, Technology and Medicine, London SW7 2BZ, UK
+AEA Technology, Culham, OXON OX14 3OB, UK

Introduction. During the 1991-92 JET experimental campaign the neutron profile monitors measured along both the horizontal and vertical lines of sight the γ emissivity produced by nuclear reactions of ^{3}He ions accelerated by ICRF heating with ^{9}Be impurities during ICRF heating experiments in a (^{3}He)D plasma [1]. In the present paper a numerical technique is presented that simulates such measurements by merging information obtained from the fast ion distribution and from nuclear reactions producing the observed γ emissivity. This technique is full of potentialities to be developed, and it can play an importat role in the identification of plasma instabilities that affect the redistribution of the fast ions in the plasma, like the TAE modes and the ripple in the tokamak magnetic field.

Production of γ photons during ^{3}He-^{9}Be reactions. High energy ^{3}He ions accelerated by ICRF heating can undergo exothermic nuclear reactions with ^{9}Be impurities present in the plasma, namely,

$$^9\mathrm{Be}+^3\mathrm{He}\rightarrow{}^{11}\mathrm{B}+\mathrm{p}+\gamma \qquad Q=10\ \mathrm{MeV}, \tag{1}$$

$$^9\mathrm{Be}+^3\mathrm{He}\rightarrow{}^{11}\mathrm{B}+\mathrm{d}+\gamma \qquad Q=1.09\ \mathrm{MeV} \tag{2}$$

$$^9\mathrm{Be}+^3\mathrm{He}\rightarrow{}^{11}\mathrm{C}+\mathrm{n}+\gamma \qquad Q=7.59\ \mathrm{MeV}. \tag{3}$$

The γ photons are produced when the residual nucleus is formed in an excited state, and subsequently decays to one of the lower excited states, or the ground state. In the present analysis Eq.(1) is considered, because the reaction energy of Eq.(2) is one order of magnitude lower, and can therefore be neglected, while Eq.(3) is the isobaric equivalent of Eq.(1). Extensive studies of the ^{9}Be(^{3}He,p)^{11}B reaction exist [2,3,4,5,6], from which information can be obtained about the differential cross-sections at 90° in the laboratory frame of reference and in the energy range between 1 and 3 MeV for protons leaving ^{11}B in its excited states. Since the γ detectors used have no energy resolution, a "total" cross-section $(d\sigma / d\omega)_{tot}$ has been derived, sum of all the excitation curves for the energy levels from first to ninth, which gives an estimate of the relative probability that a γ photon is emitted from any excited state in the energy interval of interest (see Fig.1).

Simulation of γ-ray emission. In order to describe correctly the interation of ^{3}He ions with ^{9}Be impurities it is also necessary to know the distribution of ^{3}He ions in $(v_{\parallel}, v_{\perp}, r, \theta)$ space and the orbit paths of the fast ^{3}He ions. The distribution of ^{9}Be ions is here assumed to be uniform and with a concentration equal to 1% of the electron density,

consistent with the measurements of Z_{eff} for the discharges considered. The ^{3}He distribution has been calculated by means of a 2D numerical code that solves the bounce-averaged steady-state Fokker-Planck equation in cylindrical coordinates [7]. This code does not include the effects of finite orbit width of high energy fast ions, which therefore have to be included *a posteriori*. To this end the orbit following code ORBIT [8] has been used that estimates the time $(\Delta t / T)_{T\to\infty}$ spent by the ^{3}He ions at each point in the configuration

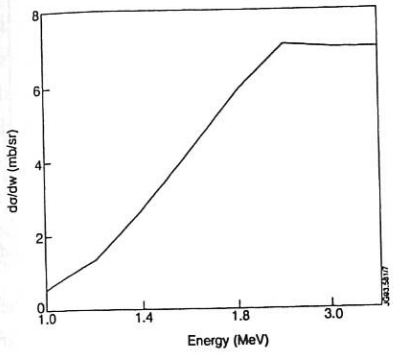


Fig.1. "Total" differential cross-section for ^{11}B.

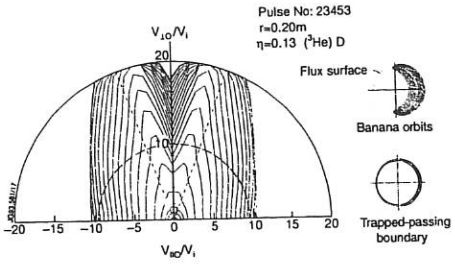


Fig.2. Minority ion distribution function in $(v_{||}, v_{\perp})$ space.

space. A plot of the intensity of γ emissivity,

$$I_\gamma \propto \int d^3r \int dE \sqrt{E} f(E,r,\theta) \left(\frac{d\sigma}{d\omega}\right)_{tot} \left(\frac{\Delta t}{T}\right)_{T\to\infty}, \qquad (4)$$

can then be generated for each energy considered and a number of test particles, once the weight function,

$$w(E,r,\theta) = \sqrt{E} f(E,r,\theta) \left(\frac{d\sigma}{d\omega}\right)_{tot} \left(\frac{\Delta t}{T}\right)_{T\to\infty}, \qquad (5)$$

is known. Information about the ^{3}He distribution in energy, pitch angle and minor radius and the excitation curves of ^{11}B have therefore been combined in the weight function Eq.(5) as input for the ORBIT code to calculate the γ-ray emission of monoenergetic test particles launched at the midplane. The results of simulations at different energies have been subsequently integrated to give the total γ emissivity.

Results and comparison with the experiment. The JET shots for which experimental measurements of the γ emissivity exist are those of Table I, where their main plasma parameters are listed. Measurements of γ emissivity can be plotted either as a 3D

reconstruction of γ intensity in the poloidal plane, or as line integrated data of γ emission along a vertical and horizontal line of sight [1]. Both cases have been simulated numerically. In Fig.3 the intensity of γ emission in the (r,z) plane is reported for the off-axis discharge JPN 23450. Analysis of these simulations show that different types of orbits contribute to determine the two γ distributions when on-axis and off-axis ICRF are considered, which leads also to a different localization of the emissivity peak (the "hot spot"). In particular, the off-axis ICRF discharge (JPN 23450) is dominated by passing particles in the plasma centre, while trapped particles are localised either on the RF resonance or nearby. On the contrary, in the case of on-axis ICRF heating (JPN 23453) trapped particles dominate near the plasma centre (on the RF resonance), with a clear contribution of high energy D-shaped orbits. If the numerical γ emissivity in the (r,z) plane is line integrated into γ intensity along the horizontal and vertical lines of sight [1], then the γ-ray calculations can be compared with the experimental curves. The results, shown in Fig.4 for JPN 23450, clearly indicate that experiment and simulation agree qualitatively, meaning that the main elements responsible for the distribution of γ emissivity (and fast ions) are all present in the model. However the picture also shows that while along the horizontal line of sight the measured and calculated intensities have the same profiles, along the vertical line of sight the intensity peaks are displaced of one channel. This means that the simulated "hot spot" is displaced horizontally with respect to the measurement. This difference could find an explanantion in the approximations used. In particular, the Fokker-Planck code calculates $f(E,r,\theta)$ in cylindrical coordinates, while the actual discharges have substantial elongation and triangulation. Also orbit

Table I - Plasma parameters

	JPN 23450	JPN 23453
time slice (s)	49.0	49.0
plasma current (MA)	3.5	3.5
B_t on-axis (T)	3	3
T_{e0} (keV)	7.3	7.4
n_{e0} (10^{19} m^{-3})	2.8	3.0
P_{RF} (MW)	7.9	11.7
magnetic axis R_0 (m)	3.10	3.12
resonance off-set (m)	0.29	0.06
fast ion energy (MJ)*	0.2	1
Z_{eff}	1.5	1.6
n_{He}/n_{e0} *	0.045	0.13

**estimated with the orbit code PHANTOM [9] and cross-checked with experimental data*

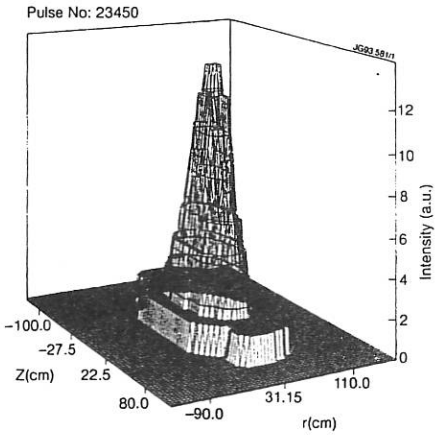


Fig.3. Numerical reconstruction of γ-ray emissivity in the poloidal plane for the off-axis ICRF heated discharge JPN 23450.

effects are not introduced self-consistently, but *a posteriori*. It is also not excluded that other nuclear reactions (of ^{12}C with ^{3}He, for instance) should be included in the analysis.

Conclusions and future work. In this paper a model has been presented that can simulate the γ emissivity in the poloidal cross-section during (^{3}He)D ICRF heated discharges in JET plasmas. Calculations show reasonable agreement with the experiment, indicating that all the main elements that produce the distribution are present. However the model is still only a first order description of the γ production. Future work will therefore be oriented especially to improve the calculation of the fast ion distribution function by including self-consistently effects of toroidal geometry and finite orbit widths of ^{3}He ions (through already available Monte-Carlo codes). This technique can be useful to analyse JET discharges in all those scenarios where the ^{3}He distribution plays a major role, like in the presence of Toroidal Alfven Eigenmode (TAE) modes or ripple in the tokamak magnetic field. In the former case the distribution is expected to lose its peakedness due to the redistribution of the passing fast ions into high energy D-shaped orbits.

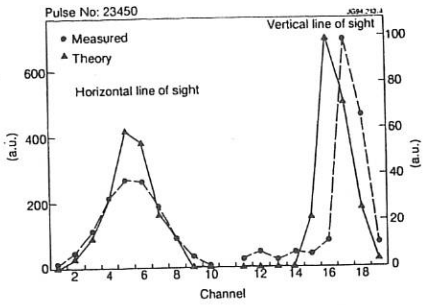


Fig.4. Comparison between experimental and theoretical line integrated intensity of γ emissivity along the horizontal and vertical lines of sight of the γ detectors for JPN 23450 (courtesy of P.J.A. Howarth).

Acknowledgements. The authors would like to acknowledge the cooperation with the JET RF Team and the Neutron Group, in particular P. van Belle, G. Sadler, P.J.A. Howarth and O.N. Jarvis. Special thanks go to Dr. E. Jelley, of the Nuclear Physics Laboratory in Oxford, for his precious help to dig out the references on ^{11}B cross-sections.

References

1. P.J.A. Howarth et al., these Proceedings.
2. H.D. Holmgren, M.L. Bullock and W.E. Kunz, Phys. Rev. **104** (1956), 1446.
3. S. Hinds and R. Middleton, Proc. Phys. Soc. **A74** (1959), 196.
4. E.A. Wolicki et al., Phys. Rev. **116** (1959), 1585.
5. S. Hinds and R. Middleton, Proc. Phys. Soc. **A75** (1960), 754.
6. W.R. Coker et al., Nucl. Physics **A91** (1967), 97.
7. M.R. O'Brien, M. Cox and D.F.H. Start, Nucl. Fusion **26** (1986), 1625.
8. P. van Belle, private communication.
9. E. Righi, Ph.D. thesis, Imperial College of Science, technology and Medicine (1994).

AN ANALYSIS OF JET FAST-WAVE HEATING AND CURRENT-DRIVE EXPERIMENTS DIRECTLY RELATED TO ITER.

V.P. Bhatnagar, L. Eriksson, C. Gormezano, J. Jacquinot, A. Kaye, D.F.H. Start.

JET Joint Undertaking, Abingdon, OXON, OX14 3EA (U.K.)

1. INTRODUCTION. The ITER fast-wave system is required to serve a variety of purposes, in particular, plasma heating to ignition, current profile and burn control and eventually, in conjunction with other schemes, a central non-inductive current drive (CD) for the steady-state operation of ITER. We analyse, in terms of dimensionless parameters, the ICRF heating and current drive data that has been obtained in JET with a view to ascertaining its direct relevance to key ITER requirements. The analysis is then used to identify areas both in physics and technological aspects of ion-cyclotron resonance heating (ICRH) and CD that require further experimentation in ITER-relevant devices such as JET to establish the required data base.

2. PLASMA HEATING. Heating to ignition is a direct extrapolation from the JET high power (22 MW) minority ICRF heating [1] including that of the high minority ($n_H/n_{He3} \leq 1$) heating [2] experiments reported earlier. Also, a 2 MA (magnetically) steady-state discharge lasting 60 s and heated by ICRH at a level of 3 MW for the entire duration of the discharge has been produced [3]. Deuterium fundamental and tritium second harmonic heating scenarios, proposed for ITER, are also scheduled to be carried out later in the D-T phase of JET.

3. MINORITY-ION CURRENT DRIVE AND BURN CONTROL. With a view to burn control, the stabilization or destabilization of sawteeth due to magnetic shear control at the $q = 1$ surface has been obtained by minority ion current drive [4,5] in JET. This behaviour results in a change in the DD reactivity of up to 60% in JET. A model calculation predicts that by changing the sawtooth period from 3 s to 0.2 s in ITER-EDA like plasmas, the D-T reactivity could be reduced by a factor of 0.75 [6]. In this preliminary calculation, the dynamic behaviour of burn control (delayed response-time due to current diffusion) has not yet been evaluated.

4. ELECTRON-TTMP CURRENT DRIVE. The scenario predicted to be the most effective for electron transit-time magnetic pumping (e-TTMP) current drive by fast waves in ITER is at a frequency (22 MHz) that lies below all ion resonances [1] so as to avoid strong ion damping. In this domain, the experimental data base is scant principally due to low β_e (ratio of kinetic to magnetic pressure) and relatively small plasma size and hence weak damping in present day devices. We note that for good current drive efficiency ($\bar{\eta}$), one should operate at normalized speed $\xi \equiv v_p/v_e \geq 2$ to avoid deleterious effects of electron trapping [7] (see Fig. 1), but optimum damping occurs at $\xi = 1/\sqrt{2}$ (see Fig. 2). This eventually reflects in lower CD efficiency. The electron damping of the fast wave can be represented as [8],

$$\frac{k_{i\perp}}{|k_\perp|} = \frac{\sqrt{\pi}}{4}\,\beta_e\,\xi\,e^{-\xi^2}$$

where $k_\perp$ is the wave vector perpendicular to the magnetic field, $k_{\perp i}$ is the imaginary part of $k_\perp$ and $\beta_e \equiv 2\mu_0 n_e T_e/B_\phi^2$ where μ_0 is the vacuum permeability. A contour plot of the right hand side of the above equation in a (β_e, ξ)-plane is plotted in Fig. 2. It is clear that the absorption increases linearly with β_e and it is optimum at $\xi = 1/\sqrt{2}$. Using ray tracing [9], we calculate single pass absorption (SPA) of fast waves by electrons launched from an antenna located on the low-field side in which the tokamak geometry, profiles and the effect of poloidal field

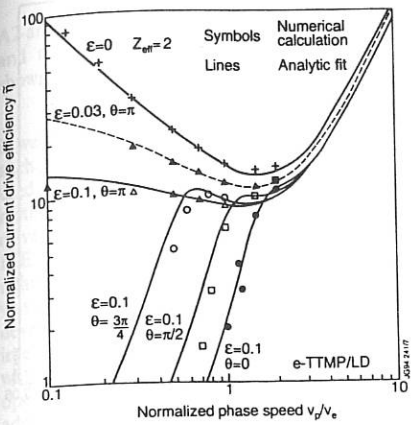


FIG. 1. $\bar{\eta}$ vs v_p/v_e for several poloidal angles (θ) and inverse aspect ratio (ε). v_e is the electron thermal speed and $v_p = \omega/k_{//}$. Courtesy Ref. 7.

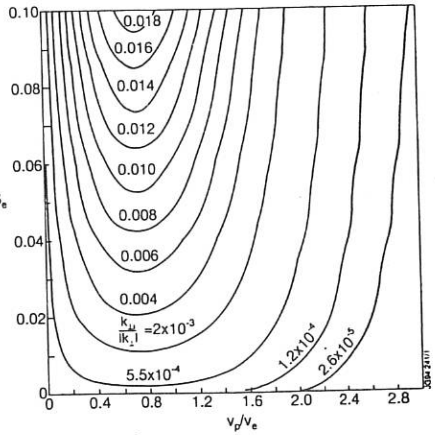


FIG. 2. Contours representing fast-wave e-TTMP/e-Landau dampings ($k_{\perp i}/|k_\perp|$) in (β_e, v_p/v_e)-plane.

are fully taken into account. An aspect ratio of 3.2 in the present divertor phase of JET allows us to exclude H and D ion resonances from the plasma (33 MHz at 3 T without introducing He3) for an operation of ITER-relevant e-TTMP current drive scheme in JET in deuterium plasmas. In Fig. 3, we plot the e-SPA as a function of the toroidal field (B_ϕ) for two values of central electron temperature (T_{e0}). To exclude the ion resonances, the ratio of frequency to B_ϕ is maintained constant. As expected, the e-SPA decreases as $B_\phi^{\frac{1}{2}}$. The same data is plotted as a function β_e in Fig. 4 and shows a linear dependence on β_e. A minimum value of SPA of about 10% appears to be necessary from other experiments (Tore Supra and DIII-D) for significant electron heating. These calculations show that at 3 T in JET, the e-SPA is poor. An operation at 2.55 T (28.3 MHz) and T_{e0} = 10keV would lead to an e-SPA of about 12%. Operation at a still lower B_ϕ would be better but then the frequency goes out of the band of the JET ICRF plant which was initially designed for heating rather than the electron current drive scheme.

We now present the e-SPA results in Fig. 5 for ITER where the operating frequency (f= 22 MHz) for electron current drive at a given B_ϕ = 6T is chosen to exclude all ion resonances from the device. These results are an average of three rays (at $\theta = -20, 0, 20°$; covering the poloidal extent of the antenna) launched from the low-field side of the tokamak. This permits us to take account of the variation of $k_{//}$ due to poloidal field in single pass calculations more correctly. The single pass damping decreases as v_p/v_e increases in the range of v_p/v_e shown. Finally, we note that e-SPA depends on β_e, v_p/v_e and plasma diameter.

In Fig. 6, we present results of normalised current drive efficiency factor ($\gamma_{CD} = < n_e > RI/P \propto T_e \bar{\eta}$) for e-TTMP current drive in JET and ITER. These results are calculated using multiple-bounce multi-ray trajectories and using CD efficiencies from Fig. 1 for ITER-EDA and JET parameters. Here, I is the current driven, P the RF power, R the major radius and $< n_e >$ the average electron density. The higher γ_{CD} values in ITER as compared to JET are principally due to higher T_{e0} and higher antenna directivity in ITER. The model assumes no loss of power on a ray reflection on the cutoff at the plasma edge which may be questionable for very weak SPA cases.

5. ICRF FAST-WAVE TECHNOLOGY. We note that on the technology side, the basic ITER ICRF system (20-60 MHz) does not need to be very different from that of the present JET system (f= 23-57 MHz and P_{GEN} = 32 MW). To take advantage of the different

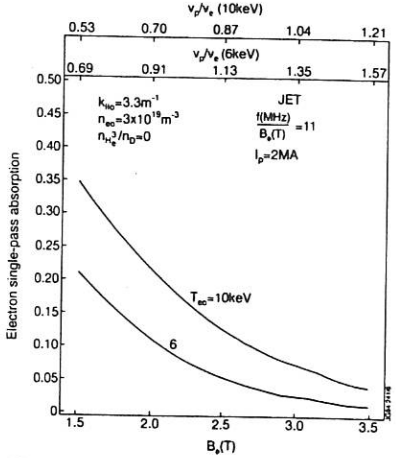


FIG. 3. e-SPA vs B_ϕ in JET when frequency is varied to exclude H and D resonances from the plasma.

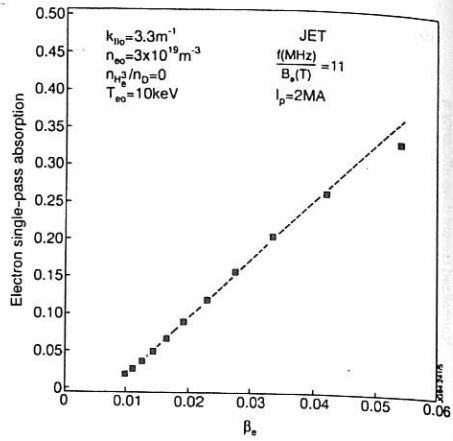


FIG. 4. Single-pass electron absorption vs β_e for the case of Fig. 3 at T_{eo} = 10 keV.

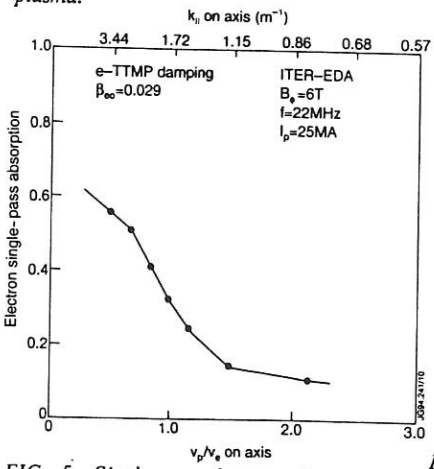


FIG. 5. Single-pass electron absorption vs v_p/v_e for ITER-EDA parameters: D-T, T_{eo} = 19 keV, $n_{eo} = 1.4x10^{20}m^{-3}$.

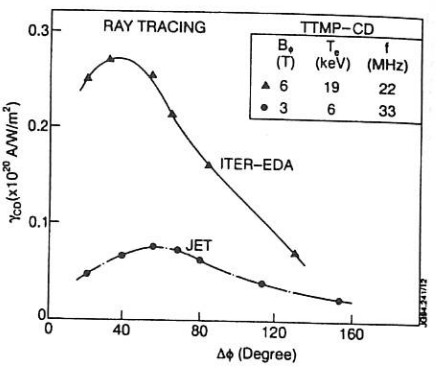


FIG. 6. Current drive efficiency factor γ_{CD} as a function of $\Delta\phi$ between successive antenna straps. ITER-EDA: 6-straps (L_z = 0.74m). JET-A2: 4-straps (L_z = 0.4m).

fast-wave scenarios spread over a large frequency range, a "violin" [10] antenna (a multiple resonance, asymmetrically excited antenna) has been proposed (see Fig. 7) in which a long strap is connected in parallel with a very short section. The latter acts as a matching element located within the antenna and improves the power coupling property especially at low frequencies. Its has high coupling resistance capability at a number of desired frequencies in a wide band [10]. The proposed violin antenna for ITER features a remote ceramic as the antenna is supported at its two short-circuited ends. The remote ceramic aspect of the ITER violin antenna is being simulated [11] with the successful operation of JET A2-antennas with 9 MW coupled up to now to a 2 MW single-null divertor plasma [12]. The antennas have also been tested up to 35 kV in vacuum without arcing. A simplified drawing of the JET

A2-antenna together with the vacuum transmission line and the remote ceramic window (also a support) is shown in Fig. 8.

6. CONCLUSIONS. The fast-wave ICRF system is well suited for heating to ignition of next-step devices such as ITER. The minority ion current drive can be used to control sawteeth. In conjunction with other methods, the fast wave central non-inductive current drive can also be used for steady-state operation of ITER. However, the demonstration of latter is in its infancy due to low β_e in present day devices. The fast wave ICRF technology does not need major developments for the next step and a successful integration of an ICRH antenna with screen into first wall of ITER constitutes the main task. The very recent operation of JET antennas with remote ceramic provides additional design flexibility.

ACKNOWLEDGEMENTS. Contribution of the JET team in this work is greatfully acknowledged.

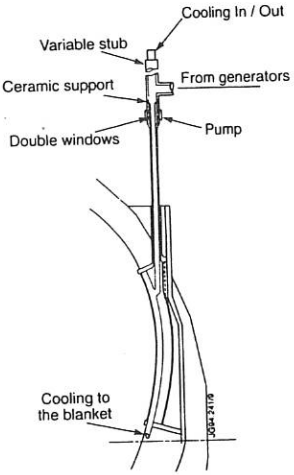


FIG. 7. A poloidal view of a proposed "violin" antenna for ITER with a short and a long section both short circuited at their far ends.

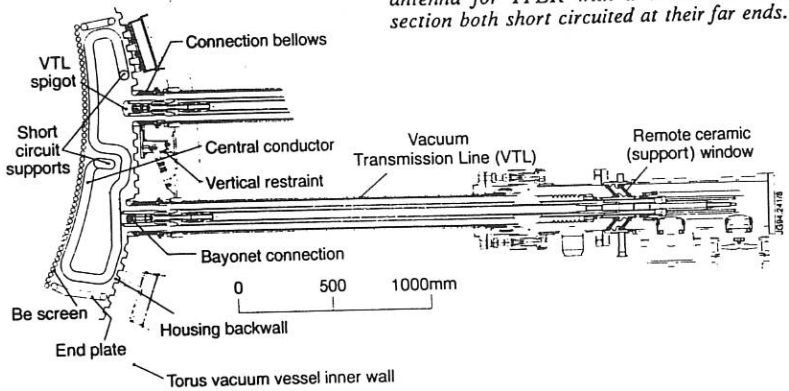


FIG. 8. A simplified drawing of a poloidal view of a strap of a JET-A2 antenna. Also shown is the connection to VTL with a remote ceramic (support) window.

REFERENCES.

[1] JACQUINOT J. et al, Plasma Phys and Contr Fusion, 35 (1993) A35.
[2] BHATNAGAR, V.P. et al., Nuclear Fusion, 33 (1993) 83.
[3] BRUSATI, M. et al., AIP Topical Conf. Proc. 244, Charleston, SC (1991) 115.
[4] START, D.F.H., et al., Proc. IAEA TCM on Fast Wave Current Drive in Reactor Scale Tokamaks, Arles, France (1991) 260.
[5] BHATNAGAR, V.P. et al., submitted to Nuclear Fusion.
[6]. START, D.F.H., ERIKSSON, L., (1993) private communication.
[7] EHST, D. et al., Nuclear Fusion, 31 (1991) 1933.
[8] START, D.F.H. et al., Nucl. Fusion 30 (1990) 2171.
[9] BHATNAGAR, V.P. et al., Nucl. Fusion 24 (1984) 995.
[10] BHATNAGAR, V.P., JACQUINOT, J., to be published in Nucl Fusion,
[11] JACQUINOT, J. et al., Proc. IAEA TCM on RF Launchers, Naka, Japan (1993).
[12] BURES, M. et al., these proceedings.

Ion energy balance during fast wave heating in TORE SUPRA

T. Hutter, A. Bécoulet, J.P. Coulon, B. Saoutic, V. Basiuk, G. T. Hoang
Association Euratom-CEA sur la Fusion
Centre d'Etudes de Cadarache
13108 Saint Paul Lez Durance (FRANCE)

Introduction

Direct coupling of the fast magnetosonic wave to the electrons has been recently studied on TORE SUPRA. Preliminary experiments were dedicated to optimise the scenario for Fast Wave Electron Heating (FWEH) and Current Drive (FWCD). In a first part, thermal kinetic and diamagnetic energy are compared when fast wave is applied to the plasma in two different regimes: 1/ the minority hydrogen heating scenario (ICRH), 2/ the direct electron damping. Effects of ion resonant layers, marginally present in the plasma in the later regime (FWEH), is then presented and discussed.

In the following, all plasmas are limited on the carbon inner wall, with R = 2.28 m and a = 0.72 m, and, unless specified, are helium plasmas with a small hydrogen concentration ($n_H/n_e < 5\%$).

Thermal energy content

On TORE SUPRA, time resolved energy spectra of fast hydrogen and deuterium neutrals are routinely measured by charge exchange (CX) analysers [1] of the E||B type (46 channels per mass, H and D, Emax = 300 keV) with different lines of sight: five in a poloidal cross-section having a tangency radius Rt = 0.43 m (near "perpendicular"), and one in the equatorial plane with Rt = 1.9 m (near "parallel" to the magnetic axis, see figure 4).

Concerning the ion energy balance, the ion temperature profiles are simulated including: 1/ a best fit to the passive measured spectra of each analyser, 2/ for all the analysers, the same normalisation factor for the neutral density profile (fast computed consistently with ion temperature[2]) and 3/ the consistency with neutron yield and plasma composition. Standard diagnostics provide the other experimental data required in the simulation code (ne(r), Te(r), Zeff, neutron yield and plasma geometry).

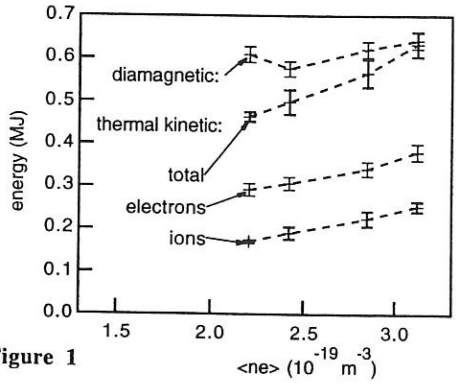


Figure 1

A 4-step electron density scan is performed on a 4 s, 4 MW ICRH pulse (f = 57.4 MHz, dipole phasing), launched in a mainly deuterium plasma ($n_D/n_{He} \approx 2$, B = 3.9 T, Ip=1.3 MA). Electron and ion kinetic thermal energies are shown on figure 1. In the ohmic phase, diamagnetic and kinetic energy are found in good agreement. The lowest density point corresponds to a monster sawtooth. For the other points, data are averaged during 100 ms (about two normal sawteeth). If we assume that perpendicular supra-thermal ion energy content is the difference between diamagnetic and thermal kinetic energy, it is within the error bars for the high density point, but clearly increases with decreasing density. The thermal energy content has also been evaluated on a 4 MW pulse of FWCD (f = 47.7 MHz, co-current phasing) launched in mainly helium plasma ($n_D/n_{He} \approx 0.7$, B = 2.2 T, Ip = 0.76 MA). It is found equal to the diamagnetic energy, indicating that the supra-thermal particle energy content, if present, is negligible.

Hydrogen spectra during FWEH optimisation

To get a better efficiency for FWEH/CD, it is necessary to avoid any ion damping of the wave. Due to the outgasing of the TORE SUPRA carbon inner wall, it is impossible to get rid of hydrogen and deuterium. A precise monitoring of the position of the ion cyclotron layers is thus a necessity. The CX analysers, both parallel and perpendicular, appear to be the best tool to optimise the scenarios. For f=47.7 MHz (dipole phasing, 2MW, 2s), the magnetic field B has been scanned between 2.10 and 2.27 T on four consecutive shots (Ip= 0.75MA). The first harmonic hydrogen layer, Ω_{CH}, is on the high field side (HFS) of the discharge, the second one, $2\Omega_{CH}$, on the low field side (LFS), and the third harmonic of majority ions (deuterium or helium, $3\Omega_{CD}$) is at the plasma centre. In the present plasma conditions, no significant damping on $3\Omega_{CD}$ is expected. This is experimentally confirmed by the usual maxwellian shape of the observed deuterium spectra (figure 6). Hydrogen neutral spectra measured during these shots (analysers time resolution: 65 ms) are shown on figure 2. One can notice that the perpendicular tail vanishes when increasing B from 2.1 to 2.24 T, and that above 2.2 T a large non maxwellian tail appears on the parallel analyser.

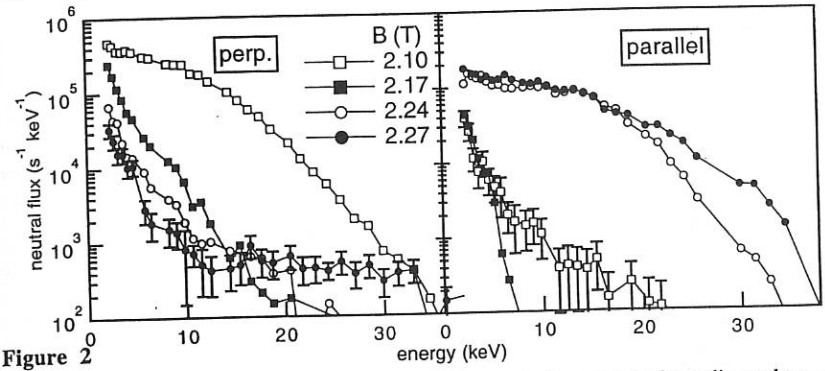


Figure 2

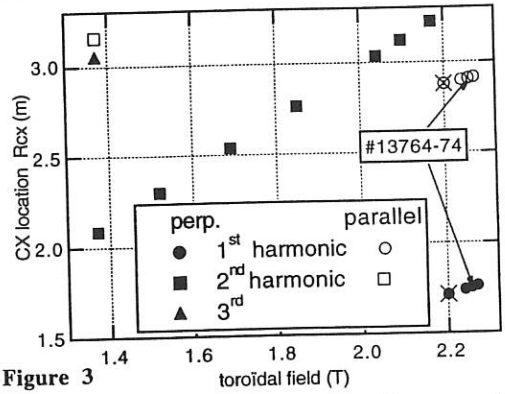


Figure 3

An ion of velocity v directed towards the CX analyser (and of parallel velocity $v_{//}$), making a CX at major radius Rcx, satisfies $Rt/Rcx = v_{//} / v$. According to the adiabatic theory of particle trajectories in tokamak, this ion, before the CX, can cross a cyclotron resonant layer ($n\Omega_{CH}$, n=1,2,...) only if $Rcx - Rt^2 / Rcx \leq R_{n\Omega CH}$. The equality corresponds to a trapped ion with banana tips on the resonant layer, which interacts strongly with the wave. The corresponding value of Rcx is shown on figure 3 for each harmonic layer present in the plasma ($1.56 < R_{n\Omega CH} < 3.2$). One can check that, in the present B-scan, particles interacting with the Ω_{CH} layer can be detected by the parallel analyser when doing their CX on the LFS and by the perpendicular analyser when doing their CX on the HFS. However the energy of the ions in the present case is low (E<20keV, cf. figure 2). The particles making their CX on the HFS are thus mostly re-ionised before reaching the perpendicular analyser. The ions accelerated on Ω_{CH} (HFS) are then

mainly detected by the parallel analyser. And in the same way, the perpendicular analyser mainly detects the ions accelerated on the $2\Omega_{CH}$ (LFS) layer. It is thus possible, using both CX analysers, to explain the B-scan experiments results as the $2\Omega_{CH}$ layer moving outside the plasma, and the Ω_{CH} layer progressively entering on the HFS. Finally B=2.17 T represents the optimum field, where no significant ion damping competes with the direct electron heating.
This is also well confirmed by the expected positions of the cyclotron layers shown in Table I, except that at B=2.10T the $2\Omega_{CH}$ layer is 4 cm outside the plasma and that a significant tail is however observed. One must remember here that the ripple effect is quite high on the low field side of TORE SUPRA. Indeed, for the case B = 2.10T, R+a increases by 3 cm and $R2\Omega_{CH}$ decreases by 15 cm between two coils[3]. So it is clear on figure 4 that confined protons can interact with the wave.

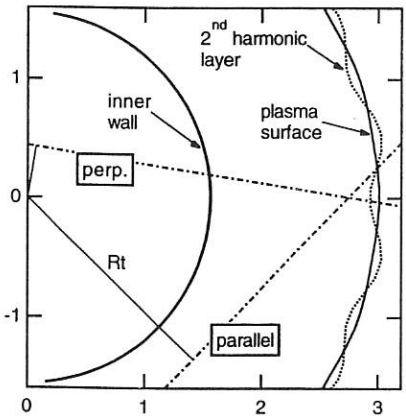


Figure 4: *lines of sight of the CX analysers in the equatorial plane.*

table I: relative position (in meter) of the harmonic resonant layers. A negative value indicate a layer outside the plasma.

B(T)	$R_{\Omega CH}$-(R-a)	R+a-$R_{2\Omega CH}$
2.10	-.04	-.04
2.17	.01	-.14
2.24	.06	-.24
2.27	.08	*(-.29)

*: no signification (out of the torus).

The Doppler effect also broadens the cyclotron layer, thus being coupled to the ions a few centimetres deeper in the plasma. Finally, since few obstacles are located on the outer part of the plasma chamber, one can expect sufficient confinement of 5-30 keV protons in the low electron, high neutral density plasma located on the low field side of the torus, thus giving rise to that relatively high neutral signal observed on the perpendicular analysers when 2.1 < B < 2.2 T ($2\Omega_{CH}$, upper right black square on figure 3).

Ion-electron competitions during FWEH/CD experiments

A larger B-scan has been performed (1.37<B(T)<2.2), at f=47.7MHz, in order to investigate the possibility for maximizing the electron single-pass absorption (which scales as B^{-3}). But lowering B also means entering the $2\Omega_{CH}$ layer into the plasma, and thus a competition with ion damping (which increase also with ion temperature Ti). Figure 5 displays the CX analysers measurements for various B values, the corresponding cyclotron layers locations being given in Table II. One clearly distinguish the increasing absorption on the $2\Omega_{CH}$ layer as it enters the plasma towards the centre (and experiences an increasing Ti, B from 2.2 to 1.69T), followed by a decrease as B varies from 1.69 to 1.37T. The FW single-pass absorption computations, as well as full-wave simulations, confirm the observations, revealing a switch between the electron and ion dampings when the $2\Omega_{CH}$ layer is at the plasma centre (B=1.69T).

Another example of such a competition between ions and electrons has been observed when phasing the currents between the FW antenna straps, for FWCD experiments. In that case, the averaged parallel wave number decreases, lowering the electron single-pass absorption. This is well confirmed by the neutral spectra measurements, in cases where the set f / B is not optimised: for 48MHz / 2.25T, Ω_{CH} layer is slightly inside the plasma on the high field side. On figure 6, hydrogen spectra measured during FWEH for two different shots, with these f / B values, are presented. We can see that spectra remain low in dipole phasing

(#13764), but with the co-current phasing (#13774), we observe a large increase of the parallel analyser signal and the appearance of a "flat" spectra on the perpendicular one for energy above 20 keV (fast neutral coming from HFS and crossing the plasma, despite higher density than in #13764!).

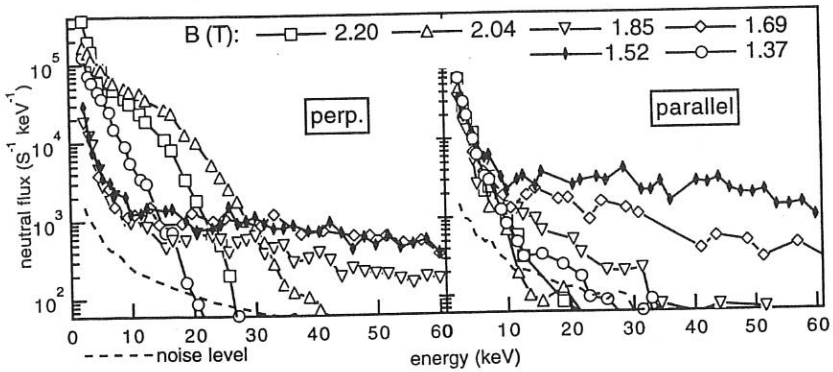


Figure 5

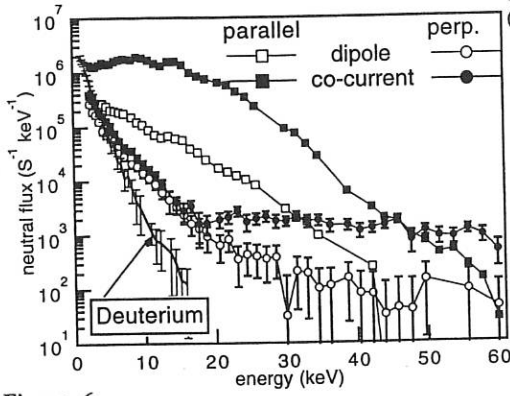


Figure 6

table II: R_m : magnetic axis radius (Ip = 0.4 MA, P_{RF} = 1.5 MW)

B(T)	$R_{\Omega CH}$-(R-a)	$R_{2\Omega CH}$-R_m	(R+a)-$R_{3\Omega CH}$
2.20	.05	.81	*
2.04	*(-.17)	.59	*
1.85	*	.31	*
1.69	*	.06	*
1.52	*	-.18	*(-.31)
1.37	*	-.39	0

*: no signification (out of the torus).

Conclusions

On TORE SUPRA CX analysers 1/ prove to be a powerful tool in the determination and optimisation of the FWEH/CD scenarios, 2/ permit direct observation of competing damping mechanisms for ions and electrons.

---

1 similar to those developed for TFTR: A. L. Roquemore et al., Rev. Sci. Instrum. 56, 1120 (1985).

2 H. Capes, P. Laporte, T. Hutter and J-C. M. de Haas, this conference.

3 R. Arslanbekov, Y. Peysson et al, this conference.

FAST EVALUATION OF THE QUASILINEAR ION DISTRIBUTION FUNCTION DURING ION CYCLOTRON HEATING

Marco Brambilla

Max-Planck Institut für Plasmaphysik – Euratom Association
Garching bei München, Germany

Abstract. The code SSFPQL solves the steady-state quasilinear kinetic equation for Ion Cyclotron heating using an expansion in Legendre polynomials in the pitch angle and cubic finite elements in the velocity. Finite Larmor radius effects are taken into account but toroidal trapping is neglected. While this restricts the use of SSFPQL to moderate heating rates, the code provides all the information needed to take into account quasilinear effects on wave propagation and absorption with minimal numerical effort. This is illustrated with an application to minority IC heating in ASDEX Upgrade.

Introduction. Investigation of the ion distribution function during ICR heating is important because deviations from Maxwellian 1) influence the propagation and absorption of IC waves; 2) are experimentally measurable through CX and therefore have diagnostic value; and 3) can modify the reactivity and the ignition temperature in the fusion reactor. This investigation has been pioniered by Stix [1] assuming isotropy in velocity space. In the case of fundamental heating of a minority species this simple model predicts the development of a suprathermal tail with the effective temperature

$$T_i^{tail} \simeq 0.353\,10^{-28} Z_i Z_M^3 T_e^{3/2} W_i / A_M^{3/2} n_e n_i \qquad (1)$$

(subscripts i, M refer to the minority and majority, respectively; W_i is the heating rate in $\mathrm{W/cm^{-3}}$; temperatures are in keV, densities in $\mathrm{cm^{-3}}$). This has been found to agree qualitatively well with experimental results. Since IC heating increases mainly the perpendicular energy of resonant ions, however, the distribution function can be expected to be quite anisotropic. In a tokamak, moreover, the quasilinear diffusion coefficient has a strong pitch–angle dependence [2], in particular due to toroidal trapping of the heated ions. To take into account these effects, whose importance increases with the plasma temperature and the size of the device, one has to solve the quasilinear Fokker-Planck kinetic equation in two velocity variables [3]. This is a very heavy numerical task, particularly if it has to be repeated on several magnetic surfaces to allow for the radial localization of the IC power deposition profile and for radial diffusion.

The code SSFPQL. If toroidal trapping is neglected, however, a two dimensional solution of the quasilinear kinetic equation can be obtained with minimal numerical effort by expanding the heated distribution function in Legendre polynomials in the pitch angle

$$F_i(\vec{v}) = \sum_n F_n(v)\, P_{2n}(\mu) \qquad (2)$$

(symmetry in $\mu = v_\parallel / v$ is assumed). The success of the Legendre expansion is due to a non-conventional representation of the quasilinear diffusion coefficient based on the

addition theorem for Bessel functions:

$$D_{ql}(v,\mu) = D_o\,(1-\mu^2)^p \sum_{k=0}^{\infty} \mathcal{J}_k^p(\xi_\perp v)\,\mu^{2k} \tag{3}$$

where we have introduced the functions

$$\mathcal{J}_k^p(\xi_\perp v) = \left(\frac{\xi_\perp v}{2}\right)^k \sum_{k'=0}^{k} \frac{1}{k'!(k-k')!} J_{p+k'}(\xi_\perp v) J_{p+k-k'}(\xi_\perp v) \tag{4}$$

Here $\xi = k_\perp v_{thi}/\Omega_i$, v is normalized to the thermal speed, and $p = 0$ for fundamental heating, $p = 1$ for first hamonic heating. For each v Eq. (3) is a Taylor expansion around the exact value of D_{ql} for perpendicular velocity. On the other hand, for $\mu \neq 0$ it is also an expansion in the Larmor radius, since the k–th term begins as $(\xi_\perp v)^{2k+p}/k!$. The advantage of using (3) instead of a power expansion of the Bessel function is that at moderate energies it ensures a rapid convergence of (2) for nearly perpendicular velocities, where it is most important, and confines possible convergence problems to nearly parallel velocities, where there are much less particles. A straightforward Larmor radius expansion of D_{ql} [4], although giving a somewhat simpler form to the quasilinear operator, localizes the worst convergence problems of the Legendre expansion near perpendicular velocities, and therefore becomes useless already at much lower energies. The code SSFPQL solves the steady–state quasilinear kinetic equation (linearized by the assumption that the heated species collides with a Maxwellian background plasma) using (2)–(3) and cubic finite elements in the velocity variable.

Due to the omission of toroidal trapping, SSFPQL cannot follow ions to very high energies; the effects of trapping on IC heating, however, although very important from other points of view, have only a modest influence on the propagation and absorption of the Fast Magnetosonic wave in the IC frequency range. Two reasons can be given for this statement. In the first place, since the wavelength of the compressional wave is always much longer than the thermal ion Larmor radius, the local dielectric tensor depends only on the distribution of parallel velocities and (roughly speaking) on two low order momenta of the distribution of perpendicular velocities, namely the density and the perpendicular pressure [5]. In the second place, ion cyclotron resonance layers in tokamaks are optically thin or at most marginally thick: this means that by far the largest fraction of the absorption is due to thermal ions, whose distribution is rather insensitive to toroidal trapping. Thus SSFPQL can provide, with a modest numerical effort, all the velocity-space information required to take into account quasilinear effects on wave propagation and absorption.

Minority Heating in ASDEX Upgrade. A description of the code will be given elsewhere [6]. Here we present an application to minority heating in ASDEX Upgrade, which illustrates the possibilities of the code and its potential use in view of a self-consistent description of IC heating. The power density available for minority IC heating in ASDEX Upgrade ranges typically from 0.5 to 2 W/cm^3 in a region extending to about one third of the radius, and decreases rapidly outside. Assuming a constant 'linear' heating rate $W_i = 1$ W/cm^3 and 5 % Hydrogen in a Deuterium plasma of electron

density $n_e = 8\,10^{13}$ cm^{-3}, we present in fig. 1 the results from SSFPQL for a scan of the background plasma temperature T_o over the range 1 to 4 keV accessible to the heating experiment. The strong anisotropy of the quasilinear distribution function is clear: while the effective perpendicular tail temperature increases from 10 to over 60 keV, the parallel temperature does not exceed 12 keV. Note that the increase of T^{tail} is sligthly less than linear due to finite Larmor radius (FLR) effects, which reduce the quasilinear heating rate by about 20 % as T_D increases from 1 to 4 kev; at the same time the power collisionally transferred by the minority to the electrons remains roughly constant around 0.4 W/cm^{-3} (these results are obtained from SSFPQL alone at constant linear W_i; they do not take into account that as the temperature increases the balance between electron and ion absorption would shift in favor of the latter, thereby increasing W_i at constant total available power). The anisotropy is also clearly visible from the level plot of the minority distribution at 2 keV, shown in fig. 2.

Approximate representation of the solution. From the solution of the quasilinear kinetic equation obtained with SSFPQL in the form (2) one could evaluate the local FLR dielectric tensor with the techniques described in [5]. In spite of the simplicity of this procedure, however, using it in large wave propagation codes would still represent a formidable numerical effort. The results of SSFPQL suggest a factorized approximation $F(\vec{v}) \simeq F_\perp(v_\perp)\, F_\parallel(v_\parallel)$, which simplifies this task substantially. Indeed, the distribution of perpendicular velocities $F(v, \mu = 0)$ is found to be essentially identical to the one-dimensional solution of Stix (properly normalized for the different number of degrees of freedom and corrected for FLR effects if required), for which a simple analytic form is known [5]. The distribution of parallel velocities on the other hand can be accurately approximated as the sum of two Maxwellians

$$F_\parallel(u) = (1-\alpha)\frac{e^{-u^2}}{\sqrt{\pi}} + \alpha\frac{e^{-u^2/\gamma}}{\sqrt{\gamma\pi}} \tag{5}$$

where $u = v_\parallel / v_{tho}$ is the parallel velocity in terms of the thermal velocity before heating, and $\gamma = T_\parallel^{tail}/T_o$; the tail population fraction α is determined by imposing that $F(u)$ has the same average energy $T_\parallel^{QL}$ as the numerical solution, i.e. $\alpha = (T_\parallel^{QL} - T_o)/(T_\parallel^{tail} - T_o)$. The accuracy of this approximation is illustraded in figs. 3 and 4 for $T_o = 2$ and 4 keV, respectively. The huge numerical advantage of using the approximated distribution function is obvious. In particular, the singular integrals over $v_\parallel$ which describe parallel dispersion and collisionless absorption can be expressed in terms of the usual Plasma Dispersion function alone, for which efficient algorithms are available [7].

[1] Stix T.H., *Nucl. Fus.* **15** (1975) 737.

[2] Lamalle P.U., Phys. Lett. **A 175** (1993) 45.

[3] Karney C.F.F., Comp. Phys. Reports **4** (1986) 183.

[4] Anderson D., Eriksson L.-G., Lisak M., Plasma Phys. Contr. Fus. **29** (1987) 891.

[5] M. Brambilla, C. Hoffman, 20th EPS Conf. on Contr. Fusion and Plasma Physics, Lisboa 1993, Vol. III, p. 957.

[6] M. Brambilla, to be published in Nucl. Fusion (1994).

[7] W. Gautschi, *SIAM Rev.* **9** (1967) 24.

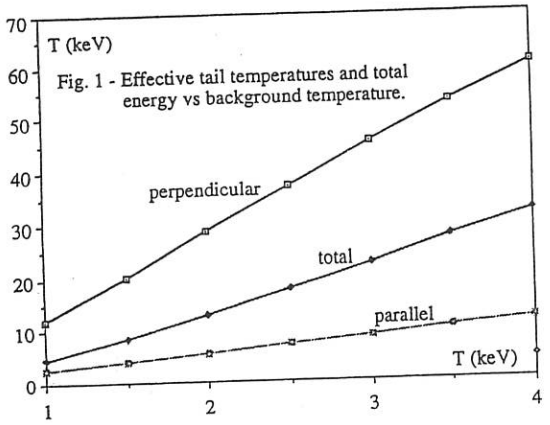


Fig. 1 - Effective tail temperatures and total energy vs background temperature.

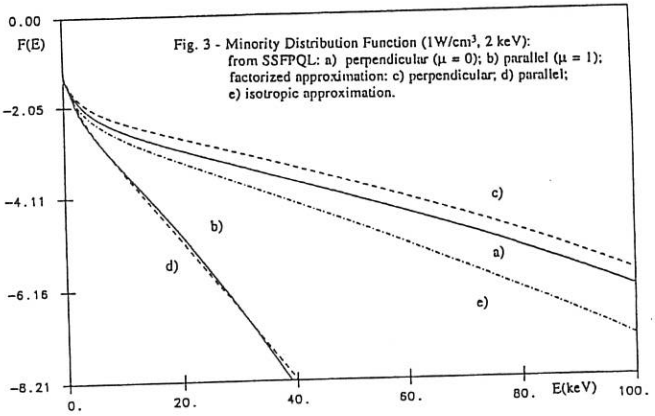
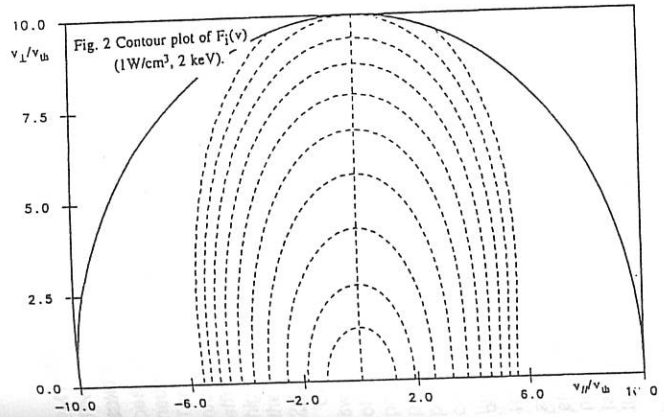


Fig. 3 - Minority Distribution Function (1W/cm³, 2 keV): from SSFPQL: a) perpendicular (μ = 0); b) parallel (μ = 1); factorized approximation: c) perpendicular; d) parallel; e) isotropic approximation.



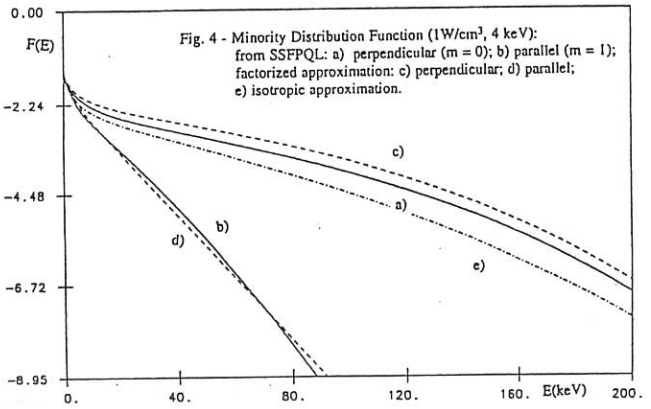


Fig. 4 - Minority Distribution Function (1W/cm³, 4 keV): from SSFPQL: a) perpendicular (m = 0); b) parallel (m = 1); factorized approximation: c) perpendicular; d) parallel; e) isotropic approximation.

STUDY OF THE THIRD HARMONIC ICR HEATING OF THE BEAM HEATED DEUTERIUM PLASMA OF TEXTOR

G. VAN WASSENHOVE[1], R. KOCH[1], D. VAN EESTER[1], P. DUMORTIER[1], F. DURODIE[1], H. EURINGER[2], F. HOENEN[2], A.M. MESSIAEN[1*], J. ONGENA[1*], H.F.TAMMEN[3], G. WAIDMANN[2].

(1) Laboratoire de Physique des Plasmas - Laboratorium voor Plasmafysica, Association "Euratom-Belgian State", Ecole Royale Militaire-Koninklijke Militaire School - B-1040 Brussels, Belgium.

(2) Institut fûr Plasmaphysik, Forschungszentrum Jülich, GmbH Association "Euratom-KFA", D-5170 Jülich, FRG.

(3) FOM Instituut voor Plasmafysica, "Rijnhuizen", Association Euratom-FOM, P.O.Box 1207, 3430 BE, Nieuwegein, The Netherlands.

(*)Researcher at the National Fund for Scientific Research, Brussels, Belgium.

Introduction

Heating scenarii combining both NBI (neutral beam injection $D \rightarrow D^+$) and third harmonic heating have been experimentally studied on TEXTOR; two scenarios were investigated: ICRH + pure Co injection and ICRH + balanced injection. During the first series of experiments with only Co beam, the neutron yield showed an enhancement of fusion reactions while temperature and energy increase are rather low [1]. The large increase in neutron production was associated with the preferential absorption of the wave energy by the fast ions of the beam, leading to the formation of a tail in the energy distribution. This tail formation was also observed in JT60 [2].
During the second campaign of experiments, both Co and Co + Counter neutral beam were combined with ICRH, showing better heating efficiency than previously observed.
These experimental results are documented and compared with predictions from the SWHAP and BECHSI codes [3].

Experimental conditions

For the two experimental programs, the same plasma discharge conditions were selected: Deuterium beam injected in a deuterium plasma target; plasma current I_p=350 kA; heating frequency = 38 MHz.
-for the co injection experiments, the energy of the beam ions was varied between 30 keV and 53 keV, which corresponds to a beam injected power varying between 0.4 MW and 1.55 MW. ICRH heating power is varied between 0 and 2 MW. The plasma density $\overline{n_{e0}}$ varied between 2.2 $10^{13}cm^{-3}$ and 4. $10^{13}cm^{-3}$. The toroïdal field B_t was varied between 1.66T and 1.81T.
-for the Co + counter beam injection, the energy of the beam was fixed at 40 KeV, which corresponds to a beam power of 800 KW for each beam. The RF power was also varied between 0 and 2 MW. For this heating scenario, larger plasma densities were reached: an input power of 1.6 MW NBI combined with 2 MW ICRH induces an unavoidable density increase from 2.2 $10^{13}cm^{-3}$ to 5.9 $10^{13}cm^{-3}$.

Experimental results

1)Co injection experiments
In these experiments the RF power was varied from 0 to 2 MW; B_t = 1.77T so that the $3f_{CD}$ absorption layer is 10 cm outboard. The plasma density increase during additional heating was rather modest : from 2 10^{13} cm^{-3} to 2.6 10^{13} cm^{-3} for P_{nb} = 1.4 MW and P_{icrh} =

2MW.
The neutron yield shows a clear linear dependence with respect to the RF power. The neutron production by RF is 10^{13} neutrons/MW at a fixed NBI power of 1.4 MW. Change in neutral beam energy makes that slope vary from 0.2 10^{13} neutrons/MW at 30 KeV to 1.2 10^{13} neutrons/MW at 53 KeV.
The plasma diamagnetic energy also increases linearly with the RF power, but the slope recorded is only half of the value obtained during minority ion heating scenario. Heating efficiencies close to values obtained during minority heating are possible when working at higher plasma density and lower magnetic field (putting the absorption layer in the centre of the plasma).
2)Co + Counter injection experiments:
Contrary to co-injection experiments, plasma density increases dramatically at the RF switch-on. Sometimes a second spontaneous density increase is observed in the plateau phase of the RF power. This large density increase is not directly correlated to the amount of RF power; indeed, for certain discharges, this large density increase occurs at very low RF power (see e.g. fig. 7-8 of [3]). In this type of plasma discharges the small amount of RF power induces a big increase of the energy and of the density of the plasma. The auxiliary confinement time one can deduce from this experiment is unrealistically high i.e. similar to the ohmic one. We interpret this as an improvement of confinement induced by the rf heating which is correlated with the large density peaking accompanying the event.
In fig (1) the time evolution of the plasma parameters for a typical high power discharge is presented.
A linear dependence of neutron yield with RF power is observed. The neutron production efficiency is 10^{13} neutrons/MW of ICRH (to compare with $\approx .6\ 10^{13}$ neutrons/MW at similar conditions but with only 1 beam).
The diamagnetic energy increases almost linearly with the RF power, the slope of the linear dependence is higher than in the co injected case. A value of 27 KJ/MW is obtained which is of the same order of magnitude as the value measured for the minority heating scenario.
Equilibrium energy also exhibits the same type of behaviour but, during ICRH, its value is always lower than the diamagnetic energy. At an Nbi power level of 1.6 MW combined with 1.6 MW RF power, a maximum value of diamagnetic energy of 121KJ is reached; this is equivalent to a Troyon factor of 2.2 which is a record value on Textor.

Comparison between theory and experiment

The neutron production in these experiments is mainly due to reactions between fast particles and the plasma target. A modest change in the neutron production is due to the change in the plasma target electron temperature (< 10%). Most of the increase in the neutron production is due to the ICRH induced change in the velocity distribution function of the fast ions.
Model description
The theoretical description of the combined ICRH and beam injection experiment proceeds in 3 steps.
-Computation of the power absorbed by the different plasma species (e^-, $D_{background}$, D_{beam}) in the neighbourhood of the 3rd harmonic of the ion cyclotron frequency, using the SWHAP code [3]. It shows that the main part of the ICRH power is absorbed by the beam ions: at a power density of 0.350 MW/m^3 this fraction is 78% , 6% is given to the electrons and 15% to the thermal plasma ions.
-Evaluation of the distribution function of the fast D ions. The distribution is obtained by solving the quasi linear Fokker-Planck equation (BECHSI code [3]). The $k_\perp$ value used in this code is that given by SWHAP for $k_{//} = 7\ m^{-1}$. This $k_\perp$ is dependent on plasma parameters , for example the plasma density.
-From the distribution of particles velocity, the neutron yield produced by fast ions plasma reactions is calculated .

Theoretical predictions

A graph of the particle velocity distribution is presented in fig. 2. We clearly see formation of a tail. The shape of the tail is independent on the RF power but its amplitude is proportional to that power. The cut-off of the tail corresponds to the first zero of the RF diffusion coefficient ($E_+ J_2 + E_- J_4$) which acts as a barrier against further particle acceleration. As a consequence, even if the number of fast ions contained in the tail increases with RF power, the tail will not significantly extend to higher velocity values. This theoretical prediction clearly explains the linear dependence of neutron production with respect to the RF power.

Neutron yield prediction: even though the experimental dependence is well explained by theory, the absolute neutron yield measured is far below the value predicted by the code. Looking at the particle velocity distribution, one can observe that a non negligible fraction of the ions of the tail is not confined. Since that fraction is directly linked to $k_\perp$, the fraction of ions lost will be linked to the plasma density and thus this effect should be accounted for when estimating the neutron production. A rough guess of the ion loss is obtained by considering an ion population that is accelerated at the plasma radius where the neutral beam absorption is maximal. First, the frontier in velocity space separating confined and lost particles is determined looking at the guiding centre trajectories of individual particles (see fig. 3). Next, the deconfined particles are removed from the distribution. If we suppose that the ion loss doesn't affect the size or shape of the distribution, but just leads to a sharp cut in that distribution, the impact of this ion deconfinement effect on neutron production can be quantitatively estimated. The number of neutron produced in function of density is given in fig. 4. For 1 MW injected power and at $n_e = 4\ 10^{13}$ cm^{-3}, the expected increase in the neutron yield is a factor 4, a doubling of the neutron yield is observed.

Plasma energy analysis: the ion deconfinement process also has an impact on the plasma energy. To quantify this effect, we investigate the reduction in ion beam distribution resulting from the deconfinement of fast ions. This is done by associating a quasi negligible confinement time with these fast particles in the Fokker-Planck equation. As expected, the loss of fast ions of the tail strongly decreases the power given to the electrons.

The loss of fast ions explains many results of the 3rd harmonic icrh experiment:

-Increase of the density results in larger $k_\perp$ values and in a decrease of the maximum velocity of the fast ions. In this way it indirectly allows for a better energy confinement.

-When the absorption of the RF power takes place in the centre, energy and neutron production is higher since, for a given particle energy, core particles are better confined than particles closer to the edge.

-The change in neutron production efficiency with the energy of the beam is also linked to the modification in the confinement .

Conclusions:

By theoretically analysing the 3rd harmonic heating scenario, we demonstrate that, when fast ions of the tail can be confined i.e. by density increase and putting the absorption layer in the centre of the plasma, heating efficiency of that scenario is at least as efficient as the minority heating scenario. Low energy increase measured during the first series of experiments [1] can be explained by the deconfinement process of the fast ions.

With 1.6 MW 3rd harmonic icrh combined with the same amount of NBI power we were able to reach the β_{limit} of Textor.

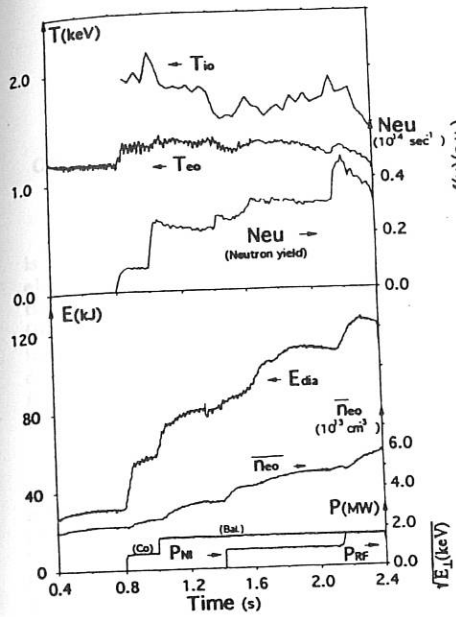
References

[1] G. Van Wassenhove et al (1992), Europhysics topical conference on Radiofrequency Heating and Current Drive of Fusion Devices, Brussels, Vol16E, 141.

[2] H. Kimura et al. , Plasma Phys. Control. Fusion 35 (1993), 845.

[3] R. Koch et al., Proc. 5th Int. Toki Conf. (1993), to be published in Fus. Eng. & Design.

[4] A. M. Messiaen et al., Plasma Phys. Control. Fusion 35 (1993), A15.



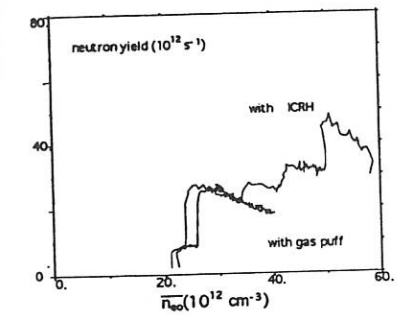


Fig. 1(a) Display of T_{io}, T_{eo}, neutron yield, E_{dia} and the additional power versus time.
(b) Neutron yield as a function of density for this shot with ICRH, compared with one without ICRH but with a gas puff induced density increase.

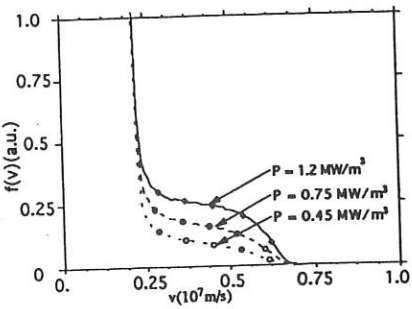


Fig. 2 Velocity distribution profile of the beam ions for 3 different values of the heating power density (n_e =9. 10^{13} cm^{-3}, T_e = 1.5 keV, T_i = 1.7 keV).

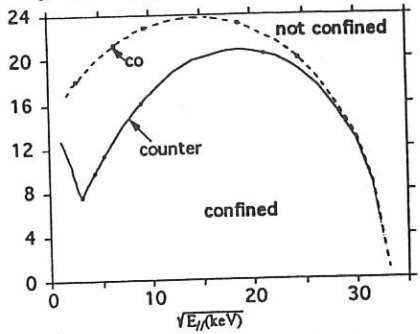


Fig. 3 Limit of confinement of fast ions as a function of $\sqrt{E_\perp}$, $\sqrt{E_{//}}$ (r=13 cm, B_t=1.7 T).

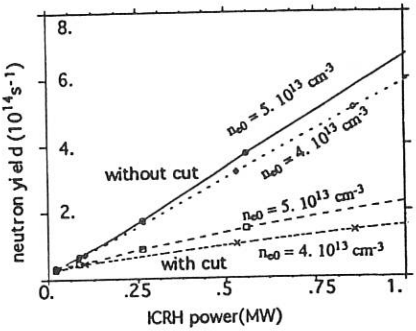


Fig. 4 Neutron production as a function of RF power for 2 values of the density, with and without taking into account the fast ions losses.

PONDEROMOTIVE EFFECTS ON THE COUPLING OF ION BERNSTEIN WAVES TO TOKAMAK PLASMA

A. Cardinali, R. Cesario, F. De Marco

Associazione EURATOM- ENEA sulla Fusione, Centro Ricerche Energia Frascati, C.P. 65 - 00044 Frascati, Rome (Italy)

I. INTRODUCTION

The ion Bernstein wave (IBW) can be excited in a tokamak plasma by launching a slow electron plasma wave (EPW), with a frequency ω_0 near the ion cyclotron frequency harmonic and the parallel wave number $n_\parallel \geq 1$. This wave propagates in the region of the scrape-off plasma where $\omega_{pe} > \omega_0 > \omega_{pi}$ and mode-transforms into an IBW near the layer $\omega_{pi}=\omega_0$. A good antenna loading is expected according to the theory [1,2], with an antenna resistance $R \geq 1\Omega$ for low plasma density values near the antenna, such that $\omega_{pi} < 0.7\text{-}0.8\omega_0$. Moreover, direct IBW coupling is expected at higher values of the plasma density so that $\omega_{pi} > \omega_0$. The direct IBW coupling is strongly dependent on the toroidal magnetic field [3].

In the recent IBW experiments on DIII-D [4] and PBX-M [5,6], good antenna coupling was found, even when operating in conditions where poor coupling was expected. The coupling was evaluated by assuming that the plasma density near the antenna has the same value as that measured at the same radial position, but in a toroidal position a few meters from the antenna. Moreover, no dependence of the antenna coupling on the toroidal magnetic field was found during the experiment on DIII-D. These results can be explained by supposing that the plasma density near the antenna is reduced during the RF pulse, due to the ponderomotive forces of the RF electric field gradient.

In the present work, the effect of the RF ponderomotive potential on the plasma density is studied, and the perturbed density is evaluated by self-consistent evaluation of the electric field. The wave-induced electric field is obtained by the amplitude transport equation (Poynting theorem).

As a result, we have found that the ponderomotive effects are strongly dependent on the operating frequency. In the IBW experiments on DIII-D and PBX-M, operating at a frequency of about 50-60 MHz, the antenna coupling is dominated by the ponderomotive effect also at low levels of injected rf power.

II. MODEL EQUATIONS AND DISCUSSION

A simple theoretical model describing the nonlinear effects of the wave field on the plasma edge is given in ref. [8], from where a formula for the evolution of the perturbed plasma density as a function of the wave field is obtained:

$$n(x) = n_0(x)\, exp\left\{ - \frac{W}{T_e(x) + T_i(x)} \right\} \qquad (1)$$

where $n_0(x)$ is the unperturbed density profile, $x=r/a$ is the normalized slab variable and

$$W = \frac{1}{4m_i}\frac{e^2E_\perp^2}{\omega_0^2-\Omega_{ci}^2} + \frac{1}{4m_e}\frac{e^2E_\parallel^2}{\omega_0^2} \qquad (2)$$

is the ponderomotive potential. In the plasma, the components of the propagating electric field are obtained by solving the amplitude transport equation (Poynting theorem) both analytically and numerically. In general, the behaviour of the electric field will depend on the plasma density, which, in turn, depends on the field. An iterative procedure is applied to Eqs. (1)-(2) to obtain the value of the perturbed density in the scrape-off plasma. The parallel and perpendicular components of the field used in Eqs. (1)-(2) are obtained from the wave potential, which is a function of the radial variable and the Fourier component of the field at the antenna:

$$\Phi^2(x, n_{\parallel 0}) = \frac{(n_e(a)/n_e(0))^{1/2}}{x n^{1/2}(x)}\,\Phi_0^2(n_{\parallel 0}) \qquad (3)$$

$n(x)$ is the density profile; $n_e(a)$ and $n_e(0)$ are the edge and the central values, respectively, of the plasma density; and $\Phi 2_0(n_{\parallel 0})$ is the spectrum of the field at the antenna. The electric field at the antenna-plasma interface is obtained by the Brambilla wave-plasma coupling theory [1], which takes into account the plasma density at the antenna position before the IBW pulse. For the PBX-M experiment,

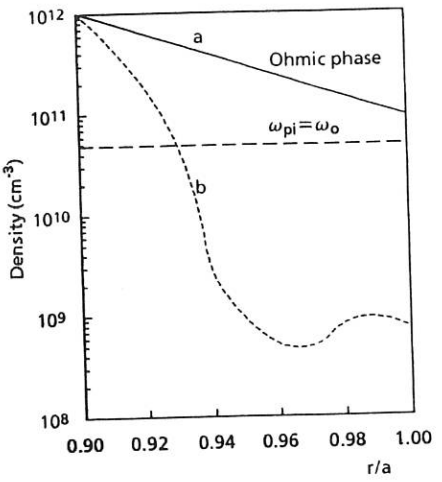


Fig. 1a,b) Scrape-off plasma density as a function of the radial variable for PBX-M IBW experiments. a) ohmic phase, b) calculated plasma density change during IBW pulse (P_{RF}=10kW, f_0=47MHz., B_T=14kG).

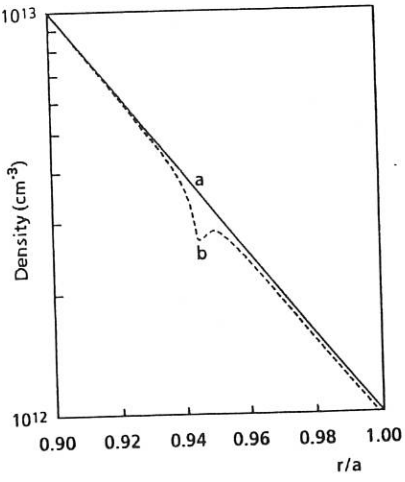


Fig. 2a,b) Scrape-off plasma density as a function of the radial variable for FTU IBW experiments. a) ohmic phase, b) calculated plasma density change during IBW pulse (P_{RF} = 500 kW, f_0=433MHz., B_T=78kG).

plasma density of about 10^{11} cm^{-3} is expected at the antenna position, which corresponds to $\omega_{pe}>>\omega_0$. In these conditions, a poor estimate of the wave electric field near the antenna is obtained in ref. [9].

From eq. (1) it is obvious that the higher the injected power, the stronger the reduction of the plasma density in the scrape-off plasma. The results of our analysis are shown in Fig. 1 for the PBX-M tokamak, which operates at a frequency f_0=47MHz. In the figure, the unperturbed (a) and perturbed (b) density is plotted in logarithmic scale vs x. A strong decrease of the density near the antenna is observed (one order of magnitude), which causes the layer $\omega_0=\omega_{pi}$, which is located outside the plasma prior to the IBW pulse, to be pushed inside the scrape-off plasma, resulting in EPW coupling. Therefore, this result can justify the good antenna coupling during the IBW experiments on PBX-M and DIII-D, which operated with similar plasma parameters in the antenna region.

For the next IBW experiment on FTU, which operates at a frequency f_0=433 MHz, the layer $\omega_0=\omega_{pi}$ should be located inside the scrape-off plasma during the ohmic phase. In Fig. 2 the ponderomotive effects are evaluated by considering the FTU [7] plasma parameters. We can observe that no significant change of the plasma density near the antenna is expected during the IBW pulse up to the maximum operating power of 500 kW.

III. CONCLUSION

Ponderomotive effects can be responsible for reducing the plasma density near the antenna and determine the coupling of the electron plasma wave to the plasma. At operating frequencies of 50-60 MHz, as in the IBW experiments on DIII-D and PBX-M, the nonlinear ponderomotive effects are very strong and are responsible for the anomalous antenna coupling observed. For the IBW planned experiment on FTU, the ponderomotive effects are not expected to modify significantly the plasma density near the antenna, and the coupling should be determined only by the antenna-plasma distance.

REFERENCES

[1] M. Brambilla, A. Cardinali, Nucl. Fusion 32, 465 (1992).
[2] A. Cardinali, R. Cesario, F. DeMarco, O. Sauter; Europhysics Topical Conference on Radiofrequency Heating and Current Drive of Fusion Devices, edited by C. Gormezano, P.U. Lamalle, R.R. Weynants (EPS, Bruxelles, July 1992), p 153.
[3] M. Brambilla, Nucl. Fusion 28, 549 (1988).
[4] R.I. Pinsker, M.J. Mayberry, C.C. Petty et. al., Proceedings of the 9th Topical Conference on Radio Frequency Power in Plasmas, edited by D.B. Batchelor, (AIP, Charleston, S.C., 1991), p. 105.
[5] M. Ono, R. Cesario, T.K. Chu et. al., Proceedings of the 10th Topical Conference on Radio Frequency Power in Plasmas, edited by M. Porkolab and J. Hosea, (AIP, Boston, MA,1993), p. 64.
[6] R. Cesario, R. Hermann, M. Ono, F. Paoletti, L. Schmitz, Nucl. Fusion 34, 261 (1994).
[7] P. Papitto, R. Cesario, F. DeMarco, G.L. Ravera, M. Sassi, Proceedings of the 17th Symposium on Fusion Technology, edited by C. Ferro, M. Gasparotto, H. Knoepfel, (North Holland, Rome, Italy, September 1992), Vol 1 p. 57.

[8] R. Klima, Soviet Phys. JETP 23 (1966) 534.
[9] M. Ono, Phys. of Fluids B 5 241 1993 (p. 258).

QUASILINEAR ANALYSIS OF IBW ELECTRON ABSORPTION

A. Cardinali, F. Paoletti*, S. Bernabei+, M. Ono+

Associazione EURATOM- ENEA sulla Fusione, Centro Ricerche Energia Frascati, C.P. 65 - 00044 Frascati, Rome (Italy)

I.INTRODUCTION

It has been shown [1,2,3] that ion Bernstein waves (IBW's), normally employed to heat the bulk ions of the plasma at a given harmonic resonance, could be used to heat the electron population directly because of the strong increase of the parallel refraction index $n_\parallel$ along the ray trajectory. As already shown [2,3], $n_\parallel$ oscillates along the trajectory, assuming positive and negative values; its amplitude depends essentially on the poloidal location of the antenna and, when the antenna lies on the equatorial plane, on the $n_\parallel$-spectrum launched by the antenna itself. Hence, a wide range of values of $n_\parallel$ are present inside the plasma. These characteristics of IBW's can be exploited to use them in conjunction with lower-hybrid waves (LHW's) to improve the efficiency of lower-hybrid current drive (LHCD) [4].

The IBW is unable, alone, to produce a net current in the plasma owing to the relevant fact that the launched wave spectrum continuously changes from positive to negative values. Instead, the LHW launched with a spectrum centred on low values of $n_\parallel$, lying just above the accessibility condition, generates a tail in the electron distribution function that extends to a very low parallel velocity, producing a net current inside the plasma. The effect of IBW's used in conjunction with LHW's can be twofold. On the one hand, IBW's can sustain this current, dissipating its energy on the side of the parallel velocity where the tail already exists due to LHW's. On the other hand, IBW's can modify the distribution function of the electrons and help to fill the LHW gap for very low parallel velocity (high values of $n_\parallel$). In this work, a quasilinear analysis of IBW absorption by the electron population of the plasma is performed, which relies on the analytical calculation of the amplitude of the electric field along the trajectory to obtain the quasilinear diffusion coefficient and the perturbed electron distribution function. The damping of IBW's is also calculated on the tail of the distribution function generated by LHW's, having supposed the filling of the $n_\parallel$ gap. This calculation assumes particular relevance bearing in mind the IBW/LHW experiments on the Princeton Beta Experiment-Modified (PBX-M) [5] machine, which are directed at demonstrating the synergy between IBW's and LHW's.

II. THE AMPLITUDE TRANSPORT EQUATION

The WKB analysis of wave propagation in the context of the geometric optics approximation leads to a set of ordinary differential equations for the position $\mathbf{r}$, the wave vector $\mathbf{k}$, time t and frequency ω, which are, formally, the classical Hamilton equations for position and momentum. At the successive order in the WKB expansion, an equation for the slowly varying amplitude of the electric field can be deduced that satisfies the Poynting theorem. This equation, in the electrostatic approximation, can be written as follows:

$$\frac{d|\Phi|^2}{dt} = -|\Phi|^2 \frac{dln\,(\partial H^{Re}/\partial\omega)}{dt} - |\Phi|^2 \nabla \cdot V_g - 2\gamma(|\Phi|^2)|\Phi|^2 \qquad (1)$$

where Φ is the amplitude of the electrostatic potential; $V_g = -\dfrac{\partial H^{Re}/\partial k}{\partial H^{Re}/\partial\omega}$ is the group velocity of the wave packet; $\gamma = -\dfrac{H^{Im}}{\partial H^{Re}/\partial\omega}$ is the wave damping rate, which, in the quasilinear regime, is a function of the electric field itself; H^{Re} is the IBW electrostatic dispersion relation; and HIm is the anti-Hermitian part of the dispersion relation.

If we suppose very small wave damping compared to the other terms of the amplitude transport equation, the evolution of the amplitude of the electrostatic potential is obtained by simple integration of Eq. (1) along the ray trajectory. We obtain:

$$\Phi^2(x) \approx \left(\frac{T_i(a)}{T_i(x)}\right)^{1/2}\left(\frac{1+\varepsilon}{1+\varepsilon x}\right)\frac{1}{x^2}\Phi_0^2(n_{\|0}) \qquad (2)$$

where $T_i(x)$ is the ion temperature, $\varepsilon = a/R_0$ is the inverse aspect ratio, x is the normalized radial vaiable and $\Phi_0(n_{\|0})$ is the Fourier component of the amplitude of the electric field at the antenna. The parallel component of the electric field, which must be used in the calculation of the quasilinear diffusion coefficient, is obtained by calculating the gradient of the electrostatic potential in the parallel direction:

$$E_{\|}^2(x,\, n_{\|0}) = \frac{n_{\|}^2(x)}{n_{\|0}^2}\left(\frac{T_i(a)}{T_i(x)}\right)^{1/2}\left(\frac{1+\varepsilon}{1+\varepsilon x}\right)\frac{1}{x^2}E_0^2(n_{\|0}) \qquad (3)$$

Knowing the evolution of the electric field inside the plasma allows us to calculate the quasilinear diffusion coefficient everywhere in the plasma and, consequently, the distribution function for the electrons as a function of the parallel velocity.

II. THE DAMPING OF IBW's IN THE PRESENCE OF A LHW-TAIL

It is possible to calculate the damping of the IBW on the distribution function tail generated by a high-power LHW. This is a typical experimental situation of PBX-*M* [5] where about 400 kW of LHW power is coupled to the plasma in current drive regime. Successively, a shorter IBW pulse at lower power level (around 100 kW) is coupled to the plasma for $6<n_{\|0}<10$, simultaneously with the LHW. The question is to establish whether the power launched by the IBW could be absorbed by the electrons present in the tail generated by the LHW, whose spectrum, inside the plasma, extends from $n_{\|0}=1.8$ to 8 (filling of the $n_{\|}$-gap).

The spatial damping is given by

$$\Gamma(x) = -\frac{2}{\delta_0}\int_1^x \frac{\gamma(x,\, \Phi^2)}{V_{gx}}\,dx \qquad (4)$$

where $\delta_0=\omega/ca$, and

$$\gamma(x,\, \Phi^2) = \frac{H^{Im}}{\partial H^{Re}/\partial\omega} = -\frac{\pi}{\partial I^{Re}/\partial\omega}\frac{\omega_{pe}^2(x)}{V_{the}^2(x)}\left(\frac{df_e(u)}{du}\right)_{u=c/n_{\|}v_{the}} \qquad (5)$$

where, $f_e(x,u)$ is the distribution function of the electrons in the parallel direction. The derivative of the distribution function is

$$\left(\frac{df_e(u)}{du}\right)_{u=c/n_\parallel v_{the}} = -\frac{C_o c}{n_\parallel v_{the}}\left\{\frac{1}{2}+\frac{2}{3}\left(\frac{c}{n_\parallel v_{the}}\right)^2\left|D_{LHW}(x)+D_{IBW}(x)\right|\right\}^{-a-1} \tag{6}$$

where C_0 is determined by imposing the boundary condition on the distribution function, which, outside the interval of resonant velocity, is the usual Maxwellian function; a is given by

$$a = \left(\frac{3}{4[D_{LHW}(x)+D_{IBW}(x)]}\right) \tag{7}$$

and

$$D_{IBW}(x) = \frac{\pi}{\omega}\left(\frac{e}{m_e}\right)^2\frac{c}{v_{the}}E_\parallel^2(x,n_{\parallel 0})\left(\frac{1}{v_0 v_{the}^2}\right) \tag{8}$$

$$D_{LHW}(x) = \frac{\pi}{\omega}\left(\frac{e}{m_e}\right)^2\left(\frac{c}{v_{the}}\right)\frac{(n_e(a)/n_e(0))^{1/2}}{xn^{1/2}(x)}E_0^2(n_{\parallel 0})\left(\frac{1}{v_0 v_{the}^2}\right)$$

are, respectively, the normalized (with respect to the electron-electron collisions, ν_0 is the collision frequency) quasilinear diffusion coefficients for IBW's and LHW's.

The IBW power decrement $\exp(\Gamma(x))$ was obtained by integration of Eq. (4).

A plot of IBW power decrement is given in Fig. (1) for plasma parameters typical of the PBX-M machine when a LHW flattens the distrbution function in a wide range of parallel velocity (solid curve). On the same plot, we also show the power decrement obtained when we can neglect the effect of D_{LHW} and D_{IBW} (dashed curve). In this case, the distribution function is Maxwellian and we consider a linear damping. Obviously, owing to the tail generated in the resonant velocity interval by the LHW, the absorption of the IBW in this interval of velocity is amplified with respect to the Maxwellian case.

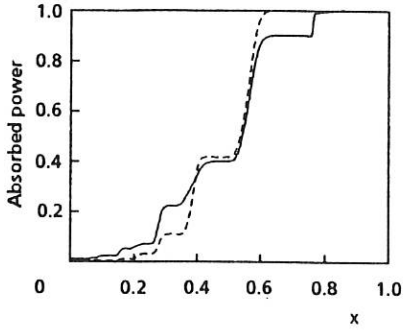


Fig. 1 Absorbed IBW power $\exp(\Gamma)$ vs x in the case of the Maxwellian distribution function (linear damping) (solid line) and modified distribution function ($D_{LHW} \geq 1$) (dashed line).

In this example, we have shown that IBW's can be absorbed by the electrons on the tail generated by a previous application of the lower hybrid wave. The electrons due to the IBW electric field would undergo a further acceleration and increase the current drive.

III-CONCLUSIONS

A quasilinear analysis of the absorption of the IBW by the electron species has been analytically developed. The parallel electric field, the diffusion coefficient and the distortion of the distribution function caused by the strong electric field present in the plasma have been analytically determined. This method has been applied to analyze the combined effects of lower hybrid and ion Bernstein waves in a typical experimental situation for the PBX-M tokamak

FOOTNOTE AND REFERENCES

+Princeton University, Plasma Physics Laboratory, Forrestal Campus, P.O. Box 451, Princeton, New Jersey 08543

*Massachusetts Institute of Technology, 77 Massachusetts Avenue, Cambridge, Massachussets 02139

[1] M. Ono; Phys. of Fluids B 5, 241 (1993)
[2] A. Cardinali, F. Romanelli; Phys. of Fluids B 4, 504 (1992)
[3] A. Cardinali; Phys. of Fluids B 5, 2778 (1993)
[4] A. Cardinali, S. Bernabei, D. Ignat, D. Lee, M. Ono, F. Paoletti, E. Valeo, and PBX-M group, 35th Annual Meeting, APS Division of Plasma Physics, St. Louis, Mo, November 1993.
[5] W. Tighe, R. Bell, S. Bernabei, A. Cardinali, T. K. Chu, S. Jones, R. Kaita, B. Leblanc, M. Ono, F. Paoletti, G. Petrovich, H. Takahashi, S. Von Goeler, A. Post Zwicker, and PBX-M group, 35th Annual Meeting, APS Division of Plasma Physics, St. Louis, Mo, November 1993.

OBSERVATION OF PLASMA EXPULSION FROM A POWERED SCREENLESS ICRF ANTENNA.

R. Van Nieuwenhove *, R. Koch, G. Van Oost

Laboratoire de Physique des Plasmas - Laboratorium voor Plasmafysica
Association "Euratom-Belgian State"
Ecole Royale Militaire - Koninklijke Militaire School 1040 Brussels - Belgium
* Researcher at NFSR Belgium

Abstract

Langmuir probe measurments have been performed for the first time inside an ICRF antenna without Faraday screen. It is found that upon RF switch-on, the low density plasma between the antenna protection limiters is promptly pushed out of this region, even at very low RF power (order 1 kW). An order of magnitude estimate indicates that this effect could be attributed to the ponderomotive force linked to the large parallel electric fields close to the antenna. The consequences of this result with respect to screenless antenna design are discussed.

1) Introduction

A crucial criterium to operate a screenless ICRF antenna succesfully [1,2] is to keep the plasma density at the central conductor below a critical density as derived by RF sheath theories. Our previous estimates [1,2,3] showed that for our present antenna design and typical TEXTOR parameters, this criterium was indeed fulfilled. These estimates depend however very critically on the perpendicular diffusion constant in front of the antenna. This diffusion constant is in general not known very accurately, especially not in RF heated discharges. Moreover, convective cells induced by sheath rectified potentials [4,5] could significantly increase the transport in front of the antenna and thus could enhance the plasma density at the central conductor. Therefore reliable measurements of the plasma density at the level of the central conductor were urgently needed, not only to investigate the above mentioned physical problems but also to establish more detailed and reliable criteria for the design of screenless ICRF antennas.

2) Experimental set-up.

A rectangular stainless steel probe with dimensions 1 mm (radial) times 10 mm (poloidal) and surrounded by a boron nitride insulator was installed 1 cm below the level of the protection limiters in one of the antenna boxes of an unshielded ICRH antenna pair (Fig.1), poloidally 3 cm away from the graphite protection plates in front of the antenna feeder. The probe was connected via a thermocoax cable and low pass filter (to block the RF component induced by the ICRF antenna) to the usual probe electronics and data acquisition. In the experiments, the probe was operated as a single Langmuir probe and the probe voltage was swept between -60 V and +60 V at a frequency of 20 Hz. Due to the low density at the probe location, the ion saturation current is too small (comparable to the noise level) to be usable. Therefore, the amplitude of the electron saturation current was used as a rough indication of the relative changes of the electron density.

3) Experiments :

3.a) Ohmic phase

A typical example of the current - voltage (I-V) probe characteristic for the Ohmic phase is shown in Fig.2. In this figure, several sweeps, corresponding to a phase without RF (0.5 - 0.7 s on Fig.4), are overlayed. As discussed before, the level of the ion saturation current I_{ii}

is comparable to the noise level, whereas the current on the electron branch attains a significant (order 30 mA) level. The electron density profile (as measured by a thermal Li-beam diagnostic) for this shot is shown in Fig.3. From this, one obtains a density of 2.4 10^{11} cm^{-3} at the level of the antenna protection limiters (r = 48 cm). Using the decay length of 3.5 mm mentioned in [1,2], one can deduce a density at the probe radius of 1.8 10^{10} cm^{-3}. The corresponding expected values of I_{sI} and I_{sE} are respectively 0.7 mA and 42 mA , and are in reasonable agreement with the measured values.

3.b) RF heated phase :

An example of a discharge in which the RF power was ramped up to 50 kW is shown in Fig.4. One can notice that the probe current drops to zero (noise level) as soon as the RF is switched on.

To determine at which RF power level this effect becomes important the RF power was ramped up to only 9 kW and then ramped down again (see Fig.5). During the ramp-up phase, neutral beam injection was applied in conjunction. From the ramp-down phase one can observe a substantial decrease of the probe current signal already for an RF power level of less than 1 kW. The signal drops completely to zero at about 5 kW. From the similarity of the edge density profiles (Li-beam) during the Ohmic and RF phase (Fig.3) one can conclude that the ponderomotive force (see Sect. 4) acts only very locally (i.e. in the immediate vicinity of the ICRF antenna), as expected.

From the ramp-up phase, one can deduce an increase of the electron density during the neutral injection phase, as compared to the pure RF phase (ramp-down phase). This can be attributed to an overall increase of the edge density during the NBI phase ; n_e at the antenna limiter radius ($r \simeq 48\ cm$) increased from 1.2 10^{11} cm^{-3} to 6 10^{11} cm^{-3}. During this phase I_{sI} becomes comparable to I_{sE}. This might be due to a significant increase in the ion to electron temperature ratio. At higher RF power levels ($\geq$ 50 kW), the low density plasma inside the antenna box is completely pushed away, even in the presence of high power NBI.

4) Interpretation of the results

These results can best be understood in terms of the ponderomotive force [6] on the plasma induced by the strong gradients of the RF parallel electric fields inside the antenna box between the antenna central conductor and the protection limiters. An elegant way to describe this effect is by means of the ponderomotive potential $\Psi = \frac{e E_z^2}{2 m_e \omega^2}$, where E_z is the rms value of the parallel RF electric field, e is the electron charge, ω is the angular frequency of the RF field and Ψ is expressed in V. In our particular case, the ponderomotive force (on the electrons) $F_p = -\nabla e n_e \Psi$ is radially inward (away from the antenna). The voltage at the antenna feeder, for the present antenna configuration, is given by $U_f[kV] = 0.5 \sqrt{P_{RF}[kW]}$. Using transmission line theory, one finds that the voltage at the position of the probe is given by 0.74 $\times$ U_f. The parallel electric field E_z is thus given by $E_z[V/m] = 0.74 \times 0.5\ 10^3 \sqrt{P_{RF}[kW]} / d$, where d (6.5 cm) is the separation between the edge of the antenna central conductor and the antenna limiter. Inserting the estimate for E_z into the expression for Ψ, one obtains $\Psi\ [V] = 50\ P_{RF}[kW]$. The ponderomotive effect will become important when Ψ is of the same order as T_e (expressed in Volt). Assuming $T_e \simeq 10eV$, one finds the required RF power to push away most of the electrons to be 0.2 kW, which is within an order of magnitude consistent with the measurement. One should of course also keep in mind here that the precision of the RF power measurement is certainly not better than 1 KW.

5) Conclusions

From Langmuir probe measurements it is found that the low density plasma inside the antenna box of an unshielded antenna is completely pushed out of this region by the ponderomotive force. Due to this effect, the screenless antenna can be operated at much higher densities as one would expect from simply taking into account cross field diffusion alone, as was done in Ref.1,2. This was indeed recently confirmed on TEXTOR, where it was demonstrated that the screenless antenna still works properly [7] at the maximum line-averaged density (7.5 10^{13} cm^{-3}) presently attainable on TEXTOR. Alternatively, for a given plasma density, one could allow for a larger width of the antenna box.
These results strengthen the case of a reactor relevant screenless ICRF antenna concept.

References

1. R. Van Nieuwenhove, R. Koch, G. Van Oost, Rep. No. 93, LPP-ERM/KMS, Brussels (1990)
2. R. Van Nieuwenhove, R. Koch, G. Van Oost, et al., Nuclear Fusion 31 (1991), 1790
3. R. Van Nieuwenhove, R. Koch, G. Van Oost, et al., Nuclear Fusion 32 (1992), 1913
4. G.R. Tynan, J.A. Boedo, D.S. Gray, et al., Journal of Nuclear Materials 196-198 (1992) 770
5. D. Bora, R.S. Ivanov, G. Van Oost, et al., Nuclear Fusion 31 (1991) 2383.
6. J.W. Schearer, J.L. Eddleman, Physics of Fluids, 16 (1973), 1753
7. A.M. Messiaen, J. Ongena, U. Samm, et al., to be published in Nuclear Fusion (1994)

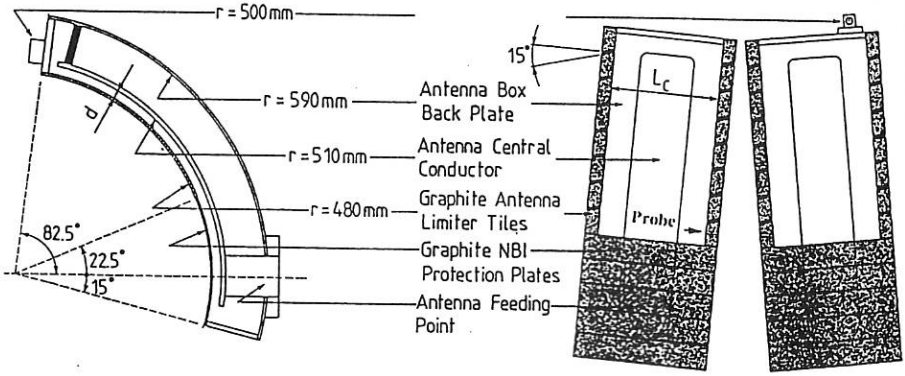


Fig.1 : Schematic view of a screenless ICRH antenna in which the position of the probe is indicated

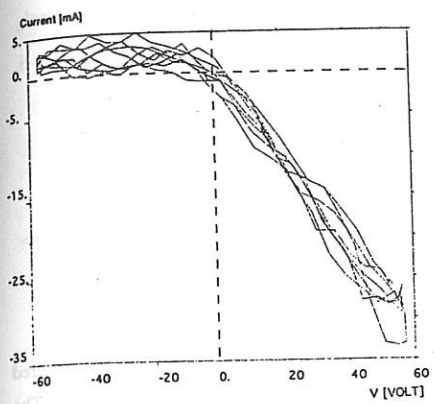


Fig.2 : Current voltage characteristic (from t =0.5 s to t=0.7 s ; see Fig.4) of the Langmuir probe inside the screenless antenna in the Ohmic phase. The plasma conditions were ; $\overline{n_e}$ = 1.9 10^{13} cm^{-3}, I_p = 360 kA, B_T = 2.25 T, #50382. The ICRH generator frequency was 38 MHz.

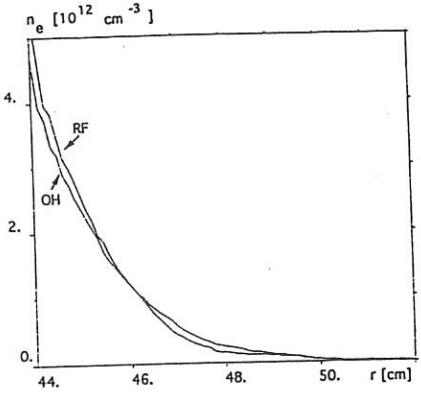


Fig.3 : Edge density profiles in the Ohmic (at t=0.7 s ; curve a) and in the RF (50 kW) heated phase (at t=1.25 s ; curve b) for the same shot as in Fig.2 and 4.

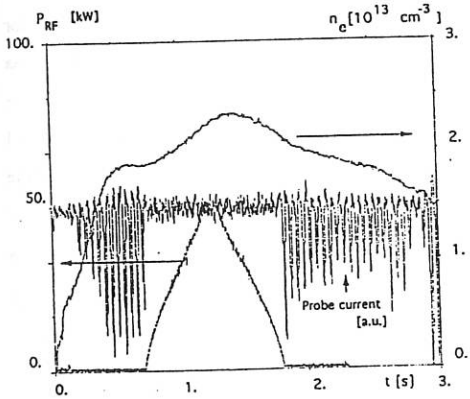


Fig.4 : Time evolution of the probe current, the line-averaged density and the RF power (ramped from 0 to 50 kW) for the shot of Fig.2.

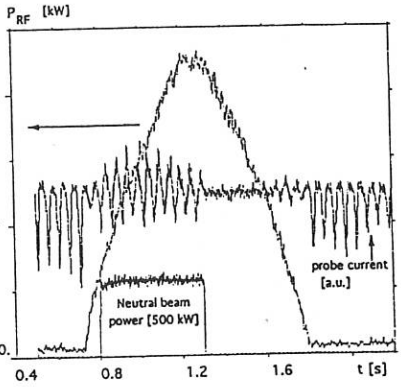


Fig.5 : Time evolution of the probe current, neutral injection power (He^3 co-injection) and the RF power (ramped from 0 to 9 kW). The plasma conditions are similar to those of Fig.4, #50384

A STUDY OF ANTENNA COUPLING DURING ICRF PLASMA BUILD-UP

V.E.Moiseenko, S.V.Kasilov, A.I.Lysoivan, V.V.Plyusnin

Institute of Plasma Physics, National Science Center "Kharkov Institute of Physics and Technology", Kharkov 310108, Ukraine

INTRODUCTION. A method of plasma build-up in ICRF has an obvious advantage compared to ECRH consisting in the possibility of operation in wide range of steady magnetic field values. The majority of experiments show that low density plasma ($n_e = 10^{12} \div 10^{13}$ cm^{-3}) can be easily produced in ICRF. The more dense plasma ($n_e = 3 \cdot 10^{13}$ cm^{-3}) has been recently obtained in the experiments on URAGAN-3M torsatron [1] using Three-Half-Turn (THT) antenna [2]. This antenna needs in initial plasma with the density order of $\cdot 10^{12}$ cm^{-3}. Therefore, a long antenna of frame type has been used for start-up plasma production in these experiments. It cannot produce dense plasma alone because its efficiency was sufficiently reduced at high density values.

In order to produce dense plasma using a single antenna, the antenna of a new crankshaft type is analized in the present paper by means of 1D numerical code.

1D CODE. 1D code solves using finite elements technique a boundary-value problem for Maxwell equations in the model of nonuniform plasma cylinder with identical ends. The plasma dielectric tensor taking into account collisional energy dissipation as well as electron Landau damping was used. Ion gyroradius was assumed to be zero. Therefore, the excitation, propagation and mutual conversion of the slow and fast waves are correctly described in the framework of the model, while kinetic ion-cyclotron waves (IBW) are neglected. Antennas are modeled as external currents which meet a condition $\mathrm{div}\,\vec{j} = 0$. The parameters of calculations are choosen to be close to those ones in URAGAN-3M experiments. The wall radius is 20cm, plasma radius is 12cm, major torus radius is 100cm, antenna radial position is 14cm, electron temperature is 30eV, toroidal magnetic field is 0.47T, heating frequency is $3.6\ 10^7$ s^{-1}. Plasma density profile is assumed as parabolic in the plasma core and falling with exponential rate near plasma boundary. The character exponentiation length is 1 cm. The parameter under analysis was the ratio of antenna loading resistance R_{pl} to plasma average density n_e in the whole range of densities (10^6 cm$^{-3} < n_e < 10^{14}$ cm^{-3}). This parameter is directly linked to the

plasma production (ionization) rate. The average radius of power deposition $\bar{r} = \int_V d^3r \cdot p_{RF} \cdot r \,/\, \int_V d^3r \cdot p_{RF}$ is also considered.

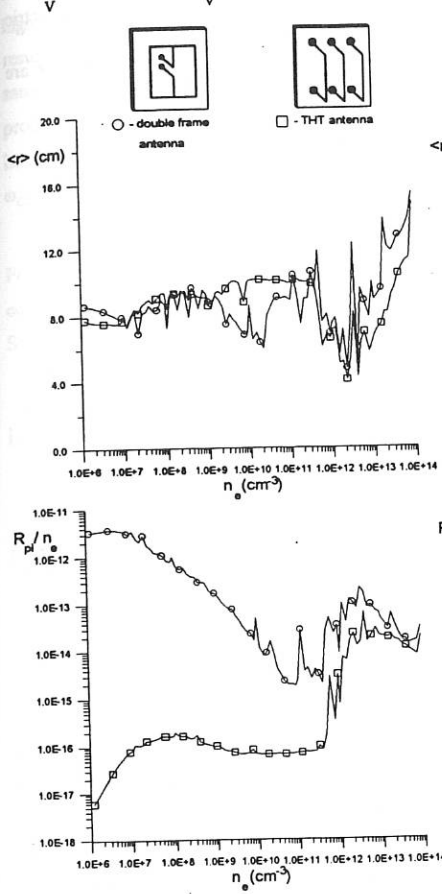


Fig.1. The dependense of average radius of power deposition (upper chart) and R_{pl}/n_e parameter (lower chart) versus plasma density for double frame (70×23 cm) and THT (24×40 cm) antennas.

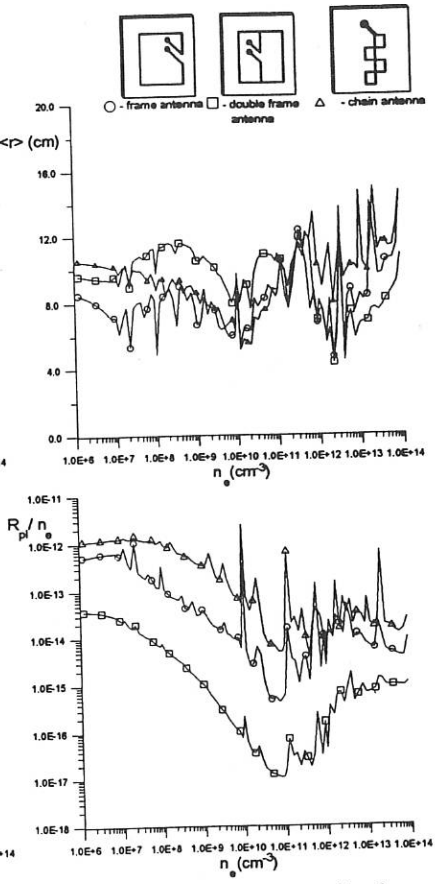


Fig.2. The dependense of average radius of power deposition (upper chart) and R_{pl}/n_e parameter for frame (2×40 cm), double frame (4×40 cm) and chain (4×40 cm) antennas.

DISCUSSION OF THE RESULTS OF CALCULATIONS. Fig.1 illustrates the properties of the long frame and THT antennas currently used in URAGAN-3M experiments. It shows that the density limitation of long-frame antenna is caused by the degradation of power deposition profile [1]. Power deposition profile for THT antenna at the densities order of 10^{13} cm^{-3} is rather good. Newertheless R_{pl}/n_e values for this antenna at low densities are too low what actually prohibits gas breakdown. This results from the very poor excitation of slow wave by THT antenna, because for the

efficient excitation of slow wave parallel external currents are required. R_{pl}/n_e rapidly increases starting from the plasma densities order of 10^{10} cm^{-3} which correspond to a rise of local Alfven resonaces for the first longitudinal modes obeying the equation $\frac{\omega^2}{c^2}\varepsilon_\perp R^2 \approx$ (here $\varepsilon_\perp$ is the dielectric tensor transverse diagonal component, R is torus major radius). The local Alfven resonances are responsible for fast wave energy coupling.

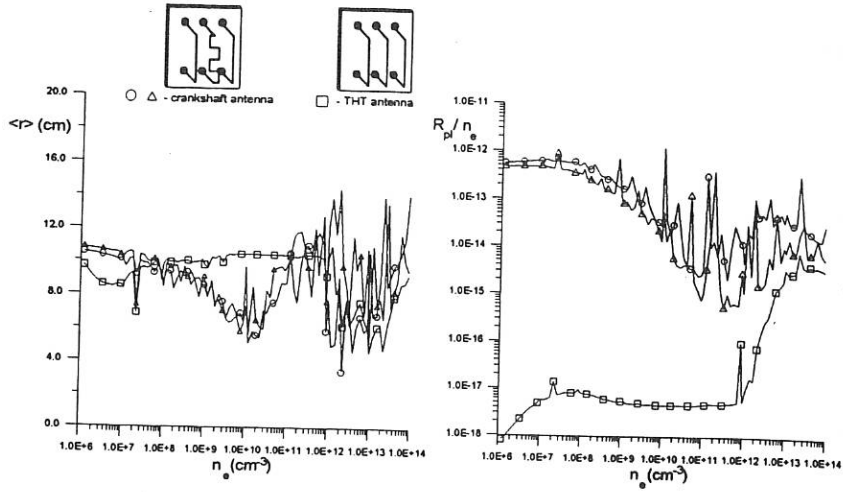


Fig.3. The dependence of average radius of power deposition (left chart) and R_{pl}/n_e parameter (right chart) versus plasma density for crankshaft antenna (24×40 cm, crankshaft amplitude - 2cm) circles - ω_{ci}=0.8, triangles - ω/ω_{ci}=0.6,.and THT antenna at ω/ω_{ci}=0.6 (squares).

The value of R_{pl}/n_e for the frame type antenna is normally higher than required for plasma production in the low density region. So the addition of small-size frame type currents to THT antenna should make it capable to perform gas breakdown. This addition is desirable not to deteriorate THT properties at high densities. Fig.2 demonstrates the behavior of R_{pl}/n_e parameter versus plasma density for the frame antennas with small parallel length (4cm). The curves have obvious minimum at $n_e \approx 10^{10} \div 10^{11}$ cm^{-3} . This minimum is a result of excitation of long wavelength electromagnetic modes, which makes worse power deposition profile at high densities. The situation can be improved by the shift of longitudinal currents poloidal spectrum to the higher wavenumbers. This allows to enhance the excitation of slow wave.and in the same time decrease the excitation of electromagnetic wave. This can be realized using a chain of frames stretching in poloidal direction. Fig. 2 shows its properties. Obviously it is more preferable as an addition to THT antenna.

If the chain of frames is displaced along the central strap of THT antenna, the combination results in the turn of straight poloidal current to the one with the shape of crankshaft. Therefore, a new

combined (crankshaft) antenna is a modification of THT antenna. Its properties are displayed in Fig.3. From this figure follows that the dependence of R_{pl}/n_e meets all criteria for plasma production. At high densities its properties do not differ significantly from those ones of THT antenna, what is the result of weak influence of central strap crankshaft shaping on fast wave modes excitation. At the same time energy deposition at low plasma densities is improved what makes possible dense plasma production by this antenna alone. The attainment of higher densities is possible with the decrease of heating frequency. In Fig.3 provides the comparison of THT and crankshaft antennas properties at $\omega/\omega_{ci}=0.8$ and $\omega/\omega_{ci}=0.6$.

ACKNOWLEDGMENTS The present report was supported in part by International Science Foundation contract No. U32000 and the Ukrainian State Committee for Science and Technology contract No. 9.02.02/094-93. The presentation of this report was made possible by International Science Foundation (grant No.1590.8).

REFERENCES

[1] S.V.Kasilov, A.I.Lysoivan, V.E.Moiseenko, V.V.Plyusnin, IAEA Technical Committee Meeting on Stellarators and Other Helical Confinement Systems (Garching, Germany, 10-14 May,1993), IAEA, Vienna, 1993, P.447.

[2] V.E.Moiseenko, IAEA Technical Committee Meeting VIII Stellarator Workshop (Kharkov, USSR, 27-31 May,1991) P.207.

ICRF Antenna Coupling and Fast Alpha Heating Models for Fusion Plasmas*

I.E. Scharer, M. Bettenhausen, N.T. Lam, and R.S. Sund

Electrical and Computer Engineering Department
University of Wisconsin, Madison, WI, USA

Abstract

Analysis and computer simulation[1] is presented for coupling Ion Cyclotron Range of Frequency (ICRF) waves to tokamak plasmas using phased coil antenna arrays. The model accounts for 3-D antenna and feeder current effects, an antenna cavity which is finite in all three dimensions and warm plasma effects. The effect of the coupled power spectrum and radiation resistance on heating and current drive performance for the possible current drive applications on TFTR and ITER are considered. The model includes parallel electric fields and Faraday shield angle for consideration of slow or ion Bernstein mode excitation as well as fast wave coupling. Radiation resistance and spectrum results from the model are presented and compared to TFTR experimental data. The influence of the edge density gradients and profiles is examined for supershot H- and L-mode regimes. We also consider the problem of fundamental deuterium heating and current drive for ITER and second harmonic tritium heating for TFTR plasmas, in the presence of a population of fast alpha particles. For the fundamental deuterium case we calculate the non-Maxwellian reactivity due to ICRF heating[2] and obtain peak fast alpha slowing down concentrations of 0.1-0.8% n_e modeled by an absorption equivalent Maxwellian of T_α = 600-1000 keV. The absorption and reflection coefficients for the fast wave are calculated using XWAVE[3], a code which treats full wave and profile effects by means of a fundamental definition of power conservation. We find that under appropriate conditions, the presence of the two-ion (D-T) hybrid resonance can give rise to a substantial enhancement of the local fast alpha particle absorbed power density (P_α = 20-80% P_{inc}). We consider profile effects and the off-axis heating as well as the on-axis ω_{DT} resonance for fast alpha particle current drive in ITER. We also consider the influence of alpha particle heating for TFTR $2\omega_{CT}$ supershot heating scenarios.

I. Description of the Antenna Model and Results. The model presented here is an extension to the models developed by Brambilla[4] and Chiu et al[5]. The model incorporates a finite length antenna in a three-dimensional recessed cavity and includes parallel electric field and warm plasma effects. A rectangular coordinate system is assumed with x, y and z corresponding to the radial, poloidal and toroidal directions. Figure 1 shows the geometry used and defines various parameters.

The electric fields excited by the assumed antenna current distribution are calculated by solving Maxwell's equations in four separate regions: in the plasma, x > 0, and in the three vacuum regions as labeled in Fig. 1. Boundary

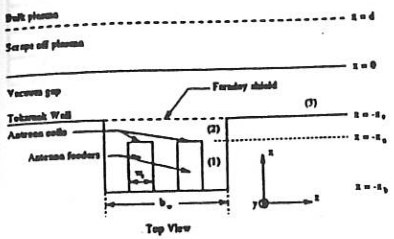


Figure 1. Antenna model geometry

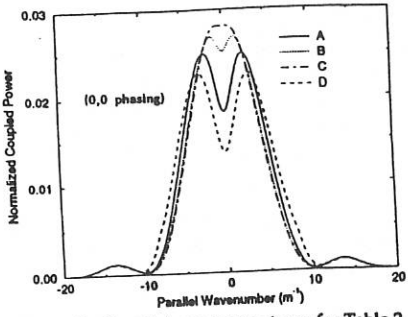


Figure 2. Coupled power spectrum for Table 2 cases.

conditions are applied between adjacent regions to produce a unique solution. The plasma wave fields are calculated using the model developed by Brambilla[4]. These results are used to calculate a plasma surface impedance relating the electric and magnetic fields at the vacuum-plasma interface.

The boundary conditions at the Faraday shield assume that the shield acts as a perfect conductor parallel to the shield bars and as a perfect insulator perpendicular to the bars. A jump condition is applied at the antenna current elements . Finally, E_y and E_z are continuous at the antenna.

The computer code WICS[1] (Wisconsin Ion Cyclotron Coupling Solver) is used to calculate the antenna radiation resistance and parallel wavenumber spectrum of the coupled power based on the model discussed above.

Table 1 shows the TFTR machine and Bay M parameters. Table 2 shows the variation of the calculated radiation resistance for the TFTR Bay M as the poloidal current distribution on the antenna is changed. The results shown are for in-phase excitation of the current coils and all parameters not specified in Table 3 are as given in Table 2. In Table 2 the column heading R_A is the per-strap radiation resistance, ck^*/ω is the ratio of the speed of light to the poloidal phase velocity of the current on the antenna coils, b_h/h is the ratio of the antenna cavity height to the antenna coil half-height and $R_A/2h$ is the radiation resistance per coil per one meter antenna length. Finally, the feeder type is either center-fed with end shorts or end-fed with a single end

$R = 261$ cm	$B_0 = 4.2T$	$x_b = 16.5$ cm	$w_s = 10.0$ cm
$h = 38.0$ cm	$n_0 = 5 \times 10^{19}$ m^{-3}	$\alpha_n = 0.5$	$L_n = 1$ cm
$T_0 = 10.0$ keV	$\alpha_T = 1.0$	$\alpha = r_v = 96$ cm	$f = 43$ MHz
$x_a = 3.8$ cm	$\Delta_s = 33.7$ cm	$ck^*/\omega = 0.5$	$n_{sep} = 5 \times 10^{18}$ m^{-3}
$\beta_n = 2.0$	$L_T = 3.0$	$T_{sep} = 0.5$ keV	$\beta_T = 2.0$

Table 1. TFTR machine and ICRF antenna (Bay M) parameters.

Feeder Type	ck^*/ω	R_A (Ω)	b_h (cm)	b_h/h	$R_A/2h$ (Ω/m)	Fig label
center	1.5	3.8	80	2.1	5.0	A
center	0.1	4.2	80	2.1	5.5	
center	0.1	12.6	240	2.1	5.5	B
center	0.1	25.5	480	2.1	5.6	C
center	0.1	20.3	480	4.2	8.9	
end	1.5	3.5	80	2.1	4.6	D

Table 2. Variation of radiation resistance with antenna and cavity height and current distribution.

$k_\parallel$ (m^{-1})	D(%)	α(%)	e(%)	R(%)
4	27.0	26.1	29.0	17.8
6	44.3	26.9	22.1	7.1
8	60.8	18.8	16.6	3.9
10	73.6	11.3	12.5	1.9

Table 3. Fraction of incident power absorbed by each species

short. The end-fed case has a lower average current and greater poloidal variation. Therefore, the end fed case has a lower radiation resistance.

II. ICRF Heating and Applications to ITER and TFTR. We consider the effects of a small concentration of alpha particles on ICRF wave propagation and absorption for an ITER plasma near the fundamental deuterium cyclotron resonance. We then consider the cases of second harmonic tritium for the TFTR supershots. For the fundamental regimes we utilize the XWAVE[3] code which includes profile effects, perpendicular gradients in the magnetic field and second order gyroradius effects for cases where $(k_\perp \rho_{\alpha t})^2 << 1$.

We consider the case of fundamental deuterium and alpha particle heating in a tritium plasma with ITER parameters. We assume the plasma to have $n_e = 9 \times 10^{13}/cm^3$, B=4.85 T, R_0=6 m, n_D/n_T=0.5, $T_e=T_T$=15 keV a self-consistent deuterium temperature of 15-25 keV with corresponding fast alpha particle concentrations of $n_{\alpha f}$=0.1-0.8% n_e. The two ion hybrid resonance lies at x=-0.7 m towards the high field side from the fundamental resonance on the axis. The corresponding left-hand circularly polarized component peaks in a localized region near the two ion hybrid resonance. The Maxwellian equivalent alpha particle distribution is chosen to have the same number of resonant particles in this region as the slowing down distribution. The $|E_{left}|$ peak extends over a comparatively narrow interval near the two-ion hybrid resonance, and most of the power that goes to the alphas is absorbed in that narrow region. Consequently, we choose the number of resonant particles at x_p, the location of the $|E_{left}|$ peak, to be the basis of equivalency between two distributions.

Table 3 shows the total power absorption and reflection for each species as a function of $k_\parallel$ for the case of the lowest temperature plasmas noted above. Note that a substantial fraction of the incident power can be absorbed by the fast alphas when the absorption by the deuterium and electrons is not complete. Figure 3 shows the total absorbed power density over the region where it is significant. We have also examined the current TFTR $2f_{cT}$ D-T heating experiments and find that a small fraction (5%) of the ICRF power can be coupled to the alphas near n_z^2=S.

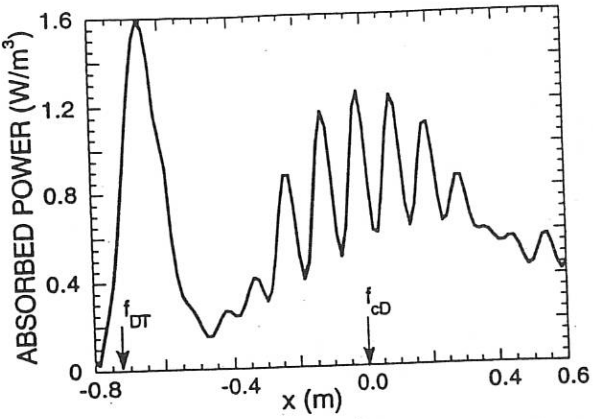


Figure 3. Radial profile of absorption corresponding to $k_{\parallel} = 6\ m^{-1}$.

III. **Summary**. We are developing a "3-D" antenna code for studies of cavity effects and shield alignment for studies of cavity effects and shield alignment for coupling to edge density profiles on TFTR, JET and TPX. The results show significant effects on the antenna spectrum at low and high k_z. The influence of alpha particle absorption on ICRF fundamental deuterium and second harmonic tritium heating can be significant and must be considered for ITER and TFTR supershot scenarios. We are currently examining an alpha particle current drive scheme using this absorption process for advanced confinement, high bootstrap fraction tokamaks.

Acknowledgments. The authors thank D. Batchelor, M. Carter, D. Stallings and R. Majeski for useful discussions and helpful suggestions and for the use of the 2D antenna coupling code RANT for benchmarking our code. We appreciate the assistance of C. Phillips, R. Majeski and R. Wilson in determining the TFTR ICRF experimental parameters.

*Research supported by U.S. DOE Grant Nos. DE-FG02-86ER53218 and DE-FG02-93ER54196.

References

1. M. Bettenhausen and J. Scharer, "An ICRF Antenna Coupling Model with a 3-D Rectangular Cavity," submitted to Nuclear Fusion (1994).
2. N. Lam, J. Scharer and R. Sund, "Influence of Alpha Particle Absorption on Fundamental Deuterium Heating in a Fusion Plasma," to appear in Nuclear Fusion (1994).
3. R.S. Sund and J.E. Scharer, Physics of Fluids B 3, 1326 (1991).
4. M. Brambilla, Nuclear Fusion, 28, 549 (1988).
5. S.C. Chiu et al., Nuclear Fusion, 23, 499 (1983).

RECENT RESULTS FROM THE TFTR ICRF DT PROGRAM

J. H. Rogers, D. Darrow, R. Majeski, M. Murakami,† C. K. Phillips, D. A. Rasmussen,†
G. Schilling, J. Stevens, G. Taylor, J. R. Wilson, K. L. Wong and the TFTR Group

Princeton Plasma Physics Laboratory, Princeton, New Jersey 08543, USA
†Oak Ridge National Laboratory, Oak Ridge, Tennessee 37831, USA

Abstract

The first experiments to be performed with ICRF heating of DT plasmas are reported. ICRF heating of minority ions, tritium (second harmonic resonance), as well as direct electron heating are being performed during the DT phase of TFTR. RF power modulation and Fourier transform techniques are used to attempt to elucidate the competition between tritium second harmonic, direct electron, and ^{3}He fundamental heating in DT plasmas. A significant fraction of the RF power has been found to couple to the tritium ions via second harmonic heating. Relevant RF coupling physics is investigated using ^{3}He minority heating (43 MHz), H minority heating (64 MHz), and mode conversion (43 MHz, comparable densities of ^{3}He and ^{4}He) at a toroidal field of 4.5T.

I. DT Supershots

ICRF on TFTR has the capability of increasing the DT reaction rate by increasing the ion temperature and by directly accelerating the tritium ions via second harmonic resonance heating. Also, ICRF has been shown to be effective at raising the electron temperature[1] which increases the alpha particle slowing down time; the increased alpha pressure will help verify thresholds for alpha instabilities. Initial DT experiments on TFTR which include both ICRF and neutral beam power have all been with an RF frequency of 43 MHz, which is resonant with second harmonic tritium and ^{3}He minority. Many shots had no ^{3}He injected, so the ICRF power was shared between the tritium second harmonic heating and direct electron heating. In order to estimate the fraction of power going to either the tritium or electrons, the ICRF power was modulated during many of the shots. Figure 1 shows the modulated ICRF waveform along with the variation in electron temperature (measured by ECE) and excess perpendicular energy ($\delta W_\perp$-$2\delta W_\parallel$ measured by the magnetics, where modulation of $\delta W_\parallel$ is assumed small) for two different tritium concentrations in which no ^{3}He was added. The variation of the electron temperature (with no phase delay) is characteristic of direct electron heating, while the variation of excess perpendicular energy is characteristic of resonant ion heating. As the number of tritium neutral beams increases, the second harmonic damping on the tritium beam ions increases, and the amount of power going directly to the electrons decreases. In fact, the modulation of the excess perpendicular energy indicates that for high tritium concentrations, about half of the RF power is coupled directly to the tritium ions.

Further evidence of tritium high energy tail formation has been observed with the escaping fast ion probe[2] 45° below the outer midplane of the tokamak. A signal modulated synchronously with the RF is observed on this probe in DT plasmas with no ^{3}He minority (tail ions are usually seen by this probe during ion minority heating). This signal is not due to neutral beam ions, because the probe is only sensitive to ions with energies in excess of 300 keV, and the gyroradius measured is less than those of fusion products. Therefore, it is inferred that the signal is due to accelerated tritium ions.

When unmodulated ICRF was added to DT supershots, the electron temperature, ion temperature, and fusion power were increased. Figure 2 shows a comparison between two shots each with 23 MW of neutral beam power (including 13 MW of tritium neutral beam power) and one in which 5.4 MW of ICRF is added. The recycled gas from the carbon limiters is primarily deuterium, so a net fraction of approximately 30% of the ions are tritium. In this case, a small ^{3}He puff precedes the neutral beam injection, which results in the ^{3}He density of approximately 2% of the electron density. The electron temperature on axis is increased from around 8.5 keV to almost 11 keV by the RF. The ion temperature increases on axis from around 25 keV to 30-35 keV until a carbon bloom develops (probably due to a shift in the

limiter strike point due to the increased stored energy). The neutron flux is increased approximately by 10% before the carbon bloom, reaching a peak fusion power of 3.2 MW.

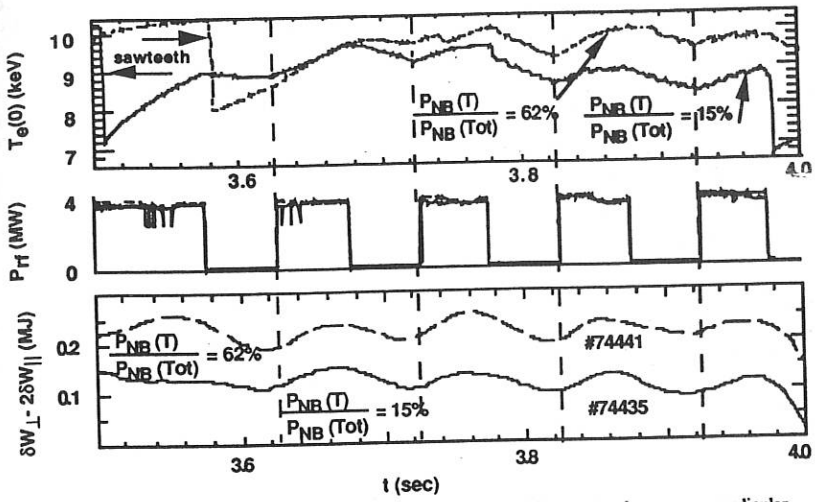


FIG. 1. Time variation of the electron temperature on axis, RF power, and excess perpendicular energy for two shots with different tritium concentrations. The power contained in the tritium beams is 3MW out of 19.5MW in shot #74435 and 11.5MW out of 18.5MW in shot #74441.

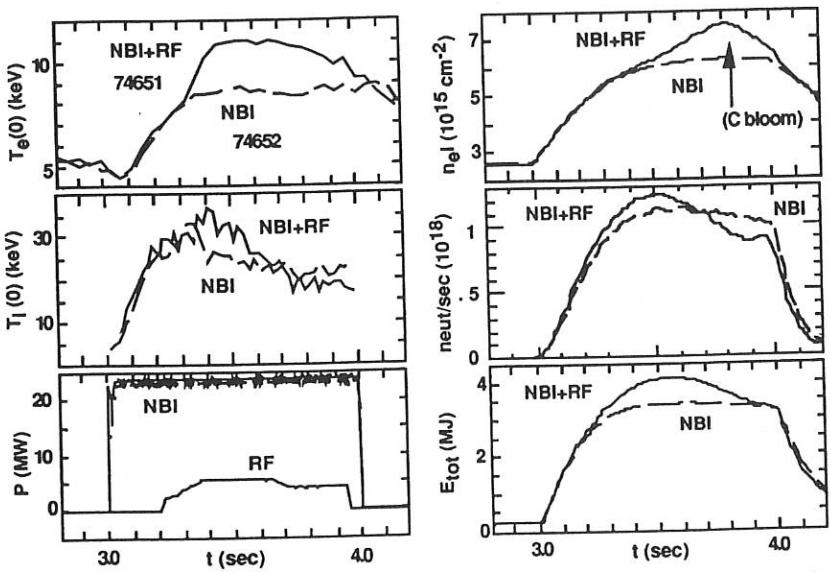


FIG. 2. A comparison of two shots, one with RF (5.4 MW peak) and one without RF. Tritium neutral beams contained 13.5 MW of the 23.5 MW total neutral beam heating. A carbon bloom in the RF shot degraded the performance near the end of the shot.

II. Mode Conversion Current Drive

One method of current drive particularly well suited for ICRF in a DT plasma is mode conversion of the fast wave to an ion Bernstein wave at the ion-ion hybrid resonance between the D and the T cyclotron resonances.[3] Recent experiments in TFTR have successfully tested the capability of this technique to efficiently couple energy to the electrons on or off axis. The experiments were performed in an ohmic plasma with comparable densities of ^{3}He and ^{4}He. In this case, the mode conversion layer is remote from either ion cyclotron resonance layer and ion heating can be avoided.[3] Amplitude modulation of the ICRF power combined with radially resolved ECE measurements are used to determine the power deposition profile for different toroidal fields (i.e. different locations in major radius of the mode conversion layer). Fig. 3a shows the Thomson scattering measurement of the electron temperature profile. With only ohmic heating and 3 MW of ICRF, the central electron temperature was increased to ~ 8 keV. The FWHM of the electron temperature is less than 30 cm, indicating that the electron heating was also very localized. Fig. 3b shows the measured electron absorption profile and the absorption profile calculated by the sixth order 1-D code FELICE[4] for a case in which the mode conversion surface is off axis (B_0=4.4 T, $n_{He\text{-}3}/n_e$=.24, $n_{He\text{-}4}/n_e$=.06, n_D/n_e=.13, n_C/n_e=.045). The small amount of absorption on axis is an indication that the direct electron damping of the fast wave is small compared to the damping due to the mode converted wave (the mode conversion layer is on the high field side of the axis). These results demonstrate that this technique could be a prime candidate for current profile control.

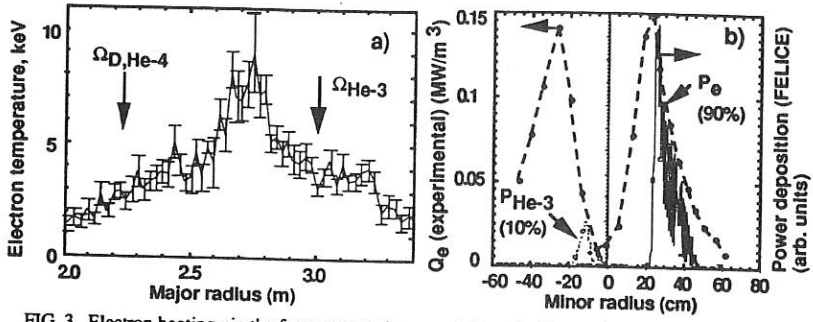


FIG. 3. Electron heating via the fast wave mode converted to a ion Bernstein wave provides localized coupling on or off axis. a) T_e profile with mode conversion layer on axis (3 MW of RF, no neutral beams). b) measured and calculated power deposition profile with mode conversion layer off axis (experimental measurements can not distinguish where on the flux surface the absorption takes place).

III. ICRF coupling to alpha particles

Coupling of the ICRF power to the alpha particles has been observed in the TFTR DT experiments. Fig. 4 shows the signal from the escaping fast ion probe[2] at the bottom of the vessel with a toroidal magnetic field of 4.1 T at the magnetic axis. The observed gyroradius of the alpha particles ejected during the RF implies energies greater than the 3.5 MeV birth energy. When the toroidal magnetic field was raised to 4.2 and 4.5 T, this signal was not present. A possible explanation for the acceleration is doppler broadened fundamental resonance heating of the alphas, i.e. $\omega_{c\alpha} = \omega - k_{\|}v_{\|}$. If this is the mechanism, it is likely that there are still alphas being

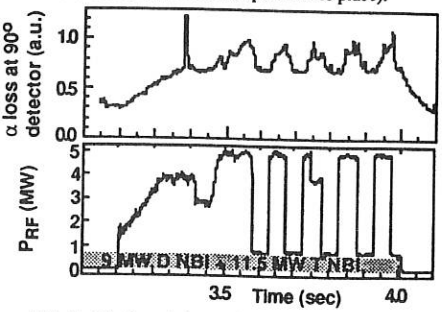


FIG. 4. The lost alpha particle signal and RF power for B_0 = 4.1 T.

accelerated by the ICRF at the higher toroidal magnetic fields, but those alphas which are lost due to the acceleration are no longer striking the wall at the fast ion probe location.

IV. Toroidal Alfven Eigenmodes (TAE)

In a fusion reactor, the energetic alpha particles may drive Toroidal Alfven Eigenmodes (TAE) unstable. TAE modes have been excited in TFTR DT supershots with the aid of an ICRF hydrogen minority. The ICRF power (63.6 MHz, $B_0 = 4.2$ T) was brought up to a level just above the TAE instability threshold (~5 MW) for a deuterium plasma (19.8 MW of neutral beams). Then 14 MW out of a total of 19 MW of neutral beams were supplied by tritium neutral beams, and the TAE signal strength was observed to increase by a large amount. The increase in the signal amplitude could be partially due to the alpha particles present in the DT shot supplying energy to the wave. Unfortunately, the dominant damping of the TAE wave is Landau damping by the beam ions, and because the tritium beam ions are moving at slower velocities than the deuterium beam ions, the damping is reduced in the DT shots. Detailed analysis of this data to determine the relative importance of these two effects is still in progress.

V. Fast Wave Current Drive (FWCD)

Though the current design of ITER relies heavily on FWCD, there have been few experiments demonstrating FWCD, and none in a DT plasma.[5] Recent improvements in the TFTR ICRF hardware have made it possible to launch several megawatts in a toroidally directed ICRF wave. Initial attempts at FWCD on TFTR used 1.5 MW of hydrogen minority heating with 43 MHz ICRF ($B_0 = 2.9$ T) to raise the electron temperature. After 200 ms, when $T_e \sim$ 3.5 keV, an additional 3 MW of 63.6 MHz ICRF was used for FWCD. With the chosen toroidal field, the hydrogen fundamental resonance for 63.6 MHz was inside the plasma near the high field limiter (but the wave polarization is dominantly right handed due to the proximity of the $n_{||}^2 = R$ cutoff, so there is little energy coupled to the H-minority) and the second harmonic hydrogen resonance is approximately 10 cm beyond the low field limiter. Comparisons between +90 degree phasing between the antenna straps and -90 degree phasing are complicated by the fact that the density and electron temperature evolved differently. Early in the pulse, while the electron temperature and density are still similar, the loop voltage was measured to be ~ 50 mV lower when trying to drive co-current than when trying to drive counter-current. This result is consistent with driving ~ 40-100 kA of current.

VI. Future Plans

During the remainder of the TFTR DT run, a number of experiments will make use of the unique capabilities on TFTR. Mode conversion current drive will be attempted in a DT plasma. The effects of ICRF on toroidal plasma rotation, which are of importance to the ITER design, will also be investigated. Future ICRF heating of supershot experiments will include using lithium pellet conditioning to reduce the carbon influx during the shot, and the simultaneous use of hydrogen minority heating and second harmonic tritium heating (64 and 43 MHz, from different antennas). This use of two simultaneous frequencies is expected to result in the maximum ICRF power coupled into TFTR supershots, and the maximum total auxiliary heating (NBI and ICRF) of DT plasmas to ever be performed on TFTR.

Acknowledgments

This work was supported by US Department of Energy contract DE-AC02-76CH03073.

References

[1]G. Taylor, et. al. Phys. Fluids B 5, 2437 (1993).

[2]S. J. Zweben, R. L. Boivin, M. Diesso, S. Hayes, H. W. Hendel, H. Park, J. D. Strachan, Nucl. Fusion 30, 1551 (1990). also, D. S. Darrow, H. W. Herrmann, D. W. Johnson, R. J. Marsala, R. Palladino, S. J. Zweben, and M. Tuszewski, accepted for publication in Rev. Sci. Instrum.

[3]R. Majeski, C. K. Phillips, J. R. Wilson, submitted to Phys. Rev. Lett.

[4]M. Brambilla, Nucl. Fusion 28, 549 (1988).

[5]R. I. Pinsker, *Radio Frequency Power in Plasmas: 10th Topical Conf., Boston, MA 1993* (AIP New York, 1994) p. 179 and errata.

ICRF EXPERIMENTS IN THE ALCATOR C-MOD TOKAMAK

S. N. Golovato, M. Porkolab, Y. Takase, R. Boivin,
P. Bonoli, F. Bombarda†, C. Fiore, J. Goetz, R. Granetz,
M. Greenwald, S. Horne, A. Hubbard, I. Hutchinson, J. Irby,
B. LaBombard, B. Lipschultz, E. Marmar, G. McCracken,
J. Rice, J. Snipes, J. Terry, S. Wolfe, B. Welch†,
C. Christensen, D. Garnier, M. Graf, T. Hsu, D. Jablonski,
C. Kurz, T. Luke, M. May§, A. Mazurenko, A. Niemczewski,
P. O'Shea, J. Reardon, J. Schachter, P. Stek, G. Tinios

MIT Plasma Fusion Center, Cambridge, MA 02139, USA

Introduction Alcator C-Mod is a compact (R=0.67 m, a=0.21 m), high field (B $\lesssim$ 9 T), high current (I_p < 3 MA), shaped ($\kappa \leq 1.7$) tokamak. It has molybdenum plasma-facing components and can be run with a closed or open single-null divertor. The auxilliary heating required for studies of dissipative divertors and transport at high densities and magnetic fields is provided solely by ICRF. For the first phase of experiments, 2 MW of power at 80 MHz was available in up to 1 sec pulses and ICRF coupling studies were carried out using a radially movable single current strap antenna and accompanying radially movable outboard limiter. The goals of the first phase were to produce diverted plasmas appropriate for the second phase experiments with high power auxilliary heating and to establish the optimal outboard limiter and antenna positions for coupling high power to the diverted plasmas. The first phase experiments were carried out at 5.3 T and 1 MA plasma currents with up to 1 MW of ICRF power injected in the hydrogen minority heating regime in deuterium majority plasmas. A detailed description of Alcator C-Mod and the results of the first phase of experiments can be found elsewhere.[1]

For the second phase of experiments, 4 MW of power will be available and rf excitation will be achieved using two fixed position antennas, each with two toroidally spaced current straps which can be driven either in-phase or out-of-phase. The radial locations of the two-strap antennas and two fixed position outboard limiters were established in the first phase experiments. Initial results from the second phase of operation can be found elsewhere.[2] Presented here are the initial ICRF results on coupling and plasma heating with up to 1.8 MW of power injected using one two-strap antenna.

Single Current Strap Antenna Results In order to incorporate radial motion in the design of the first antenna, it was necessary that it retract into the 20 cm wide Alcator C-Mod port opening. To meet this constraint and still have an antenna spectrum that coupled effectively to the plasma, a single current strap design was required. The antenna had a two layer, titanium carbonitride (TiC/N) coated Faraday shield, TiC/N coated molybdenum protection tiles, and slotted side walls for better coupling to the plasma.[3] High plasma loading (5-20 Ω) was observed, which depended mainly on density and antenna-separatrix gap and high power operation was achieved (up to 1 MW, 13 MW/m^2) at relatively low rf voltages (<30 kV). At high power ($\gtrsim$ 200 kW) the loading was about 30% lower than that observed at low power ($\lesssim$ 10 kW). Heating powers in excess of 0.5 MW in pulse lengths up to 0.4 sec were applied to plasmas with peak densities of up to 4×10^{20} m^{-3} using gas fueling. Large increases in molybdenum radiation were observed at high rf power. The molybdenum radiation was reduced by about a factor of two when the density increased above 2×10^{20} m^{-3}. Increases in radiated power were estimated from bolometers to be as high as the applied rf power in some cases. Some plasma heating was observed with central electron temperature increases of up to 100 eV, as measured by electron cyclotron emission (ECE) and ion temperature increases of up to 500 eV, as measured by the fusion neutron rate. Analysis of charge exchange neutrals in low density discharges showed a high energy hydrogen distribution and deuterium bulk heating along with a high energy deuterium tail. The neutron rate measurement of ion heating may be an overestimate because of the non-thermal deuterium distribution. More details of the single-strap antenna results can be found elsewhere.[4]

---

† ENEA Frascati

‡ University of Maryland

§ Johns Hopkins University

The primary goal of these experiments was to study effects of the antenna and outboard limiter positions on coupling to diverted discharges. Using the radial motion capability of both the antenna and limiter, the following spacings were established for the fixed position limiters and two-strap antennas. The outboard limters are 2 cm from the separatrix, the antenna protection tiles are 5 mm behind the limiters, with the Faraday shield front face 5 mm behind the protection tiles. This geometry places the front face of the current straps 4.8 cm from the separatrix.

Two-Strap Antenna Results In order to have a good spectrum for ICRF coupling, the two-strap antennas had to be made significantly wider than a port opening. An additional benefit was to increase the surface area so that 2 MW of power could be coupled by one antenna at a power density of $\sim$ 10 MW/m^2. The disruption loads in Alcator C-Mod are very large, owing to the high field and plasma current capability, and the antennas and outboard limiters have to be fixed securely to the vacuum vessel wall to withstand these loads. This precluded the possibility of incorporating radial movement into the design. The first phase experiments played an important role by establishing the fixed radial locations of these antennas and limiters. The two-strap antennas have single-layer Faraday shields with side slots to faciliate rf flux coupling to the plasma. The two antennas have different Faraday shield coatings, one is TiC/N like the single-strap antenna, and the other Boron Carbide (B_4C). The antennas are located in adjacent ports such that they form a four element array with approximately equal strap spacing, allowing the possibility of future experiments using current drive phasing. There are B_4C-coated molybdenum protection tiles on the outside edges of the antennas but not between the antennas. This can be seen in Fig. 1, which shows the two two-strap antennas installed in Alcator C-Mod. More details on the design can be found elsewhere.[5]

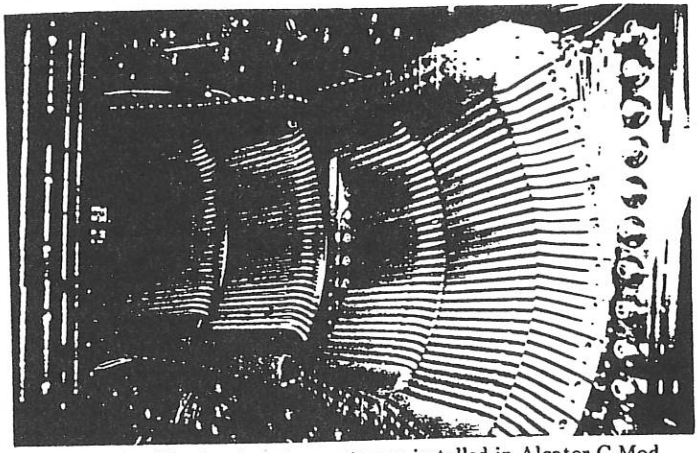


Figure 1 - The two two-strap antennas installed in Alcator C-Mod

The experiments described here have been carried out using only one of the two-strap antennas (TiC/N coated) with up to 2 MW of available rf power from a single transmitter. The second antenna will be operated shortly with an additional 2 MW of power from a second transmitter. Up to 1.8 MW has been coupled to the plasma using out-of-phase excitation of the two current straps (so-called dipole excitation), resulting in substantial plasma heating with significantly less impurity generation than was observed with the single-strap antenna. The heating follows L-mode scaling and brief periods of H-mode have been observed.[2]

Loading The plasma loading ranges from 3-25 Ohms depending on the density and antenna-separatrix spacing (outer gap), with the lowest loading observed during ELM-free H-mode periods. As with the single-strap antenna the loading is higher by about 25-30% at low power and decreases as the power is increased up to about 200 kW. Above 200 kW, the loading shows little power dependence. Figure 2 shows the loading resistance variation with line-averaged density for a set of limited discharges fueled by gas puffing. The different symbols correspond to data from

different days. The data shows a stronger than linear increase in loading with density. Using a Langmuir probe located in a protection tile of the single-strap antenna, it was observed that the density at the antenna rises faster than the central density as the gas fueling is increased. This information along with the data in Fig. 2 indiciates that the loading is most sensitive to the density immediately in front of the antenna. Figure 2 also shows the effect of varying the outer gap on the loading. The main effect of varying the outer gap is to vary the density in the immediate vicinity of the antenna. In diverted discharges with similar outer gap and density, the loading is about 20% lower.

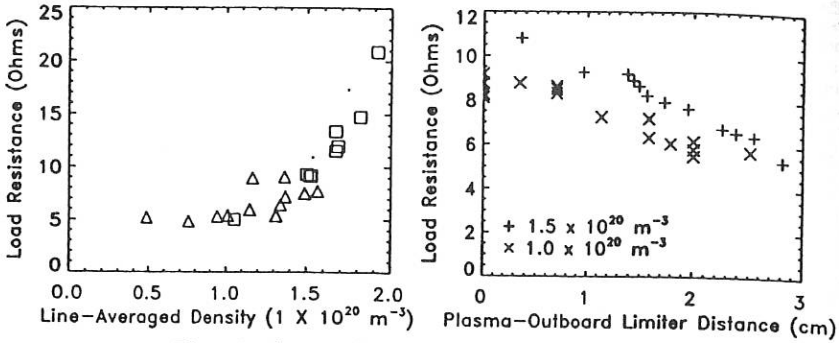


Figure 2 - Antenna loading vs. density and outer gap

Heating Significant heating is observed when high power is applied. Figure 3 shows data from a discharge where 1.65 MW of rf power is applied to an inner wall limited plasma with $\kappa = 1.5$ and a line-averaged density of 1.8×10^{20} m^{-3}. The stored energy as determined by magnetic equilibrium reconstruction (EFIT) increases by more than 30 kJ, the electron temperature at the sawtooth peak measured by ECE increases by 1.4 keV (the average increase is about 0.6 keV), and the ion temperature measured from the neutron rate increases by 0.6 keV. The diamagnetic stored energy shows a similar increase to the EFIT value and the instantaneous change in slope of the diamagnetic signal at rf turn on and turn off is consistent with absorption of 80-100% of the rf power. The ion temperature measured by Doppler broadening of Argon lines agrees well with the neutron rate measurement and the Doppler measurements show that the ion temperature increases across most of the profile. The ECE data shows an increase of the sawtooth period from 5 to 15 ms and the Ohmic heating power decreases from 1.1 to 0.8 MW. While fewer experiments have been done in diverted discharges thus far, the same rf power levels have been applied with similar heating observed.

Impurity Generation The increases in radiated power and Molybdenum radiation are significantly reduced using the two-strap antenna with dipole phasing, as has been observed on many experiments. It is important to note that this improvement is also observed in the all-Molyndenum environment of Alcator C-Mod. The Molybdenum radiation is observed to increase linearly with rf power, but with the dipole antenna the magnitude is down by as much a factor of ten at 500 kW. The total radiated power, as measured by a bolometer array, which was as much as 100% of the rf power for the single-strap antenna in diverted discharges, now is about 50-60% for rf-heated limiter discharges, with a similar 50% radiated in Ohmic limiter plasmas.

Confinement Analysis of the heating data from a large number of limiter discharges varying rf power, density, and plasma current shows good agreement with ITER89-P L-Mode scaling.[2]At low current, the rf power can be three times the Ohmic power while at high current, it is about equal to the Ohmic value. The ASDEX-U H-mode scaling indicates that the threshold power for Alcator C-Mod at 5.3 T and $\overline{n}_e = 1 \times 10^{20}$ m^{-3} is about 1.5 MW. H-modes have been previously observed in Ohmic plasmas at fields up to 5.3 T.[6]

Brief periods with H-mode signatures have been observed during ICRF heating, of inner wall limited discharges which were nearly but not quite diverted. ELMing H-modes of 40 ms duration (about twice τ_E) and ELM-free periods of 12 ms. have been observed. Figure 4 shows an example of a brief ICRF-produced ELM-free H-mode period. The ICRF H-modes are difficult to maintain because the 30% (ELMing) to 45% (ELM-free) decrease in loading causes a reduction

or an interruption of the rf power. The H-modes are identified by the characteristic drop in H_α at the edge and a concommitant density increase. During the ELM-free period, the diamagnetic stored energy continues to rise despite the sudden reduction in rf power from 1.4 to 0.8 MW, implying at least a transient increase in energy confinement. All of these effects can be seen in Fig. 4, which also shows that at the lowest loading, peak rf voltages of up to 39 kV are supported by the antenna and matching systems.

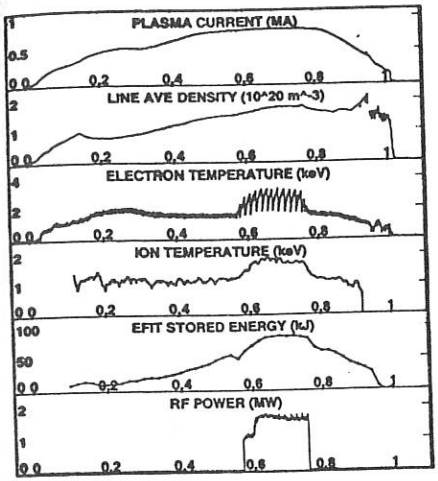


Figure 3 - Parameters with ICRF heating

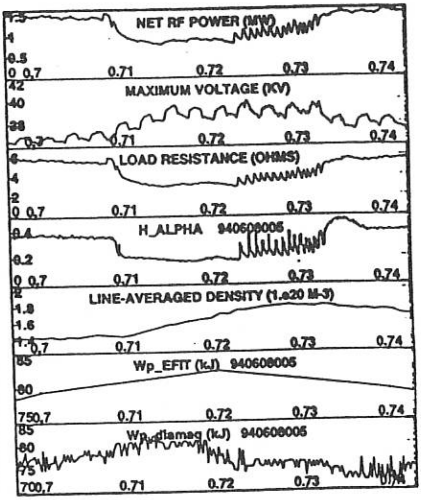


Figure 4 - Transient ELM-free ICRF H-mode

Conclusions The initial results of ICRF heating experiments using a two-strap antenna with dipole phasing are very encouraging. Effective plasma heating and control of rf-related impurity generation have been demonstrated in a tokamak with molybdenum plasma facing components. The energy confinement shows L-mode scaling and brief periods of H-mode behavior have also been observed. The first of two two-strap antennas has been operated up to 1.8 MW and experiments with two such antennas and 4 MW of available rf power will begin in the near future.

Acknowledgements It is a pleasure to acknowledge the numerous contributions of the Alcator engineering and technical staff. We are particularly grateful to M. Fridberg and W. Beck for engineering of the rf transmitters and antenna systems respectively. This work was supported by USDOE Contract No. DE-AC02-78ET51013.

References

[1] I. H. Hutchinson et al., *Phys Plasma* **1**, 1511 (1994).
[2] I. H. Hutchinson et al., Contr. Fusion Plasma Physics (21st European Conference, Montpellier, 1994), invited paper.
[3] S. N. Golovato et al., in *Proceedings of the 9th Topical Conference on Radio-Frequency Power in Plasmas*, Charleston, SC (AIP, New York, 1991), p. 185.
[4] Y. Takase et al., *Fusion Eng. and Design*, 1994 (to be published).
[5] Y. Takase et al., in *Proceedings of the 9th Topical Conference on Radio-Frequency Power in Plasmas*, Charleston, SC (AIP, New York, 1991), p. 189.
[6] J. A. Snipes et al., *Nucl. Fusion*, 1994 (to be published); J. A. Snipes et al., Contr. Fusion Plasma Physics (21st European Conference, Montpellier, 1994), post-deadline paper.

Radial Banana-Transitional Transport of Alpha Particles Driven by ICRH in a Tokamak Fusion Reactor

C.S. Chang*, K. Tani†, K. Hamamatsu†, and M. Azumi†
Courant Institute of Mathematical Sciences
New York University, New York, NY 10012, U. S. A.

Abstract

It is found that the particle trapping effect from the ion cyclotron resonance heating (ICRH) in the pitch angle direction can produce another radial transport of the DT fusion-born alpha particles whose energy is well above the critical slowing-down energy. This transport is in addition to the previously known radial transport process of the passing alphas induced by ICRH in the energy direction [C.S. Chang, J. Lee, and H. Weitzner, Phys. Fluids B 3, 3429 (1991)]. At lower energy, the Coulomb pitch angle scattering becomes dominant over the ICRH pitch angle scattering, and negates this effect.

For a steady state operation of a deutrium-tritium (DT) fusion reactor, it is essential that the helium ash particles do not accumulate in the burning core region of the plasma. It is expected that the fusion reaction rate is highly peaked toward the magnetic axis and that the radial alpha transport rate is slow, hence the helium ash deposition will be highly peaked toward the magnetic axis. The density of the accumulated helium ash will then be determined from the competition between the ash deposition rate and radial helium transport rate. Since the radial helium transport rate is expected to be similar to those of the background plasma particles, it is feared that the natural helium transport rate may be too slow to prevent the helium accumulation in a well confined tokamak fusion plasma. Therefore, it will be of great benefit to the fusion program if we can find a way to control the generation rate of the helium ash particles in the burning core.

One way to reduce the helium ash deposition rate in the burning core is to force the alpha particles move out radially while they slow down. Chang, Lee, and Weitzner [1] suggested the use of Ion Cyclotron Resonance Heating (ICRH) to achieve this. Their theoretical investigation concluded that the ICRH-induced velocity-space flow in the energy direction of the passing alphas travelling in the preferred toroidal direction can lead to radially outward motion of the passing alpha orbits, and the resulting radial transport rate of the slowing-down alpha particles was shown to be fast enough to reduce the ash deposition rate in a tokamak fusion reactor.

In the present work, we report that there is yet another important ICRH-driven radial transport mechanism of the slowing-down alpha particles, which was not discussed in

*Also at Korea Advanced Institute of Science and Technology.
†Japan Atomic Energy Research Institute, Japan.

Ref. [1]. The mechanism of Ref. [1] did not include the ICRH-induced trapping effect of the passing alphas: it included the ICRH-induced radial drift of the passing orbits only. When the passing alpha particles are heated by ICRH, the ratio of their perpendicular energy to parallel (to the magnetic field vector) energy increases and, eventually, they become trapped in the toroidal magnetic mirror. The trapped particle orbit is shifted by a banana width either inward (for co-passing alphas) or outward (for counter-passing alphas) relative to the passing orbits prior to the transition. If we can adjust the fast wave characteristics in such a way that the ICRH absorption is preferrentially to the counter passing alphas, then a radially outward shift of average alpha position occurs as a result of ICRH-induced transition from passing to trapped particles.

The radial alpha particle flux induced by ICRH heating is shown in Ref. [1] to be in the form

$$\Gamma_\psi = \left\langle \int d^3v \frac{I v_\parallel}{\Omega} \{Q\}(f_\alpha) \right\rangle, \tag{1}$$

where $I = RB_T$, R is the major radius, B_T is the toroidal component of the magnetic induction vector $\vec{B}$, Ω is the alpha gyrofrequency, $\{Q\}$ is the bounce averaged quasilinear ICRH heating operator, and f_α is the lowest order alpha distribution function. Equation (1) was obtained assuming that the Coulomb pitch angle scattering is negligible.

The plasma we consider here is within or near the burning core of a tokamak fusion reactor. It is assumed that the alpha banana orbits are well confined and the plasma is quiescent. The ICRH heating operator can be divided into the even, $\{Q^E\}$, and odd, $\{Q_O\}$, parts in the parity of $v_\parallel$: $\{Q\} = \{Q^E\} + \{Q^O\}$. It can be easily seen from Eq. (1) that, if f_α is even in $v_\parallel$, only $\{Q_O\}$ can lead to a non-vanishing Γ_ψ. For alpha particles in a fusion reactor, it is reasonable to assume that f_α is even in $v_\parallel$, and a preferential heating of alphas for one sign of $v_\parallel$ can yield the odd part $\{Q^O\}$ and, thus, a net radial alpha flow.

We use the velocity coordinate (v, λ), where λ = magnetic moment / kinetic energy. Both v and λ are constants of motion, and λ_c denotes the value of λ at the trapped passing boundary. The bounce averaged quasilinear heating operator can be cast into the following form [2]

$$\begin{aligned} \{Q^O\} &= \nabla \cdot \Gamma_v^O, \\ \Gamma_v^O &= -\Theta(\lambda_c - \lambda) D_b^O (\hat{v} - \hat{\xi}_m \eta)\left(\frac{\partial}{\partial v} + \eta \frac{\partial}{v \partial \xi_m}\right) f_\alpha, \end{aligned}$$

where $\Theta(\lambda_c - \lambda)$ is the heavy side step function, the subscript m (R) denotes the outside midplane (resonance location), $\xi = \cos^{-1}(v_\parallel / v)$, τ_b is the alpha bounce (or transit) time, $\eta = B_m \xi_R^2 / B_R \xi_m^2$, and D_b^O is the odd part of the quasilinear diffusion coefficient driven by the odd part of the left-handed circularly polarized wave electric field E_+^O: $D_b^O = (\pi q^2 / 8 M_\alpha / |d\Omega/dt|\ \tau_b) |E_+^O|^2$. It is shown in Ref. [1] that, when the zero-$v_\parallel$ resonance layer is across the magnetic axis, $|E_+^O|^2$ corresponds to the in-out asymmetric part of $|E_+|^2$. It is important to notice here the existence of the heavy side step function in the above expression for the odd part of the quasilinear v-space flux Γ_v^O. It reflects the fact that the

fast bounce motions of the trapped particles do not allow for an odd quasilinear v-space flux.

Substituting the above expression for $\{Q^O\}$ into Eq. (1), we find

$$\Gamma_\psi = \left\langle \int d^3v \frac{Iv_\parallel}{\Omega} \left[\frac{1}{v^2}\frac{\partial}{\partial v} v^2 D_b^O \Theta(\lambda_c - \lambda) + 2h_m \xi_m \frac{1}{v}\frac{\partial}{\partial \lambda} D_b^O \Theta(\lambda_c - \lambda)\sqrt{1-\xi_m^2}\eta \right] \frac{\partial f_\alpha}{\partial v} \right\rangle. \quad (2)$$

The first term in the above expression is the contribution from the ICRH in the energy direction. This is the term which has been evaluated in Ref. [1]. It is associated with the drift of the passing orbits by ICRH.

The second term is new here. It comes from the ICRH in the pitch angle direction. It is associated with the abrupt shift of the guiding center orbit as the particles get trapped, which can be seen mathematically from the fact that the contribution from the second term to the particle flux, which we call $\Gamma_\psi^{(P)}$ from now on, is mainly through the delta-function behavior at the trapped passing boundary,

$$\Gamma_\psi^{(P)} = -2Ih_m \left\langle \int d^3v \frac{\xi\xi_m}{\Omega} D_b^O \delta(\lambda - \lambda_c)\sqrt{1-\xi_m^2}\eta \frac{\partial f_\alpha}{\partial v} \right\rangle.$$

We note here that the existence of non-vanishing $\Gamma_\psi^{(P)}$ is justified only well above the critical slowing-down energy. For alphas near or below the critical slowing-down energy, the analytical procedure taken here to obtain $\Gamma_\psi^{(P)}$ is invalid due to the neglect of the Coulomb pitch angle scattering effect. In this case, the new trasnport effect considered here is negated because the Coulomb pitch-angle scattering dominates over the ICRH-driven pitch-angle scattering.

$\Gamma_\psi^{(P)}$ can be evaluated in terms of the horizontal aspect ratio $\epsilon = x/R_0$, where x is the horizontal minor radius and R_0 is the major radius at the magnetic axis;

$$\Gamma_\psi^{(P)} = \frac{3IS_\alpha\tau_s}{2\Omega_0 v_0} D_b^O(\epsilon + \epsilon_R)\frac{(1+\epsilon_R)}{\sqrt{1+\epsilon}}\mathcal{I}, \quad (3)$$

for counter passing alphas, where $\mathcal{I} = \int_0^1 dss^3/(s^3+s_c^3)^2$, S_α is the alpha birth rate, τ_s is the alpha slowing-down time, v_0 is the alpha birth speed, and $s_c = v_c/v_0$ with v_c denoting the critical slowing-down speed. For a reactor plasma, the value of the ingegral $\mathcal{I}$ is found to be approximately constant $\mathcal{I} \simeq 2.4$. In term of the radial flow speed $V_r = \Gamma_r/S_\alpha\tau_s$, we can change the above result into

$$V_r^{(P)} \simeq 1.2\epsilon[1+\sqrt{\epsilon_R/\epsilon}\,](p_{RF}^O/p_\alpha)\rho_p/\tau_s,$$

where p_{RF}^O/p_α is the local ratio of the fast wave power density to the alpha birth power density and ρ_p is the poloidal gyroradius of the newborn alpha particles.

Let us compare the radial flow speed $V_r^{(P)}$ due the ICRH in the pitch angle direction with $V_r^{(E)}$ due to the ICRH in the energy direction. According to Ref. [1], we have $V_r^{(E)} \simeq \gamma(p_{RF}^O/p_\alpha)\rho_p/\tau_s$, where γ an efficiency factor, which is typically ~ 0.3. Eventhough $V_r^{(P)}$ is formally smaller than $V_r^{(E)}$ by a factor ϵ, the small efficiency factor γ in $V_r^{(E)}$ makes $V_r^{(P)}$

to be comparable to $V_r^{(E)}$. Hence, both terms in Eq. (2) should be considered when we calculate the ICRH driven radial flow of alpha particles. The combined radial alpha flow speed can be written in the form

$$V_r^{(ICRH)} \simeq (\gamma + 2\epsilon)(p_{RF}^O/p_\alpha)\rho_p/\tau_s.$$

We notice here that $V_r^{(P)}$ increases with the minor radius r in proportion to the safety factor q, for a given p_{RF}^O/p_α value, while $V_r^{(E)}$ decreases with r in proportion to q/ϵ. Hence, $V_r^{(P)}$ can be larger than $V_r^{(E)}$ at larger minor radius. Considering this and the fact that the total particle number flowing across a flux surface is proportional to r, it can be seen that $V_r^{(P)}$ can also play an important role in spreading the helium ash distribution to larger minor radial positions outside of the burning core (theoretically, 10^{20}/sec He particle removal rate from the ITER-CDA burning core can be achieved by ICRH).

This tendency could have an important consequence when we consider an alpha current driven by the same mechanism, since the plasma current is proportional to minor radius r times current density. Hence, for ICRH-driven alpha current, the effect from the passing-trapped transition could be greater than the effect from the passing orbit shift.

A comparison of the ICRH-driven radial alpha flow rate with a neoclassical one may be helpful. Reference [3] reported an enhanced neoclassical flow of alpha particles at the speed $V_r^{(NEO)} \simeq \epsilon^2\rho_p^2/(\tau_s a)$. Comparison with $V_r^{(ICRH)}$ yields, allowing for $p_{RF}^O/p_\alpha \simeq \epsilon^{1/2}\rho_p/a$,

$$V_r^{(ICRH)}/V_r^{(NEO)} \simeq (\gamma/\epsilon + 2)/\epsilon^{1/2}.$$

It was shown in Ref. [4] that this much enhancement can have a significant effect on the alpha distribution in a fusion reactor.

The radial flow $V_r^{(ICRH)}$ of alpha particles yields a radial spread, during a slowing-down time,

$$\Delta r \sim (\gamma/\epsilon + 2)\epsilon^{1/2}(p_{RF}^O/p_\alpha)\Delta_b.$$

Taking $\epsilon \simeq 0.1$, $p_{RF}^O/p_\alpha \simeq 1/3$, and $\gamma \sim 0.3$ in the burning core, we obtain $\Delta r \sim \Delta_b/2$. This corresponds to $V_r^{(ICRH)} \sim 0.1$ m/sec, since $\tau_s \sim 1$ sec. Assuming that a high α-density, flat top region can develop without ICRH for r < 50 cm in the burning core of ITER-CDA, and taking $\Delta_b \simeq 20cm$, the volume spread factor by ICRH becomes $\sim (50+10)^2/50^2 \simeq 1.44$. Hence, the flat top He-density can be reduced to 70% in the burning core.

Reference [1] showed that the alphas at lower energy range behave differently from the higher energy alphas. The additional radial flow discussed here does not affect the lower energy alphas. It is due to the fact that the Coulomb pitch angle scattering effect reverses the physical processes discussed here.

This work is supported by the U.S. Department of Energy.

RERERENCES

[1] C.S. Chang, J. Lee, and H. Weitzner, Phys. Fluids B **3**, 3429 (1991).

[2] C.S. Chang, Phys. Fluids **28**, 3596 (1985).

[3] C.T. Hsu, P.J. Catto, and D.J. Sigmar, Phys. Fluids B **2**, 280 (1990).

[4] P. J. Catto, Phys. Rev. Lett. **60**, 1954 (1988).

ICRF Heating in CHS

R.Kumazawa, K.Nishimura, S.Masuda[1], D.A.Rasmussen[2], T.Mutoh, F.Shimbo, T.Seki, T.Watari, R.Akiyama, A.Ando, A.Ejiri, H.Idei, K.Ida, H.Iguchi, M.Isobe[1], M.Iwase[1], S.Kubo, K.Matsuoka, T.Morisaki, S.Morita, S.Mutoh, S.Okamura, T.Ozaki, S.Sakakibara, M.Sasao, C.Takahashi, T.Kawamoto, K.Tanaka, J.Xu, H.Yamada, I.Yamada

National Institute for Fusion Science
[1]The Graduate University for Advanced Studies
Furo-cho, Chikusa-ku, Nagoya, 464-01, Japan
[2]Oak Ridge National Laboratory, Oak Ridge, TN 37831, U.S.A.

Abstract

Ion cyclotron range of frequency(ICRF) heating can sustain a 2.2kJ plasma with 590kW from 5 antennas in the CHS device. The electron and ion temperatures are 330eV and 200eV with an average electron density, $n_e=3.8X10^{13}cm^{-3}$. These results were obtained following boronization of the vacuum vessel. The radiated power was reduced to 140kW following boronization. The main impurity is oxygen and its line radiation was reduced by 3 times by applying boronization.

1. Introduction

Ion cyclotron range of frequency(ICRF) heating is established as an reliable heating method in large tokamaks such as JET, JT-60U, TFTR and Tore Supra. ICRF heating experiments in heliotron/torsatron devices, however, have not yet succeeded in sustaining and heating plasmas while maintaining low radiated power conditions[1,2]. ICRF heating for the super conducting Large Helical Device(LHD) under construction at National Institute for Fusion Science(NIFS) requires steady state(30min.) operation with a moderate power up to 3MW and a pulsed operation(10sec.) up to 12MW[3,4]. ICRF heating is being studied in the existing device, the Compact Helical System(CHS) to develop the techniques required for the LHD.

ICRF heating experiments have been performed in CHS, using two-ion-hybrid and minority heatings since 1991. In initial experiments without boronization it was found that ICRF heating was effective for different heating modes:

(1)ICRF heating could sustain the plasma by itself following turn-off of electron cyclotron heating(ECH) power used to produce an afterglow decaying target plasma.

(2)The stored energy increased by 650J when ICRF power of 300kW was radiated into an ECH target plasma.

(3)A high energy ion tail was observed.

(4)The stored energy increased by 850J when ICRF power of 500kW was radiated into the NBI plasma.

In all ICRF heating experiments, Impurity radiation limited the period of effective heating to about 20ms.

2. CHS device and ICRF Heating System

CHS is a low aspect ratio helical device(l=2, m=8) with a maximum magnetic field strength, B_t=2T, the major radius, R=1m and an average minor radius, a=0.2m. Five ICRF antennas have been installed in the outward high field side. In the earliest experiments we used two single strap antennas(referred to P-port antenna, 4cm wide and 40cm long). For more recent experiments the existing P-port antennas were modified and two additional P-port antennas were installed such that every other helical period has an antenna of this type. The modified antennas have been drawn back 1cm further from the plasma boundary and their Faraday shield aligned with the magnetic field. In addition a new wide single strap antenna was designed and installed(referred to U-port antenna, 16cm wide and 40cm long, with aligned Faraday shield) with the same radial separation from the plasma boundary. The P-port antennas are fed in pairs(same phase for each antenna pair) by separate RF coaxial feed lines. The U-port antenna has its own coaxial feed line. The RF power, up to 1.5MW can be transferred to five antennas through impedance matching circuits, consisting of two stub tuners. In the most recent experiments the operating frequency for the antennas was raised from 14MHz to 26MHz in conjunction with raising the maximum CHS magnetic field to 2T. This latest operating period allowed a comparison of ICRF heating before and after boronization.

3. Experimental Results

3-1 Before Boronization

He glow discharge(1A/400V, 40mtorr) is done for vacuum wall conditioning before an experimental run. A Ti-gettering is also occasionally done during experiments to reduce hydrogen/deuterium recycling and impurity release from the vacuum wall.

Complex geometry of the hybrid and ion cyclotron resonances requires an experimental determination of the magnetic field which results in the largest increase in plasma stored energy. We performed a series of experiments at different magnetic fields with 250kW of ICRF power radiated by the U-port antenna into a plasma with an average electron density of $2X10^{13}cm^{-3}$. The time evolution of a discharge from this series is shown in Fig.1. During the first 30ms the plasma was produced by 100kW of ECH. Following the ECH power turn-off, ICRF heating power was injected along with a gas puffing which provided 10% of hydrogen minority in a deuterium majority. The plasma stored energy reaches its peak value of 600J about 30ms after RF power turn-on, but then decreases as the radiated power increases. Figure 2 shows the dependence of the peak value of the plasma stored energy on the magnetic field strength between 1.55 and 1.8T. The average electron densities are also plotted in Fig.2. There is a clear optimum in the plasma stored energy at 1.7T of magnetic field strength. The minority ratio measured by comparing H_α and D_α light was 15%. At this magnetic field strength, the hybrid resonance is located at the magnetic axis. We observed the optical emission from various impurity lines including OV, CIII, TiXII etc.. The oxygen line radiation was the dominant contributor to the total impurity radiation. The OV line radiation was larger by about 3 times than in neutral beam heated plasma. A similar series of experiments were performed using P-port antennas and the optimum magnetic field was also determined to be 1.7T.

In further experiments we applied about 600kW from all five antennas at 1.7T. The stored energy reached a maximum of 1.3kJ, 10ms after ICRF power turn-on but then decreased as the radiated power increased (similar to separate P-port and U-

port antenna heating experiments). The radiated power exceeded 600kW before the end of RF pulse.

3-2 After Boronization

The CHS vacuum vessel was boronized in an attempt to reduce impurity radiation. Vaporized decaborane($B_{10}H_{14}$) was injected into He glow discharge at pressure of about 40 mtorr through a toroidally distributed set of 4 valves. During a typical 4 or 5 hour discharge 2-3g of decaborane are consumed. The boronization glow discharge was followed by He glow discharge of more than 20 hours in order to remove hydrogen atoms from the vacuum vessel wall.

Following boronization of the vacuum vessel a series of ICRF discharge were obtained where the increase in the stored energy lasted to the end of the heating pulse. Using the P-port antennas 250kW of RF power produced a 1kJ plasma sustained by ICRF heating alone. Using the U-port antenna 240kW of RF power produced a 1.4 kJ plasmas. Figure 3 (referred to high density mode) shows the time evolution of the total injected RF power, average electron density, plasma stored energy when power was applied simultaneously to the U-port and P-port antennas. The plasma stored energy reached 2.2kJ with 590kW of combined RF power and an average electron density of $3.8X10^{13}cm^{-3}$ 50-60ms after RF power turn-on. For this discharge the radiated power was 140kW. The hydrogen minority ratio, H/(H+D) was measured to be 30% despite the fact that the gas puffing was pure deuterium(at 20torr l/sec during RF heating). The recycling from the boronized wall mainly provided the hydrogen. The radial profiles of the electron density and the electron temperature obtained from Thomson scattering are shown in Fig.4. The electron density is hollow with a peak density of $6.0X10^{13}cm^{-3}$. The multiple chord HCN far infrared interferometer also observed a hollow density profile. The electron temperature profile is peaked with a central value of 330eV. The ion temperature was measured to be 200eV using fast neutral particle analyzer(FNA), which is lower than the electron temperature.

In low gas puffing operation(at 3-4torr l/sec), another heating mode (referred to low density mode) was obtained with a plasma stored energy of 2kJ by the same RF power level. The average electron density and the central electron temperature were $2X10^{13}cm^{-3}$ and 400eV, respectively. The ion temperature was measured to be 500eV by FNA, higher than the electron temperature. In contrast to this mode, the ion temperature is lower than the electron temperature in high density mode. The plasma stored energy reached its peak value of 2kJ 20ms after RF power turn-on, but gradually decreased with times, accompanied by increase in the radiated power.

3-3 Combination heating with NBI

ICRF heating experiments were also performed in NBI plasma. The plasma was sustained by two NBI systems, where one is co-injected(38kV,1MW) and the other is counter-injected(38kV, 0.7MW). The optimum magnetic field was 1.7T where the increase in stored energy due to 400kW of ICRF was 0.7kJ. The radiated power increased by 300kW during ICRF heating pulse. The cause of this increase is not presently understood.

4. Summary

CHS plasma has been successfully heated using 26MHz ICRF power optimized at B_t=1.7T. Following boronization of CHS vacuum vessel, ICRF wave has heated and sustained the stored energy throughout the entire RF pulse. ECH-initiated

discharges were raised to 2.2kJ of stored energy at an average electron density of $3.8X10^{13}cm^{-3}$ with 590kW of RF power. The stored energy was 50% or more higher than it was for the same ICRF power level applied in the preboronization discharge. Following boronization the impurity emission remained small showing no signs of accumulation or a collapse of stored energy. ICRF heating was also effective when combined with NBI, which resulted in the increase in plasma stored energy by 0.7kJ.

References

[1] T.Mutoh, H.Okada, O.Motojima et al., Nuclear Fusion 24(1984)1003.
[2] M.Kwon, T.D. Shepard, R.H.Goulding et al., Nuclear Fusion 32(1992) 1225.
[3] T.Mutoh, R.Kumazawa, T.Watari et al., in Proc. of the 14th IEEE Symp. on Fusion Engineering, Vol.1, (1991)103.
[4] R.Kumazawa, T.Watari, T.Mutoh et al., Proc. of the 17th Symp. on Fusion Technology, Vol.1, (1992)554.

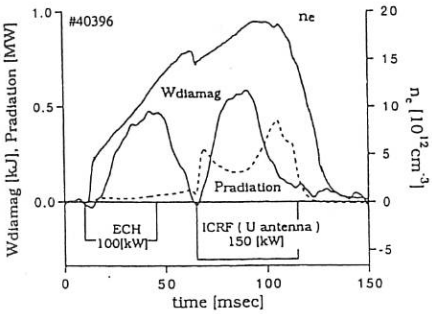


Fig.1 Average electron density, plasma stored energy and radiated power with injected RF power before boronization.

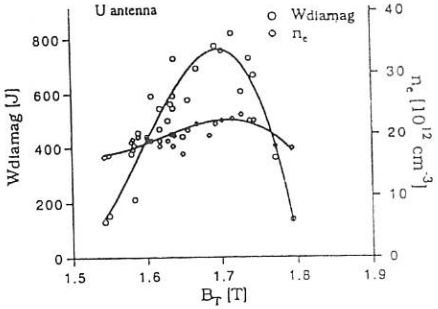


Fig2. Dependence of plasma stored energy and average electron density on magnetic field strength.

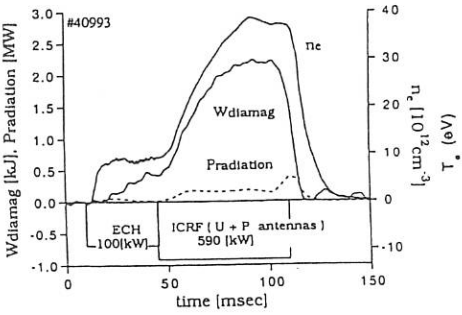


Fig.3 Average electron density, plasma stored energy and radiated power with injected RF power after boronization.

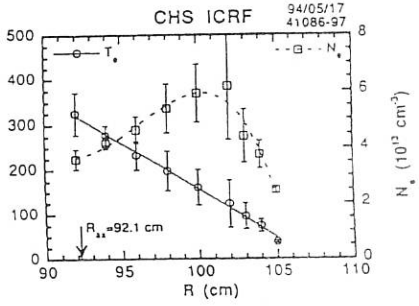


Fig.4 Radial profile of electron density and electron temperature.

MEASUREMENT OF THE OPTICAL DEPTH AT THE THIRD ELECTRON CYCLOTRON HARMONIC IN TORE SUPRA

J.L. Ségui, Y. Michelot, G. Giruzzi

Association EURATOM-CEA sur la Fusion
Département de Recherches sur la Fusion Contrôlée
Centre d'Etudes de Cadarache
13108 St. Paul-lez-Durance (FRANCE)

T. Goodman, A. Kritz[a], A. Pochelon, O. Sauter, G.R. Smith[b], M.Q. Tran

Association EURATOM-Confédération Suisse
Ecole Polythechnique Fédérale de Lausanne
Centre de Recherche en Physique des Plasmas
1007 Lausanne (SWITZERLAND)

Electron cyclotron absorption of extraordinary waves at the third harmonic has important applications for heating in toroidal plasmas, in particular for devices working at low magnetic field and in high density regimes. Such machines include stellarators, reversed-field pinches and tokamaks devoted to high-beta plasma studies; for example, TCV (Tokamak à Configurations Variables [1]) with plasma elongations up to b/a = 3. The main drawback of 3rd harmonic ECRH is related to the relatively low optical depth predicted by the linear relativistic theory [2], which sets constraints both on the launching geometry and on the minimum electron temperature for which the method is applicable. Since the value of the first-pass absorption is a critical issue of this heating scheme, it is important to verify the theoretical evaluations of the optical depth of a Maxwellian plasma with experiments. This motivated the experimental transmission measurements performed on Tore Supra, using a vertically propagating extraordinary mode at variable frequency. In contrast with horizontal propagation, the use of vertical propagation allows a detailed comparison with the relativistic theory of wave absorption and ray propagation. In fact, along a vertical chord the toroidal magnetic field is nearly constant and the cyclotron frequency is slowly varying, basically because of the poloidal field and of paramagnetic and diamagnetic effects. This means that the shape of the optical depth as a function of frequency is very close to that of the local absorption coefficient and a precise measurement of the optical depth will be a sensitive check of the absorption theory including, e.g., relativistic ray-tracing and gyrokinetic corrections [3]. In the past, optical depth measurements have been performed in stellarators [4,5] and in tokamaks in the horizontal direction [6-8]. Vertical transmission measurements have been performed basically as a diagnostic of superthermal electrons [9-11] and of MHD modes [12].

The experimental arrangement used is the following. A narrow beam of microwaves (spread angle $< 2°$) is launched into the torus from a bottom port along a vertical direction intersecting the magnetic axis of a standard discharge. Both launching and receiving antennae

---

[a] Lehigh University, Bethlehem, Pennsylvania (USA)
[b] LLNL, Livermore, California (USA)

are rectangular horns, with the longest side parallel to the direction of the magnetic field at the plasma/vacuum interface, in order to couple a pure extraordinary mode and to minimize Faraday and Cotton-Mouton effects. A millimeter wave source of the IMPATT type is used (power ≥ 5 mW; frequency range 99-109 GHz). In order to enhance the signal-to-noise ratio, the launched beam is amplitude-modulated at the frequency f_0 = 200 kHz, and the received signal is video-detected through a low-pass filter (20 kHz band). The result is an average signal-to-noise ratio higher than 20 dB. The problem of standing wave formation due to multiple wall reflections is avoided, to a large extent, because of the natural divergence of the beam used and by the presence of large oblique port windows. The time resolution is determined by the frequency sweeping time of the wave source (≈ 3 ms). The experiments have been performed in the Tore Supra tokamak (a = 0.78 m, R = 2.36 m) in Ohmic discharges at a toroidal magnetic field B ≈ 1.25 Tesla. The main parameters scanned are the density ($10^{19} < n_{e0} < 3 \times 10^{19}$ m^{-3}) and the plasma current ($150 < I_p < 600$ kA), which results in temperature variations in the range $0.8 < T_{e0} < 1.2$ keV. The density profiles are measured by a 5-chord infrared interferometer and the temperature profile by a 12-channel Thomson scattering system.

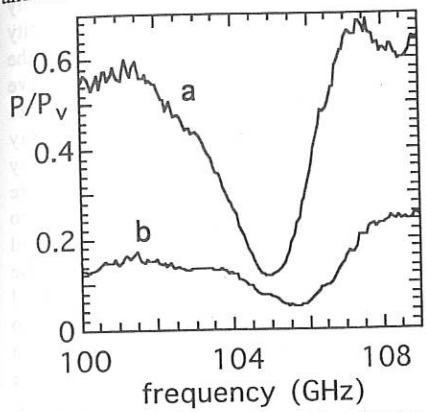


Fig. 1: Transmission spectra. a) low density; b) high density

Typical examples of measured spectra are shown in Fig. 1, for central densities of 1.4×10^{19} m^{-3} (a) and 2.8×10^{19} m^{-3} (b). The quantity plotted versus frequency is the power detected by the receiving antenna normalized to the corresponding power measured in vacuum (P/P_v). P is reduced with respect to P_v because of two effects: refraction losses (namely broadening and deflection of the wave beam) which decrease with increasing frequency, and wave absorption, which is localized close to the 3rd harmonic of the cyclotron frequency ω_c. The level of the signal far from $3\omega_c$ (i.e., where the absorption vanishes) gives a measurement of refraction losses, which are generally found to decrease linearly with frequency in the narrow frequency range considered (10 GHz). This allows the separation of refraction effects from absorption and the precise measurement of the optical depth τ_{X3}. Refraction losses grow with the

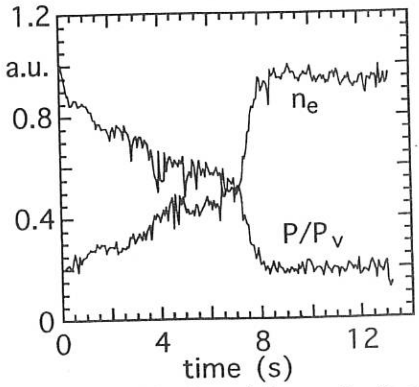


Fig. 2 : Time behaviour of electron density and transmission signal at fixed frequency

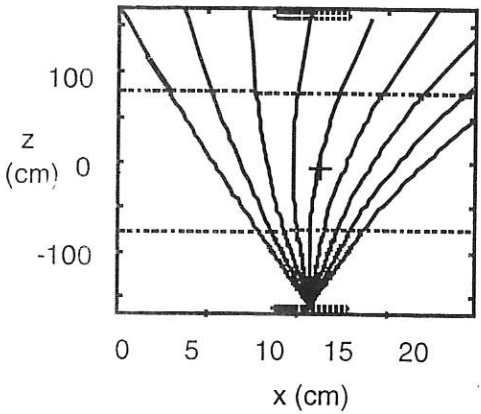


Fig. 3 : Poloidal projection of the ray trajectories between the two antennae. A + indicates the position of the magnetic axis

density, as shown in Fig. 1, as well as in Fig. 2, where the time evolution of both P/P_v and the line-averaged density is shown for a case in which the density was increased by gas puffing during the discharge. Refraction effects have limited the experimental range to moderate densities. Typical ray trajectories obtained in this density range by ray-tracing calculations are shown in Fig. 3. An important effect to be included in ray-tracing and absorption calculations is the paramagnetic correction to the toroidal field (≈ 3 % of the vacuum field) due to the plasma current. This effect causes a measurable frequency shift of the absorption line as the current is varied, as shown in Fig. 4. Note that at low current the spectra present a bump close to ω_c, on the high frequency side of the dip in transmission. This effect is systematically observed and appears related to hot plasma effects on the ray propagation. The measured transmission coefficient $\exp(-\tau_{X3})$ is now compared to the theoretical values, obtained by integrating along the ray trajectories the local absorption coefficient [2]

$$\alpha_{X3} \approx \frac{\omega}{cN_x}\left(1 - \frac{i\varepsilon_{12}}{\varepsilon_{11}}\right)^2 \left(\frac{N_x}{Y}\right)^4 \frac{9}{7!}\left(\frac{\omega_p}{\omega}\right)^2 \frac{\sqrt{2\pi}}{\mu}(2Z)^{7/2}\exp(-Z), \qquad (1)$$

where N_X is the cold plasma refractive index, ε_{12}, ε_{11} are elements of the cold dielectric tensor, $\mu = mc^2/T_e$, $Y = \omega_c/\omega$ and $Z = \mu(3Y - 1)$.

The finite size of the antennae is taken into account by averaging over multiple rays. A typical experimental spectrum is shown in Fig. 5 (dashed line), together with two theoretical curves (solid lines) which cover the error bars in the measured density and temperature profiles. The agreement is good, although the experimental curve looks somewhat broader; this is probably due to lack of precision in the evaluation of the magnetic equilibrium. Equation (1) shows that α_{X3} is maximum at $Z = 7/2$ and that the maximum optical depth for vertical propagation will be proportional to the line-averaged values of n_eT_e, at least at moderate densities. This dependence has been checked by slowly increasing the density during a

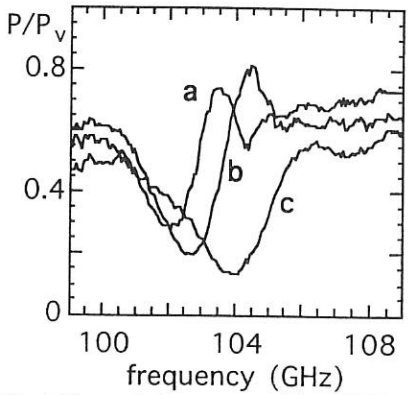


Fig. 4: Transmission spectra. a) I_p = 180 kA; b) I_p = 300 kA; c) I_p = 550 kA

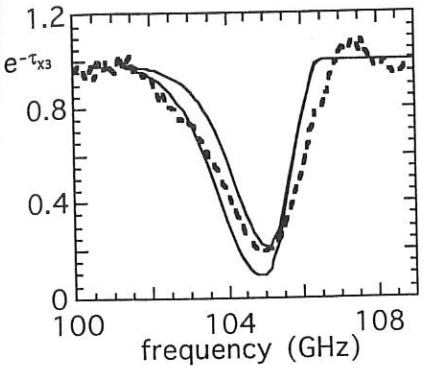


Fig. 5 : Experimental (dashed) and theoretical (solid lines) transmission coefficients

current flat-top: the temperature also changes, which gives an excursion in the parameter n_eT_e. The measured values of the maximum optical depth τ_{max} are plotted versus $n_{e0}T_{e0}$ in Fig. 6. Within the error bars, a reasonable agreement is found with the theoretical prediction.

In conclusion, direct experimental measurements of the optical depth have given a global confirmation of the relativistic theory of wave absorption at the 3rd electron cyclotron harmonic. These results are a sound basis for heating experiments at the 3rd harmonic. For adequate first-pass absorption, long path lengths are required and the microwave beam needs to be launched at a shallow angle to the resonance line, i.e., nearly vertically [13,14]. However, the absorption line being rather narrow and sensitive to paramagnetic effects, this heating scenario calls for a sophisticated launching system, providing good localization, low beam divergence and good control of the launching angles.

Acknowledgements. This work has been partly supported by the Swiss National Science Foundation.

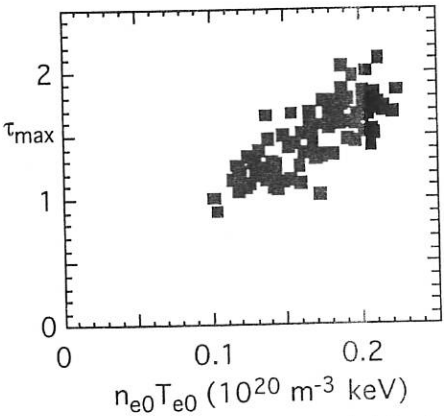


Fig. 6 : measured maximum optical depth for vertical propagation vs $n_{e0}T_{e0}$

[1] G. Tonetti et al., in *Proc. of 16th. Symp. on Fusion Technology, London 1990*, 1, 587.
[2] M. Bornatici *et al.*, Nucl. Fusion 23, 1153 (1983).
[3] D.C. Mc Donald *et al.*, Phys. Plasmas 1, 842 (1994).
[4] E.B. Meservey, S.P. Schlesinger, Phys. Fluids 8, 500 (1965).
[5] V. Arunasalam *et al.*, Phys. Fluids 11, 1076 (1968).
[6] P.C. Efthimion *et al.*, Phys. Rev. Lett. 44, 396 (1980).
[7] A. Pachtman *et al.*, Nucl. Fusion 27, 1283 (1987).
[8] F. Smits *et al.*, in *Proc. 8th Joint Workshop on ECE and ECRH, Gut Ising 1992*, (IPP, Garching, 1993) 2, 513.
[9] E.Mazzucato *et al.*, Nucl. Fusion 25, 1681 (1985).
[10] R. Kirkwood *et al.*, Nucl. Fusion 30, 431 (1990).
[11] J.L. Ségui, G. Giruzzi, Plasma Phys. Contr. Fusion 36, 897 (1994).
[12] G.Giruzzi *et al.*, Nucl. Fusion 31, 2158 (1991).
[13] R.L. Meyer, I. Fidone, in *Proc. 6th Joint Workshop on ECE and ECRH, Oxford 1987* (Culham, 1987), 57.
[14] A. Pochelon *et al.*, in *Proc. 20th JEPS Conf. Contr. Fusion Plasma Phys., Lisbon 1993* (EPS, Geneva, 1993), 17C, III, 1029.

HIGH DENSITY OPERATION WITH 140 GHz ECRH: EXPERIMENTS AT THE W7-AS STELLARATOR, PROSPECTS FOR THE W7-X STELLARATOR

V. Erckmann, N. Karulin, H. Wobig
W VII-AS Team, NBI Team [1]), IPF-ECRH group [2]), T-10 ECRH group,[3])
Gyrotron group [4]), IAP-ECRH group [5])

[1]) *Max-Planck-Institut für Plasmaphysik, EURATOM Ass., D-8046 Garching, FRG,*
[2]) *IPF, Univ.Stuttgart, FRG,* [3]) *Kurchatov Inst., Moscow, Russia,*
[4]) *SALUT, Nizhny Novgorod, Russia,*
[5]) *Inst. for Applied Physics, Nizhniy Novgorod, Russia*

INTRODUCTION

The extention of the accessible plasma density with ECRH at 140 GHz in 2nd harmonic operation (B_0=2.5 T) opens a new experimental parameter window for plasma investigations with favourable aspects: 1. The global confinement in W7-AS scales favourably with density /1/. 2. H-mode transitions occur in W7-AS once the density exceeds a certain threshold as is well known from tokamaks. 3. The investigation of the ion transport in ECR heated discharges is possible with the strong collisional coupling at high densities. The possibility of high density ECRH operation allows to combine ECRH and NBI, the latter of which inherently runs at high density. Heating with 70 GHz ECRH (up to 0.8 MW) restricts the plasma density to values below 6 10^{20} m^{-3} , which is the cut-off density for the O-mode, 1st harmonic (O1). This system is presently being replaced by a 140 GHz system with 2 MW microwave power at the 2nd harmonic X-mode (X2). Experiments with plasma densities up to $1.1 \cdot 10^{20}$ m^{-3} were performed with the presently available 140 GHz heating power of 0.5 MW for 1.1 s pulse duration (alternatively 0.9 MW for 0.4 s) which is close to the cut-off density for the X2-mode. The attractiveness of high density operation at W7-AS led us to examine the possibility to operate with the 2nd harmonic O-mode (O2) at the next step stellarator W7-X, which would allow to extend the plasma density towards 2 10^{20} m^{-3}.

BASIC OBSERVATIONS AT W7-AS

Experiments were conducted at W7-AS with pure ECRH in a wide density range. In the low density branch the electrons show only a weak collisional coupling to the ions and thus the electron confinement governs the plasma confinement. This branch is well suited to investigate the electron transport alone. In the high density branch the ions show a strong collisional coupling to the heated electrons and ion transport contributes significantly to the confinement. In Fig. 1 we have plotted the central electron (ECE and Thomson scattering) and ion temperatures (active CX diagnostics) as a function of the central electron density for an input power of 0.4 MW. It is clearly seen, that the temperatures approach each other in the high density branch. ECRH at high densities provides good experimental conditions for ion heat transport studies, because the power input to the ions is due to collisions only. A detailled transport analysis based on the measured profiles indicates, that the ion heat transport can be described by neoclassical theory within an uncertainty of a factor of two, if the ambipolar radial electric field is taken into account /2,3/.

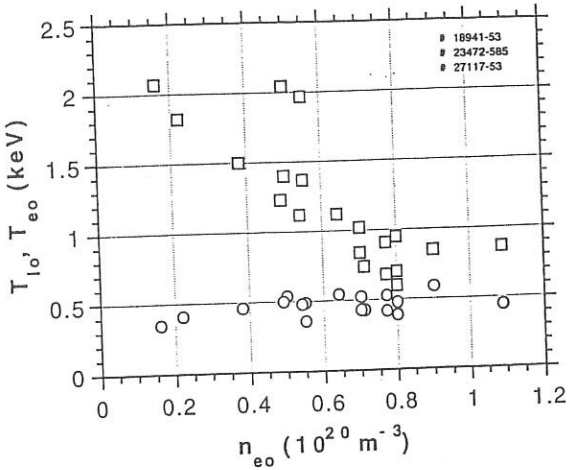


Fig.1: Central electron- and ion temperature as a function of the central plasma density for ECR heated plasmas with 0.4 MW input power.

The narrow power deposition profile with ECRH is well suited to shape the electron temperature profile in W7-AS by applying the heating power on- or off-axis. This holds also in the high density branch because of the special launching geometry, where the wave vector of the incident waves is perpendicular to the flux surfaces, which can be considered in good approximation as surfaces of constant density. Thus beam deflection is small also in the vicinity of the cut-off density. Experiments with combined heating of 140 GHz ECRH and NBI show a strong effect on the particle confinement and density control is possible despite the neutral-beam particle fuelling under combined heating conditions, whereas in general a steady density increase is observed with NBI alone due to beam fuelling and recycling fluxes /4/. A reduced impurity confinement was measured with combined heating at on-axis ECRH as compared to off-axis ECRH+NBI. There is evidence, that the reduced impurity confinement is due to the profile changes caused by additional ECRH.

PROSPECTS FOR HIGHER DENSITIES AT W7-X

The advantage of high density operation with ECRH led us to examine the possibility of a further extension of the accessible density range. The 2nd harmonic O-mode (O2) operation would in principle allow to extend the density with 140 GHz ECRH towards $2.4 \cdot 10^{20}$ m^{-3}. This mode is, however, optically thin at typical W7-AS parameters. For the expected plasma parameters and heating power (10 MW ECRH at 140 GHz) of the next step stellarator W7-X, however, this mode may become an interesting candidate. The single pass absorption for the 2nd harmonic O-mode is shown in Fig.2 for W7-X as a function of density for different launch angles at 2 and 4 keV electron temperature. The optimal launch angle for this mode is about 30° with respect to perpendicular launch. In contrast to the X2-mode, which is always optically thick at the relevant plasma parameters, the single pass absorption of the O2-mode is strongly dependent on the electron temperature within the operational

range of W7-X (1-6 keV), which in turn is determined by the heat transport. The electron temperature is expected to decrease with increasing density and due to the absoption characteristics of the O2-mode, the single pass absorption drops.

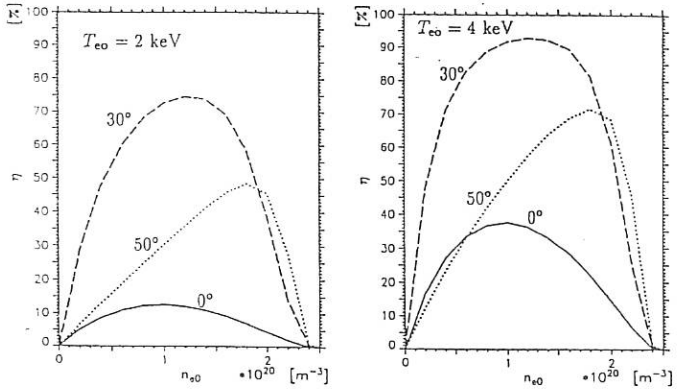


Fig.2: The single pass absorption for 2nd harmonic O-mode launch in W7-X as a function of density for different launch angles at 2 (left) and 4 keV (right) electron temperature.

Thus the plasma can in principle become thermally unstable while switching from X2- to O2-mode launch and increasing the density after switching.

We have modelled the time dependent plasma behaviour in W7-X with the ASTRA transport code during and after the transition from X2-mode to O2-mode heating. Heating scenarios were examined, where the plasma is started and maintained with the X2-mode (i.e. complete single pass absorption at all relevant W7-X parameters) at a given input power. Then the mode is changed to O2-mode and the density is increased in several steps until a thermal roll over of the plasma occurs. The result of the calculations and the onset of the thermal instability depends, of course, on the modelling of the heat transport and other plasma losses. We have used a local electron heat transport coefficient composed by the neoclassical /5/ and an anomalous term, the latter translates the Lackner-Gottardi scaling to stellarators /6/:

$$\chi_{e,an} = 2.4/R\ (2.2/B)^2\ .\ T_e^{3/2}\ (1.1-(r/a)^2)^{-4} \qquad (m, T, keV, s)$$

The ion heat conduction is assumed to be neoclassical in the optimized magnetic field geometry of W7-X including ambipolar electric fields. Bremsstrahlung losses and volume impurity line radiation losses of 30% of the absorbed power are included. The input power and the absorbed power at the onset of the thermal roll-over as obtained from the ASTRA simulations is plotted as a function of the density in Fig. 3 (left). The corresponding electron- and ion temperatures at the critical density are plotted together with the absorbed power fraction in Fig. 3 (right).

It is seen, that for an input-power level of about 4-5 MW stable operation can be achieved up to a density of about 1.8-2 10^{20} m^{-3} with a single pass absorption of

about 20-25 %. Heating with the full power of 10 MW would lead to T_{io}=2.3 and T_{eo}=2.7 keV , respectively, at an increased single pass absorption of 51 % at this density. Pushing the density even higher towards the cut-off density of the O2 mode leads to an excessively high input power with a single pass absorption of only 15 % to overcome the instability limit and is therefore considered unacceptable. The threshold temperatures of both ions and electrons are typically in the range 1-1.5 keV over the full density range.

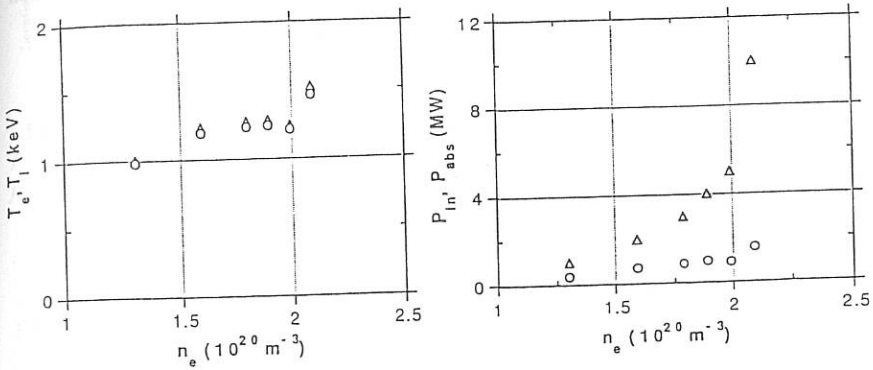


Fig.3: ASTRA code simulations for 2nd harmonic O-mode ECRH inW7-X.
Left: Input- (triangles) and absorbed power (dots) at the thermal stability limit as a function of density.
Right: Critical ion-(dots) and electron temperatures (triangles) for thermal instability as a function of the critical density.

The results are a pessimistic approach insofar, as only the single pass absorption is used for the calculations, which gives a worst case estimate for the required heating power. Multipass absorption is expected to contribute to heating as well, which would either increase the critical density for a given input-power or reduce the required input-power for a given density. From this modelling, therefore, we have high confidence that successful transition from X2- to O2-mode heating can be obtained and operation close to the cut-off density of the O2-mode is possible with the available heating power.

References:

/1/ Weller, A., et al., Plasma Phys. and Contr. Fusion, Vol.33 (1991) 1559
/2/ M.Kick, et al., Proc. 20th EPS Conf. on Contr. Fusion and Plasma Physics, Vol. 17C, Part I (1993) 357
/3/ U. Stroth, Workshop on Local Transport Studies in Fusion Plasmas, Göteborg, 1994
/4/ Erckmann, V., et al., Proc. 20th EPS Conf. on Contr. Fusion and Plasma Physics, Vol.17C, Part I (1993) 345
/5/ C.D. Beidler, Stellarators and other helical confinement systems, IAEA Technical Committee Meeting, Garching, Germany (1993) p.138
/6/ K. Lackner, N.A.O. Gottardi, Nuclear Fusion 30, No.4 (1990) 767

ELECTRON CYCLOTRON HEATING & CURRENT DRIVE IN ITER

B. Lloyd, M.R. O'Brien and C.D. Warrick

UKAEA Government Division, Fusion, Culham, Abingdon, Oxon OX14 3DB, UK
(UKAEA/Euratom Fusion Association)

Introduction

Electron cyclotron waves can fulfil a variety of roles in ITER, for example start-up assist, heating to ignition, current drive and instability control. In the present paper, we report the results of extensive calculations to examine the heating and current drive potential of electron cyclotron waves in ITER and to determine the optimum system parameters. Electron cyclotron heating is a robust, highly efficient and localised heating scheme. There is total absorption for all plasma parameters foreseen in ITER, the location of the damping is adjustable, there is no alpha particle damping, there are no requirements on plasma edge control and no specific impurity generation problems are anticipated. The calculations described here were carried out using BANDIT-3D (O'BRIEN et al, 1992) a relativistic and self-consistent ray tracing and Fokker-Planck code incorporating 2D velocity space (speed and pitch angle) and 1D real space effects. Electron radial diffusion, trapping, toroidal dc electric fields and realistic magnetic geometry (eg up-down asymmetric single null divertor configuration) can all be included and synergy with other schemes can be studied.

Parameters

A single null x-point configuration (magnetic axis at R = 8.2m, $\kappa \sim 1.55$, $I_p = 24.8$MA), was utilised in the calculations. The various values of B_ϕ quoted below correspond to the toroidal magnetic field at the nominal major radius $R_o = 8.1$m. Electron temperature and density profiles were of the form,

$$T_e(r) = (T_{eo} - T_{ea})(1-r^2/a^2) + T_{ea} \quad (1)$$

$$n_e(r) = (n_{eo} - n_{ea})(1-r^2/a^2)^{0.26} + n_{ea} \quad (2)$$

with $T_{ea} = 0.5$keV and $n_{ea} = 0.8 \times 10^{20}$m^{-3} generally assumed. Except where explicitly stated otherwise, $n_{eo} = 1.4 \times 10^{20}$m^{-3}. A flat Z_{eff} profile was assumed with $Z_{eff} = 2$. The most suitable scheme for both heating and current drive in ITER is low-field-side injection of the ordinary mode with absorption primarily at the fundamental resonance. A cone of rays with Gaussian power distribution and half-angle 3° was launched from the outboard plasma mid-plane. The effects of increasing the beam divergence up to half-angle 9°, or of launching the radiation from 30° below the plasma mid-plane, were found to be negligible for a number of cases investigated. The direction of launch is indicated by specification of the toroidal (ϕ) and poloidal (θ) launch angles, both measured with respect to the major radius. In calculating current drive efficiencies the effect of the inductive dc electric field was ignored. Similarly, for the parameters employed in this study, fast electron transport has an insignificant effect on the results and was therefore generally neglected.

Heating

Operation at 160GHz with perpendicular launch ($\phi = 0°$, $\theta = 0°$) allows core heating in ITER up to $n_{eo} > 3 \times 10^{20}$ m^{-3}. Strong localised absorption is observed even in the initial ohmic phase of an ITER discharge. For example, at $T_{eo} = 5$keV, $n_{eo} = 3 \times 10^{19}$m^{-3} ($n_{ea} = 1 \times 10^{19}$m^{-3}) the optical depth is ~30 indicating strong single pass absorption with the power absorbed inside r/a ~ 0.1 (ie., inside the flux surface which intersects the plasma mid-plane at r/a = 0.1). The optical depth increases to ~300 for parameters appropriate to the ignited phase ie., $T_{eo} = 20$keV, $n_{eo} = 1.4 \times 10^{20}$m^{-3} ($n_{ea} = 8 \times 10^{19}$m^{-3}). Thus strong heating of the core can be maintained throughout the density ramp-up and approach to

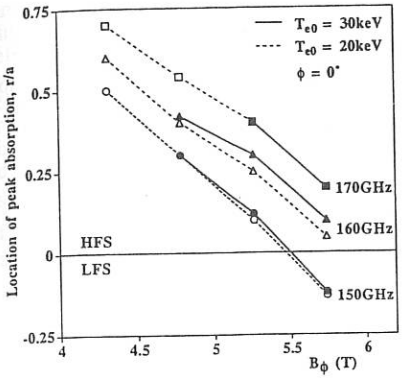


Fig 1 Location of power deposition vs $B\phi$ for fundamental absorption (perp. launch).

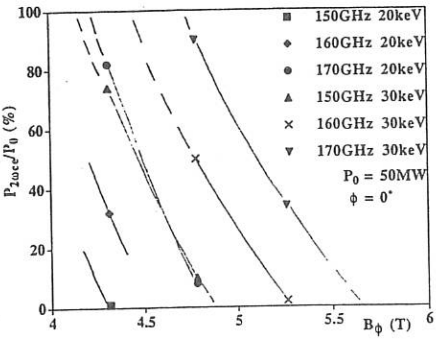


Fig 2 Fraction of second harmonic absorption vs $B\phi$ for fundamental absorption (perp. launch).

ignition. The location of the power deposition, plotted in Fig 1 as a function of $B\phi$, for f = 150 - 170GHz and T_{eo} = 20/30keV, does not depend strongly on temperature. For perpendicular launch at $B\phi$ = 5.74T, 160GHz gives the most central absorption. Of course, in all cases, as the toroidal field is reduced the absorption moves further to the high-field-side of the magnetic axis but central absorption can be recovered by imposing a toroidal launch angle which in turn leads to significant non-inductive current generation as discussed below.

Because of the high electron temperatures expected in ITER, downshifted ($\omega < 2\omega_{ce}$) second harmonic absorption, which can lead to a broadened power deposition profile, can be significant. At the nominal operating field, namely $B\phi$ ~ 5.7T at major radius R ~ 8.1m, second harmonic absorption is negligible for frequencies in the range 150 - 170GHz

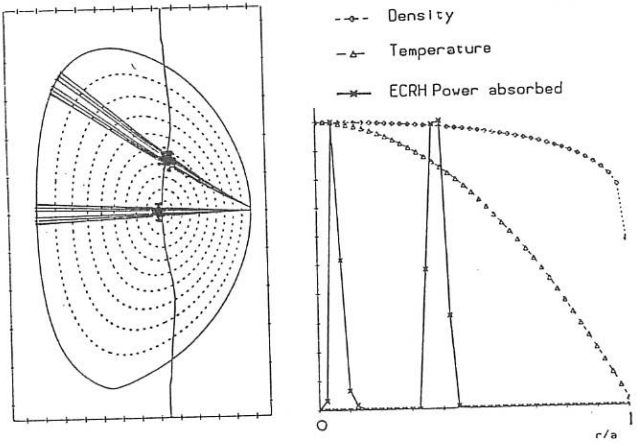


Fig 3 Control of heating zone by variation of poloidal launch angle.

(perpendicular launch) even at central temperatures up to 30keV, but soon becomes significant if B_ϕ is reduced, especially at 170GHz (Fig 2). Effective control of the heating zone at fixed magnetic field and frequency is possible by variation of the poloidal launch angle. This is illustrated in Fig 3 where imposition of a poloidal launch angle of 27° is seen to move the heating zone out to r/a ~ 0.4 whilst maintaining very localised power deposition. In this example f = 160GHz, $B_\phi = 5.74$T, $T_{eo} = 20$keV and $n_{eo} = 1.4 \times 10^{20}m^{-3}$.

Current Drive

Electron cyclotron current drive has been studied for a range of ITER parameters and for frequencies in the range 150 - 230GHz. The normalised current drive efficiency, $\eta_{20} = \langle n_e(10^{20}m^{-3})\rangle I_{rf}R_o/P_{rf}$, is plotted as a function of toroidal launch angle for a wide range of frequencies in Fig 4. The plasma parameters were $B_\phi = 5.74$T, $T_{eo} = 30$keV ($T_{ea} = 0.5$keV) and $n_{eo} = 1.4 \times 10^{20}m^{-3}$ ($n_{ea} = 8 \times 10^{19}m^{-3}$). In calculating η_{20} we have taken an average density of $1.3 \times 10^{20}m^{-3}$ consistent with the broad density profile used. It is seen that for these parameters, $\eta_{20} > 0.3$ is achievable. Very localised driven current profiles, as might be required for instability control, including error field locked mode removal, can be generated. A suitable scheme for central current drive would appear to be f ~ 220GHz with a toroidal launch angle of ~40°. The driven current is localised in the plasma core and the absorption arises from a strongly upshifted ($\omega > \omega_{ce}$) interaction. Downshifted second harmonic absorption is small (~10%) in this case, but for some combinations of frequency and toroidal launch angle can be significant. Because of relativistic and trapping effects, under many conditions the second harmonic driven current can reinforce the current arising from fundamental absorption leading to an enhancement of the current drive efficiency. Although a system at 220GHz ($\phi = 40°$) would simultaneously serve as a heating scheme, since the generation of the non-inductively driven current relies on the creation of a toroidally asymmetric resistivity (FISCH & BOOZER, 1980) through preferential heating of electrons with a particular sign of $v_{||}$, there is a great incentive to operate at as low a frequency as possible from the technological and economic point of view. Therefore it is instructive to examine in more detail the current drive capabilities of lower frequency systems in the range 150 - 170GHz which as we have seen are suitable for efficient heating over a wide range of plasma densities and temperatures. The normalised current drive efficiency is plotted as a function of toroidal launch angle for f = 150 - 170GHz, $B_\phi = 5.74$T and T_{eo} = 20/30keV in Fig 5. The current drive efficiency at 150GHz is extremely poor because

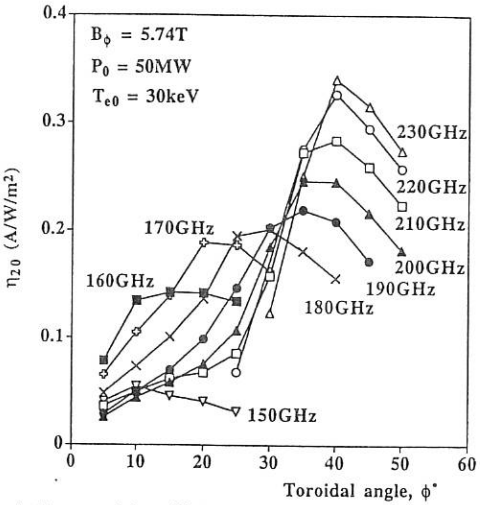


Fig 4 Current drive efficiency vs toroidal launch angle for frequencies in the range 150 - 230GHz.

imposition of a finite toroidal launch angle results in absorption significantly to the low-field side of the core where trapping can reduce the driven current. In addition it is seen that the efficiency at 170GHz appears to be somewhat better than at 160GHz primarily for the same reason. Clearly the conclusions in this case will depend to a certain extent on the equilibrium chosen and in particular the magnitude of the Shafranov shift. For operation at significantly reduced toroidal magnetic field, eg. ~4.3T, as has been proposed for some advanced high bootstrap fraction operating scenarios in ITER, there is little difference with respect to current drive capability between 160 and 170GHz. This is illustrated in Fig 6 where it may also be seen that operation at 160/170GHz with $B_\phi = 4.31T$ is essentially equivalent to operation at full field ($B_\phi = 5.74T$) and a frequency of 220GHz. In all cases the optimum toroidal launch angle is ~40°.

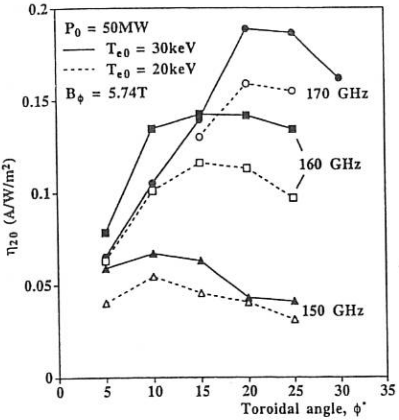


Fig 5 Comparison of current drive efficiencies for frequencies in the range 150 - 170GHz.

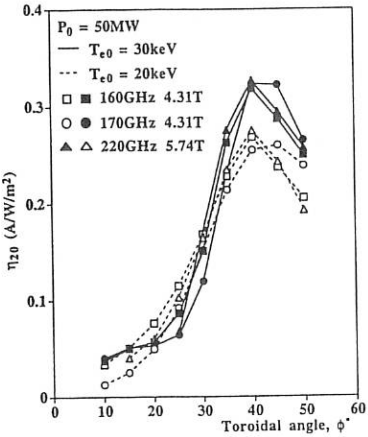


Fig 6 Current drive at reduced field & frequency and comparison with high field, high frequency operation.

There are two further important points to note from Fig 6. First, the optimum launch angle does not depend on central temperature in the range 20 - 30keV allowing the launch configuration to be specified in advance with some confidence. Second, the maximum current drive efficiency depends quite weakly on temperature in the same range.

Summary

These calculations identify ECH/ECCD as a flexible and robust tool for heating and current drive in ITER. For f = 220GHz, ϕ ~ 40°, current drive efficiencies $\eta_{20} > 0.3 (> 0.25)$ are achievable at T_{eo} = 30(20)keV. Perpendicular launch at 160GHz is ideal for efficient heating in both the ohmic and ignited phase. Effective control of heating location is possible by variation of the poloidal launch angle. An attractive option is a combined heating and current drive system at 160 - 170GHz with toroidal launch angle ~20°. 170GHz offers the potential of somewhat higher current drive efficiency but at the expense of reduced operating flexibility.

References

FISCH, N.J. & BOOZER A.H., Phys. Rev. Lett. **45** (1980) 720.
O'BRIEN, M.R. et al, Proc. IAEA Technical Committee Meeting on Advances in Simulation and Modelling of Thermonuclear Plasmas, Montreal 1992, p527.

* This work was supported by the UK Department of Trade and Industry and Euratom.

Experimental Investigation of ECRH Assisted Low Voltage Ohmic Startup in HL-1

L.H.Yao, Z.Y.Shang, D.M.Xu, T.C.Xu, S.W.Xue, Y.Liu, X.D.Li

Southwestern Institute of Physics, P.O.Box 432, Chengdu 610041,China

Introduction

Earlier experiments with microwave preionization[1] resulted in a reduction of the initial voltage and gave improved reliability and reproducibility of Ohmic startup in a variety of tokamaks. There is considerable interest in the development of low voltage startup for the requirement that the vacuum vessel of reactor scale tokamak be sufficiently robust to withstand the large forces associated with a disruption and that the vessel be constructed without any insulating toroidal breaks implies that the toroidal electrical resistance will be small, for example, it is in the order of $\mu\Omega$, which in turn limits the toroidal electric field $E \leq 0.3$v/m. Electron cyclotron resonance heating (ECRH) has been proposed as an alternative means of assisted Ohmic heating startup at low electric field in some tokamaks[2,3]. The experiments demonstrated that the O-mode launch starts the plasma more centrally than the X-mode launch and results in higher current ramp rate[3]. Studies of ECRH-assisted startup in HL-1 are considerable important, because the toroidal resistance of HL-1M, which is under construction now, will be reduced to 1.5 mΩ from 20mΩ of HL-1. It is better strengthen the breakdown of pre-fill gas and promote the plasma current ramp rate at startup phase, so as to reduce the influence of stray magnetic fields on the start up of tokamak plasma.

Experimental arrangement and results

For previous reasons the experiments of assisted startup were carried out on HL-1 device in original Ohmic discharge program for making a comparison of the effect with or without ECRH assisted. At the present, series of experiments, 240kW of microwave power for pulse lengths of up to 20ms was launched by 75GHz gyrotron with HE_{11} mode through the 3m over-mode waveguide into HL-1 torus from the low magnetic field side with O-mode polarization. When the wave pulse is launched before loop voltage is applied, breakdown takes place, which implies that we can control the position of breakdown by changing toroidal magnetic field strength and the time by microwave pulse trigger time, respectively, so the discharge will be more reliable and reproducible.

The experimental data demonstrate that substantial reductions($>50\%$) in loop voltage required for plasma current startup are obtained as ECRH assisted. During the phase of plasma current ramping up, the magnetic flux consumption saving is about 41% at the end of microwave launch as shown in table 1.

Table 1. Flux consumption during startup

Time (ms)	With ECRH (VSec consump)	Without ECRH (VSec consump)	Saving of VSec (%)
5	0.068	0.13	47.7
10	0.092	0.16	42.5
15	0.10	0.17	41.2
20	0.12	0.19	36.8
50	0.17	0.24	29.2
100	0.25	0.31	19.4

The plasma current ramping rate can be written by as following

$$\frac{dI_p}{dt} = \frac{V_\ell - I_p\left[R + \frac{1}{2}\frac{d}{dt}L_{tot}\right]}{L_{tot}},$$

where V_ℓ is the loop voltage, R is the plasma resistance and L_{tot} is the total plasma inductance. Owing to the effect of ECRH, the electron temperature increases promptly resulting in the decrease of plasma resistance($\eta \propto T_e^{-3/2}$), the variation of total plasma inductance can be neglected owing to the fact that the plasma current position shift is small for O-mode launch[3]. Thus, the current ramping rate increased with ECRH by 1.3 times can be attributed to a reduction in the resistive voltage(Fig.1). The curve of current ramping up with ECRH is smoother than that of without. In the meanwhile, the electron density rises quickly after the loop electric field is applied, resulting in the decrease of run away electrons(Fig.2), as well as the decrease of non-thermal electron radiation during the phase startup as shown in Fig.3.

Conclusion

The experiment is also a pre-test of HL-1M tokamak low voltage Ohmic heating startup. It seems to be useful to make up the programmable plasma current at start-up phase for HL-1M experiments.

References

1 Xu Yaocong, Liu Yukui, Zhu Xuewu, et al. Preionization Experiments in HL-1 Tokamak with a 4mm Gyrotron. Nuclear Fusion and Plasma Physics (in chinese), 8(1988)163

2 Lloyd B, Jackson G L, Taylor T S, et al. Low Voltage Ohmic and Electron Cyclotron Heating Assisted Startup in DIII-D. Nuclear Fusion, 31(1991)2031

3 Whaley D R, Goodman T P, Pochelon A, et al. X-and O-mode Electron Cyclotron Heating Breakdown and Startup in TCA. Nuclear Fusion, 32(1992)757

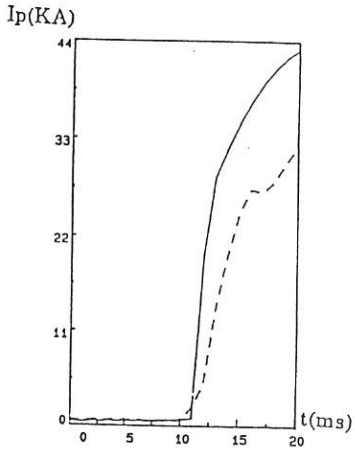


Fig.1 Plasma current ramping rate comparison with (solid line) and without (dashed line) ECRH assisted

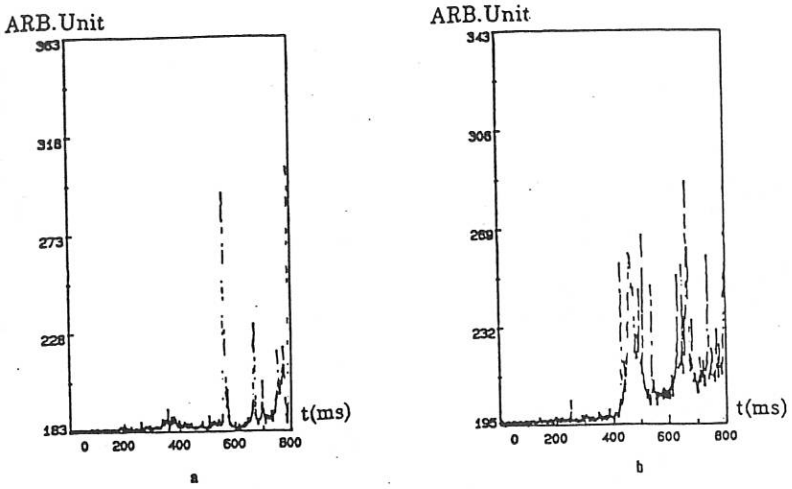


Fig.2 Hard X-ray emissions comparison
a,with ECRH b,without ECRH

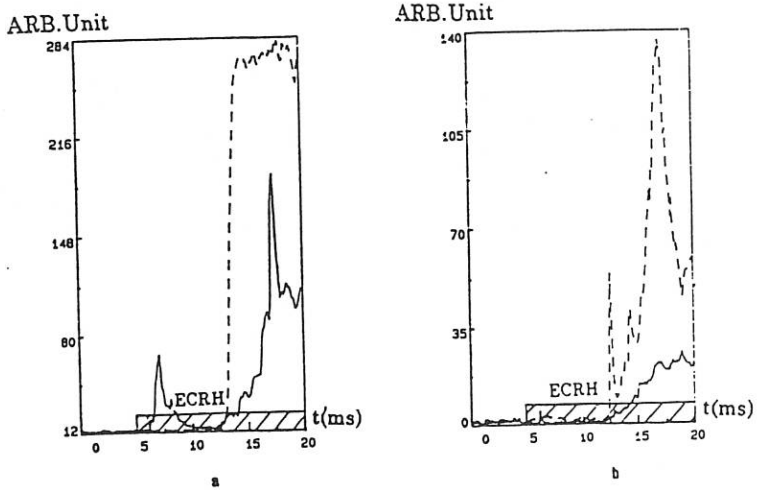


Fig.3 Non-thermal electron radiation comparison with (solid line) and without (dashed line) ECRH assisted
a,3cm microwave radiation b,10cm microwave radiation

Influence of different Heating Schemes on High-Z Contamination from a Tungsten Test Limiter in TEXTOR

G. Van Oost[1], A.M. Messiaen[1*], V. Philipps[2], M. Wada[3], N. Hawkes[4], R. Koch[1], J. Ongena[1*], A. Pospieszczyk[2], M. Rubel[5], B. Schweer[2], T. Tanabe[6], Y. Ueda[6], R. Van Nieuwenhove[1*], G. Van Wassenhove[1], P. Wienhold[2]

[1]Laboratoire de Physique des Plasmas - Laboratorium voor Plasmafysica - Association "Euratom-Belgian State", Ecole Royale Militaire - Koninklijke Militaire School, B-1040 Brussels - Belgium
[2]Institut für Plasmaphysik, Forschungszentrum Jülich, Association EURATOM-KFA, Germany
[3] Dep. Electronic Engineering, Doshisha University, Kyoto 602, Japan
[4] UKAEA-Euratom Association, Culham, UK
[5]Royal Institute of Technology, Physics Department-Frescati, Association-EURATOM-NFR, Stockholm, Sweden
[6] Faculty of Engineering, Osaka University, Suita, Osaka 565, Japan
[*] Researcher at NFSR, Belgium

ABSTRACT

Test limiter experiments have been carried out in TEXTOR under various plasma- and heating conditions to broaden the database for the evaluation of the suitability of high-Z materials as plasma facing components in large machines.

The heat flux to the test limiter reached values on the order of 20 MW/m^2, representative of ITER divertor target conditions. Under OH conditions W-radiation increases with plasma density. Above a critical density, accumulation in the centre leads to an instability characterized by strong central radiation and hollow T_e profiles. In most discharges heated with NBI($H^0 \rightarrow D^+$) no strong central radiation was observed although the release of W was comparable with that in OH discharges, and the W-radiation decreases with increasing plasma density. In some discharges heated with NBI ($D^0 \rightarrow D^+$) a centrally peaked radiation profile was observed. Remarkably, this central radiation decreases as soon as ICRH is added to NBI and disappears afterwards, enabling to maintain a sufficiently clean core plasma in a steady state with good confinement. A similar RF-induced expulsion of W from the centre was also observed in an ohmic target plasma. No accumulation of W in the centre was found in discharges with edge radiative cooling using neon and heated with NBI and/or ICRH.

I. INTRODUCTION

At present, plasma-facing components belong to the most difficult design issues for ITER. The current database for plasma-facing materials (PFM's) in large machines is concentrated on low-Z materials (carbon-based and Be)[1] which, together with wall conditioning techniques have been an essential element in the attainment of improved plasma parameters. However, there are serious concerns about the applicability of low-Z materials in future fusion devices[1] such as erosion (life-time), degradation of thermal conductivity due to neutron irradiation, safety problem of Be and its low melting point (1277°C), etc. From the materials point of view, poor ductility and low thermal shock

resistance used to be a problem of most refractory metals. However, recent advances in production and purification techniques are bringing high-Z PFM's within engineering feasibility[1]. These materials have high melting points, advantageous sputtering properties, good thermal conductivity and acceptable thermomechanical properties. Tungsten and molybdenum impurity production was found to be mainly due to physical sputtering by carbon and oxygen impurities[2]; W and Mo have a high threshold energy for physical sputtering and their use in the high density, low temperature ITER divertor might be attractive to overcome problems of excessive materials erosion.

The main concerns for the utilization of high-Z materials as PFM's are[1]: (1) impurity production and accumulation (very low tolerable high-Z impurity concentration due to strong line radiation), (2) hydrogen recycling in the high recycling regime, and (3) material performance under high heat load conditions (4) metal impurities during ICRH[7].

Since TEXTOR is dedicated to the study of plasma-surface interactions and PFM's, and is particularly well edge-diagnosed, a high-Z test limiter programme has been initiated [2,3] to broaden the poor database for the evaluation of the suitability of high-Z materials as PFM's.

2. EXPERIMENTAL SET-UP

The test limiter experiments were performed under standard TEXTOR conditions with boronized walls (ALT-II belt limiter at 46 cm, B_t = 2.25 T, I_p = 350 kA) in ohmically and auxiliary heated plasmas (NBI: $D^o \rightarrow D^+$ and $H^o \rightarrow D^+$; ICRH: 32.5 MHZ, screenless antenna, H-minority heating). A tungsten test limiter was inserted through a limiter lock at the bottom of the vessel up to a minor radius r = 44 cm. The limiter was made of highly purified W and had dimensions of 10 cm in toroidal direction, 6 cm in poloidal direction and 5 cm in height (toroidal curvature 8.5 cm and poloidal curvature 6 cm). The plasma-facing area of the test limiter represents only about 1/500 that of ALT-II (3.3 m^2). Hence, the major part of the plasma still interacts with the graphite belt limiter which dominates the general impurity behaviour.

The test limiter was thermally isolated and used as a calorimeter. A maximum fraction of about 8 % of the total convective energy was deposited onto the test limiter, resulting in a heat flux of about 20 MW/m^2 (representative of ITER divertor target conditions) and a peak surface temperature of about 2900 °C (melting point of W: 3410 °C). determined from CCD camera measurements. The local impurity release was studied by means of a spectrometer. High-Z contamination of the plasma was observed by VUV-spectroscopy (SPRED spectrometer), soft-X-ray emission and by radial profiles of the radiated power from bolometry. Edge electron temperature and density profiles were measured using He- and Li-beams. Surface collector probes were used in the SOL to trace deuterium and impurity fluxes[4].

3. EXPERIMENTAL RESULTS

Under OH conditions with the test limiter inserted at 44 cm the W-impurity radiation increases with increasing plasma density although the relative strength of the W-source decreases; the local W-emission from the test limiter as well as the deposition of W on the deposition probes in the SOL both decrease with increasing density and decreasing edge temperature as is expected from a sputter erosion process. Figure 1 shows the evolution of the radiation profile during a density scan with the limiter inserted and withdrawn. The additional radiation due to W-impurity ions is rather low at low n_e, increases at medium n_e and rises dramatically as the central line-averaged density n_{eo} exceeds a critical value of $3 \cdot 10^{13}$ cm^{-3}. At this critical density W accumulates in the

plasma centre, leading to strong W-radiation and hollow electron temperature profiles resulting in a minor disruption (thermal instability). At a density of $2.5 \cdot 10^{13}$ cm^{-3} the evaluated W-concentration profile is flat with a value of typically $2 \cdot 10^{-4}$, in good agreement with the relative W-deposition rate on the collector probe.

In NBI-heated discharges the impurity behaviour as a function of density is totally different although the impurity source changes in the same way. Similar results were obtained with a Mo-limiter[2,3]. A density scan with NBI-Co (1.3 MW, $H^0 \rightarrow D^+$) showed that the W-radiation decreases with increasing plasma density similar to the W-source at the limiter (decreasing edge temperature). At high density (n_{e0} around $5 \cdot 10^{13}$ cm^{-3}) the contribution of the high-Z limiter to the plasma impurity content and its influence on the plasma performance are negligible. No instability was observed under these conditions. The evaluated profiles are peaked at the outer plasma regions. However, with $D^0 \rightarrow D^+$ accumulation of W in the plasma centre was observed in some discharges leading to centrally peaked radiation profiles.

It is remarkable to note that this central radiation decreased as soon as ICRH was added to NBI and disappeared afterwards, enabling to maintain a sufficiently clean core plasma in a steady state with good confinement (confirmed by neutron yield measurements, see in the next paragraph), in spite of a slight increase of the W-release with respect to NBI alone. A similar RF-induced expulsion of W-impurities from the centre was also observed in an OH target plasma. Figure 2a shows a clear decrease of the central radiated power at the onset of ICRH while the time evolution of the radiation profile in Fig. 2b reflects the accumulation during the OH phase and the expulsion at the onset of ICRH. No thermal instability occurred in discharges heated by ICRH (with or without NBI).

Preliminary results from discharges with edge radiative cooling using neon and heated with NBI-Co ($D^0 \rightarrow D^+$) and/or ICRH show that there is almost no increase of the W-concentration in the plasma centre, in contrast with the results from discharges with Ne-cooling and hydrogen NBI-Co where a Mo-test limiter was inserted[3]. The absence of a significant decrease of reactivity of the plasma (from neutron yield measurements[5]) is a clear indication for a low central impurity concentration[6] (and stationary in time) which is confirmed by the radiation profiles.

4. DISCUSSION

The impurity concentration is determined by the source strength and the transport of impurity ions. The striking difference in W-concentration and radiation profiles between OH- and auxiliary heated discharges can be due to several factors such as impurity production, impurity transport, shielding effects by the edge plasma, occurrence of sawteeth, etc. ... The results show that in both types of discharge the impurity source changes in the same way as a function of density (limiter erosion reduced by decrease of edge temperature). Impurity screening depends on the heating scheme. The ionization lengths of singly charged Mo-ions in NBI-heated high density discharges were found to be shorter than their Larmor radius, leading to prompt local redeposition[3]. The interactions between the plasma boundary and ICRH can differ strongly from those between the plasma boundary and NBI depending on the conditions[7].

Sawtooth activity may lead to the disappearance of a peaked radiation profile. Preliminary results indicate that no strong central radiation occurred in case of strong sawtooth activity, but not vice versa. The limited database does e.g. not allow to conclude whether the disappearance of central radiation after the onset of ICRH is linked to a modification of the sawtooth behaviour caused by the RF or if the cause of the change in

sawtoothing is the reduction of central radiation due to RF-induced expulsion of tungsten.

An analytical model[2] taking into account energy and impurity particle transport has recently been proposed to explain the central radiation behaviour. Further test limiter experiments are planned on TEXTOR with a view to a detailed study of high-Z contamination under a variety of plasma- and heating conditions, including edge biasing.

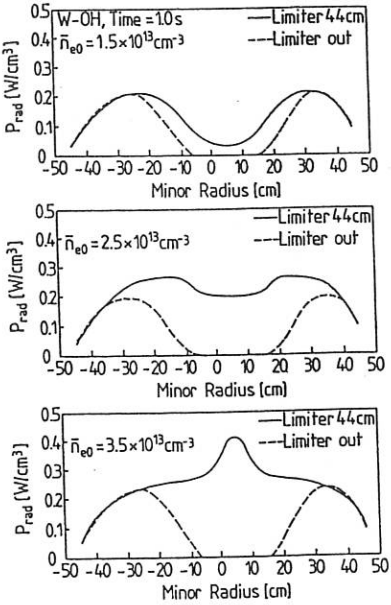


Fig. 1 Radiation profiles with the tungsten limiter inserted (r = 44 cm) and withdrawn for different plasma densities under ohmic heating conditions.

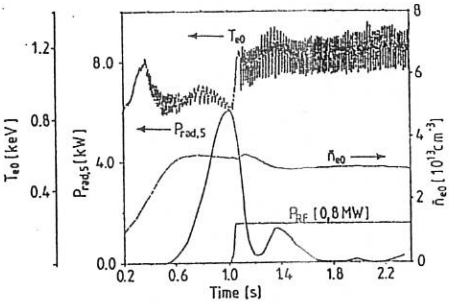


Fig. (2a) Time evolution of central electron temperature, central line-averaged density, central radiated power (inside r = 5 cm), and RF power (#55813). Tungsten limiter at r = 44.5 cm.

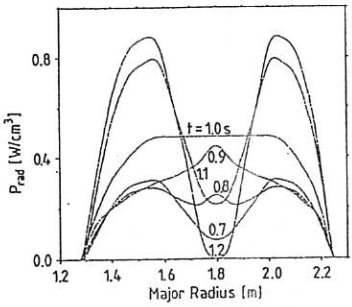


Fig. (2b) Radiation profiles at different times.

REFERENCES

/1/ T. Tanabe et al., J. Nucl. Mater. 196-198 (1992) 11

/2/ V. Philipps et al., to be published in Nucl. Fusion

/3/ Y. Ueda et al., tp be published in J. Nucl. Mater.

/4/ M. Rubel and P. Wienhold, to be published in Contrib. Plasma Physics (1994)

/5/ G. Van Wassenhove et al., Proc. 17th Eur. Conf., Amsterdam 1990, Vol. 14 B, Part III, p. 1040

/6/ A.M. Messiaen et al., Nucl. Fusion (1994) in press

/7/ J.M. Noterdaeme and G. Van Oost, Plasma Phys. Control. Fusion 35 (1993) 1481

Physics Issues and Design Aspects of ITER Ion and Electron Cyclotron Systems

G. Bosia, M. Makowski, T. Nagashima, D. Remsen
ITER Joint Central Team
Garching, Max-Planck-Institute für Plasmaphysik,
D-85748 Garching bei München, FRG

1. Introduction

The primary purpose of the ITER RF System is to provide the auxilliary power necessary to reach ignition. This varies with the assumed transport scaling, impurity level, and plasma operating conditions. A total of 50 MW deposited in the plasma appears to be adequate for heating to ignition under a variety of scenarios. A secondary goal of the RF program is to provide ITER with means of non-inductive current drive for discharge control, extension of the pulse length, and possibly steady state operation. However, the experimental basis for such scenarios is not sufficiently established so that detailed requirements cannot at this time be determined. The prevailing approach now is to note the development of steady-state concepts (such as high β_p scenarios) and ensure that the auxiliary power system can be adapted to potential needs as they arise.

2. ICRF Heating and Current Drive Scenarios

Several ICRF heating scenarios (20-80 MHz) can be used in ITER [1]. The target objective of the heating scenario is single pass central plasma heating during the pre-ignited phase.

The second harmonic tritium (T) scheme has a number of advantages: there is little power going to the α-particles, it can be used in deuterium (D) rich mixtures and directly heats a reacting species. At the high electron densities in ITER, there is no concern about large T tail formation. Heating at the second harmonic is a finite gyro radius effect and requires a high temperature for absorption at the second harmonic of T ($n_D / n_T = 1$). The addition of ~5 % of He^3 resonating at the same radial position but at its fundamental resonance may be required. Simulations using the ALCYON 3D code [2, 3] show that 50 % of the power is absorbed by the He^3 with good ray focusing (Fig. 1) while 50 % is still absorbed by electrons. As the temperature increases, fuelling in He^3 can be stopped. The He^3 will progressively disappear through D-He^3 reactions providing a small additional heating gain (~10 % for 5 % He^3). Second harmonic heating of T ions then takes place as the temperature increases. Under ignited conditions and for $n_T/n_D = 1$, the power partition is typically 46 % to T ions, 50 % to electrons and 3 % to D ions, and can be influenced by the choice of toroidal mode number (the phasing between the antennas); a lower toroidal mode number favours the deposition to the T ions.

Heating at the fundamental resonance of D gives the highest single pass damping and ion heating in T rich mixtures. In a reacting plasma, the power deposition in the α-particles ($f_{CHe^4} = f_{CD}$) is a concern, though the choice of $k_\parallel$ can influence the partition of power. In ohmic conditions and for $n_D/n_T = 0.4$ and a central toroidal mode number $n \sim k_\parallel R$ of 69 only a small fraction of power is absorbed by D ions (20 %) [3]. The main fraction (80 %) is absorbed by electrons through the cumulative effort of Landau damping and mode conversion at the D-T hybrid layer. An increase of the D concentration to $n_D/n_T = 1$ leads to a power fraction of 90 % to the electrons. For an ignited plasma, assuming 5 % of α-particles at 1 MeV, the power distribution is 50 % to D, 25 % to electrons and 25 % to the α-particles (Fig. 2). Decreasing n to 34 leads to an increase in the power deposited on the α-particles to 48 %, while D ions retain 36 % and electrons 16 %.

The ICRF current drive (CD) scheme relies on the absorption of the fast magnetosonic wave through electron Landau damping and transit time magnetic pumping.

A frequency below the lowest cyclotron harmonic is chosen (~20 MHz) in order to avoid parasitic ion damping. This, together with a suitable choice of the antenna spectrum, realize a compromise ($\omega \sim 2k_{\|}v_{\|}$) where the adverse effect of trapped particle and direct cyclotron resonance wave absorption are minimized [4]. In this scheme, single pass absorption on electrons lies between 20 to 60 % depending on $k_{\|}$ value. The mode converted fraction of the wave power at the Alfven resonance is about 10 % of the unabsorbed power.

The CD scenario is viable only in high-β_p, high temperature low plasma current plasmas. A simulation of the CD efficiency has been computed in a typical low plasma current (I_p = 15 MA, n_D/n_T = 1, f = 20 MHz, B_T = 6 T, $T_{e0} = T_{i0}$ = 27 keV, n_{e0} = 1.4 x 10^{20} m^{-3}, edge temperature 0.3 keV, edge density 0.6 x 10^{20} m^{-3}). The CD figure of merit is γ_{IC} = 0.3 x 10^{20} A/Wm^2 not including trapped particle effects. Sources of inefficiency are the off mid-plane poloidal position of the antenna (20-30 %), which causes an enrichment of the poloidal wavenumber spectrum. It should be noted that we have made no attempt to optimize parameters.

3. ECRF Heating and Current Drive Scenarios

For the magnetic field and range of densities and temperatures relevant to ITER, outside launch of Ordinary-Mode (OM) polarized ECW meets the accessibility requirements for ITER applications. Since ECWs propagate in free space the power can be coupled through the vacuum layer without impurity generation or density feedback control.

Central heating for ignition requires a frequency in the range of 150-170 GHz and allows propagation to peak densities up to 3 x 10^{20} m^{-3}. Simulations using the BANDIT 3D code indicate that full single pass absorption can be obtained in both the ohmic and ignited phases of the discharges [5]. The optical depths for these two cases are 30 and 300, respectively. The loss due to second harmonic absorption is not significant for the range of temperatures, densities, and central fields of interest to ITER. For the frequency range proposed there is no significant second harmonic absorption in the pre-ignited (T_e < 15 keV) and ignited phases for a field of 6 T. In ignition, assuming T_{e0} = 32 keV, fundamental power is completely accessible to the centre of the plasma at the full field of 6 T offering some prospect for burn control [5].

Detailed studies of core CD recommend scenarios based on upshifted ($\omega > \omega_{ce}$) absorption of elliptically polarized OM waves launched from low-field-side midplane [6]. Such scenarios are compatible with high-bootstrap-current operation. A survey of runs has been performed on ITER reference ignition plasmas at two different T_{e0} of 20 keV and 30 keV; n_{e0} = 1.7 x 10^{20} m^{-3}. The peak value of 0.3 x 10^{20} A/Wm^2 is obtained for frequencies between 180 and 220 GHz and launch angles between 30° and 40° (Fig. 3).

CD in ITER plasmas with a central electron temperature of 30 keV, central density of 1.6 x 10^{20} m^{-3}, central field of 5.9 T, but with an equilibrium confining a current of 10-15 MA, of which > 70 % is bootstrap current, has been modelled [5]. This equilibrium features a large shift in the position and field value of the magnetic axis. The optimum launch parameters were found near a frequency of 190 GHz, a poloidal launch angle of 20° above horizontal, and a toroidal launch angle of 45° corresponding to γ_{EC} = 0.3. Even in these condition of oblique launch angle and high central electron temperature, the amount of second harmonic absorption is small (under 5 %) due to the peaked electron temperature profile. At 170 GHz a significant CD of γ_{EC} = 0.24 is obtained.

4. ICRF Antenna Concept

The proposed system [5] is composed of two arrays of 18 RF antennas (36 in total for 100 MW), toroidally located in two opposite 45° sectors of the vacuum vessel. Each array is integrated in 9 adjacent shield modules (two RF antenna per module). The

antennas are installed in the lower section of the outboard shield, which can be routed through the radial ports. A triax feeder, carrying RF power, inlet and outlet coolant in a compact 260 mm OD tube is proposed (Fig. 4). Water cooling is used, at the same temperature (100-150°C) and the pressure (20 Bars), as for the shield cooling. The proposed poloidal position is a trade-off between optimized RF performances and the requirements of not removing any TF coils shielding where the neutron flux is maximum.

The proposed antenna [7] is a stripline short circuited at both ends, having an electrical length approximately equal to $\lambda/2$ at the lowest frequency used resonant at n $\lambda/2$ with n = 1, 2, 3, 4, asymmetrically fed at an intermediate point. This scheme provides a good antenna efficiency at most of the interesting frequency ranges and has practical advantages: i) the current strap is self supporting, and supports also the feeder's end; ii) the antenna has self tuning properties, and the feeder's tap point can be selected where the antenna and feeder impedances approximately match.

5. ECRF Antenna Concept

A design goal is to minimize the impact of the ECRF antenna on the shield design while fulfilling physics requirement [5]. To that extent, the main feature of the optical design are: i) 50 MW of power delivered to plasma; ii) two horizontal ports used for 100 MW; iii) minimum size of the shield penetration; iv) minimal extension of primary vacuum boundary.

50 MW of ECW is injected through an elliptical blanket aperture 44 x 34 cm^2 in size corresponding to an average density of 420 MW/m^2 (800 MW/m^2 already achieved on DIII-D).

The antenna system is mounted into a steel structure supported by the cryostat and linked to the vessel through double walled bellows (Fig. 5). From the inner window block waveguides are brought together with mitre bends to form a compact waveguide launcher. The power from each waveguide is projected onto a parabolic reflector (0.9 x 1.04 m^2) which focuses and directs the power along a major radius (perpendicular injection) into the plasma, or onto a second flat mirror (1.1 x 0.4 m^2). From this mirror the beam is reflected at an oblique toroidal angle (35°) into the plasma for CD applications.

Acknowledgements

The authors would like to thank Home Team members for their excellent contributions.

References

[1] J. Jacquinot et al., :*Ion Cyclotron Summary*, ITER Tech. Meeting on RF H&CD, Garching JWS (Nov. 21-26, 1993).
[2] D. Edery, H. Picq, A. Samain, D. Gambier, EUR-CEA-FC Report No. 1334 (1987).
[3] A. Bècoulet, Fast Wave Task Force, Subtask No. TAC 4 FW-1 and FW-2.
[4] M.V. Dimitrieva, L. Eriksson, D. Gambier, JET Report R(92) 09 (1992).
[5] 4th TAC Report, *DETAIL OF THE ITER OUTLINE DESIGN REPORT*, Vol. 1, Jan. 10-12, 1994.
[6] R. Freeman et al., :*Electron Cyclotron Summary*, ITER Tech. Meeting on RF H&CD, Garching JWS (Nov. 21-26, 1993).
[7] V.P. Bhatnagar, J. Jacquinot, JET-P(93)76, submitted for publication in Nuclear Fusion.

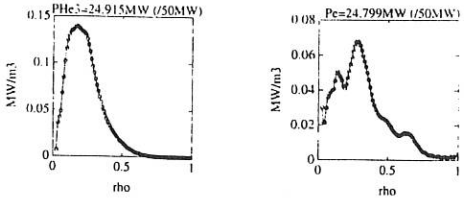


Fig. 1 ICRF wave absorption; n_D/n_T =1 and 5 % He^3, 60 MHz

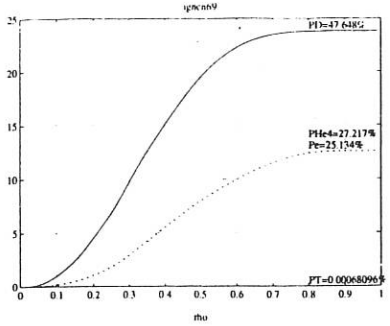


Fig. 2 ICRF wave absorption; ignited condition, $n_D/n_T = 1$ and 5 % α-particles at 1 MeV, 43 MHz

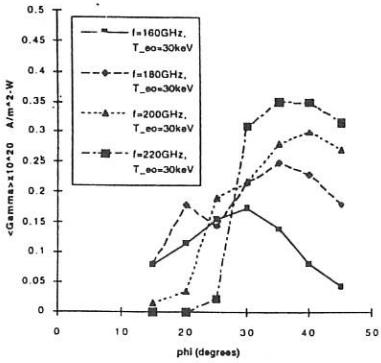


Fig. 3 ECCD figure-of-merit γ vs. toroidal injection angle; $I_p = 24$ MA, $n_{e0} = 1.7 \times 10^{20}$ m^{-3}

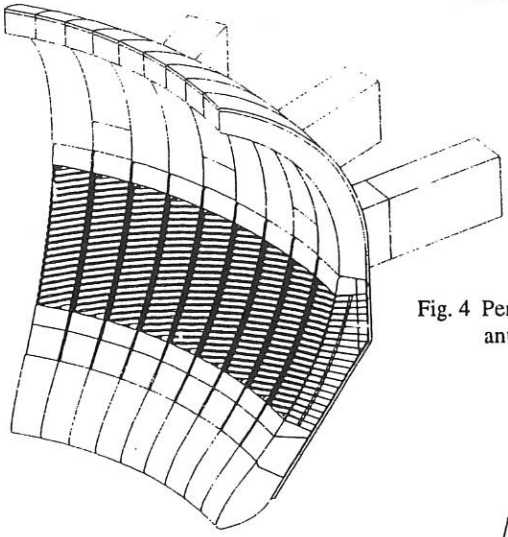


Fig. 4 Perspective view of an ICRF antenna array for ITER

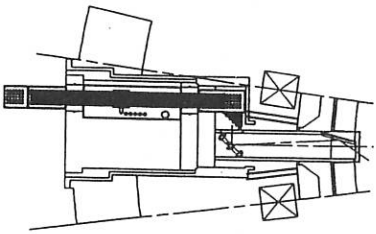


Fig. 5 Top view of the ECRF antenna for heating and current drive in ITER

EFFECTIVE LOWER HYBRID HEATING OF ELECTRONS AND IONS IN THE FT-2 TOKAMAK

V.N.Budnikov, V.V.Dyachenko, L.A.Esipov, E.R.Its, M.A.Irzak, S.I.Lashkul, K.A.Podushnikova, A.Yu.Stepanov

The Ioffe Physiko–Technical Institute, St.Petersburg, Russia

The experiments on the lower hybrid (LH) heating in the FT-2 tokamak [1] have demonstrated that the wave absorption and ion heating are associated with the development of the parametric decay instability of the pump wave f_0 that takes place in the plasma centre at a local density $n_d < n_{LH}$ (n_{LH} — LH density, i.e. the density at the wave linear transformation point estimated by the dispersion relation with finite temperature corrections [2]). Here the daughter wave $f_1 \approx 0.7\, f_0$ has its local LH resonance which provides an effective interaction with ions. The fast ions generation starts at the centre at a minimum energy $E_{min} \approx 8T_i$. At the increase of the plasma density $\bar{n}$ the decay region shifts to the periphery, its local density n_d slightly rises and the ions of successively higher energies are produced (this can be considered as an evidence of the development of parametrically excited long wave spectra). At the same time the current drive switches off. The bulk ion heating is observed at these intermediate densities $n_0 \approx 1.5\, n_d$.

The fact of ion heating in the intermediate density region has been proved by the plasma heating experiments on the tokamaks ASDEX [3] and FT [4] and it does not contradict with the experiments in Petula-B [5] (considered earlier as an example of classical heating). However in the previous LH heating experiments little attention has been paid to the investigation of this density region. The goal of the present work is a detailed study of the electron and ion heating at the intermediate plasma density.

The main device and discharge parameters are: $R = 55\,\text{cm}$, $a = 8\,\text{cm}$, $I_p = 22\,\text{kA}$, $B = 22\,\text{kGs}$, $\bar{n} = (1.2 - 3.0) \cdot 10^{13}\,\text{cm}^{-3}$, H^+ plasma. In the ohmic regime the electron and ion temperatures were 500 – 600 eV and 100 eV, respectively. The RF power up to 140 kW at a frequency 920 MHz and with pulse duration 3 ms was launched from the outer side of the torus through a 2-waveguide grill ($N_\parallel = 2 - 4$).

After the end of the RF pulse a transition to the regime of the improved confinement of particles and energy was observed [6]. It was accompanied by typical processes: drop of the H_β line emission at the rise of the average density, sharp reduction of MHD activity, ELM's appearance. The energy confinement time $\tau_E^{OH} = 0.8\,\text{ms}$ in the ohmic regime. During the RF heating it decreased with the increase of the RF power and came down to 0.5 ms at 100 kW. After the end of RF pulse it rose sharply up to 2 ms. It was observed in a wide range of RF powers 40 – 140 kW.

The general scheme of the plasma-wave interaction is shown in fig. 1. Here the loop voltage drop $\Delta U/U_l$, CX fluxes at energies 1.5 and 3.7 keV, electron and ion temperatures (measured by SXR and CX spectra, respectively) are presented as a function of the central density n_0. The loop voltage drop (representing the current drive efficiency) was observed only below those densities at which the fast ions generation started. The electron and ion heating began at the same densities. In the experiments the ion temperature increased by 4 times (from 100 eV to 400 eV) and the electron temperature increased by 2 times (from 500 eV to 1000 eV) at RF power $\approx 100\,kW$ which is comparable to the ohmic heating power (90 kW). The heating efficiency $\eta = (\Delta T_i + \Delta T_e)/P$ reached $10 \cdot 10^{13}\, eV\, cm^{-3}\, kW^{-1}$

and was independent of the power. However such effective heating was observed in a very narrow density range $\Delta n \approx \pm 0.15\, n$. It is of interest that the densities of maximum electron and ion heating differ by $\Delta n \approx 0.1\, n$.

The CX hydrogene spectra are presented in fig. 2. It can be seen that the temperature $T_i \approx 400 - 500eV$ is determined not by the fast ion tail but by the thermal part of the ion energy distribution (300 – 500 eV). It should be noted also that the spectra satisfy the condition of normalizing by the number of particles with account of its growth.

Time behavior of the electron temperature measured by the SXR emission at various densities is shown in fig. 3. At low densities $n_0 \geq n_d$ (on the left side of the effective heating density range) the heating rate increases at the increase of the initial density. At a density corresponding to the maximum heating ($n_0 = 3.4 \cdot 10^{13}\,\mathrm{cm}^{-3}$, curve 2) T_e increases at the beginning of RF pulse but then it starts to decrease as the density reaches a certain value ($n_0 = 4.2 \cdot 10^{13}\,\mathrm{cm}^{-3}$). It could indicate at the change in the ratio of electron and ion absorption. The electron absorption prevails at $n_0 < n^* = 4.2 \cdot 10^{13}\,\mathrm{cm}^{-3}$ though a direct wave-ion interaction is present (fast ion tails are observed). In the opposite case $n_0 > n^*$ the wave-electron interaction ceases and the wave-ion interaction prevails. In this respect the curve 4 is typical for the high density: as $n_0 = 4.3 \cdot 10^{13}\,\mathrm{cm}^{-3} \geq \mathrm{n}^*$ already at the beginning of the RF pulse the derivative dT_e/dt is negligible, i.e.the wave energy is practically not transferred to the electrons. A slight T_e rise at the end of the pulse can be explained by the reduced energy transfer from the electrons to the ions due to the decrease of $T_e - T_i$ as the ions are directly heated by the wave. The rise of T_e after the end of RF pulse (curves 1, 2) observed in some shots is explained by the transition to the improved confinement regime.

Diamagnetic loop measurements were carried out to confirm effective ion heating. The diamagnetic signal at $n_0 = 3.9 \cdot 10^{13}\,\mathrm{cm}^{-3}$ is shown in fig. 4. It continues to increase slightly after the end of RF pulse which proves the transition to the improved confinement regime. The CX flux at an energy 500 eV is also presented here. It drops after the end of RF pulse but it correlates well with the drop of H_β line emission [6] and so can be explained by the reduction of the target neutral hydrogen density. Taking it into account, the presented CX flux indicates at a fairly large confinement time of thermal ions (≈ 3 ms).

As can be seen from fig. 1, the maximum of the diamagnetic signal correponds to the maximum of the ion heating at $n_0 = 3.9 \cdot 10^{13}\,\mathrm{cm}^{-3}$. At this density the measured $T_e(r)$ profile was approximated by $T_e(r) \propto (1 - \frac{r^2}{a^2})^2$ in the ohmic regime and by $\propto (1 - \frac{r^2}{a^2})^5$ at the end of the RF pulse. The density profile was $n \propto (1 - \frac{r^2}{a^2})^{2.2}$. Using the radial profiles and the measured diamagnetic signal one can estimate the increase of the ion temperature and the power of its radial parabolic profile. We found that for the case of $P_{RF} = 100\,kW$ (when $\Delta T_{i0} = 300\,eV$ from the CX measurements) ΔT_{i0} is equal to 300 eV from the diamagnetic measurements at a parabolic profile with a power $\alpha = 1$. It is important as the CX spectra give the maximum temperature (in the centre) and the diamagnetic signal gives the cross-section averaged value $\langle \Delta(n_i T_i) \rangle$, so taking narrow profiles (i.e. large α) one can prove any large ΔT_i. However the reliability of the result would be low in this case. The power $\alpha = 1$ means a broad ion temperature profile (when $\langle \Delta T_i \rangle = \Delta T_{i0}/2$) which, together with $\Delta T_{i0} = 300\,eV$, confirms the effective ion heating.

Turning to the discussion of the obtained results we note that unlike our previous experiments the fast ion generation starts at a density $n_0 = 2.9 \cdot 10^{13}\,\mathrm{cm}^{-3}$ which is only slightly less than the lower hybrid one ($n_{LH} = 3.5 \cdot 10^{13}\,\mathrm{cm}^{-3}$ at $T_e = 500\,eV$, $T_i = 100\,eV$,

$Z_{eff} = 3$ ($H^+ + O^{+6}$), $B = 22$ kGs and $N_\parallel = 3$). However if we take into account that there are waves with $N_\parallel = 4$ in the excited spectrum we can think that the generation starts in fact at a lower hybrid density. At the maximum heating the initial central density $n_0 = 3.9 \cdot 10^{13}\,\mathrm{cm}^{-3} \geq n_{LH}$ is close to the lower hybrid one. During the RF pulse the density rises up to $n = 5 \cdot 10^{13}\,\mathrm{cm}^{-3}$ and Z_{eff} rises up to 5.5. With the account of the enhanced temperature and Z_{eff} the increased central density is equal to the LH density for the frequency 920 MHz. Therefore, though the parameters of the central plasma regions change, the LH resonance conditions are satisfied and the heating can be considered as classical. However, there are some facts which do not agree with this picture and rather resemble the parametric mechanism: 1). The sequence of the fast ions generation (fig. 1) — less energetic ions appear at lower density. 2). The inclination of both electron and ion heating tends to the threshold density on the left side and that could indicate at a common heating mechanism. It can be a parametric decay process at which ion heating is related to the $k_\perp$ of a daughter wave and the electron heating — to the $k_\parallel$. A fast drop of the heating on the right side at the density increase to $n_0 = 5 \cdot 10^{13}\,\mathrm{cm}^{-3}$ indicates that the energy absorption takes place not in the centre, i.e. not at the LH density. So a slight further increase of the density results in a drastic reduction of the heating efficiency. A direct proof of the wave absorption mechanism could be obtained by the enhanced MW scattering, like in [1]. But we could not use it in these experiments because of the high plasma density (the decay region was unaccessible for the probing wave).

Thus we obtained a really effective ion and electron heating in the intermediate densities range following the idea of the parametric absorption mechanism. However the LH resonance conditions appeared to be satisfied in the centre of the plasma column and the heating is classical *pro forma*. Further study is necessary to clarify the details of the absorption mechanism.

The research described in this publication was made possible in part by Grant N^o R23000 from the International Science Foundation.

References

[1] V.N.Budnikov, *Nucl. Fusion* **31** (1991), p. 611.

[2] A.Bers, *Proc. of the 3rd Topical Conf. on Radio Frequency Plasma Heating*, Pasadena, California, Jan 11–13, 1978, **A1**, p. 1–10.

[3] F.Leuterer, F.Söldner, D.Eckhartt et al, *Plasma Physics and Controlled Fusion* **27** (1985) No 12A, pp. 1399–1409.

[4] V.N.Budnikov, L.A.Esipov, M.A.Irzak, S.I.Lashkul, "Interpretation of the Lower Hybrid Heating Experiments on the FT Tokamak." *Preprint of the Ioffe PTI* **1532** (1991).

[5] O.Van Houtte, G.Agarici, P.Blank et al *Proc. 4th Int. Symp. on Heating in Toroidal Plasmas*, Rome, 1984 vol.1,
International School of Plasma Physics, Varenna, 1984, p. 554.

[6] V.O.Alexandrov, V.N.Budnikov, V.V.Dyachenko et al. *Proc. 20th EPS Conf. on Contr. Fusion and Plasma Phys.*, Lisboa, 1993, **4**, p. 1505.

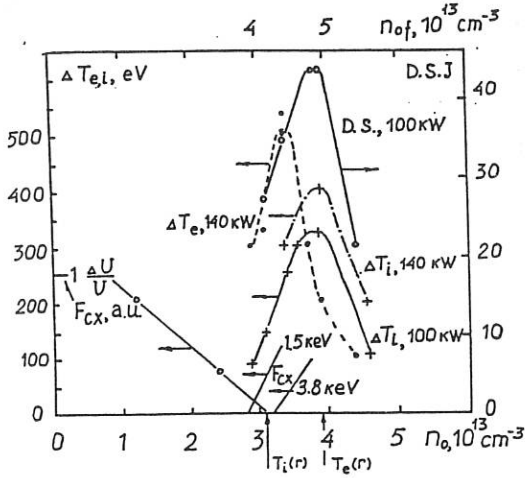


Fig. 1

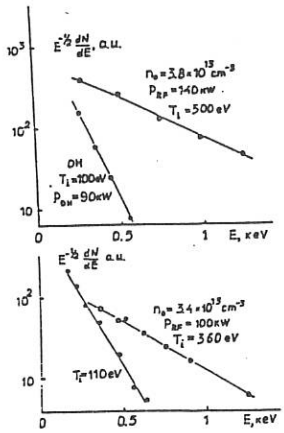


Fig. 2

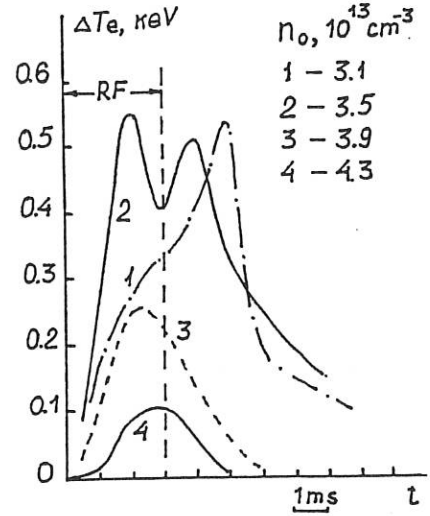


Fig. 3

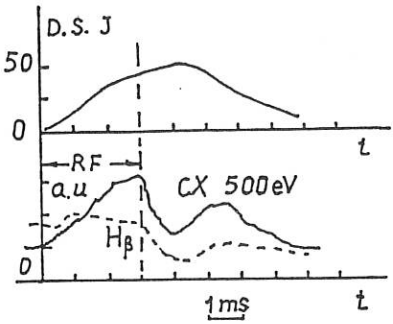


Fig. 4

M.TRIBECHE, T.H.ZERGUINI

UNIVERSITE DES SCIENCES ET DE LA TECHNOLOGIE HOUARI BOUMEDIENE
PHYSICS INSTITUTE, THEORETICAL PHYSICS LABORATORY,
B.P.32, EL-ALIA, ALGIERS, ALGERIA

ELECTRON CYCLOTRON HEATING AND CURRENT DRIVE IN THE PRESENCE OF A LOWER HYBRID WAVE; A FINITE ELEMENT SOLUTION OF THE RELATIVISTIC QUASILINEAR FOKKER-PLANCK EQUATION

Introduction:

It is widely recognized that auxiliary heating is desirable in almost all contemporary fusion devices. Tokamaks, the largest devices at present, are the principal customers for auxiliary heating. Ohmic heating alone cannot raise ion temperatures to the required fusion threshold value because of inherent limitations in the physics. The Tokamak is a much more attractive concept as a fusion power device if is run at steady state. This can be accomplished with an efficient source of toroidal current, other than an inherently pulsed inductive drive. A method of continuously driving the toroidal current is then essential.Various methods for producing continuous toroidal currents in TOKAMAK plasmas have been proposed and widely investigated to date. Among these methods, the current drive using electromagnetic field of radio frequency (RF) waves launched into the plasma were successful in several TOKAMAK experiments. A net toroidal momentum is then delivered to one of the plasma species, usually the electrons. This leads to the production of a plasma current which, simultaneously, plays the role of sustaining plasma equilibrium and plasma heating because of its ohmic heat power.
Electron Cyclotron (EC) waves are particularly suitable for this purpose because they readily penetrate into high density; high temperature TOKAMAK plasma and because their damping process is easily controlled in configuration and velocity space. Electron cyclotron heating (ECH) has proved to be a successful method of auxiliary heating in present day tokamak devices. This is of great interest in tokamak reactors not only for attaining the ignition temperature but also for its bearing on the crucial problem of the reactor lifetime. Almost all of the problems encountered with this technique have been with the generation and transmission of millimeter waves at high power device. Unfortunately, for $T_e << 15$ Kev, EC current drive can only be of interest if the current drive efficiency is significantly enhanced compared with that of maxwellien target plasma. This enhancement can be achieved through interaction of the EC waves with Lower Hybrid waves.

Basic equations:

The electron cyclotron resonance heating and current drive in TOKAMAK plasma in the presence of lower hybrid waves is investigated numerically using the quasilinear relativistic Fokker-Planck equation:

$$L(f) = \frac{\partial f}{\partial \tau} = \left(\frac{\partial f}{\partial \tau}\right)_{Coll} + \left(\frac{\partial f}{\partial \tau}\right)_{LH} + \left(\frac{\partial f}{\partial \tau}\right)_{EC} + \left(\frac{\partial f}{\partial \tau}\right)_{DC} \quad (1)$$

where

$$\left(\frac{\partial f}{\partial \tau}\right)_{Coll} = \frac{\gamma(Z+1)}{P^3}\frac{\partial}{\partial \mu}\left[(1-\mu^2)\frac{\partial f}{\partial \mu}\right] + \frac{2}{P^2}\frac{\partial}{\partial p}\left[\frac{\gamma^3}{P}\frac{\partial f}{\partial p} + \gamma^2 f\right] \quad (2)$$

is the relativistic Fokker-Planck collision operator[1].
f is the momentum distribution of the resonant electron
τ is the normalized time
γ is the relativistic mass factor
μ is the particle cosine angle
P is the particle normalized momentum

$$\left(\frac{\partial f}{\partial \tau}\right)_{EC} = \sum_n \frac{\gamma}{P\sqrt{1-\mu^2}} L'\left[\frac{P(1-\mu^2)}{\gamma} DL''(f)\right] \quad (3)$$

is the relativistic quasilinear contribution for EC harmonics

$$L' = \frac{n\omega_c}{\gamma\omega}\sqrt{(1-\mu^2)}\left(\frac{\partial}{\partial P} - \frac{\mu}{P}\frac{\partial}{\partial \mu}\right) + P\frac{\sqrt{(1-\mu^2)}}{\gamma}\left(\mu\frac{\partial}{\partial P} + \frac{1-\mu^2}{P}\right)\left(\frac{\gamma - n\frac{\omega_c}{\omega}}{P\mu}\right) \quad (4)$$

$$L'' = \frac{n\omega_c}{\gamma\omega}\sqrt{1-\mu^2}\left(\frac{\partial}{\partial P} - \frac{\mu}{P}\frac{\partial}{\partial \mu}\right) + \frac{P\sqrt{1-\mu^2}\left(\gamma - n\frac{\omega_c}{\omega}\right)}{\gamma P\mu}\left(\mu\frac{\partial}{\partial P} + \frac{1-\mu^2}{P}\frac{\partial}{\partial \mu}\right) \quad (5)$$

D is the electron cyclotron diffusion coefficient,

$$\left(\frac{\partial f}{\partial \tau}\right)_{LH} = \left[\mu\frac{\partial}{\partial P} + \frac{1-\mu^2}{P}\frac{\partial}{\partial \mu}\right]\left[D_{LH}\left(\mu\frac{\partial f}{\partial p} + \frac{1-\mu^2}{P}\frac{\partial f}{\partial \mu}\right)\right] \quad (6)$$

describes the LH parallel diffusion
D_{LH} is the lower-hybrid diffusion coefficient,

$$\left(\frac{\partial f}{\partial \tau}\right)_{DC} = -E\left(\mu\frac{\partial f}{\partial p} + \frac{1-\mu^2}{P}\frac{\partial f}{\partial \mu}\right) \quad (7)$$

is the DC electric field term and E an external electric field

Numerical solution:
We assume a steady state and solve for the equilibrium of EQ.1 which is a 2-D partial differential equation. Since the combined problem of velocity and configuration space is rather difficult to treat, we assume a spatially homogeneous plasma.
Our study develops a rapid approximate solution of the quasilinear Fokker-Planck equation, suitable for parametric studies of Electron Cyclotron Resonance Heating. The numerical procedure we use is appropriate to solve both static and dynamic problems evolving either the diffusion theory or transport theory model[2]. A finite element technique is used to compute the momentum distribution of the resonant electron. As elements, we consider "hat functions" that satisfy the boundary conditions. The distribution function is then approximated by a sum of products of angular and velocity hat functions with the expansion coefficients λ_{KL}. We seek an approximate solution of the form:

$$f(\mu, p) = \sum_{Kl} \lambda_{KL} \psi_L(\mu)\, \Phi_K(p) \qquad (8)$$

To find the coefficients of the assumed finite element expansion,we substitute the trial solution for the momentum distribution in the governing differential equation.This will result in a residual which we write:

$$R = L\left[\sum_{k,1} \lambda_{kl} \psi_1(P)\, \phi_k(\mu)\right] \qquad (9)$$

To obtain the best solution, we then attempt to distribute the residual through the domain of solution of the function f by trying to minimize the integral of the residual. We employ GALERKIN's method of using a weighted value of the residuals technique with the hat functions themselves as weight functions. For a mesh point (m,n), corresponding to the hat functions $\Psi_m(p)$ and $\phi_n(\mu)$,we have to take the sum over all the k's and l's for which the product of the four hat functions $\phi_k\phi_n\Psi_l\Psi_m$ is not zero.So we have each time a sum of nine terms,each involving integral over p and μ in the ranges where the hat function products are non zero. The coefficients λ_{KL} involved for the mesh point (m,n) are:

$\lambda_{m-1,n-1}$, $\lambda_{m,n-1}$, $\lambda_{m+1,n-1}$, $\lambda_{m-1,n}$, $\lambda_{m,n}$, $\lambda_{m+1,n}$, $\lambda_{m-1,n+1}$, $\lambda_{m,n+1}$, $\lambda_{m+1,n+1}$

This approach results at each iteration, in a linear system of equations that can be represented by a matrix of nine diagonals where all matrix element have been calculated analytically. To invert the matrix at each iteration,we apply a vectorized gaussian elimination technique. By doing so, we find the distribution function f_1^i, which is then used to calculate a new distribution function f_1^{i+1} until convergence occurs.
The presence of RF power in the plasma results in parallel velocity diffusion. The evolution of the space-averaged electron velocity distribution in the absence of any DC electric field is governed by:

$$\frac{\partial f}{\partial t} = \frac{\partial}{\partial V_z}\left[D_{QL}\frac{\partial f}{\partial V_z}\right] + \left(\frac{\partial f}{\partial t}\right)_{Coll} \qquad (10)$$

where D_{QL} is the quasilinear diffusion coefficient.

In order to investigate the dynamics in the parallel direction, Fish[3] integrated EQ.10 over the perpendicular velocity direction, obtaining for high velocity electrons:

$$\frac{\partial f}{\partial \tau}=\frac{\partial}{\partial \omega}\left[D(\omega)\frac{\partial f}{\partial \omega}\right]+\frac{\partial}{\partial \omega}\left[\frac{1}{\omega^3}\frac{\partial f}{\partial \omega}+\frac{f}{\omega^2}\right] \qquad (11)$$

where ω is the electron normalized velocity.
We have considered the situation when $D(\omega)$ is constant in a finite velocity interval:

$$D(\omega)=D_0 \ , \ if \ : \ \omega_1<\omega<\omega_2 \qquad (12)$$

and vanishes elsewhere. We have then obtained an exact steady-state solution:

$$f(\omega) = C\left[\frac{D^{2/3}\omega^2-D^{1/3}\omega+1}{(D^{1/3}\omega+1)^2} + \exp\left(-\frac{1}{\sqrt{3}D^{2/3}}arctg\frac{(2D^{1/3}\omega-1)}{\sqrt{3}}\right)\right] \qquad (13)$$

where C is a constant determined by the conservation of the particles, and a figure of merit:

$$\frac{J}{P_d}=\frac{3(\omega_2^2-\omega_1^2)}{2Log\frac{(1+D\omega_1^3)}{(1+D\omega_2^3)}} \qquad (14)$$

Conclusion:
A rapid solution of the quasilinear relativistic Fokker- Planck(QRFPE) equation has been developed to investigate the heating and current drive by the combined effects of Lower Hybrid and Electron Cyclotron waves. Various possible diagnostics and the calculation of physical quantities have been developed. Better results should be obtained if we bounce-average the QRFPE over the electron orbit and take into account electron trapping effects. The conventional 1-D treatment which assumes a Maxwellien distribution at bulk temperature in the perpendicular direction for all parallel velocities is a good approximation over the quasilinear plateau region.

REFERENCES:
[1] I.FIDONE and Al. Nuclear Fusion,Vol.27,N°04,(87)
[2] T.H.ZERGUINI,Nuclear Sci.and Engineering,Vol.92,N°01,(86)
[3] N.J.FISH,Physical Rev.Lett.,Vol.41,N°13,(78)

PARASITIC ABSORPTION AT THE ALFVÉN RESONANCE IN SCRAPE-OFF LAYERS

D.W. FAULCONER and R. KOCH

Laboratoire de Physique des Plasmas - Laboratorium voor Plasmafysica
Association "Euratom-Etat belge" - Association "Euratom-Belgische Staat"
Ecole Royale Militaire - B 1040 Brussels - Koninklijke Militaire School

INTRODUCTION

When plasma is heated or current driven in a tokamak with the fast wave at a frequency ω just below the lowest ion cyclotron frequency ω_{ci}, the Alfvén resonance appears to the high field side of the cyclotron resonance and can be of concern as a source of parasitic absorption ([1] and Refs. therein; [2]). Notably, a fast wave current drive scheme has been proposed which pushes electrons, avoiding detrimental ion absorption by operating at a frequency $\omega<\omega_{ci}$; for the low parallel wavenumber spectra employed, the Alfvén resonance can run in extended portions of the scrape-off layer (SOL) and in the bulk plasma edge [3]. Here lower single-pass bulk absorption of the fast wave makes its parasitic energy loss a sensitive issue.

ANALYTIC PRELIMINARIES

We model such parasitic loss by integrating the wave equation for a cold plasma in slab geometry with Fourier analysis in the invariant y,z directions. Our neglect of collisions highlights the effect of the Alfvén resonance. With equilibrium magnetic field B_0 in the z-direction, the fast wave approximation, $E_z=0$, reduces this equation to the following system [4]

$$\frac{d}{dx}\begin{pmatrix} i\omega B_z \\ E_y \end{pmatrix} = \begin{pmatrix} \frac{-dk_y}{u} & -u + \frac{d^2}{u} \\ 1 - \frac{k_y^2}{u} & \frac{dk_y}{u} \end{pmatrix} \begin{pmatrix} i\omega B_z \\ E_y \end{pmatrix} \qquad (1)$$

where $d=k_0{}^2\varepsilon_{12}/i$, $u=k_0{}^2\varepsilon_{11}-k_z{}^2$ in terms of dielectric tensor elements. The Alfvén resonance appears at the singular point where $u=0$; choosing this point as the origin in x with $u'(0)\equiv u_0'$, one can develop Eqn.(1) as

$$\frac{d}{dx}\begin{pmatrix} i\omega B_z \\ E_y \end{pmatrix} = \left(\frac{A_0}{u_0' x} + A_1 + A_2 x + \ldots\right) \begin{pmatrix} i\omega B_z \\ E_y \end{pmatrix} \qquad (2)$$

where $$A_0 = \begin{pmatrix} -dk_y & d^2 \\ -k_y^2 & dk_y \end{pmatrix}.$$

Noting $A_o{}^2=0$, the solution to Eqn.(2) can be written in a small neighborhood of x=0 as [5]

$$\begin{pmatrix} i\omega B_z \\ E_y \end{pmatrix} \approx \left(I + \frac{A_o}{u_o'} \ln(x) \right) \begin{pmatrix} C_1 \\ C_2 \end{pmatrix} \tag{3}$$

where the C_i are constants. Multiplication from the left by $(-k_y,d)$ annihilates A_o in the right member of Eqn.(3) showing

$$-ik_y\omega B_z + dE_y = -k_yC_1 + dC_2 \tag{4}$$

to be nonsingular at the origin.

The power lost at the resonance can be evaluated as the difference in the Poynting flux, $Re\{E_yH_z{}^*\}/2$, evaluated at $x=\pm\delta$, $\delta\to 0$; here one eliminates the two field components using Eqn.(3), then reidentifies with these components the terms which survive the indicated limit. The proper branch of the logarithm is found by the usual addition of an infinitesimal positive imaginary part to ω. There results

$$P = \frac{-\pi}{2\omega\mu_o|u_o'|} \left| -ik_y\omega B_z + dE_y \right|^2 \tag{5}$$

where the nonsingular combination of field components of Eqn.(4) reappears. Solutions (3) with C_i which annul the right member of Eqn.(4) are seen from Eqn.(5) to suffer no absorption.

PHYSICAL REMARKS

Other authors have taken $k_y=0$ [1] and found that the proximity of machine wall and resonance can play an important role in reducing both E_y at the resonance (E_y is nonsingular (Eqn.(4), $k_y=0$) and vanishes at the metallic wall) and fast wave absorption thereupon ($\propto |E_y|^2$, Eqn.(5)). However, in the case of nonzero k_y, a glance at Eqn.(5) shows absorption to be proportional to a combination of field components which, though nonsingular, need not vanish at the wall. One might plausibly conjecture absorption to increase with $|k_y|$.

On the other hand, as $|k_y|$ grows, another effect finally intervenes to eliminate absorption. For propagation from the plasma core toward the Alfvén resonance the cold fast wave dispersion, $k_x{}^2=k_\perp{}^2(k_z)-k_y{}^2$, exhibits successively a cutoff, a resonance and another cutoff; an incident wave must tunnel between the first cutoff and the resonance before losing its energy. As increase in $|k_y|$ causes a uniform downward shift of the dispersion curve, the tunneling distance increases so as to finally suppress energy loss. Thus we must refine our conjecture and predict lobes of higher absorption in k_y to either side of $k_y=0$.

NUMERICAL STUDY

Plasma density is taken to increase exponentially from the metallic wall across a SOL of width L_{sol} with e-folding length L_{exp}. Our objective being to study fast wave absorption at an Alfvén resonance near the plasma edge, we model the bulk density locally, taking it to increase linearly from the edge value n_{edge} with slope dn/dx, B_o being assumed constant. With this profile and field value Eqn.(1) is integrated numerically, the resonance singularity being resolved as above by the addition of a small imaginary part to ω. At high density the solution is matched to

incident and reflected combinations of Airy functions and the fraction of the incident Poynting flux which is absorbed, q, is calculated.

We now examine parasitic energy loss of the fast wave in relation to the abovementioned low-frequency current drive method applied to an ITER-type DT plasma [3] with $n_D/n_T=0.4$, $L_{sol}=0.15$ m, $L_{exp}=0.02$ m, $n_{edge}=0.8\ 10^{20}\ m^{-3}$, edge value of $dn/dx=4.6\ 10^{20}\ m^{-4}$, on-axis $B_o=6$ T, and $\omega/2\pi=22$ MHz. Such a frequency is just low enough to exclude the tritium cyclotron resonance from the outboard side of the tokamak. Central temperature and density profiles are nonessential for our study of the cold edge though the latter implicitly determines the choice of dn/dx edge value. Since an outboard launched fast wave will initially reflect from the inboard wall, we examine the energy flux in the incident wave which is lost to the Alfvén resonance in front of this wall, using an appropriately augmented inboard confinement field of 9T.

Absorption coefficient $q(k_y,k_z)$ for this case appears in the figures, Fig.2 being simply a blowup of Fig.1 showing the critical region around the origin. High absorption ($q\approx 1.0$, Fig.1; $q\approx 0.5$, Fig.2) occurs in the white regions, and low (descending to essentially zero) in the black with isoclines being equispaced. There is a minimum in absorption at $k_y=0$ with values on the order of 0.2 [1], whereas higher absorption appears in two lobes to either side of this value, as conjectured in the preceding section. High absorption is seen to occur for k_y, k_z values well within the spectral distribution expected in the given plasma. Though the detailed prediction of this spectral distribition of the fast wave is the affair of large computer codes, one should remark that if the "beam" of fast waves emitted by an outboard antenna remains vertically collimated in its first transit of the tokamak, the beam will arrive at the inner wall with a k_y distribution having half-width roughly π divided by its vertical beam height, i.e. a figure on the order of 1. Were poloidal phasing feasible one could exploit the asymmetry of q in k_y to minimize parasitic loss.

CONCLUSION

Theoretical expectations for heating/current drive at $\omega<\omega_{ci}$ are borne out in markedly higher parasitic Alfvén absorption of the fast wave appearing for nonzero k_y. Essentially total absorption is seen for certain regions of the k_y,k_z plane; high absorption regions intersect the zones excited in experiment. The thinness of the resonance layer seen in sharp SOL density profiles does not prevent this.

ACKNOWLEDGEMENTS

Fruitful discussions with Dr. M.P. Evrard and Professor R.R. Weynants are gratefully recognized.

REFERENCES

[1] J.A. Heikkinen, T. Hellsten, M.J. Alava, Nucl. Fusion 31, 417 (1991).
[2] A.M. Messiaen, 7th European Conf. on Cont. Fusion and Plasma Phys., Lausanne, Sept., 1975, I, 155 (1975).
[3] V.P. Bhatnagar, J. Jaquinot, and the JET Team, JET Report JET-P(94)23, submitted for publication in Fusion Engineering and Design.
[4] C.F.F. Karney et al., Phys. Rev. Lett. 42, 1621 (1979).
[5] W. Wasow, *Asymptotic Expansions for Ordinary Differential Equations*, Wiley-Interscience, New York, 1965, Theorem 5.5.

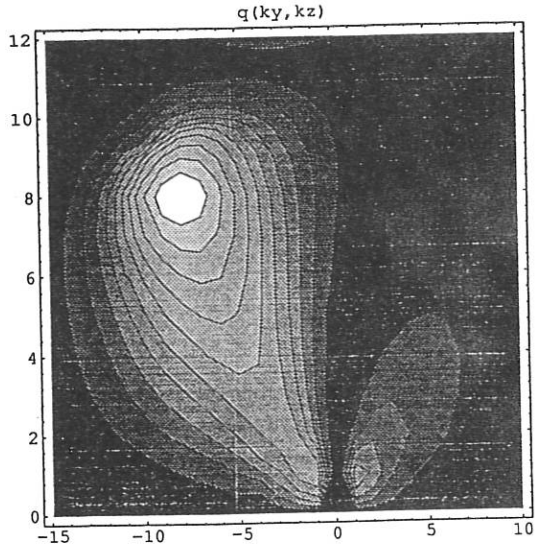


Fig.1 Power absorbed at edge Alfvén resonance for ITER current drive case indicated in text.; k_y on abscissa.

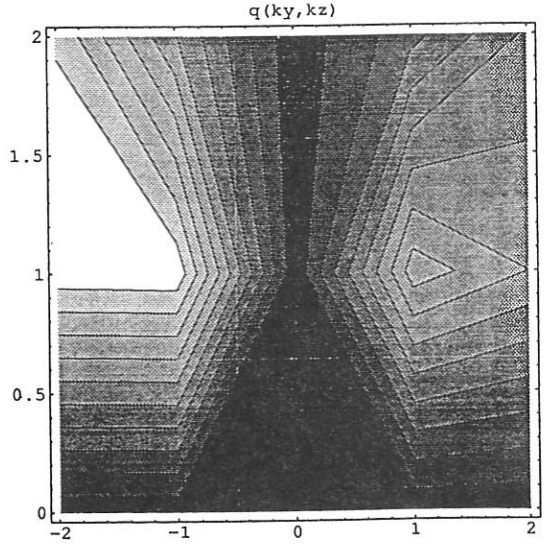


Fig.2 Blowup of Fig.1.

Abel, G. I-38, III-1086, III-1090
Abramov, V.A. II-596
Aceto, S.C. I-412
Adams, J.M. I-262, I-274
Adler, H. I-82
Agostini, E. III-1414
Akhmetov, T.D. I-446
Akiyama, R. I-432, II-940, II-1000
Al-Karkhy, A. I-490
Alava, M.A. II-664
Alava, M.J. III-1114
Albrecht, M. III-1188
Alejaldre, C. I-376
Alexander, M. I-306, I-330
Ali-Arshad, S. I-54, I-206
Allen, S.L. II-834
Allibert, J.-P. III-1058
Almagri, A. I-482
Alper, B. I-102, I-198, I-202, I-206, III-1304
Amano, T. II-940
Anderson, D. II-644
Ando, A. I-310, II-940, II-1000
Andrew, P. II-746
Ané, J.-M. II-688, III-1058
Anikeev, A.V. I-442
Antoni, V. I-454, I-458, I-462, II-762
Apicella, M.L. II-818
Appel, L.C. II-620
Apruzzese, G. II-802
Arimoto, H. I-432
Arkhipenko, V.I. III-1200
Arkhipov, N.I. II-830
Arslanbekov, R. I-278, III-1046, III-1054, III-1058
Asano, E. II-940
Ashall, J.D. I-322
Ashkenazy, J. III-1536
Asmussen, K. II-730
Astrelin, V.T. I-498
Axnäs, I. III-1520
Axon, K.B. I-322, II-910
Azumi, M. II-996
Bachmann, P. II-794
Baelmans, M. II-676
Bagatin, M. I-462, III-1352
Bagryansky, P.A. I-442
Baity, F.W. III-1118
Bakhtin, V.P. II-830
Bakos, J.K. III-1336
Balbin, R. I-162, II-870
Baldzuhn, J. I-384, I-392
Balescu, R. II-576
Balet, B. I-58, I-106, I-206, I-258, I-346
Baranov, Y. III-1122, III-1126
Baranowski, J. III-1320, III-1348
Barnes, C.W. I-18, I-182
Barnes, D.C. III-1386
Barnsley, R. I-134, I-322
Barth, C.J. I-154, III-1248
Bartiromo, R. II-818
Bartlett, D.V. II-786

Basiuk, V. I-278, II-956, III-1046
Basylev, B. II-742
Batani, D. III-1448
Batha, S. I-354, III-1094
Bâtzner, R. I-282, III-1344
Baylor, L.R. I-412
Bazdenkov, S.V. II-600, II-886
Beaumont, B. II-790, II-898, III-1054
Bécoulet, A. II-660, II-898, II-956, III-1054, III-1130
Behn, R. III-1224, III-1252
Behrendt, H. III-1328
Behringer, K. II-722
Behrisch, R. II-718
Beidler, C.D. I-368, I-400, II-568
Belkin, V.S. I-446
Bell, G.L. I-412
Bell, J.D. I-412
Bell, M. G. I-82, I-354
Bell, R. I-186, III-1094
Bell, R.E. I-354
Belo, J. III-1150
Bender, E.D. I-446
Bengtson, R.D. I-78, I-174
Benuzzi, A. III-1448
Berezhiani, V.I. III-1474
Bergsaker, H. II-762, II-866, III-1352
Berk, H.L. II-648
Bernabei, S. II-972, III-1094
Bers, A. III-1134, III-1460
Bertrand, P. III-1082, III-1430, III-1434
Bessenrodt-Weberpals III-1312
Besshou, S. I-416, I-420, I-424, I-428, I-502, III-1368
Bettenhausen, M. II-984
Bhatnagar, V.P. I-314, II-944, II-952, III-1110, III-1126
Bickley, A.J. III-1126
Biener, J. III-1524
Bigelow, T.S. I-412
Biskamp, D. II-564
Bizarro, J.P. III-1046, III-1150
Blackler, K. III-1304
Blackwell, B.D. I-436
Bliman, S. III-1510
Boedo, J.A. I-74, I-130
Bogomolov, L.M. I-170
Bohmeyer, W. III-1328
Boivin, R. II-992
Bombarda, F. II-992
Bond, D.S. I-262, I-274
Bondeson, A. II-544
Bonnin, X. I-78
Bonoli, P.T. II-992
Booth, M. I-322, II-910
Borass, K. II-698
Borba, D. II-612, II-616
Bornatici, M. III-1422
Börner, P. II-676, II-758
Borovski, B. V. I-170
Bosch, H.-S. I-326, II-680, II-706
Bosia, G. II-1024
Bossi, S. III-1448

Boucher, C. III-1086
Boucher, D. II-524
Boudenne, J.M. III-1448
Bourgoin, D. III-1086
Braams, B. II-706, II-846
Bracco, G. I-70, I-142
Braga, G. III-1236
Brakel, R. I-388, I-400
Brambilla, M. II-842, II-960
Branas, B. I-162, II-870, III-1176
Brasilio, Z.A. II-918
Braun, F. II-838
Brémond, S. II-688, III-1058
Brenning, N. III-1520
Bretz, N.L. I-354
Brooker, P. III-1086
Brooks, N.H. II-834
Brown, T. II-944
Browning, P.K. I-490
Brusati, M. III-1122
Brzozowski, J.H. I-470, I-474, II-866
Büchl, K. I-222, I-306, I-326, II-680, II-710, II-726, II-850, III-1364
Budaev, V.P. I-170
Budnikov, V. N. II-1028, III-1196, III-1200
Budny, R.V. I-82, I-246, I-290, I-354
Buffa, A. I-458, I-462
Buhlmann, F. III-1224
Bulanov, S.V. III-1456
Bunting, C.A. I-322
Buratti, P. I-70, I-142
Burdakov, A.V. I-498
Bures, M. I-54, I-206, II-944
Bürger, G. III-1336
Burgos, C. I-162, III-1296
Burrell, K.H. II-858
Bush, C.E. I-82, I-354
Caldas, I.L. II-918
Camargo, S.J. II-564
Campbell, D.J. I-2, I-314, II-746
Campbell, R.D. II-834
Campostrini, P. I-458
Cantu, P. III-1236
Caorlin, M. I-18
Cap, F.F. II-672
Capes, H. I-62, II-734
Capobianco, A. I-462
Cappello, S. I-458
Cardinali, A. II-968, II-972
Carlson, A. I-326, II-710
Carolan, P.G. I-214, I-322
Carpignano, F. I-10
Carraro, L. I-466
Carrasco, J. I-278, III-1046
Casarotto, E. I-466
Casper, T.A. I-190
Castejón, F. I-162, I-166
Castro, R.M. II-918
Cecil, F.E. III-1340
Cekic, M. I-482
Cercek, M. III-1332

Cesario, R. II-968
Challis, C. D. III-1126
Chamouard, C. II-738, II-754
Chance, M. III-1094
Chang, C.S. I-290, II-996
Chang, Z. I-82, I-246, I-354
Chapman, B. I-482
Chareau, J.M. I-110, III-1172
Chatelier, M. II-754
Chatenet, J.H. II-862
Cheng, C.Z. I-246, I-290, II-628
Chitarin, G. I-458
Cho, T. II-922
Chow, C.C. III-1460
Christensen, C. II-992
Christiansen, J.P. I-54, II-508
Chu, C.C. I-154, III-1248
Chu, M.S. I-190
Chu, S.C. III-1118
Chu, T. K. III-1094
Cicconi, G. III-1360
Cima, G. I-178
Clairet, F. II-862, III-1172
Clement, S. I-2, II-746
Coda, S. II-854
Coffey, I.H. I-134
Colas, L. I-110
Colchin, R.J. I-22, I-412
Collarin, P. I-462
Connor, J.W. I-138, II-512, II-580, II-616
Conroy, S.W. I-270
Conway, N.J. I-322
Cooper, W.A. II-548
Coppi, B. I-10, II-520
Cordey, J.G. I-58, I-106, I-314, I-346
Cordier, J.J. II-750
Core, W.G.F. I-254
Cornelis, J. I-338
Cornille, M. III-1510
Correa-Restrepo, D. III-1398
Corrigan, G. II-694, II-698
Costa, S. I-462, I-466
Coster, D. II-706, II-842, II-846
Costley, A. III-1168, III-1184
Côté, A. I-38, I-46, III-1086, III-1090
Côté, C. III-1086, III-1090
Coulon, J.P. II-956
Counsell, G. III-1130
Cox, M. II-636, III-1110, III-1122, III-1130
Craig, J.L. I-174
Cramer, N.F. III-1532
Cristofani, P. I-210
Crocker, N. I-482
Cui, Z.Y. I-342
Cukier, M. III-1510
Cummings, R. III-1378
Cunningham, G. I-486, I-490
Cupido, L. III-1184, III-1188
D'Angelo, F. II-572
D'Ippolito, D.A. II-894

Da Costa, O.	III-1216
da Cruz, D.F.	III-1204
da Silva, R.P.	II-918
Darrow, D.S.	I-290, I-354, II-988
Das, J.	I-388
Daughton, W.	II-520
Davies, S.	II-746
Davydenko, V.I.	I-446
de Assis, A.S.	I-450
De Baar, M.R.	III-1204
De Blank, H. J.	I-226, II-632, II-850, III-1394
De Esch, H.	I-54, I-206, I-314
De Grassie, J.S.	III-1118
De Haas, J.C.M.	I-62
De la Cal, E.	I-162
de la Luna, E.	I-404, II-870, III-1176, III-1180
de la Rosa, I.	III-1288
De Lauri, A.	I-146
De Lorenzi, A.	I-458
De Luca, F.	I-66, I-146, I-158
De Marco, F.	II-968
De Michelis, C.	II-734, II-738, II-790, II-810, II-814, III-1042, III-1280
de Pena Hempel, S.	I-6, II-774
de Rover, M.	II-584
de Vries, P.C.	I-230, I-286
Décoste, R.	I-38, I-46, III-1086
Degtyarev, L.	II-556
Deichuli, P.P.	I-442
Deliyanakis, N.	I-206, I-346
Demchenko, V.	III-1154
Dementjev, G.N.	I-170
Demers, Y.	I-38, III-1086, III-1090
Den Hartog, D.J.	I-482
Dendy, R.O.	II-616, II-652
Deng, X.W.	I-342
Deschamps, P.	II-750
Desgranges, C.	I-30, I-210, I-298
Desideri, D.	II-762, III-1352
Detragiache, P.	I-10
Deutsch, C.	III-1444
Devynck, P.	I-110, I-118, II-862
di Vita, A.	III-1122
Dietrich, L.	III-1328
Dillon, S.F.	III-1304
Dimov, G.I.	I-446
Diver, D.A.	III-1478
Dommaschk, W.	I-360
Donné, A.J.H.	I-230, III-1232, III-1248, III-1316
Dory, R.A.	I-412
Drake, J.R.	I-470, II-866
Dranichnikov, A.N.	I-446
Drawin, H.W.	I-298
Dreval, V.V.	II-886, III-1192
Druetta, M.	II-814
Duan, X.R.	I-342
Dubois, M.A.	I-30
Duck, R.C.	I-22, I-138, I-490
Dudnikova, G. I.	III-1490
Dudok de Wit, T.	III-1050
Dumbrajs, O.	III-1240

Dumortier, P.	I-74, I-130, II-964
Dunlap, J.L.	I-186, I-246, I-412, III-1094
Durodie, F.	II-964
Dux, R.	I-6
Dyachenko, V. V.	II-1028, III-1196
Dyer, G.R.	I-412
Dziubek, R.	I-482
Edenstrasser, J.W.	II-540
Edlington, T.	I-322
Edmonds, P.H.	I-78
Edwards, A.M.	I-322
Edwards, A.W.	I-198, III-1304
Edwards, M.	I-214, I-318
Efthimion, P.C.	I-182, I-354
Egorov, S. M.	III-1364
Ehrenberg, J.	II-746
Ejiri, A.	I-432, II-1000
Ekedahl, A.	III-1122
Eliezer, S.	III-1464
Elliott, J.A.	III-1378
Elsässer, K.	III-1066, III-1406
Endler, M.	II-874
Engelhardt, W.	II-730
England, A.C.	I-412, III-1094
England, A.C.	I-186
Eninger, J.E.	III-1520
Enk, Th.	III-1500
Erba, M.	I-106
Erckmann, V.	I-158, II-1008
Erents, S.K.	I-138, II-746
Eriksson, L.-G.	II-644, II-648, II-952
Ernst, D.	I-82, I-354
Esipov, L. A.	II-1028, III-1196
Estrada, T.	I-162, I-404, II-870, III-1176
Euringer, H.	I-130, II-964
Eusébio, F.	III-1188
Fahrbach, H.-U.	II-838
Fahy, M.	II-936
Fall, T.	I-38, III-1086
Falter, H.	II-786
Faral, B.	III-1448
Fasoli, A.	II-612, III-1382
Faulconer, D.W.	II-1036
Fechner, B.	II-944
Feist, J.H.	II-936
Feix, M.	III-1434
Feng, Y.	I-282, I-388
Fernandes, J.	III-1188
Ferreira, J.	I-138, I-322, II-910, III-1046
Ferro, C.	II-822
Ferron, J.R.	I-86, I-242
Fiedler, S.	III-1268, III-1272
Field, A.R.	I-392, II-722, II-726, II-730, II-774
Fielding, S. J.	I-134, I-318, I-322, II-910
Figueiredo, A.	III-1150
Fijalkow, E.	III-1410, III-1434
Fiksel, G.	I-482
Filchenkov, S.E.	III-1070
Filippov, V.N.	I-446
Finken K.H.	I-74, I-130, I-238

Fiore, C. II-520, II-992
Fiorentin, P. I-458
Fisch, N.J. II-640
Fischer, B. III-1126, III-1500
Fishpool, G. I-54, I-194, I-206
Fitzpatrick, R. I-214
Fontanesi, M. III-1236, III-1374, III-1414
Forest, C.B. III-1118, III-1146
Fraboulet, D. II-660, II-898
Fraguas, A.L. I-376
Francés, M. III-1176
Franke, S. III-1252
Fredrickson, E. I-82, I-246, I-354
French, P.A. I-490
Frigione, D. II-818
Froissard, P. III-1122
Fu, G.Y. I-246, I-290, II-628
Fuchs, Ch. I-326, I-330
Fuchs, G. I-238
Fuchs, J.C. I-6, I-222, III-1308
Fuchs, V. III-1086, III-1134
Fuji, Y. II-528
Fujita, T. I-98
Fukuyama, A. II-528
Fussmann, G. II-730, III-1328
Gabellieri, L. II-802
Gadeberg, M. II-746
Gaillard, R. I-118
Galassi, A. III-1236
Gao, Q. II-608, III-1162
Garbet, X. I-114, I-118, I-210, II-862
Garcia-Cortes, I. I-162, II-870
Garcia-Rosales, C. I-222, II-718, II-722, II-770, II-774
Garcin, M. III-1050
Gardner, C. III-1122
Garnier, D. II-992
Garzotti, L. I-454
Gasquet, H. I-178
Gates, D. I-218, I-318, I-322
Gauthier, E. II-738, II-750, II-790
Gauvreau, J.-L. I-38, I-46, III-1086
Gee, S.J. I-490, I-494
Geiger, J. I-372, I-392, I-400
Geist, T. I-404
Gentle, K.W. I-78, I-178
Geraud, A. I-210, I-298
Gernhardt, J. II-842
Gerstel, U.C. I-254
Gervais, F. I-118, II-862
Gettelfinger, G. III-1094
Ghendrih, Ph. II-734, II-738, II-750, II-754, II-810, II-862, III-1042
Ghizzo, A. III-1082, III-1430, III-1434
Giannella, R. I-102, III-1260
Giannone, L. I-158, II-874
Gibson, A. I-58
Giesen, B. I-74, I-238
Gil, C. I-114, I-210, I-298, III-1054
Gilev, E.A. I-446
Gill, R.D. I-198, III-1304
Gimblett, C.G. I-214

Giroud, C. I-486
Giruzzi, G. II-1004, III-1050, III-1208
Glaude, V. III-1086
Gnesotto, F. I-458
Goedbloed, J.P. I-234, III-1126
Goetz, J. II-992
Gohil, P. I-190, II-858
Goldfinger, R. C. I-412
Golovato, S.N. II-992
Gondhalekar, A. I-266, II-746
Goniche, M. II-790, III-1042, III-1054
Goodall, D.H. J. I-22, I-138
Goodman, T. II-1004
Gorini, G. I-66, I-146, I-158
Gormezano, C. I-314, II-612, II-944, II-952, III-1122, III-1126
Gottardi, N. I-2, II-698, II-746
Goulding, R.H. II-944, III-1118
Gowers, C. I-2
Graf, M. II-992
Granetz, R. II-520, II-992
Grashin, S.A. II-886
Gray, D.S. I-130
Greenough, N. III-1094
Greenwald, M. II-520, II-992
Gregory, B. I-38, III-1086
Grek, B. I-82
Grésillon, D. I-110, I-118, III-1212, III-1216, III-1244
Greuner, H. III-1328
Grigull, P. I-388, I-400
Grisham, L.R. I-82
Grisolia, C. II-738
Grobben, B.J.J. III-1248
Groebner, R.J. II-858
Grosman, A. II-734, II-738, II-750, II-754, II-790, II-862, II-898, III-1042
Grossmann, T. III-1188
Grote, H. III-1328
Gruber, O. I-222, I-326, I-330, II-680, II-706, II-936
Grützmacher, K. III-1288
Gryaznevich, M. I-22, I-138
Gu, Y.B. III-1386
Guatieri, R. I-466
Gudowska, I. II-762
Guerra, R. III-1256
Guilhem, D. II-734, II-750, II-790, II-810, II-898, III-1042
Guirlet, R. II-734, II-738, II-790, II-810, II-814, III-1280
Guiziou, L. I-114
Gulec, K. I-380
Gunn, J. III-1086
Guo, S.C. II-536
Gusakov, E.Z. III-1200, III-1212
Gyergyek, T. III-1332
Haas, G. I-326, II-680, II-726
Haddad, E. I-38, III-1086
Haines, M.G. II-656
Hallock, G.A. I-178
Hamada, T. I-416, I-424, I-428, III-1368
Hamada, Y. I-310
Hamamatsu, K. II-996
Hamberger, S.M. I-436
Hanatani, K. I-416, I-428, III-1368

Hanson, G.R. I-412, III-1180
Hantzsche, E. II-926
Harbour, P.J. I-2, II-746
Harin, A.O. III-1438
Harmeyer, E. I-368, I-400
Harris, J.H. I-412, II-898
Hartfuß, H.J. I-158, I-396, I-404, III-1220
Harvey, R. I-482
Haste, G.R. II-898
Hastie, R.J. II-616
Hatayama, A. III-1102
Hatcher, R. III-1094
Hawkes, N. I-314, II-1020
Hawryluk, R. I-82
Hayashi, T. I-364
Hedin, G. I-470
Heidbrink, W.W. I-190
Heijnen, S.H. I-230, III-1204
Heikkinen, J.A. III-1114, III-1158, III-1240
Hellblom, G. II-866, III-1352
Heller, M.V.A.P. II-918
Hellsten, T. III-1114
Hender, T.C. I-206, I-214, I-218, I-318, II-620
Hennequin, P. I-118, II-862
Henry, J. I-482
Hermann, A. II-936
Hermann, W. II-838
Herre, G. I-400
Herrmann, A. I-222, I-326, II-710, II-726, III-1308
Herrmann, H. I-290
Hermegger, F. I-360
Hess, W.R. II-734, II-738, II-790, II-810, II-814, III-1280, III-1300
Hey, J.D. I-126
Hidalgo, C. I-162, I-404, II-870
Hidekuma, H. I-416
Hildebrandt, D. II-718
Hill, D.N. II-834
Hillis, D. L. I-130
Hintz, E. I-126
Hirose, A. I-46
Hirsch, M. I-404, I-408
Hirsch, S. II-722, II-730
Hirshman, S. III-1094
Hoang, G.T. I-114, I-118, I-210, I-278, II-956, III-1046, III-1054, III-1058
Hoenen, F. II-964
Hoffman, D.J. III-1118
Hoffmann, C. II-838, II-842
Hofmann, F. III-1224
Hofmann, J.V. I-392, I-400
Hofmeister, F. II-842
Hogan, J. T. II-810, II-898, III-1300
Hogeweij, G.M.D. I-66, I-146, I-150, I-158
Hokin, S. I-482
Holakovsky, J. II-878
Holly, D. I-482
Holties, H.A. I-234, III-1126
Hone, M.A. I-270, I-274
Honrubia, J.J. III-1464
Höpfl, R. III-1464
Hora, H. III-1464

Hörling, P. I-470, I-474
Horne, S. II-992
Horton, L. I-2, I-314, II-698, II-746, II-826
Howarth, P.J.A. I-262, I-274
Hsu, T. II-992
Hubbard, A. II-520, II-992
Hübner, K. I-282, III-1344
Hugenholtz, C.A.J. III-1204
Hugill, J. I-22, I-138, I-318, I-322, II-910
Hunaba, H. I-416
Hurt'ak, O. III-1074
Hurwitz, P.D. I-78
Husmann, K.C.E. III-1232
Hutchinson, D.P. I-412
Hutchinson, I. II-992
Hutter, T. I-62, II-956
Huysmans, G.T.A. I-202, I-206, I-234, II-612, II-616, II-620, III-1126
Hwang, D. I-46
Hyatt, A. W. I-14, I-190
Ichimura, M. II-922
Ida, K. I-392, I-416, I-432, II-1000
Ide, S. III-1138
Idei, H. I-432, II-1000
Igitkhanov, Yu. L. II-714, II-766
Ignacz, P.N. III-1336
Ignat, D. III-1090, III-1094
Iguchi, H. I-432, II-1000
Ikeda, Y. III-1138
Ikezi, H. III-1118
Imre, K. II-668
Ingesson, L.C. III-1316
Ingrosso, L. III-1344
Innocente, P. I-454, I-458, I-462
Inutake, M. II-922
Irby, J. II-520, II-992
Ireland, J. III-1478
Irzak, M.A. II-1028
Isayama, A. I-416, I-428, I-502
Ishida, S. I-94, I-98
Ishii, K. II-922
Ishii, S. III-1528
Isler, R.C. I-42, I-186, I-412, II-810, III-1094, III-1300
Isobe, M. II-1000
Itoh, K. II-528
Itoh, S. III-1106
Itoh, S.I. II-528, III-1106
Its, E. R. II-1028, III-1196
Ivanov, A.A. I-442
Ivanov, R. S. I-170
Iwase, M. II-1000
Jablonski, D. II-992
Jacchia, A. I-66, I-146, I-158
Jäckel, H.J. II-786
Jacquet, Ph. III-1086
Jacquinot, J. II-952, III-1122
Jaenicke, R. I-396, I-408
Jakovets, A.N. II-886
Jakubka, K. III-1078
Jakubowski, L. III-1320
James, R.A. I-190

Janeschitz, G. II-714
Janicki, C. I-46
Janos, A. I-246
Jardin, S. III-1090, III-1094
Jarvis, O.N. I-54, I-206, I-258, I-262, I-270, I-274, III-1340
Jassby, D. L. I-82, I-290
Javedani, J.B. III-1386
Jenkins, I. I-22, I-138
Jernigan, T.C. I-412
Ji, H. I-482
Jiménez, J.A. I-376, III-1356
Joffrin, E. I-30, I-34, I-114, I-210, I-298, III-1054, III-1058
Johnson, L. C. I-82, I-182
Jones, S. III-1094
Jones, T.T.C. I-54, I-106, I-206, I-314
Jong, R. I-190
Jotaki, E. III-1106
Junker, W. I-6, I-326, II-680, II-726
Jüttner, B. II-718
Kabantsev, A.A. I-446
Kado, S. I-416
Kaganskaya, N.M. III-1200
Kaita, B. III-1180
Kaita, R. I-42, I-186, III-1094
Kaleck, A. II-758
Kallenbach, A. I-6, I-326, I-330, II-722, II-774, II-850, II-936, III-1188
Kamada, Y. I-98
Kamelander, G. III-1154
Kammeyer, M. III-1328
Kamperschroer, J. I-18
Kaneko, O. II-940
Kano, Y. I-310
Kardaun, O. I-90, II-936
Kardon, B. III-1336
Karliner, V.M. I-446
Karney, C.F.F. II-640
Karpushov, A.N. I-442
Karttunen, S. III-1082, III-1434, III-1452
Karulin, N. II-1008
Kasilov, S.V. II-980
Kass, T. I-306
Kassab, M.M. II-540
Kastelewicz, H. II-680
Kato, Y. III-1528
Katsonis, K. III-1444, III-1510, III-1514
Kaufmann, M. I-326, I-330, II-680, II-706, II-774, II-850, III-1364
Kawahata, K. I-432
Kawamoto, T. II-940, II-1000
Kawano, Y. I-94, I-98
Kawasaki, S. III-1106
Kawashima, H. II-890
Kaye, A. II-944, II-952
Kaye, S. I-186, III-1094
Kazarian, F. III-1058
Kedves, M.A. III-1336
Kerner, W. I-206, I-234, II-612, II-616, II-620, II-882, III-1126
Kesner, J. I-354, III-1094
Kick, M. I-392, I-400, I-408
Kienle, St. III-1320
Kikuchi, M. I-94, I-98

Kim, J. II-858
Kimura, K. III-1102
Kißlinger, J. I-368, I-400
Kiwamoto, Y. II-922
Kiyama, H. I-250
Kiyama, S. I-250
Klepper, C. C. II-810, II-898, III-1300
Kletecka, P. III-1078
Klima, R. III-1078
Koch, R. I-74, I-238, II-806, II-964, II-976, II-1020, II-1036
Koch, S. I-282
Koch, St. III-1344
Koenig, M. III-1448
Koenig, R. I-206
Koidan, V.S. I-498
Koide, Y. I-98
Komar, W. III-1348
Kondo, K. I-416, I-420, I-424, I-428, I-502, III-1368
Kondoh, T. I-94, III-1138
König, R.W.T. I-54, I-254, II-826, III-1264
Konings, J.A. I-66, I-146, I-150, I-158
Konrad, C. I-408
Köppendörfer, W. I-326, I-330, II-680
Kornejew, P. III-1328
Korotkov, A.A. I-266
Koslowski, H.R. I-26, I-74
Kovalenko, Yu. V. I-446
Kovalev, N.F. III-1070
Kovrizhnykh, L.M. I-380
Krämer, M. III-1500
Krämer-Flecken, A. I-74, I-122
Krieger, K. II-834
Kritz, A. II-1004
Krivenski, V. III-1228, III-1324
Krlin, L. II-878
Kroegler, H. II-802
Kryska, L. III-1078
Kubo, S. I-432, II-1000
Kubota, T. II-528
Kugel, H.W. I-42, I-186, III-1094
Kühner, G. I-392, I-400
Kukushkin, A.S. II-714, II-766
Kumazawa, R. I-432, II-1000
Kupfer, K. III-1146
Küppers, J. III-1524
Kurata, M. II-922
Kurimoto, Y. I-416, I-424, I-428, I-502
Kurki-Suonio, T.K. II-664
Kuroda, T. II-940
Kurz, C. II-992
Kuteev, B.V. I-306, III-1364
Kuus, H. II-898, III-1054
Kuvshinov, B. N. II-588, II-592
La Marche, P.H. I-18
LaBombard, B. II-992
Lachambre, J.L. I-38, I-46, III-1086
Lackner, K. I-222, I-326, II-680, II-706, III-1308
Laing, E.W. III-1482
Lam, N.T. II-984
Lamalle, P. II-944

Landman, I. II-742
Lang, P.T. I-306, III-1364
Lang, R.S. I-306, III-1364
Langhoff, M. II-782
Langley, R.A. I-412
Lao, L. L. I-86, I-190, I-242, III-1146
Laporte, P. I-62
Lashkul, S. I. II-1028, III-1196
Lashmore-Davies, C.N II-652, III-1130
Laurent, L. I-110
Lauro-Taroni, L. I-102, III-1260
Laux, M. I-326, II-680, II-726
Laviron, C. I-118, II-862, III-1168
Lawson, K. I-54, I-102, I-194, I-206
Lazarus, E.A. I-14
Lebedev, S. V. I-498
LeBlanc, P.B. I-42, I-186, III-1094
Ledyankin, A.I. II-810, II-814
Lee, D.K. I-412
Lehnert, Bo III-1426
Lengyel, L.L. II-778, III-1364
Lennholm, M. II-944
Leonard, A.W. II-834
Levinton, F. I-186, I-354, III-1094
Li, G.X. I-470, II-866
Li, X.D. II-1016
Liang, R. I-310
Lie, Y.T. I-126
Lieder, G. II-722, II-730, II-774
Likin, K.M. I-412
Lin-Liu, Y.R. III-1118
Lingertat, H. I-2
Lingertat, J. II-698, II-786
Lipa, M. II-750
Lipschultz, B. II-992
Litaudon, X. I-278, III-1046, III-1054, III-1058
Litwin, C. I-482
Liu, C. II-608, III-1162
Liu, Y. II-1016
Lloyd, B. I-322, II-1012, III-1130
Lo Surdo, C. II-536
Loarer, T. II-754
Loarte, A. I-2, II-698, II-746
Lok, J. I-154
Lomas, P.J. I-314
Lomas, P.J. I-54, I-58, I-106, I-206
Lopes Cardozo, N.J. I-66, I-146, I-150, I-154, I-158, I-286, II-584, III-1248
Lotz, W. II-568
Loughlin, M. J. I-18, I-182, I-258, I-274
Lowry, C.G. I-2, I-314, II-746
Luce, T.C. III-1118, III-1146
Luckhardt, S. III-1094
Luke, T. II-520, II-992
Lundstrõm, I. III-1352
Lutterloh, C. III-1524
Lyadina, E. III-1304
Lyon, J.F. I-380, I-412
Lysoivan, A.I. II-980
Ma, C.H. I-412
Maafa, N. III-1244

Maas, A.C. I-254
Maassberg, H. I-158, II-568
Mabong, S. III-1444
Maddison, G.P. II-906, II-910
Maggi, C.F. II-746, II-826
Mahajan, S.M. III-1410, III-1474
Mai, H.H. III-1086
Mailloux, J. I-38, III-1086
Majeski, R.P. II-640, II-894, II-988
Makino, K. III-1106
Makowski, M. I-190, II-1024
Mandl, W. I-400, III-1276
Manfredi, G. III-1434
Manhood, S.J. I-322
Manickam, J. II-552, III-1094
Mank, G. I-74, I-130, I-238
Mansfield, D.K. I-82, I-294
Manso, M.E. III-1184, III-1188
Mantica, P. I-66, I-146, I-158
Mantsinen, M.J. II-684
Maraschek, M. III-1312
Marchiori, G. I-458
Marcus, F.B. I-54, I-102, I-206, I-254, I-262, I-274
Marmar, E. II-520, II-992
Marrelli, L. I-462, I-466
Martin, F. I-38, I-46, III-1086
Martin, G. I-278
Martin, P. I-462, I-466
Martin, R. I-22, I-138, I-490
Martin, Y. III-1224
Martinell, J.J. III-1098
Martines, E. I-458, I-462, I-466, II-762
Martinez-Val, J.M. III-1464
Martini, S. I-454, I-458, I-462
Martynov A. II-556
Mast, F. I-222, I-326, II-726, III-1308
Masuda, S. II-1000
Matsuo, K. I-416
Matsuoka, K. I-432, II-1000
Matsuoka, M. III-1138
Matsuura, H. III-1368
Mattioli, M. I-102, II-814, III-1280
Mauel, M.E. I-354
Maximov, V.V. I-442
May, M. II-992
Maynard, G. III-1444, III-1510, III-1514
Mazur, S. I-470, I-478
Mazurenko, A. II-992
Mazzitelli, G. II-802, II-818
Mazzucato, E. I-246
Mc Carthy, P.J. II-936
McCarthy, K.J. I-162, III-1296
McClements, K.G. II-652
McCormick, K. II-746, II-874, III-1268, III-1272
McCracken, G. M. II-992
McCune, D. I-82, I-182
McGuire, K. M. I-246
Medina, F. I-162, II-870
Medvedev, S. II-556
Mekler, K.I. I-498

Melnick, I.M. I-134, I-322
Melnikov, P.I. I-498
Mendanha Dias, J.A. III-1256
Mendonça, J.T. III-1150, III-1256
Ménicot, O. I-118
Méo, F. III-1086
Merkel, P. I-364
Mertens, V. I-6, I-306, I-326, I-330, II-680, II-726, II-936, III-1364
Messiaen, A. I-74, I-130, II-806, II-964, II-1020
Meyer, W. I-190
Michaud, D. I-38, III-1086, III-1090
Michelot, Y. II-1004, III-1050, III-1208
Micozzi, P. I-142
Miedema, H.S. III-1232
Migliuolo, S. I-10
Miley, G.H. III-1386
Millot, P. III-1168
Minardi, E. III-1418
Miroshnikov, I. V. III-1364
Mirus, K. I-482
Misguich, J. II-576
Mizuuchi, T. I-416, I-420, I-424, I-428, I-502, III-1368
Moeckli, R. II-548
Moiseenko, V.E. I-50, II-980
Möller, A. II-762, II-866, III-1352
Monier-Garbet, P. II-734, II-738, II-790, II-810, II-814, III-1042
Monk, R. I-2
Monticello, D. II-552
Montvai, A. II-584
Moreau, D. I-278, III-1046, III-1050, III-1054, III-1058
Moreira, A. III-1150
Mori, M. I-94, I-98
Morisaki, T. I-432, II-1000
Morita, S. I-432, II-1000
Morozov, D. Kh. II-596
Morris, A.W. I-214, I-218, I-318, I-322
Mueller, D. I-18
Mullier, B. I-74
Mulligan, W. III-1304
Murakami, M. I-82, I-412, II-988
Murakami, S. II-940
Muraoka, K. I-416
Murari, A. I-466
Mutoh, S. II-1000
Mutoh, T. II-1000
Myra, J.R. II-894
Nadler, J.H. III-1386
Nagasaka, K. III-1102
Nagasaki, K. I-416, I-420, I-424, I-428, I-502, III-1368
Nagashima T. II-1024
Naito, O. III-1138
Nakajima, N. I-392, II-940
Nakamura, K. III-1106
Nakamura, Y. I-416, I-424
Nakasuga, M. I-416, III-1368
Nakayama, T. I-502
Napiontek, B. II-722, II-726
Nassi, M. I-10
Naujoks, D. II-722, II-730
Nave, M.F.F. I-202, I-206

Navratil, G.A.	I-354
Nazikian, R.	I-246
Nebel, R.A.	III-1386
Neu, R.	I-6, II-730, II-774
Neuhauser, J.	I-222, I-306, I-326, II-680, II-706, II-710, II-726, II-842, II-846
Nguyen, F.	II-734, II-750, II-944
Nicolai, A.	I-238
Niedermeyer, H.	I-388, I-400, II-874
Niemczewski, A.	II-992
Nieswand, C.	III-1224
Nilsson, J.O.	III-1520
Nishimura, K.	I-432, II-1000
Nishitani, T.	I-94, I-98
Nocentini, A.	II-902
Nordlund, P.	I-470, I-478
Noterdaeme, J.-M.	II-838, II-842
Novik, K.M.	III-1200, III-1240
Nührenberg, J.	I-364
Nunes, I.	III-1188
O'Brien, D.P.	I-206, I-346, II-746
O'Brien, M. R.	II-636, II-1012, III-1122, III-1130
O'Connell, R.	I-214, I-322
O'Mullane, M.J.	I-134
O'Shea, P.	II-992
Obiki, T.	I-416, I-420, I-424, I-428, I-502, III-1368
Ochando, M.	I-162, II-870
Ödblom, A.	II-644
Ogasawara, M.	III-1102
Ogata, K.	I-420, I-502
Ohlendorf, W.	I-384
Oka, Y.	II-940
Okabayashi, M.	I-186, III-1094
Okada, H.	I-416, I-420, I-424, I-428, I-502, III-1368
Okajima, S.	I-432
Okamoto, M.	II-940
Okamura, S.	I-432, II-1000
Ongena, J.	I-74, I-130, II-964, II-1020
Ono, M.	I-42, I-186, II-972, III-1094
Oomens, A.A.M.	I-150, I-154, I-286, III-1204
Osborne, T.H.	I-14, I-86
Osipenko, M.V.	II-600, II-886
Ott, W.	I-392
Ottaviani, M.	II-532
Owens, D.K.	I-18
Ozaki, T.	I-432, II-1000
Ozeki, T.	I-98
Paccagnella, R.	II-536, II-572
Pacher, G.W.	II-914, III-1062
Pacher, H.D.	II-914
Painter, S.L.	I-380
Paoletti, F.	II-972, III-1094
Paquin, L.	III-1122
Parail, V. V.	I-106, I-234, I-350, III-1126
Park, H. K.	I-82
Park, W.	II-628
Parlange, F.	I-34
Pasch, E.	III-1328
Pasqualotto,	I-466
Patel, A.	I-134, I-322
Pättikangas, T.	III-1082, III-1434, III-1452

Paul, S.F. I-42, I-186, III-1094
Paume, M. I-110, III-1172
Pautasso, G. I-222
Pavlo, P. II-604, III-1078, III-1204
Payan, J. II-862
Peacock, N.J. I-134, I-322
Pearson, D. I-198
Pecquet, A.-L. I-210, I-298, III-1280
Pedrosa, M.A. I-162, II-870
Pegoraro, F. II-588, II-592, III-1456
Pégourié, B. I-298
Pelletier, G. II-660
Peng, X. II-608, III-1162
Penningsfeld, F.P. I-392, I-408, II-932
Penso, A. III-1374
Perematko, A.O. III-1196
Pereverzev, G.V. III-1126
Petelin, M.I. III-1070
Peters, M. I-66, I-146, I-158
Peterson, B.J. I-416
Petrie, T.W. II-834
Petty, C.C. III-1118
Peysson, Y. I-278, III-1042, III-1046, III-1050, III-1054, III-1058
Pfirsch, D. III-1390, III-1398
Philipps, V. II-1020
Philips, C.K. I-354
Phillips, C.K. II-988
Phillips, P. E. I-78, I-174, I-178
Pickalov, V.V. III-1316
Piera, M. III-1464
Pieroni, L. II-802, II-818
Pietrzyk, Z.A. III-1252
Pijper, F.J. I-154, III-1248
Piliya, A. D. III-1240
Pinches, S.D. II-620
Pinsker, R.I. III-1118
Pinsonneault, D. I-46, III-1086
Piovan, R. I-458, I-462
Pitcher, C.S. II-680, II-722
Piterskii, V.V. II-886
Platzer, P. III-1268
Pletzer, A. II-552
Plyusnin, V.V. II-980
Pocheau, C. III-1050
Pochelon, A. II-1004
Pod'minogin, A.A. I-442
Podushnikova, K. A. II-1028
Pogutse, O. II-882
Polevoy, A.R. I-138, II-600
Politzer, P.A. I-190, III-1146
Pomaro, N. I-458, III-1352
Popel, S.I. III-1066, III-1402, III-1406
Porcelli, F. II-532, II-612, II-648
Porkolab, M. II-854, II-992, III-1118
Porter, G.D. I-190
Poschenrieder, W. II-722, II-774
Pospieszczyk, A. II-798, II-1020
Post-Zwicker, A.P. I-42, I-186, III-1094
Postupaev, V.V. I-498
Prager, S. I-482

Prater, R. III-1118
Preinhaelter, J. III-1074, III-1078
Prentice, R. III-1168, III-1184
Puiatti, M.E. I-462, I-466
Pütz, Th. II-758
Qin, J. II-870
Qualls, A.L. I-412
Quemeneur, A. I-118, II-862
Rachlew-Källne, E. I-474
Radford, G. II-694
Radtke, R. II-722, II-730
Ram, A.K. III-1134, III-1460
Raman, R. I-46
Ramsey, A.T. I-18, I-82
Ran, L.B. I-342
Rapozo, C. da C. I-450
Rasmussen, D.A. I-412, II-988, II-1000
Rau, F. I-368, I-372, I-392, I-400
Reardon, J. II-992
Redi, M. I-290
Reichle, R. II-746, II-786
Reiter, D. II-676, II-706, II-758, II-842, II-846
Rem, J. II-592
Remsen, D. II-1024
Renner, H. I-368, II-750
Rey, G. III-1054
Reznichenko, P.V. III-1364
Ribeiro, C. I-22, I-138
Riccardi, C. III-1236, III-1374, III-1414
Rice, B. I-190, I-242
Rice, J. II-520, II-992
Richard, N. I-38, I-46, III-1086
Richards, B. I-174
Richards, R.K. I-412
Riedel, K.S. II-668
Rigato, V. II-762
Righi, E. I-314, II-944, II-948
Rimini, F. I-314, II-944, III-1122, III-1126
Ringler, H. I-392, I-400
Roach, C. I-138
Robinson, D.C. I-322
Robouch, B.V. I-282, III-1344
Rodriguez-Rodrigo, L I-162, I-166
Rogers, B. I-10
Rogers, J.H. II-988
Rogister, A. I-238
Rogozin, A.I. I-442
Röhr, H. II-680
Rommers, J.H. I-230, III-1204
Rooney, C.E. III-1482
Roquemore, A.L. I-182
Rosatelli, C. III-1360
Rosmej, F.B. III-1292
Rosmej, O.N. III-1292
Roth, J. II-722, II-770
Rowan, W.L. I-78, I-178
Rozhanski, V. I-302, II-516
Rubel, M. II-1020
Rudakov, D.L. I-436
Rudyj, A. II-874

Runov, A.M. II-766
Rusbridge, M.G. I-490, I-494, III-1378
Rusbüldt, D. I-126
Ryter, F. I-326, I-330, I-334, II-850, II-936
Sabbagh, S.A. I-354
Sabot, R. I-30, I-350
Sadler, G. I-206, I-262, I-270, I-274, III-1340
Sadowski, Marek III-1320
Safronov, V.M. II-830
Sager, G.T. II-834
Saghiri, A.A. III-1344
Sahara, A. I-502
Saibene, G. I-2, I-314, II-746
Saito, T. II-922
Sakakibara, S. I-432, II-1000
Sakakita, H. I-310
Sakamoto, K. III-1368
Sakamoto, M. I-310, III-1106
Sakurai, S. II-890
Salomaa, R.R.E. II-684, III-1082, III-1434
Saltmarsh, M.J. I-412
Samm, U. I-126, I-130, II-798, II-806
Sanchez, E. I-404
Sanchez, J. I-404, II-870, III-1176, III-1180
Sandeman, J. III-1378
Sano, F. I-416, I-420, I-424, I-428, I-502, III-1368
Saoutic, B. I-298, II-660, II-790, II-898, II-956, III-1054
Sardei, F. I-388
Sarff, J. I-482
Sarkissian, A. I-38, III-1086
Sarksyan, K.A. I-412
Sarparanta, K. III-1240
Sartori, R. I-54, I-314
Sasao, M. I-294, II-1000
Sato, K. I-310
Sato, M. I-416
Satsangi, A.J. III-1386
Sattin, F. I-466
Sattler, S. I-408, III-1220
Sauter, O. I-86, I-242, II-1004
Sauthoff, N. I-186, III-1094
Savkin, V. Ya. I-446
Sawatzky, B. I-46
Scanlan, J.V. I-214, I-322
Scarin, P. I-466
Schachter, J. II-992
Schaffer, M.J. II-834
Scharer, J. II-984
Schenk, A. III-1524
Schep, T.J. II-588, II-592
Scherzer, B.M.U. II-782
Schiavi, A. I-462, I-466
Schilling, G. II-988
Schivell, J. I-82, I-290
Schlüter, A. I-360
Schmidt, H. III-1320
Schmitz, L. III-1094
Schneider, R. II-680, II-706, II-842, II-846
Schneider, U. I-388
Schneider, W. I-222, I-330, II-718

Schokker, B.C. I-286
Schönmann, K. I-6
Schram, D. C. III-1316
Schroder, K. I-78
Schüller, F.C. I-154, I-230, I-286
Schultz, S.D. III-1134
Schunke, B. I-54, II-668
Schweer, B. II-798, II-1020
Schweinzer, J. III-1268, III-1272
Schwenn, U. I-364
Scott, B.D. II-560, II-564
Scott, S.D. I-82, I-290, I-354
Segui, J.-L. II-1004, III-1050, III-1208
Seidel, J. III-1288
Seidel, U. II-710
Seki, M. III-1138
Seki, T. I-432, II-1000
Selenin, V.L. III-1200
Sen, A.K. I-174
Senju, T. III-1368
Seraydarian, R.P. II-858
Sergeev, V.Yu III-1364
Serianni, G. I-454, I-462, I-466, II-762, III-1352
Serra, F. III-1184, III-1188
Sesnic, S. I-186, III-1094
Shang, Z.Y. II-1016
Sharapov, S. II-612, II-616, II-620
Sharp, L.E. I-436
Shats, M. I-412, I-436
Shcheglov, M.A. I-498
Shichovtsev, I.V. I-442
Shimbo, F. II-1000
Shirai, H. I-98, I-502
Shkarofsky, I. III-1082, III-1086, III-1090, III-1434
Shorikov, V. Yu. III-1196
Shoucri, M. III-1082, III-1086, III-1090, III-1430, III-1434
Shukla, P.K. III-1470
Sibley, A. II-944
Silipā, S.K. II-664, III-1158, III-1240
Silva, A. III-1184, III-1188
Silva, F. III-1188
Simonchik, L.V. III-1200
Simonini, R. II-694, II-698, II-746
Simpkins, J.E. I-412
Simpson, P.R. I-322
Sindoni, E. III-1236, III-1374, III-1414
Singleton, M.A. I-134, I-322
Sips, A.C.C. I-202, III-1126
Sips, G. I-314
Skarka, V. III-1410, III-1474
Skiff, F.N. III-1382
Skinner, C.H. I-82
Skladnik-Sadowska, E III-1320, III-1348
Smeulders, P. I-54, I-102, I-106, I-206
Smirnov, A. I. III-1070
Smith, G.R. II-1004
Snipes, J. A. II-992
Sokolov, V.G. I-446
Solano, E.R. I-78
Soldatov, S.V. II-886, III-1192

Söldner, F.X. I-234, III-1126
Soltwisch, H. I-26
Sonato, P. I-458, II-754
Sosenko, P.P. III-1244
Sovinec, C. I-482
Spathis, P.N. II-778
Spence, J. II-694, II-746
Speth, E. II-936
Spetz, A. III-1352
Spineanu, F. II-576
Spong, D.A. I-290, I-408
Springmann, E.M. I-106, III-1126
Squire, J.P. III-1118
St John, H. I-190
St-Onge, M. III-1086
Stäbler, A. I-326, I-330, II-936
Staebler, G.M. II-834
Stallard, B.W. I-190
Stammers, K. I-322
Stamp, M. I-2, II-698, II-746, II-826
Stangeby, P.C. II-698, II-906
Stanojevic, M. III-1332
Stansfield, B. I-38, I-46, III-1086
Start, D.F.H. I-314, II-612, II-944, II-948, II-952, III-1110, III-1122
Stauton-Lambert, S. III-1304
Steiger, A. III-1288
Stek, P. II-992
Stenflo, L. III-1470
Stepanov, A.Yu. II-1028, III-1196
Steuer, K.-H. II-680, II-774
Stevens, J. II-988
Stöckel, J. II-878, III-1078
Stoneking, M. I-482
Storek, D.J. I-78
Stork, D. I-2, I-54, I-206, I-314, II-746
Strachan, J.D. I-82, I-182, I-290
Strait, E.J. I-86, I-190, I-242
Strasser, V.O. III-1438
Streibl, B. II-706
Stroth, U. I-158
Strumberger, E. II-702
Stubberfield, P. I-58, I-106, I-206, I-258, I-346
Stupishin, N.V. I-442
Sudo, S. I-416
Sugihara, M. II-714
Sugiyama, L.E. II-520
Summers, H. P. I-486, II-826
Sun, Y. III-1094
Sund, R.S. II-984
Sünder, D. II-794
Sundgren, H. III-1352
Sushkov, A.V. II-886
Suttrop, W. II-838, II-850
Suvorov, E.V. III-1070
Suzuki, Y. I-416, I-424, I-428, I-502
Svensson, J. III-1264
Svoboda, V. II-878
Swain, D.W. III-1118
Sychev, V.N. I-170
Sykes, A. I-22, I-138

Synakowski, E.J.	I-82, I-182, I-354
Szigeti, J.	III-1336
Tabares, F.	I-162, II-870
Tafalla, D.	I-162, II-870
Taguchi, M.	III-1142
Takada, H.	I-428, I-502
Takahashi, C.	I-432, II-1000
Takahashi, H.	I-186, III-1094
Takahashi, T.	II-922
Takamura, S.	II-890
Takase, Y.	II-992
Takeiri, Y.	II-940
Talvard, M.	III-1050, III-1094
Tamano, T.	II-922
Tammen, H.F.	II-964
Tanabe, T.	II-1020
Tanaka, K.	I-432, II-1000
Tani, K.	II-996
Tanzi, C.P.	I-226, I-230
Tarditi, A.	III-1360
Taroni, A.	I-54, I-106, II-694, II-698, II-746, III-1126
Taskaev, S.Yu.	I-446
Tatematsu, Y.	II-922
Taylor, G.	I-82, I-354, II-988
Taylor, J.B.	II-580
Taylor, T. S.	I-86, I-242
Telesca, G.	II-806
Tendler, M.	II-516
Terreault, B.	III-1086
Terry, J.	II-992
Theimer, G.	II-874
Thomas, C.E.	II-660, II-898
Thomas, J.	I-46
Thomas, P.R.	I-54, I-58, I-206, I-314
Thompson, D.G.	III-1304
Thompson, S.J.	I-86, I-190, I-242
Thomsen, K.	I-54, I-106, I-206, I-314
Thouvenin, D.	III-1050
Throumoulopoulos, G.	III-1390
Tighe, W.	I-42, I-186, III-1094
Tinios, G.	II-992
Tobin, S.J.	II-810, II-898, III-1300
Tobita, K.	I-290
Toda, S.	II-528
Todd, T. N.	I-322
Tohshi, K.	III-1368
Toi, K.	I-432
Tokar, M.Z.	I-126, I-238
Tomas, J.	I-138, I-322
Toporkov, D.A.	II-830
Tramontin, L.	I-462, II-762, III-1352
Tran, M.Q.	II-1004
Trevisan, F.	I-458
Tribaldos, V.	III-1228
Tribeche, M.	II-1032
Troyon, F.	II-548, II-556
Trubnikov, B.A.	III-1486
Truc, A.	I-118, II-862
Tsois, N.	II-874
Tsumori, K.	I-432, II-940

Tu, K. III-1510
Tubbing, B.J.D. I-314
Tudisco, O. I-70, I-142
Tumlos, R. I-436
Turlur, S. III-1054
Turnbull, A.D. I-86, I-190, I-242
Turner, M.F. I-138, II-512
Tynan, G. III-1094
Uchimoto, E. I-482
Uckan, T. I-174
Uddholm, P. III-1378
Ueda, Y. II-1020
Uglum, J.R. I-78, I-174
Ulrich, M. II-710
Unterberg, B. I-130, II-798, II-806
Urquijo, G. II-688
Ushigusa, K. III-1138
Vaessen, P.H.M. III-1256
Vahala, G. II-604
Vahala, L. II-604
Valeo, E.J. II-640, III-1094
Valisa, M. I-466
Vallet, J.-C. II-734, II-738, II-790, II-814, III-1042
Valovic, M. I-134, I-318, I-322
Valter, J. II-734
Van Belle, P. I-262, I-270, III-1340
Van de Pol, M.J. III-1204
Van Eester, D. II-964
Van Gelder, J.F.M. III-1232
Van Houtte, D. I-114
van Milligen, B.Ph. I-404, III-1296, III-1356
Van Nieuwenhove, R. I-238, I-338, II-798, II-976, II-1020
Van Oost, G. I-74, I-130, I-238, I-338, II-798, II-976, II-1020
Van Wassenhove, G. I-74, I-130, II-964, II-1020
Vanden Eijnden, E. II-576
Vander Sluis, K.L. I-412
Varandas, C.A.F. III-1150
Varela, P. III-1184, III-1188
Varias, A. I-376
Vega, J. I-162, III-1296
Verhaag, G.C.H.M. III-1248
Vershkov, V.A. II-886, III-1192
Veselova, I. I-302
Villard, L. II-556
Vlad, M. II-576
Vladimirov, S.V. III-1402, III-1494, III-1504
Vlases, G. II-746
Vlasov, V. P. III-1486
Voitsekhovitch, I.A. III-1098
Vollmer, O. I-326, I-330, II-936
Von Goeler, S. III-1094
von Hellermann, M. I-102, I-254, I-314, II-746, III-1264
Voorhees, D. I-18
Voropaev, S.G. I-498
Voskoboynikov, S. I-302
Voslamber, D. III-1284, III-1288
Vshivkov, V.A. III-1490
Wada, M. II-1020
Wade, T. II-944
Waidmann, G. I-122, I-230, II-964

Wakatani, M.	I-416, I-424
Walsh, M.J.	I-22, I-138
Walter, H.	I-400
Walter, J.	II-898
Wang, E.Y.	I-342
Wang, H.	II-576
Ward, D.	I-314
Ward, D.J.	II-544
Warrick, C.D.	II-948, II-1012, III-1110, III-1130
Watari, T.	I-432, II-1000
Watkins, N.	I-262, I-274
Watts, C.	I-178
Weber, S.	II-694
Wegrowe, J.-G.	III-1062
Weinlich, M.	I-326, II-710, II-722, II-726
Welcht, B.	II-992
Weller, A.	I-372, I-396, I-408
Wenzel, U.	II-726, II-730
Wesley, J.	II-524
Wesson, J.	I-206
West, W. P.	II-834
Weynants, R.	I-338, II-798
Whyte, D.	II-834
Wienhold, P.	II-1020
Wijnands, T.J.	I-34
Wilgen, J.B.	I-412, III-1180
Wilson, D.J.	III-1304
Wilson, H.R.	I-22, I-138, II-580
Wilson, J.R.	II-988
Winslow, D.	I-174
Winter, B.	III-1524
Winter, H.P.	III-1272
Wobig, H.	I-368, I-400, II-1008
Wolf, H.	II-718
Wolfe, S.	II-520, II-992
Wolle, B.	I-282, III-1344
Wong, K.L.	I-246, II-988
Wood, R.D.	II-834
Wootton, A.J.	I-174
Wroblewski, D.	I-190, I-242, III-1146
Wurden, G.A.	I-294
Würz, H.	II-742, II-830
Wutte, D.	II-722, III-1268
Xu, D.M.	II-1016
Xu, J.	I-432, II-1000
Xu, T.C.	II-1016
Xue, S.W.	II-1016
Yaguchi, K.	III-1368
Yamada, H.	I-432, II-1000, II-1000
Yamada, I.	I-432, II-1000
Yamagajo, T.	III-1106
Yamaguchi, H.	II-528
Yang, J.W.	I-342
Yang, S.K.	I-342
Yao, L.H.	II-1016
Yoshimura, Y.	II-922
Young, K. M.	I-290
Yu, M.Y.	III-1504
Zacek, F.	III-1078
Zaitsev, F.S.	II-636

Zandolin, S. II-762
Zanino, R. II-822
Zarnstorff, M. C. I-82, I-182, I-354
Zastrow, K.-D. I-470, I-474
Zaveriaev, V. I-290
Zebrowski, J. III-1320
Zehrfeld, H.-P. II-706
Zerguini, T.H. II-1032
Zhang, Y.-Z. II-902
Zhdanov, S.K. III-1486
Zheng, Y.Z. I-342
Zhitlukhin, A.M. II-830
Zhong, G.W. I-342
Zhuravlev, V. II-870, III-1176, III-1180
Zielinski, J.J. I-412
Zohm, H. I-306, I-326, I-330, I-396, II-632, II-842, II-846, II-850, II-936, III-1188, III-1312
Zoler, D. III-1536
Zoletnik, S. II-722, II-874, III-1268
Zolfaghari, A. I-186
Zonca, F. II-624
Zou, X.L. I-110
Zurro, B. I-162, III-1296
Zushi, H. I-416, I-420, I-424, I-428, I-502, III-1368
Zuzak, W. I-38, I-46, III-1086
Zweben, S. J. I-82, I-246, I-290, I-354

Achevé d'imprimer en Novembre 1994
sur les presses de l'imprimerie Esmenjaud à Gardanne

Dépôt légal 3ème trimestre 1994